Natural Resources Canada | Ressources naturelles Canada

GEOLOGICAL SURVEY OF CANADA
OPEN FILE 8549

Targeted Geoscience Initiative: 2018 report of activities

N. Rogers (ed.)

2019

Canada



GEOLOGICAL SURVEY OF CANADA
OPEN FILE 8549

Targeted Geoscience Initiative: 2018 report of activities

N. Rogers (ed.)

2019

© Her Majesty the Queen in Right of Canada, as represented by the Minister of Natural Resources, 2019

Information contained in this publication or product may be reproduced, in part or in whole, and by any means, for personal or public non-commercial purposes, without charge or further permission, unless otherwise specified.
You are asked to:

- exercise due diligence in ensuring the accuracy of the materials reproduced;
- indicate the complete title of the materials reproduced, and the name of the author organization; and
- indicate that the reproduction is a copy of an official work that is published by Natural Resources Canada (NRCan) and that the reproduction has not been produced in affiliation with, or with the endorsement of, NRCan.

Commercial reproduction and distribution is prohibited except with written permission from NRCan. For more information, contact NRCan at nrcan.copyrightdroitdauteur.rncan@canada.ca.

Permanent link: https://doi.org/10.4095/313623

This publication is available for free download through GEOSCAN (http://geoscan.nrcan.gc.ca/).

Recommended citation
Rogers, N., (ed.) 2019. Targeted Geoscience Initiative: 2018 report of activities; Geological Survey of Canada, Open File 8549, 448 p. https://doi.org/10.4095/313623

Publications in this series have not been edited; they are released as submitted by the author.

Targeted Geoscience Initiative: 2018 report of activities

Edited and compiled by
Neil Rogers

Foreword – Targeted Geoscience Initiative: 2018 report of activities
N. Rogers 7

Gold project:
Subproject 1: System controls on gold through time and space (source to trap)

Geological setting and mineralization styles of the Sunday Lake and Lower Detour 'gold trends', northwestern Abitibi greenstone belt, Ontario and Quebec
S. Castonguay, B. Dubé, P. Mercier-Langevin and N. Wodicka 9

Lithological and structural controls on the nature and distribution of gold at the LaRonde Zone 5 project, Doyon-Bousquet-LaRonde gold camp, Abitibi, Quebec
E. Boily-Auclair, P. Mercier-Langevin, P.-S. Ross and D. Pitre 23

Characteristics of diagenetic and epigenetic sulphides in deformed and metamorphosed Archean carbonaceous metasedimentary rocks of the Timmins-Matheson corridor: establishing a framework for fingerprinting ore-forming processes in shear zone-hosted orogenic gold systems
J.-L. Pilote, S.E. Jackson, P. Mercier-Langevin, B. Dubé and D. Rhys 33

Mantle metal mobility: preliminary gold and platinum group element geochemical results
C.J.M. Lawley, S.E. Jackson, D.C. Petts, D. Savard, D.G. Pearson, S. Zhang, A. Zagorevski and B.A. Kjarsgaard 43

Gold project:
Subproject 2: Tectonic influences on gold deposits (tectonic drivers and conduits)

Superimposed auriferous structural events along the Llewellyn-Tally Ho deformation corridor in southern Yukon and northwest British Columbia
L. Ootes, S. Castonguay, R. Friedman and F. Devine 49

Lithological and structural setting of structurally controlled gold mineralization in the Wilding Lake region, central Newfoundland belt
I.W. Honsberger, W. Bleeker, H.A.I. Sandeman and D.T.W. Evans 59

Paleoproterozoic gold and its tectonic triggers and traps
C.J.M. Lawley, W.J. Davis, S.E. Jackson, D.C. Petts, E. Yang, S. Zhang, D. Selby, A.R. O'Connor and D.A. Schneider 71

Structural and lithological controls on the nature and distribution of gold at the Tiriganiaq deposit, Meliadine district, Rankin Inlet greenstone belt, Nunavut
B. St.Pierre, P. Mercier-Langevin, M. Simard, O. Côté-Mantha, M. Malo and G. Servelle 77

Geological setting of the 5.2 Moz Au Amaruq banded iron formation-hosted gold deposit, Churchill Province, Nunavut
M. Valette, S. De Souza, P. Mercier-Langevin, V.J. McNicoll, N. Wodicka, R.A. Creaser, O. Côté-Mantha and M. Simard 83

Macroscopic control on Carlin-type gold mineralization in north-central Yukon
N. Pinet and P.J. Sack 89

Volcanic- and sedimentary-hosted base metal mineralization project:
Subproject 1: Seafloor ore deposition through space and time

Reconnaissance molybdenum isotope study of vent-distal SEDEX zinc-lead mineralization and host rocks in the Howard's Pass district, Selwyn Basin, Yukon: potential application to paleoredox determinations
J.M. Peter, M.G. Gadd, D. Layton-Matthews and A. Voinot 105

Application of pyrite chemistry to recognize a distal expression of hydrothermal activity in the MacMillan Pass SEDEX district, Yukon
C. Leighton, D. Layton-Matthews, J.M. Peter and M.G. Gadd 125

Toward the application of molybdenum and thallium isotopes as indicators of paleoredox conditions and genesis of hyper-enriched black shale (HEBS) deposits, Peel River, Yukon
I. Crawford, D. Layton-Matthews, J.M. Peter, M.G. Gadd and A. Voinot 139

Lithogeochemical and sulphur isotope indicators of environment of formation and genesis of the Moss hyper-enriched black shale showing, Yukon
M.G. Gadd, J.M. Peter, T.A. Fraser and D. Layton-Matthews 163

Metal transport by liquid hydrocarbons: Evidence from metalliferous shale and pyrobitumen, Yukon
K.M. Henderson, A.E. Williams-Jones and J.R. Clark 179

Volcanic- and sedimentary-hosted base metal mineralization project: Subproject 2: Base metal sources and mineralizing processes

Fluid inclusion LA-ICP-MS and whole rock geochemical investigation of possible magmatic contributions to the giant Windy Craggy Besshi-type VMS deposit
M.A. Schmidt, M.I. Leybourne, J.M. Peter, D. Petts and D. Layton-Mathews 189

Preliminary carbon and oxygen isotope analyses of hydrothermal carbonates from Mississippi Valley-type and REE-F-Ba deposits of the southern Canadian Rocky Mountains – a comparison
S. Paradis and G.J. Simandl 205

Three-dimensional forward modelling and inversion of magnetotelluric data using unstructured meshes for understanding realistic geological systems: method development, algorithms and model construction for the Lalor deposit, Manitoba
S.M. Ansari, E.M. Schetselaar and J.A. Craven 217

Porphyry-style mineral systems project: Subproject 1: Temporal and spatial controls on porphyry-style mineralization

Analysis of wireline logs and vertical seismic profiling data acquired with fibre-optic cable at the copper-gold New Afton porphyry deposit, British Columbia
G. Bellefleur, E.M. Schetselaar, D. Wade, D. White, R. Enkin and D.R. Schmitt 235

Petrogenesis and associated mineralization of Acadian related granitoids in New Brunswick
Z. Azadbakht, N. Rogers, D.R. Lentz and C.R.M. McFarlane 243

The relationship between the Ganderian Aspy and Bras d'Or terranes explored using Devonian plutonic rocks, Cape Breton, Nova Scotia
C. Grant, D.B. Archibald, D.A. Kellett and J.M. Cottle 279

Contrasts in petrological features between Silurian-Devonian plutons in the Mira and Aspy terranes of Cape Breton Island, Nova Scotia: implications for porphyry-style mineralization
A. Moning, S.M. Barr, C.E. White and D. van Rooyen 287

Reactivation of the Eastern Highlands Shear Zone, Cape Breton Island, Appalachian Orogen
N. Piette-Lauzière, R. Graziani, K.P. Larson and D.A. Kellett 295

SHRIMP U-Pb zircon dating of the South Mountain Batholith, Nova Scotia: Timing and duration of crystallization and evidence for inheritance
L. Bickerton, D.J. Kontak, I.M. Samson, J.B. Murphy and D.A. Kellett 307

Porphyry-style mineral systems project: Subproject 3: Mineral markers of porphyry processes

Discovering the next generation of copper porphyry deposits using mineral markers
A. Plouffe, I.M. Kjarsgaard, C.H. Kobylinski, K. Hattori, D.C. Petts, K.E. Venance and T. Ferbey 321

Mineral and geochemical signatures of porphyry copper mineralization: work in progress for the Casino Cu-Au-Mo-Ag porphyry deposit, Yukon
M.B. McClenaghan, M.W. McCurdy, R.G. Garrett, C.E. Beckett-Brown, M.E. Leybourne, S.G. Casselman and P. Pelchat 333

Unravelling tourmaline in mineralized porphyry systems: assessment as a valid indicator mineral
C.E. Beckett-Brown, A.M. McDonald and M.B. McClenaghan 345

Uranium-rich ore systems project:
Subproject 1: Uranium fluid pathways

Origin of boron-rich fluids in the formation of unconformity associated deposits of the Sibley Basin
C.J. Kelly, W.J. Davis, E.G. Potter, R. Metsaranta and M. Puumala 353

Quantifying fertile alteration in the Patterson Lake corridor, Saskatchewan, through visible-near infrared-shortwave infrared spectroscopy
J.W. Powell, E.G. Potter, V. Tschirhart, J.B. Percival, S. Mount, B. McEwan, R. Ashley and K. Wheatley 365

Uranium-rich ore systems project:
Subproject 2: Uranium-rich deep metasomatic processes

Geochemistry of U±Cu±Mo±V mineralization, Central Mineral Belt, Labrador: differentiating between mineralization styles using a principal component analysis approach
P. Acosta-Góngora, E.G. Potter, L. Corriveau, C.J.M. Lawley and G.W. Sparkes 381

Ni-Cr-PGE ore systems project:
Subproject 1: System scale and deposit scale controls on Ni-Cu-PGE mineralization in cratonic areas and their margins

Volcanology, geochemistry and petrogenesis of the Expo-Raglan magmatic system in the eastern Cape Smith Belt, Nunavik, northern Quebec
D.J. McKevitt, C.M. Lesher and M.G. Houlé 393

Ni-Cu-PGE potential of the Nipissing sills as part of the ca. 2.2 Ga Ungava large igneous province
S. Davey, W. Bleeker, S. Kamo, D. Davis, M. Easton and R.H. Sutcliffe 403

Characteristics of Ni-Cu-PGE sulphide mineralization within the 1.1 Ga Midcontinent Rift
J.Smith, W. Bleeker, D.A. Liikane, M. Hamilton, R. Cundari and P. Hollings 421

Ni-Cr-PGE ore systems project:
Subproject 2: Magmatic architecture of Cr-bearing ore systems

Overview of chromium, Fe-Ti-V and Ni-Cu-PGE metal endowment of the Superior Province
M.G. Houlé, C.M. Lesher and A.-A. Sappin 433

Architecture of magmatic conduits in chromium-(PGE) and Ni-Cu-(PGE) ore systems in Superior Province: example from the 'Ring of Fire' region, Ontario
M.G. Houlé, C.M. Lesher, R.T. Metsaranta and A.-A. Sappin 441

Foreword – Targeted Geoscience Initiative: 2018 report of activities

N. Rogers

Geological Survey of Canada, 601 Booth Street, Ottawa, Ontario K1A 0E8

The Targeted Geoscience Initiative (TGI) is a Government of Canada led geoscience research program directed towards advancing geoscience knowledge in support of more effective mineral exploration. To achieve this goal, TGI is focused on resolving knowledge gaps on the geological processes responsible for liberating, transporting and depositing metals. A secondary objective of TGI is the mentoring and training of students to become the next generation of highly qualified personnel available to the mineral exploration industry.

The Targeted Geoscience Initiative employs a thematic, 'ore system' approach to its research. Ore systems encompass a range of mineral deposits that share common genetic and geologic characteristics. Deposits within an ore system can differ in style, position in the crust and timing, but share common causative ore-forming processes and controlling parameters. For the TGI program, four aspects of the ore system concept are more specifically addressed, namely: what terrane, region or geological/tectonic setting to look in; where to look in a specific terrane, region or geological/tectonic setting; how to vector towards mineralized rocks; and detection methods.

The thematic, ore systems approach to research program design enables TGI to conduct its research on the best-suited areas, districts and deposits from across Canada to support, develop and test next generational geoscience knowledge. The program is divided into five projects representing Canada's major mineral systems: namely gold, Ni-Cr-PGE, porphyry-style mineralization, uranium and volcanic- and sedimentary-hosted base metal. Each of the ore system projects are split into series of activities focused on resolving specific problems by integrating data and studies from multiple sites across Canada. Herein, we present interim results and interpretations from a selection of the research activities currently being conducted under the auspices of TGI.

Corresponding author: Neil Rogers (neil.rogers@canada.ca)

Rogers, N., 2019. Foreword – Targeted Geoscience Initiative: 2018 report of activities; *in* Targeted Geoscience Initiative: 2018 report of activities, (ed.) N. Rogers; Geological Survey of Canada, Open File 8549, p. 7–8. https://doi.org/10.4095/313624

Geological setting and mineralization styles of the Sunday Lake and Lower Detour 'gold trends', northwestern Abitibi greenstone belt, Ontario and Quebec

S. Castonguay[1], B. Dubé[1], P. Mercier-Langevin[1] and N. Wodicka[2]

[1]*Geological Survey of Canada, 490 rue de la Couronne, Québec, Quebec G1K 9A9*
[2]*Geological Survey of Canada, 601 Booth Street, Ottawa, Ontario K1A 0E8*

Abstract

The Detour Lake gold mine (approximately 25 Moz Au) and Lower Detour zones (e.g. Zone 58N; 534 000 oz Au) are in the northwestern part of the Abitibi greenstone belt in Ontario. They are spatially associated with the Sunday Lake and Lower Detour deformation zones that delineate gold trends extending eastward into Quebec, where gold mineralized zones, such as the Vortex and Martiniere – Bug Lake deposits, also occur. Gold is associated with quartz -carbonate±tourmaline veins and/or silicified zones and disseminated to locally semi-massive sulphides in veins or sericitized, chloritized, or biotitized wall rocks. These structurally controlled auriferous zones are hosted in volcanic sequences of the 2734 to 2724 Ma Deloro assemblage and in porphyritic rocks near faulted contacts with Porcupine-like turbidite of the less than 2.70 Ga Caopatina assemblage. Strained Timiskaming-like polygenic conglomerate locally delineates the regional-scale deformation zones. These relationships are analogous to parts of the southern Abitibi belt, such as in Timmins – Porcupine or Val d'Or areas. Geochemical and geochronological analyses are underway to document the lithotectonic setting and alteration associated with gold mineralization and to better constrain the timing of deformation, magmatism, sedimentation, and mineralization along the Sunday Lake and Lower Detour deformation zones.

.

Introduction

The principal first-order metallotects of Archean orogenic quartz-carbonate vein gold deposits, such as regional-scale long-lived fault zones, synorogenic polygenic conglomerate, intermediate to felsic intrusions, tholeiitic and komatiitic basalt, and extensive iron-carbonate alteration, are documented in the well-studied southern Abitibi greenstone belt, as well as elsewhere (e.g. Robert at al., 2005; Dubé and Gosselin, 2007; Bleeker, 2015; Dubé et al., 2017; Poulsen, 2017). These metallotects also occur in the poorly exposed and underexplored northwestern Abitibi belt, most specifically along two regional-scale deformation zones termed the Sunday Lake (Fig. 1) and Lower Detour deformation zones (Fig. 2; Ayer et al., 2009, 2010; Oliver et al., 2012; Faure, 2015; Castonguay et al., 2018). The primary focus of this study is to examine the significance and relationship between deformation zones and spatially related gold mineralization in the Detour Lake and Lower Detour areas in Ontario and their along-strike eastward extensions into Quebec. A secondary objective is to compare these mineralized deformation corridors with those of the southern Abitibi, such as the Destor – Porcupine and Larder Lake – Cadillac deformation zones (Fig. 1). The present paper is a descriptive overview of the visited localities, active mine, or exploration properties being principally studied via the examination of numerous diamond drillholes to establish the setting of gold mineralization and its relationships with the regional deformation zones. Samples for geochemical and geochronological analyses were collected to characterize the host rocks, the alteration associated with gold mineralization and the timing of events.

Geological setting

The northwestern Abitibi greenstone belt comprises the 2734 to 2724 Ma volcanic rocks of the Deloro assemblage and the younger than 2700 Ma Caopatina turbititic assemblage that forms an east- trending elongated Porcupine/Cadillac-like sedimentary belt (Fig. 1, 2; Thurston et al., 2008; Ayer et al., 2009; Oliver et al., 2012). Eastward, in Quebec, these belts comprise the Manthet and Rivière Turgeon assemblages, respectively (Lacroix, 1994; Faure, 2015). Synvolcanic to syntectonic, tonalitic to granodioritic intrusive complexes and plutons surround and intrude the volcanic and sedimentary assemblages.

In the Detour Lake area (Fig. 2, 3), the Deloro assemblage has been assigned to the Detour Lake Formation (Oliver et al., 2012). The latter comprises ultramafic-dominated flows, sills, and dykes of the lower Detour Lake Formation and mafic-dominated volcanic and volcaniclastic rocks of the upper Detour Lake Formation, separated by the 2725.1 ± 1.4 Ma "Chert Marker Horizon" (CMH; Oliver et al., 2012). The CMH is not a primary chert, but rather a fine-grained felsic to intermediate volcaniclastic unit of calc-alkaline affinity (Oliver et al., 2012).

Corresponding author: Sébastien Castonguay (sebastien.castonguay@canada.ca)

Castonguay, S., Dubé, B., Mercier-Langevin, P., and Wodicka, N., 2019. Geological setting and mineralization styles of the Sunday Lake and Lower Detour 'gold trends', northwestern Abitibi greenstone belt, Ontario and Quebec; *in* Targeted Geoscience Initiative: 2018 report of activities, (ed.) N. Rogers; Geological Survey of Canada, Open File 8549, p. 9–22. https://doi.org/10.4095/313625

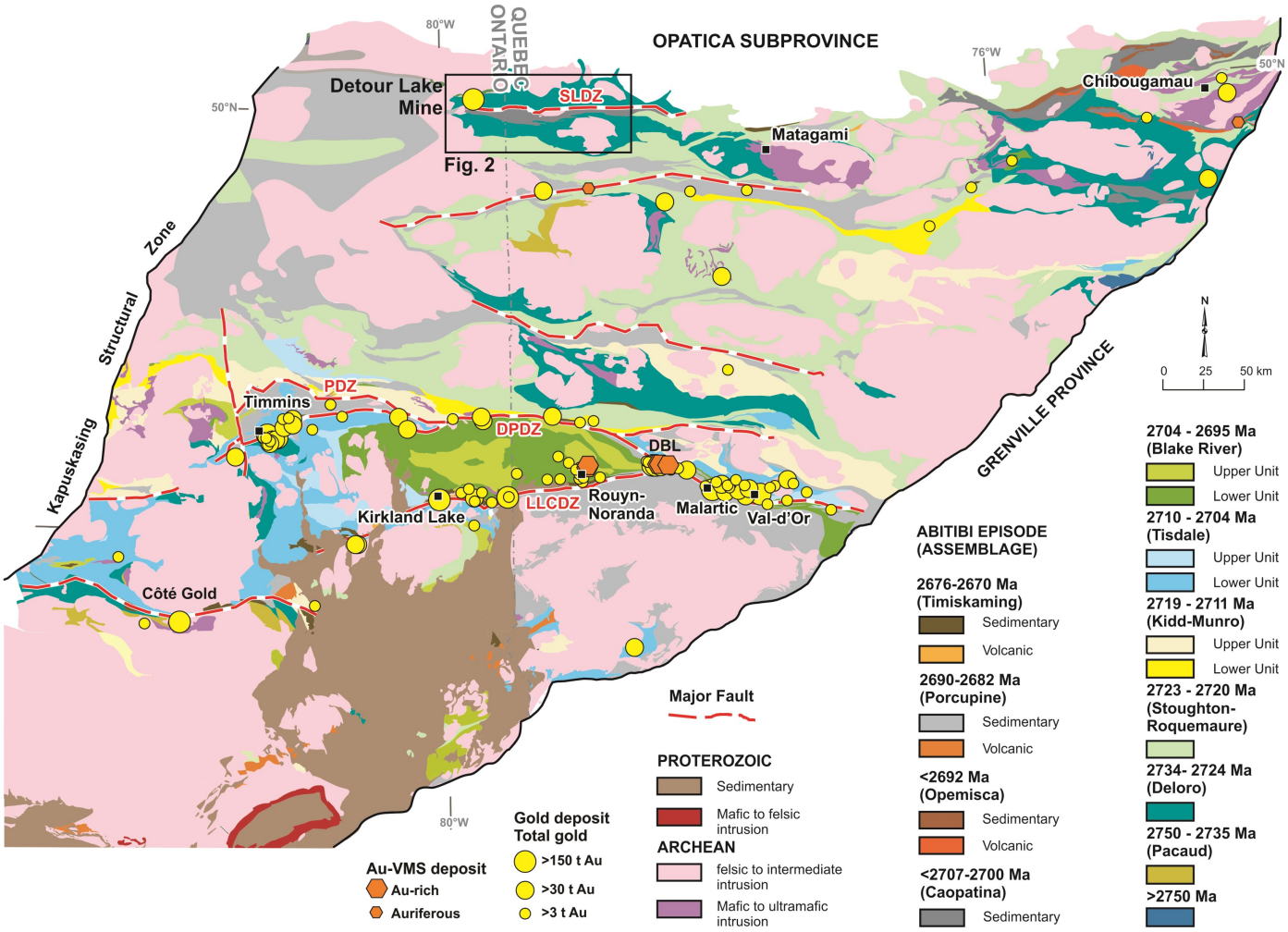

Figure 1. Generalized geological map of the Abitibi subprovince showing the main lithotectonic assemblages and location of major gold deposits, including the Detour Lake Mine. *Modified from* Ayer et al. (2010). Data for major gold and gold-rich volcanogenic massive sulphide (VMS) deposits *modified from* Gosselin and Dubé (2005) and Mercier-Langevin et al. (2011). Abbreviations: DBL = Doyon – Bousquet – Laronde camp; DPDZ = Destor – Porcupine deformation zone; LLCDZ = Larder Lake – Cadillac deformation zone; PDZ = Pipestone deformation zone; SLDZ = Sunday Lake deformation zone.

In drill core, intervals assigned to the CMH correspond to silicified and sulphidized mafic volcanic to volcaniclastic rocks and intermediate sills and/or dykes. Felsic to gabbroic, massive to porphyritic ca. 2722 to 2700 Ma plutons and dykes intrude the Detour Lake Formation (Oliver et al., 2012). The Sunday Lake deformation zone (SLDZ; Fig. 2) juxtaposes the Deloro assemblage to the north against the Caopatina assemblage to the south (Ayer et al., 2009, 2010). The latter consists of younger than ca. 2697 Ma quartz wacke, argillaceous siltstone and mafic volcaniclastic units, cut by gabbroic intrusive rocks (Oliver et al., 2012).

The Lower Detour (Zone 58N) area lies 7 km south of the SLDF, across the Caopatina belt in the structural hanging wall of the Lower Detour (LDDZ) and Massicotte (MDZ) deformation zones (Fig. 2). It is underlain by the Deloro assemblage, including komatiitic and tholeiitic mafic volcanic rocks (Malcolm et al., 2015; Detour Gold Corporation, 2017). Deformed and locally iron carbonate-altered polygenic conglomerate beds occur in the immediate structural footwall of the LDDZ. Locally altered, alkaline feldspar porphyritic dykes were emplaced along the LDDZ and commonly obscure the contact between the volcanic and sedimentary units.

In Quebec, the Harricana-Turgeon volcano-sedimentary belt comprises the Deloro-correlative Manthet assemblage, which consists of massive, pillowed, and locally brecciated tholeiitic basalt, gabbro sills, and interlayered volcaniclastic and locally graphitic argillite occurring north of the SLDZ (Fig. 2; Lacroix, 1994; Faure, 2015). Ultramafic volcanic rocks also occur in the hanging wall of the SLDZ (most probably correlative with the Lower Detour Formation), and gabbro-pyroxenite sills and intrusions, such as the Grasset ultramafic complex (Fig. 2), are interlayered with basalt (Lacroix, 1994; Faure, 2015). A lenticular, fault-bounded basin of polygenic conglomerate has been outlined by Midland Exploration's drilling since

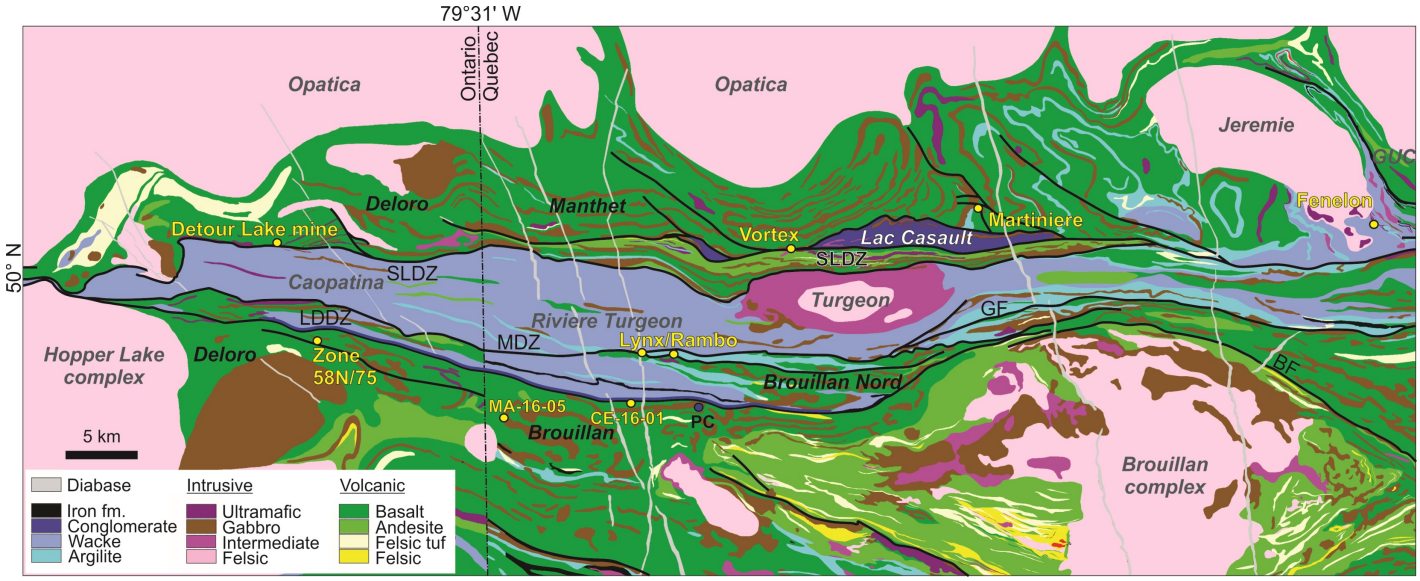

Figure 2. Simplified regional geological map of the Sunday Lake and Lower Detour 'gold trends' area (*modified from* Faure, 2015) with identification of the main lithological assemblages and deformation/fault zones and the location of gold mines, mineralized zones, and cited exploration drillholes. The location of the figure is outlined on Figure 1. Abbreviations: BF = Bapst fault zone; GF = Grasset fault zone; GUC = Grasset ultramafic complex; LDDZ = Lower Detour deformation zone; MDZ = Massicotte deformation zone; SLDZ = Sunday Lake deformation zone.

2013 and is informally called the Lac Casault basin (Faure, 2015). The sedimentary belt south of the SLDZ comprises the Caopatina-correlative Rivière Turgeon assemblage [termed the La Peltrie-Matagami group or "Matagami sediments" by Lacroix et al., (1990) and Lacroix (1994)], which consists of turbiditic siltstone, sandstone and locally argillite. A band of magnetite banded iron formation and of polygenic conglomerate occurs in the southern part of the belt, in the immediate structural footwall of the LDDZ. The mafic volcanic rocks occurring south of the MDZ and LDDZ comprise the Brouillan Nord

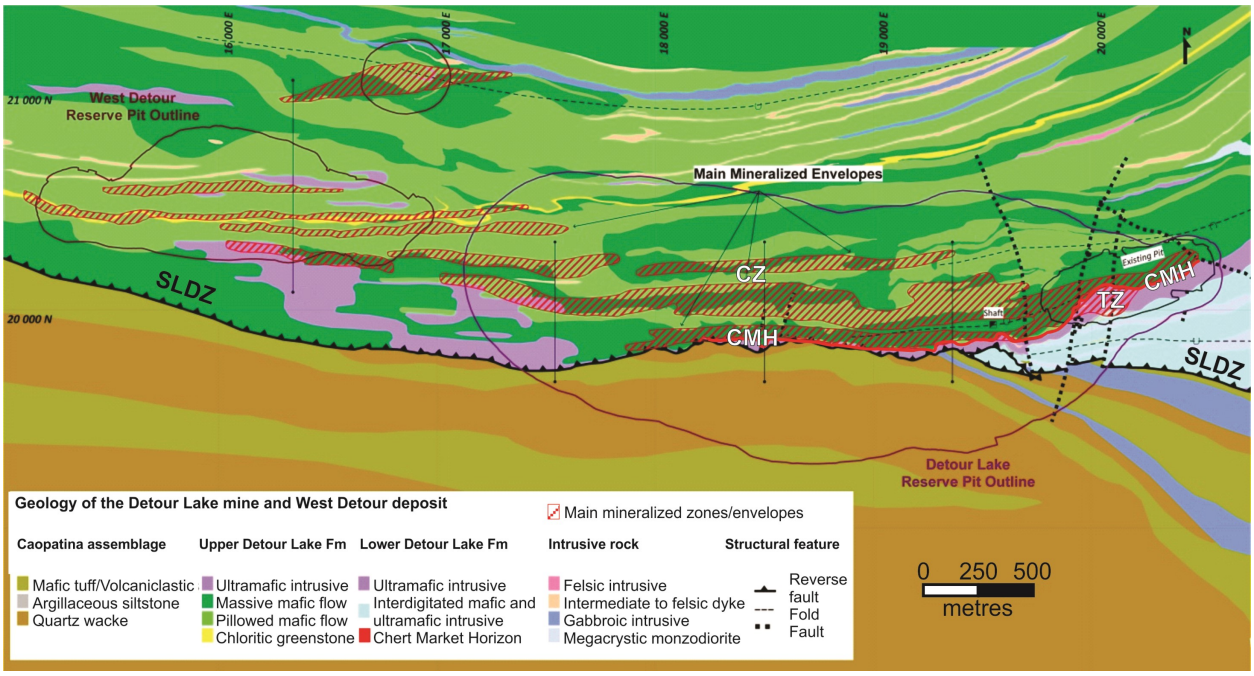

Figure 3. Simplified geological map of the Detour Lake deposit area, with location of the main mineralized zones and historical and future pit outlines (modified from Oliver et al., 2012 and Detour Gold Corporation, 2017). Abbreviations: CMH = Chert marker horizon; CZ = Calcite Zone; SLDZ = Sunday Lake deformation zone; TZ = Talc zone.

assemblage and Brouillan volcanic complex, respectively (Lacroix, 1994). Rock units of the latter are principally massive and pillow basalt and gabbro sills. These units extend southeastward in the Selbaie deposit area, where they are interlayered with ca. 2729 Ma felsic volcanic rocks (Barrie and Krogh, 1996), attesting a correlation with the Deloro assemblage. The syntectonic Turgeon pluton intrudes the Riviere Turgeon assemblage south of the SLDZ and is composed of quartz diorite with a core of quartz monzodiorite (Fig. 2; Lacroix, 1994). North of the SLDZ, the Jeremie pluton (Fig. 2) has a similar composition to syntectonic granitic to granodioritic intrusions of the Opatica subprovince (Lacroix, 1994; Davis et al., 1995), although its southern part may comprise an early synvolcanic phase (Faure, 2015).

Rock units of the study area have been polydeformed and metamorphosed. In the Detour Lake mine area, Oliver et al. (2012) recognized four phases of deformation. The earliest phase, related to Caopatina basin formation and sedimentation, is not associated with any penetrative regional fabric. The main regional fabric, S_2, is generally steeply dipping and axial-planar to west-trending tight to isoclinal F_2 folds. Early displacement along the SLDZ is dominated by D_2 reverse faulting. Broad, open, southeast-trending F_3 folds, mostly occurring north of the SLDZ, clearly affect the contact with the Opatica subprovince (Fig. 2). The fourth phase of deformation is characterized by a series of southeast-trending late faults, which are locally intruded by Proterozoic diabase dykes. In general, the metamorphic grade increases toward the contact with the Opatica subprovince. In and north of the Detour Lake mine area, amphibolite facies assemblages in mafic rocks comprise biotite, actinolite, albite and almandine garnet (Marmont, 1986; Oliver et al., 2012; Dubosq, 2017). Farther south from the Opatica contact, such as in the Martiniere and Lower Detour areas, typical greenschist facies assemblages predominate. Hydrothermal alteration related to gold mineralization overprints the regional metamorphic paragenesis, as documented at the Detour Lake deposit (Marmont, 1986; Oliver et al., 2012).

Sunday Lake 'gold trend'

The Sunday Lake 'gold trend' is informally defined by gold mineralized zones occurring within the SLDZ and along its splays or second-order structures in a broad (approximately 4 km) corridor. The Detour Lake gold mine (approximately 25 Moz Au: Detour Gold Corporation, 2017), the Vortex zones, and the Martiniere-Bug Lake deposits (591 000 oz Au: Balmoral Resources, 2018a) comprise the Sunday Lake gold trend (Fig. 2).

Detour Lake gold mine

Auriferous zones of the Detour Lake gold deposit are hosted in a sequence of lower amphibolite-facies pillowed and massive basaltic (upper Detour Lake Formation) and altered ultramafic rocks (lower Detour Lake Formation), both as low-grade disseminated quartz-sulphide zones or as quartz±carbonate veins and silicified high-grade zones (Marmont, 1986; Oliver et al., 2012; Detour Gold Corporation, 2017; Dubosq et al., 2018). Ore zones are commonly oriented subparallel to a series of high-strain zones occurring coplanar and in the hanging wall of the SLDZ (Fig. 3).

Previously mined high-grade zones (i.e. the Main Zone) focused on the CMH and included the hanging wall 'Q-Veins' and footwall 'Talc Zone' (Fig. 3; Oliver et al., 2012; Detour Gold Corporation, 2017). The mineralization associated with the CMH is hosted in silicified fine-grained intermediate intrusive rocks and silicified-sulphidized volcanic or volcaniclastic layers (Fig. 4a, b; e.g. 15.8 g/t Au/2.5 m: Oliver et al., 2012). The Q-Veins (e.g. 8.6 g/t Au/5.4 m) are strongly deformed centimetric quartz±carbonate fault-fill veins and 0.5 to 5 volume % pyrrhotite-pyrite±chalcopyrite stringers occurring in potassic-altered, biotite-rich, massive and pillowed mafic volcanic rocks. Gold associated with sulphides also occurs in the Talc Zone (e.g. 9.4 g/t Au/3.2 m) along the footwall of the CMH in strongly sheared, serpentinized and talcose ultramafic rocks adjacent to an intermediate intrusive body (Oliver et al., 2012; Detour Gold Corporation, 2017).

Since late 2012, open-pit mining has been concentrated in the low-grade (approximately 1 g/t Au) high-tonnage Calcite Zone (Fig. 3), which consists of steep west-trending zones comprising boudinaged quartz-calcite-pyrite-pyrrhotite veinlets in potassic (biotite) altered mafic volcanic rocks (Fig. 4c), preferentially occurring at contacts between pillow and massive basalt. There are several types and generations of veins (syn- to post-D_2; Dubosq et al, 2018), including sulphide-rich brecciated veins that are associated with late brittle-ductile strain and Au remobilization.

Vortex zones

The Vortex zones (part of the Midland – SOQUEM Casault property; Midland Exploration, 2018) are located along a splay of the SLDZ, at the western tip of the Lac Casault conglomeratic basin, about 40 km east of the Detour Lake mine (Fig. 2). They comprise several west-trending auriferous high-strain zones in mafic volcaniclastic rocks at the contact between tholeiitic and calc-alkaline volcanic units, and are locally spatially associated with reddish alkaline porphyritic intrusions (Fig. 5). The calc-alkaline units mainly comprise andesitic and lesser rhyolitic volcaniclastic rocks that have been tentatively correlated with the CMH occurring along strike of the SLDZ at the Detour Lake deposit (Faure, 2015).

From north to south and following an increasing strain gradient, there are three mineralized corridors (Fig. 5): (1) Zone 475 consists of deformed quartz-carbonate-sulphide veins in sheared mafic blocky tuff, locally with semi-massive pyrite (e.g. 0.4 g/t Au over 8 m, including 2.7 g/t Au over 0.5 m; drillhole CAS-17-94; Fig. 6a); (2) Zone 450, the most important to date (e.g. 1.4 g/t Au over 26 m, including 7.9 g/t Au over 2.2 m; drillhole CAS-17-96), comprises quartz-carbonate-sericite veins and disseminated pyrite associated with a high-strain,

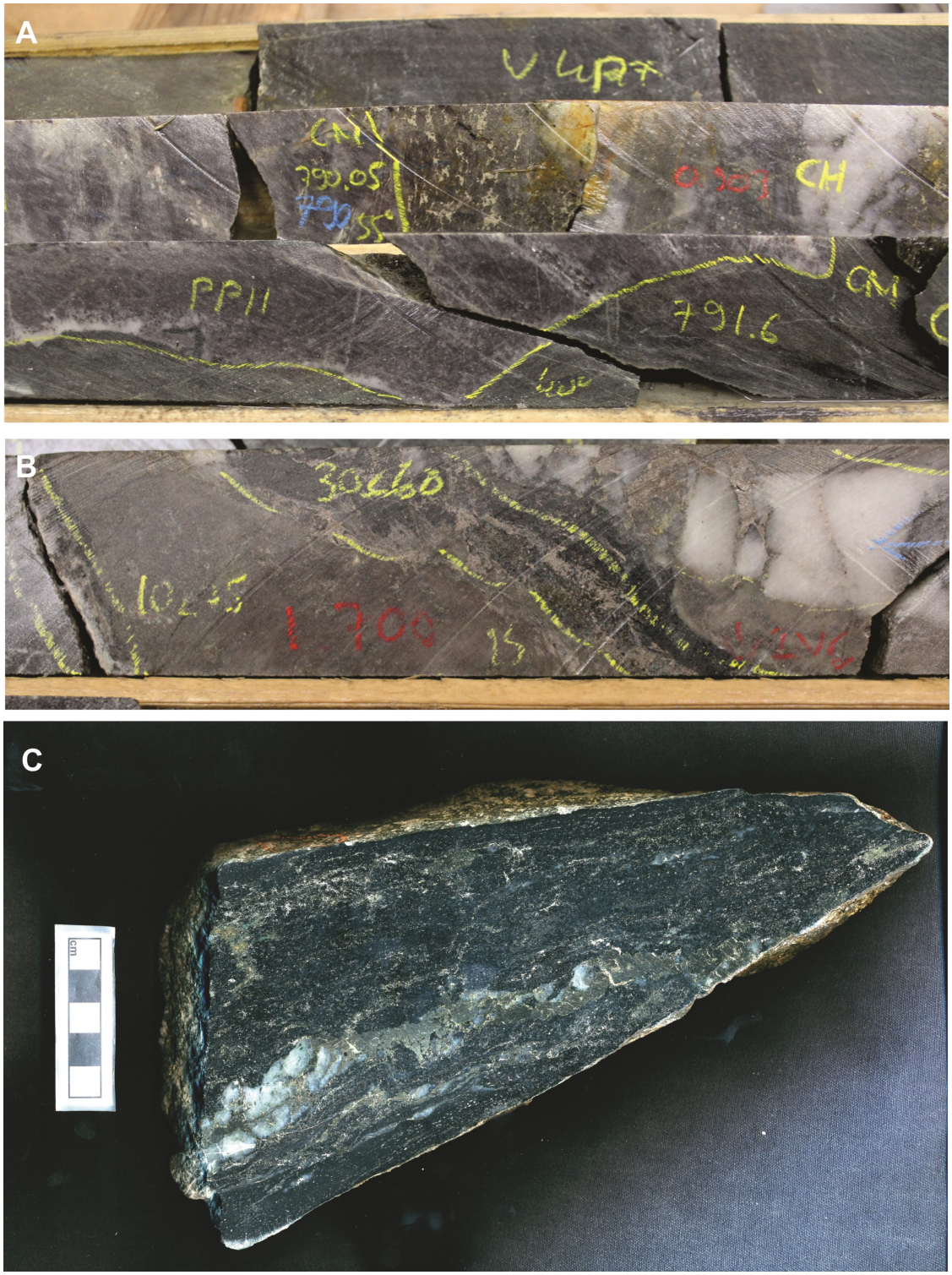

Figure 4. Photographs of samples from Detour Lake mine: a) CMH: Silicified biotite-chlorite-2 volume % pyrrhotite-pyrite intermediate feldspar porphyry intruding silicified mafic volcanic unit with quartz vein and 5 volume % pyrrhotite stringer (interval is 1 g/t Au/0.5 m; NQ core diameter is 47.6 mm). Note evidence of folding with lithological contact locally at a high angle to the main fabric. b) Silicified-biotitized pillow basalt with 10 to 15 volume % pyrrhotite stringer and pyrrhotite filling fractures of quartz-calcite veins (1.7 g/t Au/0.5 m; NQ core diameter is 47.6 mm). c) Sawed piece of low-grade (approximately 0.5–0.9 g/t Au) ore from the Detour Lake open pit consisting of boudinaged/fractured quartz-calcite-pyrite-pyrrhotite veins and stringer in biotitized mafic volcanic rocks.

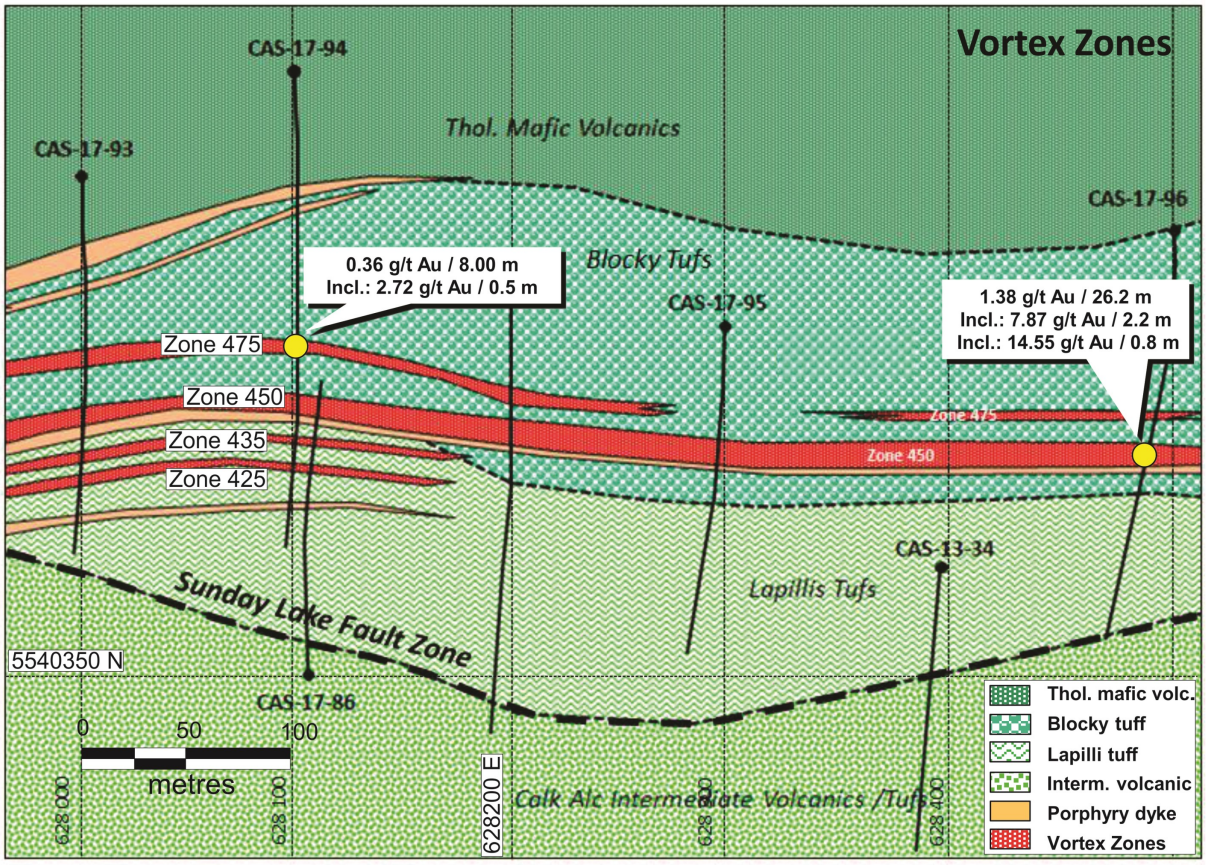

Figure 5. Simplified geological map of parts of the Vortex zones (*modified from* Midland Exploration, 2018). Abbreviations: Incl. = including; Interm. volcanic = intermediate volcanic rocks; Tholeitic mafic volc. = Thol mafic volcanic rocks.

brecciated zone between mafic volcaniclastic rocks and an albitized-sericitized granitic dyke (Fig. 6b, c); and 3) secondary zones 435 and 425 consist of quartz-carbonate veins and disseminated pyrite in strongly deformed, hematitized-sericitized lapilli tuff (e.g. Zone 435, 3.5 g/t Au over 2.8 m, including 5.0 g/t Au over 0.95 m; drillhole CAS-17-93). In general, disseminated sulphides reach 5 to 7 volume % in the high-grade brecciated silicified zones. Quartz veins are boudinaged and folded, but some locally cut foliation, suggesting an overall early- to syn-deformation relative chronology. The brecciation is late-main phase deformation as it affected a previously foliated rock and is spatially associated with a locally strongly developed crenulation fabric nearing the mineralized zones (e.g. Zone 425; Fig. 6d).

Martiniere West-Bug Lake deposits

The Martiniere West and Bug Lake deposits (Martiniere property), located about 50 km east of the Detour Lake mine and 12 km east of Vortex, are hosted in greenschist-grade Manthet basalt and intrusive rocks occurring roughly 2 km from the northern splay of the SLDZ (Fig. 2, 7; Balmoral Resources, 2018a). In general, rock units are weakly foliated, except in mineralized high-strain zones.

The Martiniere West deposit comprises a series of 1 to 2 m thick silicified, carbonatized high-strain zones and breccia with multiple generations of quartz-dolomite/ankerite-tourmaline veins and 1 to 5 volume % pyrite±arsenopyrite (Fig. 8a). Northeast-trending mineralized zones (e.g. 17.1 g/t Au over 1.4 m in a 1.6 g/t Au 20 m envelope; drillhole MDW13-88) are hosted in moderately foliated, sericitized, leucoxene-bearing quartz gabbro near, and subparallel to, the contact with mafic volcanic and sedimentary units. Away from mineralized high-strain zones, the host gabbro is massive to weakly foliated and contains magnetite.

The Bug Lake trend is defined by the Bug North and Bug South deposits consisting of en échelon, moderately to steeply eastward-dipping high-strain zones occurring along contacts of the north-northwest-trending Bug Lake porphyry dyke (BLP), which lies almost perpendicular to the stratigraphic layering of host rocks (Fig. 7, 9). The BLP is a buffy grey fine-grained quartz porphyry with 1 to 2 volume % disseminated pyrite. It is mostly massive to weakly foliated, with decametric brecciated margins. Gold is typically associated with fine-grained pyrite and occurs in several discrete altered and silicified high-strain zones in the hanging wall ('Upper Bug zone') and footwall ('Lower Bug zone') of the BLP. At Bug North, mineralization

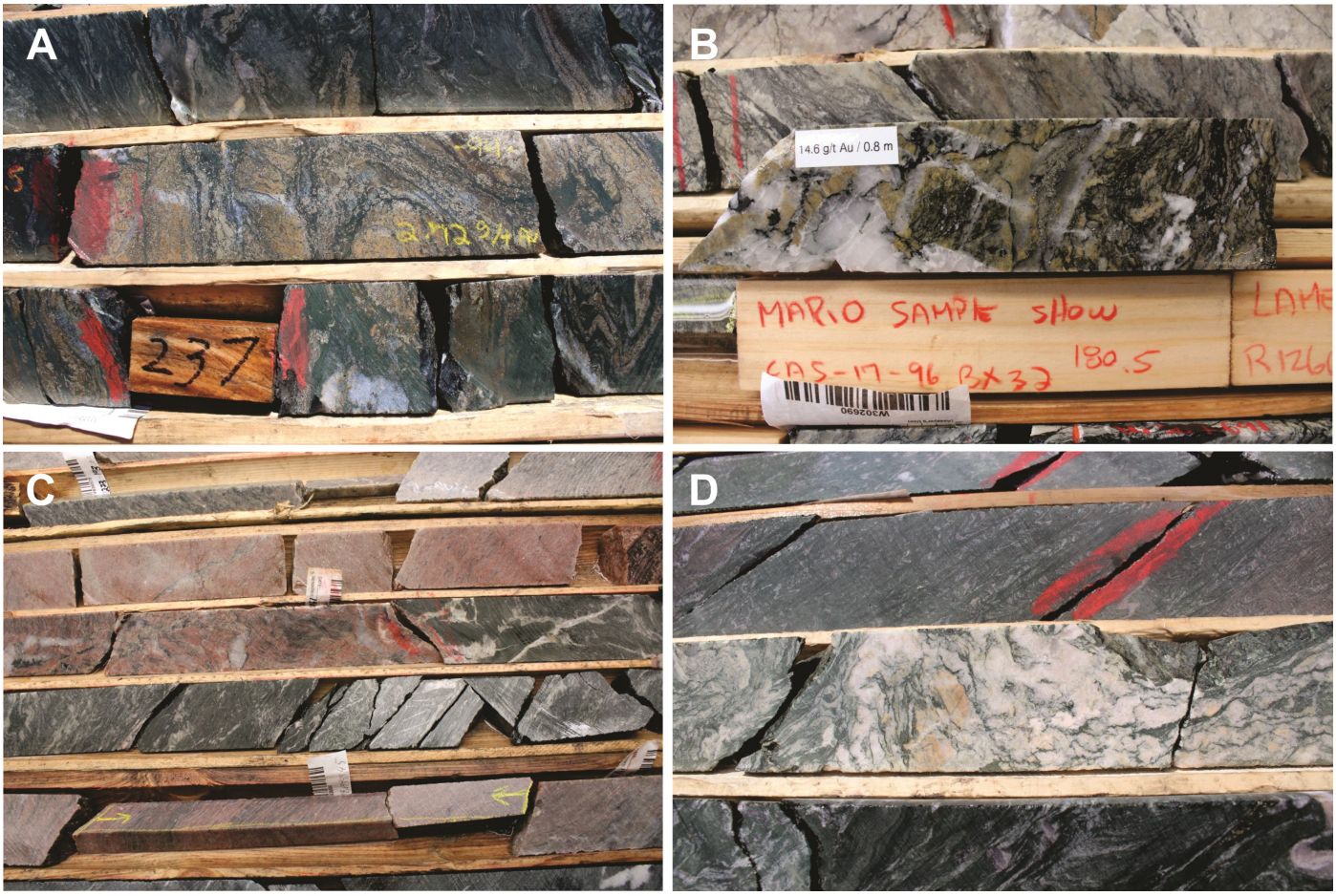

Figure 6. Photographs of drill core (NQ core diameter is 47.6 mm) from the Vortex zones: a) Zone 475: deformed quartz-carbonate-sulphide veins in sheared mafic blocky tuff, locally with semi-massive pyrite (2.7 g/t Au over 0.5 m; drillhole CAS -17-94). b) Zone 450: quartz-carbonate±tourmaline±sericite veins and disseminated pyrite associated with a high-strain, brecciated zone between mafic volcaniclastic rocks and an albitized-sericitized granitic dyke (see Fig. 5). c) Hematitized granitic intrusive and mafic volcanic rocks associated with Zone 450. Contacts are strongly foliated, brecciated and marked by quartz-carbonate veins. d) Folded, boudinaged and brecciated quartz-carbonate veins spatially associated with a locally strongly developed crenulation in Zone 425 (0.96 g/t Au/1.1 m; drillhole CAS-17-94).

(e.g. 6.1 g/t Au over 11.7 m; drillhole MDE-16-236) in the hanging wall is characterized by brecciated silicified zones with pyrite stringer and minor quartz-carbonate veining hosted in sericite-calcite-chlorite-altered mafic volcanic rocks. Auriferous zones (e.g. 4.2 g/t Au over 1.8 m in a 1.0 g/t Au 43 m envelope; drillhole BLD-16-03) in the footwall occur in silicified-sulphidized leucoxene-bearing quartz gabbro and quartz-dolomite-pyrite veins (Fig. 8b). Both the Upper and Lower zones of the Bug South deposit are hosted in sericitized mafic volcanic rocks. Here, the Upper Bug zone (e.g. 6.5 g/t Au over 1.9 m in a 1.8 g/t Au 39 m envelope; drillhole MDE-17-287B) is generally thicker than at Bug North and characterized by more abundant quartz-carbonate veins (Fig. 8c, d). The lower zone at Bug South is thinner and lower grade (e.g. 0.8 m at 5.0 g/t Au in a 1.2 g/t Au 6.1 m envelope; drillhole MDE-17-287B) than along strike at Bug North. In general, better grades are associated with increased silicification and more than 5 volume % pyrite stringer. It is noteworthy that several layers of massive to semi-massive sulphide occur in the hanging wall of the Bug Lake deposits, where they are related to an early pervasive chlorite-calcite-sericite alteration in the surrounding mafic volcanic rocks (Balmoral Resources, 2018a).

Lower Detour gold trend

The Lower Detour gold trend lies roughly 7 km south of the SLDF, across the Caopatina belt (Fig. 2). It comprises gold mineralization spatially associated with the Massicotte and Lower Detour deformation zones, including zones 58N and 75 (534 000 oz Au; Detour Gold Corp., 2018) and the auriferous intersections in Quebec, such as those of the Lynx and Rambo zones (Balmoral Resources) and Probe Metals-SOQUEM 'Detour Quebec' project. The MDZ and LDDZ correlate eastward with the Grasset fault zone (Fig. 2; Faure, 2015).

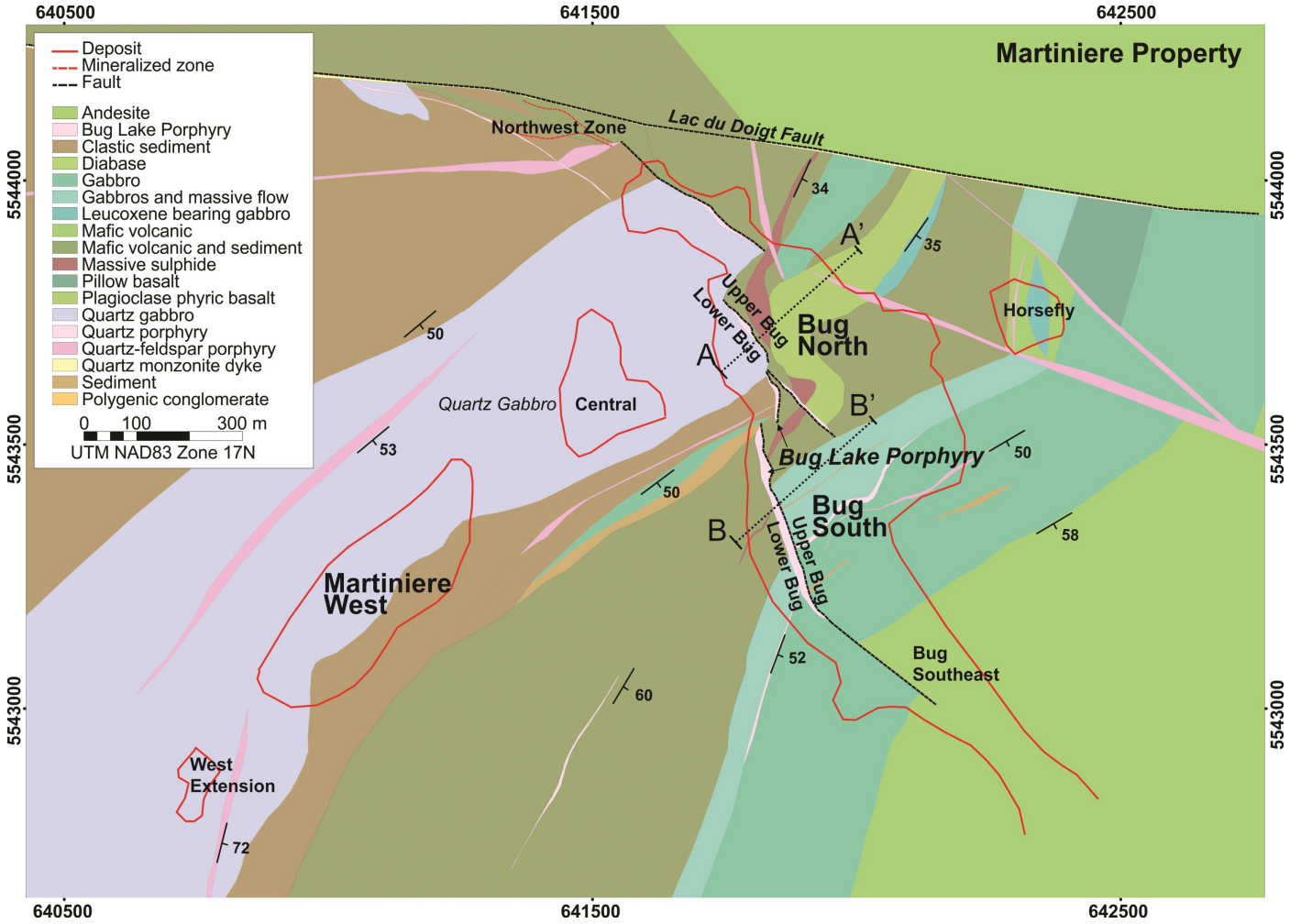

Figure 7. Geological map of the Martiniere West and Bug Lake deposits, Martiniere property (*modified from* Balmoral Resources, 2018a). Cross-sections through A-A' and B-B' are shown in Figure 9.

Zones 58N and 75

The Lower Detour area of the Detour Gold Corporation property is underlain by volcanic units correlated with the Detour Lake Formation (Deloro assemblage; Ayer et al., 2009) occurring to the north (Fig. 2). Here, gold mainly occurs in the steeply south-dipping zones 75 and 58N, in the structural hanging wall of an intermediate intrusion (Fig. 10 and 11; Malcolm et al., 2015; Castonguay et al., 2018). Zone 75 is hosted in a high-strain zone separating tholeiitic and komatiitic mafic volcanic units that have been silicified and biotite-sericite altered and locally in a fine-grained or feldspar porphyritic intrusive (Fig. 12a). It represents a similar lithological setting and style of mineralization as those of the CMH at the Detour Lake mine. Zone 75 mineralization comprises sulphide-rich zones reaching locally up to 20 volume % as mainly pyrite, and lesser pyrrhotite, chalcopyrite and sphalerite (Fig. 12b). Higher gold content (e.g. 8.0 g/t over 6 m; drillhole DLD-16-203) generally correlates with increasing strain. The much wider Zone 58N consists of discrete laminated quartz-tourmaline-carbonate veins and stockworks (e.g. 52 g/t Au over 1 m in a 6.5 g/t Au 22 m interval; drillhole DLD-15-140) hosted in a swarm of leucocratic feldspar porphyry dykes. The auriferous veins are associated with a decimetre-wide sericite-, silica-, and biotite-alteration zone (Fig. 12c). Sulphides generally vary between 0.5 and 5 volume % occurring as disseminated pyrite within the veins or their immediate selvages, along with trace amounts of sphalerite and chalcopyrite. Structurally below Zone 58N, the ore-hosting porphyry is intruded and brecciated by a melanocratic intermediate porphyry (Malcolm et al., 2015; Fig. 12d). The melanocratic phase is mostly barren, except in high-strain zones, suggesting that it is probably not a post-mineralization phase.

Lower Detour gold trend in Quebec

Most of the Lower Detour metallotects (i.e. deformed and locally altered polygenic conglomerate porphyritic intrusive rock and contacts between contrasting volcanic sequences, and carbonate hydrothermal alteration, all spatially related to regional-scale deformation zones) extend eastward in an exten-

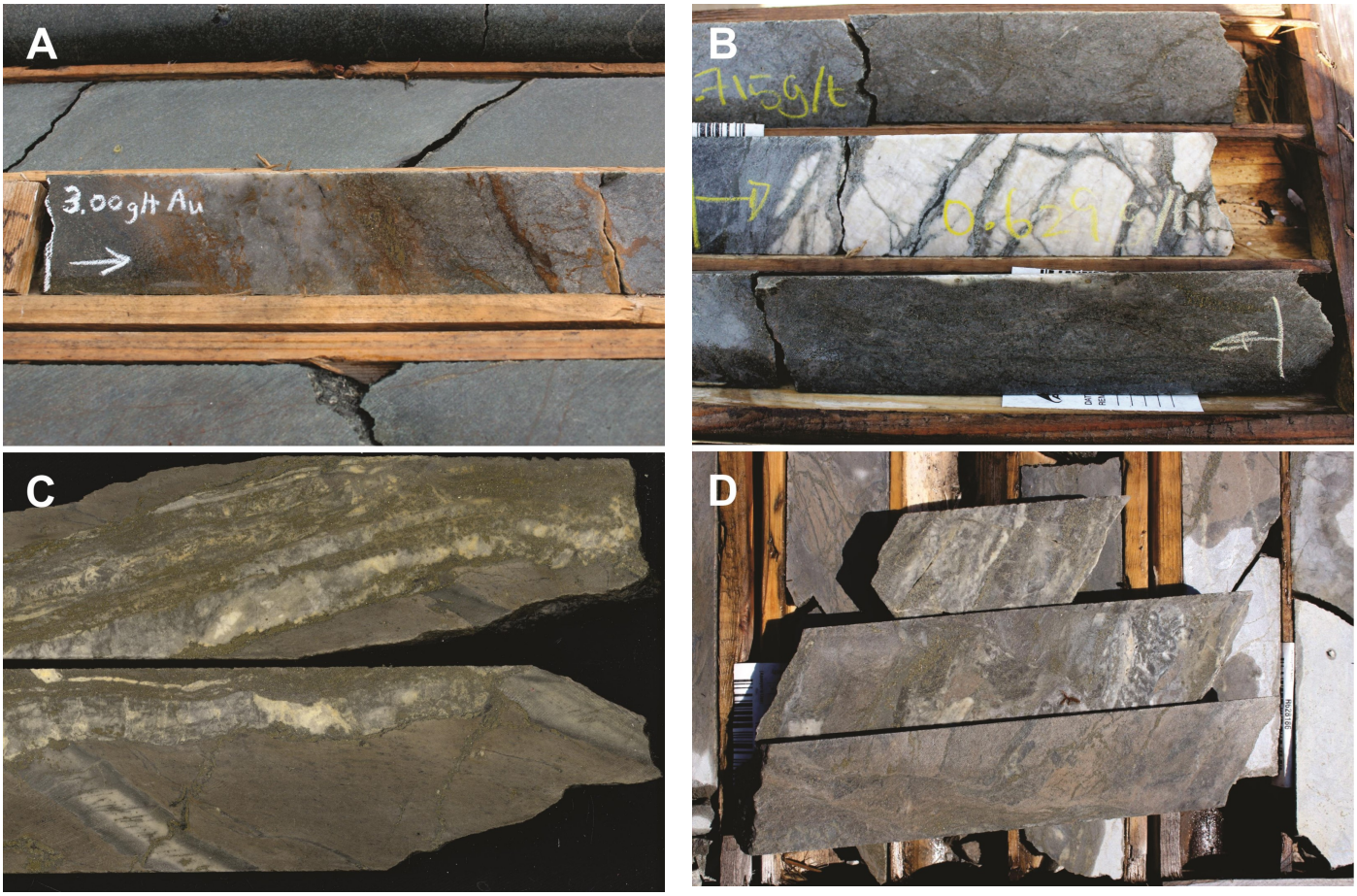

Figure 8. Photographs of drill core (NQ core diameter is 47.6 mm) from the Martiniere West and Bug Lake deposits: a) Quartz-dolomite/ankerite-pyrite (5 volume %)-tourmaline veins in quartz gabbro at Martiniere West. b) Lower zone of Bug North, pyrite (3–7 volume %) stringer and quartz-dolomite veins in silicified leucoxene-bearing gabbro. c) Upper zone of Bug South: quartz-dolomite-pyrite veins in a 4.6 g/t Au interval in sericitized pillow basalt. d) Upper zone of Bug South: pyrite (5–10 volume %) stringer and quartz-dolomite veins in a 7.9 g/t Au interval of sericitized pillow basalt.

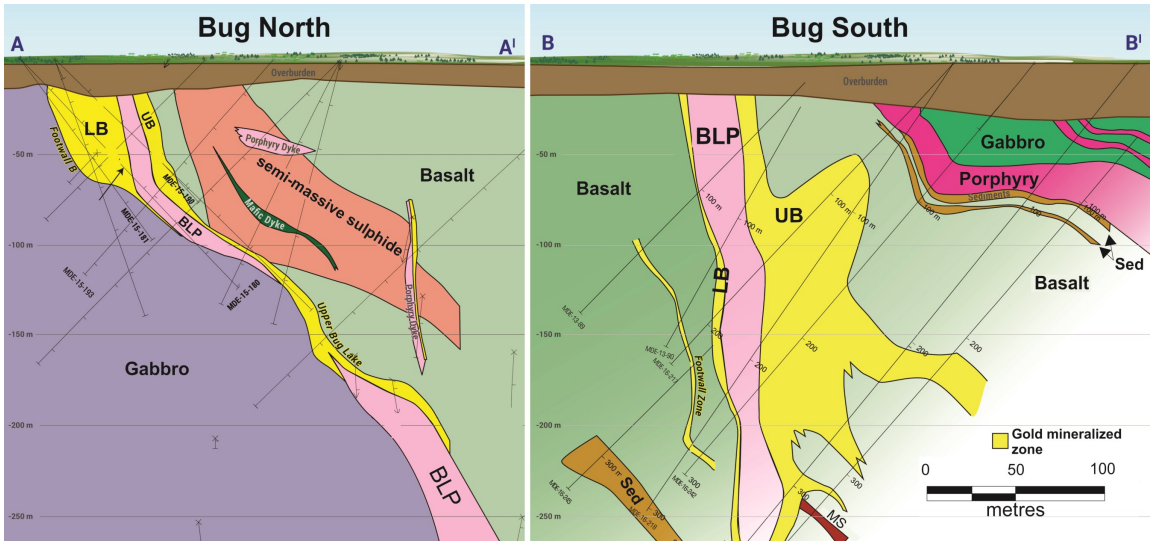

Figure 9. Simplified geological sections of the Bug Lake deposit, see Figure 7 for location: Cross-section A-A') Bug North. Cross-section B-B') Bug South (*modified from* Balmoral Resources, 2018a). Abbreviations: BLP = Bug Lake porphyry; LB = Lower Bug zone; MS = massive sulphide; Sed = sedimentary rocks; UB = Upper Bug zone.

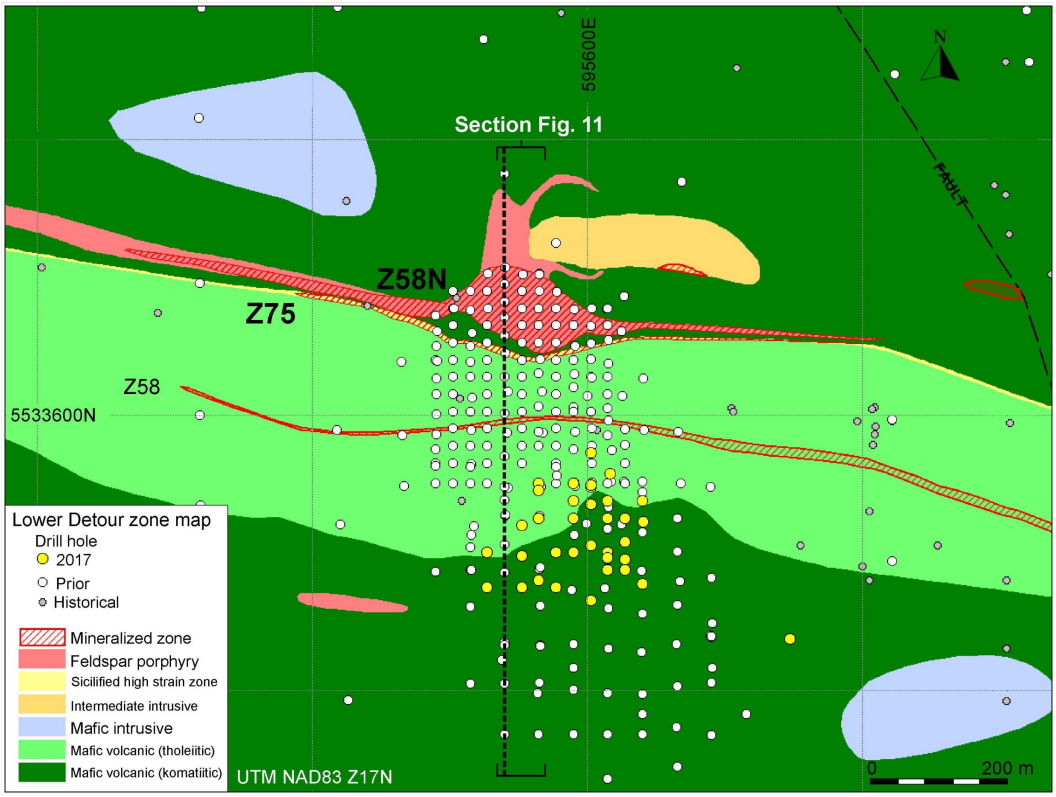

Figure 10. Simplified geological map of the Lower Detour area extrapolated from drill core data, with location of the main mineralized zones (zones 75 and 58 N; *modified from* Malcolm et al., 2015; Detour Gold Corporation, 2017). Cross section shown in Figure 11.

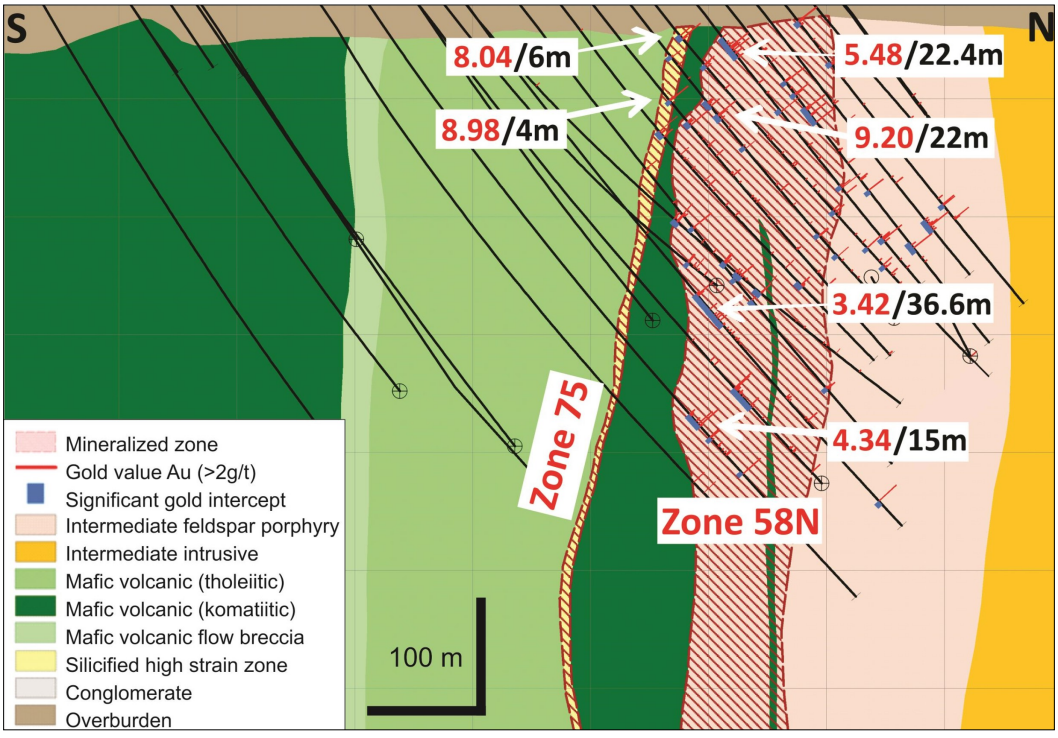

Figure 11. Simplified geological section of the Lower Detour zones 75 and 58 N with representative gold intercepts (*modified from* Malcolm et al., 2015; Detour Gold Corporation, 2017).

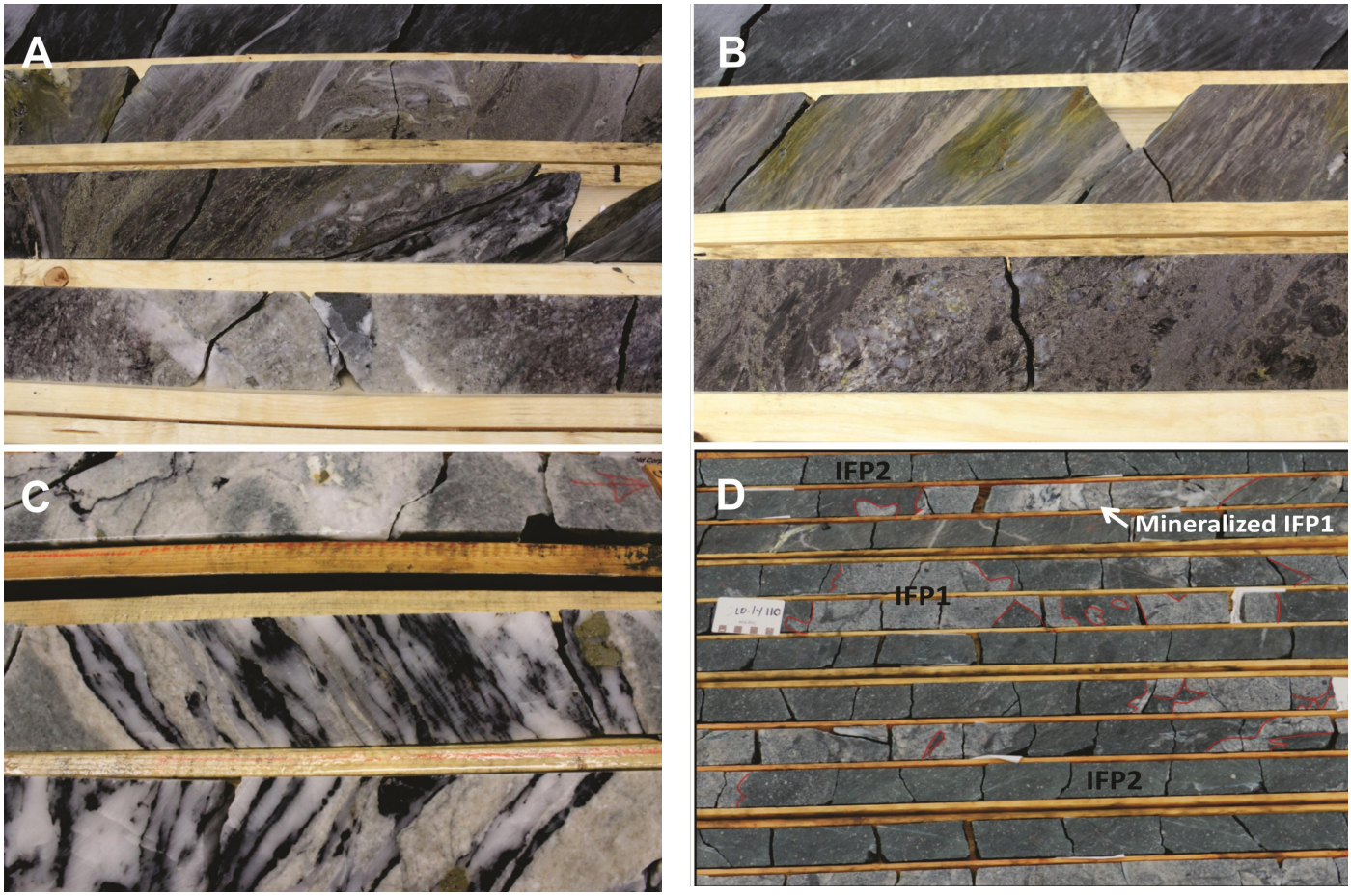

Figure 12. Photographs of drill core (NQ core diameter is 47.6 mm) from the Lower Detour zones. a) Zone 75; silicified, sulphidized, and biotite-sericite-altered mafic volcanic units and feldspar-quartz porphyry. b) Zone 75; sulphide-rich zone (mainly pyrite, and lesser pyrrhotite, chalcopyrite and sphalerite) in highly strained and altered mafic volcanic rocks. c) Typical zone 58 N, with laminated quartz-tourmaline veins in silica-sericite-altered feldspar porphyry with trace to 2 volume % coarse pyrite along vein contacts with the feldspar porphyry (interval is 34.9 g/t over 1 m). d) Ore-hosting leucocratic porphyry (IFP1) is intruded and brecciated by a melanocratic intermediate porphyry (IFP2; *modified from* Malcolm et al., 2015). The melanocratic phase is mostly barren, except in high-strain zones.

sively overburden-covered and under-explored area of Quebec.

The Lynx (7.8 g/t Au/7.2 m) and Rambo (6.3 g/t Au/2.7 m) zones are east-trending 0.4 to 13.4 m thick zones of quartz-carbonate-pyrite veins hosted along the contact between andesitic and mafic volcanic rocks (Balmoral Resources, 2018b) along the MDZ (Fig. 2). A preliminary exploration model suggests that the mineralization is linked with a fault-related fold structure, similar to that associated with the Casa Berardi gold deposit to the south (Balmoral Resources, 2018b).

The Massicotte and Casgrain-Extension properties lie roughly 3 km southward and are part of the Detour Quebec project covering a long (approximately 74 km) corridor along the LDDZ in Quebec (Probe Metals, 2018). Recent exploration, including sparse diamond drilling, has intersected auriferous zones (e.g. 2.8 g/t Au/0.74m; drillhole CE-16-01; Fig. 2) along the LDDZ and probable second-order splays to the south. These zones comprise pyrite±galena±sphalerite veins in a sericite schist (e.g. 5.3 g/t Au/3.4 m, including 17.5 g/t Au/1 m; drillhole MA-16-05; Probe Metals, 2016) or quartz-tourmaline-pyrite veins at sheared contacts between hematitized-sericitized reddish felsic intrusive and chloritized mafic volcanic rocks (Fig. 13a). In addition, exploration drilling has intersected several thick intervals of polygenic conglomerate. One approximately 260 m thick polygenic conglomerate interval occurs just north of the LDDZ, at the same structural position as that of the Lower Detour area to the west (Fig. 2). It consists of flattened subrounded to subangular clasts, principally of mafic volcanic origin with lesser felsic volcanic, porphyritic, and quartz vein clasts. The strongly deformed conglomerate is intruded by buff -coloured intermediate porphyritic dykes, at the contact of which occur brecciated zones marked by strong carbonate-sericite alteration, disseminated pyrite, and quartz-tourmaline veinlets (Fig.13b). Immediately south of LDDZ, another conglomerate unit (>80 m thick) is intersected at the bottom of the

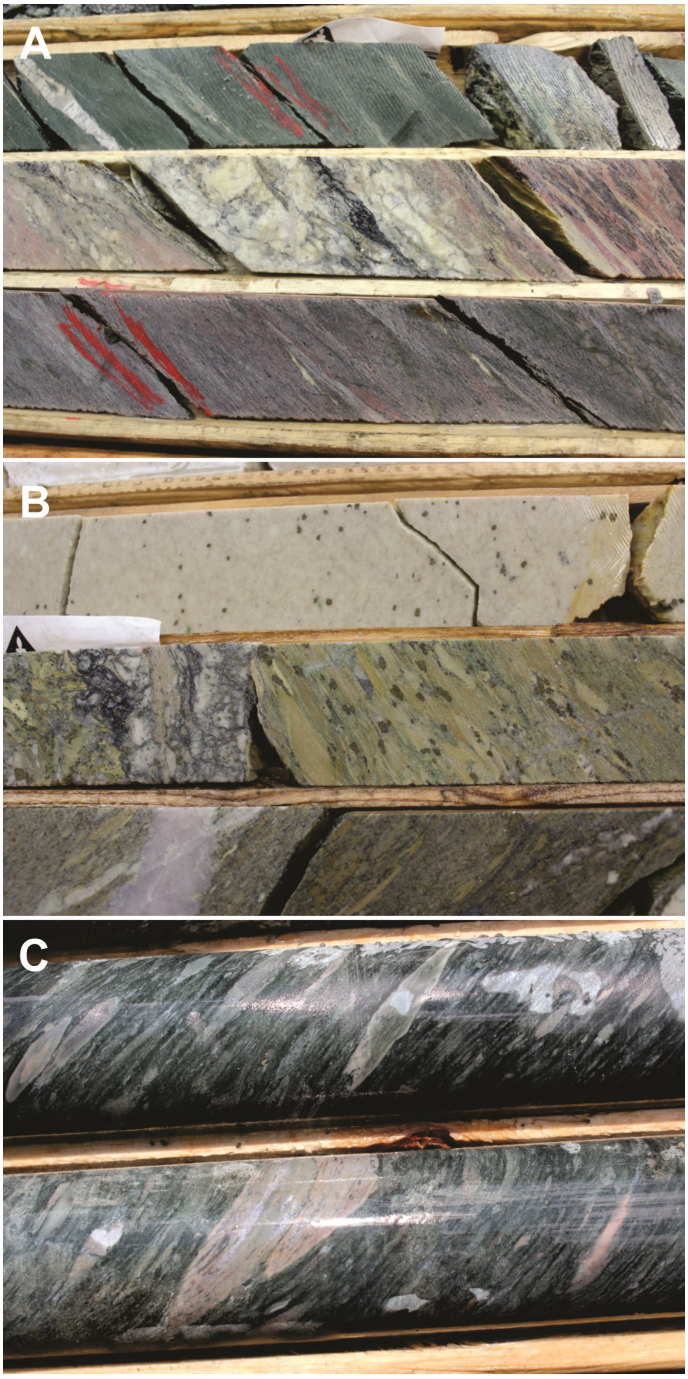

Figure 13. Photographs of drill core (NQ core diameter is 47.6 mm). a) Brecciated quartz-tourmaline-pyrite vein (anomalous in gold) at sheared contact between hematitized-sericitized felsic intrusive and chloritized mafic volcanic units. b) Contact between sericitized-pyritized intermediate feldspar porphyry and polygenic conglomerate, with brecciated zones marked by quartz-tourmaline veinlets in a 1.27 g/t Au/1 m interval. c) Highly strained polygenic conglomerate with mafic and lesser felsic volcanic clasts and hematitized fine-grained, locally porphyritic felsic intrusive clasts in a chlorite-rich matrix.

drillhole (PC in Fig. 2). Here again, the conglomerate is strongly deformed and intensely flattened polygenic clasts include mafic and felsic volcanic rocks, reddish porphyries, and chert (Fig. 13c).This setting shares analogies, but as a mirror image, with the position of the Lac Casault basin occurring northward along the SLDZ.

Discussion and future work

The ongoing study on the geological setting of the Detour Lake gold mine and various deposits and exploration properties along what we informally refer to as the Sunday Lake and Lower Detour gold trends, suggest that gold is distributed along, and structurally controlled by high-strain zones commonly occurring at contacts between different volcanic units or with competent intrusive rocks. These mineralized zones occur within regional deformation/fault zones or their subsidiary splays, which are spatially related to a Porcupine/Cadillac-like sedimentary basin and Timiskaming-like polygenic conglomerate, and to contacts between mafic-ultramafic volcanic assemblages, all locally intruded by intermediate to felsic, typically reddish, alkaline porphyritic dykes and plutons. Gold is associated with quartz-carbonate±tourmaline veins and/or silicified zones and disseminated to locally semi-massive sulphides in veins or as replacement in sericitized, chloritized or biotitized wall rocks. These relationships are analogous to various gold camps (e.g. Robert at al., 2005), such as those of the southern Abitibi belt (e.g. Bleeker, 2015; Dubé et al., 2017; Poulsen, 2017, and references therein). Geochemical and geochronological analyses are underway to document the lithotectonic setting and hydrothermal alteration signature, and better constrain the timing of deformation, magmatism, sedimentation and mineralization along both the Sunday Lake and Lower Detour gold trends.

Acknowledgments

This report is a contribution to NRCan's Targeted Geoscience Initiative Program (TGI). Support for this study was provided through the Gold Project's 'Activity G-1.1: Gold through space and time at the Archean'.

Detour Gold Corporation, Midland Exploration, Balmoral Resources, Probe Metals, SOQUEM and their exploration staff are acknowledged for giving access to their property, sharing knowledge and data sets, and providing logistical support. This report benefited from reviews by Jennifer Smith, Jeremy Powell and Neil Rogers.

References

Ayer, J.A., Chartrand, J.E., Duguet, M., Rainsford, D.R.B., and Trowell, N.F., 2009. Geological compilation of the Burntbush-Detour lakes area, Abitibi greenstone belt; Ontario Geological Survey, preliminary maps P3609, scale 1:100 000.

Ayer, J.A., Goutier, J., Thurston, P.C., Dubé, B., and Kamber,

B.S., 2010. Tectonic and metallogenic evolution of the Abitibi and Wawa subprovinces; *in* Summary of Fieldwork and Other Activities 2010; Ontario Geological Survey, Open Files Report 6260, p. 3-1–3-6.

Balmoral Resources, 2018a. Technical (N.I. 43-101) Report on the Martiniere Property, March 27, 2018; Balmoral Resources, 113 p. <http://www.balmoralresources.com/assets/docs/Martiniere%202018%20NI%2043-101%20report%20redsize-20180329174245.pdf> [accessed November 5, 2018]

Balmoral Resources, 2018b. The Detour East Property; Balmoral Resources <http://www.balmoralresources.com/projects/detour-east/mineralization> [accessed November 5, 2018]

Barrie, C.T. and Krogh, T.E., 1996. U-Pb zircon geochronology of the Selbaie Cu-Zn-Ag-Au Mine, Abitibi subprovince, Canada; Economic Geology, v. 91, p. 563–575.

Bleeker, W., 2015. Synorogenic gold mineralization in granite-greenstone terranes: The deep connection between extension, major faults, synorogenic clastic basins, magmatism, thrust inversion, and long-term preservation; *in* Targeted Geoscience Initiative 4: Contributions to the Understanding of Precambrian Lode Gold Deposits and Implications for Exploration, (ed.) B. Dubé and P. Mercier-Langevin; Geological Survey of Canada, Open File 7852, p. 25–47.

Castonguay, S., Dubé, B., Mercier-Langevin, P., McNicoll, V.J., DeLazzer, A., and Malcolm, K., 2018. Nature and significance of deformation zones on gold mineralization in the Detour Lake area: Implications for exploration in Ontario and Quebec; *in* Targeted Geoscience Initiative: 2017 Report of Activities, Volume 1, (ed.) N. Rogers; Geological Survey of Canada, Open File 8358, p. 105–111.

Davis, W.J., Machado, N., Gariépy, C., Sawyer, E.W., and Benn, K., 1995. U-Pb geochronology of the Opatica tonalite-gneiss belt and its relationship to the Abitibi greenstone belt, Superior Province, Quebec; Canadian Journal of Earth Sciences, v. 32, p. 113–127.

Detour Gold Corporation, 2017. Detour Lake operation Ontario, Canada: NI 43-101 Technical Report; Detour Gold Corporation, 304 p. <http://s22.q4cdn.com/327131108/files/doc_news/archive/DGC-PR-17-03-22-LOM-Plan.pdf> [accessed October 31, 2017]

Detour Gold Corporation, 2018. Detour Gold Reports an Initial Mineral Resource for Zone 58N; Detour Gold Corporation <https://s22.q4cdn.com/327131108/files/doc_news/2018/07/25/DGC-PR_18-07-25-Zone-58N-MR.pdf> [accessed November 5, 2018]

Dubé, B. and Gosselin, P., 2007. Greenstone-hosted quartz-carbonate vein deposits; *in* Mineral Deposits of Canada: A Synthesis of Major Deposit-Types, District Metallogeny, the Evolution of Geological Provinces, and Exploration Methods, (ed.) W.D. Goodfellow; Geological Association of Canada, Mineral Deposits Division, Special Publication No. 5, p. 49–73.

Dubé, B., Mercier-Langevin, P., Ayer, J., Atkinson, B., and Monecke, T., 2017. Orogenic greenstone-hosted quartz-carbonate gold deposits of the Timmins-Porcupine camp; *in* Archean Base and Precious Metal Deposits, southern Abitibi Greenstone Belt, Canada, (ed.) T. Monecke, P. Mercier-Langevin, and B. Dubé; Reviews in Economic Geology, v. 19, p. 51–79.

Dubosq, R., 2017. Assessing the structural and alteration controls on gold mineralization at Detour Lake mine, Ontario, Canada; M.Sc. thesis, University of Ottawa, Ottawa, Ontario, 278 p.

Dubosq, R., Lawley, C.J.M., Rogowitz, A., Schneider, D., and Jackson, S.E., 2018. Pyrite deformation and connections to gold mobility: Insight from micro-structural analysis and trace element mapping; Lithos, v. 310-311, p.86–104.

Faure, S., 2015. Prolongement de la faille Sunday Lake (mine Detour Gold, Ont.) au Québec et son potentiel pour les minéralisations aurifères et en métaux de base; CONSOREM Project Report 2013-02, 41 p.

Gosselin, P. and Dubé, B., 2005. Gold deposits of Canada: distribution, geological parameters and gold content; Geological Survey of Canada, Open File 4896, 105 p., 1 CD-ROM.

Lacroix, S., 1994. Géologie de la partie oust du sillon Harricana-Turgeon, Abitibi; Ministère des Ressources naturelles du Québec, MB 94-54, 26 p.

Lacroix, S., Simard, A., Pilote, P., and Dubé, L.M., 1990. Regional geologic elements and mineral potential resources of the Harricana-Turgeon belt, Abitibi of NW Quebec; *in* The northwestern Quebec Polymetallic Belt: A summary of 60 years of mining exploration, Proceedings of the Rouyn-Noranda 1990 symposium, (ed.) M. Rive, P. Verpaelst, Y. Gagnon, J.M. Lulin, G. Riverin and A. Simard; Canadian Institute of Mining and Metallurgy, Special Volume 43, p. 313–26.

Malcolm, K.J., Kontak, D.J., Tinkham, D.K., Ayer, J.A., and MacGillivray, G., 2015. The Lower Detour Lake Au discovery, Ontario, Canada: A high-grade oxidized intrusion-related Au deposit; Abstract 34977 *in* Abstracts and Proceedings; American Geophysical Union-Geological Association of Canada-Mineralogical Association of Canada-Canadian Geophysical Union Joint Assembly, Montréal, Quebec, p. 302–303.

Marmont, S., 1986. The geological setting of the Detour Lake gold mine, Ontario, Canada; *in* Gold '86: An International Symposium on the Geology of Gold Deposits, (ed.) A.J. Macdonald; Toronto, p. 3–22.

Mercier-Langevin, P., Hannington, M., Dubé, B., McNicoll, V., Goutier, J., and Monecke, T., 2011. Geodynamic influences on the genesis of Archean world-class gold-rich VMS deposits: examples from the Blake River Group, Abitibi greenstone belt, Canada; *in* Proceedings 11th Biennial Society of Geology Applied to Mineral Deposits, 26-29 Septem-

ber, 2011, Antofagasta, Chile, p. 85–87.

Midland Exploration, 2018. Midland et SOQUEM découvrent un important système aurifère (zone Vortex) de type "Syenite-Associated" à l'est de Detour Lake; Midland Exploration <http://www.midlandexploration.com/fr/Communique.aspx?ResourceId=00fcfdc2-9d04-45df-a69e-8eca5336e39b> [accessed November 5, 2018]

Oliver, J., Ayer, J., Dubé, B., Aubertin, R., Burson, M., Panneton, G., Friedman, R., and Hamilton, M., 2012. Structure, stratigraphy, U-Pb geochronology, and alteration characteristics of gold mineralization at the Detour Lake gold deposit, Ontario, Canada; Exploration and Mining Geology, v. 20, p. 1–30.

Poulsen, K.H., 2017. The Larder Lake-Cadillac Break and its gold districts; Reviews in Economic Geology, v. 19, p. 133–167.

Probe Metals, 2016. Probe Metals and SOQUEM Drill 17.5 g/t Au Over 1 Metre Along the Lower Detour Gold Trend and Commence Drilling on Phase II Program; Probe Metals <https://www.probemetals.com/site/assets/files/1069/2016-08-24_nr.pdf> [accessed November 5, 2018]

Probe Metals, 2018. Detour Quebec project overview Probe Metals <https://www.probemetals.com/projects/detour-quebec/overview/> [accessed November 5, 2018]

Robert, F., Poulsen, K.H., Cassidy, K.F., and Hodgson, C.J., 2005. Gold metallogeny of the Superior and Yilgarn Cratons; *in* Economic Geology 100th Anniversary Volume (1905–2005), (ed.) J.W. Hedenquist, J.F.H. Thompson, R.J. Goldfarb and J.P. Richards; Society of Economic Geologists, p. 1001–1033.

Thurston, P.C., Ayer, J.A., Goutier, J., and Hamilton, M.A., 2008. Depositional gaps in Abitibi greenstone belt stratigraphy: A key to exploration for syngenetic mineralization; Economic Geology, v. 103, p. 1097–1134.

Lithological and structural controls on the nature and distribution of gold at the LaRonde Zone 5 project, Doyon-Bousquet-LaRonde gold camp, Abitibi, Quebec

E. Boily-Auclair[1], P. Mercier-Langevin[2], P.-S. Ross[1] and D. Pitre[3]

[1]*Institut national de la recherche scientifique, Centre Eau Terre Environnement, 490 rue de la Couronne, Québec, Quebec G1K 9A9*

[2]*Geological Survey of Canada, 490 rue de la Couronne, Québec, Quebec G1K 9A9*

[3]*Agnico Eagle Mines limited, LaRonde Division, 2 chemin Bousquet, Preissac, Quebec J0Y 2E0*

Abstract

The LaRonde Zone 5 (LZ5) is in the Doyon-Bousquet-LaRonde mining camp (DBL), eastern Blake River Group, Abitibi greenstone belt. LaRonde Zone 5 and the satellite zones 4 and 4.1 are hosted within steeply south-dipping (80 –90°) and south-facing volcanic and volcaniclastic units (mafic to felsic tuff and lapilli tuff) of the lower member of the Bousquet Formation. The mineralization of all three zones consists of discordant networks of millimetre to centimetre thick pyrite±chalcopyrite veinlets (10–20 volume %) and, to a lesser extent, of very finely disseminated pyrite (1 volume %) in chlorite-carbonate-sericite alteration zones. Gold is present as microscopic inclusions in fine-grained granoblastic pyrite in both the veinlets and disseminations.

The study area was affected by major tectonic deformation and the mineralized zones were intensely transposed into the steeply dipping, east-trending penetrative foliation. Uncertainty remains about the exact timing of gold mineralization, deformation, and metamorphism. Also, the style of mineralization at LZ5 (pyrite±chalcopyrite veins and veinlets, ± disseminated pyrite) and its setting (mafic-intermediate rocks of the lower member of the Bousquet Formation) largely differs from most of the ore in the rest of the DBL, which is considered to be synvolcanic. Ongoing research at LZ5 aims to document the ore styles and setting, establish the relative timing of events, compare mineralization with the other ore styles of the camp and contribute to the metallogenic models for Archean gold deposits in the southern Superior Province.

Introduction

The LaRonde Zone 5 (LZ5) in the prolific Doyon-Bousquet -LaRonde mining camp (DBL) of the Blake River Group, the southern Abitibi greenstone belt (Fig. 1, 2), contained a defined resource as of December 31, 2017, of approximately 15 Mt of ore at 1.9 g/t Au with a total resource of 28 t Au (0.9 Moz) (Agnico Eagle Mines Ltd., 2018a). The LZ5 that was formerly part of the Bousquet 1 mine, and exploited in an open pit by Lac Minerals and Barrick Gold, is currently operated by Agnico Eagle Mines Ltd. as an underground mine. Although the DBL, and most of its deposits (LaRonde Penna 20 North lens, LaRonde Penna zone 6 and 7 and the 20 south lens; Fig. 3), have been extensively studied over recent years, limited or no access to LZ5 has prevented its complete integration in revised metallogenic models for the camp (e.g. Dubé et al., 2007, 2014; Mercier-Langevin et al., 2007a–d, 2009, 2017; Yergeau, 2015; Yergeau et al., 2015). Renewed exploration at LZ5 has provided the opportunity to study some of the stratigraphically lowermost mineralized ore zones of the camp (Fig. 3).

To gain a more comprehensive understanding of the LZ5 mineralized zones we aim to (1) accurately establish the stratigraphic position of the LZ5 mineralized corridors and the nature of the host rocks; (2) document the distribution of gold relative to key geological elements; and (3) define the mineral paragenesis and relative timing of events, with an emphasis on gold mineralization.

In this paper, we present preliminary observations from detailed underground mapping and drill-core logging that was conducted in the summer of 2018 and allowed acquisition of preliminary information about the LZ5 geology. Samples collected in this study were obtained from drill-core and underground stopes. In total, 251 samples were collected to provide a representative suite of LZ5 lithologies and mineralization. The samples were analyzed by Activation Laboratories, Lancaster, Ontario, and ALS Minerals, Val-d'Or, Quebec, for lithogeochemistry, with thin sections produced by Vancouver Petrographic. Ongoing compilation of available data, petrographic and lithogeochemical analysis of samples, and 3-D modelling of the deposit will help establish the nature of the auriferous zones at LZ5 and determine the relative importance of factors controlling the distribution of ore.

Corresponding author: Emile Boily-Auclair (emile.boily-auclair@ete.inrs.ca)

Boily-Auclair, E., Mercier-Langevin, P., Ross, P.-S., and Pitre, D., 2019. Lithological and structural controls on the nature and distribution of gold at the LaRonde Zone 5 project, Doyon-Bousquet-LaRonde gold camp, Abitibi, Quebec; *in* Targeted Geoscience Initiative: 2018 report of activities, (ed.) N. Rogers; Geological Survey of Canada, Open File 8549, p. 23–32. https://doi.org/10.4095/313631

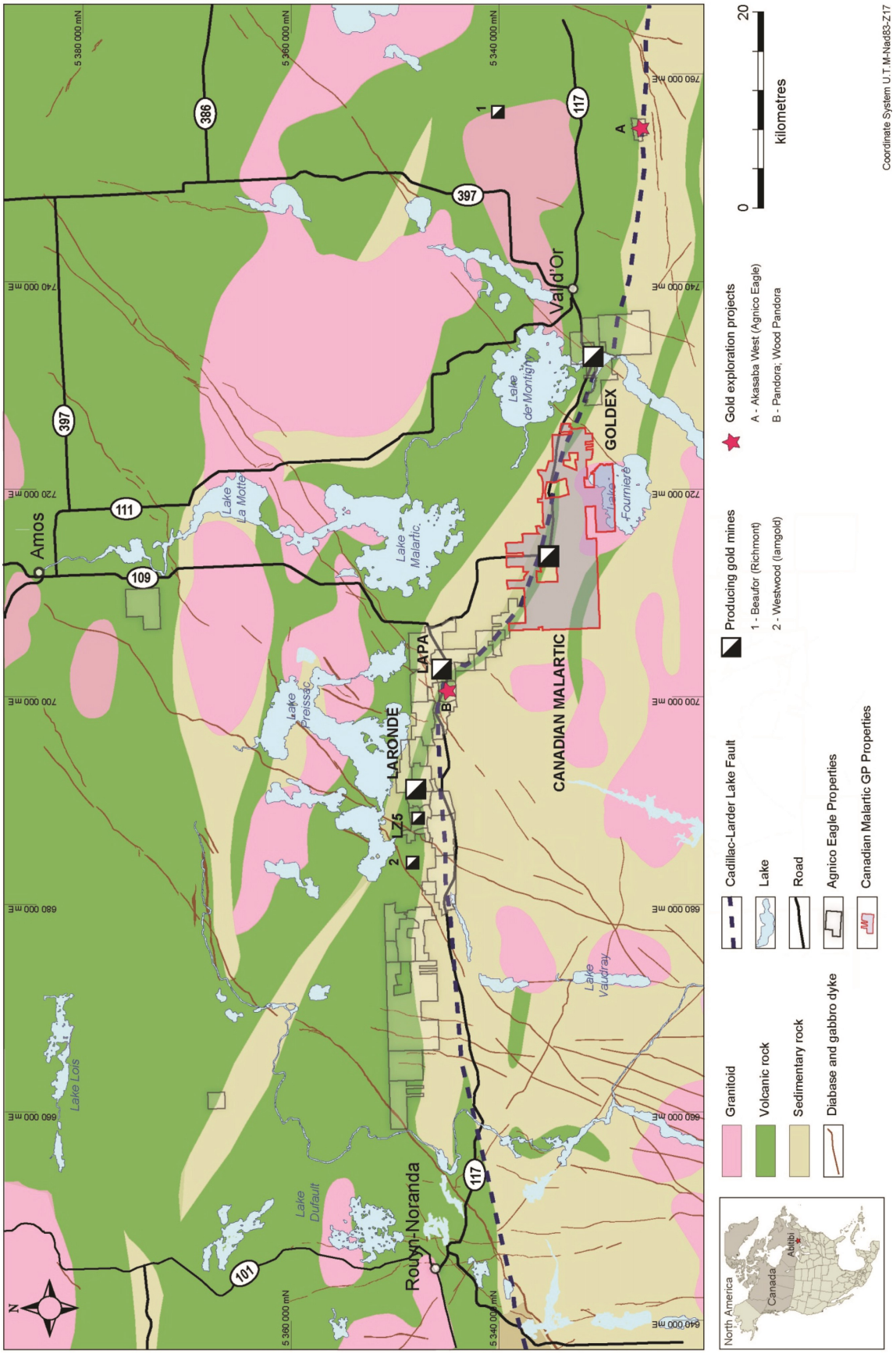

Figure 1. Geology of the southern Abitibi greenstone belt. From Agnico Eagle Mines Limited website. (2018b).

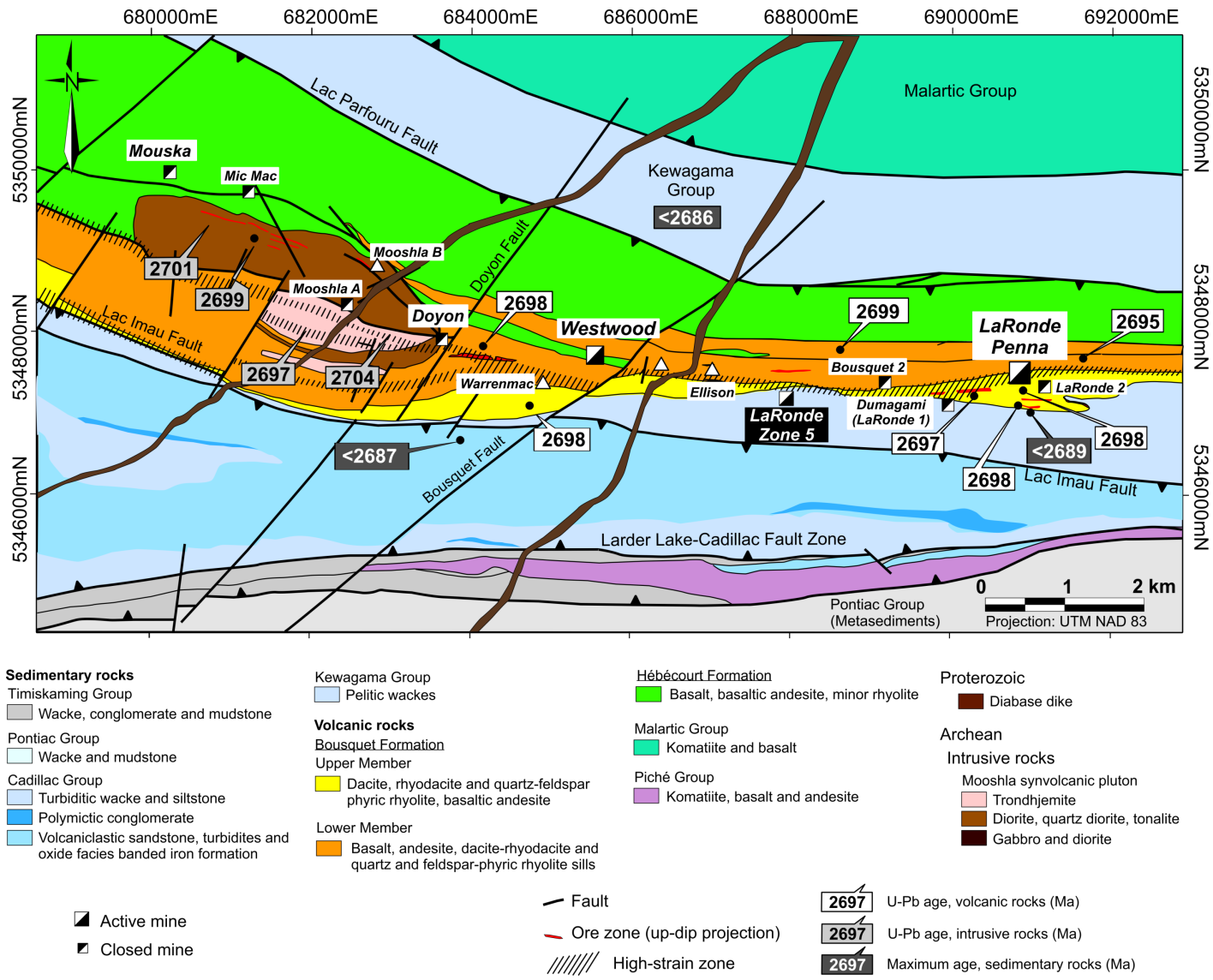

Figure 2. Geology of the Doyon-Bousquet-LaRonde mining camp. *From* Mercier-Langevin et al. (2017).

LaRonde Zone 5 deposit geology

The DBL has a total endowment of 71.3 Mt of ore at 3.91 g/t Au, for approximately 280 t Au (Mercier-Langevin et al., 2017). The stratigraphy of the DBL consists of a succession of volcanic and volcanoclastic rocks allocated to the Hébécourt and Bousquet formations that show a stratigraphic polarity to the south and form a tilted east-trending volcanic pile with subvertical dip (70–80˚) to the south (Fig. 2, 3). The Hébécourt Formation consists of tholeiitic basalt and basaltic andesite flows, with associated gabbro sills, and is stratigraphically overlain by the Bousquet Formation, which consists of basaltic to rhyolitic flows, domes, synvolcanic intrusions and volcaniclastic units (Lafrance et al., 2003).

Mineralization at LZ5 is hosted within a succession of volcanic and volcaniclastic units (tuff and lapilli tuff) that vary in composition from mafic to felsic (Fig. 4), and is spread over three separate mineralized horizons (namely zone 5 and satellite zones 4 and 4.1). The main ore horizon of LZ5 is hosted in dominantly mafic to intermediate massive rocks (Tourigny et al., 1992) that are tentatively correlated with those of the Bousquet heterogeneous unit (i.e. unit 4.4 of Lafrance et al., 2003; Fig. 3). The rocks are strongly deformed, moderately to intensely foliated, locally stretched and sheared into the main east-trending foliation that dips steeply to the south (Lafrance et al., 2003; Mercier-Langevin, 2005).

Gold grades are generally higher in zone 5 (mean 2.2 g/t for study samples; Boily-Auclair, work in progress, 2018) than in zones 4 and 4.1 (means 1.8 and 0.8 g/t for study samples; Boily -Auclair, work in progress, 2018). The LZ5 ore horizon has a maximum thickness of approximately 30 m and extends over approximately 600 m. Mineralization consists dominantly of millimetre to centimetre thick pyrite veinlet stockworks (10–20

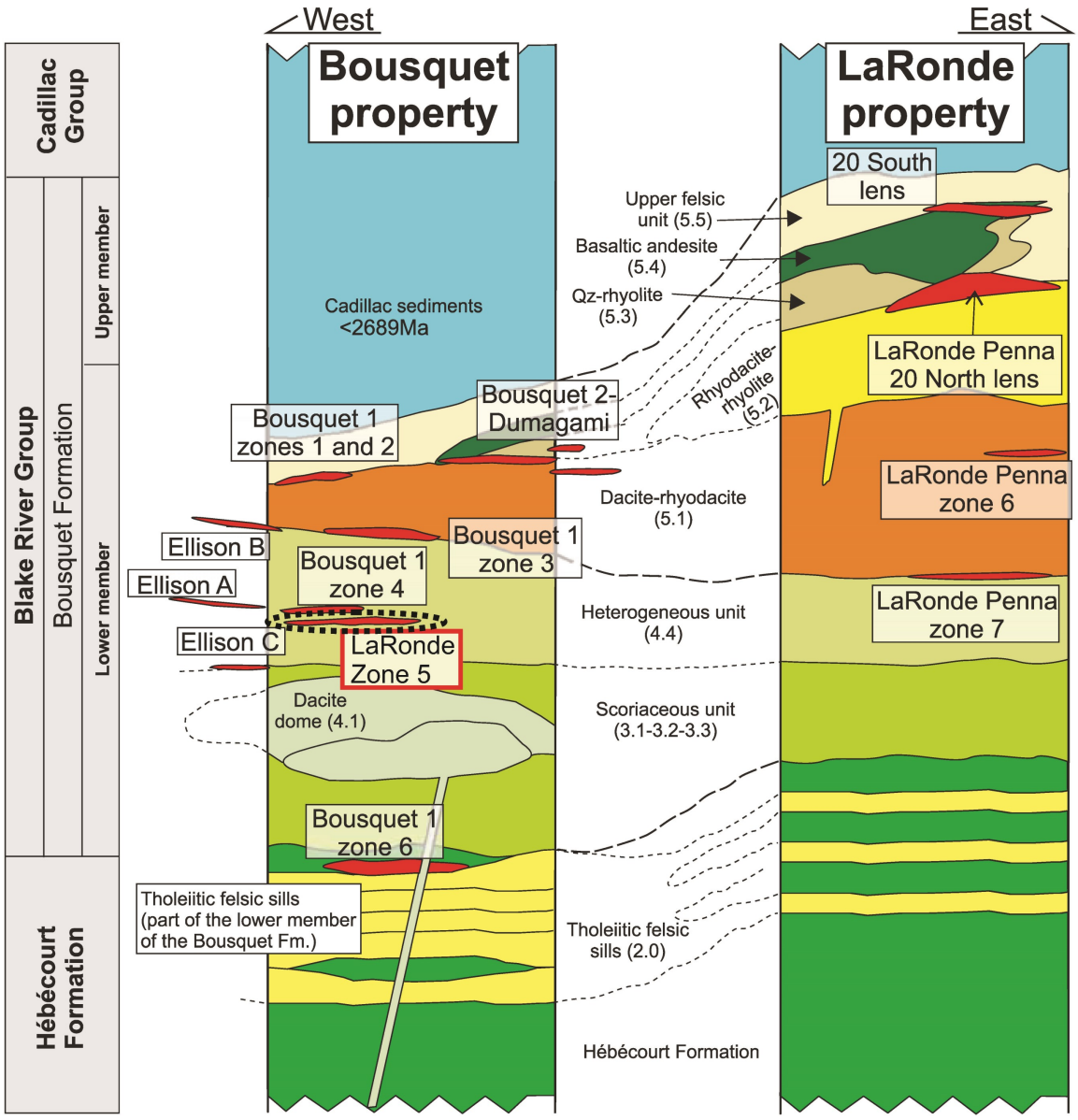

Figure 3. Simplified stratigraphy of the Doyon-Bousquet-LaRonde mining camp, showing the stratigraphic setting of the main ore lenses in the LaRonde Zone 5 project. The ore lenses are not to scale. *Modified from* Lafrance et al. (2003) and Mercier-Langevin et al. (2007d).

volume %) (Fig. 4a), along with to a lesser extent very finely disseminated pyrite (Fig. 4c), and clusters and/or elongated centimetre long fragments (≤10 volume %) (Fig. 4b, f). Chalcopyrite, sphalerite, and pyrrhotite are also present in minor to trace amounts in association with the pyrite. Gold is mainly present as inclusions in granoblastic pyrite and typically grades from 1 to 5 g/t over 0.5 to 1.5 m long intervals (Tourigny et al., 1989a, b). However, discordant, centimetre to decimetre thick quartz-carbonate veins are present within the mineralized zones (Fig. 4e). Gold grades of up to 60 g/t (Boily-Auclair, work in progress, 2018) have been obtained in some of these veins, which suggests that this may represent a separate auriferous event, or remobilization of previously formed mineralization. These veins commonly contain significant amounts (<30 volume %) of pyrite, chalcopyrite and/or sphalerite. Some are subparallel to foliation, but others are discordant to foliation. More work will be needed to fully understand the events that may have led to the formation of these high-grade veins.

Figure 5 shows the spatial distribution of the three mineralized bands that constitute the LZ5 project. Zone 4.1 consists of a discontinuous, variably mineralized corridor that is approximately 3 m wide (Fig. 5). Its horizontal and vertical continuity is difficult to estimate due to the lack of underground development and the scarcity of drill holes intersecting it. Zone 4 consists of a variably mineralized, 3 to 4 m thick corridor, charac-

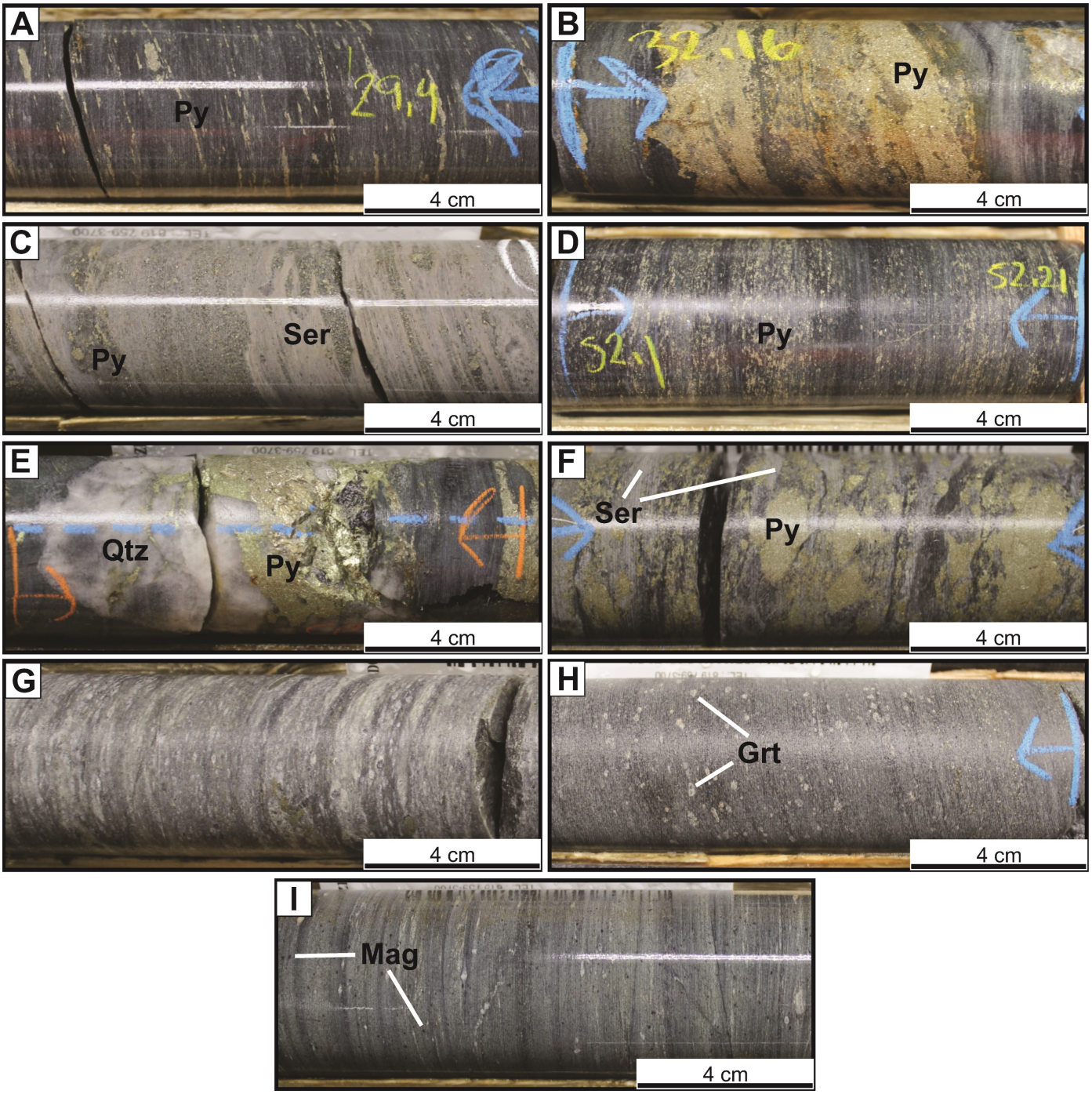

Figure 4. a) Massive and homogeneous andesitic rock (typical of Zone 5) with 10 to 12 volume % of millimetre thick pyrite stringers, drillhole BZ-0905120-1. b) Massive pyrite veins in an andesitic rock in Zone 5, drillhole BZ-0905120-1. c) Very fine grained, strongly sericitized unit. The mineralization is very finely disseminated in the matrix, Zone 4; drillhole BZ-1805136-1. d) Banded unit located north of Zone 5. Finely disseminated sulphides and discontinuous millimetre thick stringers; drillhole BZ-0905120-1. e) Quartz vein with a massive chalcopyrite cluster in a typical andesitic unit in Zone 5 (7.5 g/t Au); drillhole BZ-0905116-1. f) Centimetre thick pyrite fragments in an intermediate rock with sericitization of the matrix; drillhole BZ-0905116-1. g) Intermediate quartz-phyric unit; drillhole BZ-1805136-1. h) Intermediate unit with fine grained garnet porphyroblasts north of Zone 5, drillhole BZ-1805136-1. i) Intermediate unit with 1 volume % of millimetre wide magnetite; drillhole BZ-1805136-1 .

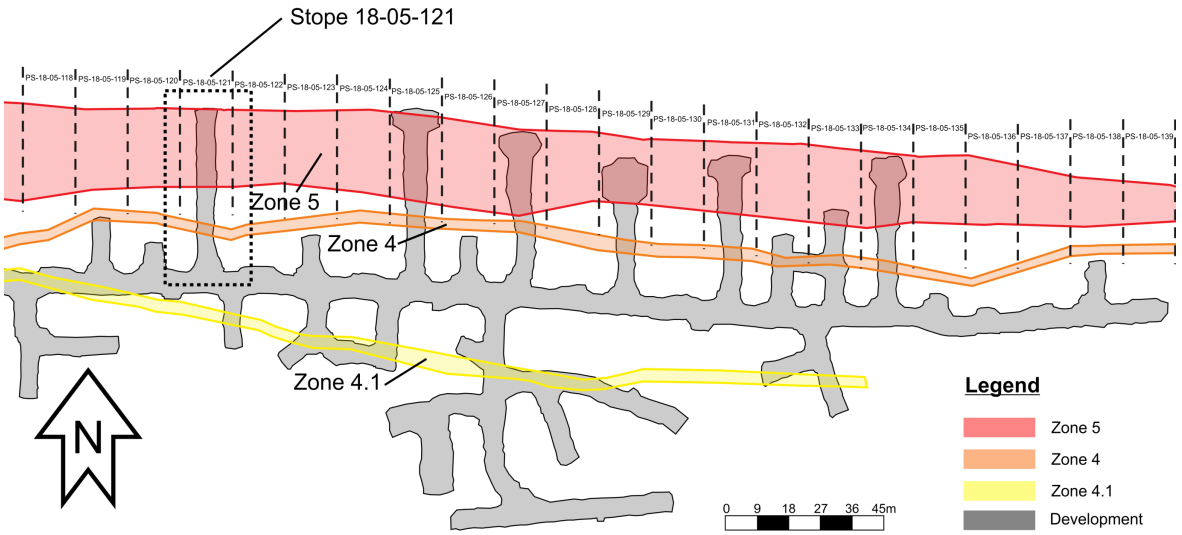

Figure 5. Plan view of mineralized zones 4, 4.1, and 5 on level 18 (180 m below surface) of the LaRonde Zone 5 deposit. *Modified from* Agnico Eagle Mines Ltd. (pers. comm., 2018).

terized by meter wide, intensely altered bands (mostly sericite) and is hosted in a fragmented intermediate tuff unit (Fig. 5). Zones 4.1 and 4 may merge to the west of the LZ5 deposit to form a single mineralized corridor. Mineralization in zones 4 and 4.1 is similar in style (stockwork), although sulphides are slightly less abundant (5–10 volume %).

The LZ5 mineralization has previously been interpreted as syntectonic (e.g. Tourigny et al., 1988, 1989a, b) or synvolcanic (e.g. Valliant and Barnett, 1982; Valliant and Hutchinson, 1982; Valliant et al., 1982, 1983; Mercier-Langevin et al., 2007c). The contrasting interpretations about the nature of the ore in the studied area result from ambiguous timing relationships between the sulphides, the associated gold and the structural features. At stope scale, the veinlets at LZ5 cross-cut each other and are often at a slight angle to or seemingly transposed into the foliation (Fig. 6). In section view, veinlets are commonly intensely folded and transposed (Fig. 7).

Throughout LZ5 multiple pale grey horizons that contrast strongly in colour with the surrounding rocks are present (Fig. 6). These bands, containing up to 20 volume % sulphides, have previously been classified as felsic tuff (Fig. 4c). Irregular contacts between the alteration fronts and the surrounding rocks, occasional decimetre thick quartz-carbonate veins on either side of the pale grey bands, and the presence of discordant centimetre wide faults across these pale bands suggest that they more likely represent hydrothermal alteration corridors (Boily-Auclair et al., 2017). The protoliths of the light grey bands correspond, for the most part, to fragmented tuff units of intermediate composition that have undergone significant sericitic alteration. It is noted though that the geochemical signature of

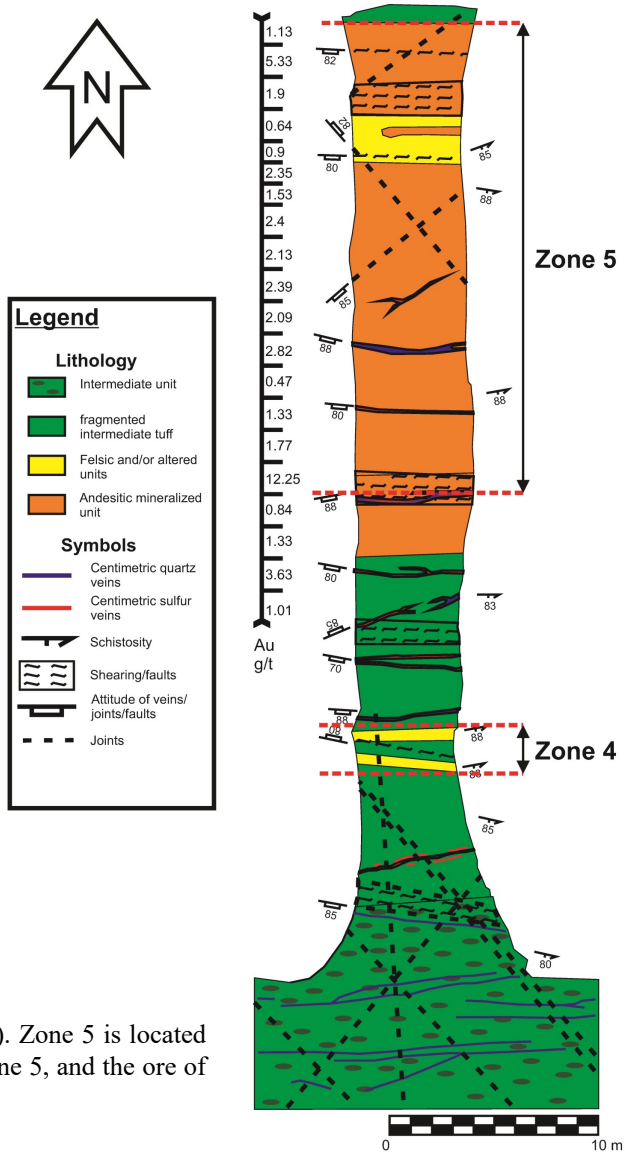

Figure 6. Plan view of stope 121 on level 18 (180 m below surface). Zone 5 is located between two intermediate tuff units. Zone 4 is not as wide as Zone 5, and the ore of Zone 4 is hosted in strongly altered intermediate and felsic rocks.

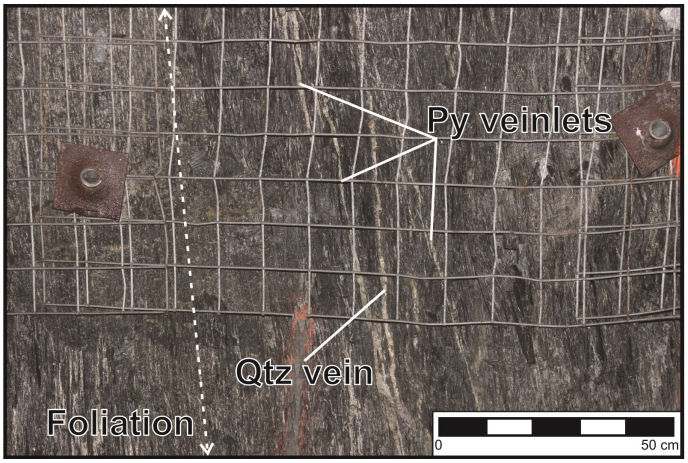

Figure 7 Typical mineralized andesite of Zone 5. The millimetre thick pyrite veinlets are at a slight angle to the foliation, seemingly transposed into the foliation. Some larger veinlets overlap each other and are even more transposed into the foliation, level 15, stope 121. Abbreviation: Py – pyrite.

one of the light grey bands studied does correspond to a felsic protolith. The discontinuity of this felsic unit indicates that it could be a small sill or lava flow. Petrography and lithogeochemical analyses of core samples taken along borehole S11-44 that crosscuts the entire LZ5 host succession were used to characterize the composition of the deposit's host rocks. The rocks are subalkaline and range in composition from basalt to rhyolite (Fig. 8), however, given the intense alteration (chlorite -carbonate-sericite) present the Zr/TiO_2 versus Nb/Y plot is likely the more reliable (Fig. 8b). The rocks hosting LZ5 show composition ranging from basalt to andesite, whereas the zone 4 host rocks are more evolved (Fig. 8b).

A geochemical profile of borehole S11-44 is shown in Figure 9 (analytical methods and data: Boily-Auclair, work in progress, 2018). With increasing downhole depths, an increase in Fe_2O_3 content, as well as a decrease in MnO content, marks the contact between the intermediate tuff and LZ5 mineralized andesite. The Al_2O_3 contents do not vary significantly across the different units. The MgO content increases, but the Na_2O content generally decreases in the main mineralized zone. In LZ5 mineralized andesite, a local decrease in gold content near 330 m appears to be accompanied by a decrease in the carbonate saturation index (CSI: $CO_2/(CaO + FeO + MgO + MnO)$ molar) of Kishida and Kerrich (1987) and a decrease in the carbonate discrimination index (CDI: CO_2/CaO molar) of Whitehead and Davies (1988), which could indicate that the mineralization is associated with iron-magnesium carbonate minerals. The local drop in gold content is also accompanied by an increase in Na_2O indicating that mineralization is closely related to alteration intensity. The CDI makes it possible to differentiate the types of carbonate minerals present and the CSI makes it possible to assess the intensity of carbonation. On the Nabil and Lafrance (2009) plot, which combines CSI and CDI, the samples plot in the calc-silicate and calcite-ankerite-

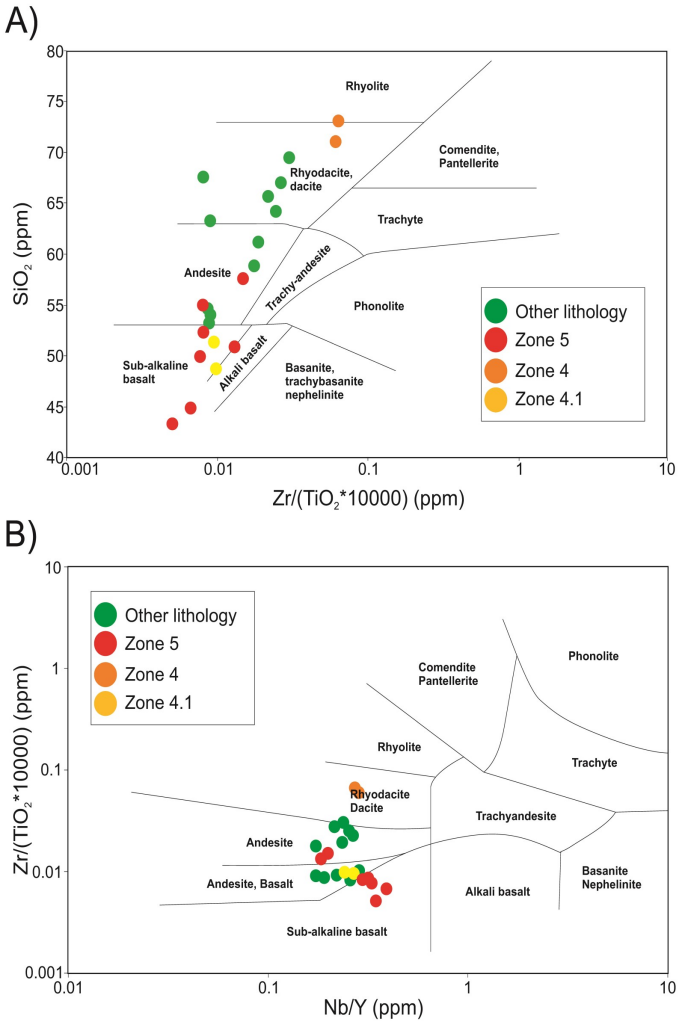

Figure 8. Lithological classification plots for volcanic rocks (Winchester and Floyd, 1977). a) SiO_2 vs. Zr/TiO_2. b) Zr/TiO_2 vs. Nb/Y. Samples from drillhole S11-44.

dolomite fields (Fig. 10). This plot can differentiate carbonate associated with orogenic deposits from those present in volcanogenic deposits, however as all the samples plot in the field of orogenic and/or volcanogenic deposits, this alone does not resolve the two competing origin hypotheses. In addition, this plot can help to differentiate between distal and proximal carbonate alterations (Nabil and Lafrance, 2009). The samples taken from zones 4, 4.1 and 5 plot mostly in the distal range, while other lithologies plot between the distal and proximal range. In the main mineralization (LZ5), there is also a slight increase in the Hashimoto alteration index (AI: $(100(MgO + K_2O)/(MgO + K_2O)/(MgO + K_2O + CaO + Na_2O + CaO + Na_2O))$ of Ishikawa et al. (1976), which quantifies magnesium chlorite and sericite alteration in volcanic environments, implying that the LZ5 has undergone strong alteration. Visual observation of drill core confirms that most of LZ5 is strongly chloritized. Copper is anomalous in the ore zone, and mimics the gold distribution.

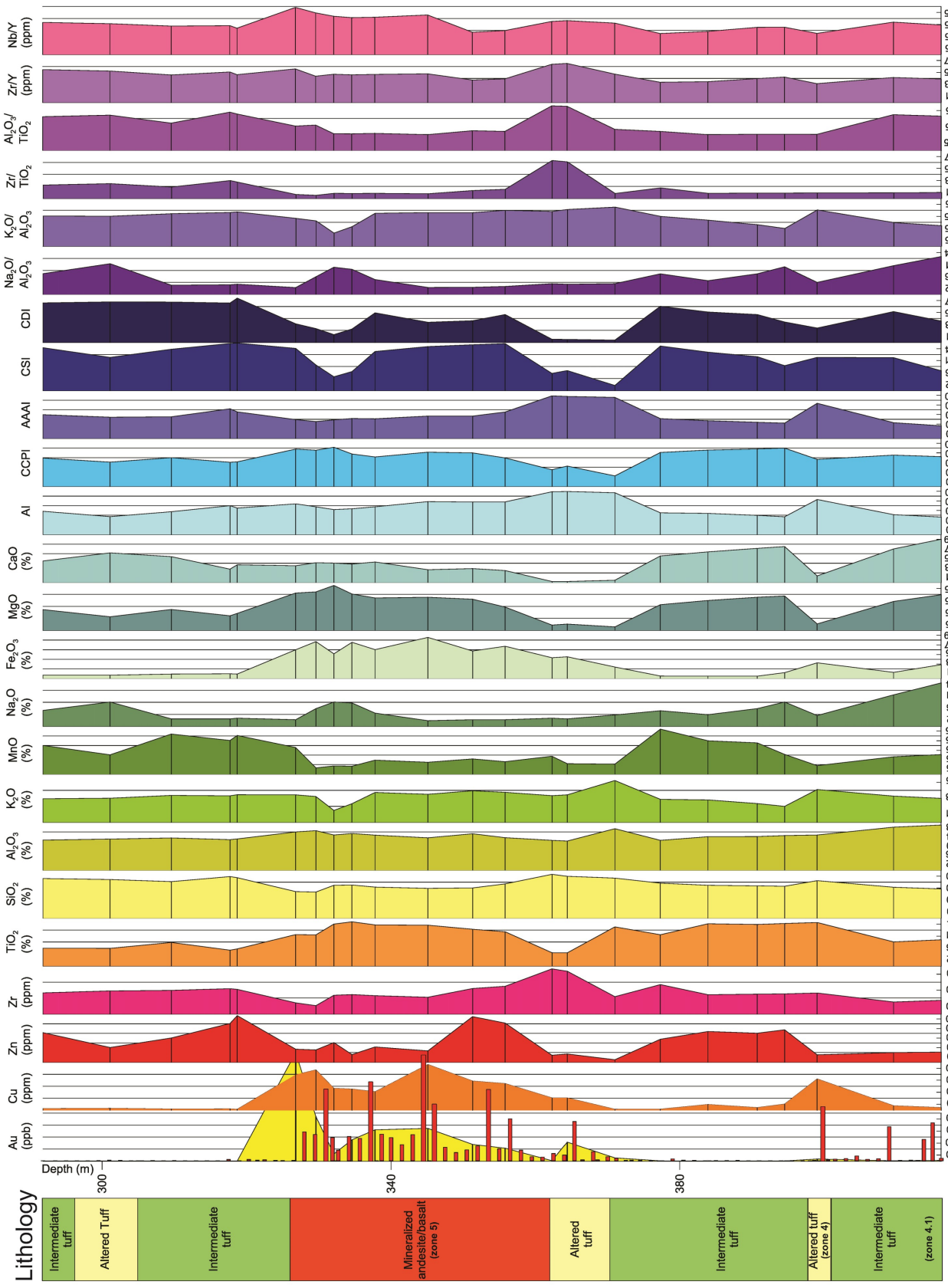

Figure 9. Geochemical profile of drillhole S11-44. Locations of samples and geochemical data are shown by short horizontal lines. Red bars in the Au column represent assays obtained by Agnico Eagle Mines Ltd. (pers. comm., 2018). AAAI – advanced argillic alteration index (Williams and Davidson, 2004); AI – Hashimoto alteration index (Ishikawa et al., 1976); CCPI – chlorite-carbonate-pyrite index (Large et al., 2001); CDI – carbonate discrimination index (Kishida and Kerrich, 1987); CSI – carbonate saturation index (Whitehead and Davies, 1988). All oxides are in weight %.

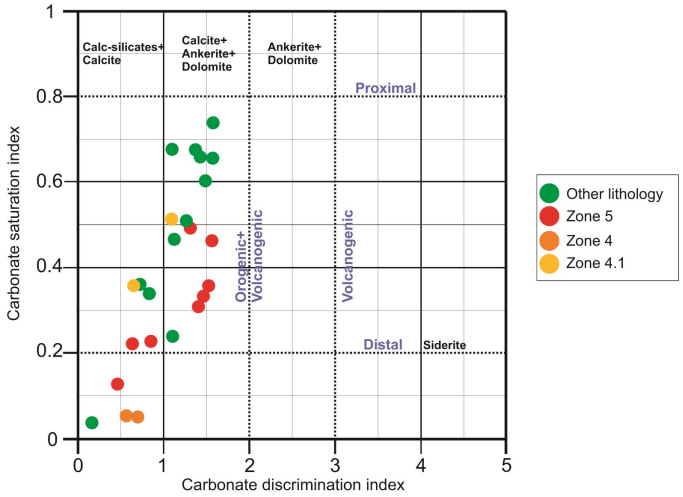

Figure 10. The carbonate alteration plot (Nabil and Lafrance, 2009) compares the carbonate discrimination index (CDI: Whitehead and Davies, 1988) with the carbonate saturation index (CSI: Kishida and Kerrich, 1987). Samples from drillhole S11-44.

Preliminary interpretations (largely from field observations) are that LZ5 mineralization is pre-main deformation, and thus probably synvolcanic, followed by strong deformation and potential local remobilization of gold into structural sites in a previously altered and mineralized corridor. This differs from previous interpretations that had sulphide mineralization as synvolcanic, but followed by an epigenetic episode of gold mineralization related to the main phase of regional metamorphism and tectonism (Tourigny et al., 1989a, b).

Future work

Future work will aim at properly documenting the nature of the host rocks and the style of mineralization of the LZ5 project at various scales. Analysis of lithogeochemical results, data compilation, detailed petrography and mineral chemistry (e.g. chlorite, carbonate minerals, garnet, white micas, biotite, feldspars), as well as 3-D modelling of the distribution of mineralization and alteration zones will advance understanding of the deposit's evolution and camp metallogeny.

Acknowledgments

This report is a contribution to NRCan's Targeted Geoscience Initiative Program (TGI). Support for this study was provided through the Gold Project's '*Activity G-1.1: Gold through space and time at the Archean*'.

Emile Boily-Auclair is conducting a TGI-supported M.Sc. study at the Institut national de la recherche scientifique – Centre Eau, Terre et Environnement, Québec. Agnico Eagle Mines Ltd., LaRonde Division, and its personnel, in particular D. Fortin, R. Dubuc, D. Pitre, D. Lussier and M. Bernier, are thanked for their support and access to the LaRonde Zone 5 deposit, access to the drill core and database, as well as for numerous constructive discussions. This report benefited from the review of Colter Kelly, Jennifer Smith and Neil Rogers.

References

Agnico Eagle Mines Ltd., 2018a. LaRonde mine operations; Agnico Eagle Mines Ltd. <https://www.agnicoeagle.com/English/operations-and-development-projects/operations/laronde/default.aspx> [accessed December 29, 2018]

Agnico Eagle Mines Ltd., 2018b. LaRonde mine geological maps; Agnico Eagle Mines Ltd. <https://www.agnicoeagle.com/English/operations-and-development-projects/operations/laronde/maps-and-surveys/default.aspx> [accessed December 29, 2018]

Boily-Auclair, E., 2017. Nature et style de l'altération hydrothermale associée aux minéralisations aurifères du projet LaRonde Zone 5 (LZ-5), Abitibi, Québec; B.Sc. thesis, Université Laval, Québec, Quebec, 69 p.

Dubé, B., Mercier-Langevin, P., Hannington, M., Lafrance, B., Gosselin, G., and Gosselin, P., 2007. The LaRonde Penna world-class Au-rich volcanogenic massive sulphide deposit, Abitibi, Québec: mineralogy and geochemistry of alteration and implications for genesis and exploration; Economic Geology, v. 102, p. 633–666.

Dubé, B., Mercier-Langevin, P., Kjarsgaard, I., Hannington, M., Bécu, V., Côté, J., Moorhead, J., Legault, M., and Bédard, N., 2014. The Bousquet 2-Dumagami world class Archean Au-rich volcanogenic massive sulfide deposit, Abitibi, Québec: Metamorphosed submarine advance argillic alteration footprint and genesis; Economic Geology, v. 109, p. 121–166.

Ishikawa, Y., Sawaguchi, T., Iwaya, S., and Horiuchi, M., 1976. Delineation of prospecting targets for Kuroko deposits based on modes of volcanism of underlying dacite and alteration haloes; Mining Geology, v. 26, p. 105–117.

Kishida, A. and Kerrich, R., 1987. Hydrothermal alteration zoning and gold concentration at the Kerr- Addison Archean lode gold deposit, Kirkland Lake, Ontario; Economic Geology, v. 82, p. 649–690.

Lafrance, B., Moorhead, J., and David, D.W., 2003. Cadre géologique du camp minier Doyon-Bousquet-LaRonde; Ministère des Ressources naturelles, de la Faune et des Parcs du Québec, report ET 2002-07, 45 p.

Large, R. R., Gemmell, J. B., Paulick, H., and Huston, D. L., 2001a. The alteration box plot: a simple approach to understanding the relationship between alteration mineralogy and lithogeochemistry associated with volcanic-hosted massive sulfide deposits. Economic Geology, v. 96, p. 957–971.

Mercier-Langevin, P., 2005. Géologie du gisement de sulfures massifs volcanogènes aurifères LaRonde, Abitibi, Québec; Ph.D. thesis, Institut national de la Recherche scientifique – Centre Eau, Terre et Environnement, Québec, Quebec, 694 p.

Mercier-Langevin, P., Dubé, B., Hannington, M.D., Davis, D.,

Lafrance, B., and Gosselin, G., 2007a. The LaRonde Penna Au-rich volcanogenic massive sulphide deposit, Abitibi greenstone belt, Quebec: Part I. Geology and geochronology; Economic Geology, v. 102, p. 585–609.

Mercier-Langevin, P., Dubé, B., Hannington, M.D., Richer-Laflèche, M., and Gosselin, G., 2007b. The LaRonde Penna Au-rich volcanogenic massive sulphide deposit, Abitibi greenstone belt, Quebec: Part II. Lithogeochemistry and paleotectonic setting; Economic Geology, v. 102, p. 611–631.

Mercier-Langevin, P., Dubé, B., Lafrance, B., Hannington, M., Galley, A., Moorhead, J., and Gosselin, P., 2007c. Metallogeny of the Doyon-Bousquet-LaRonde mining camp, Abitibi greenstone belt, Quebec; *in* Mineral Deposits of Canada: A Synthesis of Major Deposit Types, District Metallogeny, the Evolution of Geological Provinces, and Exploration Methods; Geological Association of Canada, Mineral Deposits Division, Special Publication No. 5, p. 673–701.

Mercier-Langevin, P., Dubé, B., Lafrance, B., Hannington, M.D., Galley, A., and Moorhead, J., 2007d. A group of papers devoted to the LaRonde Penna Au-rich volcanogenic massive sulfide deposit, eastern Blake River Group, Abitibi greenstone belt, Quebec: Preface: Economic Geology, v.102, P. 577–583.

Mercier-Langevin, P., Wright-Holfeld, A., Dubé, B., Bernier, C., Houle, N., Savoie, A., and Simard, P., 2009. Stratigraphic setting of the Westwood-Warrenmac ore zones, Westwood Project, Doyon-Bousquet-LaRonde mining camp, Abitibi, Québec; Geological Survey of Canada, Current Research Paper 2009-3, 20 p.

Mercier-Langevin, P., Dubé, B., Blanchet, F., Pitre, D., and Laberge, A., 2017. The LaRonde Penna Au-rich volcanic-hosted massive sulfide deposit; Reviews in Economic Geology, v. 19, p. 225–245.

Nabil, H. and Lafrance, B., 2009. Outil de discrimination des carbonates et exemples d'applications pour l'exploration; CONSOREM workshop, Québec Exploration conference 2009, Ministère des Ressources Naturelles et Faune. <http://www.consorem.ca/presentation_pub/quebec_exploration_2009/quebec_exploration_2009_ateliers/Outil%20carbonatation%20Atelier%20QC%20Explo%202009.pdf> [accessed December 29, 2018]

Tourigny, G., Hubert, C., Brown, A.C., and Crépeau, R., 1988. Structural geology of the Blake River at the Bousquet mine, Abitibi, Quebec; Canadian Journal of Earth Sciences, v. 25, p. 581–592.

Tourigny, G., Brown, A.C., Hubert, C., and Crépeau, R., 1989a. Synvolcanic and syntectonic gold mineralization at the Bousquet mine, Abitibi greenstone belt, Quebec; Economic Geology, v. 84, p. 1875–1890.

Tourigny, G., Hubert, C., Brown, A.C., and Crépeau, R., 1989b. Structural control on gold mineralization at the Bousquet mine, Abitibi, Quebec; Canadian Journal of Earth Sciences, v. 26, p. 157–175.

Tourigny, G., Hubert, C., Brown, A.C., Crépeau, R., Trudel, P., Hoy, L., and Kheang, L., 1992. Géologie de la mine Bousquet; Ministère de l'Énergie et des Ressources du Québec, ET 89-09, 99 p.

Valliant, R.I. and Barnett, R.L., 1982. Manganiferous garnet underlying the Bousquet gold orebody, Quebec: metamorphosed manganese sediment as a guide to gold ore; Canadian Journal of Earth Sciences. v. 19, p. 993–1010.

Valliant, R.I. and Hutchinson, R.W., 1982. Stratigraphic distribution and genesis of gold deposits, Bousquet region, Northwestern Quebec; *in* Geology of Canadian Gold Deposits, (ed.) R.W. Hodder and W. Petruk; Canadian Institute of Mining, Metallurgy, and Petroleum, Special Volume 24, p. 27–40.

Valliant, R.I., Mongeau, C., and Doucet, R., 1982. The Bousquet pyritic gold deposit, Bousquet region, Quebec: descriptive geology and preliminary interpretations on genesis; *in* Geology of Canadian Gold Deposits, (ed.) R.W. Hodder and W. Petruk; Canadian Institute of Mining, Metallurgy, and Petroleum, Special Volume 24, p. 41–49.

Valliant, R.I., Barnett, R.L., and Hodder, R.W., 1983. Aluminium silicate-bearing rock and its relation to gold mineralization: Bousquet mine, Bousquet township, Quebec; Canadian Institute of Mining, Metallurgy, and Petroleum Bulletin, v. 76, p. 81–90.

Whitehead, R.E. and Davies, J.F., 1988. Discriminant analysis involving CO_2/CaO and arsenic in gold exploration; Journal of Geochemical Exploration, v. 30, p. 243–253.

Williams, N.C. and Davidson, G.J., 2004. Possible submarine advanced argillic alteration at the Basin Lake prospect, western Tasmania, Australia; Economic Geology, v. 99, p. 987–1002.

Winchester, J.A. and Floyd, P.A., 1977. Geochemical discrimination of different magma series and their differentiation products using immobile elements; Chemical Geology, v. 20, p. 325–343.

Yergeau, D., 2015. Géologie du gisement synvolcanique aurifère atypique Westwood, Abitibi, Québec; Ph.D. thesis, Institut national de la recherche scientifique. – Centre Eau, Terre et Environnement, Québec, Quebec, 643 p.

Yergeau, D., Mercier-Langevin, P., Dubé, B., Malo, M., McNicoll, V.J., Jackson, S.E., Savoie, A., and La Rochelle, F., 2015. The Archean Westwood Au deposit, southern Abitibi: telescoped Au-rich VMS and intrusion-related Au systems; in Targeted Geoscience Initiative 4: Contributions to the understanding of Precambrian lode gold deposits and implications for exploration, (ed.) B. Dubé and P. Mercier-Langevin; Geological Survey of Canada, Open File 7852, p. 177–191.

Characteristics of diagenetic and epigenetic sulphides in deformed and metamorphosed Archean carbonaceous metasedimentary rocks of the Timmins-Matheson corridor: establishing a framework for fingerprinting ore-forming processes in shear zone-hosted orogenic gold systems

J.-L. Pilote[1], S.E. Jackson[2], P. Mercier-Langevin[1], B. Dubé[1] and D. Rhys[3]

[1]*Geological Survey of Canada, 490 rue de la Couronne, Québec, Quebec G1K 9A9*
[2]*Geological Survey of Canada, 601 Booth Street, Ottawa, Ontario K1A 0E8*
[3]*Panterra Geoservices Inc., 14180 Greencrest Drive, Surrey, British Columbia V4P 1L9*

Abstract

This research activity investigates the origin of gold-rich (up to approximately 10 ppm) iron sulphide nodules and the timing of gold introduction in Archean carbonaceous metasedimentary rocks near and distal to orogenic gold mineralization in the Timmins-Matheson area, Ontario. It provides insights into the factors controlling gold enrichment and tests the hypothesis asserting a genetic link between sedimentary sulphides and orogenic gold deposits. Preliminary textural examination of numerous iron sulphide (e.g. pyrite) nodules hosted in various sedimentary sequences from assemblages, including Kidd-Munro, Tisdale, Porcupine, and Timiskaming, reveals evidence of nucleation and formation prior to the main regional deformation events. Pyrite grains that are unequivocally metamorphic/hydrothermal in origin (e.g. coarse-grained euhedral porphyroblasts, overgrowths, and cross-cutting stringers) show distinct geochemical signatures compared to the nodules, with lower contents of Sb, Tl, Ag and Au. There are also consistent intra-nodule chemical trends, including, for example, systematic decreases in Au and Ni/Tl from core to rim. These trends are observed across the region, regardless of the setting of the nodules (i.e. shear-hosted, proximal or distal to mineralization, stratigraphic depths). The systematic core to rim decrease in gold content may reflect increasing pH and/or redox potential of the ambient fluid during the development of the nodules. Further geochemical and isotopic work is being conducted to better understand the genesis of the gold-rich nodules and any potential genetic link that may exist between orogenic Au mineralization and an earlier gold enrichment event in the Timmins-Matheson area.

Introduction

Sulphides in ancient carbonaceous metasedimentary units that host or are proximal to orogenic quartz-carbonate gold deposits have received a significant amount of attention in recent years, mainly due to a growing interest in the hypothesis that gold-enriched sedimentary pyrite could be a primary source of gold in some deposits (e.g. Mumin et al., 1994; Large et al., 2007). Some workers have suggested that the trace element composition of pyrite can be used as a fertility proxy to vector towards gold mineralization (Sack et al., 2018). The applicability of this premise remains to be tested for different gold deposit types. The Timmins-Matheson area (Fig. 1) in the western Abitibi greenstone belt offers an opportunity to determine if the iron sulphides in several volcano-sedimentary assemblages in a region that is well endowed in gold mineralization (>75 Moz Au produced: Dubé et al., 2017) served as a source of gold in the deposits in the area.

Among the various features present in carbonaceous metasedimentary rocks, iron sulphide nodules present unique characteristics, including concentric textural zoning, which is also reflected by their geochemical compositions. Remarkably, some of these nodules can contain up to about 10 ppm Au in their cores or concentric layers (Jackson et al., 2017), raising many questions regarding the timing of, and controls on this enrichment. Addressing these questions will provide further constraints on the possible genetic relationships between gold-enriched sulphide nodules, fertility of a region, and the development and timing of orogenic gold mineralization.

It is widely accepted that iron sulphide nodules in near unmetamorphosed to weakly metamorphosed sedimentary packages are products of diagenetic processes (e.g. Raiswell, 1982; Rickard, 2012). In structurally complex settings, however, where volcano-sedimentary sequences with carbonaceous mudstone horizons are affected by polyphase deformation and overprinted by greenschist metamorphism or higher and/or ore-related hydrothermal alteration, the assertion that the nodules originated from diagenesis and were preserved throughout the

Corresponding author: Jean-Luc Pilote (jean-luc.pilote@canada.ca)

Pilote, J.-L., Jackson, S.E., Mercier-Langevin, P., Dubé, B., and Rhys, D., 2019. Characteristics of diagenetic and epigenetic sulphides in deformed and metamorphosed Archean carbonaceous metasedimentary rocks of the Timmins-Matheson corridor: establishing a framework for fingerprinting ore-forming processes in shear zone-hosted orogenic gold systems ; *in* Targeted Geoscience Initiative: 2018 report of activities, (ed.) N. Rogers; Geological Survey of Canada, Open File 8549, p. 33–41. https://doi.org/10.4095/313632

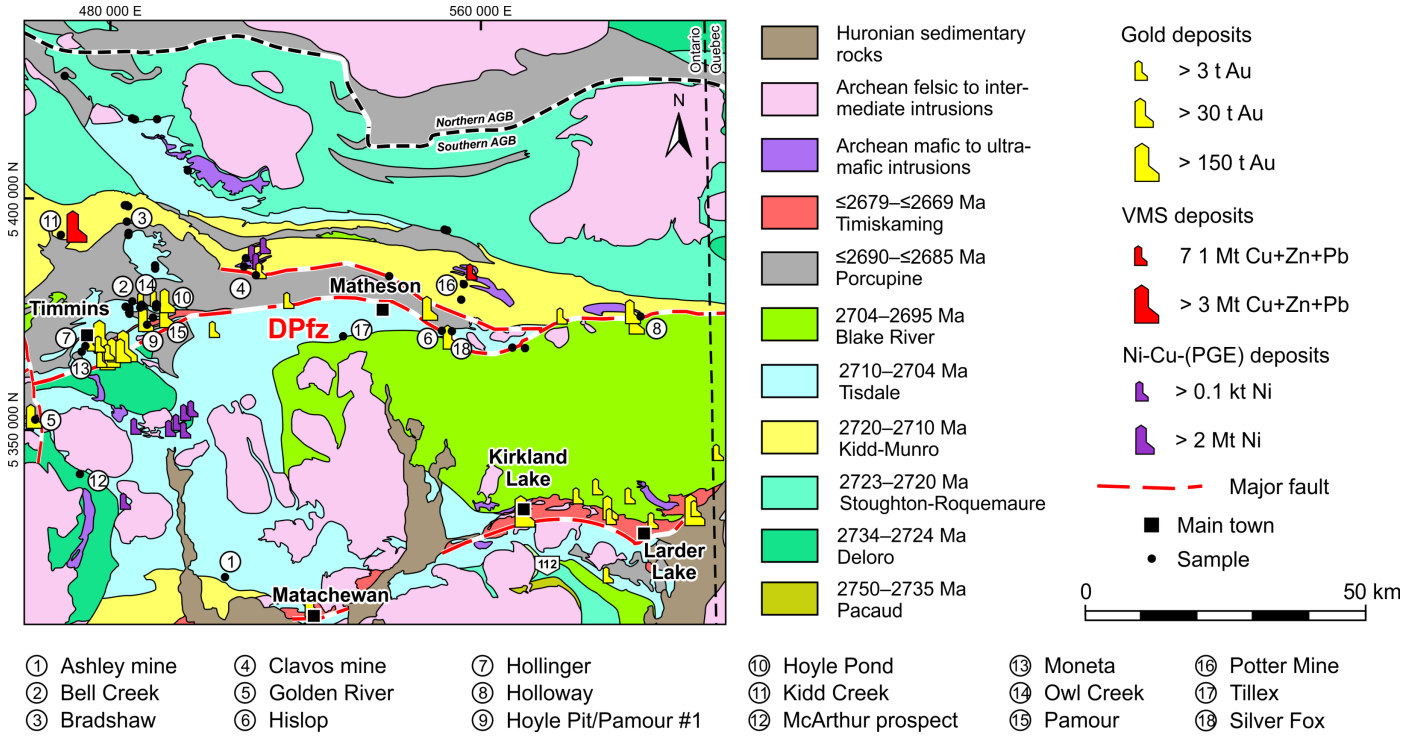

Figure 1. Simplified geological map of the western portion of the southern Abitibi greenstone belt (AGB) and locations of samples collected (note: only analyzed samples are numbered). Map *after* Dubé et al. (2017), *modified from* Thurston et al. (2008). DPfz = Destor-Porpcupine fault zone.

overprinting events becomes equivocal. As stated in Jackson et al. (2017), preliminary observations at mega- to mesoscopic scales suggested that the nodules at the Bell Creek, Hoyle Pond, and Holloway deposits in the Timmins-Matheson area are restricted to high-strain zones, proximal to shear-hosted gold mineralized quartz-carbonate veins, suggesting that they could be of hydrothermal, rather than diagenetic, origin. Multi-ppm abundances of Au in similar pyrite nodules have been measured in the southern Abitibi greenstone belt through this activity and other studies (e.g. Kingston, 1987; Jonasson et al., 1999; Gray and Hutchinson, 2001; Mercier-Langevin et al., 2016; Jackson et al., 2017).

Access to new sample material, together with recent developments in laser ablation inductively coupled plasma mass spectrometry (LA-ICP-MS) element mapping techniques (Jackson et al., 2017) present the opportunity to conduct a thorough, multi-disciplinary, and multi-scale investigation to constrain the timing of the formation of the argillite-hosted iron sulphide nodules of the Timmins-Matheson corridor. The same is true for other sulphide textures/generations commonly spatially associated with gold deposits. Additionally, characterizing in a systematic and detailed way the various sulphide textures, including argillite-hosted iron sulphide nodules, and defining their paragenetic evolution provides an expanding framework on which geochemical and isotopic work can be conducted. If the nodules are mainly of diagenetic nature throughout the region, then the question whether the sedimentary sulphides were a potential source of metals to the auriferous systems can be addressed. If, however, the nodules are of hydrothermal origin, or are multi-stage, with diagenetic cores and hydrothermal overgrowths, some of their features (e.g. concentric zoning expressed by fluctuating element abundances and textural changes) could potentially be used as proxies of the physico-chemical conditions of the ore-forming fluids. The origin of the nodules and the timing of gold introduction are the two critical aspects that need to be addressed. This report highlights some key observations and preliminary results substantiating the timing of formation of pyrite nodules in carbonaceous argillite of the Timmins-Matheson area.

Sampling strategies and analytical methods

Samples were collected or provided to us by collaborators from 18 gold deposits and prospects that occur over a large portion of the Timmins-Matheson area (Fig. 1). These deposits/prospects occur in various units, including (from oldest to youngest) interflow sedimentary horizons within the Kidd-Munro and Tisdale assemblages, lowermost portions of the deep-water basin-related Porcupine assemblage, and the synorogenic clastic sedimentary rocks of the Timiskaming assemblage. The depositional age of these assemblages spans a range of more than 50 Ma, from approximately 2720 to 2669 Ma (e.g. Bleeker and van Breemen, 2011; Frieman et al., 2017). Sampling was conducted on a number of scales, includ-

ing: 1) proximal (≤5 m) and peripheral (>5 m) to known mineralization; 2) laterally and vertically along strike within units that are cut by ore zones; 3) at different stratigraphic depths along ore-bearing or mineralized structures; 4) within carbonaceous metasedimentary units that are structurally bounded by shear zones; and 5) within mineralized zones that have entrained primary or secondary carbonaceous material. Intrusive and volcanic rocks containing epigenetic sulphides were also sampled for geochemical comparison with carbonaceous wall rocks and mineralized vein-hosted sulphides. This systematic approach allows us to examine variations in the geochemical and textural nature of the sulphides and evaluate their chronological relationship to mineralization and deformation.

Two deposits were visited during the 2017 and 2018 field seasons, the Bell Creek and Bradshaw gold deposits, where sampling was carried out underground and in strategically selected drill cores. Samples were then prepared for petrographic, scanning electron microprobe (SEM), and LA-ICP-MS analyses. Over 1000 in situ analyses have been completed so far and 20 element maps have been generated by LA-ICP-MS.

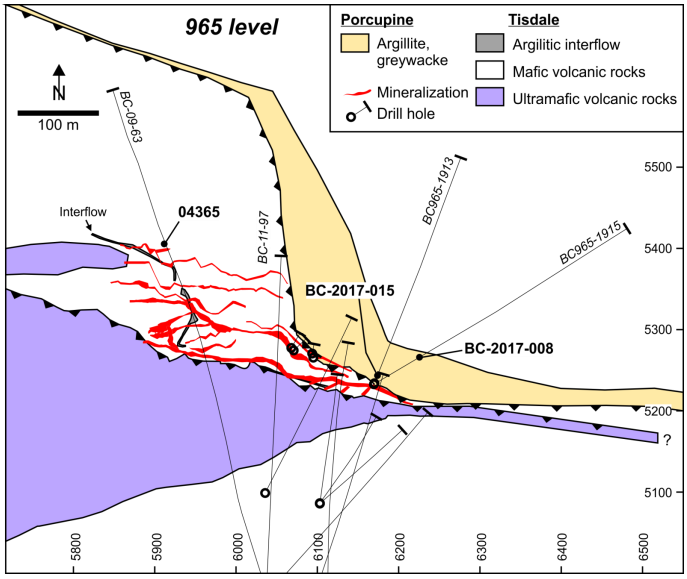

Figure 2. Plan view map of level 965 at the Bell Creek deposit and sample location (*after* unpublished map A. Camuti, Tahoe Canada, pers. comm., 2018).

Morphologies, textural, and preliminary geochemical characteristics of iron sulphide nodules of the Timmins-Matheson area

Several key field and geochemical observations were made during the 2018 field season, including the documentation of textures that are common to all the sulphide nodules throughout the Timmins-Matheson area.

1) At the Bell Creek gold deposit, nodules occur in interflow sediments between mafic volcanic rocks of the Tisdale assemblage, which is host to the mineralization (Fig. 2). The nodules are composed of pyrite and typically developed most abundantly along bedding planes. The pyrite has recorded at least one of the two principal phases of shortening that are apparent in the area, and nodules are transposed along the overprinting deformation fabric (Fig. 3).
2) Pyrite nodules occur at all stratigraphic depths in the overlying wedge of ore-barren Porcupine assemblage at Bell Creek (Fig. 2, 4a, b). Although the nodules vary in size (about 0.5–3 cm), their distribution is not controlled by proximity to gold mineralization or quartz-carbonate veins. Other Porcupine assemblage wedges to the south of Bell Creek, intersected by historical drillholes, contain pyrite nodules (not shown).
3) A semi-massive layer of abundant pyrite nodules that locally coalesce into pyritic layers in an interflow mudstone unit in ultramafic and mafic volcanic flows at the Bradshaw deposit contains thin, millimetre thick, boudinaged silty layers in which elongated concretions/nodules are developed (Fig. 4c). Locally, the coarser grained nature of the sedimentary rock extends across the entire band of pyrite, where it sharply transitions to a more massive, inclusion-free mass (Fig. 4d). Some of these in situ nodules containing the bedding-parallel features were rotated during deformation, showing an oblique relationship to bedding in the host unit. Nodules developed in adjacent mudstone layers contain non-sulphide inclusions of much smaller grain size (Fig. 4e), which indicates that the size of the inclusions inside the nodules reflects the grain size of the sediment in which the nodule grew.
4) In situ bedding features like those present at Bradshaw also occur in a sulphide breccia unit 9 km east-southeast of Bradshaw. These bedding features in a transported semi-massive sulphide horizon reflect their primary nature (Fig. 4f).
5) Trails of non-sulphide inclusions occur in pyrite nodules at the Owl Creek, Bell Creek, Bradshaw, and Silver Fox (80 km east of Timmins) gold deposits. The inclusions are generally equigranular and angular, and show limited point contacts between grains. They form an assemblage of quartz, plagioclase, calcite, muscovite, and potassium-feldspars with trace amounts of apatite, ilmenite, and titanite. These trails are interpreted as relicts of the bedding on which the nodules grew.
6) Evidence for the interpreted relicts of sedimentary bedding within the nodules is also shown on LA-ICP-MS element maps, where layers are apparent on immobile element (Al, Ti, Zr, Hf and U) distribution maps (Fig. 5). These layers are parallel to the relict bedding planes within the nodules, extend across their entire width and are oblique to the main foliation in the argillite.
7) In situ LA-ICP-MS analyses were performed on nodules and on pyrite grains that exhibit metamorphic or hydrothermal textures. Examples of metamorphic and hydrothermal pyrite include cubic porphyroblasts, remobilized/recrystallized pyrite, and euhedral overgrowths on earlier generations of pyrite within quartz-carbonate veins and pressure shadows. Preliminary data from 240 spot analyses on pyrite nodules and 250

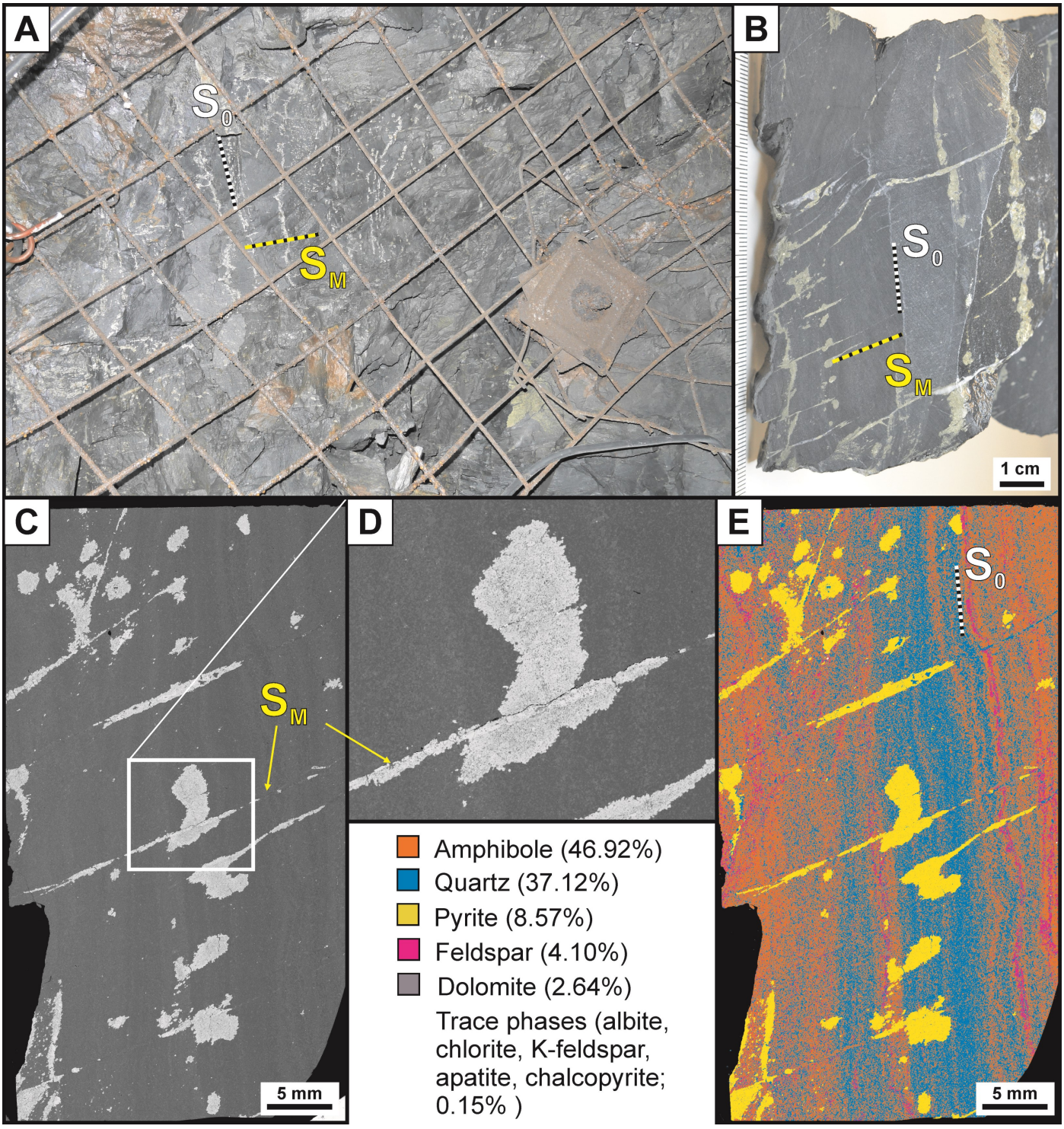

Figure 3. Nodular argillite interflow from level 1020, Bell Creek mine, Timmins, Ontario. a) Photograph of the drift ceiling showing the distribution of pyrite and the relationship to the east-west-oriented overprinting fabric (S_M), which controls the auriferous quartz veins at Bell Creek (spacing of the wire mesh is approximately 10 cm across). b) Photograph of a slab from rock shown in photograph (a) (sample JL-2018-028). c) Backscattered electron image of a polished thin section prepared from the sample shown in photograph (b). d) Close-up image of photograph (c). e) False-coloured energy dispersive spectrometry (EDS) image of the thin section in photo (c) showing the distribution of mineral phases (with relative proportions).

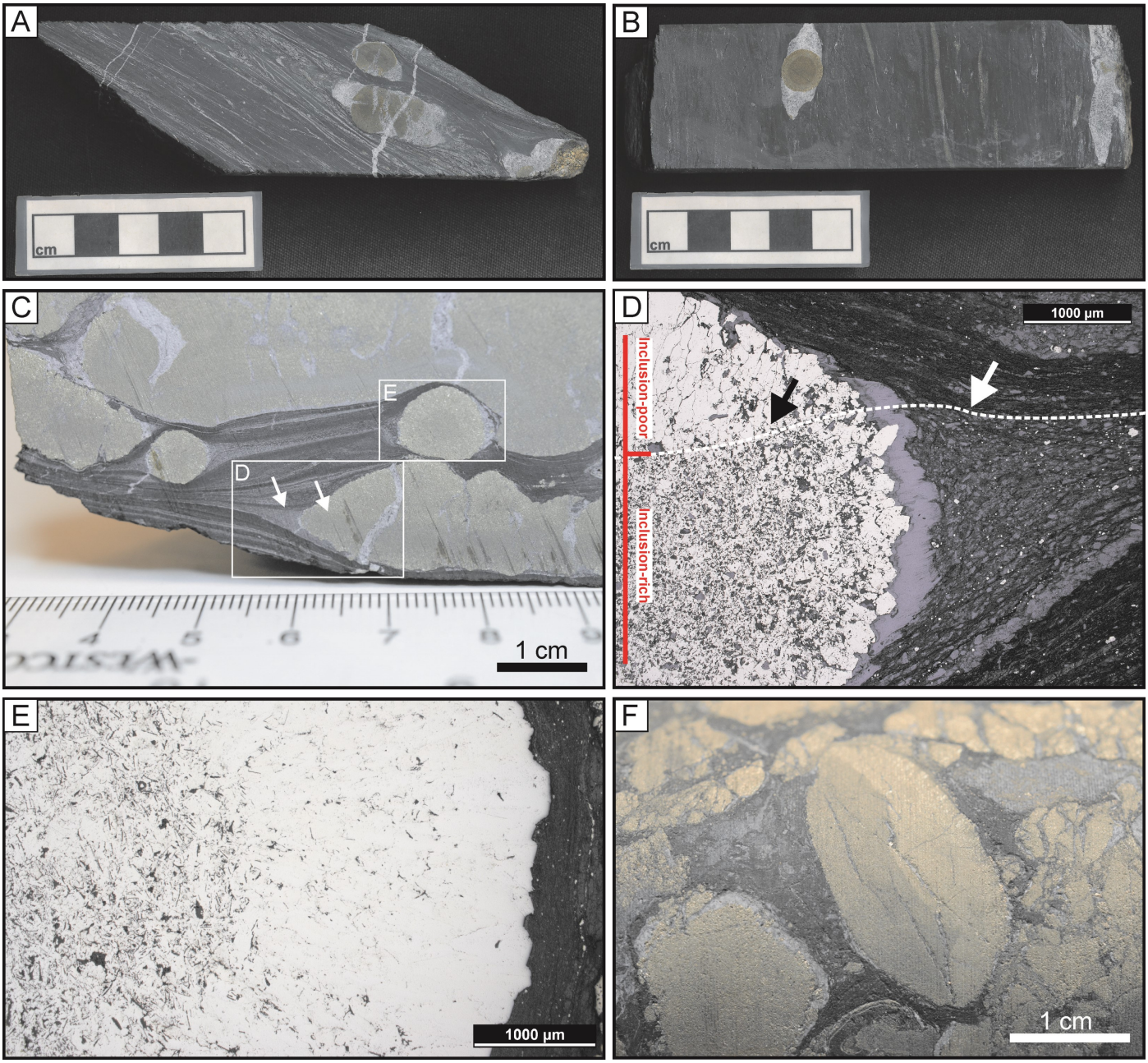

Figure 4. Photographs and photomicrographs of samples from the Bell Creek and Bradshaw deposits. Representative samples of (a) the lower section and (b) the upper section of the structurally juxtaposed Porcupine assemblage at Bell Creek (samples BC -2017-008 and BC-2018-015, respectively). c) Sample from the Bradshaw deposit of nodular intercalated shale and siltstone with nodules developed both in the argillitic and silty layers, exhibiting textural artefacts of the primary lithologies (sample JL -2018-039). d) and e) close-ups of photograph (c). f) Sulphide breccia with fragments showing textures similar to those shown in photograph (c). Note the silty fragment in the top right of the photo.

spot analyses on metamorphic/hydrothermal pyrite grains from across the Timmins-Matheson area exhibit significant differences between the two types of pyrite. These differences are shown by plotting Ag, Sb, Tl and Au against Ni (Fig. 6). The core and rim of the nodules show systematically higher values, and/or element/Ni ratios (see Ni/Tl below), than those of the metamorphic/hydrothermal pyrite, with minimal overlaps. This is interpreted to reflect the distinct conditions in which they formed. Values from analyzed ore vein-hosted (hydrothermal) pyrite from the Bradshaw deposit are also plotted (Fig. 6), which show clear distinctions from the rest of pyrite within and outside the deposit.

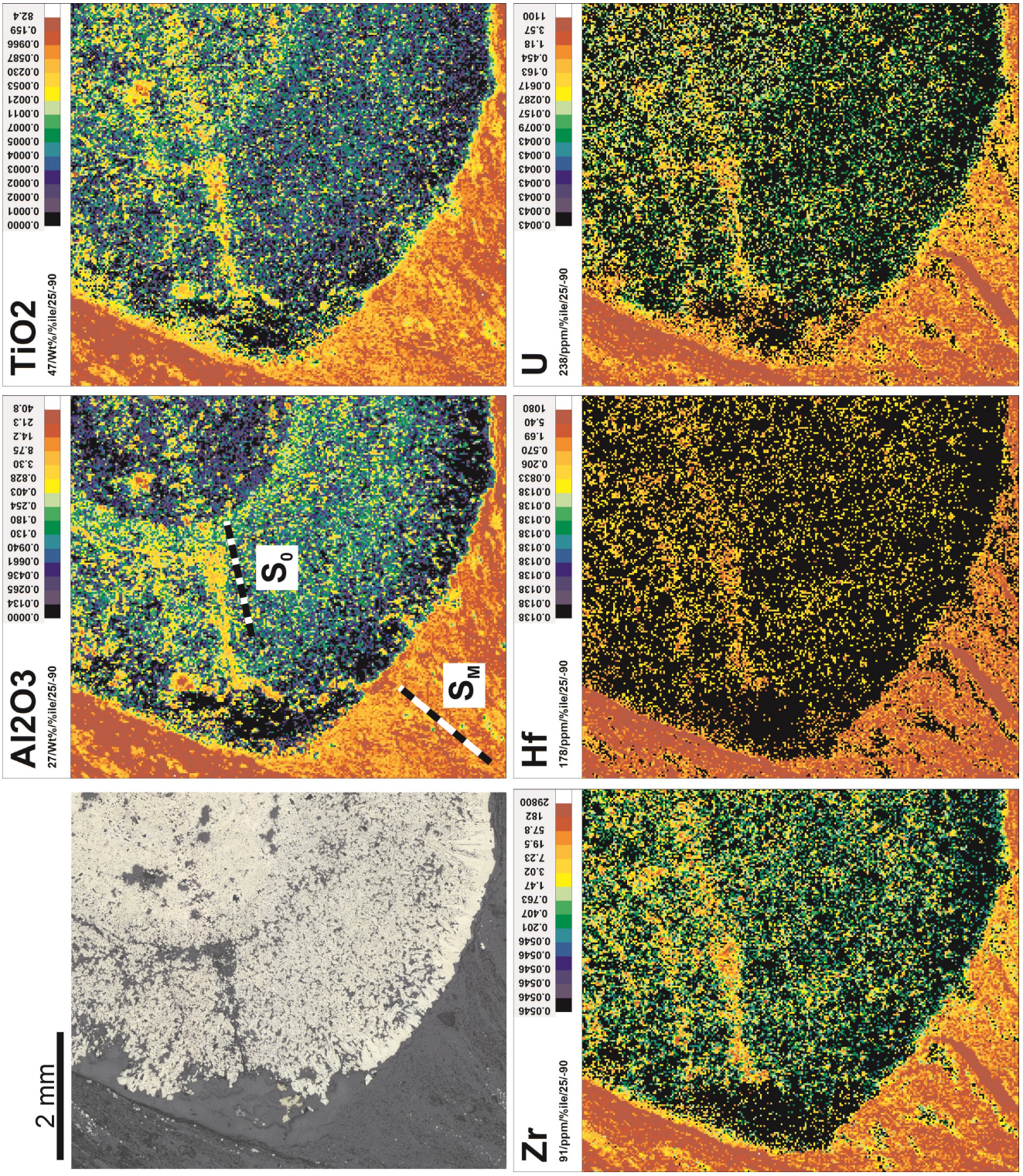

Figure 5. Laser ablation inductively coupled plasma mass spectrometry (LA-ICP-MS) element maps of a pyrite nodule from an argillite interflow in the Tisdale assemblage, Bell Creek deposit (sample 04365, DDH BC-09-63). The element maps use a percentile scaling function. Note the lamination (S_0) expressed by conservative elements such as Al_2O_3, TiO_2, Zr, Hf and U and its oblique relationship with the well-developed foliation (S_M).

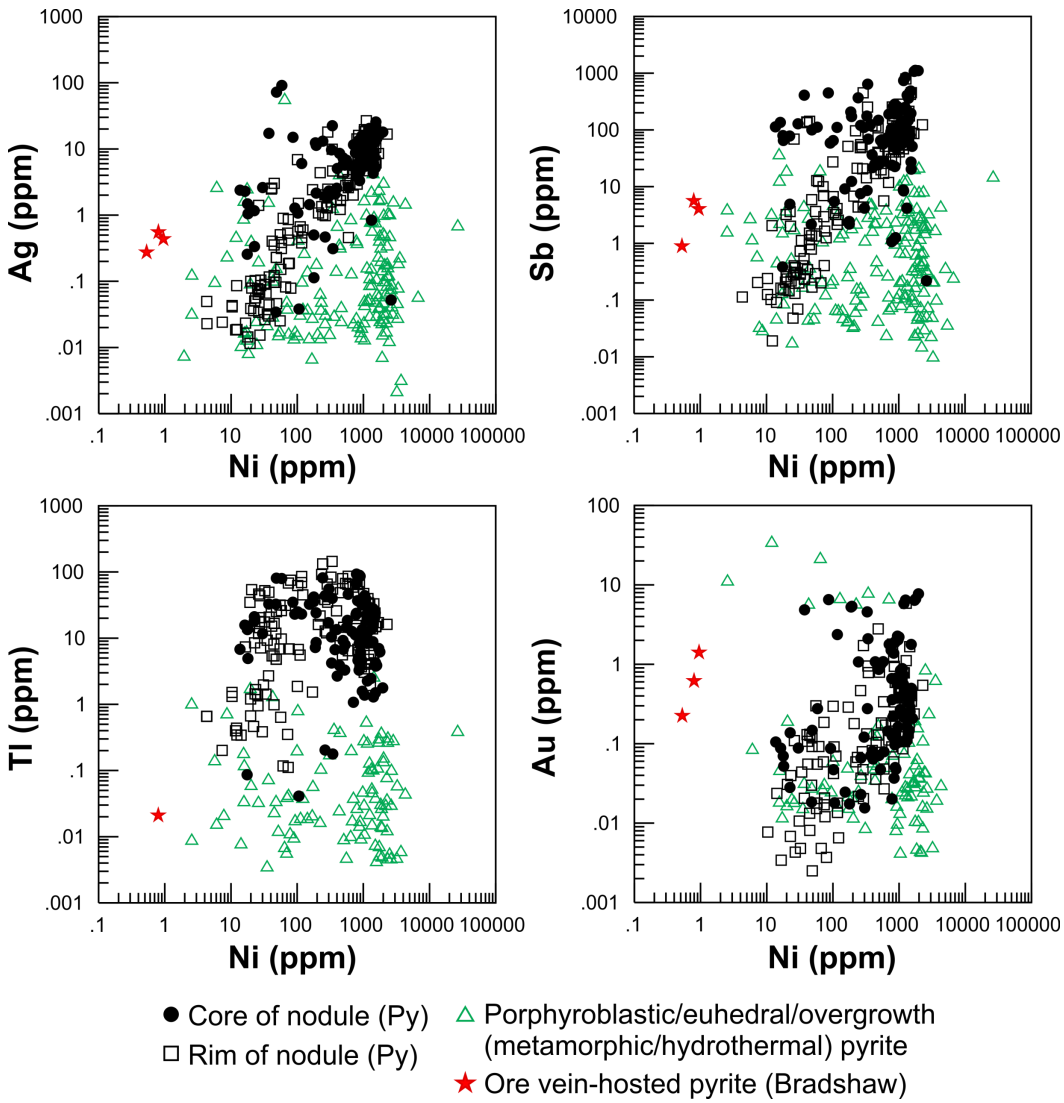

Figure 6. Bivariate plots of selected trace metals in pyrite from the Timmins-Matheson area (*see* text for the list of locations), as determined by LA-ICP-MS. Ni vs. (a) Ag, (b) Sb, (c) Tl, and (d) Au. The ore vein-hosted pyrite from the Bradshaw deposit is from an auriferous quartz-arsenopyrite(±pyrite) vein (level 45), in which arsenopyrite is the main host of the gold.

8) When plotting Ni/Tl against Au, both show a systematic decrease from core to rim in the nodules, regardless of the deposit/prospect within or proximal to which they formed (Fig. 7). This trend is the same for nodules developed in interflow and deep-basin sedimentary rocks. An increase in pH, oxidizing potential, and/or a decrease of available base and precious metals from the ambient fluids during growth of the nodules are possible factors explaining this region-wide trend (e.g. Rickard, 2012).

Conclusions

Despite deformation, the nodules documented in the Bell Creek and Bradshaw deposits, which are the focus of this report, are generally well preserved, ubiquitous and show preserved sedimentary features. Furthermore, no indication of a hydrothermal or structural control to their distribution has been observed. The common geochemical trends in pyrite nodules from the deposits studied in the Timmins-Matheson area suggest that their growth was controlled by similarly evolving conditions in the sediments and that, regardless of the intensity of deformation, metamorphism, alteration, or mineralization, the nodules preserve their primary signatures very well. If a genetic relationship exists between carbonaceous argillite, pyrite nodules and greenstone-hosted quartz-carbonate vein-type gold deposits, the geochemical and/or isotopic signatures reflecting this remain to be defined. On a regional scale, it is unclear if a relationship exists between the contents of gold and other elements present in the nodules and the distribution of the orogenic gold deposits. It is, however, evident that gold contents of

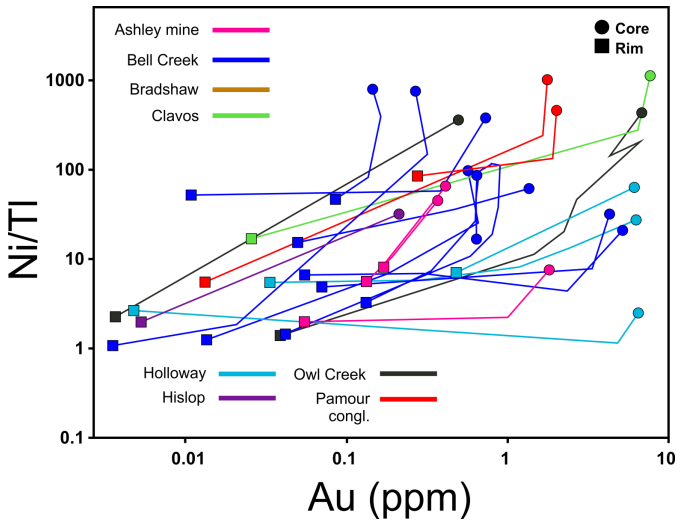

Figure 7. Ni/Tl vs. Au plot from in situ Laser ablation inductively coupled plasma mass spectrometry (LA-ICP-MS) data of nodules collected throughout the Timmins-Matheson area. Multiple analyses were done on each region of the nodule, including the core, outer core, inner rim and rim. Values for each region were averaged for simplicity.

the pyrite nodules from the Timmins-Matheson area are generally much higher than typical sedimentary pyrite globally (Gregory et al., 2015), suggesting that the sediments underwent an early phase of gold enrichment.

Future work

Although this work has revealed textures that have rarely been documented in Archean deformed and metamorphosed rocks, ongoing research is intended to address the processes controlling their formation. This could in turn provide key information about the potential contribution (or lack thereof) of metals from metal-enriched pyrite nodules to ore-forming solutions in Archean orogenic gold deposits and their potential use as a fertility indicator. The implications of the anomalous gold enrichment (and the processes that led to it) in the Timmins-Matheson area remain to be clarified.

Multiple S, Fe, and Pb isotopic analyses on various sulphide generations will be performed on nodular and ore-related sulphides, which will be used to constrain the controlling physico-chemical conditions or reactions during the evolution of the Timmins-Matheson area. The production of numerous LA-ICP-MS element maps are planned for selected samples from deposits throughout the region that have representative textural features. These maps contain a tremendous amount of data and so machine learning tools available in the "R" language are being applied to classify sulphide generations that have formed or overprinted the nodules, using geochemical assemblages derived from LA-ICP-MS mapping (Lawley et al., work in progress, 2018). Thin sections from the samples collected during the 2017 and 2018 field season are currently being characterized by automated SEM analysis (as shown in Fig. 3). This method will provide maps of the various mineral phases present in the thin sections and the average mineral compositions (semi-quantitative) of each classified phase. Moreover, over 80 whole-rock samples of carbonaceous argillite are being analyzed for complete major, trace and rare-earth elements, and these data will provide another geochemical dimension to the study. Paleoredox conditions during sediment deposition will be assessed using redox-sensitive elements such as U, As, Sb, V and Mo and, since many of them can partition into sulphides, only sulphide-barren argillite samples have been submitted for whole-rock analyses where possible.

Other deposits in strongly deformed or hydrothermally altered argillite units where the genesis of nodules have not been fully addressed, such as at Hoyle Pond (Tisdale-hosted), Holloway (Kidd-Munro-hosted) and the historical Pamour #1 mine (Timiskaming-hosted), have characteristics (i.e. distribution restricted to high strain zones proximal to shear-hosted mineralized quartz-carbonate veins) that remain for now difficult to reconcile with the results presented here. Ongoing analyses from the latter deposits will hopefully provide insights on these remaining ambiguities.

Acknowledgments

This report is a contribution to NRCan's Targeted Geoscience Initiative Program (TGI). Support for this study was provided through the Gold Project's '*Activity G-1.4: Fingerprinting ore processes in auriferous systems*'.

The authors thank Anthony Camuti, Alain Mainville, and Keith Green from Tahoe Resources Inc. (Bell Creek mine) and Rochelle Collins from Gowest Gold Ltd. (Bradshaw mine) for providing access to the sites, data, and samples. Sincere thanks to Dr. Ed van Hees of the Ontario Geological Survey for scientific and technical support. Drs. Mark Hannington and Matthew Gray are acknowledged for providing samples from several localities in the district. We thank Lionel Bonhomme and Wayne Corstorphine of International Explorers and Prospectors Inc. for access to historical drillcores from various exploration projects. David Diekrup and Ashley Abraham are thanked for sample preparation and description and SEM work. Drs. Duane Petts and Zhaoping Yang are thanked for LA-ICP-MS support. Valérie Bécu and Francis Aucoin helped with compilation work and maps. This report benefited from the review of Gilles Bellefleur, Jan Peter and Neil Rogers.

References

Bleeker, W. and van Breemen, O., 2011. New geochronological, stratigraphic, and structural observations on the Kidd-Munro assemblage and the terrane architecture of the south-central Abitibi greenstone belt, Superior craton, Canada; Ontario Geological Survey, Open File Report 6258, 35 p.

Dubé, B., Mercier-Langevin, P., Ayer, J., Atkinson, B., and Monecke, T., 2017. Orogenic greenstone-hosted quartz-carbonate gold deposits of the Timmins-Porcupine camp;

Reviews in Economic Geology, v. 19, p. 51–79.

Frieman, B.M., Kuiper, Y.D., Kelly, N.M., Monecke, T., and Kylander-Clark, A., 2017. Constraints on the geodynamic evolution of the southern Superior Province: U-Pb LA-ICP-MS analysis of detrital zircon in successor basins of the Archean Abitibi and Pontiac subprovinces of Ontario and Quebec, Canada; Precambrian Research, v. 292, p. 398–416.

Gray, M.D. and Hutchinson, R.W., 2001. New evidence for multiple periods of gold emplacement in the Porcupine mining district, Timmins area, Ontario, Canada; Economic Geology, v. 96, p. 453–475.

Gregory, D.D., Large, R.R., Halpin, J.A., Baturina, E.L., Lyons, T.W., Wu, S., Danyushevsky, L., Sack, P., Chappaz, A., Maslennikov, V.V., and Bull, S.W., 2015. Trace element content of sedimentary pyrite in black shales; Economic Geology, v. 110, p. 1389–1410.

Jackson, S.E., Dubé, B., Mercier-Langevin, P., and Rhys, D., 2017. Fingerprinting ore processes in auriferous systems; *in* Targeted Geoscience Initiative – 2016 Report of Activities, (ed.) N. Rogers; Geological Survey of Canada, Open File 8199, p. 29–32.

Jonasson, I.R., Kingston, D.M., Watkinson, D.H., and Elliot, S.R., 1999. Role of pyrite in the formation and localisation of gold mineralization at the Owl Creek mine, Timmins, Ontario; *in* The Giant Kidd Creek Volcanogenic Massive Sulfide Deposit, Western Abitibi Subprovince, Canada, (ed.) M.D. Hannington and C.T. Barrie; Economic Geology, Monograph 10, p. 627–660.

Kingston, D.M., 1987. Geology and geochemistry of the Owl Creek gold deposit, Timmins, Ontario; M.Sc. thesis, Carleton University, Ottawa, Ontario, 108 p.

Large, R.R., Maslennikov, V., Robert, F., Danyushevsky, L.V., and Chang, Z., 2007. Multistage sedimentary and metamorphic origin of pyrite and gold in the giant Sukhoi Log deposit, Lena gold province, Russia; Economic Geology, v. 102, p. 1232–1267.

Mercier-Langevin, P., Dubé, B., Jackson, S.E., Layne, G.D., and Piercey, S.J., 2016. Synvolcanic gold at the Archean: Evidences from LA-ICP-MS mapping, SEM analyses, and in-situ SIMS $\delta^{34}S$ isotope analyses on pyrite – Examples from the LaRonde Penna Au-rich VMS deposit and Rainy River gold project; Geological Association of Canada – Mineralogical Association of Canada (GAC-MAC) Annual Joint Meeting, Abstracts Volume 39, p. 63.

Mumin, A.H., Fleet, M.E., and Chryssoulis, S.L., 1994. Gold mineralisation in As-rich mesothermal gold ores of the Bogosu-Prestea mining district of the Ashanti gold belt, Ghana: Remobalization of "invisible' gold; Mineralium Deposita, v. 29, p. 445–460.

Raiswell, R., 1982. Pyrite texture, isotopic composition and the availability of iron; American Journal of Science, v. 282, p. 1244–1263.

Rickard, D.T., 2012. Sulfidic sediments and sedimentary rocks: Developments in sedimentology: Amsterdam, Elsevier, 816 p.

Sack, P.J., Large, R.L., and Gregory, D.D., 2018. Geochemistry of shale and sedimentary pyrite as proxy for gold fertility in the Selwyn basin area, Yukon; Mineralium Deposita, v. 53, p. 997–1018.

Thurston, P.C., Ayer, J.A., Goutier, J., and Hamilton, M.A., 2008. Depositional gaps in Abitibi greenstone belt stratigraphy: A key to exploration for syngenetic mineralization; Economic Geology, v. 103, p. 1097–1134.

Mantle metal mobility: preliminary gold and platinum group element geochemical results

C.J.M. Lawley[1], S.E. Jackson[1], D.C. Petts[1], D. Savard[2], D.G. Pearson[3], S. Zhang[4], A. Zagorevski[1] and B.A. Kjarsgaard[1]

[1]*Geological Survey of Canada, 601 Booth Street, Ottawa, Ontario, K1A 0E8*

[2]*Sciences de la Terre, Université du Québec à Chicoutimi, 555 Boulevard de l'Université, Chicoutimi, Québec, Canada, G7H 2B1*

[3]*Department of Earth & Atmospheric Sciences, University of Alberta, Edmonton, Alberta T6G 2E3*

[4]*Department of Earth Sciences, Carleton University, 1125 Colonel By Drive, Ottawa, Ontario K1S 5B6*

Abstract

Mantle sulphides are rare but relatively important mineral phases that dominate the chalcophile and/or siderophile element budget of the silicate Earth. The macro- to micro-scale distribution of mantle sulphides and their trace chalcophile and siderophile elements, however, remains poorly understood. Herein we present new laser ablation inductively coupled plasma mass spectrometry (LA-ICPMS) spot and element mapping results for an assemblage of naturally occurring sulphide, alloy, and native metal minerals recovered from ophiolitic mantle peridotite and pyroxenite (Atlin, British Columbia). Sulphide (pentlandite, pyrrhotite, chalcopyrite), alloy (awaruite) and native metal (copper and iron) phases are interstitial to variably serpentinized olivine and pyroxene relicts at the micro-scale. Pentlandite (±pyrrhotite) occurs with magmatic clinopyroxene and is typically replaced by awaruite and native iron, suggesting super-reduced conditions during serpentinization and de-sulphidation of the low-temperature equilibrated mantle sulphide assemblage rather than the late addition of sulphide minerals during and/or after ophiolite emplacement. Element mapping results further suggest that gold, platinum and other metals were remobilized during serpentinization. New whole-rock nickel sulphide fire-assay (NiS-FA) platinum group element (PGE) results for the same Atlin ultramafic suite, however, yield flat chondrite-normalized profiles that scatter around the composition of the primitive mantle, suggesting that precious metal remobilization was limited to the micro-scale. Future work will focus on the paragenetic history of this ultramafic suite using a combination of whole-rock ultratrace geochemistry and isotopic studies.

Introduction

The factors that control the metal endowment of mantle-derived melts remains unclear despite the importance of ultramafic- to mafic-hosted nickel, copper, gold and platinum group element (PGE) ore deposits in modern and ancient settings. Mantle Metal Mobility seeks to address that knowledge gap by documenting the macro- to micro-scale distribution and geochemical behaviour of metals within mantle source regions. Research is split between studies focused on ancient cratonic mantle underlying the Canadian Shield (i.e. Superior and Slave cratons) and young ophiolitic mantle exposed in and around Atlin, British Columbia (Fig. 1). Research results for the Abitibi cratonic mantle are published in Lawley et al. (2018a–c).

Preliminary geochemical results from a research subactivity focused on sulphide, alloys, and native metal minerals recovered from mantle peridotite at Atlin, British Columbia are discussed below. We demonstrate that sulphide, alloy and native metals phases represent important mineral hosts for gold and PGE within Atlin mantle peridotite and pyroxenite. The petrogenetic history of these phases within mantle source regions therefore likely represents an important factor controlling melt fertility. Geochemical studies of mantle sulphide phases reported herein complement on-going whole-rock ultratrace element and isotopic studies to better understand the melting and refertilization history of Atlin peridotite with implications for metal-enrichment processes that operate in mantle source regions.

Preliminary LA-ICP-MS mantle sulphide results

Sample preparation and petrography

Samples were collected over the course of two field seasons at several ultramafic massifs within the Cache Creek terrane (Fig. 1). Ultramafic rocks are interpreted as dismembered remnants of a Late Permian to Early Triassic ophiolite, however, the tectonic setting and emplacement history of Atlin peridotite samples are the focus of ongoing study as part of the Cordillera Project within the Geo-mapping for Energy and Minerals (GEM) program (Zagorevski et al., 2016; McGoldrick et al.,

Corresponding author: Chris Lawley (christopher.lawley@canada.ca)

Lawley, C.J.M., Jackson, S.E., Petts, D.C., Savard, D., Pearson, D.G., Zhang, S., Zagorevski, A. and Kjarsgaard, B.A., 2019. Mantle metal mobility: preliminary gold and platinum group element geochemical results; *in* Targeted Geoscience Initiative: 2018 report of activities, (ed.) N. Rogers; Geological Survey of Canada, Open File 8549, p. 43–48. https://doi.org/10.4095/313635

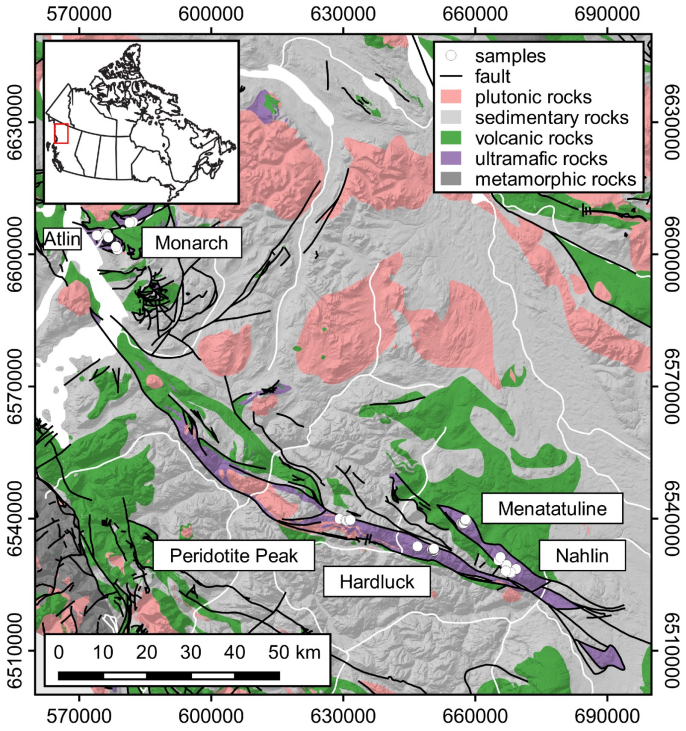

Figure 1. Regional geologic map of northwestern British Columbia (Ciu et al., 2017) showing the distribution of mantle peridotites and sampling localities during the 2016 and 2017 field seasons. Shuttle radar topography mission (SRTM) elevation data shown for reference (Farr et al., 2007).

2017). Several ultramafic lithologies were identified and sampled during field work, including spinel-bearing peridotite (dunite, harzburgite, lherzolite) and pyroxenite dykes (olivine websterite, orthopyroxenite and websterite). Samples were submitted to Overburden Drilling Management (Ottawa, Ontario) for electric pulse disaggregation followed by magnetic and heavy liquid separation. Sulphide, alloy and native metal mineral phases were mostly recovered from the heavy and magnetic grain fractions due to the presence of magnetite and awaruite mineral intergrowths with nonmagnetic minerals (e.g. pentlandite). The coarsest sulphide and alloy mineral phases were then mounted in epoxy, polished to approximately half the original thickness, and imaged with a Tescan Mira-3 field-emission scanning electron microscope (SEM) at the Geological Survey of Canada (Ottawa) prior to analysis. Examples of sulphide, alloy, and native metal mineral phases were also identified in situ following automated mineral phase scanning on polished thick sections using SEM back scatter electron (BSE) images and the Oxford Instruments Aztec software package (i.e. Feature function). The coarsest in situ sulphide minerals were selected for LA-ICPMS mapping (Fig. 2).

Coarse pentlandite crystals occur with rare magmatic clinopyroxene and chrome-spinel. This close, co-spatial relationship suggests that pentlandite represents a low-temperature equilibrated mantle mineral phase, rather than a hydrothermal sulphide phase precipitated during and/or after ophiolite emplacement. Pentlandite is interstitial to serpentinized olivine relicts and cut by ultrafine (a few microns thick) chalcopyrite vein networks, suggesting that this low-temperature equilibrated assemblage may have originally occurred as a metasomatic nickel (± copper)-rich sulphide melt (e.g. Lorand, 1987). The paragenesis of the observed mantle sulphide assemblage is the subject of further study (discussed below). Pyrrhotite, awaruite, magnetite, and native copper and iron wrap pentlandite, but also occur as isolated crystals within serpentine meshes in the absence of pentlandite. Serpentinization reactions can generate super-reduced conditions and represent one of the few terrestrial settings where native iron is stable (e.g. Tominaga et al., 2017). Super-reduced conditions, in turn, likely destabilized the mantle sulphide assemblage, a supposition that is supported by awaruite and native iron replacing pentlandite at the micro-scale. We therefore interpret pentlandite as a relict sulphide mineral phase that escaped complete desulphidation during serpentinization.

Nickel sulphur fire assay (NiS-FA) methods and results

Whole-rock NiS-FA analyses of the Atlin mantle peridotite suite (n = 67) were completed at the Université du Quebec à Chicoutimi (UQAC) following the approach of Savard et al. (2010). Mantle peridotite tends to yield a flat, chondrite-normalized PGE patterns, similar to that of the primitive mantle (Palme and O'Neill, 2014), despite including lithologies that range from refractory dunite to relatively fertile lherzolite (Fig. 3a). Linking the whole-rock PGE signature to the petrogenetic history of the ultramafic suite is the subject of future research, however, whole-rock PGE concentrations are recalculated to 100% sulphide for comparison with the in situ LA-ICP-MS results reported below (Fig. 3b).

LA-ICP-MS methods and results

All LA-ICP-MS mapping and spot analyses were completed at the Geological Survey of Canada (Ottawa) using an Agilent Technologies 7700 x ICP-MS coupled to a Photon Machines Analyte 193 nm excimer laser ablation system (Cabri and Jackson, 2011). Spot analyses (20–30 µm) were calibrated using standard-sample-bracketing with the United States Geological Survey (USGS) doped synthetic basaltic glass standard GSE-1G (Guillong et al., 2005) and doped synthetic pyrrhotite standard Po726 (Au, Pt, Pd, Os and S; prepared by L. Cabri and G. Laflamme at CANMET) in *Glitter* (Griffin et al., 2008). Sulphide reference material FeS1 was used as a quality control standard to monitor instrument performance. Spot analyses are relatively precise and accurate with lower analytical detection limits compared to mapping results due to larger sampling volumes and counting statistic considerations.

Element mapping was completed using the same analytical setup as spot analyses, but with a significantly smaller spot size (5–6 µm) due to the fine crystal size of the mapped mineral assemblage. Data processing for element maps was completed

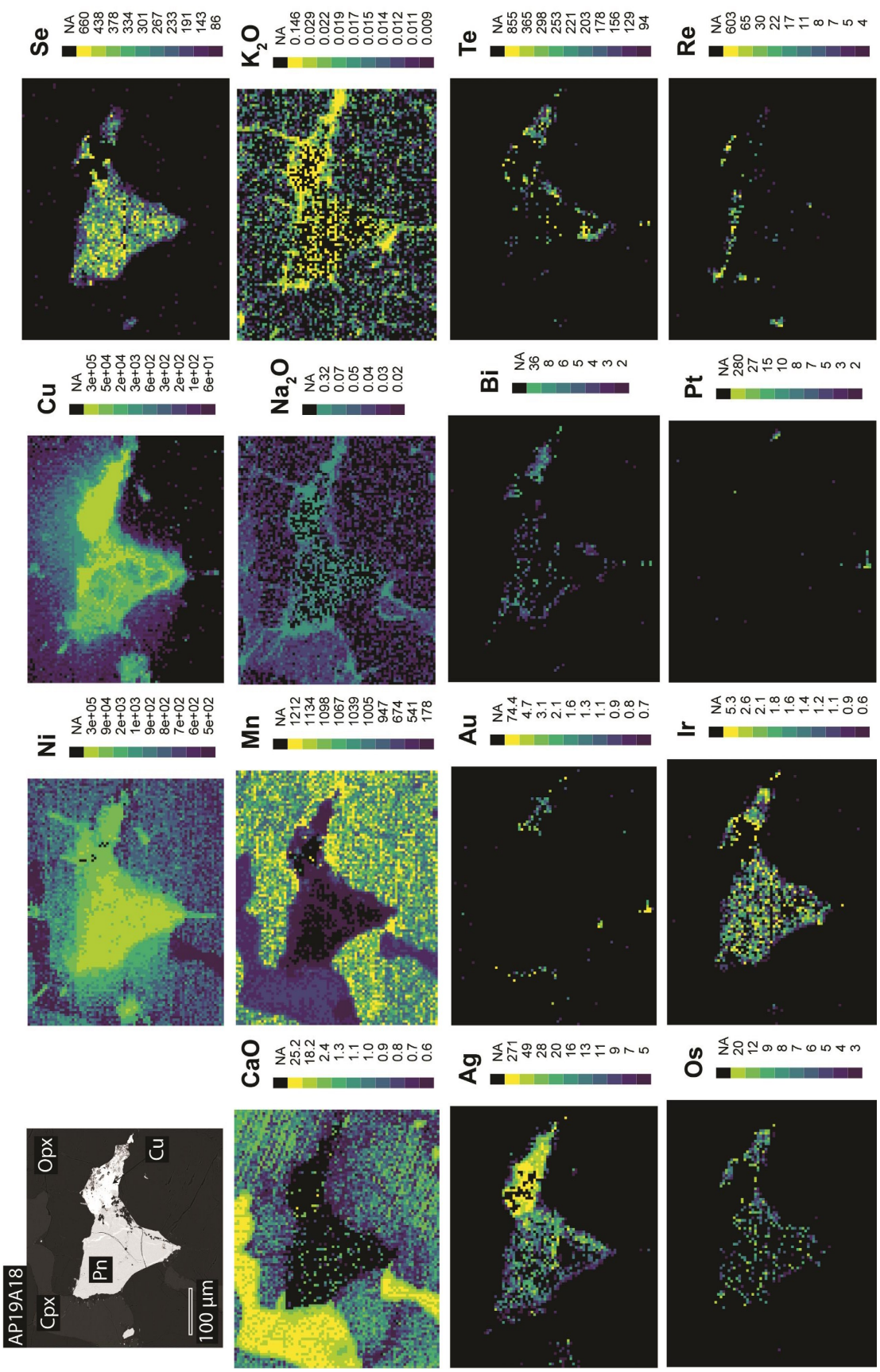

Figure 2. a) Scanning electron microscopy electron backscatter image (SEM-BSE) of composite pentlandite, alloy, and native metal grain. b–g) Laser ablation inductively coupled plasma mass spectrometry (LA-ICP-MS) element maps showing the distribution of major, minor, and trace elements (reported in ppm). Data processing and plotting were completed in R using new code and functions derived from dplyr and gpplot2 (Wickham, 2009, 2011, 2014). Concentrations are plotted using percentile colour scaling after internal standardization and 100% normalization following the approach of Longerich et al. (1996). Concentrations below the analytical detection limit are not shown (NA).

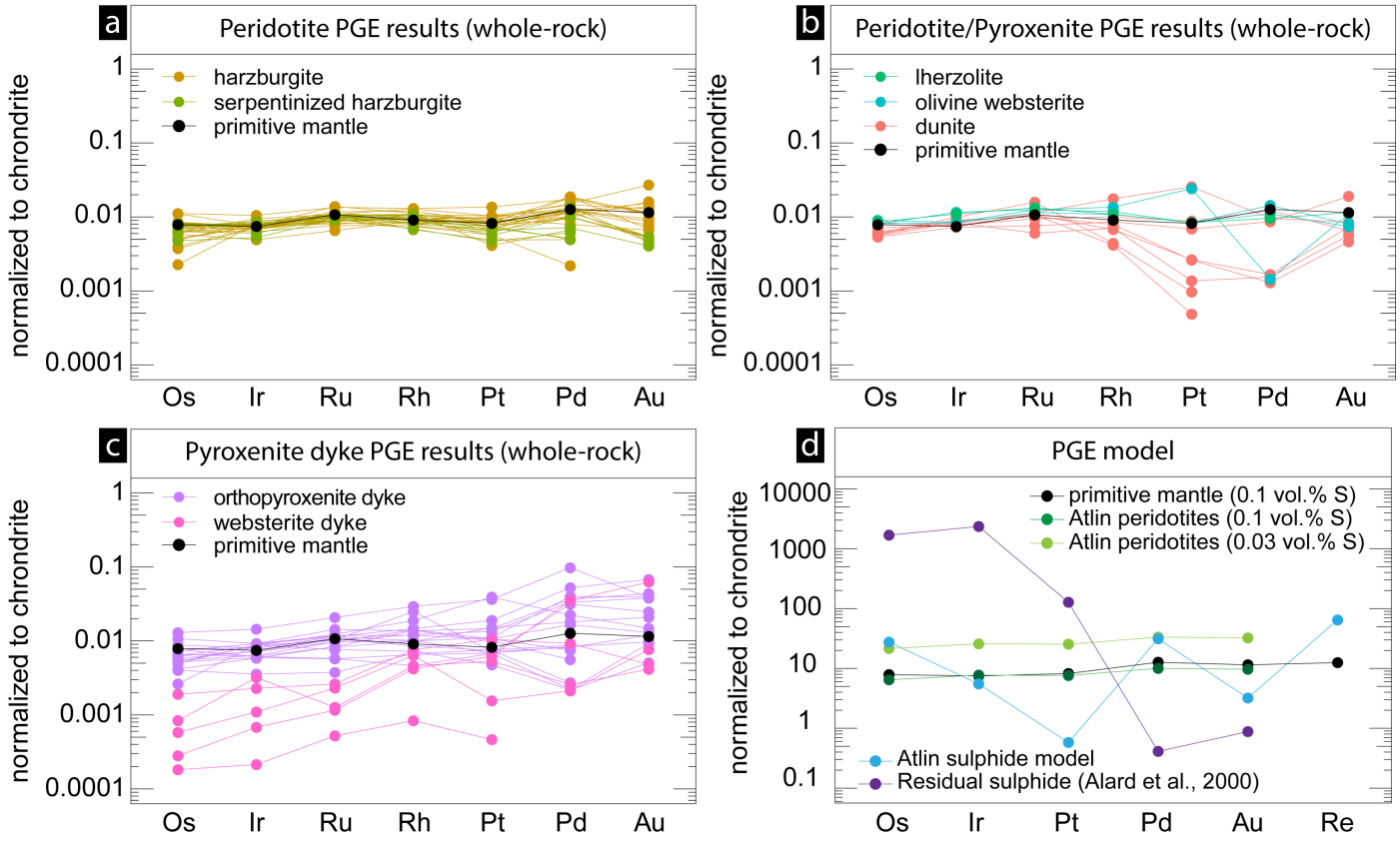

Figure 3. a–c) Whole-rock, chondrite-normalized (Palme and O'Neill, 2014) PGE profiles for mantle peridotite and pyroxenite sampled in and around Atlin, British Columbia (Fig. 1); d) Primitive mantle and median whole-rock PGE profiles recalculated to 100% sulphide and normalized to chondrite (Palme and O'Neill, 2014). The sulphide model is based on the median of LA-ICP-MS spot analyses and typical modal abundance for each mineral phase. The overlap between whole-rock PGE profiles recalculated to 100% sulphide and the model sulphide composition, suggests that mantle sulphides are the dominant host for PGEs and gold. However, the platinum- and gold-poor signature of the modelled pentlandite suggests that a proportion of these elements likely also occurs in some other form (e.g. nuggets and/or inclusions). The steep, negative-sloping PGE profile of residual sulphides (Alard et al., 2000) is shown for reference.

in *R* (R Core Development Team, 2018) using several data manipulation and plotting packages (e.g. *dplyr* and *ggplot2*; Wickham, 2009, 2011, 2014) and new *R* code. Element maps are quantitative with each pixel corresponding to a 5–6 micron analytical spot and calibrated using internal standardization (standard-sample-standard bracketing with GSE-1G and Po726) and 100% normalization following the approach of Longerich et al. (1996) and Jackson (2008). Element concentrations below the analytical detection limit are reported as NA; whereas all other element concentrations are reported as percentile colour scaling in Figure 2.

Pentlandite-hosted trace elements tend to be heterogeneously distributed at the micro-scale (Fig. 2) but are consistently osmium- and iridium-rich (typically 1–100 ppm; Fig. 2). Other chalcophile and siderophile elements (e.g. Au, Ag, Pt and Bi), however, are concentrated in alloy and native metal phases (e.g. awaruite and native copper) at the margins of pentlandite (Fig. 2). The heterogeneous micro-scale distribution of gold and platinum suggests that a proportion of these elements likely occurs as submicron inclusions within serpentinized veinlets.

Future work

New LA-ICP-MS mapping and spot results demonstrate that gold, platinum and other so-called chalcophile elements (i.e. silver, bismuth) are concentrated within the super-reduced alloy assemblage, suggesting precious metals may have been remobilized from destabilized sulphide phases during serpentinization. Other PGEs (osmium and iridium) are almost entirely pentlandite-hosted, which suggests that these elements were immobile during serpentinization. Reconstructed mantle sulphide compositions, based on median spot analyses results and modal mineralogy, suggest that the mantle sulphide phase assemblage (e.g. pentlandite±chalcopyrite) was the dominant mineral host prior to serpentinization (Fig. 3b). Osmium and iridium concentrations are fully accounted for by the modelled primary mantle sulphide composition, whereas a small propor-

tion of gold and platinum must also occur in some other form to balance the whole-rock precious metal budget.

Element-mapping results demonstrate the heterogeneous, micro-scale distribution of gold and platinum inclusions and/or nuggets within the serpentinized silicate matrix distal to pentlandite (Fig. 2). Further work is required to test whether these inclusions are sufficient to balance the 'missing' gold and platinum predicted by whole-rock mass balance calculations. Both elements yield whole-rock concentrations that overlap with the primitive mantle, suggesting that precious metal mobility was limited to the micro-scale. The limited mobility of gold during the earliest stages of serpentinization is consistent with experimental studies on its solubility within super-reducing fluids (e.g. Williams-Jones et al., 2009). The mobility of gold and PGE during serpentinization may therefore depend on the stability of the super-reduced alloy and native metal mineral assemblage, which were effective mineral traps at the micro-scale during desulphidation of mantle sulphides. Oxidized fluids are better geochemical agents for gold transport, consistent with experimental studies of auriferous fluids (e.g. Williams-Jones et al., 2009). The relationship between gold mobility and redox conditions during serpentinization may have implications for the genesis of ultramafic-hosted gold deposits (i.e. listvenite) and is the subject of ongoing study.

Acknowledgments

This report is a contribution to NRCan's Targeted Geoscience Initiative Program (TGI). Support for this study was provided through the Gold Project's *Activity G-1.2: Mantle metal mobility*.

This report benefited from the review of Colter Kelly, Jim Craven and Neil Rogers.

References

Alard, O., Griffin, W.L., Lorand, J.P., Jackson, S.E., and O'Reilly, S. Y., 2000. Non-chondritic distribution of the highly siderophile elements in mantle sulphides; Nature, v. 407, p. 891–894.

Cabri, L. and Jackson, S., 2011. New developments in characterization of sulfide refractory Au ores; *in* World Gold 2011; 50th Conference of Metallurgists, MetSoc, Montreal, Quebec, p. 51–62.

Cui, Y., Miller, D., Schiarizza, P., and Diakow, L.J., 2017. British Columbia digital geology; British Columbia Ministry of Energy, Mines and Petroleum Resources, British Columbia Geological Survey, Open File 2017-8, p. 9.

Farr, T.G., Rosen, P.A., Caro, E., Crippen, R., Duren, R., Hensley, S., Kobrick, M., Paller, M., Rodriguez, E., Roth, L., Seal, D., Shaffer, S., Shimada, J., Umland, J., Werner, M., Oskin, M., Burbank, D., and Alsdorf, D.E., 2007. The shuttle radar topography mission; Reviews of Geophysics, v. 45, no. 2, RG2004.

Griffin, W., Powell, W., Pearson, N., and O'Reilly, S., 2008. GLITTER: Data reduction software for laser ablation ICP-MS; *in* Laser Ablation ICP-MS in the Earth Sciences: Current Practices and Outstanding Issues, (ed.) P.J. Sylvester; Mineralogical Association of Canada, Short Course 40, p. 308–311.

Guillong, M., Hametner, K., Reusser, E., Wilson, S.A., and Günther, D., 2005. Preliminary characterisation of new glass reference materials (GSA-1G, GSC-1G, GSD-1G and GSE-1G) by laser ablation-inductively coupled plasma-mass spectrometry using 193 nm, 213 nm and 266 nm wavelengths; Geostandards and Geoanalytical Research, v. 29, p. 315–331.

Jackson, S., 2008. LAMTRACE data reduction software for LA-ICP-MS; *in* Laser Ablation ICP-MS in the Earth Sciences: Current Practices and Outstanding Issues, (ed.) P.J. Sylvester; Mineralogical Association of Canada, Short Course 40, p. 305–307.

Lawley, C.J.M., Kjarsgaard, B.A., Jackson, S.E., Yang, Z., Petts, D., and Roots, E., 2018a. Trace metal and isotopic depth profiles through the Abitibi cratonic mantle; Lithos, v. 314–315, p. 520–533.

Lawley, C.J.M., Kjarsgaard, B.A., Jackson, S.E., Yang, Z., and Petts, D.C., 2018b. Olivine and clinopyroxene mantle xenocryst geochemistry from the Kirkland Lake kimberlite field, Ontario; Geological Survey of Canada, Open File 8376, 1 zip file.

Lawley, C.J.M., Kjarsgaard, B.A., Jackson, S.E., Yang, Z., Petts, D.C., and Roots, E., 2018c. Mapping the ore element signature of the Abitibi greenstone belt cratonic mantle, Ontario; Geological Survey of Canada, Open File 8387, 1 poster.

Longerich, H.P., Jackson, S.E., and Günther, D., 1996. Laser ablation inductively coupled plasma mass spectrometric transient signal data acquisition and analyte concentration calculation; Journal of Analytical Atomic Spectrometry, v. 11, p. 899–904.

Lorand, J.P., 1987. Cu-Fe-Ni-S mineral assemblages in upper-mantle peridotites from the Table Mountain and Blow-Me-Down Mountain ophiolite massifs (Bay of Islands, Newfoundland): Their relationships with fluids and silicate melts; Lithos, v. 20, p. 59–76.

McGoldrick, S., Zagorevski, A., and Canil, D., 2017. Geochemistry of volcanic and plutonic rocks from the Nahlin ophiolite with implications for a Permo-Triassic arc in the Cache Creek terrane, northwestern British Columbia; Canadian Journal of Earth Science, v. 54, p. 1214–1227.

Palme, H. and O'Neill, H.S.C., 2014. Cosmochemical estimates of mantle composition; *in* Treatise on Geochemistry (2nd edition), (ed.) R.W. Carlson; Elsevier, p. 1–39.

R Core Development Team, 2018, R: A language and environment for statistical computing; R Foundation for Statistical Computing, Vienna, Austria. <http://www.R-project.org/>

[accessed December 12, 2018]

Savard, D., Barnes, S.-J., and Misel, T., 2010. Comparison between Nickel-Sulfur Fire Assay Te co-precipitation and isotope dilution with high-pressure asher digestion for the determination of platinum-group elements, rhenium and gold; Geostandards and Geoanalytical Research, v. 34, p. 281–291.

Tominaga, M., Beinlich, A., Lima, E.A., Tivey, M.A., Hampton, B.A., Weiss, B., and Harigane, Y., 2017. Multi-scale magnetic mapping of serpentinite carbonation; Nature Communications, v. 8, p. 1–10.

Wickham, H., 2009. ggplot2: Elegant Graphics for Data Analysis; Springer New York, New York, 213 p.

Wickham, H., 2011. The split-apply-combine strategy for data analysis; Journal of Statistical Software, v. 40, p. 1–29.

Wickham, H., 2014. Tidy data; Journal of Statistical Software, v. 59, p. 1–23.

Williams-Jones, A.E., Bowell, R.J., and Migdisov, A.A., 2009. Gold in solution; Elements, v. 5, p. 281–287.

Zagorevski, A., Mihalynuk, M.G., McGoldrick, S., Bedard, J.H., Golding, M., Joyce, N., Lawley, C. Canil, D., Corriveau, A.S., Bogatu, A., and Tremblay, A., 2016. Geological framework of ancient oceanic crust in northwestern British Columbia and southwestern Yukon, GEM 2 Cordillera; Geological Survey of Canada, Open File 8140, 13 p.

Superimposed auriferous structural events along the Llewellyn-Tally Ho deformation corridor in southern Yukon and northwest British Columbia

L. Ootes[1], S. Castonguay[2], R. Friedman[3] and F. Devine[4]

[1]*British Columbia Geological Survey, Ministry of Energy, Mines and Petroleum Resources, Victoria, British Columbia V8W 9N3*

[2]*Geological Survey of Canada, Natural Resources Canada, Québec, Quebec G1K 9A9*

[3]*Pacific Centre for Geochemical and Isotopic Research, University of British Columbia, Vancouver, British Columbia V6T 1Z4*

[4]*Merlin Geosciences Inc., Atlin, British Columbia V0W 1A0*

Abstract

The Llewellyn-Tally Ho deformation zone in northwest British Columbia and southern Yukon demarcates the eastern limit of the Nisling terrane and the western limit of the Stikine terrane and has spatially related epithermal, mesothermal, and intrusion-related gold deposits and occurrences. The Llewellyn fault is a southeast-striking, steeply dipping brittle dextral strike-slip structure that overprints 'early' penetrative fabrics and ductile deformation. The Tally Ho shear zone, in the Yukon, represents an early ductile deformation zone, comprising one penetrative foliation (S_{main}) and mylonite zones that are overprinted by late brittle faulting, analogous to the Llewellyn fault. Previous work and this study demonstrate that brittle strike-slip deformation along the Llewellyn fault occurred between ca. 56 and 50 Ma. Two granodiorite intrusions (ca. 75 Ma) crosscut the early ductile deformation fabrics. In the Tally Ho shear zone, S_{main} crosscuts a granodiorite pluton and porphyry dyke, which have yielded preliminary U-Pb zircon dates of ca. 98 and 95 Ma, respectively. As such, we infer that the early ductile fabrics formed before ca. 75 Ma and after ca. 95 Ma. This study further demonstrates that the early ductile and late brittle deformation are separated by at least ca. 20 Ma, indicating the various styles of gold mineralization developed during temporally distinct tectonic events: an 'early' late Cretaceous ductile event typical of the Tintina gold belt; and a 'later' Eocene brittle event matching the timing and structural framework of the Juneau gold camp.

Introduction

In collaboration with the Yukon Geological Survey, this joint British Columbia Geological Survey (BCGS)-Geological Survey of Canada (GSC), Targeted Geoscience Initiative (TGI) supported study was designed to document the geological setting and controls of gold mineralization that is spatially associated with selected major fault zones of the Canadian Cordillera. The chosen field area extends from the Tagish Lake area of northwest British Columbia northward to the Wheaton River area in southern Yukon (Fig. 1, 2). This area is the locus of a series of vein-hosted gold prospects and deposits, including past-producing mines (e.g. Engineer, Mount Skukum), that are spatially related to the Llewellyn fault and Tally Ho shear zone, which affect multiple lithotectonic suites (Fig. 2; e.g. Hart and Radloff, 1990; Mihalynuk et al., 1999; Tizzard et al., 2009). This study aims at providing better constraints on the timing of deformation along the fault zones and the temporal and genetic relationships with intrusion-related, mesothermal and epithermal-style gold systems. Herein, we build on previous reports (Castonguay et al., 2017, 2018; Ootes et al., 2017, 2018) regarding the relationship between the Llewellyn fault and the Tally Ho shear zone (Hart and Radloff, 1990; Mihalynuk et al., 1999; Tizzard et al., 2009) and provide further constraints on the timing of ductile strain and associated gold mineralization that characterizes parts of this deformation corridor.

Geological setting

The Llewellyn fault, in northwest British Columbia, extends directly along strike with the Tally Ho shear zone in southwest Yukon (Fig. 1, 2). This northwest-striking deformation zone marks the boundary between the Nisling terrane to the west and Stikine terrane to the east (Fig. 2; Hart and Radloff, 1990; Mihalynuk et al., 1999) and is spatially associated with a variety of gold prospects and minor past producers (Fig. 2). This gold mineralization has characteristics that range from mesothermal (Montana Mountain mines; Fig. 2; Roots, 1981; Walton, 1986; Hart and Pelletier, 1989), to epithermal (Mount Skukum and Engineer mines; Love, 1990, Love et al., 1998; Millinog et al., 2017), to intrusion-related (Bennett plateau and

Corresponding author: Sébastien Castonguay (sebastien.castonguay@canada.ca)

Ootes, L., Castonguay, S., Friedman, R., and Devine, F., 2019. Superimposed auriferous structural events along the Llewellyn-Tally Ho deformation corridor in southern Yukon and northwest British Columbia; *in* Targeted Geoscience Initiative: 2018 report of activities, (ed.) N. Rogers; Geological Survey of Canada, Open File 8549, p. 49–58. https://doi.org/10.4095/313636

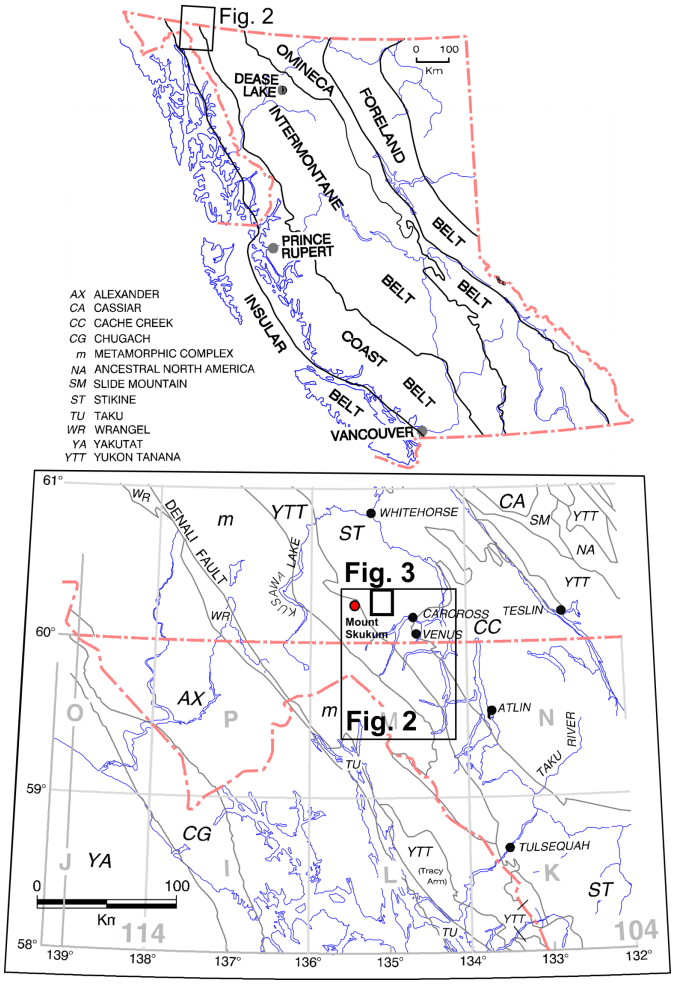

Figure 1. Location map with regional geography and terranes (*modified from* Mihalynuk et al., 1999).

Middle Ridge prospects, Golden Eagle project; Mihalynuk et al., 2003; Troymet Exploration Corporation, 2012).

Reconnaissance fieldwork, data compilation and preliminary reports (Castonguay et al., 2017, 2018; Ootes et al., 2017, 2018) have underlined that the epithermal gold mineralization at the Engineer and Mount Skukum deposits coincide both spatially and temporally with Eocene magmatism (also *see* Love et al., 1998; Millonig et al., 2017). These first-order observations led to the suggestion of a relationship between large-scale deformation zones, gold mineralization and Eocene magmatism in southwest Yukon and northwest British Columbia.

Llewellyn fault

The Llewellyn fault is an over 100 km long, northwest-striking, steeply dipping, brittle dextral strike-slip structure that occurs from the Tulsequah area in the south to the British Columbia-Yukon border in the north (Mihalynuk et al., 1994, 1999). The Llewellyn fault juxtaposes the Boundary Ranges metamorphic suite to the west (pre-Triassic; part of Stikine or Nisling terrane?) against the Stuhini and Laberge groups volcano-sedimentary rocks to the east (Triassic-Jurassic; part of the Stikine Terrane; Fig. 2; Mihalynuk et al., 1999). The Llewellyn structure overprints rocks affected by earlier south-southeast-trending penetrative fabrics that have been interpreted to indicate sinistral shear (Mihalynuk et al., 1999). The ductile deformation post-dates deposition of the Jurassic Laberge Group, and is much more penetrative in the Boundary Ranges metamorphic complex. Upper Cretaceous and Eocene plutons crosscut the ductile fabrics, providing a minimum age for the ductile deformation (Mihalynuk et al., 1999).

Brittle deformation along the Llewellyn fault is temporally constrained by vein-hosted gold mineralization at Engineer Mine. There, vanadian illite was produced by fluid-rock interaction during epithermal vein formation at ca. 50 Ma ($^{40}Ar/^{39}Ar$ data: Millonig et al., 2017). This timing coincides with Cordillera-wide dextral strike-slip faulting (e.g. Gabrielse et al., 2006).

Ootes et al. (2017, 2018) documented and sampled for geochronological study some localities along the Llewellyn fault, south of the British Columbia – Yukon border, including the Bennett plateau area and a few others southeastward toward Tagish Lake, British Columbia (Fig. 2, 3). The geology of sampled localities and age data (Table 1; *see* Ootes et al. (2018) for the description of analytical techniques) are briefly described

Table 1. Geochronological data for the Llewellyn and Tally Ho deformation corridor area.

Sample	Location	Rock type	Field relationship	Method	Age (Ma)	Reference
	Engineer vein/mine	quartz-vanadian mica vein	mineralized vein	$^{40}Ar/^{39}Ar$ V-illite	ca. 50	Millonig et al. (2017)
	Mount Skukum deposit	Au-quartz-calcite-adularia vein	mineralized vein	$^{40}Ar/^{39}Ar$ Adularia	ca. 54	Love et al. (1998)
16lo22A	Bennett Lake	biotite-hornblende granite	unfoliated	U-Pb Zircon	56.46 ± 0.06	Ootes et al. (2018)
16lo20A	Bennett Lake	K-feldspar granite	unstrained	U-Pb Zircon	56.58 ± 0.07	Ootes et al. (2018)
16lo05B	west of Moon Lake	biotite-hornblende granodiorite	unfoliated	U-Pb Zircon	ca. 74	Ootes et al. (2018)
16lo11B	Bennett plateau	granodiorite porphyry	unfoliated	U-Pb Zircon	76.30 ± 0.05	Ootes et al. (2018)
17lo16	Mount Hodnett	monzonite dyke	weakly-foliated/folded	U-Pb Zircon	ca. 95	This report; preliminary data
17lo10	Mount Hodnett	biotite-hornblende granodiorite	foliated	U-Pb Zircon	ca. 98	This report; preliminary data
16lo18B	SW of Racine Lake	rhyolitic unit	foliated	U-Pb Zircon	ca. 121	Ootes et al. (2018)
	Middle Ridge	volcanic unit	openly folded	U-Pb Zircon	ca. 125	Mihalynuk et al. (2003)
	Tally Ho Mountain	megacrystic granite	massive	U-Pb Zircon	ca. 173	Tizzard et al. (2009)
	Tally Ho Mountain	Tally Ho leuco-gabbro	foliated	U-Pb Zircon	ca. 208	Tizzard et al. (2009)

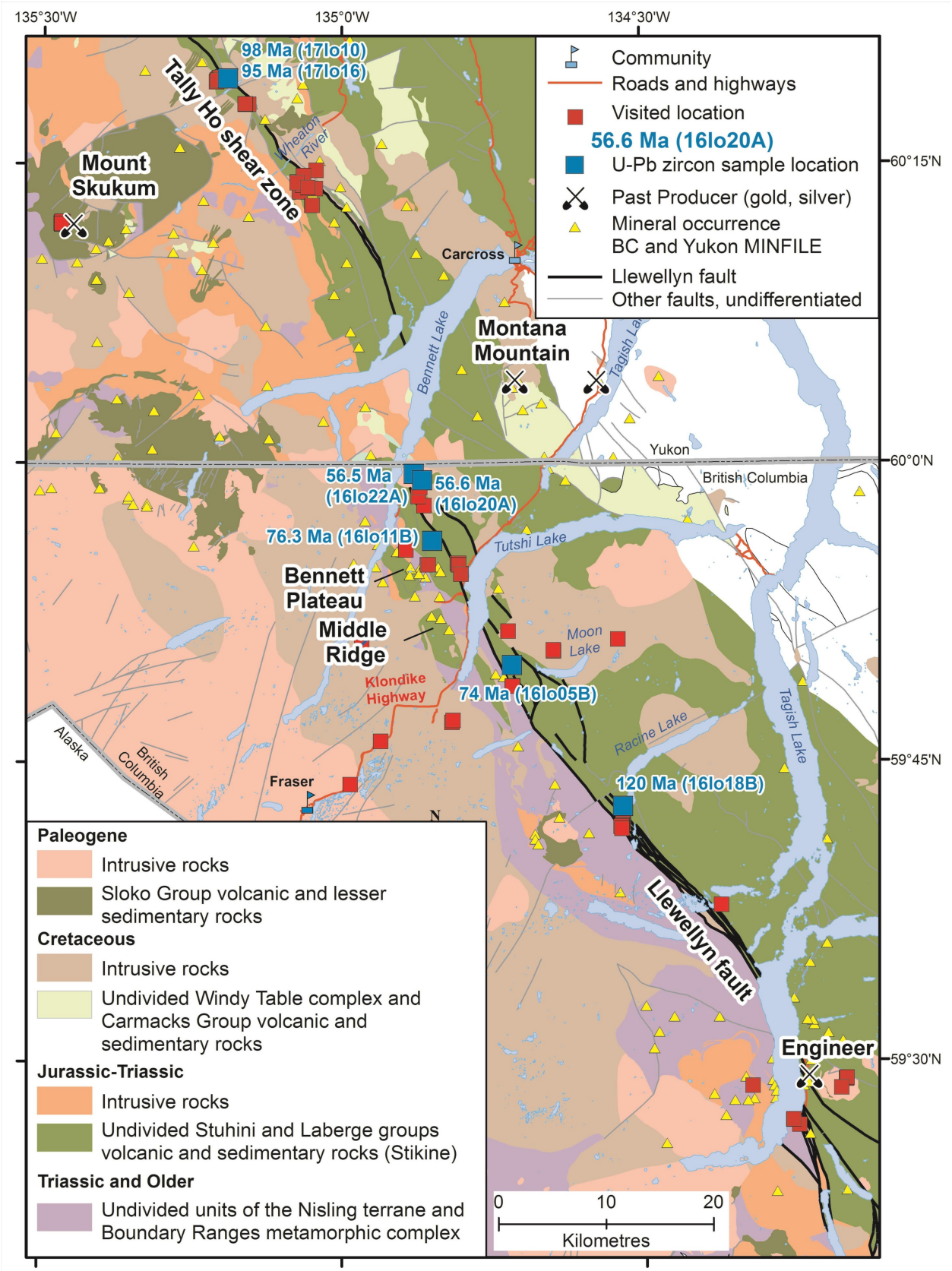

Figure 2. Generalized geology near the Llewellyn fault and Tally Ho shear zone (*modified from* Ootes et al., 2018). Geology is *after* Doherty and Hart (1988), Hart and Pelletier (1989), Hart and Radloff (1990), and Mihalynuk et al. (1999). Rocks of the Cache Creek assemblage (upper right) are unfilled.

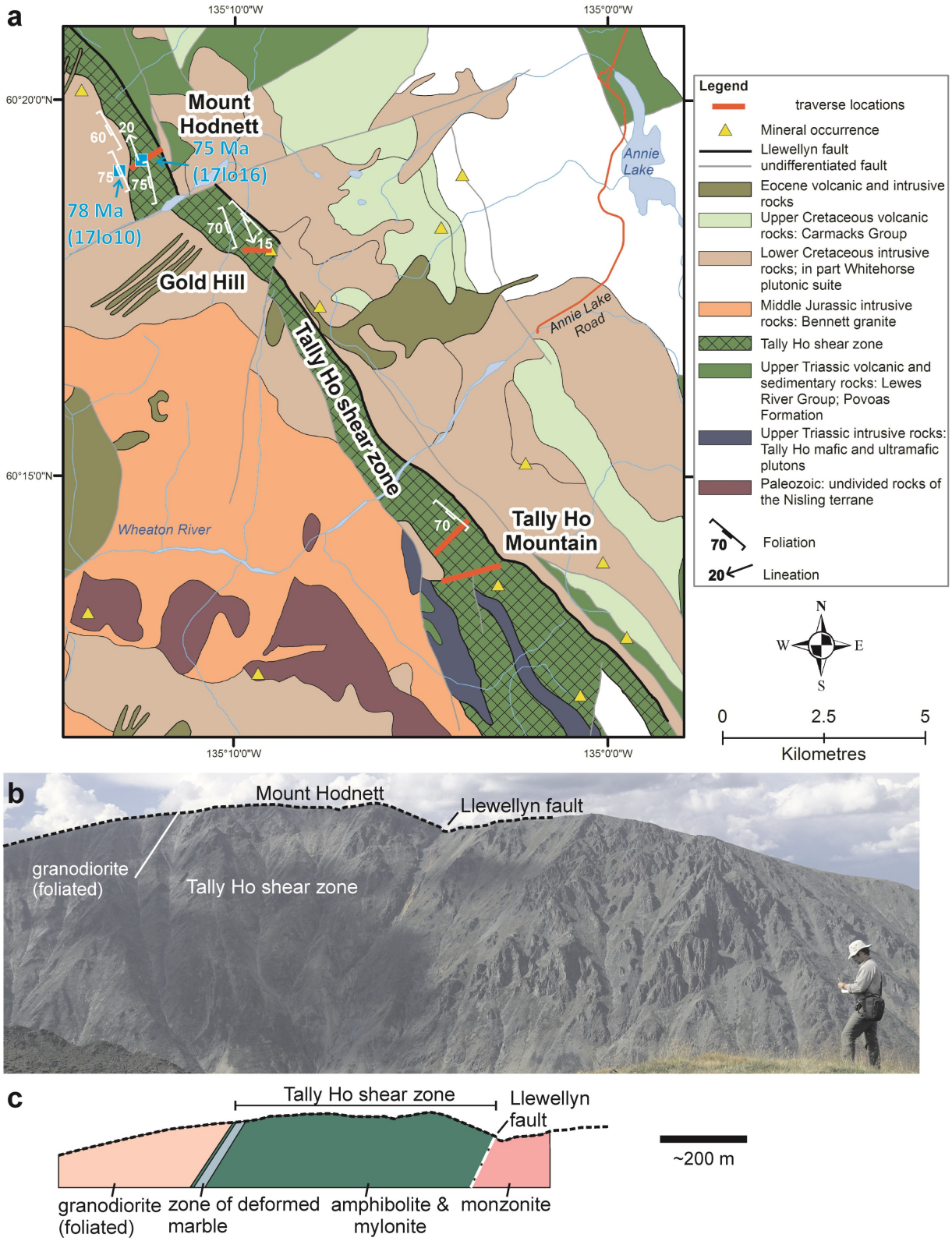

Figure 3. a) Generalized geology of the Tally Ho shear zone, southern Yukon (*modified after* Hart and Radloff, 1990). Generalized foliations (line with pendants) and lineations (arrows) are from this study and Hart and Radloff (1990). b) View to the northwest of Mount Hodnett and the Tally Ho shear zone from Gold Hill. c) Geological sketch of Mount Hodnett, in upper left of photo; in part *modified after* Tizzard et al. (2009).

below.

Two different granitic intrusions from east of Bennett Lake were sampled for U-Pb dating (Fig. 2). Sample 16lo20A was collected from a medium-grained granite with K-feldspar phenocrysts. The granite pluton, which was mapped as middle Cretaceous to Tertiary (unit LKqm in Mihalynuk et al., 1999), intrudes foliated Laberge Group metasedimentary rocks. The granite does not contain a foliation. Five prismatic zircon grains were selected for $^{206}Pb/^{238}U$ age dating, and the weighted mean of the three youngest overlapping concordant results yields an age of 56.58 ± 0.07 Ma, which is interpreted as the crystallization age of the granite (Ootes et al., 2018). Another sample (16lo22A) consists of equigranular biotite-hornblende granite, mapped as middle Cretaceous to Tertiary pluton and interpreted to crosscut both ductile and brittle Llewellyn structures (unit LKg1 in Mihalynuk et al., 1999; Pennington pluton discussed in Hart and Radloff, 1990). The granite lacks a ductile fabric but contains closely spaced (<30 cm), moderately east-dipping, brittle fractures, subparallel and probably related to the Llewellyn fault (Fig. 2). From the five prismatic igneous zircons selected for analysis, a $^{206}Pb/^{238}U$ weighted mean of four results yields a crystallization age of 56.46 ± 0.06 Ma (Ootes et al., 2018).

At Bennett plateau (Fig. 2), the 'Skarn zone' hosts gold and base-metal mineralization that developed with a series of hydrothermal quartz-actinolite veins hosted in metasedimentary rocks of the Stuhini Group (Mihalynuk et al., 1999; Troymet Exploration Corporation, 2012). These veins are boudinaged and folded. A two metre thick unfoliated granodiorite porphyry, which intruded the Skarn zone parallel to the host-rock fabrics, post-dates the ductile deformation. A sample of the granodiorite porphyry (sample 16lo11B) yielded good quality igneous zircons, four of which have overlapping, concordant $^{206}Pb/^{238}U$ ages with a weighted mean age of 76.30 ± 0.05 Ma, which is interpreted as the crystallization of the intrusion (Ootes et al., 2018).

A fine- to medium-grained, granodiorite pluton (unit #gd in Mihalynuk et al., 1999) was sampled within the trace of the Llewellyn fault, west of Moon Lake (Fig. 2), where it cuts across the contact between the Stuhini Group and the Boundary Ranges metamorphic uite. It is weakly porphyritic, with moderate carbonate alteration and partially chloritized biotite and hornblende. The granodiorite lacks a foliation and post-dates the ductile deformation preserved in the host argillite. The granodiorite is cut by a southeast-striking brittle fault, comprising a two metre wide gouge zone (Ootes et al., 2017). The sample represents the least-altered part of the granodiorite, near the contact with the host argillite. The sample (16lo05B) yielded concordant to slightly discordant zircon with a range of $^{206}Pb/^{238}U$ ages from ca. 92 to 74 Ma (Ootes et al., 2018). The youngest zircons, at ca. 74 Ma, give the best estimate for the time of crystallization of the granodiorite, whereas the older zircon is interpreted as an antecryst.

Southwest of Racine Lake is a zone of imbricated Stuhini Group and minor Laberge Group rocks (Mihalynuk et al., 1999) that are juxtaposed against those of the Boundary Ranges metamorphic suite along splays of the Llewellyn fault. At that locality, Mihalynuk et al. (1999) identified fault-bounded slices of 'rhyolite' and associated rocks. The rhyolitic rock contains plagioclase and quartz phenocrysts and is affected by a penetrative moderate to strong foliation and is carbonate altered, potentially related to brittle faulting along this zone. The rhyolitic sample 16lo18B was selected for geochronology and two zircons yielded overlapping and concordant results, with a $^{206}Pb/^{238}U$ weighted mean age of ca. 121 Ma, which is interpreted to represent the timing of crystallization (Ootes et al., 2018).

Tally Ho shear zone

In southern Yukon, the Tally Ho shear zone is defined by a corridor of strongly deformed amphibolite, marble, and schist assigned to the Povoas Formation of the Lewes River Group (Upper Triassic; equivalent to Stuhini Group in British Columbia), which are bounded on either side by younger intrusions (Fig. 2; Doherty and Hart, 1988; Hart and Radloff, 1990; Tizzard et al., 2009). The approximately 40 km long shear zone is best exposed between Tally Ho Mountain and Mount Hodnett (Fig. 3) where it comprises marble, mafic schist, and amphibolite that have a steep southwest-dipping penetrative foliation to mylonitic fabric, locally marked by a shallow southeast- or northwest-plunging mineral lineation (Fig. 3; Hart and Radloff, 1990). Bedding is locally preserved in strongly deformed marble layers, but is strongly folded and transposed into the foliation as the mylonite zones are approached (Hart and Radloff, 1990; Tizzard et al., 2009). Brittle deformation features are parallel to and overprint the Tally Ho shear zone ductile fabrics. These include faults with dextral offset, one of which occurs along the east side of the Tally Ho shear zone, which Hart and Radloff (1990) correlated to the Llewellyn fault (Fig. 2, 3).

Hart and Radloff (1990) interpreted that the Tally Ho shear zone records predominantly sinistral deformation between 230 and 220 Ma, and speculated on its potential importance as a terrane-bounding thrust fault. Revising this interpretation, Tizzard et al. (2009) considered that the shear zone represents a top-to-the-east crustal-scale thrust fault that juxtaposed foliated gabbro and pyroxenite (hanging wall) over Povoas Formation (shear zone and footwall) and was subsequently affected by upright folds during Nisling-Stikine collision. Tizzard et al. (2009) provided uranium-lead zircon ages of ca. 208 Ma for a foliated leucogabbro in the hanging wall and ca. 173 Ma for a massive megacrystic granite west of the shear zone, which they interpreted as bracketing the timing of thrusting and subsequent folding.

Traverses across the Tally Ho shear zone were conducted in the Tally Ho Mountain, Gold Hill, and Mount Hodnett areas of Yukon (Fig. 2, 3; Castonguay et al., 2018; Ootes et al., 2018). The best exposed and accessible section at Mount Hodnett (Fig. 3) was selected for geochronological sampling (see pre-

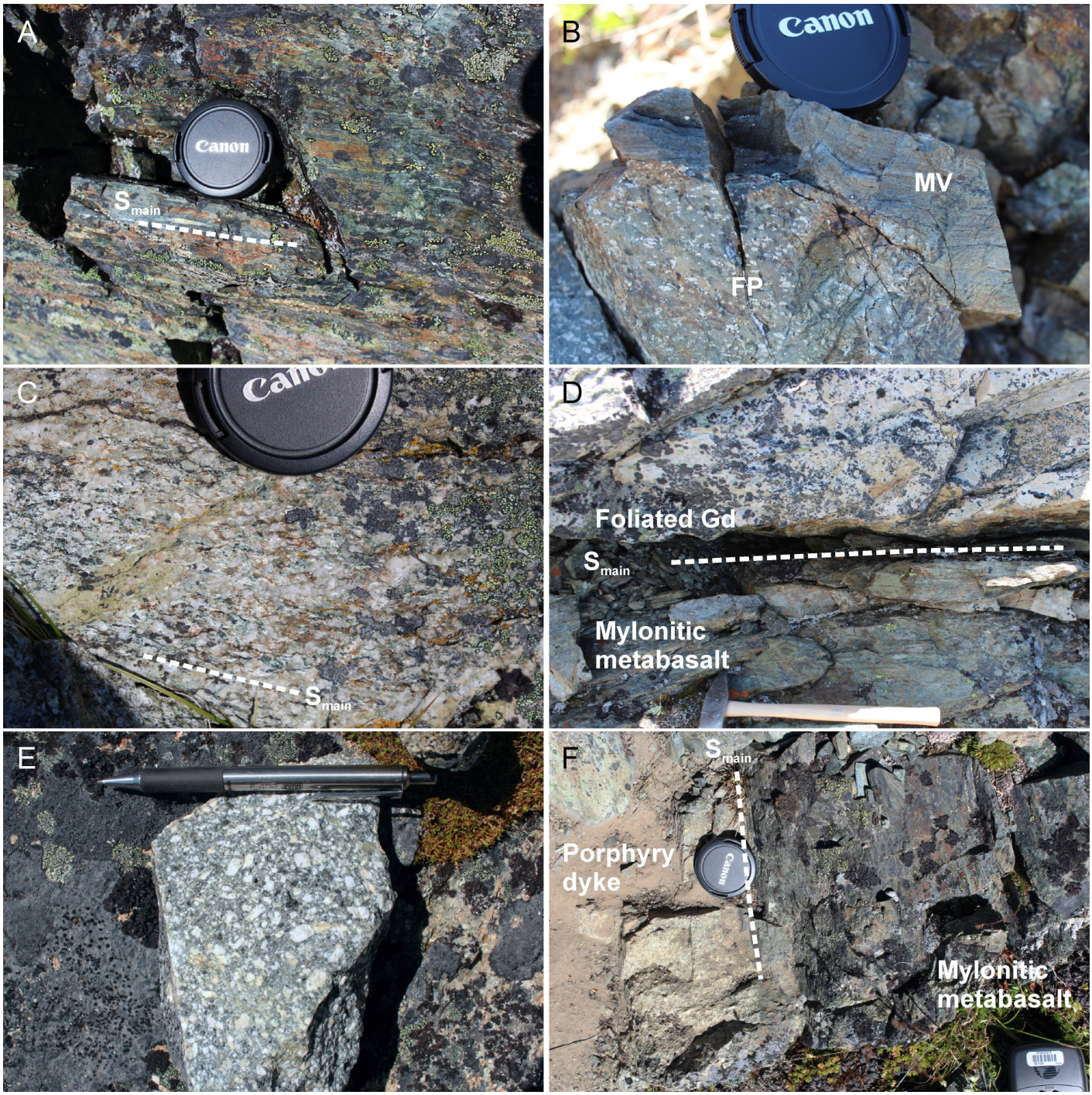

Figure 4. Tally Ho shear zone at Mount Hodnett. a) Strongly foliated to mylonitic metabasalt/amphibolite. b) Late, unfoliated feldspar porphyritic dyke (FP) intruding mylonitic mafic volcaniclastic rock (MV). c) Foliated granodiorite near sampled locality 17lo10. d) Sheared intrusive contact between foliated granodiorite (Gd) and mylonitic mafic schist (rotated view to the northwest, top is to the right side). e) Relatively massive sample (near locality 17lo16) in the central part of an approximately 8 m thick feldspar porphyritic monzonite dyke intruding the metabasalt within the shear zone. f) Sheared intrusive contact, subparallel to S_{main}, between a weakly foliated dyke and mylonitic metabasalt. For scale, lens cap is 6 cm in diameter, pen is 14 cm in length and hammer is 37.5 cm in length.

liminary results below). Exposed units include (from west to east): weakly to moderately foliated granodiorite in sheared intrusive contact with steeply west-dipping amphibolite and marble; strongly sheared mafic volcaniclastic rocks (mylonite), and foliated metabasalt (Fig. 3), locally intruded by massive to weakly foliated (at contacts) intermediate feldspar porphyry dykes. The steep southwest-dipping main foliation (S_{main}) occurs in most rocks (except late feldspar porphyry dykes), but is best developed in mylonitic volcaniclastic beds. East of this, the shear zone is mostly strongly foliated (S_{main}) amphibolite and metabasalt (mafic schist; Fig. 4a). Rare kinematic indicators include shear bands, sigmoidal clasts, and quartz vein boudins, which indicate apparent northeast-directed motion (Ootes et al., 2018). However, the shallowly plunging stretching and/or mineral lineation on S_{main} indicates strike-slip movement. Along the eastern side of the shear zone, the foliated amphibolite/metabasalt is structurally interlayered with moderately foliated monzonite (Fig. 3). This juxtaposition is the result of a less than 10 m wide subvertical brittle high-strain zone marked by cataclasite and carbonate alteration that overprints the foliation in the metabasalt. All units are intruded by late unfoliated intermediate to felsic feldspar-porphyritic dykes (Fig. 4b).

The granodiorite west of the shear zone (Fig. 3) was assigned to the Whitehorse plutonic suite (ca. 120 Ma: Hart and Radloff, 1990). This granodiorite contains a steep southwest-dipping heterogeneously developed foliation (Fig. 4c), defined by chlorite-altered biotite and hornblende, which occurs in southeast-trending high-strain corridors, and increases in intensity northeastward toward the contact with the mylonitic metabasalt that comprises the shear zone (Fig. 4d). This foliation in the granodiorite strikes south-southeast, dips west, and is subparallel to the S_{main} foliation in the shear zone (Ootes et al., 2018; Fig. 3). The contact is a zone in which the foliated intrusion becomes progressively finer grained, more felsic, and interfingered with the mylonitic metabasalt. Basalt xenoliths also occur in strongly foliated granodiorite. The contact is overprinted by brittle fault and breccia zones and intruded by a late unfoliated intermediate dyke. Based on these relationships, including the eastward-increasing heterogeneous strain gradient observed in the granodiorite and the occurrence of only one subparallel penetrative foliation across both units, the zone is interpreted as a sheared intrusive contact, at which strain was strongly partitioned in the metabasalt, during a single ductile deformation event (Ootes et al., 2018).

Two samples were collected in 2017 and recently analyzed for uranium-lead zircon geochronology. Both age results are herein considered as preliminary data (Table 1). The first sample comes from a moderately foliated granodiorite (sample 17lo10; Fig. 3, 4c) collected roughly 110 m west of the main contact with the Tally Ho shear zone. The analysis (3 concordant grains) yielded a preliminary $^{206}Pb/^{238}U$ weighted mean age of ca. 98 Ma. The second sample (17lo16; Fig. 3, 4e) is from the central part of a approximately 8 m thick feldspar porphyritic monzonite dyke intruding the metabasalt within the shear zone. The dyke is massive to locally weakly foliated (marked by the alignment of amphibole and biotite grains) and is probably folded: the eastern contact is oriented at high angle with the mylonitic fabric in the host rock, whereas it is at low angle with the fabric along the western contact, where the dyke is weakly foliated (Fig. 4f). Three grains from this sample have been analyzed thus far. Two grains gave an age of ca. 98 Ma; the third yielded a $^{206}Pb/^{238}U$ age of 95 Ma, which constitutes the preliminary maximum age of the dyke.

Discussion

Timing of deformation

Two spatially superposed structural events occur along the Llewellyn-Tally Ho deformation corridor. An early ductile deformation phase exemplified by the Tally Ho shear zone in the Yukon, and by correlative, albeit lesser documented, ductile deformation zones in the Boundary Ranges metamorphic suite and Stuhini Group in British Columbia. Brittle fault zones related to the Llewellyn fault overprint these early ductile deformation zones. The ongoing study including U-Pb geochronology (Ootes et al., 2018, and herein) allows the timing of deformation of these superposed structural events and associated gold mineralization to be better bracketed (Fig. 5; Table 1).

Early ductile event

Only one penetrative foliation (S_{main}) has been observed along the entire Llewellyn fault and Tally Ho shear zone corridor. The rhyolite occurring along the Llewellyn fault southwest of Racine Lake, has an age of ca. 121 Ma (sample 16lo18B) and is interpreted to predate the development of S_{main} foliation (Ootes et al., 2018). To further bracket the maximum age of S_{main}, we investigated the Tally Ho shear zone at Mount Hodnett. There, S_{main} foliation and related mylonitic fabric in the shear zone are parallel and probably formed at the same time as the heterogeneously developed, but locally penetrative foliation in the neighbouring granodiorite pluton (again mapped as Whitehorse plutonic complex: Hart and Radloff, 1990). Tizzard et al. (2009) preferred the explanation that the foliation in the granodiorite is distinct and related to a fault that juxtaposes the granodiorite and Tally Ho shear zone. Based on field relationships and geochronology at Tally Ho Mountain (south of Mount Hodnett), they have interpreted that S_{main} foliation and the development of the Tally Ho shear zones occurred between 208 and 173 Ma.

Based on our preliminary U-Pb zircon data from the granodiorite at Mount Hodnett (ca. 98 Ma: sample 17lo10), the penetrative foliation (in the granodiorite pluton), the S_{main} foliation and consanguineous mylonitic fabric must have developed after ca. 98 Ma. Within the shear zone, if the foliation in the margins of the dyke (sample 17lo16) is S_{main}, which is our preferred interpretation, then the maximum age of ductile deformation would be even younger (<95 Ma).

The ca. 74 Ma granodiorite pluton west of Moon Lake (sample 16lo05B) and the ca. 76 Ma granodiorite porphyry on Bennett plateau (sample 16lo11B) both postdate ductile defor-

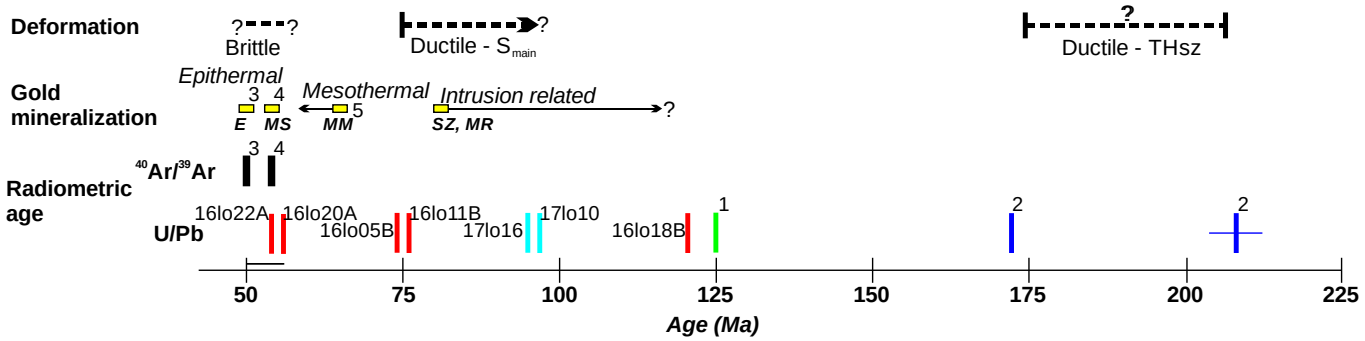

Figure 5. Timeline summary of deformation and gold mineralization in the vicinity of the Llewellyn fault and Tally Ho shear zone (THsz). Uranium-lead age constraints from this study are labelled by sample number (red bar *for* Ootes et al. (2018) data; light blue bar for preliminary data *from* this report): (1) *from* Mihalynuk et al. (2003; green bar); and (2) *from* Tizzard et al. (2009; blue bar). $^{40}Ar/^{39}Ar$ mica results are *from* (3) Millonig et al. (2017) and (4) *from* Love et al. (1998), and also constrain the time of epithermal gold mineralization at Engineer Mine (E) and Mount Skukum (MS). The suggested timing of mesothermal gold mineralization at Montana Mountain mines (MM; 5) is *from* Hart and Pelletier (1989) and intrusion-related mineralization at the Skarn zone (SZ) is from this study and at Middle ridge (MR) is from Mihalynuk et al. (2003). Notes: ? – uncertainty; S_{main} – main foliation along Llewellyn and Tally Ho deformation corridor. *See* text for discussion.

mation in the Stuhini and Laberge groups and Boundary Ranges metamorphic suite. Therefore, ductile deformation fabrics along the Llewellyn fault predate ca. 75 Ma.

Late brittle event

The granodiorite west of Moon Lake (sample 16lo05B) is crosscut by the Llewellyn fault, constraining the brittle deformation to younger than ca. 74 Ma. The two granitic plutons sampled near the British Columbia-Yukon border along the Llewellyn fault (samples 16lo20A, 16lo22A; Fig. 2) yield indistinguishable ages of ca. 56 Ma. Both intrusive phases postdate ductile deformation. The slightly older K-feldspar porphyritic granite lacks evidence of brittle deformation. However, the slightly younger equigranular granite pluton (sample 16lo20A) contains fractures that are along strike, and parallel to, the fault trace, and is interpreted to have acted as a rigid body during brittle faulting (Ootes et al., 2018). Brittle deformation continued after the granite intruded, as indicated by $^{40}Ar/^{39}Ar$ dating of vanadian illite from Engineer Mine (about 70 km to the southeast, Fig. 2), which indicates brittle movement and associated epithermal veining along the fault at ca. 50 Ma (Millonig et al., 2017). This timing is coeval with Cordilleran-scale brittle dextral strike-slip faulting (e.g. Gabrielse et al., 2006). It does remain possible that brittle movement began prior to ca. 56 Ma and the plutons overlap the initiation of brittle deformation along the Llewellyn fault.

Gold mineralization and deformation

One of the goals of this study was to test the apparent relationship between the various styles of gold mineralization and structural and magmatic events along the Llewellyn-Tally Ho deformation corridor. An additional question arises as to whether the gold mineralization styles are part of the same system in which ductile and brittle deformation are contemporaneous, and gold mineralization occurs synchronously at various depths in the crust (e.g. Goldfarb et al., 2005). The field relationships and U-Pb zircon geochronology presented herein demonstrate a time gap of at least ca. 20 Ma between the ductile and the brittle deformation (Fig. 5). The older ductile deformation is defined by a regional foliation (S_{main}) in the Stikine terrane rocks (Stuhini, Lewes River, and Laberge groups) and possibly the Boundary Ranges metamorphic complex. The S_{main} foliation is older than ca. 75 Ma (Fig. 5) so that the intrusion-related gold mineralization that formed before or during the early-ductile phase of deformation, such as in the Skarn zone at Bennett plateau and perhaps Middle Ridge (Mihalynuk et al., 2003), predates ca. 75 Ma. If intrusion-related gold mineralization at Bennett plateau, and possibly Middle Ridge, developed between 95 to 75 Ma, then this mineralization falls within the timeframe and style typical of the Tintina gold belt in Yukon and Alaska (e.g. Hart, 2007).

The epithermal-styles of gold mineralization, such as at Engineer Mine and Mount Skukum, have been dated at ca. 55 to 50 Ma and are clearly related to brittle deformation and volcanism (Fig. 5; Love, 1990; Love et al., 1998; Millonig et al., 2017; Ootes et al., 2017). This timeframe of brittle deformation corresponds to that of similar major Cordilleran faults (e.g. Gabrielse et al., 2006) and of the timing of orogenic gold mineralization in the Juneau gold camp, Alaska (Miller et al., 1994).

Conclusions

The Llewellyn fault overprints early ductile fabrics in British Columbia and the Tally Ho shear zone in Yukon. Epithermal gold mineralization at the past-producing Mount Skukum and Engineer mines are related to this brittle deformation that occurred between ca. 56 and 50 Ma. That event matches the timing and structural framework of the Juneau gold camp in Alaska (Miller et al., 1994), suggesting a similar first-order

genetic process led to gold mineralization in both environments.

Previous work suggested the Tally Ho shear zone developed between 208 and 173 Ma (Tizzard et al., 2009). Observations and preliminary U-Pb zircon data from this study suggest that the Tally Ho shear zone and related fabric (S_{main} foliation) affected a ca. 95 Ma dyke within the shear zone and a neighbouring ca. 98 Ma granodiorite pluton, considered part of the Whitehorse plutonic complex (Hart and Radloff, 1990). A ca. 120 Ma rhyolite along the Llewellyn fault contains S_{main} foliation, indicating that the fabric developed after 120 Ma. Two granodiorite intrusions crosscut and provide a minimum age of ductile deformation at ca. 76 and 74 Ma. Intrusion-related gold mineralization, for example at the Skarn zone and possibly at Middle ridge (Mihalynuk et al., 2003; Troymet Exploration Corporation, 2012), are deformed and pre-date 75 Ma. If these intrusion-related gold mineralizing systems developed between 95 and 75 Ma, then they may correlate with those of the Tintina gold belt in Yukon and Alaska (Hart, 2007).

The Llewellyn fault and related brittle splays extend into Yukon and crosscuts the Tally Ho shear zone (Hart and Radloff, 1990; Mihalynuk et al., 1999). A ca. 20 Ma time-gap between early and late deformation (Fig. 5) shows that gold mineralization associated with ductile and brittle fabrics and structures formed at different times, and therefore are related to distinct tectonic events.

Acknowledgments

This report is a contribution to NRCan's Targeted Geoscience Initiative Program (TGI). Support for this study was provided through the Gold Project's '*Activity G-2.3: Epithermal and orogenic gold along Cordilleran faults*'.

This joint British Columbia Geological Survey – TGI study is conducted in collaboration with the Yukon Geological Survey. We thank BC Gold Corp. (Engineer Mine now owned by Blind Creek Resources), Troymet Exploration Corp., and Teralogic Exploration Inc. for access to properties and data. Helicopter support was provided by Capital Helicopters (Whitehorse, Yukon) and Discovery Helicopters (Atlin, British Columbia). The study benefited from field assistant Jessica Elliott (in 2016) and Reid Simmonds (in 2017), both from the University of Victoria, and logistical support, field visits, and discussions with Scott Casselman and Craig Nicholson (Yukon Geological Survey), Stephen Rowins and Adrian Hickin (British Columbia Geological Survey), and Patrick Mercier-Langevin (GSC Quebec). This report benefited from the review of Pedro Acosta-Góngora, Suzanne Paradis and Neil Rogers.

References

Castonguay, S., Ootes, L., Mercier-Langevin, P., Rowins, S., and Devine, F., 2017. Orogenic gold along Cordilleran faults; key characteristics and analogies between Phanerozoic and Archean settings; *in* Targeted Geoscience Initiative – 2016 Report of Activities, (ed.) N. Rogers; Geological Survey of Canada, Open File 8199, p. 35–37.

Castonguay, S., Ootes, L., Mercier-Langevin, P., and Devine, F., 2018. Gold along Cordilleran faults: Key characteristics and analogies between Phanerozoic and Archean settings; *in* Targeted Geoscience Initiative: 2017 report of activities, volume 1, (ed.) N. Rogers; Geological Survey of Canada, Open File 8358, p. 139–145.

Doherty, R.A. and Hart, C.J.R., 1988. Preliminary geology of Fenwick Creek (105D/3) and Alligator Lake (105D/6) map areas; Yukon Geological Survey, Open File 1988-2, 2 maps, 1:50,000 scale**.**

Gabrielse, H., Murphy, D.C., and Mortensen, J.K., 2006. Cretaceous and Cenozoic dextral orogen-parallel displacements, magmatism, and paleogeography, north-central Canadian Cordillera; *in* Paleogeography of the North American Cordillera: Evidence For and Against Large-Scale Displacements, (ed.) J.W. Haggart, R.J. Enkin, and J.W.H. Monger; Geological Association of Canada, Special Paper 46, p. 255–276.

Goldfarb, R.J., Baker, T., Dubé, B., Groves, D.I., Hart, C.J.R., and Gosselin, P., 2005. Distribution, character, and genesis of gold deposits in metamorphic terranes; *in* Economic Geology 100th Anniversary Volume (1905-2005), (ed.) J.W. Hedenquist, J.F.H. Thompson, R.J. Goldfarb, and J.P. Richards; Society of Economic Geologist, Littleton, Colorado, p. 407–450.

Hart, C.J.R., 2007. Reduced intrusion-related gold-systems, *in* Mineral Deposits of Canada: A Synthesis of Major Deposit-Types, District Metallogeny, the Evolution of Geological Provinces, and Exploration Methods, (ed.) W.D. Goodfellow; Geological Association of Canada, Mineral Deposits Division, Special Publication No. 5, p. 95–112.

Hart, C.J.R. and Pelletier, K.S., 1989. Geology of Carcross (105D/2) and Part of Robinson (105D/7) Map Areas; Indian and Northern Affairs Canada, Yukon Geological Survey, Open File 1989-1, 84 p.

Hart, C.J.R. and Radloff, J.K., 1990. Geology of Whitehorse, Alligator Lake, Fenwick Creek Carcross and part of Robinson map areas (105D/11, 6, 3, 2 & 7); Yukon Geological Survey, Open File 1990-4.

Love, D.A., 1990. Structural controls on veins of the Mount Skukum gold deposit, southwestern Yukon; *in* Current Research, Part E, Cordillera and Pacific Margin; Geological Survey of Canada, Paper 90-1E, p. 337–346.

Love, D.A., Clark, A.H., Hodgson, C.J., Mortensen, J.K., Archibald, D.A., and Farrar, E., 1998. The timing of adularia-sericite-type mineralization and alunite-kaolinite-type alteration, Mount Skukum epithermal gold deposit, Yukon Territory, Canada: ^{40}Ar-^{39}Ar and U-Pb geochronology; Economic Geology, v. 93, p. 437–462.

Mihalynuk, M.G., Smith, M., Hancock, K.D., Dudka, S.F., and Payne, J., 1994. Geology of the Tulsequah River and Glacier Creek Area (NTS 104K/12, 13); Ministry of Energy,

Mines and Petroleum Resources, British Columbia Geological Survey, Open File 1994-03, 3 sheets, 1:50 000 scale.

Mihalynuk, M.G., Mountjoy, K.J., Currie, L.D., Smith, M.T., and Rouse, J.N., 1999. Geology and mineral resources of the Tagish Lake area (NTS 104M/8, 9, 10E, 15 and 104N/12W) northwestern British Columbia; Ministry of Employment and Investment, British Columbia Geological Survey, Bulletin 105, 190 p.

Mihalynuk, M.G., Devine, F., and Friedman, R.M., 2003. Marksmen partnership: potential for shallow submarine VMS (Eskay-style) and intrusive-related gold mineralization, Tutshi Lake area; Ministry of Energy and Mines, British Columbia Geological Survey, Geofile 2003-09, 1 poster.

Miller, L.D., Goldfarb, R.J., Gehrels, G.E., and Snee, L.W., 1994. Genetic links among fluid cycling, vein formation, regional deformation, and plutonism in the Juneau gold belt, southeastern Alaska; Geology, v. 22, p. 203–206.

Millonig, L.J., Beinlich, A., Raudsepp, M., Devine, F., Archibald, D.A., Linnen, R.L., and Groat, L.A., 2017. The Engineer Mine, British Columbia: An example of epithermal Au -Ag mineralization with mixed alkaline and subalkaline characteristics; Ore Geology Reviews, v. 83, p. 235–257.

Ootes, L., Elliott, J.M., and Rowins, S.M., 2017. Testing the relationship between the Llewellyn fault, gold mineralization, and Eocene volcanism in northwest British Columbia: A preliminary report; *in* Geological Fieldwork 2016; British Columbia Ministry of Energy and Mines, British Columbia Geological Survey, Paper 2017-1, p. 49–59.

Ootes, L., Castonguay, S., Friedman, R., Devine, F., and Simmonds, R., 2018. Testing the relationship between the Llewellyn fault, Tally Ho shear zone, and gold mineralization in northwest British Columbia; *in* Geological Fieldwork 2017; British Columbia Ministry of Energy, Mines and Petroleum Resources, British Columbia Geological Survey, Paper 2018-1, p. 67–81.

Roots, C.F., 1981. Geological setting of gold-silver veins on Montana Mountain; *in* Yukon Geology and Exploration 1979-80; Indian and Northern Affairs Canada/Department of Indian and Northern Development: Exploration and Geological Services Division, p. 116–122.

Tizzard, A.M., Johnston, S.T., and Heaman, L.M., 2009. Arc imbrication during thick-skinned collision within the northern Cordilleran accretionary orogen, Yukon, Canada; *in* Earth Accretionary Systems in Space and Time, (ed.) P.A. Cawood and A. Kröner; Geological Society, London, Special Publications, v. 318, p. 309–327.

Troymet Exploration Corporation, 2012. Technical Report, Golden Eagle Property; 43-101 Technical Report, July 9, 2012; Troymet Exploration Corporation, 471 p. <https://www.troymet.com/assets/docs/projects/GE_TechRpt_Jul-12.pdf> [accessed December 27, 2018]

Walton, L., 1986. Textural characteristics of the Venus vein and implications for ore shoot distribution; *in* Yukon Geology Volume 1, (ed.) J.A. Morin and D.S. Emond; Exploration and Geological Services Division, Indian and Northern Affairs Canada, p. 67–71.

Lithological and structural setting of structurally controlled gold mineralization in the Wilding Lake region, central Newfoundland

I.W. Honsberger[1], W. Bleeker[1], H.A.I. Sandeman[2] and D.T.W. Evans[3]

[1]*Geological Survey of Canada, 601 Booth Street, Ottawa, Ontario K1A 0E8*

[2]*Newfoundland and Labrador Department of Natural Resources, Mineral Deposits Section, St. John's, Newfoundland A1B 4J6*

[3]*Antler Gold Inc., Suite 2001-1969 Upper Water Street, Halifax, Nova Scotia B3J 3R7*

Abstract

The structurally controlled central Newfoundland gold belt is emerging as one of the next significant mining jurisdictions in Canada. Gold mineralization is associated with crustal-scale faults that preserve synorogenic conglomerates, similar to the setting of orogenic gold in the Archean Abitibi greenstone belt. Recent exploration in the Wilding Lake region exposed a system of auriferous quartz veins hosted within sedimentary and volcanic rocks. Detailed lithological and structural documentation of these newly exposed zones was conducted to examine controls on gold mineralization and place the vein system into a regional context.

Field data demonstrate that the main 'Elm' quartz vein extends for approximately 230 m along strike, is up to 2 m wide and cuts the conglomerate host within an oblique sinistral shear zone that accommodated north-northeast-directed thrusting. An early set of moderately dipping extensional quartz veins, consistent with oblique sinistral shear, emanate from the main vein. A later, more steeply dipping set of extensional quartz veins crosscut the main vein and the earlier vein set, and are consistent with a component of horizontal extension. Chalcopyrite and malachite occur locally in the early vein set, but are more abundant overall within the younger vein set. A nearly conjugate set of steeply dipping extension fractures crosscut the main vein and the two vein sets. These fractures are filled typically with vuggy quartz and unaltered and altered sulphides. Field data are consistent with progressive deformation characterized by early oblique compressional sinistral shear and subsequent components of subhorizontal extension and minor dextral strike-slip.

Introduction

Structurally controlled gold systems comprise the most economically significant gold deposit type in Canada (Hodgson, 1993). These systems are characterized by synorogenic quartz±carbonate veins that form during deformation along crustal-scale fault zones (Hodgson, 1993; Kerrich and Cassidy, 1994; Groves et al., 1998; Kerrich et al., 2000; Goldfarb et al., 2001, 2005), as in the Archean Abitibi greenstone belt of the Canadian Shield (e.g. Poulson et al., 2000; Dubé and Gosselin, 2007; Bleeker, 2015; Dubé et al., 2017). In central Newfoundland, epigenetic gold mineralization appears to be associated spatially with crustal-scale fault zones that preserve footwall panels of synorogenic clastic sedimentary rocks (Fig. 1), similar to the structurally controlled orogenic gold system of the Abitibi (Bleeker, 2015).

The top emerging gold mining jurisdiction in Newfoundland, and among the top in Canada, is Marathon Gold's Valentine Lake gold property along the Victoria Lake shear zone in central Newfoundland (Fig. 1 and 2a; Lycopodium Minerals Canada Ltd., 2018). Presently, this gold property is reporting 4.2 Moz of structurally controlled total gold resource grading between 1.77 and 1.85 g/t (Lycopodium Minerals Canada Ltd., 2018). The recent expansion of the Valentine Lake gold property has stimulated renewed prospecting, staking, exploration, and study elsewhere along the major encompassing structural corridor. Recent soil sampling programs and exploratory drilling on industry lands adjacent to Valentine Lake along the Victoria Lake shear zone confirm the economic potential and the need for local geological studies in these areas. The research herein documents the lithological and structural setting of recently discovered gold mineralization on Antler Gold Inc. property adjacent to and northeast of the Valentine Lake gold property (Fig. 2a, b). This is the first detailed geological and structural study conducted on this highly prospective ground for gold mineralization along strike from the known Valentine Lake gold property. An overarching research goal is to provide a coherent geological and structural framework for assessing the mineral potential of Antler Gold's property and, as well, inform future targeted exploration vectors.

Corresponding author: Ian Honsberger (ian.honsberger@canada.ca)

Honsberger, I.W., Bleeker, W., Sandeman, H.A.I., and Evans, D.T.W., 2019. Lithological and structural setting of structurally controlled gold mineralization in the Wilding Lake region, central Newfoundland; *in* Targeted Geoscience Initiative: 2018 report of activities, (ed.) N. Rogers; Geological Survey of Canada, Open File 8549, p. 59–69. https://doi.org/10.4095/313640

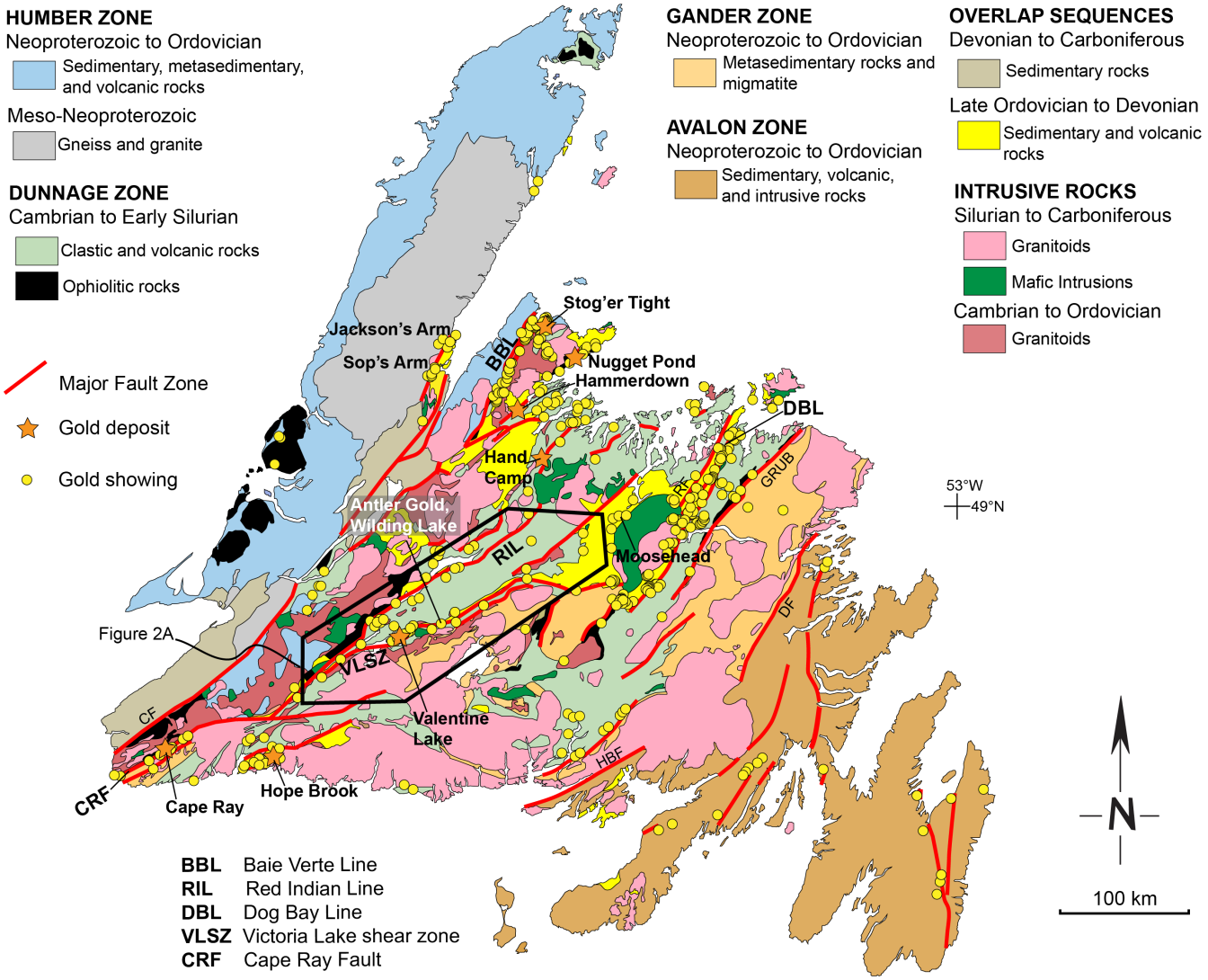

Figure 1. Generalized geological map of Newfoundland showing the distribution of crustal-scale faults (red lines) and locations of gold deposits (orange stars) and showings (yellow circles). The area outlined in black is enlarged in Figure 2a. Map modified from Colman-Sadd et al. (1990). Abbreviations: CF – Cabot Fault; DF – Dover Fault; GRUB – Gander River Ultrabasic Belt; HBF – Hermitage Bay Fault.

Geological and structural setting of epigenetic gold mineralization, central Newfoundland

Numerous epigenetic gold deposits and showings occur along crustal-scale faults within the Dunnage Zone of central Newfoundland (Fig. 1; Tuach et al., 1988; Evans, 1996, 1999). The eastern Dunnage Zone, termed the Exploits subzone, is particularly well endowed in gold deposits and showings (Evans, 1996). The main structural corridor in central Newfoundland with respect to gold mineralization extends northeast from Cape Ray along the Cape Ray fault and Victoria Lake shear zone (Fig. 1). The Valentine Lake gold property occurs towards the southwestern end of the Victoria Lake shear zone, and the Antler Gold Inc. property in the Wilding Lake region is immediately adjacent to the northeast (Fig. 1, 2).

The geology of the gold-bearing corridor is characterized by accreted Neoproterozoic to Ordovician magmatic-sedimentary arc terranes of peri-Gondwanan affinity and overlying Early Ordovician to Silurian sequences composed of volcanic and sedimentary rocks (Williams, 1978; Williams et al., 1988, 1993; Colman-Sadd et al., 1990; Evans and Kean, 2002; O'Brien, 2003; Rogers et al., 2005, 2006; Valverde-Vaquero et al., 2005; van Staal et al., 2005). The Valentine Lake pluton (Fig. 2a), a Neoproterozoic granitoid of the Crippleback Intrusive Suite (Colman-Sadd et al., 1990; Evans et al., 1990; van Staal et al., 2005) hosts gold mineralization at the Valentine Lake gold property (Fig. 2a). The gold resource at Valentine Lake occurs in the hanging wall of the steeply northwest-dipping Valentine Lake thrust, which places the Valentine Lake pluton over Silurian polymict Rogerson Lake Conglomer-

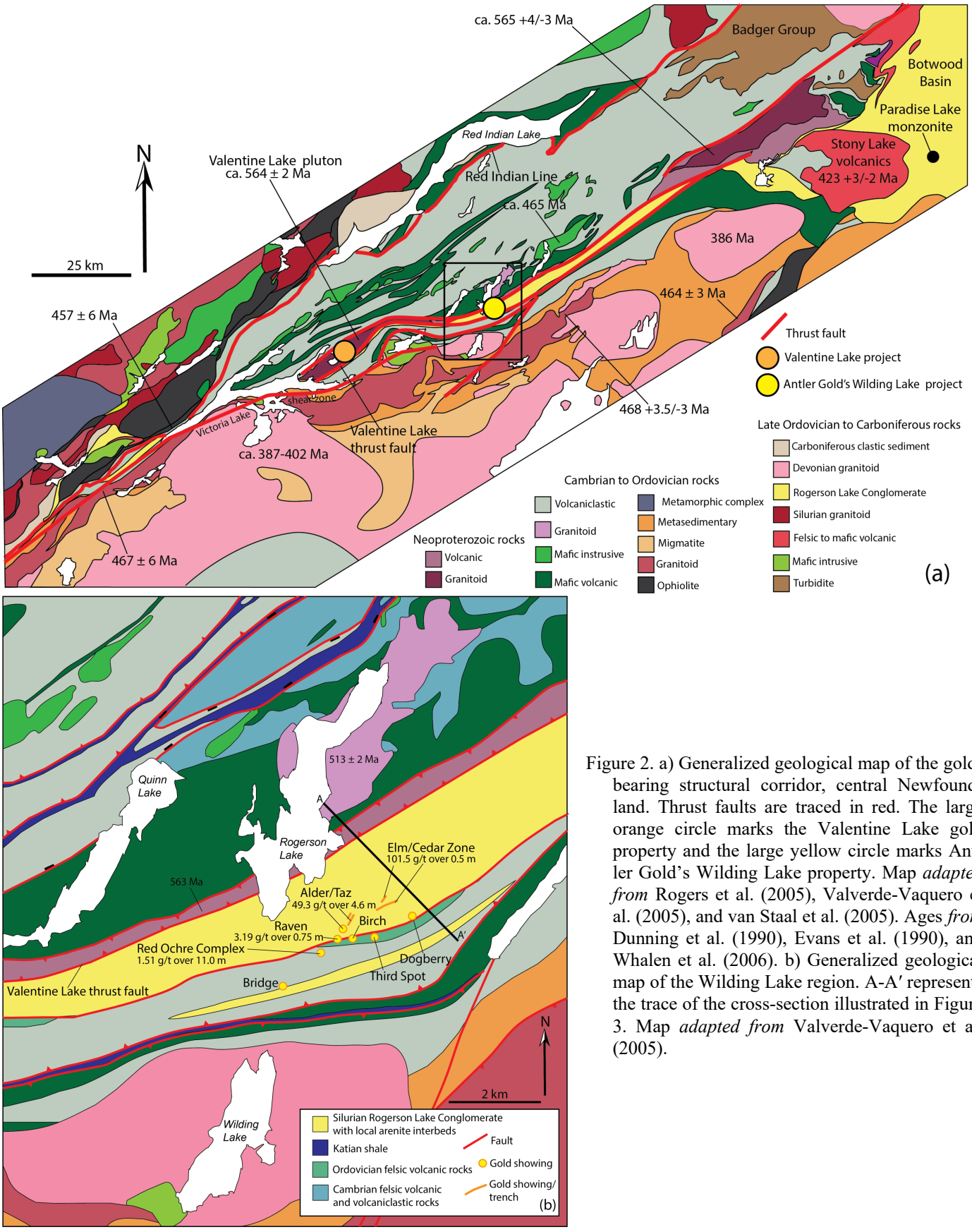

Figure 2. a) Generalized geological map of the gold-bearing structural corridor, central Newfoundland. Thrust faults are traced in red. The large orange circle marks the Valentine Lake gold property and the large yellow circle marks Antler Gold's Wilding Lake property. Map *adapted from* Rogers et al. (2005), Valverde-Vaquero et al. (2005), and van Staal et al. (2005). Ages *from* Dunning et al. (1990), Evans et al. (1990), and Whalen et al. (2006). b) Generalized geological map of the Wilding Lake region. A-A′ represents the trace of the cross-section illustrated in Figure 3. Map *adapted from* Valverde-Vaquero et al. (2005).

ate (Lycopodium Minerals Canada Ltd., 2018). Rogerson Lake Conglomerate represents the southwestern continuation of the Botwood Basin (Williams, 1972), which is dominated by red, green, and grey sandstone beds of the Wigwam Formation farther to the northeast (Colman-Sadd et al., 1990; O'Brien, 2003; van Staal et al., 2014). A sedimentary sequence associated with gold along the Cape Ray fault (Dubé et al., 1996; van Staal et al., 1996) occurs in a comparable structural position to Rogerson Lake Conglomerate.

Gold mineralization on Antler Gold's property in the Wilding Lake region occurs along the northeastern extension of the Valentine Lake thrust, but within footwall rocks composed of Rogerson Lake Conglomerate and Ordovician volcanic and volcaniclastic rocks (Fig. 2b, 3). Grey, muscovitic quartz arenite beds interlayered with Rogerson Lake Conglomerate in the Wilding Lake region preserve local younging directions consistent with a synclinal structure for the Silurian rocks and underlying Ordovician rocks (Fig. 3, 4a, b). The syncline is truncated to the northwest by the northeastern extension of the Valentine Lake thrust, which displaces Neoproterozoic volcanics and Cambrian to Ordovician arc rocks toward the southeast over the Silurian sequence (Fig. 3). The contact between Silurian Rogerson Lake Conglomerate and the Ordovician volcanic and volcaniclastic sequence is not exposed in this region; however, overall younging directions of sandstones throughout the Silurian section are consistent with the contact being a deformed unconformity that dips steeply to the northwest (Fig. 3). In the Wilding Lake area, gold mineralization is hosted by Silurian Rogerson Lake Conglomerate and, as well, Ordovician volcanic and volcaniclastic rocks. The Red Ochre Complex, an auriferous feldspar porphyry unit, occurs within the Ordovician volcaniclastic sequence (Fig. 3, 4c), whereas smaller gold showings (e.g. Birch Zone) occur near the Rogerson Lake Conglomerate – Ordovician felsic volcanic contact (Fig. 3, 4d). Within Rogerson Lake Conglomerate, gold mineralization occurs in laterally extensive quartz veins (Elm Zone and Alder Zone) that dip moderately to the southeast and preserve structural evidence for oblique sinistral shear. Gold is associated with quartz, chalcopyrite, malachite, tourmaline, and altered sulphides.

Exploration history of the Valentine Lake and Wilding Lake regions

From the early 1960s to 1983, base metal exploration in the Valentine Lake region by Asarco and HBOG led to the discovery of quartz veins containing gold (Micon International Ltd., 2012). Following this discovery, gold exploration was conducted in the area by Abitibi-Price Inc., BP Canada, Noranda Inc., Mountain Lake Resources Inc. and Richmont Mines Inc. In 2006, InnovExplo studied the structural geology of the Valentine Lake gold system and compared the overall structure to the

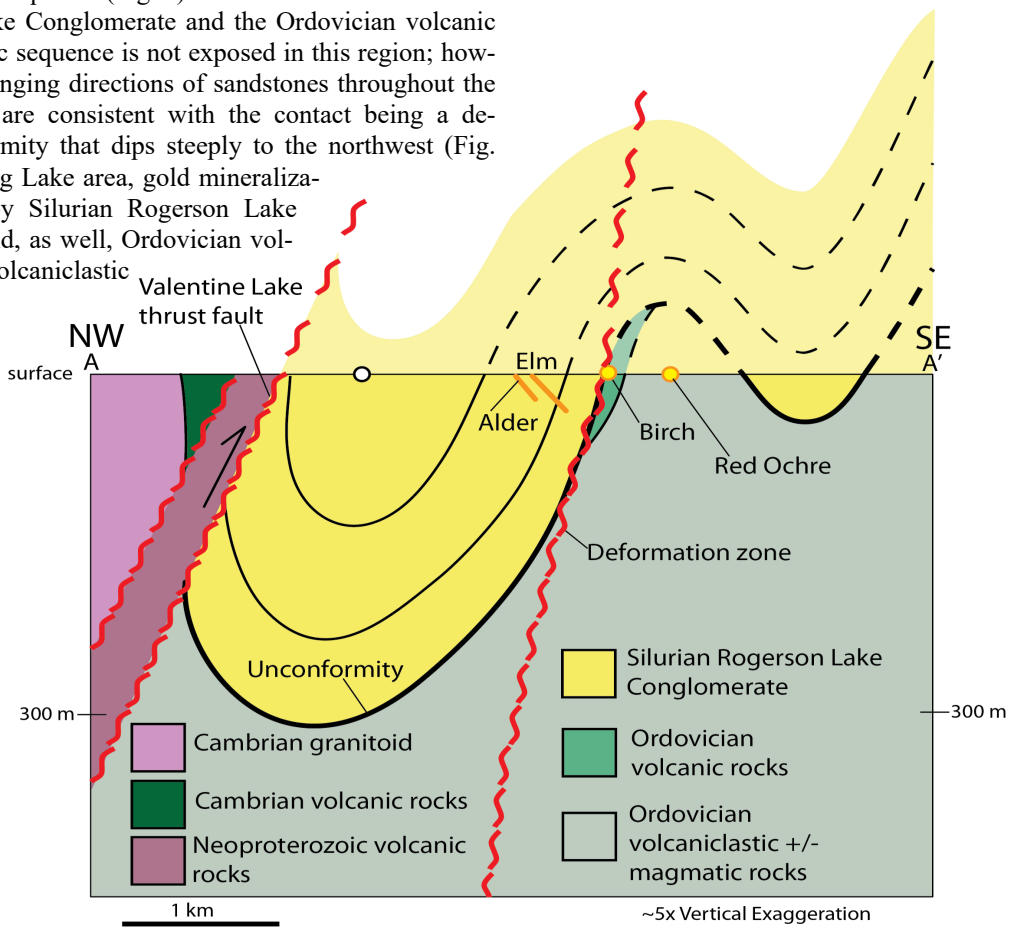

Figure 3. Cross-sectional view along A-A′ shown in Figure 2b. Locations of mineralized zones are indicated with yellow circles and short orange lines (Elm and Alder). White circle marks the location of field photographs of Rogerson Lake Conglomerate shown in Figure 4a and b.



Figure 4. Field photographs. a) Interlayered polymict Rogerson Lake Conglomerate and sandstone. b) Basal scour in sandstone. Hammer along top of image for scale. c) Gold-bearing quartz vein in feldspar porphyry of the Red Ochre Complex. d) Altered Rogerson Lake Conglomerate from the Birch Zone.

quartz-tourmaline-bearing gold camp at Val-d'Or in the Abitibi (Micon International Ltd., 2012). Marathon Gold Corporation acquired the Valentine Lake property in 2010; they now report 4.2 Moz of total gold resource (Lycopodium Minerals Canada Ltd., 2018). The main deposit is presently constrained by an open pit-shell that extends to approximately 1 km depth (Lycopodium Minerals Canada Ltd., 2018).

Gold exploration in the Wilding Lake area began in 2015, when prospectors discovered visible gold in quartz boulders as the result of new road construction for logging activities. Prospecting and soil sampling by Altius Resources in the summer of 2016 led to the discovery of additional quartz-tourmaline boulders with visible gold. In September 2016, Antler Gold Inc. optioned the Wilding Lake property from Altius Resources. Subsequent trenching between September 2016 and November 2016 by Antler Gold Inc. exposed five new gold showings, including Alder, Taz, Elm, Cedar, and Dogberry hosted in Rogerson Lake Conglomerate (Fig. 2b; Antler Gold Inc., 2017a). Prospecting also identified three additional showings near the boundary with underlying felsic volcanic rocks (Birch, Third Spot, and Bridge). In 2017, Antler discovered the Red Ochre Complex within a volcaniclastic rock dominated terrane south of the contact with Rogerson Lake Conglomerate and, as well, uncovered additional gold mineralization in the conglomerate (Raven). A first phase of channel sampling and drilling was completed by Antler in 2017, including 3 drillholes in the Alder Zone and 13 drillholes in the Elm Zone (Antler Gold Inc., 2017b). Gold values of 19.2 g/t over 0.9 m and 49.92 g/t over 0.98 m were reported for the Alder and Elm zones, respectively, with local gold values up to 101.5 g/t along channel samples at Elm (Antler Gold Inc., 2017c).

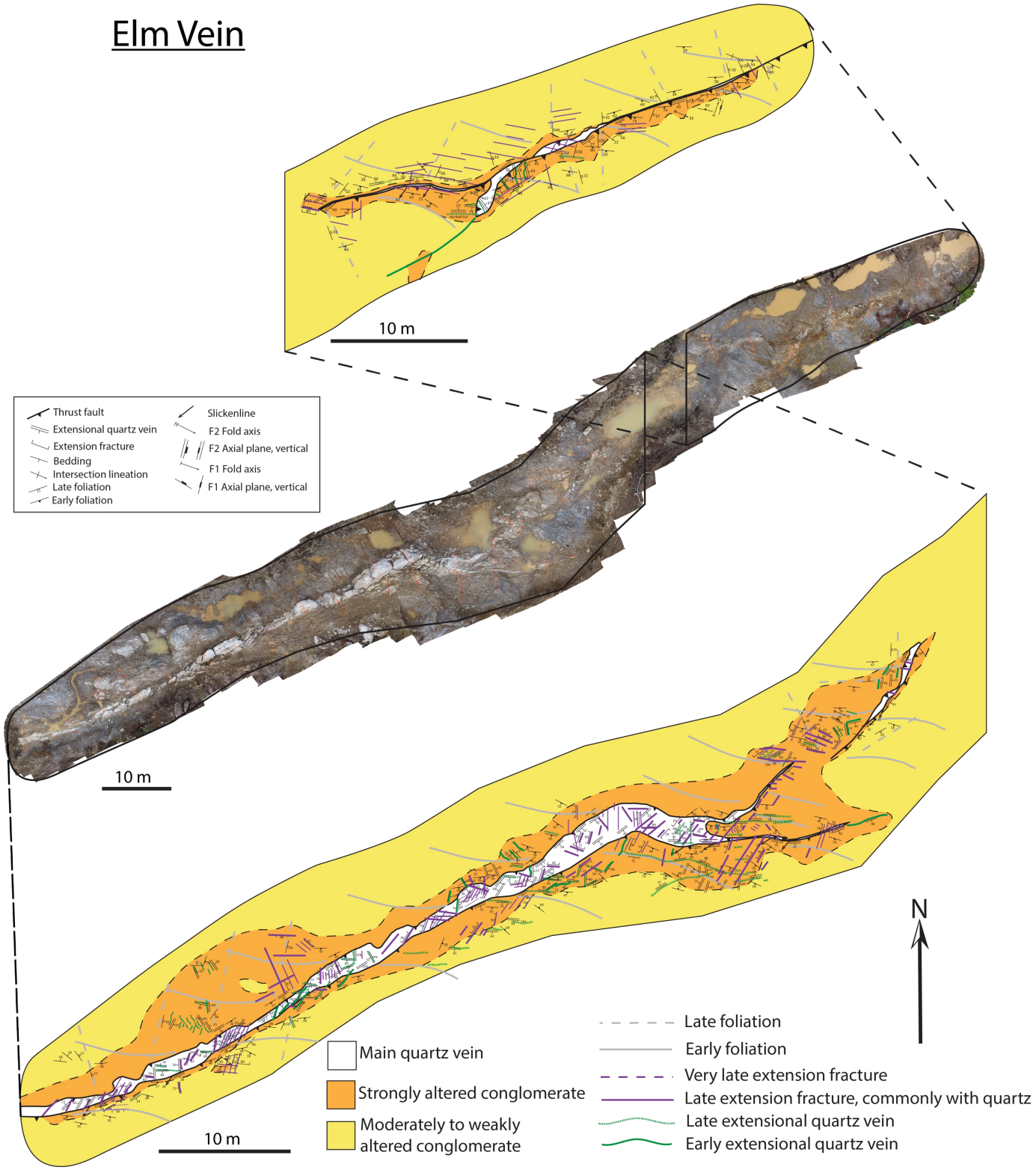

Figure 5. Geological and structural maps of the northeastern portion of the Elm Zone (top and bottom images) as compared to an orthorectified unmanned aerial vehicle (UAV) image (middle image). Altered and deformed Rogerson Lake Conglomerate occurs on either side of the main quartz vein (white lineament). The smaller map area covers the northeastern-most portion of the UAV image, whereas the larger map area covers the southwestern portion of the UAV image. Foliations (grey lines), extension veins (green lines), and fractures (purple lines) are superimposed. Different line thicknesses represent schematically varying thicknesses of veins and fractures.

Lithology and structure, Elm Zone, Wilding Lake region

The gold-bearing quartz vein system of the Elm Zone (Fig. 5) is the focus of this report because it is the most extensive vein system on the property and yielded the highest gold values. The main quartz vein dips moderately (35–65°) to the southeast, cutting Rogerson Lake Conglomerate (Fig. 6a). The main vein is exposed for about 230 m northeast along strike and is up to 2.5 m wide (Fig. 5). It is composed of massive, milky white quartz, which is unaltered towards the hanging-wall contact, but more laminated and carbonate altered towards the footwall contact. The footwall contact is marked by a zone of strongly deformed conglomerate that is locally transformed into a fault breccia. Disseminated chalcopyrite, malachite, and tourmaline occur locally in the main vein.

The surrounding conglomerate is clast-supported, polymict, and contains angular, subangular, and subrounded clasts up to approximately 15 cm across of felsic to intermediate plutonic and volcanic rocks, clastic sedimentary rocks, and jasper. The conglomerate is strongly altered close to the main vein (Fig. 6b) and moderately to weakly altered elsewhere (Fig. 6c). Light to dark brown alteration of conglomerate is likely ankerite and/or siderite, whereas fine-grained muscovite (sericite) is likely responsible for the waxy lustre in altered conglomerate.

Primary bedding is preserved locally as sub-metre-scale sandy layers in the conglomerate that strike subparallel to the oldest foliation generation. At least two generations of foliation are preserved in the conglomerate. The older generation, defined by alignment of muscovite, is well preserved in the hanging wall of the main vein, and on average strikes to the east-southeast and dips moderately to steeply towards the south-southwest. Deflection and shallowing of this foliation towards the main vein is consistent with oblique sinistral shear and a component of thrusting towards the north-northeast (Fig. 7). The younger, crosscutting foliation generation defines a spaced cleavage in the conglomerate that dips shallowly to the northeast and southeast, and is locally dominant in the footwall of the main vein. Where both are present, the two foliations form an intersection lineation that plunges shallowly to the southeast.

The older foliation generation is cut by the main vein, which itself defines the main shear plane. The main vein displays slickenlines that plunge moderately towards the southwest along the sheared contact with hanging-wall conglomerate. These linear features are compatible with oblique thrust motion towards the north-northeast. Deformed extensional quartz veins consistent with sinistral shearing occur within the strongly altered conglomerate surrounding the main vein (Fig. 5, 7). These extension veins emanate from the main vein, dip moderately towards the southeast or northeast (Fig. 6d), and are locally folded into open to tight reclined folds that plunge moderately to steeply to the northeast. The geometry of such folds is consistent with drag folding during protracted oblique sinistral shearing. A younger fold set, defined by fold axes that plunge moderately toward the southeast, is compatible with oblique compression. A late steeply dipping set of extensional quartz veins cuts the moderately dipping vein set as well as the main quartz vein (Fig. 6e, 7). This late vein set is richer in chalcopyrite, malachite, and tourmaline than the older vein set. Next, steeply dipping sets of nearly conjugate extension fractures cut the main vein and both generations of extension veins (Fig. 5). These fractures are very tightly spaced in portions of the main vein and contain vuggy quartz, chalcopyrite, malachite±tourmaline±pyrite±hematite±goethite (Fig. 6f). One of these fracture sets is subparallel to the plane of motion (Fig. 7), thus, forming an intersection lineation on the main vein that is subparallel to the slip lineations. The youngest planar structures in the Elm Zone are very late, weakly developed fracture sets that parallel both the early foliation and laminations in the main quartz vein.

Kinematic interpretation, Elm Zone

The main conglomerate-hosted quartz vein system of the Elm Zone defines a moderately- to steeply- dipping oblique sinistral compressional shear zone that involved north-northeast-directed hanging-wall motion (Fig. 7), compatible with reverse sinistral movement documented along the Valentine Lake thrust on Marathon Gold's property (Lycopodium Minerals Canada Ltd., 2018). Preservation of both brittle and ductile structures at Wilding Lake may suggest formation of the vein system during exhumation of the conglomerate through the brittle-ductile transition.

The overall coherent geometry of the quartz vein system and relatively consistent mineralogy of the different vein sets is compatible with one progressive deformation cycle that began with tight folding of Rogerson Lake Conglomerate. Next, the main gold-bearing quartz vein and associated early extensional veins cut across the deformed conglomerate. Thickness variations in the main quartz vein, coupled with left-lateral kinematic indicators in the conglomerate and oblique attitudes of slip lineations on the main vein, are consistent with infilling of quartz in semi-brittle dilatational jogs formed during sinistral shearing. Local folding of the early extensional flat veins that emanate from the main vein supports the proposal of progressive compressional semi-ductile deformation.

The presence of the late, brittle, steep crosscutting vein set and late, shallow foliation suggests rotation of the maximum principal stress to subvertical, compatible with a transient phase of subhorizontal extension. Locally, late crosscutting extensional veins display right lateral kinematics, which may suggest a late minor component of dextral strike-slip. Although the late sets of brittle extension fractures crosscut many of the late extensional veins, their geometries suggest that they may have formed under a similar state of stress, just later in time. The abundance of chalcopyrite, malachite and carbonate alteration in the late extensional veins and fractures may indicate that progressive deformation influenced metasomatism of Cu^{2+} and CO_2, and likely Au. Considering the tectonic evolution of the

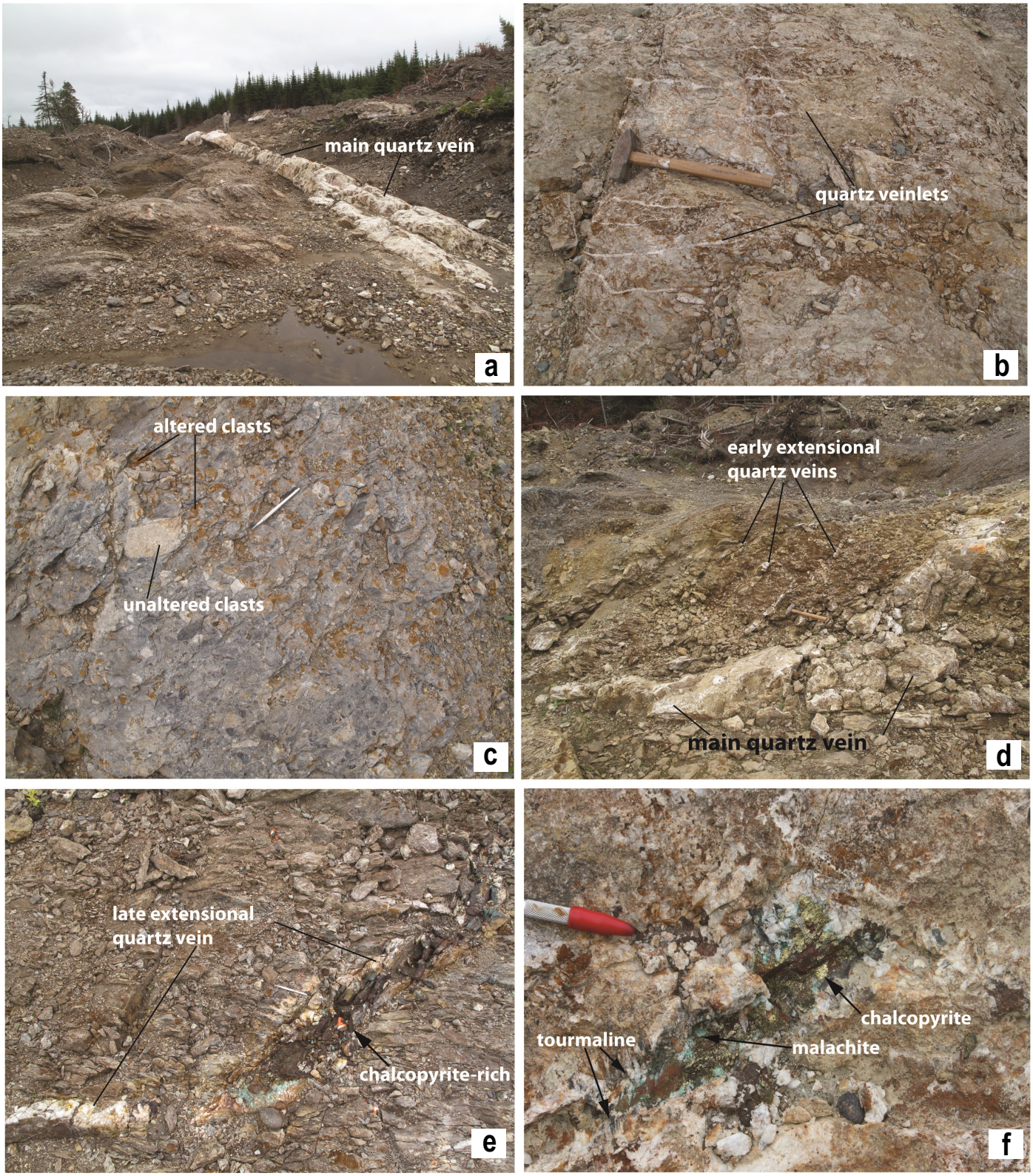

Figure 6. Field photographs of the Elm Zone. a) Main quartz vein cutting deformed conglomerate. b) Strongly altered conglomerate. c) Moderately to weakly altered conglomerate. d) Early, moderately dipping extensional quartz veins. e) Late, steeply dipping extensional quartz vein with chalcopyrite and malachite. Veins cuts conglomerate. f) Vuggy quartz, tourmaline, malachite, and chalcopyrite in a late extension fracture.

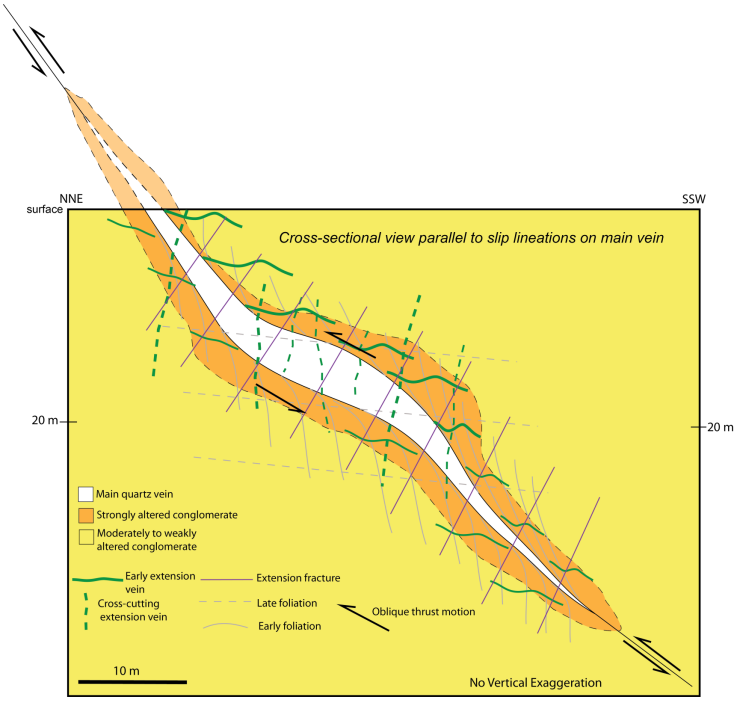

Figure 7. Structural cross-section interpretation of the main quartz vein in the Elm zone parallel to slip lineations. Structural data are superimposed. The arrows describe the sense of oblique sinistral thrust motion.

regional terrane (Dunning et al., 1990; van Staal et al., 2014), progressive deformation may have spanned portions of both the latest Salinic and earliest Acadian orogenies during the late Silurian and Devonian, respectively.

Conclusions

The field data herein confirm that the Elm Zone and related mineralization occur within a structurally controlled gold-bearing quartz vein system that is an extension of the auriferous Valentine Lake structure to the southwest. Mineralization in the Wilding Lake region, however, occurs in the structural footwall of the Valentine Lake thrust structure. Footwall gold mineralization in association with synorogenic clastic sedimentary rocks bears close structural resemblance to the major gold-bearing structures of the Abitibi greenstone belt (Honsberger and Bleeker, 2018). Deeper drillholes into Rogerson Lake Conglomerate on the Antler property will be important for determining the property's full economic potential, as unexposed, deep-seated plutonic rocks may be rheologically favourable for gold-bearing fluid entrapment (e.g. Valentine Lake pluton). Future exploration and drilling in the Wilding Lake region might consider targeting the extension of the Valentine Lake thrust, which preserves significant gold mineralization in its hanging wall farther southwest.

Acknowledgments

This report is a contribution to NRCan's Targeted Geoscience Initiative Program (TGI). Support for this study was provided through the Gold Project's '*Activity G-2.1: Deep faults, synorogenic clastic sequences, alkaline magmatism and gold deposits: testing and refining the Timmins-Kirkland Lake model in areas with high gold potential*'.

Ian Honsberger is conducting TGI supported post-doctoral research at GSC Ottawa. Thanks to Cees van Staal (GSC Vancouver) and Neil Rogers (GSC Ottawa) for field guidance. A special thanks to the Lakeview Inn for providing comfortable lodging. Collaboration with Antler Gold Inc. and the Newfoundland and Labrador Department of Natural Resources, Mineral Deposits Section is gratefully acknowledged. This report benefited from the review of Dawn Kellett, Michel Houlé and Neil Rogers.

References

Antler Gold Inc., 2017a. Antler gold discovers new mineralized zones at the Wilding Lake gold project, Newfoundland; Antler Gold. <antlergold.com/files/PR_20170830_final_with_maps.pdf> [accessed December 2, 2018]

Antler Gold Inc., 2017b. Antler gold drills 10.01 grams per tonne gold over 5.35 metres at the Wilding Lake gold project, Newfoundland. <antlergold.com/files/PR_20171213_final_with_appendix_and_maps.pdf> [accessed December 2, 2018]

Antler Gold Inc., 2017c. Antler gold announces high grade gold assays from the elm trench and confirms increased widths at alder zone, Wilding Lake gold project, Newfoundland. <antlergold.com/files/20170123_final_2_for_website.pdf> [accessed December 2, 2018]

Bleeker, W., 2015. Synorogenic gold mineralization in granite-greenstone terranes: The deep connection between extension, major faults, synorogenic clastic basins, magmatism, thrust inversion, and long-term preservation; *in* Targeted Geoscience Initiative 4: Contributions to the Understanding of Precambrian Lode Gold Deposits and Implications for Exploration, (ed.) B. Dubé and P. Mercier-Langevin; Geological Survey of Canada, Open File 7852, p. 25–47.

Colman-Sadd, S., Hayes, J., and Knight, I., 1990. The geology of the Island of Newfoundland; map 90-01; Government of Newfoundland and Labrador, Department of Mines and Energy, Geological Survey Branch, GS# NFLD/2192, scale: 1:1 000 000.

Dubé, B. and Gosselin, P., 2007. Greenstone-hosted quartz-carbonate vein deposits; *in* Mineral deposits of Canada: A synthesis of major deposit-types, district metallogeny, the evolution of geological provinces, and exploration methods, (ed.) W.D. Goodfellow; Mineral Deposits Division, Geological Association of Canada, Special Publication no. 5, p. 49–73.

Dubé, B., Dunning, G.R., Lauziere, K., and Roddick, J.C., 1996. New insights into the Appalachian Orogen from geology and geochronology along the Cape Ray fault zone, southwest Newfoundland; Geological Society of America Bulletin, v. 108, p. 101–116.

Dubé, B., Mercier-Langevin, P., Ayer, J., Atkinson, B., and Monecke, T., 2017. Orogenic greenstone-hosted quartz-carbonate gold deposits of the Timmins-Porcupine gold camp; Reviews in Economic Geology, v. 19, p. 51–79.

Dunning, G.R., O'Brien, S.J., Colman-Sadd, S.P., Blackwood, R.F., Dickson, W.L., O'Neil, P.P., and Krogh, T.E., 1990. Silurian Orogeny in the Newfoundland Appalachians; The Journal of Geology, v. 98, p. 895-913.

Evans, D.T.W., 1996. Epigenetic gold occurrences, eastern and central Dunnage Zone, Newfoundland; Government of Newfoundland and Labrador, Department of Mines and Energy, Geological Survey, Mineral Resources Report 9, 135 p.

Evans, D.T.W., 1999. Epigenetic gold mineralization, Baie Verte Peninsula, Newfoundland; *in* Current Research; Government of Newfoundland and Labrador, Department of Mines and Energy, Geological Survey Branch, Report 99-1, p. 163–182.

Evans, D.T.W. and Kean, B.F., 2002. The Victoria Lake Supergroup, central Newfoundland - its definition, setting and volcanogenic massive sulphide mineralization; Newfoundland Department of Mines and Energy, Geological Survey, Open File NFLD/2790, 68 p.

Evans, D.T.W., Kean, B.F., and Dunning, G.R., 1990. Geological studies, Victoria Lake Group, central Newfoundland; *in* Current Research; Government of Newfoundland and Labrador, Department of Mines and Energy, Geological Survey Branch, Report 90-1, p. 135–144.

Goldfarb, R.J., Groves, D.I., and Gardoll, S., 2001. Orogenic gold and geologic time: A global synthesis; Ore Geology Reviews, v. 18, p. 1–75.

Goldfarb, R.J., Baker, T., Dubé, B., Groves, D.I., Hart, C.J.R., and Gosselin, P., 2005. Distribution, character and genesis of gold deposits in metamorphic terranes; Economic Geology 100th Anniversary, p. 407–450.

Groves, D.J., Goldfarb, R.J., Gebre-Mariam, M., Hagemann, S.G., and Robert, F., 1998. Orogenic gold deposits: A proposed classification in the context of their crustal distribution and relationships to other gold deposit types; Ore Geology Reviews, v. 13, p. 7–27.

Hodgson, C.J., 1993. Mesothermal lode-gold deposits; *in* Mineral Deposit Modelling, (ed.) R.V. Kirkham, W.D. Sinclair., R.I. Thorpe and J.M. Duke; Geological Association of Canada, Special Paper 40, p. 635–678.

Honsberger, I. and Bleeker, W., 2018. Orogenic comparison of structurally controlled gold systems of the Abitibi greenstone belt and central Newfoundland Appalachians: Implications for Newfoundland gold potential and recurring tectonic drivers of gold mineralization; *in* Targeted Geoscience Initiative: 2017 report of activities, volume 2, (ed.) N. Rogers; Geological Survey of Canada, Open File 8373, p. 65–70.

Kerrich, R. and Cassidy, K.F., 1994. Temporal relationships of lode gold mineralization to accretion, magmatism, metamorphism and deformation – Archean to present: A review; Ore Geology Reviews, v. 9, p. 263–310.

Kerrich, R., Goldfarb, R., Groves, D., and Garwin, S., 2000. The geodynamic of world-class gold deposits: characteristics, space-time distribution and origins; *in* Gold in 2000, (ed.) S.G. Hagemann, and P.E. Brown; Society of Economic Geologists, Reviews in Economic Geology, v. 13, p. 501–551.

Lycopodium Minerals Canada Ltd., 2018. Preliminary economic assessment of the valentine lake gold project Newfoundland, NL, Canada; Marathon Gold. <www.marathon gold.com/site/assets/files/5047/2018-10-pea.pdf> [accessed December 2, 2018]

Micon International Limited, 2018. On the updated mineral resource estimate for the Leprechaun gold deposit Valentine Lake property central Newfoundland, Canada; Marathon Gold. <www.marathon-gold.com/site/assets/files/4319/valentine_lake_lep_deposit_2012.pdf> [accessed December 2, 2018]

O'Brien, B.H., 2003. Geology of the central Notre Dame Bay region (parts of NTS areas 2E/3,6,11), northeastern Newfoundland; Government of Newfoundland and Labrador, Department of Mines and Energy, Geological Survey Branch, Report 03-03, p. 147.

Poulsen, K.H., Robert, F., and Dubé, B., 2000. Geological classification of Canadian gold deposits; Geological Survey of Canada, Bulletin 540, 106 p.

Rogers, N., van Staal, C.R., McNicoll, V.J., Squires, G.C., Pollock, J., and Zagorevski, A., 2005. Geology, Lake Ambrose and part of Buchans, Newfoundland and Labrador; Geological Survey of Canada, Open File 4544, scale 1:50 000.

Rogers, N., van Staal, C.R., McNicoll, V.J., Pollock, J., Zagorevski, A., and Whalen, J., 2006. Neoproterozoic and Cambrian arc magmatism along the eastern margin of the Victoria Lake Supergroup: A remnant of Ganderian basement in central Newfoundland?; Precambrian Research, v. 147, p. 320–341.

Tuach, J., Dean, P.L, Swinden, H.S., O'Driscoll, C.F., Kean, B.F., and Evans, D.T.W., 1988. Gold mineralization in Newfoundland: A 1988 review; *in* Current Research. Government of Newfoundland and Labrador, Department of Mines, Mineral Development Division, Report 88-1, p. 279 –306.

Valverde-Vaquero, P., van Staal, C.R., and Rogers, N., 2005. Geology, Snowshoe Pond, Newfoundland and Labrador; Geological Survey of Canada, Open File 4597, scale 1:50 000.

van Staal, C.R., Hall, L., Schofield, D., and Valverde, P., 1996. Geology, Port aux Basques, Newfoundland (part of NTS 11 -O/11); Geological Survey of Canada, Open File 3165,

scale 1:25 000.

van Staal, C.R., Valverde-Vaquero, P., Zagorevski, A., Rogers, N., Lissenberg, C.J., and McNicoll, V.J., 2005. Geology, Victoria Lake, Newfoundland and Labrador; Geological Survey of Canada, Open File 1667, scale 1:50 000.

van Staal, C.R., Zagorevski, A., McNicoll, V.J., and Rogers, N., 2014. Time-transgressive Salinic and Acadian orogenesis, magmatism, and Old Red Sandstone sedimentation in Newfoundland; Geoscience Canada, v. 41, p. 138–164.

Whalen, J.B., McNicoll, V.J., van Staal, C.R., Lissenberg, C.J., Longstaffe, F.J., Jenner, G.A., and van Breemen, O., 2006. Spatial, temporal and geochemical characteristics of Silurian collision zone magmatism, Newfoundland Appalachians: An example of a rapidly evolving magmatic system related to slab break-off; Lithos, v. 89, p. 377–404.

Williams, H., 1972. Stratigraphy of Botwood map-area, northeastern Newfoundland; Geological Survey of Canada, Open File Report 113, 98 p.

Williams, H., 1978. Tectonic lithofacies map of the Appalachian Orogen; Memorial University of Newfoundland, St John's, Newfoundland and Labrador, scale 1:1 000 000.

Williams, H., Colman-Sadd, S.P., and Swinden, H.S., 1988. Tectonic-stratigraphic subdivisions of central Newfoundland; *in* Current Research, Part B; Geological Survey of Canada, Paper 88-1B, p. 91–98.

Williams, H., Currie, K.L., and Piasecki, M.A.J., 1993. The Dog Bay Line: A major Silurian tectonic boundary in northeast Newfoundland; Canadian Journal of Earth Sciences, v. 30, p. 2481–2494.

Paleoproterozoic gold and its tectonic triggers and traps

C.J.M. Lawley[1], W.J. Davis[1], S.E. Jackson[1], D.C. Petts[1], E. Yang[2], S. Zhang[3], D. Selby[4], A.R. O'Connor[5] and D.A. Schneider[5]

[1]*Geological Survey of Canada, 601 Booth Street, Ottawa, Ontario, K1A 0E8*
[2]*Manitoba Geological Survey, 360-1395 Ellice Ave, Winnipeg, Manitoba R3G 3P2*
[3]*Department of Earth Sciences, Carleton University, 1125 Colonel By Drive, Ottawa, Ontario K1S 5B6*
[4]*Department of Earth Sciences, Durham University, Science Labs, Durham, DH1 3LE, United Kingdom*
[5]*Department of Earth and Environmental Sciences, University of Ottawa, 120 University, Ottawa, Ontario K1N 6N5*

Abstract

The tectonic trigger(s) that controls the formation of large gold deposits hosted within ancient greenstone belts remain poorly understood. Herein we address that knowledge gap by merging macro- to micro-scale field relationships and multiple mineral chronometers to constrain the timing of magmatism, deformation, metamorphism, and gold in the Lynn Lake greenstone belt, Manitoba. Preliminary monazite and xenotime ages from the MacLellan gold deposit (1.83–1.75 Ga) are coeval with previously reported metamorphic ages for northern Manitoba (1.81–1.78 Ga), which also marks the terminal collision of the composite Hearne-La Ronge-Lynn Lake block and Sask-Superior craton at 1.83 to 1.80 Ga. The peak metamorphic mineral assemblage and dated phosphate minerals define the main structural fabric (D_2) of the Lynn Lake greenstone belt, which coupled with the folded, transposed auriferous veins, places a lower limit for the timing of gold at or before 1.75 Ga. However, xenotime within a garnet-hosted and gold-bearing veinlet dated at ca. 1.83 Ga may provide the first evidence for a cryptic early stage of gold mineralization that is coeval with the onset of collisional orogenesis between the composite Hearne and Superior cratons. Ongoing thermochronology (e.g. apatite, biotite) and Re-Os pyrite and arsenopyrite dating at gold deposits within the Lynn Lake greenstone belt will further constrain the timing of gold deposition relative to the different stages of the Trans-Hudson orogeny. New ages will inform ore system models by identifying the tectonic trigger(s) for gold and improving exploration targeting in ancient greenstone belts.

Introduction

Ancient greenstone belts represent geological collages that juxtapose rocks with different histories, compositions, and metal endowment. Differentiating barren from prospective rocks packages in these complex settings represents a major challenge for mineral exploration. The challenge is particularly acute for greenstone-hosted orogenic gold deposits, which are structurally complex deposits hosted in a variety of rock types, often with uncertain timing relative to magmatism, deformation, and metamorphism. The equivocal timing of gold deposition represents one of the major knowledge gaps that limits progress on ore system models for orogenic gold mineralization.

Herein we address that knowledge gap with a field-based, petrochronological approach, integrating macro- to micro-scale field observations with multiple geochronometers. Geochronology results with their textural context will help to constrain the timing of magmatism, deformation, metamorphism, and gold deposition. Progress on a regional compilation of the Lynn Lake greenstone belt's geological setting and preliminary geochronology results are presented below.

Unravelling the orogenic collage

The Lynn Lake greenstone belt represents one segment of the larger Paleoproterozoic Trans-Hudson orogeny that extends from Saskatchewan and Manitoba into the Canadian Arctic Archipelago (Fig. 1). The broad chronological framework of this continent-scale orogenic belt is fairly well developed and defined by magmatic and metamorphic ages ranging between 1.9 and 1.8 Ga (e.g. Corrigan et al., 2009). In detail, however, the Trans-Hudson orogeny actually represents a collage of geological settings, including accretionary, collisional, and intracontinental stages prior to final cratonization (e.g. Schneider et al., 2007). Ore deposits can occur in a variety of these tectonic settings over its 100 Ma orogenic history, which makes robust and precise dating of mineralization an important component for effective exploration targeting in greenstone belts that may have formed and/or been reworked during multiple stages of orogenesis.

Mafic to felsic volcanic rocks and synvolcanic sedimentary successions comprising the Wasekwan Group represent the oldest rocks exposed in the Lynn Lake greenstone belt (1.90–1.87 Ga Wasekwan Group; Fig. 2; Gilbert et al., 1980; Baldwin

Corresponding author: Chris Lawley (christopher.lawley@canada.ca)

Lawley, C.J.M., Jackson, S.E., Petts, D.C., Savard, D., Pearson, D.G., Zhang, S., Zagorevski, A. and Kjarsgaard, B.A., 2019. Mantle metal mobility: Preliminary gold and platinum group element geochemical results; *in* Targeted Geoscience Initiative: 2018 report of activities, (ed.) N. Rogers; Geological Survey of Canada, Open File 8549, p. 71–75. https://doi.org/10.4095/313641

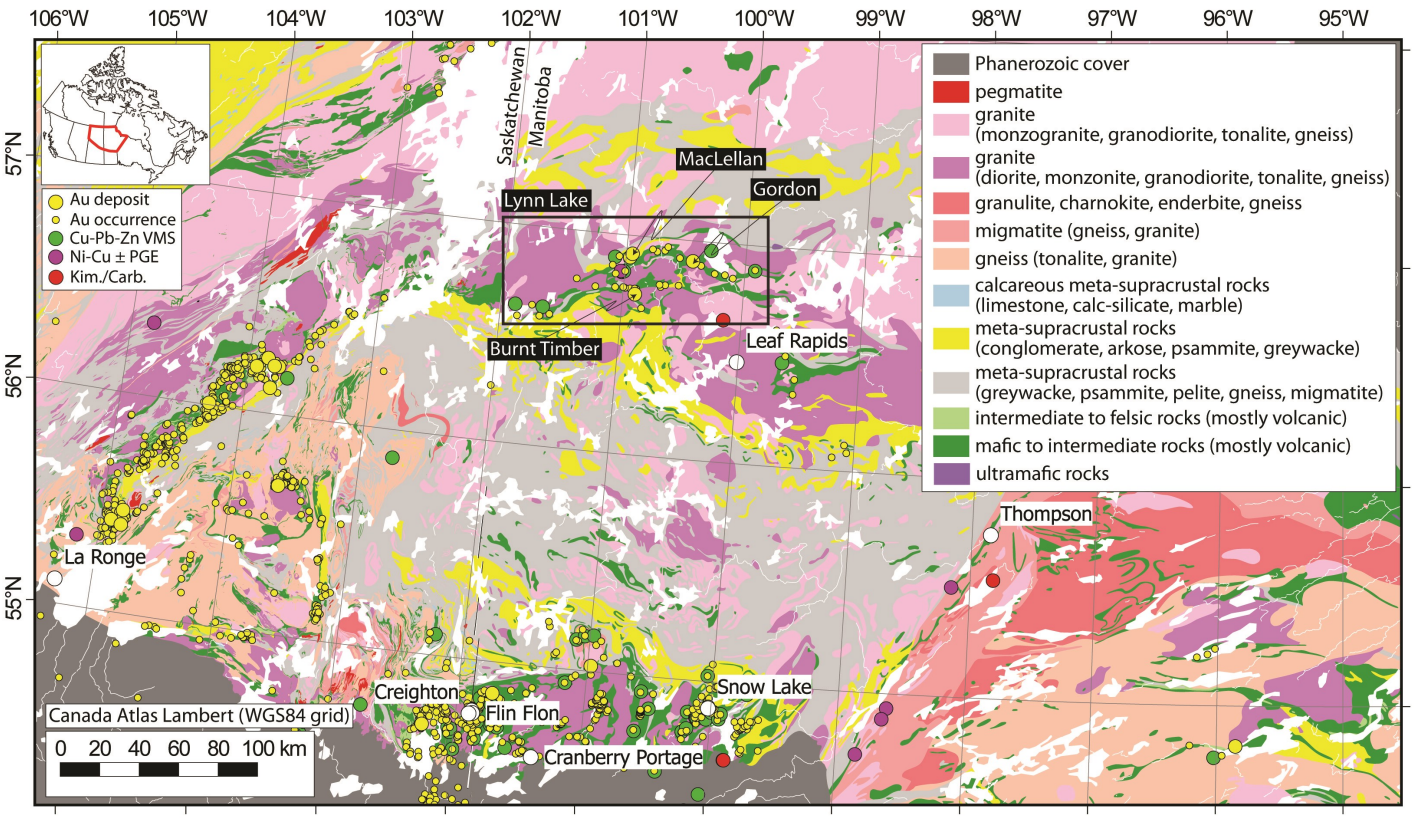

Figure 1. Regional geological map of Saskatchewan and Manitoba [Saskatchewan geology polygons from the Saskatchewan Mining and Petroleum GeoAtlas; Manitoba geologic polygons *from* Manitoba Mineral Resources (2013)]. Volcanogenic massive sulphide (VMS; Galley et al., 2007), nickel-platinum group element (Eckstrand and Hulbert, 2007), gold deposits (Gosselin and Dubé, 2015), kimberlites (Kom.; Faure, 2010) and carbonatites (Carb.; Wooley and Kjarsgaard, 2008) are shown for reference. Gold occurrences are also shown for reference (data are commodity-filtered from the provincial mineral occurrence databases).

et al., 1987). The diverse trace element composition of these rocks suggests that they represent the structural juxtaposition of disparate volcanic rock packages (Zwanzig et al., 1999). Structural juxtaposition must have occurred prior to ca. 1.87 based on the magmatic ages of a diverse suite of mafic to felsic intrusive phases, known locally as the 1.89 to 1.87 Ga Pool Lake suite (Gilbert et al., 1980), that stitch the amalgamated greenstone belt. The timing of mafic volcanism and the Pool Lake suite corresponds with the earliest, accretionary stage of Trans-Hudson orogenesis (Ansdell, 2003; Corrigan et al., 2004). Volcanogenic massive sulphide deposits (VMS), such as the syn-volcanic mineralization at the Fox deposit (Fig. 1, 2) and orthomagmatic nickel deposits, such as the ca. 1.87 Ga El and Fraser gabbros that host the Lynn Lake nickel deposit (Fig. 1, 2; Turek et al., 2000) pre-date and/or are coeval with the Pool Lake suite, respectively, providing a temporal link between metallogenesis and accretionary orogenesis. Additional metallogenic evidence for this accretionary orogenic stage is, however, extremely limited and difficult to recognize in the rock record due to overprinting deformation and metamorphism during the later stages of collisional orogenesis. Large batholiths (e.g. 1.86–1.85 Ga Wathaman batholith; Fumerton et al., 1984; Meyer et al., 1992) and smaller intrusions of calc-alkaline and continental arc-like affinity stitch the southern margin of the Hearne craton (Fig. 1, 2), suggesting that the accretion of the Lynn Lake belt was completed prior to ca. 1.85 Ga (Ansdell, 2003; Corrigan et al., 2004). The ages of the Lynn Lake plutonic suites, such as the Pool Lake suite (e.g. Beaumont-Smith et al., 2006; Lawley et al., 2017) and Wathaman-age intrusions (Turek et al., 2000; Beaumont-Smith and Böhm et al., 2003; Lawley et al., 2017), therefore represent important temporal pins to unravel the tectonic history of the Lynn Lake greenstone belt (Fig. 2).

Sedimentary basin development closely followed accretionary orogenesis, as suggested by the 1.85 to 1.84 Ga depositional timing of the Burntwood Group at the southern limit of the Lynn Lake greenstone belt (Fig. 2; Ansdell et al., 1995; Zwanzig, 1999). Structurally dismembered remnants of smaller basins with similar lithological associations (e.g. Ralph Lake conglomerate and Sickle group) are intercalated and/or unconformably overlie older mafic to felsic volcanic rocks (1.90–1.87 Ga; Wasekwan Group) around the town of Lynn Lake (Fig. 2). The depositional timing of the Sickle group and its relationship to the Burntwood Group are the subject of further study, although previous work suggests that the Sickle-like meta-sandstone and -conglomerate unconformably overlie the

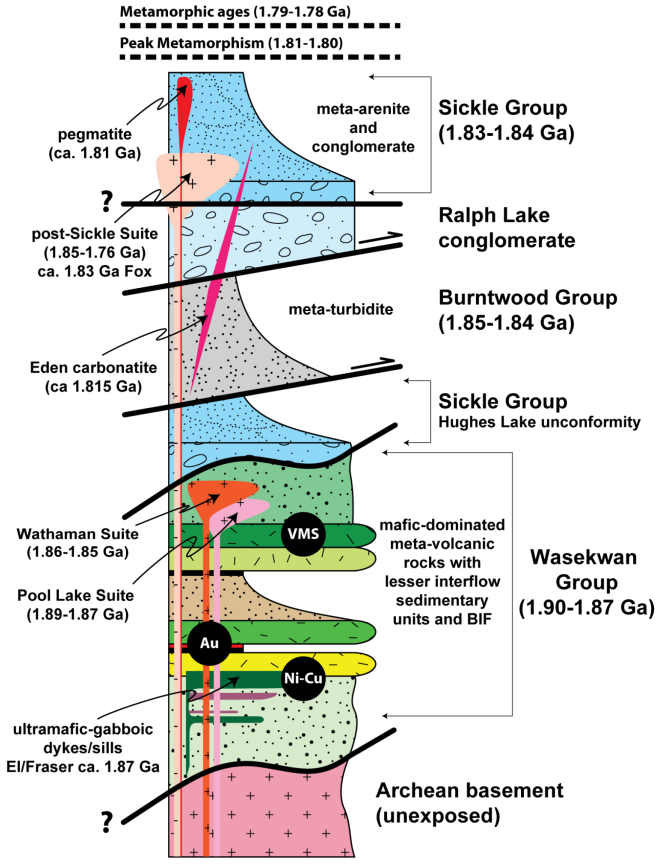

Figure 2. Schematic stratigraphic column summarizing the main supracrustal groups and plutonic suites comprising the Lynn Lake greenstone belt. Ages are summarized from several sources (*see* text for further details; Turek et al., 2000; Beaumont-Smith and Böhm, 2002, 2003; Beaumont-Smith et al., 2006; Schneider et al., 2007; Elliot, 2009; Couëslan et al., 2013; Lawley et al., 2017). Abbreviations: BIF – banded iron formation; VMS – volcanogenic massive sulphides.

Burntwood Group (e.g. Gilbert et al., 1980; Maxeiner and Demmans, 2000; Zwanzig, 2000). The depositional timing is further constrained by the ca. 1.83 Ga felsic plutons that intrude the Sickle group (e.g. ca. 1.83 Ga Fox mine tonalite: Turek et al., 2000). Late and relatively rare pegmatite (1.81–1.78 Ga: Beaumont-Smith and Böhm, 2002) and tonalitic dykes (ca. 1.76: Beaumont-Smith and Böhm, 2002), which along with the ca. 1.815 Ga Eden Lake carbonatite complex distal to Lynn Lake belt (Fig. 1; Elliot, 2009), likely represent the final magmatic expression(s) of the collisional stage of Trans-Hudson orogenesis (Fig. 2).

Auriferous veins from gold deposits included as part of the current study contain metamorphic minerals and are folded and transposed by the main, penetrative deformation fabric at Lynn Lake. The timing of metamorphism at Lynn Lake, which is the main focus of the current study, is presently constrained by 1.81 to 1.78 Ga metamorphic monazite ages reported from rocks south and east of the Lynn Lake greenstone belt (Fig. 2; e.g. Schneider et al., 2007; Couëslan et al., 2013). These metamorphic ages are broadly consistent with the preliminary results for monazite and xenotime ages from the MacLellan gold deposit (1.83–1.75 Ga), which were determined from samples that were collected in situ as part of the current study and ana-

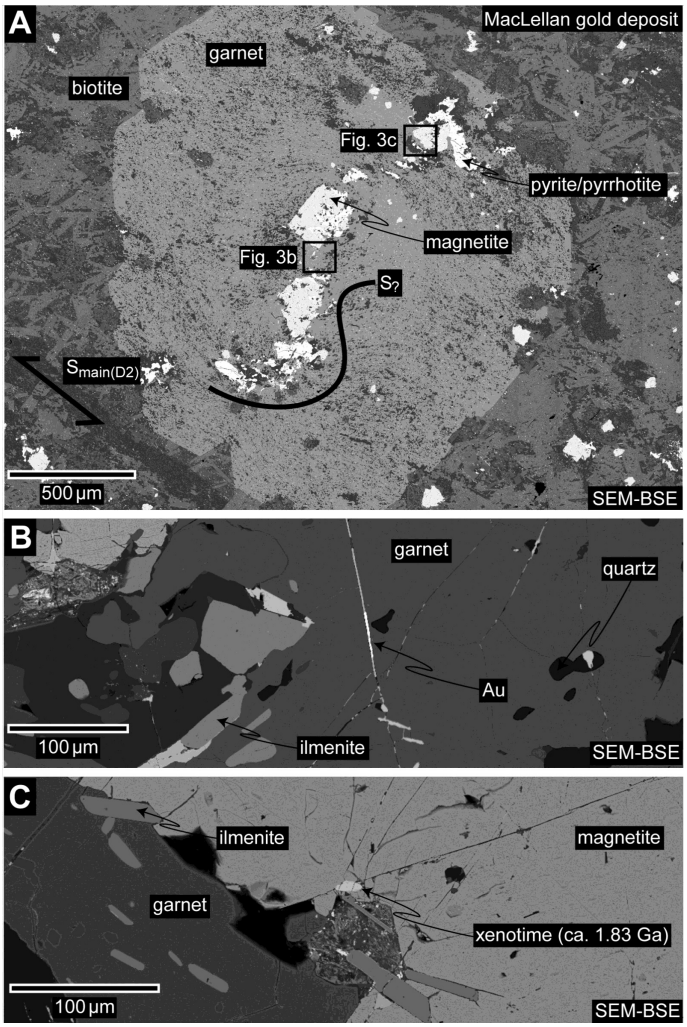

Figure 3. a) Scanning electron microscopy back-scatter (SEM-BSE) image of garnet porphyroblast at the MacLellan gold deposit. Garnet is wrapped and rotated by the main regional deformation fabric (Smain) that developed during D2. b) Close-up image showing native gold filling a fractured garnet within the pressure shadow of magnetite-bearing veinlet. c) Close-up photograph of magnetite-hosted xenotime within a garnet porphyroblast. In situ sensitive high-resolution ion microprobe (SHRIMP) U-Pb geochronology results for this xenotime crystal yielded an age of ca. 1.83 Ga. Because xenotime and gold are associated with the same veinlet, we speculate whether this xenotime age also reflects the timing of early pyrite and gold. Xenotime within the rock matrix of this sample (not shown) also yielded broadly coeval ages at ca. 1.83 Ga, but are not co-spatial.

lyzed using the sensitive high-resolution ion microprobe (SHRIMP) at the Geological Survey of Canada, Ottawa. However, xenotime associated with a garnet-hosted sulphide and gold-bearing micro-veinlet yielded nominally older ages of ca. 1.83 Ga (Fig. 3a). Xenotime hosted within this unusual microtextural setting and within the adjoining volcanic rock matrix potentially document a cryptic, and previously unknown, early phase of gold mineralization (Fig. 3b, c) that pre-dates peak metamorphism. Deformation and hydrothermal alteration related to this early phase of mineralization are obscured by younger overprints during the later stage of collisional orogenesis (Fig. 3a). Constraining the timing of gold relative to magmatism, metamorphism, and deformation is the subject of continued research, as discussed below.

Future work

Work to further constrain the timing of metamorphism in the Lynn Lake greenstone belt is ongoing. Metamorphic mineral assemblages and mineral thermometry will map how pressure and temperature varied across the belt during the main, collision-stage of the Trans-Hudson orogen. Thermochronology (e.g. apatite and biotite) results will be used to better understand how metamorphic conditions varied in space and time, which may shed light on the geological setting of the Lynn Lake greenstone belt during orogenesis and its relationship to gold endowment. Geochronological, isotopic and trace element work is ongoing on sulphide minerals from the MacLellan, Gordon and Burnt Timber deposits. Together these datasets will further constrain the timing of gold deposition, metamorphism and deformation in the Lynn Lake greenstone belt. Results will also inform ore system models by constraining the possible tectonic trigger(s) for orogenic gold-style mineralization, which may also be applicable in other ancient greenstone belts.

Acknowledgments

This report is a contribution to NRCan's Targeted Geoscience Initiative Program (TGI). Support for this study was provided through the Gold Project's *'Activity G-1.2: Paleoproterozoic Gold: Tectonic Triggers and Traps'.*

This report benefited from the review of Alain Plouffe, Pedro Acosta-Góngora and Neil Rogers.

References

Ansdell, K.M., Lucas, S.B., Connors, K., and Stern, R.A., 1995. Kisseynew metasedimentary gneiss belt, Trans-Hudson orogen (Canada): Back-arc origin and collisional inversion; Geology, v. 23, p. 1039–1043.

Ansdell, K.M., 2003. Tectonic evolution of the Manitoba–Saskatchewan segment of the Paleoproterozoic Trans-Hudson Orogen, Canada; Canadian Journal of Earth Science, v. 42, p. 741–759.

Baldwin, D.A., Syme, E.C., Zwanzig, H.V., Gordon, T.M., Hunt, P.A., and Stevens, R.P., 1987. U-Pb zircon ages from the Lynn Lake and Rusty Lake metavolcanic belts, Manitoba: Two ages of Proterozoic magmatism; Canadian Journal of Earth Sciences, v. 24, p. 1053–1063.

Beaumont-Smith, C.J. and Böhm, C.O., 2002. Structural analysis and geochronological studies in the Lynn Lake greenstone belt and its gold-bearing shear zones (NTS 64C10, 11, 12, 14, 15 and 16), Manitoba; *in* Report of Activities 2002; Manitoba Industry, Trade and Mines, Manitoba Geological Survey, p. 159–170.

Beaumont-Smith, C.J., and Böhm, C.O., 2003. Tectonic evolution and gold metallogeny of the Lynn Lake greenstone belt, Manitoba (NTS 64C10, 11, 12, 14, 15 and 16); *in* Report of Activities 2003; Manitoba Industry, Trade and Mines, Manitoba Geological Survey, p. 39–49.

Beaumont-Smith, C.J., Machado, N., and Peck, D.C., 2006. New uranium-lead geochronology results from the Lynn Lake greenstone belt, Manitoba (NTS 64C11–16); Manitoba Geological Survey, Geoscientific Paper GP2006-1, 11 p.

Corrigan, D., Hajnal, Z., Németh, B., and Lucas, S.B., 2004. Tectonic framework of a Paleoproterozoic arc-continent to continent-continent collisional zone, Trans-Hudson Orogen, from geological and seismic reflection studies; Canadian Journal of Earth Sciences, v. 42, p. 421–434.

Corrigan, D., Pehrsson, S., Wodicka, N., and de Kemp, E., 2009. The Palaeoproterozoic Trans-Hudson Orogen: A prototype of modern accretionary processes; *in* Ancient Orogens and Modern Analogues, (ed.) J.B. Murphy, J.D. Keppie, and A.J. Hynes; Geological Society, London, Special Publications, v. 327, p. 457–479.

Couëslan, C.G., Pattison, D.R.M., and Dufrane, S.A., 2013. Paleoproterozoic metamorphic and deformation history of the Thompson Nickel Belt, Superior Boundary Zone, Canada, from in situ U–Pb analysis of monazite; Precambrian Research, v. 237, p. 13–35.

Eckstrand, R. and Hulbert, L., 2007. Magmatic nickel-copper-platinum group element deposits *in* Mineral Deposits of Canada: A Synthesis of Major Deposit-Types, District Metallogeny, the Evolution of Geological Provinces, and Exploration Methods, (ed.) W.D. Goodfellow; Geological Association of Canada, Special Publication no. 5, p. 205–222.

Elliot, B.A., 2009, A mineralogical, geochemical and geochronological study of postorogenic carbonatites in the Eden Lake complex, northern Manitoba; M.Sc. thesis, University of Manitoba, Winnipeg, Manitoba, 213 p.

Faure, S., 2010, World Kimberlites CONSOREM Database (Version 3), Consortium de Recherche en Exploration Minérale CONSOREM, Université du Québec à Montréal. <http://www.consorem.ca> [accessed December 12, 2018].

Fumerton, S.L., Stauffer, M.R., and Lewry, J.F., 1984. The Wathaman batholith: Largest known Precambrian pluton; Canadian Journal of Earth Science, v. 21, p. 1082–1097.

Galley, A., Hannington, M., and Jonasson, I., 2007. Volcano-

genic massive sulphide deposits; *in* Mineral Deposits of Canada: A Synthesis of Major Deposit-Types, District Metallogeny, the Evolution of Geological Provinces, and Exploration Methods, (ed.) W.D. Goodfellow; Geological Association of Canada, Special Publication no. 5, p. 141–162.

Gilbert, H.P., Syme, E.C., and Zwanzig, H.V., 1980. Geology of the metavolcanic and volcaniclastic metasedimentary rocks in the Lynn Lake area; Manitoba Energy and Mines, Geological Services, Geological Paper GP80-1, 118 p.

Gosselin, P. and Dubé, B., 2015. World lode gold deposit database; Geological Survey of Canada, Open File 7930.

Lawley, C.J.M., Schneider, D., Yang, E., Davis, W.J., Jackson, S.E., Yang, Z., Zhang, S., and Selby, D., 2017. Age relationships and preliminary U-Pb zircon geochronology results from the Lynn Lake greenstone belt; *in* Targeted Geoscience Initiative: 2017 report of activities, volume 1, (ed.) N. Rogers; Geological Survey of Canada, Open File 8358, p. 133–137.

Manitoba Mineral Resources, 2013. Bedrock geology, Manitoba; *in* Map Gallery – Geoscientific Maps, Manitoba Mineral Resources. <https://web33.gov.mb.ca/mapgallery/mgg-gmm.html> [accessed July 1, 2018]

Maxeiner. R.O. and Demmans, C.J., 2000. The final pieces of the 'Bridge': Geology of the southern Reindeer Lake and Laurie Lake areas; *in* Summary of Investigations 2000, Volume 2; Saskatchewan Geological Survey, Saskatchewan Energy Mines, Miscellaneous Report 2000-4.2.

Meyer, M.T., Bickford, M.E., and Lewry, J.F., 1992. The Wathaman batholith: An early Proterozoic continental arc in the Trans-Hudson orogenic belt, Canada; Geological Society of America Bulletin, v. 104, p. 1073–1085.

Schneider, D.A., Heizler, M.T., Bickford, M.E., Wortman, G.L., Condie, K.C., and Perilli, S., 2007. Timing constraints of orogeny to cratonization: Thermochronology of the Paleoproterozoic Trans-Hudson orogen, Manitoba and Saskatchewan, Canada; Precambrian Research, v. 153, p. 65–95.

Turek, A., Woodhead, J., and Zwanzig H.V., 2000. U-Pb age of the gabbro and other plutons at Lynn Lake (part of NTS 64C); *in* Report of Activities 2000; Manitoba Industry, Trade and Mines, Manitoba Geological Survey, p. 97–104.

Woolley, A.R., Kjarsgaard, B.A., 2008. Carbonatite occurrences of the world: map and database; Geological Survey of Canada, Open File 5796, 28 p.

Zwanzig, H.V., 1999. Structure and stratigraphy of the south flank of the Kisseynew Domain in the Trans-Hudson Orogen, Manitoba: Implications for 1.845–1.77 Ga collision tectonics; Canadian Journal of Earth Science, v. 36, p. 1859–1880.

Zwanzig, H.V., Syme, E.C., and Gilbert, H.P., 1999. Updated trace element geochemistry of ca. 1.9 Ga metavolcanic rocks in the Paleoproterozoic Lynn Lake Belt; Manitoba Industry, Trade and Mines, Geological Services, Open File Report 99-13, 46 p.

Zwanzig, H.V., 2000. Geochemistry and tectonic framework of the Kisseynew Domain-Lynn Lake belt boundary (part of NTS 63P/13); *in* Report of Activities 2000; Manitoba Industry, Trade and Mines, Manitoba Geological Survey, p. 91–96.

Structural and lithological controls on the nature and distribution of gold at the Tiriganiaq deposit, Meliadine district, Rankin Inlet greenstone belt, Nunavut

B. St.Pierre[1], P. Mercier-Langevin[2], M. Simard[3], O. Côté-Mantha[4], M. Malo[1] and G. Servelle[5]

[1]*Institut national de la Recherche scientifique, Centre Eau Terre Environnement, 490 rue de la Couronne, Québec, Quebec G1K 9A9*

[2]*Geological Survey of Canada, 490 rue de la Couronne, Québec, Quebec G1K 9A9*

[3]*Agnico Eagle Mines Ltd., Technical Services, 200, route de Preissac, Rouyn-Noranda, Quebec J0Y 1C0*

[4]*Agnico Eagle Mines limited, Exploration Division, 765 chemin de la mine Goldex, Val-d'Or, Quebec J9P 4N9*

[5]*Agnico Eagle Mines Limited - Meliadine Division - Rankin Inlet, Nunavut X0C 0G0*

Abstract

The Archean Meliadine gold district, Rankin Inlet greenstone belt, Nunavut, contains numerous gold deposits and prospects that are spatially associated with the crustal-scale Pyke Fault and its splays. Many of these deposits are partially to dominantly hosted within banded iron formation (BIF), including at the Tiriganiaq mine where gold is hosted in complexly folded and sheared BIF-associated zones.

The Tiriganiaq deposit is hosted in the structural hanging wall of the Lower Fault, a west-trending splay of the Pyke Fault located further to the south. The Lower Fault marks a break between the footwall mafic volcanic-dominated sequence (south) and a turbiditic dominated sequence in the hanging wall (north). The hanging wall units host the ore -bearing, decimetre- to metre-wide laminated quartz-ankerite shear vein referred to as the 1000 lode.

A large part of the ore at Tiriganiaq is hosted within the Upper Oxide Formation, a package of iron-rich sedimentary rocks and BIF units. The southernmost ore zone (1100 lode) consists of a geometrically planar mineralized corridor associated with the transposed long limb of the folded BIF. The more geometrically and structurally complex 1150 and 1250 lode series are controlled by Lower Fault-parallel, narrow, north-dipping, reverse shear zones that overprint the slightly steeper, north-dipping S_2 foliation that is axial planar to tight F_2 folds. Shallowly south-dipping extensional veins, associated with the shear zones and related fault-fill veins, are preferentially developed in tightly folded decimetre- to metre-thick BIF layers around the moderately north-dipping reverse shear zones.

Introduction

Orogenic gold deposits form in granite-greenstone-slate belts that are deformed and metamorphosed synchronously with the late stages of an orogeny. Orogenic deposits typically form at depths greater than five kilometres in a variety of host rocks, including banded iron formations (BIF), in which case they are referred to as BIF-hosted orogenic gold deposits (Poulsen et al., 2000; Goldfarb et al., 2005). These deposits are structurally controlled, from the distribution of deposits to the internal textures and structures of the ore. Typically they are found adjacent to major crustal-scale fault zones in association with long-lived high-strain corridors and shear zones in a variety of rock types (Dubé and Gosselin., 2007). Layer anisotropy of the host units, such as BIFs, induces significant structural complexities throughout the evolution of these deposits. Understanding these complexities is critical to optimize exploration models and mine development (Robert et al., 1994).

The Meliadine gold district, located within the (>2.66 Ga) Rankin Inlet greenstone belt (RIGB), Nunavut (Fig. 1), is one of Canada's largest emerging gold districts with 3.7 million ounces (105 t) of gold in proven and probable reserves, 3.1 million ounces (88 t) of gold in indicated mineral resources, and 2.7 million ounces (77 t) of gold in inferred resources (Agnico Eagle, 2018). The RIGB is located within the Hearne Craton of the Western Churchill Province, an understudied, remote region of eastern Nunavut. It has a very complex geological and metallogenic history (Berman et al., 2007; Pehrsson et al., 2013; Lawley et al., 2015a, b, c, 2016). The major terrane boundary between the Hearne and Chesterfield block likely played a key role in the formation of the Meliadine district's gold deposits, acting as a locus for a first-order crustal-scale fault zone to form (Lawley et al., 2015a, b, 2016), a crucial

Corresponding author: Brayden St.Pierre (Brayden.St-Pierre@ete.inrs.ca)

St.Pierre, B., Mercier-Langevin, P., Simard, M., Côté-Mantha, O., Malo, M., and Servelle, G., 2019. Structural and lithological controls on the nature and distribution of gold at the Tiriganiaq deposit, Meliadine district, Rankin Inlet greenstone belt, Nunavut; *in* Targeted Geoscience Initiative: 2018 report of activities, (ed.) N. Rogers; Geological Survey of Canada, Open File 8549, p. 77–82. https://doi.org/10.4095/313642

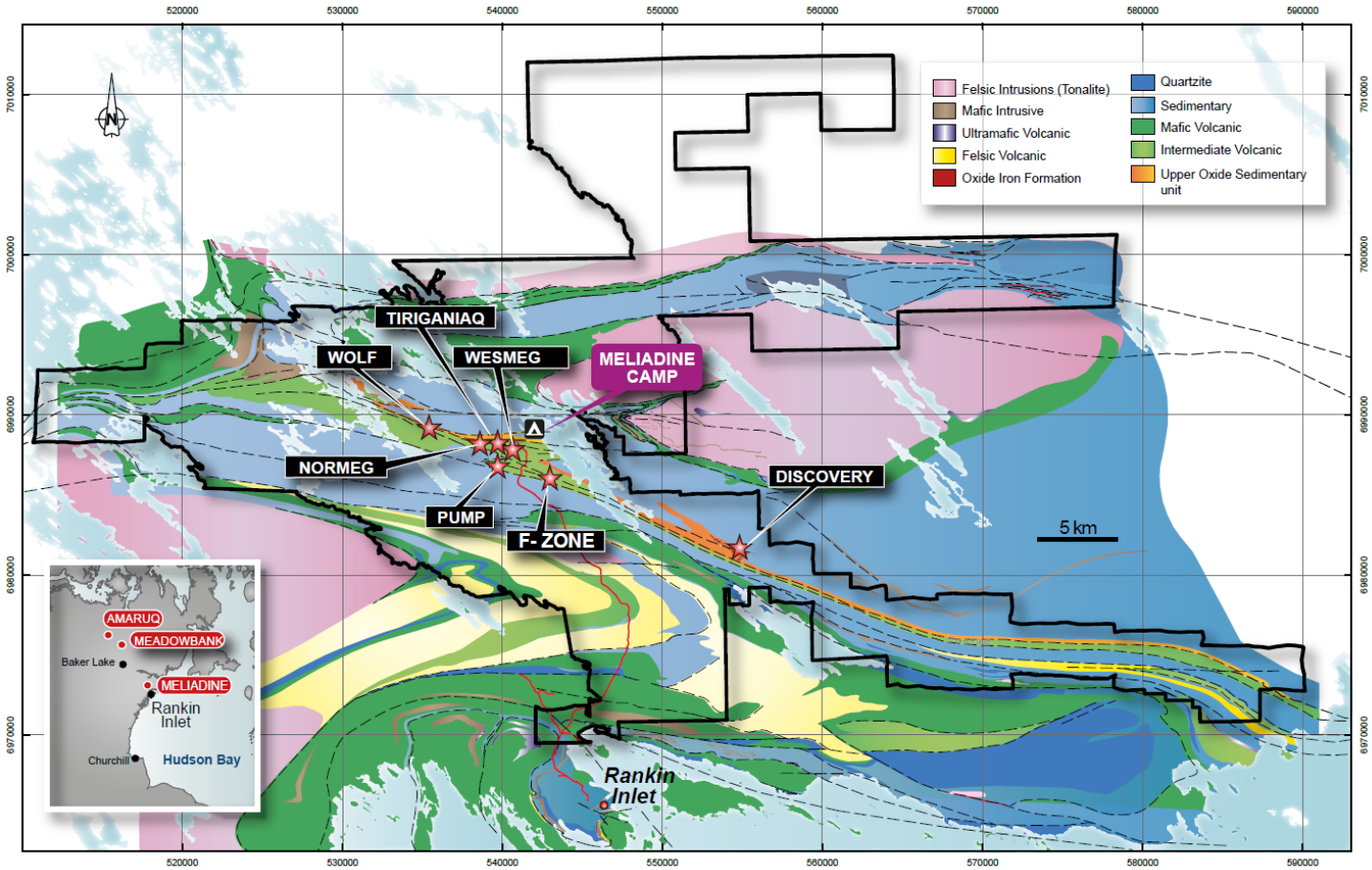

Figure 1. Meliadine area regional geology and location of the Tiriganiaq deposit. The trend of the Meliadine property is defined by the northwest-trending major Pyke Fault zone (*modified from* Agnico Eagle Mines Ltd., pers. comm., 2016).

element in the formation of orogenic gold deposits.

The deformation history of the Meliadine gold district has been divided into four increments (Carpenter and Duke, 2004). The first documented phase (D_1) is associated with the juxtaposition of turbiditic and volcanic rock packages along an ancestral expression of what most probably now forms the Pyke Fault. The second phase of deformation (D_2) consisted of folding of the Archean succession by southwest-directed shortening, developing F_2 folds with an axial planar S_2 cleavage. The third phase of deformation (D_3) occurred in a slightly different direction causing southern shortening (Carpenter and Duke, 2004) forming a west-trending fabric. At Tiriganiaq, there is one main deposit fabric oriented N265/65 on average, which likely represents the main regional S_2 foliation transposed into a west-trending orientation by D_3 strain (Miller et al., 1995). The fourth deformation (D_4) resulted in kink banding and north - to northwest-trending crenulation cleavage.

Tiriganiaq, the principal deposit of the Meliadine district, is a subtype of BIF-hosted gold deposits in which only part of the mineralization is hosted in BIF (Dubé et al., 2015; Lawley et al., 2015a). The mineralization at Tiriganiaq largely consists of decimetre- to metre-thick laminated fault-fill and associated extensional veins with coarse arsenopyrite replacement of magnetite-rich BIF units along vein selvages (Carpenter et al., 2005; Lawley et al., 2015a, b, c, 2016).

The Tiriganiaq mine, the focus of this study, is currently in a pre-production and development phase, and is scheduled to enter full production in 2019. This study is part of a larger thematic research project that aims at better understanding the controls on BIF-hosted gold deposits in general, and at unravelling the interplay between Archean and Paleoproterozoic events in forming the Churchill Province BIF-hosted gold deposits.

Tiriganiaq deposit geology

The Tiriganiaq deposit, located in the central part of the Meliadine district, is hosted in the overturned dominantly turbiditic sequence present in the structural hanging wall of the Lower Fault, a west-oriented splay of the Pyke Fault (Fig. 2). The 1000 lode vein is a quartz-ankerite laminated shear vein with a sericitic alteration halo and associated sulphidation comprising mainly arsenopyrite and pyrrhotite (Lawley et al., 2015c). The vein is hosted in the Tiriganiaq Formation, a package of laminated siltstone with graphitic argillite at the base in contact with the Lower Fault. There are sections along the

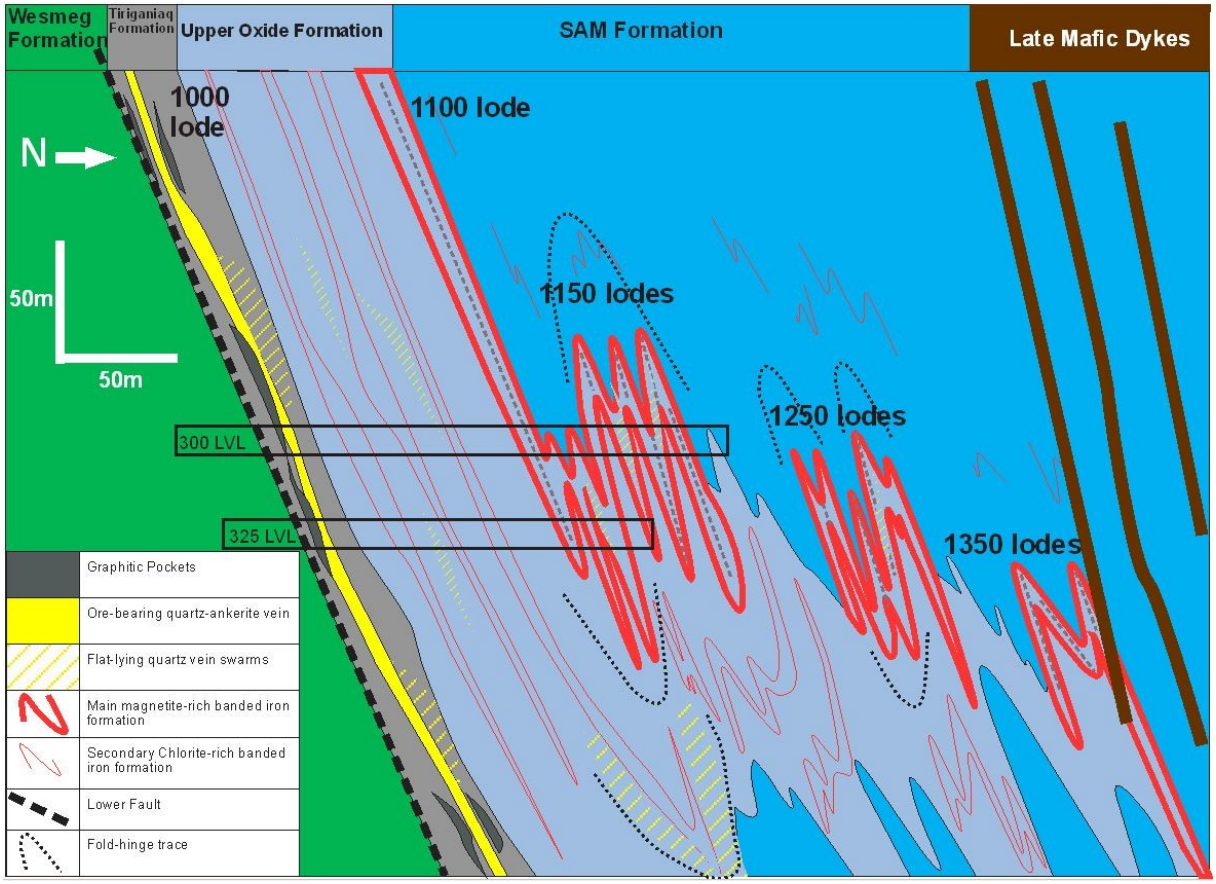

Figure 2. Schematic cross-section looking west of the deposit, showing the geometry of the lithologies, vein distribution, and location of ore zones (*modified from* Agnico Eagle Mines Ltd., pers. comm., 2018).

1000 lode vein with abundant deformed, ore-bearing, shallowly north-dipping, syn- to late-D_2 quartz-ankerite extensional vein arrays. Most of the ore is hosted in the Upper Oxide Formation, a package of iron-rich sedimentary rocks and complexly folded BIF units. The 1100 lode, north of the 1000 lode, is associated with the long limb of the F_2-folded BIF succession in the Upper Oxide Formation. The 1150, 1250, and 1350 lode series, north of the 1100 lode, have a more complex geometry, which is controlled by Lower Fault-parallel, syn- to late-D_2 narrow north-dipping reverse shear zones, which overprint the slightly steeper, north-dipping S_2 foliation that is axial planar to tight F_2 folds. Shallowly south-dipping extensional veins, associated with the shear zones and related fault-fill veins, are preferentially developed in tightly F_2-folded decimetre- to metre-thick BIF layers around the moderately north-dipping reverse shear zones (St.Pierre et al., 2018).

1150 Lodes

In the summer of 2018, new underground developments exposing the 1150 lodes were mapped and yielded the same characteristics as shown in St.Pierre et al. (2018). The 1150 lodes are associated with multiple parallel narrow (decimetre to metre-wide) syn- to late-D_2 shear zones localized within the chloritic siltstone between complexly F_2-folded BIF intervals, which act as a first-order control on mineralization at ore-zone scale (Fig. 3). These shear zones, which dip moderately to the north and are parallel to the Lower Fault to the south, control the location of vein corridors (deformed fault-fill/shear veins). Extensional quartz±ankerite veins are associated with the shear zones and are particularly well mineralized in BIF units, forming stratabound zones of coarse arsenopyrite replacement of magnetite layers along vein margins. The mineralized extensional veins dip shallowly to the south in north-dipping units. The veins are late- to post-F_2 folding, and syn- to late-shearing. The shear zones have a slightly shallower dip than the main foliation, which are at N270/55 and N270/60, respectively (Fig. 3; St.Pierre et al., 2018).

Deposit kinematics

Although the main deposit fabric is cut by distinct ore-controlling shear planes, they both seem to be part of a protracted deformation event (St.Pierre et al., 2018). The main S_2 deposit fabric is axial planar to F_2 folds, and all units are folded, although folding is most prominent in decimetre- to metre-thick BIF units. Lithological contacts are generally parallel to subparallel with the main foliation at drift scale, except in hinge zones. Kinematic indicators almost uniformly show reverse motion in the shear zones (Fig. 4). At drift scale, the lat-

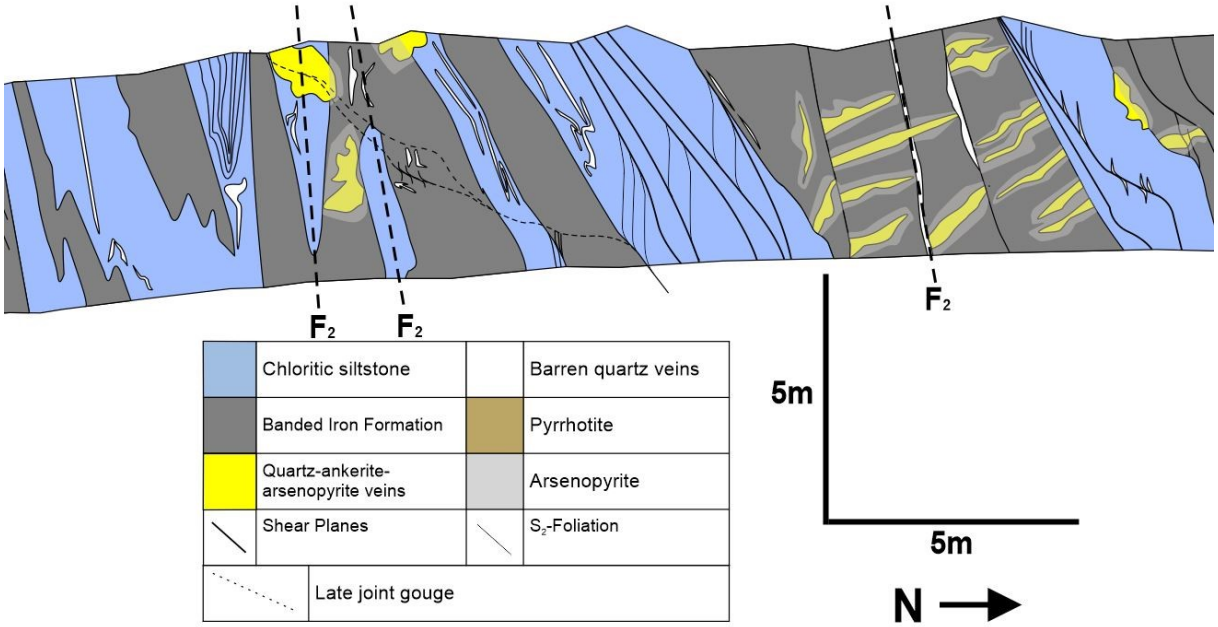

Figure 3. Underground detailed geological and structural map of west wall of drift CC300-152. Shear zones are localized within chloritic siltstone, between tightly folded BIF intervals with quartz-ankerite shear veins controlled by distinct shear planes. Also refracted, shallowly south-dipping quartz-ankerite extensional veins, associated with shear zones, with stratabound arsenopyrite replacement of magnetite-rich layers within BIF intervals along vein selvages.

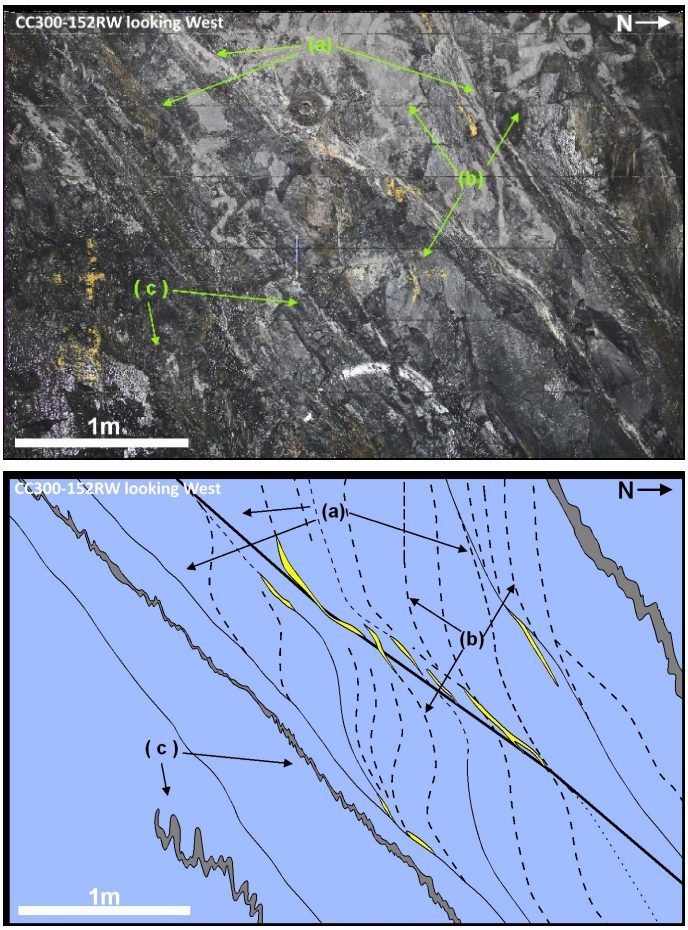

eral component of these shear zones is not readily apparent at drift scale. Further investigation of oriented samples, in plan view, revealed that there are distinct shear bands cutting the main deposit fabric with a dextral shear sense within the chloritic siltstone samples taken from within the shear zones (Fig. 5a). This suggests the main deformation and associated deposit fabric and related shear zones have an oblique reverse dextral shear sense in agreement with a major, syn-ore reverse component of motion in the deposit area.

Interveining lodes

New drifts and stopes were developed at Tiriganiaq, exposing what is informally referred to as the "interveining lodes", a section of abundant, deformed shallowly north-dipping ore-bearing quartz-ankerite veins (Fig. 5b). The interveining lodes, just north of the 1000 lode, form a series of multiple generations of deformed extensional vein arrays hosted within the Tiriganiaq Formation sedimentary rocks, with distinct sericitic alteration halos (Fig. 5b). Most of these veins preserve horizontal vein tips as an indication of their original mode of formation

Figure 4. Underground picture and schematic west wall of drift CC300-152. A relatively thick shear zone with systematic reverse motion indicators. a) Discrete shear planes that are moderately dipping (north), i.e. more shallowly than the main foliation. b) Main foliation is dragged on the shear planes, indicating a reverse component of motion. c) Tightly folded chert beds also indicate a reverse component of motion.

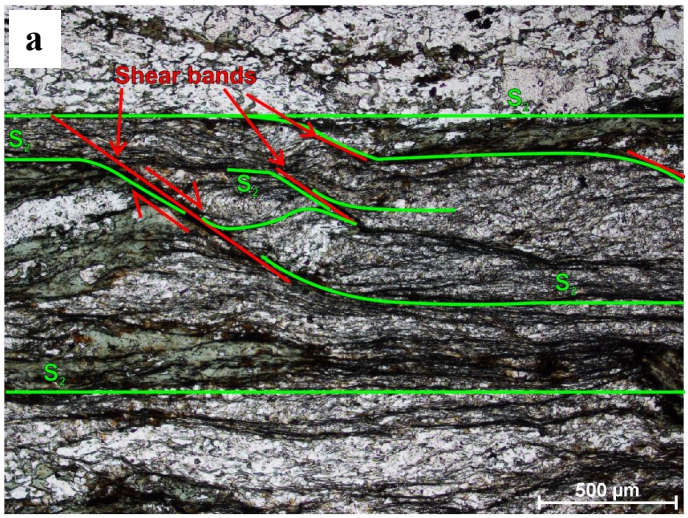

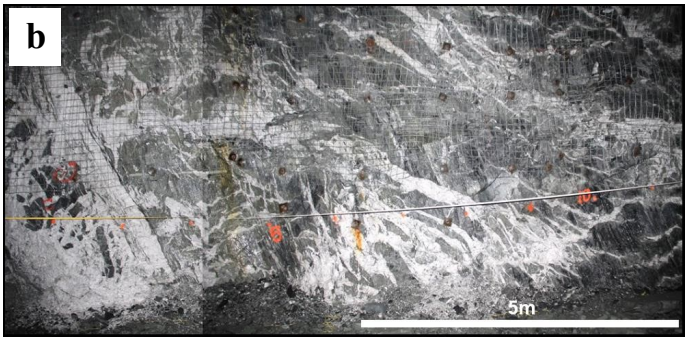

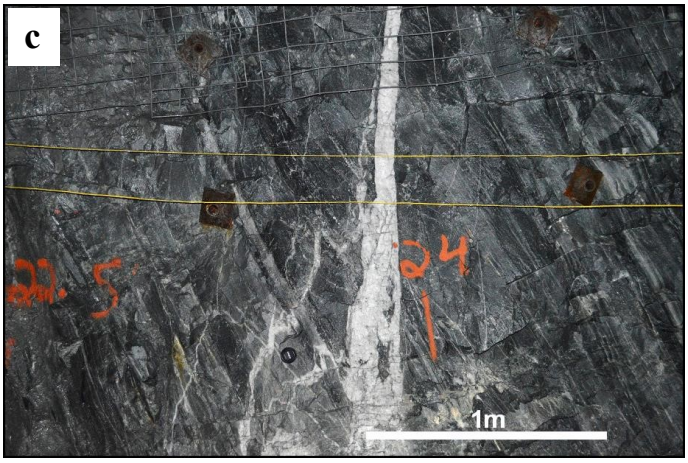

Figure 5. a) Plan view of oriented sample of chloritic siltstone taken from drift CC300-152 within one of the shear zones between folded banded iron formation intervals. Main deposit fabric S_2 is cut by shear bands suggesting a dextral shear sense. Plane polarized light; x10. b) Left wall of drift CC200-157 (looking west). "Interveining lodes", just north of the 1000 lode, are a series of multiple generations of progressively deformed extensional vein arrays hosted within the Tiriganiaq Formation sedimentary rocks. The extensional veins are predominantly subhorizontal to shallowly dipping north. The partly folded geometry of extensional vein arrays suggests reverse (north over south) movement. Less predominant extensional veins are more intensely transposed and folded. c) Left wall of drift CC325 -155 (looking west). Relatively weakly deformed subvertical ore-bearing quartz-ankerite vein, with weak sericite alteration halo, cross-cutting S_2 foliation in chloritic siltstone.

and far-field stress regime compatible with progressive deformation, indicating horizontal shortening, vertical extension, and syn- to late-D_2 reverse shearing, which is in agreement with observations made elsewhere in the deposit (e.g. St.Pierre et al., 2018). These areas of intense veining represent major concentrations of gold and ongoing work aims to better understand the controls on their development and to determine if they define ore shoots that could be used to vector towards similarly enriched zones at deposit scale.

In addition to the ore-bearing shear veins and associated extensional veins typical of the 1150 lode series, there are also rare relatively weakly deformed subvertical quartz-ankerite veins, some of which are mineralized (Fig. 5c).

Expected outcomes and future work

Ongoing work includes additional geochemical characterization of the host rocks and mineralized zones, and microstructural analysis of key fabrics registered by the host rocks using thin section microscopy and rocks slab observation and documentation. Analysis of the larger scale geometry of the ore zones and high-grade gold intercepts in section, plan view, and longitudinal view is ongoing. Geochemical characterization of the host rocks and mineralized zones will be applied as lithological controls on gold grades and distribution and to find reliable stratigraphic markers. The results from this study will directly contribute at developing improved reserve modelling and exploration models by providing key information on the structural controls (conduits and traps) of the ore zones at various scales.

Acknowledgments

This report is a contribution to NRCan's Targeted Geoscience Initiative Program (TGI). Support for this study was provided through the Gold Project's '*Activity G-2.4: Lithotectonic controls on Paleoproterozoic gold distribution in the Archean rocks of the Amaruq area, Nunavut*'.

Brayden St.Pierre is conducting a TGI-supported M.Sc. program at Institut national de la recherche scientifique – Centre Eau, Terre et Environnement, Québec. This activity is conducted in close collaboration with the Meliadine and Technical Services divisions of Agnico Eagle Mines Ltd. that provide essential scientific and technical support and access to material

and data. We are particularly grateful to J.-C. Blais and M. Horjth, from the Meliadine division, and to W. Bleeker for fruitful discussions of the geology of orogenic gold districts. This report benefited from the review of Beth McClenaghan, Vicki Tschirhart and Neil Rogers.

References

Angico Eagle, 2018. Agnico Eagle Mines Limited Detailed Mineral Reserves and Resources Data: As of December 31, 2017; Agnico Eagle Mines Limited. <https://www.agnicoeagle.com/English/operations-and-development-projects/reserves-and-resources/default.aspx> [accessed January 23, 2019]

Berman, R., Davis, W., and Pehrsson, S., 2007. Collisional Snowbird tectonic zone resurrected: Growth of Laurentia during the 1.9 Ga accretionary phase of the Hudsonian orogeny; Geology, v. 35, p. 911-914.

Carpenter, R.L. and Duke, N.A., 2004. Geological setting of the West Meliadine gold deposits, Western Churchill Province, Nunavut, Canada; Exploration and Mining Geology Journal, v. 13, p. 49–65.

Carpenter, R.L., Duke, N.A., Sandeman, H.S., and Stern, R., 2005. Relative and absolute timing of gold mineralization along the Meliadine trend, Nunavut, Canada: Evidence for Paleoproterozoic gold hosted in an Archean greenstone belt; Economic Geology, v. 100, p. 567−576.

Dubé, B. and Gosselin, P., 2007. Greenstone-hosted quartz-carbonate vein deposits; *in* Mineral Deposits of Canada: A Synthesis of Major Deposit Types, District Metallogeny, the Evolution of Geological Provinces, and Exploration Methods, (ed.) W.D. Goodfellow; Geological Association of Canada, Mineral Deposits Division, Special Publication no. 5, p. 49–83.

Dubé, B., Mercier-Langevin, P., Castonguay, S., McNicoll, V.J., Bleeker, W., Lawley, C.J.M., De Souza, S., Jackson, S.E., Dupuis, C., Gao, J.-F., Bécu, V., Pilote, P., Goutier, J., Beakhouse, G.P., Yergeau, D., Oswald, W., Janvier, V., Fontaine, A., Pelletier, M., Beauchamp, A.-M., Katz, L.R., Kontak, D.J., Tóth, Z., Lafrance, B., Gourcerol, B., Thurston, P.C., Creaser, R.A., Enkin, R.J., El Goumi, N., Grunsky, E.C., Schneider, D.A., Kelly, C.J., and Lauzière, K., 2015. Precambrian lode gold deposits — a summary of TGI-4 contributions to the understanding of lode gold deposits, with an emphasis on implications for exploration; *in* Targeted Geoscience Initiative 4: Contributions to the Understanding of Precambrian Lode Gold Deposits and Implications for Exploration, (ed.) B. Dubé and P. Mercier- Langevin; Geological Survey of Canada, Open File 7852, p. 1–24.

Goldfarb, R., Baker, T., Dube, B., Groves, D., Hart, C., and Gosselin, P., 2005. Distribution, character and genesis of gold deposits in metamorphic terranes; *in* 100th Anniversary Volume (1905-2005), (ed.) J.W. Hedenquist, J.R.H. Thompson, R.J. Goldfarb and J.P. Richards; Society of Economic Geologists, p. 407–450.

Lawley, C.J.M., Dubé, B., Mercier-Langevin, P., McNicoll, V.J., Creaser, R.A., Pehrsson, S., Castonguay, S., Blais, J.-C., Simard, M., Davis, W.J., and Jackson, S.E., 2015a. Setting, age, and hydrothermal footprint of the emerging Meliadine gold district, Nunavut; *in* Targeted Geoscience Initiative 4: Contributions to the understanding of Precambrian lode gold deposits and implications for exploration, (ed.) B. Dubé and P. Mercier-Langevin; Geological Survey of Canada, Open File 7852, p. 99–111.

Lawley, C.J.M., Creaser, R.A., Jackson, S., Yang, Z., Davis, B., Pehrsson, S., Dubé, B., Mercier-Langevin, P., and Vaillancourt, D., 2015b. Unravelling the Western Churchill Province Paleoproterozoic gold metallotect: Constraints from Re-Os arsenopyrite and U-Pb xenotime geochronology and LA-ICP-MS arsenopyrite trace element chemistry at the BIF-hosted Meliadine gold district, Nunavut, Canada; Economic Geology, v. 110, p. 1425–1454.

Lawley, C.J.M., Dubé, B., Mercier-Langevin, P., Kjarsgaard, B.A, Knight, R., and Vaillancourt, D., 2015c. Defining and mapping hydrothermal footprints at the BIF-hosted Meliadine gold district, Nunavut, Canada; Journal of Geochemical Exploration, v. 155, p. 33–55.

Lawley, C.J.M., McNicoll, V.J., Sandeman, H., Pehrsson, S., Simard, M., Castonguay, S., Mercier-Langevin, P., and Dubé, B., 2016. Age and geological setting of the Rankin Inlet greenstone belt and its relationship to the gold endowment of the Meliadine gold district, Nunavut, Canada; Precambrian Research, v. 275, p. 471–795.

Miller, A.R., Balog, M.J. and Tella, S., 1995. Oxide iron-formation hosted lode gold, Meliadine Trend, Rankin Inlet Group, Churchill Province, Northwest Territories; Current Research 1995-C, Geological Survey of Canada, p. 163-174.

Pehrsson, S., Berman, R., and Davis, W., 2013. Paleoproterozoic orogenesis during Nuna aggregation: A case study of reworking of the Rae craton, Woodburn Lake, Nunavut; Precambrian Research, v. 232, p. 167–188.

Poulsen, K.H., Robert, F., and Dubé, B., 2000. Geological classification of Canadian gold deposits; Geological Survey of Canada, Bulletin 540, 106 p.

Robert, F., Poulsen, K.H., and Dubé, B., 1994. Structural analysis of lode gold deposits in deformed terranes; Geological Survey of Canada, Open File 2850, p. 5-17.

St.Pierre, B., Mercier-Langevin, P., Simard, M., Côté-Mantha, O., Malo, M., and Servelle, G., 2018. Structural and lithologic controls on the nature and distribution of gold in the BIF-associated 1150 and 1250 lode series at Tiriganiaq, Meliadine district, Rankin Inlet greenstone belt, Nunavut; *in* Targeted Geoscience Initiative: 2017 report of activities, volume 1, (ed.) N. Rogers; Geological Survey of Canada, Open File 8358, p. 157–161.

Geological setting of the 5.2 Moz Au Amaruq banded iron formation-hosted gold deposit, Churchill Province, Nunavut

M. Valette[1], S. De Souza[1], P. Mercier-Langevin[2], V.J. McNicoll[3], N. Wodicka[3], R.A. Creaser[4], O. Côté-Mantha[5] and M. Simard[6]

[1]*Université du Québec à Montréal, 201 Avenue du Président-Kennedy, Montreal, Quebec H2X 3Y7*
[2]*Geological Survey of Canada, 490 rue de la Couronne, Québec, Quebec G1K 9A9*
[3]*Geological Survey of Canada, 601 Booth Street, Ottawa, Ontario K1A 0E8*
[4]*University of Alberta, 116th Street and 85th Avenue, Edmonton, Alberta T6G 2R3*
[5]*Agnico Eagle Mines Ltd., Exploration Division, 765 chemin de la mine Goldex, Val-d'Or, Quebec J9P 4N9*
[6]*Agnico Eagle Mines Ltd., Technical Services, 10 200 route de Preissac, Rouyn-Noranda, Quebec J0Y 1C0*

Abstract

The recently discovered 5.2 Moz Au Amaruq deposit in Nunavut is part of the Neoarchean (ca. 2.72–2.63 Ga) Woodburn Lake greenstone belt, Churchill Province. It is hosted in polydeformed, upper greenschist facies banded iron formation (BIF), volcanic, and detrital sedimentary rocks of the Rumble assemblage of the Woodburn Lake group. The orebodies are primarily hosted in Algoma-type silicate-facies BIF and chert, and occur as stratabound to discordant pyrrhotite-rich replacements and arsenopyrite (± löllingite)-bearing zones of silica flooding. Several sets of discordant quartz±carbonate auriferous veins are present and include fault-fill laminated veins in high-strain zones preferentially developed along sheared/folded contacts between sedimentary and volcanic rocks. The host rocks are affected by at least three episodes of deformation. Textural relationships between silicate and sulphide minerals provide evidence for prograde metamorphism associated with the main phase of deformation and main fabrics affecting the ore. Gold was exsolved from löllingite during retrograde metamorphism to lower greenschist facies. Possible Archean gold heritage and the timing of the gold mineralization represent key issues that are being addressed to help improve exploration models for BIF-hosted/associated gold deposits in the Churchill Province and other Archean terranes.

Introduction and problem statement

The study area is in the Rae domain of the Churchill Province, in the Canadian Shield (Fig. 1). The Rae domain is composed of a Mesoarchean (2.9–2.8 Ga) gneissic basement, and several Archean greenstone belts (ca. 2.73–2.63 Ga), which spread out over one thousand kilometres and are locally covered by Paleoproterozoic sedimentary basins (ca. 2.2–1.9 Ga: Jefferson et al., 2015). With a total of almost 560 metric tons of gold (approximately 20 million ounces) in reserves and resources (Agnico Eagle Mines Ltd., 2018), the nearby Meliadine, Meadowbank, and Amaruq deposits are part of a new emerging gold province where exploration is mostly based on orogenic Algoma-type BIF-hosted/associated gold deposits (Fig. 1; Côté-Mantha et al., 2015, 2017; Mercier-Langevin et al., 2017). The ore zones at these sites are structurally controlled and associated with faults, shear zones, and/or polydeformed banded iron formation (BIF), which are the principal metallotects in the region (Janvier, 2016; Lawley et al., 2016; Mercier-Langevin et al., 2017).

The Amaruq gold deposit is hosted in the Woodburn Lake greenstone belt, which has been deformed and metamorphosed during Archean and Proterozoic orogens (Perhsson et al., 2013; Janvier et al., 2015; Janvier, 2016). Several studies and Re-Os geochronology on the Meliadine and Meadowbank districts (e.g. Lawley et al., 2015; Janvier, 2016; Mercier-Langevin et al., 2018) suggest that gold was introduced during the Trans-Hudson Orogen (ca. 1.91–1.81 Ga). However, a series of Re-Os model ages as old as 2.65 Ga were also obtained for the Meliadine (Lawley et al., 2015) and Amaruq (Mercier-Langevin et al., 2018) deposits.

Uncertainties about the structural controls on the ore zones, the effects of metamorphism, the relative timing of events, and the nature and age of the hydrothermal and metamorphic events raise questions about ore-forming processes in the region, from province- to deposit-scale. For example, was there an early Archean gold event affected by, and possibly upgraded, by later Proterozoic orogenesis, or was gold only introduced during the Paleoproterozoic? How is this gold minerali-

Corresponding author: Manon Valette (valette.manon@courrier.uqam.ca)

Valette, M., De Souza, S., Mercier-Langevin, P., McNicoll, V.J., Wodicka, N., Creaser, R.A., Cote-Mantha, O., and Simard, M., 2019. Geological setting of the 5.2 Moz Au Amaruq banded iron formation-hosted gold deposit, Churchill Province, Nunavut; *in* Targeted Geoscience Initiative: 2018 report of activities, (ed.) N. Rogers; Geological Survey of Canada, Open File 8549, p. 83–87. https://doi.org/10.4095/313643

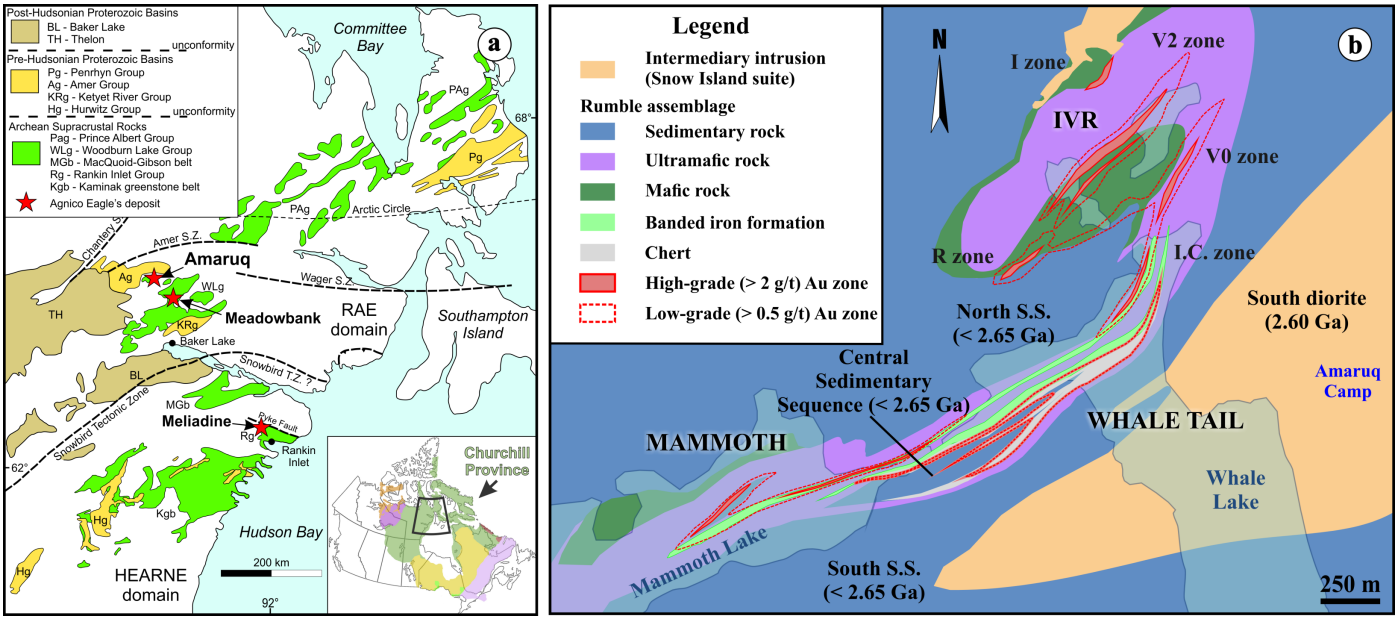

Figure 1. a) Simplified bedrock geological map of the Rae and Hearne domains of the western Churchill Province with the location of the Amaruq gold project in the Woodburn Lake greenstone belt (*modified from* Hrabi et al., 2003). b) Simplified bedrock geological map of the Amaruq area showing the location of the Whale Tail and IVR zones (*modified from* Agnico Eagle Mines Ltd., 2018).

zation event(s) reflected in the rocks and what is the age gap between the host stratigraphy and the main gold events? Answering these fundamental questions and clarifying numerous aspects specific to the Amaruq deposit necessitate a multidisciplinary study of the main controls on ore deposition (i.e. timing, geometry).

This paper is presenting the geology and the work undertaken at the Amaruq deposit, which will contribute to the understanding of the nature and age of the principal ore-forming processes in this part of Nunavut and improve understanding of the nature and role of conduits and traps responsible, and their roles in the formation (and preservation) of orogenic BIF-hosted/associated gold deposits.

Geology of the Amaruq gold deposit

At Amaruq, the Woodburn Lake group comprises a 250 m thick volcano-sedimentary sequence that consists of mafic-ultramafic volcanic rocks and greywacke interlayered with chert and silicate-facies iron-formation (Fig. 1). The greywacke is subdivided into south, central, and north packages separated by slivers of volcanic and fine-grained/chemical sedimentary rocks (Fig. 1). Preliminary SHRIMP U-Pb geochronology of detrital zircons from the three greywacke packages indicate that the central, ore-hosting sedimentary rock package has a younger overall heritage, with detrital zircons varying in age between 2.65 and 2.73 Ga, whereas zircons in the north and south packages vary between 2.65 and 3.15 Ga. All three packages have a preliminary maximum depositional age of 2.65 Ga. The minimum age of the sedimentary and volcanic rocks is constrained at 2.6 Ga by a crosscutting diorite intrusion of the Snow Island Suite (Pehrsson et al., 2013; Jefferson et al., 2015).

Detailed mapping and analyses of drill sections highlight that at least two main phases of deformation controlled the geometry of the ore zones. The main phase of deformation, D_2, is represented by a shallow to steeply southeast-dipping schistosity, which is affected by a shallow-dipping crenulation cleavage associated with D_3 deformation (Fig. 2a). Evidences of deformation D_1 are locally preserved and can be observed in the hinge zone of F_2 folds. Petrographic relationships among metamorphic minerals, such as garnets in BIF, provide evidence for prograde and peak metamorphism at upper greenschist facies associated with D_2 deformation (Fig. 2b, c). There is also evidence of retrograde and/or probably another metamorphic event at lower greenschist facies related to the formation of the crenulation cleavage, which is locally associated with the crystallization of andalusite in sedimentary rocks (Fig. 2d).

Two principal gold zones exist, the Whale Tail and the IVR zones, which comprise distinct types of ore and structural domains (Fig. 1). The mineralized zones have contrasting styles, geometry, and distribution (Coté-Mantha et al., 2017; Valette et al., 2017, 2018). The Whale Tail zone is mainly characterized by pyrrhotite-rich stratabound replacement-style ore zones with 'silica flooding' and veining developed along BIF, chert, and lithological contacts with mafic-ultramafic rocks in open fold hinge zones (Fig. 2e). Gold is mostly present as inclusions in arsenopyrite or at the contact between arsenopyrite and

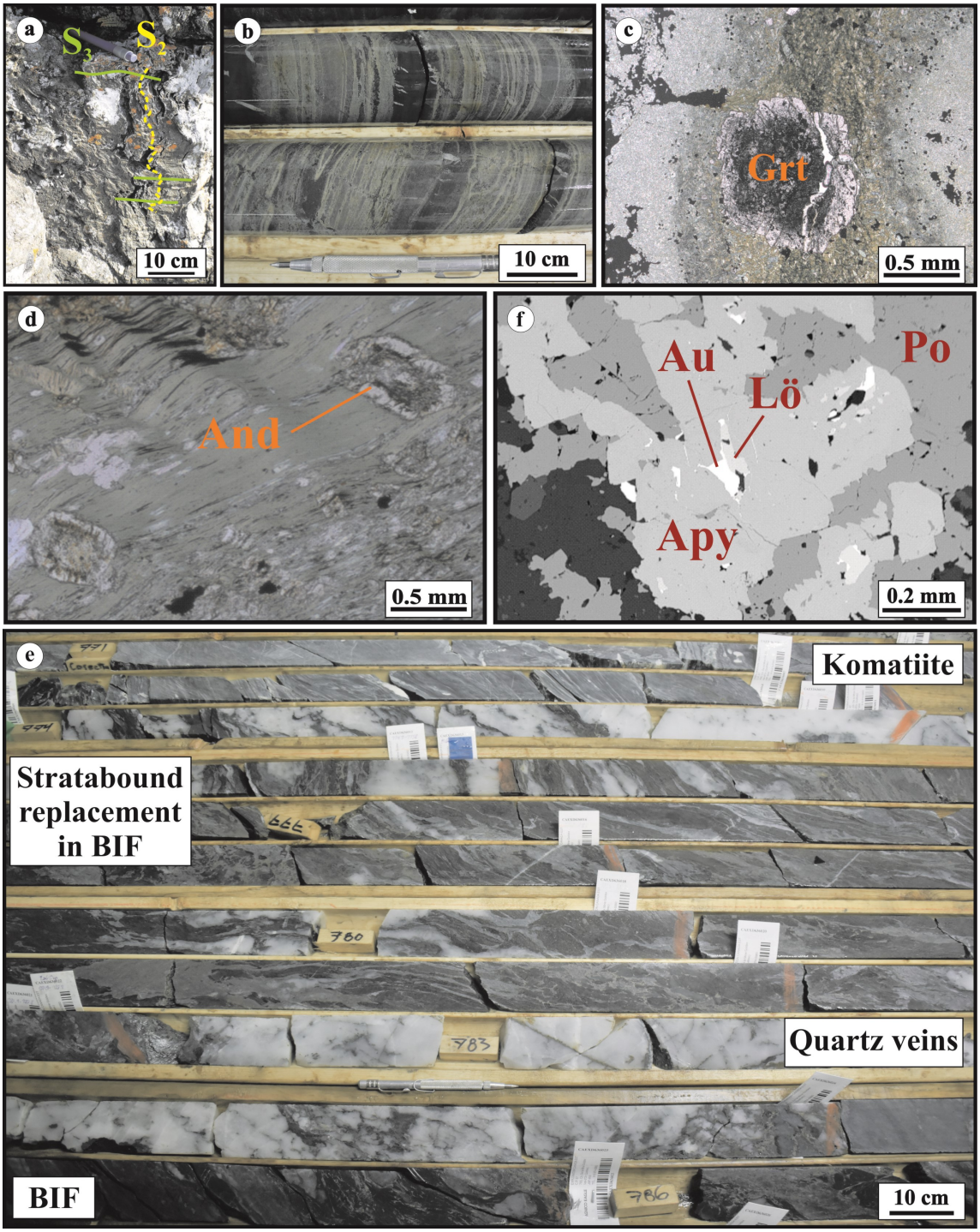

Figure 2. Photographs of deformed, mineralized, and hydrothermally altered rocks and veins of the Whale Tail and IVR zones, Amaruq area. a) S_2 schistosity affected by subhorizontal S_3 crenulation cleavage, IVR zone. b) Typical banding of silicate-facies iron formation composed of alternating layers of chert-grunerite (+/- magnetite) and stilpnomelane-chlorite (+/-garnet), drillhole AMQ18-1845A, IVR zone. c) Syn-D_2 garnet porphyroblast in alternating layers of biotite-chlorite(±gersdorffite) and amphibole-chert in banded iron formation, drillhole AMQ17-1187, Whale Tail zone. d) Syn-D_3 andalusite porphyroblasts oriented parallel to the S_3 crenulation cleavage and superimposed onto the S_2 schistosity in greywacke, IVR zone. e) Stratabound, replacement-type, disseminated pyrrhotite-arsenopyrite, mineralized zones in iron formation, cut by quartz veins at the contact between komatiite and banded iron formation layers, drillhole AMQ18-1834, Whale Tail zone. f) Typical metamorphic texture between retrograded arsenopyrite, relict of löllingite, and free gold in high-grade ore zones, drillhole AMQ16-592, IVR zone. Abbreviations: And = andalusite; Apy = arsenopyrite; Grt = garnet; Lö = löllingite; Po = pyrrhotite.

löllingite crystals (Fig. 2f). The latter texture (cf. Tomkins and Mavrogenes, 2001) suggests that gold was introduced before or during peak metamorphism, and was exsolved from löllingite during retrograde metamorphism (Mercier-Langevin et al., 2018).

In the IVR zone, gold is mainly associated with several sets of laminated and sulphide-poor quartz±carbonate veins preferentially developed in the hinge of a shallow-plunging fold affecting the volcano-sedimentary sequence (Fig. 1). The main auriferous veins, with free and native gold, have been recrystallized and deformed, and are interpreted as contemporaneous with early to syn-D_2 deformation. Both the orebodies associated with Algoma-type BIF and the main auriferous quartz veins are characterized by metamorphosed calcic and potassic alterations halos, and shallowly east-plunging ore shoots, which correspond to the orientation of the regional fold axis or σ2.

Future work

During the 2018 field season, several samples were selected for U-Pb isotope dilution-thermal ionization mass spectrometry (ID-TIMS) and/or sensitive high-resolution ion microprobe (SHRIMP) geochronology of zircon and titanite in an attempt to date the mafic (-ultramafic) volcanic rocks of the Rumble assemblage hosting the Amaruq deposit. The Rumble assemblage is regionally poorly understood and geochemical characterization of the host rocks coupled with detailed petrographic descriptions will help refine the stratigraphy at Amaruq and elsewhere in the Woodburn Lake group.

An $^{40}Ar/^{39}Ar$ amphibole and muscovite geochronology study has also been undertaken to date the metamorphic and hydrothermal events affecting the ore and their host rocks. These results will allow a better understanding of the age and thermal history of the Amaruq volcano-sedimentary sequence and provide necessary data for regional correlation of the stratigraphy and tectono-metamorphic events. Preliminary Re-Os geochronology results indicate that the arsenopyrite associated with the gold mineralization has a complex history that is perhaps over four hundred million years long, and as old as Archean (Mercier-Langevin et al., 2018). Geochemical characterization of the alteration zones coupled with scanning electron microscope (SEM) and laser ablation-inductively coupled plasma mass spectrometry (ICP-MS) analyses are planned and aim to constrain the mineralogical and chemical composition of the ores and ore-forming conditions.

Documentation of the Amaruq deposit geology, mineralogy, and geochemistry will help establish the relative timing of the hydrothermal, structural, and metamorphic events of the area and define the key controls on the formation of the deposit, and could provide better constraints on the potential metal sources and processes leading to gold concentration. Combination of U-Pb and $^{40}Ar/^{39}Ar$ data with ongoing Re-Os geochronology will significantly enhance the understanding of the timing of gold mineralization during the tectono-metamorphic history of the Rae domain. Banded iron formation-hosted gold deposits are usually sparse and isolated, but this part of Nunavut, and especially the Amaruq area, provides one of the best field research laboratories to understand their formation and formulate more robust exploration models in the Churchill Province and other Archean and Paleoproterozoic terranes.

Acknowledgments

This report is a contribution to NRCan's Targeted Geoscience Initiative Program (TGI). Support for this study was provided through the TGI Gold Project's *'Activity G-2.4: Lithotectonic controls on Paleoproterozoic gold distribution in the Archean rocks of the Amaruq area, Nunavut'*.

Manon Valette is a Ph.D. candidate at Université du Québec à Montréal. This activity is conducted in close collaboration with the Chaire de Recherche Industrielle CRSNG-Agnico Eagle - thème Minéraux indicateurs pour les gîtes d'or orogéniques led by G. Beaudoin (Université Laval), I. McMartin (Geological Survey of Canada), V. De Bronac De Vazelhes (Université Laval), N. Boulianne-Verschelden (Université Laval), and Alexandre Mendizabal (Université Laval). Agnico Eagle Mines Ltd. is most gratefully acknowledged for the logistical and scientific support, and for access to their property, drill core, and data. This report benefited from the review of Beth McClenaghan, Suzanne Paradis and Neil Rogers.

References

Agnico Eagle Mines Ltd., 2018. Technical Report on the Mineral Resources and Mineral Reserves at Meadowbank Gold Complex including the Amaruq Satellite Mine Development, Nunavut, Canada as at December 31, 2017; Agnico Eagle Mines Ltd., Toronto, Ontario, 331 p. <https://s21.q4cdn.com/374334112/files/doc_downloads/operations/meadowbank/Meadowbank-Technical-Report-Feb-14-2018-Final-poasted-on-Sedar.pdf> [accessed December 23, 2018]

Côté-Mantha, O., Gosselin, G., Vaillancourt, D., and Blackburn, A., 2015. Amaruq: A new gold discovery in Nunavut, Canada; *in* Extended Abstracts; NewGenGold 2015 meeting, Perth, Australia, November 17–18, 2015, p. 41–56.

Côté-Mantha, O., Gosselin, G., Vaillancourt, D., and Blackburn, A., 2017. The Amaruq deposits – building a customized toolset and using a flexible geomodel: optimization from discovery to mine development; *in* Proceedings of Exploration 17, (ed.) V. Tschirhart and M.D. Thomas; Sixth Decennial International Conference on Mineral Exploration, p. 553–567.

Hrabi, R.B., Barclay, W.A., Fleming, D., and Alexander, R.B., 2003. Structural evolution of the Woodburn Lake group in the area of the Meadowbank gold deposit, Nunavut; Geological Survey of Canada, Current Research 2003-C27, 12 p.

Janvier, V., 2016. Géologie du gisement d'or Meadowbank encaissé dans des formations de fer rubanées, Nunavut,

Canada; Ph.D. thesis, Institut National de Recherche Scientifique – Centre Eau Terre Environnement (INRS-ETE), Québec, Quebec, 472 p.

Janvier, V., Castonguay, S., Mercier-Langevin, P., Dubé, B., Malo, M., McNicoll, V.J., Creaser, R.A., de Chavigny, B., and Pehrsson, S.J., 2015. Geology of the banded iron formation-hosted Meadowbank gold deposit, Churchill Province, Nunavut; *in* Targeted Geoscience Initiative 4: Contributions to the Understanding of Precambrian Lode Gold Deposits and Implications for Exploration, (ed.) B. Dubé and P. Mercier-Langevin; Geological Survey of Canada, Open File 7852, p. 255–269.

Jefferson, C.W., White, J.C., Young, G.M., Patterson, J., Tschirhart, V.L., Pehrsson, S.J., Calhoun, L., Rainbird, R.H., Peterson, T.D., Davis, W.J., Tella, S., Chorlton, L.B., Scott, J.M.J., Percival, J.A., Morris, W.A., Keating, P., Anand, A., Shelat, Y., and MacIsaac, D., 2015. Outcrop and remote predictive geology of the Amer Belt and basement beside and beneath the northeast Thelon Basin, in parts of NTS 66-A, B, C, F, G and H, Kivalliq Region, Nunavut; Geological Survey of Canada, Open File 7242, 1 sheet.

Lawley, C.J.M., Creaser, R.A., Jackson, S.E., Yang, Z., Davis, B.J., Pehrsson, S.J., Dubé, B., Mercier-Langevin, P., and Vaillancourt, D., 2015. Unravelling the Western Churchill Province Paleoproterozoic gold metallotect: constraints from Re-Os arsenopyrite and U-Pb xenotime geochronology and LA-ICP-MS arsenopyrite trace element chemistry at the BIF-hosted Meliadine Gold District, Nunavut, Canada; Economic Geology, v. 110, p. 1425–1454.

Mercier-Langevin, P., Rogers, N., Dubé, B., Castonguay, S., McNicoll, V.J., Lawley, C.J.M., Bleeker, W., Bellefleur, G., Chapman, J.B., Pinet, N., Jackson, S.E., Davis, W.J., Bécu, V., Peter, J.M., Paradis, S., Potter, E.G., Bjerkelund, C., Villeneuve, M.E., and Evans, R., 2017. Targeted Geoscience Initiative: 2016 Report of Activities – An Overview; *in* Targeted Geoscience Initiative – 2016 Report of Activities, (ed.) N. Rogers; Geological Survey of Canada, Open File 8199, p. 7–16.

Mercier-Langevin, P., Valette, M., De Souza, S., Creaser, R.A., McNicoll, V.J., Grondin-LeBlanc, P., St.Pierre, B., Lauzon, M.-C., Malo, M., Côté-Mantha, O., and Simard, M., 2018. Lithologic controls on Paleoproterozoic BIF-hosted/ associated gold: Overview of Re-Os geochronology and Pb isotopes preliminary results; *in* Targeted Geoscience Initiative: 2017 Report of Activities, Volume 1, (ed.) N. Rogers; Geological Survey of Canada, Open File 8358, p. 147–152.

Pehrsson, S.J., Berman, R.G., and Davis, W.J., 2013. Paleoproterozoic orogenesis during Nuna aggregation: A case study of reworking of the Rae craton, Woodburn Lake, Nunavut; Precambrian Research, v. 232, p. 167–188.

Tomkins, A.G. and Mavrogenes, J.A., 2001. Redistribution of gold within arsenopyrite and löllingite during pro- and retrograde metamorphism: Application to timing of mineralization; Economic Geology, v. 96, p. 525–534.

Valette, M., De Souza, S., Mercier-Langevin, P., Côté-Mantha, O., Simard, M., McNicoll, V.J, and Barbe, P., 2017. Geology of the 4.2 Moz Au Amaruq project, Nunavut; *in* Proceedings of the 14th Biennial Society for Geology Applied to Mineral Deposits (SGA) Meeting, Québec, Quebec, p. 199–202.

Valette, M., De Souza, S., Mercier-Langevin, P., McNicoll, V.J., Grondin-LeBlanc, P., Côté-Mantha, O., Simard, M., and Malo, M., 2018. Lithological, hydrothermal, structural and metamorphic controls on the style, geometry and distribution of the auriferous zones at Amaruq, Churchill Province, Nunavut; *in* Targeted Geoscience Initiative: 2017 Report of Activities, Volume 1, (ed.) N. Rogers; Geological Survey of Canada, Open File 8358, p. 153–156.

Macroscopic control on Carlin-type gold mineralization in north-central Yukon

N. Pinet[1] and P.J. Sack[2]

[1]*Geological Survey of Canada, 490 rue de la Couronne, Québec, Quebec G1K 9A9*
[2]*Yukon Geological Survey, 91807 Alaska Hwy, Whitehorse, Yukon Y1A 5B7*

Abstract

This open file summarizes observations from diamond drillhole logging on a section through the Sunrise prospect, in north-central Yukon, and to a lesser extent the Osiris prospect. Carlin-type mineralization is hosted in a lime-mudstone unit (Osiris limestone, Neoproterozoic Gametrail Formation) bounded on both sides by a non-calcareous mudstone unit (Osiris Mudstone, Nadaleen Formation), which is interpreted to have low porosity and permeability. This geometry provides first-order control on mineralized zones that are grossly concordant with bedding. Discontinuous rudstone and floatstone intervals in the Gametrail Formation also played an important role in focussing mineralizing fluids and influenced the location, geometry, and characteristics of orebodies. Clast-supported rudstone intervals (flat pebble conglomerate) deposited through short-transport gliding acted as impermeable barriers, whereas matrix supported floatstone and coarse grainstone intervals, deposited through debris flows, preferentially channelled fluids. Variation of the pre-mineralization fracture permeability, due to bed thickness and lithology or specific tectonic features (e.g. cataclastic zone, fold hinge zone), also influenced the location of the mineralization.

Introduction

Carlin-type gold deposits are a major source of gold and significant exploration targets because of the gold endowment of this deposit style in southwest United States (Muntean, 2018). The vast majority of production and knowledge of Carlin-style gold deposits comes from Nevada, where greater than 147 Moz of Au has been produced from these deposits (Berger et al., 2014; Muntean, 2018; Muntean and Cline, 2018). In Nevada, mineralizing fluids are often described as 'passive' or 'opportunistic', because the fluids are interpreted to have exploited a variety of permeable pathways (Cline et al., 2005). The opportunistic nature of the fluids is mainly due to the relatively shallow depth (a few kilometres) of mineralization and low regional differential stress during mineralization, which was coeval with minor extension but succeeded the main pre-Tertiary shortening and preceded the main period of basin-and-range extension (Cline et al., 2005). The high structural level of Carlin-type deposits results in greatly variable ore shapes at the deposit scale and difficulty in predicting mineralized zones at the exploration stage. In Nevada, parameters that influenced the location of the orebodies include a) the location below low-angle faults (e.g. the Roberts Mountain Thrust) that could have formed a regional aquitard to any upward fluid flow (Cline et al., 2005); b) favourable lithological units such as silty limestone and matrix-supported debris flow deposits (Cook, 2015); c) zones characterized by a network of either pre-Tertiary or Tertiary, shallowly or steeply dipping faults and fractures (Rhys et al., 2015); and d) the proximity of premineralization magmatic rocks that acted as rigid bodies during post-intrusion deformation, favouring heterogeneous strain and an increase in fault and fracture density near these bodies (Heitt et al., 2003).

In north-central Yukon, the recent discovery of mineralized zones with distinct Carlin-type gold deposit characteristics makes the Nadaleen trend one of the rare examples of true Carlin-type gold mineralization that has been identified outside of Nevada (Tucker et al., 2012; Tucker, 2015). Previous studies indicate that mineralized zones hosted by Neoproterozoic rocks are grossly concordant with lithological units (Tucker et al., 2012; Tucker, 2015; Pinet et al., 2017, 2018; Coulter et al., 2018; Ristorcelli et al., 2018). However, in detail, orebody geometries are complex and the correlation between drillholes located a few tens of metres apart can be problematic. A reappraisal of the detailed geometry and mineralization characteristics of one representative section through each of the Osiris and Sunrise prospects and two perpendicular sections through the Conrad prospect was the main objective of core logging done during the summer 2018. This open file summarizes observations from the Sunrise and, to a lesser extent, the Osiris prospects.

Geological setting

In northern Canada, the outer zone of the Cordillera (foreland) forms an arcuate mountain belt of deformed mainly Neoproterozoic to Carboniferous sedimentary rocks. Regional-scale folds and faults change in strike from north to north-northwest in the Northwest Territories, to west to west-northwest in north-central Yukon, where the Rackla belt is located.

The Rackla belt is a 5 to 15 km wide fold-and-fault belt

Corresponding author: Nicolas Pinet (nicolas.pinet@canada.ca)

Pinet, N. and Sack, P.J., 2019. Macroscopic control on Carlin-type gold mineralization in north-central Yukon; *in* Targeted Geoscience Initiative: 2018 report of activities, (ed.) N. Rogers; Geological Survey of Canada, Open File 8549, p. 89–103. https://doi.org/10.4095/313644

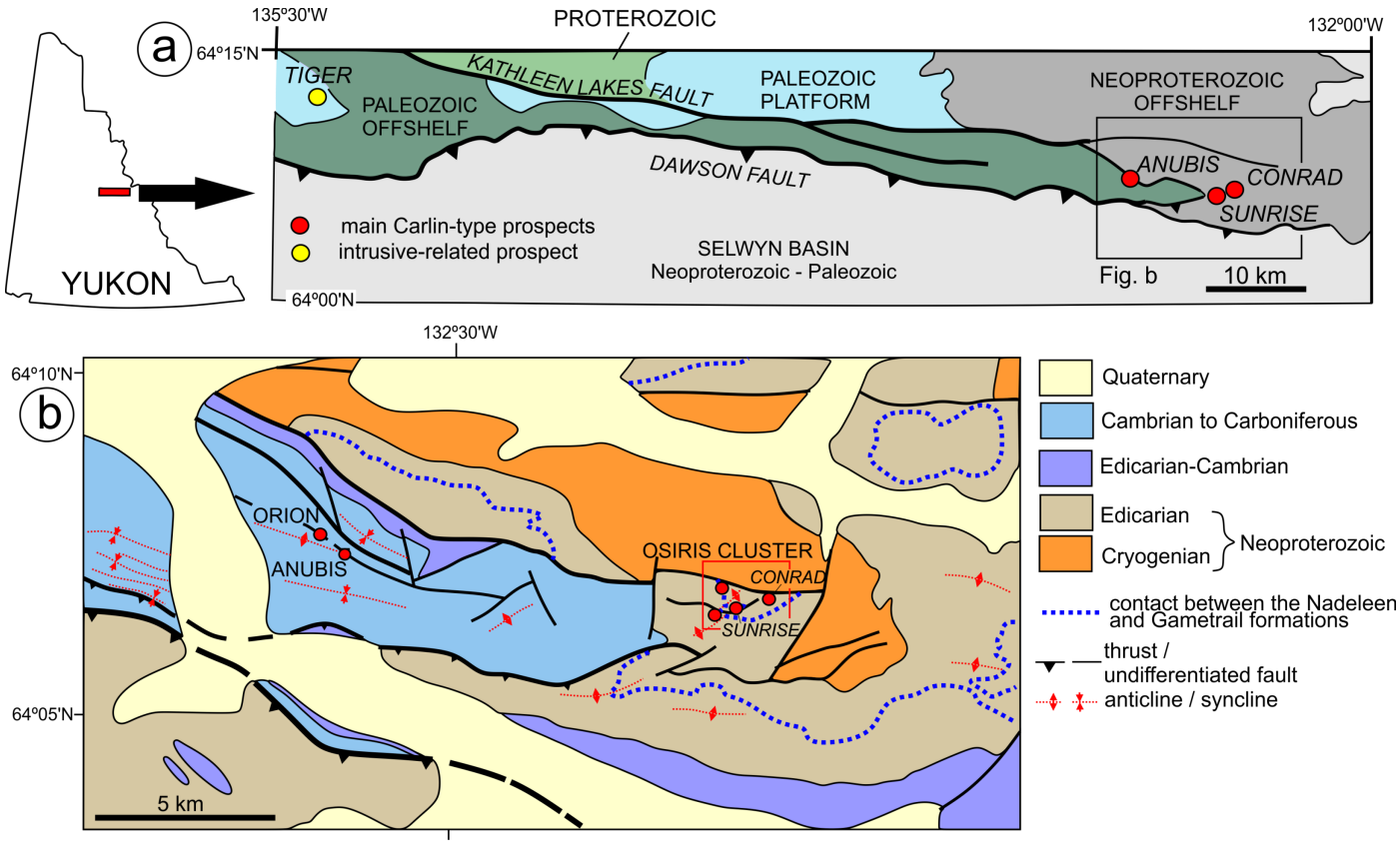

Figure 1. a) Geological setting of the Rackla belt in east-central Yukon (*from* Pinet et al., 2017; *modified from* Colpron et al., 2013). b) Geological map of the eastern Rackla belt (*from* Pinet et al., 2017; *simplified from* Moynihan, 2016). The Osiris cluster includes the Ibis, Osiris, Sunrise and Conrad prospects.

bounded to the north by the Kathleen Lake Fault and to the south by the Dawson Fault (Fig. 1). The Rackla belt roughly coincides with the location of 'offshelf' platform-basin facies boundaries during the Neoproterozoic and part of the Paleozoic (Fig. 1a). This spatial coincidence suggests that depositional patterns were controlled by a major, long-lived, probably deep-seated, structure that may have been reactivated during mountain building (Abbott, 1997).

In the eastern Rackla belt, where the Carlin-type gold prospects are located, the Dawson Fault splits into several splays (Moynihan, 2016; Fig. 1). In this area, the sedimentary succession consists of a relatively diverse assemblage of Neoproterozoic (Windermere Supergroup and Hyland Group) and overlying Cambrian to Carboniferous strata. Igneous rocks are scarce and limited to a poorly exposed Ordovician gabbroic pluton (Fig. 2) and a few intermediate to mafic Late Cretaceous dykes (Tucker, 2015). The succession is complexly faulted and folded and several phases of deformation are documented (Moynihan, 2013, 2016; Steiner et al., 2018). Major faults are steeply dipping with a significant strike-slip component.

Gold prospects in the eastern Rackla belt forms the Nadaleen trend. They are mainly hosted by Neoproterozoic limestone (with a few mineralized intervals in siltstone) belonging to the Nadaleen and Gametrail formations (Windermere Supergroup) and in mid-Paleozoic calcareous siltstone (Moynihan, 2016). The age of mineralization is poorly constrained to only a older age limit of less than 74.4 ± 1.0 Ma provided by a Late Cretaceous dyke that is locally mineralized (Tucker, 2015). All prospects exhibit characteristics consistent with Carlin-type mineralization including i) the 'invisible' nature of the gold; ii) the association of gold with pathfinder elements such as Tl, As, Hg and Sb and the general association of realgar and orpiment with gold at the macroscopic scale; iii) the low base metal and Ag content; and iv) the partial to complete decalcification of mineralized intervals.

Sunrise prospect

The Sunrise gold prospect is one of the Neoproterozoic-hosted prospects in the Osiris cluster, eastern Rackla belt. It is in the hanging wall of the Osiris fault, on the east-striking flank of an anticline with complex geometry (Fig. 2, 3; Steiner et al., 2018). The Osiris and Ibis gold prospects are hosted in the same sedimentary unit (Gametrail Formation). The Osiris prospect is located in the north-south striking flank of the same anticline and the Ibis prospect in the hanging wall of the Osiris fault (Fig. 2). Farther to the east, the Conrad gold prospect is mainly hosted in an older limestone unit (lower Nadaleen Formation; Tucker, 2015; Moynihan et al., in press).

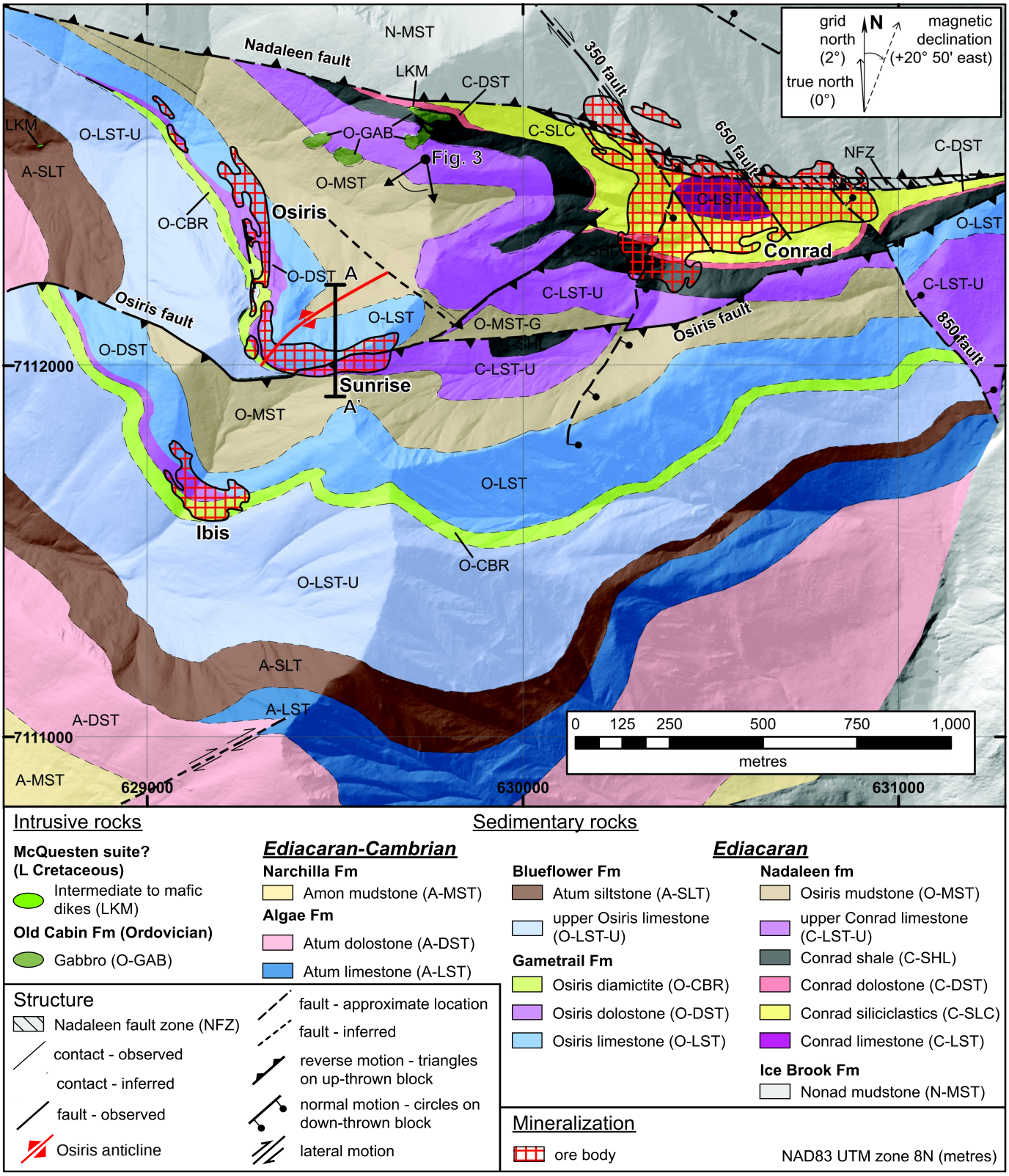

Figure 2. Geological map of the Osiris cluster with Ibis, Osiris, Sunrise, and Conrad orebodies projected to surface. Cross section 629500E shown as bold black line (A-A'; Fig. 4). Orebodies are defined in ATAC Resources Ltd. July 2018 resource estimate (open pit resource cut-off of 1.3 g/t Au and underground resources of 2.6 g/t Au; Ristorcelli et al., 2018). Note the location of Figure 3. Geology *modified from* A. Steiner (pers. comm., 2018) and Steiner et al. (2018).

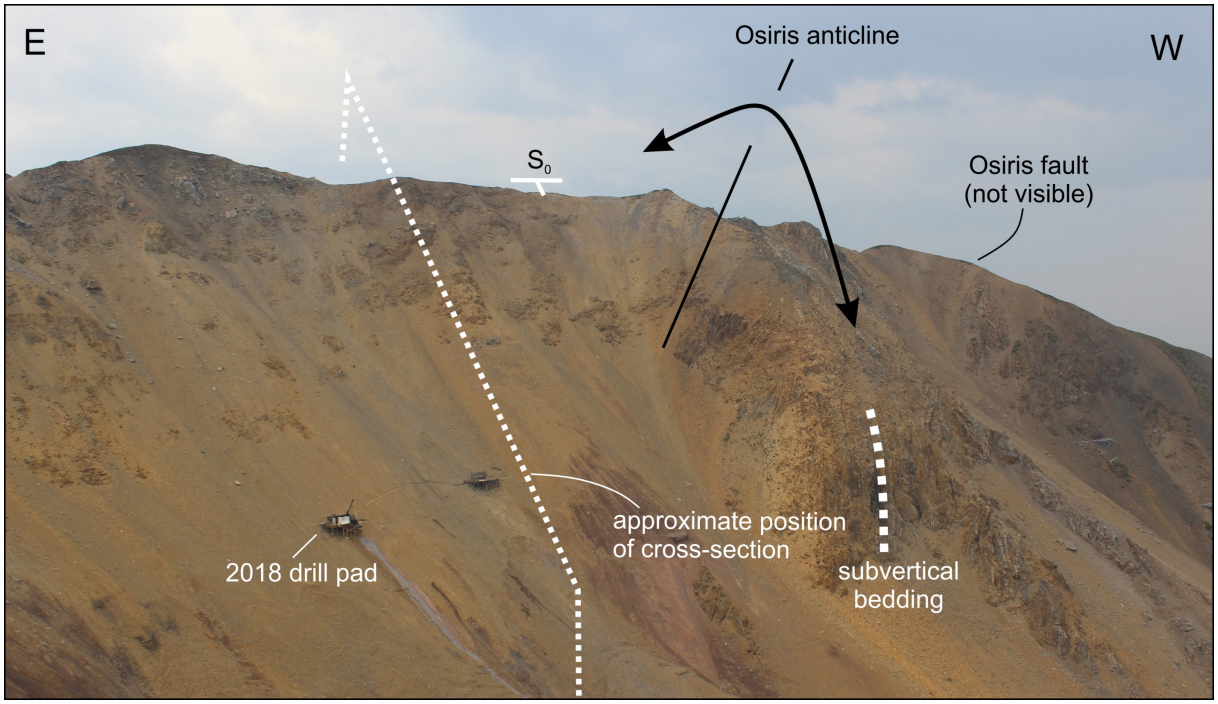

Figure 3. Panoramic view toward the South of the Sunrise area. The location where the photograph was taken is labelled on Figure 2.

On the studied cross-section (629500E; Fig. 2, 4), the sedimentary succession is structurally repeated by the steeply (75˚) dipping Osiris fault. This fault has a mixed dextral-reverse sense of motion as attested by the apparent offset of rock units (Fig. 2) and kinematic indicators (Fig. 4b). On the section, three main sedimentary units are recognized. The oldest unit is limestone-dominated and is locally known as the upper Conrad limestone. It is composed of alternating centimetre to decimetre thick layers of medium to dark grey lime-mudstone and decimetre-thick packstone interbeds. The upper Conrad limestone also includes a few poorly calcareous mudstone intervals and polymictic matrix-supported floatstones with millimetre to decimetre carbonate and siltstone clasts in a dark grey to dark green variably calcareous matrix. Clasts are generally subrounded and locally show evidence of soft-sediment deformation. A finely (millimetre to few centimentre) laminated vari-coloured (brown, grey, green, purple) non-calcareous mudstone and siltstone unit (Osiris mudstone) stratigraphically overlies the upper Conrad limestone. On section 629500E (Fig. 4), the Osiris mudstone is found above the upper Conrad limestone and below the Osiris limestone. The Osiris mudstone is also recognizable in a 10 m thick fault-bounded interval (Fig. 4, 5), except in drillhole OS-13-214 where it is missing, likely due to fault truncation (Fig. 4). This mudstone unit contains up to 3 volume % fine-grained pyrite and has textures typical of soft-sediment deformation. Both the upper Conrad limestone and Osiris mudstone are correlated with the Nadaleen Formation (Moynihan, 2016; Moynihan et al., in press). On the studied cross-section, the unit that hosts the orebodies corresponds to a 130 m thick limestone interval, locally known as the Osiris limestone, and has been correlated with the Gametrail Formation of the Windermere Supergroup (Aitken, 1989; Moynihan, 2016). This unit is a medium grey lime-mudstone with over 80 volume % micrite matrix (Fig. 6). Beds are generally 1 to 80 mm in thickness (with a few metre thick beds), and exhibit planar (Fig. 6a) or wavy contacts (Fig. 6b). Some intervals show only weak reaction to HCl, indicating partial fabric-retentive dolomitization. Coarse-grained fabric-destructive dolostone with irregular dolomite veins, which are common in the Osiris prospect (Beaton, 2015), are notably absent on section 629500E. The Osiris limestone also includes rudstone and floatstone intervals. Both types of intervals are interpreted as mass transport complexes, but they result from different transport mechanisms that have contrasting effects on porosity/permeability development (Fig. 7; *see below*). The rudstone intervals correspond to decimetre to metre thick clast-supported conglomerate with elongated lime-mudstone fragments centimetre to decimetre in size (flat pebble conglomerate; Myrow et al., 2004). Fragments are variably oriented and exhibit stylolitic and indented relationships (Fig. 6c). Interclast space is filled with lime-mudstone. The rudstone intervals are interpreted to have been formed through short-transport translational sliding (‘gliding’) on a moderate slope, which led to bed disruption and the development of tabular clasts with either angular or subrounded terminations. This interpretation is substantiated by a variety of synsedimentary deformation features (Fig. 6e, f) recording the transition from undisturbed sediments to buckled or partially dismembered beds to fully developed flat pebble conglomerate. The number of rudstone intervals varies between drillholes, suggesting that they pinch-out later-

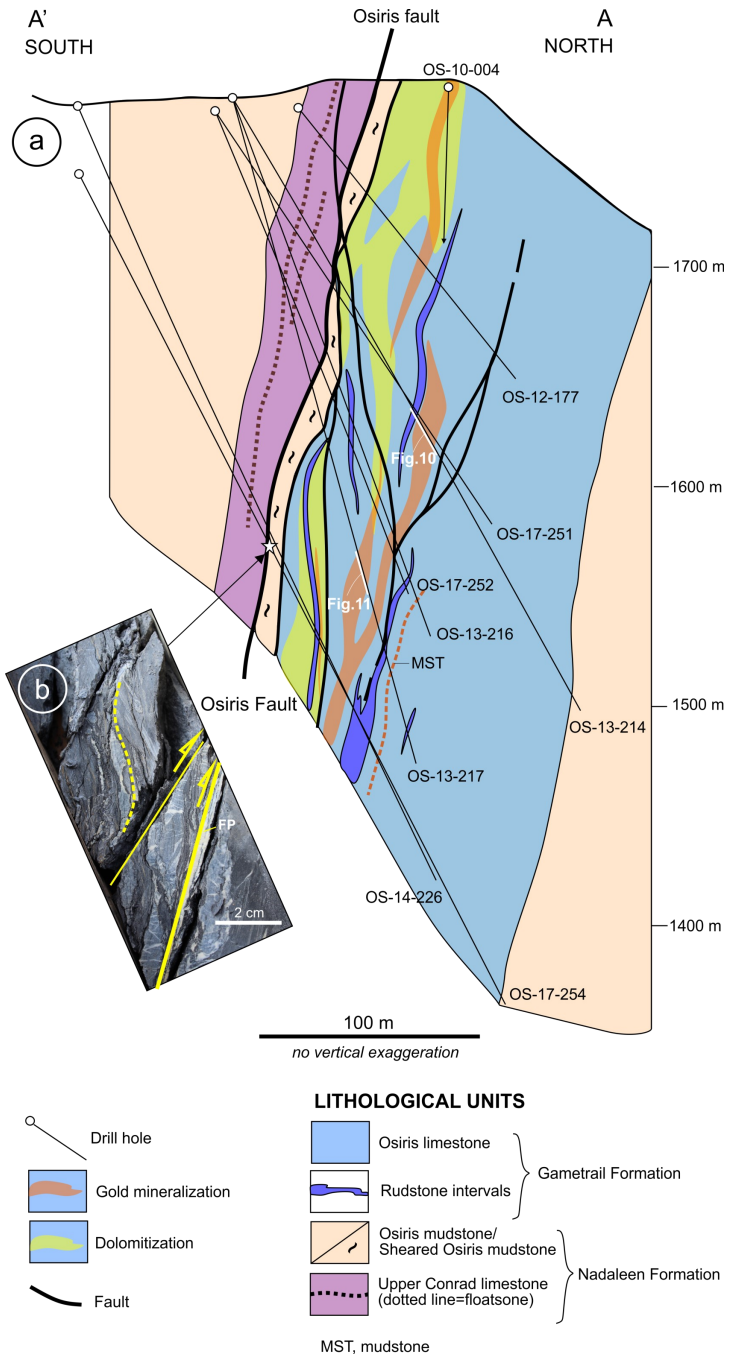

Figure 4. a) Geological section 629500E across the Sunrise prospect, showing the locations of Figures 10 and 11. The depth of the overburden is less than 3 m. The dolomitization envelope is based on core logging and whole-rock magnesium content. Rudstone (i.e. flat pebble conglomerate) envelopes may include more than one interval. Floatstone intervals are not shown due to uncertainty correlating across drillholes. b) Osiris fault in drillhole OS-17-254. Slickenlines on the fault plane indicate oblique dextral-reverse motion (yellow arrows). Note the warping of bedding near shearing planes. Abbreviation: FP – fault plane.

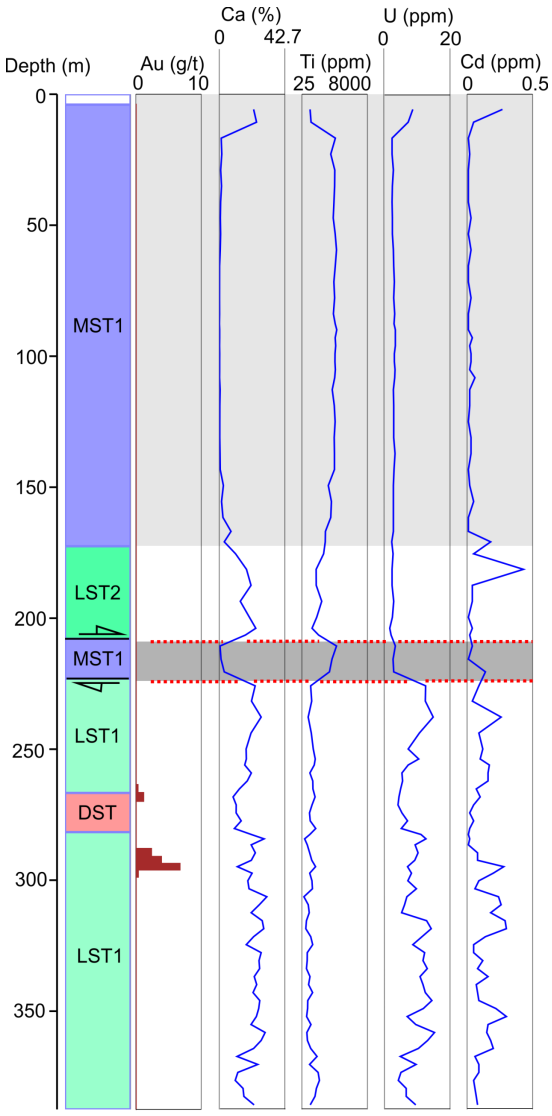

Figure 5. Strip logs with rock units and select elements, drillhole OS-14-226. Grey colours correspond to mudstone intervals. Geochemical analysis *from* ATAC Resources Ltd. (pers. comm., 2018). Note the clear decrease in Ca content and increase in Ti content at the lower and upper contacts of the mudstone unit (MST1) at -208 and 222 m (dotted line). Rock unit boundaries *from* ATAC Resources Ltd. (pers. comm., 2018). Abbreviations: DST – dolostone; LST2 – upper Conrad limestone; LST1 – Osiris limestone; MST1 – Osiris mudstone.

ally. In contrast to the clast-supported rudstone, the floatstone is a poorly sorted polymictic matrix-supported sedimentary breccia with variable clast size and matrix content. Clasts are millimetre to decimetre in size, angular with sharp terminations, and exhibit a chaotic organization. The number and thickness (5–120 cm) of floatstone intervals also varies between drillholes, suggesting that they occur as sheet or channel -shaped bodies. The floatstone intervals are interpreted to have been deposited through debris flows in which the flows were

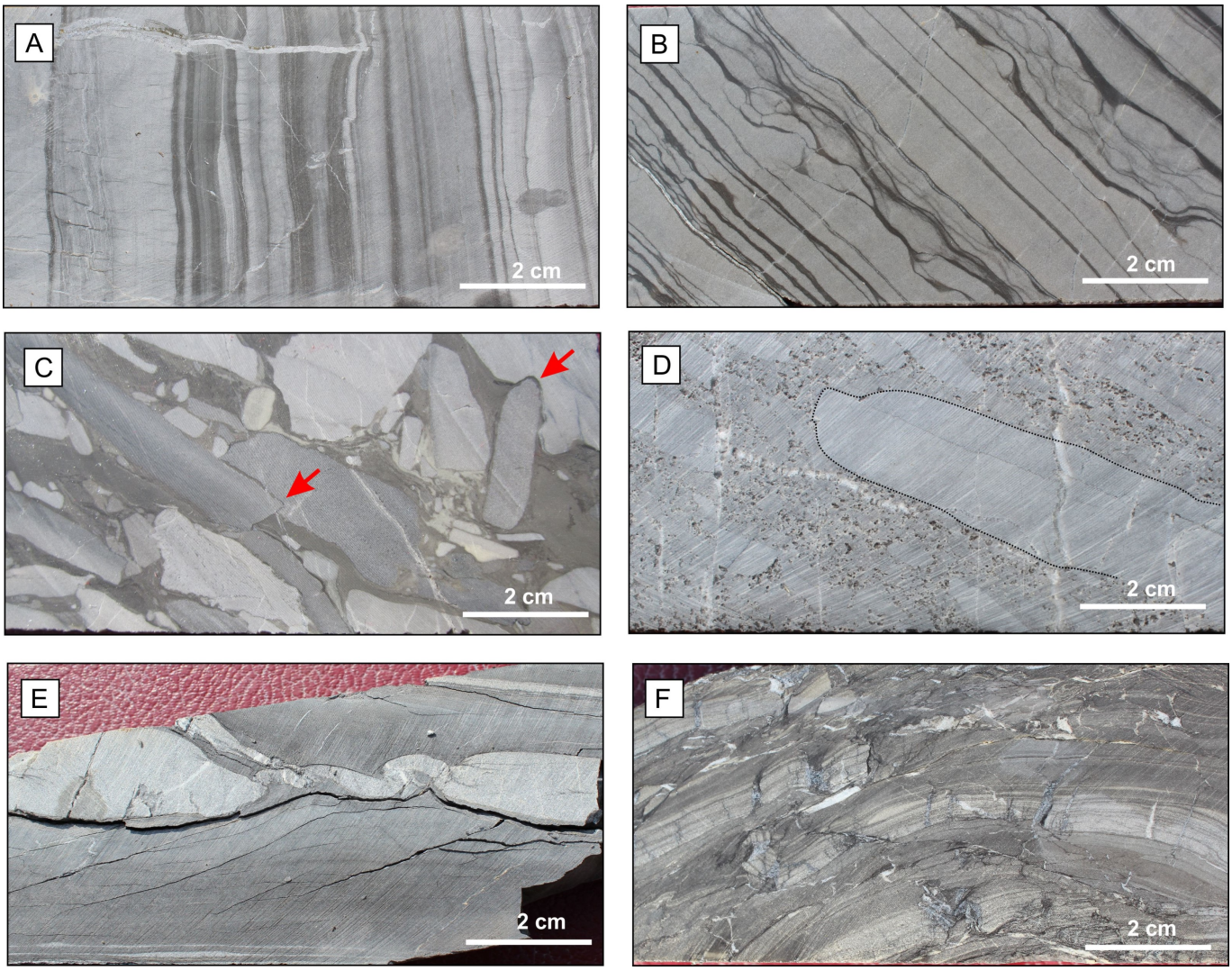

Figure 6. Photographs showing the lithology of the Osiris limestone, Gametrail Formation: a) typical lime-mudstone with planar bedding; b) typical lime-mudstone with wavy bedding; c) clast-supported rudstone characterized by elongate clasts of lime mudstone. Note the indentation contacts between clasts indicated by the red arrow. This type of contact between clasts is associated with a decrease in permeability; d) clast- to matrix-supported rudstone characterized by elongated clasts of lime mudstone (note that the amount of matrix is higher than in the lime mudstone shown in photograph (c)). In this specific case, the matrix is porous, which may be the result of syn-mineralization(?) decalcification; e) and f) initial stages of bed fragmentation.

supported above the sediment-water interface by matrix strength and buoyancy that allowed larger clasts to 'float' in a muddy/sandy matrix. In the Osiris limestone, some of the grainstone beds (Fig. 8) may have formed through the deposition of mixed mud- and sand-sized material at the top or in the distal parts of debris flow deposits.

On the studied cross section, multiple generations of veins showing cross-cutting relationships are documented. These veins are mainly filled with calcite (and dolomite/quartz) and vary significantly in abundance among the lithological units. They represent less than 1% of the rock in the Osiris mudstone and reach a maximum of 10% in the Osiris limestone, close to the faulted contact with mudstone.

Mineralization

On the studied section, orebodies are confined to the Osiris limestone (Fig. 4). In all drillholes, except hole OS-12-177, two main mineralized zones are divided by a barren interval (Fig. 4). These zones are grossly concordant with bedding, are located 35 to 65 m from the Osiris fault, and are hosted by both dolomitized and 'fresh' limestone (Fig. 4). In several cases, clast-supported rudstone (flat pebble conglomerate) are found close (<5 m) to mineralized zones. Contacts of mineralized zones are relatively sharp and gold grades decrease from several grams/tonne to background values in a few metres at most.

Realgar and orpiment (±fluorite) are generally a good visual

GRAVITY-INDUCED DEPOSITS			TRANSPORT MECHANISM	SEDIMENTARY FEATURES
MASS-TRANSPORT COMPLEX	SLIDE	translational (glide)	Failure along a discrete planar shear plane	Essentially undeformed continuous bedding *Sunrise area: rudstone intervals*
		rotational	Failure along a discrete concave-upward shear plane	Deformation concentrated near the base and at the front
	SLUMP		Shear failure with various degree of internal deformation	Plastic deformation particularly at the toe and base: 'pinch and swell' structures, folds, rotational blocks
	DEBRIS FLOW		Shear distributed throughout the sediment mass. Sediments supported above the sediment-water interface by matrix strength and buoyancy which allow larger clasts to 'float' along in a muddy-sandy matrix	Matrix-supported, random fabric, clast variable in size, often polymictic *Sunrise area: floatstone intervals*
TURBIDITY CURRENT	TURBIDITE		Supported by fluid turbulence (newtonian rheology)	Normal size grading, sharp basal contact, gradational upper contact

Figure 7. Classification of gravity-induced deposits. *Modified from* Moscardelli and Wood (2008).

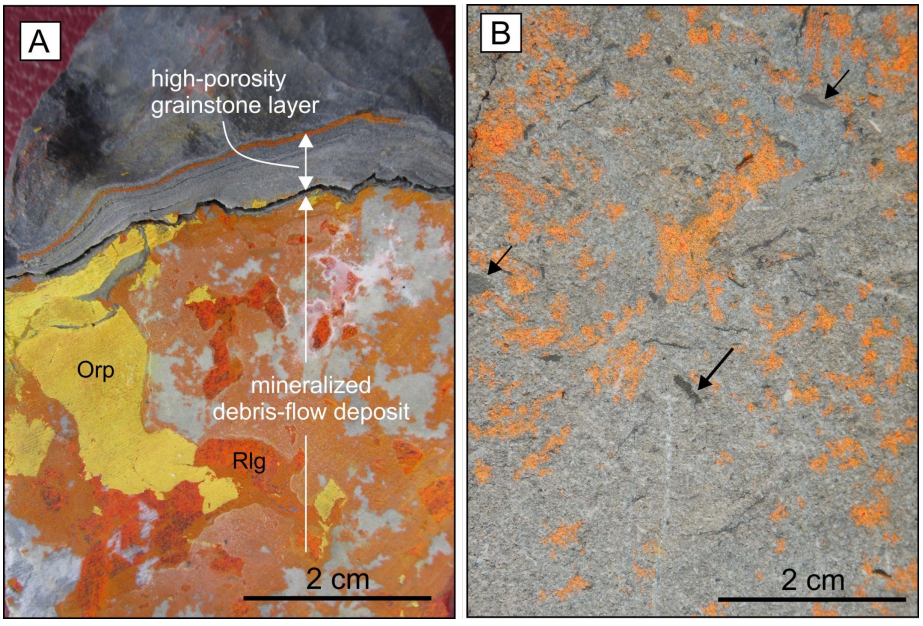

Figure 8. Grainstone beds possibly formed through debris flows. a) Greater than 1 cm thick grainstone layer overlying a floatstone interval. b) Mineralized medium grey grainstone layer with a few millimetre long darker clasts (arrows). Orange colour variations are linked to the amount of realgar.

guide for mineralization in the Sunrise prospect. These minerals are always found in gold mineralized intervals with greater than 1 g/t Au, and, in a few cases, also in intervals with less than 1 g/t Au. Realgar is often found in calcite veins that post-date the main stage of gold mineralization (see below). However, the spatial coincidence of realgar and orpiment with gold mineralized intervals strongly suggest that these minerals formed in the late stage of a single event, not during a distinct hydrothermal pulse. Within the Osiris limestone, mineralized intervals show significant increase in As, Sb, Hg, Tl, S, Ag, Cd, Mn, W and Zn compared to the non-mineralized host rocks.

Bedding is still visible close to, or even within, mineralized intervals. Decalcification (removal of calcite; Teal and Jackson, 2002) is the main alteration type associated with gold mineralization, which is clearly illustrated in the Ca-Au plot for the Osiris limestone (Fig. 9). Within mineralized intervals, decarbonatization (removal of both calcite and dolomite; Teal and Jackson, 2002) is highly variable with some decimetre-scale core segments still reacting with HCl a few centimetres from decarbonatized core segments. Silicification or argillization are much more discrete alteration types and have been only observed locally.

At the macroscopic scale, gold mineralization styles vary significantly, even within the same mineralized interval. In general, realgar is more common and abundant than orpiment. In Figures 10 and 11, seven mineralization styles are distinguished:

1) Selective replacement of beds. This mineralization type is restricted to millimetre-thick beds (Fig. 11b) with a saccharoidal texture (originally packstone/grainstone) alternating with millimetre thick fine grained beds (originally calcareous (?) mudstone). The along-bed continuity of mineralization is difficult to determine from core observation, but in a few cases, mineralization appears confined to a few centimetres to decimetres from a central feeder vein.

2) Mineralized fractures. Mineralization occurs along planes that recorded almost no displacement and no calcite infill. In most cases, fractures are perpendicular to bedding (Fig. 11c), strongly suggesting that they formed as joints, under low deviatoric stresses, before the mineralizing event.

3) Veining. Veins associated with the late stage of mineralization are found within and adjacent to (<10 m) gold mineralized intervals. Late-stage mineralization veins are defined by the presence of realgar (± orpiment) with either calcite or less commonly quartz. The late-stage calcite veins often have centimetre-size calcite crystals and both the calcite and quartz veins can have open-space features. In mineralized intervals, these late-stage mineralization veins may be visually attractive, but they probably represent only a very small part of the gold endowment. These veins frequently form a well organized sets that are either oblique or parallel to bedding (Fig. 10f) or are irregular and anastomosing (Fig. 10e). Minor faults cutting calcite-realgar veins (Fig. 10f) attest to some post-veining deformation. Paragenetic vein sequence varies with realgar both predating and postdating calcite.

4) Mineralized floatstone (debris flow). Mineralization occurs in matrix-supported, polymictic, floatstone with variably oriented angular to subangular clasts (Fig. 11 d, e). In this style, mineralization is usually confined to the matrix and to a few fractures within clasts. The amount of realgar varies significantly at the decimetre-scale and some fragments are almost surrounded by realgar though others are not.

5) Mineralized tectonic breccia. This type of breccia is characterized by calcite vein fragments and boundaries that often show evidence of brittle deformation (Fig. 10d). In several cases, a few finely laminated angular fragments are recognizable, suggesting these intervals correspond to mineralized floatstone that were brecciated post-mineralization.

6) Massive replacement. These decimetre to metre mineralized intervals are characterized by high amounts of realgar and orpiment and an almost total lack of preserved sedimentary features, which makes the original host rocks difficult to recognized. Their boundaries may be either concordant with bedding or highly irregular (Fig. 11f). In a few cases, irregular shapes mimic floatstone clasts, suggesting that these intervals were originally debris flows.

7) Dark grey to black decarbonatized interval. These decimetre to metre thick decarbonatized intervals are visually almost featureless and do not show preserved laminations. They are tentatively interpreted as high-matrix-content debris flow deposits.

Gold grades are highest (typically >10 g/t Au) in mineralization types 4 to 7. If our interpretations are correct, a significant portion of the gold is concentrated in debris flow intervals that have variable matrix content and variable post-mineralization deformation features.

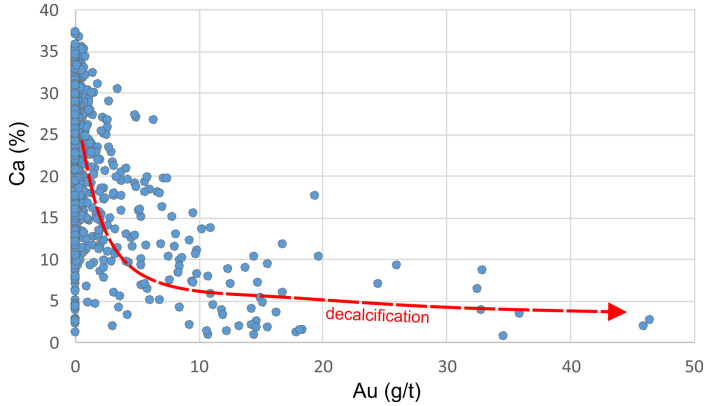

Figure 9. Plot of Ca vs. Au. Note the decrease in Ca content with increasing Au mineralization due to decalcification. Geochemical analysis from ATAC Resources Ltd. (pers. comm., 2018).

Discussion

The location of the orebodies in the Sunrise prospect was controlled by parameters that either favoured or prevented mineralization. The location of the Osiris limestone between two

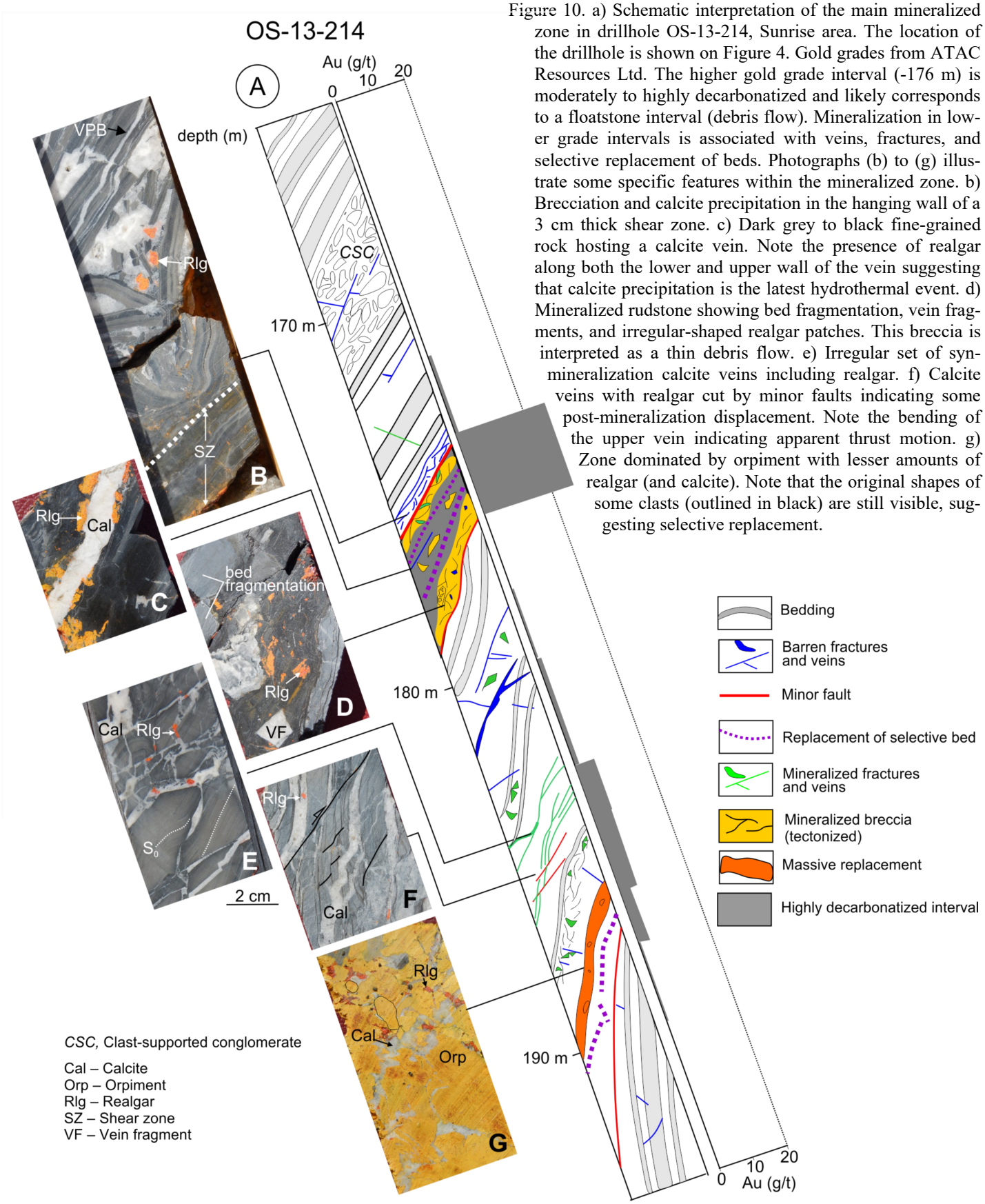

Figure 10. a) Schematic interpretation of the main mineralized zone in drillhole OS-13-214, Sunrise area. The location of the drillhole is shown on Figure 4. Gold grades from ATAC Resources Ltd. The higher gold grade interval (-176 m) is moderately to highly decarbonatized and likely corresponds to a floatstone interval (debris flow). Mineralization in lower grade intervals is associated with veins, fractures, and selective replacement of beds. Photographs (b) to (g) illustrate some specific features within the mineralized zone. b) Brecciation and calcite precipitation in the hanging wall of a 3 cm thick shear zone. c) Dark grey to black fine-grained rock hosting a calcite vein. Note the presence of realgar along both the lower and upper wall of the vein suggesting that calcite precipitation is the latest hydrothermal event. d) Mineralized rudstone showing bed fragmentation, vein fragments, and irregular-shaped realgar patches. This breccia is interpreted as a thin debris flow. e) Irregular set of syn-mineralization calcite veins including realgar. f) Calcite veins with realgar cut by minor faults indicating some post-mineralization displacement. Note the bending of the upper vein indicating apparent thrust motion. g) Zone dominated by orpiment with lesser amounts of realgar (and calcite). Note that the original shapes of some clasts (outlined in black) are still visible, suggesting selective replacement.

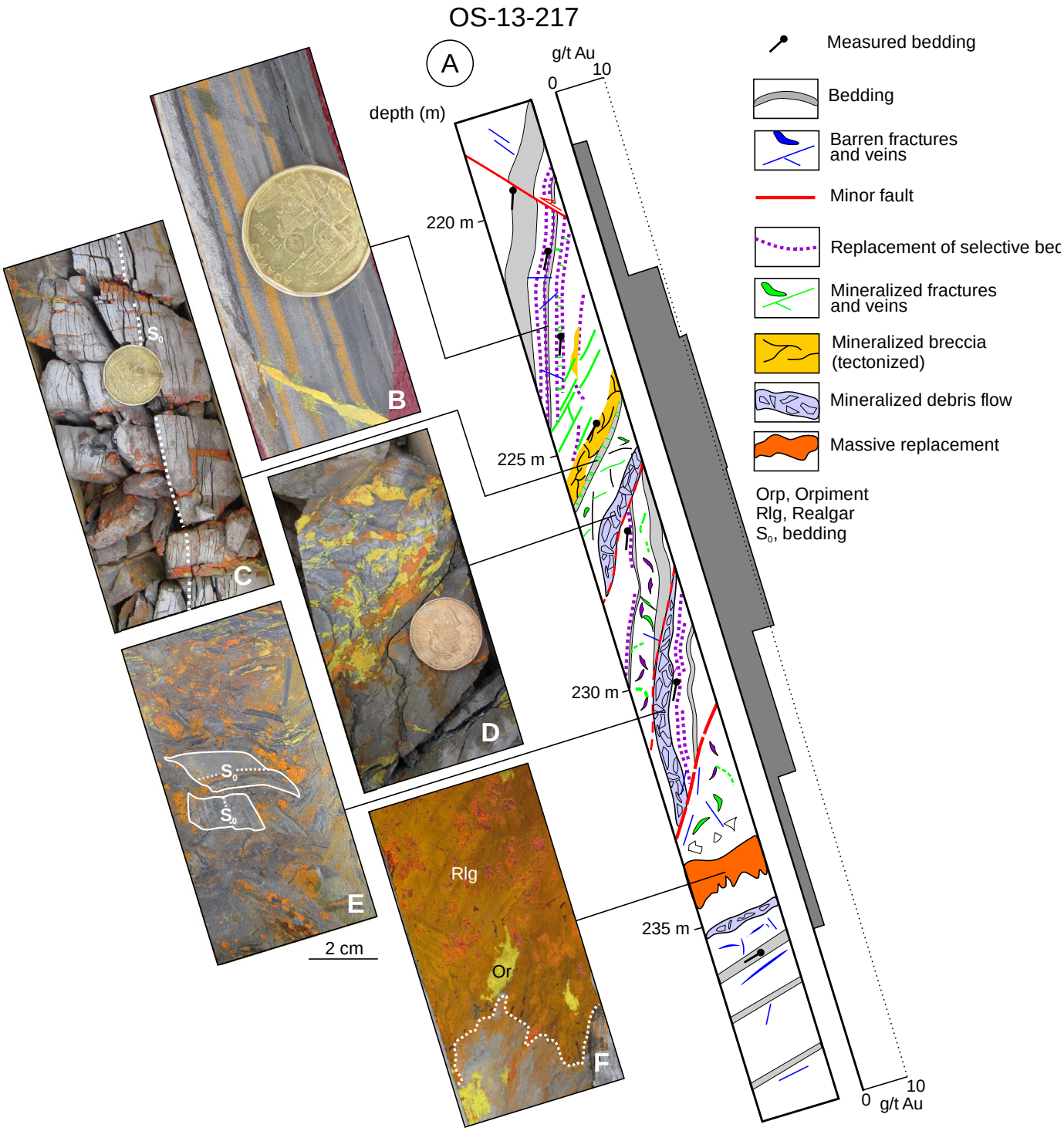

Figure 11. a) Schematic interpretation of the main mineralized zone in drillhole OS-13-217, Sunrise area. The location of the drillhole is shown on Figure 4. Gold grades *from* ATAC Resources Ltd. (pers. comm., 2018). Note that even in intervals with greater than 10 g/t Au, bedding is visible. Mineralization is associated with veins, joints perpendicular to bedding, selective replacement of specific beds, replacement of the matrix in floatstone (debris flows), and massive replacement. b) Selective replacement of millimetre-thick beds. c) Realgar within fractures perpendicular to bedding. These fractures are interpreted as joints formed before the main deformation event. d) Mineralized matrix-supported floatstone (debris flow). e) Mineralized floatstone. Note the angular shape of fragments and the variable orientation of internal bedding (S_0, dotted line). Mineralization occurs only in the matrix and in a few fractures within clasts. f) Massive replacement with realgar and orpiment. Note the very irregular geometry of the lower contact (dotted line).

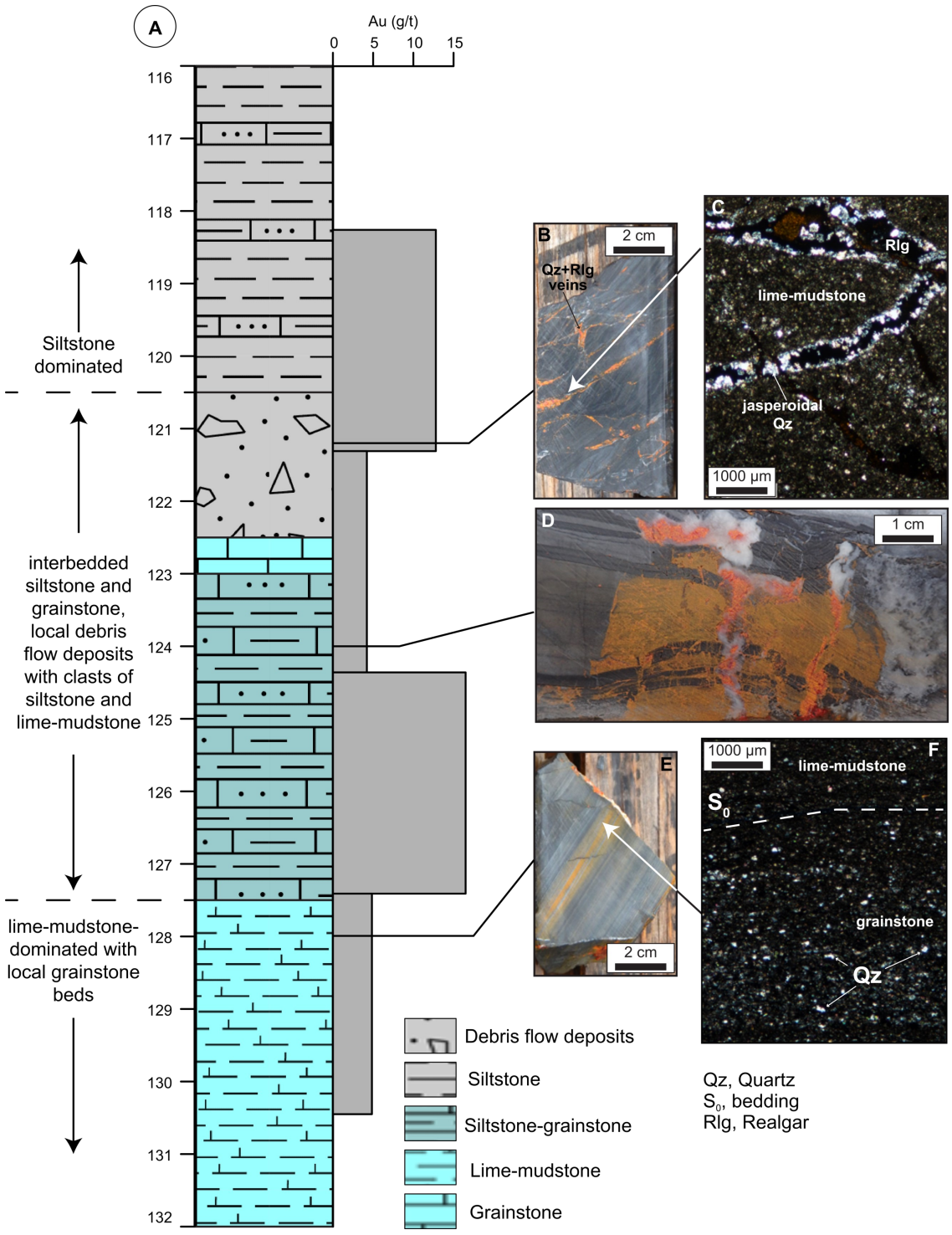

Figure 12. Strip logs of mineralized interval from drillhole OS-17-244. Cross-section 7112475N, Osiris prospect. Gold grades from ATAC Resources Ltd. a) Detail lithology from 116 to 132 m. Depth (m) on left side and assay Au values (g/t) on right. b) Matrix-rich portion of floatstone with realgar + jasperoidal quartz (Qz) ± calcite veins exploiting soft sediment deformation planes; 12.8 g/t Au over 3.05 m, sample from 121.2 m. White box shows thin section 121.2 m location. c) Mineralized realgar and jasperoidal quartz vein cutting lime-mudstone host rock. d) Selective realgar replacement of grainstone beds outwards from feeder calcite + realgar vein. e) Planar laminated lime-mudstone beds with selective realgar replacement along beds that are slightly coarser with more detrital quartz grains; 4.9 g/t Au over 3.04 m, samples from 128.0 m. Images (c) and (e) are cross-polarized light photomicrographs. f) Note the increase in detrital quartz grains towards bottom of photomicrograph that corresponds to an increase in selective realgar replacement.

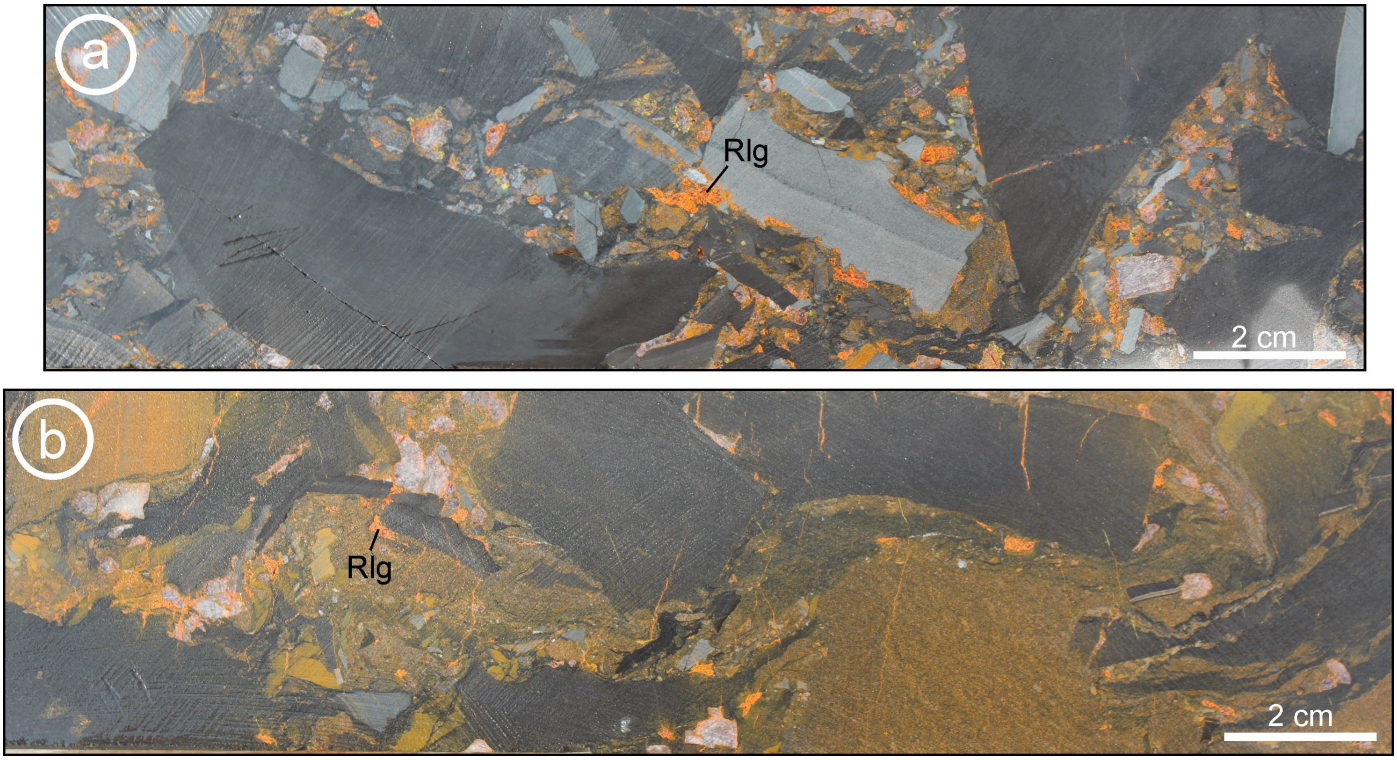

Figure 13. a) and b) Photographs of the mineralized floatstone interval (debris flow) in Osiris drillhole OS17-244 at 218 m depth. Note that realgar (Rlg) is located primarily in the matrix and in a few fractures within clasts. Orange colour variations are linked to the amount of realgar.

low-permeability mudstone intervals is a first-order control on fluid flow. However, other parameters influenced the location and characteristics of mineralized intervals at the centimetre to tens of metre scale (Fig. 12–14).

Among the sedimentary units, floatstone intervals appear to be the most favourable host-rocks for gold mineralization in the Sunrise prospect (Fig. 14e). In some cases, the porosity and permeability of the debris flow deposits was enhanced by the rheological contrast between floatstone and well-bedded lime-mudstone that favoured shearing along the lithological contacts and fracture development. The relationship between floatstone units and mineralized intervals is also documented in the Osiris prospect (also hosted by the Osiris limestone; Fig. 2) at metre (Fig. 12) to decimetre (Fig. 13) scales. In several Carlin-type deposits of Nevada, high-grade gold mineralization is preferentially hosted in floatstone intervals (debris flow deposits; Creel and Bradley, 2013; Cook, 2015) reinforcing the idea that they were more porous and/or permeable than surrounding slope or base of slope background sedimentary rocks. Carbonate gravity -flow deposits, including debris flows may also represent uncommon, but locally significant petroleum reservoirs. In a study of the Tamabra Formation (Mexico), a classic example of a carbonate debris apron, Loucks et al (2010) demonstrated that several types of breccia and clast-bearing mud limestone lithofacies might coexist over a short distance, reflecting different density flow mechanisms or different ratios of carbonate mud, sand and clasts. In this case, porosity development is post depositional (removal of lime mud; dolomitization of the matrix; Enos, 1988), but is closely linked with the original properties of carbonate debris flows. In the Sunrise and Osiris prospects, the interpretation of the centimetre to decimetre thick grainstone beds as being late and/or distal products of debris flows (Fig. 14h), and what their preferential mineralization is, is harder to establish, but conforms to both depositional models (Cook and Mullins, 1983; Loucks et al., 2010; Cook, 2015) and macroscopic observation at the Nadaleen trend (Fig. 8).

Fracture permeability also favours mineralizing fluid flow. In most cases, fractures predate the mineralization and the more permeable intervals are linked with the higher original density of joints (likely controlled by bed thickness and lithology; Rustichelli et al., 2013; Afşar et al., 2014) or associated with fault damaged zones (Fig. 14f; including structural intersections difficult to document by core logging) or preferential cleavage development in fold hinges (Fig. 14g). In a few cases, fracture permeability may have developed during mineralization. Pre-mineralization fracture porosity/permeability is generally partly filled by calcite cement. This calcite cement would have been susceptible to dissolution by acidic fluids, which are common in the early stages of Carlin-type systems, and the resulting increase in porosity and permeability of these rocks could have been exploited by gold-bearing fluids (Cline et al., 2005)

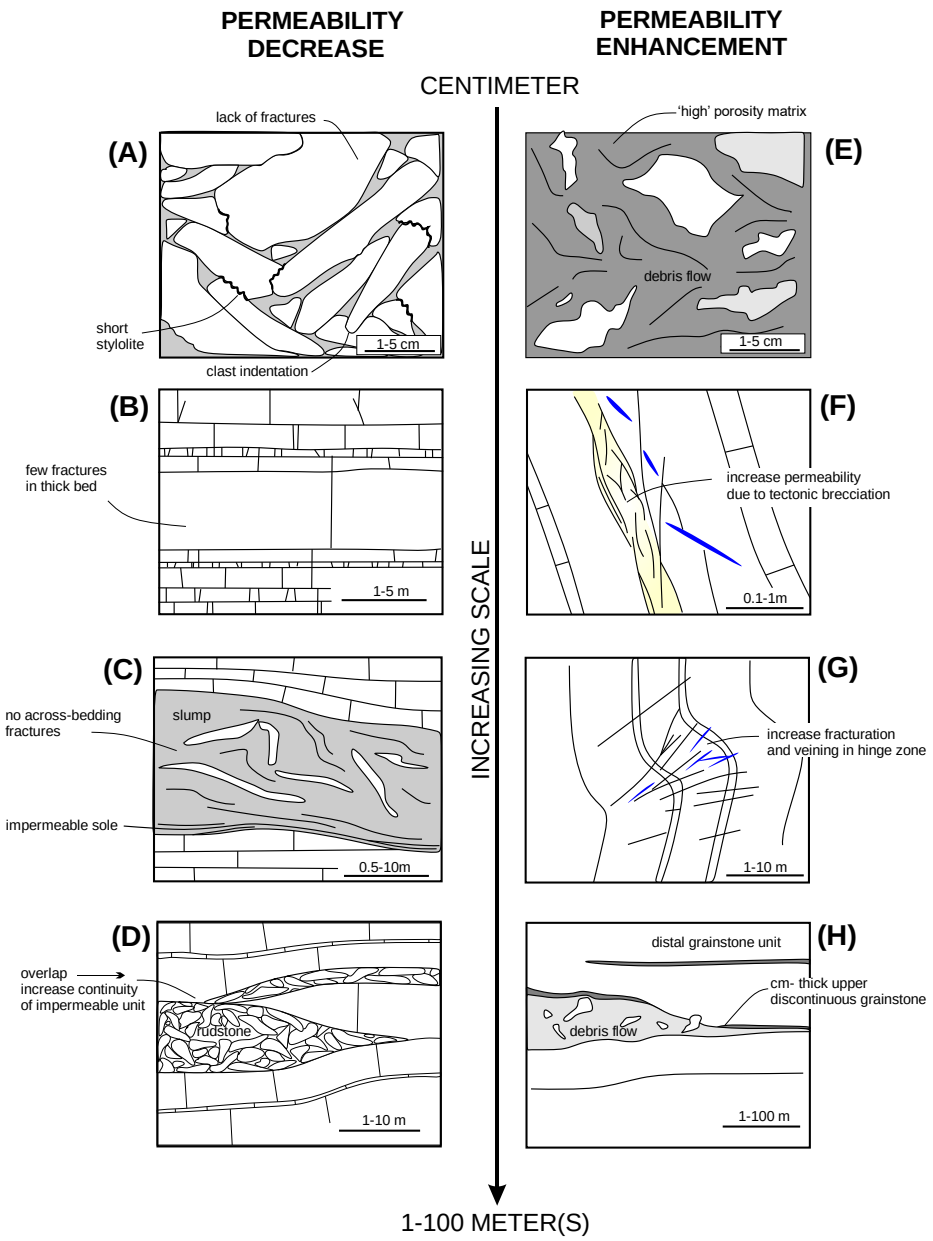

Figure 14. Schematic illustration of some of the geological features that relate to permeability and porosity and thus control the flow of mineralizing fluids. Grey colours enhance matrix and pale yellow a fault zone. Calcite veins are in blue. Illustrations (a) to (d) depict the features inhibiting fluid flow. a) Clast-supported rudstone intervals with elongate fragments (flat pebble conglomerate) act as impermeable barriers due to short stylolites at clast boundaries, clast indentation, non-connected matrix, and the scarcity of fractures at the clast and interval scales. b) Thick limestone beds tend to have fewer fractures and act as impermeable layers. c) Slump intervals deposited through short distance sliding are characterized by bed disruption and monomictic fragments with few fractures crossing the interval. These intervals may also include a relatively impermeable sole. d) At the 10 to 100 m scale, rudstone intervals are discontinuous but complex sedimentary architecture, such as overlapping relationships, may have enhanced the continuity of impermeable barriers, restricting fluid flow. Illustrations (e) to (h) show features that facilitate fluid flow. e) Debris flows are characterized by a more porous matrix compared to surrounding lime mudstones. Even if this porosity was partly filled by calcite cement before ore stage, these later were most easily dissolved than surrounding host rocks during the mineralization event. f) Pre- or syn-mineralization tectonic brecciation increased fracture permeability. g) Fracture cleavage in hinge fold zones. h) Thin, relatively high-porosity grainstone layers may cap floatstone intervals or be the distal portions of debris flow events. These grainstone beds have a slightly higher detrital quartz grain content than surrounding rocks that may have provided a framework to keep fluid pathways open after initial calcite dissolution by early mineralizing fluids.

In the Sunrise prospect, some clast-supported rudstone intervals (flat pebble conglomerate) exhibit clasts with stylolitic and indented relationships, and almost no matrix. These intervals also influenced fluid flow by acting as discontinuous impermeable barriers (Fig. 14 a, d). Other low-permeability units include relatively thick massive limestone beds generally characterized by a low density of fractures (Fig. 14b) and dismembered units with a relatively impermeable sole and only a few crosscutting fractures (Fig. 14c).

The detailed study of the Sunrise prospect demonstrates that mineralization exploited a variety of porous and permeable pathways indicating a 'passive' or 'opportunistic' nature for the mineralizing fluids. This is similar to Nevada Carlin-type gold deposits, which occur across a spectrum from lithologically controlled to structurally controlled deposits (Teal and Jackson, 2002). However, there are also differences between Nadaleen and Carlin. For example, the steep dip of the sedimentary units at the Nadaleen trend and the lack of shallowly dipping units or structures that could have behaved as regional aquitards as the Roberts Mountain Thrust did in Nevada are major differences between the two districts.

Acknowledgments

This report is contribution to NRCan's Targeted Geoscience Initiative Program (TGI). Support for this study was provided through the Gold Project's *Activity G-2.5: 'Lithotectonic controls on the genesis and distribution of carbonate replacement-type ('Carlin style') gold zones, northeastern Selwyn Basin, Yukon'*.

ATAC Resources Ltd. is thanked for their tremendous logistical and scientific support. This report beneficiated from discussions with J. Cline, M. Colpron, A. Coulter, B. Dubé, J. Lane, D. Lavoie, P. Mercier-Langevin, D. Moynihan, and A. Steiner. This report benefited from the review of Suzanne Paradis, Wouter Bleeker and Neil Rogers.

References

Abbott, G., 1997. Geology of the upper Hart River area, eastern Olgivie Mountains, Yukon Territory (116A/10, 116A/11); Yukon Geological Survey, Bulletin 9, 92 p.

Afşar, F., Westphal, H., and Philipp, S.L., 2014. How facies and diagenesis affect fracturing of limestone beds and reservoir permeability in limestone-marl alternations; Marine and Petroleum Geology, v. 57, 418–432.

Aitken, J.D., 1989. Uppermost Proterozoic formations in central Mackenzie Mountains, Northwest Territories; Geological Survey Canada, Bulletin 368, 26 p.

Beaton, N.I., 2015. Diagenetic controls on hydrothermal fluid flow in the Osiris, Isis and Isis East Carlin-type showings, Nadaleen Trend, Yukon; M.Sc. thesis, University of Alberta, Edmonton, Alberta, 180 p.

Berger, V.I., Mosier, D.L., Bliss, J.D., Moring, B.C., 2014. Sediment-hosted gold deposits of the world- database and grade and tonnage models; United States Geological Survey, Open File report 2014-1074, 45 p.

Cline, J.S., Hofstra, A.H., Muntean, J.L., Tosdal, R.M., and Hickey, K.A., 2005. Carlin-type gold deposits in Nevada: critical geologic characteristics and viable models; *in* Economic Geology, 100*th* Anniversary volume (1905–2005), (ed.) J.W. Hedenquist, J.F.H. Thompson, R.J. Goldfarb and J.P Richards; Society of Economic Geologist, p. 541–484.

Colpron, M., Moynihan, D., Israel, S., and Abbott, G., 2013. Geologic map of the Rackla belt, east-central Yukon (NTS 106C/1-4, 106D/1); Yukon Geological Survey, Open File 2013-13, 5 maps, scale 1:50 000.

Cook, H.E., 2015. The evolution and relationship of the western North American Paleozoic carbonate platform and basin depositional environments to Carlin-type gold deposits in the context of carbonate sequence stratigraphy; *in* New Concepts and Discoveries: GSN 2015 Symposium Proceedings, (ed.) W.M. Pennell and L.J. Garside; DEStech Publications Inc., Lancaster, Pennsylvania, p. 1–80.

Cook, H.E. and Mullins, H.T., 1983. Basin margin environment; *in* Carbonate Depositional Environments, (ed.) P.A. Scholle, D.G. Bebout and C.H. Moore; American Association of Petroleum Geologists, Memoir 33, p. 539–617.

Coulter, A.B., Lane, J., and Steiner, A., 2018. Osiris cluster Carlin-type gold, east-central Yukon, *in* Yukon Exploration and Geology 2017, (ed.) K.E. MacFarlane; Yukon Geological Survey, p. 65–74.

Creel, K.D. and Bradley, M.A., 2013. Gold Rush: lessons learned from the latest giant gold deposit discovered in Nevada; *in* Tectonics, Metallogeny, and Discovery: The North American Cordillera and Similar Accretionary Settings, (ed.) M. Colpron, T. Bissig, B.G. Rusk and J.F.H. Thompson; Society of Economic Geologists, Special Publication 17, p. 403–413.

Enos, P., 1988. Evolution of pore space in the Poza Rica trend (Mid-Cretaceous), Mexico; Sedimentology, v. 35, p. 287–325.

Heitt, D.G., Dunbar, W.W., Thompson, T.B., and Jackson, R.G., 2003. Geology and geochemistry of the Deep Star Gold Deposit, Carlin Trend, Nevada; Economic Geology, v. 98, p. 1107–1135.

Loucks, R.G., Kerans, C., Janson, X., and Rajano, M.A.M, 2010. Lithofacies analysis and stratigraphic architecture of a deep-water carbonate debris apron: Lower Cretaceous (Latest Aptian to Latest Albian) Tamabra Formation, Poza Rica field area, Mexico; *in* Mass-Transport Deposits in Deepwater Settings, (ed.) C. Shipp, P. Weimer and H.W. Posamentier; SEPM Society for Sedimentary Geology, Special Publication No 96, p. 367–390.

Moscardelli, L. and Wood, L., 2008. New classification system for mass-transport complexes in offshore Trinidad; Basin Research, v. 20, p. 73–98.

Moynihan, D., 2013. Bedrock Geology of NTS 106B/04, eastern Rackla belt; *in* Yukon Exploration and Geology 2017, (ed.) K.E. MacFarlane, M.G. Nording and P.J. Sack; Yukon Geological Survey, p. 147–167.

Moynihan, D., 2016. Bedrock geology compilation of the eastern Rackla Belt, NTS 105N/15, 105N/16, 105O/13, 106B/4, 106C/1, 106C/2, east-central Yukon; Yukon Geological Survey. Open File 2016-2, scale 1:75 000.

Moynihan, D., Strauss, J.V., Padget, C.D., and Nelson, L.L., in press. Upper Windermere Supergroup and the transition from rifting to continent-margin sedimentation, Nadaleen River area, northern Canadian Cordillera; Geological Society of America Bulletin.

Muntean, J., 2018. The Carlin gold system: Applications to exploration in Nevada and beyond; *in* Diversity of Carlin-Style Gold Deposits, (ed.) J. Muntean; Society of Economic Geologists, Reviews in Economic Geology, Volume 20, p. 39–88.

Muntean, J. and Cline, J.S., 2018. Diversity of Carlin-style gold deposits; *in* Diversity of Carlin-Style Gold Deposits, (ed.) J. Muntean; Society of Economic Geologists, Reviews in Economic Geology, Volume 20, p. 1–6.

Myrow, P.M., Tice, L., Archuleta, B., Clark, B., Taylor, J.F., and Ripperdant, R.L., 2004. Flat-pebble conglomerate: its multiple origins and relationship to metre-scale depositional cycles; Sedimentology, v. 51, p. 973–996.

Pinet, N., Mercier-Langevin, P., Dubé, B., Brake, V., Lane, J., and Colpron, M., 2017. Geological characteristics of Carlin -type gold mineralization prospects in a 'frontier' area, Rackla belt, Yukon, Canada; Proceedings of the 14th Society for Geology Applied to Mineral Deposits (SGA), Biennial Meeting, Québec, Quebec, p. 179–182.

Pinet, N., Sack, P., Mercier-Langevin, P., Lavoie, D., Dubé, B., Lane, J., and Brake, V., 2018. Breccia styles and controls on carbonate replacement type ('Carlin type') gold zones, Rackla belt, east-central Yukon; *in* Targeted Geoscience Initiative – 2017 Report of Activities, (ed.) N. Rogers; Geological Survey of Canada, Open File 8358, p. 163–168.

Ristorcelli, S., Ronning, P., Martin, C., and Christensen, O., 2018. Technical report and estimate of mineral resources for the Osiris project, Yukon, Canada; Technical report ATAC Resources Ltd.

Rhys, D., Valli, F., Burgess, R., Heitt, D., Griesel, G., and Hart, K., 2015. Controls of fault and fold geometry on the distribution of gold mineralization on the Carlin Trend; in New Concepts and Discoveries, (ed.) W.M. Pennell and L.J. Garside; Geological Society of Nevada-Nevada Bureau of Mines and Geology-Society of Economic Geologists-United States Geological Survey, 2015 Symposium, DESTech Publication Inc., p. 333–389.

Rustichelli, A., Agosta, F., Tondi, E., and Spina, V., 2013. Spacing and distribution of bed-perpendicular joints throughout layered, shallow-marine carbonates (Granada Basin, southern Spain); Tectonophysics, v. 582, p. 188–204.

Steiner, A., Hickey, K., and Coulter, A., 2018. The structural framework for Carlin-type gold mineralization in the Nadaleen trend, Yukon; *in* Yukon Exploration and Geology 2017, (ed.) K.E. MacFarlane; Yukon Geological Survey, p. 139–149.

Teal, L. and Jackson, M., 2002. Geologic overview of the Carlin Trend gold deposits; *in* Gold Deposits of the Carlin Trend, (ed.) T.B. Thompson, L. Teal and R.O. Meeuwig; Nevada Bureau of Mines and Geology, Bulletin 111, p. 9–19.

Tucker, M.J., 2015. Geology, mineralization and geochronology of the Conrad zone Carlin-type prospect, east-central Yukon Territory, Canada; M.Sc. thesis, University of British Columbia, Vancouver, British Columbia, 160 p.

Tucker, M.J., Hart, C.J.R., and Carne, R.C., 2012. Geology, alteration, and mineralization of the Carlin-type Conrad zone, Yukon; *in* Yukon Exploration and Geology 2012, (ed.) K.E. MacFarlane, M.G. Nordling and P.J. Sack; Yukon Geological Survey, p. 163–178.

Reconnaissance molybdenum isotope study of vent-distal SEDEX zinc-lead mineralization and host rocks in the Howard's Pass district, Selwyn Basin, Yukon: potential application to paleoredox determinations

J.M. Peter[1], M.G. Gadd[1], D. Layton-Matthews[2] and A. Voinot[2]

[1]*Geological Survey of Canada, 601 Booth Street, Ottawa, Ontario K1A 0E8*

[2]*Department of Geological Sciences and Geological Engineering, Queen's University, 36 Union Street, Kingston, Ontario K7L3N6*

Abstract

Recent work on the largest sedimentary exhalative (SEDEX) district in Canada, the Howard's Pass district (HPD) in Selwyn Basin, Yukon, has shown that a persistently euxinic water column was not the source of sulphur in the mineralization, and that the redox conditions of the water column (and shallow subsurface) varied from anoxic to suboxic to euxinic. We have conducted a bulk geochemical and molybdenum isotopic traverse through a mineralized intersection in a single drill hole from the Anniv East vent-distal lead-zinc SEDEX deposit in the HPD. Bulk geochemical redox proxies generally show that redox conditions varied between (intermittently to permanently) suboxic, dysoxic, anoxic and euxinic. Herein we present new molybdenum isotope data for these same samples, and evaluate the efficacy of the application of this isotopic system to determining redox conditions of the water column and shallow subsurface, and examine the utility of molybdenum isotopes in providing genetic information for SEDEX deposits.

Molybdenum isotope values range from δ^{98}Mo -0.29 to 2.27‰. There is good general agreement between the molybdenum isotope values and certain redox sensitive elements and established redox indicators for the unmineralized and mineralized host rocks; these relationships reflect suboxic or oxic conditions for the most negative values, and anoxic and euxinic conditions for the most positive values. This indicates that the application of molybdenum isotopes as a redox indicator in seafloor hydrothermal deposits in sedimentary (or volcano-sedimentary) settings shows great promise. Unlike thallium isotopes, molybdenum isotopes do not appear to be of use in fingerprinting SEDEX mineralization.

Introduction and background

In the long-standing genetic model for SEDEX deposits, metal-bearing sedimentary basinal fluids rise along growth faults in second- or third-order marine basins and vent into anoxic (no free O_2 present) and euxinic (free H_2S present) waters (Fig. 1) (e.g. Goodfellow and Lydon, 2007). The H_2S originates from seawater sulphate that was bacterially reduced. The metals (dominantly Fe, Zn, Pb) in the venting fluids are fixed by the H_2S in the water column upon mixing, and the precipitated pyrite, sphalerite, and galena subsequently settle to the seafloor in layers. A key implication of this model to exploration is that the presence of reduced, fine-grained marine strata (black shales) is a first-order requisite. However, some workers have suggested that water column anoxia and euxinia are not of paramount importance (e.g. Taylor and Beaudoin, 2000; Saez et al., 2011; Gadd et al., 2016a, b, 2017; Magnall et al., 2015, 2016). Recent Targeted Geoscience Initiative Program (TGI) funded research on SEDEX systems in the Selwyn Basin, Yukon has led to the conclusion that persistent anoxia (and euxinia) in the water column did not prevail throughout the time interval of mineralization (e.g. Gadd et al., 2016a, b, 2017; Magnall et al., 2016, 2018; Peter et al., 2018). Providing primary and supporting evidence to corroborate or discount the role of anoxia and/or euxinia in the deposit-forming environments of Canada's premier SEDEX deposit district will contribute to revolutionizing genetic and exploration models for SEDEX deposits.

Recent advancements in stable isotope analysis of non-traditional, redox-sensitive metals (e.g. Ni, Mo, Se, U, Cr) by multi-collector-inductively coupled plasma-mass spectrometry (MC-ICP-MS) in geological materials (e.g. Anbar and Rouxel, 2007) have facilitated studies that have shown that some metal isotope systems are useful as paleoredox proxies (e.g. Cr: Frei et al., 2009; Mo: Anbar and Gordon, 2008; Tl: Owens et al., 2017). Herein, we present the results of a reconnaissance study of the application of molybdenum isotope analyses as a potential redox indicator in a sedimentary exhalative (SEDEX) lead-zinc deposit environment. To date, there have been relatively few studies that employ Mo isotopes in a seafloor hydrothermal mineral deposit environment (e.g. Magnall et al., 2018; Song et al., 2011).

Corresponding author: Jan Peter (jan.peter@canada.ca)

Peter, J.M., Gadd, M.G., Layton-Matthews, D., and Voinot, A., 2019. Reconnaissance molybdenum isotope study of vent-distal SEDEX zinc-lead mineralization and host rocks in the Howard's Pass district, Selwyn Basin, Yukon: potential application to paleoredox determinations; *in* Targeted Geoscience Initiative: 2018 report of activities, (ed.) N. Rogers; Geological Survey of Canada, Open File 8549, p. 105–123. https://doi.org/10.4095/313645

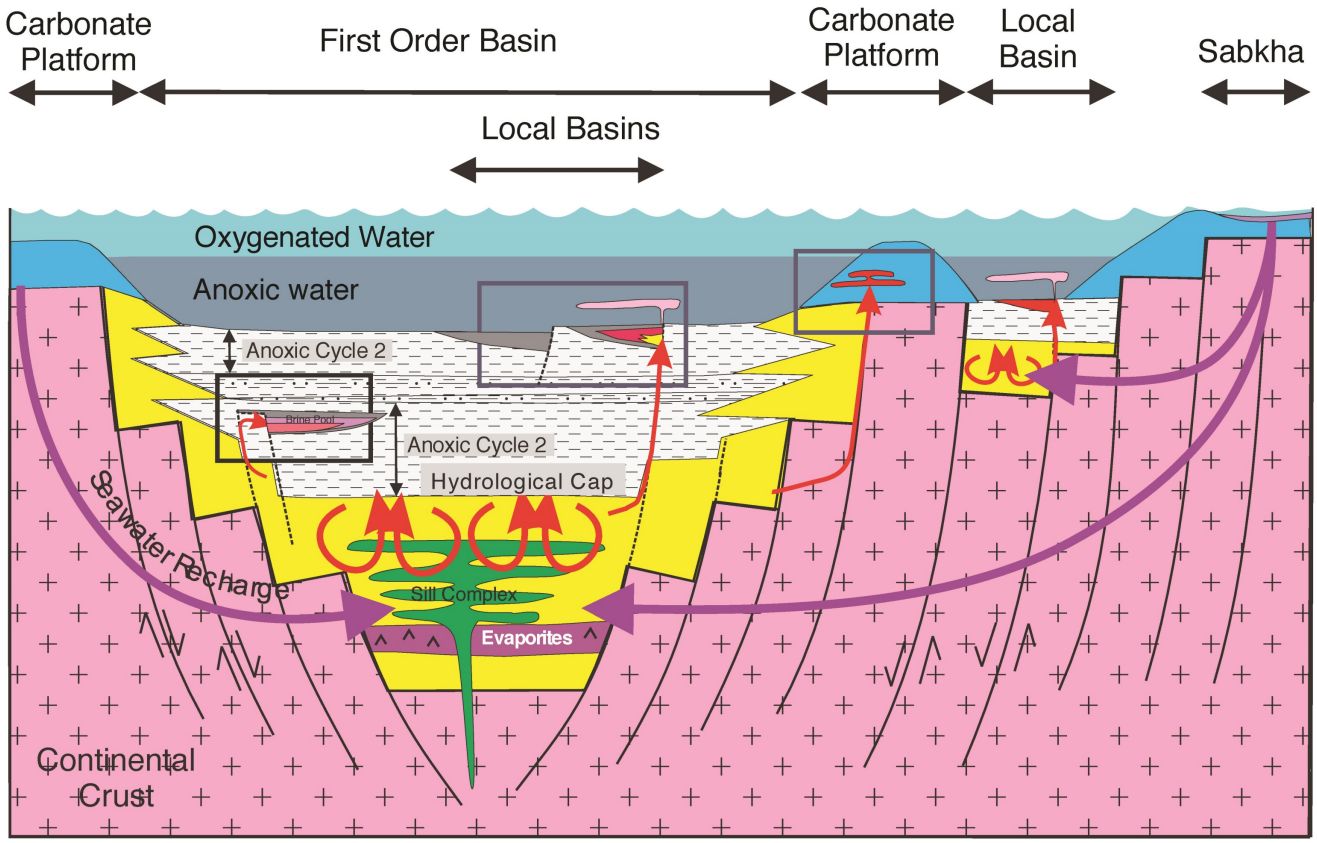

Figure 1. Generalized, schematic model for formation of SEDEX deposits (*modified from* Goodfellow and Lydon, 2007).

Molybdenum geochemistry

Molybdenum is a transition element with atomic number 42 and has a large number of oxidation states, with IV to VI being most common in surficial environments (Barling et al., 2001). The crustal abundance of Mo is 1 to 2 ppm (Taylor and McLennan, 1985). Molybdenum is essential for biological processes (e.g. Siebert et al., 2003), and the biological fixation of nitrogen (e.g. Glass et al., 2009). In oxygenated waters, molybdenum is highly mobile and conservative; it is accumulated in seawater so effectively that it is the most abundant of the oceanic transition elements (approximately 107 nmol/kg; Collier, 1985). The oceanic residence time of molybdenum is 770 000 years (Algeo, 2004), far greater than the ocean mixing time (1500 years; Sarmiento and Gruber, 2006), and this results in a homogenized seawater Mo content of 9.6 ppm (Collier, 1985).

In solid Earth materials such as continental crust, molybdenum occurs as Mo(IV) and Mo(V). Under oxidizing conditions in typical seawater and freshwater, Mo(VI) is stable and the dominant aqueous species is the molybdate ion (MoO_4^{2-}) (Barling et al., 2001). In oxic seawater molybdenum is scavenged onto ferromanganese nodules (Barling et al., 2001; McManus, 2002). In euxinic ocean waters, molybdenum is rapidly removed as Mo(IV)-sulphide compounds on sinking particles, where they accumulate in anoxic muds and organic-rich mudstones (e.g. Helz et al., 1996; Emerson and Huested, 1991; Scott and Lyons, 2012). Molybdenum is also scavenged by and adsorbed onto pyrite, pyrrhotite and clays (Helz et al., 2004), as well as organic matter (Biswas et al., 2009). Therefore, the abundance of this redox sensitive element in marine sediments has been used a paleoredox proxy over the last several decades (e.g. Dahl et al., 2010a; Helz et al., 2011; Scott et al., 2008; Scott and Lyons, 2012).

Molybdenum isotope systematics and fractionation processes

Molybdenum has seven naturally occurring stable isotopes that range in abundance from 10 to 25%. These are (in decreasing abundance; Mayer and Weiser, 2014): ^{98}Mo (24.29%), ^{96}Mo (16.67%), ^{95}Mo (15.87%), ^{92}Mo (14.65%), ^{100}Mo (9.74%), ^{97}Mo (9.58%) and ^{94}Mo (9.19%). Molybdenum stable isotope fractionation is reported in δ^{98}Mo notation in per mil (parts per thousand) deviation from the ^{98}Mo/^{95}Mo ratio relative to the international reference standard NIST-SRM-3134 (Nägler et al., 2014):

$$\delta^{98}\mathrm{Mo} = \left(\frac{(^{98}\mathrm{Mo}/^{95}\mathrm{Mo})_{\mathrm{sample}}}{(^{98}\mathrm{Mo}/^{95}\mathrm{Mo})_{\mathrm{NIST3134}}} - 1 \right) \times 1000\ (‰)$$

Molybdenum isotope data reported in the literature using the SPEC Mo standard as a reference were converted by adding 0.25‰ to reported values. Literature data reported as δ^{97}Mo were converted to δ^{98}Mo by multiplying by 1.5.

Earth materials in the geosphere and hydrosphere display significant variability in their molybdenum isotopic compositions (Fig. 2). Kendall et al. (2017) provide a useful, succinct summary of the geological applications of molybdenum isotopes. Molybdenum in crustal materials ranges from slight negative to slightly positive δ^{98}Mo values, with an average of 0.3‰ (Breillat et al., 2016; Voegelin et al., 2014). Open (i.e. oxic) ocean water has δ^{98}Mo = 2.34 ±0.10‰ (Barling et al., 2001; Siebert et al., 2003; Greber et al., 2012; Nakagawa et al., 2012; Goldberg et al., 2013). In oxic seawater, isotopically light molybdenum (δ^{95}Mo) is sequestered by adsorption onto ferromanganese and manganese oxyhydroxide precipitates, and this process results in the large isotopic fractionation (up to 3‰) and negative molybdenum isotopic compositions (approximately -0.7‰; Barling et al., 2001; Siebert et al., 2003; Arnold et al., 2004; Goldberg et al., 2009). The temperature dependence of this fractionation is weak (Wasylenki et al., 2008). In strongly sulphidic seawater, MoO_4^{2-} is transformed into thiomolybdate species (e.g. Saxena et al., 1968) and rapidly deposited, with little to no isotopic fractionation between seawater Mo and Mo in the sulphidic sediments (Barling et al., 2001; Siebert et al., 2003). In weakly sulphidic seawater, molybdenum is only partly converted (to thiomolybdate) and this results in a molybdenum isotopic fractionation (Δ) of -0.7‰ from modern seawater (McManus, 2002; Poulson et al., 2006; Barling and Anbar, 2004; Wasylenki et al., 2008), such that molybdenum within reducing sediments (typically in continental margin settings, with high productivity and upwelling) are enriched in isotopically light molybdenum (Siebert et al., 2006). Organic matter-rich mudstones and shales likely host most of the molybdenum in Earth's crust, and have the greatest range in δ^{98}Mo (from -1.3 to +2.5‰; e.g. Dahl et al., 2010b; Duan et al., 2010; Wille et al., 2013; Chen et al., 2015; Kendall et al., 2015; Partin et al., 2015). This variability, thought to be largely due to variability in oceanic redox at both the local and global levels, importantly controls crustal and mantle cycling of molybdenum.

Geology

The Howard's Pass District (HPD) is located within the Selwyn Basin (Fig. 3a), a metallogenic province known for its world-class Zn-Pb(±Ag±Ba) SEDEX deposits (Gadd et al., 2016a; Fig. 3b). The Selwyn Basin is a continental margin ba-

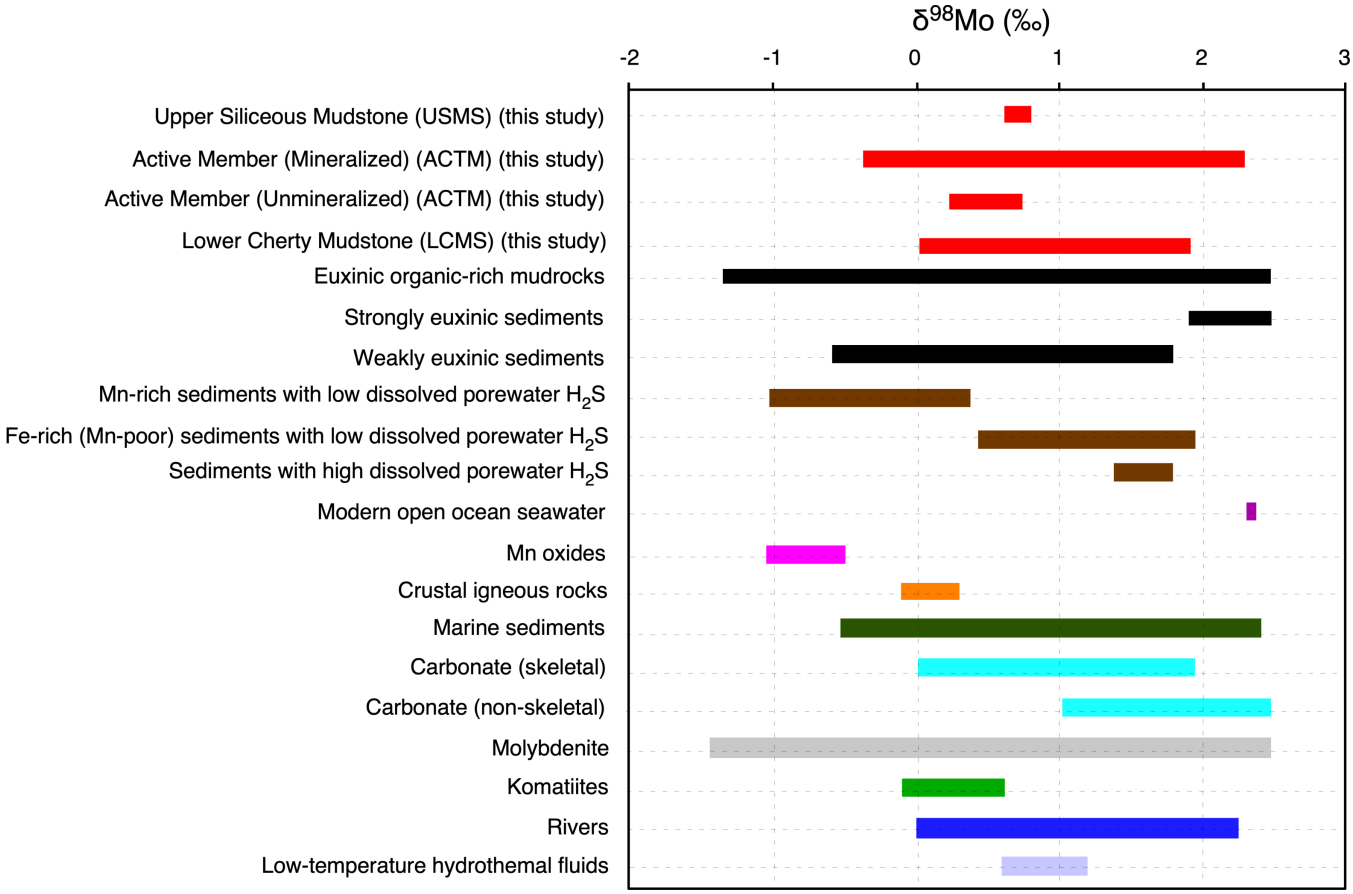

Figure 2. Synthesis of natural molybdenum isotope variations within various reservoirs on Earth, together with data from the present study. *Modified from* Kendall et al. (2017).

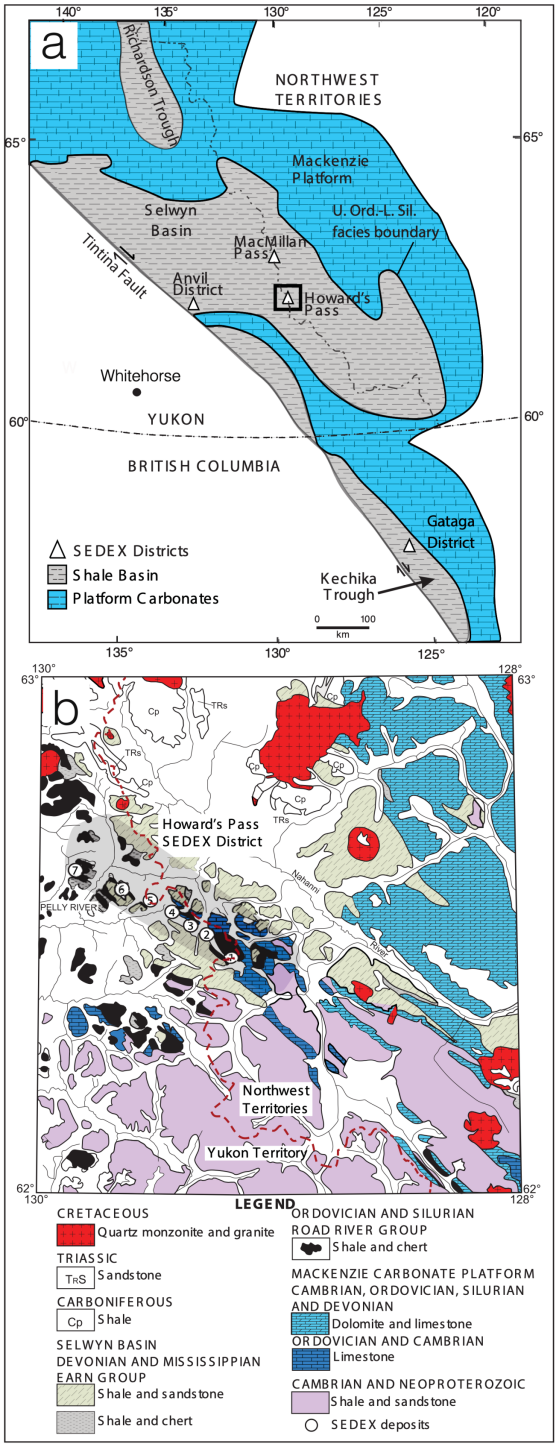

Figure 3. a) General geological map of the Selwyn basin and Mackenzie platform with major SEDEX Zn-Pb-(Ag-Ba) districts labelled (Goodfellow, 2007). b) Geological map of the Howard's Pass district, showing locations of SEDEX deposits (*modified from* Goodfellow, 2004). 1: XY zone (XY, XY Central and XY West deposits); 2: Brodel deposit; 3: HC zone (HC and HC West deposits); 4: Don zone (Don and Don East deposits); 5: Anniv Zone (Anniv and Anniv East deposits); 6: OP deposit; 7: Pelly North deposit.

sin characterized by the deposition of thick Lower Ordovician to Lower Devonian sequences of fine-grained siliciclastic rocks with calcareous intercalations (Fig. 3a; Goodfellow and Jonasson, 1986). The Paleozoic stratigraphy of the Selwyn Basin overlies Upper Proterozoic to Lower Cambrian shale, siltstone and sandstone of the Vampire Formation. The Vampire Formation, in turn, is unconformably overlain by massive to wavy-banded limestone of the Upper Cambrian to Lower Ordovician Rabbitkettle Formation (Goodfellow and Jonasson, 1986; Gordey and Anderson, 1993). The Middle Ordovician to Silurian Road River Group structurally overlies these limestones within the HPD (Hodder et al., 2014) and is divided into the Duo Lake and the Steel formations. The Duo Lake Formation comprises carbonaceous siliceous and calcareous mudstone, cherty mudstone and minor limestone. The Steel Formation conformably overlies the Duo Lake Formation and consists of grey bioturbated mudstone. The Lower Devonian to Middle Mississippian Earn Group conformably overlies the Steel Formation and is divided into the Portrait Lake and Prevost formations (Fig. 4; Gordey and Anderson, 1993). The rocks of the Earn Group comprise cherty clastic turbidites and carbonaceous mudstone. The Duo Lake, Steel and Portrait Lake formations are subdivided into informal members in the HPD (Fig. 4). The Duo Lake Formation consists of the Pyritic Siliceous Mudstone member (PSMS), Lower Cherty Mudstone member (LCMS) and Calcareous Carbonaceous Mudstone member (CCMS), which are the immediate stratigraphic footwall to the mineralization (Fig. 5a), the Active Member (ACTM), which hosts the mineralization (Fig. 5b, c), and the Upper Siliceous Mudstone

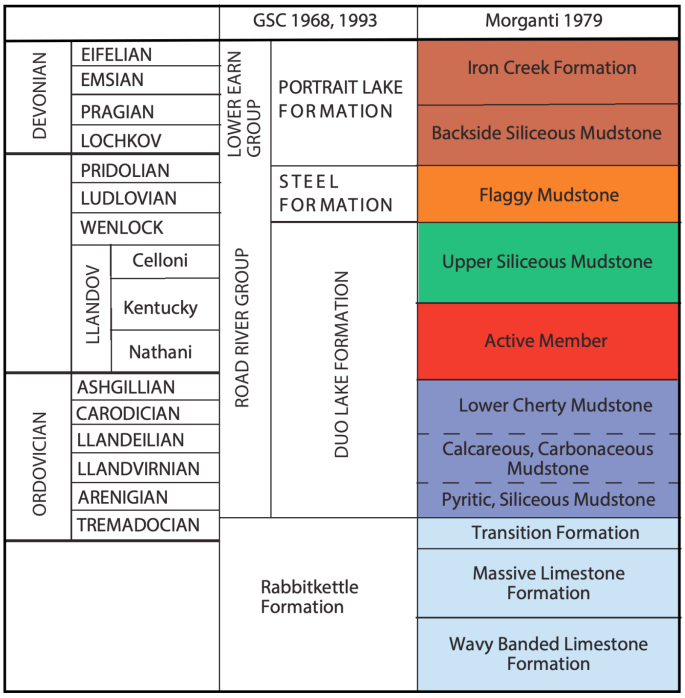

Figure 4. Stratigraphic section of the Howard's Pass district. The zinc-lead mineralization is hosted entirely within the ACTM (*modified from* Gordey and Anderson, 1993).

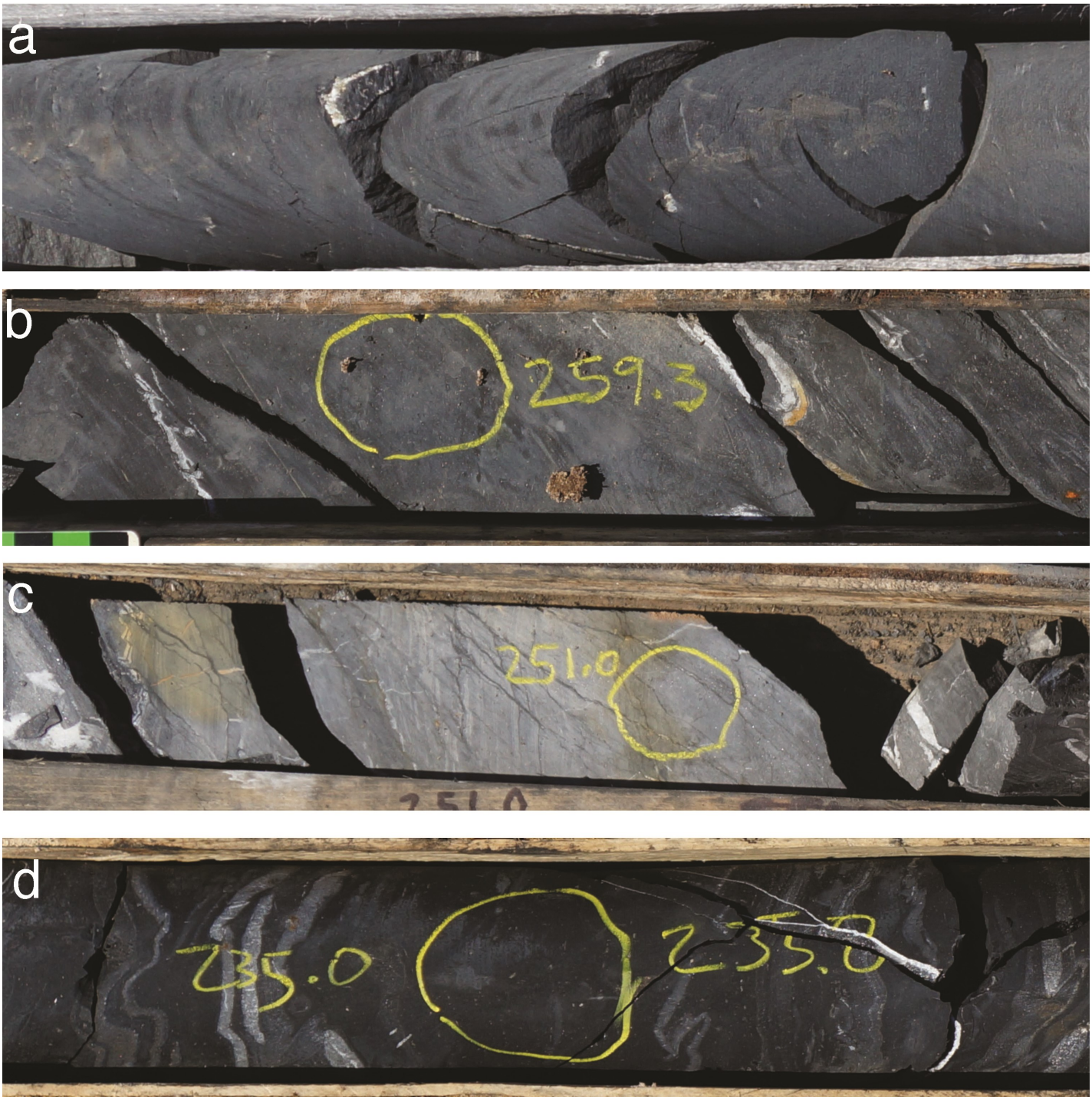

Figure 5. Representative photographs of drill core samples from ANE-108 used in this study. A) Lower Cherty Mudstone member (LCMS). Downhole depth 284.0 m; B) unmineralized Active Member (ACTM) which hosts the mineralization. Downhole depth 259.3 m; C) Lead-zinc mineralized Active Member (ACTM). Downhole depth 251.0 m; D) Upper Siliceous Mudstone member (USMS) which is the immediate stratigraphic hanging wall to the mineralization; downhole depth 235.0 m. Diameter of drill core is 4.8 cm for all photographs.

member (USMS), which is the immediate stratigraphic hanging wall to the mineralization (Fig. 5d). The Steel Formation is designated as the Flaggy Mudstone member (FLMD) and the basal Portrait Lake Formation is designated as the Backside Siliceous Mudstone member (BSSM) (Morganti, 1979).

Conodonts recovered from the ACTM place the time of formation near the Lower to Middle Llandoverian (443–439 Ma: Norford and Orchard, 1985). The PSMS member (2–10 m thick) is the basal unit of the Duo Lake Formation in the HPD and consists of grey to black pyritic, carbonaceous shale. The CCMS (50–100 m thick) overlies the PSMS member and consists of highly carbonaceous mudstone with variable amounts of intercalated limestone and carbonate concretions. Minor wispy pyrite and calcite veins (2.5 mm–1 cm wide) occur locally. The LCMS (15–30 m thick) consists of highly carbonaceous and siliceous mudstone. The CCMS and LCMS have similar appearances in that they are massive and monotonous, highly carbonaceous cherty mudstones with variable contents of calcite. The ACTM (0–60 m thick, although typically 20–30 m) hosts the zinc-lead mineralization in the HPD. The USMS (20–90 m thick) consists of carbonaceous and cherty mudstones with minor to abundant laminations (0.5–1.5 cm thick) of carbonate-rich fluorapatite and locally abundant carbonate concretions. The FLMD (100–140 m thick) is a grey siliceous to dolomitic silty mudstone and contains minor carbonaceous intercalations. The BSSM (60–180 m thick) is a carbonaceous, siliceous mudstone that contains locally abundant concretions and also contains trace amounts of laminated sphalerite and framboidal pyrite. Pyrite is a widespread, but minor, constituent in all of the members.

Mineralization in the HPD occurs along what is termed the 'Zinc Corridor', a 38 km long, northwest-southeast trend comprising 14 zinc-lead sedimentary exhalative (SEDEX) deposits that contain an estimated 400.7 Mt grading 4.5 weight % Zn and 1.5 weight % Pb (Kirkham et al. 2012). All of these deposits are located on the same Early Silurian time-stratigraphic horizon, and are composed dominantly of massive and semi-massive sphalerite and galena hosted in calcareous and cherty mudstones; pyrite is a minor (approx. 5.5 weight %) part of the mineralization (e.g. Fig. 5c). The mineralized horizon is generally 20 to 30 m thick. The Anniv East zone has an indicated resource of 16.92 Mt grading 4.15 weight % Zn and 1.2 weight % Pb, and an inferred resource of 16.05 Mt grading 4.04 weight % Zn and 1.08 weight % Pb (Kirkham et al., 2012). Anniv East has a strike length of 2.6 km and is interpreted to be an antiform (Yukon Geological Survey, 2012).

Sampling and methods

Twelve samples were collected from drill hole ANE-108 that cored a continuous stratigraphic section through the Anniv East mineralized horizon. The samples span a stratigraphic interval from 225.6 to 284.0 meters downhole. Three samples are from the LCMS, six from the ACTM, and three from the USMS (Table 1).

Table 1. Metadata for samples of drill core ANE-108 from the Duo Lake Formation at the Anniv East deposit, together with molybdenum isotope compositions.

Drillhole	Depth (m)	Unit	Comment	δ^{98Mo} (‰)	2-sigma
ANE-108	225.6	USMS		0.69	0.41
ANE-108	235	USMS		0.77	0.70
ANE-108	244.9	USMS		—	—
ANE-108	251	ACTM	mineralized	-0.29	0.17
ANE-108	252.5	ACTM	unmineralized	0.26	0.30
ANE-108	259.3	ACTM	unmineralized	0.57	0.10
ANE-108	262.2	ACTM	mineralized	1.24	0.21
ANE-108	271.5	ACTM	mineralized	2.27	0.51
ANE-108	273	ACTM	unmineralized	1.62	0.21
ANE-108	275.2	LCMS		0.71	0.20
ANE-108	281.6	LCMS		1.85	0.28
ANE-108	284	LCMS		0.04	0.23

— sample lost from column

Bulk geochemistry

Samples of drill cores were prepared and analyzed by Acme Analytical Laboratories (now Bureau Veritas Upstream Minerals), Vancouver. Samples were crushed and then pulverized in a ceramic mill. The following analytical methods were used (*see* Table 2): 1) method 4B, lithium metaborate/tetraborate fusion followed by 5% HNO_3 dissolution and analysis by ICP-MS; 2) method 1F30 ultra-trace using a 4 acid (HF, HNO_3, $HClO_4$, HCl) near-total digestion, and analysis by ICP-MS; 3) method LOI (loss on ignition), sintering at 1000°C; 4) method G806, digestion with sulphuric and hydrofluoric acid and titration using potassium dichromate; 5) method 2A-F, fusion and analysis by specific ion electrode; 6) TC001 and TC002, ignition in induction furnace, and measurement by adsorption in an infrared spectrometric cell; 7) method 2A-C: leaching with dilute HCl, followed by ignition at 500°C, and analysis of residue by LECO; 8) method 2A11, perchloric acid leach, and measurement by LECO; and 9) organic C: by difference (= total C – inorganic C – graphite C).

Precision and accuracy were monitored using laboratory in-house standards, as well as by replicate analysis of certified reference materials. Detection limits are listed in Table 2. For plotting purposes, half detection limits were used. For three analyses of mineralized ACTM, upper detection limits of 10 000 ppm were exceeded for some elements and for those elements, a value of 10 000 was used for plotting purposes.

Chemical treatment, separation and mass spectrometry of molybdenum

Sample preparation and isotope analyses were conducted at the Queen's Facility for Isotope Research (QFIR). To minimize procedure blanks and allow for measurement of molybdenum isotope ratios using low amounts of molybdenum (<500ng), high purity reagents were used for the preparation of all the solutions described below. Concentrated HNO_3 and HCl were prepared by distillation of technical grade HCl and HNO_3

Table 2. Summary of geochemical data for samples analyzed for molybdenum isotopic composition in this study. Ranges (minimum to maximum) are given for LCMS, unmineralized ACTM, mineralized ACTM and USMS. Also shown are lower limits of detection and analytical methods used (*see* text for details).

Element	Detection Limit	Unit	LCMS Range	Unmin. ACTM Range	Min ACTM Range	USMS Range	Analytical Method Code
Ag	2	ppb	1069 - 2227	196 - 1000	547 - 1256	265 - 1182	1F30
Al	0.01	wt%	0.43 - 0.57	0.07 - 0.13	0.05 - 0.10	0.43 - 1.37	1F30
As	0.1	ppm	21.6 - 36.1	16.3 - 23.5	12.0 - 28.3	3.2 - 38.9	1F30
Au	0.2	ppb	0.1 - 0.4	0.1	0.1	0.1 - 0.3	1F30
B	1	ppm	10 - 14	3 - 4	2 -3	14 - 40	1F30
Ba	0.5	ppm	687 - 875	52 - 468	50 - 276	2053 - 3784	4B
Be	0.1	ppm	2 - 5	0.5 - 5	0.5 - 4	0.5 - 11	1F30
Bi	0.02	ppm	0.19 - 0.36	0.01 - 0.12	0.01 - 0.08	0.12 - 0.16	1F30
CO2	0.02	wt%	0.02 - 0.66	0.08 - 28.43	0.21 - 26.59	0.94 - 3.27	2A11
C tot	0.02	wt%	3.75 - 9.37	6.16 - 13.12	3.04 - 10.71	6.74 - 12.76	2A LECO
C org	0.02	wt%	3.54 - 9.33	3.65 - 6.14	1.84 - 3.01	6.46 - 11.67	2A-C
Ca	0.01	wt%	0.61 - 0.98	0.25 - 31.49	0.83 - 32.03	2.55 - 3.91	1F30
Cd	0.01	ppm	0.07 - 6.53	1.01 - 4.82	46.29 - 68.83	0.005 - 0.20	1F30
Ce	0.1	ppm	50.3 - 64.1	4.7 - 23.9	10.5 - 20.2	20.5 - 60.6	1F30
Co	0.1	ppm	10.9 - 14.3	1.4 - 6.4	0.8 - 3.5	5.4 - 11.1	1F30
Cr	0.5	ppm	13.3 - 30.0	6.2 - 17.0	4.8 - 19.5	20.0 - 64.6	1F30
Cs	0.02	ppm	2.5 - 7.1	0.3 - 0.8	0.2 - 0.5	1.6 - 7.3	1F30
Cu	0.01	ppm	47.66 - 82.67	12.81 - 105.05	20.59 - 24.84	43.15 - 48.61	1F30
Dy	0.05	ppm	3.5 - 7.13	1.15 - 3.23	0.91 - 1.72	1.86 - 2.99	4B
Er	0.03	ppm	2.63 - 4.61	0.47 - 2.36	0.68 - 1.16	1.95 - 3.91	4B
Eu	0.02	ppm	1.0 - 1.78	0.14 - 0.72	0.26 - 0.44	0.45 - 1.68	4B
F	10	ppm	1096 - 1764	286 - 740	223 - 323	220 - 1604	2A-F
Fe tot	0.01	wt%	1.61 - 2.93	0.48 - 0.85	0.79 - 1.82	0.58 - 1.11	G806
Ga	0.5	ppm	14.1 - 18.3	0.25 - 4.7	0.25 - 1.4	4.1 - 10.8	1F30
Gd	0.05	ppm	3.83 - 8.68	0.96 - 4.11	1.33 - 1.84	1.83 - 8.82	4B
Ge	0.1	ppm	0.05	0.05	0.1 - 0.3	0.05 - 0.10	1F30
Hf	0.02	ppm	3.4 - 4.6	0.05 - 0.6	0.05 - 0.5	1.6 - 5.2	1F30
Hg	5	ppb	195 - 239	102 - 160	1271 - 1772	77 - 136	1F30
Ho	0.02	ppm	0.81 - 1.51	0.16 - 0.77	0.2 - 0.4	0.5 - 1.45	4B
H2O+	0.01	wt%	9.04 - 13.94	2.28 - 7.85	0.005 - 5.64	8.15 - 14.94	LOI
In	0.02	ppm	0.01 - 0.03	0.01	0.01 - 0.05	0.01	1F30
K	0.01	wt%	0.28 - 0.38	0.05 - 0.09	0.03 - 0.06	0.28 - 0.76	1F30
La	0.5	ppm	33.5 - 37.6	1.7 - 22.2	4.2 - 12.2	16.2 - 51.8	1F30
Li	0.1	ppm	1.7 - 4.3	0.6 - 2.0	0.3 - 1.1	3.3 -28.5	1F30
LOI	0.1	wt%	10.5 - 15.1	8.8 - 37.4	5.8 - 32.0	9.5 - 19.3	LOI
Lu	0.01	ppm	0.40 - 0.58	0.08 - 0.31	0.05 - 0.19	0.26 - 0.53	4B
Mg	0.01	wt%	0.05 - 0.14	0.03 - 0.08	0.01 - 0.06	0.07 - 1.51	1F30
Mn	1	ppm	29 - 77	36 - 433	81 - 437	33 -110	1F30
Mo	0.01	ppm	3.27 - 57.15	9.5 - 50.63	5.34 - 16.26	1.92 - 38.23	1F30
Na	0.001	wt%	0.0005	0.0005 - 0.003	0.0005 - 0.002	0.0005 0.002	1F30
Nb	0.02	ppm	13.9 - 25.5	0.9 - 5.9	0.6 - 2.3	5.2 - 10.5	1F30
Nd	0.3	ppm	24.6 - 39.8	3.9 - 16.0	5.9 - 12.2	11.0 - 41.7	4B
Ni	0.1	ppm	100.8 - 192.1	32.2 - 79.7	18.5 - 47.8	75.2 - 91.3	1F30
P	0.001	wt%	0.08 - 0.44	0.03 - 0.25	0.05 - 0.06	0.04 - 1.24	1F30
Pb	0.01	ppm	37.46 - 49.26	104.73 - 113.08	3699.21 - >10000	11.07 - 17.07	1F30
Pd	10	ppb	5 - 18	5 - 12	5	5	1F30
Pr	0.02	ppm	6.89 - 9.54	0.85 - 4.11	1.33 - 2.71	3.26 - 10.92	4B
Pt	2	ppb	1 - 8	1 - 3	1 - 3	1 - 6	1F30
Rb	0.1	ppm	103.7 - 150.1	8.0 - 28.7	6.0 - 15.2	64.0 - 122.5	1F30
Re	1	ppb	17 - 77	14 - 79	3 - 23	20 - 28	1F30
S	0.02	wt%	1.84 - 3.29	0.52 - 0.95	1.76 - 3.30	0.66 - 1.09	1F30
S tot	0.02	wt%	1.91 - 3.42	0.60 - 1.04	2.04 - 3.43	0.73 - 1.25	2A LECO
Sb	0.02	ppm	3.12 - 9.08	1.68 - 3.47	3.55 - 7.94	1.82 - 2.06	1F30
Sc	0.1	ppm	2.0 - 4.0	0.5 - 1.4	0.3 - 1.2	1.4 - 4.3	1F30
Se	0.1	ppm	5.9 - 8.8	0.7 - 2.3	1.0 - 5.4	4.3 - 7.6	1F30
Sm	0.05	ppm	3.91 - 7.86	0.77 - 3.56	1.06 - 1.69	1.67 - 8.11	4B
Sn	0.1	ppm	1.0 - 2.0	0.5	0.5	0.5 - 2.0	1F30
Sr	0.5	ppm	16.1 - 27.9	5.8 - 229.6	10.1 - 209.0	50.8 - 78.4	1F30
Ta	0.05	ppm	0.9 - 1.8	0.05 - 0.3	0.05 - 0.2	0.3 - 0.6	1F30
Tb	0.01	ppm	0.61 - 1.29	0.16 - 0.61	0.18 - 0.33	0.27 - 1.26	4B
Te	0.02	ppm	0.1 - 1.24	0.04 - 0.12	0.03 - 0.09	0.07 - 0.17	1F30
Th	0.1	ppm	7.8 - 10.7	0.5 - 2.8	0.6 - 1.3	6.4 - 9.9	1F30
Ti	0.001	wt%	0.004 - 0.005	0.001 - 0.002	0.0005 - 0.001	0.005 - 0.027	1F30
Tl	0.02	ppm	0.35 - 1.12	0.26 - 0.40	0.81 - 3.14	0.07 - 0.16	1F30
Tm	0.01	ppm	0.40 - 0.62	0.09 - 0.36	0.07 - 0.21	0.27 - 0.59	4B
U	0.1	ppm	10.4 - 29.7	3.2 - 51.0	2.6 - 4.2	9.6 - 12.8	1F30
V	2	ppm	273 - 1674	281 - 974	168 - 275	125 - 750	1F30
W	0.1	ppm	0.9 - 1.1	0.25 - 0.9	0.25	0.25 - 1.4	1F30
Y	0.01	ppm	22.5 - 52.5	6.2 - 27.8	6.5 - 14.7	19.4 - 61	1F30
Yb	0.05	ppm	2.14 - 3.71	0.66 - 1.89	0.46 - 1.06	2.11 - 3.08	4B
Zn	0.1	ppm	30.4 - 654.4	251.1 - 780.7	>10000	5.0 - 18.7	1F30
Zr	0.1	ppm	119.5 - 165.2	11.7 - 27.2	7.2 - 19.6	70 - 144.3	1F30

(VWR Technical), HF and H_2O_2 were sourced from Seastar Chemical (Baseline). PFA containers (Savillex) were used throughout the sample preparation.

Sample digestion was similar to that in Peter et al. (2018). About 50 mg of solid material was weighed in a Savillex container. About 4 mL of aqua regia was added to each container and put on the hotplate to digest overnight at 180˚C. The samples were then centrifuged at 3500 rpm for 10 min, and the liquid phase was evaporated to dryness at 85˚C. This solid residue was then dissolved in 1 to 2 mL of 1N HCl/0.5N HF (volume adjusted to achieve complete dissolution of the residue), and run through an ESI PrepFast® automated chromatography system for molybdenum purification. A 250 µL (8 cm long) PFA column loaded with BioRad® AG1X8 resin was used for Mo separation (modified from Pearce et al., 2009). A minimum of 50 ng of molybdenum was loaded onto the resin in a 200 µL volume. Additional steps were added to ensure that the final Mo elution would not contain Zr and Ru separation (3N HCl and 8N HNO_3, respectively), and to eliminate isobaric interferences with some molybdenum isotopes. Additional details about the procedure are given in Table 3.

Table 3. Molybdenum purification procedure with PrepFast® parameters used in this study.

Reagent	Volume	Flow rate	Purpose
8N HNO_3	4 mL	1000µL/min	Resin cleaning
2N HNO_3	1.5 mL	1000µL/min	
3N HCl	3 mL	1000µL/min	
1N HCl/0.5N HF	1.5 mL	1000µL/min	Conditioning
Sample load	200 µL	50µL/min	
1N HCl/0.5N HF	1.5 mL	1000µL/min	Matrix elution
3N HCl	3 mL	1000µL/min	Zr elution
2N HNO_3	2.5 mL	1000µL/min	Mo elution
8N HNO_3	3 mL	1000µL/min	Ru elution

After the elution, the molybdenum fraction was evaporated to dryness on a hotplate at 80˚C overnight. Once dry, 2 drops of concentrated HNO_3 were added to the samples, which were then put on the hotplate at 180˚C with the container capped for several hours to allow for the digestion of any potential residual organic matter resulting from the degradation of the resin. The samples were then evaporated again and taken back in about 500 µL of 2% HNO_3 before being brought to the Thermo -Finnigan Neptune MC-ICPMS for molybdenum isotope measurement. Sensitivity was about 30 to 40 V/ppm.

An ESI microFAST® autosampler setup with a 300 µL injection column was used for sample introduction. The injection flowrate was 30 µL, and 80 µL of solution was pushed through for each sample or standard. Measurement time was about 100 seconds per sample. Because of the dual loop system, time between consecutive bracketing standards was about 8 minutes, thus minimizing any potential effect of the drift of the instrument (<0.05‰). Samples were measured using a Standard-Sample Bracketing (SSB) method, using NIST3134 and PTC-1 reference materials for the entire procedure. PTC-1 yielded a molybdenum isotopic composition of -0.52‰ (2s 0.08‰, n = 2). Overall procedure blank for the entire procedure was below detection limit on the Neptune faraday cups (<10 pg Mo, or less than 0.1% of the Mo coming from the sample). Errors reported are 2SD.

Data analysis and statistics

Several REE ratios were calculated from the bulk geochemical data. All were normalized to average post-Archean Australian Shale (PAAS; Taylor and McLennan, 1985) and designated as shale-normalized (SN) as follows:

$Ce/Ce^*_{SN} = 2Ce_{SN}/(La_{SN}+Pr_{SN})$

$Eu/Eu^*_{SN} = 2Eu_{SN}/(Sm_{SN}+Gd_{SN})$.

$Gd/Gd^*_{SN} = Gd_{SN}/((Sm_{SN})^{0.33} \times (Tb_{SN})^{0.67})$

Non-parametric Spearman's rank correlations were used rather than Pearson Product-Moment, as the latter is susceptible to the effects of outliers, particularly in small sample sizes (n = 12 in this study). Correlation coefficients are expressed as r_s.

Results

Bulk geochemical compositions

USMS Mo contents range from 1.92 to 38.23 ppm. Unmineralized ACTM Mo contents range from 9.5 to 50.63 ppm, whereas mineralized ACTM Mo contents range from 5.34 to 16.26 ppm. LCMS Mo contents range from 3.27 to 57.15 ppm (Table 2).

Molybdenum isotopic compositions

Molybdenum isotopic compositions and 2SD are shown in Table 1. The overall δ^{98}Mo range for all samples is -0.29 to 2.27‰. The highest δ^{98}Mo value is near the base of the (mineralized) ACTM, whereas the lowest δ^{98}Mo value is from the upper part of the (mineralized) ACTM (n = 3). There is a systematic decrease upwards for mineralized ACTM samples, and a general overall upward increase for all ACTM samples, mineralized and unmineralized. USMS sample have a δ^{98}Mo range from 0.69 to 0.77‰ (n = 2). Unmineralized ACTM have δ^{98}Mo values that range from 0.26 to 1.62‰ (n = 3). As mentioned above, mineralized ACTM samples have δ^{98}Mo values that range from -0.29 to 2.27‰. LCMS samples have δ^{98}Mo values that range from 0.04 to 1.85‰ (n = 3).

Discussion

Mineralogical residence of molybdenum

A key question is: What are the mineralogical residence(s) of molybdenum in the rocks and mineralization at Anniv East? Gadd et al. (2016a) show that pyrite in mineralization and host rocks to the HPD contain abundant Mo (typically between 10–100 ppm, but up to 3000 ppm). These authors also showed that for pyrite in mineralization and host rocks of the HPD, Mo

groups together with Co, Ni, Cu, Se and Bi, indicating that these elements are of hydrogenous (seawater) origin. Chappaz et al. (2014) studied pyrite in euxinic shales and determined that, although pyrite is a significant molybdenum sink (20%), matrix material is the host for most (80%) of the molybdenum.

Our bulk geochemical data show somewhat positive correlations between Mo and TOC (Fig. 6a; $r_s = 0.3287$, two-tailed P = 0.2969), C org (Fig. 6b; $r_s = 0.5524$, two-tailed P = 0.0625), Ag (Fig. 6c; $r_s = 0.4336$, two tailed P = 0.1591), Re (Fig. 6d; $r_s = 0.6573$, two-tailed P = 0.0202), Te (Fig. 6e; $r_s = 0.3328$, two-tailed P = 0.2906), U (Fig. 6f; $r_s = 0.6154$, two-tailed P = 0.0332), V (Fig. 6g; $r_s = 0.7552$, two-tailed P = 0.0045) and V/Cr (Fig. 6h; $r_s = 0.6434$, two-tailed P = 0.0240). The correlations of Mo with TOC (TOC = C org + graphite) and organic carbon (C org) are due to the organic matter sequestration of molybdenum (and other trace elements) from seawater and porewater during sedimentation and diagenesis (e.g. Large et al., 2014), by forming organometallic bonds. Breakdown of the organic matter by bacterial sulphate reduction during diagenesis liberates molybdenum (under reducing conditions), and it is incorporated into diagenetic pyrite (Tribovillard et al., 2006), where it occurs as non-stoichiometric lattice substitutions, similar to other elements such as copper and bismuth (Huston et al., 1995). Molybdate is likely adsorbed onto organic matter, and thiomolybdate is scavenged onto sulphurized organic matter in the black shales, similar to the process proposed by Kurzweil et al. (2015).

Molybdenum displays weak negative correlations (plots not shown) with CO_2 ($r_s = -0.3357$, P = 0.2861), Ca ($r_s = -0.3916$, P = 0.2081), Li ($r_s = -0.3783$, P = 0.2253), Mg ($r_s = -0.4343$, P= 0.1583), Na ($r_s = -0.4956$, P = 0.1013) and Sr ($r_s = -0.4056$, P = 0.1908), indicating varying dilution with carbonate, micas and

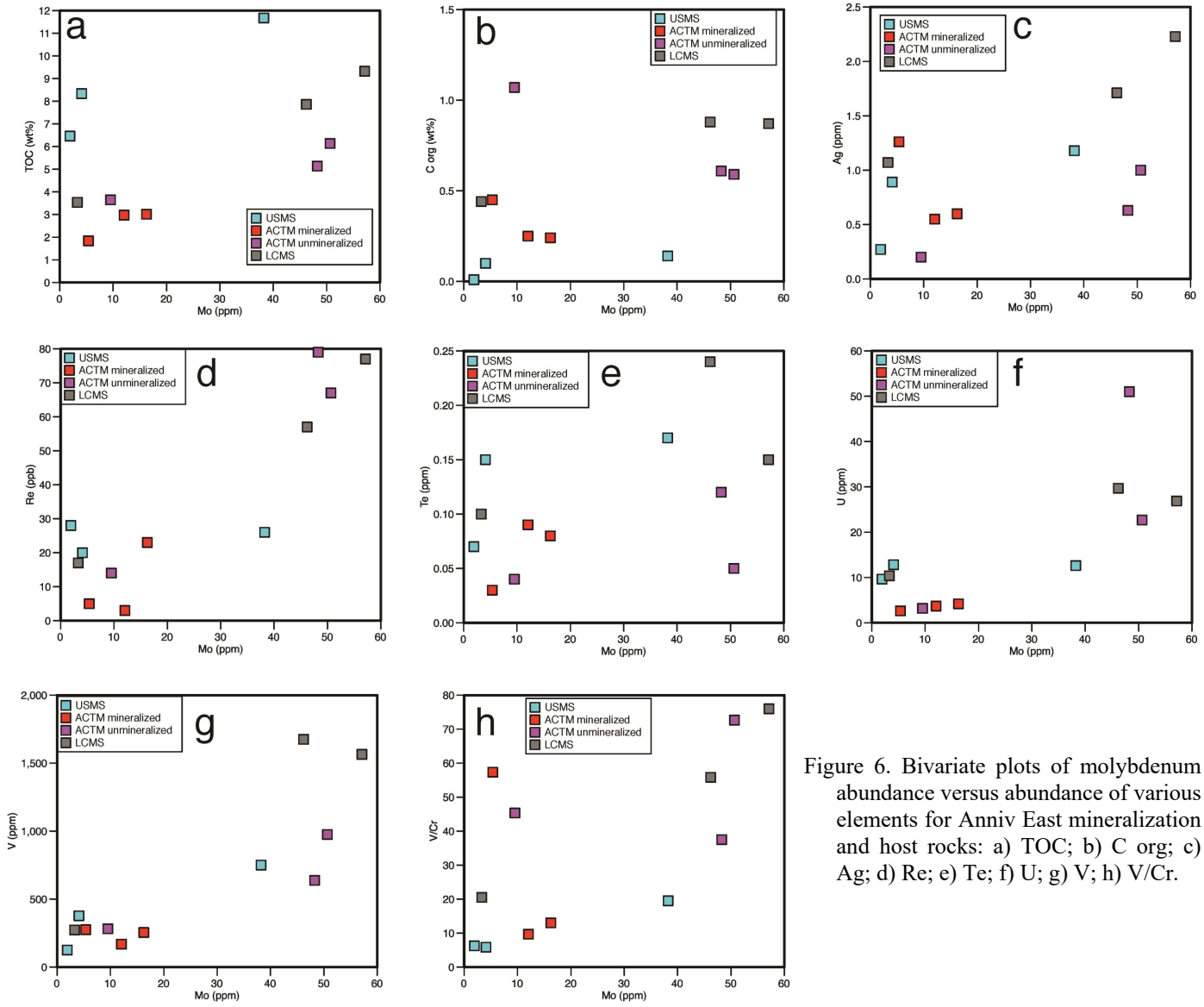

Figure 6. Bivariate plots of molybdenum abundance versus abundance of various elements for Anniv East mineralization and host rocks: a) TOC; b) C org; c) Ag; d) Re; e) Te; f) U; g) V; h) V/Cr.

clays. Collectively, these positive and negative correlations suggest that molybdenum is hosted both in pyrite and organic matter.

Bulk geochemical paleoredox indicators

Below, we paraphrase our findings in Peter et al. (2018) regarding paleoredox in the ANE drill core. In order to assess the potential viability of molybdenum isotopes as a paleoredox indicator in Canadian Paleozoic SEDEX settings, it is instructive to first evaluate the bulk geochemical paleoredox indicators, and then (later, below) compare them directly with the molybdenum isotopic data. A caveat is that the redox conditions of bottom waters may not reflect the redox conditions of pore waters in the sediments and (immediately below) the seafloor (e.g. oxic bottom waters overlying sediments with anoxic and/or sulphidic pore waters). Indeed, this scenario is that proposed for deposition of the SEDEX deposits in the HPD (Gadd et al., 2016b, 2017). Table 4 is a compilation of some selected (least problematic or contradictory) geochemical paleoredox proxies taken from the literature, and the redox conditions for each of the following: LCMS, unmineralized ACTM, mineralized ACTM and USMS.

Cerium andnd europium are the only REE that can have valence states other than +3 (III). Cerium has two oxidation states (Ce^{3+} and Ce^{4+}) that are strongly redox dependent, with Ce fractionated from it neighbouring REE according to redox state (e.g. De Baar et al., 1988). In oxygenated marine waters, Ce^{4+} predominates and is scavenged onto highly surface-reactive Fe-Mn oxyhydroxides, leaving the oxic seawater depleted in Ce (Elderfield and Greaves, 1982). The magnitude of the Ce anomaly (Ce/Ce*) varies with water depth in the modern oceans; it is absent (i.e. Ce/Ce* = 1) in surface waters, but becomes increasingly negative with depth due to oxidative scavenging onto Fe-Mn oxyhydroxides in the water column (Alibo and Nozaki, 1999). The Fe-Mn oxyhydroxides capture Ce^{4+} (and therefore have Ce/Ce* > 1). In anoxic marine settings, Ce occurs as Ce^{3+} (same valence state as the other REE), and nil (Ce/Ce* = 1) to weakly positive anomalies occur in seawater. The magnitude of cerium anomalies can serve as a proxy for oxygen levels (e.g. Wright et al., 1987).

Values of Ce/Ce* vary widely from 0.58 to 1.02 in our samples, and are in good agreement with time-stratigraphically equivalent rocks elsewhere in the HPD (Slack et al., 2017). Most of the Ce anomalies are real, based on a plot (not shown) of Pr/Pr* versus Ce/Ce*, following Bau and Dulski (1996). The Ce/Ce* anomalies are shown in Figure 7, a PAAS-normalized REE plot, with samples classified as LCMS, unmineralized ACTM, mineralized ACTM and USMS. Cerium anomalies between 0.4 to 0.9 are taken to indicate deposition under suboxic conditions (i.e. 0.2–2 mL O_2/L H_2O; Tribovillard et al., 2006), and most of our analyses fall within this range (Fig. 7). Our analyses also have gadolinium anomalies (Gd/Gd*) that range from 1.02 to 1.30, and are indicative of the higher stability of Gd in seawater over the other REE (Alibo and Nozaki, 1999; Gadd et al. 2016b).

Total organic carbon contents themselves are not diagnostic of anoxia, as there is considerable overlap in values between anoxic and oxic settings (e.g. Raiswell et al., 1988) and are influenced by high sedimentation rates (e.g. Tyson, 2001) and clay mineralogy (e.g. Kennedy et al., 2002). Values of Ni/Co, previously proposed to be effective redox indicators (e.g. Jones and Manning, 1994; Ross and Bustin, 2009), display a positive correlation with TOC (r_s = -0.41, two-tailed P = 0.1283), whereas V/Cr and U/Th, both of which have been cited as effective redox indicators (e.g. Jones and Manning, 1994), show no correlation with TOC (V/Cr r_s = +0.02, two-tailed P = 0.9484; U/Th r_s = -0.31, two-tailed P = 0.3306). However, there is positive correlation between V and TOC (r_s = +0.63, two-tailed P = 0.02832; plot not shown). The two uppermost samples of LCMS have V greater than 1000 ppm, indicative of hyper-sulphidic conditions (Scott et al., 2017).

Molybdenum contents of sediments are considered to be a robust paleoredox proxy, with Mo contents below 25 ppm indicative of euxinic conditions within pore waters; Mo greater than 100 ppm signifies permanently euxinic conditions within the water column itself, and Mo between 25 and 100 ppm indicates an intermittently euxinic water column (Scott and Lyons, 2012). According to these criteria, the LCMS, ACTM and USMS were deposited in conditions that varied between eux-

Table 4. Summary of selected (least problematic, viable) bulk geochemical paleoredox proxies, and salient references for these. Shown are the value ranges (minimum to maximum) for each of each of these, subdivided into LCMS, unmineralized ACTM, mineralized ACTM, and USMS.

Paleoredox Proxy:	V	Mo	Re/Mo	Ni/Co	V/Cr	U/Th	Mo/TOC	Ce/Ce* PAAS norm
LCMS Range	273 - 1674 ppm	3.3 - 57.1 ppm	0.0012 - 0.0052	8.0 - 16.7	20.6 - 76.0	1.0 - 3.8	0.9 - 6.1	0.74 - 0.78
LCMS Redox	e (i)	e (i)	a (i) to s (i)	a & s (p)	a & s (p)	a (i) to d (i)	a	s (p)
Unmin. ACTM Range	281 - 974 ppm	9.5 - 50.6 ppm	0.0013 - 0.0016	12.4 - 23.0	37.5 - 72.7	6.4 - 34.0	2.6 - 9.4	0.62 - 0.90
Unmin. ACTM Redox	?	e (i)	a (p)	a & s (p)	a & s (p)	a & s (p)	a	s (p)
Min ACTM Redox	168 - 275 ppm	5.3 - 16.3 ppm	0.00025 - 0.0015	13.7 - 23.1	9.7 - 57.3	2.8 - 4.3	2.9 - 5.4	0.70 - 1.02
Min. ACTM Redox	?	e (p porewater)	a (i) to s (i)	a & s (p)	a & s (p)	a & s (p)	a	s (i) and a (i)
USMS Range	125 750 ppm	1.9 - 38.2 ppm	0.0007 - 0.015	6.8 - 16.4	5.9 - 19.5	1.3 - 1.6	0.3 - 3.3	0.59 - 0.84
USMS Redox	?	e (p porewater; i water)	a (i) to s (i)	a & s (p)	a & s (p)	a & s (p)	a	s (p)
References	Breit & Wanty, 1991; Scott et al., 2013	Scott & Lyons, 2012	Ross & Bustin, 2009; Crusius et al., 1996	Ross & Bustin, 2009; Jones & Manning, 1994	Ross & Bustin, 2009; Jones & Manning, 1994	Ross & Bustin, 2009; Jones & Manning, 1994	Algeo & Lyons 2006; Algeo & Rowe, 2012	Wright et al., 1987; Tribovillard et al., 2006

o oxic (>2 ml O2)/L H2O); s suboxic (0.2 to 2 ml O2/L H2O); d dysoxic (<0.2 ml O2/L H2O); a anoxic (<0 ml O2/L H2O); e euxinic (>0 ml H2S/L H2O); i intermittent; p permanent

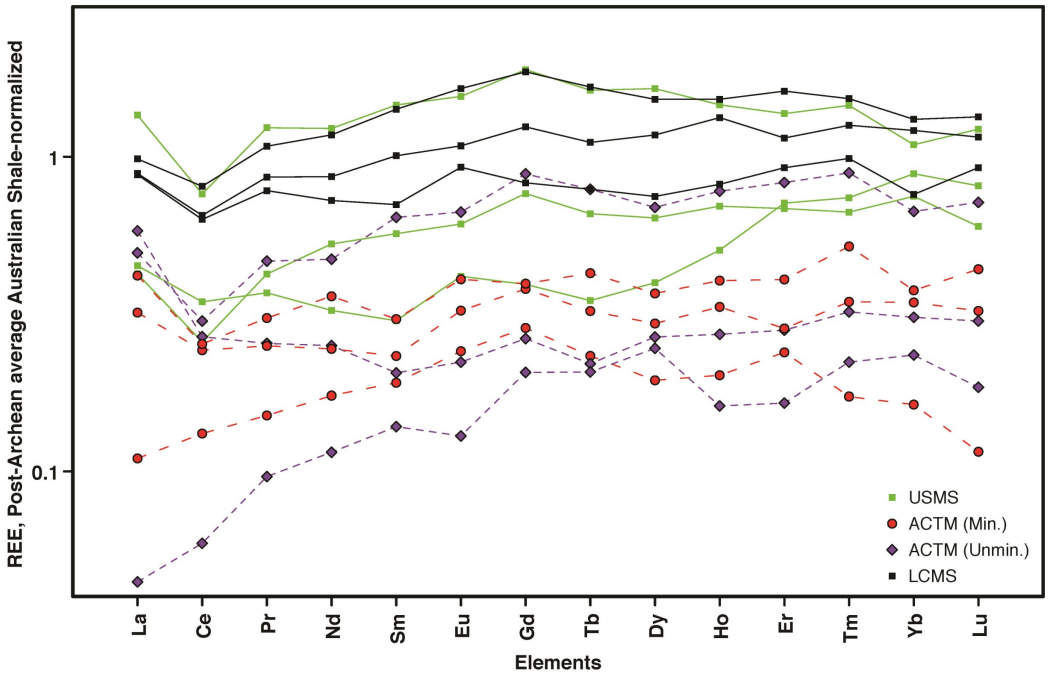

Figure 7. PAAS-normalized REE plot, with samples classified into LCMS, unmineralized ACTM, mineralized ACTM and USMS.

inic pore waters and an intermittently euxinic water column. The two uppermost LCMS samples have Mo contents of 46 and 57 ppm, indicative of predominantly anoxic conditions (Mo > 25–100 ppm; *see* Slack et al., 2017).

Molybdenum (ppm)/TOC (weight %) (Mo/TOC) values have also been used as potential redox indicators (e.g. Algeo and Lyons, 2006; Algeo and Rowe, 2012). Our data (Mo/TOC = 0.3–9.4) are in the range of modern anoxic silled basins. Further, based on the residence time of Mo in seawater (770 ka; Algeo, 2004), and comparison with deep-water renewal times of modern anoxic basins, the LCMS experienced a deep-water renewal time of approximately 400 years, whereas at the base of the ACTM this decreases to approximately 200 years (*see* figure 3 of Algeo and Rowe, 2012).

According to Crusius et al. (1996), and Ross and Bustin (2009), Re/Mo between 0.0008 and 0.004 indicate anoxic conditions and Re/Mo over 0.004 indicate suboxic conditions, whereas Re/Mo similar to seawater (0.0008) indicate deposition under euxinic conditions. Re/Mo values for Anniv East samples are low (<0.015) and suggest anoxic to sulphidic depositional conditions: LCMS Re/Mo = 0.0012 to 0.005 (anoxic), mineralized ACTM Re/Mo = 0.0002 to 0.0014 (euxinic to anoxic), unmineralized ACTM Re/Mo = 0.0013 to 0.0016 (anoxic), and USMS Re/Mo = 0.0007 to 0.015 (anoxic to suboxic). Furthermore, there is an excellent negative correlation between Re/Mo and Ce/Ce* (i.e. the higher/closer to unity for Ce anomaly, the lower the Re/Mo value).

Although the Anniv East deposit (present study) is approximately 20 km northwest of the XY Central deposit where Slack et al. (2017) conducted their bulk geochemical paleoredox studies, our paleoredox indicators show similar trends, suggesting that all the deposits/zones in the HPD formed within similar water column and/or (early diagenetic) sedimentary environmental conditions.

Molybdenum isotopes as paleoredox indicators?

The Anniv East host rocks and mineralization collectively fall within the overall range for euxinic organic-rich mudrocks (Fig. 2; Kendall et al., 2017). The highest and lowest δ^{98}Mo values are in mineralized ACTM (2.27‰ and -0.29‰, respectively); unmineralized ACTM has a more restricted range (1.62 –0.26‰). LCMS footwall shales form a range (1.19–0.76‰) that is intermediate between mineralized and unmineralized ACTM. USMS samples, however, have a much more restricted (tighter) range (0.77–0.69‰). Based on comparison with modern marine sediments, such isotopic values are indicative of suboxic to anoxic, to euxinic conditions (Scott and Lyons, 2012).

In order to assess the potential of molybdenum isotopes as paleoredox proxies, it is instructive to examine correlations between the molybdenum isotopic compositions and various elements, element ratios, and geochemical indicators for the same samples (Fig. 8). Our data show positive correlations between δ^{98}Mo and C_{tot} (Fig. 8a; r_s = 0.4100, two-tailed P = 0.2104), LOI (Fig. 8b; r_s = 0.3909, two-tailed P = 0.2345), Ag (Fig. 8c; r_s = 0.463 two-tailed P = 0.1509), Mo (Fig. 8d; r_s = 0.2909, two-tailed P = 0.3855), Mo/TOC (Fig. 8e; r_s = 0.2909, two-tailed P = 0.3855), Ni/Co (Fig. 8f; r_s = 0.4091, two-tailed P = 0.2115), Re (Fig. 8g; r_s = 0.4091, two-tailed P = 0.2115) and

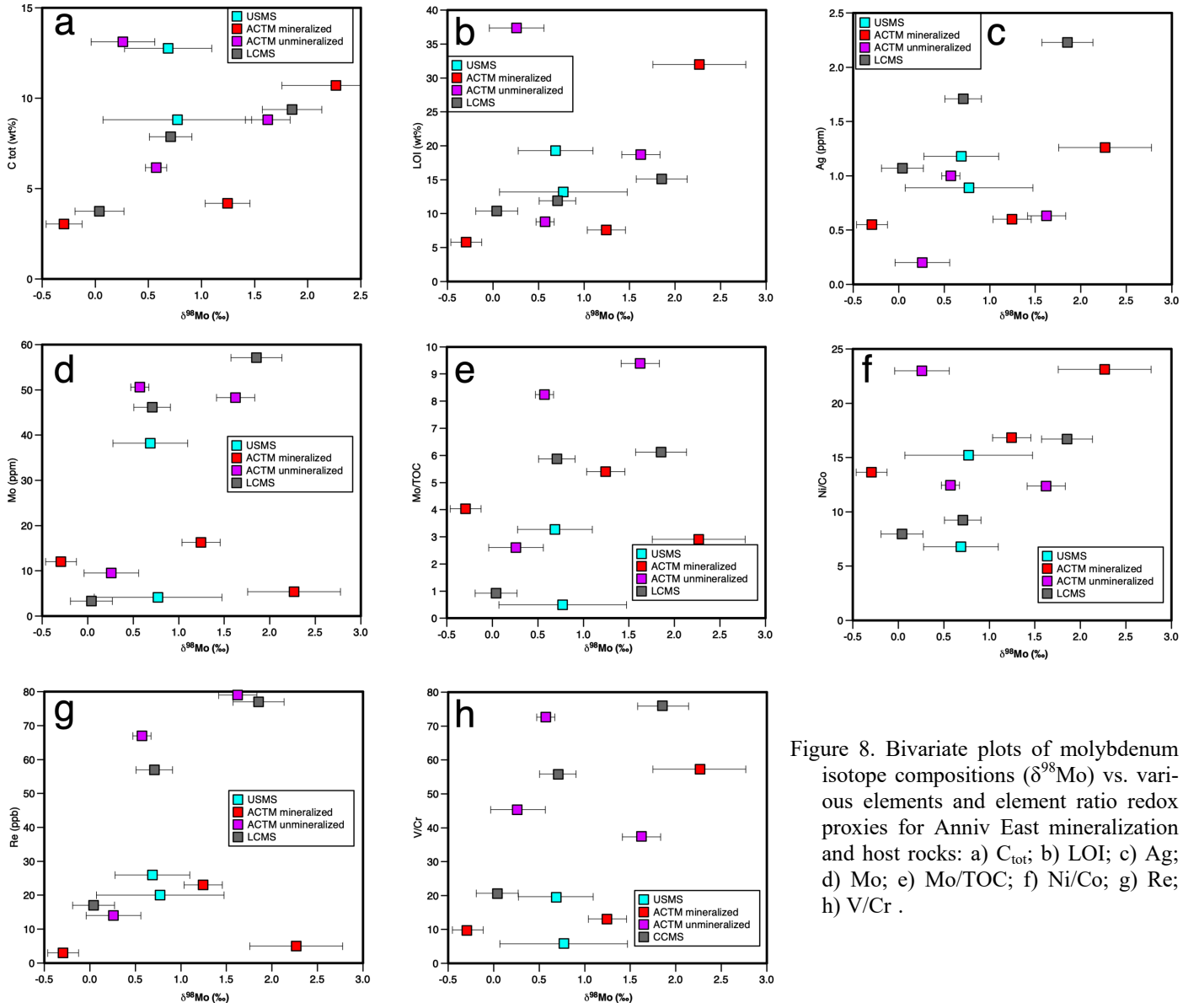

Figure 8. Bivariate plots of molybdenum isotope compositions (δ^{98}Mo) vs. various elements and element ratio redox proxies for Anniv East mineralization and host rocks: a) C_{tot}; b) LOI; c) Ag; d) Mo; e) Mo/TOC; f) Ni/Co; g) Re; h) V/Cr .

V/Cr (Fig. 8h; r_s = 0.3545, two-tailed P = 0.2847).

Silver is a trace element that is sourced from seawater and sequestered in pyrite (e.g. Large et al., 2014). Nickel, rhenium, rhenium and uranium are redox sensitive elements present in seawater. In oxic marine settings, nickel is complexed with organic matter in the water column and sedimented, leading to its enrichment in the sediments (Algeo and Maynard, 2004). Evidence for such nickel-organic matter complexation in the Anniv East samples is the positive correlation between Ni and TOC (r_s = +0.66, two-tailed P = 0.02019; plot not shown). In reducing sediments, nickel is mobilized from the sediments into the overlying water column.

The correlations of δ^{98}Mo with C_{tot} and LOI are due to carbonate (strong positive correlation between CO_2 and LOI and between C_{tot} and CO_2; both not shown). This relationship might reflect formation of carbonate by anaerobic oxidation of methane (AOM) in the sulphate-methane transition zone, as suggested by Johnson et al. (2018).

In comparison to the selected bulk geochemical paleoredox indicators, δ^{98}Mo values show positive correlations with V/Cr (Fig. 8h; r_s = 0.3545, two-tailed P = 0.2847), Ni/Co (Fig. 8f; r_s = 0.4091, two -tailed P = 0.2115), Mo (Fig. 8d; r_s = 0.2909, two-tailed P = 0.3855). This implies that the Mo isotopic compositions of the sedimentary rocks and mineralization (see below) have potential to serve as paleoredox indicators.

A manganese-oxide cycling shuttle, as proposed by Magnall et al. (2018) for the MacMillan Pass SEDEX district, likely did not operate to fractionate molybdenum isotopes in the Howard's Pass system. Evidence for this is the extremely low Mn contents of the unmineralized and mineralized shales; the maximum Mn content is 437 ppm and most samples contain below 110 ppm.

Lithologic and stratigraphic variation in molybdenum isotopic compositions

Figure 9, a plot of drillhole depth versus δ^{98}Mo (and other geochemical parameters and thallium isotopic composition), shows (from the lowermost sample at 284 m depth, and progressing stratigraphically upward to 271.5 m depth) that there is a systematic increase in δ^{98}Mo values (with one outlier) through the LCMS and to the lower part of the ACTM, from 0.04‰ to a maximum of 2.27‰. This trend can be interpreted to reflect increasingly reducing to euxinic conditions with time and deposition. From 271.5 m upward to 251 m there is a progressive decrease in δ^{98}Mo from 2.27 to -0.29‰ that can be interpreted as a decrease in reducing conditions with time and deposition. The USMS hanging wall rocks have intermediate δ^{98}Mo values of 0.69 to 0.77‰ (note that one sample at 244.9 m was not analyzed as no sample was recovered from the column); this may reflect a return to slightly more reduced, but still suboxic conditions.

These findings corroborate recent research at Howard's Pass (and other) SEDEX districts (Gadd et al., 2016a, b, 2017; Slack et al., 2017; Magnall et al., 2016, 2018). Namely, that persistent euxinic conditions did not exist, nor were requisite to form the deposits. The dynamic conditions that we document probably favoured the formation of SEDEX deposits in the HPD by making available organic matter, nutrients and sulphur for SEDEX mineralizing fluids to interact/react with. This resulted in metal fixation by the precipitation of sulphides either from sulphide generated by thermochemical reduction of seawater sulphate (e.g. Gadd et al., 2017) and/or by sulphide produced via seawater sulphate reduction within the sulphate-methane transition zone in association with AOM in the organic-rich sediments (e.g. Johnson et al., 2018).

Relationship between molybdenum and thallium isotopic compositions

The molybdenum (present study) and thallium isotope data (Peter et al., 2018) for the Anniv East samples are not inversely correlated (Fig. 9, 10), which is not in agreement with the proposed idea of the authigenic behaviour in various redox environments, whereby molybdenum and thallium isotopes fractionate in opposite directions with respect to manganese oxide burial (e.g. Nielsen et al., 2011; Nielsen and Rehkämper, 2011; Kendall et al., 2017). There is a positive, albeit weak, correlation between δ^{98}Mo and ε^{205}Tl (Fig. 10a; $r_s = 0.2545$, two-tailed $P = 0.4500$).

The LCMS, unmineralized ACTM and USMS were deposited from both clastic sedimentary and hemipelagic and pelagic sedimentary processes, and the molybdenum and thallium isotopic compositions likely reflect a mixture between continental material, hemipelagic and pelagic sediments (possessing a seawater isotopic signature), and seawater that were deposited in suboxic to anoxic to euxinic conditions (Fig. 10b, c). Lower Silurian seawater is estimated to have δ^{98}Mo of approximately 1.5‰ (reported to NIST3134; Dahl et al., 2010b; Gordon et al., 2009). Samples that are close to (above and below) this value reflect deposition under euxinic conditions. Samples substantially below this Lower Silurian seawater value reflect less euxinic and more oxidized conditions.

Modern seawater has an ε^{205}Tl value of -6.3 ± 0.3 (Rehkämper et al., 2002; Nielsen et al., 2004; Nielsen et al., 2006; Owens et al., 2017); however, the ε^{205}Tl for Lower Silurian seawater remains unconstrained. Over the last 70 Ma, the ε^{205}Tl of seawater has been shown to vary by approximately 10 epsilon units (Nielsen et al., 2017) and there is no *a priori* reason to suggest that the Lower Silurian seawater value was the same as present day seawater. The thallium isotopic compositions of the Anniv East host rock and mineralization are intermediate between continental crustal and modern seawater, with mineralization having less negative values (Fig. 10c). Peter et al. (2018) concluded that the mineralized samples more closely resemble continental crustal values (due to leaching of continental detritus in the basinal sediments by the SEDEX mineralizing fluid), whereas the unmineralized samples reflect deposition under anoxic to euxinic conditions.

The lack of an obvious inverse correlation between the molybdenum and thallium isotopic compositions (Fig. 10a) may relate to differences in the residence sites for both of these metals in the samples. Peter et al. (2018) showed that pyrite is the predominant residence site of thallium in the host rocks and mineralization, with some also resident in white mica. Molybdenum, however, resides in pyrite and organic matter (sub-graphite). More work is required to understand the relationship between the two isotopic systems in our samples and we will investigate this using selective extractions.

Mineralizing fluid control on molybdenum isotopic compositions?

Peter et al. (2018) showed that thallium isotopes were useful in distinguishing thallium introduced by the SEDEX mineralizing fluid (i.e. fingerprinting mineralization); however, the positive element correlations of Mo abundance with Ag (Fig. 8c), Re (Fig. 8e), Te (Fig. 8f), U (Fig. 8g) and V (Fig. 8h) indicate that this mostly redox-sensitive element suite is sourced from seawater, and not the SEDEX mineralizing fluid. Ancillary supporting evidence for this conclusion comes from the hydrogenous trace element suite of Co, Ni, Cu, Se, Mo and Bi of pyrite from the mineralization in the HPD (Gadd et al., 2016a). For this reason, molybdenum isotopes cannot be used to fingerprint SEDEX mineralization.

Conclusions

A bulk geochemical and molybdenum isotopic stratigraphic traverse through a mineralized intersection (and immediate stratigraphic footwall and hanging wall) was conducted in a single drill hole from the Anniv East vent-distal lead-zinc SEDEX deposit in the HPD of the Selwyn Basin, Yukon. Bulk geochemical redox proxies commonly accepted to have the least problems (V, Mo, Re/Mo, Ni/Co, V/Cr, U/Th, Mo/TOC

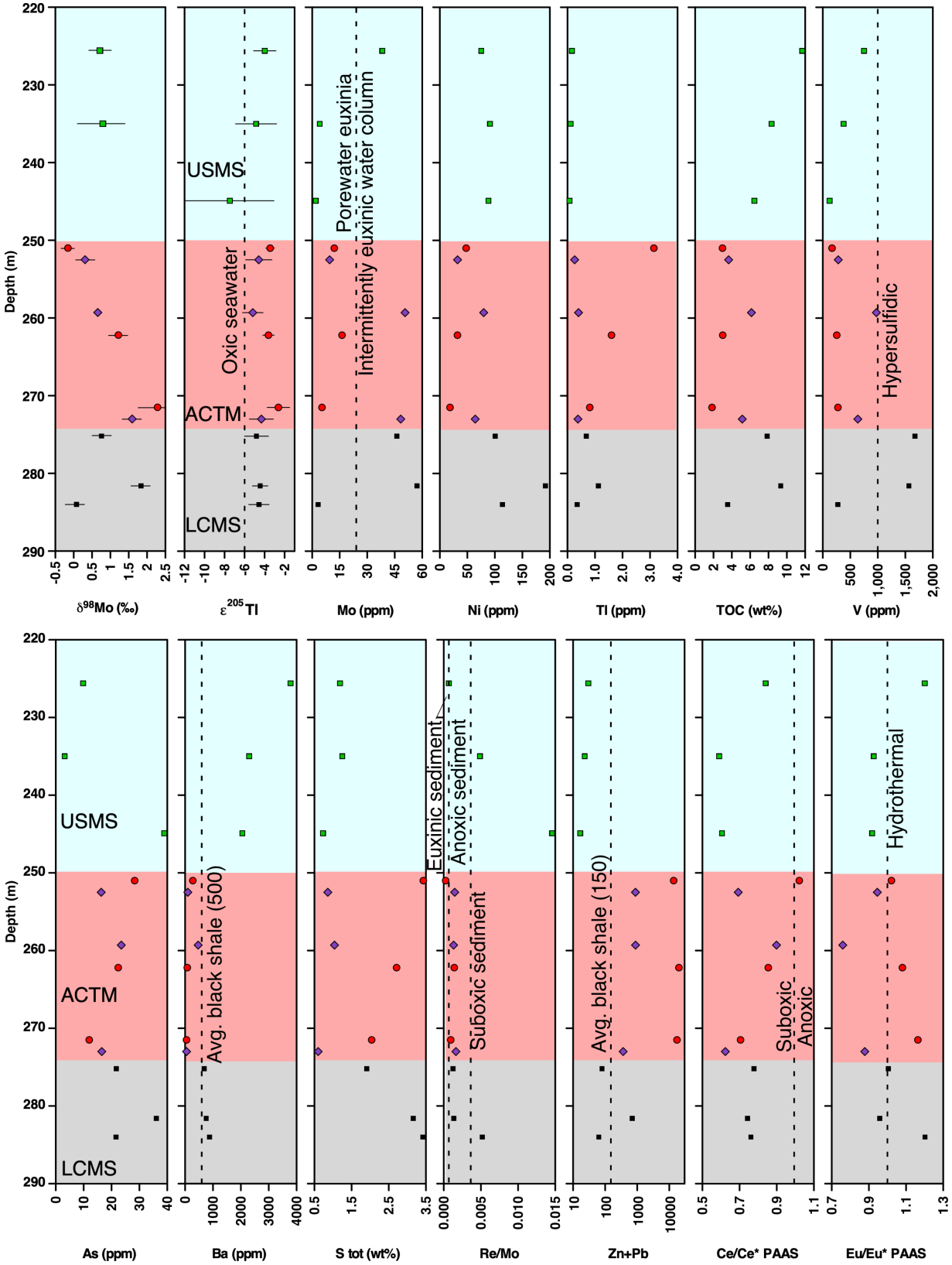

Figure 9. Stratigraphic molybdenum isotope, thallium isotope (Peter et al., 2018) and bulk geochemical profiles for samples from drill hole ANE-108. Black squares = LCMS; purple diamonds = unmineralized ACTM; red circles = mineralized ACTM; green squares = USMS.

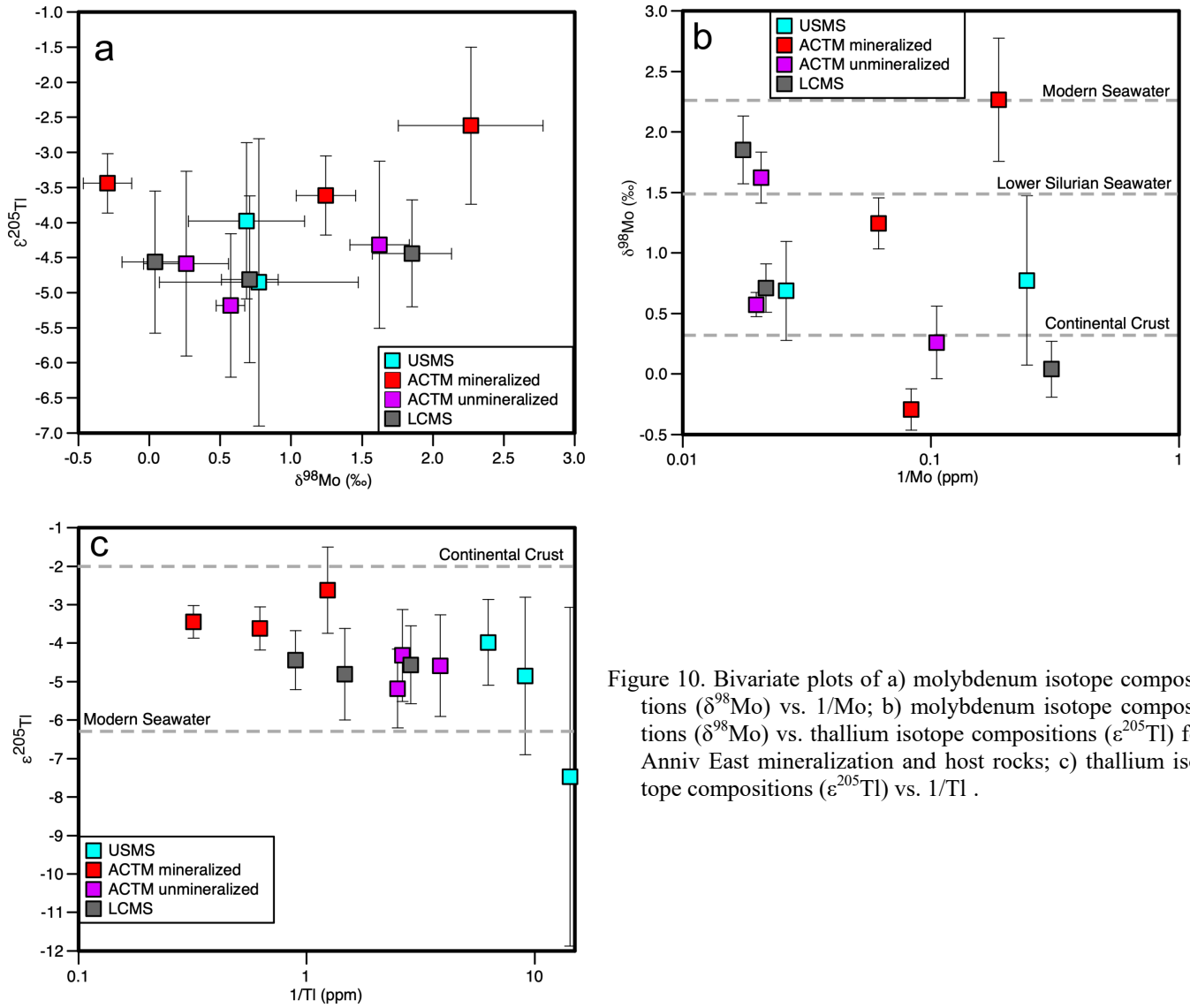

Figure 10. Bivariate plots of a) molybdenum isotope compositions (δ^{98}Mo) vs. 1/Mo; b) molybdenum isotope compositions (δ^{98}Mo) vs. thallium isotope compositions (ε^{205}Tl) for Anniv East mineralization and host rocks; c) thallium isotope compositions (ε^{205}Tl) vs. 1/Tl .

and Ce/Ce*$_{SN}$), though somewhat contradictory amongst each other, generally show that redox conditions varied between suboxic, anoxic, and euxinic (intermittently to permanently). Given our (widely spaced) sample density, we cannot place constraints on the time durations that these disparate conditions existed for. We can conclude, however, that conditions were dynamic over the stratigraphic interval sampled.

Molybdenum isotope compositions of host rocks range from δ^{98}Mo 0.26 to 1.85‰, whereas mineralization ranges from δ^{98}Mo -0.29 to 2.27‰. There is good general agreement between molybdenum isotope values and certain redox sensitive elements (Mo, Ni, Co, Re, V, Cr) and established redox indicators (Mo, Mo/TOC, Ni/Co, V, V/Cr) for the unmineralized and mineralized host rocks, reflecting conditions that ranged from suboxic to anoxic to euxinic. This indicates that the application of molybdenum isotopes as a redox indicator in seafloor hydrothermal deposits in sedimentary (or volcanosedimentary) settings shows great promise. However, unlike thallium isotopes, molybdenum isotopes do not appear to be of use in fingerprinting mineralization in the HPD, as molybdenum was not introduced by the mineralizing fluid.

Acknowledgments

This report is a contribution to NRCan's Targeted Geoscience Initiative Program (TGI). Support for this study was provided through the Volcanic- and Sedimentary-Hosted Base Metal Mineralization Project's '*Activity VS-1.1: Role of anoxia, euxinia and microbes in seafloor hydrothermal sulphide (VMS and SEDEX) deposit formation*'.

The authors thank Jason Dunning, Gabe Xue, Wolfgang Schleiss, and Jelle DeBruyckere of Selwyn Chihong Mining Ltd. for providing access to drill core samples and technical information, without which this work could not have been done. This report benefited from the review of Ian Honsberger and Neil Rogers.

References

Algeo, T.J., 2004. Can marine anoxic events draw down the trace-element inventory of seawater?; Geology, v. 32, p. 1057–1060.

Algeo, T. and Lyons, T., 2006. Mo-total organic carbon covariation in modern anoxic marine environments: Implications for analysis of paleoredox and paleohydrographic conditions; Paleoceanography, v. 21, PA1016, 16 p.

Algeo, T.J. and Maynard, J.B., 2004. Trace-element behaviour and redox facies in core shales of Upper Pennsylvanian Kansas-type cyclothems; Chemical Geology, v. 206, p. 289 –318.

Algeo, T.J. and Rowe, H., 2012. Paleoceanographic applications of trace-metal concentration data; Chemical Geology, v. 324–325, p. 6–18.

Alibo, D.S. and Nozaki, Y., 1999. Rare earth elements in seawater; particle association, shale-normalization, and Ce oxidation; Geochimica et Cosmochimica Acta, v. 63, p. 363 –372.

Anbar, A.D. and Rouxel, O., 2007. Metal stable isotopes in paleoceanography; Annual Review of Earth and Planetary Sciences, v. 35, p. 717–746.

Anbar, A.D. and Gordon, G.W., 2008. Redox renaissance; Geology, v. 36, p. 271–272.

Arnold, G.L., Anbar, A.D., Barling, J., and Lyons, T.W., 2004. Molybdenum isotope evidence for widespread anoxia in mid-Proterozoic oceans; Science, v. 304, p. 87–90.

Barling, J. and Anbar, A.D., 2004. Molybdenum isotope fractionation during adsorption by manganese oxides; Earth and Planetary Science Letters, v. 217, p. 315–329.

Barling, J., Arnold, G., and Anbar, A.D., 2001. Natural mass-dependent variations in the isotopic composition of molybdenum; Earth and Planetary Science Letters, v. 193, p. 447–457.

Bau, M. and Dulski, P., 1996. Distribution of yttrium and rare-earth elements in the Penge and Kuruman iron-formations, Transvaal Supergroup, South Africa; Precambrian Research, v. 79, p. 37–55.

Breillat, N., Guerrot, C., Marcoux, E., and Négrel, P., 2016. A new global database of δ^{98}Mo in molybdenites: a literature review and new data; Journal of Geochemical Exploration, v. 161, p. 1–15.

Breit, G.N. and Wanty, R.B., 1991. Vanadium accumulation in carbonaceous rocks: a review of geochemical controls during deposition and diagenesis: Chemical Geology, v. 91, p. 83–97.

Biswas, K., Woodards, N., Xu, H., and Barton, L., 2009. Reduction of molybdate by sulfate-reducing bacteria; Biometals, v. 22, p. 131–139.

Chappaz, A., Lyons, T.W., Gregory, D.D., Reinhard, C.T., Gill, B.C., Li, C., and Large, R.R., 2014. Does pyrite act as an important host for molybdenum in modern and ancient euxinic sediments?; Geochimica et Cosmochimica Acta, v. 126, p. 112–122.

Chen, X., Ling, H.F., Vance, D., Shields-Zhou, G.A., Zhu, M., Poulton, S.W., Och, L., Jiang, S.-Y., Cremonese, L., and Archer, C., 2015. Rise to modern levels of ocean oxygenation coincided with the Cambrian radiation of animals; Nature Communications, v. 6, 7 p.

Collier, R.W., 1985. Molybdenum in the northeast Pacific Ocean; Limnology and Oceanography, v. 30, p. 1351–1354.

Crusius, J., Calvert, S., Pedersen, T., and Sage, D., 1996. Rhenium and molybdenum enrichments in sediments as indicators of oxic, suboxic and sulfidic conditions of deposition; Earth and Planetary Science Letters, v. 145, p. 65–78.

Dahl, T.W., Anbar, A.D., Gordon, G.W., Rosing, M.T., Frei, R., and Canfield, D.E., 2010a. The behavior of molybdenum and its isotopes across the chemocline and in the sediments of sulfidic Lake Cadagno, Switzerland; Geochimica et Cosmochimica Acta, v. 74, p. 144–163.

Dahl, T.W., Hammarlund, E.U., Anbar, A.D., Bond, D.P., Gill, B.C., Gordon, G.W., Knoll, A.H., Nielsen, A.T., Schovsbo, N.H., and Canfield, D.E., 2010b. Devonian rise in atmospheric oxygen correlated to the radiations of terrestrial plants and large predatory fish; Proceedings of the National Academy of Sciences, v. 107, p. 17 911-17 915.

De Baar, H.J.W., German, C.R., Elderfield, H., and Van Gaans, P., 1988. Rare earth element distributions in anoxic waters of the Cariaco Trench; Geochimica et Cosmochimica Acta, v. 52, p. 1203–1219.

Duan, Y., Anbar, A., Arnold, G., Lyons, T., Gordon, G., and Kendall, B., 2010. Molybdenum isotope evidence for mild environmental oxygenation before the Great Oxidation Event; Geochimica et Cosmochimica Acta, v. 74, p. 6655–6668.

Elderfield, H. and Greaves, M.J., 1982. The rare earth elements in seawater; Nature, v. 296, p. 214–218.

Emerson, S.R. and Huested, S.S., 1991. Ocean anoxia and the concentrations of molybdenum and vanadium in seawater; Marine Chemistry, v. 34, p. 177–196.

Frei, R., Gaucher, C., Poulton, S.W., and Canfield, D.E., 2009. Fluctuations in Precambrian atmospheric oxygenation recorded by chromium isotopes; Nature, v. 461, p. 250–254.

Gadd, M.G., Layton-Matthews, D., Peter, J.M., and Paradis, S.J., 2016a. The world-class Howard's Pass SEDEX Zn-Pb district, Selwyn Basin, Yukon. Part I. trace element compositions of pyrite record input of hydrothermal, diagenetic, and metamorphic fluids to mineralization; Mineralium Deposita, v. 51, p. 319–342.

Gadd, M.G., Layton-Matthews, D., and Peter, J.M., 2016b. Non-hydrothermal origin of apatite in SEDEX mineralization and host rocks of the Howard's Pass district, Yukon, Canada; American Mineralogist, v. 101, p. 1061–1071.

Gadd, M.G., Layton-Matthews, D., Peter, J.M., Paradis, S., and Jonasson, I.R., 2017. The world-class Howard's Pass

SEDEX Zn-Pb district, Selwyn Basin, Yukon. Part II. the roles of thermochemical and bacteria sulphate reduction in metal fixation; Mineralium Deposita, v.52, p. 405–419.

Glass, J., Wolfe-Simon, F., and Anbar, A., 2009. Coevolution of metal availability and nitrogen assimilation in cyanobacteria and algae; Geobiology, v. 7, p. 100–123.

Goldberg, T., Archer, C., Vance, D., and Poulton, S.W., 2009. Mo isotope fractionation during adsorption to Fe (oxyhydr) oxides; Geochimica et Cosmochimica Acta, v. 73, p. 6502–6516.

Goldberg, T., Gordon, G., Izon, G., Archer, C., Pearce, C., McManus, J., Anbar, A., and Rehkämper, M., 2013. Resolution of inter-laboratory discrepancies in Mo isotope data: an intercalibration; Journal of Analytical Atomic Spectrometry, v. 28, p. 724–735.

Goodfellow, W.D., 2004. Geology, genesis and exploration of SEDEX deposits, with emphasis on the Selwyn Basin, Canada; *in* Sediment-hosted lead-zinc sulphide deposits, (ed.) M. Deb and W.D. Goodfellow; Narosa, New Delhi, p. 24–99.

Goodfellow, W.D., 2007. Base metal metallogeny of the Selwyn Basin, Canada; *in* Mineral Resources of Canada: A Synthesis of Major Deposit-types, District Metallogeny, the Evolution of Geological Provinces, and Exploration Methods, (ed.) W.D. Goodfellow; Mineral Deposits Division, Geological Association of Canada, Special Publication 5, p. 553–579.

Goodfellow, W.D. and Jonasson, I.R., 1986. Environment of formation of the Howards Pass (XY) Zn-Pb deposit, Selwyn Basin, Yukon; *in* Mineral Deposits of Northern Cordillera, (ed.) J.A. Morin; Canadian Institute of Mining and Metallurgy, p.19–50.

Goodfellow, W.D. and Lydon, J.W., 2007. Sedimentary-exhalative (SEDEX) deposits; *in* Mineral Deposits of Canada: A Synthesis of Major Deposit-types, District Metallogeny, the Evolution of Geological Provinces, and Exploration Methods, (ed.) W.D. Goodfellow: Mineral Deposits Division, Geological Association of Canada Special Publication 5, p. 163–183.

Gordey, S.P. and Anderson, R.G., 1993. Evolution of the Northern Cordillera Miogeocline, Nahanni map area (105I), Yukon and Northwest Territories; Geological Survey of Canada Memoir 428, 214 p.

Gordon, G.W., Lyons, T.W., Arnold, G.L., Roe, J., Sageman, B.B., and Anbar, A.D., 2009. When do black shales tell molybdenum isotope tales?; Geology, v. 37, p. 535–538.

Greber, N., Siebert, C., Nägler, T., and Pettke, T., 2012. $\delta^{98/95}$Mo values and molybdenum concentration data for NIST SRM 610, 612 and 3134: Towards a common protocol for reporting Mo data; Geostandards and Geoanalytical Research, v. 36, p. 291–300.

Helz, G.R., Miller, C.V., Charnock, J.M., Mosselmans, J.F.W., Pattrick, R.A.D., Garner, C.D., and Vaughan, D.J., 1996. Mechanism of molybdenum removal from the sea and its concentration in black shales: EXAFS evidence; Geochimica et Cosmochimica Acta, v. 60, p. 3631–3642.

Helz, G., Vorlicek, T., and Kahn, M., 2004. Molybdenum scavenging by iron monosulfide; Environmental Science and Technology, v. 38, p. 4263–4268.

Helz, G.R., Bura-Nakic, E., Mikac, N., and Ciglenecki, I., 2011. New model for molybdenum behaviour in euxinic waters; Chemical Geology, v. 284, p. 323–332.

Hodder, R., Bain, D., and Martel, E., 2014. Interpretive structural geology map and cross- sections of the Howard's Pass Pb-Zn district, Yukon and Northwest Territories; Northwest Territories Geoscience Office, Yellowknife, NT, Open File 2014-2002, scale 1:50 000.

Huston, D.L., Sie, S.H., Suter, G.F., Cooke, D.R., and Both, R.A., 1995. Trace elements in sulfide minerals from eastern Australian volcanic-hosted massive sulfide deposits .1. Proton microprobe analyses of pyrite, chalcopyrite, and sphalerite, and .2. Selenium levels in pyrite: Comparison with delta S-34 values and implications for the source of sulfur in volcanogenic hydrothermal systems; Economic Geology, v. 90, p. 1167–1196.

Johnson, C.A., Slack, J.F., Dumoulin, J.A., Kelley, K.D., and Falck, H., 2018. Sulfur isotopes of host strata for Howards Pass (Yukon-Northwest Territories) Zn-Pb deposits implicate anaerobic oxidation of methane, not basin stagnation; Geology, v. 46, p. 619-622.

Jones, B. and Manning, D.A.C., 1994. Comparison of geochemical indices used for the interpretation of palaeoredox conditions in ancient mudstones; Chemical Geology, v. 111, p. 111–129.

Kendall, B., Komiya, T., Lyons, T.W., Bates, SM., Gordon, G. W., Romaniello, S.J., Jiang, G., Creaser, R.A., Xiao, S., McFadden, K., Sawaki, Y., Tahata, M., Shu, D., Han, J., Li, Y., Chu, X., and Anbar, A.D., 2015. Uranium and molybdenum isotope evidence for an episode of widespread ocean oxygenation during the late Ediacaran Period; Geochimica et Cosmochimica Acta, v. 156, p. 173–193.

Kendall, B., Dahl, T.W., and Anbar, A.D., 2017. The stable isotope geochemistry of molybdenum; Reviews in Mineralogy and Geochemistry, v. 82, p. 683–732.

Kennedy, M.J., Pevear, D.R., and Hill, R.J., 2002. Mineral surface control of organic carbon in black shale; Science, v. 295, p. 657-660.

Kirkham, G., Dunning, J., and Schleiss, W., 2012. Update for Don deposit mineral resource estimate, Howard's Pass property, eastern Yukon; Selwyn Resources Ltd., NI 43–101 Technical Report. 145 p.

Kurzweil, F., Wille, M., Schoenberg, R., Taubald, H., and Van Kranendonk, M., 2015. Continuously increasing δ^{98}Mo values in Neoarchean black shales and iron formations from the Hamersley Basin; Geochimica et Cosmochimica Acta, v. 164, p. 523–542.

Large, R.R., Halpin, J.A., Danyushevsky, L.V., Maslennikov, V.V., Bull, S.W., Long, J.A., Gregory, D.D., Lounejeva, E., Lyons, T.W., Sack, P.J., McGoldrick, P.J., and Calver, C.R., 2014. Trace element content of sedimentary pyrite as a new proxy for deep-time ocean–atmosphere evolution; Earth and Planetary Science Letters, v. 389, p. 209–220.

Magnall, J.M., Stern, R., Gleeson, S.A., and Paradis, S., 2015, Widespread euxinic conditions are not a prerequisite for sediment-hosted base metal (Pb-Zn-Ba) mineralization at Macmillan Pass, Yukon; *in* Targeted Geoscience Initiative 4: Sediment-hosted Zn-Pb Deposits: Processes and Implications for Exploration, (ed.) S.J. Paradis, Geological Survey of Canada Open File 7838: Ottawa, Ontario, p. 43–57.

Magnall, J.M., Gleeson, S.A., Stern, R.A., Newton, R.J., Poulton, S.W., and Paradis, S., 2016. Open system sulphate reduction in a diagenetic environment – Isotopic analysis of barite ($\delta^{34}S$ and $\delta^{18}O$) and pyrite ($\delta^{34}S$) from the Tom and Jason Late Devonian Zn–Pb–Ba deposits, Selwyn Basin, Canada; Geochimica et Cosmochimica Acta, v. 180, p. 46–163.

Magnall, J.M., Gleeson, S.A., Poulton, S.W., Gordon, G.W., and Paradis, S., 2018. Links between seawater paleoredox and the formation of sediment-hosted massive sulphide (SHMS) deposits — Fe speciation and Mo isotope constraints from Late Devonian mudstones; Chemical Geology, v. 490, p. 45–60.

Mayer, A. and Wieser, M., 2014. The absolute isotopic composition and atomic weight of molybdenum in SRM 3134 using an isotopic double spike; Journal of Analytical Atomic Spectrometry, v. 29, p. 85–94.

McManus, J., 2002. Oceanic molybdenum isotope fractionation: Diagenesis and hydrothermal ridge-flank alteration; Geochemistry, Geophysics, Geosystems, v. 3, p. 1–9.

Morganti, J.M. 1979. The geology and ore deposits of the Howards Pass area, Yukon and Northwest Territories: the origin of basal sedimentary stratiform sulphide deposits; Ph.D. thesis, University of British Columbia, Vancouver, British Columbia, 351 p.

Nägler, T., Anbar, A., Archer, C., Goldberg, T., Gordon, G., Greber, N., Siebert, C., Sohrin, Y., and Vance, D., 2014. Proposal for an international molybdenum isotope measurement standard and data representation; Geostandards and Geoanalytical Research, v. 38, p. 149–151.

Nakagawa, Y., Takano, S., Firdaus, M., Norisuye, K., Hirata, T., Vance, D., and Sohrin, Y., 2012. The molybdenum isotopic composition of the modern ocean; Geochemical Journal, v. 46, p. 131–141.

Nielsen, S.G. and Rehkämper, M., 2011. Thallium isotopes and their application to problems in earth and environmental science; *in* Handbook of Environmental Isotope Geochemistry: Advances in Isotope Geochemistry, (ed.) M. Baskaran; Berlin, Germany, Springer-Verlag, p. 247–269.

Nielsen, S.G., Rehkämper, M., Baker, J., and Halliday, A.N., 2004. The precise and accurate determination of thallium isotope compositions and concentrations for water samples by MC-ICPMS; Chemical Geology, v. 204, p. 109–124.

Nielsen, S.G., Rehkämper, M., Teagle, D.A.H., Butterfield, D.A., Alt, J.C., and Halliday, A.N., 2006. Hydrothermal fluid fluxes calculated from the isotopic mass balance of thallium in the ocean crust; Earth and Planetary Science Letters 251, 120–133.

Nielsen, S.G., Goff, M., Hesselbo, S.P., Jenkyns, H.C., LaRowe, D.E., and Lee, C.T.A., 2011. Thallium isotopes in early diagenetic pyrite - A paleoredox proxy?; Geochimica et Cosmochimica Acta, v. 75, p. 6690–6704.

Nielsen, S.G., Rehkämper, M., and Prytulak, J., 2017. Investigation and Application of thallium isotope fractionation; Reviews in Mineralogy and Geochemistry, v. 82, p. 759–798.

Norford, B. and Orchard, M., 1985. Early Silurian age of rocks hosting lead-zinc mineralization at Howards Pass, Yukon Territory and District of Mackenzie; Geological Survey of Canada Paper 83-18, 35 p.

Owens, J.D., Nielsen, S.G., Horner, T.J., Ostrander, C.M., and Peterson, L.C., 2017. Thallium-isotopic compositions of euxinic sediments as a proxy for global manganese-oxide burial; Geochimica et Cosmochimica Acta, v. 213, p. 291–307.

Partin, C., Bekker, A., Planavsky, N., and Lyons, T., 2015. Euxinic conditions recorded in the ca. 1.93 Ga Bravo Lake Formation, Nunavut (Canada): implications for oceanic redox evolution; Chemical Geology, v. 417, p. 148–162.

Pearce, C.R., Cohen, A.S., and Parkinson, I.J., 2009. Quantitative separation of molybdenum and rhenium from geological materials for isotopic determination by MC-ICP-MS; Geostandards and Geoanalytical Research, v. 33, p. 219–229.

Peter, J.M., Gadd, M.G., Layton-Matthews, D., and Voinot, A., 2018. Reconnaissance thallium isotope geochemistry study of SEDEX mineralization and host rocks in the Howard's Pass district, Selwyn Basin, Yukon: Potential application to paleoredox determinations and fingerprinting of mineralization; *in* Targeted Geoscience Initiative: 2017 report of activities, volume 1, (ed.) N. Rogers; Geological Survey of Canada, Open File 8358, p. 173–191.

Poulson, R.L., Siebert, C., McManus, J., and Berelson, W.M., 2006. Authigenic molybdenum isotope signatures in marine sediments; Geology, v. 34, p. 617–620.

Raiswell, R., Buckley, F., Berner, R.A., and Anderson, T.F., 1988. Degree of pyritization of iron as a paleoenvironmental indicator of bottom-water oxygenation; Journal of Sedimentary Petrology, v. 58, p. 812–819.

Rehkämper, M., Frank, M., Hein, J.R., Porcelli, D., Halliday, A., Ingri, J., and Liebetrau, V., 2002. Thallium isotope variations in seawater and hydrogenetic, diagenetic, and hydrothermal ferromanganese deposits; Earth and Planetary Science Letters, v. 197, p. 65–81.

Ross, D.J.K. and Bustin, R.M., 2009. Investigating the use of

sedimentary geochemical proxies for paleoenvironment interpretation of thermally mature organic-rich strata: examples from the Devonian-Mississippian shales, western Canada sedimentary basin; Chemical Geology, v. 260, p. 1–19.

Saez, R., Moreno, C., González, F., and Amodódovar, G., 2011. Black shales and massive sulfide deposits: causal or casual relationships? Insights from Rammelsberg, Tharsis, and Draa Sfar; Mineralium Deposita, v. 46, p. 585–614.

Sarmiento, J. and Gruber, N., 2006. Ocean Biogeochemical Dynamics; Princeton University Press, New Jersey, 528 p.

Saxena, R., Jain, M., and Mittal, M., 1968. Electrometric investigations of an acid-thiomolybdate system and the formation of polyanions; Australian Journal of Chemistry, v. 21, p. 91–96.

Scott, C. and Lyons, T., 2012. Contrasting molybdenum cycling and isotopic properties in euxinic versus non-euxinic sediments and sedimentary rocks: refining the paleoproxies; Chemical Geology, v. 324–325, p. 9–27.

Scott, C., Lyons, T.W., Bekker, A., Shen, Y., Poulton, S.W., Chu, X., and Anbar, A.D., 2008. Tracing the stepwise oxygenation of the Proterozoic ocean; Nature, v. 452, p. 456–460.

Scott, C., Slack, J., and Kelley, K., 2013, The origin of vanadium hyper-enriched black shales: Geological Society of America Abstract and Program, v. 45, p. 427.

Scott, C., Slack, J., and Kelley, K., 2017. The hyper-enrichment of V and Zn in black shales of the Late Devonian-Early Mississippian Bakken Formation (USA); Chemical Geology, v. 452, p. 24–33.

Siebert, C., Nägler, T.F., von Blanckenburg, F., and Kramers, J.D., 2003. Molybdenum isotope records as a potential new proxy for paleoceanography; Earth and Planetary Science Letters, v. 211, p. 159–171.

Siebert, C., McManus, J., Bice, A., Poulson, R.L., and Berelson, W., 2006. Molybdenum isotope signatures in continental margin sediments; Earth and Planetary Science Letters, v. 241, p. 723–733.

Slack, J.F., Falck, H., Kelley, K.D., and Xue, G.G., 2017. Geochemistry of host rocks in the Howards Pass district, Yukon -Northwest Territories, Canada: implications for sedimentary environments of Zn-Pb and phosphate mineralization; Mineralium Deposita, v. 52, p. 565–593.

Song, S., Hu, K., Wen, H., Zhang, Y., Li, K., and Fan, H., 2011. Molybdenum isotopic composition as a tracer for low -medium temperature hydrothermal ore-forming systems: A case study on the Dajiangping pyrite deposit, western Guangdong Province, China; Chinese Science Bulletin, v. 56, p. 2221–2228.

Taylor, S.R. and McLennan, S.M., 1985. The Continental Crust: its composition and evolution; Oxford, Blackwell Scientific Publications, 312 p.

Taylor, B. and Beaudoin, G., 2000. Sulphur isotope stratigraphy of the Sullivan Pb-Zn-Ag deposit, B.C.: Evidence for hydrothermal sulphur, and bacterial and thermochemical sulphate reduction; *in* The Geological Environment of the Sullivan deposit, British Columbia, (ed.) J. Lydon, T. Höy, J. Slack and M. Knapp; Mineral Deposits Division, Geological Association of Canada, p. 696–719.

Tribovillard, N., Algeo, T., Lyons, T., and Riboulleau, A., 2006. Trace metals as paleoredox and paleoproductivity proxies: An update; Chemical Geology, v. 232, p. 12–32.

Tyson, R.V., 2001. Sedimentation rate, dilution, preservation and total organic carbon: some results of a modelling study; Organic Geochemistry, v. 32, p. 333-339.

Voegelin, A., Pettke, T., Greber, N., von Niederhäusern, B., and Nägler, T., 2014. Magma differentiation fractionates Mo isotope ratios: evidence from the Kos Plateau Tuff (Aegean Arc); Lithos, v. 190, p. 440–448.

Wasylenki, L.E., Rolfe, B.A., Weeks, C.L., Spiro, T.G., and Anbar, A., 2008. Experimental investigation of the effects of temperature and ionic strength on Mo isotope fractionation during adsorption to manganese oxides; Geochimica et Cosmochimica Acta, v. 72, p. 5997–6005.

Wille, M., Nebel, O., Van Kranendonk, M., Schoenberg, R., Kleinhanns, I., and Ellwood, M., 2013. Mo-Cr isotope evidence for a reducing Archean atmosphere in 3.46-2.76 Ga black shales from the Pilbara, Western Australia; Chemical Geology, v. 340, p. 68–76.

Wright, J., Schrader, H., and Holser, W.T., 1987. Paleoredox variations in ancient oceans recorded by rare earth elements in fossil apatite; Geochimica et Cosmochimica Acta, v. 51, p. 631–644.

Yukon Geological Survey, 2012. Yukon Minfile 105I 037: Anniv deposits; Yukon Geological Survey. <http://data.geology.gov.yk.ca/Occurrence/DownloadOccurrenceDirect/13393> [accessed January 21, 2019]

Application of pyrite chemistry to recognize a distal expression of hydrothermal activity in the MacMillan Pass SEDEX district, Yukon

C. Leighton[1], D. Layton-Matthews[1], J.M. Peter[2] and M.G. Gadd[2]

[1]*Department of Geological Sciences and Geological Engineering, Queen's University, 36 Union Street, Kingston, Ontario K7L 3N6*

[2]*Geological Survey of Canada, 601 Booth Street, Ottawa, Ontario K1A 0E8*

Abstract

The Tom and Jason sedimentary exhalative (SEDEX) Pb-Zn-Ag-(Ba) deposits in Yukon grade 7.4 weight % and 7.0 weight % Zn, and 6.5 weight % and 4.6 weight % Pb, with zinc and lead tonnages of 15.7 and 10.1 Mt, respectively. Pyrite is ubiquitous in SEDEX deposits and can potentially reveal much information about the environment and nature of deposition, hydrothermal fluid properties, genesis of mineralization, and may provide vectors toward mineralization. Pyrite-bearing samples from three drillholes situated 2 to 4 km from mineralization (but time-stratigraphically equivalent) were sampled, and four generations of pyrite were identified (Py1, Py2, Py3, Py4), each with distinct morphological characteristics and mineralogical associations. Synsedimentary (Py1), diagenetic (Py2), hydrothermal (Py3) and metamorphic (Py4) morphologies were identified. A representative subset of pyrite grains was analyzed for trace element contents by laser ablation-inductively coupled plasma mass spectrometry using raster grids to create quantitative trace element composition maps, in order to characterize the trace element composition of each pyrite generation.

A distal (2–4 km) expression of hydrothermal mineralization is recognized in Py3, which displays mineral associations and a trace element assemblage typical of hydrothermally precipitated pyrite. The trace element geochemistry of pyrite distal to SEDEX mineralization (and time-stratigraphically equivalent to it) displays enrichment in Zn, Mn, As and Co, and these elements are generally more abundant in Py3 than other generations, indicating the presence of nearby concealed mineralization.

Introduction

The Selwyn Basin hosts stratiform sedimentary exhalative (SEDEX) deposits in the Howard's Pass, Anvil and MacMillan Pass districts. The MacMillan Pass Pb-Zn-Ag-(Ba) district hosts the Tom and Jason deposits, which are the product of precipitation from hydrothermal brines exhaled along faults, on or near the seafloor in a sedimentary basin (Goodfellow and Lydon, 2007). The deposits contain base metal sulphides, including pyrite, sphalerite and galena. The Tom and Jason deposits grade 7.4 weight % and 7.0 weight % Zn, and 6.5 weight % and 4.6 weight % Pb, respectively, with zinc and lead tonnages of 15.7 and 10.1 Mt, respectively (Goodfellow and Lydon, 2007) (Fig. 1).

There are two end members of SEDEX deposits – vent-distal and vent-proximal; the Tom and Jason deposits belong to the latter (Goodfellow, 2007). The deposits have the four facies characteristic of vent-proximal deposits: bedded sulphides, vent complex, sulphide stringer zone and distal hydrothermal sediments. Most of the minerals of economic importance are hosted in the vent complex and bedded sulphide facies, near the fault-related upflow zone (Goodfellow, 2007). Thinly bedded distal hydrothermal deposition is characteristic of vent-proximal deposits. The bedded facies is present 1 to 2 km from the Tom and Jason vents (Goodfellow, 2007). Pyrite is ubiquitous in all SEDEX mineralization facies, making it potentially valuable for vectoring studies. Herein, we evaluate the use of trace elements variability in pyrite as a tool for vectoring toward mineralization.

Pyrite can reveal much information about the environment and nature of deposition, hydrothermal fluid properties, and genetic processes of SEDEX deposit formation (Goodfellow, 2007; Gadd et al., 2016; Large et al., 2017). The textural and geochemical characteristics and genesis of pyrite in marine sedimentary settings are influenced by ambient and subsurface diagenetic conditions. Consequently, pyrite can be used as an archive of paleo-environmental or paleo-ocean environmental conditions (Large et al., 2017).

Pyrite sequesters ambient trace elements into its chemical structure, and the resultant trace element composition of pyrite is controlled by the fluid composition from which it precipitates (Berner et al., 2013). The trace elements sequestered from seawater into sedimentary and diagenetic pyrite can act as paleo-environmental proxies for atmospheric or oceanic O_2 content (Mo, U, V, Se), marine nutrients (Mo, Cd, Zn, Se, Cu,

Corresponding author: Claire Leighton (claireleighton95@gmail.com)

Leighton, C., Layton-Matthews, D., Peter, J.M., and Gadd, M.G., 2019. Application of pyrite chemistry to recognize a distal expression of hydrothermal activity in the MacMillan Pass SEDEX district, Yukon; *in* Targeted Geoscience Initiative: 2018 report of activities, (ed.) N. Rogers; Geological Survey of Canada, Open File 8549, p. 125–137. https://doi.org/10.4095/313646

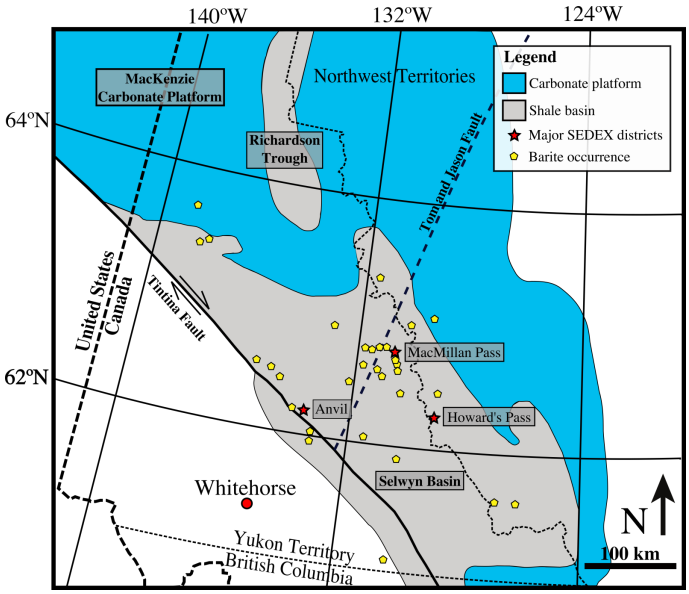

Figure 1. Simplified geological map of the Selwyn Basin, Yukon, showing the locations of major SEDEX districts and barite occurrences. *Modified from* Goodfellow (2007) and Magnall et al. (2015).

Ni) and ocean pH (Ag, Cd) (Gregory et al., 2015; Large et al., 2017). SEDEX deposits contain hydrothermal pyrite with a trace element composition that is representative of the metal content of the hydrothermal fluids from which it precipitated (Gadd et al., 2016). Sedimentary, hydrothermal and metamorphic pyrite can all comprise the same mineral grain if overgrowth occurs, and trace element compositions and textures will be different for each generation. Therefore, pyrite, particularly with multiple generations, can be used to decipher the history of its formation, including mineralizing processes. We examine pyrite textures and chemical compositions from the MacMillan Pass SEDEX district to elucidate the hydrothermal history of the area following the examples of Gadd et al. (2016) and Magnall et al. (2016).

We aim to determine the morphologies, textures, paragenesis and the trace element compositions of pyrite grains from unmineralized, time-stratigraphically equivalent rocks located 2 to 4 km along strike from SEDEX mineralization in MacMillan Pass district Yukon (Fig. 1). Key objectives are to characterize the multiple generations of pyrite and determine if pyrite records a distal (i.e. 2–4 km from mineralization) expression of mineralizing hydrothermal activity.

Regional geology

The Tom and Jason deposits are hosted by Late Devonian to Early Mississippian carbonaceous and siliciclastic marine basinal strata. Immediate host rocks are sedimentary diamictite breccia and basinal black shale and mudstone of the MacMillan Pass and Tom Members of the Lower Earn Group (Abbott and Turner, 1991) (Fig. 2).

The Tom and Jason deposits are within the Central Block of the 125 km long MacMillan Fold Belt (MFB) (Abbott and Turner, 1991). The MFB is a structural anomaly within the broader Selwyn and Mackenzie fold belts. The MFB is a Mesozoic deformational feature that dominates the MacMillan Pass, and has driven the formation of west-northwest-trending folds, caused stratigraphic dismemberment of Earn Group rocks, and deformed the Tom deposit into an anticline structure (Fig. 2a), such that mineralized horizons are within tight, upright folds (Abbott and Turner, 1991).

Mineralization and faulting at the MacMillan Pass are considered coeval with local sedimentation, and therefore an age of the host rock provides an age of the mineralizing hydrothermal event (Goodfellow, 2007). The age of the MacMillan mineralization is Frasnian (372–383 Ma), based on conodonts in host chert-pebble conglomerate and chert grit clasts from the Tom West Zone (Fig. 2a; Irwin and Orchard, 1991).

Pyrite-bearing drill cores (drilled by Hudson Bay Exploration and Development Ltd.) were previously collected from eight holes drilled in and around the Tom and Jason deposits (Fig. 2a). The pyrite and matrix in the drill cores were analyzed with a handheld and benchtop X-ray fluorescence analyzer (pXRF), logged and sampled for whole-rock geochemistry (Peter et al., 2015). Pb-Zn-Ag SEDEX mineralization (intersected in drillholes TYK-001, TYK-005, TS-009, TS91-014) can be identified in whole-rock and pXRF geochemistry. Mineralized intervals displayed clear spikes in Mn, Ag, Ba, Zn, Pb, Ti, V and Sn content (Fig. 3), moderate spikes in Ca, Ni, Cu, Tl Sb, P, Hg, Cl, Cd, Sr, Pt, Au and REEs, and a depletion (relative to background) in K, Zr and Rb.

Distal drillholes (JS76-017, TS91-019, JS76-008) do not intersect Pb-Zn mineralization. Whole-rock and pXRF data from these barren drill cores were inspected to determine if there is a similar geochemical expression to that observed in the mineralized intervals in distal drillholes (Fig. 3). Of the elements that were enriched in the mineralized interval in drillhole TYK-001, few elements (Ba, Ag, V, Cr, Sn) display enrichments in distal holes. Vanadium and Cr are redox-sensitive elements, and are likely to be scavenged from seawater; Sn is typically sourced from sediments (Large et al., 2017). Silver may relate to hydrothermal mineralization (Magnall et al., 2016). Barium is not intrinsically related to hydrothermal activity; barite is related to slightly older mineralization (Magnall et al., 2015, 2016). However, barite is significant because it can provide a source of sulphur and is an important mechanism of sulphide formation through replacement, as at Red Dog (Kelley et al., 2004) and MacMillan Pass (Magnall et al., 2016).

Methods

Pyrite-bearing rocks were sampled from three drill cores (TS91-019, JS76-017 and JS76-008) to investigate a possible distal expression of hydrothermal (Pb-Zn mineralization) activ-

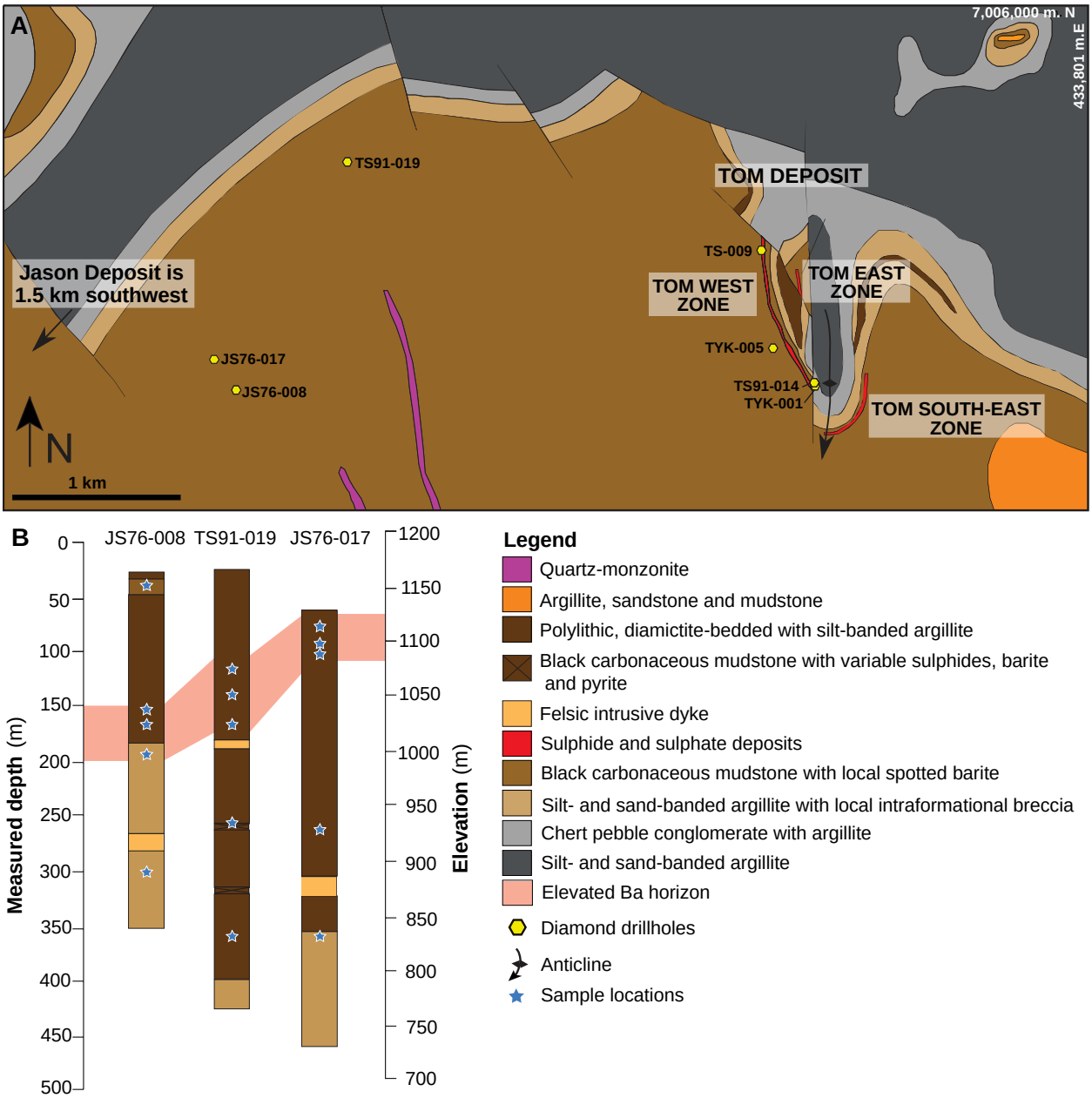

Figure 2. a) Simplified geological map of the MacMillan Pass SEDEX district, focused on the Tom deposit area. Locations of diamond drillhole that were sampled are shown. b) Stratigraphy of the drillholes sampled for this study. *Modified from* Peter et al. (2015).

ity (Fig. 2b).

Fifteen polished thin sections were made (five from each drillhole), at 20 ± 10 m spacing within high Ba horizons and 100 ± 10 m spacing outside these horizons (Fig. 2b).

Polished thin sections were studied using optical light and scanning electron microscopy to determine mineralogy and to classify pyrite textures and paragenesis (Fig. 2b). Geochemical analyses for trace elements were performed at the Queen's University Facility for Isotope Research using a ThermoScientific X Series 2® quadrupole inductively coupled plasma mass spectrometry (ICP-MS) coupled to a New Wave/ESI 193-nm ArF Excimer laser system. A representative subset of pyrite grains was analyzed for trace element contents by laser ablation-inductively coupled plasma mass spectrometry (LA-ICPMS) using raster grids (20–50 µm beam diameter, 70–100% energy, 10 Hz laser rate, 5 s laser warm-up, 10 s wash-out delay and beam fluence of 5–10 J/cm^2) to create quantitative trace element composition maps. Sets of pyrite analyses were bracketed by analyses of National Institute of Standards

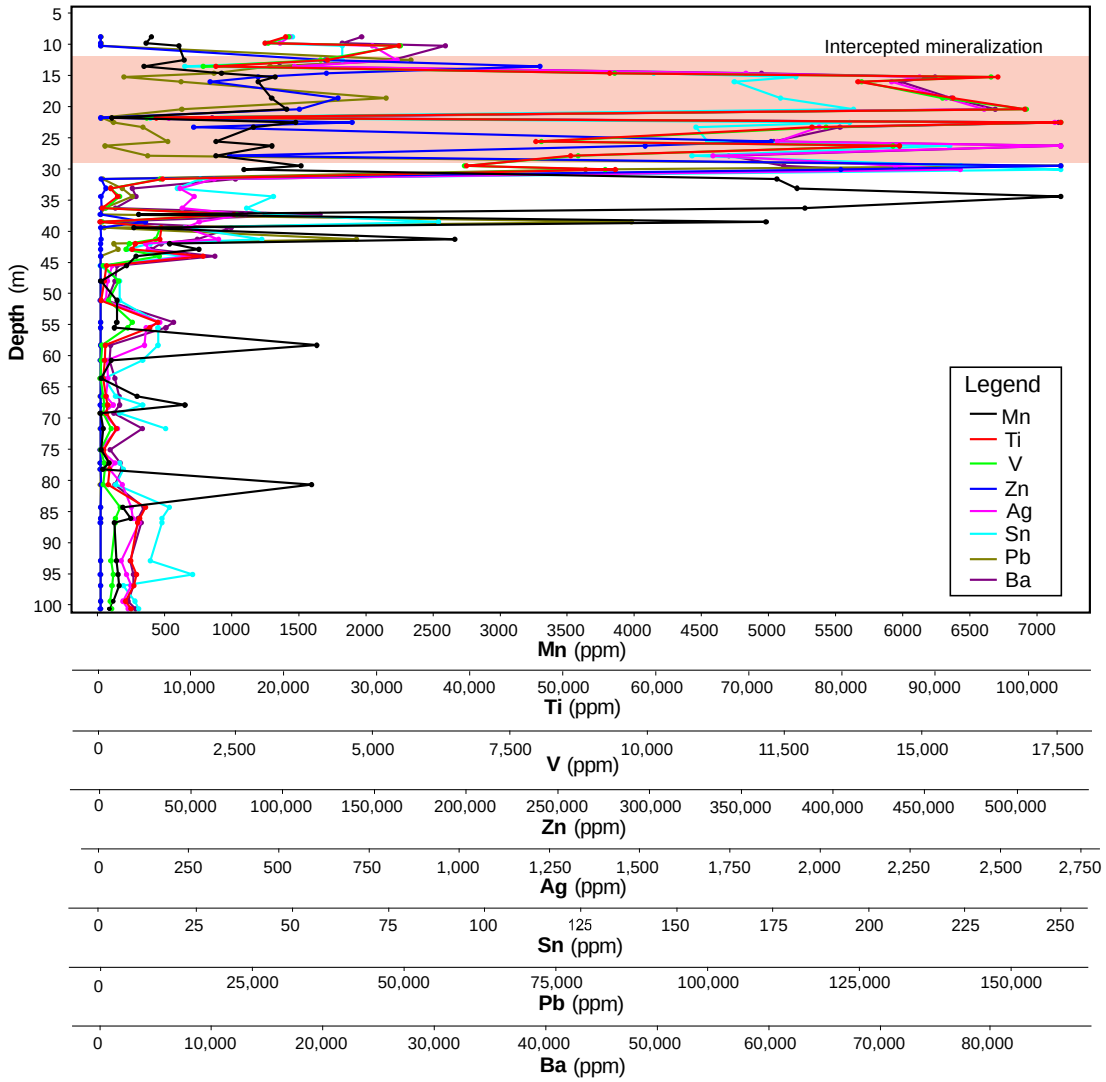

Figure 3. Downhole geochemistry of matrix in drill core TYK-001 by pXRF (location shown in Fig. 2a) that shows high Mn, Ti, V, Zn, Ag, Sn, Pb and Ba in the mineralized horizon (5–28 m depth).

and Technology (NIST) 614, NIST 612, MASS 1, BHVO-2G and BCR2G standards to calibrate the results and to correct for analytical drift, elemental bias and laser yield. Raw LA-ICPMS data in counts per second were converted to parts per million (ppm) using Iolite 4.0 (Paton et al., 2011). Detection limits varied depending on the spot size of the laser. Principal component analysis (PCA) was applied to pyrite trace element data using the PCA routine in ioGAS. Trace element abundances that were below detection were assigned a value of half detection for statistical analyses.

Pyrite generations and paragenesis

Scanning electron, reflected light and transmitted light microscopic investigations of fifteen polished thin sections (Fig. 2b) revealed four generations of pyrite: Py1, Py2, Py3 and Py4 (Table 1; Fig. 4).

Framboidal Py1 pyrite is the earliest formed generation (Table 1) and the range of framboid sizes (approximately 5–50 µm) indicate formation from H_2S-bearing seawater within shallow, unconsolidated sediments and/or within the water column during syngenesis or in early diagenesis (Fig. 4a; Berner et al., 2013). Py1 pyrite is present throughout all unmineralized mudstones at all depths. Magnall et al. (2016) identified an early generation of anhedral, interstitial to microcrystalline quartz and less than 25 µm barite crystals that occur as replacements in mudstone beds.

Py2 pyrite overprints the framboid-bearing matrix and has a sooty (inclusion-rich, framboid-bearing) texture, indicating it is later than Py1 (Fig. 4a). Pyrite Py2 formed from H_2S-bearing sediment porewaters during diagenesis.

Hydrothermal Py3 pyrite is only identified in high-Ba horizons (Fig. 2b) and is characterized by the minerals that co-

Table 1. Pyrite generations with their key textural features described.

Generation	**Synsedimentary pyrite** (Py1)	**Diagenetic pyrite** (Py2)	**Hydrothermal pyrite** (Py3)	**Metamorphic pyrite** (Py4)
Texture	Framboidal, poly-framboid, aggregates, micro-crystals, arranged along bedding planes; ubiquitous	Anhedral, nodular, ragged edges, sooty, inclusion-rich, commonly overgrown, overprints Py1 and matrix; ubiquitous	Variable morphology (anhedral – subhedral), can be disseminated or in veins, sooty, inclusion-rich, in high-Ba horizons	Euhedral, in veins, overgrowth texture, veins, pressure shadows, aligned with tectonic fabric, inclusion-free, cuts bedding; ubiquitous
Size	<50 µm	50 – 3000 µm	100 – 2000 µm	100 – 3000 µm
Inferred origin	Early diagenetic and/or syngenetic	Late diagenetic	Hydrothermal	Metamorphic

precipitated with it, such as chlorite, sphalerite, monazite, epidote, Ba-feldspar and barite (Fig. 4d). Py3 and these associated minerals form veins that crosscut Py1- and Py2-bearing bedding (Fig. 4d, f), indicating it is later stage (Fig. 5).

It is possible early forming diagenetic barite was dissolved when hot hydrothermal fluids interacted with the host rock. Onset of hydrothermal activity would have increased the temperature of the system and promoted barite dissolution, due to change in the solubility of barite from prograde to retrograde at 100°C (Bowers et al., 1985). This process leached sulphur from diagenetic barite into the mineralizing fluid. Sulphur and barium availability in the fluid creates a chemical trap for Pb-Zn-

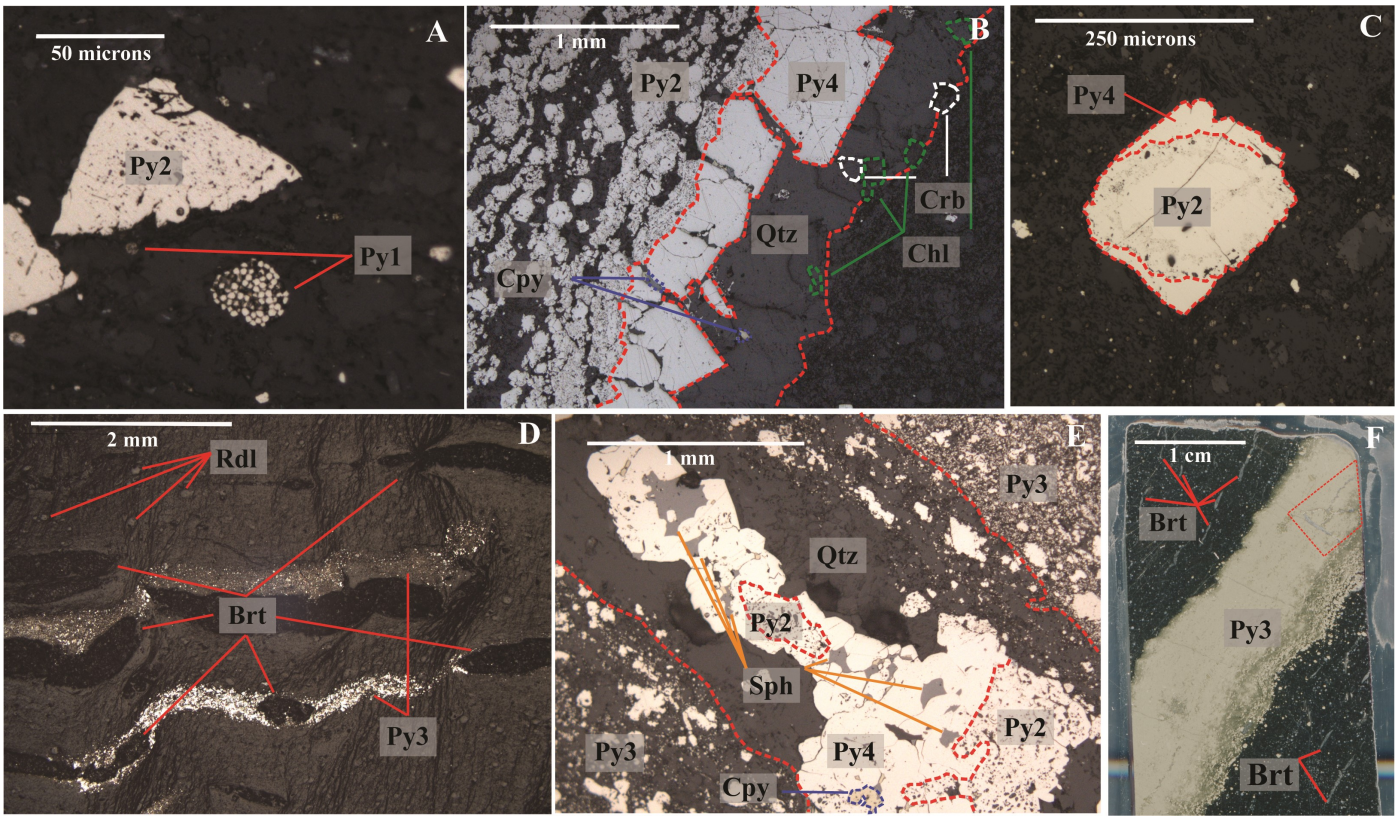

Figure 4. Reflected light photomicrographs of pyrite generations and associated minerals. a) Large Py1 framboid with nearby Py1 and Py2 grain, surrounded by matrix (DDH TS91-019, 358 m). b) Disseminated Py2 in a vein, overgrown by euhedral Py4, within a coat of recrystallized quartz, fringed by chlorite and minor chalcopyrite (DDH JS76-008, 194 m). c) Nodular Py2 grain overgrown by euhedral Py4 (DDH TS91-019, 162 m). d) Py3 and barite intergrown in veins that crosscut bedding; minor sphalerite within disseminated Py3 and radiolarians in the matrix (DDH TS91-019, 137.1 m). e) Py2 grain overgrown by Py4 and fringed by a quartz vein that is within an area of disseminated Py3. Minor chalcopyrite and sphalerite intergrowths (DDH JS76-008, 194 m). f) Polished thin section showing barite veins within a shale matrix, and a Py3 vein that is cut by late-stage quartz (associated with Py4) in the red box (DDH JS76-008, 165.8 m). Abbreviations: Brt – barite; Chl – chlorite; Cpy – chalcopyrite; Crb – carbonate; Py1 – synsedimentary pyrite; Py2 – diagenetic pyrite; Py3 – hydrothermal pyrite; Py4 – metamorphic pyrite; Qtz – quartz; Rdl – radiolaria; Sph – sphalerite.

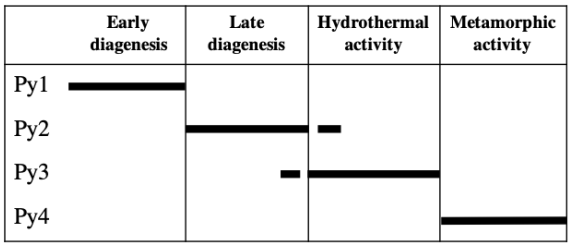

Figure 5: Paragenesis of pyrite at the MacMillan Pass. Abbreviations: Py1 = synsedimentary pyrite; Py2 = diagenetic pyrite; Py3 = hydrothermal pyrite; Py4 = metamorphic pyrite.

Ag sulphide mineralization, forming recrystallized barite, Py3 pyrite and minor (<500 µm) sphalerite (Fig. 4e) (Magnall et al., 2016). Scanning electron microscope (SEM) analysis reveals that galena and Ag-sulphosalts are minor constituents in samples from the high-Ba intervals. The minor occurrence of sulphide minerals (other than pyrite) is the distal expression of SEDEX Pb-Zn-Ag mineralization. It is possible the high-Ba horizons in distal drillholes (Fig. 2a) represent a change in the thermal regime (and resultant change in barite solubility) concomitant with the hydrothermal activity that formed the nearby Tom and Jason deposits.

Py4 pyrite is late-stage and is associated with recrystallized quartz, phyllosilicate minerals (muscovite, chlorite, paragonite) (Fig. 4b), minor chalcopyrite (<100 µm; Fig. 4b) and Fe-oxide (Fig. 6). Py4 is interpreted to be metamorphic in origin because it is associated with quartz-filled (and minor carbonate) pressure shadows and veins that are fringed by mica minerals (dominantly chlorite), and the quartz has a texture that is typical of low-grade (sub-greenschist) metamorphism (Fig. 4b, 6) (Magnall et al., 2015). Py4 occurs as euhedral crystals and overgrowths on previous generations, particularly common Py2 (Fig. 4b, c, 6). The formation of Py4 may have involved the dissolution of Fe and S from pre-existing pyrite (Py1 and Py2) during metamorphism, after which the available iron and sulphur recombined to form Py4. During this metamorphism, inclusions loosely held in the pyrite structure were expelled, and this resulted in the inclusion-free (or 'clean') morphology of Py4 (Fig. 7).

Deformed pyrite and quartz pressure shadows (Fig. 6) preserve evidence for compressive stresses. The principal stress (S1) is compressive and horizontal, and the direction of least stress (S3) is perpendicular and vertical (S3) (Fig. 7). Compression (or metamorphism) drives the pressure solution of Fe and S from Py2, and these elements migrate and recrystallize along the S3 axis, where there is less stress, as euhedral Py4 and Fe-oxide surrounded by a quartz pressure shadow. These features are present throughout all distal unmineralized rocks that were sampled in this study (Fig. 2b).

The lithological units sampled are hosted in the Earn Group, which is within in the Mackenzie Fold Belt deformation structure; hence, it is unsurprising that evidence of deformation is observed at a microscopic scale in these samples. Ansdell et al. (1989) also identified post-mineralization quartz veins that crosscut mineralization and host rocks in the MacMillan Pass area. Additionally, quartz-filled pressure shadows were observed in proximity to Py4. The quartz that forms these veins and pressure shadows is likely sourced from the siliceous mudstone matrix during late tectonic activity. Py4 is associated with minor chalcopyrite (Fig. 4b), and the quartz veins may contain carbonate (calcite or ankerite). The Cu is probably sourced from the matrix, and carbonate could be sourced either from hydrothermal carbonate minerals (siderite and ankerite

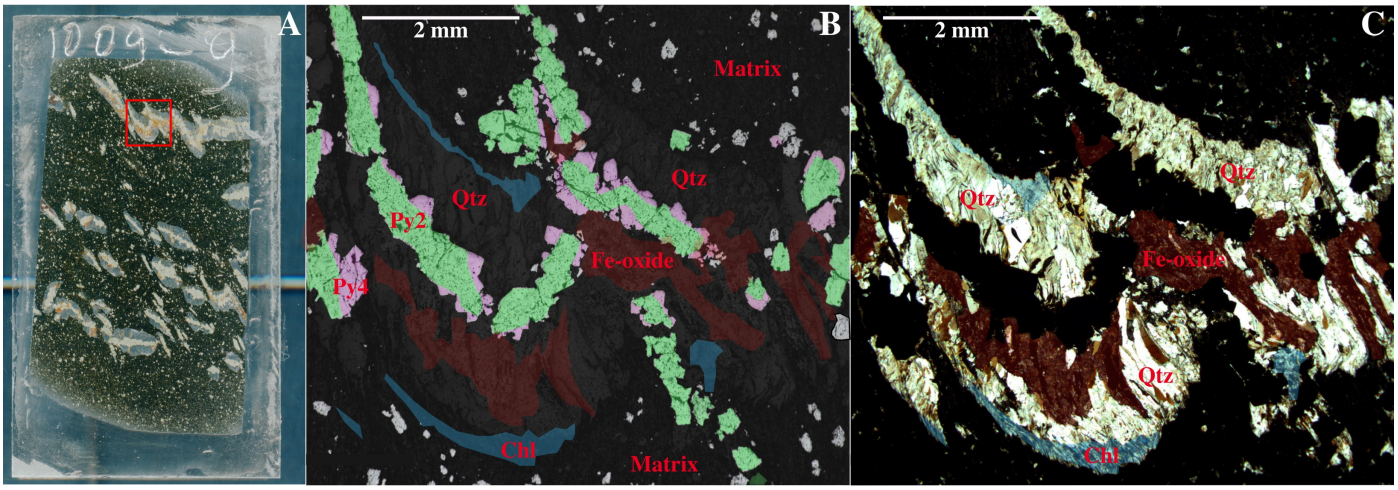

Figure 6. a) Scan of a polished thin section of core from drillhole TS91-019 at 106.1 m depth, with a box showing the location of photographs (b) and (c). b) Reflected light photomicrograph in which Py2 is shown as a false-coloured green, Py4 is false-coloured pink, chlorite (Chl) is false-coloured blue, and Fe-oxide is false-coloured red c) Plane polarized light PPL photomicrograph of the same area as is shown in (b); quartz pressure shadows are discernible as the colourless/yellow mineral. The colours relate to Figure 7. Abbreviations: Chl – chlorite; Py2 – diagenetic pyrite; Py4 – metamorphic pyrite; Qtz- quartz.

Table 2. Trace element composition of each pyrite generation.

Generation	**Synsedimentary pyrite** (Py1)	**Diagenetic pyrite** (Py2)	**Hydrothermal pyrite** (Py3)	**Metamorphic pyrite** (Py4)
Trace element composition	Wide range of trace elements (Ag, As, Bi, Cs, Co, Cr*, Cu, Hg, Mn, Mo, Ni, Pb, Rb*, Sb, Sc, Se, Ti, Tl, Te, V*, Zn), enriched (1–1,000s ppm)	Moderate range of trace elements (As, Cr*, Mo, Ni, Pb, REEs, Sb, Se, Th, Tl, Zn), moderately enriched (10–100s ppm)	Wide range of trace elements (Ag, As, Bi, Cd, Co, Cu, Mn, Mo, Ni, Sb, Se, Te, Tl, V*, Zn, enriched (10–1,000s ppm)$^{+}$	Narrow range of trace elements (Co, Ni, Se, ±As), moderately enriched (1–100s ppm)

*These elements are unlikely to represent stoichiometric substitution, rather they may be resident in micro-inclusions of matrix (organic particles or silicate inclusions) that are beyond the resolution of the laser.

$^{+}$Elements are considered to be enriched in Py3 if the average abundances are an order of magnitude higher in Py3 than in Py2 and Py4.

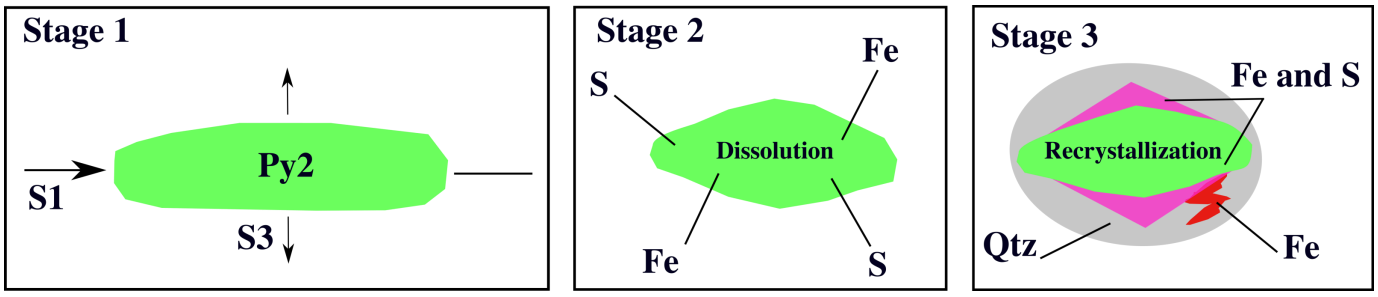

Figure 7. Schematic diagram of how compressive metamorphic stresses impact diagenetic Py2, through pressure solution of Fe and S, which migrate and recrystallize as Py4 and Fe-oxide. This same process dissolved matrix-sourced quartz to form a pressure shadow or vein around the Py4. The colours relate to Figure 6, where green is Py2, pink is Py4, red is Fe-oxide, and quartz is grey. Abbreviations: Py2 – diagenetic pyrite; Py4 – metamorphic pyrite; S1 – direction of principal stress; S3 – direction of least stress.

are abundant in the proximal deposits) but is more likely sourced from organic material in the matrix (Ansdell et al., 1989). Figure 4f shows that metamorphic quartz (that formed with Py4, as shown in Fig. 4, 6) crosscuts Py3, providing evidence that the metamorphic processes that formed Py4 postdated Py3 (Fig. 5).

Pyrite geochemistry

Pyrite sequesters ambient trace elements into its chemical structure as it crystallizes, and the resultant trace element composition is controlled by the fluid from which it precipitates (Berner et al., 2013). LA-ICP-MS element maps reveal compositional differences that correlate with variation in pyrite textures and generations, as is summarized in Table 2.

Principal component analysis (PCA) is a statistical technique that applies an orthogonal transformation to organize possibly interrelated variables into groups called principal components (PC) (Gregory et al., 2015). PCA attempts to identify patterns that exist in a dataset and it may reveal any underlying relationships between variables in the dataset. Each principal component in a given geochemical dataset will contain a suite of elements that may be controlled by one or more geological processes. PCA of the trace element geochemical data for 43 pyrite grains identified five principal components that account for 74.58% of the variance in the data (Table 3). This analysis was conducted in ioGAS using the "Classical" PCA method. The elements selected for PCA are outlined in Table 4.

Principal component one (PC1) accounts for 39.5% of the element variance, with strong (>0.8) loadings (scaled eigenvalues) for Ag, Bi, Sb, Se and Tl, and moderate (0.6–0.8) loadings for Mn, Co, Mo, Ni and Rb (Table 3, 4). PC1 represents trace elements that are incorporated in pyrite. Elements with strong or moderate loadings in PC1 (except Rb) can be incorporated into the crystal structure of pyrite. These elements are known to readily substitute into the pyrite lattice (Gregory et al., 2015). There are variable abundances of these elements in each generation (Fig. 8) but the PCA does not discriminate between generations.

Table 3. Results of principal component analysis of pyrite trace element data. Concentrations below detection were assigned a value of half detection.

Principal component	**Eigenvalues**	**Percent**	**Cumulative %**
PC1	9.095	39.54	39.54
PC2	3.07	13.35	52.89
PC3	2.424	10.54	63.43
PC4	1.44	6.259	69.69
PC5	1.124	4.887	74.58

Table 4. Scaled coordinates of principal components 1 through 5 (PC1–PC5) from the principal component analysis of pyrite trace element data. Concentrations below half detection was removed. Moderate (0.6–0.8) to strong (>0.8) values are in bold font.

Scaled Coordinates	**Principal component 1** (PC1)	**Principal component 2** (PC2)	**Principal component 3** (PC3)	**Principal component 4** (PC4)	**Principal component 5** (PC5)
Ag	**0.8776**	-0.2196	0.0473	0.0023	-0.1516
As	**0.9320**	-0.1697	-0.1351	0.0732	-0.0199
Bi	**0.8876**	-0.1565	0.0031	0.0460	-0.1107
Cd	0.0928	-0.1525	-0.1342	**-0.8377**	0.1547
Ce	0.2409	0.5322	-0.1751	0.0510	-0.0801
Co	**0.7981**	-0.1343	-0.1441	0.0656	0.2167
Cs	0.3874	0.1245	**0.7959**	-0.0386	0.0596
Cu	-0.2221	-0.0671	-0.0986	-0.3970	**-0.7027**
Ga	0.5930	**0.6892**	0.1219	-0.0833	0.0169
La	0.2742	**0.6560**	-0.2375	0.0095	-0.0229
Mn	**0.6063**	0.0591	-0.0284	0.0100	0.2956
Mo	**0.7431**	-0.0976	-0.1478	0.0081	0.0307
Nd	0.3143	**0.8429**	-0.2358	-0.0997	-0.0372
Ni	**0.8955**	-0.1985	-0.0877	0.0905	0.0326
Pb	0.5897	-0.1644	-0.0361	0.0377	-0.5281
Rb	**0.6061**	0.1227	**0.6768**	-0.0538	0.1181
Sb	**0.9373**	-0.1754	-0.1242	0.0369	-0.0203
Sc	0.3315	0.1915	**0.6839**	-0.1319	0.0108
Se	**0.8760**	-0.1751	-0.1525	0.0437	-0.0965
Sm	0.3116	**0.8521**	-0.2440	-0.1072	-0.0413
Ti	0.0330	0.1066	**0.6975**	-0.0843	-0.2658
Tl	**0.9243**	-0.1502	-0.0898	0.0510	-0.0276
Zn	0.3074	-0.2360	-0.1167	**-0.7020**	0.2156

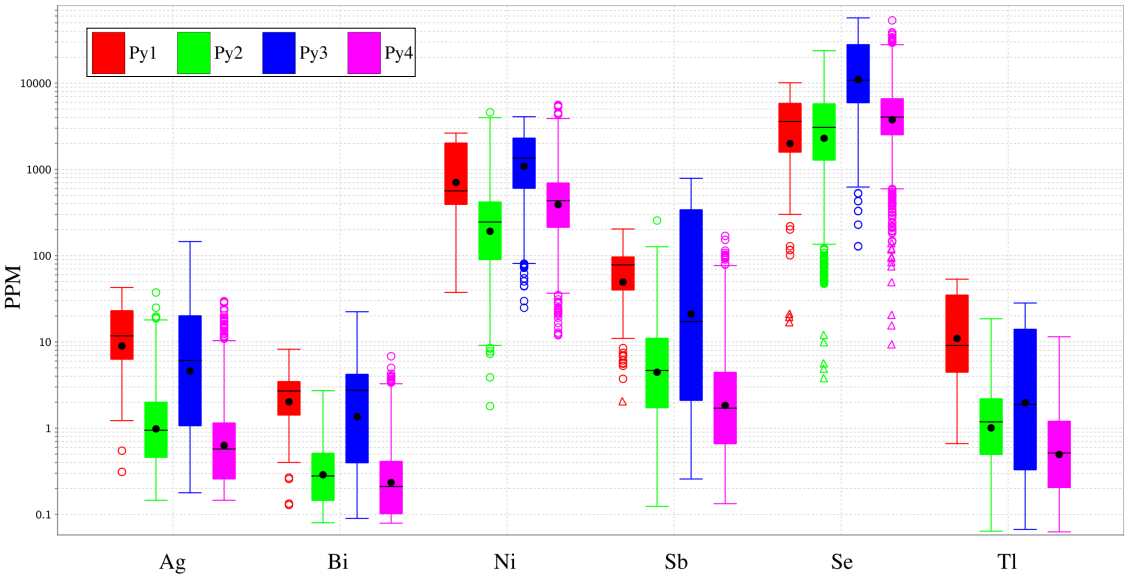

Figure 8. Box and whisker plot of Ag, Bi, Ni, Sb, Se and Tl (logged ppm): Py1 n = 92; Py2 n = 3158; Py3 n = 1901; and Py4 n = 2551. Abbreviations: n – number of pyrite grains; Py1 – synsedimentary pyrite; Py2 – diagenetic pyrite; Py3 – hydrothermal pyrite; Py4 – metamorphic pyrite.

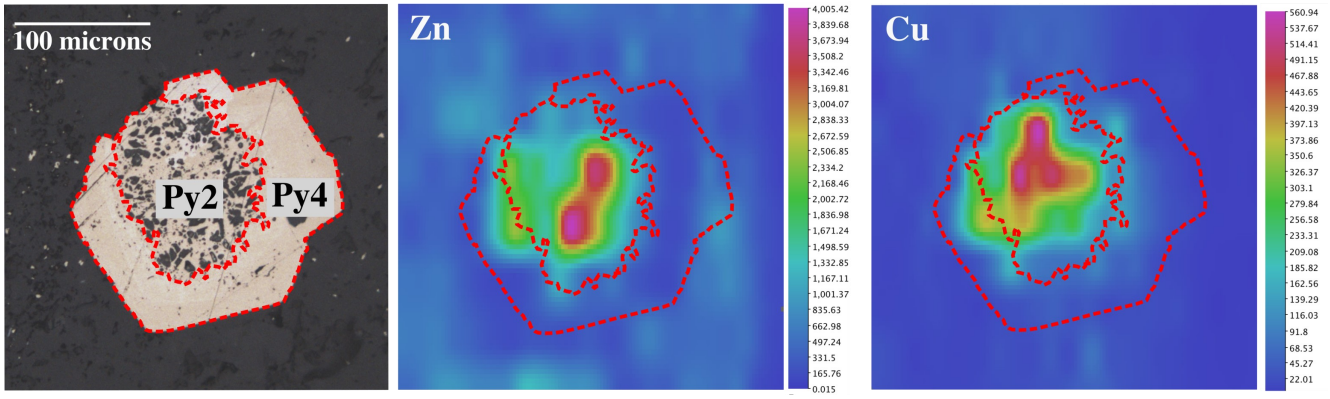

Figure 9. LA-ICP-MS raster map of a Py2 grain overgrown by Py4, with Co, Ni and Se colour ramps for intensity in ppm. Sample from drillhole JS76-017 at 212.1 m depth. Abbreviations: Py2 – diagenetic pyrite; Py4 – metamorphic pyrite.

PC2 accounts for 13.35% of element variance, with strong loadings for Nd and Sm (Table 3, 4). PC2 is interpreted to represent Py2, because it appears enriched in rare earth elements relative to the other generations (Fig. 9). These elements are not known to substitute into the pyrite lattice (Gregory et al., 2015). These REEs represent micro-inclusions of REE-rich carbonate or silicate minerals that exist in Py2.

PC3 accounts for 10.54% of element variance with moderately strong loadings for Cs, Rb, Sc and Ti. These elements are typically hosted in mica and clay minerals. PC3 represents Py1, because Py1 has high contents of these elements, which are the result of micro-inclusions of clay and mica that were trapped during rapid synsedimentary growth (Fig. 10).

PC4 accounts for 6.26% of element variance with strong

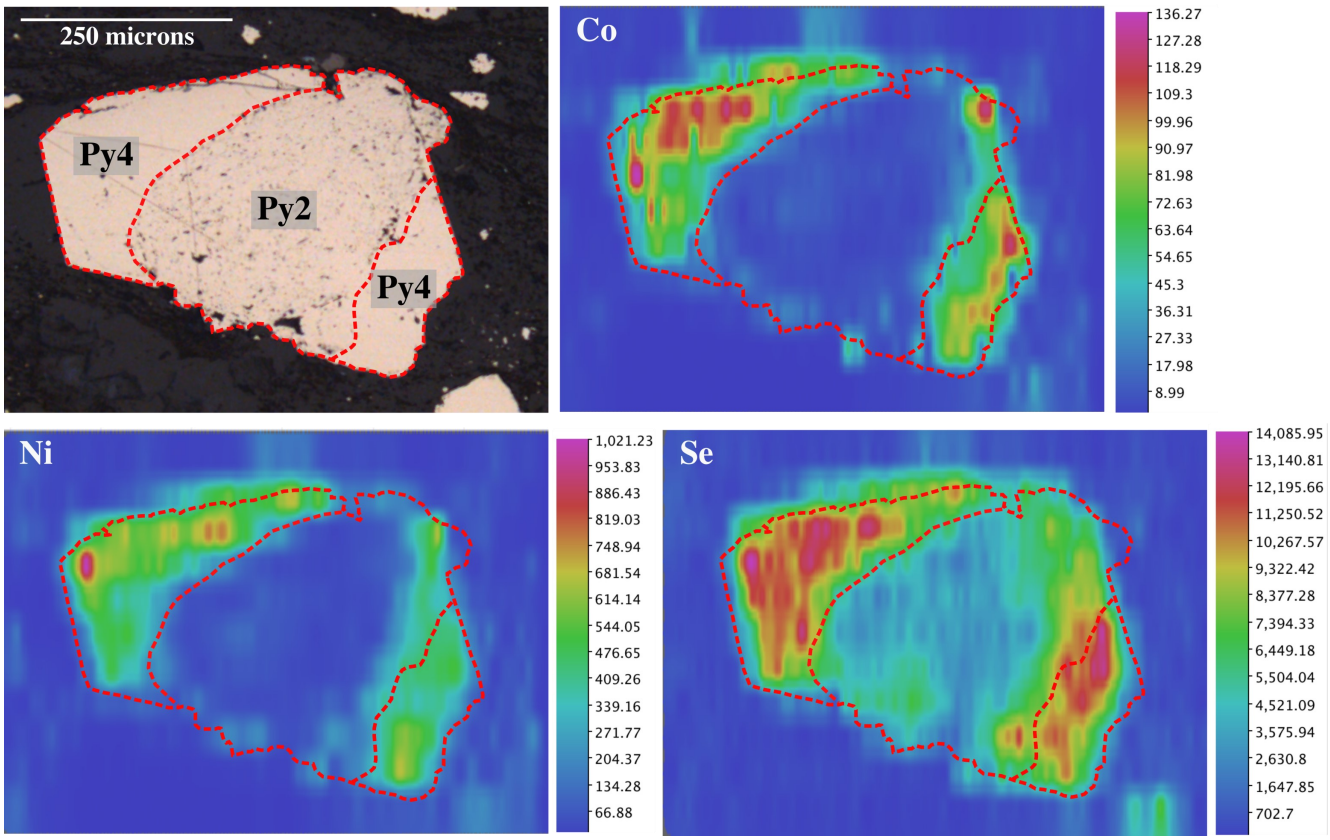

Figure 10. LA-ICPMS raster map of a Py2 grain overgrown by Py4, with Zn and Cu colour ramps for intensity in ppm. The inclusions in Py2 are matrix/silicates. Sample from drillhole TS91-019 at 162 m depth. Abbreviations: Py2 – diagenetic pyrite; Py4 – metamorphic pyrite.

loadings for Cd, and moderate loadings for Zn. PC5 accounts for 4.89% of element variance, with moderate loadings for Cu. In other pyrite chemistry studies (Gadd et al., 2015; Gregory et al., 2015), Zn, Cd and Cu was interpreted to substitute into the pyrite lattice. However, these elements are also known to be associated with other sulphide minerals. Zinc is incorporated into sphalerite, as is cadmium, through direct $Zn^{2+} \leftrightarrow Cd^{2+}$ substitution (Cook et al., 2009), and copper is incorporated into chalcopyrite. Minor chalcopyrite and sphalerite intergrowths and inclusions have been observed in these samples (Fig. 4b, e) and in other studies (Gadd et al., 2015). All attempts were made to avoid inclusions during LA-ICPMS analyses, however, the small size of micro-inclusions and intergrowths (Fig. 4b, e) were beyond the resolution of the laser (20–50 µm beam width). Thus, PC4 and PC5 may represent micro-inclusions and/or intergrowths of sulphide that co-occur with pyrite. PC4 is interpreted to represent sphalerite inclusions/co-precipitations that are associated with Py3.

Similarly, PC2 and PC3 may also be influenced by micro-inclusions and intergrowths in pyrite that were beyond the resolution of the laser. This caused elements that are not incorporated in the pyrite lattice, such as Cs, Rb, Sc and Ti, to have spurious abundances (Fig. 9, 10).

Synsedimentary Py1 is a sink for ambient, hydrogenous trace elements, and preferentially sequesters trace elements from ocean water relative to the shale/mudstone matrix. This imparts into Py1 an enrichment (>5 ppm, <1000 ppm) in many trace elements that reflect the diverse, ppt-scale concentrations of metals in ocean water, as sedimentary pyrite is a sink for trace elements (Table 2; Large et al., 2017). Framboidal pyrite precipitates rapidly, and forms when the precipitating fluid is supersaturated with respect to precursor iron monosulphides. Rapid nucleation enhances the uptake of a range of trace elements into Py1 (Table 2; Berner et al., 2013).

Py2 is late diagenetic and postdates Py1, shown by the overgrowth of Py2 on Py1 (Fig. 4a). Diagenetic Py2 formed within interstitial pore space in sediment or through displacive growth of sediment, giving it an inclusion-rich (shale matrix, oxides) texture from overprinting. The composition of Py2 is influenced by ambient sedimentary and bacteriogenic processes as well as ocean water (Berner et al., 2013). This bacteriogenic influence causes high contents of transition metals in Py2, such as Cu and Zn, with average abundances of 225 and 205 ppm, respectively (Table 2; Fig. 11). There is less ambient H_2S in the lower sediment column relative to the unconsolidated seawater -saturated upper sediment column where Py1 formed, which favoured a slower rate of precipitation for Py2 and imparted a trace element assemblage that is slightly less diverse in Py2 relative to Py1 (Table 2; Berner at al., 2013).

Element maps display a compositional contrast between Py4 overgrowths and preceding generations, whereby the interior of these grains (Py2) are enriched in a wider range of trace elements at similar abundances (Table 2). The formation of Py4 may have involved the recrystallization and migration of

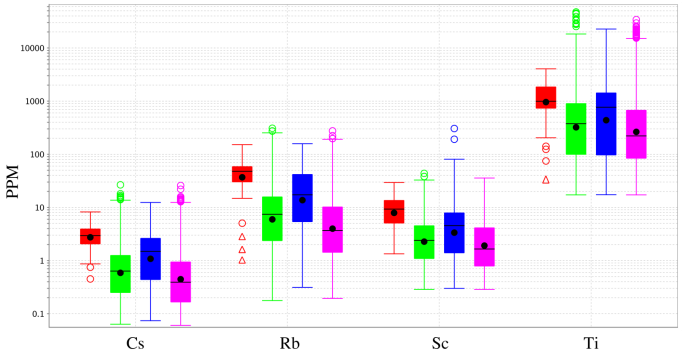

Figure 11. Box and whisker plot of Cs, Rb, Sc and Ti (logged ppm). *See* Figure 8 for the legend and 'n' values.

Fe and S from existing pyrite during metamorphism, during which trace elements loosely held in the pyrite lattice were expelled; this can explain the less diverse range of trace elements in Py4 and lack of inclusions (Fig. 7, 11) (Gregory et al., 2015). Cobalt, nickel and selenium are preferentially incorporated into Py4 relative to Py2 (Fig. 12), with average abundances of 29, 389 and 3761 ppm, respectively. The abrupt contrast in trace element composition across Py2 and Py4 geochemically distinguishes Py4 from the other generations of pyrite (Fig. 11, 13). Steadman and Large (2016) documented enrichments of As, Ni and Co, and Large et al. (2007) similarly found enrichments in As, Co, Ni and Se in metamorphic pyrite. Non-stoichiometric As and stoichiometric Co, Ni and Se are held strongly in the pyrite lattice, which causes them to be retained or possibly enriched during metamorphism (Large et al., 2007).

Py3 occurs within the high-Ba horizons of each drill core (Fig. 2b). Py3 generally contains greater abundances (5–2000 ppm) of trace elements compared to Py2 and Py4 (<500 ppm) (Table 2). Py3 contains enrichments in trace elements that are likely to be hydrothermal in origin, based on a similar pyrite metal enrichment suite in the Howard's Pass SEDEX district (HPD), 100 km southeast (Fig. 1; Gadd et al., 2016), and the pyrite-bearing black shales of the Lena Gold Province, Russia (Large et al., 2007). Most trace elements, except Bi and Cd, enriched in Py3 in this study are also enriched in hydrothermal

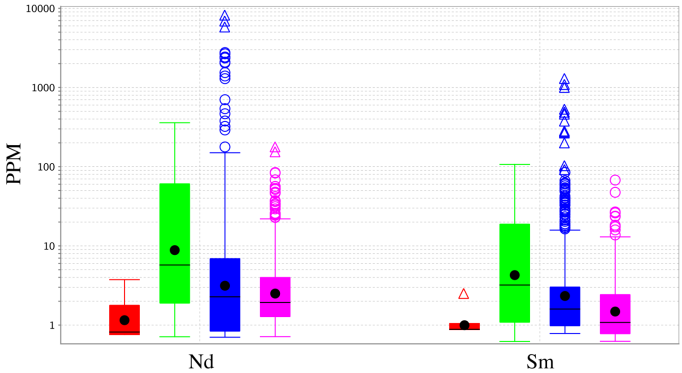

Figure 12. Box and whisker plot of Nd and Sm (logged ppm). *See* Figure 8 for the legend and 'n' values.

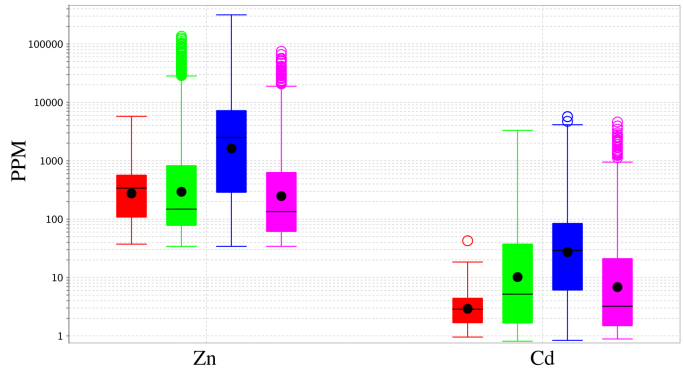

Figure 13. Box and whisker plot of Zn and Cd (logged ppm). *See* Figure 8 for the legend and 'n' values.

pyrite in other studies (Table 5).

Arsenic, cobalt and zinc are notably more enriched in Py3 relative to other generations, with average abundances of 1034, 95 and 1399 ppm, respectively (Fig. 14). This is also supported by the PCA, where PC1 has heavy or moderately heavy loadings for most elements that were found to be enriched in HPD and/or Lena Gold Province hydrothermal pyrite (Table 5).

It is also noteworthy that most elements enriched in Py3 (Table 2) are also either enriched or moderately enriched in the mineralized zone intercepted in drillhole TYK-001 (Fig. 3), based on field pXRF (Layton-Matthews et al., work in progress, 2018). Selenium, tellurium and cobalt are not enriched in whole-rock (matrix, and not macroscopic pyrite) pXRF data. This is because they are stoichiometrically substituted into the pyrite lattice in the place of S^{2-} (Se and Te) or Fe^{2+} (Co) preferentially over other minerals in the rock or matrix (Gregory et al., 2015).

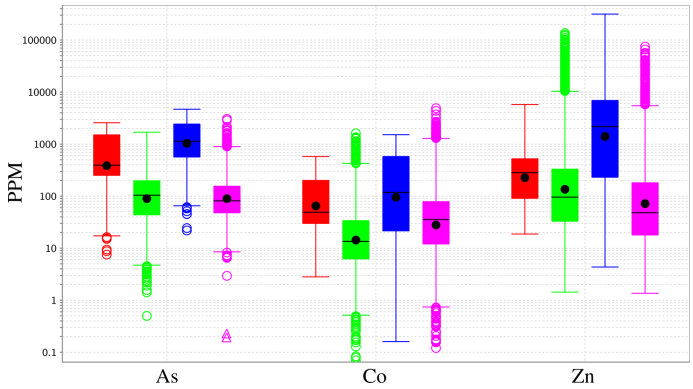

Figure 14. Box and whisker plot of As, Co and Zn (logged ppm). *See* Figure 8 for the legend and 'n' values.

These lines of evidence suggest Py3 was precipitated from (spent) mineralizing fluids that exhaled or travelled within the subsurface from an upflow zone 2 to 4 km away (i.e. the same fluids that formed the Tom and Jason Pb-Zn-Ag-(Ba) deposits).

Conclusions

Four pyrite types are recognized, each displaying distinct textures and mineralogical associations. These types (i.e. generations) were placed into a paragenetic sequence: Py1 – framboidal, synsedimentary; Py2 – anhedral, sooty, diagenetic; Py3 – disseminated, associated with barite, hydrothermal; and Py4 – euhedral, metamorphic.

Each of these generations has a distinct suite of trace elements, as determined by LA-ICPMS, that is controlled by the composition of the fluid from which it precipitated. Py1 has a diverse element suite (Ag, As, Bi, Cs, Co, Cr*, Cu, Hg, Mn, Mo, Ni, Pb, Rb, Sb, Sc, Se, Ti, Tl, Te, V*, Zn) that is strongly enriched (1s to 1000s ppm); Py2 has a moderately diverse element suite (As, Cr*, Mo, Ni, Pb, REEs, Sb, Se, Th, Tl, Zn), that is moderately enriched (10s to 100s ppm); Py3 has a diverse element suite (Ag, As, Bi, Cd, Co, Cu, Mn, Mo, Ni, Sb, Se, Te, Tl, V*, Zn) that is enriched (10s to 1000s ppm); Py4 has a limited element suite (Co, Ni, Se, ± As) that is moderately enriched (1s to 100s ppm) (Table 2).

Py1 formed from seawater within shallow unconsolidated sediment and/or the water column, whereas Py2 formed from pore-fluid within sediment, overprinting Py1. Thus, the trace element assemblage of Py1 is more representative of ocean water than Py2, because the pyrite-forming pore-fluid composition of Py2 is also impacted by diagenetic and bacteriogenic processes. A distal expression of SEDEX mineralizing fluid is recognized in Py3, which has unique morphologies, associations with other minerals and chemical characteristics. The hydrothermal suite of elements in Py3, and hydrothermal pyrite interpreted elsewhere (Table 5), suggests that it could potentially be used to vector toward concealed SEDEX mineraliza-

Table 5. Trace elements enriched in 'hydrothermal' pyrite from the Howard's Pass district (Gadd et al., 2016), the Lena Gold Province (Large et al., 2007) and this study. Trace elements in hydrothermal pyrite (Py3) in this study that are also found in hydrothermal pyrites of the other two studies are bolded.

	Howard's Pass District*	**Lena Gold Province◆**	**MacMillan Pass⁺**
Enrichment suite in hydrothermal pyrite	Zn, Pb, Mn, Tl, As, Ag, Sb	Sb, Ni, Co, Se, Te, Ag, Cu, Pb, Zn, Mo, Mn	**Ag**, **As**, Bi, Cd, **Co**, **Cu**, **Mn**, **Mo**, **Ni**, **Sb**, **Se**, **Te**, Ti, **Tl**, V, **Zn**

* Gadd et al. (2015)
◆Large et al. (2007)
⁺ This study

tion in the MacMillan Pass area and possibly other SEDEX horizons in the Selwyn Basin. Py4 overgrows all other pyrite generations and is the latest stage pyrite. Py4 is inclusion-free due to remobilization and recrystallization of previous pyrite generations under metamorphic stresses.

Future work

We are currently conducting similar analyses on samples from drillholes proximal to and within Pb-Zn stratiform mineralization (drillholes TYK-001, TK-005, TS91-014, TS-009: Fig. 2). These will be used to further evaluate efficacy of pyrite trace element geochemistry as a potential tool to vector from distal, mineralization-equivalent rocks toward concealed mineralization and the major mineralizing fluid upflow sites. The applicability of the findings to other SEDEX systems in the Selwyn Basin, and elsewhere in the world will be evaluated.

Further, as trace elements sequestered from seawater into sedimentary and diagenetic pyrite (Py1 and Py2) can act as paleo-environmental proxies for atmospheric or oceanic O_2 content, marine nutrients and ocean pH (Gregory et al., 2015; Large et al., 2017), the trace element enrichment suites of Py1 and Py2 will be evaluated as potential paleo redox proxies for the Late Devonian to Early Mississippian.

We also plan to conduct Secondary Ion Mass Spectrometry (SIMS) to analyze sulphur isotopic composition at the micron scale ($d^{34}S$), following methods similar to that of Magnall et al. (2016), in order to determine fluid source.

Acknowledgments

This report is a contribution to NRCan's Targeted Geoscience Initiative Program (TGI). Support for this study was provided through the Volcanic- and Sedimentary-Hosted Base Metal Mineralization Project's '*Activity VS-1.1: Role of anoxia, euxinia and microbes in seafloor hydrothermal sulphide (VMS and SEDEX) deposit formation*'.

We gratefully acknowledge funding from the Queen Elizabeth II Diamond Jubilee Scholarship. We thank Alex Voinot for invaluable help with analyses and data reduction. This report benefited from the review of Bill Davis, Michel Houlé and Neil Rogers.

References

Abbott, J. G. and Turner, R. J., 1991. Character and paleotectonic setting of Devonian stratiform sediment-hosted Zn, Pb, Ba deposits, Macmillan Fold Belt, Yukon*; in* Mineral Deposits of the northern Canadian Cordillera, Yukon - northeastern British Columbia [Field Trip 14], (ed.) J. G. Abbott and R. J. Turner; Geological Survey of Canada Open File 2169, p. 99–136.

Ansdell, K., Nesbitt, E., and Longstaffe, F.J., 1989. A Fluid Inclusion and Stable Isotope Study of the Tom Ba-Pb-Zn Deposit, Yukon Territory, Canada; Economic Geology, v. 84, p. 841–856.

Berner, Z., Puchelt, H., Nöltner, T., and Kramar, U., 2013. Pyrite geochemistry in the Toarcian Posidonia Shale of southwest Germany: Evidence for contrasting trace-element patterns of diagenetic and syngenetic pyrites; Sedimentology, v. 60, p. 548–573.

Bowers, T.S., Von Damm, K.L., and Edmond, J.M., 1985. Chemical evolution of mid-ocean ridge hot springs; Geochimica et Cosmochimica Acta, v. 49, p. 2239–2252.

Cook, N.J., Ciobanu, C.L., Pring, A., Skinner, W., Shimizu, M., Danyushevsky, L., Sainieidukat, B., and Melcher, F., 2009. Trace and minor elements in sphalerite : A LA-ICPMS study; Geochimica et Cosmochimica Acta, v. 73, p. 4761–4791.

Gadd, M.G., Layton-Matthews. D., Peter, J.M., and Paradis, S.J., 2016. The world-class Howard's Pass SEDEX Zn-Pb district, Selwyn Basin, Yukon. Part I. Trace element compositions of pyrite record input of hydrothermal, diagenetic, and metamorphic fluids to mineralization; Mineralium Deposita, v. 51, p. 319–342.

Goodfellow, W.D., 2007. Base metal metallogeny of the Selwyn Basin, Canada; *in* Mineral deposits of Canada: A synthesis of major deposit-types, district metallogeny, the evolution of geological provinces, and exploration methods, (ed.) W.D. Goodfellow; Geological Association of Canada, Mineral Deposits Division, Special Publication No. 5, p. 553–579.

Goodfellow, W.D. and Lydon, J.W., 2007. Sedimentary-exhalative (SEDEX) deposits; *in* Mineral Deposits of Canada: A Synthesis of Major Deposit-types, District Metallogeny, the Evolution of Geological Provinces, and Exploration Methods, (ed.) W.D. Goodfellow; Geological Association of Canada, Mineral Deposits Division, Special Publication 5, p. 163–183.

Gregory, D.D., Large, R.R., Halpin, J.A., Baturina, E.L., Lyons, T.W., Wu, S., Danyushevsky, L., Sack, P., Chappaz, A., Maslennikov, V., and Bull, S.W., 2015. Trace element content of sedimentary pyrite in black shales; Economic Geology, v. 110, p. 1389–1410.

Irwin, S.E.B. and Orchard, M.J., 1991. Upper Devonian-Lower Carboniferous conodont stratigraphy of the Earn Group and overlying units, northern Canadian Cordillera; *in* Ordovician to Triassic Conodont Paleontology of the Canadian Cordillera, (ed.) M.J. Orchard and A.D. McCracken; Geological Survey of Canada, Bulletin 417, p. 185–213.

Kelley, K.D., Leach, D.L., Johnson, C.A., Clark, J.L., Fayek, M., Slack, J.F., and Ridley, W.I., 2004. Textural, compositional, and sulfur isotope variations of sulfide minerals in the Red Dog Zn-Pb-Ag deposits, Brooks Range, Alaska: Implications for ore formation; Economic Geology, v. 99, p. 1509–1532.

Large, R.R., Maslennikov, V.V., Robert, F., Danyushevsky, L.V., and Chang, Z., 2007. Multistage sedimentary and

metamorphic origin of pyrite and gold in the giant Sukhoi Log deposit, Lena Gold Province, Russia; Economic Geology, v. 102, p. 1233–1267.

Large, R.R., Mukherjee, I., Gregory, D.D., Steadman, J.A., Maslennikov, V.V., and Meffre, S., 2017. Ocean and atmosphere geochemical proxies derived from trace elements in marine pyrite: Implications for ore genesis in sedimentary basins; Economic Geology, v. 112, p. 423–450.

Magnall, J.M., Stern, R., Gleeson, S.A., and Paradis, S., 2015. Widespread euxinic conditions are not a prerequisite for sediment-hosted base metal (Pb-Zn-Ba) mineralization at Macmillan Pass, Yukon; *in* Targeted Geoscience Initiative 4: Sediment-hosted Zn-Pb (±Ag, ±Ba) Deposits: Processes and Implications for Exploration, (ed.) S. Paradis; Geological Survey of Canada, Open File 7838, p. 43–57.

Magnall, J.M., Gleeson, S.A., Stern, R.A., Newton, R.J., Poulton, S.W., and Paradis, S., 2016. Open system sulphate reduction in a diagenetic environment – Isotopic analysis of barite ($\delta^{34}S$ and $\delta^{18}O$) and pyrite ($\delta^{34}S$) from the Tom and Jason Late Devonian Zn–Pb–Ba deposits, Selwyn Basin, Canada. Geochimica et Cosmochimica Acta, v. 180, p. 146–163.

Paton, C., Hellstrom, J., Paul, B., Woodhead, J., and Hergt, J., 2011. Iolite: Freeware for the visualisation and processing of mass spectrometric data; Journal of Analytical Atomic Spectrometry, v. 26, p. 2508–2518.

Peter, J. M., Layton-Matthews, D., Gadd, M. G., Gill, S., Baker, S., Plett, S., and Paradis, S., 2015. Application of visible-near infrared and shortwave infrared spectroscopy to SEDEX deposit exploration in the Selwyn Basin, Yukon; *in* Targeted Geoscience Initiative 4: Sediment-hosted Zn-Pb (±Ag, ±Ba) Deposits: Processes and Implications for Exploration, (ed.) S. Paradis; Geological Survey of Canada, Open File 7838, p. 152–172.

Steadman, J.A. and Large, R.R., 2016. Synsedimentary, diagenetic, and metamorphic pyrite, pyrrhotite, and marcasite at the Homestake BIF-hosted gold deposit, South Dakota, USA: Insights on Au-As Ore Genesis from Textural and LA-ICP-MS trace element studies; Economic Geology, v. 111, p. 1731–1752.

Toward the application of molybdenum and thallium isotopes as indicators of paleoredox conditions and genesis of hyper-enriched black shale (HEBS) deposits, Peel River, Yukon

I. Crawford[1], D. Layton-Matthews[1], J.M. Peter[2], M.G. Gadd[2] and A. Voinot[1]

[1]*Department of Geological Sciences and Geological Engineering, Queen's University, 36 Union Street, Kingston, Ontario K7L 3N6*

[2]*Geological Survey of Canada, 601 Booth Street, Ottawa, Ontario K1A 0E8*

Abstract

Hyper-enriched black shale (HEBS) deposits such as those hosted in Devonian black shales of northern Yukon are a globally significant source of a variety of economically important metals, particularly nickel, copper, zinc and platinum group elements (PGE). The Yukon HEBS occurs as a thin (<10 cm) but laterally extensive (10 000s km^2) stratiform and stratabound mineralized layer that is hyper-enriched in Ni-Mo-Zn-PGE. The genesis of such deposits and the ambient paleoenvironment in which they formed are the subject of vigorous debate. Non-traditional stable isotopes, particularly molybdenum and thallium, are shown to be robust paleoredox indicators. Systematic sampling with molybdenum and thallium isotopic analysis of a 200 m stratigraphic section through the Yukon HEBS mineralization and the footwall and hanging-wall strata at the Peel River north and south bank localities give δ^{98}Mo values of -1.1 to -0.53‰ and ε^{205}Tl values of -8.1 to -5.2 for the mineralization and 0.05 to 0.60‰ and -4.8 to -4.4 for the unmineralized strata, respectively. These values, together with bulk geochemical redox indicators and rare earth elements, indicate that the Peel River HEBS mineralization formed from seawater in a quiescent, euxinic basinal paleoenvironment.

Introduction

Black shales tend to be enriched in a variety of trace metals (i.e. they are polymetallic) (e.g. Vine and Tourtel, 1970; Scott et al., 2017). Some examples exhibit extreme metal enrichments, ranging from 10 to 60 000 times average black shales (Vine and Tourtel, 1970; Mao et al., 2002; Slack et al., 2015) and are known as hyper-enriched black shales (HEBS). In some locales (e.g. Kupfershiefer, Germany: Püttman et al., 1989; Talvivaara, Finland: Loukola-Rusekeenieni and Heino, 1996; Yangtze, China: Mao et al., 2002), sizes of accumulations, together with metal abundances are of economic interest. Worldwide, they represent a significant repository of a variety of economically important metals, including nickel, copper, platinum group elements (PGE), and in some cases molybdenum, zinc, manganese, vanadium and uranium (Jowitt and Keays, 2011; Peter et al., 2018).

The origin of the metal enrichment in HEBS is controversial, with diverse origins proposed, including scavenging from seawater under certain redox and organic matter availability conditions, seafloor hydrothermal fluids, by means of diagenetic processes, hydrocarbon carriers, seeding from meteorite impacts and influx of metal-rich riverine sediments (e.g. Hulbert et al., 1992; Rimmer, 2004; Lehmann et al., 2007; Slack et al., 2015). Both hydrothermal and hydrogenous sources have been suggested for the largest known Ni-PGE HEBS deposit, the Talvivaara mine in Finland (Loukola-Ruskeeniemi and Heino, 1996; Kontinen et al., 2006; Jowitt and Keays, 2011), and the HEBS in the Niutitang Formation throughout China, including the Huangjiawan mine (Steiner et al., 2001; Mao et al., 2002; Jiang et al., 2006; Lehmann et al., 2007; Lingang et al., 2011). The latter have been presented as an analogue for the Yukon HEBS deposits (Hulbert et al., 1992; Jowitt and Keays, 2011; Gadd and Peter, 2018). The present incomplete understanding of HEBS deposit formation currently hinders exploration (Gadd and Peter, 2018).

A variety of geochemical tools, such as redox sensitive trace elements (e.g. V, Mo, Cr), elemental ratios (e.g. Ni/Co, U/Th), total organic carbon (TOC) and degree of pyritization (DOP), have been applied to shales to investigate the paleoredox conditions under which they were deposited. These redox indicators, aside from DOP, rely on bulk geochemical compositions and all of them have limitations. However, some redox proxies have been shown to be more sensitive, and more robust than others. Using multiple proxies not uncommonly results in contradictory and/or equivocal paleoredox conditions (e.g. Peter et al., 2018). This has resulted in a movement in recent years to investigate the development of more robust and independent paleo redox indicators.

Corresponding author: Isobel Crawford (isobelrosecrawford@gmail.com)

Crawford, I., Layton-Matthews, D., Peter, J.M., Gadd, M.G., and Voinot, A., 2019. Toward the application of molybdenum and thallium isotopes as indicators of paleoredox conditions and genesis of hyper-enriched black shale (HEBS) deposits, Peel River, Yukon; *in* Targeted Geoscience Initiative: 2018 report of activities, (ed.) N. Rogers; Geological Survey of Canada, Open File 8549, p. 139–161. https://doi.org/10.4095/313647

Isotopes provide a powerful geochemical tool in the study of the natural world. The isotopic composition of certain redox-sensitive elements (e.g. Fe, S, C, Mo, U, Tl, Cr, Cu, Sb) has recently emerged as a new avenue for marine and sedimentary redox studies (Anbar and Rouxel, 2007; Andersen et al., 2014). Two such isotopes with strong sensitivities to ambient redox conditions are molybdenum and thallium. Molybdenum (based on bulk abundance or isotopic composition) has been shown to be a useful indicator of marine paleoredox conditions by numerous workers (Barling et al., 2001; Arnold et al., 2004; Scott et al., 2008; Dahl et al., 2010; Helz et al., 2011; Kendall et al., 2011). Molybdenum isotopes have been employed in the study of HEBS deposits in China. Chinese HEBS mineralization has δ^{98}Mo of - 0.94 to 1.38‰ and the host sedimentary rocks range from 0.81 to 1.70‰ (Lehmann et al., 2007; Xu et al., 2013). The authors suggested these values represent suboxic to euxinic conditions, and with other PGE and rare earth elements (REE) data indicated a seawater source for mineralization (Lehmann et al., 2007; Xu et al., 2013).

Thallium isotopic compositions have been less widely used as a paleoredox indicator (Nielsen et al., 2011; Nielsen and Rehkämper, 2012; Owens et al., 2017). A recent study investigated the use of thallium isotopes as a redox proxy in sedimentary exhalative (SEDEX) lead-zinc deposits and the authors concluded the application of thallium isotopes in seafloor hydrothermal deposits in sedimentary environments are useful in fingerprinting sulphide precipitation processes in hydrothermal mineralization, however, seem to be untenable as a redox indicator (Peter et al., 2018).

Molybdenum and thallium geochemistry

Molybdenum is a transition metal with a wide range of oxidation states (Barling et al., 2001). Although it is only a minor constituent of the Earth's crust at 1 to 2 ppm (Taylor and McLennan, 1985), Mo is considered to be the most abundant transition metal in the modern, oxygenated ocean, at a uniform concentration of 9.6 ppm with a conservative distribution due to a long residence time of 800 ka (Collier, 1985; Emerson and Huested, 1991; Morford and Emerson, 1999). Molybdenum is redox-sensitive, and its behaviour is dictated by changes in redox state in the natural environment (Barling et al., 2001). Molybdenum in continental crust occurs in the reduced or partially reduced forms Mo(IV) and Mo(V). Under oxidizing surface conditions, reduced Mo is oxidized to Mo(VI), and is transported in solution as the highly stable tetrahedral molybdate ion MoO_4^{2-} to the oceans (Barling et al., 2001). In oxygenated seawater, Mo is scavenged into ferromanganese nodules (Barling et al., 2001; McManus, 2002). Molybdenum is also concentrated in reducing, sulphidic, organic-rich shales (Barling et al., 2001).

Thallium occurs in nature as Tl^+ and Tl^{3+}, but in both oxic and anoxic aqueous systems it occurs predominantly as Tl^+ (Nielsen et al., 2011); because of the high redox potential of the oxidized form Tl^{3+}, it is only stable under extremely oxidizing and highly alkaline conditions (Kaplan and Mattigod, 1998), rendering it uncommon in natural environments (Nriagu, 1998; Nielsen et al., 2011). Tl^+ has a large ionic radius and behaviours similar to an alkali metal, whereas Tl^{3+} is much smaller and is more similar to transition metals; this exerts a control on its distribution in the natural environment (Shannon, 1976; Heinrichs et al., 1980).

Thallium occurs in much higher abundances in continental crust than in the mantle (Shaw, 1952; McDonough and Sun, 1995; Wedepohl, 1995), but it occurs in low concentrations in river water and at a low concentration of 12 to 14 ppb in the oceans (Flegal and Patterson, 1985; Nielsen et al., 2005). In seawater Tl has a conservative distribution, which in conjunction with a residence time of approximately 21 ka (significantly greater than the mixing time of ocean water), gives Tl a uniformly distributed invariant ocean composition (Rehkämper and Nielsen, 2004; Baker et al., 2009).

Thallium has a strong affinity for organic matter (Wade and Banister, 1973) and is commonly incorporated into clay minerals, such as mica, illite, and other similar phyllosilicate minerals (where it substitutes for K) (Matthews and Riley, 1970; McGoldrick et al., 1979; Kaplan and Mattigod, 1998; Turner et al., 2010). Thallium also shows slight to moderate chalcophile behaviour and hence has a strong affinity for mantle sulphides, early diagenetic pyrite, and sulphides in low-temperature hydrothermal systems (Xiong, 2007; Nielsen et al., 2011, 2014; Kiseeva and Wood, 2013; Wickham, 2014).

Molybdenum and thallium isotope systematics

There are seven naturally occurring molybdenum stable isotopes that range in mass number from 92 to 100 (Barling et al., 2001; McManus, 2002; Anbar and Rouxel, 2007). The isotopic composition of molybdenum is reported as a variation relative to the NIST 3134 standard, and is expressed in delta notation (parts per thousand, or ‰) as follows:

$$\delta^{98}\text{Mo} = \left(\frac{(^{98}\text{Mo}/^{95}\text{Mo})_{\text{sample}}}{(^{98}\text{Mo}/^{95}\text{Mo})_{\text{NIST3134}}} - 1 \right) \times 1000^{*} \ (‰)$$

*This varies by +0.25‰ to other reference materials (Nägler et al., 2014).

Molybdenum isotopic composition of geosphere and hydrosphere materials vary significantly (Fig. 1). Crustal molybdenum ranges from slightly negative to slightly positive δ^{98}Mo values, with an average of 0.3‰; ocean water is isotopically significantly heavier (2.3–2.4‰) (Barling et al., 2001; McManus, 2002; Siebert et al., 2003; Arnold et al., 2004; Voegelin et al., 2014; Breillat et al., 2016).

At a dissolved sulphide (H_2S_{aq}) concentration of 0.44 ppm or greater, highly effective scavenging of molybdenum in anoxic sediments by the rapid formation of thiomolybdates results in little to no isotopic fractionation between seawater molybdenum and molybdenum in euxinic sediments (Barling et

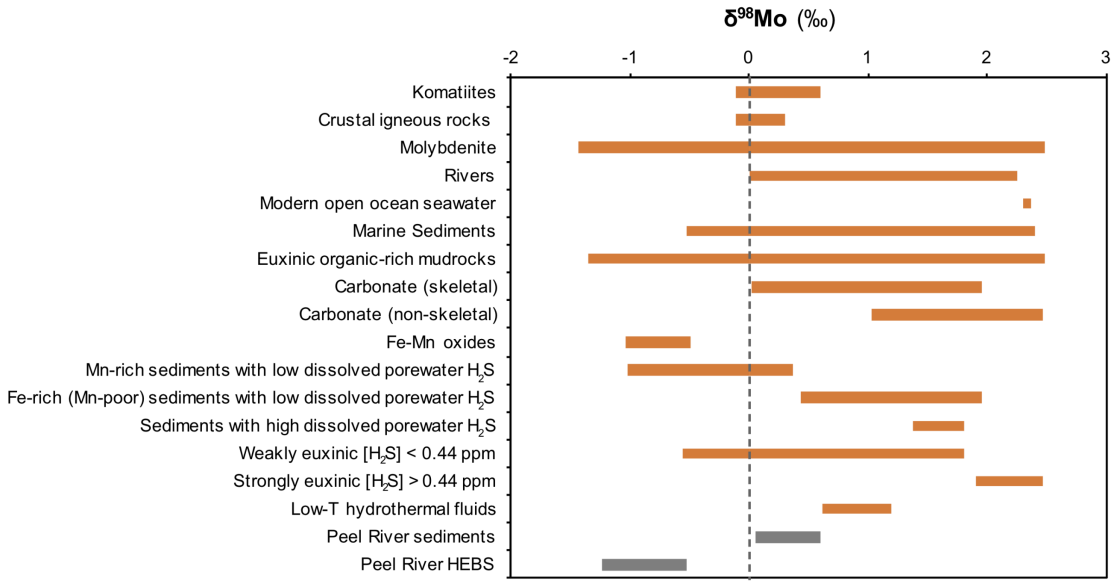

Figure 1. Compositional variations of δ^{98}Mo in selected reservoirs in the geosphere and hydrosphere (*after* Kendall et al., 2011, 2017) Peel River sample values also shown.

al., 2001; Siebert et al., 2003). Below 0.44 ppm the conversion of the dissolved Mo phase is incomplete and is associated with a molybdenum isotopic fractionation of -0.7‰, relative to modern seawater (McManus, 2002; Poulson et al., 2006). In oxic marine sedimentary environments, Mo is sequestered via adsorption onto ferromanganese oxyhydroxides, with preferential incorporation of the light molybdenum isotope (^{95}Mo) in the solid phase, resulting in a large isotopic fractionation of up to 3‰ associated with the conversion of MoO_4^{2-} to $Mo(OH)_6$ (Calvert and Pedersen, 1993). This large isotopic fractionation produces a negative Mo isotopic value in the solid phase, which averages -0.7‰ (Barling et al., 2001; Siebert et al., 2003).

Thallium has two stable isotopes, ^{203}Tl and ^{205}Tl, with natural abundances of 29.5% and 70.5%, respectively (Nielsen et al., 2011; Nielsen and Rehkämper, 2012). Thallium is conventionally reported using ε-notation (part per 10 000 variation) due to its original development for cosmochemical radiogenic isotope systematics, which traditionally uses ε-notation (Nielsen and Rehkämper, 2012). This notation is also convenient in recording the small variations measured in nature. The thallium isotopic composition is reported as:

$$\varepsilon^{205}\mathrm{Tl} = \left(\frac{(^{205}\mathrm{Tl}/^{203}\mathrm{Tl})_{\mathrm{sample}}}{(^{205}\mathrm{Tl}/^{203}\mathrm{T})_{\mathrm{NIST997}}} - 1 \right) \times 10^4 \ (\varepsilon\text{-units})$$

Classical stable isotope fractionation theory predicts that fractionation of these two isotopes of thallium would result in a very small isotope effect (Bigeleisen and Mayer, 1947; Urey, 1947); however, substantially larger fractionations have been observed in the natural environment on Earth (Fig. 2) (Rehkämper et al., 2002; Nielsen et al., 2006, 2011; Nielsen and Rehkämper, 2012; Coggon et al., 2014).

The Tl isotopic composition of upper continental crust, determined as an average from loess and an ultrapotassic dyke, is ε^{205}Tl = –2 ± 1 (Williams et al., 2001; Nielsen et al., 2005, 2006, 2007, 2017). Modern seawater is significantly lower in comparison, with an average ε^{205}Tl value of -6.0 ± 0.3 (Rehkämper et al., 2002; Nielsen et al., 2004, 2006; Owens et al., 2017). The lowest known ε^{205}Tl values (-20: Nielsen et al., 2017) have been measured in low-temperature hydrothermally altered oceanic crust, although these rocks have an average isotope value of ε^{205}Tl = -7.2. The mechanism(s) responsible for the observed isotopic fractionation in these altered rocks are still unknown (Nielsen et al., 2017).

Ferromanganese oxyhydroxides have the highest known ε^{205}Tl values (up to +15: Nielsen et al., 2017), and have been proposed to be the result of a change of oxidation state between Tl^+ to Tl^{3+}(Nielsen and Rehkämper, 2012; Yang and Liu, 2015). This large Tl isotope fractionation is due to the combination of pure mass-dependent equilibrium isotopic effects and mass-independent nuclear valence effect fractionation, although mass-dependent effects can only explain a small part of the variation (Bigeleisen et al., 1996; Knyazev and Myasoedov, 2001; Schauble, 2007). Both isotope effects act in the same direction and, collectively, they have been shown to reproduce the magnitude of variation observed; however, specific natural mechanism(s) remain largely unidentified (Schauble, 2007; Nielsen and Rehkämper, 2012). Thallium adsorption onto clay minerals results in minimal to no mass-dependent isotopic fractionation (Schauble, 2007), and for this reason seafloor clays inherit the thallium isotopic composition of modern seawater (ε^{205}Tl = -6; Nielsen et al., 2017). Unless the thallium in pelagic clays originates from manganese oxides; these will have thallium isotopic compositions akin to ferromanganese oxyhydroxides (Nielsen et al., 2017).

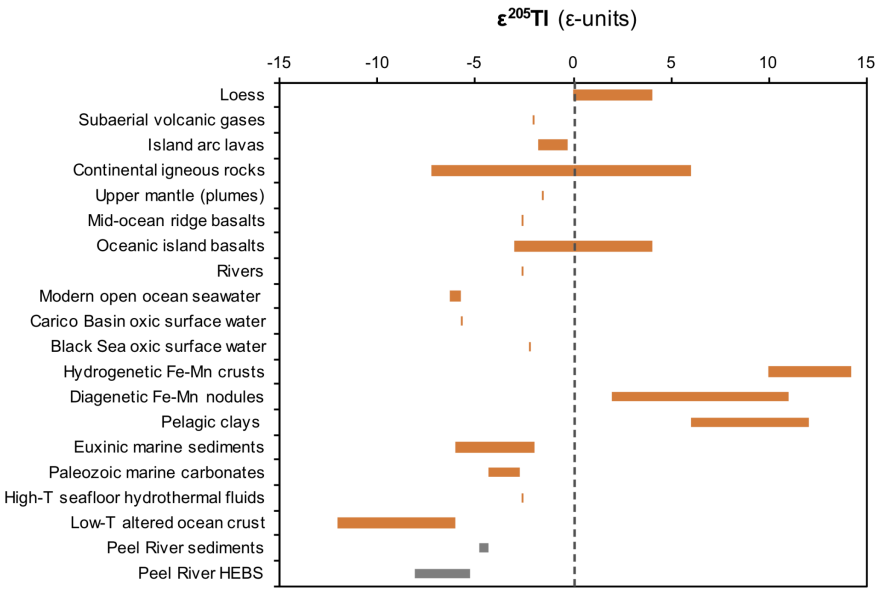

Figure 2. Compositional variations of $\varepsilon^{205}Tl$ in selected reservoirs in the geosphere and hydrosphere (adapted from Kersten et al., 2014) Peel River sample values also shown.

Geology

The rocks that are the focus of this study outcrop on the banks of the Peel River; they overlie a fault-bounded block of shallowly west-southwest dipping Paleozoic shales that were deposited in a deep basin to slope facies setting within the Richardson Trough, an eroded and folded sub-basin on the continental side of the Selwyn Basin (Parry and Carne, 1990; Heon, 2006; Goodfellow et al., 2010; Fig. 3). The Selwyn Basin formed in response to rifting of the continental margin of ancient North America during the early Paleozoic (Goodfellow, 1981, 2007; Cecile, 1982). The Richardson Trough is a Cambrian to Late Devonian intracratonic depression thought to be an aulacogen that formed as the result of episodic activation of old deep-seated structures marked by the faults of the Richardson Fault Array (Gabrielse, 1967; Norris, 1985; Hulbert et al., 1992). The Richardson Trough separated extensive Cambrian and Ordovician carbonate platforms, the Mackenzie Platform and the Yukon Stable Block (Norris, 1985; Morrow et al., 1999).

The Yukon HEBS deposits (including those at Peel River) lie within a unique and strikingly uniform stratigraphic succession (Fig. 4) (Goodfellow et al., 2010). The oldest rocks in the stratigraphic section exposed in the field area are calcareous, finely laminated, graptolitic black shale belonging to the Road River Group (RRG). The youngest is black non-calcareous, finely laminated, siliceous and pyritic shale and chert of the Canol Formation (Hulbert et al., 1992). At the unconformable contact between these two stratigraphic units there is a distinctive lithological sequence referred to as the 'Transition Zone'. The Transition Zone consists of, from oldest to youngest: 1) a limestone ball (concretion) member with shale that drapes around concretions in places; 2) a barite- and calcite-bearing nodular, siliceous, and carbonaceous shale unit; and 3) the Ni-PGE-rich sulphide horizon; collectively, these units record a period of prolonged condensed sedimentation (Dumala, 2007a; Fraser and Hutchison, 2017; Gadd and Peter, 2018). During field work in the summer of 2017, multiple stratigraphically distinct HEBS layers were found, two at the South El site and three at the North Pe site (Gadd and Peter, 2018). Conodont age determinations give an age range of Upper Eifelian to Lower Givetian (386.9–389.2 Ma) for the deposition of the two upper HEBS sulphide horizons (Gadd et al., work in progress, 2018).

The mineralized HEBS layers are stratiform, semi-massive sulphide that are enriched in nickel, molybdenum, zinc, and PGEs. The upper mineralized horizon at the El property, which was traced over a 2000 m strike length and a maximum of 1500 m down-dip (Dumala, 2007b; Gregory, 2008), outcrops over a strike length of approximately 300 m at a thickness of 2 cm, although drill core intersections have an average true thickness of 3 cm, with local variations from below 1 to 14 cm (Dumala, 2007b). Samples from the 16 diamond drillholes that intersected the horizon give an average of 3.7 weight % Ni, 0.23 weight % Mo, 1.07 weight % Zn, 91 ppb Au, 223 ppb Pt, 120 ppb Pd, and 26.9 ppm Re (Dumala, 2007b).

Mineralization consists of approximately 60 volume % sulphide minerals and approximately 40 volume % gangue minerals (Hulbert et al., 1992; Heon, 2006; Goodfellow et al., 2010). The sulphide minerals are pyrite, vaesite (NiS_2), millerite, gersdorffite (NiAsS), sphalerite and wurtzite ([Zn,Fe]S); the gangue minerals are silica, barite, apatite, (Ba) K-feldspar and pyrobitumen (Parry and Carne, 1990; Hulbert et al., 1992; Heon, 2006; Goodfellow et al., 2010; Gadd and Peter, 2018). At the Peel River north and south bank localities, millerite is the dominant sulphide mineral, whereas vaesite prevails at the Nick property (Gadd and Peter, 2018). Laser ablation - induc-

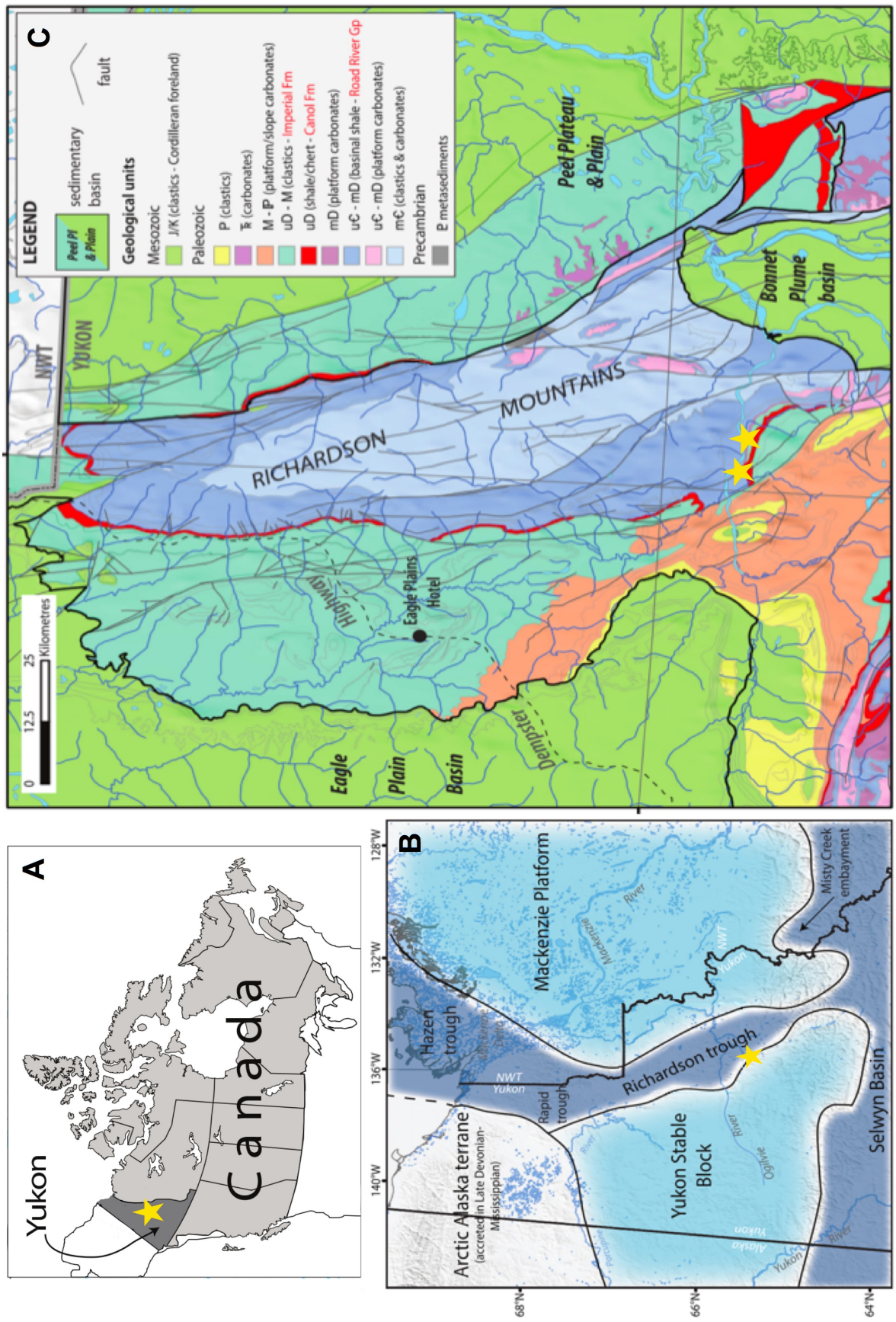

Figure 3. Location of field area (yellow star) (*adapted from* Fraser and Hutchison, 2017). a) Within Canada. b) Devonian paleography of north Yukon and northwest Northern Territories. c) Geological map of the Richardson Mountains; the western star is the north bank locality, and the eastern star is the south bank locality.

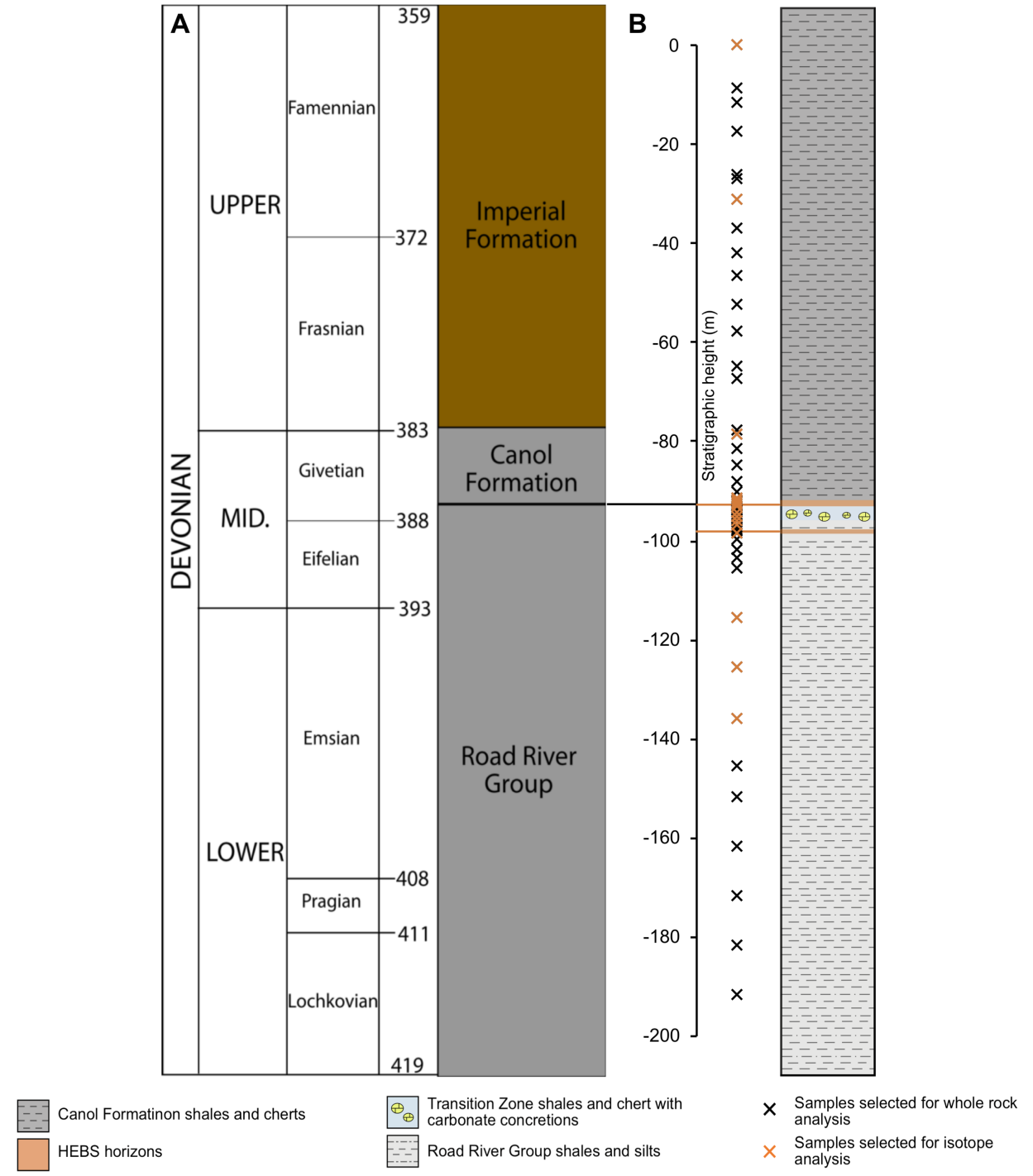

Figure 4. a) Devonian stratigraphy of the Richardson Trough (*modified from* Gadd and Peter, 2018). b) Schematic stratigraphic section for the Peel River field area.

tively coupled plasma - mass spectrometry (LA-ICP-MS) analysis of samples from the north bank of the Peel River reveals that the PGE are hosted in fine-grained sulphidic carbonaceous matrix material, predominately in pyrite and a minor amount in millerite (Gadd et al., work in progress, 2018).

Sampling and methods

Forty-seven samples were collected from the outcropping cliff exposure along the southern bank of the Peel River (65° 51'56" N, 135°50'47" W). In addition, 17 samples were collected from the nearby drillhole EL07-10 (65°51'48" N, 135°

51'40" W) to cover the complete stratigraphic section through the mineralized horizons, spanning a continuous stratigraphic interval of approximately 200 m. Samples depths were recorded relative to a 0 m baseline from the top sample collected. Six samples were collected from the three HEBS horizons from the north Peel River bank (65°53'35" N, 135°55'51" W). Overall, there is 29 samples of the Road River Group shales, 7 of the Ni -PGE HEBS mineralization, 8 of the transition zone, and 26 of the Canol Formation shale.

Bulk geochemistry

Samples were crushed, pulverised, and analyzed by Activation Laboratories Ltd, Ancaster, Ontario. Four acid ('near total') digestion, peroxide 'total' fusion digestion, and analysis by ICP-MS and optical emission spectrometry (OES) was undertaken for major and trace element contents (Table 1). A certified reference material considered to be a good chemical match to the samples being analysed (LKSD-1) was used as a quality control standard to evaluate accuracy and precision. All elements are within ±2 standard deviations of the expected values (for elemental abundances less than 10x lower limit of detection; LOD) and are within the expected values for elements greater than 10x LOD for standard LKSD-1. Silica blanks were also analyzed (inserted every 20 samples) to test for contamination between runs. No contamination was recorded.

Sample preparation for molybdenum and thallium isotope analyses

Twenty-four samples covering the entire stratigraphic section were chosen for Mo and Tl isotopic analysis: 6 Canol Formation samples, 8 HEBS mineralization samples, 1 Transition Zone shale sample, and 9 Road River Group samples. High purity reagents were used throughout the sample preparation process to keep contamination low. Sample digestion was undertaken with use of an Anton Paar Multiwave 3000 microwave at the Queen's Facility for Isotope Research, Queen's University, Kingston, Ontario. Eighty to 100 mg of powdered sample and certified reference materials (SDO-1, SGR-1, and PTC-1) were weighed into 10 mL PTFE-TFM microwave digestion vessels. The high organic content of the shale necessitated use of the following at specific concentrations: 4 mL of concentrated HNO_3, 1 mL of concentrated HF, 1 mL of concentrated HCl, and 2 mL of H_2O_2. Digestions were run at the following settings: 1400W, 30 min period with an added 5 min for ramp and 15 min for cooling, and infrared (IR) at 210°C. In -house purified reagents were used for the preparation of all solutions described above and below. Samples were moved into Savillex® containers in a clean lab and evaporated to dryness on a hot plate at 85°C. Three millilitres of 0.5N HCl were added to the evaporated samples, 300 mL were then run through an ESI PrepFast® automated ion exchange chromatography system with a 1 mL 4 cm AG1-50x12 column to purify Mo from the major cations (Ca, Na, Mg, Si, K, Al). This method used a flow rate of 125 mL/min, 0.5N HCl and 6N HCl to remove the cations, elute Mo, and clean the resin before loading the next sample through. The remaining reactant was then evaporated to dryness at 80°C for subsequent Tl elution. The eluted product was evaporated to dryness at 80°C, taken back in 2 mL 1N HCl/0.5N HF, loaded onto a 250mL 8 cm AG1x8 column, and processed on the ESI PrepFast® for Mo recovery by a method modified from Pearce et al. (2009). Additional steps using 3N HCl and 8N HNO_3 were added for Zr and Ru separation, respectively, as these elements can generate isobaric interferences with some Mo isotopes. 1.5 mL of 0.2N HBr with 2% Br_2 was added to the dried Tl aliquot and subsequently loaded onto a 100 mL AG1x8 column for thallium recovery following the method of Rehkämper and Halliday (1999).

Thallium and molybdenum isotope analyses

Following elution, the molybdenum and thallium fractions were evaporated overnight at 80°C to complete dryness. Two drops of concentrated HNO_3 were added to both fractions and placed on a hotplate for a few hours at 180°C to remove any potential residual organic matter from the resins, and evaporated to dryness at 80°C. Five hundred mL of 2% HNO_3 were added to each sample before measurement of Mo and Tl isotopes on a Thermo-Finnigan Neptune multicollector inductively coupled plasma-mass spectrometer (MC-ICP-MS), using a standard-sample bracketing method. Certified reference materials NIST 3134 and NIST 997 were used as the bracketing standards for molybdenum and thallium, respectively. Samples were introduced using an ESI microFAST autosampler setup with a 300 mL injection column. The dual-loop system of the autosampler created a 6 minute and 12 minute time-interval between consecutive bracketing standards for Mo and Tl, respectively, which minimized the potential effect of instrument drift (<0.05‰ for Mo, <0.02 ε-units for Tl).

During the measurement of thallium, all solutions (blank, wash, NIST 997 bracketing standard) were prepared in 2% HNO_3 with 0.1% v/v H_2SO_4 to match the sample matrix, as residual H_2SO_4 is present in the samples at the end of thallium recovery (Rehkämper and Halliday, 1999; Nielsen et al., 2004). Blanks run through the entire procedure were below the lower limit of detection on the MC-ICP-MS faraday cups (<<50pg Mo; <<20pg Tl). Drift between consecutive NIST 3134 and NIST 997 standards was monitored throughout the sequence. The reference materials were within error from published values and within 2 standard deviation of the average value typically measured for that reference material in the Queen's Facility for Isotope Research (Table 2).

Results

Bulk geochemical compositions

Elemental ranges for the Road River Group shale, Transition Zone, mineralized horizon, and Canol Formation shale are given in Table 1. The lowest Mo and Tl contents occur in the Transition Zone carbonate concretions (3.13–9.93 ppm Mo; 0.45–1.99 ppm Tl) and the Canol Formation (5.1–79 ppm Mo; 0.38–6.06 ppm Tl), followed by the upper Road River Group

Table 1. Summary of bulk geochemical data. Ranges are given for the Canol Formation, the HEBS horizon, Transition Zone shales and concretions, and Road River Group. Lower limits of detection and analytical methods are shown also.

Analyte Symbol	Detection Limit	Unit Symbol	Canol Formation	HEBS	Transition Zone (shale)	Transition Zone (concretion)	Road River Group	Analysis Method
H_2O+	0.1	wt. %	0.2–2.7	2–4.6	1.9–5.0	0.3–0.6	0.2–3.7	H_2O+
LOI		wt. %	2.07–26.84	15.4–29.7	8.24–25.1	32.36–37.43	6.51–38.11	FUS-ICP
LOI 500°C		wt. %	0.61–4.87	4.53–10.3	1.72–5.86	0.68–1.76	0.16–6.96	GRAV
TOC	0.5	wt. %	0.8–2.4	0.5–1	1.1–1.3	0.5–1.4	0.8–3.5	IR
Al_2O_3	0.01	wt. %	1–8.4	1.47–4.32	7.39–17.0	0.71–2.5	1.17–11.88	FUS-ICP
C tot	0.01	wt. %	1.13–9.5	1.49–3.82	1.88–7.48	10.7–11.3	2.09–11.6	CS
CaO	0.01	wt. %	0.06–39.9	0.06–5.66	0.17–20.68	35.15–54.38	0.37–38.63	FUS-ICP
Fe	0.01	wt. %	0.43–4.85	9.79–26.5	3.01–3.66	0.19–0.82	0.41–3.27	TD-MS
Fe tot	0.01	wt. %	0.63–6.95	14.46–38.29	4.72–5.77	0.33–1.25	0.68–4.51	FUS-ICP
K_2O	0.01	wt. %	0.11–1.96	0.36–1.12	1.57–4.31	0.06–0.39	0.25–5.29	FUS-ICP
Na_2O	0.01	wt. %	0.07–1.18	0.04–0.08	0.10–0.11	0.02–0.05	0.04–0.12	FUS-ICP
MgO	0.01	wt. %	0.06–4.36	0.05–2.08	0.72–8.71	0.63–9.63	0.21–10.34	FUS-ICP
MnO	0.001	wt. %	0.004–0.052	0.012–0.019	0.006–0.07	0.017–0.07	0.008–0.074	FUS-ICP
P_2O_5	0.01	wt. %	0.01–0.22	0.02–0.97	0.08–0.11	0.04–0.09	0.04–0.15	FUS-ICP
S	0.01	wt. %	0.24–5.78	14.6– >20	1.05–4.02	0.24–0.96	0.36–2.92	TD-ICP
S tot	0.01	wt. %	0.3–5.65	15.9–37.6	1.09–4.27	0.24–1.0	0.36–2.95	CS
SiO_2	0.01	wt. %	21.7–94.7	24.7–52.34	23.9–70.3	2.6–11.02	12.13–85.01	FUS-ICP
TiO_2	0.001	wt. %	0.044–0.42	0.072–0.152	0.28–0.66	0.029–0.095	0.056–0.496	FUS-ICP
Ba	2	ppm	1322–29180	1924–9433	2097–28420	417–3099	729–4676	FUS-ICP
Cr	20	ppm	20–270	80–120	60–120	<20	30–170	FUS-MS
Mo	0.05	ppm	5.1–79	554–3170	33.6–66.0	3.13–9.93	13.3–88.7	TD-MS
Ni	0.5	ppm	13.4–140	11800–49000	47.2–503	9.2–76.1	41.6–241	TD-MS
Se	0.1	ppm	0.4–20.1	497– >1000	25.3–61.1	1.1–8.6	2.1–21.7	TD-MS
Sr	2	ppm	33–1312	34–241	75–675	214–1426	58–778	FUS-ICP
V	5	ppm	56–1191	121–796	548–1554	80–345	262–1610	FUS-ICP
Zn	0.2	ppm	15.9–854	938–27200	148–3850	58.1–461.0	104–853	TD-MS
Ag	0.05	ppm	0.06–0.68	0.69–6.89	0.2–0.46	0.07	0.1–0.53	TD-MS
As	0.1	ppm	4.4–52.8	961–3930	47.3–93.9	2.9–12.4	4.3–38.6	TD-MS
Au	0.5	ppb	0.2–5.5	39.7–102	0.7–2.7	0.5–1.5	0.8–8.9	NI-FINA
Bi	0.02	ppm	0.03–0.25	0.31–1.03	0.12–0.28	0.03–0.05	0.03–0.22	TD-MS
Cd	0.1	ppm	0.3–10.4	4.1–74.7	0.7–103	0.8–11.8	1.1–9.6	TD-MS
Ce	0.05	ppm	4.63–57.4	9.08–69.3	24.2–48.4	4.63–13.1	11.3–93.4	FUS-MS
Co	0.1	ppm	0.5–14.9	57.4–243	1.8–23.1	0.5–3.3	1.1–10.9	TD-MS
Cs	0.1	ppm	0.2–4.2	0.7–2.0	4.2–14.2	0.1–0.8	0.6–9.0	FUS-MS
Cu	0.2	ppm	3.8–84	94.5–493	17.3–59.5	3.5–10.7	12.2–67.9	TD-MS
Dy	0.01	ppm	0.86–17.8	0.81–8.59	1.2–7.26	0.5–2.43	1.22–6.74	FUS-MS
Er	0.01	ppm	0.49–9.71	0.45–5.04	0.91–4.26	0.33–1.58	0.73–4.26	FUS-MS
Eu	0.005	ppm	0.144–3.930	0.186–2.370	0.244–1.200	0.12–0.59	0.272–1.83	FUS-MS
Ga	0.1	ppm	1.9–11.5	3.5–26.2	8.4–25.8	2.2	0.8–15.3	TD-MS
Gd	0.01	ppm	0.63–18.7	0.86–9.78	1.0–6.47	0.49–2.55	1.17–7.56	FUS-MS
Ge	0.1	ppm	<0.1	2.3–11.9	<0.1	<0.1	<0.1	TD-MS
Hf	0.1	ppm	0.3–1.7	0.5–1.1	1.2–2.6	0.1–0.4	0.3–2.0	FUS-MS
Hg	10	ppb	20–330	800–3460	60–180	40–60	30–270	TD-MS
Ho	0.01	ppm	0.17–3.63	0.15–1.78	0.28–1.52	0.11–0.51	0.24–1.39	FUS-MS
Ir	0.1	ppb	<0.1	0.5–1.6	<0.1	<0.1	0.1	NI-FINA
La	0.05	ppm	2.94–43.2	5.25–55.1	15.6–28.7	3.81–16.9	7.25–71.6	FUS-MS
Li	0.5	ppm	4.2–11.9	4.9–15.7	9.8–24.7	1.8–3.6	3.7–18.2	TD-MS
Lu	0.002	ppm	0.057–1.21	0.063–0.526	0.169–0.479	0.054–0.285	0.113–0.749	FUS-MS

Table 1. Cont.

Analyte Symbol	Detection Limit	Unit Symbol	Canol Formation	HEBS	Transition Zone (shale)	Transition Zone (concretion)	Road River Group	Analysis Method
Nb	0.2	ppm	0.8–4.6	1.0–3.1	4.0–10.2	0.3–1.5	0.8–8.1	FUS-MS
Nd	0.05	ppm	3.17–48	5.18–54.6	11.5–21.8	2.41–10.9	6.6–50.5	FUS-MS
Pb	0.5	ppm	1.3–12.1	11.7–64.2	6.3–13.6	0.7–3.2	2.3–15.5	TD-MS
Pd	2	ppb	06-Feb	45–168	3	<2	2.0–4.0	NI-FINA
Pr	0.01	ppm	0.73–8.98	1.26–13.4	3.24–6.20	0.85–2.7	1.71–13.5	FUS-MS
Pt	5	ppb	<5	64–239	<5	<5	<5	NI-FINA
Rb	1	ppm	4–78	14–37	69–198	3.0–18.0	10–139	FUS-MS
Re	0.001	ppm	0.003–0.079	7.55–32.0	0.048–0.119	0.002–0.018	0.016–0.11	TD-MS
Rh	0.2	ppb	0.2–0.4	1.0–2.6	<0.2	0.2	0.2–0.6	NI-FINA
Ru	5	ppb	<5	08-May	<5	<5	10	NI-FINA
Sb	0.1	ppm	0.2–13.9	33.4–155	2.9–11.7	0.9–2.7	1.6–10.2	TD-MS
Sc	1	ppm	10-Jan	2.0–5.0	7.0–14.0	2.0–8.0	2.0–15.0	FUS-ICP
Sm	0.01	ppm	0.67–15.1	1.05–10.9	1.26–4.28	0.43–2.51	1.27–8.85	FUS-MS
Sn	1	ppm	<1	08-Jan	03-Jan	<1	1.0–2.0	TD-MS
Ta	0.01	ppm	0.05–0.61	0.05–0.45	0.33–0.77	0.02–0.17	0.05–0.55	FUS-MS
Tb	0.01	ppm	0.13–3.12	0.14–1.51	0.17–1.13	0.08–0.39	0.2–1.17	FUS-MS
Te	0.1	ppm	<0.1	3.1–31.0	0.1	<0.1	0.1–0.3	TD-MS
Th	0.05	ppm	0.64–5.8	1.01–11.7	3.84–8.27	0.34–1.31	0.84–6.83	FUS-MS
Tl	0.05	ppm	0.38–6.06	107–434	5.1–13.4	0.45–1.99	1.52–11.6	TD-MS
Tm	0.005	ppm	0.064–1.24	0.062–0.651	0.147–0.547	0.052–0.241	0.107–0.651	FUS-MS
U	0.1	ppm	1.6–14.9	3.6–49.7	5.5–14.9	1.1–4.5	4–28.3	TD-MS
W	0.5	ppm	0.5–3.4	1.4–6.2	1.0–1.7	0.6–1.9	0.5–10.9	FUS-MS
Y	0.5	ppm	8.2–169	5.2–77.6	9.0–65.6	5.8–21.3	9.0–63.3	FUS-MS
Yb	0.01	ppm	0.38–7.83	0.4–3.74	1.04–3.21	0.37–1.75	0.7–4.5	FUS-MS
Zr	1	ppm	13–62	19–44	48–101	9.0–27.0	15–89	FUS-ICP

(19.1–78.7 ppm Mo; 2.58–11.6 ppm Tl), lower Road River Group (13.3–88.7 ppm Mo; 1.52–9.19 ppm Tl), and Transition Zone shales (33.6–55.6 ppm Mo; 5.1–13.4 ppm Tl). Molybdenum and Tl contents are highest in mineralization at abundances that are two to three orders of magnitude greater that in the unmineralized units (554–3170 ppm Mo; 107–434 ppm Tl).

Molybdenum and thallium isotopic compositions

Molybdenum and Tl isotopic compositions and the standard deviations are shown in Table 3. The δ^{98}Mo values range from a low of -1.24‰ to a high of +0.60‰. The Canol Formation, Road River Group, and Transition Zone samples have universally positive values (0.05–0.60‰), whereas the mineralized sulphide horizons have universally negative values (-1.24 to -0.53 ‰).

The ε^{205}Tl values range from a low of -8.1 to a high of -4.4 ε-units. The Canol Formation, Road River Group, and Transition Zone samples have the least negative ε^{205}Tl values (-4.8 to -4.5), and the mineralized sulphide horizons have the most negative ε^{205}Tl values (-8.1 to -5.2).

Discussion

Bulk geochemical paleoredox indicators

Seven bulk geochemical paleoredox proxies have been selected from the literature and applied to the Peel River stratigraphic succession (Table 4). A representative subset of these data has been plotted to highlight the stratigraphic variability among the key stratigraphic units over a 10 m interval (entire stratigraphic section Fig. 5a; 10 m interval Fig. 5b–f)

Table 2. Summary of certified reference material data for thallium and molybdenum isotopic determinations. Abbreviation: QFIR = Queen's Facility for Isotope Research.

	CRM	δ^{98}Mo (‰)	Stdev	n	Reference
This study	SDO-1	0.74	0.098	5	
	SGR-1	0.28	0.088	4	
	PTC-1	-0.53	0.056	2	
Published values	SDO-1	0.79	0.08 (2sd)		Dickson et al., 2016
	SGR-1				
	PTC-1	-0.52	0.08 (2sd)	2	QFIR, Peter et al., 2018

	CRM	ε^{205}T	Stdev	n	Reference
This study	SDO-1	-2.6	0.7	1	
	SGR-1	-3.3	1.95	1	
	PTC-1	-5.5	1.4	1	
Published values	SDO-1	-1.7 and -1.6			Rehkämper et al., 2004
	SGR-1				
	PTC-1	-5.8	0.5	10	QFIR, Peter et al., 2018

Table 3. Molybdenum and thallium isotope compositions of the Peel River samples. HEBS – hyper-enriched black shale; Std Dev – standard deviation.

Sample ID	Depth (m)	Lithologic Unit	δ^{98}Mo (‰)	Std Dev	ε^{205}Tl	Std Dev
17-POA-31	-98.09	Middle HEBS	-1.24	0.1	-6.37	0.51
17-POA-49a	19.1	Upper HEBS (N)	-0.94	0.13	-6.11	0.83
17-POA-49b	19.05	Upper HEBS (N)	-0.74	0.1	-8.09	0.9
17-POA-49c	19	Upper HEBS (N)	-0.53	0.33	-5.24	0.57
17-POA-72	15.7	Middle HEBS (N)	-0.69	0.23	-6.35	0.87
17-POA-73	15.7	Middle HEBS (N)	-1.08	0.19	-7.08	1.04
17-POA-89	8.28	Lower HEBS (N)	0.4	0.06	-7.01	0.74
17-POA-134	-98.69	Road River Group	0.35	0.36	-4.74	1.2
17-POA-138	-96.69	Road River Group	0.38	0.16		
17-POA-140	-95.99	Road River Group	0.45	1.37		
17-POA-143	-95.39	Road River Group	0.33	0.11		
17-POA-144	-95.19	Road River Group	0.05	0.1	-4.51	0.66
17-POA-148	-94.39	Road River Group	0.39	0.14		
17-POA-156	-92.99	Transition Zone (shale)	0.37	0.12	-4.69	0.78
17-POA-158	-92.59	Upper HEBS	-0.79	0.09	-6.08	0.61
17-POA-159	-92.49	Canol Formation	0.52	0.1		
17-POA-162	-91.99	Canol Formation	0.6	0.13	-4.36	1.06
17-POA-164	-91.59	Canol Formation	0.58	0.11		
17-POA-169	-115.69	Road River Group	0.13	0.21	-4.8	1.23
17-POA-170	-125.69	Road River Group	0.47	0.17		
17-POA-171	-136.19	Road River Group	0.15	0.13		
17-POA-179	0	Canol Formation	0.06	0.1		
17-POA-185	-31.1	Canol Formation	0.41	0.3		
17-POA-195	-78.5	Canol Formation	0.46	0.11		

Note: (N) refers to samples collected from the north bank of the Peel River, all other samples are from the south bank

The abundance of molybdenum in fine-grained sedimentary rocks is considered to be a robust paleoredox proxy, where less than 25 ppm denotes euxinic pore waters and oxic to suboxic overlying water; over 100 ppm Mo represents persistent euxinic bottom waters; and Mo abundances between 25 and 100 ppm signify intermittently euxinic bottom water conditions or extreme bottom basin restriction (Scott and Lyons, 2012; Scott et al., 2017). Following the above criteria, the Canol Formation and the Road River Group were deposited under conditions that varied from oxic to suboxic, intermittently euxinic bottom waters with euxinic pore waters (Fig. 5b). Transition Zone shales were deposited during intermittent euxinic bottom water conditions, Transition Zone concretions were deposited during euxinic pore water conditions, and the HEBS mineralization

Table 4. Summary of a selection of bulk geochemical paleoredox proxies. Ranges of each proxy is given for the Canol Formation, HEBS horizon, Transition Zone shales and concretions, and Road River Group.

	Canol Formation		HEBS		Transition Zone (shale)		Transition Zone (concretion)		Road River Group		References
V (ppm)	56.0-1126	e(i)	121-796	?	548-1554	e(i)	80.0-345	?	262-1610	e(i)	Breit and Wanty, 1991; Scott et al., 2013
Mo (ppm)	5.10-79.0	e(p to i)	554-3170	e(pers)	50.6-66.0	e(i)	3.13-9.93	e(p)	13.3-88.7	e(p to i)	Scott and Lyons, 2012; Scott et al., 2017
Re/Mo	0.0004-0.0032	e(i) to a(i)	0.003-0.021	a(i) to s(i)	0.001-0.002	a(p)	0.0006-0.0018	e(i) to a(i)	0.0004-0.0016	e(i) to a(i)	Crusius et al., 1996; Ross and Bustin, 2009
V/Cr	0.44-23.86	a & s(p)	1.10-7.96	a & s(p)	9.13-12.95	a & s(p)			2.44-21.1	a & s(p)	Jones and Manning, 1994; Ross and Bustin, 2009
Ni/Co	2.61-65.6	a & s(p)	162-299	a & s(p)	17.24-26.2	a & s(p)	18.4-27.3	a & s(p)	13.2-63.1	a & s(p)	Jones and Manning, 1994; Ross and Bustin, 2009
U/Th	1.03-13.44	a & s(p)	2.92-25.0	a(p)	1.41-3.30	a(p) & s(i)	1.76-5.23	a & s(p)	1.10-8.67	a & s(p)	Jones and Manning, 1994; Ross and Bustin, 2009
Ce/Ce*	0.55-0.94	s(i) to a(i)	0.59-0.81	s(p)	0.78-0.83	s(p)	0.61-0.77	s(p)	0.48-0.84	s(p)	Wright et al., 1987; Tribovillard et al., 2006

Note: e – euxinic; a – anoxic; s – suboxic; i – intermittently; p – pore water; pers – persistent

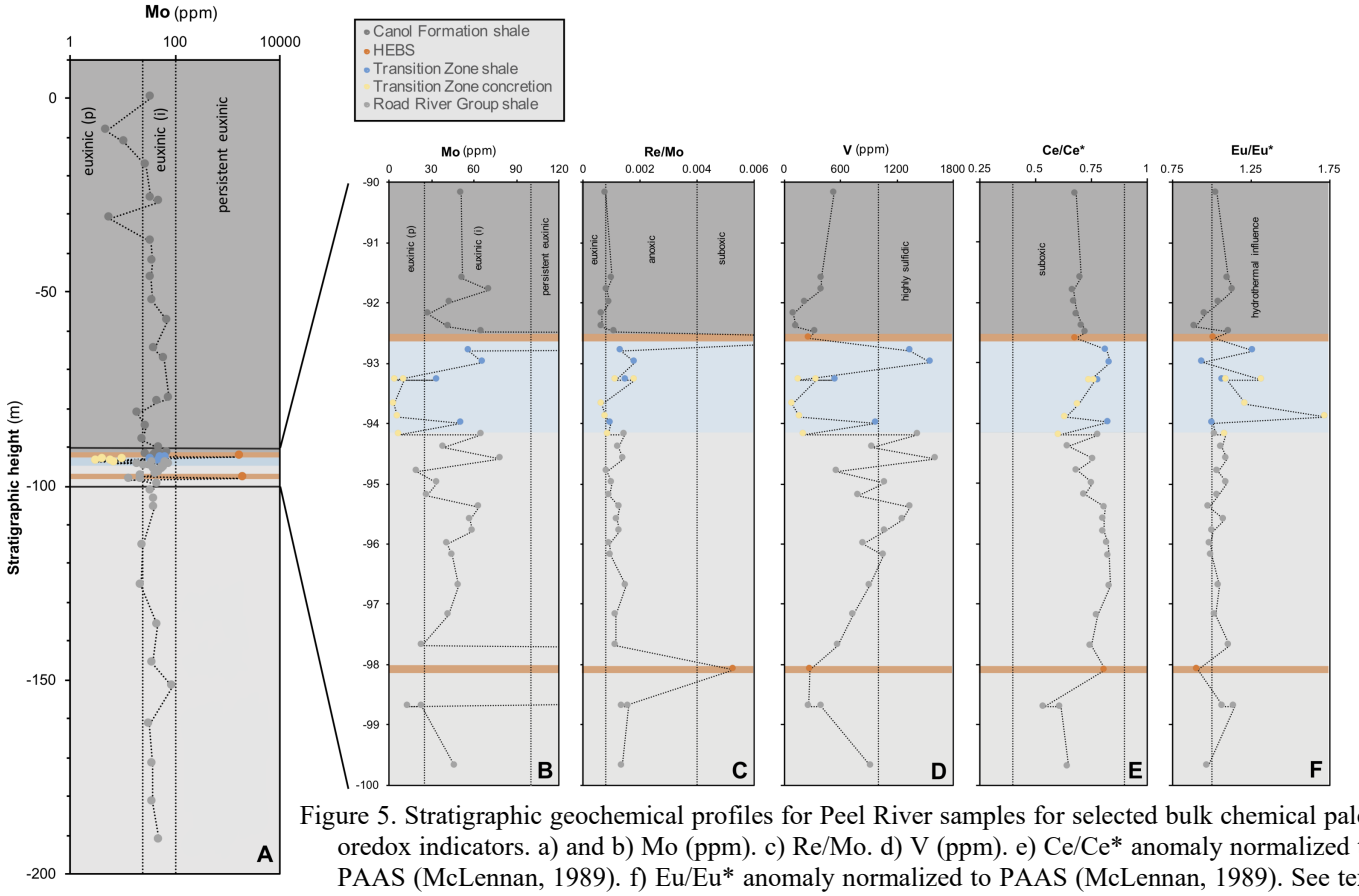

Figure 5. Stratigraphic geochemical profiles for Peel River samples for selected bulk chemical paleoredox indicators. a) and b) Mo (ppm). c) Re/Mo. d) V (ppm). e) Ce/Ce* anomaly normalized to PAAS (McLennan, 1989). f) Eu/Eu* anomaly normalized to PAAS (McLennan, 1989). See text for details regarding redox fields or boundaries. Note p – pore; i – intermittent.

was deposited under persistent euxinic conditions.

Values of Re/Mo between 0.0008 and 0.004 are considered to indicate anoxic conditions and Re/Mo values over 0.004 represent suboxic conditions (Jones and Manning, 1994; Ross and Bustin, 2009). These criteria indicate that all the Peel River stratigraphic units were deposited under anoxic pore water conditions, although some samples from the Canol Formation shale, the Transition Zone concretions, and the Road River Group shale have Re/Mo values below 0.0008, which are interpreted to have been deposited under euxinic conditions (Fig. 5c). Furthermore, some of the HEBS mineralized samples have Re/Mo values greater than 0.004, which suggest suboxic depositional conditions.

Total organic carbon (TOC) contents have been linked to anoxia due to conditions required for preservation; however, they show considerable overlap between oxic and anoxic environments (Raiswell et al., 1988) and thus are an equivocal diagnostic tool. Total organic carbon may, however, be useful as a comparison with other redox indicators. Comparison with proposed redox indicators, V/Cr, Ni/Co and U/Th (Jones and Manning, 1994; Ross and Bustin, 2009), shows no correlation to TOC (Fig. 6). The Cr contents of Transition Zone concretions are below the limit of detection and thus V/Cr values could not be calculated for these samples.

Vanadium abundances of over 1000 ppm in fine-grained sedimentary rocks are indicative of hyper-sulphidic depositional conditions (Scott et al., 2013); some samples from the Canol Formation shale, some shales of the Transition Zone, and sam-

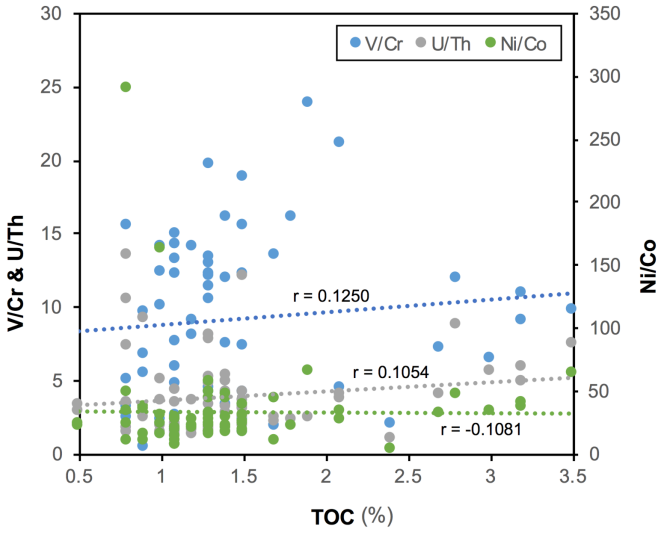

Figure 6. Bivariate plots of V/Cr, Ni/Co, and U/Th plotted against total organic content (TOC, %) with best fit lines and r values shown.

ples of the Road River Group shale meet this criterion (Fig. 5d).

Amongst the REE, cerium and europium are the only elements that have multiple oxidation states (Ce^{3+} and Ce^{4+}; Eu^{2+} and Eu^{3+}), a characteristic that makes them useful geochemical tracers. Europium enrichment in REE patterns resulting in a positive Eu (Eu/Eu*) anomaly relative to its neighbours in the lanthanide series, reflects preferential scavenging of Eu^{2+} from hydrothermal solutions (Goldstein and Jacobsen, 1988; Olivarez and Owen, 1991). Cerium depletion relative to its lanthanide neighbours produces a negative Ce anomaly (Ce/Ce*) that indicates the involvement of oxygenated seawater (Wright et al., 1987). Europium and cerium anomalies were calculated from the bulk geochemical data and normalized to average post -Archean Australian Shale (PAAS; McLennan, 1989), designated by the shale-normalized (SN) label, as follows:

$$Ce/Ce^*_{SN} = \frac{Ce_{SN}}{\sqrt{(La_{SN} \times Pr_{SN})}}$$

$$Eu/Eu^*_{SN} = \frac{Eu_{SN}}{\sqrt{(Sm_{SN} \times Gd_{SN})}}$$

The oxidation state of Ce is strongly redox dependent; Ce predominantly occurs as Ce^{4+} in oxygenated waters and is subsequently scavenged into Fe-Mn oxyhydroxides, leaving the seawater relatively depleted in Ce (De Baar et al., 1988; Alibo and Nozaki, 1999). Sediments deposited under these conditions will capture the negative Ce anomaly (i.e. Ce/Ce* $\leq$1). In anoxic marine environments, however, Ce occurs as Ce^{3+} and there is no (negative) Ce anomaly. Values of Ce/Ce* between 0.4 and 0.9 are considered to represent suboxic depositional conditions (Tribovillard et al., 2006). All stratigraphic units, aside from the Transition Zone concretions, have Ce/Ce* values within the range of 0.4 to 0.9 (Fig. 5e). The Peel River samples show insignificant positive Eu anomalies (Fig. 5f, 7).

Overall, the bulk geochemical paleoredox indicators are contradictory; we propose that they reflect conditions for two different environments. The Ce anomalies indicate suboxic conditions in the paleo-water column, whereas other indicators (e.g. Mo, V, Re/Mo) reflect anoxic to euxinic conditions of the pore fluids in the shallow subsurface.

Significance of molybdenum and thallium isotopic compositions of host sediments

The mineralized samples are significantly more enriched in both molybdenum and thallium than the enclosing, unmineralized host sedimentary rocks (Fig. 8a, b). They also have molybdenum and thallium isotopic compositions that are distinct from the unmineralized rocks of the Peel River stratigraphic section (Fig. 8a, b). In both isotopic systems, the samples of HEBS mineralization have lighter (more negative) values than the host rocks. The molybdenum and thallium isotope systems of the Peel River samples are not inversely correlated (Fig. 9), however, which is not in agreement with the proposed idea of the authigenic behaviour in various redox environments (Nielsen et al., 2011).

The Canol Formation, Transition Zone shale, and Road River Group sedimentary rocks were deposited from both clastic sedimentary (turbidite sequences) and pelagic sedimentary processes, and the molybdenum and thallium isotopic compositions likely also reflect a mixture between continental material, pelagic sediments (possessing a seawater isotopic signature) that were deposited in the suboxic water column, and seawater (Fig. 8a, b). Important assumptions and potential caveats are associated with estimating the molybdenum and thallium isotopic compositions of Middle Devonian seawater (age of HEBS mineralization). The molybdenum isotopic composition of Devonian seawater is assumed to be 1.5‰ (reported to NIST3134; Gordon et al., 2009; Magnall et al., 2018). Modern seawater has a ε^{205}Tl value of -6.3 ±0.3; (Rehkämper et al., 2002; Nielsen et al., 2004, 2006; Owens et al., 2017); however, the ε^{205}Tl of seawater for the past 80 Ma varied between approximately -14.5 and -4.5 (Nielsen et al., 2009, 2017). Nielsen et al., (2017) showed there is an close correlation between the Tl and S isotopic composition of seawater. At 387.7 Ma (Givetian-Eifelian boundary) the S isotopic composition of seawater was 18 to 19‰ (Kampschulte and Strauss, 2004), which corresponds to a Tl isotopic composition of -13 to -11 (Fig. 10)—significantly different from modern seawater.

The unmineralized samples show a moderate positive correlation between K and Mo, a strong positive correlation between K and Tl (r = 0.46 and 0.88, respectively; Fig. 11a, c), a weak positive correlation between S and Mo, and a moderate correlation between S and Tl (r = 0.28 and 0.57, respectively; Fig. 12a, c). The mineralized samples are enriched in sulphur coinciding with enrichments with molybdenum and thallium (Fig. 12b, d); however, they mostly contain much lower potassium (Fig. 11b, d). This suggests that molybdenum and thallium occur in both K-bearing clay and sulphide minerals in the Peel River host sediments and are predominantly hosted in sulphides in the HEBS mineralization. Their occurrence in the sulphide minerals in the HEBS mineralization is supported by LA-ICP-MS analyses of mineralized sulphide samples from the north bank of the Peel River, which show that molybdenum or thallium are resident predominantly in pyrite (Gadd et al., work in progress, 2018). Thallium is preferentially incorporated into clays and sulphides as Tl^+, the stable cation in oxic seawater (Schauble, 2007; Nielsen et al., 2017). Molybdenum and thallium incorporation into clays in the Peel River host sediments likely did not fractionate molybdenum and thallium isotopes, given the extremely low manganese abundances of these rocks (140 ppm; Table 2). Incorporation of molybdenum and thallium into sulphides during background sedimentation, i.e., non-mineralized, is unlikely to have fractionated molybdenum or thallium isotopes if the system is considered open.

Given the above, we suggest that the molybdenum and thallium isotopic compositions of the Peel River unmineralized

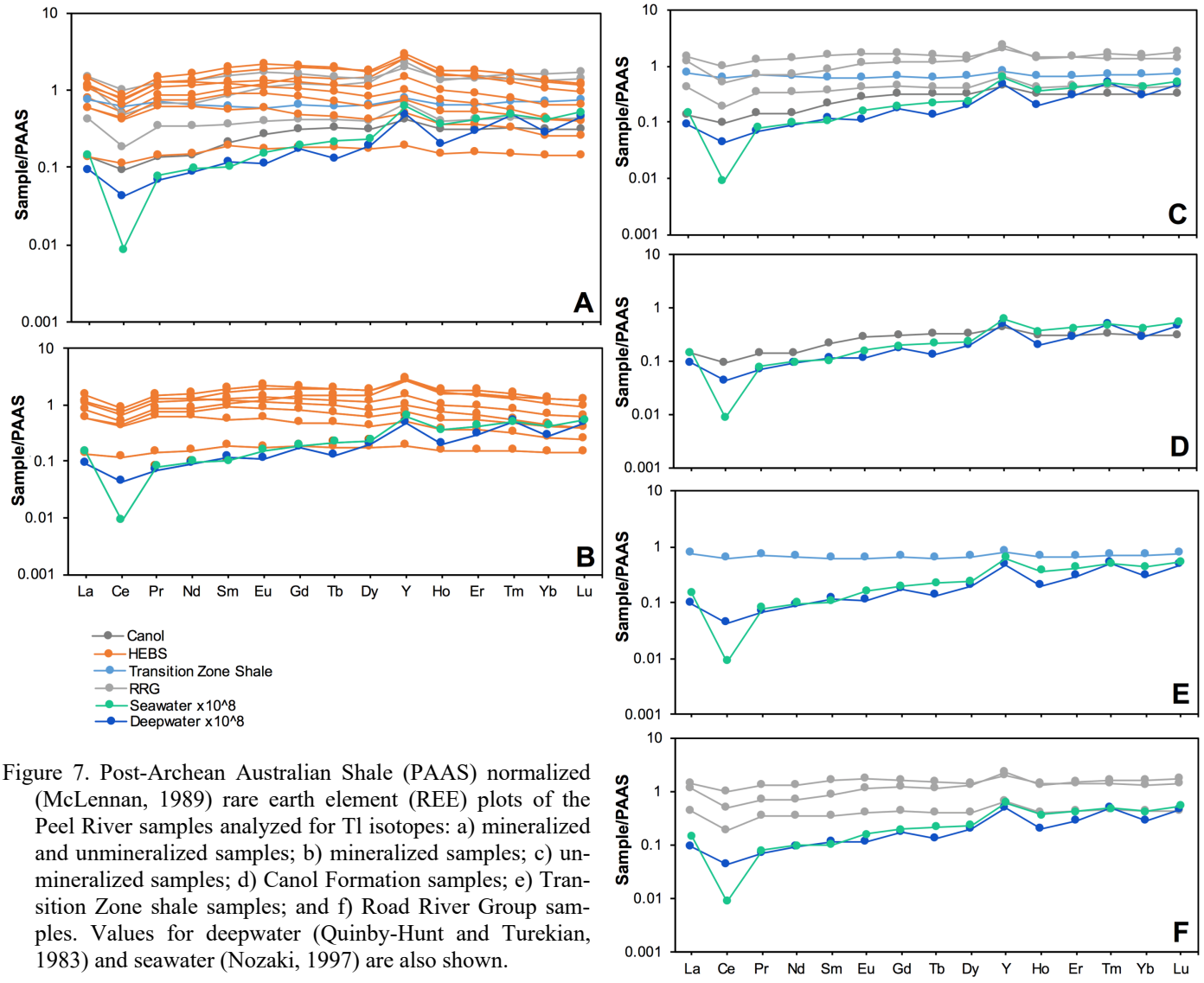

Figure 7. Post-Archean Australian Shale (PAAS) normalized (McLennan, 1989) rare earth element (REE) plots of the Peel River samples analyzed for Tl isotopes: a) mineralized and unmineralized samples; b) mineralized samples; c) unmineralized samples; d) Canol Formation samples; e) Transition Zone shale samples; and f) Road River Group samples. Values for deepwater (Quinby-Hunt and Turekian, 1983) and seawater (Nozaki, 1997) are also shown.

rock samples reflect the isotopic compositions of the infilling seawater at the time they were deposited.

Relevance of bulk geochemistry and molybdenum and thallium isotopic data to genetic models for mineralization

Two genetic models for the Yukon Ni-PGE-rich HEBS mineralization that have generated the most traction over the last 15 years are (1) seafloor-hydrothermal, syndiagenetic hot, dense, hydrothermal brine carrying metal complexed organic-matter that migrated laterally within bottom sediments to precipitate metals (Hulbert et al., 1992); and (2) seeding of the water column with metals of meteoritic and crustal origin that settled on the seafloor in an anoxic basinal setting following meteoritic impact (Goodfellow et al., 2010). Recently, both models have been disputed (Gadd and Peter, 2018). The seafloor-hydrothermal model (Hulbert et al., 1992) was proposed for the Nick deposit. However, with the discovery of other HEBS localities over 100s of kilometres contradicts the validity of this model, as it is unlikely that a single fault had the orientation and extent to reach all the Yukon HEBS occurrences. It is also not tenable that a sequence of growth faults discharged fluids simultaneously to precipitate mineralization over such a widespread area, over three discrete episodes at the Peel River location. Furthermore, no vent-like complexes have been identified and the Peel River samples lack significant Eu anomalies that would provide evidence of high-temperature (<250°C), reduced hydrothermal fluid (Fig. 5f, 7).

The Tl isotopic composition of the HEBS mineralization (ε^{205}Tl = -8.1 to -5.2) is lower than any mineral deposits reported in the literature (ε^{205}Tl = -4.1 to +1.1; Hettmann et al., 2014; Wickham, 2014; Peter et al., 2018). The δ^{98}Mo values are also much lower than those for hydrothermal or magmatic-hydrothermal fluids that have reacted with and/or traversed

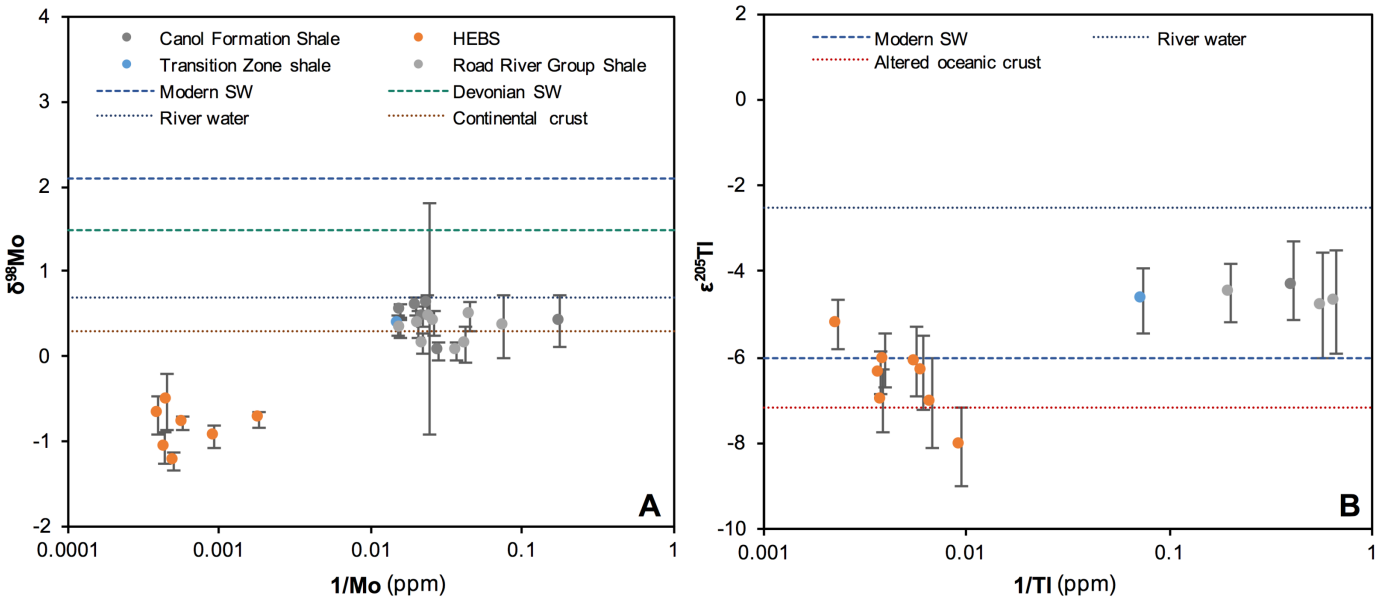

Figure 8. a) Bivariate plot of δ^{98}Mo vs. 1/Mo for the Peel River hyper-enriched black shale (HEBS) and sedimentary rock samples. b) Bivariate plot of ε^{205}Tl vs. 1/Tl of the Peel River samples. Isotopic values for seawater (Mo modern: Kendall et al., 2017, Devonian: Gordon et al., 2009 reported to NIST3134; Tl: Nielsen et al., 2017), terrestrial sources (Mo: Voegelin et al., 2014; Breillat et al., 2016; Tl: Rehkämper and Nielsen, 2004; Nielsen et al., 2005), and altered oceanic crust (Tl: Rehkämper and Nielsen, 2004; Nielsen et al., 2017) are also shown.

upper continental crust (δ^{98}Mo = 0.1‰; Breillat et al., 2016). The molybdenum and thallium isotopic compositions of the Peel River HEBS, therefore, do not support a (seafloor) hydrothermal origin.

The bolide impact model proposed for the Yukon HEBS (Goodfellow et al., 2010) lacks validity, as the quiescent sedimentary nature of the concretions associated with the mineralization and the presence of several discrete mineralized horizons cast severe doubt on the possibility of such a catastrophic event. In previous models these concretions were misinterpreted to be large rip-up clasts related to tsunami deposits caused by the bolide impact. Furthermore, the bolide was surmised to have been emplaced at the Frasnian-Famennian boundary (ca. 376 Ma; Tucker et al., 1998), whereas the HEBS conodonts are

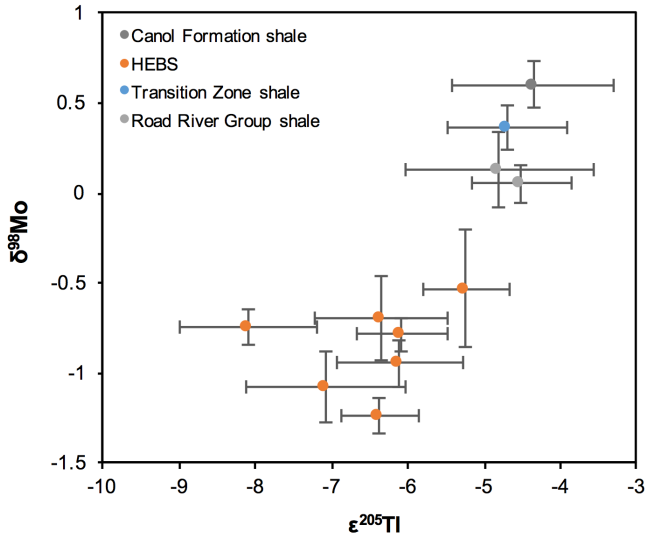

Figure 9. Bivariate plot of δ^{98}Mo vs. ε^{205}Tl of the Peel River samples.

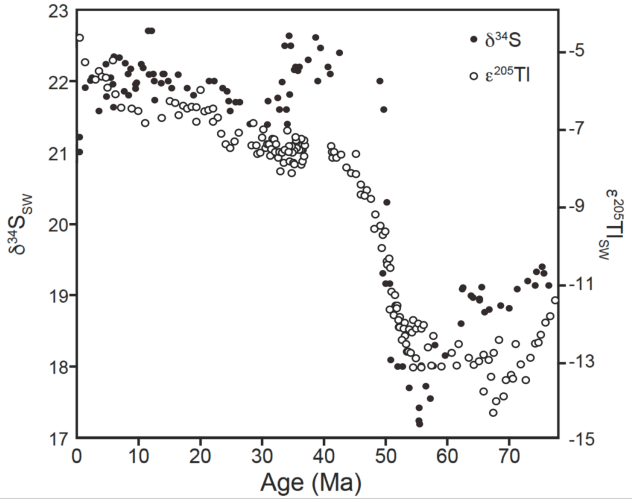

Figure 10. Tl and S isotope composition of seawater for the last 75 Ma. Tl isotope values are from Nielsen et al. (2009) and Tl chronology-based Os isotope data are from Burton (2006). S values from Paytan et al. (1998, 2004). Adapted from Nielsen et al. (2017) .

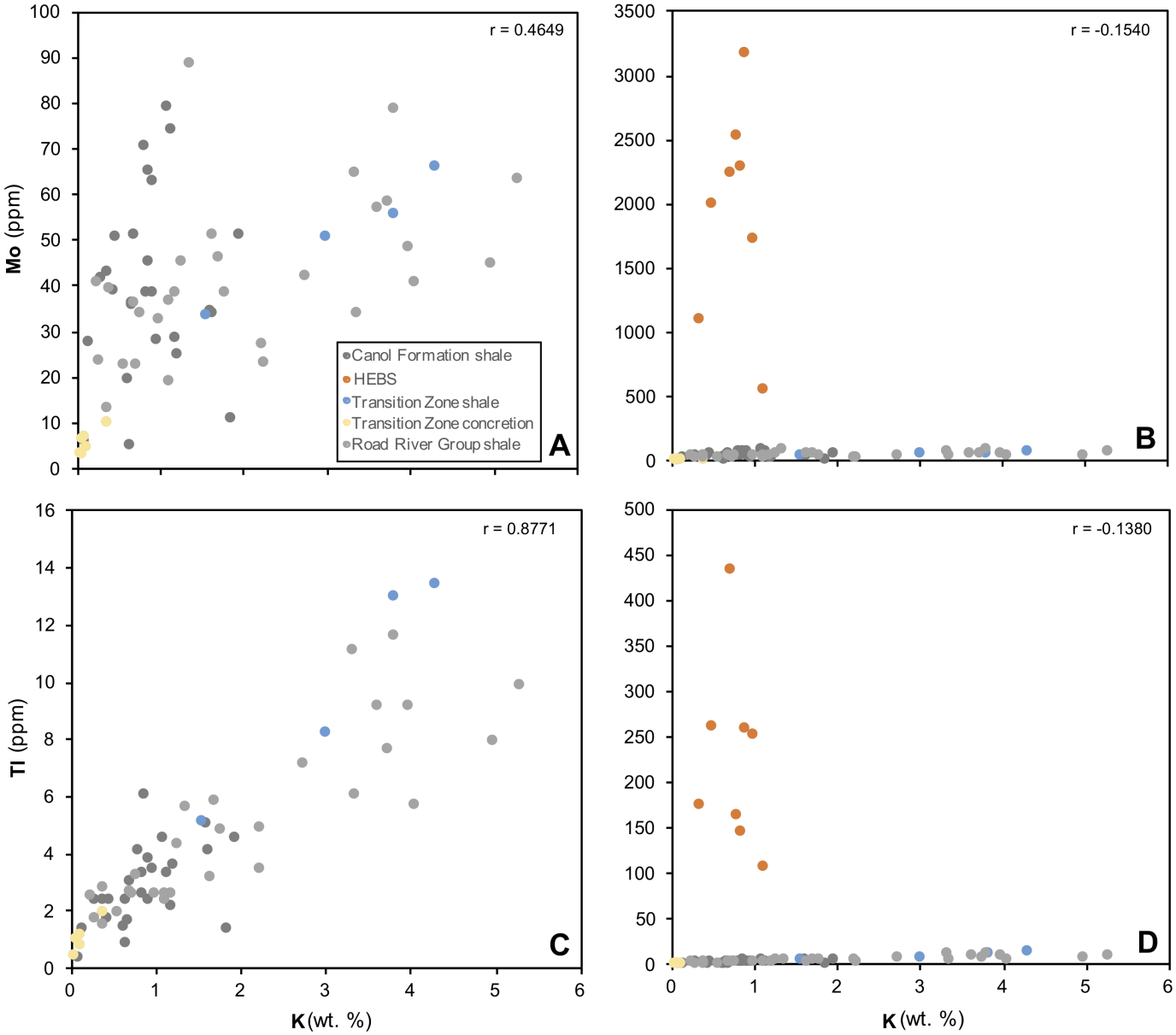

Figure 11. Bivariate plots of (a) Mo vs. K of unmineralized samples, (b) Mo vs. K for all samples, (c) Tl vs. K of unmineralized samples, and (d) Tl vs. K for all samples. r values are also shown.

about 20 Ma older (Gadd et al., work in progress, 2018).

Very recently, a model of highly efficient seawater scavenging under similar conditions to those proposed for the HEBS in China (i.e. an anoxic paleoenvironment with little clastic input and a high degree of organic matter remineralization) has been proposed for the Yukon HEBS (Gadd and Peter, 2018). Fractionation away from seawater values may explain the δ^{98}Mo and ε^{205}Tl composition of the Peel River HEBS mineralization. A predominantly marine influence is supported by the REE patterns. REE patterns of the Peel River samples are similar to PAAS (i.e. pelagic shale) and show a strong seawater -influence exhibited by negative Ce and positive Y anomalies. They also lack significant (negative or positive) Eu anomalies (Fig. 7). Ratios of Y/Ho for the Peel River sedimentary host rocks range from 27 to 59. Yttrium and Ho are geochemical 'twins' due to the similarities in charge, ionic radii, and electronegativites, and because they do not fractionate in igneous and clastic sedimentary rocks (i.e. they exhibit chondritic Y/Ho ratio of 28; Bau and Dulski, 1996; Nozaki et al., 1997). Post-Archean Australian Shale (PAAS) has a Y/Ho value of 27 (McLennan, 1989). Yttrium, however, has a lower scavenging affinity with iron oxyhydroxides compared to Ho (Bau, 1999; Bau and Dulski, 1999), resulting in higher Y/Ho values for seawater (>36; Bau and Dulski, 1995; Tostevin et al., 2016) in

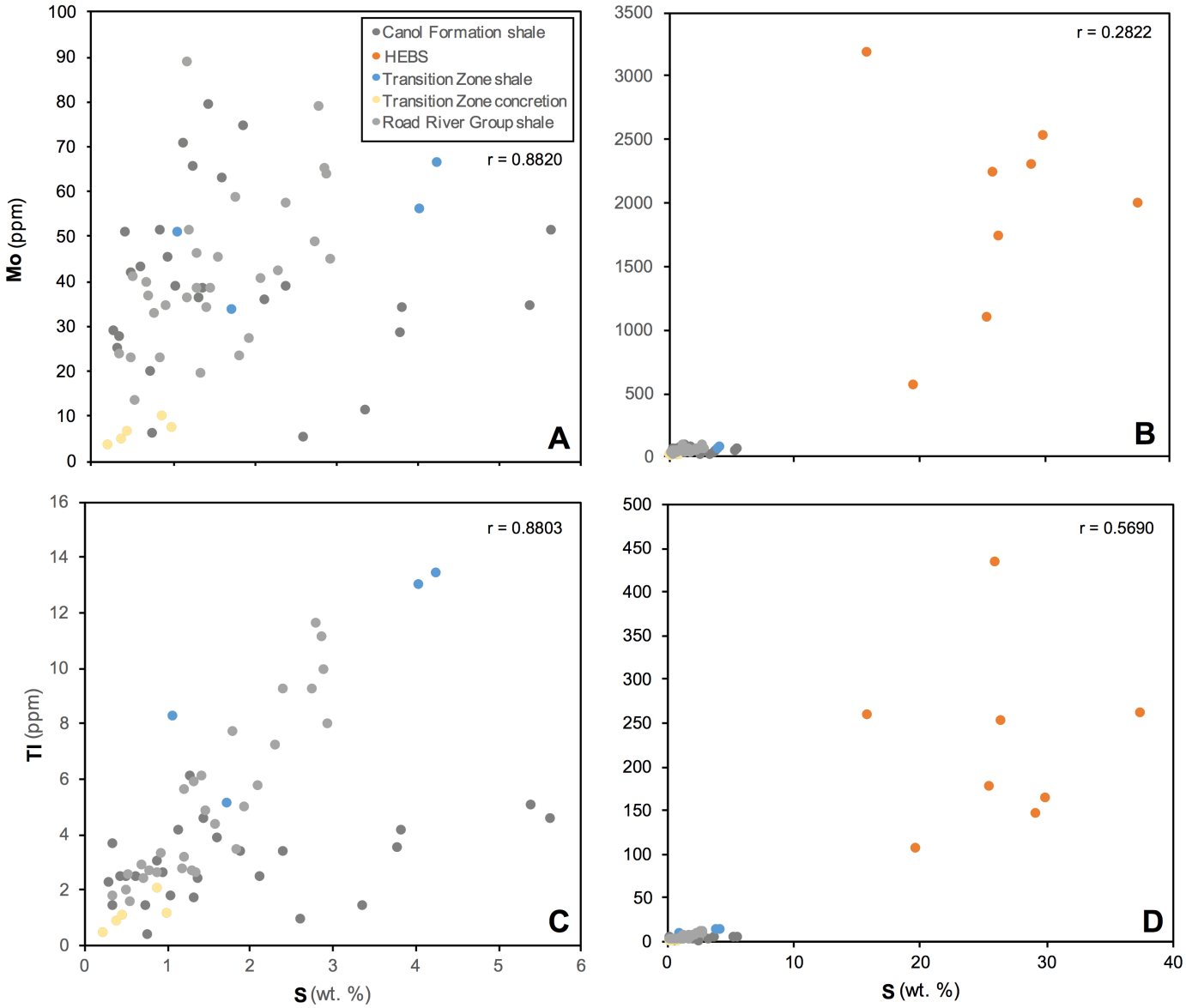

Figure 12. Bivariate plots of (a) Mo vs. S plot of unmineralized samples, (b) Mo vs. S plot for all samples, c) Tl vs. S plot of unmineralized samples, d) Tl vs. S plot for all samples. r values are shown.

open marine settings and lower values in near shore or restricted settings (De Baar et al., 1985a,b; Nozaki and Zhang, 1995; Bau et al., 1997). On a plot of Ce/Ce* versus Y/Ho (Fig. 13), the Peel River samples display a mixing trend between seawater and clastic sediments and/or other crustal material (i.e. chondritic).

The molybdenum isotopic compositions of the sedimentary rock and sulphide samples are markedly different, and not part of a single population (Fig. 8a). The higher molybdenum abundances and the lower δ^{98}Mo in the sulphide samples (than the sedimentary samples) suggests that a process is fractionating molybdenum isotope values away from coeval seawater in a manner that is not typical of modern oxic seawater, assuming the sediments above and below the HEBS horizon contain a mix of molybdenum sourced from coeval seawater and detrital molybdenum. Given the association of molybdenum with the abundant sulphide minerals, we proposed that the fractionation process occurring in the Peel River HEBS is linked to reducing or euxinic processes.

As mentioned previously, pyrite is the dominant host of molybdenum and thallium within the mineralization. Thallium is preferentially taken up in pyrite as Tl^{+}, for which the light thallium isotope (^{203}Tl) has a high affinity (Schauble, 2007; Peacock and Moon, 2012; Yang and Liu, 2015); therefore, thallium uptake by scavenging into sulphides could result in isotopic fractionation. Within the HEBS mineralized samples, ε^{205}Tl increases with increasing thallium content (Fig. 8b). Here, ε^{205}Tl acts as an indicator of the amount of thallium pre-

cipitated from the reservoir in a closed system. Precipitation of a small amount of thallium and sulphide results in larger fractionation as ^{203}Tl is preferentially scavenged in the sulphide phase and a lower sulphide thallium isotopic composition. With increasing scavenging, the produced sulphide thallium isotopic composition closer resembles the signature of the reservoir. At the Peel River site, we suggest thallium was partly scavenged at first, producing a large initial fractionation, but as sulphide formation continued, thallium sequestration increased to the point where the $\varepsilon^{205}Tl$ values of the HEBS reached values similar to the unmineralized shales, more closely approaching seawater.

Based on conodont biostratigraphy, each Peel River HEBS horizon formed over 1 to 2 Ma (Gadd et al., work in progress, 2018). During these lengthy time intervals, the basin was starved of clastic sediments. At the same time, the Richardson Trough was also subject to marine transgression(s) (i.e. rising sea level) as evidenced by the abundance of woody plant fossils (Gadd and Peter, 2018) and pelagic and chemical condensed sedimentation that forms the Transition Zone shales and concretions (Fraser and Hutchinson, 2017). The lack of sediments accumulating on the seafloor and the prolonged exposure of the seafloor to the water column would have promoted authigenic metal enrichment from ambient seawater, ultimately forming the thin mineralized horizon. Such a relatively long timespan of exposure on the seafloor would have enabled continued incomplete scavenging of molybdenum, resulting in the high molybdenum abundance in the Peel River sediments and the observed isotopic fractionation. Transgressive/regressive cycles periodically refilled/replenished the Richardson Trough with upwelling, nutrient-rich, suboxic to anoxic bottom water over a timespan of several million years. Such pulses could have readily provided sufficient metals and sulphur to form the HEBS horizons, similar to an upwelling deepwater source suggested for the HEBS deposits along the Yangtze Platform in China (Lehmann et al., 2007, 2016; Och et al., 2013).

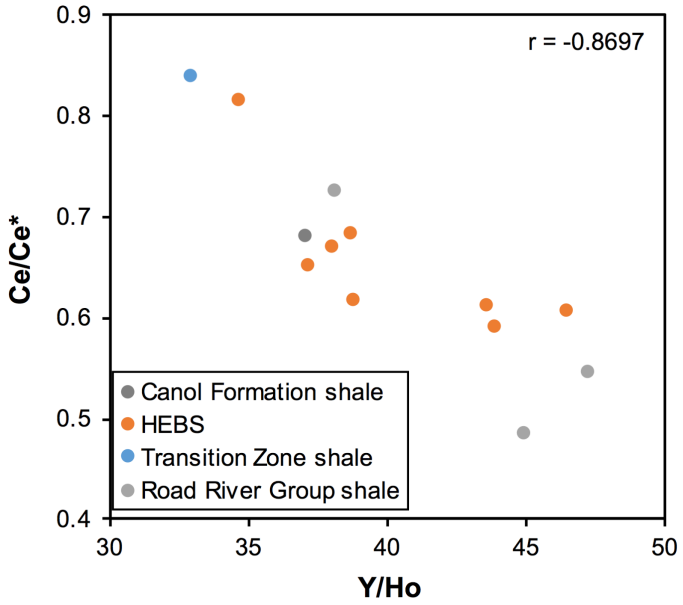

Figure 13. Bivariate plot of Ce/Ce* vs. Y/Ho for samples selected for Tl isotope analyses. The r value is shown.

Molybdenum and thallium isotopic compositions as paleoredox indicators?

The Peel River sulphide $\delta^{98}Mo$ values are lower that most known reservoirs, although they do fall within the range cited for euxinic organic-rich mudstones (Kendall et al., 2017). Given the association of molybdenum with abundant sulphide minerals in the HEBS, the molybdenum isotope fractionation mechanism away from seawater must be linked to reducing and euxinic processes. Anoxic to euxinic conditions are evidenced by the presence of organic matter, including preserved wood and the replacement of organic material by pyrite. Euxinic marine sediments have low $\varepsilon^{205}Tl$, although not as low as the values for the Peel River sediments. However, the association of thallium with abundant sulphide minerals similarly suggests the thallium isotope fractionation mechanism away from seawater must be linked to reducing or euxinic processes.

In comparison to the selected bulk geochemical paleoredox indicators, both $\delta^{98}Mo$ and $\varepsilon^{205}Tl$ values show no correlation with Ce anomaly (Fig. 14a, b), however, they both show moderate to strong positive correlations with V/Cr (r = 0.56 and 0.45, respectively; Fig. 14c, d), Ni/Co (r = -0.76 and -0.75; Fig. 14e, f), Mo (r = -0.66 and -0.61; Fig. 14g, h), and Re/Mo (r = -0.67 and -0.64; Fig. 14i, j). This implies that at the Peel River site both molybdenum and thallium isotopic compositions of the sedimentary rocks and mineralization together have potential to serve as paleoredox indicators of pore fluid conditions in the shallow subsurface, but they are of limited use in the interpretation of paleowater column conditions.

Conclusions

Molybdenum and thallium isotopic compositions of representative samples collected over a 200 m stratigraphic traverse through Middle Devonian Ni-PGE HEBS at the Peel River, northern Yukon show clear differences between the host marine sedimentary rocks and HEBS mineralization. The footwall and hanging-wall strata exhibit slightly positive $\delta^{98}Mo$ values (0.05 to 0.60‰) and negative $\varepsilon^{205}Tl$ values (-4.8 to -4.4), whereas the HEBS mineralization exhibits lower $\delta^{98}Mo$ values and $\varepsilon^{205}Tl$ values (-1.1 to -0.53‰ and -8.1 to -5.2, respectively) than the host sedimentary rocks. These isotopic compositions rule out a seafloor-hydrothermal genesis for the mineralization and suggest that the Mo and Tl isotopic compositions of the Peel River sediments may be used as indicators of sub-seafloor paleoredox conditions, but not the paleowater column.

The background sedimentation at the Peel River localities took place in ambient suboxic water column conditions. The HEBS sulphide mineralization, however, was precipitated in anoxic to euxinic conditions in the sub-seafloor. The $\delta^{98}Mo$ and $\varepsilon^{205}Tl$ values of the Peel River sedimentary rock and HEBS

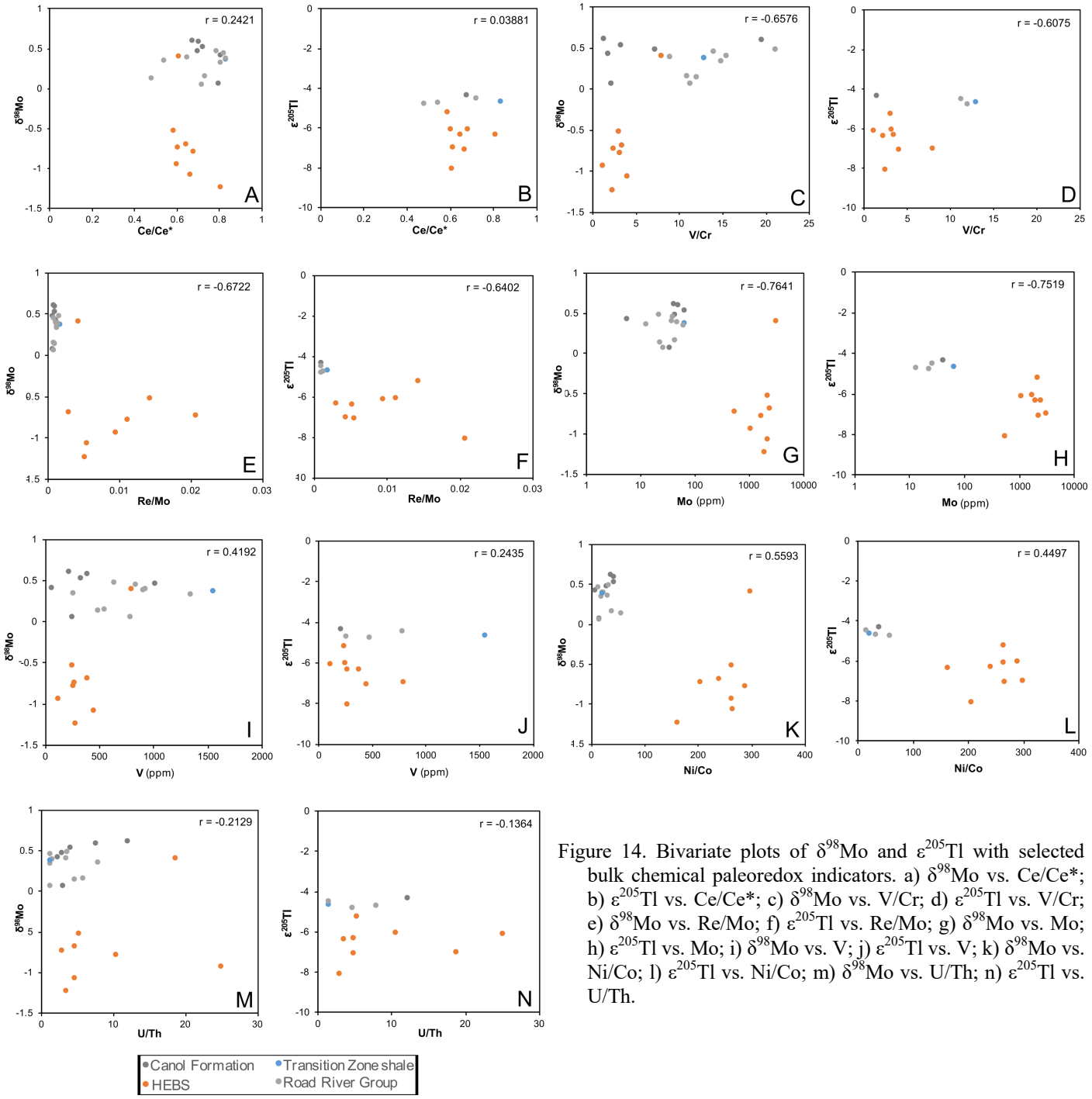

Figure 14. Bivariate plots of δ^{98}Mo and ε^{205}Tl with selected bulk chemical paleoredox indicators. a) δ^{98}Mo vs. Ce/Ce*; b) ε^{205}Tl vs. Ce/Ce*; c) δ^{98}Mo vs. V/Cr; d) ε^{205}Tl vs. V/Cr; e) δ^{98}Mo vs. Re/Mo; f) ε^{205}Tl vs. Re/Mo; g) δ^{98}Mo vs. Mo; h) ε^{205}Tl vs. Mo; i) δ^{98}Mo vs. V; j) ε^{205}Tl vs. V; k) δ^{98}Mo vs. Ni/Co; l) ε^{205}Tl vs. Ni/Co; m) δ^{98}Mo vs. U/Th; n) ε^{205}Tl vs. U/Th.

samples, together with the other bulk paleoredox indicators and REE, indicate that the molybdenum and thallium were both sourced from seawater. We suggest the molybdenum and thallium isotopic compositions of the Peel River sediments reflects the molybdenum and thallium isotopic compositions of seawater at the time of deposition. Precipitation of the HEBS deposits occurred under closed system isotopic fractionation of coeval seawater under reducing and euxinic conditions, resulting in both molybdenum and thallium isotopic shifts, relative to the host sediments. Each HEBS horizon in the Richardson Trough was precipitated on the seafloor over a lengthy time (ca. 1–2 Ma) during periods of extremely low sedimentation. During this time, upwelling, nutrient-rich anoxic bottom waters filled the basin, and periodically replenished it. Together these two factors supplied the seafloor with adequate metals and sulphur from which the HEBS horizons were formed.

Ongoing and future work

The molybdenum and thallium isotope analyses presented here are only a subset of samples chosen for isotopic analysis. Analysis of the remaining samples is proceeding, and this will contribute to more robust interpretations. We also plan to undertake partial leaches on a subset of the Peel River samples to better understand the mineral hosts of molybdenum and thallium in both the sedimentary rocks and the mineralization.

Acknowledgments

This report is a contribution to NRCan's Targeted Geoscience Initiative Program (TGI). Support for this study was provided through the Volcanic- and Sedimentary-Hosted Base Metal Ore System '*Activity VS-1.2: "Development of genetic and exploration models for hyper-enriched black shale (HEBS) deposits*".

The authors thank the Polar Continental Shelf Program (Project 00717) for additional funding and field logistical support. Personal funding to the senior author came from the Queen Elizabeth II Diamond Jubilee Scholarship. Claire Leighton of Queen's University is thanked for assistance in the field, and Tiffani Fraser and Leyla Weston of the Yukon Geological Survey graciously shared their knowledge of Yukon shales in the field. We are sincerely grateful to the Gwich'in Tribal Council for allowing us to perform research on their traditional lands. This report benefited from the review of Simon Jackson, Wouter Bleeker and Neil Rogers.

References

Alibo, D.S. and Nozaki, Y., 1999. Rare earth elements in seawater: Particle association, shale-normalization, and Ce oxidation; Geochimica et Cosmochimica Acta, v. 63, p. 363–372.

Anbar, A.D. and Rouxel, O., 2007. Metal stable isotopes in paleoceanography; Annual Review of Earth and Planetary Science, v. 35, p. 717–746.

Andersen, M.B., Romaniello, S., Vance, D., Little, S.H., Herdman, and R., Lyons, T.W., 2014. A modern framework for the interpretation of $^{238}U/^{235}U$ in studies of ancient ocean redox; Earth and Planetary Science Letters, v. 400, p. 184–194.

Arnold, A.G.L., Anbar, A.D., Barling, J., and Lyons, T.W., 2004. Molybdenum isotope evidence for widespread anoxia in Mid-Proterozoic oceans; Science, v. 304, p. 87–90.

Baker, R.G.A., Rehkämper, M., Hinkley, T.K., Nielsen, S.G., and Toutain, J.P., 2009. Investigation of thallium fluxes from subaerial volcanism-Implications for the present and past mass balance of thallium in the oceans; Geochimica et Cosmochimica Acta, v. 73, p. 6340–6359.

Bau, M., 1999. Scavenging of dissolved yttrium and rare earths by precipitating iron oxyhydroxide: experimental evidence for Ce oxidation, Y-Ho fractionation, and lanthanide tetrad effect; Geochimica et Cosmochimica Acta, v. 63, p. 67–77.

Bau, M. and Dulski, P., 1995. Comparative study of yttrium and rare-earth element behaviours in fluorine-rich hydrothermal fluids; Contributions to Mineralogy Petrology, v. 119, p. 213–223.

Bau, M. and Dulski, P., 1996. Distribution of yttrium and rare-earth elements in the Penge and Kurumaniron-formations, Transvaal Supergroup, South Africa; Precambrian Research, v. 79, p. 37–55.

Bau, M. and Dulski, P. 1999. Comparing yttrium and rare earths in hydrothermal fluids from the Mid-Altantic Ridge: implications for Y and REE behaviour during near-vent mixing and for the Y/Ho ratio of Proterozoic seawater; Chemical Geology, v. 155, p. 77–90.

Bau, M., Moller, P., and Dulski, P., 1997. Yttrium and lanthanides in eastern Mediterranean seawater and their fractionation during redox-cycling; Marine Chemistry, v. 56, p. 123–131.

Barling, J., Arnold, G.L., and Anbar, A.D., 2001. Natural mass-dependent variations in the isotopic composition of molybdenum; Earth and Planetary Science Letters, v. 193, p. 447–457.

Bigeleisen, J., Brook, S., and York, N., 1996. Nuclear size and shape effects in chemical reactions: Isotope chemistry of the heavy elements; Journal of the American Chemical Society, v. 118, p. 3676–3680.

Bigeleisen, J. and Mayer, M.G., 1947. Calculation of equilibrium constants for isotopic exchange reactions; Journal of Chemical Physics, v. 15, p. 261–267.

Breillat, N., Guerrot, C., Marcoux, E., and Négrel, P., 2016. A new global database of $\delta^{98}Mo$ in molybdenites: a literature review and new data; Journal of Geochemical Exploration, v. 161, p. 1–15.

Breit, G.N. and Wanty, R.B., 1991. Vanadium accumulation in carbonaceous rocks: A review of geochemical controls during deposition and diagenesis; Chemical Geology, v. 91, p. 83–97.

Burton, K.W., 2006. Global weathering variations inferred from marine radiogenic isotope records; Journal of Geochemical Exploration, v. 88, p. 262-265.

Calvert, S.E. and Pedersen, T.F., 1993. Geochemistry of Recent oxic and anoxic marine sediments: Implications for the geological record; Marine Geology, v. 113, p. 67–88.

Cecile, M.P., 1982. The lower Paleozoic Misty Creek embayment, Selwyn Basin, Yukon and Northwest Territories; Geological Survey of Canada, Bulletin 335, 78 p.

Coggon, R.M., Rehkämper, M., Atteck, C., Teagle, D.A.H., Alt, J.C., and Cooper, M.J., 2014. Controls on thallium uptake during hydrothermal alteration of the upper ocean crust; Geochimica et Cosmochimica Acta, v. 144, p. 25–42.

Collier, R.W., 1985. Molybdenum in the Northeast Pacific Ocean; Limnology and Oceanography, v. 30, p. 1351–1354.

Crusius, J., Calvert, S., Pedersen, T., and Sage, D., 1996. Rhe-

nium and molybdenum enrichments in sediments as indicators of oxic, suboxic and sulfidic conditions of deposition; Earth and Planetary Science Letters, v. 145, p. 65–78.

Dahl, T.W., Anbar, A.D., Gordon, G.W., Rosing, M.T., Frei, R., and Canfield, D.E., 2010. The behaviour of molybdenum and its isotopes across the chemocline and in the sediments of sulfidic Lake Cadagno, Switzerland; Geochimica et Cosmochimica Acta, v. 74, p. 144–163.

De Baar, H.J.W., Bacon, M.P., Brewer, P.G., and Bruland, K.W., 1985a. Rare earth elements in the Pacific and Atlantic Oceans; Geochimica et Cosmochimica Acta, v. 49, p. 1943–1959.

De Baar, H.J., Brewer, P.G., and Bacon, M.P., 1985b. Anomalies in rare earth distributions in sea- water: Gd and Tb; Geochimica et Cosmochimica Acta, v. 49, p. 1961–1969.

De Baar, H.J.., German, C.R., Elderfield, H., and Van Gaans, P., 1988. Rare earth element distribution in anoxic waters of the Cariaco Trench. Geochimica et Cosmochimica Acta, v. 52, p. 1203–1219.

Dickson, A.J., Jenkyns, H.C., Porcelli, D., van den Boorn, S., Idiz, E., and Owens, J.D., 2016. Basin-scale controls on the molybdenum-isotope composition of seawater during Oceanic Anoxic Event 2 (Late Cretaceous); Geochimica et Cosmochimica Acta, v. 189, p. 404–405.

Dumala, M.R., 2007a. Assessment report describing prospecting, mapping, geochemical sampling, geophysical surveys and diamond drilling at the Pe property, prepared for Southampton Ventures Inc. and Strategic Metals Ltd.; Archer, Cathro & Associates (1981) Ltd., Whitehorse, Yukon, 151 p.

Dumala, M.R., 2007b. Assessment report describing prospecting, mapping, geochemical sampling, geophysical surveys and diamond drilling at the El property, prepared for Southampton Ventures Inc. and Strategic Metals Ltd.; Archer, Cathro & Associates (1981) Ltd., Whitehorse, Yukon, 279 p.

Emerson, S.R. and Huested, S.S., 1991. Ocean anoxia and the concentrations of molybdenum and vanadium in seawater; Marine Chemistry, v. 34, p. 177–196.

Flegal, A.R. and Patterson, C.C., 1985. Thallium concentrations in seawater; Marine Chemistry, v. 15, p. 327–331.

Fraser, T.A. and Hutchison, M.P., 2017. Lithogeochemical characterization of the Middle – Upper Devonian Road River Group and Canol and Imperial formations on Trail River, east Richardson Mountains, Yukon: age constraints and a depositional model for fine-grained strata in the Lower Paleozoic Richardson trough; Canadian Journal of Earth Science, v. 54, p. 731–765.

Gabrielse, H., 1967. Tectonic evolution of the northern Canadian Cordillera; Canadian Journal of Earth Science, v. 4, p. 271–298.

Gadd, M.G. and Peter, J.M., 2018. Field observations, mineralogy and geochemistry of Middle Devonian Ni-Zn-Mo-PGE hyper-enriched black shale deposits, Yukon; *in* Targeted Geoscience Initiative: 2017 report of activities, volume 1, (ed.) N. Rogers; Geological Survey of Canada, Open File 8358, p. 193–206.

Goldstein, S.J. and Jacobsen, S., 1988. Rare earth elements in river waters; Earth and Planetary Science Letters, v. 89, p. 35–47.

Goodfellow, W.D., 1981. Geochemistry of shales and cherts hosting stratabound Zn-Pb deposits, Selwyn Basin, Yukon Territory; Geological Society of America, Program Abstracts v, 12, p. 461.

Goodfellow, W.D., 2007. Base metal metallogeny of the Selwyn Basin, Canada; *in* Mineral Resources of Canada: A Synthesis of Major Deposit-Types, District Metallogeny, the Evolution of Geological Provinces, and Exploration Methods, (ed.) W.D. Goodfellow; Geological Association of Canada, Mineral Deposits Division, Special Publication 5, p. 553–579.

Goodfellow, W.D., Geldsetzer, H., Gregoire, C., Orchard, and M., Cordey, F., 2010. Geochemistry and origin of geographically extensive Ni-(Mo, Zn, U)-PGE sulphide deposits hosted in Devonian black shales, Yukon; *in* TGI-3 Workshop: Public Geoscience in Support of Base Metal Exploration, Simon Fraser University, Vancouver, British Columbia, p. 15–18.

Gordon, G.W., Lyons, T.W., Arnold, G.L., Roe, J., Sageman, B.B., and Anbar, A.D., 2009. When do black shales tell molybdenum isotope tales? Geology, v. 37, p. 535–538.

Gregory, D., 2008. Assessment report describing prospecting, mapping, geochemical sampling, geophysical surveys and diamond drilling at the El property, prepared for Southampton Ventures Inc. and Strategic Metals Ltd. Archer, Cathro & Associates (1981) Limited; Whitehorse, Yukon, 56 p.

Heinrichs, H., Schulz-Dobrick, B., and Wedepohl, K.H., 1980. Terrestrial geochemistry of Cd, Bi, Tl, Pb, Zn and Rb; Geochimica et Cosmochimica Acta, v. 44, p. 1519–1533.

Helz, G.R., Bura-Nakić, E., Mikac, N., and Ciglenečki, I., 2011. New model for molybdenum behaviour in euxinic waters; Chemical Geology, v. 284, p. 323–332.

Héon, D., 2006. Mineral Assessment of the Eagle Plain Study Area, Yukon; Energy, Mines and Resources. Yukon Geological Survey, Open File 2006-3, 126 p.

Hettmann, K., Kreissig, K., Rehkämper, M., Wenzel, T., Mertz -Kraus, R., and Markl, G., 2014. Thallium geochemistry in the metamorphic Lengenbach sulfide deposit, Switzerland: Thallium-isotope fractionation in a sulfide melt; American Mineralogist, v. 99, p. 793–803.

Hulbert, L.J., Conrad Gregoire, D., Paktunc, D., and Carne, R.C., 1992. Sedimentary nickel, zinc, and platinum-group-element mineralization in Devonian black shales at the Nick property, Yukon, Canada: A new deposit type; Exploration Mining Geology, v. 1, p. 39–62.

Jiang, S.Y., Chen, Y.Q., Ling, H.F., Yang, J.H., Feng, H.Z., and Ni, P., 2006. Trace- and rare-earth element geochemistry and Pb-Pb dating of black shales and intercalated Ni-Mo-PGE-

Au sulfide ores in Lower Cambrian strata, Yangtze Platform, South China; Mineralium Deposita, v. 41, p. 453–467.

Jones, B. and Manning, D.A.C., 1994. Comparison of geochemical indices used for the interpretation of palaeoredox conditions in ancient mudstones; Chemical Geology, v. 111, p. 111–129.

Jowitt, S.M. and Keays, R.R., 2011. Shale-hosted Ni–(Cu–PGE) mineralisation: a global overview. A global overview; Transactions of the Institution of Mining and Metallurgy Section B – Applied Earth Science, v. 120, p. 187–197.

Kampschulte, A. and Strauss, H., 2004. The sulfur isotopic evolution of Panerozoic seawater based on the analysis of structurally substituted sulfate in carbonates; Chemical Geology, v. 204, p. 255–286.

Kaplan, D.I. and Mattigod, S.V., 1998. Aqueous geochemistry of thallium; *in* Thallium Environment, volume 2, (ed.) J.O. Nriagu; Wiley & Sons, p. 15–29.

Kendall, B., Gordon, G.W., Poulton, S.W., and Anbar, A.D., 2011. Molybdenum isotope constraints on the extent of late Paleoproterozoic ocean euxinia; Earth and Planetary Science Letters, v. 307, p. 450–460.

Kendall, B., Dahl, T.W., and Anbar, A.D., 2017. The stable isotope geochemistry of molybdenum; Reviews in Mineralogy and Geochemistry, v. 82, p. 683–732.

Kersten, M., Xiao, T., Kreissig, K., Brett, A., Coles, B.J., and Rehkämper, M., 2014. Tracing anthropogenic thallium in soil using stable isotope compositions; Environmental Science and Technology, v. 48, p. 9030–9036.

Kiseeva, E.S. and Wood, B.J., 2013. A simple model for chalcophile element partitioning between sulphide and silicate liquids with geochemical applications; Earth and Planetary Science Letters, v. 383, p. 68–81.

Knyazev, D.A. and Myasoedov, N.F., 2001. Specific effects of heavy nuclei in chemical equilibrium; Separation Science and Technology, v. 36, p. 1677–1696.

Kontinen, A., Peltonen, P., and Huhma, H., 2006. Description and genetic modelling of the Outokumpu-type rock assemblage and associated sulphide deposits. Final technical report for GEOMEX JV; Report number M10?4/2006/1, Geological Survey of Finland, Espoo, Finland, p. 378.

Lehmann, B., Nägler, T.F., Holland, H.D., Wille, M., Mao, J., Pan, J., Ma, D., and Dulski, P., 2007. Highly metalliferous carbonaceous shale and Early Cambrian seawater; Geology, v. 35, p. 403–406.

Lehmann, B., Frei, R., Xu, L., and Mao, J., 2016. Early Cambrian black shale-hosted Mo-Ni and V mineralization on the rifted margin of the Yangtze platform, China: Reconnaissance chromium isotope data and a refined metallogenic model; Economic Geology, v. 111, p. 89–103.

Lingang, X., Lehmann, B., Jingwen, M., Wenjun, Q., and Andao, D., 2011. Re-Os age of polymetallic Ni-Mo-PGE-Au mineralization in Early Cambrian black shales of South China - A reassessment; Economic Geology, v. 106, p. 511–522.

Loukola-Rusekeeniemi, K. and Heino, T., 1996. Geochemistry and genesis of the black shale-hosted Ni-Cu-Zn deposit at Talvivaara, Finland; Economic Geology, v. 91, p. 80–110.

Magnall, J.M., Gleeson, S.A., Poulton, S.W. Gordon, G.W., and Paradis, S., 2018. Links between seawater paleoredox and the formation of sediment-hosted massive sulphide (SHMS) deposits – Fe speciation and Mo isotope; Chemical Geology, v. 490, p. 45–60.

Mao, J., Lehmann, B., Du, A., Zhang, G., Ma, D., Wang, Y., Zeng, M., and Kerrich, R., 2002. Re-Os dating of polymetallic Ni-Mo-PGE-Au mineralization in Lower Cambrian black shales of South China and its geologic significance; Economic Geology, v. 97, p. 1051–1061.

Matthews, A.D. and Riley, J.P., 1970. The occurrence of thallium in sea water and marine sediments; Chemical Geology, v. 6, p. 149–152.

McDonough, W.F. and Sun, S.S., 1995. The composition of the Earth; Chemical Geology, v. 120, p. 223–253.

McGoldrick, P.J., Keays, R.R., and Scott, B.B., 1979. Thallium: a sensitive indicator of rock/seawater interaction and of sulfur saturation of silicate melts; Geochimica et Cosmochimica Acta, v. 43, p. 1303–1311.

McManus, J., 2002. Oceanic molybdenum isotope fractionation: Diagenesis and hydrothermal ridge-flank alteration; Geochemistry, Geophysics, Geosystems, v. 3, p. 1–9.

McLennan, S.M., 1989. Rare earth elements in sedimentary rocks: influence of provenance and sedimentary processes; Reviews in Mineralogy and Geochemistry, v. 21, p. 160–200.

Morford, J.L. and Emerson, S., 1999. The geochemistry of redox sensitive trace metals in sediments; Geochimica et Cosmochimica Acta, v. 63, p. 1735–1750.

Morrow, D.W., Dubord, M.P., Uyeno, T.T., Norris, A.W., and Norford, B.S., 1999. Lower Paleozoic stratigraphy of northern Yukon Territory and northwestern District of Mackenzie; Geological Survey of Canada, Bulletin 538, 202 p.

Nägler, T.F., Anbar, A.D., Archer, C., Goldberg, T., Gorden, G.W., Greber, N.D., Siebert, C., Sohrin , Y., and Vance, D., 2014. Proposal for an international molybdenum isotope measurement standard and data representation. Geostandards and Geoanalytical Research, v. 38, p. 149–151.

Nielsen, S.G. and Rehkämper, M., 2012. Thallium isotopes and their application to problems in earth environmental science; *in* Handbook of Environmental Isotope Geochemistry, Advances in Isotope Geochemistry, (ed.) M. Baskaran; Springer, v. 1, p. 247–269.

Nielsen, S.G., Rehkämper, M., Baker, J., and Halliday, A.N., 2004. The precise and accurate determination of thallium isotope compositions and concentrations for water samples by MC-ICPMS; Chemical Geology, v. 204, p. 109–124.

Nielsen, S.G., Rehkämper, M., Porcelli, D., Andersson, P., Halliday, A.N., Swarzenski, P.W., Latkoczy, C., and Günther, D., 2005. Thallium isotope composition of the upper continental crust and rivers - An investigation of the conti-

nental sources of dissolved marine thallium; Geochimica et Cosmochimica Acta, v. 69, p. 2007–2019.

Nielsen, S.G., Rehkämper, M., Teagle, D.A.H., Butterfield, D.A., Alt, J.C., and Halliday, A.N., 2006. Hydrothermal fluid fluxes calculated from the isotopic mass balance of thallium in the ocean crust; Earth and Planetary Science Letters, v. 251, p. 120–133.

Nielsen, S.G., Rehkämper, M., Brandon, A.D., Norman, M.D., Turner, S., and O'Reilly, S.Y., 2007. Thallium isotopes in Iceland and Azores lavas - Implications for the role of altered crust and mantle geochemistry; Earth and Planetary Science Letters, v. 264, p. 332–345.

Nielsen S.G., Mar-Gerrison, S., Gannoun, A., LaRowe, D.E., Klemm, V., Halliday, A.N., Burton, K.W., and Hein, J.R., 2009. Thallium isotope evidence for increased marine organic carbon export in the early Eocene; Earth and Planetary Science Letters, v. 278, p. 297–307.

Nielsen, S.G., Goff, M., Hesselbo, S.P., Jenkyns, H.C., LaRowe, D.E., and Lee, C.T.A., 2011. Thallium isotopes in early diagenetic pyrite - A paleoredox proxy?; Geochimica et Cosmochimica Acta, v. 75, p. 6690–6704.

Nielsen, S.G., Rehkämper, M., and Prytulak, J., 2017. Investigation and Application of thallium isotope fractionation; Reviews in Mineralogy and Geochemistry, v. 82, p. 759–798.

Norris, A.W., 1985. Stratigraphy of Devonian outcrop belts in northern Yukon Territory and northwestern District of Mackenzie (Operation Porcupine area); Geological Survey of Canada, Memoir 410, p. 81.

Nozaki, Y., 1997. A fresh look at element distribution in the North Pacific Ocean; EOS, Transactions American Geophysical Union, v. 78, p. 221.

Nozaki, Y. and Zhang, J., 1995. The rare earth elements and yttrium in the coastal/offshore mixing zone of Tokyo Bay waters and the Kuroshio; *in* Biogeochemical Processes and Ocean Flux in the Western Pacific, (ed.) H. Sakai and Y. Nozaki; Terra, p. 171–184.

Nriagu, J.O., 1998. Thallium in the environment; *in* Advances in Environmental Sciences and Technology; Wiley & Sons, New York, v. 29, p. 284.

Och, L.M., Shields-Zhou, G.A., Poulton, S.W., Manning, C., Thirlwall, M.F., Li, D., Chen, X., Ling, H., Osborn, T., and Cremonese, L., 2013. Redox changes in Early Cambrian black shales at Xiaoton section, Yunnan Province, South China; Precambrain Research, v. 225, p. 166–189

Olivarez, A.M. and Owen, R.M., 1991. The europium anomaly of seawater: implications for fluvial versus hydrothermal REE inputs to the oceans; Chemical Geology, v. 92, p. 317–328.

Owens, J.D., Nielsen, S.G., Horner, T.J., Ostrander, C.M., and Peterson, L.C., 2017. Thallium-isotopic compositions of euxinic sediments as a proxy for global manganese-oxide burial; Geochimica et Cosmochimica Acta, v. 213, p. 291–307.

Parry, D. and Carne, R.C., 1990. Geological mapping, geochemical sampling and diamond drilling at the Nick Property, Yukon. Nick Property; Yukon Territory assessment report, Archer, Cathro & Associates (1981) Ltd., p. 1–34.

Paytan, A., Kastner, M., Campbell, D., and Thiemens, M.H., 1998. Sulfur isotopic composition of Cenozoic seawater sulfate; Science v. 282, p. 1459–1462.

Paytan, A., Kastner, M., Campbell, D., and Thiemens, M.H., 2004. Seawater sulfur isotope fluctuations in the cretaceous; Science, v. 304, p. 1663–1665.

Peacock C.L. and Moon E.M., 2012. Oxidative scavenging of thallium by birnessite: explanation for thallium enrichment and stable isotope fractionation in marine ferromanganese precipitates; Geochimica et Cosmochimica Acta, v. 84, p. 297–313.

Pearce, C.R., Cohen, A.S., and Parkinson, I.J., 2009. Quantitative separation of molybdenum and rhenium from geological materials for isotopic determination by MC-ICP-MS; Geostandards and Geoanalytical Research, v. 33, p. 219–229.

Peter, J.M., Gadd, M.G., Matthews, D.L., and Voinot, A., 2018. Reconnaissance thallium isotope study of zinc - lead SEDEX mineralization and host rocks in the Howard's Pass district, Selwyn Basin, Yukon: Potential application to paleoredox determinations and fingerprinting of mineralization; *in* Targeted Geoscience Initiative: 2017 report of activities, volume 1, (ed.) N. Rogers; Geological Survey of Canada, Open File 8358, p. 173–191.

Poulson, R.L., Siebert, C., McManus, J., and Berelson, W.M., 2006. Authigenic molybdenum isotope signatures in marine sediments; Geology, v. 34, p. 617–620.

Püttman, W., Heppenheimer, H., and Diesel, R., 1989. Accumulation of copper in the Permain Kupferschiefer: A result of post-depositional redox reactions; Advances in Organic Geochemistry, v. 16, p. 1145–1156.

Quinby-Hunt, M.S. and Turekian, K.K., 1983. Distribution of elements in sea water; EOS, Transactions of the American Geophysical Union, v. 64, p. 130–132.

Raiswell, R., Buckley, F., Berner, R., and Anderson, T.F., 1988. Degree of pyritization of iron as a paleoenvironmental indicator of bottom-water oxygenation; Journal of Sedimentary Petrology, v. 58, p. 812–819.

Rehkämper, M. and Halliday, A.N., 1999. The precise measurement of Tl isotopic compositions by MC-ICPMS: Application to the analysis of geological materials and meteorites; Geochimica et Cosmochimica Acta, v. 63, p. 935–944.

Rehkämper, M. and Nielsen, S.G., 2004. The mass balance of dissolved thallium in the oceans; Marine Chemistry, v. 85, p. 125–139.

Rehkämper, M., Frank, M., Hein, J.R., Porcelli, D., Halliday, A., Ingri, J., and Liebetrau, V., 2002. Thallium isotope variations in seawater and hydrogenetic, diagenetic, and hydrothermal ferromanganese deposits; Earth and Planetary Science Letters, v. 197, p. 65–81.

Rimmer, S.M., 2004. Geochemical paleoredox indicators in Devonian-Mississippian black shales, Central Appalachian

Basin (USA); Chemical Geology, v. 206, p. 373–391.

Ross, D.J.K. and Bustin, R.M., 2009. Investigating the use of sedimentary geochemical proxies for paleoenvironment interpretation of thermally mature organic-rich strata: Examples from the Devonian-Mississippian shales, Western Canadian Sedimentary Basin; Chemical Geology, v. 260, p. 1–19.

Schauble, E.A., 2007. Role of nuclear volume in driving equilibrium stable isotope fractionation of mercury, thallium, and other very heavy elements; Geochimica et Cosmochimica Acta, v. 71, p. 2170–2189.

Scott, C. and Lyons, T.W., 2012. Contrasting molybdenum cycling and isotopic properties in euxinic versus non-euxinic sediments and sedimentary rocks: Refining the paleoproxies; Chemical Geology, v. 324–325, p. 19–27.

Scott, C., Lyons, T.W., Bekker, A., Shen, Y., Poulton, S.W., Chu, X., and Anbar, A.D., 2008. Tracing the stepwise oxygenation of the Proterozoic ocean; Nature, v. 452, p. 456–459.

Scott, C.T., Slack, J.F., and Kelley, K.D., 2013. The origin of vanadium hyper-enriched black shales; Geological Society of America, Abstracts and Program, v. 45, p. 427.

Scott, C.T., Slack, J.F., and Kelley, K.D., 2017. The hyper-enrichment of V and Zn in black shales of the Late Devonian-Early Mississippian Bakken Formation (USA); Chemical Geology, v. 452, p. 24–33.

Shannon, R.D., 1976. Revised effective ionic radii and systematic studies of interatomic distances in halides and chalcogenide; Acta Crystallographica, v. 32, p. 751–767.

Shaw, D.M., 1952. The geochemistry of thallium; Geochimica et Cosmochimica Acta. v. 2, p. 118–154.

Siebert, C., Nägler, T.F., von Blanckenburg, F., and Kramers, J.D., 2003. Molybdenum isotope records as a potential new proxy for paleoceanography; Earth and Planetary Science Letters. v. 211, p. 159–171.

Slack, J.F., Selby, D., and Dumoulin, J.A., 2015. Hydrothermal, biogenic, and seawater components in metalliferous black shales of the Brooks Range, Alaska: Synsedimentary metal enrichment in a carbonate ramp setting; Economic Geology, v. 110, p. 653–675.

Steiner, M., Wallis, E., Erdtmann, B.D., Zhao, Y., and Yang, R., 2001. Submarine-hydrothermal exhalative ore layers in black shales from South China and associated fossils - Insights into a Lower Cambrian facies and bio-evolution; Palaeogeography, Palaeoclimatology, Palaeoecology, v. 169, p. 165–191.

Taylor, S.R. and McLennan, S.M., 1985. The Continental Crust: Its Composition and Evolution: An Examination of the Geochemical Record Preserved in Sedimentary Rocks; Blackwell Science, Oxford, 312 p.

Tribovillard, N., Algeo, T.J., Lyons, T., and Riboulleau, A., 2006. Trace metals as paleoredox and paleoproductivity proxies: An update; Chemical Geology, v. 232, p. 12–32.

Tostevin, R., Shields, G.A., Tarbuck, G.M., He, T., Clarkson, M.O., and Wood, R.A., 2016. Effective use of cerium anomalies as a redox proxy in carbonate-dominated marine settings; Chemical Geology, v. 438, p. 146–162.

Tucker, R.D., Bradley, D.C., Van Straeten, C.A., Harris, A.G., Ebert, J.R., and McCutcheon, S.R., 1998. New U–Pb zircon ages and the duration and division of Devonian time; Earth and Planetary Science Letters, v. 158, p. 175–186.

Turner, A., Cabon, A., Glegg, G.A., and Fisher, A.S., 2010. Sediment-water interactions of thallium under simulated estuarine conditions; Geochimica et Cosmochimica Acta, v. 74, p. 6779–6787.

Urey, H.C., 1947. The thermodynamic properties of isotopic substances; Journal of Chemical Society, v. 85, p. 562–581.

Vine, J.D. and Tourtel, E.B., 1970. Geochemistry of black shale deposits - A summary report; Economic Geology, v. 65, p. 253–272.

Voegelin, A.R., Pettke, T., Greber, N.D., von Niederhäusern, B., and Nägler, T.F., 2014. Magma differentiation fractionates Mo isotope ratios: evidence from the Kos Plateau Tuff (Aegean Arc); Lithosphere, v. 190, p. 440–448.

Wade, K. and Banister, A.J., 1973. The Chemistry of Aluminum, Gallium, Indium, and Thallium; Pergamon Press, Pergamon Texts in Inorganic Chemistry, v. 12, 214 p.

Wedepohl, K.H., 1995. The composition of the continental crust; Geochimica et Cosmochimica Acta, v. 59, p. 1217–1232.

Wickham, K., 2014. Thallium isotope implications for the metalliferous source of Carlin-type deposits in northern Nevada; M.Sc. thesis, University of Nevada, Reno, Nevada, 49 p.

Williams, H., Turner, S., Kelley, S., and Harris, N., 2001. Age and composition of dikes in Southern Tibet: New constraints on the timing of east-west extension and its relationship to post-collisional volcanism; Geology, v. 29, p. 339–342.

Wright, J., Schrader, H., and Holser, W.T., 1987. Paleoredox variations in ancient oceans recorded by rare earth elements in fossil apatite; Geochimica et Cosmochimica Acta, v. 51, p. 631–644.

Xiong, Y., 2007. Hydrothermal thallium mineralization up to 300°C: A thermodynamic approach; Ore Geology Reviews, v. 32, p. 291–313.

Xu, L., Lehmann, B., and Mao, J., 2013. Seawater contribution to polymetallic Ni-Mo-PGE-Au mineralization in Early Cambrian black shales of South China: Evidence from Mo isotope, PGE, trace element, and REE geochemistry; Ore Geology Reviews. v. 52, p. 66–84.

Yang, S. and Liu, Y., 2015. Nuclear volume effects in equilibrium stable isotope fractionations of mercury, thallium and lead; Scientific Reports, v. 5, p. 1–12.

Lithogeochemical and sulphur isotope indicators of environment of formation and genesis of the Moss hyper-enriched black shale showing, Yukon

M.G. Gadd[1], J.M. Peter[1], T.A. Fraser[2] and D. Layton-Matthews[3]

[1]*Geological Survey of Canada, 601 Booth Street, Ottawa, Ontario K1A 0E8*
[2]*Yukon Geological Survey, P.O. Box 2703 (K-14), Whitehorse, Yukon Y1A 2C6*
[3]*Department of Geological Sciences and Geological Engineering, Queen's University, 36 Union Street, Kingston, Ontario K7L 3N6*

Abstract

The Moss Ni-Mo-Zn-Pt-Pd-Re-Au hyper-enriched black shale (HEBS) showing is located in the western Richardson Mountains and is one of several in northern Yukon. The mineralization consists of a thin, stratiform semi-massive Fe-Ni-Mo-Zn sulphide horizon that occurs at the stratigraphic contact between the Road River Group and Canol Formation. This study evaluates the ambient paleoenvironmental conditions using several robust lithogeochemical proxies. Prior to HEBS formation, terrigenous clastic sedimentation predominated, whereas chemical sedimentation predominated during and immediately after HEBS formation. Rare earth element-Y data indicate that the water column was (weakly) oxygenated ($Ce/Ce^*_{SN} < 1$), that hydrothermal activity was absent ($Eu/Eu^*_{SN} \approx 1$), and that there was a significant seawater influence on the sedimentary environment (Y/Ho > 28) throughout the deposition interval, even during HEBS mineralization.

High (>10) authigenic Mo/U ratios suggest that a ferromanganese particulate shuttle delivered metals sourced from seawater to the seafloor. Negative bulk $\delta^{34}S$ values (-19.3 to -23‰) in the HEBS indicate that microbially reduced seawater sulphate was the source of reduced sulphur for the mineralization. Collectively, these data signify a basinal environment that experienced varying degrees of restriction and stratification, but fresh (i.e. unfractionated) marine waters delivered metals, metalloids, and sulphur. This type of geological setting is considered critical for the formation and preservation of HEBS mineralization.

Introduction

Hyper-enriched black shales (HEBS; also referred to as polymetallic metalliferous shales) are an important global resource for Zn, Ni, Cu, Mo, Se, U, V, ± Cr, Co, Ag, Au, platinum group elements (PGE) and rare earth elements (REE) (Jowitt and Keays, 2011). These deposits are thin (<10 cm) and laterally widespread, covering 1000s of km^2 (e.g. Cambrian, Yangtze Platform, China; Devonian, Mackenzie Platform, Yukon). Canada hosts some of the best examples globally (e.g. Nick prospect, Yukon: Hulbert et al., 1992). At the Nick Ni-Mo-Zn-PGE-Au-Re prospect, the first documented site of this style of mineralization in Yukon, the Ni sulphide horizon is thin (3–10 cm) and discontinuously crops out in several stream -cuts (Carne, 1989). Nick has been studied in detail (Hulbert et al., 1992; Horan et al., 1994; Orberger et al., 2003a, b, 2005; Pagés et al., 2018; Pasava et al., 2018), but there are several HEBS showings in north Yukon (Fig. 1a), with only Peel River receiving recent study (Gadd et al., 2017; Gadd and Peter, 2018).

A lack of understanding of how HEBS deposits formed hinders exploration for them. Several genetic models have been presented for HEBS; the two that have received the most favour are seafloor hydrothermal venting (Hulbert et al., 1992; Steiner et al., 2001) and hydrogenous (i.e. seawater) scavenging (Lehmann et al., 2007, 2016; Xu et al., 2011, 2013). Both genetic models require that enrichment of metals occurs on the seafloor or within the shallow subsurface, meaning that ambient paleoenvironmental redox conditions likely played a significant role in the formation and preservation of the HEBS. However, determining unambiguously ancient paleoenvironmental depositional conditions is difficult due to incomplete sedimentary records and post-depositional modifications to primary signatures. Bulk and trace element geochemical compositions of organic carbon-rich shales are commonly used to infer ancient depositional conditions, with the aim of resolving oxic (>2 mL O_2/L H_2O), suboxic (0.2–2 mL O_2/L H_2O), anoxic (0 mL O_2/L H_2O), and euxinic (>0 mL H_2S/L H_2O) environments (Tribovillard et al., 2006). These proxies are based on the behaviours of redox-sensitive elements in modern marine environments, and are commonly used to infer past oceanic conditions. Although many proxies have been developed to assess paleoredox, some of the most robust are REE-Y based (e.g. Ce) and Mo based (Mo/TOC: Algeo and Lyons, 2006; authigenic Mo and U: Algeo and Tribovillard, 2009; Re/Mo: Ross and Bustin, 2009).

Corresponding author: Michael Gadd (michael.gadd@canada.ca)

Gadd, M.G, Peter, J.M., Fraser, T.A., and Layton-Matthews, D., 2019. Lithogeochemical and sulphur isotope indicators of environment of formation and genesis of the Moss hyper-enriched black shale showing, Yukon; *in* Targeted Geoscience Initiative: 2018 report of activities, (ed.) N. Rogers; Geological Survey of Canada, Open File 8549, p. 163–178. https://doi.org/10.4095/313648

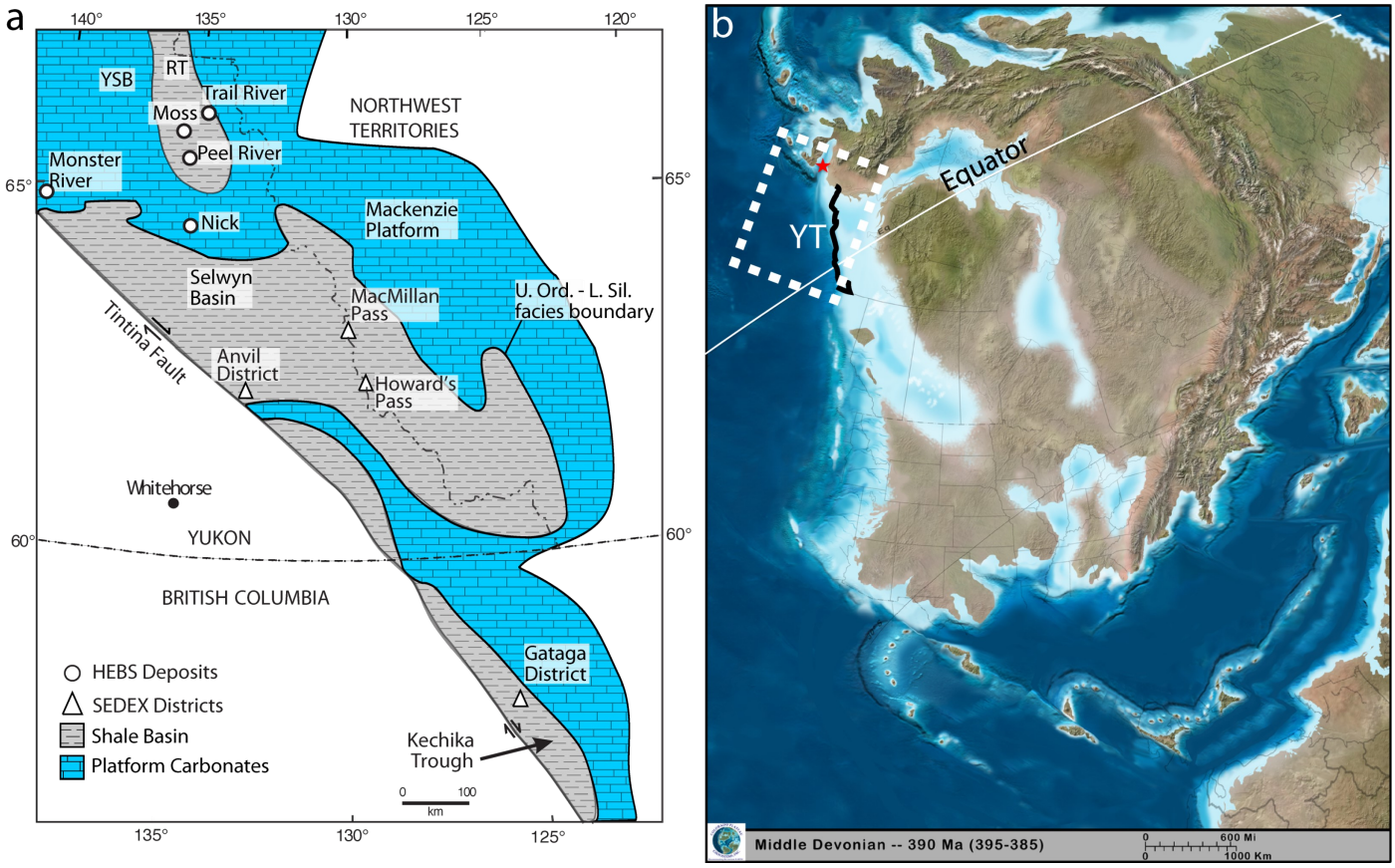

Figure 1. a) Map of the Paleozoic sedimentary facies in the northern Cordillera showing locations of key HEBS deposits and SEDEX districts. b) Middle Devonian paleogeographic reconstruction of North America at ca. 390 Ma (Blakey, 2013); white box outlines the Richardson trough area. Abbreviations: RT – Richardson trough; YSB – Yukon Stable Block.

Within the near-surface environment of reducing basinal sediments, bacterial reduction of seawater sulphate is generally the mechanism responsible for generating reduced sulphur (Berner, 1989). Negative $\delta^{34}S$ values (<<0‰) in sulphides are characteristic of biogenic sulphide (Sweeney and Kaplan, 1980), and such values have been determined for HEBS at the Nick prospect (Hulbert et al., 1992) and also for HEBS in China (Murowchick et al., 1994). Sulphur isotope analyses can provide additional details about the paleoenvironment and are commonly used to determine the source(s) and pathway(s) of sulphur in base metal sulphide deposits in sedimentary settings.

This contribution focuses on the lesser-known Moss HEBS locality in the western Richardson Mountains. Herein, the HEBS outcrop locality will be referred to as the "Moss" showing to differentiate it from the "Rich" Property showings (Dumala, 2007) observed in nearby exploration drill cores. This report presents a detailed lithogeochemical and paleoredox evaluation of a narrow interval that encompasses the rocks immediately beneath, within, and above HEBS. These data are supplemented with sulphur isotope measurements from the HEBS mineralization and barren massive pyrite beds from stratigraphy underlying the HEBS. As such, this research provides insight into some of the factors that control HEBS formation, which include basinal redox stratification, availability of metals and sulphur, very low sedimentation rate, and high biological productivity.

Regional geology

The Moss showing, and several other HEBS prospects, are located within Paleozoic basinal strata of the Richardson trough (Fig. 1a). This tectonic depression has been interpreted as a failed rift (Lane, 2007; Norris, 1985), and is bound to the east by the Mackenzie platform and to the west by the Yukon Stable Block, which for much of the early Paleozoic was a stable shelf (Fig. 1a; Morrow, 1999). At the time of formation, the Richardson trough was situated near the equator (Fig. 1b). The Richardson trough is characterized by >100 m of fine-grained, carbonaceous siliciclastic rocks of the Late Cambrian to Middle Devonian Road River Group (Fig. 2a; Morrow 1999). The Canol Formation overlies the Road River Group, and consists of up to approximately 220 m of Middle Devonian to early Late Devonian siliceous, carbonaceous shale (Hutchison and Fraser, 2015). The nature of the contact between the Road River Group and the overlying Canol Formation has been de-

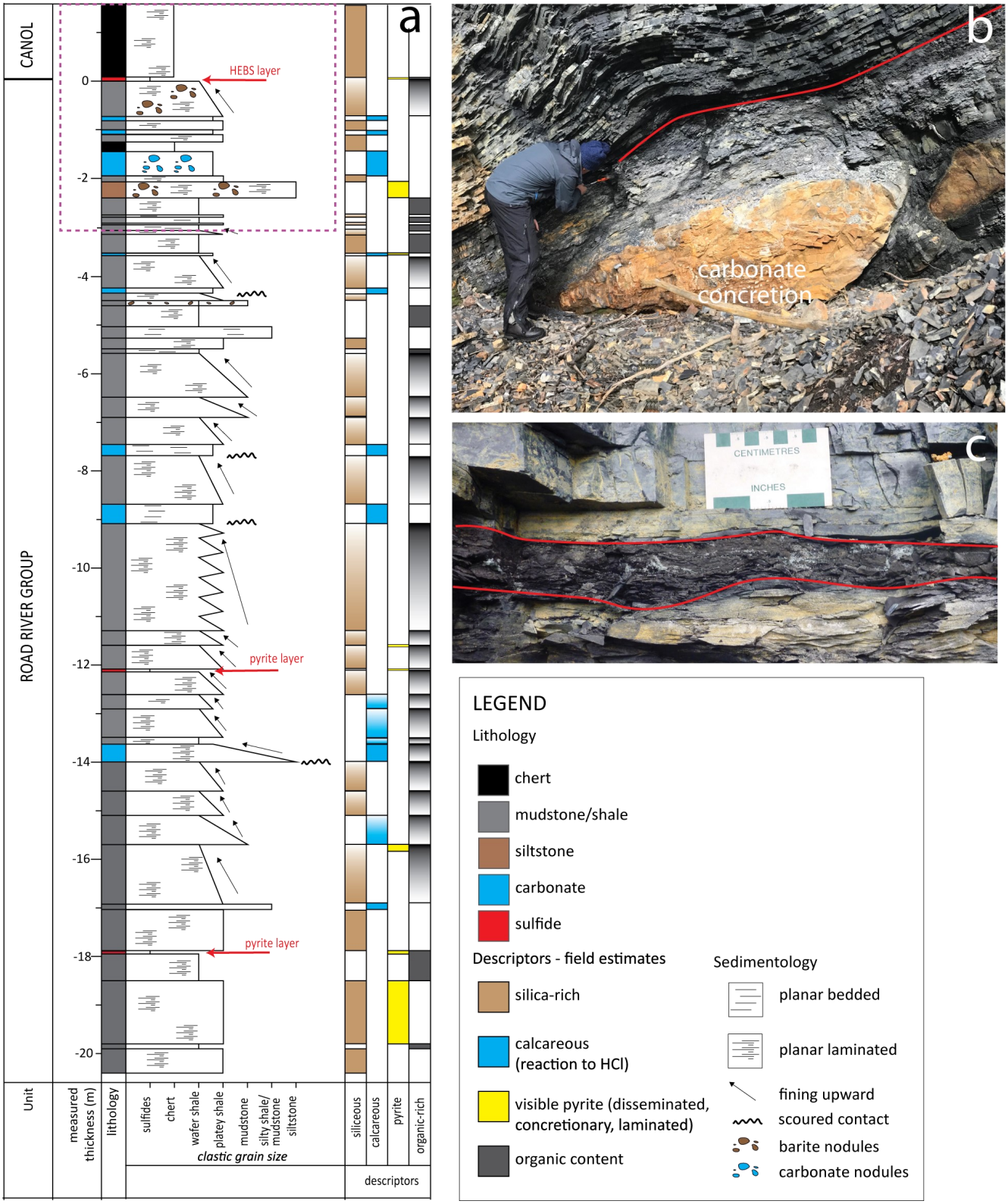

Figure 2. a) Schematic sketch of the stratigraphic succession at the Moss locality showing lithological descriptors and sedimentary features. The '0 m' stratigraphic marker defines the HEBS mineralized zone. Note that lithogeochemical results shown in Figures 3 to 5 are confined to the bounding box at the upper end of the section. b) Photograph of the upper portion of the stratigraphic succession at Moss showing a large carbonate concretion and its relationship to the overlying HEBS layer (red line). c) Close-up photograph of the HEBS layer at the Moss showing (outlined by red lines).

scribed as both conformable (Lenz and Pedder, 1972; Williams, 1983; Morrow, 1999; Fraser and Hutchison, 2017) and unconformable (Bassett and Stout, 1967; Norris, 1985). At this contact, a discontinuous and thin (1–10 cm thick) Ni-Mo-Zn-PGE-rich HEBS layer occurs at many localities throughout northern Yukon (Hulbert et al. 1992; Goodfellow et al. 2010; Fraser and Hutchison, 2017; Gadd and Peter, 2018). The Late Devonian Imperial Formation, a deep-water shale interbedded with turbiditic sandstone, overlies the Canol Formation (Pugh, 1983; Lane, 2007).

Local geology

The stratigraphy of the Moss showing (Fig. 2a) comprises the following (from the base to the top): 1) Carbonaceous and siliceous shale with minor calcareous and pyritic intercalations. The rocks consist of several fining-upward sequences with minor scoured surfaces (Fig. 2a). The bottom of the section is not constrained at the Moss showing. 2) Carbonaceous shale (1 to 2 m thick) with 0.5 to 1.5 m diameter elongated calcareous concretions. Shale beds drape around concretions (Fig. 2b); bedding is preserved within some concretions that conform to surrounding shale laminae. 3) Up to 120 cm thick siliceous, carbonaceous shales with centimetre scale, spheroidal barite and carbonate nodules. 4) A 1 to 4 cm thick stratabound, stratiform semi-massive sulphide HEBS layer (Fig. 2b, c). 5) Carbonaceous, siliceous shale to cherty shale that is in sharp contact with the underlying HEBS mineralization.

Previously published bulk geochemical data for the HEBS mineralization across northern Yukon show enrichments in a broad suite of elements relative to the enclosing sedimentary rocks (Hulbert et al., 1992; Goodfellow et al., 2010). The HEBS mineralization at the Moss showing occurs as a single (Fig. 2c) Ni-Mo-Zn-PGE-Au-Re-bearing horizon at the Road River Group-Canol Formation contact. The mineralogy is similar to that observed at the Peel River locality in that it consists of approximately 60 volume % sulphides as pyrite and millerite (and lesser sphalerite) and 40 volume % gangue (quartz, Ba-bearing feldspar, pyrobitumen, apatite) (cf. Gadd and Peter, 2018). There is also sedimentary pyrite in the stratigraphic section (Fig. 2a), but this does not possess the characteristic metal suite of the HEBS and is considered "unmineralized" (i.e. barren). Dumala (2007) reports 1.96 m (true stratigraphic thickness) of mineralization containing 1.31 weight % Ni and approximately 500 ppb Au+Pt+Pd that was intersected by Southampton Ventures in exploration drilling in the nearby Rich prospect; this thickness of HEBS is not present at the Moss outcrop. Other diamond drillholes in the area intersected only centimetre-scale thicknesses of HEBS mineralization on the Rich property (Dumala, 2007), similar to what we documented in outcrop.

Horan et al. (1994) conducted Re-Os isotope analyses of the HEBS layer and host black shales at the Nick prospect. They concluded that metal enrichment occurred during or shortly after deposition of the host rocks, and the age of mineralization is between 380 and 367 Ma. Although conodonts are preserved within the mineralization at the Nick prospect (Orberger et al., 2003b), as yet, there are no age estimates based on these conodonts. Conodonts recovered from the middle HEBS layer at Peel River yield ages of middle to late Eifelian (Gouwy, 2018), and Gadd and Peter (2018) recovered conodont elements from the upper HEBS mineralization at Peel River that yield an age of Givetian (i.e. late Middle Devonian). Radiolarians recovered from the shale 40 cm above the HEBS layer yield ages of Middle Frasnian to Early Famennian (Goodfellow et al., 2010). Conodonts have not been recovered from the rocks at the Moss showing. However, the HEBS at this locality occurs at the same stratigraphic position, and has the same contact relationships as the upper HEBS at Peel River (and the Nick property), suggesting that the mineralization at all occurrences is coeval.

Methods

Shale and semi-massive sulphide samples were collected from outcrop at the Moss showing (66°18'13"N, 136° 11'36"W). The samples were collected at 10 to 25 cm spacings and bulk samples were homogenized within sampled intervals for lithogeochemical analyses. The rocks were submitted to Activation Laboratories Ltd., Ancaster, Ontario. The samples were crushed, and splits were ground to finer than 63 µm in a ceramic mill. Quartz sand was milled between each sample to clean the mill and prevent cross-contamination. Major and refractory trace elements were measured in 5 g splits using a lithium metaborate/tetraborate fusion followed by inductively couple plasma-mass spectrometry (ICP-MS). Trace elements were measured in 0.5 g splits using a four-acid (hydrochloric-nitric-perchloric-hydrofluoric) digestion followed by ICP-MS. Ruthenium, Rh, Pd, Os, Ir, Pt, and Au contents were measured in 10 to 25 g splits of powered rock by instrumental neutron activation analysis (INAA). Platinum group elements and Au were preconcentrated in Ni-sulphide beads produced by fire-assay prior to INAA. The abundances of carbon (i.e. C_{org} and CO_2) and sulphur were determined using infrared mass spectrometry.

Measured REE-Y abundances were normalized against post -Archean Australian shale (PAAS; Taylor and McLennan, 1985). PAAS-normalized values are marked with subscript 'SN'. Anomalies are quantified ratios that are denoted by '*' and quantified using the geometric means of the neighbouring elements following the convention of McLennan (1989): $Ce/Ce^* = Ce_{SN}/(La_{SN}*Pr_{SN})^{0.5}$, $Eu/Eu^* = Eu_{SN}/(Sm_{SN}*Gd_{SN})^{0.5}$. Elemental enrichment factors are expressed as X_{EF}, where X is an element and the enrichment factors are calculated using the expression $(X/Al_2O_3)_{sample}/(X/Al_2O_3)_{PAAS}$ (Algeo and Tribovillard, 2009). Enrichment factors are useful for rapidly identifying elemental enrichments, where values greater than 3 signify a detectable authigenic enrichment and values greater than 10 signify substantial enrichment (Algeo and Tribovillard, 2009).

A split of pulps of semi-massive sulphide samples were analyzed for their sulphur isotope compositions ($^{34}S/^{32}S$) at

Queen's Facility for Isotope Research at Queen's University, Kingston, Ontario. Two HEBS samples and three bedded to massive pyrite were analyzed. The samples were weighed in tin capsules, where they were combusted at 1700 to 1800°C in a Costech ECS 4010 elemental analyzer. The sulphur isotope compositions were measured using a MAT 253 stable isotope ratio mass spectrometer coupled to the analyzer. Sulphur isotope compositions are reported using the delta ($\delta^{34}S$) notation in units of permil (‰), relative to that in the Vienna-Cañon Diablo troilite (V-CDT) international reference standard. Based on analyses of primary and secondary standards, results are reproducible to 0.2‰.

Results

Lithogeochemistry

Elemental ranges and geochemical proxies in the unmineralized host black shales of the Road River Group (footwall), HEBS mineralization, and Canol Formation carbonaceous siliceous shales and carbonaceous cherty shales (hanging wall) are presented in Table 1 and summarized below:

- The Road River Group sedimentary rocks are characterized by shale-like (e.g. PAAS; Taylor and McLennan, 1995) SiO_2 contents (Fig. 3a), low to moderate terrigenous input (TIP; Fig. 3b) contents (TIP = $Al_2O_3 + TiO_2 + K_2O + Na_2O$; Fraser and Hutchison, 2017), low $Fe_2O_{3(tot)}$ contents (Fig. 3c), moderate to high total organic carbon (TOC) contents (Fig. 3d), low to high carbonate contents ($CaO+CO_2$) (Fig. 3e), weak to moderate negative Ce anomalies (Ce/Ce*) (Fig. 3f), weakly negative to weakly positive Eu anomalies (Eu/Eu*) (Fig 3g), crustal to super-chondritic Y/Ho ratios (>28) (Fig. 3h), moderate to high Mo contents (Fig. 3i) and low to moderate Mo/TOC ratios (Fig. 3j).
- The HEBS layer is characterized by low SiO_2 content (Fig. 3a), extremely low TIP content (Fig. 3b), high $Fe_2O_{3(tot)}$ content (Fig. 3c), low to moderate TOC content (Fig. 3d), low carbonate content (Fig. 3e), moderate negative Ce/Ce* (Fig. 3f), weakly negative Eu/Eu* (Fig 3g), super-chondritic Y/Ho ratios (Fig. 3h), extremely high Mo abundances (Fig. 3i) and extremely high Mo/TOC ratios (Fig. 3j).
- The Canol Formation is characterized by extremely high SiO_2 contents (Fig. 3a), low TIP contents (Fig. 3b), low $Fe_2O_{3(tot)}$ contents (Fig. 3c), moderate to high TOC contents (Fig. 3d), extremely low carbonate contents (Fig. 3e), weak to moderate negative Ce/Ce* (Fig. 3f), weakly negative to nil Eu/Eu* (Fig 3g), super-chondritic Y/Ho ratios (Fig. 3h), moderate to high Mo contents (Fig. 3i) and low to moderate Mo/TOC ratios (Fig. 3j).

Sulphur isotopes

Bulk sulphur isotope compositions for two samples of HEBS mineralization and three samples of bedded pyrite are given in Table 2. The HEBS mineralization (n = 2) is isotopically negative, with $\delta^{34}S$ values of -19.3 and -23.0‰. In stark contrast, the bedded pyrite (n = 3) is isotopically positive, with $\delta^{34}S$ values of 13.8 to 17.3‰.

Discussion

Rare earth element-yttrium geochemistry

The REE-Y provide important information about the conditions under which sedimentary rocks are deposited. At Moss, REE-Y abundances are principally controlled by the TIP (Fig. 4a), but the PAAS-normalized profiles reveal important information about the conditions under which sediments were deposited and the evolution of the sedimentary porewaters. The flat topology of the PAAS-normalized REE-Y profiles indicates normal, shale-like behaviour (i.e. no fractionation). Samples from the Road River Group (Fig. 4b), HEBS (Fig. 4c), and Canol Formation (Fig. 4d) do not have flat profiles. Indeed, a notable and consistent feature is a middle-REE 'bulge', quantified by $La_N/Sm_N<1$ and $Sm_N/Yb_N>1$. This occurs because MREE are remobilized from metastable phases within the sediment pile (e.g. ferromanganese particles and labile organic matter; Hu et al., 2014) into authigenic precipitates (e.g. carbonate; Himler et al., 2010), and is a characteristic of anoxic diagenesis (Himler et al., 2010). In the Road River Group (Fig. 4b), calcareous samples have MREE bulges, whereas the shale samples have troughs. This suggests remobilization at a highly localized scale within the shallow subsurface, which contributes to the complex diagenesis of the rocks that host HEBS. Although this probably affected Eu/Eu* to some degree, it is unlikely to have significantly affected Ce/Ce* and Y/Ho ratios (*see* below).

Among the lanthanide series elements, only Ce and Eu deviate from the trivalent state. Cerium has two valences in nature, Ce^{3+} and Ce^{4+}, and this is principally controlled by redox; Ce fractionates relative to La and Pr based primarily on the ambient oxidation state (De Baar et al., 1988). Cerium (IV) is the dominant ion in oxygenated marine environments, where it is efficiently scavenged by particle-reactive ferromanganese oxyhydroxides (Elderfield and Greaves, 1982). Further, the magnitude of Ce depletion in seawater depends on water depth and, in modern oxygenated marine environments, surface waters typically do not to have Ce anomalies; however, oxidative scavenging of Ce by ferromanganese particles progresses at depth, resulting in significant Ce depletion in marine waters (Nozaki, 1997; Alibo and Nozaki, 1999). Authigenic phases that precipitate or adsorb REE from Ce-depleted marine waters have negative Ce anomalies (Ce/Ce* < 1). Significantly, Ce in anoxic marine conditions behaves like the other trivalent REE, producing nil to weakly positive anomalies (Ce/Ce* ≈ 1).

Samples of the Moss mineralization and host rock possess exclusively negative Ce/Ce* anomalies, regardless of their stratigraphic position (Figs. 3f, 4b–d). These anomalies are real and not related to anomalous La behaviour, based on comparisons with Pr/Pr* (not shown; Bau and Dulski, 1996). Cerium anomalies with values of 0.4 to 0.9 indicate deposition under

Table 1. Summary of lithogeochemical data for the Moss showing.

Element	Detection limit	Unit	Road River Group Range	HEBS Range	Canol Formation Range	Analytical method
Na_2O	0.01	wt.%	0.03–0.7	0.02–0.11	0.03–0.1	Fusion-ICP-MS
MgO	0.01	wt.%	0.24–5.12	0.03–0.19	0.04–0.45	Fusion-ICP-MS
SiO_2	0.01	wt.%	30.4–86.86	23.29–35.9	70.3–93.8	Fusion-ICP-MS
Al_2O_3	0.01	wt.%	1.55–17.5	0.87–2.66	1.54–7.5	Fusion-ICP-MS
P_2O_5	0.01	wt.%	0.01–0.28	0.01–0.06	0.05–0.08	Fusion-ICP-MS
K_2O	0.01	wt.%	0.28–3.93	0.08–0.52	0.23–1.51	Fusion-ICP-MS
CaO	0.01	wt.%	0.05–29.56	0.06–0.22	0.01–0.5	Fusion-ICP-MS
TiO_2	0.001	wt.%	0.08–0.94	0.03–0.1	0.05–0.34	Fusion-ICP-MS
MnO	0.001	wt.%	0.004–0.06	0.01–0.03	0–0.01	Fusion-ICP-MS
Fe_2O_3(T)	0.01	wt.%	0.3–4.4	22.8–40.21	0.1–1.23	Fusion-ICP-MS
H_20+	0.1	wt.%	0.9–3.7	2.6–3.6	0.5–1	Fusion-ICP-MS
LOI	n/a	wt.%	5.76–21.86	24.95–30.63	2.95–5.51	Fusion-ICP-MS
C org	0.5	wt.%	1.06–3.9	1.47–2.9	1.3–4.3	LECO
CO_2	0.01	wt.%	0.03–23	0.1–0.99	0.05–0.11	LECO
C-total	0.01	wt.%	2.03–7.21	1.65–1.98	1.53–3.31	LECO
S-total	0.01	wt.%	0.41–8.7	23.7–39.5	0.26–2.29	LECO
Sc	1	ppm	2–15	1–2.4	1.6–7.6	Fusion-ICP-MS
V	5	ppm	184–1787	5–304	123–434	Fusion-ICP-MS
Cr	20	ppm	23–140	40–70	10–170	Fusion-ICP-MS
Co	0.1	ppm	0.9–11	89–149	0.7–5	4-acid
Ni	0.5	ppm	31–390	31100–41000	34–270	4-acid
Cu	0.2	ppm	1–66	120–211	1–17.6	4-acid
Zn	0.2	ppm	10–990	320–1720	7–42.3	4-acid
Ga	0.1	ppm	0.7–20.5	2.9–5.7	1.5–1.5	4-acid
Ge	0.1	ppm	0.2–0.2	10.6–13.5	0–0	4-acid
As	0.1	ppm	4.8–126	2863–5500	1.7–47	4-acid
Se	0.1	ppm	7.7–123	1760–2460	4.7–89	4-acid
Rb	1	ppm	13–178	7–22	10–73	Fusion-ICP-MS
Sr	2	ppm	36–1000	26–210	21–310	Fusion-ICP-MS
Y	0.5	ppm	4–105	3.4–12.3	2.7–9.9	Fusion-ICP-MS
Zr	1	ppm	16–100	12–22	15–68	Fusion-ICP-MS
Nb	0.2	ppm	1–9.2	0.5–1.3	0.9–1.9	Fusion-ICP-MS
Mo	0.05	ppm	16–110	2370–2980	24–82	4-acid
Ag	0.05	ppm	0.08–2.8	2.07–2.25	0.06–0.22	4-acid
Cd	0.1	ppm	0.2–23	2.1–6.6	0.2–0.4	4-acid
In	0.1	ppm	0.02–0.11	0.08–0.08	0.02–0.02	4-acid
Sn	1	ppm	1–3	1–1	0–0	4-acid
Sb	0.1	ppm	1.5–24	109–129	1.7–18	4-acid
Te	0.1	ppm	0.1–0.4	0.4–21.3	0.2–0.3	4-acid
Cs	0.1	ppm	0.7–11.1	0.3–1	0.9–1.6	Fusion-ICP-MS
Ba	2	ppm	740–280000	415–1600	942–58000	Fusion-ICP-MS
La	0.05	ppm	3.25–83	2.91–7.01	3.1–10.7	Fusion-ICP-MS
Ce	0.05	ppm	5.7–123	5.35–12.5	6.19–20	Fusion-ICP-MS
Pr	0.01	ppm	0.77–19	1.04–2.55	0.96–3.3	Fusion-ICP-MS
Nd	0.05	ppm	2.82–65	5.13–13.6	3.94–14	Fusion-ICP-MS
Sm	0.01	ppm	0.87–14.8	0.96–3.57	0.62–2.2	Fusion-ICP-MS
Eu	0.005	ppm	0.22–3.36	0.17–0.72	0.09–0.46	Fusion-ICP-MS
Gd	0.01	ppm	0.7–15.4	0.68–3.27	0.37–1.8	Fusion-ICP-MS
Tb	0.01	ppm	0.11–2.17	0.1–0.45	0.06–0.25	Fusion-ICP-MS
Dy	0.01	ppm	0.59–12.3	0.57–2.28	0.37–1.6	Fusion-ICP-MS
Ho	0.01	ppm	0.1–2.47	0.11–0.38	0.08–0.31	Fusion-ICP-MS
Er	0.01	ppm	0.3–6.49	0.29–1.02	0.25–0.91	Fusion-ICP-MS
Tm	0.005	ppm	0.05–0.82	0.04–0.13	0.04–0.17	Fusion-ICP-MS
Yb	0.01	ppm	0.29–4.82	0.26–0.77	0.27–1.2	Fusion-ICP-MS
Lu	0.002	ppm	0.04–0.69	0.04–0.1	0.04–0.19	Fusion-ICP-MS
Hf	0.1	ppm	0.4–4.4	0.2–0.36	0.3–1.6	Fusion-ICP-MS
Ta	0.01	ppm	0.1–2.1	0.05–0.11	0.06–0.48	Fusion-ICP-MS
W	0.5	ppm	0.8–2.5	2.1–3.7	1.7–2.5	Fusion-ICP-MS

Table 1. cont.

Element	Detection limit	Unit	Road River Group Range	HEBS Range	Canol Formation Range	Analytical method
Re	0.001	ppm	0.012–0.169	21.2–58.5	0.025–0.038	4-acid
Hg	10	ppm	80–340	2060–2410	80–130	4-acid
Tl	0.05	ppm	1.17–20	180–402	0.9–24	4-acid
Bi	0.02	ppm	0.03–0.27	0.53–0.67	0.04–0.08	4-acid
Pb	0.5	ppm	1.6–19.9	35–52.7	2–7	4-acid
Th	0.05	ppm	1.06–10	0.56–1.1	0.87–3.1	Fusion-ICP-MS
U	0.01	ppm	2.6–15	2.6–7.2	3.08–13	Fusion-ICP-MS
Ir	0.05	ppm	0.05–0.07	0.8–1.3	0.05–0.05	NiS bead-INAA/ICP-MS
Ru	0.05	ppm	0.05–0.15	1.8–9	0.05–0.09	NiS bead-INAA/ICP-MS
Rh	0.2	ppm	0.2–0.2	2.9–9.3	0.2–0.2	NiS bead-INAA/ICP-MS
Pt	1	ppm	1.9–51.8	255–368	1–8.4	NiS bead-INAA/ICP-MS
Pd	2	ppm	2–10.1	154–228	1.4–10.5	NiS bead-INAA/ICP-MS
Au	0.5	ppm	1–4	66.5–167	0.5–2.6	NiS bead-INAA/ICP-MS
Re/Mo			0.0007–0.003	0.0088–0.0196	0.0007–0.0012	
Mo (EF)			24.99–278.01	17052.63–61044.83	199.46–466.36	
U (EF)			1.94–10.62	15.1–26.56	8.9–25.1	
Mo/TOC			6.15–34.38	827.59–1922.58	11.03–27.69	
Mo/U (auth)			4.55–44.29	1033.33–3553.08	10.63–37.04	
Pt/Pd			0.5–9.59	1.48–1.69	0.38–2.53	
Sum REE-Y			19.99–335.11	21.88–60.65	20.29–65.39	
Ce/Ce* (PAAS)			0.7–0.87	0.63–0.71	0.71–0.84	
Pr/Pr* (PAAS)			1.04–1.22	1.11–1.22	1.05–1.25	
Eu/Eu* (PAAS)			0.73–1.32	0.78–0.98	0.84–1.15	
Y/Ho			29.41–43.64	30.91–39.47	30–35	
Ba/Eu			220.24–1037037.04	1080.78–8265.06	2941.18–126086.96	
TIP (Al+Ti+K+Na)			1.97–22.03	1.03–3.39	1.98–9.45	
Th/U			0.36–1.76	0.15–0.26	0.12–0.35	

suboxic bottom-water conditions (Tribovillard et al., 2006). Ce/Ce* values show minor fluctuation within the Road River Group, and systematically decrease upward to the lower contact with the HEBS (Fig. 3f). This suggests that the water column became more oxygenated immediately preceding, and during, HEBS formation. The negative Ce anomalies in the sulphide mineralization are somewhat counterintuitive. The formation and preservation of semi-massive sulphides in the HEBS indicate that the sedimentary environment was highly reducing; however, the domain of reducing conditions may have been restricted to the sediment-porewaters or a chemocline near the sediment-water interface.

In a redox-stratified ambient paleoenvironment, detrital minerals and/or biogenic debris that sank through the water column and settled on the seafloor may have acquired a negative Ce anomaly from the suboxic seawater through which they sank, prior to settling on/in the reducing environment. The terrigenous contribution to the HEBS bulk compositional makeup is extremely low (Fig. 3b), indicating that there was little clastic detrital sedimentation. Indeed, Gadd and Peter (2018) concluded that this is one of primary controls on HEBS formation in Yukon. Within the siliceous and cherty shale of the Canol Formation, Ce/Ce* anomalies steadily decrease from the upper contact of the HEBS through the upper 1.5 m (Fig. 3f). The extremely high silica in this unit is consistent with its regional composition, which is thought to be derived biogenically from radiolarian blooms (Fraser and Hutchison, 2017). The consistently high silica abundances in the Canol Formation likely represents high paleoproductivity, and the decreasing Ce/Ce* probably reflect basin ventilation associated with the incursion of nutrient-rich waters.

Europium also has two oxidation states, Eu^{2+} and Eu^{3+}, and their valence states are controlled by temperature, pH and redox. At ambient temperature, near-surface conditions, Europium (III) predominates (Sverjensky, 1984). Europium is not fractionated under these conditions relative to its neighbouring REE, and no Eu anomaly is produced (i.e. Eu/Eu* ≈ 1). However, Eu (III) is reduced to Eu (II) under extremely reducing (i.e. anoxic) alkaline conditions or high temperature (above 250°C) hydrothermal conditions. Positive Eu anomalies can occur in samples with high Ba (i.e. $^{137}Ba^{16}O^{+}$ on $^{153}Eu^{+}$), but

Table 2. $\delta^{34}S$ values of hyper-enriched black shale HEBS mineralization and barren authigenic pyrite from the Moss showing.

Sample ID	Lithology	Stratigraphic height (cm)	$\delta^{34}S$ ‰ vs VCDT
17_POA_105	HEBS	0	-19.3
17_POA_106	HEBS	0	-23.0
17_POA_111	Road River Group	-1000	13.8
17_POA_113	Road River Group	-1000	17.3
17_POA_116	Road River Group	-500	16.5

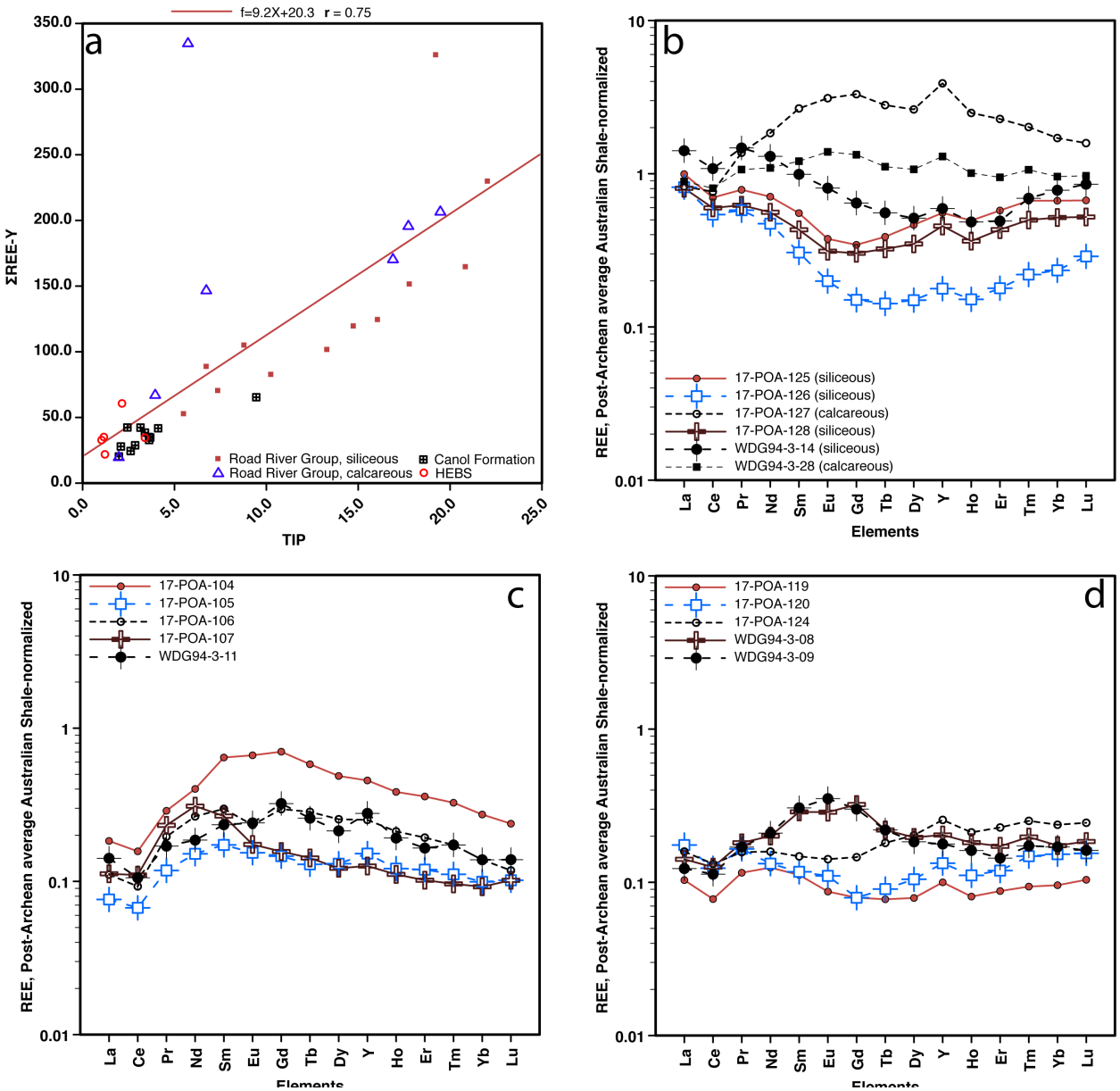

Figure 4. a) Bivariate plot of SREE-Y versus TIP showing Pearson product moment correlation co-efficient. Representative PAAS-normalized REE-Y plots of b) Road River Group, c) HEBS mineralization, and d) Canol Formation.

are spurious analytical artefacts (Jarvis et al., 1989). This can be monitored by plotting Eu/Eu* versus Ba/Sm (not shown), which shows the relative importance of Ba interferences. Although Yukon shale samples have moderate to high barite contents, our data indicate that there are no significant interferences (i.e. the Eu/Eu* are real).

The shales at Moss record Eu/Eu* values that range from weakly negative to weakly positive. The HEBS layers have weakly negative to nil Eu/Eu*, indicating that there was no significant fractionation of Eu relative to the neighbouring REE. The lack of large positive Eu anomalies negates precipitation of the sulphide minerals from high-temperature (above 250°C), reduced, acid seafloor hydrothermal vent fluids (Douville et al., 1999). The weakly negative to weakly positive values in barren shale suggest that the principal control on Eu/Eu* is detrital, whereas more positive values are attributed to contributions from authigenic phases (e.g. carbonate) (Shuster et al., 2018). Indeed, the highly reducing, alkaline environment within which the carbonate concretions precipitated would certainly favour the development of positive Eu anomalies.

The extent to which the clastic sedimentary rocks have been influenced by authigenic/hydrogenous input of REE-Y can be evaluated using Y/Ho ratios. This ratio is tightly coupled in marine environments and the relative fractionation of Y to Ho

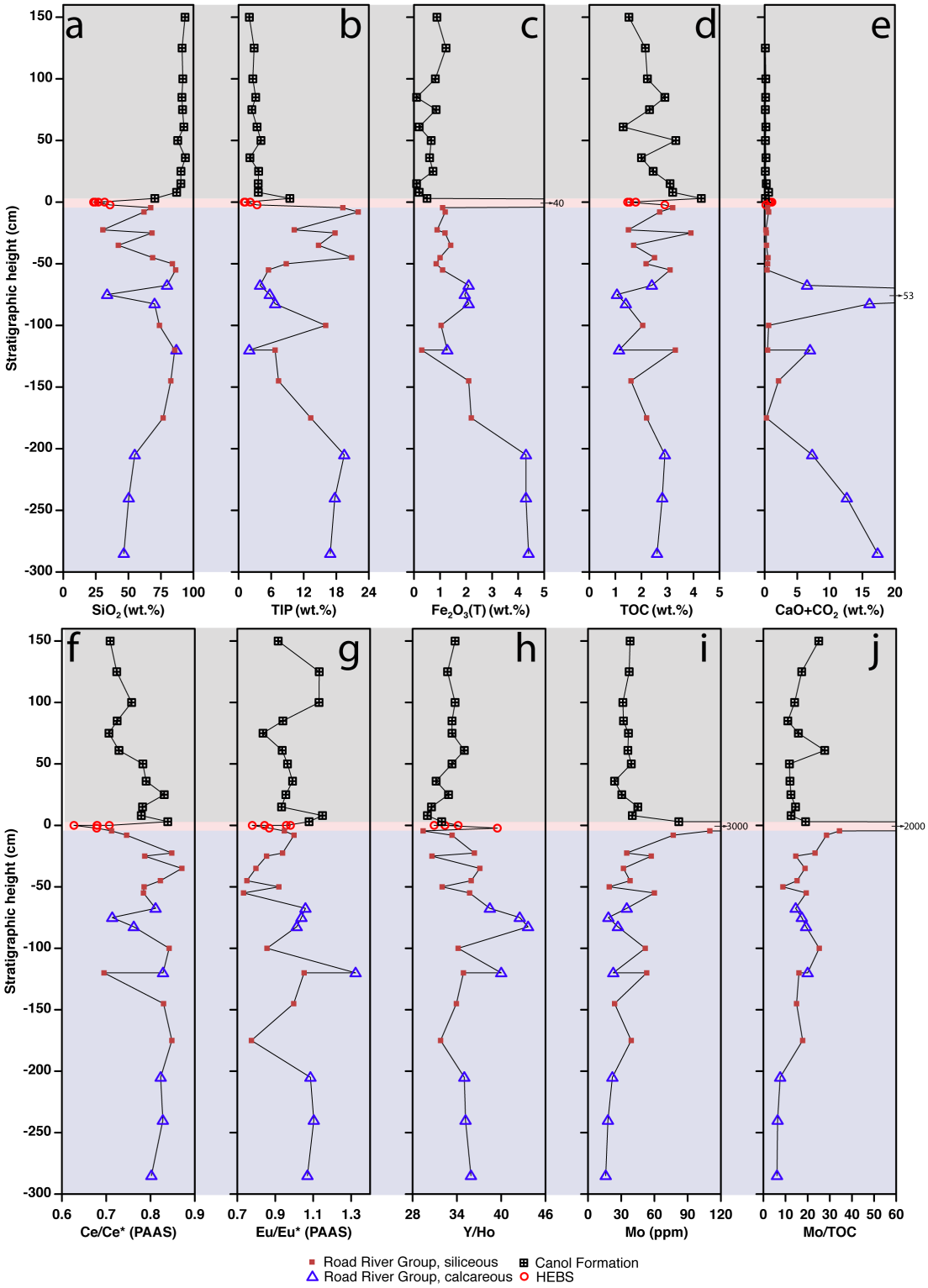

Figure 3. Lithostratigraphic profiles of selected elements, oxides and element ratios for the Moss HEBS showing outcrop section in western Richardson Mountains. The '0 cm' stratigraphic marker defines the HEBS mineralized zone (red shading), with strata above assigned to the Canol Formation (grey shading) and below to the Road River Group (blue shading). *See* Figure 2a for location of samples in measured section. a) SiO_2; b) TIP (Al_2O_3 + TiO_2 + K_2O + Na_2O); c) Fe_2O_3 (total); d) total organic carbon (TOC); e) CaO + CO_2; f) Ce/Ce* (post-Archean Australian shale (PAAS)-normalized); g) Eu/Eu* (PAAS-normalized); h) Y/Ho; i) Mo; and j) Mo/TOC. These data are based on whole-rock analyses. The different symbols correspond to the different lithostratigraphic units.

within seawater is useful for interpreting their ultimate source (Bau and Dulski, 1996). Bulk continental crust, clastic sedimentary rocks, and chondrites have a fairly consistent Y/Ho ratio of 28 (Mclennan, 2001), whereas ratios in seawater are between 44 and 74 (Bau, 1996). Most of the rocks at Moss have Y/Ho ratios of over 28, but the magnitude varies based on the dominant lithology. The lower Y/Ho ratios in the host black shales indicate that the REE+Y budget is dominated by terrigenous input, with only minor contributions from seawater.

The HEBS also have higher Y/Ho ratios, which indicate a moderate to significant contribution of these elements (and other REE) from ambient seawater. This characteristic is similar to that for analogous mineralization in the Nuititang Formation on the Yangtze Platform, where polymetallic shales have consistently higher Y/Ho ratios than their barren host rocks (Xu et al., 2013). Calcareous rocks underlying the Moss HEBS have uniformly super-chondritic Y/Ho ratios (34–44), indicating a strong hydrogenous influence on the REE-Y content in these rocks.

Molybdenum and uranium geochemistry

The bulk molybdenum abundance in fine-grained marine sedimentary rocks is a robust indicator for estimating the presence and extent of euxinia in ancient depositional environments (Scott and Lyons, 2012). This assumes that all molybdenum is hydrogenous and that dilution by clastic (or carbonate) detritus, pH or low aqueous molybdenum concentrations did not affect the bulk molybdenum abundance. Scott and Lyons (2012) define three abundance ranges for molybdenum in shale that determine the extent and magnitude of euxinia: 1) Mo contents less than 2 to 25 ppm are indicative of sulphidic pore waters; 2) Mo contents of 25 to 100 ppm are indicative of intermittently euxinic to persistent euxinic water column; and 3) a Mo content greater than 100 ppm is indicative of sustained euxinia. The Mo content of the Road River Group increases upward to the contact with the HEBS layer (Fig. 3i), suggesting that sulphidic porewaters transitioned into euxinic bottom-waters. Concomitant (with increasing total Mo) increasing Mo/TOC ratios (Fig. 3j) indicate that the basinal environment transitioned from restricted to moderately/weakly restricted (Algeo and Lyons, 2006). Molybdenum abundance and Mo/TOC ratios increase two orders of magnitude at the sharp contact between Road River Group shale and the overlying HEBS (Fig. 3i, j). Gadd and Peter (2018) proposed that the HEBS is a condensed section because it is nearly devoid of clastic sedimentary rocks (Fig. 3b; see also: Fraser and Hutchison, 2017) and is replete with microfossils (e.g. conodont elements) and macrofossils (e.g. pyrite permineralized wood).

Enrichment plots, developed originally for measurements in modern marine environments, have provided useful insights into ancient basin evolution (Algeo and Tribovillard, 2009) and the relationship between authigenic Mo (Mo_{EF}) and authigenic U (U_{EF}) is commonly used to discriminate between different types of depositional environments in carbonaceous shale basins (Fig. 5a). The relationship of Mo_{EF} with U_{EF} may elucidate basinal processes because the marine cycling of these redox-sensitive trace elements responds to sedimentation and basinal restriction (Algeo and Tribovillard, 2009; Tribovillard et al.,

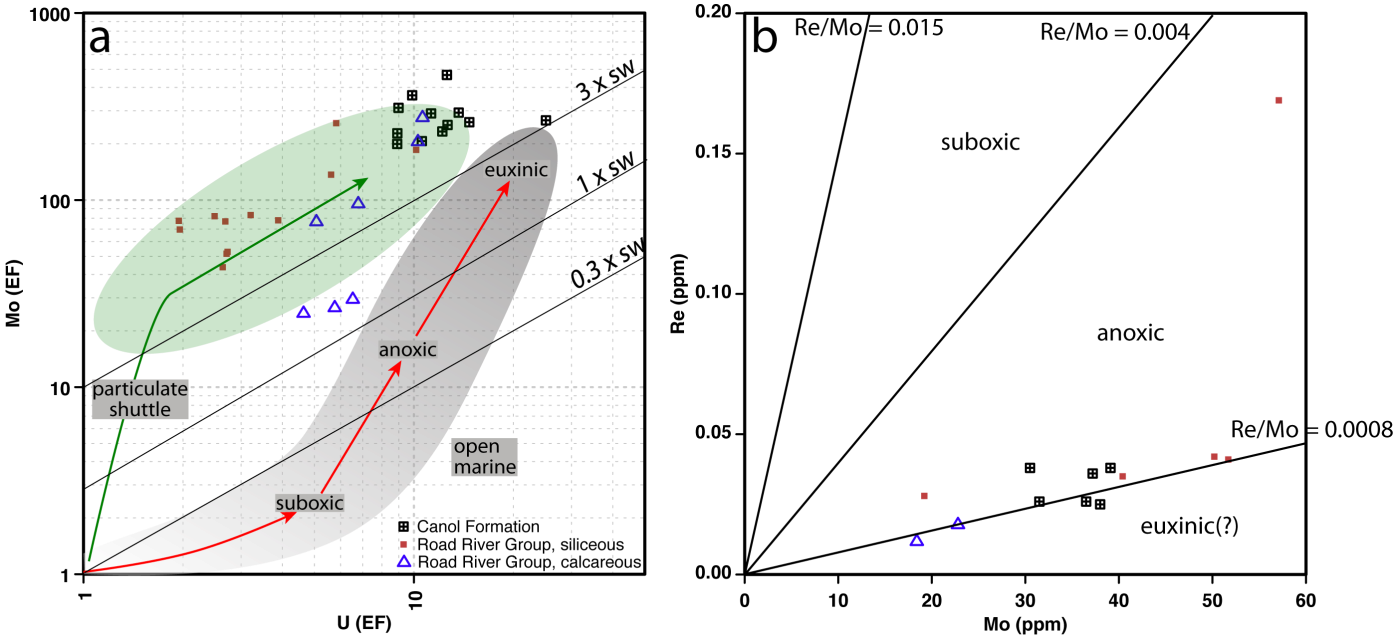

Figure 5. a) Scatterplot of Mo versus U (EF) using fields *from* Algeo and Tribovillard (2009) and Tribovillard et al. (2012). The green line (arrow) and green-shaded field represent the trajectory of an active particulate shuttle (Algeo and Tribovillard, 2009). The red line (arrows) and grey-shaded field represent redox zonation in unrestricted (i.e. open) marine environments (Algeo and Tribovillard, 2009). b) Scatterplot of Re versus Mo showing regions of different redox zonations as *defined by* Crusius et al. (1996) and Ross and Bustin (2009). Note that neither plot shows mineralized samples.

2012; Cheng et al., 2016). Authigenic Mo/U ratios greater than three times that of seawater indicate that a particulate ferromanganese shuttle (i.e. ferromanganese oxyhydroxide chemical sediments that form in oxygenated seawater; Koschinsky and Hein, 2017 and references therein) was active during deposition of the uppermost Road River Group and lower Canol Formation (Fig. 5a). The strong enrichment of Mo_{EF} relative to U_{EF} indicates that a particulate shuttle intensified the delivery of these elements to the basin floor during HEBS formation. Both elements are particle-reactive, but only Mo is retained during diagenesis in sulphidic sediments (Algeo and Tribovillard, 2009). Within the sediments, molybdates are thiolated (i.e. containing a sulfhydryl [-sH] group) and may be sequestered by Fe sulphides and not released back into the water column (Helz et al., 2011). Uranium is not retained during sulphidic diagenesis and it is released back into the water column (Algeo and Tribovillard, 2009).

Fraser and Hutchison (2017) present authigenic Mo and U data for time-stratigraphically equivalent rocks at Trail River, approximately 40 km east of the Moss locality, where there is also strong evidence of a particulate shuttle operating in the water column during deposition of the Canol Formation. Kabanov (2018) similarly presents authigenic Mo and U data for age-equivalent, correlative rocks on the Mackenzie Platform that also indicate the presence of an active particulate shuttle. Thus, it is likely that a particulate shuttle was widespread during the Middle to early Late Devonian along the Laurentian continental margin. A major sea-level transgression juxtaposed Mo- and TOC-rich rocks onto the Mackenzie Platform carbonates, and several sea-level fluctuations are recognized throughout the Middle Devonian (Haq and Schutter, 2008). The Richardson trough, where these shales were deposited, is an aulacogen (Lane, 2007; Norris, 1985; Pugh, 1983). Plate reconstructions indicate that it was bound to the east by the Mackenzie Platform and to the west by the Yukon Stable Block; carbonate build-ups apparently also occurred on the southern margin, but the northern margin in the Middle Devonian is unclear (Colpron and Nelson, 2009, 2011). Nevertheless, it seems likely that the Richardson trough was periodically restricted, especially during sea level low-stands, such as during the late Early Devonian (Haq and Schutter, 2008; Fraser and Hutchison, 2017). Thus, we interpret the combination of periodic restriction and ventilation in a continent-marginal trough to be a key aspect in the formation and preservation of HEBS.

Rhenium and molybdenum relationships

Bulk rhenium and molybdenum during sedimentation are both affected minimally by detrital input, behave conservatively in seawater, and have relatively long oceanic residence times (Mo: t = 4.4×10^5 years; Re: t = 1.3×10^5 years; Colodner et al., 1993; Crusius et al., 1996; Tribovillard et al., 2006; Miller et al., 2011). Because of these behaviours, bulk Re/Mo ratios are also accepted to be a robust indicator of paleoredox and have been determined for many modern and ancient basins. Unlike molybdenum, rhenium accumulation is not related to ferromanganese oxyhydroxide cycling, but rather is conserved in both oxic and anoxic marine conditions (Crusius et al., 1996; Ross and Bustin, 2009). Rhenium sequestration is thought to be either by direct reduction of ReO_4^- (Crusius et al., 1996) or by thiolation of the perrhenate oxyanion (ReO_4^-) (Helz and Dolor, 2012). In either case, rhenium is trapped more efficiently than molybdenum in suboxic conditions, which results in higher Re/Mo ratios (Helz and Dolor, 2012).

Crusius et al. (1996) and Ross and Bustin (2009) demonstrated that Re/Mo ratios in modern carbonaceous sediments and ancient sedimentary rocks can be used as a proxy for redox conditions. Ratios between 0.0008 and 0.004 indicate anoxic conditions, whereas values less than 0.0008 are possibly euxinic. Values greater than 0.004 are indicative of suboxic conditions. At the Moss locality, all the barren samples have Re/Mo ratios that are less than 0.004 and many are close to 0.0008 (Fig. 5b), indicative of deposition under anoxic to possibly euxinic conditions. The HEBS samples have Re/Mo ratios that range from 0.009 to 0.02 (not shown in Fig. 5b), indicative of deposition under suboxic conditions; however, the absolute abundances of these elements are several orders of magnitude higher than in the barren rocks. Assuming the metals were derived directly from ambient seawater (Gadd and Peter, 2018; Pagés et al., 2018), an intense particulate shuttle may have efficiently delivered massive quantities of metals (and metalloids) to the marine environment; however, it is difficult to reconcile the extremely high Re abundances with its conservative behaviour in the presence of ferromanganese oxyhydroxides. The average Re (approximately 40 ppm, n = 5) abundance at the Moss showing is higher than the highest-grade Re mineralization globally (<30 ppm; John et al., 2017), and resolving its enrichment mechanism will be the focus of future study.

The Re/Mo values give redox information that conflicts with the Ce/Ce* values for the same rocks. Whereas Ce/Ce* ratios are uniformly negative, most of the Re/Mo ratios for barren shale fall into a tight range (approximately 0.0008) that indicate anoxic depositional conditions. Only within the HEBS do these two redox proxies agree with each other, with both indicating a suboxic environment. A suboxic environment is in stark contradiction to the observed extreme Mo abundances, which almost certainly formed in response to euxinia (Scott and Lyons, 2012). Although it is generally accepted that euxinia plays an essential role in forming HEBS, it is likely that basinal redox stratification played an important role in forming and preserving HEBS (Johnson et al., 2017). Under these conditions, anoxia may have been driven by high biological productivity within nutrient trace element-rich waters (i.e., marine waters that fuel biological growth). Discrepancies among paleoredox proxies are common (for recent discussion, *see* Peter et al., 2018). At the Moss showing, the contradictory nature of the lithogeochemical redox proxies is likely a reflection of the mineralogical residence that relates to different environmental conditions. Adsorption of seawater REE onto detrital and/or biogenic sedimentary particles as they sank

through the water column prior to settling on the seafloor reflect the suboxic conditions of the water column. Rhenium and molybdenum, however, are associated with authigenic sulphides that precipitated during early diagenesis and probably reflect the remineralization of organic and ferromanganese particulates (Gadd et al., work in progress, 2018). Therefore, the various redox proxies record and retain the ambient paleoredox state of the different media with which they have the most interaction.

Sulphur geochemistry

Seawater sulphate is generally implicated as the ultimate source of sulphur in low-temperature, reduced sedimentary environments. Sulphate is transformed to sulphide by the following (simplified) reaction: $2CH_2O + SO_4^{2-} \longrightarrow 2HCO_3^- + H_2S$. Microbes consume labile sedimentary organic matter and sulphate is the terminal electron acceptor (Sweeney and Kaplan, 1980). The sulphur isotope composition of sulphide generated during bacterial sulphate reduction may vary from extremely negative ($\delta^{34}S << 0$) to positive. Several factors contribute to the $\delta^{34}S$ values preserved in sedimentary sulphides, which include whether the environment is open (or closed) and the concentration of dissolved sulphate. Biogenic sulphides are typically negative in open systems with high sulphate concentrations (e.g. Phanerozoic marine environments), where fractionations between parent sulphate and daughter sulphide, expressed as $\Delta^{34}S_{SO4\text{-}H2S}$, is approximately 45 ± 20‰ (Sweeney and Kaplan, 1980; Strauss, 1999). As the marine sulphate reservoir is exhausted, it is possible for the $\delta^{34}S$ values preserved in sedimentary pyrite to equal or exceed the $\delta^{34}S$ value of coeval sulphate (Goodfellow and Jonasson, 1984; Goodfellow, 1987).

The strongly negative sulphur isotope composition of the HEBS mineralization is consistent with bacterial sulphate reduction of a relatively unfractionated seawater sulphate source. These negative values are similar to the negative values of HEBS mineralization at the Nick Prospect (Hulbert et al., 1992). Murowchick et al. (1994) analyzed *in situ* the sulphur isotope composition of pyrite in HEBS mineralization in China, and determined that pyrite $\delta^{34}S$ values range from highly negative to highly positive. Although grain- to millimetre-scale variations in sulphur isotope compositions may exist in the Moss HEBS samples, our bulk analyses preclude an assessment of this. Seawater sulphate in the Middle Devonian is thought to have a $\delta^{34}S$ value of approximately 20‰ (Kampschulte and Strauss, 2004), implying that the abundant sulphur (≤40 weight %) in the HEBS mineralization did not originate by quantitative removal (i.e. closed-system Rayleigh fractionation) of seawater sulphate. Indeed, the $\delta^{34}S$ values of the HEBS indicate that unfractionated seawater sulphate diffused from the overlying water column into the sediment porewaters.

The $\delta^{34}S$ values of barren bedded and nodular pyrite in Road River Group shale at Moss are positive and are approximately the same as Middle Devonian seawater. The positive values may also have resulted from bacterial sulphate reduction, but deeper within the sediments where diffusional exchange of seawater sulphate with the overlying water column was cut off. Closed-system sulphate reduction exhausts a diminishing supply of seawater sulphate (i.e. Rayleigh fractionation) such that the sulphate is completely converted to sulphide and no fractionation exists (i.e. $\delta^{34}S_{sulphide} \approx \delta^{34}S_{sulphate}$). Alternatively, positive $\delta^{34}S$ values in authigenic, stratiform pyrite may be the result of rapid anaerobic sulphate respiration above the sulphate-methane transition zone in the organic-rich host sediments (Borowski et al., 2013).

Platinum-palladium geochemistry

Our current working hypothesis for the Moss property (and the other HEBS in Yukon) is that metal enrichment is a product of highly efficient scavenging of metals from seawater (Gadd and Peter, 2018; Gadd et al., work in progress, 2018). This is broadly supported by research on the HEBS in China (Lehmann et al., 2007, 2016; Xu et al., 2011, 2013). There is a range of Pt/Pd values (0.27–9.59, n = 10) in barren shales at Moss, but most (0.27–1.21, n = 8) are close to modern seawater (0.83; Nozaki, 1997). The average Pt/Pd ratio of the HEBS is approximately 1.62, which is approximately double that of modern seawater. In the modern, oxygenated ocean, authigenic ferromanganese crusts and nodules have Pt/Pd ratios of approximately 20 to 50 (Halbach et al., 1989; Koschinsky and Hein, 2017). Ratios substantially higher than seawater are the result of differing scavenging potentials, where negatively charged platinum-chloro complexes are oxidatively scavenged by adsorption(?) onto Mn-oxides (Halbach et al., 1989) or Fe-O(OH) (Koschinsky et al., 2005). Palladium is not scavenged at the same rate because it is not oxidatively scavenged (Koschinsky et al., 2005); however, the HEBS in Yukon formed under reducing conditions (suboxic to euxinic) that may have facilitated similar degrees of scavenging of both platinum and palladium, producing the observed ratios. HEBS mineralization in the Nuititang Formation in China also has seawater-like Pt/Pd values, and these deposits are also thought to form under euxinic conditions (Xu et al., 2013). Lehmann et al. (2016) suggested that HEBS mineralization is the reduced equivalent to hydrogenous ferromanganese crusts that form on the modern seafloor. Perhaps the similar degree of Pd scavenging is an artefact of this type of environment.

Conclusions

Our study of the Moss showing reveals that sedimentation shifted dramatically from the uppermost Road River Group through to the basal Canol Formation. Terrigenous detritus predominated up to the formation of HEBS, but the clastic supply was effectively cut off during and after HEBS formation. The paucity of clastic sedimentation marked the onset of Ni-Mo-Zn-PGE-Au-Re hyper-enrichment, and this condensed sedimentation is perhaps fundamental to the formation of HEBS. The HEBS was terminated by the onset of silica-dominant sedimentation of the Canol Formation, which deliv-

ered and deposited blooms of radiolarians.

Lithogeochemical data for the host rocks and HEBS show that the paleoenvironmental redox conditions were complex (i.e. non-static) and likely fluctuated between suboxic, anoxic, and euxinic. The REE-Y systematics suggest a predominantly suboxic water body, whereas the Mo abundances and Re/Mo ratios indicate anoxic to euxinic conditions in the shallow subsurface below the seafloor. Authigenic enrichments of molybdenum and uranium indicate an active particulate shuttle operated during deposition of the Road River Group through to deposition of the Canol Formation, and it was most intense during HEBS formation. Collectively, these data signify a basinal environment that experienced varying degrees of restriction and stratification, with pulses of fresh (i.e. unfractionated) marine waters that delivered metals, metalloids, and sulphur. This type of geological setting is considered critical for the formation and preservation of HEBS mineralization.

Future research

Future work will investigate lithogeochemical redox proxies at the other HEBS localities in order to generate a holistic model of the formation of this style of mineralization in the Richardson trough. We aim to use LA-ICP-MS analyses at other HEBS localities to establish the PGE host minerals. We will also conduct *in situ* S isotope analyses of samples from the HEBS mineralization in order to better constrain isotopic variability at the sample- to grain-scale.

Acknowledgments

This report is a contribution to NRCan's Targeted Geoscience Initiative Program (TGI). Support for this study was provided through the Volcanic- and Sedimentary-Hosted Base Metal Ore System '*Activity VS-1.2: "Development of genetic and exploration models for hyper-enriched black shale (HEBS) deposits*".

The authors would like to acknowledge the Polar Continental Shelf Program (Project 00717) for providing additional funding and field logistical support. We also thank Claire Leighton and Izzy Crawford of Queen's University and Leyla Weston of the Yukon Geological Survey for their assistance in the field. Finally, we express our gratitude to the Gwich'in Tribal Council for permitting us to perform research on their traditional lands. This report benefited from the review of Chris Lawley, Michel Houlé and Neil Rogers.

References

Algeo, T.J. and Lyons, T., 2006. Mo-total organic carbon covariation in modern anoxic marine environments: Implications for analysis of paleoredox and paleohydrographic conditions; Paleoceanography, v. 21, p. PA1016.

Algeo, T.J. and Tribovillard, N., 2009. Environmental analysis of paleoceanographic systems based on molybdenum–uranium covariation; Chemical Geology, v. 268, p. 211–225.

Alibo, D.S. and Nozaki, Y., 1999. Rare earth elements in seawater: Particle association, shale-normalization, and Ce oxidation; Geochimica et Cosmochimica Acta, v. 63, p. 363–372.

Bassett, H.G. and Stout, J.G., 1968. Devonian of western Canada; *in* Proceeding of the International Symposium on the Devonian System, Calgary, 1967; Alberta Society of Petroleum Geologists, Calgary, Alberta, v.1, p. 717–752.

Bau, M., 1996. Controls on the fractionation of isovalent trace elements in magmatic and aqueous systems: Evidence from Y/Ho, Zr/Hf, and lanthanide tetrad effect; Contributions to Mineralogy and Petrology, v. 123, p. 323–333.

Bau, M. and Dulski, P., 1996. Distribution of yttrium and rare-earth elements in the Penge and Kuruman iron-formations, Transvaal Supergroup, South Africa; Precambrian Research, v. 79, p. 37–55.

Berner, R.A., 1989. Biogeochemical cycles of carbon and sulfur and their effect on atmospheric oxygen over phanerozoic time; Palaeogeography, Palaeoclimatology, Palaeoecology, v. 75, p. 97–122.

Blakey, R., 2013. Middle Devonian (395–385 Ma) paleogeographic reconstruction of North America; *in* North American Key Time Slices, (ed.) R. Blakey; Colorado Plateau Geosystems Inc. <http://deeptimemaps.com/north-america-key-time-slices-details/> [accessed January 25, 2019]

Borowski, W.S., Rodriguez, N.M., Paull, C.K., and Ussler, I.W., 2013. Are ^{34}S-enriched authigenic sulfide minerals a proxy for elevated methane flux and gas hydrates in the geologic record?; Marine and Petroleum Geology, v. 43, p. 381–395.

Carne, R., 1989. Nick Property; Yukon Territory assessment report, p. 8.

Cheng, M., Li, C., Zhou, L., Algeo, T. J., Zhang, F., Romaniello, S., Jin, C., Lei, L., Feng, L., and Jiang, S.Y., 2016. Marine Mo biogeochemistry in the context of dynamically euxinic mid-depth waters: A case study of the lower Cambrian Niutitang shales, South China; Geochimica et Cosmochimica Acta, v. 183, p. 79–93.

Colodner, D., Sachs, J., Ravizza, G., Turekian, K., Edmond, J., and Boyle, E., 1993. The geochemical cycle of rhenium: a reconnaissance; Earth and Planetary Science Letters, v. 117, p. 205–221.

Colpron, M. and Nelson, J.L., 2009. A Palaeozoic Northwest Passage: incursion of Caledonian, Baltican and Siberian terranes into eastern Panthalassa, and the early evolution of the North American Cordillera; *in* Accretionary Orogens through Earth History, (ed.) P.A. Cawood, A. Kröner, W.J. Collins, T.M. Kusky, W.D. Mooney and B.F. Windley; Geological Society, London, Special Publications, v. 318, p. 273–307.

Colpron, M. and Nelson, J.L., 2011. A Palaeozoic NW Passage and the Timanian, Caledonian and Uralian connections of

some exotic terranes in the North American Cordillera, *in* Arctic Petroleum Geology, (ed.) A.M. Spencer, A.F. Embry, D.L. Gautier, A.V. Stoupakova and K. Sørensen; Geological Society London, Memoirs, v. 35, p. 463–484.

Crusius, J., Calvert, S., Pedersen, T., and Sage, D., 1996. Rhenium and molybdenum enrichments in sediments as indicators of oxic, suboxic and sulfidic conditions of deposition; Earth and Planetary Science Letters, v. 145, p. 65–78.

De Baar, H.J.W., German, C.R., Elderfield, H., and van Gaans, P., 1988. Rare-earth element distributions in anoxic waters of the Cariaco Trench; Geochimica et Cosmochimica Acta, v. 52, p. 1203–1219.

Douville, E., Bienvenu, P., Charlou, J.L., Donval, J.P., Fouquet, Y., Appriou, P., and Gamo, T., 1999. Yttrium and rare earth elements in fluids from various deep-sea hydrothermal systems; Geochimica et Cosmochimica Acta, v. 63, p. 627–643.

Dumala, M., 2007. Assessment report describing prospecting, mapping, geochemical sampling, geophysical surveys and diamond drilling at the Rich property, prepared for Southampton Ventures Inc. and Strategic Metals Ltd.; Whitehorse, Yukon Territory, p. 455.

Elderfield, H., and Greaves, M.J., 1982. The rare earth elements in seawater; Nature, v. 296, p. 214–218.

Fraser, T.A. and Hutchison, M.P., 2017. Lithogeochemical characterization of the Middle–Upper Devonian Road River Group and Canol and Imperial formations on Trail River, east Richardson Mountains, Yukon: age constraints and a depositional model for fine-grained strata in the Lower Paleozoic Richardson trough; Canadian Journal of Earth Sciences, v. 54, p. 731–765.

Gadd, M. G., and Peter, J.M., 2018. Field observations, mineralogy and geochemistry of Middle Devonian Ni-Zn-Mo-PGE hyper-enriched black shale deposits, Yukon; *in* Targeted Geoscience Initiative: 2017 report of activities, volume 1, (ed.) N. Rogers; Geological Survey of Canada, Open File 8358, p. 193–206.

Gadd, M.G., Peter, J.M., Goodfellow, W., Jackson, S.E., and Yang, Z., 2017. Geology, geochemistry and mineralogy of hyper-enriched black shale deposits, Yukon; *in* Proceedings of Exploration '17; 6th Decennial International Conference on Mineral Exploration, Toronto, Ontario, p. 841–845.

Goodfellow, W.D., 1987. Anoxic stratified oceans as a source of sulphur in sediment-hosted stratiform Zn-Pb deposits (Selwyn Basin, Yukon, Canada); Chemical Geology, Isotope Geoscience Section, v. 65, p. 359–382.

Goodfellow, W.D., and Jonasson, I.R., 1984. Ocean stagnation and ventilation defined by $\delta^{34}S$ secular trends in pyrite and barite, Selwyn Basin, Yukon; Geology, v. 12, p. 583–586.

Goodfellow, W., Geldsetzer, H.H.J., Pride, K., Uyeno, T., and Gregoire, C., 2010. Geochemistry and origin of geographically extensive Ni-(Mo, Zn, U)-PGE sulphide deposits hosted in Devonian black shales, Yukon, *in* TGI-3 Workshop: Public Geoscience is Support of Base Metal Exploration; Simon Frasier University, Vancouver, British Columbia, p. 15–18.

Gouwy, S.G., 2018. Report on fifteen conodont samples from the Canol and Road River formations from the Peel River banks and Moss (Yukon) NTS 106E and NTS 116I collected and submitted by Tiffani Fraser (Yukon Geological Survey) and Mike Gadd (GSC-Ottawa) under the TGI 5 Volcanic- and sediment-hosted base metal deposits or system program (VS1.2) (Con no. 1819-1 to 1819-15); Geological Survey of Canada, Paleontological Report 4-SAG-2018, p. 14.

Halbach, P., Kriete, C., Prause, B., and Puteanus, D., 1989. Mechanisms to explain the platinum concentration in ferromanganese seamount crusts; Chemical Geology, v. 76, p. 95–106.

Haq, B. and Schutter, S., 2008. A chronology of Paleozoic sea-level changes; Science, v. 322, p. 64–68.

Helz, G.R. and Dolor, M.K., 2012. What regulates rhenium deposition in euxinic basins?; Chemical Geology, v. 304, p. 131–141.

Helz, G. R., Bura-Nakić, E., Mikac, N., and Ciglenečki, I., 2011. New model for molybdenum behavior in euxinic waters; Chemical geology, v. 284, p. 323–332.

Himler, T., Bach, W., Borhmann, G., and eckmann, J., 2010. Rare earth elements in authigenic methane-seep carbonates as tracers for fluid composition during early diagenesis; Chemical Geology, v. 277, p. 126–136.

Horan, M.F., Morgan, J.W., Grauch, R.I., Coveney, J.R.M., Murowchick, J.B., and Hulbert, L.J., 1994. Rhenium and osmium isotopes in black shales and Ni-Mo-PGE-rich sulfide layers, Yukon Territory, Canada, and Hunan and Guizhou provinces, China; Geochimica et Cosmochimica Acta, v. 58, p. 257–265.

Hu, Y., Feng, D., Peckmann, J., Roberts, H.H., and Chen, D., 2014. New insights into cerium anomalies and mechanisms of trace metal enrichment in authigenic carbonate from hydrocarbon seeps; Chemical Geology, v. 381, p. 55–66.

Hulbert, L.J., Gregoire, D., Paktunc, D., and Carne, R., 1992. Sedimentary nickel, zinc, and platinum-group-element mineralization in Devonian black shales at the Nick Property, Yukon, Canada: A new deposit type; Exploration and Mining Geology, v. 1, p. 39–62.

Hutchison, M.P. and Fraser, T.A., 2015. Paleoenvironment, paleohydrography and chemostratigraphic zonation of the Canol Formation, Richardson Mountains, north Yukon, *in* Yukon Exploration and Geology 2014, (ed.) K.E. MacFarlane, M.G. Nordling, and P.J. Sack; Whitehorse, Yukon Territory, Yukon Geological Survey, p. 73–98.

Jarvis, K., Gray, A., and McCurdy, E., 1989. Avoidance of spectral interference on europium in inductively coupled plasma mass spectrometry by sensitive measurement of the doubly charged ion; Journal of Analytical Atomic Spectrometry, v. 4, p. 743–747.

John, D., Seal II, R.R., and Polyak, D., 2017. Rhenium; Chapter P *in* Critical Mineral Resources of the United States - Economic and Environmental Geology and Prospects for Future Supply, (ed.) K. Schulz, J. DeYoung, R.R. Seal II, and D. Bradley; United States Geological Survey, Professional Paper 1802, p. P1–P49.

Johnson, S.C., Large, R.R., Coveney, R.M., Kelley, K.D., Slack, J.F., Steadman, J. ., Gregory, D.D., Sack, P.J., and Meffre, S., 2017. Secular distribution of highly metalliferous black shales corresponds with peaks in past atmosphere oxygenation; Mineralium Deposita, v. 52, p. 791–798.

Jowitt, S.M. and Keays, R.R., 2011. Shale-hosted Ni-(Cu-PGE) mineralisation: a global overview; Transactions of the Institution of Mining and Metallurgy, Section B-Applied Earth Science, v. 120, p. 187–197.

Kabanov, P., 2018. Devonian (c. 388–375 Ma) Horn River Group of Mackenzie Platform (NW Canada) is an open-shelf succession recording oceanic anoxic events; Journal of the Geological Society, v. 176, p. 29–45.

Kampschulte, A. and Strauss, H., 2004. The sulfur isotopic evolution of Phanerozoic seawater based on the analysis of structurally substituted sulfate in carbonates; Chemical Geology, v. 204, p. 255–286.

Koschinsky, A. and Hein, J.R., 2017. Marine ferromanganese encrustations: Archives of changing oceans; Elements, v. 13, p. 177–182.

Koschinsky, A., Audroing, J., and Hein, J.R., 2005. The enrichment of platinum and the fractionation of Pt from Pd in marine ferromanganese crusts; *in* 10th International Platinum Symposium, (ed.) T. Törmänen and T. Alapieti; Oulu, Finland, p. 429–432.

Lane, L., 2007. Devonian–Carboniferous paleogeography and orogenesis, northern Yukon and adjacent Arctic Alaska; Canadian Journal of Earth Sciences, v. 44, p. 679–694.

Lehmann, B., Nägler, T.F., Holland, H.D., Wille, M., Mao, J., Pan, J., Ma, D., and Dulski, P., 2007. Highly metalliferous carbonaceous shale and Early Cambrian seawater; Geology, v. 35, p. 403.

Lehmann, B., Frei, R., Xu, L., and Mao, J., 2016, Early Cambrian Black Shale-Hosted Mo-Ni and V mineralization on the rifted margin of the Yangtze Platform, China: Reconnaissance chromium isotope data and a refined metallogenic model; Economic Geology, v. 111, p. 89–103.

Lenz, A.C. and Pedder, A.E.H., 1972. Lower and Middle Paleozoic sediments and paleontology of Royal Creek and Peel River, Yukon and Powell Creek, Northwest Territories; International Geological Congress XXIV, Field Excursion Guidebook, A14.

McLennan, S.M., 1989, Rare-earth elements in sedimentary-rocks: Influence of provenance and sedimentary processes; Reviews in Mineralogy and Geochemistry, v. 21, p. 169–200.

McLennan, S.M., 2001. Relationships between the trace element composition of sedimentary rocks and upper continental crust; Geochemistry, Geophysics, Geosystems, v. 2, p. 1–24.

Miller, C.A., Peucker-Ehrenbrink, B., Walker, B.D., and Marcantonio, F., 2011. Re-assessing the surface cycling of molybdenum and rhenium; Geochimica et Cosmochimica Acta, v. 75, p. 7146–7179.

Morrow, D., 1999. Lower Paleozoic stratigraphy of northern Yukon Territory and northwestern District of Mackenzie; Geological Survey of Canada, Bulletin 538, 202 p.

Murowchick, J.B., Coveney, J., Raymond M, Grauch, R.I., Eldridge, C.S., and Shelton, K.L., 1994. Cyclic variations of sulfur isotopes in Cambrian stratabound Ni-Mo-(PGE-Au) ores of southern China; Geochimica et Cosmochimica Acta, v. 58, p. 1813–1823.

Norris, A.W., 1985. Stratigraphy of Devonian outcrop belts in northern Yukon Territory and northwestern District of Mackenzie (Operation Porcupine area); Geological Survey of Canada, Memoir 410, 81 p.

Nozaki, Y., 1997. A fresh look at element distribution in the north Pacific Ocean; EOS Transactions of the American Geophysical Union, v. 78, p. 221–223.

Orberger, B., Pasava, J., Gallien, J.P., and Daudin, L., 2003a. Se, As, Mo, Ag, Cd, In, Sb, Pt, Au, Tl, Re traces in biogenic and abiogenic sulfides from Black Shales (Selwyn Basin, Yukon territories, Canada): A nuclear microprobe study; Nuclear Instruments and Methods in Physics Research Section B, Beam Interactions with Materials and Atoms, v. 210, p. 441–448.

Orberger, B., Pasava, J., Gallien, J.P., Daudin, L., and Pinti, D.L., 2003b. Biogenic and abiogenic hydrothermal sulfides: controls of rare metal distribution in black shales (Yukon Territories, Canada); Journal of Geochemical Exploration, v. 78, p. 559–563.

Orberger, B., Gallien, J.P., Pinti, D.L., Fialin, M., Daudin, L., Gröcke, D.R., and Pasava, J., 2005. Nitrogen and carbon partitioning in diagenetic and hydrothermal minerals from Paleozoic Black Shales,(Selwyn Basin, Yukon Territories, Canada); Chemical geology, v. 218, p. 249–264.

Pagés, A., Barnes, S., Schmid, S., Coveney, J.R.M., Schwark, L., Liu, W., Grice, K., Fan, H., and Wen, H., 2018. Geochemical investigation of the lower Cambrian mineralised black shales of South China and the late Devonian Nick deposit, Canada; Ore Geology Reviews, v. 94, p. 396–413.

Pasava, J., Chrastny, V., Loukola-Ruskeeniemi, K., and Sebek, O., 2018. Nickel isotopic variation in black shales from Bohemia, China, Canada, and Finland: a reconnaissance study; Mineralium Deposita, in press.

Peter, J.M., Gadd, M.G., Layton-Matthews, D., and Voinot, A., 2018. Reconnaissance thallium isotope study of zinc-lead SEDEX mineralization and host rocks in the Howard's Pass district, Selwyn Basin, Yukon: Potential application to paleoredox determinations and fingerprinting of mineralization; *in* Targeted Geoscience Initiative: 2017 Report of Activities, volume 1, (ed.) N. Rogers; Geological Survey of Cana-

da, Open File 8358, p. 173–291.

Pugh, D.C. 1983. Pre-Mesozoic geology in the subsurface of Peel River map area, Yukon Territory and District of Mackenzie. Geological Survey of Canada, Memoir 401, 61 p.

Ross, D.J.K. and Bustin, R.M., 2009. Investigating the use of sedimentary geochemical proxies for paleoenvironment interpretation of thermally mature organic-rich strata: Examples from the Devonian–Mississippian shales, Western Canadian Sedimentary Basin; Chemical geology, v. 260, p. 1–19.

Scott, C. and Lyons, T., 2012. Contrasting molybdenum cycling and isotopic properties in euxinic versus non-euxinic sediments and sedimentary rocks: Refining the paleoproxies;Chemical Geology, v. 324–325, p. 19–27.

Shuster, A., Wallace, M.W., van Smeerdijk Hood, A., and Jiang, G., 2018. The Tonian Beck Spring Dolomite: Marine dolomitization in a shallow, anoxic sea; Sedimentary Geology, v. 368, p. 83–104.

Steiner, M., Wallis, E., Erdtmann, B.-D., Zhao, Y., and Yang, R., 2001. Submarine-hydrothermal exhalative ore layers in black shales from South China and associated fossils — insights into a Lower Cambrian facies and bio-evolution; Palaeogeography, Palaeoclimatology, Palaeoecology, v. 169, p. 165–191.

Strauss, H., 1999. Geological evolution from isotope proxy signals — sulfur; Chemical Geology, v. 161, p. 89–101.

Sverjensky, D.A., 1984. Europium redox equilibria in aqueous-solution; Earth and Planetary Science Letters, v. 67, p. 70–78.

Sweeney, R. and Kaplan, I., 1980. Stable isotope composition of dissolved sulfate and hydrogen sulfide in the Black Sea; Marine Chemistry, v. 9, p. 145–152.

Taylor, S.R. and McLennan, S.M., 1985. The Continental Crust: Its Composition and Evolution; Oxford, Blackwell, 312 p.

Taylor, S.R. and McLennan, S.M., 1995. The geochemical evolution of the continental crust; Reviews of Geophysics, v. 33, 241 p.

Tribovillard, N., Algeo, T.J., Lyons, T., and Riboulleau, A., 2006. Trace metals as paleoredox and paleoproductivity proxies: An update; Chemical Geology, v. 232, p. 12–32.

Tribovillard, N., Algeo, T.J., Baudin, F., and Riboulleau, A., 2012. Analysis of marine environmental conditions based onmolybdenum–uranium covariation—Applications to Mesozoic paleoceanography; Chemical Geology, v. 324-325, p. 46–58.

Williams, G.K., 1983. What does the term ‘Horn River Formation’ mean?; Bulletin of Canadian Petroleum Geology, v. 31, p. 117–122.

Xu, L., Lehmann, B., Jingwen, M., Wenjun, Q., and Andao, D., 2011. Re-Os age of polymetallic Ni-Mo-PGE-Au mineralization in Early Cambrian black shales of south China—A reassessment; Economic Geology, v. 106, p. 511–522.

Xu, L., Lehmann, B., and Mao, J., 2013. Seawater contribution to polymetallic Ni–Mo–PGE–Au mineralization in Early Cambrian black shales of South China: Evidence from Mo isotope, PGE, trace element, and REE geochemistry; Ore Geology Reviews, v. 52, p. 66-84.

Metal transport by liquid hydrocarbons: Evidence from metalliferous shale and pyrobitumen, Yukon

K.M. Henderson, A.E. Williams-Jones and J.R. Clark

McGill University, Earth and Planetary Sciences 238-3450 University Street, Montreal, Quebec H3A0E8

Abstract

Hyper-enriched black shale (HEBS) occurs within Yukon Devonian stratigraphy as a thin (approximately 3 cm thick) laterally extensive (100–1000s km2) sulphide-rich unit. These shale beds contain an average of 4 weight % Ni, 0.5 weight % Zn, and 0.3 weight % Mo, as well as anomalous concentrations of Cu, Ag, Se, As, P, Ba, U, platinum group and rare earth elements. The origin of these HEBS deposits is strongly debated; possible mechanisms include metals being derived from seawater in a sediment-starved, stratified euxinic basin or by addition from hydrothermal fluids. However, a process that has not been considered is mobilization of metals by hydrocarbon liquids. These liquids are produced during diagenesis, and are capable of transporting nickel, vanadium and zinc.

Pyrobitumen occurs as centimetre-scale veins within the hyper-enriched black shale (HEBS) layer, but also much thicker metre-wide veins in the surrounding shale packages. Bulk analysis shows that these veins have high metal concentrations; most notably nickel and vanadium. Pyrobitumen within the HEBS horizon has average Ni and V concentrations of 1300 ppm and 1400 ppm, respectively. A vein above the HEBS horizon has 2000 ppm Ni and 3700 ppm V, as well as 8000 ppm Zn and 220 ppm Mo. Nickel-vanadium sulphur phases are present within the organic material as small (2–10 μm long) laths. The presence of nickel- and vanadium-bearing phases within pyrobitumen veins is consistent with the notion of metal-transportation by liquid hydrocarbons.

Introduction

Deep-marine black shale has an enriched metal content compared to other fine-grained clastic sedimentary rocks. The metal signature is derived from a combination of detrital debris, biogenic material, and metals precipitated from seawater (Piper and Calvert, 2009). Certain metals (Ag, Mo, Zn, Ni, Cu, Cr and V) appear to be universally enriched in the organic component of black shale, and there is a strong positive correlation of these metals with the total organic carbon content (Vine and Tourtelot, 1970). Hyper-enriched black shales (HEBS) exhibit extreme metal endowment of metals such as Ni, Zn and Mo. Such rocks also host anomalously high concentrations of Cu, Se, U V, Cr, Co, As, Ag, Au, platinum group elements (PGE) and rare earth elements (REE). These types of shales have been observed in two areas: southeastern China in the Early Cambrian Niutitang Formation (Lehmann et al., 2007), and in the Devonian of northern Yukon (Hulbert et al., 1992; Goodfellow, 2011). In both cases, the rocks are thin (<15 cm), laterally extensive (>1600 km strike length in China; 100 km strike length in Yukon) units composed of approximately 60 to 70 volume % sulphide minerals. First documented by Fan (1983), the origin of HEBS is still contested. Although many models have been proposed for its genesis, the two favoured models are: 1) derivation of metals from hydrothermal fluid venting on the seafloor (Hulbert et al., 1992; Lott et al., 1999; Steiner et al., 2001; Coveney, 2003; Jiang et al., 2007; Pašava et al., 2008; Och et al., 2013); or 2) their derivation from seawater directly (Mao et al., 2002; Lehmann et al., 2007, 2016; Xu et al., 2013).

A common feature of deep-marine sediments, metalliferous black shale, and even black shale-hosted base metal ore deposits is the presence of pyrobitumen. Pyrobitumen, an amorphous mineraloid that results from the linking of hydrocarbon polymers has been reported in HEBS in southeast China (Kříbek et al., 2007) and in northern Yukon (Hulbert et al., 1992; Gadd and Peter, 2018). Kříbek et al. (2007) reported that solidified products of a migrating oil (migrabitumen) are present in the Chinese HEBS horizon but are absent in the surrounding shale units. Hulbert et al. (1992) noted the occurrence of a 3 m wide pyrobitumen vein with a vertical extent of 9 m and strike length of 21 m near the Nick Property, Yukon. Stratigraphically, the vein occurs in the shale underlying the Nick HEBS (Road River Group, see below; Hulbert et al., 1992). More recently, a pyrobitumen vein with similar dimensions has been found in the shale overlying the HEBS near the Nick Property (T. Fraser, pers. comm., 2017; the exact relationship between the bitumen outcrop and the Nick HEBS is currently unknown). The significance of pyrobitumen veins within and surrounding HEBS horizons is the focus of the present research. Key questions being addressed include: the origin of the pyrobitumen; whether the pyrobitumen was generated from the HEBS horizon or the surrounding shale; and whether hydrocarbon generation or migration contributed to the metal endowment of these shales.

Corresponding author: Kyle Henderson (kyle.henderson@mail.mcgill.ca)

Henderson, K.M., Williams-Jones, A.E., and Clark, J.R., 2019. Metal transport by liquid hydrocarbons: Evidence from metalliferous shale and pyrobitumen, Yukon; *in* Targeted Geoscience Initiative: 2018 report of activities, (ed.) N. Rogers; Geological Survey of Canada, Open File 8549, p. 179–187. https://doi.org/10.4095/313650

Regional geology

Devonian strata in northern Yukon were deposited within the Paleozoic Richardson Trough. The Trough is a tectonic depression between two carbonate platforms, the Mackenzie Platform to the east and the Yukon Stable Block to the west (Fig. 1). The sedimentary sequence begins with the Late Cambrian to Early Devonian Road River Group, a greater than 100 m thick unit of fine-grained, carbonaceous siliciclastic rocks including limestone, shale, chert, dolostone, and conglomeratic debris flows (Norford, 1997; Fraser and Hutchison, 2017). A period of transgression drowned the carbonate platforms, depositing the Canol Formation during the Middle to Late Devonian. Between the Road River Group and Canol Formation is a 1 to 13 cm thick metalliferous layer that has been recognized in several locations in northern Yukon (HEBS horizon). The Canol Formation marks the conclusion of black shale deposition, with turbiditic sandstone deposition during the Late Devonian (Fraser and Hutchison, 2017).

Stratigraphy

The stratigraphy at the different Yukon HEBS localities is very similar. The base of the section is marked by a carbonaceous shale (5–10 m at Peel River; Road River Group); this is overlain by a 1 to 2 m thick carbonaceous shale with 1 to 1.5 m diameter calcareous concretions (Limestone Ball member), followed by a 0.3 to 1.1 m thick carbonaceous shale with centimetre-scale barite concretions (Transition Shale member). Above this layer is a 1 to 13 cm thick Ni-sulphide HEBS layer which is, in turn, overlain by a siliceous-cherty shale of unknown thickness (Canol Formation).

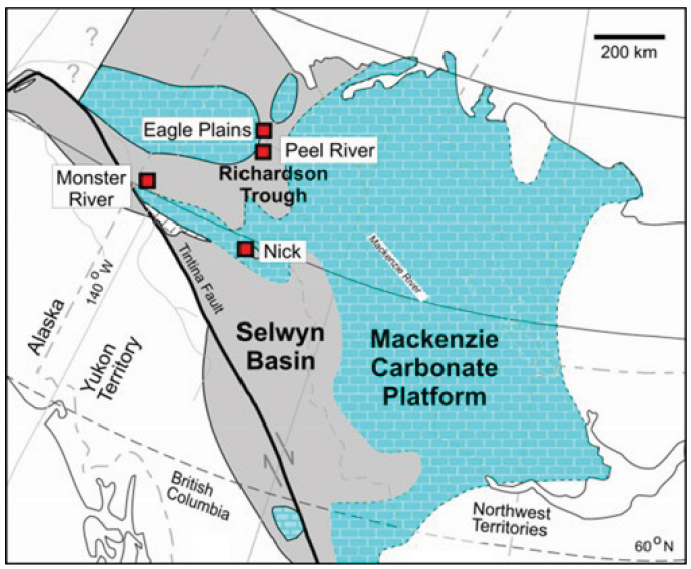

Figure 1. Regional Yukon geology with hyper-enriched black shale (HEBS) localities indicated by red squares. The fieldwork conducted in 2017 was at Peel River and Eagle Plains. Image *from* Goodfellow et al. (2010).

Stratigraphic sections for the Nick property (approximately 100 km south of Peel River, *see* Fig. 1; Hulbert et al., 1992) contain similar units. The Canol Formation has an equivalent unit called the Imperial Formation. Previously, the HEBS horizon was only documented as a single layer between the Road River Group and the Canol Formation. However, Gadd and Peter (2018) identified three discrete (not structurally repeated) horizons at the Peel River North Bank site, and two discrete HEBS horizons at the Peel River South Bank (located approximately 2 km southeast of the North Bank). These newly recognized horizons occur approximately 5 and 10 m below the previously identified HEBS layer, and are hereafter referred to as the upper, middle, and lower HEBS horizons, respectively. Only one HEBS layer occurs at the Eagle Plains site, though two pyritic, non-nickeliferous layers, 1 to 1.5 cm thick, occur in a similar stratigraphic position as the middle and lower HEBS horizons. The relationship (if any) between the nickeliferous and non-nickeliferous sulphidic layers is not yet known.

Methods

Multi-acid digestion using HF-$HClO_4$-HNO_3 in a 2:1:1 ratio for inductively coupled plasma emission spectroscopy (ICP-ES) and inductively coupled plasma mass spectroscopy (ICP-MS) was conducted in Vancouver by Bureau Veritas. Approximately 15 to 20 g of rock was crushed to 75 µm (200 mesh), then a 0.25 g spilt was taken for analysis. A PerkinElmer ELAN 9000 was used for ICP-MS analyses, and a Spectro Ciros Vision for ICP-ES analyses. Standards and blanks were used for accuracy and precision calculations. Total organic carbon (TOC) was determined by pyrolysis using a Rock-Eval 6 Turbo 4.10 instrument with between 50 to 100 mg of sample material. Calibration was performed using standard IFP#160000.

An Agilent 7700x ICP-MS connected to a Photon Machine Analyte G2 Excimer for trace element ablation of pyrobitumen was used at the Geological Survey of Canada, Ottawa. Helium served as the carrier gas. Analyses were conducted at a laser repetition rate of 10 Hz, and a laser pulse energy of 3.785 J cm^{-2}. Synthetic oil standard S-21 was used as the primary standard. The oil was spiked with 50 ppm each of Ag, Al, B, Ba, Ca, Cd, Cr, Cu, Fe, Mg, Mn, Mo, Na, Ni, Pb, Si, Sn, Ti, V and Zn. Solid standard GSD-1G was used to extend the element list to include As, Au, Bi, Co, Hf, Nb, Pd, Pt, REE, Ru, Sb, Sc, Sr, Ta, Te, Th Tl, U, W, Y and Zr. Samples were analyzed in cycles of 20 unknowns bracketed by standard analyses. Data reduction was performed using a multi-standard approach, with carbon as an internal standard for S-21, and Al for GSD-1G. Iolite software was used to select regions of integration to calculate element concentrations and 2σ uncertainties (Woodhead, 2007; Paton et al., 2011). Results are presented as integrations of stable signal intensities, free of spikes or peaks that may represent micro-inclusions. Future work will investigate potential analytical problems associated with inclusions within pyrobitumen.

Results

Whole-rock geochemistry

The HEBS horizons contain up to 7 weight % Ni, 2.4 weight % Zn, 0.38 weight % Mo, 0.6 weight % As and 3.5 weight % TOC (Fig. 2). The Nick Property has the highest median Ni concentration (6.3 weight %), followed by Eagle Plains, South Bank, and North Bank with 4.0, 3.4 and 2.8 weight %, respectively. These median values represent a combination of all HEBS horizons at the different locations. At North Bank, the upper and middle HEBS horizons have median Ni concentrations of 2.7 and 3.8 weight %, median Zn concentrations of 0.19 and 0.12 weight %, and median Mo concentrations of 0.16 and 0.19 weight %, respectively. The one sample collected from the lower HEBS horizon at North Bank has Ni, Zn, and Mo concentrations of 4.5, 0.93, and 0.28 weight %, respectively. The total organic carbon content varies among different locations and horizons. The respective median TOC contents for Nick, North Bank, South Bank, and Eagle Plains are 2.59, 1.46, 1.58, and 1.33 weight %. At North Bank, the upper and middle HEBS layers have median TOC values of 1.5 and 1.3 weight %. The single North Bank lower HEBS sample contains 2.4 weight % TOC.

The surrounding black shale units are also relatively metal-rich. At South Bank, the Transition Shale member has median Ni, Zn and Mo contents of 306, 678 and 55 ppm, respectively. The median TOC value is 2.29 weight %. The Road River Group shale has median Ni, Zn and Mo contents of 313, 849, and 77 ppm, respectively, and a median TOC value of 2.7 weight %. Metal values decrease further down section. Shale 20 m below the upper HEBS layer has median Ni, Zn and Mo concentrations of 100, 370 and 31 ppm, respectively. The vanadium concentration is very low within the HEBS horizon (median 205 ppm) but is higher in the Transition Shale member (1300 ppm), and the Road River Group (1400 ppm); V concentrations appear to decrease with depth away from the HEBS layer (870 ppm at 20 m down stratigraphy).

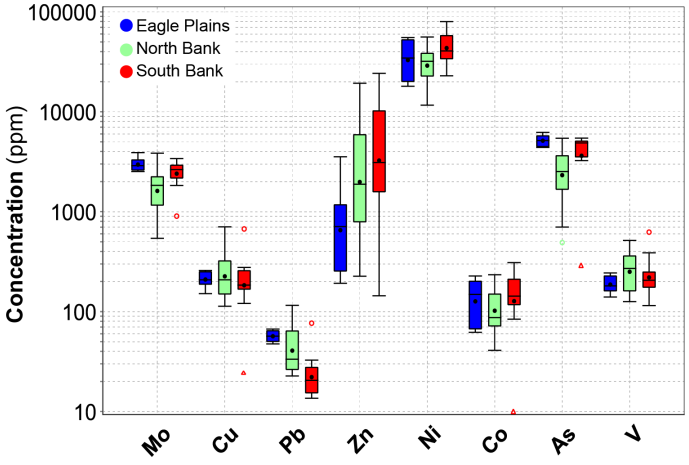

Figure 2. Box plot for the Eagle Plains and two Peel River sites. Some elements display similar distributions in the three locations (e.g. Cu, Ni, Co, V), whereas Mo, Pb, Zn and As show different distributions.

Spearman correlations were calculated using upper HEBS horizon data from the North and South Bank locations ($p > 0.05$): nickel shows positive correlations with Co (0.86), As (0.81) and S (0.81); zinc correlates positively with Cu (0.86), Cd (0.96) and Sn (0.90); and molybdenum shows strong correlations with As (0.86) and S (0.83). The TOC has no significant correlation with any trace elements in the HEBS horizon.

Six pyrobitumen samples were collected: two near the Nick horizon—one in the underlying Road River Group (R. Coveney, pers. comm., 2018) and the second in the overlying Canol Formation (T. Fraser, pers. comm., 2017); two within the upper HEBS layer at North Bank; and two below the HEBS horizon (T. Fraser, pers. comm., 2017). The two pyrobitumen veins found significantly below the HEBS layer at North Bank are metal-poor, but the two from within the HEBS horizon are relatively rich in Ni (median 1360 ppm) and V (1440 ppm). In addition, one of the veins contains 1500 ppm Mo and 680 ppm As. The two pyrobitumen veins near the Nick horizon have different geochemical characteristics. The vein from below the horizon contains 900 ppm Ni, 4200 ppm V and 1000 ppm Cu, whereas the vein above the horizon contains 2000 ppm Ni, 3700 ppm V and 8000 ppm Zn (Fig. 3).

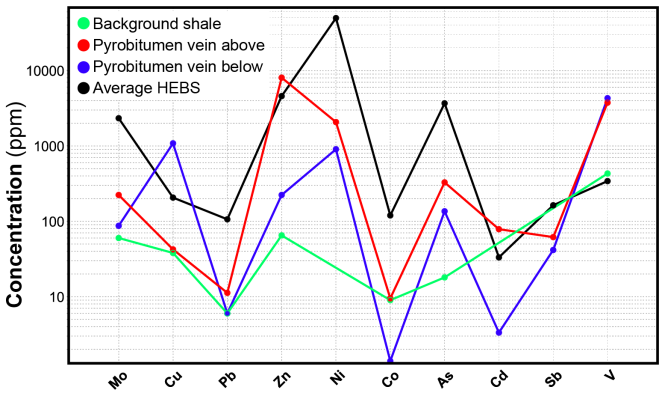

Figure 3. Spider diagram comparing trace-element concentrations in pyrobitumen veins with average background shale (Canol Formation equivalent) and Nick hyper-enriched black shale (HEBS) concentrations. The data for background shale *from* Hulbert et al. (1992).

LA-ICP-MS

Laser ablation ICP-MS analyses on the two pyrobitumen samples collected near the Nick HEBS horizon (samples KH01 and KH16) yielded mostly similar results, with relatively abundant Ni (median 400 ppm for both veins) and V (2400 and 2500 ppm). Differences in Cu and Zn concentrations were noted: sample KH01 from above the Nick horizon had a median Zn concentration of 4.5 ppm versus 0.9 ppm in sample KH16 from below the Nick horizon. Similarly, the vein above the Nick HEBS horizon has a higher median Cu concentration than

the vein below it (23 vs. 3 ppm).

Correlation coefficients (Spearman's Rho) for trace elements in pyrobitumen indicate that nickel exhibits strong (>0.8) and significantly ($p < 1E-15$) positive correlations with V (0.92), As (0.95), Se (0.86), Mo (0.89) and Ag (0.91). Vanadium exhibits strong and significantly ($p < 1E-11$) positive correlations with Ni (0.92), As (0.88), Se (0.80), Mo (0.91) and Ag (0.82).

Mineralogy

The mineralogy of the Yukon HEBS horizons is broadly similar at all locations, and is dominated by pyrite, millerite (NiS), vaesite (NiS_2), gersdorffite (NiAsS) and sphalerite. Vaesite occurs mainly at the Nick showing, and less so at the other sites. Non-sulphide phases include quartz, barite, apatite, pyrobitumen and minor hyalophane ($(K,Ba)[Al(Si,Al)Si_2O_8]$).

Pyrite is the most abundant sulphide mineral and exhibits multiple textural forms. Most commonly, it occurs as framboids ranging from less than 1 to 150 µm in diameter that are composed of microcrystalline particles (<15 µm). Pyrite also occurs as a replacement of organic material and as anhedral masses. Variable degrees of recrystallization suggest multiple pyrite stages. The diameter of the framboids and the particles within them can provide insight into redox conditions during deposition (Wilkin and Barnes, 1997). Further work will document pyrite grain size distributions from the different HEBS horizons.

Millerite occurs as anhedral blebs and acicular needles, interspersed with microcrystalline pyrite, and infills framboids. Locally, it encases anhedral pyrite masses. Sphalerite occurs as minor inclusions in pyrite, but more commonly is related to replacement of hyalophane or apatite nodules. Such nodules are typically elliptical, have major axes between 80 and 350 µm long, and are commonly replaced by sphalerite and gersdorffite, and less frequently by millerite and chalcopyrite. The origin and relationships between the nodules and sulphides are not always clear. Barite is texturally late, and typically overprints pyrite and millerite.

Pyrobitumen below the Nick horizon

The pyrobitumen vein below the Nick horizon is relatively copper-rich and is characterized by dense fracture networks with a maximum width of 50 µm. The fractures are infilled by quartz and carbonate. Carbonate compositions range from calcite to iron-rich ankerite. Within the quartz-carbonate material, a bronze-yellow sulphide was tentatively identified by scanning electron microscope - energy-dispersive spectrometry (SEM-EDS) as sulvanite (Cu_3VS_4).

Within the organic material, various sulphide minerals occur as 2 to 10 µm long laths (Fig. 4), approximately 1 µm wide and as 1 to 2 µm diameter spheres; the latter probably represent the laths viewed perpendicularly to the c-axis. Preliminary SEM-EDS analyses suggest that these minerals are vanadium and vanadium-nickel sulphides. Future electron microprobe work will establsh the stoichiometry of these minerals.

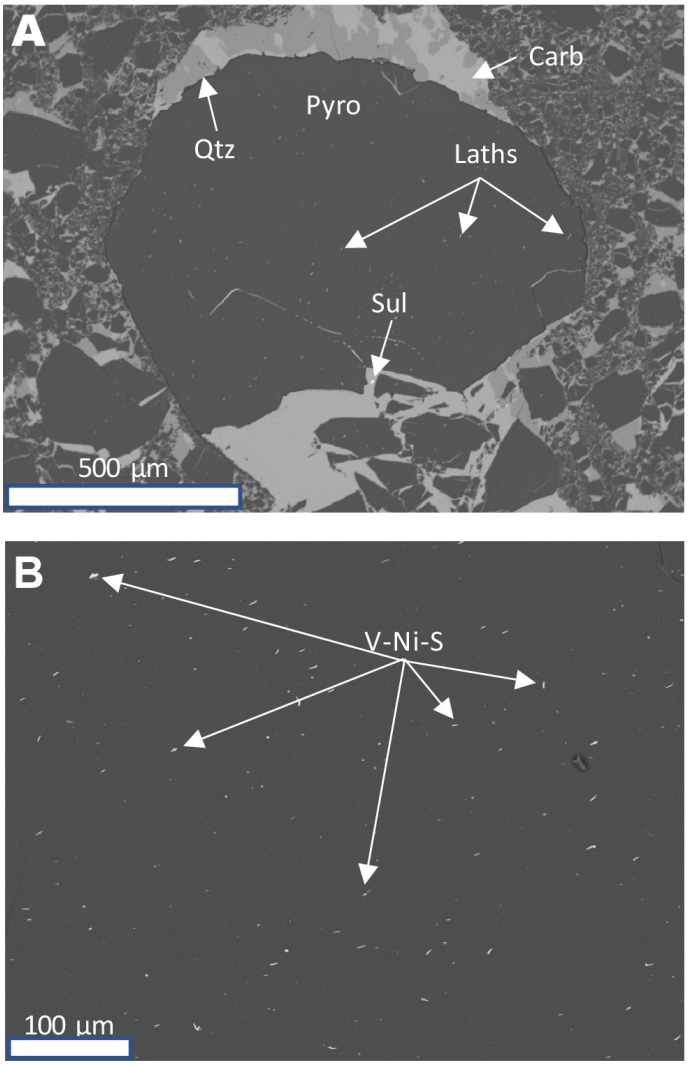

Figure 4. Pyrobitumen vein occurring a few kilometres from the Nick hyper-enriched black shale (HEBS) horizon: a) Scanning electron microscope backscattered electron image of pyrobitumen (black) with a surrounding quartz-carbonate matrix. Sulvanite (Cu_3VS_4) occurs in the quartz-carbonate matrix. b) Close-up of (a) showing white laths disseminated in pyrobitumen. Scanning electron microscope energy-dispersive spectrometry (SEM-EDS) analyses suggest that these are a vanadium-nickel sulphide. Abbreviations: Carb – carbonate; Qtz – quartz; Pyro – pyrobitumen; Sul – sulvanite.

Pyrobitumen above the Nick Horizon

Texturally, the pyrobitumen vein above the Nick horizon is like that below the horizon, although the former is relatively zinc-rich. The vein above the Nick horizon is also characterized by a dense fracture network infilled by a quartz-carbonate matrix. No copper sulphide minerals have been identified in the quartz-carbonate matrix, but vanadium and nickel-vanadium sulphide laths occur in the organic material (Fig. 4). Sphalerite

occurs only in the fracture network and not in the organic material.

Pyrobitumen within the HEBS layer (North Bank)

The pyrobitumen vein within the HEBS horizon at North Bank hosts worm-like pyrite intergrowths that exhibit varying degrees of recrystallization (Fig. 5). The intergrowths are approximately 38 to 42 µm in width and average 400 µm in length (maximum 1.1 mm). Texturally, the intergrowths vary from early framboids to later (recrystallized) massive pyrite. The only non-sulphidic phases in the veins are pyrobitumen and quartz. Microcrystalline pyrite occurs between the worm-like pyritic intergrowths. Future work will investigate the origin of these textures and their paragenetic relationship with the mineralized horizon.

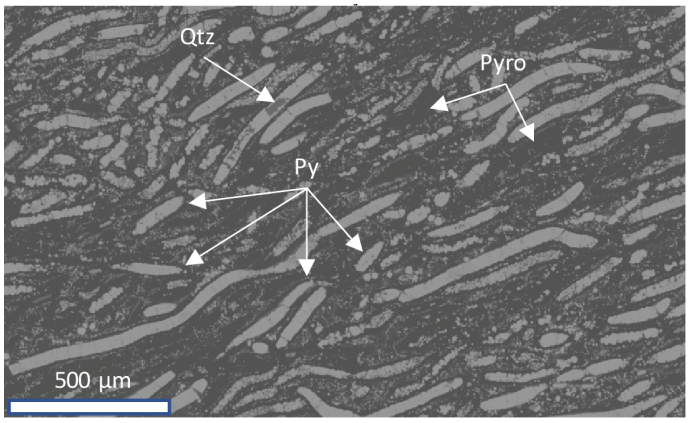

Figure 5. Scanning electron microscope backscattered electron image of a pyrobitumen vein found within the hyper-enriched black shale (HEBS) at North Bank, Yukon. Pyrite forms worm-like intergrowths within a bituminous medium. Variable degrees of crystallization are observed with some intergrowths appearing as solid pyrite and others veining framboidal pyrite. Quartz is the only non-sulphide mineral present and occurs throughout the sample in small quantities (approximately 5% of sample). Some worm-like voids are also present. The origin of this texture and relationship with the HEBS horizon is unclear. Abbreviations: Py – pyrite; Pyro – pyrobitumen; Qtz – quartz.

Discussion

Mineralogy and paragenesis

The mineralized horizons host a variety of sulphide minerals, most notably pyrite, millerite, vaesite, gersdorffite and sphalerite (Fig. 5). The complex mineral textures makes evaluation of the paragenesis and mineralization process difficult. The size and diversity of framboidal pyrite textures suggest that some formed below an anoxic water column (larger framboids), whereas smaller framboids may have formed under euxinic conditions (Wignall and Newton, 1998). Generally, the size of pyrite framboids reflects the competition between processes involving nucleation and growth of crystals (Wilkin and Barnes, 1997). Smaller framboids (<7 µm) typically form in euxinic conditions where the nucleation of new pyrite crystals is facilitated by an abundance of free H_2S. Under anoxic conditions, the growth of framboids is favoured, resulting in larger structures (Wilkin et al., 1996; Wilkin and Barnes, 1997). Millerite fills voids in framboidal pyrite (Fig. 6, 7), forms crusts around anhedral pyrite masses, and occurs in the shale matrix as acicular needles and blebs (Fig. 6). This suggests that millerite precipitated after pyrite. Whether these different types of millerite represent discrete phases or long-lived nickel-sulphide deposition is unknown.

Hyper-enriched black shale (HEBS) genesis—source of metals

Hydrothermal venting has been proposed to explain the extreme metal endowment of HEBS layers in both southeast China (Lott et al., 1999; Steiner et al., 2001) and north Yukon (Hulbert et al., 1992). Steiner et al. (2001) proposed that during a regional transgression of a carbonate platform, there was an expulsion of metal-rich saline hydrothermal fluids along a 1600 km arc-parallel fracture zone, leading to the formation of the HEBS horizon. Hulbert et al. (1992) suggested that in Yukon, the discharge of hydrothermal brines, enriched in metals, sulphate, phosphate and organic compounds, into stagnate unconsolidated bottom sediment was responsible for formation of the HEBS horizon. For the Chinese HEBS, hydrothermal models

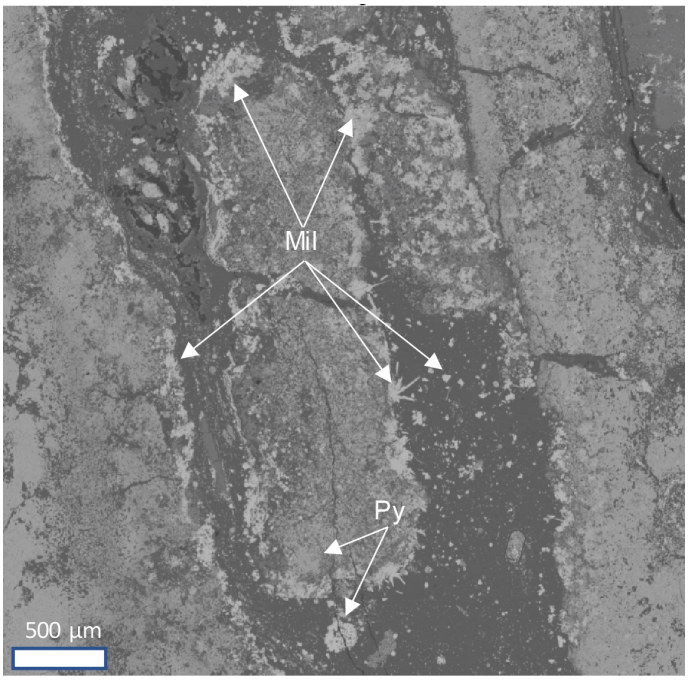

Figure 6. Scanning electron microscope backscattered electron image of millerite in the Peel River hyper-enriched black shale (HEBS). Millerite forms crusts around masses of anhedral pyrite and acicular needles. Abbreviations: Mil – millerite; Py – pyrite.

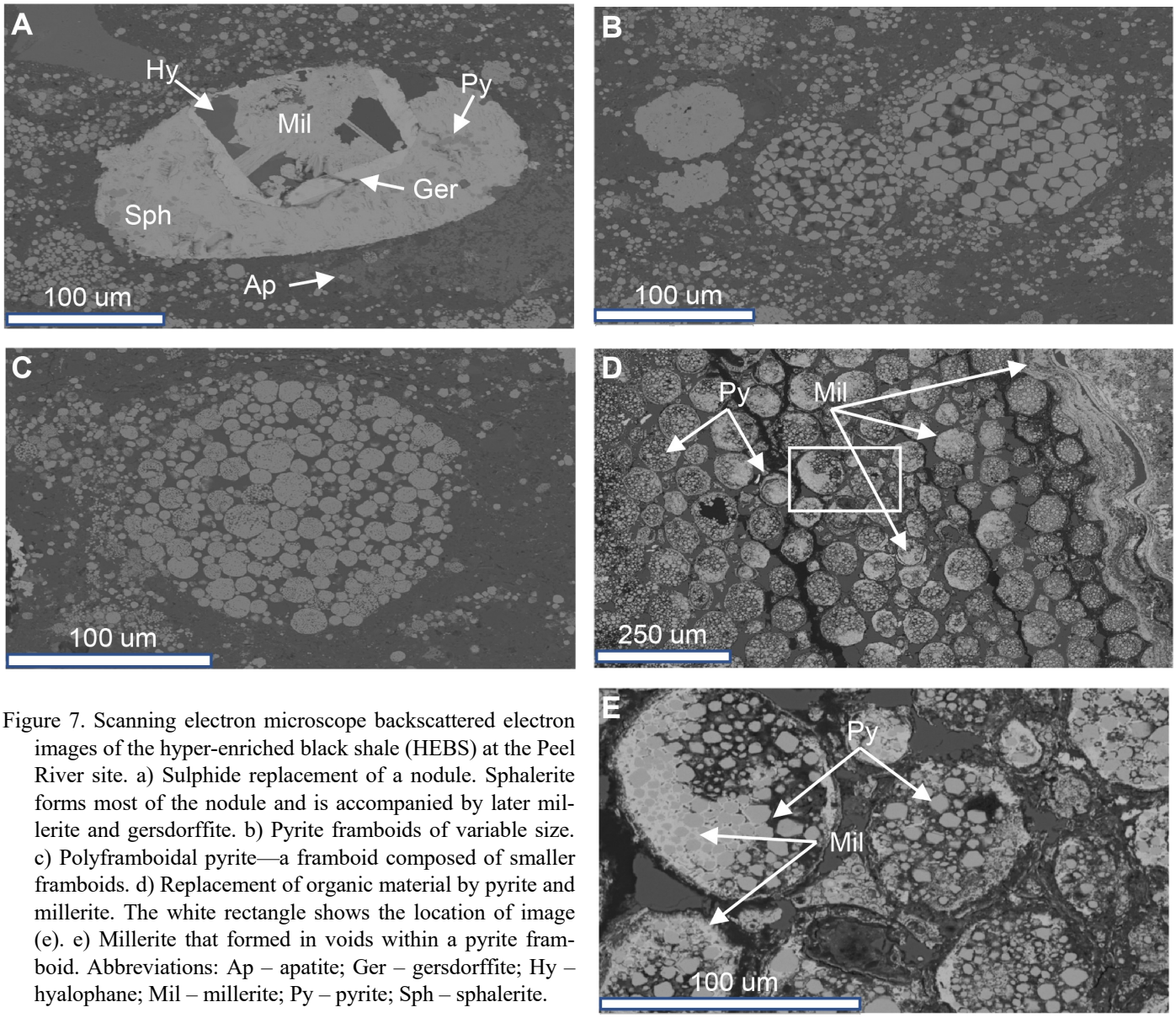

Figure 7. Scanning electron microscope backscattered electron images of the hyper-enriched black shale (HEBS) at the Peel River site. a) Sulphide replacement of a nodule. Sphalerite forms most of the nodule and is accompanied by later millerite and gersdorffite. b) Pyrite framboids of variable size. c) Polyframboidal pyrite—a framboid composed of smaller framboids. d) Replacement of organic material by pyrite and millerite. The white rectangle shows the location of image (e). e) Millerite that formed in voids within a pyrite framboid. Abbreviations: Ap – apatite; Ger – gersdorffite; Hy – hyalophane; Mil – millerite; Py – pyrite; Sph – sphalerite.

assume that ultramafic-mafic rocks were the ultimate source of nickel (Lott et al., 1999; Steiner et al., 2001). As no ultramafic-mafic units are present in the northern Yukon, the underlying shale units are thought to be the source of metals transported by organic complexes (Hulbert et al., 1992). High nickel concentrations in other shale units globally (500–2000 ppm) may be related to leaching of nickel from nearby ultramafic rocks (e.g. Talvivaara: Loukola-Ruskeeniemi and Lahtinen, 2013). Regional variations in the composition of the underlying ultramafic-mafic source rocks was used by Steiner et al. (2001) to explain variable Pb/Co ratios in the HEBS horizons in China. This regional variance was also used by Han et al. (2015), who proposed that the cobalt was sourced from mafic rocks and black shale with high lead content was associated with underlying lead-zinc deposits.

A challenge for any model explaining the HEBS occurrences is the laterally extensive nature of the horizons. Although discontinuous, the horizons extend for more than 1600 km in southeast China and 100 km in Yukon; this feature is a significant problem for most hydrothermal exhalative models. This is especially true for those in Yukon, as a large pyrobitumen vein underlying the Nick HEBS, which was interpreted by Hulbert (1992) to be a vent-like system that acted as a fluid conduit, has only been found in one location. The petroleum-exhalative ('petrex') model proposed by Emsbo et al. (2005) involves the discharge of petroleum onto the seafloor. Lehmann et al. (2016) argued that this could not account for the metal tenors of the HEBS horizons, noting that black shale is consistently higher in Re, Os, Mo and Ni than the extracted oil fractions.

In the Yukon occurrences, pyrobitumen veins above the Nick HEBS contain 2000 ppm Ni, 3700 ppm V, and 8000 ppm Zn; below the Nick HEBS these veins contain 900 ppm Ni, 4200 ppm V and 1000 ppm Cu. To assess the source of these veins, we have compared the metal distribution in the veins with that in the Nick HEBS layer and surrounding black shale (Fig. 3). The latter data comprise the average background values for the shale given in Hulbert et al. (1992). For consistency, the average value for the HEBS layer was used, rather than the median. Following the approach of Lehmann et al. (2016), if the Nick area black shale is consistently higher in molybdenum and nickel than any derived oil products, it follows that the HEBS horizon contributed to the hydrocarbon generation and is a potential source of the metals found in the pyrobitumen. By contrast, Hulbert et al. (1992) suggested that the pyrobitumen vein below the horizon was evidence for a vent-complex system that acted as a conduit for mineralizing fluids. How the pyrobitumen vein above the Nick HEBS, which hosts higher concentrations of metals than the vein below the Nick HEBS, fits into the model of Hulbert et al. (1992) is unclear. A salient question is whether such metal concentrations can be derived from a metalliferous, but not hyper-enriched, shale, as suggested by Hulbert et al. (1992). In the exhalative model, hydrocarbon generation that resulted in the formation of the pyrobitumen veins above and below the Nick HEBS must have occurred at different times, as the proposed HEBS-related hydrothermal fluid, which discharged into an unconsolidated seafloor mud (the Canol Formation) was not deposited until the Middle Devonian.

The two metals most enriched in both veins are nickel and vanadium. Lewan (1984) described several regimes that potentially affect vanadium to nickel ratios in crude oils, citing Eh, pH and sulphide activity as critical factors. In one scenario, vanadyl or trivalent vanadium cations partition into an oil, whereas nickelous cations are hindered from doing so by the presence of sulphide ions. Oil generated under such conditions would have high V:Ni ratios and high sulphur contents. As noted by Lewan (1984), these concentrations might change during migration by addition or subtraction of more labile crude oils. For example, as vanadium and nickel form strong bonds with organometallic complexes of high molecular weight, migration could increase metal concentrations, although the ratios should remain fairly constant (Lewan, 1984). However, pyrolysis experiments indicate that vanadium organometallic complexes have higher thermal stability than similar nickel complexes (Filby and Van Berkel, 1987; Van Berkel and Filby, 1987), which suggests that V:Ni ratios increase during migration.

In the absence of an external source of metals, it is possible that the enriched elements were wholly derived from seawater. In this model, a protected basin with very low lithogenic and biogenic accumulation and anoxic/euxinic water conditions may sequester percentage levels of metals into the sediments (Lehmann et al., 2007, 2016; Xu et al., 2013). The apparent congruency between trace metal and PGE element ratios in HEBS horizons and seawater in both Yukon and China has been cited as evidence for their seawater origin (Lehmann et al., 2016; Gadd and Peter, 2018). Lehmann et al. (2016) concluded that an exotic seawater composition is not required to achieve such metal endowment and that the ultimate metal supply is related to the oxidative weathering of continental crust. A similar conclusion was reached by Johnson et al. (2017) for highly metalliferous shale (i.e. black shale with above average metal concentration, including HEBS). They documented trace element concentrations in sedimentary pyrite through the Neoproterozoic and Phanerozoic, and noted that metalliferous shale is associated with periods of elevated atmospheric O_2. However, the congruency between atmospheric O_2 and metal-rich shale is not perfect, as the Devonian lacks an oxygen peak. Gadd and Peter (2018) suggested that condensed sedimentation may have been the additional process needed to explain metal endowments. If a special seawater chemistry is not required to generate HEBS layers, and the key factors necessary to generate metal enrichment are low lithogenic input and high rates of organic matter remineralization, it is difficult to explain the apparent gap in Ni concentrations observed in shale globally. The HEBS horizons in China and Yukon have the highest Ni concentrations. The next most metalliferous shale apparently unaffected by hydrothermal input or post-deposition metal mobility, is the Road River Group underlying the HEBS layer at North Bank, with a maximum 540 ppm Ni. This is followed by the shale of the Heath Formation in Montana, which has a maximum Ni content of 500 ppm (Dumoulin et al., 2015). The shale-hosted Talvivaara deposit in Finland has an average Ni value of 0.2 weight %. However, its genesis is debated, with some authors suggesting that the Ni was leached from nearby ophiolite (Loukola-Ruskeeniemi and Lahtinen, 2013). The gap between a maximum of approximately 500 ppm Ni in black shale and 50 000 to 80 000 ppm Ni in HEBS horizons has yet to be accounted for in seawater models of metal-rich black shale formation.

Impacts of hydrocarbon generation on metal mobility

One of the objectives of this research is to assess whether hydrocarbon generation has contributed to the metal endowment seen in the HEBS layers in Yukon and China. Laser ablation ICP-MS analyses of Yukon pyrobitumen indicate that the overall abundance of trace metals is low, except for nickel and vanadium. By contrast, the HEBS horizons are depleted in vanadium relative to the surrounding shale packages, yet this metal is enriched in the pyrobitumen veins. The HEBS horizons may have undergone maturation and hydrocarbon generation, thus, depleting vanadium in the HEBS horizon. In anoxic conditions, pentavalent vanadium is reduced to tetravalent vanadium and can deposit from organometallic complexes or adsorb onto organic matter (Morford and Emerson, 1999). With decreasing redox potential, tetravalent vanadium can be reduced to trivalent vanadium, which will readily substitute for aluminium in the octahedral sites of clays (Breit and Wanty, 1991). The HEBS horizons, however, have very low lithogenic

input (Lehmann et al., 2016) and thus low clay content, but correlation coefficients calculated using whole rock data nevertheless suggest that some vanadium resides in the detrital component, rather than in sulphide minerals.

Future work

Future LA-ICP-MS analyses will be conducted on additional pyrobitumen veins to determine metal concentrations in the different phases in order to improve understanding of the metal-enrichment process and the timing of millerite deposition. Given the wide variation in the sizes of pyrite framboids, LA-ICP-MS analyses will also be conducted to determine whether framboidal pyrite sizes affected metal-enrichment. The paragenetic relationship between the pyrite 'worm' intergrowths and framboidal pyrite observed within the HEBS horizon will be also be evaluated.

Maturation of the HEBS horizon would have occurred concurrently with that of the surrounding black shale. Further work is required to resolve the partitioning of metals into an oil-phase and to determine the nature of the prevailing conditions were during deposition. Samples from different locations and HEBS formations have been submitted for whole rock analysis. Additional statistical analysis will be undertaken to characterize the upper, middle and lower HEBS horizons. This will enable a better evaluation of existing models for the hyper-enrichment of metals in black shales.

Acknowledgments

This report is a contribution to NRCan's Targeted Geoscience Initiative Program (TGI-5). Support for this study was provided through the Volcanic- and Sedimentary-Hosted Base Metal Mineralization Project's '*Activity VS-1.2: Development of genetic and exploration models for hyper-enriched black shale (HEBS) deposits*'.

The Polar Continental Shelf Program (Project 00717) is acknowledged for providing logistical support for fieldwork. We would especially like to thank Jan Peter and Michael Gadd of the Geological Survey of Canada for fieldwork logistical support, LA-ICP-MS usage and their invitation to submit this manuscript. We would also like to thank Tiffani Fraser of the Yukon Geological Survey, Dan Gregory of University of Toronto and Ray Coveney of the University of Missouri-Kansas City for sample materials. Zhaoping Yang is gratefully acknowledged for her assistance with the LA-ICP-MS analyses. This report benefited from the review of Dawn Kellett, Eric Potter and Neil Rogers.

References

Breit, G.N. and Wanty, R.B., 1991. Vanadium accumulation in carbonaceous rocks: A review of geochemical controls during deposition and diagenesis; Chemical Geology, v. 91, p. 83–97.

Coveney, R.M., Jr., 2003. Re-Os dating of polymetallic Ni-Mo-PGE-Au mineralization in lower cambrian black shales of south china and its geological significance-A discussion; Economic Geology, v. 98, p. 661–662.

Dumoulin, J.A., Johnson, C.A., Kelley, K.D., Scott, C., and Slack, J.F., 2015. Transgressive-regressive cycles in the highly metalliferous, oil shale-bearing Heath Formation (Upper Mississippian), Central Montana; American Association of Petroleum Geologists, Annual Convention and Exhibition, Denver, Search and Discovery Article #90216.

Emsbo, P., Zhang, X., Hofstra, A.H., Hu, R., Johnson, C.A., Su, W., Pi, D., Koenig, A., and Grauch, R., 2005. Lower Cambrian metallogenesis of south China: Interplay between diverse basinal hydrothermal fluids and marine chemistry; Proceedings of the 8th Biennial SGA Meeting, v. 1, p. 115–118.

Fan, D., 1983. Polyelements in the Lower Cambrian black shales series in southern China; *in* The Significance of Trace Elements in Solving Petrogenetic Problems and Controversies, (ed.) S.S. Augsitithis; Theophrastus Publications, Athens, Greece, p. 447–474.

Filby, R.H. and Van Berkel, G.J.V., 1987. Geochemistry of Metal Complexes in Petroleum Source Rocks and Coals: An Overview; *in* Metal Complexes in Fossil Fuels: Geochemistry, Characterization and Processing, (ed.) R.H. Filby and J.F. Branthaver; American Chemical Society, Symposium Series Volume 344, p. 2–39.

Fraser, T.A. and Hutchison, M.P., 2017. Lithogeochemical characterization of the Middle–Upper Devonian Road River Group and Canol and Imperial formations on Trail River, East Richardson Mountains, Yukon: Age constraints and a depositional model for fine-grained strata in the Lower Paleozoic Richardson Trough; Canadian Journal of Earth Sciences, v. 54, p. 731–765.

Gadd, M.G. and Peter, J.M., 2018. Field observations, mineralogy and geochemistry of Middle Devonian Ni-Zn-Mo-PGE hyper-enriched black shale deposits, Yukon; *in* Targeted Geoscience Initiative: 2017 Report of Activities, Volume 1, (ed.) N. Rogers; Geological Survey of Canada, Open File 8358, p. 193–206.

Goodfellow, W.D., 2011. Devonian shale-hosted Ni-Zn-Mo-PGE sulfide deposits, Yukon; Geological Association of Canada-Mineralogical Association of Canada, Program with Abstracts, v. 34, p. 77.

Goodfellow, W.D., Geldsetzer, H., Gregoire, C., Orchard, M., and Cordey, F., 2010. TGI-3 Workshop: Public Geoscience in Support of Base Metal Exploration; Geological Association of Canada, Cordilleran Section 2010, Programme and Abstracts, p. 15–18.

Han, T., Zhu, X., Li, K., Jiang, L., Zhao, C., and Wang, Z., 2015. Metal sources for the polymetallic Ni-Mo-PGE mineralization in the black shales of the Lower Cambrian Niutitang Formation, South China; Ore Geology Reviews, v. 67,

p. 158–169.

Hulbert, L.J., Gregoire, D.C., Paktunc, D., and Carne, R.C., 1992. Sedimentary nickel, zinc, and platinum-group-element mineralization in Devonian black shales at the Nick Property, Yukon, Canada: a new deposit type; Exploration and Mining Geology, v. 1, p. 39–62.

Jiang, S.Y., Yang, J.H., Ling, H.F., Chen, Y.Q., Feng, H.Z., Zhao, K.D., and Ni, P., 2007. Extreme enrichment of polymetallic Ni-Mo-PGE-Au in Lower Cambrian black shales of South China: An Os isotope and PGE geochemical investigation; Palaeogeography, Palaeoclimatology, Palaeoecology, v. 254, p. 217–228.

Johnson, S.C., Large, R.R., Coveney, R.M., Jr., Kelley, K.D., Slack, J.F., Steadman, J.A., Gregory, D.D., Sack, P.J., and Meffre, S., 2017. Secular distribution of highly metalliferous black shales corresponds with peaks in past atmosphere oxygenation; Mineralium Deposita, v. 52, p. 791–798.

Kříbek, B., Sýkorová, I., Pašava, J., and Machovič, V., 2007. Organic geochemistry and petrology of barren and Mo-Ni-PGE mineralized marine black shales of the Lower Cambrian Niutitang Formation (South China); International Journal of Coal Geology, v. 72, p. 240–256.

Lehmann, B., Nägler, T.F., Holland, H.D., Wille, M., Mao, J., Pan, J., Ma, D., and Dulski, P., 2007. Highly metalliferous carbonaceous shale and Early Cambrian seawater; Geology, v. 35, p. 403–406.

Lehmann, B., Frei, R., Xu, L., and Mao, J., 2016. Early Cambrian black shale-hosted Mo-Ni and V mineralization on the rifted margin of the Yangtze platform, China: Reconnaissance chromium isotope data and a refined metallogenic model; Economic Geology, v. 111, p. 89–103.

Lewan, M.D., 1984. Factors controlling the proportionality of vanadium to nickel in crude oils; Geochimica et Cosmochimica Acta, v. 48, p. 2231–2238.

Lott, D.A., Coveney, R.M., Jr., Murowchick, J.B., and Grauch, R.I., 1999. Sedimentary exhalative nickel-molybdenum ores in south China; Economic Geology, v. 94, p. 1051–1066.

Loukola-Ruskeeniemi, K. and Lahtinen, H., 2013. Multiphase evolution in the black-shale-hosted Ni–Cu–Zn–Co deposit at Talvivaara, Finland; Ore Geology Reviews, v. 52, p. 85–99.

Mao, J., Lehmann, B., Du, A., Zhang, G., Ma, D., Wang, Y., Zeng, M., and Kerrich, R., 2002. Re-Os dating of polymetallic Ni-Mo-PGE-Au mineralization in Lower Cambrian black shales of South China and its geologic significance; Economic Geology, v. 97, p. 1051–1061.

Morford, J.L. and Emerson, S., 1999. The geochemistry of redox sensitive trace metals in sediments; Geochimica et Cosmochimica Acta, v. 63, p. 1735–1750.

Norford, B.S., 1997. Ordovician and Silurian; *in* The Geology, Mineral and Hydrocarbon Potential of northern Yukon Territory and northwestern District of Mackenzie, (ed.) D.K. Norris; Geological Survey of Canada, Bulletin 422, p. 119–162.

Och, L.M., Shields-Zhou, G.A., Poulton, S.W., Manning, C., Thirlwall, M.F., Li, D., Chen, X., Ling, H., Osborn, T., and Cremonese, L., 2013. Redox changes in Early Cambrian black shales at Xiaotan section, Yunnan Province, South China; Precambrian Research, v. 225, p. 166–189.

Pašava, J., Kříbek, B., Vymazalová, A., Sýkorová, I., Žák, K., and Orberger, B., 2008. Multiple sources of metals of mineralization in Lower Cambrian black shales of South China: Evidence from geochemical and petrographic study; Resource Geology, v. 58; p. 25–42.

Paton, C., Hellstrom, J., Paul, B., Woodhead, J., and Hergt, J., 2011. Iolite: Freeware for the visualisation and processing of mass spectrometric data; Journal of Analytical Atomic Spectrometry, v. 26, p. 2508.

Piper, D.Z. and Calvert, S.E., 2009. A marine biogeochemical perspective on black shale deposition; Earth-Science Reviews, v. 95, p. 63–96.

Steiner, M., Wallis, E., Erdtmann, B.D., Zhao, Y., and Yang, R., 2001. Submarine-hydrothermal exhalative ore layers in black shales from South China and associated fossils - Insights into a Lower Cambrian facies and bio-evolution; Palaeogeography, Palaeoclimatology, Palaeoecology, v. 169, p. 165–191.

Van Berkel, G.J. and Filby, R.H., 1987. Generation of nickel and vanadly prophyrins from kerogen during siulated catagenesis; *in* Metal Complexes in Fossil Fuels: Geochemistry, Characterization, and Processing, (ed.) R.H. Filby and J.F. Branthaver; American Chemical Society Symposium Series Volume 344, p. 110–134.

Vine, J.D. and Tourtelot, E.B., 1970. Geochemistry of black shale deposits - A summary report; Economic Geology, v. 65, p. 253–272.

Wignall, P.B and Newton, R., 1998. Pyrite framboid diameter as a measure of oxygen deficiency in ancient mudrocks; American Journal of Science, v. 298, p. 537–552.

Wilkin, R.T. and Barnes, H.L., 1997. Formation processes of framboidal pyrite; Geochimica et Cosmochimica Acta, v. 61, p. 323–339.

Wilkin, R.T., Barnes, H.L., and Brantley, S.L., 1996. The size distribution of framboidal pyrite in modern sediments: An indicator of redox conditions; Geochimica et Cosmochimica Acta, v. 60, p. 3897–3912.

Woodhead, J., Hellstrom, J., Hergt, J., Greig, A., and Maas, R., 2007. Isotopic and elemental imaging of geological materials by laser ablation Inductively Coupled Plasma mass spectrometry; Journal of Geostandards and Geoanalytical Research, v. 31, p. 331.

Xu, L., Lehmann, B., and Mao, J., 2013. Seater contribution to polymetallic Ni-Mo-PGE-Au mineralization in Early Cambrian Black Shales of South China: Evidence from Mo isotope, PGE, trace element, and REE geochemistry; Ore Geology Reviews, v. 52, p. 66–84.

Fluid inclusion LA-ICP-MS and whole rock geochemical investigation of possible magmatic contributions to the giant Windy Craggy Besshi-type VMS deposit

M.A. Schmidt[1], M.I. Leybourne[1], J.M. Peter[2], D. Petts[2] and D. Layton-Matthews[1]

[1]*Department of Geological Sciences and Geological Engineering, Queen's University, 36 Union Street, Kingston, Ontario K7L 3N6*

[2]*Geological Survey of Canada, 601 Booth Street, Ottawa, Ontario K1A 0E8*

Abstract

The world-class Windy Craggy Cu-Co-Au deposit, northwestern British Columbia, is investigated to assess potential magmatic contributions to mineralizing fluids in volcanogenic massive sulphide (VMS) deposits. Windy Craggy is of particular interest for two reasons: 1) its atypically large size and high-grade; and 2) the observation of fluid inclusions with anomalously high salinities. The deposit has recorded fluids with salinities up to 17 weight % equivalent NaCl (most 6–16 weight % equivalent). The Ca/Na values in fluid inclusions determined by laser ablation-inductively coupled plasma-mass spectrometry (LA-ICP-MS) are greater than seawater and similar to values from other mafic-dominated VMS systems. The fluid inclusions have variable metal and metalloid concentrations, with positive correlations between Cu, Mn, Zn, Sb, Sn and Bi. Also analyzed are Windy Craggy host lithologies, including footwall argillites, relatively fresh to highly altered footwall mafic volcanic rocks and stringer and massive sulphides. These inclusions show similar trends and overlap the host rocks in Fe versus Mn and Cu versus Zn, but show clear excesses over host rocks in antimony, tin, bismuth and similar elements that are commonly ascribed as indicative of magmatic input. We suggest that these excess values strongly point to direct magmatic contributions to the Windy Craggy ore-forming fluids, as opposed to simply reflecting leaching of metals from the footwall sedimentary and igneous rocks.

Introduction

In the currently accepted genetic model for volcanogenic massive sulphide (VMS) deposits, there is a geochemical disconnect between the magmatic heat source present at depth and the circulating hydrothermal fluid system responsible for the mineralization (Shanks and Thurston, 2012). The mineralizing fluids are generally accepted to be modified seawater with a salinity typically close to that of seawater (3.2 weight % NaCl; Bischoff and Rosenbauer, 1985) and falling within the range of 2 to 6 weight % NaCl equivalent (Bodnar et al., 2014). VMS deposits form at or near the seafloor from rising metal-bearing hydrothermal fluids that are quenched by mixing with cold seawater to precipitate sulphide minerals (Hannington, 2013; Tornos et al., 2015). However, there is continued debate as to the source of metals in seafloor hydrothermal systems and the role of magmatic volatiles in the formation of ore deposits (Beaudoin et al., 2007; de Ronde, 1995; Huston et al., 2001; Leybourne et al., 2012; Timm et al., 2012; Wysoczanski et al., 2012; Yang and Scott, 1996; Yang and Scott, 2006). In this standard model for the formation of VMS deposits, metals are leached from proximal volcanic rocks, with the magma chamber primarily providing heat to drive hydrothermal circulation of seawater (Galley et al., 2007).

There is evidence of magmatic contribution in some modern seafloor hydrothermal systems at arcs, back-arcs and mid-ocean ridges. An example of direct magmatic contribution to a seafloor hydrothermal system in a modern arc/back-arc environment is Brothers Volcano located on the Kermadec arc northeast of New Zealand. Indications of magmatic contribution to a back-arc hydrothermal system (i.e. magmatic hydrothermal) includes the following: 1) hydrothermal discharge significantly more acidic than typically found at mid-ocean ridges (de Ronde et al., 2001; Leybourne et al., 2012; Massoth et al., 2003); 2) presence of ^{3}He anomalies in modern vent fluids and ancient fluid inclusions (Leybourne et al., 2012; Lupton, 1983); 3) elemental S precipitate (Giggenbach, 1996; Lyon, 1974); 4) high total dissolved copper and iron in the vent fluids (de Ronde et al., 2001) and 5) high Fe/Mn values in the vent fluids (Massoth et al., 2003). Although there are clear indications of magmatic volatile contributions to seafloor massive sulphide systems, the extent to which metals and metalloids of economic interest are also contributed from exsolving magmas driving hydrothermal circulation is still widely debated (Agangi et al., 2018; Chen et al., 2015; de Ronde et al., 2005; Huston et al., 2011; Yang and Scott, 2006).

The Windy Craggy Cu-Co-Au deposit in northwestern Brit-

Corresponding author: Madison Schmidt (m.schmidt@queensu.ca)

Schmidt, M.A., Leybourne, M.I., Peter, J.M., Petts, D., and Layton-Matthews, D., 2019. Fluid inclusion LA-ICP-MS and whole rock geochemical investigation of possible magmatic contributions to the giant Windy Craggy Besshi-type VMS deposit; *in* Targeted Geoscience Initiative: 2018 report of activities, (ed.) N. Rogers; Geological Survey of Canada, Open File 8549, p. 189–204. https://doi.org/10.4095/313651

ish Columbia is the largest Besshi-type VMS deposit in the world (Peter and Scott, 1999). Windy Craggy is the focus of the present study due to its atypically large size, relatively high salinity fluids compared to other VMS deposits and its back-arc setting (Peter et al., 2014). A previous study suggested that the impressive metal endowment and anomalous salinity of the fluids could be explained by a direct magmatic contribution to the mineralizing fluids (Peter and Scott, 1993). Through better understanding of world-class deposits such as Windy Craggy we can further refine and improve exploration models. A more refined and detailed model could allow for the targeting of atypically large deposits as well as those containing atypically high grades and specific metals or trace elements of interest.

To investigate potential magmatic contributions to large VMS systems, we have conducted a laser ablation inductively coupled plasma-mass spectrometry (LA-ICP-MS) study of fluid inclusions from the Windy Craggy deposit (Schmidt et al., 2018). We have also obtained ultra-trace ICP-MS analyses of the volcanic and sedimentary host rocks, together with mineralization at Windy Craggy in order to characterize their bulk geochemical composition and extend the element suite previously analyzed by Peter and Scott (1993). The application of LA-ICP-MS to the analysis of major and trace elements in ore deposits has proven to be an effective tool for microanalysis of major and trace elements in minerals (Bodnar et al., 2014; Gagnon et al., 2003). Further application of this method to fluid inclusions has allowed for in situ, multi-element analysis of single fluid inclusions (Audétat et al., 1998; Batchelor and Mcdonald, 1992; Hennings et al., 2017).

Analysis of individual fluid inclusions by LA-ICP-MS provides a more detailed understanding of the fluid history without the errors and lack of resolution that accompanied the previously used methods such as grinding/crushing the sample under vacuum (Roedder, 1972); decrepitation by stepwise heating (Piperov and Penchev, 1973); and decrepitation under vacuum (Welhan, 1988). Previous applications of LA-ICP-MS to fluid inclusion studies have generally focused on high salinity fluids (e.g. magmatic-hydrothermal deposits). High salinity fluids contain a higher concentration of total dissolved solids and, given the already small sample size presented by fluid inclusions, this results in a more reliable analysis (Audétat et al., 1998). The relative lower salinity of the fluid inclusions in our study, however, necessitated further method development to optimize the process and provide the best possible results.

Herein, we detail refined LA-ICP-MS methods for the analysis of single, low salinity fluid inclusions typical of VMS deposits. We show that LA-ICP-MS analyses of fluid inclusions in VMS deposits can provide metal and metalloid abundances that may reflect direct magmatic contributions to the Windy Craggy hydrothermal system. Finally, we compare the trace element geochemical compositions of host rocks (i.e. footwall and hanging wall sedimentary and volcanic rocks, and sulphide -rich samples) against fluid inclusions to demonstrate the potential magmatic origin of metals and metalloids.

Geology

The Windy Craggy deposit (Peter and Scott, 1999) is located in extreme northwestern British Columbia, within rocks of the Alexander Terrane, one of the largest accreted terranes in the North American Cordillera (Coney et al., 1980) (Fig. 1). The terrane is comprised of a thick succession of weakly metamorphosed, complexly deformed, Precambrian to Permian basinal and platformal carbonate and clastic rocks with a minor volcanic component. This succession is unconformably overlain by Upper Triassic calcareous, proximal to distal, turbidites and a bimodal volcanic suite (Campbell and Dodds, 1979, 1983; MacIntyre, 1984).

1) The Windy Craggy deposit is hosted in the Late Triassic section commonly referred to as the Tats Volcanic Complex. The complex has been subdivided into five major units described in order, moving down through stratigraphy.
2) The upper most unit is an approximately 1500 m-thick section dominated by Upper Triassic pillow basalts referred to as the Upper Tats.
3) An approximately 2000 m thick section of interbedded graphitic and calcareous argillites, pillowed and massive mafic flows, tuff, agglomerate and limestone referred to as the Middle Tats. Conodont assemblages in the limestone are Upper Triassic (ca. 225 Ma) (Orchard, 1986).
4) An approximately 1000 m thick section of Upper Triassic mafic flows and sills referred to as the Lower Tats.
5) A lower sedimentary unit, part of the Tats group, divided into a section of interlayered calcareous and graphitic shale, argillite and limestone of undefined age and overlying a gray limestone unit, possibly Siluro-Devonian.

The Windy Craggy deposit is hosted in the lower portion of the Middle Tats group. The deposit consists of several lenses of Cu-Co-Au mineralization, each with a discrete stockwork zone (Peter and Scott, 1999). Collectively, these lenses contain over 300 million tonnes grading 2.12 weight % Cu, 0.083 weight % Co, 0.16 g/t Au, and 3.30 g/t Ag (Downing et al., 1990). Felsic volcanic rocks are not present in the immediate area of the Windy Craggy deposit. However, other parts of the Alexander Terrane do contain felsic volcanic rocks or their metamorphosed equivalents, and their presence indicates volcanism was bimodal at the regional scale (Taylor et al., 2008).

Methods

Fluid inclusions

Doubly polished thin rock chips were prepared from the feeder/stockwork zone of the deposit. This study focused only on quartz-hosted fluid inclusions. Photomicrographs were taken of each sample to allow for careful mapping of each fluid inclusion to be analyzed. Fluid inclusions were classified using the criteria of Roedder (1984). Microthermometric measurements were made on 46 inclusions and include first melting temperature (T_f), final melting temperature (T_m), and tempera-

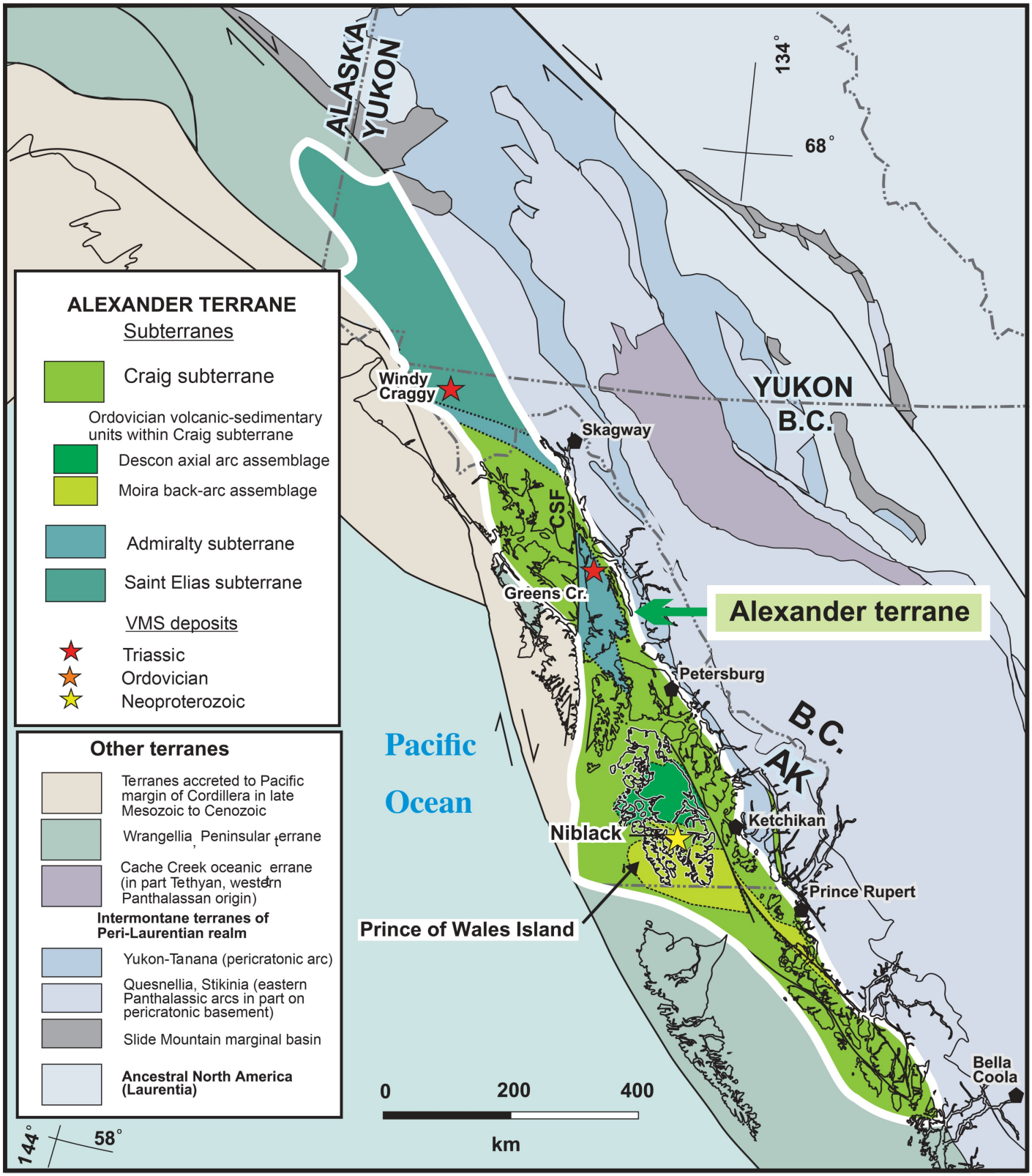

Figure 1. Location map of the Windy Craggy deposit in northwestern British Columbia (*from* Peter et. al., 2014).

ture of homogenization (T_h). The percentage of vapour and liquid, and the size of each inclusion were also recorded. The measurements were made using a Linkham THMSG600 heating freezing stage coupled to an automated controller unit and Nikon Optiphot microscope. The system was calibrated using synthetic fluid inclusion standards for CO_2 (-56.6°C), the freezing point of H_2O (0°C) and the critical point of H_2O (374.1°C). The salinity of each fluid inclusion was calculated using the H_2O-NaCl system based on Bodnar (1994).

Laser ablation-inductively coupled plasma-mass spectrometry

The LA-ICP-MS analyses of the fluid inclusions were performed at the Geological Survey of Canada, Ottawa, using a Teledyne Photon Machines Analyte G2 excimer laser ablation system (l = 193 nm) with a HelEx ablation cell coupled to an Agilent 7700x ICP-MS equipped with a second rotary vacuum pump that improves instrument sensitivity across the mass range by 2 or 3 times (Cabri and Jackson, 2011). Data were collected over two multi-day sessions. The instrumental parameters for session 1 (March 2017) and session 2 (July 2018) are presented in Table 1.

For session 1, an in-house aqueous solution standard (SOL2017) was used in addition to two standard reference materials (SRM), synthetic glass SRM NIST 610 (Norman et al., 1996), and pyrrhotite SRM Po689 (Mungall et al., 2005). The in-house solution was contained within wells constructed of pipette tips, which were sealed on the bottom and top with Parafilm. This was intended to limit the evaporation of the solution within the ablation chamber. Prior to analysis, the wells were opened by ablation of a hole through the Parafilm using a 40 mm spot size. The solution was then ablated directly using a 30 mm spot size.

The fluid inclusion chips were positioned on a thin circular (cross-sectional) slice of a pipette tip resting on a glass slide that was then placed in the sample chamber. The sample was observed using 100% magnification of the LA-ICP-MS optical system and the fluid inclusions were located using chip photomicrographs obtained during the preliminary stages of the study. The laser spot size was chosen to be the smallest that encompassed the entire fluid inclusion, typically between 10 and 15 mm. The laser optics was then set to 50% magnification and focused on the surface of the chip. The data collection program was set to collect 40 seconds of gas blank (no ablation), ablate the sample for 20 seconds and then continue to collect until a total count of 100 seconds. A small mixing chamber was added to the line to allow for the monitoring of all the elements of interest (^{109}Ag, ^{75}As, ^{11}B, ^{137}Ba, ^{209}Bi, ^{79}Br, ^{42}Ca, ^{111}Cd, ^{140}Ce, ^{35}Cl, ^{59}Co, ^{133}Cs, ^{65}Cu, ^{57}Fe, ^{202}Hg, ^{115}In, ^{39}K, ^{7}Li, ^{25}Mg, ^{55}Mn, ^{95}Mo, ^{23}Na, ^{208}Pb, ^{85}Rb, ^{34}S, ^{121}Sb, ^{77}Se, ^{29}Si, ^{118}Sr, ^{125}Te, ^{205}Ti, ^{182}W and ^{66}Zn).

For session 2, an in-house aqueous solution standard (SOL2018) was used in addition to synthetic glass standard reference material NIST 610 (Norman et al., 1996) and the previously prepared in-house aqueous solution (SOL2017). The in-house aqueous solutions were contained within borosilicate capillary tubes. The capillary was rinsed with the solution 3 times before the sample was loaded and positioned in the centre of the tube. The ends were sealed using hot glue to prevent leakage and the capillary was affixed to the slide using double sided tape.

The fluid inclusion chips were positioned on a slide and held in place using double-sided tape. The sample chips were cleaned prior to placement in the sample chamber using a solution of 2% nitric acid and a precision tip cotton swab. This was intended to remove any surface contamination due to polishing and atmospheric exposure. The sample was observed using the 100% magnification of the LA-ICP-MS optical system and the fluid inclusions were located using chip photomicrographs obtained during the preliminary stages of the study. The laser spot

Table 1. Instrumental and analytical parameters for LA-ICP-MS analyses comparing session 1 and session 2.

	Session 1 (March 2017)	Session 2 (July 2018)
Laser system type	Teledyne Photon Machines Analyte G2 Excimer	Teledyne Photon Machines Analyte G2 Excimer
Wavelength	193 nm	193 nm
Energy density for pre cleaning	N/A	1.09 J/cm2
Repetition rate for pre cleaning	N/A	1
Energy density for quartz ablation	4.54 J/cm^2	4.54 J/cm^2
Repetition rate for quartz ablation	8 hz	8 hz
Crater size for Standard analysis	NIST610 40 µm, Po689 40 µm, SOL2017 30 µm	Consistent at 20 µm
Crater size for FI analysis	Varied from 10 µm to 20 µm	Consistent at 20 µm
ICP-MS	Agilent 7700x	Agilent 7700x
Carrier gas flow	1.00 L/min He	1.00 L/min He
Rf power	1550 W	1550 W
Dwell time per isotope	5 ms seconds with the exception of Na, K, Si, at 2.5 ms & Au at 10 ms	5 ms seconds with the exception of Na, K, Si, at 2.5 ms & Au at 10 ms

size was kept constant at 20 mm for samples and standards. The laser optics was set to 50% magnification and focused on the surface of the chip. A pre-ablation cleaning sequence consisted of single low energy pulse (*see* Table 1 for laser settings). The data collection sequence was the same as session 1: 40 seconds of gas blank, ablation of the sample for 20 seconds, and data collection for 100 seconds.

The LA-ICP-MS tests were performed using a signal extender (Squid) added to the line. The element list outlined above for session 1 was reduced from the original list of 33 elements to ^{109}Ag, ^{75}As, ^{137}Ba, ^{209}Bi, ^{79}Br, ^{42}Ca, ^{111}Cd, ^{140}Ce, ^{35}Cl, ^{59}Co, ^{65}Cu, ^{57}Fe, ^{115}In, ^{39}K, ^{25}Mg, ^{55}Mn, ^{95}Mo, ^{88}Sr, ^{23}Na, ^{206}Pb, ^{207}Pb, ^{208}Pb, ^{85}Rb, ^{121}Sb, ^{77}Se, ^{29}Si, ^{118}Sn, ^{205}Ti, ^{182}W, ^{181}Ta, ^{197}Au and ^{66}Zn. The reasons for this are detailed below.

Data reduction

The data were processed using SILLS, a Matlab computer program designed for the reduction of LA-ICP-MS data obtained from both mineral grains and fluid inclusions (Guillong et al., 2008). SILLS is designed to allow for the isolation of the fluid inclusion signal from that of the host mineral. This is achieved through the use of an internal defined standard and the manual selection of various peaks and time spans by the user. Sodium was defined as the internal standard for these reductions in this study. The internal standard was determined for each inclusion prior to ablation using fluid inclusion microthermometric ice melting temperatures. The size of the inclusion and matrix signal varied by inclusion as does salinity (internal standard). For this reason, SILLS allowed each variable to be defined independently for each fluid inclusion.

Back calculations were performed to verify the validity of the SILLS corrections, by converting the concentrations of the cations (Na, K, Ca, Mg) to weight % NaCl equivalent and then calculating the required Cl assuming all of the cations are present as salt. The sum of these values equates the calculated salinity. The calculated weight % equivalent salinities were compared to the salinities determined by the microthermometric measurements. The veracity of data processing in SILLS for session 2 was also verified using the SOL2017 solution. This was accomplished by ablating SOL2017 as a standard and treating it as an unknown in SILLS. The weight % NaCl equivalent (0.38) for SOL2017 was calculated from the known concentrations of Ca, K, Na, Mg and Fe to be used as the internal standard required for SILLS. The known concentrations were then compared to the SILLS output.

Whole rock geochemistry

Pulverized samples were analyzed at ALS Geochemistry, Vancouver, for whole rock geochemical composition. The following analyses were performed: 1) major element determinations by inductively coupled plasma atomic emission spectroscopy (ICP-AES) following lithium metaborate fusion (method ME-ICP06); 2) trace elements (Ba, Cr, Cs, Ga, Hf, Nb, Rb, Sr, Ta, Th, U, V, Y, Zr and rare earth elements (REE)) determinations by ICP mass spectrometry (ICP-MS) following lithium metaborate fusion (method ME-MS81) to include elements within phases resistant to acid digestion (zircon, chromite, monazite); 3) trace and some major elements (Ag, Al, As, Ba, Be, Bi, Ca, Cd, Ce, Co, Cr, Cs, Cu, Fe, Ga, Ge, Hf, In, K, La, Li, Mg, Mn, Mo, Na, Nb, Ni, P, Pb, Rb, Re, S, Sb, Sc, Se, Sn, Sr, Ta, Te, Ti, Tl, U, V, W, Y, Zn, Zr) determinations by an ultra-trace four-acid digestion (HF, $HClO_4$, HCl, HNO_3; method ME-MS61L) followed by a mixture of ICP-AES and ICP-MS analysis, to allow lower detection limits on elements not incorporated in resistant phases; 4) lead oxide fire assay was used to preconcentrate and collect Au, prior to analysis by ICP-MS (method Au-MS23L). The Pb isotopes were also determined on the 4-acid digestions with analysis by quadrupole ICP-MS. A proprietary ALS method is used to eliminate interferences of ^{204}Hg on ^{204}Pb.

Results

Fluid Inclusions

Both primary and secondary inclusions are present in the samples, with the latter predominating over the former. Secondary inclusions are defined predominantly by their occurrence along fractures and planes crossing growth features in the quartz. Secondary inclusions range in size from 1 to 16 mm, are oval and circular in cross section. The secondary inclusions have varying liquid/vapour (L/V) values ranging from 5 to 100% (monophase liquid). The primary inclusions are defined by the negative crystal structure or occurrences along growth planes of the quartz. They range in size from 5 to 24 mm and are circular, oval or hexagonal in cross section. The primary inclusions display consistent L/V values indicating that the fluids did not boil at the time of entrapment, consistent with the observations of Peter and Scott (1993). There is also a large abundance of monophase inclusions present in the samples. The monophase inclusions are not useful for salinity measurements; however, rare two-phase (liquid-vapour) inclusions occur within particular clusters of monophase inclusions. No daughter minerals were observed within any of the inclusions.

Forty-six additional microthermometric measurements have been made beyond those of Peter and Scott (1993). The salinities range from 3.2 to 13.1 weight % equivalent NaCl (Fig. 2). The homogenization temperatures range from 101.4 to 414.4°C (Fig. 3). The first melting temperatures (eutectic melting) range from -39.6 to -4.8°C (Fig. 4). The microthermometric observations of the L-V inclusions agree closely with the ice melting in the monophase inclusions. Therefore, salinity data for these monophase liquid inclusions are deemed to be representative of this population of inclusions as a whole.

Development of LA-ICP-MS technique

The methods developed during the present study have led to an effective methodology and work flow for performing LA-ICP-MS analysis of low salinity fluid inclusions (3.2–13.1 weight % NaCl equivalent). The method allows for the reliable analysis of more than 30 isotopes. Several issues that arose in

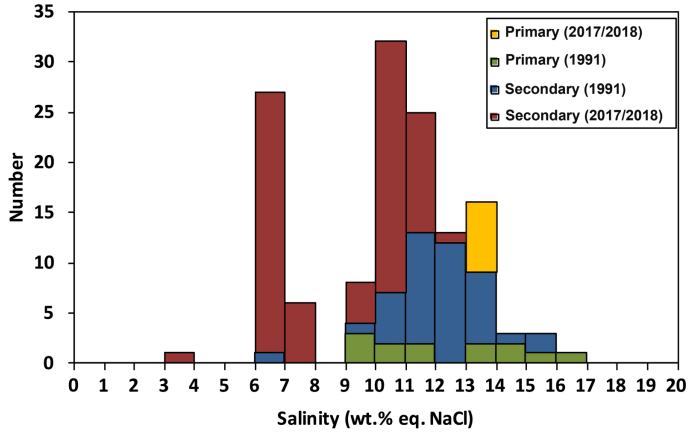

Figure 2. Histogram of microthermometric data showing the distributions of measured salinities (weight % NaCl equivalent). Data *from* Peter and Scott (1993) and this study.

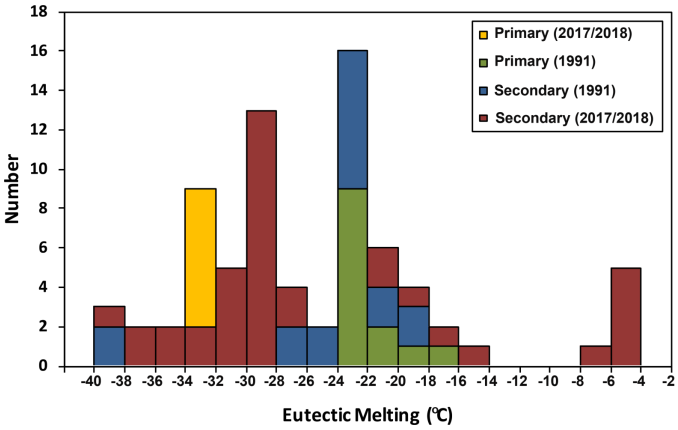

Figure 4. Histogram of microthermometric data showing the distributions of measured first melts (eutectic melting). Data *from* Peter and Scott (1993) and this study.

session 1 (March 2017) were remedied in session 2 set up (July 2018). Standard Po689 was used in session 1 to obtain S/Fe signal intensity values for calibration of S. This standard was not used in session 2 to eliminate a source of contamination. In both sessions, the NIST610 glass standard was used to calibrate the in-house solution, the primary standard for the data correction of the fluid inclusion LA-ICP-MS data. In session 1, the in-house solution contained within wells constructed from pipette tips and sealed with Parafilm did not provide effective containment, and once the well was opened it continued to leak Cl, Br and other contaminants into the chamber throughout the following analyses. This was solved in session 2 through modification of the in-house solution containment vessels. The capillary action of the capillary tubes contained the solution even after the wall was breached by the laser.

In session 1, the positioning of the chips on a slide without the aid of an adhesive resulted in the loss of samples. Although samples remained stationary inside the vacuum chamber, loading and unloading was difficult due to the small size of the samples and their propensity to shift on the slide, with the potential for them to slide/bounce off the slide. The use of double-sided tape in session 2 prevented any samples from being lost. However, some chips broke during their removal after analysis.

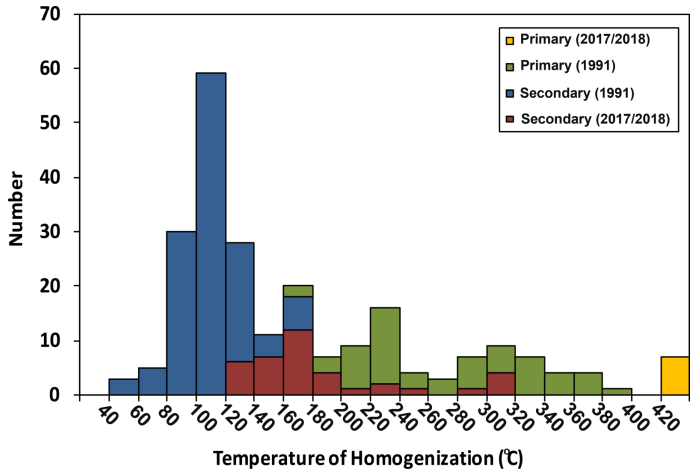

Figure 3. Histogram of microthermometric data showing the distributions of measured temperatures of homogenization. Data *from* Peter and Scott (1993) and this study.

The laser spot size in session 1 was variable and dependent on the size of the fluid inclusion. This was changed in session 2 to a consistent laser spot size (20 mm) on the unknowns as well as the standards. This removed potential for variability and improved the data confidence for comparison between standards and unknowns. The initial LA-ICP-MS test analyses were performed without the use of a signal smoothing device and using a dwell time of 4 ms per element. This setup was found to produce a signal that was too transient to obtain data for all of the elements of interest. To remedy this problem a small mixing chamber was added to the line. The mixing chamber was constructed from a plastic test tube and nylon tubing. This allowed for dwell times to be lengthened to 5 ms with the exception of Na, K, Si (2.5 ms) and Au (10 ms), which improved the duty cycle and provided greater accuracy and precision in the measurements. In session 2, the mixing chamber was replaced with a signal extender (Squid), lengthening the signal.

In session 2, the element list was shortened to ^{109}Ag, ^{75}As, ^{137}Ba, ^{209}Bi, ^{79}Br, ^{42}Ca, ^{111}Cd, ^{140}Ce, ^{35}Cl, ^{59}Co, ^{65}Cu, ^{57}Fe, ^{115}In, ^{39}K, ^{25}Mg, ^{55}Mn, ^{95}Mo, ^{88}Sr, ^{23}Na, ^{206}Pb, ^{207}Pb, ^{208}Pb, ^{85}Rb, ^{121}Sb, ^{77}Se, ^{29}Si, ^{118}Sn, ^{205}Ti, ^{182}W, ^{181}Ta, ^{197}Au and ^{66}Zn from the original list of 33 elements. Elements that were not detected during the first round, or those that were deemed no longer of interest to the study, were removed. Anomalously high Pb concentrations were noted in the data from session 1. To remove any possible surface contamination, two cleaning steps were added to the method for session 2. The samples were manually cleaned using 2% HNO_3 and a pre-ablation cleaning sequence was added to the laser program. The pre-ablation consisted of single low energy pulse that effectively removed the Pb anomalies without destroying the underlying inclusions.

Fluid inclusion LA-ICP-MS results

Laser ablation-ICP-MS was performed on over 130 inclusions, 46 for which there are salinity data collected directly from the same inclusion that was analyzed (i.e. not inferred). This study successfully analyzed 34 elements from relatively low salinity fluid inclusions (3.2–13.1 weight % NaCl) obtained from a VMS deposit with a complex history of multiple fluid events. Out of the 34 elements monitored, Na, Mg, K, Ca, Mn, Fe, Co, Cu, Zn, Sr, Sn, Ba, Ce, Pb and Bi were detected consistently throughout the analyses. Chlorine, Sb, Cd, Mo, Rb, Br, and As were also detected in a significant number of inclusions. Boron, Ag, In, Ta, Au and Ti were not detected in any of the inclusions. Comparison of the Ca/Na and Mg/Na values of the inclusions reveals a continuous trend in the data population (Fig. 5). The fluids from this study contain higher Ca/Na values than seawater. As Ca concentrations increase, the Pb, Zn, Fe, Mn, As, Se, Br, Sn, Sb and Ba values also show a general increasing trend, although most are not statistically relevant. Calcium versus Zn and Ca versus Sn do show statistically significant correlations (all values based on Spearman Rank correlations) at r = 0.341 (p = 0.012, n = 47) and r = 0.357 (p = 0.015, n = 46), respectively. There is large variation observed in the metal concentrations obtained from different fluid inclusions. For example, Cu ranges from below a detection limit of 0.154 ppm to 39500 ppm, Zn ranges from 0.181 ppm to 3490 ppm and Fe ranges from below a detection limit of 7.69 ppm to 18 500 ppm. Ranges and averages of all elements are presented in Table 2.

Whole rock geochemistry

Whole rock trace element analyses were performed on 19 samples from throughout the deposit. Representative samples of sulphides, argillite, hanging wall, footwall, altered footwall flows and stockwork stringer zones were analyzed to provide a general understanding of the distribution and sources of all elements (including those of potential magmatic origin) within the deposit (Table 3). Detailed interpretations of the geochemistry of Windy Craggy lithologies have been presented elsewhere (Peter, 1992; Peter et al., 2014). Here, we briefly discuss our new geochemical data in the context of understanding potential magmatic contributions. As such, we have subdivided the data into four groups: 1) metasedimentary rocks (argillites); 2) mafic volcanic and intrusive mafic rocks; 3) hydrothermally altered mafic rocks; and 4) sulphide-rich and stringer zone samples.

The chemical composition for each of the rock groups is listed in Table 3. The least altered mafic volcanic samples were differentiated from the altered mafic volcanic rock samples using a Chlorite-Carbonate-Pyrite Index (CCPI) versus Alteration Index (AI) plot of Large et al. (2001) (Fig. 6). The average Al_2O_3 values of the least altered mafic volcanic rock samples are 2x that of the altered mafic volcanic rocks (16.76 versus

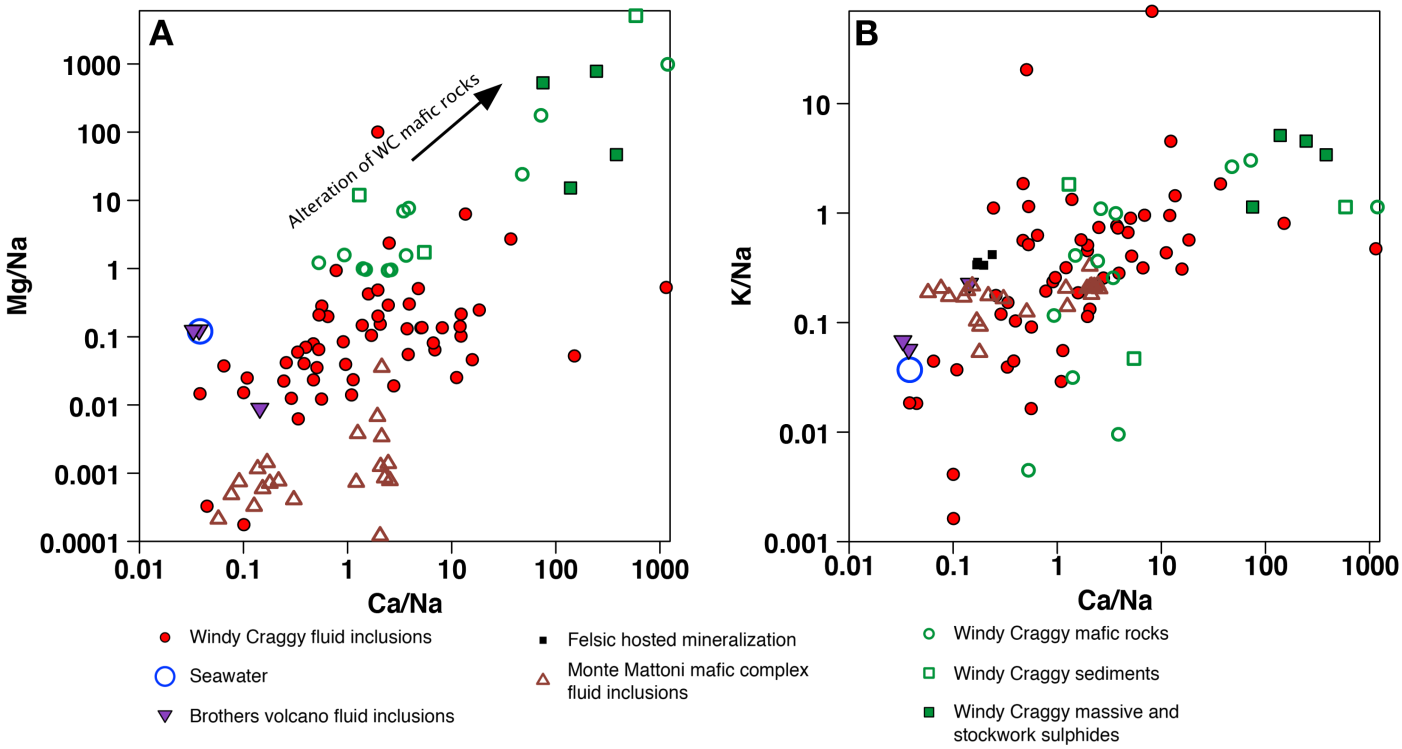

Figure 5. a) Mg/Na vs. Ca/Na and b) K/Na vs. Ca/Na plot of Windy Craggy fluid inclusions. Also plotted are fluid inclusions from the Monte Mattoni mafic complex (Hennings et al., 2017), as well as fluid inclusion data from felsic systems including Brothers Volcano on the modern Kermadec arc (de Ronde et al., 2011), Bajo de la Alumbrera (Ulrich et al., 2001), Butte (Rusk et al., 2004), El Teniente (Williams-Jones and Heinrich, 2005), modern seawater and Windy Craggy host lithologies.

Table 2. Summary table describing the fluids that occur within the deposit compared to ambient sea water composition.

	Fluid inclusions		Seawater
	Average (n = 123)	Range	
Temperature of Homogenization (˚C)	153.4	101.4–414.1	
Salinity (wt.% NaCl Equivalent)	9.3	3.2–13.1	
Na	16108	BD–44264	10800
Ca	23647	BD–36012	411
Mg	1986	BD–19733	1290
K	6371	BD–55183	392
Cu	912.1	BD–39508	0.0009
Sn	125.9	BD–882.3	0.00081
Zn	370.7	BD–6534.8	0.000003
Mo	17.24	BD–237.44	0.01
Se	466.4	BD–2667.2	0.00009
Rb	54.88	BD–3674.2	0.12
Cs	9.51	BD–48.381	0.0003
W	11.85	BD–56.486	BD
Br	9074.3	BD–154500	67.3
Sb	85.16	BD–3139.1	0.00033
Ce	66.69	BD–7251.6	0.0000012
Li	123.62	BD–456.56	0.17
Hg	542.1	BD–999.02	0.00015
Te	28.59	BD–31.39	N/A
Mn	138.84	BD–2321.1	0.0004
Co	21.09	BD–76513	0.00039
As	221	BD–3643.1	0.0026
Cd	54.46	BD–410.83	0.00011
Ba	87.36	BD–1266.1	0.021
Bi	98.38	BD–191.68	0.00002
Fe	3723.74	BD–44728	0.0034

8.19 weight %) (Table 3). The altered mafic rocks range from moderately to strongly silicified (28–71.8 weight % SiO_2). The Pb isotope compositions for the metasedimentary, least altered basalts, altered basalts and sulphides are listed in Table 3 and shown in Figure 7. "Massive sulphides" include massive sulphide and stringer samples. The new data follows the same trend as the older data (Peter and Scott, 1999), trending from non-radiogenic sulphide-rich samples (higher $^{207}P/^{206}Pb$ and $^{208}Pb/^{206}Pb$ values) to more radiogenic host rocks (lower $^{207}P/^{206}Pb$ and $^{208}Pb/^{206}Pb$ values) (Fig. 7).

Discussion

Major ion chemistry of Windy Craggy fluid inclusions

Few studies have investigated the LA-ICP-MS major and trace element composition of fluid inclusions in relatively low salinity, mafic volcanic (or plutonic) rock-associated hydrothermal or magmatic-hydrothermal systems. Hennings et al. (2017) collected data by LA-ICP-MS on fluid inclusions from the Monte Mattoni mafic complex in northern Italy. We have compared the Windy Craggy fluid inclusions to those from Monte Mattoni as it is one of the few studies of a mafic rock-dominated system, with broadly similar inclusion salinities, and some trace metal and metalloid results. Their study recog-

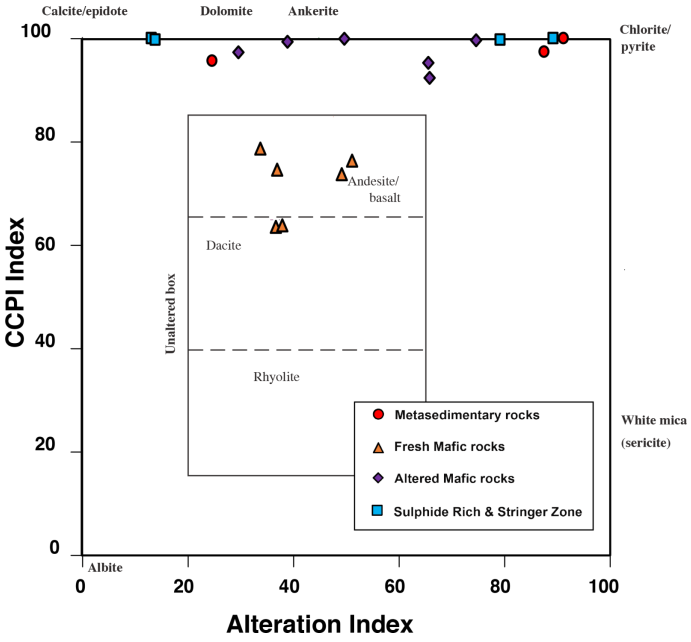

Figure 6. Chlorite-carbonate-pyrite index (CCPI) versus alteration index (AI) plot (*after* Large et al., 2001) showing the extent of alteration for the basalt, metasedimentary and mineralized samples. CCPI = 100(MgO + Fe))/(MgO + FeO + Na_2O + K_2O). AI = 100(K_2O + MgO)/(K_2O + MgO + Na_2O + CaO).

nized five distinct fluids, which represent a clear chronological picture of the hydrothermal fluid evolution. Types A, B and C inclusions are CO_2-rich and range from liquid-liquid-vapour to two-phase inclusions with daughter crystals. Types B and C have high homogenization temperatures of 334 ± 10°C and 310 ± 3°C, respectively. Salinities of these inclusions vary from 7.9 ± 0.3, 5.5 ± 0.3, and 3.6 ± 0.4 weight % NaCl equivalent for

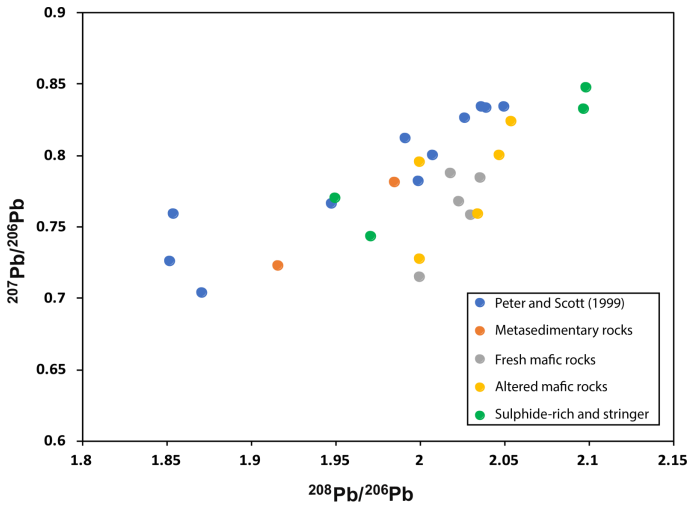

Figure 7. $^{207}Pb/^{206}Pb$ vs. $^{208}Pb/^{206}Pb$ for Windy Craggy sulphides, basalts and metasedimentary rock groups compared to previous lead isotope data for Windy Craggy *from* Peter (1992).

Table 3. Major, trace and rare earth element composition of representative samples of the host rocks and mineralization from the Windy Craggy deposit.

Sample No.	S131319	S131302	S131317	S131315	S131303	S131304	S131307	S131308	S131310	S131301	S131305	S131316	S131306	S131309	S131311	S131312	S131313	S131314	S131318
Clasification	Metasedimentary rock	Metasedimentary rock	Metasedimentary rock	Fresh mafic rock	Fresh mafic rock	Fresh mafic rock	Fresh mafic rock	Fresh mafic rock	Fresh mafic rock	Altered mafic rock	Altered mafic rock	Altered mafic rock	Altered mafic rock	Altered mafic rock	Altered mafic rock	Sulphide Rich and stringer	Sulphide Rich and stringer	Sulphide Rich and stringer	Sulphide Rich and stringer
(wt. %)																			
SiO_2	56.5	51.2	40.9	54	48.7	51	49.4	46.5	42.4	71.8	67.7	41.5	43.7	42.9	28	28	34.6	0.35	0.43
TiO_2	0.21	0.5	0.52	1.14	2.07	1.12	0.87	1.02	0.66	0.08	0.05	0.95	0.85	1.7	0.39	0.9	0.96	0.001	0.001
Al_2O_3	7.08	9.82	8.23	15.75	18.05	18.1	16.45	15.25	16.95	2.53	1.33	13.15	12.9	13.2	6.08	13.7	14.15	0.09	0.15
Fe_2O_3	25.8	23.1	27.6	7.56	8.07	6.23	8.56	12.35	9.72	17.6	15.25	27.6	15.6	11.3	18.45	33.2	33.3	62.9	57.9
MnO	0.08	0.07	0.31	0.04	0.12	0.11	0.09	0.22	0.28	0.18	0.05	0.1	0.19	0.16	0.34	0.11	0.19	1.07	1.16
CaO	0.37	0.6	6.75	2.74	8.5	6.92	4.37	6.22	8.91	1.46	0.7	2.21	4.7	5.45	12.15	2.51	0.77	3.91	2.83
MgO	4.07	6.19	2.55	7.5	3.71	5.34	8.85	5.27	4.53	0.88	0.32	6.43	11.15	13.1	12	9.5	6.44	0.57	0.37
Na_2O	0.28	0.001	1.21	5.07	3.18	4.54	4.6	4.33	2.39	0.03	0.28	0.03	1.19	1.55	0.01	0.01	0.01	0.01	0.02
K_2O	0.45	0.001	0.05	0.02	3.07	1.64	0.47	0.12	2.09	0.07	0.09	0.08	0.01	0.35	0.01	0.04	0.01	0.03	0.09
Cr_2O_3	0.005	0.011	0.024	0.02	0.001	0.01	0.039	0.022	0.002	0.003	0.002	0.039	0.088	0.064	0.222	0.011	0.018	0.001	0.001
P_2O_5	0.23	0.42	1.09	0.53	0.98	0.87	0.36	0.6	0.33	0.16	0.09	0.59	0.28	0.42	0.23	0.51	0.58	0.03	0.02
SrO	0.001	0.001	0.02	0.01	0.18	0.13	0.04	0.02	0.04	0.001	0.01	0.01	0.01	0.02	0.05	0.01	0.01	0.04	0.02
BaO	0.02	0.001	0.001	0.001	0.11	0.06	0.03	0.01	0.12	0.001	0.001	0.001	0.001	0.001	0.001	0.001	0.001	0.001	0.001
Total	100.47	98.09	94.62	99.17	98.79	98.57	99.26	99.01	97.08	100.37	97.47	99.43	98.19	98	98.13	98.33	98.04	92	89.29
C	0.5	1.12	2.11	0.49	0.04	0.03	0.54	1.24	1.96	0.82	0.13	0.54	0.83	0.81	5.52	0.78	0.5	3.58	3.26
S	1.12	2.79	5.37	0.01	0.001	0.01	0.07	0.1	0.01	5.93	8.29	1.74	0.15	0.04	0.1	6.46	0.89	32.3	34.8
(ppm)																			
Ba	223	0.001	18.3	15.7	1095	615	317	62.4	1100	9	16.1	4.9	3.4	33.4	3.8	9.1	3.4	5.6	11.2
Ce	16.7	0.001	30.5	80.3	156.5	121.5	43.1	71.1	23.6	1.6	2.4	62.8	42	65.6	26.4	55.9	56.1	0.8	0.9
Cr	40	0.001	180	170	5	80	290	170	10	20	20	300	690	450	1650	90	140	5	5
Cs	3.22	0.001	0.17	0.23	0.46	0.3	0.15	0.14	0.59	0.05	0.05	0.07	0.2	0.69	0.18	0.14	0.1	0.05	0.03
Dy	1.77	0.001	3.16	4.02	4.98	4.14	3.27	3.64	2.96	0.65	0.4	3.44	3.09	3.18	1.76	3.27	2.94	0.05	0
Er	1.12	0.001	1.82	2.53	2.41	2.01	1.84	1.92	1.66	0.32	0.26	2.06	2.06	1.5	0.84	2.04	1.69	0.015	0.06
Eu	0.22	0.001	1.18	0.98	3.02	2.11	0.92	1.56	1.21	0.07	0.31	0.81	1.06	1.62	0.85	0.74	0.7	0.11	0.18
Ga	6.8	0.001	13.3	18.4	21.3	19.3	13.3	14.6	17	12.2	4.2	24.9	13.4	13.6	7.5	36.3	31.2	6.5	9.4
Gd	2.02	0.001	4.21	4.64	7.58	5.74	3.21	4.34	3.59	0.64	0.48	3.45	3.12	4.17	1.87	3.68	3.23	0.07	0.08
Hf	1.3	0.001	1.5	3.6	6	3.9	2	3	1.6	0.5	0.4	2.8	2.1	2.6	1.1	2.6	2.6	0.1	0.1
Ho	0.42	0.001	0.74	0.85	0.95	0.8	0.69	0.68	0.57	0.15	0.12	0.67	0.74	0.63	0.36	0.8	0.69	0.01	0.01
La	11.5	0.001	19	44.2	78.3	66.6	22.6	35.9	10.4	1	1.5	33.4	20.5	29.3	13.7	28.1	27.6	0.7	0.9
Lu	0.22	0.001	0.21	0.42	0.32	0.31	0.23	0.32	0.23	0.09	0.05	0.3	0.25	0.19	0.11	0.33	0.28	0.01	0.01
Nb	2	0.001	9.3	27.8	64.2	37.6	17.7	26.2	3.2	0.8	0.4	24.6	12.8	20.4	9.4	23.8	19.9	0.1	0.1
Nd	11.5	0.001	18.8	31.7	66.6	44.6	17.4	27.7	14.8	2	2	25.3	17.3	28.7	11.1	23.5	22.8	0.3	0.3
Pr	2.69	0.001	4.14	8.22	17.4	12.4	4.57	7.48	3.2	0.44	0.5	6.73	4.6	7.87	3.04	6.3	6.32	0.09	0.12
Rb	12.3	0.001	0.7	0.3	49.7	18.8	4.3	1.9	51.1	0.3	1.7	0.2	0.4	8.9	0.3	0.2	0.2	0.1	0.4
Sm	2.23	0.001	3.43	5.55	10.8	7.62	3.56	4.62	3.92	0.48	0.43	4.29	3.34	5.75	2.32	4.05	4.19	0.015	0.09
Sn	1	0.001	1	2	2	1	1	2	1	1	1	1	1	1	1	1	1	4	2
Sr	23.5	0.001	130	106.5	1615	1180	323	198.5	324	35.1	32.1	84.9	105.5	178.5	393	94.5	33	302	140.5
Ta	0.2	0.001	0.6	1.8	3.3	2	1	1.5	0.2	0.1	0.2	1.4	0.7	1.2	0.6	1.3	1.3	0.2	0.3
Tb	0.27	0.001	0.53	0.76	0.92	0.79	0.54	0.67	0.59	0.1	0.09	0.55	0.52	0.65	0.31	0.59	0.52	0.02	
Th	0.77	0.001	1.09	4.09	4.84	5.85	2.18	2.9	1.07	0.41	0.25	2.84	1.78	1.18	1.05	3.02	2.97	0.025	0.025
Tm	0.21	0.001	0.29	0.4	0.34	0.33	0.23	0.31	0.24	0.04	0.05	0.28	0.24	0.23	0.11	0.29	0.29	0.01	0.01
U	1.66	0.001	2.38	1.41	1.54	1.82	0.74	0.83	0.61	1.27	1.4	0.94	0.7	0.34	0.3	1.94	1.38	0.58	0.33
V	54	0.001	173	201	228	156	185	206	231	33	40	188	184	206	90	202	199	7	19
W	2	0.001	1	1	1	1	1	3	2	2	3	13	1	1	2	7	2	2	2
Y	12.6	0.001	20.8	23.1	26.1	21.7	17.2	19.9	16.1	5.2	3.5	17.8	18.5	14.8	8.9	21.3	16.7	0.3	0.4
Yb	1.56	0.001	1.55	2.71	2.19	2.08	1.58	2.12	1.67	0.39	0.34	2.03	1.88	1.39	0.79	2.31	1.84	0.04	0.03
Zr	48	0.001	68	174	264	205	85	134	59	23	16	130	88	104	50	114	127	1	1
As	0.2	0.3	0.7	0.2	0.5	0.1	0.5	1.4	18.4	13.8	28.6	20.6	0.3	0.1	76.8	59.3	7.6	250	250
Bi	0.08	0.68	0.15	0.01	0.01	0.01	0.01	0.02	0.01	1.39	4.08	0.47	0.02	0.01	0.04	0.6	0.21	6.01	16.95
Hg	0.001	0.001	0.001	0.001	0.013	0.001	0.001	0.001	0.001	0.047	0.047	0.001	0.001	0.001	0.005	0.105	0.019	1.035	0.394
In	0.1	0.03	0.106	0.018	0.012	0.006	0.025	0.055	0.019	0.033	0.4	0.025	0.061	0.049	0.069	0.094	0.057	1.18	1.755
Re	0.016	0.019	0.018	0.001	0.001	0.001	0.001	0.001	0.001	0.007	0.006	0.001	0.001	0.001	0.001	0.001	0.001	0.017	0.005
Sb	0.08	0.13	0.21	0.29	0.025	0.025	0.025	0.09	0.025	2.59	0.61	0.76	0.07	0.05	0.08	1.66	0.22	27.6	24.8
Se	1.9	3.2	13.1	0.1	0.1	0.1	0.5	0.1	0.3	3.2	21.8	1.3	0.2	0.3	0.2	6.3	1.6	24.1	27
Te	0.04	0.35	0.15	0.01	0.01	0.01	0.01	0.01	0.01	0.63	2.67	0.96	0.03	0.01	0.02	1.5	0.32	7.33	11.75
Tl	0.21	0.02	0.02	0.01	0.06	0.02	0.01	0.08	1.34	0.07	0.19	0.05	0.02	0.16	0.15	0.37	0.04	4.16	1.33
Au	0.007	0.015	0.011	0.002	0.004	0.005	0.001	0.001	0.001	0.007	0.081	0.039	0.001	0.001	0.005	0.025	0.003	0.542	0.742
Ag	0.03	0.001	0.372	0.026	0.04	0.04	0.007	0.018	0.029	0.299	3.84	0.575	0.009	0.013	0.007	0.577	0.493	15.5	14
Cd	0.016	0.001	0.068	0.08	0.14	0.083	0.005	0.001	0.009	5.44	0.236	0.073	0.009	0.015	0.038	0.05	0.399	34.8	5.52
Co	17.05	0.001	58.5	14.1	19.9	19.3	29.5	20.4	27.8	188	141	51	44.1	54.8	62.9	184.5	42.7	531	363
Cu	188	0.001	607	12	45.2	28.6	25	54.4	86.9	1285	23400	575	25	40	15.95	2150	2970	16950	44600
Li	2	0.001	3.9	6.3	8.9	11	11	8.2	17.3	1	1.2	12.5	4.5	8.7	1.5	5.8	4.5	0.2	0.3
Mo	1.19	0.001	5.23	1.5	0.81	0.47	1.58	0.79	0.39	3.97	2.64	1.11	0.76	0.52	0.45	1.21	1.7	24.1	7.06
Ni	7.89	0.001	57.1	69.9	18	56.1	101	61.3	15.5	6.33	1.91	92.6	293	225	858	67.5	17	4.67	5.09
Pb	1.04	0.001	5.04	0.75	4.06	4.22	0.35	1.22	1.63	11.6	2.96	3.12	0.83	0.42	1.12	3.7	1.29	392	429
Sc	5.48	0.001	14.25	19.9	20.4	18.9	31.1	30.2	22.2	2.71	1.27	26	29.9	23.5	15.05	25.4	27.4	0.07	0.22
Zn	28.3	0.001	149.5	31.7	76.9	65.5	20.3	84.1	70.3	1370	61.8	73.3	45.1	81.6	62.2	61.9	323	13050	1665
^{204}Pb	0.02	0.001	0.07	0.01	0.05	0.06	0.01	0.02	0.02	0.15	0.04	0.04	0.01	0.01	0.01	0.05	0.02	5.32	5.9
^{206}Pb	0.36	0.001	1.37	0.28	1.08	1.11	0.1	0.33	0.43	2.94	0.78	0.85	0.22	0.11	0.29	1	0.35	101.5	113
^{207}Pb	0.26	0.001	1.07	0.2	0.85	0.87	0.05	0.25	0.33	2.42	0.62	0.68	0.16	0.07	0.22	0.77	0.26	86	94
^{208}Pb	0.69	0.001	2.72	0.56	2.18	2.26	0.19	0.67	0.87	6.04	1.56	1.74	0.44	0.22	0.59	1.95	0.69	213	237

types A, B and C, respectively (Hennings et al., 2017). Types D and E are two phase (L-V) inclusions, like those at Windy Craggy, with homogenization temperatures of 353 ± 11°C and approximately 179°C, respectively but have higher salinities than types A, B and C at 9.5 ± 1 and 27.1 ± 0.9 weight % NaCl equivalent, respectively. We have compared the major ion chemistry of the Windy Craggy inclusions with those of the Monte Mattoni inclusions, as well as fluid inclusion data from felsic systems including Brothers Volcano on the modern Kermadec arc (de Ronde et al., 2011), Bajo de la Alumbrera (Ulrich et al., 2001), Butte (Rusk et al., 2004), El Teniente (Williams-Jones and Heinrich, 2005), modern seawater and host lithologies from Windy Craggy (Fig. 5). We have included the results from more mafic systems as these are associated with copper-rich mineralization and are recognized as magmatic-hydrothermal systems; one of the goals of this study is to determine the extent, if any, of the magmatic contributions to the Windy Craggy ore-forming fluids. Fluid inclusions from Windy Craggy display generally similar Ca/Na values to inclusions from Monte Mattoni, although Windy Craggy inclusions extend to higher Ca/Na values. Both Windy Craggy and Monte Mattoni inclusions Ca/Na values are elevated in comparison to those from the felsic systems noted above and seawater (Fig. 5). Host lithologies at Windy Craggy have Ca/Na values that overlap those at the upper range of the Windy Craggy inclusions and extend to more elevated Ca/Na values in more altered mafic volcanic rocks and semi-massive and stockwork sulphide -rich samples. The elevated Ca/Na in the altered Windy Craggy rocks is in part due to addition of carbonate via hydrothermal or metamorphic fluids, but may also be associated with high temperature calcic alteration, as observed in the core of the hydrothermal upflow zone in Middle Valley on the Juan de Fuca Ridge (Leybourne and Goodfellow, 1994). The calcium-rich nature of the fluid inclusions is likely related to high temperature alteration of the mafic rocks in the footwall to the deposit; conversion of calcic plagioclase to albite will produce more calcium-rich hydrothermal fluids. Hennings et al. (2017) noted that the highest Ca/Na values for the inclusion fluids at Monte Mattoni were observed in the later, higher salinity types D and E inclusions, consistent with water-rock interaction, as also observed for calcic groundwaters in crystalline rocks elsewhere (Leybourne and Goodfellow, 2007).

Windy Craggy fluid inclusions have generally higher Mg/Na values compared to those from Monte Mattoni (Fig. 5). The Monte Mattoni inclusions are characterized by Mg concentrations less than 350 ppm (one outlier, type E = 1714 ppm), with most below 65 ppm (27 of 31 analyses). By contrast, Windy Craggy inclusions vary from approximately 6 to 20 000 ppm Mg, with a median of 920 ppm Mg. Hydrothermal fluids recovered from active vents on the seafloor are typically modelled to have end-member fluid compositions with no magnesium (e.g. Humphris and Klein, 2018). Magnesium that is recovered in hydrothermal fluids is interpreted to represent mixing with entrained seawater during collection or in the shallow subsurface; magnesium is assumed to be removed from downwelling seawater in the reaction zone overlying the magmatic system driving the hydrothermal circulation in the formation of chlorite, actinolite and amphibole (e.g. Alt et al., 1986; Goodfellow and Peter, 1994). However, recent studies of modern arc and back-arc settings have suggested that end-member vent fluids in these environments may contain significant amounts of magnesium (and SO_4) owing to the lower pH, higher magmatic gas concentrations (H_2S, CO_2, SO_2) and consequently, greater water-rock interaction in the hydrothermal upflow zones (e.g. Leybourne et al., 2012; Reeves et al., 2011). Thus, the elevated magnesium concentrations and high Mg/Na values in the Windy Craggy inclusions likely reflects hydrothermal fluids that have stripped magnesium through water-rock reactions by fluids similar to magmatic-hydrothermal fluids observed at arcs and back-arcs.

Windy Craggy fluid inclusions have K/Na values that are generally higher and have a wider range than the ones at Monte Mattoni (Fig. 5). Some inclusions at Windy Craggy have K/Na values greater than sea water. The high K/Na values of the Windy Craggy fluid inclusions are most likely the result of contributions from footwall sedimentary rocks and from water-rock reactions with the footwall mafic rocks; at Windy Craggy, the footwall flows and sills/dykes are alkalic (Peter et al., 2014), compared to the calc-alkalic host rocks at Monte Mattoni and the felsic rocks represented on Figure 5. However, Na/K_{molar} values for Windy Craggy fluid inclusions range from approximately 1 to 400 (average = 17, median = 6, excluding one outlier at 1043). These Na/K_{molar} values are more varied and generally elevated compared to Na/K_{molar} values for the more felsic porphyry copper-associated fluid inclusions from Butte (Rusk et al., 2004). The mafic compositions of the Windy Craggy lithologies, lack of primary potassium feldspar and common white mica (sericite) alteration of plagioclase (Peter, 1992; Peter et al., 2014), results in lower Na/K_{molar} values than at Butte, where fluid reactions with potassium and plagioclase feldspar, at least in part, buffer the range in Na/K_{molar} (Rusk et al., 2004).

Trace metals and metalloids in Windy Craggy fluid inclusions

Late-stage inclusions (types D, E) of magmatic-hydrothermal fluids from Monte Mattoni have salinities between 9.5 and 27.1 weight % equivalent NaCl, high Ca/Na values (Fig. 5), lower S and Cu and higher Pb, Zn, Fe and Mn concentrations than type A, B or C fluids (Hennings et al., 2017). These trends were attributed to fluid-melt partitioning of volatiles in the crystalizing magma followed by fluid-rock interaction with the host lithologies (Hennings et al., 2017). The Windy Craggy fluid inclusions are similar to the late-stage fluids from Monte Mattoni in that they also have high salinities 3.2 to 13.1, average 9.20 weight % equivalent NaCl, and high Ca/Na values (Fig. 5). Calcium shows statistically significant positive correlations with zinc, lead and tine, but not with copper, iron or manganese. Calcium is also positively correlated with salinity, with $r = 0.424$ ($p = 0.0010$, $n = 57$). Conversely,

manganese shows statistically significant correlations with copper (Log Cu versus Log Mn, r = 0.632, p = < 0.0001, n = 79), zinc (Log Zn versus Log Mn, r = 0.671, p = < 0.0001, n = 70), iron (Log Fe versus Log Mn, r = 0.434, p = < 0.0009, n = 55; Fig. 8), tin (Log Sn versus Log Mn, r = 0.646, p = < 0.0001, n = 53), antimony (Log S versus Log Mn, r = 0.457, p = < 0.0018, n = 44), and barium (Log Ba versus Log Mn, r = 0.423, p = 0.0002, n = 73). Other positive correlations of note include barium versus cerium (r = 0.520, p = < 0.0001, n = 58), copper versus strontium (Log Cu versus Log Sr, r = 0.331, p = 0.0001, n = 128) and copper versus barium (Log Cu versus Log Ba, r = 0.420, p = < 0.0001, n = 101) (Fig. 8). Compared to the Monte Mattoni fluid inclusions, those from Windy Craggy differ in having generally lower manganese and higher iron concentrations (Fig. 8). The positive correlation between cerium and barium is not shown by the host lithologies at Windy Craggy, except for the most altered of the mafic rocks (Fig. 8b), suggesting that cerium and barium were mobilized into the hydrothermal fluids through water-rock reaction. Cerium is generally considered immobile, but in these fluids it appears to have been transported by the hydrothermal fluids. This is consistent with the altered mafic rocks and massive sulphide samples from Windy Craggy having lost barium, cerium and strontium (Fig. 8).

Figure 7 plots $^{207}Pb/^{206}Pb$ versus $^{208}Pb/^{206}Pb$ for Windy Craggy sulphides, basalts and metasedimentary rock groups compared to historical lead isotope data for Windy Craggy (Peter, 1992). The Pb isotope data collected from this study

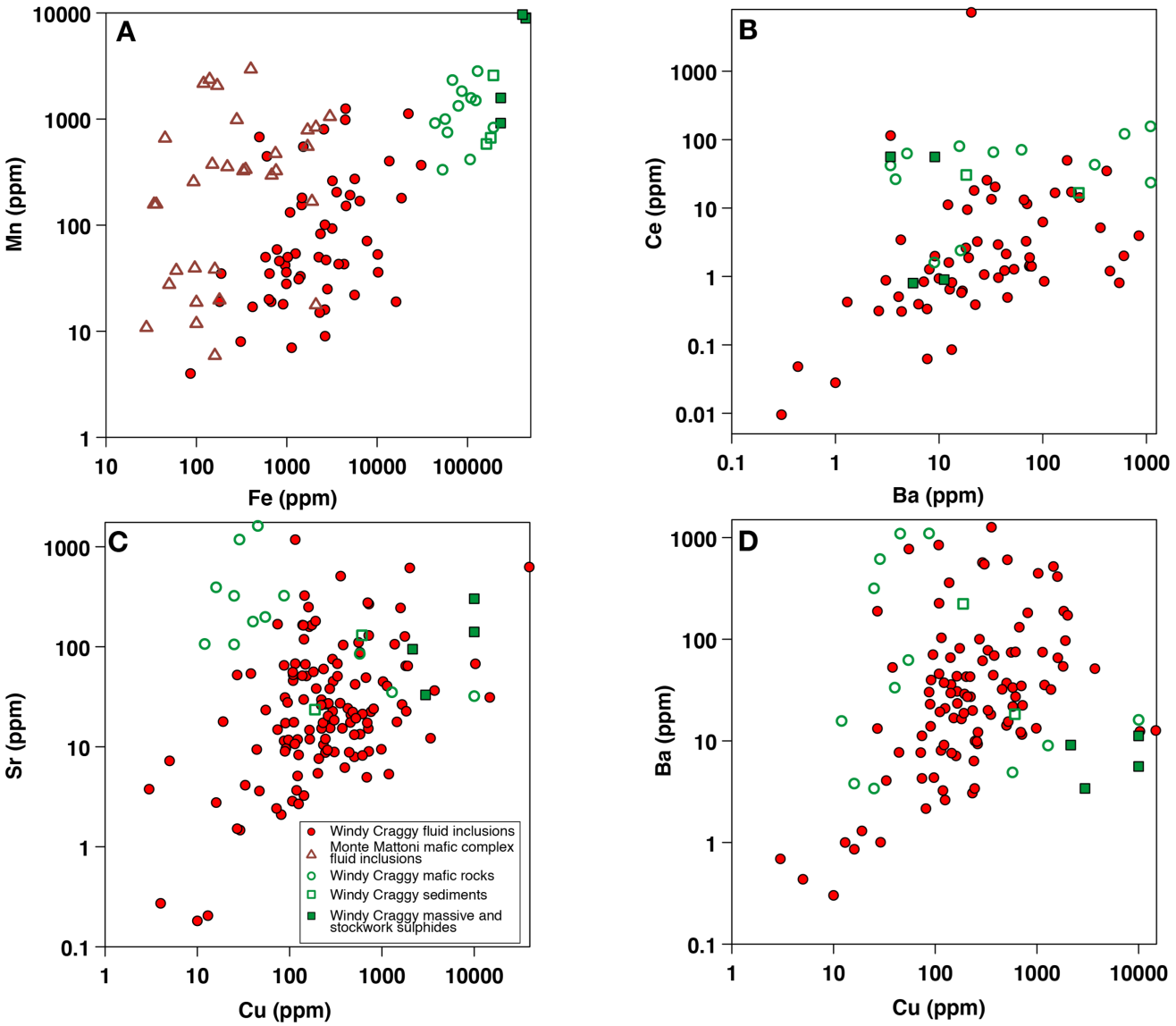

Figure 8. Plots of a) Fe vs. Mn, b) Ba vs. Ce, c) Cu vs. Sr, and d) Cu vs. Ba for Windy Craggy fluid inclusions compared to the host rocks. Also shown is Fe and Mn data for fluid inclusions from the Monte Mattoni mafic complex (Hennings et al., 2017).

follows the same trend as that seen previously (Peter, 1992). The linear trend of the sulphide isotope data was previously described as a reflection of mixing of mantle lead with crustal lead, contributed from the footwall basalts and footwall sediments, respectively (Peter, 1992; Peter and Scott, 1999).

Magmatic-hydrothermal fluids and metal contributions to VMS

Although there has been some debate as to the relative contributions of leaching versus metal-rich magmatic volatiles to seafloor ore-forming systems (Agangi et al., 2018; Chen et al., 2015; de Ronde et al., 2005; Huston et al., 2011; Yang and Scott, 2006), there is to some extent, a circularity to the argument; the footwall rocks from which metals are interpreted to be leached by modified seawater were themselves the products of crystallization of magmas similar to those interpreted to be the exsolved source of metals. Perhaps one approach to partition contributions from magmatic fluids over hydrothermal fluids, in the absence of available gas chemistry (i.e. on modern systems on arcs, magmatic contributions are evident from ^{4}He, gas chemistry and isotopic compositions; de Ronde et al., 2005), would be to determine if there is an excess in metals and metalloids commonly interpreted to be magmatic in other ore-forming systems such as epithermal and porphyry copper. Metals and metalloids commonly considered as evidence of a magmatic source in epithermal systems include As, Bi, Mo, Sb, Sn, In, W, Te, Tl and Se. For the fluid inclusions investigated here, we were able to quantify values for molybdenum (n = 20), tin (n = 76), antimony (n = 58), bismuth (n = 52) and arsenic (n = 31). Although we cannot state with a high degree of certainty that these metals and metalloids represent direct magmatic contributions to the hydrothermal fluids at Windy Craggy, as opposed to leaching of the footwall lithologies, these elements are in excess compared to iron and copper. For example, the fluid inclusions generally fall on the same trend as host rocks in manganese versus iron (Fig. 8a), barium versus cerium (Fig. 8b) and zinc versus copper (Fig. 9a), but show significant excesses in the magmatic metals/metalloids compared to the host lithologies (e.g. Sn, Sb and Bi versus Cu and Fe; Fig. 9b–f). Although these differences in antimony, tin and bismuth may simply relate to a greater affinity to be leached from the host rocks, the excesses of these elements in the fluid inclusions compared to host rocks, even the massive sulphide samples, suggest that the magmatic-hydrothermal fluids are the main source of these elements.

Conclusions

We have successfully developed and refined a method to allow for the collection of quantitative analyses of inclusion fluids from relatively low salinity fluid inclusions, for a large suite of elements from a deposit with a complex fluid history. The variations in the composition of these fluids is suspected to have resulted from interaction with the host rocks and/or mixing with another fluid introduced into the system. The lead isotope data obtained from the whole rock analyses of the different rock groups within the deposit reveal a mixing trend between mantle derived lead and crustal lead. Although we were unable to distinguish primary and secondary fluid inclusions on a geochemical basis, the excess of some metals/metalloids in the fluid inclusions over copper, zinc, maganese and iron compared to the host rocks, and in particular the sulphide-rich samples, is consistent with the fluids trapped in the inclusions representing magmatic-hydrothermal fluids rather than reflecting simple hydrothermal leaching of the host rocks.

Acknowledgments

This report is a contribution to NRCan's Targeted Geoscience Initiative Program (TGI). Support for this study was provided through the Volcanic and Sedimentary Hosted Base Metal Mineralization Project's '*Activity VS-2.4: Fingerprinting fluid source regions and pathways of volcanogenic massive sulphide deposits*'.

Madison Schmidt is conducting a TGI supported M.Sc. at Queen's University, Kingston, Ontario. This report benefited from the reviews of Alain Plouffe and Neil Rogers.

References

Agangi, A., Reddy, S.M., Plavsa, D., Vieru, C., Selvaraja, V., LaFlamme, C., Jeon, H., Martin, L., Nozaki, T., Takaya, Y., and Suzuki, K., 2018. Subsurface deposition of Cu-rich massive sulphide underneath a Palaeoproterozoic seafloor hydrothermal system—the Red Bore prospect, Western Australia; Mineralium Deposita, v. 53, p. 1061–1078.

Alt, J.C., Honnorez, J., Laverne, C., and Emmermann, R., 1986. Hydrothermal alteration of a 1 km section through the upper oceanic crust, Deep Sea Drilling Project Hole 504B: Mineralogy, chemistry, and evolution of seawater-basalt interactions; Journal of Geophysical Research, v. 91, p. 10 309–10 335.

Audétat, A., Günther, D., and Heinrich, C.A., 1998. Formation of a Magmatic-Hydrothermal Ore Deposit: Insights with LA-ICP-MS Analysis of Fluid Inclusions; Science, v. 279, p. 2091.

Batchelor, R. and Mcdonald, M., 1992. Composition of fluids in quartz: discrimination of magma pulses in a Caledonian granitoid; Mineralogical Magazine, v. 56, p. 335–342.

Beaudoin, Y., Scott, S.D., Gorton, M.P., Zajacz, Z., and Halter, W., 2007. Pb and other ore metals in modern seafloor tectonic environments; evidence from melt inclusions; Marine Geology, v. 242, p. 271–289.

Bischoff, J.L. and Rosenbauer, R.J., 1985. An empirical equation of state for hydrothermal seawater (3.2 percent NaCl) American Journal of Science, v. 285, p. 725–763.

Bodnar, R.J., 1994. Synthetic fluid inclusions: XII. The system H_2O-NaCl. Experimental determination of the halite liquidus and isochores for a 40 wt% NaCl solution; Geochimica

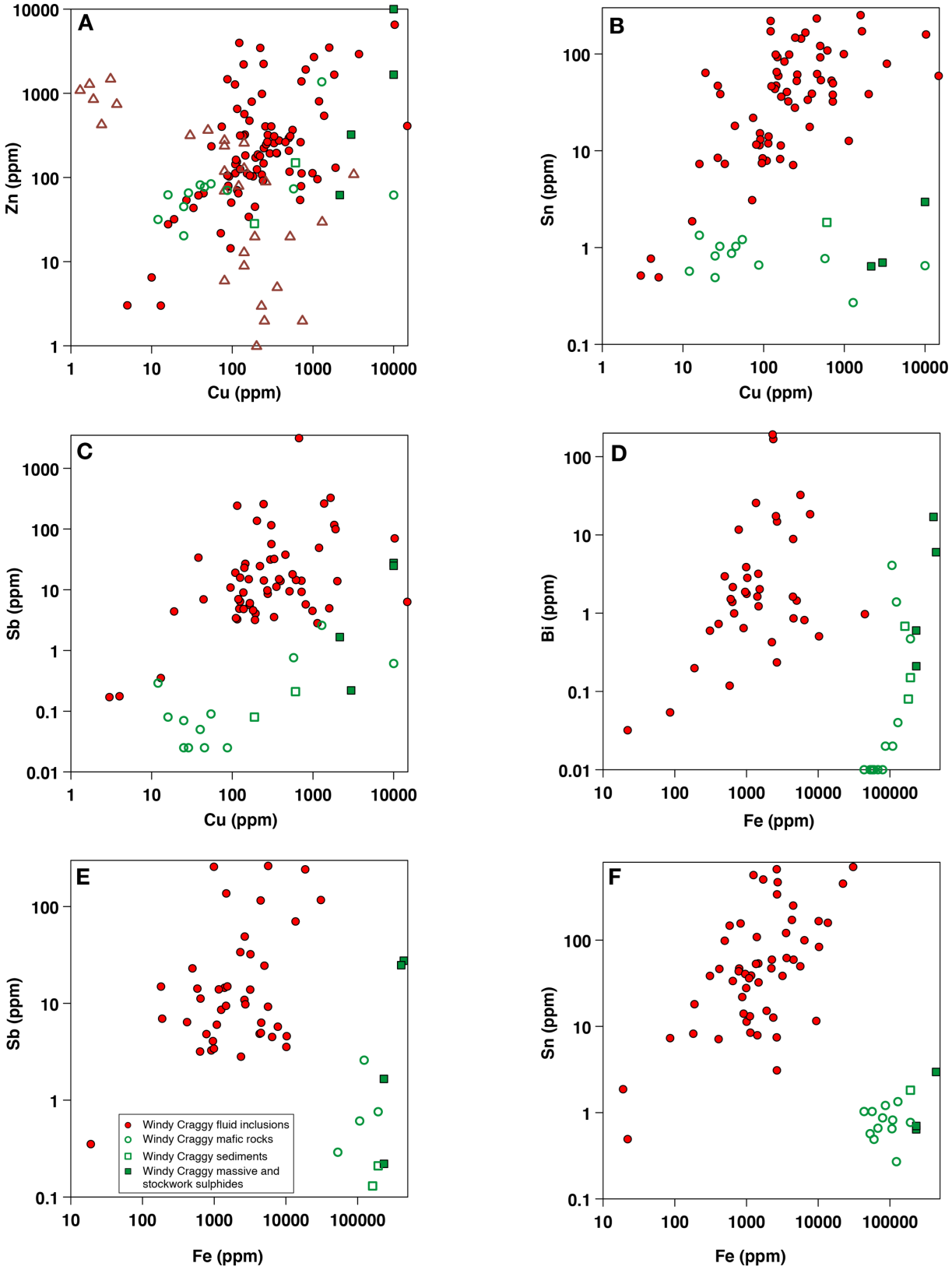

Figure 9. Plots of a) Zn vs. Cu, b) Sn vs. Cu, c) Sb vs. Cu, d) Bi vs. Fe, e) Sb vs. Fe and f) Sn vs. Fe for Windy Craggy fluid inclusions compared to the host rocks. Also shown is Zn and Cu data for fluid inclusions from the Monte Mattoni mafic complex (Hennings et al., 2017).

et Cosmochimica Acta, v. 58, p. 1053–1063.

Bodnar, R.J., Lecumberri-Sanchez, P., Moncada, D., and Steele -MacInnis, M., 2014. 13.5 - Fluid Inclusions in Hydrothermal Ore Deposits; *in* Treatise on Geochemistry (Second Edition), (ed.) H.D. Holland and K.K. Turekian; Elsevier, Oxford, p. 119–142.

Cabri, L. and Jackson, S., 2011. New developments in characterization of sulfide refractory Au ores; Abstracts World Gold 2011, 50th Conference of Metallurgists. Montreal, Quebec, p. 51–62.

Campbell, R.B. and Dodds, C.J., 1979. Operation Saint Elias, British Columbia; Geological Survey of Canada Current Research, Paper no. 79-1A, p. 17–20.

Campbell, R.B. and Dodds, C.J., 1983. Geology of Tatshenshini River Map Area (114P), British Columbia; Geological Survey of Canada Open File, v. 926.

Chen, M., Campbell, I.H., Xue, Y., Tian, W., Ireland, T.R., Holden, P., Cas, R.A.F., Hayman, P.C., and Das, R., 2015. Multiple sulfur isotope analyses support a magmatic model for the volcanogenic massive sulfide deposits of the Teutonic Bore Volcanic Complex, Yilgarn Craton, Western Australia; Economic Geology, v. 110, p. 1411–1423.

Coney, P.J., Jones, D.L., and Monger, J.W.H., 1980. Cordilleran suspect terranes; Nature, v. 288, p. 329–333.

de Ronde, C.E.J., 1995. Fluid chemistry and isotopic characteristics of seafloor hydrothermal system and associated VMS deposits; potential for magmatic contributions; Short Course Handbook, v. 23, p. 479–509.

de Ronde, C.E.J., Baker, E.T., Massoth, G.J., Lupton, J.E., Wright, I.C., Feely, R.A., and Greene, R.R., 2001. Intra-oceanic subduction-related hydrothermal venting, Kermadec volcanic arc, New Zealand; Earth and Planetary Science Letters, v. 193, p. 359–369.

de Ronde, C.E.J., Hannington, M.D., Stoffers, P., Wright, I.C., Ditchburn, R.G., Reyes, A.G., Baker, E.T., Massoth, G.J., Lupton, J.E., Walker, S.L., Greene, R.R., Soong, C.W.R., Ishibashi, J., Lebon, G.T., Bray, C.J., and Resing, J.A., 2005. Evolution of a submarine magmatic-hydrothermal system: Brothers volcano, southern Kermadec arc, New Zealand; Economic Geology, v. 100, p. 1097–1133.

de Ronde, C.E.J., Massoth, G.J., Butterfield, D.A., Christenson, B.W., Ishibashi, J., Ditchburn, R.G., Hannington, M.D., Brathwaite, R.L., Lupton, J.E., Kamenetsky, V.S., Graham, I.J., Zellmer, G.F., Dziak, R.P., Embley, R.W., Dekov, V.M., Munnik, F., Lahr, J., Evans, L.J., and Takai, K., 2011. Submarine hydrothermal activity and gold-rich mineralization at Brothers Volcano, Kermadec arc, New Zealand Mineralium Deposita, v. 46, p. 541–584.

Downing, B.W., Webster, M.P., and Beckett, R.J., 1990. The Windy Craggy massive-sulphide deposit, northwestern British Columbia, Canada; Geological Survey of Canada Open File Report, v. 2169, p. 31–67.

Gagnon, J., Samson, I., and Fryer, B., 2003. Laser ablation ICP -MS analysis of fluid inclusions; *in* Fluid Inclusions: Analysis and Interpretation, (ed.) I. Samson, A. Anderson and D. Marshall; Mineralogical Association of Canada Short Course Series Volume 32, p. 291–322.

Galley, A., Hannington, M., and Jonasson, I., 2007. Volcanogenic massive sulfide deposits *in* Mineral Resources of Canada: A Synthesis of Major Deposit-types, District Metallogeny, the Evolution of Geological Provinces, and Exploration Methods, (ed.) W.D. Goodfellow; Geological Association of Canada, Mineral Deposits Division, Special Publication no. 5, p. 141–161.

Giggenbach, W.F., 1996. Chemical Composition of Volcanic Gases; *in* Monitoring and Mitigation of Volcano Hazards, (ed.) R. Scarpa and R.I. Tilli; Springer, Berlin, Heidelberg, p. 221–256.

Goodfellow, W. and Peter, J.M., 1994. Geochemistry of hydrothermally altered sediment, Middle Valley, Northern Juan de Fuca Ridge; *in* Proceedings of the Ocean Drilling Program, (ed.) M.J. Mottl, E.E. Davis, A.T Fisher and J.F. Slack' Science Results, 139, p. 207–290.

Guillong, M., Meier, D.L., Allan, M.M., Heinrich, C.A., and Yardley, B.W.D., 2008. SILLS: A Matlab-based program for the reduction of laser ablation ICP–MS data of homogeneous materials and inclusions; Mineralogical Association of Canada Short Course Series, v. 40, p. 328–333.

Hannington, M.D., 2013. Volcanogenic Massive Sulfide Deposits, Treatise on Geochemistry: Second Edition; Elsevier, p. 463–488.

Hennings, S.K., Wagner, T., Ulmer, P., and Heinrich, C.A., 2017. Fluid evolution of the Monte Mattoni Mafic Complex, Adamello Batholith, Northern Italy: Insights from fluid inclusion analysis and thermodynamic modelling; Journal of Petrology, v. 58, p. 1645–1670.

Humphris, S.E. and Klein, F., 2018. Progress in deciphering the controls on the geochemistry of fluids in seafloor hydrothermal systems; Annual Review of Marine Science, v. 10, p. 315–343.

Huston, D.L., Brauhart, C.W., Drieberg, S.L., Davidson, G.J., and Groves, D.I., 2001. Metal leaching and inorganic sulfate reduction in volcanic-hosted massive sulfide mineral systems: Evidence from the paleo-Archean Panorama district, Western Australia; Geology, v. 29, p. 687–690.

Huston, D.L., Relvas, J.M.R.S., Gemmell, J.B., and Drieberg, S., 2011. The role of granites in volcanic-hosted massive sulphide ore-forming systems: an assessment of magmatic–hydrothermal contributions; Mineralium Deposita, v. 46, p. 473–507.

Large, R.R., Gemmell, J.B., Paulick, H., and Huston, D.L., 2001. The alteration box plot: a simple approach to understanding the relationship between alteration mineralogy and lithogeochemistry associated with volcanic-hosted massive sulfide deposits; Economic Geology, v. 96, p. 957–971.

Leybourne, M.I. and Goodfellow, W.D., 1994. Mineralogy and

mineral chemistry of hydrothermally altered sediment, Middle Valley, Juan de Fuca Ridge; *in* Proceedings of the Ocean Drilling Program, (ed.) M.J. Mottl, E.E. Davis, A.T Fisher and J.F. Slack' Science Results, 139, p. 155–206.

Leybourne, M.I. and Goodfellow, W.D., 2007. Br/Cl ratios and O, H, C, and B isotopic constraints on the origin of saline waters from eastern Canada; Geochimica et Cosmochimica Acta, v. 71, p. 2209–2223.

Leybourne, M.I., Schwarz-Schampara, U., de Ronde, C.E.J., Baker, E.T., Faure, K., Walker, S., Butterfield, D., Resing, J., Lupton, J., Hannington, M., Massoth, G., Clark, M., Timm, C., Graham, I., and Wright, I., 2012. Submarine magmatic-hydrothermal systems at the Monowai Volcanic Centre, Kermadec Arc; Economic Geology, v. 107, p. 1669–1694.

Lupton, J.E., 1983. Terrestrial inert gases: isotope tracer studies and clues to primordial components in the mantle; Annual Review of Earth and Planetary Science, v. 11, p. 371–414.

Lyon, G.L., 1974. Geothermal Gases; *in* Natural Gases in Marine Sediments, (ed.) I.R. Kaplan; Springer, Boston, MA, p. 141–150.

MacIntyre, D.G., 1984. Geology of the Alsek-Tatshenshini Rivers Area (114P); *in* Geological Fieldwork 1983; B.C. Ministry of Energy, Mines and Petroleum Resources Paper, p. 173–184.

Massoth, G.J., De Ronde, C.E.J., Lupton, J.E., Feely, R.A., Baker, E.T., Lebon, G.T., and Maenner, S.M., 2003. Chemically rich and diverse submarine hydrothermal plumes of the southern Kermadec volcanic arc (New Zealand); Geological Society Special Publication, p. 119–139.

Mungall, J.E., Andrews, D.R.A., Cabri, L.J., Sylvester, P.J., and Tubrett, M., 2005. Partitioning of Cu, Ni, Au, and platinum-group elements between monosulfide solid solution and sulfide melt under controlled oxygen and sulfur fugacities; Geochimica et Cosmochimica Acta, v. 69, p. 4349–4360.

Norman, M.D., Pearson, N.J., Sharma, A., and Griffin, W.L., 1996. Quantitative analysis of trace elements in geological materials by laser ablation ICPMS: instrumental operating conditions and calibration values of NIST glasses; Geostandards Newsletter, v. 20, p. 247–261.

Orchard, M.J., 1986. Conodonts from Western Canadian Chert: their nature, distribution and stratigraphic application; *in* Conodonts: Investigative Techniques and Applications, (ed.) R.L. Austin; Ellis Horwood Ltd. for British Micropaleontological Society, Chichester, England, p. 94–119.

Peter, J.M., 1992. Comparative geochemical studies of the Upper Triassic Windy Craggy and modern Guaymas Basin deposits: A contribution to the understanding of massive sulfide formation in volcano-sedimentary environments; Ph.D. thesis, University of Toronto, Toronto, Ontario, 562 p.

Peter, J.M., Leybourne, M.I., Scott, S.D., and Gorton, M.P., 2014. Geochemical constraints on the tectonic setting of basaltic host rocks to the Windy Craggy Cu-Co-Au massive sulphide deposit, northwestern British Columbia; International Geology Review, v. 56, p. 1484–1503.

Peter, J.M. and Scott, S.D., 1993. Fluid inclusion and light stable isotope geochemistry of the Windy Craggy Besshi-type massive sulfide deposit, northwestern British Columbia; Resource Geology Special Issue, v. 17, p. 229–248.

Peter, J.M. and Scott, S.D., 1999. Windy Craggy, northwestern British Columbia: The world's largest Besshi-type deposit; *in* Volcanic-associated massive sulfide deposits: processes and examples in modern and ancient settings: Reviews in Economic Geology 8, (ed.) C.T. Barrie and M.D. Hannington; Society of Economic Geologists, Littleton, Colorado, p. 261–295.

Piperov, N.B. and Penchev, N.P., 1973. A study on gas inclusions in minerals. Analysis of the gases from micro-inclusions in allanite; Geochimica et Cosmochimica Acta, v. 37, p. 2075–2097.

Reeves, E.P., Seewald, J.S., Saccocia, P., Bach, W., Craddock, P.R., Shanks, W.C., Sylva, S.P., Walsh, E., Pichler, T., and Rosner, M., 2011. Geochemistry of hydrothermal fluids from the PACMANUS, Northeast Pual and Vienna Woods hydrothermal fields, Manus Basin, Papua New Guinea; Geochimica et Cosmochimica Acta, v. 75, p. 1088–1123.

Roedder, E., 1972. Composition of fluid inclusions; v. 440JJ, p. 1–164.

Roedder, E., 1984. Fluid Inclusions; Reviews in Mineralogy, Vol. 12, Mineralogical Society of America, 644 p.

Rusk, B.G., Reed, M.H., Dilles, J.H., Klemm, L.M., and Heinrich, C.A., 2004. Compositions of magmatic hydrothermal fluids determined by LA-ICP-MS of fluid inclusions from the porphyry copper–molybdenum deposit at Butte, MT; Chemical Geology, v. 210, p. 173–199.

Schmidt, M.A., Peter, J.M., Jackson, S.E., Yang, Z., Leybourne, M.I., and Layton-Mathews, D., 2018. Laser ablation-inductively coupled plasma-mass spectrometric analysis of fluid inclusions from the Windy Craggy Cu-Co-Au volcanogenic massive sulphide deposit: Method development and preliminary results; *in* Targeted Geoscience Initiative: 2017 report of activities, volume 1, (ed.) N. Rogers; Geological Survey of Canada, Open File 8358, p. 243–252.

Shanks, W.C.P.I. and Thurston, R., 2012. Volcanogenic massive sulfide occurrence model; U.S. Geological Survey Scientific Investigations Report 2010–5070—C, p. 1–345.

Taylor, C.D., Premo, W.R., Meier, A.L., and Taggart, J.E., Jr., 2008. The Metallogeny of Late Triassic rifting of the Alexander Terrane in southeastern Alaska and northwestern British Columbia; Economic Geology, v. 103, p. 89–115.

Timm, C., De Ronde, C.E.J., Leybourne, M.I., Layton-Matthews, D., and Graham, I.J., 2012. Sources of chalcophile and siderophile elements in Kermadec Arc lavas; Economic Geology, v. 107, p. 1527–1538.

Tornos, F., Peter, J.M., Allen, R., and Conde, C., 2015. Controls on the siting and style of volcanogenic massive sulphide deposits; Ore Geology Reviews, v. 68, p. 142–163.

Ulrich, T., Günther, D., and Heinrich, C.A., 2001. The Evolution of a porphyry Cu-Au deposit, based on LA-ICP-MS analysis of fluid inclusions: Bajo de la Alumbrera, Argentina; Economic Geology, v. 96, p. 1743–1774.

Welhan, J.A., 1988. Methane and hydrogen in mid-ocean-ridge basalt glasses: analysis by vacuum crushing; Canadian Journal of Earth Sciences, v. 25, p. 38–48.

Williams-Jones, A.E. and Heinrich, C.A., 2005. Vapor transport of metals and the formation of magmatic-hydrothermal ore deposits; Economic Geology, v. 100, p. 1287–1312.

Wysoczanski, R.J., Handler, M.R., Schipper, C.I., Leybourne, M.I., Creech, J., Rotella, M.D., Nichols, A.R.L., Wilson, C.J.N., and Stewart, R.B., 2012. The tectonomagmatic source of ore metals and volatile elements in the Southern Kermadec Arc; Economic Geology, v. 107, p. 1539–1556.

Yang, K.H. and Scott, S.D., 1996. Possible contribution of a metal-rich magmatic fluid to a sea-floor hydrothermal system; Nature, v. 383, p. 420–423.

Yang, K.H. and Scott, S.D., 2006. Magmatic fluids as a source of metals in seafloor hydrothermal systems; in Back-Arc Spreading Systems: Geological, Biological, Chemical, and Physical Interactions, (ed.) D.M. Christie, C.R. Fisher, S. Lee and S. Givens, p. 163–184.

Preliminary carbon and oxygen isotope analyses of hydrothermal carbonates from Mississippi Valley-type and REE-F-Ba deposits of the southern Canadian Rocky Mountains – a comparison

S. Paradis[1] and G.J. Simandl[2, 3]

[1]*Geological Survey of Canada, 9860 West Saanich Road, Sidney, British Columbia V8L 4B2*

[2]*British Columbia Geological Survey, Ministry of Energy and Mines, P.O. Box 9333, Stn Prov Gov't, Victoria, British Columbia V8W 9N3*

[3]*School of Earth and Ocean Sciences, University of Victoria, P.O. Box 1700 Stn CSC, Victoria, British Columbia V8W 2Y2*

Abstract

Zinc-lead Mississippi Valley-type (MVT), carbonate-hosted REE-F-Ba and magnesite deposits of the southern Canadian Rocky Mountain Foreland Belt occur along the southwestern edge of the Kicking Horse Rim, a paleotopographic high that coincides with a carbonate platform-to-basin facies transition along the ancient Paleozoic margin. Mineralization is hosted in dolostone and is typically associated with sparry and saddle dolomite (ferroan dolomite in association with REE-F-Ba). Carbon and oxygen isotopes done on these carbonate phases show differences and similarities. All sparry, saddle and ferroan dolomite associated with mineralization have similar $\delta^{18}O_{VPDB}$ values that are lower than those of their host dolostone. However, their $\delta^{13}C_{VPDB}$ values are different with lower values for dolomites at the REE-F-Ba Rock Canyon Creek deposit than those for the MVT deposits. The depletion in ^{18}O suggests that dolomites associated with mineralization precipitated from or interacted with hydrothermal fluids. The $\delta^{18}O_{VPDB}$ and $\delta^{13}C_{VPDB}$ values of dolomite associated with mineralization at Rock Canyon Creek plot outside the field of primary igneous carbonatites, and lies on the general trend connecting the southeastern British Columbia carbonatite field to the field for unmineralized host carbonates in the same area.

Introduction

The term 'sediment-hosted deposits' as used in this paper includes a variety of deposits commonly referred to in the literature as Mississippi Valley-type (MVT: Leach et al., 2005), sedimentary exhalative (SEDEX: Goodfellow and Lydon, 2007; Wilkinson, 2014), sparry magnesite (Simandl and Hancock, 1991, 1999; Simandl, 2004), and stratabound barite-sulphide vein and replacement deposits. In the Canadian Cordillera, these deposits are located along a series of Cordillera-long tectono-stratigraphic belts. Starting in the west, the Kootenay Terrane consists of deformed and metamorphosed volcano-sedimentary rocks that host numerous MVT and SEDEX deposits (Fig. 1; Paradis et al., 2006). Farther east lies less deformed and metamorphosed platformal sedimentary rocks of the Rocky Mountain Foreland Belt, which host numerous MVT, magnesite, along with rare SEDEX deposits and a REE-F-Ba deposit, among others (Dawson et al., 1991). This study focuses on sediment-hosted deposits of the southern Rocky Mountains and investigates the geological and genetic links among various types of mineralization (e.g. zinc-lead MVT, barite-sulphide vein and replacement, magnesite and REE-F-Ba). These links are investigated by detailed integrated field-work studies, petrography, mineralogy, stable (O, C, S) and radiogenic (Sr, Pb) isotope analyses, fluid inclusion studies, and Re-Os geochronology on pyrite. Herein, we report on work in progress on stable isotope analyses (O, C) on selected MVT deposits of the southern Rocky Mountains (i.e. Oldman, Hawk Creek, Boivin and Shag). We compare our results to published and unpublished data for the carbonate-hosted Rock Canyon Creek (REE-F-Ba) deposit of southeastern British Columbia.

Regional geological setting

The carbonate-hosted deposits studied in this paper are in the Main and Front ranges of the southern Rocky Mountain Foreland Belt, along and east of the projection of the Cathedral Escarpment (Fig. 1). The strata there are deformed into a thin-skinned thrust-and-fold belt that formed along a basal-detachment fault system initiated by eastward accretion of allochthonous terranes in the Late Jurassic to Early Tertiary (McMechan, 2012; Nelson et al., 2013). They represent the late Proterozoic to Mid-Jurassic shelf and platform of the western margin of the North American craton. Upper Proterozoic to Lower Cambrian rocks of the Windermere Supergroup were deposited during intracontinental rifting (Price, 1994), and

Corresponding author: Suzanne Paradis (Suzanne.paradis@canada.ca)

Paradis, S., and Simandl, G.J., 2019. Preliminary carbon and oxygen isotope analyses of hydrothermal carbonates from Mississippi Valley-type and REE-F-Ba deposits of the southern Canadian Rocky Mountains – a comparison; *in* Targeted Geoscience Initiative: 2018 report of activities, (ed.) N. Rogers; Geological Survey of Canada, Open File 8549, p. 205–216. https://doi.org/10.4095/313652

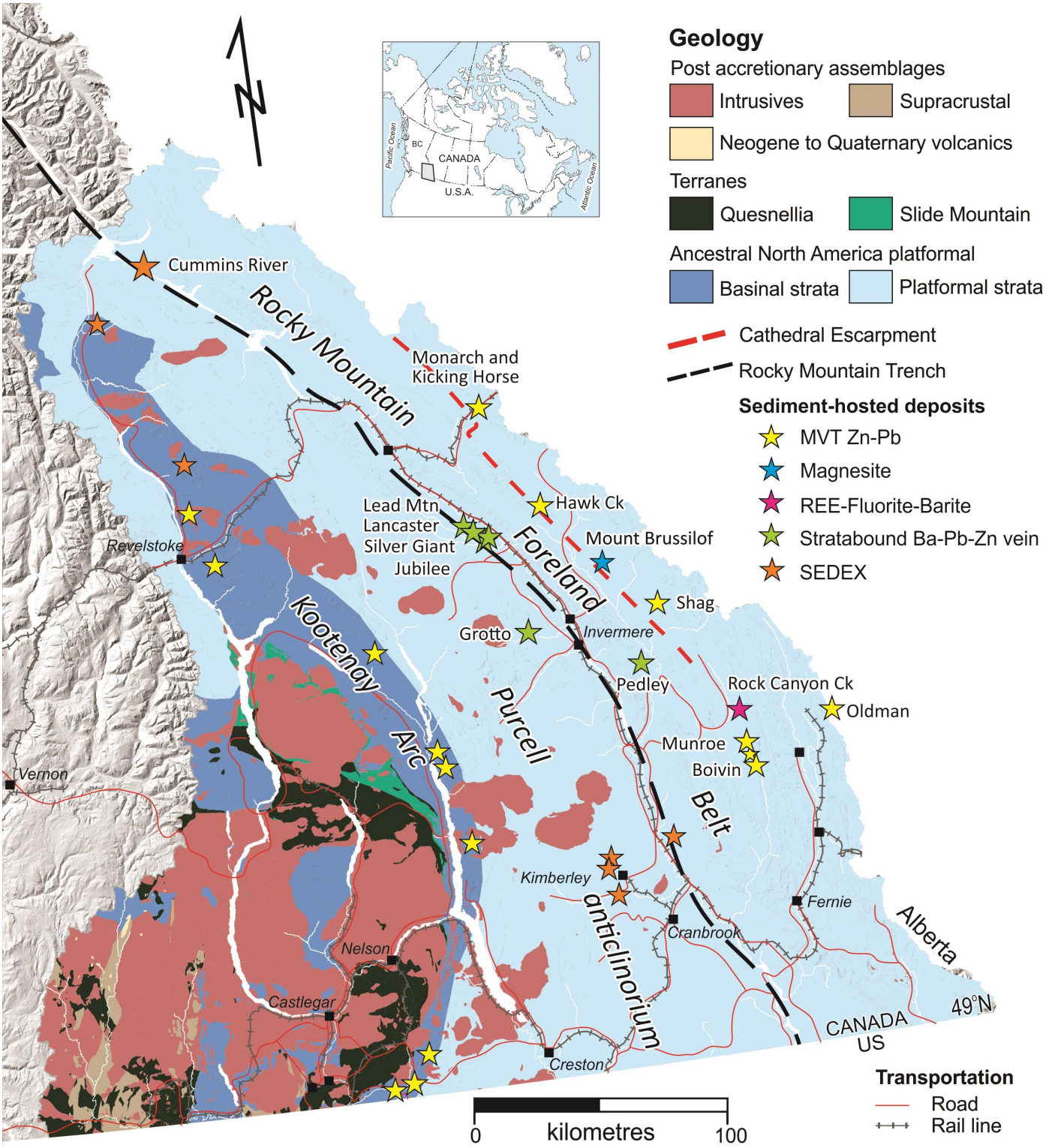

Figure 1. Regional geological map of southeastern British Columbia showing locations of sediment-hosted deposits. Those identified are studied in this project. Note that the Oldman deposit is located in Alberta. The projection of the Cathedral Escarpment corresponds approximately to the western margin location of the Kicking Horse Rim, a paleogeographic high that was initiated in the early Middle Cambrian and persisted into the Ordovician (Aitken, 1971, 1989). Both mark the change from shallow-water carbonate to the east and basinal slope lithofacies to the west during the early Paleozoic. *Modified from* Katay (2017). Terranes *from* Cui et al. (2015).

were followed by Middle Cambrian platform-basin transition sequences that formed along a paleogeographic high known as the Kicking Horse Rim (Aitken, 1971, 1989). During the Cambrian, the platform-basin transition repeatedly developed along the western margin of the Kicking Horse Rim, which corresponds approximately to the projection of the Cathedral Escarpment (shown on Fig. 1) and other escarpments. The emplacement of the Kicking Horse Rim was probably controlled by underlying basement faults (Aiken, 1971, 1989). Many MVT, SEDEX, fracture-controlled replacement Ba-Pb-Zn, magnesite, REE-F-Ba and talc deposits occur along this facies change (Simandl and Hancock, 1991; Simandl et al., 1992; Powell et al., 2006; McMechan, 2012; Paradis and Simandl, 2017, 2018). Platformal carbonate rocks hosting MVT (e.g. Monarch, Kicking Horse, Boivin, Shag and Oldman) and REE-F-Ba (e.g. Rock Canyon Creek) deposits dominate east of the projected western margin of the Kicking Horse Rim. West of the escarpments lie the Chancellor Group basinal sequences that consist predominantly of argillaceous units, including the Burgess Shale Formation, and lesser accumulations of limestone and lenses of MgO- and Ba-rich chloritic rocks. The latter were interpreted as precipitates from dense magnesian-rich brines that seeped onto the seafloor through the adjacent platform (Powell et al., 2006; Johnston et al., 2017). This regional tectono-sedimentary environment remained until the Middle Jurassic during which Cambrian-Ordovician carbonate of the Cathedral, Eldon, Stephen and Jubilee formations (to cite a few), and Middle to Upper Devonian carbonate of the Cedared, Burnais and Palliser formations were deposited. Following this period, Middle Jurassic to Eocene Cordilleran orogenic tectonism deformed, imbricated and transported these sequences north-eastward (McMechan, 2012).

Selected mineral deposits

Oldman

Oldman is a stratabound Pb-Zn-Ag deposit hosted in the upper part of the Late Devonian Palliser Formation in southwestern Alberta on the eastern slope of Mount Gass, near the British Columbia-Alberta border (Fig. 1). The host dolostone contains disseminated pyrite, sphalerite and galena, and is cut by barren and mineralized (pyrite, sphalerite, galena) white calcite (±dolomite, ±ankerite) veins, limonite-rich veinlets and fault gouges parallel to and crosscutting bedding. Galena is the dominant sulphide at Oldman and is present as disseminations in the dolostone and coarse-grained aggregates in the calcite veins. Sphalerite occurs as disseminated, equant, dark brown grains that are interstitial to the subhedral to slightly interlocking, equant grains of the host dolostone. Sphalerite also forms yellow to brown-coloured replacement patches and occurs as open-space filling. Sphalerite is accompanied by fine-grained pyrite (<0.04 mm in diameter) and locally galena.

The Oldman deposit is different from the other MVT deposits in the region in that its sulphide mineralization is associated mainly with coarse-grained white calcite (as opposed to dolomite) and occurs as open-space fillings of breccia-veins, fractures and vugs, with minor replacement (Drage and Paradis, 2018).

Boivin

Boivin is one of three zinc-lead stratabound sulphide showings (the others are Munroe and Alpine) that form a north-northwest to south-southeast linear trend (Fig. 1) in the overturned limb of an east-verging asymmetrical anticline in the Upper Devonian Morro Member of the Palliser Formation. Major westward-dipping thrust faults have positioned the Devonian rocks above Mississippian carbonate rocks and below Cambrian to Ordovician strata (Gibson, 1979a, b).

Sulphide mineralization at Boivin is identical to Munroe and Alpine and consists predominantly of sphalerite with lesser pyrite. It replaces a grey, supratidal, muddy to silty host dolostone and consists of pale yellow to orange sphalerite disseminations and aggregates forming bands and layers that alternate with white sparry dolomite-filled elongated porosity.

Shag

The Shag deposit consists of seventeen Zn-Pb (±Ag) showings in Middle to Upper Cambrian sedimentary rocks of the Stephen, Eldon and Waterfowl formations (Jensen, 1991). The main ones are BM, C-4 and Red Bed. Most of the showings are stratabound and occur at different stratigraphic levels in platformal carbonate rocks along the Kicking Horse Rim. Mineralization forms discontinuous, elongated lenses, pods and thin layers in the upper part of dolostone units, close to their contact with limestone units (Lenters, 1981). Mineralization occurs as massive replacement of the dolostone, disseminations within the dolostone, vug- and fracture-fillings, and breccia matrix. Sulphides are pale yellow to bright orange sphalerite, galena and minor pyrite in a gangue of dolomite and quartz (Drage and Paradis, 2018). Sulphide content of the zones increases from the oldest stratigraphic unit (Stephen Formation) to the top of the late Middle Cambrian Waterfowl Formation.

Hawk Creek

The Hawk Creek Zn-Pb-Ag-Au deposit is located at the carbonate platform-to-basin facies transition along the ancient Paleozoic margin (Fig. 1). It is hosted by thin-bedded argillaceous limestone and argillite of the Cambrian McKay Formation of the Chancellor Group (basinal facies time-equivalent to the platformal carbonate rocks). A geological map published in the 1930 Annual Report of the Minister of Mines of British Columbia MinEMPR shows the mineralized zone at the contact between the argillaceous limestone and the argillite. A northwest-trending shear zone of regional extent cuts the mineralized beds. Mineralization exposed at surface forms an irregular-shaped cylindrical zone roughly 15 m wide and 75 m long (Henderson, 1953; Grieve and Hoy, 1981). It forms disseminations, stringers and massive aggregates that broadly follow the layering of the sedimentary rocks. Sulphides are fine- to coarse-grained, dark grey to amber-coloured sphalerite, galena and

lesser pyrite which replaces the host rocks. Gangue minerals are dolomite and calcite.

Rock Canyon Creek

The Rock Canyon Creek REE-F-Ba deposit is in the footwall of the northwest-southeast Munroe Lake thrust, which divides the Main Ranges from the Front Ranges of the southern Canadian Rocky Mountains (Mott, 1989). It is located along the same trend as the Munroe and Boivin MVT deposits (Fig. 1). It is hosted by Middle Devonian carbonate rocks of the Cedared and Burnais formations, which consist mainly of dolostone, dolomitic limestone, carbonate breccia and laminated silty, calcareous gypsum (Pell and Hora, 1987; Green et al., 2017).

A zone of dolostone-fragment crackle breccia, coincident with REE-F-Ba mineralization, forms a steeply dipping stratabound zone extending along strike for more than 1100 m subparallel to the contact of the Cedared and Burnais formations with the overlying argillaceous lime mudstone of the Maligne Formation (Green et al., 2017). Mineralization consists of disseminations, veins, veinlets and breccia-matrix of pale and purple fluorite with associated barite and rare earth elements (Green et al., 2017). In addition, boulders of massive fluorite containing REE and aluminofluoride minerals have been found near the southeastern part of the deposit, as described by Zhu (2000) and Samson et al. (2001).

Minerals identified in the ore zone are dolomite, fluorite, quartz, K-feldspar, barite, apatite, pyrite, REE-bearing fluorocarbonate minerals such as bastnaesite-(Ce), parisite-(Ce), synchysite-(Ce) and REE-bearing phosphate minerals (such as monazite-(Ce) and crandallite group minerals (Hoshino et al., 2017a, b)). Rare earth elements, which are accompanied by fluorite and pyrite, are hosted mainly by bastnaesite-(Ce), synchysite-(Ce), parisite-(Ce) and REE-bearing phosphate minerals (mainly monazite), which may be coexisting with bastnaesite (Fig. 2). Dolomite, barite and several generations of fluorite are the main gangue minerals. Calcite is the latest gangue mineral.

A carbonatite-related origin for Rock Canyon Creek has been suggested previously by Graf (1985), Hora and Kwong (1986), Pell and Hora (1987) and Zhu (2000) based to a large extent on its mineralogy and chondrite-normalized REE profile (Fig. 3). This is in full agreement with recent studies (summarized by Simandl and Paradis, 2018) showing that globally most carbonatite-related REE deposits of economic interest are post-magmatic and could be referred to as carbohydrothermal in origin. Figure 3 illustrates the outer envelope of 41 REE profiles corresponding to the main mineralized zone of the Rock Canyon Creek deposit. The shape of this envelope is similar to mineralization at Bayan Obo (China) and Mountain Pass (U.S.A.), both considered carbonatite-related deposits. If the mineralization at Rock Canyon Creek is directly related to a peralkaline intrusion, the REE pattern would be expected to be flatter and richer in heavy REE, more akin to the profile corresponding to the Kipawa intrusion in Quebec. However, not all REE-fluorite occurrences are carbonatite- or peralkaline intrusion-related (Simandl, 2014). A good example is the Hicks Dome and Sparks Hill REE (±fluorite) mineralization located in the Illinois-Kentucky Fluorite District (U.S.A.), where the mineralization is related to ultramafic alkaline intrusions, diatremes, dykes and sills (Denny et al., 2015; Denny et al., 2017). This example may be highly relevant because at least 10 alkaline

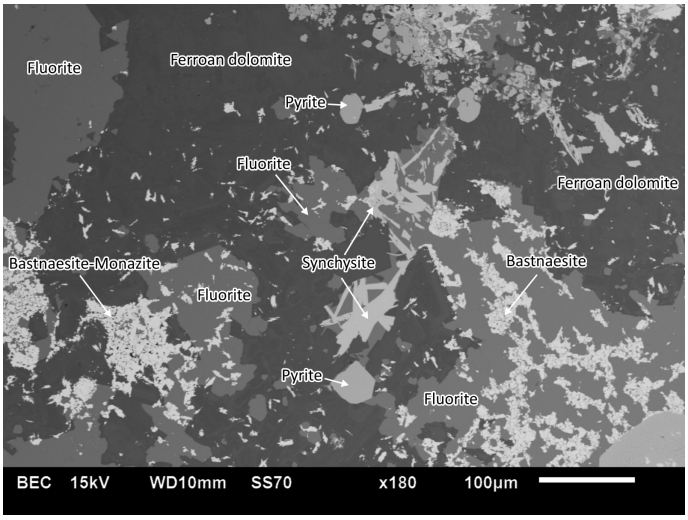

Figure 2. Backscatter electron (BSE) image of mineral assemblage from the REE-F-Ba mineralization at the Rock Canyon Creek deposit, British Columbia. Minerals identified in this image are ferroan dolomite, fluorite, pyrite and REE-bearing fluorocarbonates, bastnaesite and synchysite.

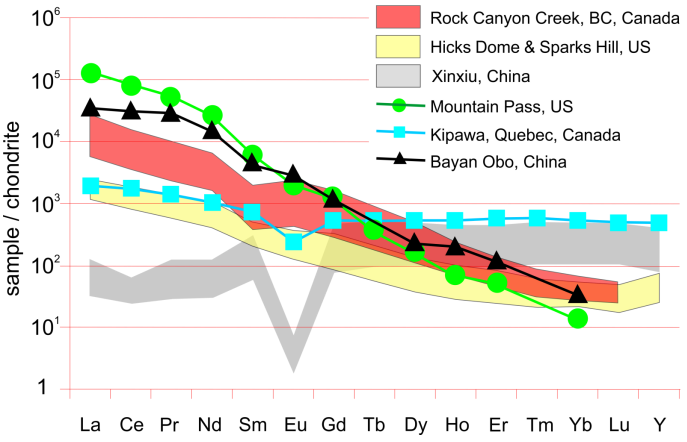

Figure 3. Typical chondrite-normalized patterns of REE for the Rock Canyon Creek REE-F-Ba deposit, Bayan Obo in China and Mountain Pass in California (carbonatite-related REE deposits), Kipawa in Quebec (peralkaline intrusion-hosted HREE deposit), Xinxiu in Southern China (ion adsorption clay deposits), and Hicks Dome and Sparks Hill in Illinois-Kentucky Fluorite District (ultramafic alkaline intrusions and diatremes). Figure *modified from* Simandl (2014).

ultrabasic diatremes and dykes are located within 40 km of Rock Canyon Creek, the nearest of which is approximately 4 km away. Most of these ultrabasic diatremes and dykes are described by Pell (1994), although the one nearest to Rock Canyon Creek remains undocumented. Furthermore, a number of recent studies (e.g. Williams-Jones et al., 2012; Migdisov and Williams-Jones, 2014; Trofanenko et al., 2016) demonstrate that REE can be effectively mobilized and transported by hydrothermal fluids in the form of REE-chloride or possibly sulphate complexes. These studies suggest that ore-forming fluids transport REE-chloride complexes and fluorine (in the form of HF) and that REE minerals precipitate when the pH of the fluid increases through interactions with carbonate rocks (Migdisov and Williams-Jones, 2014). The source of boulders of massive fluorite-REE mineralization containing aluminofluoride minerals at Rock Canyon Creek (Zhu, 2000; Samson et al., 2001) remains enigmatic, but points to an affiliation with alkaline rocks. Geographically, the source of these boulders should be up ice (i.e. north-northwest).

Analytical methods

To constrain the nature of the ore-forming elements and processes related to sediment-hosted mineral deposits, a variety of petrography and in situ geochemical and isotopic methods are applied and are in progress (*see* Paradis and Simandl, 2018, for more information).

For stable oxygen and carbonate isotopes, representative samples of carbonate from unaltered host rocks, replacive dolomitized carbonate rocks (i.e. replacive dolomite) and mineralization (i.e. sparry, saddle and ferroan dolomite) for each deposit were selected and analyzed. A few milligrams of pure carbonate were drilled at the Geological Survey of Canada and analyzed at G.G. Hatch Stable Isotope Laboratory, University of Ottawa, using a Thermo Finnigan GasBench coupled to a DeltaPlus XP IRMS. Ratios were determined on evolved CO_2 gas released from carbonate minerals by reaction with anhydrous phosphoric acid at 25°C for calcite and at 50°C for dolomite. Oxygen isotope values for dolomite and calcite were corrected using the phosphoric acid fractionation factors given by Kim and O'Neil (1997) and Sharma et al. (2002). Results are reported in conventional per mil notation (‰) relative to Vienna Pee-Dee Belemnite standard (VPDB). Accuracy of the analyses (VPDB standard) was ±0.2‰ for $\delta^{18}O$ and ±0.1‰ for $\delta^{13}C$, and the analytical precision was better than ±0.1‰ for $\delta^{18}O$ and $\delta^{13}C$. A limited number of analyses are presented in this paper; additional samples are being analyzed at the Stable Isotope Geochemistry Laboratory (Delta-Lab) of the Geological Survey of Canada.

Preliminary results

Petrography of MVT deposits

Mississippi Valley-type deposits of the southern Rocky Mountains have similar mineralogy and mineral paragenesis (i.e. Drage and Paradis, 2018). This is common for MVT deposits occurring in the same geological environment (Leach et al., 2010). The mineral paragenesis observed varies from simple (e.g. Boivin, Munroe) to complex (e.g. Monarch, Kicking Horse). One explanation for this could be related to the size of deposit and that larger deposits are the result of multiple pulses of ore-forming hydrothermal fluids and cumulative superimposing events. The generalized mineralogy and paragenesis defined for the studied deposits are summarized here.

1) Mineralized samples consist mainly of sphalerite, galena, pyrite, dolomite and calcite. Quartz is associated with sphalerite at the BM, C-4 and Red Bed showings of the Shag deposit, and is mostly absent elsewhere (except rare quartz at Kicking Horse). Chalcopyrite is only reported at Monarch in trace amounts (Goranson, 1937).

2) Dolostone hosts the sulphide mineralization. Several dolomite phases (replacement and cementation) are observed throughout the paragenesis and are associated with sulphides (except at Oldman, where only dolomitization of the carbonate precursor is present and the main carbonate associated with sulphides is calcite).

- Regional dolomitization of the limestone precursor preceded sulphide mineralization. This dolomitization has been the subject of numerous studies (e.g. Wilson et al., 1990; Qing and Mountjoy, 1994; Machel et al., 1996; Warren, 2000; Machel and Lonnee, 2002). It is a fine-grained (approximately 0.01–0.15 mm in diameter) dolostone (≤60 volume %) that may contain remnant allochems and inclusions of organic material. This dolomite preserves primary fabrics.
- The regional dolostone is replaced by a fabric-destructive, light grey, fine- to medium-grained crystalline dolomite identified as 'replacive dolomite' in this paper. The dolomite crystals exhibit non-planar texture and occur in a closely packed mosaic of anhedral to euhedral crystals ranging in diameter from 0.1 to 1 mm.
- The most recent dolomite phase is a coarse, crystalline, white sparry dolomite filling remaining open spaces (i.e. pore spaces, fractures, vugs, veinlets) after the main phase of sulphide replacement. Crystals can reach 2 mm in diameter. Large saddle dolomite crystals locally accompany it, which have characteristic undulose extinction, curved crystal faces and abundant inclusions that define growth banding. These dolomite phases are observed at Monarch, Kicking Horse, Boivin, Munroe, some showings of Shag (BM and C-3) and Hawk Creek. At Oldman, coarse-grained white calcite cement (±traces of dolomite) fills the cavities and fractures.

3) In the MVT deposits, the generalized sulphide mineral paragenesis is pyrite, followed by sphalerite and galena.

4) Generally, a single phase of sphalerite precipitation is identified, except at Monarch and Kicking Horse where two phases are observed (see Drage and Paradis, 2018).

5) Galena is one of the last sulphides to precipitate and occurs mainly as open-space filling.

6) Pyrite occurs intermittently in the paragenetic sequence: first as very fine, diagenetic grains disseminated in dolostone (pre-mineralization), second as coarser grains and aggregates associated with sphalerite (mineralization stage) and third as coarse -grained pyritohedrons filling open spaces (post-mineralization).

Petrography of the Rock Canyon Creek REE-F-Ba deposit

A brief description of the mineralogy was presented earlier in the section entitled 'Selected mineral deposits' and was derived mainly from Zhu (2000), Sampson et al. (2001), Green et al. (2017) and Hoshino et al. (2017a, b). However, more work is needed to eliminate the contradictions between these studies, as well as documentation of textures, mineral paragenesis and mineral chemistry, and to determine the age of the mineralization. A substantial portion of this work has been completed; however, interpretation is in the preliminary stage.

Oxygen and carbon isotope results for MVT deposits

The host dolostone samples from the Oldman deposit have $\delta^{13}C_{VPDB}$ values between 0.4 and 0.6‰ and $\delta^{18}O_{VPDB}$ values between -9.2 and -12‰ (pale yellow diamonds, Fig. 4). These values plot outside the field for Devonian marine carbonate rocks (Veizer et al., 1999). One coarse-grained calcite sample associated with sulphides has a $\delta^{13}C_{VPDB}$ value of -2.2‰ and $\delta^{18}O_{VPDB}$ value of -11.7‰ (dark yellow diamond in Fig. 4).

Samples from the Boivin deposit form a cluster with small variations in $\delta^{18}O_{VPDB}$ (-12 to -13.2‰) and $\delta^{13}C_{VPDB}$ (0.6 to 1.1‰) values (pale and dark green squares, Fig. 4). Isotopic compositions of the saddle and sparry dolomite are similar to the fine-grained replacive dolomite.

The $\delta^{18}O_{VPDB}$ values for the replacive dolomite of the Shag deposit vary between -9.8 to -12.1‰, and $\delta^{13}C_{VPDB}$ values vary between -1.6 to -1.9‰ (pale orange dots, Fig. 4). The replacive dolomite has more depleted $\delta^{13}C_{VPDB}$ values (-1.6 to -1.9‰) than the replacive dolomite from the other deposits covered by this study (-1.4 to 1.1‰). The $\delta^{18}O_{VPDB}$ values for replacive dolomite are similar to that of the other deposits. The $\delta^{13}C_{VPDB}$ (0.8 to -0.6‰) and $\delta^{18}O_{VPDB}$ (-13.5 to -16.5‰) values for the saddle and sparry dolomite associated with the mineralization (dark orange dots, Fig. 4) are higher and lower, respectively, than the replacive dolomite.

The argillaceous limestone (unaltered host rock) of the

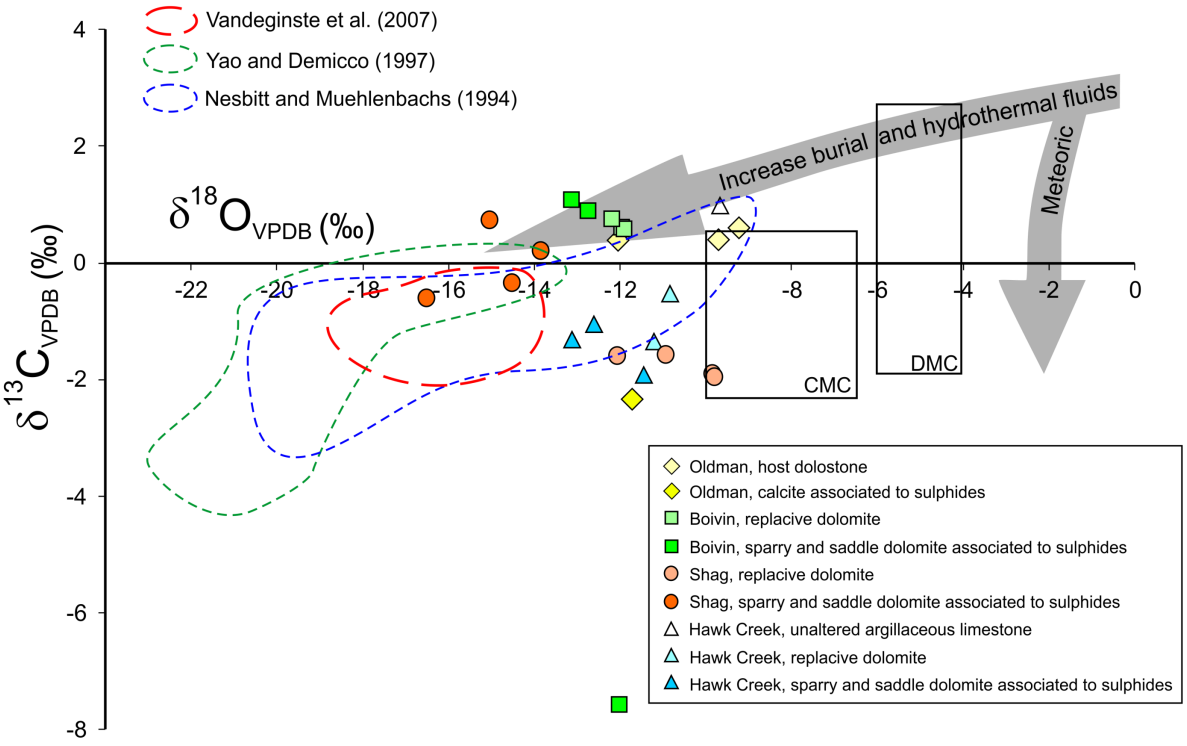

Figure 4. Plot of $\delta^{13}C_{VPDB}$ versus $\delta^{18}O_{VPDB}$ values for various unmineralized host rocks, replacive dolomite, and sparry and saddle dolomite associated with sulphides from selected deposits of the southern Canadian Rocky Mountains. The fields of Cambrian (CMC) and Devonian (DMC) marine carbonate (Veizer et al. 1999) are shown for comparison. Also shown are fields for hydrothermal dolomite from Monarch and Kicking Horse deposits (Vandeginste et al., 2007), Cambrian hydrothermal dolomite from the southern Canadian Rocky Mountains (Nesbitt and Muehlenbachs, 1994; Yao and Demicco, 1997). The generalized trends for burial, hydrothermal and meteoric fluids of Choquette and James (1987) are illustrated by arrows. All isotope values were reported relative to Vienna Pee-Dee Belemnite standard (VPDB).

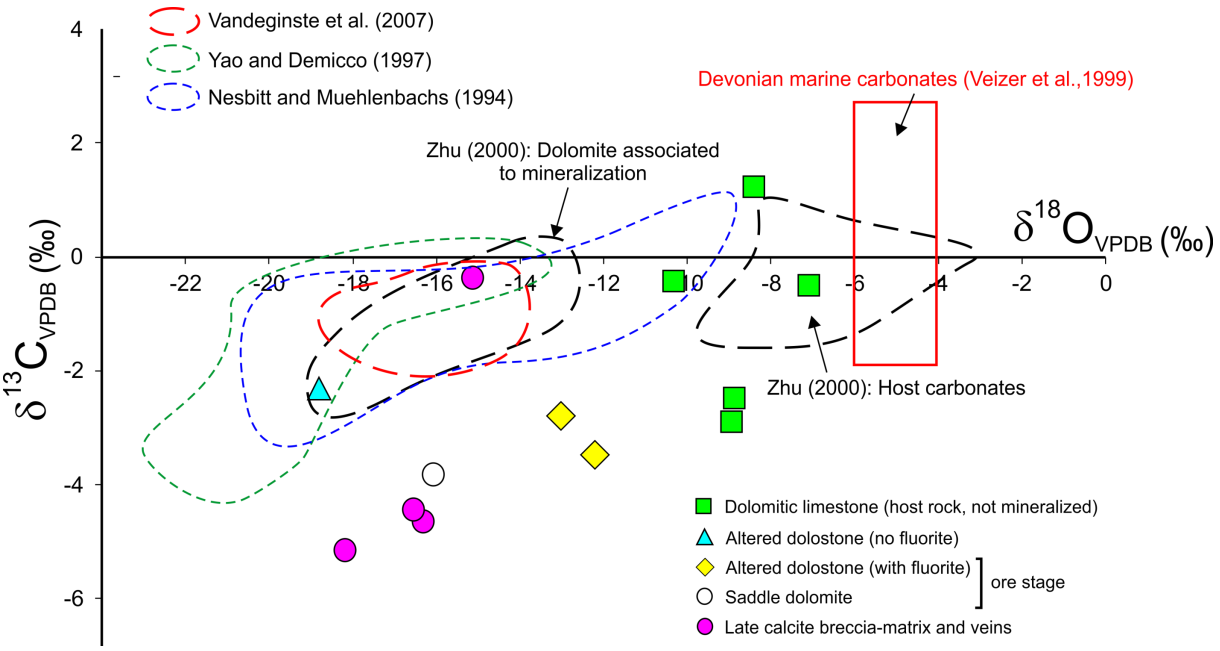

Figure 5. Plot of $\delta^{13}C_{VPDB}$ versus $\delta^{18}O_{VPDB}$ values for different carbonate phases at the Rock Canyon Creek REE-F-Ba deposit. Fields *from* Zhu (2000) are shown for comparison. Other fields are the same as in Figure 4. All isotope values were reported relative to Vienna Pee-Dee Belemnite standard (VPDB).

Hawk Creek deposit has $\delta^{13}C_{VPDB}$ and $\delta^{18}O_{VPDB}$ values of 0.99‰ and -9.6‰, respectively (white triangle, Fig. 4). These values fall close to the field for Cambrian marine carbonate rocks (Veizer et al., 1999). Samples of the replacive dolomite have lower $\delta^{18}O_{VPDB}$ values (-10.9 and -11.2‰) and $\delta^{13}C_{VPDB}$ values (-0.5 and -1.4‰) (light blue triangles, Fig. 4) than the argillaceous limestone. The sparry and saddle dolomite associated with the sulphide mineralization has $\delta^{13}C_{VPDB}$ values comparable to replacive dolomite (ranging from -1.1 to -1.9‰); however it has lower $\delta^{18}O_{VPDB}$ values (-11.5 to -13.2‰) (dark blue triangles, Fig. 4).

Oxygen and carbon isotope results for the Rock Canyon Creek REE-F-Ba deposit

The dark grey dolomitic limestone samples (host rock; not mineralized) from the Rock Canyon Creek deposit have $\delta^{13}C_{VPDB}$ values between +1.2 and -2.9‰ and $\delta^{18}O_{VPDB}$ values between -7.1 and -10.3‰ (green squares; Fig. 5). Zhu (2000) obtained similar values of +1 to -1.4‰ $\delta^{13}C_{VPDB}$ and -8.1 to -9.4‰ $\delta^{18}O_{VPDB}$ for Devonian limestone.

Two altered dolostone samples with fluorite have $\delta^{13}C_{VPDB}$ values of -2.8‰ and -3.5‰, and $\delta^{18}O_{VPDB}$ values of -13.1‰ and -12.2‰ (yellow diamonds; Fig. 5). This weathered light grey to pale brown dolostone has a mottled texture, and is crosscut by numerous fluorite veinlets and fluorite-filled vugs. It is equivalent to the 'replacive dolomite' associated with MVT deposits, and may correspond to the mineralized ferroan dolomite of Zhu (2000), which has $\delta^{13}C_{VPDB}$ and $\delta^{18}O_{VPDB}$ values ranging from -0.3 to -2.6‰ and -13 to -18.8‰, respectively. Another sample of altered dolostone (blue triangle; Fig. 5) has $\delta^{13}C_{VPDB}$ and $\delta^{18}O_{VPDB}$ values of -2.4‰ and -18.8‰, respectively. It is a whitish to light grey, mottled arenaceous micritic dolostone with no visible fluorite veinlets and vugs.

One sample of saddle dolomite associated with fluorite veinlets and vugs has a $\delta^{13}C_{VPDB}$ value of -3.8‰ and a $\delta^{18}O_{VPDB}$ value of -16.1‰ (white dot, Fig. 5). Saddle dolomite associated with fluorite-REE mineralization analyzed by Zhu (2000) had $\delta^{13}C_{VPDB}$ values of -1.1‰ and -1.9‰ and $\delta^{18}O_{VPDB}$ values between -13‰ and -18.9‰. Late calcite vein and breccia matrix cement have $\delta^{13}C_{VPDB}$ values between -0.3 and -5.2‰ and $\delta^{18}O_{VPDB}$ values between -15.1 and -18.2‰ (pink dots, Fig. 5).

Discussion and future work

Carbon and oxygen isotopes combined with strontium isotopes and fluid inclusion data of host, altered, and mineralized carbonate rocks in conjunction with mineral chemistry can provide important constraints on the origin and nature of dolomitization (associated with mineralization), sources of mineralizing fluids, and temperature of dolomitization.

We present and compare preliminary carbon and oxygen isotope data on carbonate phases associated with dolomitization (replacive) and mineralization (sparry, saddle, and ferroan) for selected MVT deposits (Oldman, Boivin, Hawk Creek and Shag) and a REE-F-Ba deposit (Rock Canyon Creek) of the southern Canadian Rocky Mountains.

Coarse-grained white sparry and saddle dolomites are spa-

tially associated with sulphide mineralization at most MVT deposits, and with REE-F-Ba mineralization at Rock Canyon Creek. In some deposits, they are mostly syn-mineralization (e.g. Monarch and Kicking Horse, Rock Canyon Creek), and in others they are mostly post-mineralization and fill fractures and vugs (e.g. Shag, Boivin, Mount Brussilof). Spatial coexistence of sparry and saddle dolomites with MVT Zn-Pb mineralization is used as an exploration guide and as evidence for interaction of high temperature hydrothermal fluids with the host rocks (e.g. Warren, 2000; Davies and Smith, 2006).

Carbon and oxygen isotope results show that, in our study area, distinct fields are identified for sparry and saddle dolomites associated with MVT mineralization and their respective host carbonate rocks. The host limestone and dolostone are depleted in ^{18}O relative to the range of values for Cambrian and Devonian marine carbonate rocks as established by Veizer et al. (1999) but have similar $\delta^{13}C_{VPDB}$ values (Fig. 4). Replacive dolomite, and sparry and saddle dolomite associated with sulphides form distinct populations for all individual MVT deposits. All carbonate rocks show large variations in $\delta^{18}O_{VPDB}$ values (-9.2 to -16.5‰) and less variations in $\delta^{13}C_{VPDB}$ values (+1.1 to -2.2‰; except for late calcite and one sparry dolomite at -7.6‰). However, overlap suggests formation from fluids of comparable isotopic chemistry and temperature (Al-Aasm, 2003). The MVT sample with an anomalously low $\delta^{13}C_{VPDB}$ value of -7.6‰ is a sparry dolomite associated with sphalerite from the Boivin deposit. This value, if correct, suggests that the dolomite incorporated organic carbon derived from the microbial or thermal breakdown of organic matter.

For the MVT and Rock Canyon Creek deposits, sparry and saddle dolomites associated with mineralization tend to have lower $\delta^{18}O_{VPDB}$ values than their respective carbonate host rocks (Fig. 6). This depletion in ^{18}O suggests that this dolomite was precipitated from or interacted with hydrothermal fluids. This phenomenon has been observed in other MVT and hydrothermal deposits around the world (e.g. Pine Point and Prairie Creek in NWT, Canada; Nanisivik in Nunavut, Canada; Cadjebut in Australia) where it has been attributed to increased fluid:rock interaction (Adams et al., 2000) and elevated temperatures of dolomite formation caused by greater burial depths or interaction with hotter mineralizing fluids (Tompkins et al., 1994; Paradis, 2007).

The $\delta^{18}O_{VPDB}$ and $\delta^{13}C_{VPDB}$ values of the MVT sparry and saddle dolomites compare well (see Fig. 6) to hydrothermal dolomites from the Monarch and Kicking Horse deposits (Vandeginste et al., 2007), Robb Lake (Nelson et al., 2002) and

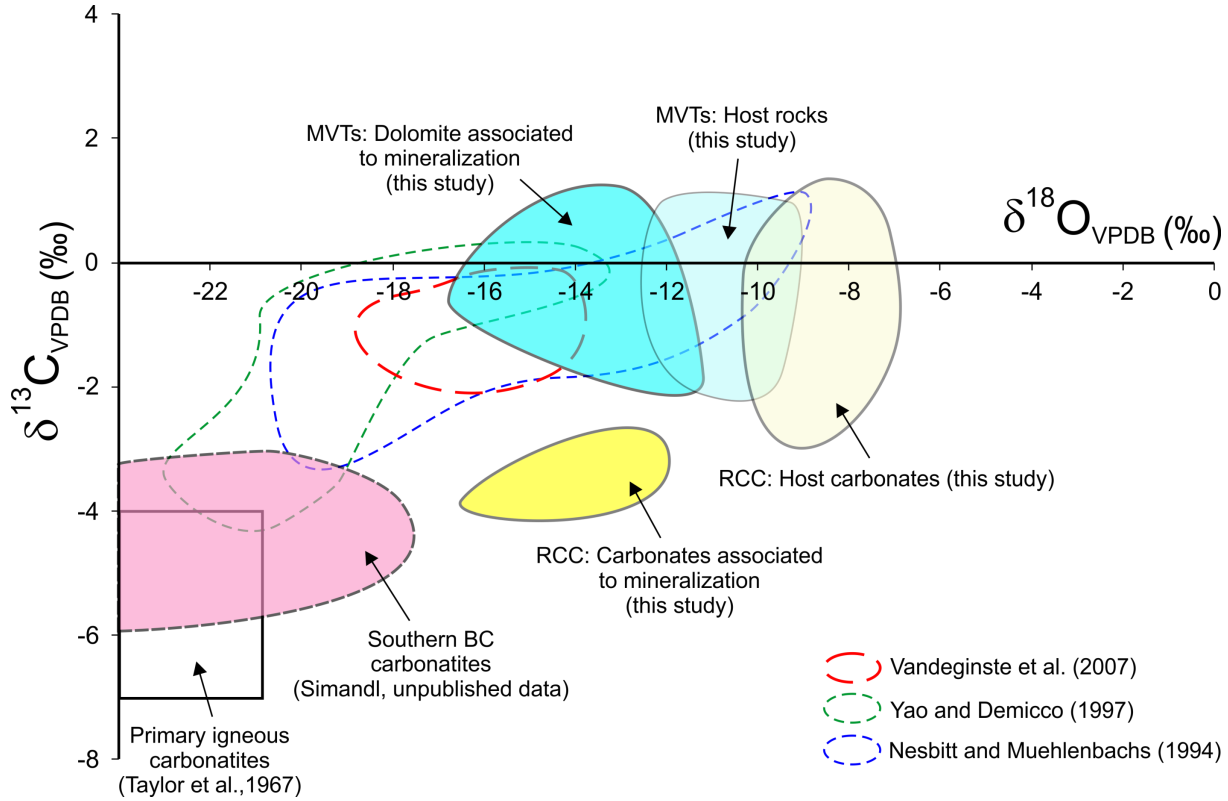

Figure 6. Plot of $\delta^{13}C_{VPDB}$ versus $\delta^{18}O_{VPDB}$ showing the fields for host rocks to MVT deposits (pale blue), dolomite associated to MVT sulphide mineralization (dark blue), host carbonate rocks to the Rock Canyon Creek (RCC) deposit (pale yellow), carbonates associated to fluorite (yellow), field of southern British Columbia carbonatite (pink; Simandl et al., work in progress, 2018), and field of primary igneous carbonatite as established by Taylor et al. (1967). The other fields are the same as in Figure 4. All isotope values were reported relative to Vienna Pee-Dee Belemnite standard (VPDB).

the southern Rocky Mountains studied by Nesbitt and Muehlenbachs (1994) and Yao and Demicco (1997). However, most of our $\delta^{13}C_{VPDB}$ values for replacive dolomite and saddle dolomite associated with REE-F-Ba mineralization at Rock Canyon Creek are slightly lower than those of Zhu (2000) for dolomites associated with mineralization; the $\delta^{18}O_{VPDB}$ values are identical. More data are needed to confirm that the gap between these two data sets is real. An interesting observation is that the $\delta^{18}O_{VPDB}$ and $\delta^{13}C_{VPDB}$ values of dolomite associated with mineralization at Rock Canyon Creek (our data; dark yellow field on Fig. 6) plot outside the field of primary igneous carbonatite as established by Taylor et al. (1967), and its $\delta^{18}O_{VPDB}$ values are comparable or slightly higher than those corresponding to carbonatites of southern British Columbia (Simandl et al., in prep.), which includes Upper Fir, Verity, Roadside, Serpentine Creek and Mount Grace. The field for dolomite that is related to the Rock Canyon Creek mineralization lies on the general trend connecting the British Columbia carbonatite field to the field for unmineralized host carbonate rocks in the same area (Fig. 6). The significance of this trend alone is not conclusive, but it suggests that the fluids responsible for formation of the Rock Canyon Creek deposit may have had a significant carbonatite-related fluid component. However, further investigation is warranted to avoid drawing a premature conclusion about the validity of this trend. After all, the fields of Yao and Demicco (1997) and Nesbitt and Muhlenbachs (1994) slightly overlap the carbonatite field (Fig. 6). New data for Rock Canyon Creek (REE-F-Ba), MVT and carbonatite-related hydrothermal deposits are being acquired, and will allow us to reconcile the differences among the various fields, identify any different trends and further compare the deposits.

The additional isotopic analyses (e.g. O, C, Sr, S, Pb) on sulphide, sulphate and carbonate minerals combined with fluid inclusion microthermometry and evaporate mound analyses of ore and gangue minerals, will provide information about the chemical composition, temperatures and salinities of ore-forming fluids and associated dolomitization, and constrain the sources of ore-forming fluids and metals in hydrothermal mineral deposits.

In situ trace element analyses of sulphide, carbonate and selected accessory minerals by laser ablation inductively coupled plasma mass spectrometry (LA ICP-MS) for trace element (including REE and Y) content of carbonate minerals and specialty metal content (e.g. Ge, Ga, In) of sulphide minerals may provide insight into dolomite- and ore-forming fluid chemistry.

Pyrite-rich samples from selected carbonate-hosted deposits were submitted for Re-Os isotopic analyses to help constrain the age of sulphide mineralization. The samples are prescreened and tested for their Re concentration, which should be higher than 0.5 ppb for reliable isotopic measurements. Age dating of accessory minerals (e.g. mica, apatite, rutile and monazite) hosted locally by sparry carbonate associated with mineralization is also being attempted. If interpretable data are obtained, the dates will help to constrain the ages of MVT mineralization, sparry dolomitization and other mineral deposit types in southeast British Columbia.

Acknowledgments

This report is a contribution to NRCan's Targeted Geoscience Initiative Program (TGI-5). Support for this study was provided through the Volcanic- and Sedimentary-Hosted Base Metal Mineralization Project's '*Activity VS-2.1: Is there a genetic link between various types of sediment-hosted deposits of the Canadian Cordillera?*' and the Specialty Metals Ore Systems Project.

This study benefited from the field assistance and collaboration of Fiona Katay (British Columbia Ministry of Energy and Mines, Regional Geologist based in Cranbrook) and assistant Natashia Drage. We thank David Pighin and Chris Graf for their perspectives on the geology of southeastern British Columbia. Dave Pighin provided access to drill cores stored at the Vine property south of Cranbrook, and Chris Graf provided guidance in the field and permission to sample the drill cores of the Rock Canyon Creek deposit, as well as samples of the Shag deposit. Carlee Akam of the British Columbia Ministry of Energy and Mines and Natashia Drage of the Geological Survey of Canada are thanked for providing a critical review. This report benefited from the review of Nicolas Pinet, Simon Jackson and Neil Rogers.

References

Adams, J.J., Rostron, B.J., and Mendoza, C.A., 2000. Evidence for two fluid mixing at Pine Point, NWT; Journal of Geochemical Exploration, v. 69-70, p. 103–108.

Aitken, J.D., 1971. Control of lower Paleozoic sedimentary facies by the Kicking Horse Rim, southern Rocky Mountains, Canada; Bulletin of Canadian Petroleum Geology, v. 19, p. 557–569.

Aitken, J.D., 1989. Birth, growth and death of the Middle Cambrian Cathedral carbonate lithosome, southern Rocky Mountains; Bulletin of Canadian Petroleum Geology, v. 37, p. 316–333.

Al-Aasm, I.S., 2003. Origin and characterization of hydrothermal dolomite in the Western Canada Sedimentary Basin; Journal of Geochemical Exploration, v. 78, p. 9–15.

Choquette, P.W. and James, N.P., 1987. Diagenesis 12. Diagenesis in limestones 3. The deep burial environment; Geoscience Canada, v. 14, p. 3–35.

Cui, Y., Miller, D., Nixon, G., and Nelson, J., 2015. British Columbia digital geology; British Columbia Ministry of Energy and Mines, British Columbia Geological Survey, Open File 2015-2.

Davies, G.R. and Smith, L.B. Jr, 2006. Structurally controlled hydrothermal dolomite reservoir facies: An overview; American Association of Petroleum Geologists, Bulletin, v. 90, p. 1641–1690.

Dawson, K.M., Panteleyev, K.M., Brown, A.S., and Woodworth, G.J., 1991. Regional metallogeny; *in* Geology of the Precambrian Superior and Grenville Provinces and Precambrian Fossils in North America, (ed.) S.B. Lucas and M.R. St-Onge; Geological Survey of Canada, Geology of Canada, no. 4, p. 709–768.

Denny, F.B., Guillemette, R.N., and Lefticariu, L., 2015. Rare earth mineral concentrations in ultramafic alkaline rocks and fluorite within the Illinois-Kentucky Fluorite District: Hicks Dome cryptoexplosive complex, southeast Illinois and northwest Kentucky, USA; *in* Proceedings of the 47th Forum on the Geology of Industrial Minerals, (ed.) Z. Lasemi; Illinois State Geological Survey, Circular 587.

Denny, F.B., Maria, A.H., Mulvaney-Norris, J.L., Guillemette, R.N., Cahill, R.A., Fifarek, R.H., Freiburg, J.T., and Anderson, W.H., 2017. Geochemical and petrographic analysis of the Sparks Hill Diatreme and its relationship to the Illinois-Kentucky Fluorspar District; Illinois State Geological Survey, Circular 588, 51 p.

Drage, N. and Paradis, S., 2018. Geology and petrography of selected carbonate-hosted Zn-Pb deposits of the southeastern Cordillera, British Columbia and Alberta; Geological Survey of Canada, Open File 8410, 29 p.

Gibson, G., 1979a. Geology of the Munroe-Alpine-Boivin carbonate-hosted zinc occurrences; Rocky Mountain Front Ranges, southeastern British Columbia; British Columbia Ministry of Energy, Mines and Petroleum Resources, Preliminary Map No. 46.

Gibson, G., 1979b. Geological report on the SOAB 4 and SOAB 5 mineral claims within the Boivin Group, Fort Steele Mining Division, 82J/3E, 82J/14E; British Columbia Ministry of Energy, Mines and Petroleum Resources, Assessment Report 7489, 9 p.

Goodfellow, W.D. and Lydon, J.W., 2007. Sedimentary exhalative (SEDEX) deposits; in: Mineral deposits of Canada: A synthesis of major deposit types, district metallogeny, the evolution of geological provinces, and exploration methods, (ed.) W.D. Goodfellow; Geological Association of Canada, Mineral Deposits Division, Special Publication No. 5, p. 163–183.

Goranson, E.A., 1937. Geology of the monarch and kicking horse ore deposits, British Columbia; Economic Geology, v. 32, p. 471–493.

Graf, C., 1985. Geological report on the D.P. 1,2,3 and Candy Claims REE-Ba-F-P carbonatite prospect, Golden Mining Division southeastern British Columbia NTS 82J/3E; British Columbia, Geological Branch Assessment Report 14677.

Green, C., Simandl, G.J., Paradis, S., Katay, F., Hoshino, M., Kon, Y., Kodama, S., and Graf, C., 2017. Geological setting of the Rock Canyon Creek REE-fluorite deposit, British Columbia, Canada; *in* Geological Fieldwork 2016; British Columbia Ministry of Energy and Mines, British Columbia Geological Survey, Paper 2017-1, p. 195–203.

Grieve, D.A. and Hoy, T., 1981. Lead-zinc showings in carbonate rocks, southern Rocky Mountains; *in* Geological Fieldwork 1980; British Columbia Ministry of Energy, Mines and Petroleum Resources, British Columbia Geological Survey, Paper 1981-1, p. 105–110.

Henderson, G.G.L., 1953. Hawk Creek; Minister of Mines, Province of British Columbia, Annual Report, 1953, p. 155–156.

Hora, Z.D. and Kwong, Y.T.J., 1986. Anomalous rare earth elements (REE) in the Deep Purple and Candy claims; *in* Geological Fieldwork 1985; British Columbia Ministry of Energy, Mines, and Petroleum Resources, British Columbia Geological Survey, Paper 1986-1, p. 241–242.

Hoshino, M., Kon, Y., Kodama, S., Simandl, G.J., Paradis, S., Green, C., Namatame, C., Matsunaga, I., and Takagi, T., 2017a. Mineralogy of the Rock Canyon Creek REE-Fluorite Deposit, British Columbia, Canada, *in* Geological Fieldwork 2016; British Columbia Ministry of Energy and Mines, British Columbia Geological Survey, Paper 2017-1, p. 205–213.

Hoshino, M., Kon, Y., Kodama, S., Simandl, G.J., Namatame, C., Matsunaga, I., and Takagi, T., 2017b. Mineralogy of the Rock Canyon Creek REE-fluorite deposit, British Columbia, Canada; British Columbia Ministry of Energy and Mines, British Columbia Geological Survey, Geofile 2017-8.

Jensen, S., 1991. Geochemical assessment report on the Shag property, Golden Mining Division; British Columbia Ministry of Energy, Mines and Petroleum Resources, Assessment Report 21885, 39 p.

Johnston, P.A., Collom, C.J., and Desjardins, P., 2017. Lower to Middle Cambrian of the southern Canadian Rockies; *in* Geologic Field Trips of the Canadian Rockies, (ed.) J.C.C. Hsieh; 2017 Meeting of the Geological Society of America, Rocky Mountain Section, Field Guide 48, p. 71–121.

Katay, F., 2017. Exploration and mining in the Southeast Region, British Columbia; *in* Exploration and Mining in British Columbia, 2016; British Columbia Ministry of Energy and Mines, British Columbia Geological Survey, Information Circular 2017-1, p. 73–107.

Kim, S.-T. and O'Neil, J.R., 1997. Equilibrium and nonequilibrium oxygen isotope effects in synthetic carbonates; Geochimica et Cosmochimica Acta, v. 61, p. 3461–3475.

Leach, D.L., Sangster, D.L., Kelly, K.D., Large, R.R., Garven, G., Allen, C.R., Gutzmer, J., and Walter, S., 2005. Sediment-hosted lead-zinc deposits: A global perspective; *in* Economic Geology, 100th anniversary Volume, 1905–2005, (ed.) J.W. Hedenquist, J.F.H. Thompson, R.J. Goldfarb and J.P. Richards; Society of Economic Geologists, Littleton, Colorado, p. 561–607.

Leach, D.L., Bradley, D.C., Huston, D., Pisarevsky, S.A., Taylor, R.D., and Gardoll, S.J., 2010. Sediment-hosted lead-zinc deposits in Earth history; Economic Geology, v. 105, p. 593–625.

Lenters, M.H., 1981. Geological mapping and geochemical

sampling, Shag Claims, Golden Mining Division; British Columbia Ministry of Energy, Mines and Petroleum Resources, Assessment Report 9678, 74 p.

Machel, H.G. and Lonnee, J., 2002. Hydrothermal dolomite—A product of poor definition and imagination; Sedimentary Geology, v. 152, p. 163–171.

Machel, H.G., Cavell, P.A., and Patey, K.S., 1996. Isotopic evidence for carbonate cementation and recrystallization, and for tectonic expulsion of fluids into the Western Canada Sedimentary Basin; Geological Society of America Bulletin, v. 108, p. 1108–1119.

McMechan, M.E., 2012. Deep transverse basement structural control of mineral systems in the southeastern Canadian Cordillera; Canadian Journal of Earth Sciences, v. 49, p. 693–708.

Migdisov, A. and Williams-Jones, A.E., 2014. Hydrothermal transport and deposition of the rare earth elements by fluorine-bearing aqueous liquids; Mineralium Deposita, v. 49, p. 987–997.

Mott, J.A., 1989. Structural and stratigraphic relations in the White river region, eastern Main Ranges, southern Rocky Mountains, British Columbia; Ph.D. thesis, Queen's University, Kingston, Ontario, 404 p.

Nelson, J.L., Paradis, S., Christensen, J., and Gabites, J., 2002. Canadian Cordilleran Mississippi Valley-type deposits: A case study for Devonian-Mississippian back-arc hydrothermal origin; Economic Geology, v. 97, p. 1013–1036.

Nelson, J.L., Colpron, M., and Israel, S., 2013. The Cordillera of British Columbia, Yukon, and Alaska: tectonics and metallogeny; *in* Tectonics, Metallogeny, and Discovery: The North American Cordillera and Similar Accretionary Settings, (ed.) M. Colpron, T. Bissig, B.G. Rusk and J.F.H. Thompson; Society of Economic Geologists, Special Publication 17, p. 53–109.

Nesbitt, B.E. and Muehlenbachs, K., 1994. Paleo hydrogeology of the Canadian Rockies and origins of brines, Pb-Zn deposits and dolomitization in the Western Canada Sedimentary Basin; Geology, v. 22, p. 243–246.

Paradis, S., 2007. Isotope geochemistry of the Prairie Creek carbonate-hosted zinc-lead-silver deposit, southern MacKenzie Mountains, Northwest Territories; *in* Mineral and Energy Resource Assessment of the Greater Nahanni Ecosystem under Consideration for the Expansion of the Nahanni National Park Reserve, Northwest Territories; (ed.) D.F. Wright, D. Lemkow and J.R. Harris; Geological Survey of Canada, Open File 5344, p. 131–176.

Paradis, S. and Simandl, G.J., 2017. Is there a genetic link between the SEDEX and MVT deposits of the Canadian Cordillera?; *in* Targeted Geoscience Initiative - 2016 Report of Activities, (ed.) N. Rogers; Geological Survey of Canada, Open File 8199, p. 107–113.

Paradis, S. and Simandl, G.J., 2018. Are there genetic links between carbonate-hosted barite-zinc-lead sulphide deposits and magnesite mineralization in southeast British Columbia?; *in* Targeted Geoscience Initiative: 2017 Report of Activities, Volume 1; (ed.) N. Rogers; Geological Survey of Canada, Open File 8358, p. 217–227.

Paradis, S., Bailey, S., Creaser, R.A., Piercey, S.J., and Schiarizza, P., 2006. Paleozoic magmatism and syngenetic massive sulphide deposits of the Eagle Bay assemblage, Kootenay terrane, southern British Columbia; *in* Paleozoic Evolution and Metallogeny of Pericratonic Terranes at the Ancient Pacific Margin of North America, Canadian and Alaskan Cordillera, (ed.) M. Colpron and J.L. Nelson; Geological Association of Canada, Special Paper 45, p. 383–414.

Pell, J., 1994. Carbonatites, nepheline syenites, kimberlites and related rocks in British Columbia; British Columbia Ministry of Energy, Mines, and Petroleum Resources, Bulletin 88, 44 p.

Pell, J. and Hora, Z.D., 1987. Geology of the Rock Canyon Creek fluorite/rare earth element showing southern Rocky Mountains (82J/3E); *in* Geological Fieldwork 1986; British Columbia Ministry of Energy, Mines and Petroleum Resources, British Columbia Geological Survey Paper 1987-1, p. 255–258.

Powell, W.G., Johnston, P.A., Collom, C.J., and Johnston, K., 2006. Middle Cambrian brine seeps on the Kicking Horse Rim and their relationship to talc and magnesite mineralization and associated dolomitization, British Columbia; Economic Geology, v. 101, p. 431–451.

Price, R.A., 1994. Cordilleran tectonics and the evolution of the Western Canada Sedimentary Basin; Chapter 2 *in*: Geological Atlas of the Western Canada Sedimentary Basin, (ed.) G. Mossop and I. Sheltsin; Alberta Research Council and Canadian Society of Petroleum Geologists, Calgary.

Qing, H. and Mountjoy, E.W., 1994. Formation of coarsely crystalline, hydrothermal dolomite reservoirs in the Presqu'ile barrier, Western Canada Sedimentary Basin; American Association of Petroleum Geologists, Bulletin, v. 78, p. 55–77.

Samson, I.M., Kerr, I.D., and Graf, C., 2001. The Rock Canyon Creek Fluorite-REE deposit, British Columbia; *in* Industrial Minerals in Canada, (ed.) S. Dunlop and G.J. Simandl; Canadian Institute of Mining and Metallurgy, Special Volume 53, p. 35–44.

Sharma, D.S., Patil, D.J., and Gopalan, K., 2002. Temperature dependence of oxygen isotope fractionation of CO_2 from magnesite-phosphoric acid reaction; Geochimica et Cosmochimica Acta, v. 66, p. 589–593.

Simandl, G.J., 2004. Magnesite and related opportunities in British Columbia, *in* Industrial Minerals with an Emphasis on Western North America, (ed.) G.J. Simandl, W.J. McMillan and N.D. Robinson; British Columbia Ministry of Energy and Mines, British Columbia Geological Survey, Paper 2004-2, p. 57–60.

Simandl, G.J., 2014. Geology and market-dependent signifi-

cance of rare earth element resources; Mineralium Deposita, v. 49, p. 889–904.

Simandl, G.J. and Hancock, K.D., 1991. Geology of the Mount Brussilof magnesite deposit, southeastern British Columbia; *in* Geological Fieldwork 1990; British Columbia Ministry of Energy, Mines and Petroleum Resources, British Columbia Geological Survey, Paper 1991-1, p. 269–278.

Simandl, G.J. and Hancock, K.D., 1999. Sparry magnesite; *in* Selected British Columbia Mineral Deposit Profiles, Volume 3, Industrial Minerals and Gemstones, (ed.) G.J. Simandl, Z.D. Hora and D.V. Lefebure; British Columbia Ministry of Energy and Mines, p. 39–41.

Simandl, G.J. and Paradis, S., 2018. Carbonatites: Related ore deposits, resources, footprint, and exploration methods; Transactions of the Institutions of Mining and Metallurgy, v. 127, p. 123–152.

Simandl, G.J., Hancock, K.D., Fournier, M., Koyanagi, V.M., Vilkos, V., Lett, R., and Colbourne, C., 1992. Geology and major element geochemistry of the Mount Brussilof magnesite deposit, southeastern British Columbia, (82J/12m 13); British Columbia Ministry of Energy, Mines and Petroleum Resources, Open File 1992-14, 14 p.

Taylor, H.P., Frechen, J., and Degens, E.T., 1967. Oxygen and carbon isotope studies of carbonatites from the Laacher See district, West Germany and the Alnö district, Sweden; Geochimica et Cosmochimica Acta, v. 31, p. 407–430.

Tompkins, L.A., Pedone, V.A., Roche, M.T., and Groves, D.I., 1994. The Cadjebut Deposit as an example of Mississippi Valley-type mineralization on the Lennard Shelf, Western Australia; single episode or multiple events?; Economic Geology, v. 89, p. 450–466.

Trofanenko, J., Williams-Jones, A.E., Simandl, G.J., and Migdisov, A.A., 2016. The nature and origin of the REE mineralization in the Wicheeda carbonatite, British Columbia, Canada; Economic Geology, v. 111, p. 199–223.

Vandeginste, V., Swennen, R., Gleeson, S.A., Ellam, R.M., Osadetz, K., and Roure, F., 2007. Geochemical constraints on the origin of the Kicking Horse and Monarch Mississippi Valley-type lead-zinc ore deposits, southeast British Columbia, Canada; Mineralium Deposita, v. 42, p. 913–935.

Veizer, J., Ala, D., Azmy, K., Bruckschen, P., Buhl, D., Bruhn, F., Carden, G.A.F., Diener, A., Ebneth, S., Godderis, Y., Jasper, T., Korte, C., Pawellek, F., Podlaha, O.G., Strauss, H., 1999. $^{87}Sr/^{86}Sr$, $\delta^{13}C$ and $\delta^{18}O$ evolution of Phanerozoic seawater; Chemical Geology, v. 161, p. 59–88.

Warren, J., 2000. Dolomite: occurrence, evolution and economically important associations; Earth Science Reviews, v. 52, p. 1–81.

Wilkinson, J.J., 2014. Sediment-hosted zinc-lead mineralization: Processes and perspectives; *in*: Geochemistry of Mineral Deposits: Treatise on Geochemistry (second edition), (ed.) S.D. Scott; Elsevier, v. 13, p. 219–249.

Williams-Jones, A.E., Migdisov, A.A., Samson, I.M., 2012. Hydrothermal mobilisation of the rare earth elements—a tale of "Ceria" and "Yttria"; Elements, v. 8, p. 355–360.

Wilson, E.N., Hardie, L.A., and Phillips, O.M., 1990. Dolomitization front geometry, fluid flow patterns, and the origin of massive dolomite: The Triassic Latemar buildup, northern Italy; American Journal of Science, v. 290, p. 741–796.

Yao, Q. and Demicco, R.V., 1997. Dolomitization of the Cambrian carbonate platform, southern Canadian Rocky Mountains: Dolomite front geometry, fluid inclusion geochemistry, isotopic signature and hydrogeologic modelling studies; American Journal of Science, v. 297, p. 892–938.

Zhu, L., 2000. An isotopic and fluid inclusion study of the Rock Canyon Creek, Fluorite-REE deposit, southeastern British Columbia; MSc thesis, University of Windsor, Windsor, Ontario, 114 p.

Three-dimensional forward modelling and inversion of magnetotelluric data using unstructured meshes for understanding realistic geological systems: method development, algorithms and model construction for the Lalor deposit, Manitoba

S.M. Ansari, J.A. Craven and E. Schetselaar

Geological Survey of Canada, 601 Booth Street, Ottawa, Ontario K1A 0E8

Abstract

The work presented here covers three major branches of geophysical prospecting including the development of model construction routines for realistic subsurface structures, forward modelling and magnetotelluric inversion strategies. Using a combination of tools, a routine is developed that produces a sealed model using tessellated geological surfaces representing lithostratigraphic contacts between rock units of the Lalor VMS deposit. This model is suitable for generating volumetric tetrahedral meshes required for mesh-based modelling and inversion of geophysical data. A finite-element based forward modelling technique is developed that discretizes the magnetotelluric problem on unstructured tetrahedral meshes. These meshes are suitable for producing realistic complex-shaped features. Magnetotelluric responses for the Lalor model are successfully calculated. A model space minimum-structure inversion is developed that is based on the iterative Gauss-Newton approach using sensitivity matrix-vector products calculated implicitly by finite-element based forward and pseudo-forward solutions.

Introduction

Geophysical modelling and imaging of geological targets, such as volcanogenic massive sulphide (VMS) and porphyry deposits, can be challenging due to lens-shaped orebodies and the complex structures of the host rocks. For such complex models, it is important to implement suitable geophysical modelling tools to capture the subtle geophysical responses associated with irregularities in the model. Three-dimensional (3D) inversion of magnetotelluric (MT) data has undergone significant improvements in the past few decades (*see* Miensopust et al., 2013). The goal of MT inverse modelling is to infer information regarding the variations in the Earth's conductivity using electromagnetic fields measured at the surface. The discretization in the forward modelling problem and subsequently the parametrization of the conductivity variations in the inversion is traditionally performed using rectilinear grids. Orthogonal meshing uses simple workflows for the discretization and numerical solution, but it produces inaccurate responses for real-life complex geological targets and models that include topography. Unstructured meshes offer the potential to better reproduce irregular geometries and can accommodate efficient refinement schemes (*see* Ansari et al., 2017, and Dunham et al., 2018). Iterative, enhanced refinement of unstructured meshes enable more accurate response estimations and can facilitate a relatively detailed inversion model.

Using natural electromagnetic fields, MT traces conducting subsurface structures by monitoring a wide range of electric and magnetic field signals related to both near surface conductive features, as well as features from deeper within the crust and mantle. For mineral deposits, MT responses are sensitive to the high electrical conductivity of buried sulphide ore zones, and also the intermediate conductivity of disseminated sulphides (e.g. Zhang and Chouteau, 1991; Bournas et. al., 2013). The forward modelling work presented here examines the range of MT frequencies that are appropriate for deposits modelling and discusses how to design a survey that will detect the lateral extent of a small-sized ore deposit relative to the MT skin depth.

More reliable understanding of MT responses from complex structures require correct allocation of electrical resistivity for each geological unit. By combining a variety of geological and geophysical data, well-constrained geological models can be constructed that also include detailed electric resistivity models. This report summarizes the principles of the inversion methodology and outlines how to conduct MT forward modelling using unstructured meshes.

Model construction using unstructured grids

This study used triangulated surfaces residing in 3D space to represent the boundaries between rock units. When undertaking geological modelling, triangular surfaces can conform to a wide range of geometries and be adaptively or locally refined in the regions of interest for accuracy and resolution (Caumon, 2010). The input model for grid-based geophysical modelling

Corresponding author: Seyedmasoud Ansari (seyedmasoud.ansari@canada.ca)

Ansari, S.M., Craven, J.A., and Schetselaar, E., 2019. Three-dimensional forward modelling and inversion of magnetotelluric data using unstructured meshes for understanding realistic geological systems: method development, algorithms and model construction for the Lalor deposit, Manitoba; *in* Targeted Geoscience Initiative: 2018 report of activities, (ed.) N. Rogers; Geological Survey of Canada, Open File 8549, p. 217–234. https://doi.org/10.4095/313656

in 3D focuses on the variation of physical properties (i.e. electrical conductivity in the case of MT) in a volumetric space subdivided into individual polyhedra. Among these, tetrahedral elements naturally conform to the triangular tessellations of the geobodies, and if distributed in an unstructured manner, are capable of accurately constructing complexly shaped geometries, such as topographic undulations or curvilinear ore bodies. Developing routines for the construction of these models is an on-going challenge (e.g. Pellerin et al., 2014; Zehner et al., 2015). Given the geological complexity of the herein examined Lalor zone (Newton and Vowles, 2017), it was necessary to develop a set workflow to construct an input geological model suitable for MT modelling.

The Lalor VMS deposit, located in the Snow Lake area, Manitoba, is hosted by Eastern Flin Flon greenstone belt volcanic rocks (Schetselaar et al., 2017). Figure 1 shows a northeast to southwest cross-section of the mine camp (Bailes et al., 2013). The Chisel-Lalor structural contact (CHLSC in Fig. 1), is interpreted as a thrust fault separating the Lower and Upper Chisel sequences (Bailes and Galley, 2007). The Lalor deposit is northeast-oriented and hosted within the Lower Chisel sequence, occurring in the footwall of the Chisel thrust at a depth between 570 and 1160 m (Schetselaar et al., 2017). Chisel thrust footwall rocks have undergone intense hydrothermal alteration from the Richards subvolcanic intrusion, with the immediate footwall to the VMS transformed into granoblastic accumulations of schists and gneisses (Bailes et al., 2016). Mineralization consisting of pyrite, pyrrhotite, sphalerite, chalcopyrite and galena, occurs as relatively thin lenses due to the ductile deformation (Caté et al., 2013). For a model to accurately represent the deposit must take into account the complex sequence of folding, faulting and alteration impacting the footwall rocks (Fig. 1).

Geological modelling of the area was undertaken by Schetselaar (2013) using Paradigm's 3D SKUA/GOCAD® (SKUA: structural knowledge universal approach), in particular its structure and stratigraphy (SnS) workflow, that led to a curvilinear grid of generalized lithostratigraphic units. To generate a 3D grid for our geophysical model, we used 3D models of individual surfaces as input in the SKUA's SnS workflow. The original triangulated surfaces used to represent the fault network is shown in Figure 2a. In this model, the triangles are discontinuous at the shared contact lines between the geobodies. Using the SnS workflow the corresponding chronostratigraphic column, volume of interest and fault network are constructed. The final product extracted from SKUA (Fig. 2b) resamples all the triangular surfaces such that the geobodies are welded properly at the contact lines.

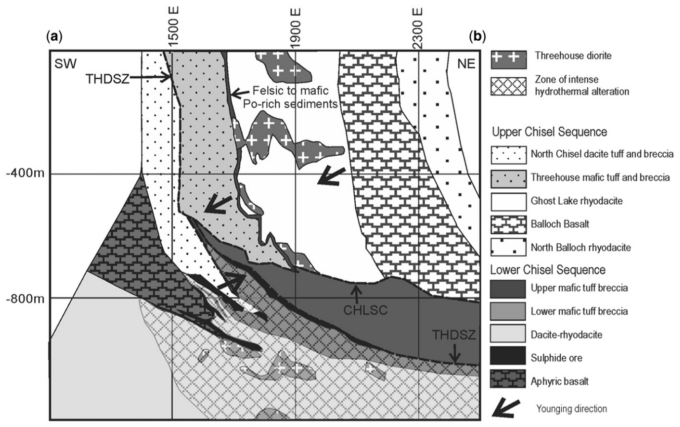

Figure 1. A southwest to northeast cross-section of the geological map of the Lalor volcanogenic massive sulphide deposit and host rocks (*after* Bailes et al., 2013). CHLSC = Chisel-Lalor structural contact; THDSZ = Threehouse ductile shear zone.

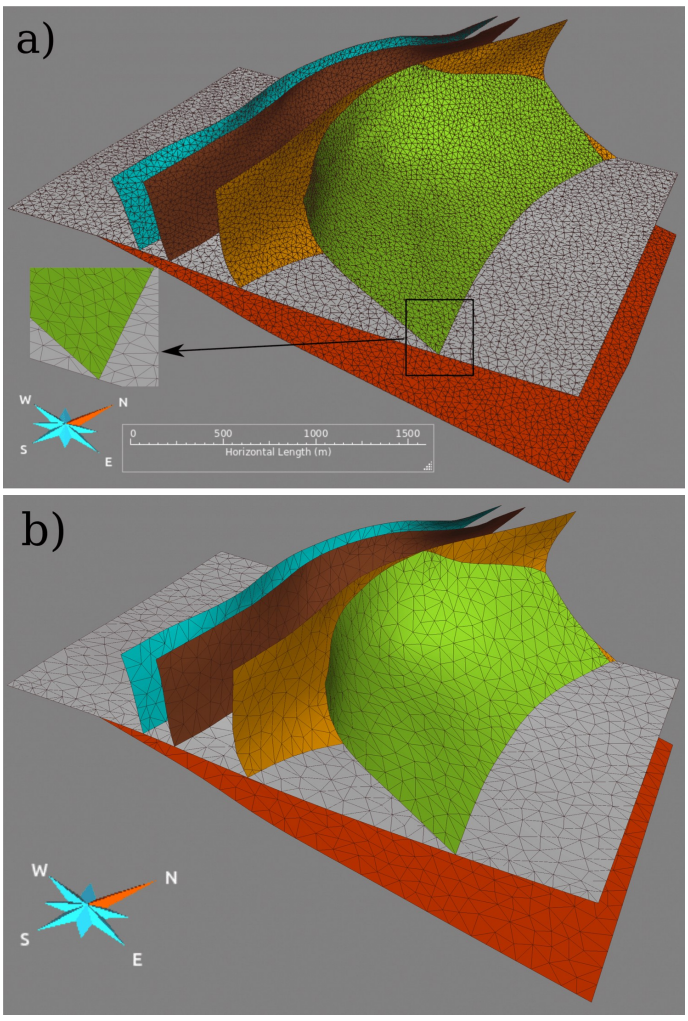

Figure 2. Workflow of sewing geobodies in SKUA-GOCAD. a) Original 3D lithostratigraphic surfaces model in SKUA; small subimage extracted to the left shows triangular discontinuities at the shared boundary between the two bodies. b) The same view but with all surfaces resampled in the SnS workflow of SKUA subject to a user-defined resolution; the triangles are properly sewn at all the contacts between geobodies.

Proceeding with the 3D grid-model construction process, the RINGMesh platform (Pellerin et al., 2017) is used to extract the triangular node- and cell-based data from the SKUA tetrahedral mesh model (Fig. 3a). Next, FacetModeller (Lelièvre et al., 2018) is used to add padding regions around the tetrahedral mesh (Fig. 3b). The padding region in the model is required for the numerical modelling of MT (*see* later). The output from FacetModeller is then introduced to the meshing library TetGen (Si, 2007), to give a quality volumetric mesh populated by tetrahedral cells (Fig. 3c, d).

Forward modelling of magnetotelluric data

Finite-element (FE) frequency domain forward modelling schemes have been the subject of active research over the past decade (e.g. Puzyrev et al., 2013; Ansari et al., 2017). The methodology presented herein is a new potential formulation that uses a smaller system of equations and is adjusted for MT. In the frequency domain and nonquasi-static situation, MT fields are functions of angular frequency (ω) and position ($\mathbf{r}$), and obey Faraday's law of induction and Ampère's law:

$$\nabla \times \boldsymbol{E} + i\omega\mu\boldsymbol{H} = 0 \quad (1)$$

$$\nabla \times \boldsymbol{H} - (\sigma + i\varepsilon\omega)\boldsymbol{E} = 0 \quad (2)$$

Herein, $\boldsymbol{E}$ is the electric field, $\boldsymbol{H}$ is the magnetic field intensity, $\sigma = \sigma(\boldsymbol{r})$ is the electrical conductivity, ε is the electric permittivity and μ is the magnetic permeability that is assumed equal to that of free space for Earth's materials. A combination of these equations gives a partial differential equation, the

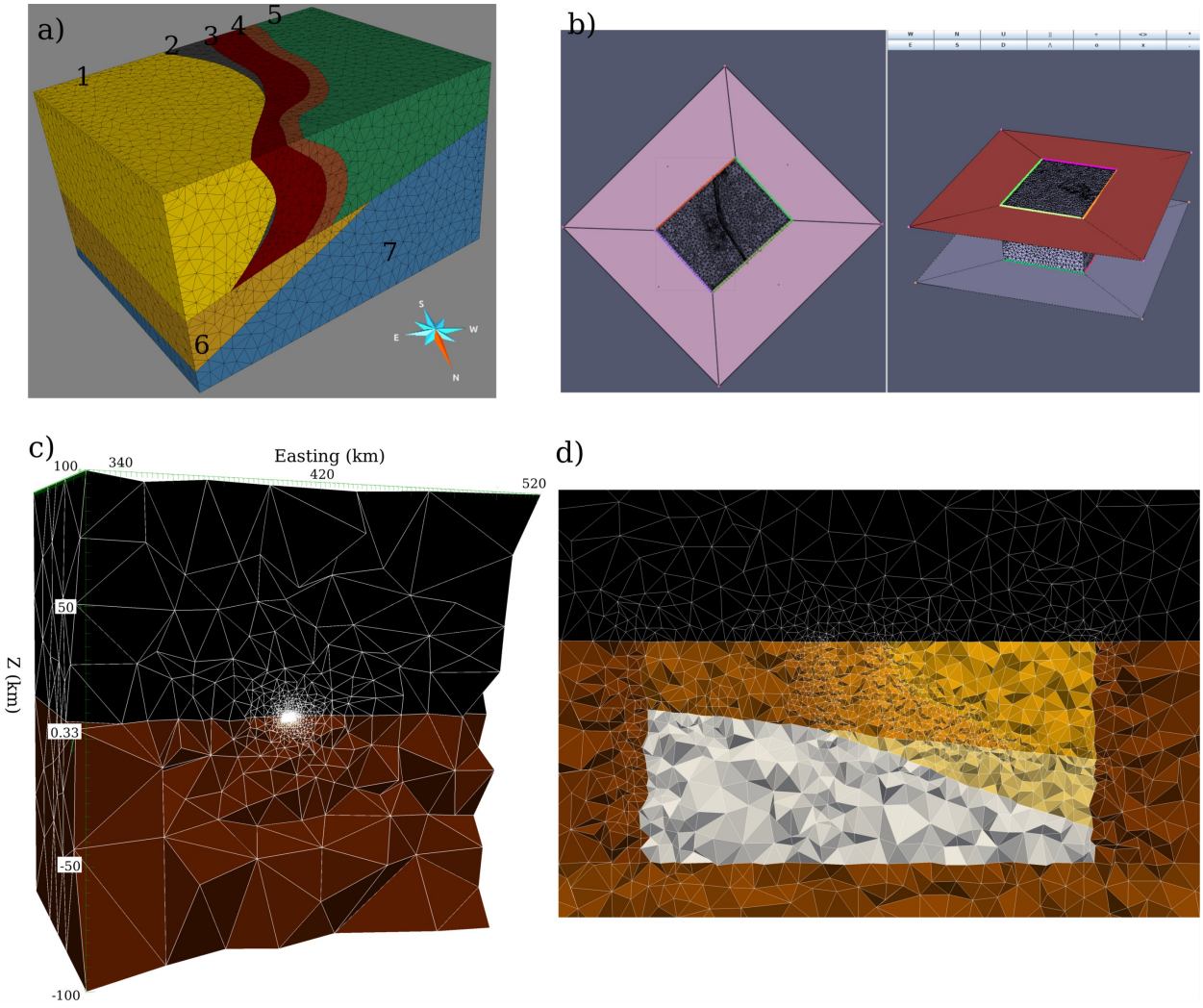

Figure 3. The process of producing a 3D tetrahedral mesh for forward modelling. a) Grid model produced in SKUA-GOCAD showing the regions between geobodies. b) View from FacetModeller showing the process of attaching the tetrahedral mesh to an internal padding region. c) Section from the 3D mesh used for the MT forward modelling. d) Zoomed-view from the central part of the 3D tetrahedral mesh showing the lithostratigraphic units and faults, background and air.

Helmholtz E-field equation, that is the conventional system to solve for electric (and magnetic) field(s):

$$\nabla \times \nabla \times \boldsymbol{E} + i\omega\mu\sigma\boldsymbol{E} - \omega^2\,\mu\epsilon\boldsymbol{E} = 0 \quad (3)$$

The approach taken here, uses the decomposition of the electric field ($\boldsymbol{E}$) into vector ($\boldsymbol{A}$) and scalar (ϕ) potentials to solve the system of equations:

$$\boldsymbol{E} = -i\omega\boldsymbol{A} - \nabla\phi \quad (4)$$

Incorporating equation (3) into equation (4) the following partial differential equation is derived for the vector and scalar potentials:

$$\nabla \times \nabla \times \boldsymbol{A} + (i\omega\mu\sigma - \omega^2\mu\epsilon)\boldsymbol{A} + (\mu\sigma + i\omega\mu\epsilon)\nabla\phi = 0 \quad (5)$$

This equation is squared with the following Coulomb gauge condition, which is declared as a second equation, to obtain unique vector and scalar potentials:

$$\nabla.\boldsymbol{A} = 0 \quad (6)$$

The goal is to solve equations (5) and (6) subject to imposing the MT boundary condition on the introduced physical domain. The electric field vector and scalar potentials relate to inductive and galvanic modes and their relative contributions to the MT response. Induction phenomena is quantified through the vector potential, providing insight about the vortex-type currents generated by the external time-varying magnetic field. An abstract meaning of the galvanic concept in MT is the background telluric currents that flow in the conducting host and channels into conductive targets or deflects around resistive targets. It is the secondary goal of this study to image these effects for realistic 3D geological targets. Concerning the enforcement of the MT boundary conditions for the $\boldsymbol{A}$ - ϕ system (equations (5) and (6) together) the tangential component of $\boldsymbol{A}$ and the value of ϕ were quantified by conducting 1D and 2D solutions on the outer boundaries of the domain. Here the system of equations for all 1D, 2D and 3D problems are discretized using the finite-element (FE) approach.

Finite-element discretization

The solution of the partial differential equations using the FE method is based on variational principles or weighted residuals (Monk, 2003; Jin, 2014). Here we used the latter that minimizes the weighted norms of the residuals in an average sense, in particular replacing the exact partial differential equations with approximate equations, their weak form, over the entire physical domain. This is done by orthogonalizing the residuals of equations (5) and (6) with relevant weight functions leading to the following equations:

$$\int_\Omega (\nabla \times \mathbf{W}).\left(\nabla \times \widetilde{\boldsymbol{A}}\right)\mathrm{d}\Omega + i\omega\mu\int_\Omega \sigma\mathbf{W}.\widetilde{\boldsymbol{A}}\mathrm{d}\Omega - \omega^2\mu\int_\Omega \epsilon\mathbf{W}.\widetilde{\boldsymbol{A}}\mathrm{d}\Omega + \mu\int_\Omega \sigma\mathbf{W}.\nabla\widetilde{\varphi}\mathrm{d}\Omega + i\omega\mu\int_\Omega \epsilon\mathbf{W}.\nabla\widetilde{\varphi}\mathrm{d}\Omega = \int_{\Gamma+\partial K} \mathbf{W}\times\left(\nabla\times\widetilde{\boldsymbol{A}}\right).\boldsymbol{n}ds \quad (7)$$

$$\int_\Omega \nabla v.\widetilde{\boldsymbol{A}}\mathrm{d}\Omega = \int_{\Gamma+\partial K} v[\boldsymbol{n}.\widetilde{\boldsymbol{A}}]ds \quad (8)$$

Here $\mathbf{W}$ and v are vector and scalar weight functions respectively that appear as the coefficients in the expansion of the original $\boldsymbol{A}$ and ϕ into their relevant approximations $\widetilde{\boldsymbol{A}}$ and $\widetilde{\varphi}$. Also, $\mathbf{n}$ is the outward normal vector, Ω stands for the volume of the domain, and ∂K and Γ represent the internal and outer boundaries of the domain. Applying the FE method to the above equations requires dividing the physical domain into a grid of smaller subdomains, that in this case are unstructured tetrahedral elements. Also used are linear edge and nodal basis functions for vector and scalar potentials respectively (Whitney, 1957; Silvester and Ferrari, 1983). By using these polynomial expansions and also adopting the Galerkin variant of the FE method closed-form formulas are calculated for the integrals in the above equations. The surface integral terms have also been calculated on the side and top boundaries of the computational domain. In order to solve for the $\widetilde{\boldsymbol{A}}$ and $\widetilde{\varphi}$ equations (7) and (8) are coupled into the following matrix form:

$$\begin{pmatrix} \boldsymbol{S} + i\omega\mu\,\boldsymbol{M} - \omega^2\,\mu\,\mathbf{N} & \mu\,\boldsymbol{F} + i\omega\mu\,\boldsymbol{G} \\ \boldsymbol{H} & \mathbf{0} \end{pmatrix}\begin{pmatrix} \widetilde{A_e} \\ \widetilde{\varphi_n} \end{pmatrix} = \begin{pmatrix} S_{\Gamma_{air}} + S^{A,2D}_{\Gamma_{sides}} \\ S^{\varphi,2D}_{\Gamma_{sides}} \end{pmatrix} \quad (9)$$

The entries in bold are the inner product integrals on the left of equations (7) and (8), and are associated with the interaction of edge and nodal elements within each tetrahedral element. The term $S_{\Gamma_{air}}$ deals with the surface integral term on the right-hand side of equation (7) that is calculated for the two polarization mode on the topmost boundary of the mesh. It is important to mention that, at this boundary, a constant real value is considered the magnetic as a result of hyper-resistive magnetosphere acting as the MT source. Approximations of the other two terms on the right-hand side of equation (9), $S^{A,2D}_{\Gamma_{sides}}$ and $S^{\varphi,2D}_{\Gamma_{sides}}$ are obtained by the imposition of the 2D boundary conditions for MT and solving the relevant numerical problems at the side boundaries. The solution of this system gives the value of vector ($\widetilde{A_e}$) and scalar ($\widetilde{\varphi_n}$) potentials for edges and nodes, respectively. The system of equations here is solved using the direct solver MUMPS (Multi-frontal Massively Parallel Solver; Amestoy et al., 2001, 2006). Despite consuming large computing memory space, MUMPS efficiently solves the system of equations subject to activating the multi-processing (OpenMP) architecture. The pre-solution components of the numerical codes written here compute the FE inner-product integrals of equation (9) also in a multi-threaded fashion.

Solving equation (9) for the vector and scalar potentials gives rise to calculating the electric and magnetic field at each point in the computational domain. Using equation (4) the approximate vector and scalar potentials are interpolated to the electric field (and magnetic field using $= \mu\nabla\times\boldsymbol{A}$) at each observation location. The primary MT response functions that include impedances and transfer functions (tipper vector) are then calculated using E_x, E_y, H_x, H_y and H_z components. The

entries of the impedance tensor were also used to calculate the apparent resistivity and phases at each observation location.

Modelling and computations for Lalor

Prior to applying forward modelling, the tetrahedral mesh is populated with relevant electrical conductivities. For the Lalor study, we have access to a number of lithology and resistivity drillhole logs. Rock units are classified into 15 groups, including the ore zone. Mean values were extracted from the resistivity logs; Figure 4 shows the distribution plots for a number of rock types. The mean value of the volcanic/volcaniclastic rocks vary within a relatively narrow resistive range between 1000 and 10 000 Ω m.

It is apparent from this data that the hanging wall units are relatively more resistive than those of footwall units. In order to produce the ore shells in the mesh we introduced a cluster of points associated with the surface of the shells to the mesh generator library. Subject to imposing suitable quality constraints the mesh generator refines the mesh at depth where the ore bodies are seated. A raster-like representation of the ore shells is then constructed using a linear interpolation scheme by which the conductivity in each tetrahedral cell is assumed a 3D linear function. Assuming the known value of conductivities at each node (i.e. from the conductivity of each region), systems of equations were solved for each tetrahedron and then an average conductivity value is obtained at the centre of each cell. Figure 5 shows the progression of placing the ore shells in the unstructured gird.

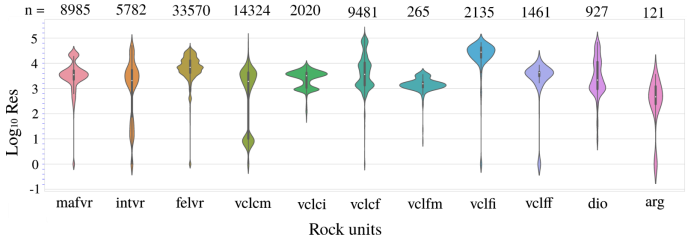

Figure 4. Log resistivity kernel distribution plots for the major rock types of the Lalor mine camp. The number of samples for each rock is given using the numbers on the top. The vertical bold lines show the resistivity distribution of the second and third quartiles and the white circle shows the mean value of resistivity (arg – argillite; dio – diorite; felvr – felsic volcanic; intvr – intermediate volcanic; mafvr – mafic volcanic; vclcm – coarse grained mafic volcaniclastic; vclci – coarse grained intermediate volcaniclastic; vclcf – coarse grained felsic volcaniclastic; vclfm – fine grained mafic volcaniclastic; vclfi – fine grained intermediate volcaniclastic; vclff – fine grained felsic volcaniclastic) .

The mesh used for the forward modelling consists of two

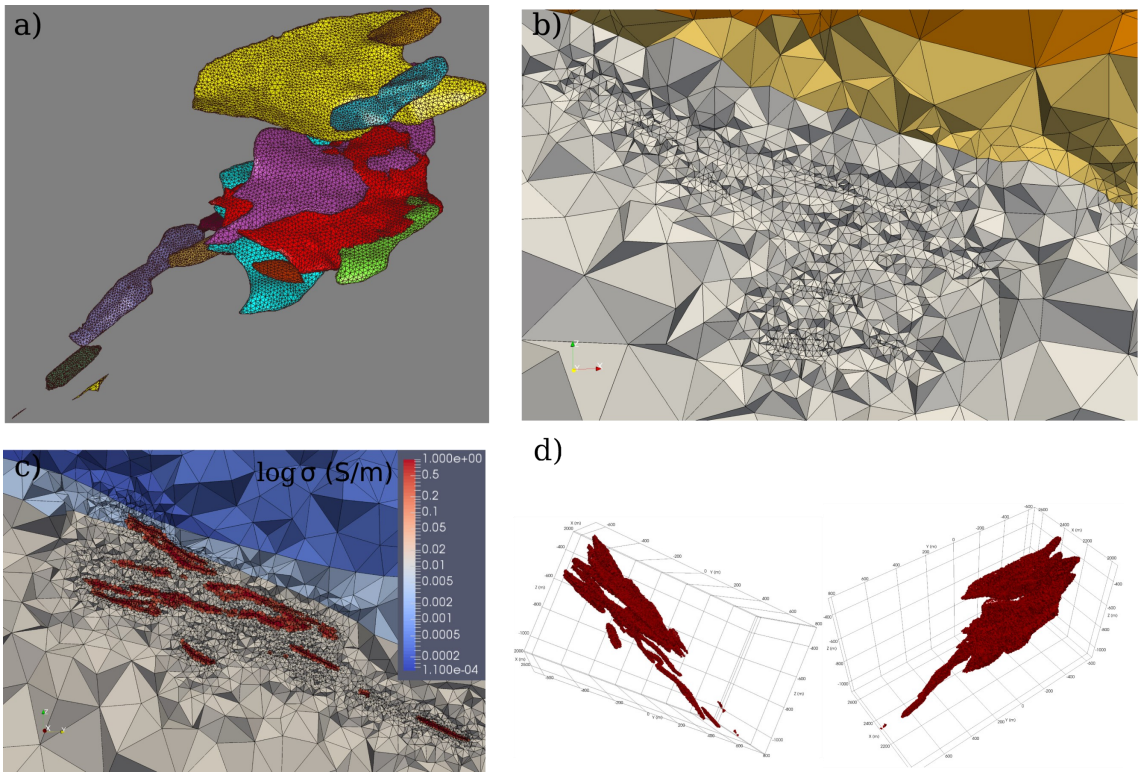

Figure 5. Workflow to include the complex structure of the ore lenses into the tetrahedral mesh. a) Original surfaces of the ore shells (Hudbay Minerals Ltd., pers. comm., 2014). b) Zoomed section from depth showing the refined region generated after inserting vertices from the ore shells. c) Zoomed-in section showing highly conductive tetrahedral of ore produced after interpolation. d) Two opposing views illustrating the reproduced 3D geometries of the ore bodies.

padding regions. The first of these (internal padding zone) extends the Lalor model by 5 km horizontally and restricts it vertically to the base of the Lalor model (Fig. 3a). An average conductivity of 0.000166 S/m is used for this region, based on an assumed volcanic nature of the background rocks. In terms of choosing the conductivity values for the second padding zone that includes the region below the ore zone and also outside the internal padding zone, two scenarios are being tested here. 'Scenario 1' used an average conductivity of volcanic rocks (0.000166 S/m), whereas 'scenario 2' employed a more conductive value of 0.01 S/m. The MT responses of models with these conductivity combinations were examined for a range of frequencies from 5.49 x 10-3 to 15 000 Hz. Here the MT sites on the surface are chosen based on the original survey undertaken by Quantec Geosciences (report by Martinez and Hearst, 2009). As shown in Figure 6a the mesh is refined at the individual sites on the surface by inserting regular tetrahedral elements. The mesh used here consists of 995 614 cells, 159 857 nodes and 115 607 edges. The MUMPS solver required 70 Gb of memory to solve the system of equations for this mesh. For each of the 47 frequencies used here the computation has taken an average time of 900 s.

For both scenarios 1 and 2, Figure 7 shows the behaviour of the off-diagonal component of the impedances at a central site above the deposit (circled in red in Fig. 6a). Considering the general trend of the impedance curves the choice of the resistivity for the external padding zone (i.e. below the ore zone), influences the data towards the long periods (e.g. compare panels (a) and (e)). It is also seen here that the impedance data shows very little difference to a calculated model without ore shells. We also included the data for a configuration where the impedance is calculated for a fixed magnetic field that comes from a remote station. The impedance data for this configuration (shown in triangles in Fig. 7) begins to deviate from those of regular impedances for periods less than 0.1 s prior to becoming noisy for the lower periods. The reason for this noisiness is because for higher frequencies the lateral skin depth begins to reduce and as a result the magnetic field at the remote site becomes irrelevant to the electric field at the central site. The corresponding curves of the apparent resistivity and phase data for this example are shown in Figure 8. It is observed here that for scenario 2, where a relatively conductive block is considered below the ore zone, the apparent resistivity data start to become slightly sensitive to the ore body (see panels (e) and (f) in Fig. 8) at periods greater than 0.05 s. It is also seen that the phase data for both scenarios elevate a hint of the ore shells at slightly high to intermediate period ranges from 0.001 to 0.1 s. In terms of the data synthesized using the remote configuration both apparent resistivity and phase are similar for the long periods. The difference starts to become more obvious in the apparent resistivity data for periods less than 0.1 s. The phase data however is sensitive within a relatively broader period range. We have also calculated the magnetic transfer functions (tippers) along the three profiles shown in Figure 6a. Figure 9

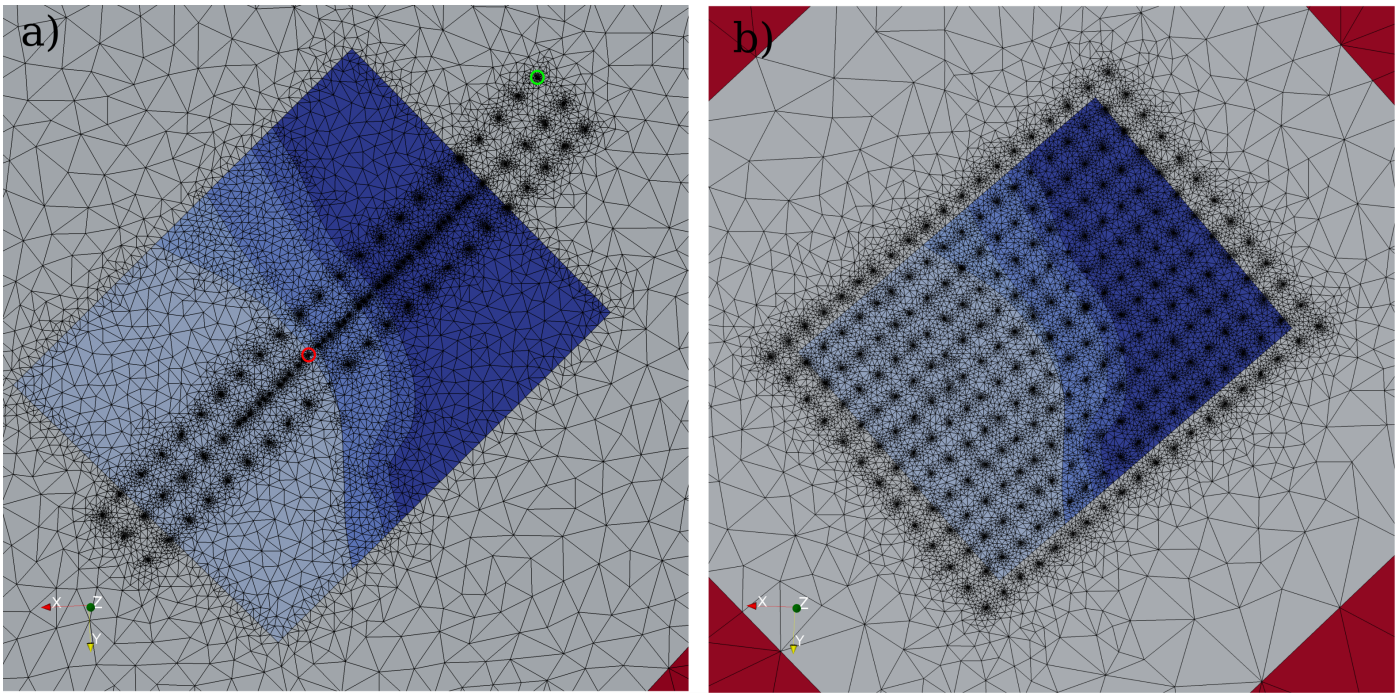

Figure 6. Horizontal views from the Earth surface showing the MT site locations over the Lalor deposit. a) Mesh refinement at MT sites for the three profile of observation. The circle in red represent the central site over approximately over the ore shells and the circle in green shows the remote site. b) Network of observation locations on the surface for the synthetic study in this paper. Grey and red coloured regions represent the internal and external padding zones, respectively.

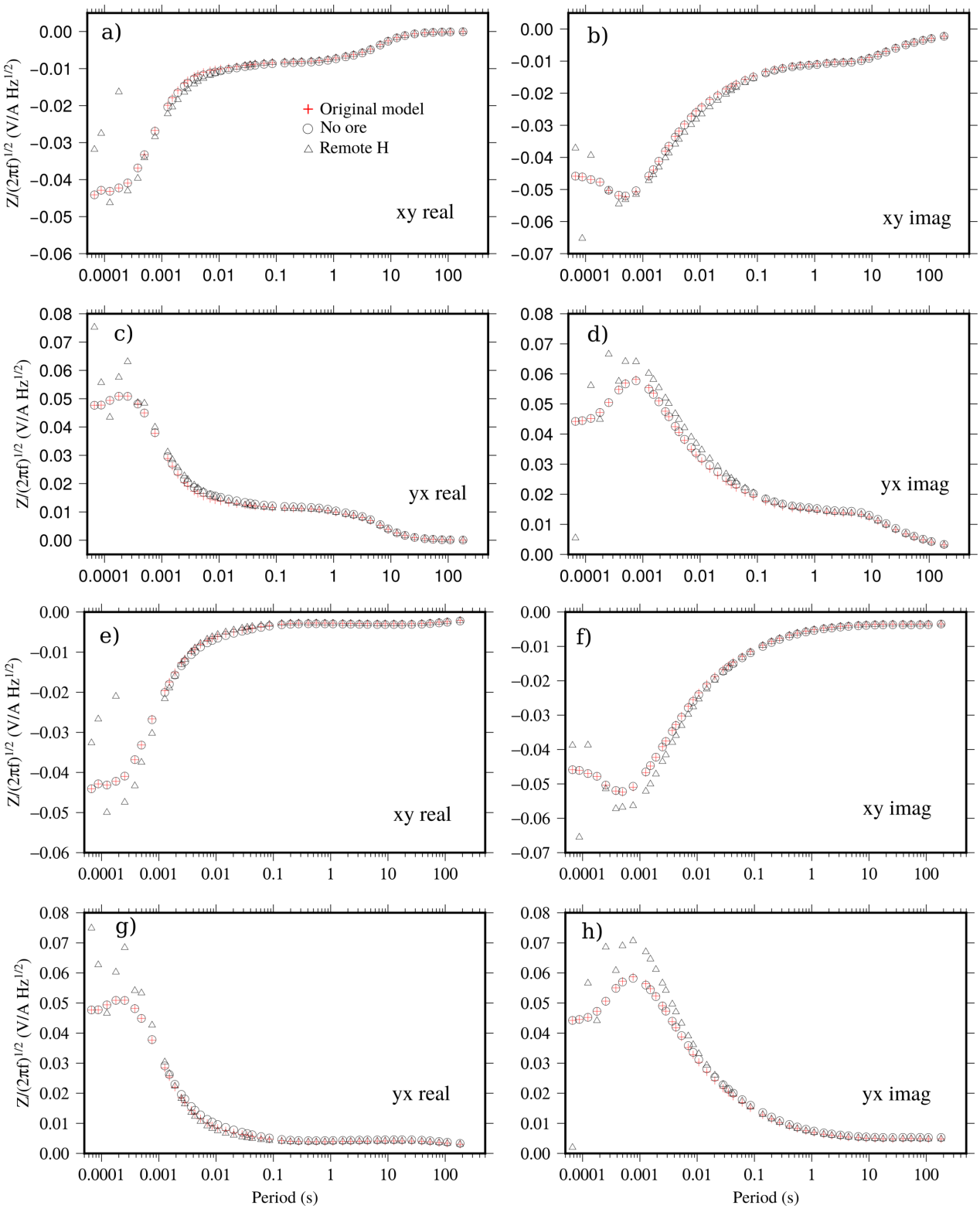

Figure 7. Impedance curves calculated at the central site for the two MT polarization modes (red circle in Fig. 6). The impedance is normalized by the square root of the angular frequency. The response for the original model that includes the fault network, layering and the ore shells is shown using cross symbols in red; the response for the same model but with no ore shells is shown using circles; the response again for the original model but for a configuration with H-fields coming from a remote site (circled in green in Fig. 6a) is shown using triangles. Panels (a) to (d) correspond to the data for a resistive padding zone (scenario 1) and panels (e) to (g) show the data for a more conductive padding zone (scenario 2).

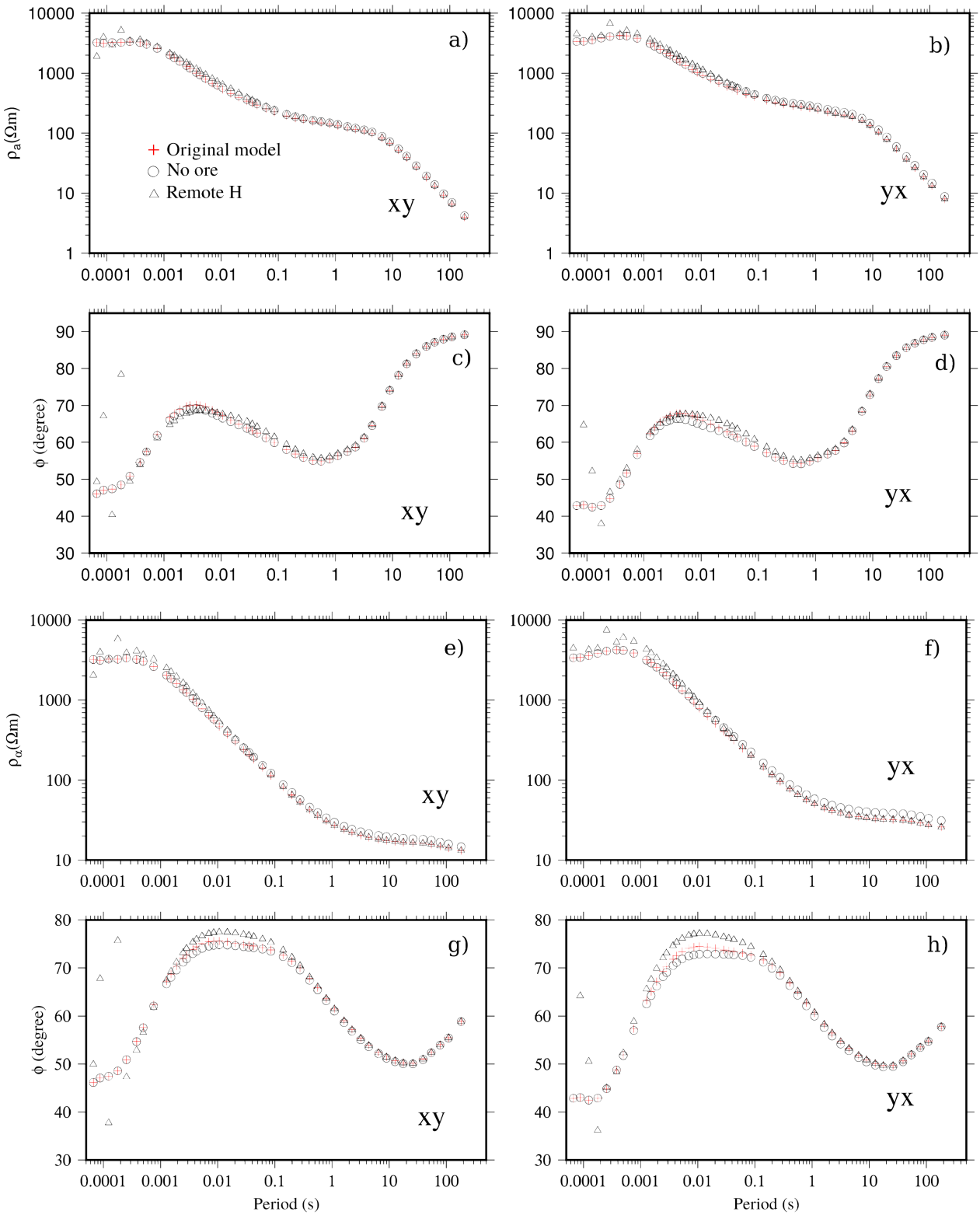

Figure 8. Curves of apparent resistivity and phase calculated at the central site (red circle in Fig. 6) for the two MT polarization modes. Panels (a) to (d) correspond to the data for a resistive padding zone (scenario 1) and panels (e) to (g) show the data for a more conductive padding zone (scenario 2).

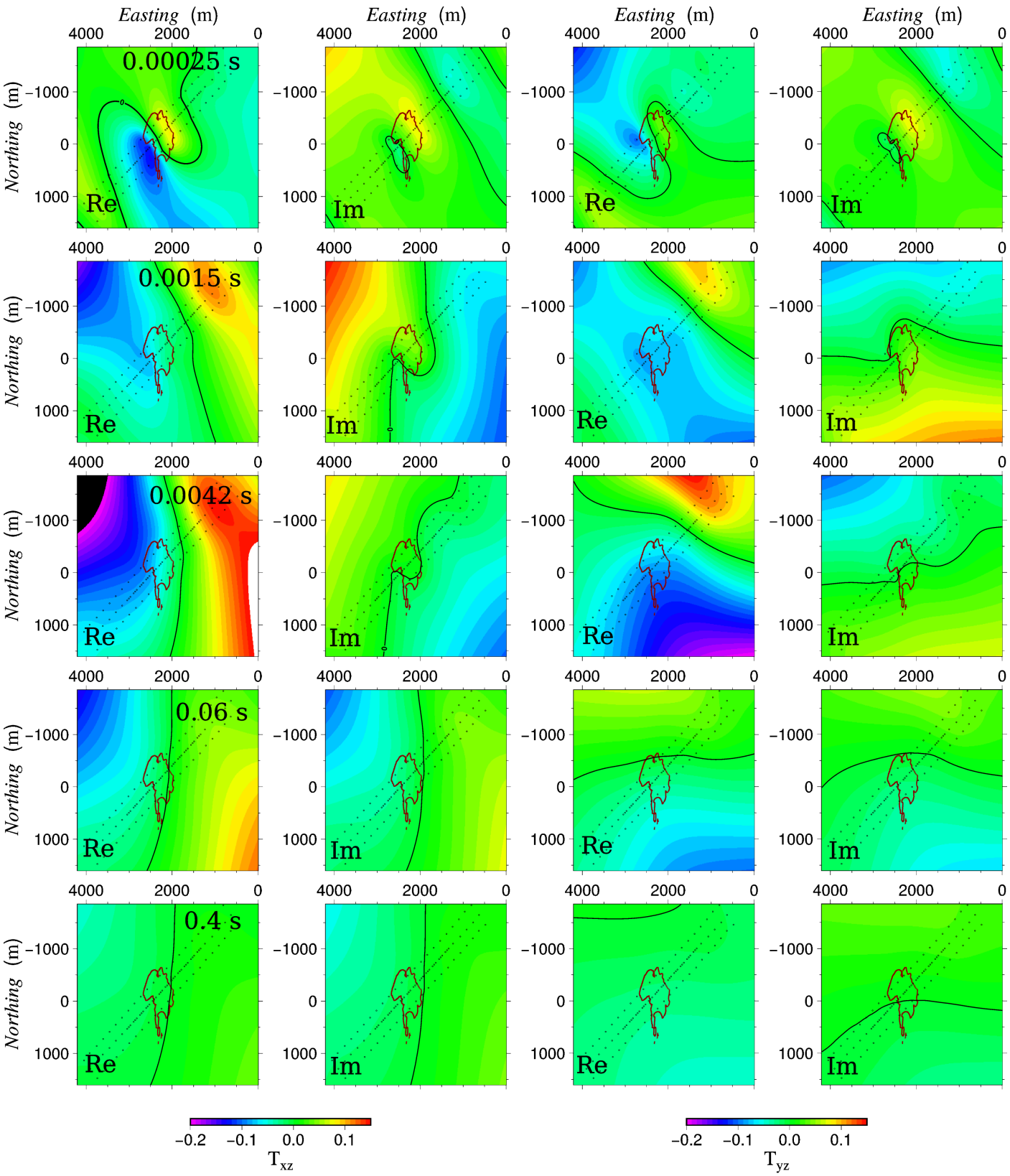

Figure 9. Contours of tipper vector for five periods for the original model that includes all conductivity information. Real and imaginary parts of the tipper for the xz and yz components are shown. Dots coloured in dark red show the projection of the outlines of the ore shells marked using the maximum and minimum lateral extends of all shells for a top view from the Earth surface.

shows a contour of tippers for five periods. Here the anomaly observed on the surface for the lowest period of 0.00025 s (highest frequency) shown, is thought to be coming from the geometry of the conductive ore zones (marked as regions 6 and 7 in Fig. 3a) at depth.

In order to investigate a relatively regional-type MT response of the Lalor model the data are calculated for a network of 260 observations on the surface (Fig. 6b). Again, in order to simulate accurate responses, the mesh is locally refined at the observation sites by inserting individual tetrahedrons. Figures 10 to 13 show surface contours of apparent resistivity and phase for the xy and yx modes over a range of periods. The results shown here follow scenario 2, where a relatively conductive block is considered below the ore zone, although similar results were also produced for scenario 1. Again, the data shown here represents the responses associated with the original model and also the background structural model with no ore shell included. It is apparent that the differences between the data (column three in Fig. 10, 11 for each period) is very small, and in particular the medium to short period (e.g. 0.14–182.14 s) responses from the entire conducting ore zone (regions 6 and 7 in Fig. 3) dominate, leading to a smeared-out and weak signal from the relatively more conductive ore shells. Phase data are indicative of more localized responses from the ore shells (Fig. 12, 13). Again, the synthesized data show similar behaviour for all periods, irrespective of the inclusion of conductive ore bodies in the model. As anticipated, the phase data demonstrates a relatively strong ore shell signature for a 0.01 s period (third column of Fig. 12, 13). This response diminishes for longer periods.

Inversion of MT data

The above process is optimized for MT forward modelling of VMS-style mineralization. In order to directly image the electrical conductivity of the subsurface materials (i.e. geologic structures and mineralization), inversion is required. The conventional approach for inversion is based on Tikhonov regularized optimization methods, where the solution is given by minimizing data misfit and model roughness with respect to conductivity. For MT inversion, this is a non-linear process that is treated by linearizing the problem by incorporating the Jacobian (sensitivity) matrix and approaching the solution through a least square iterative scheme (such as Gauss-Newton or Conjugate gradient). We adopted the Gauss-Newton iterative method, and used Krylov subspace methods for solving the matrix form of the inverse equation. An advantage of the use of Krylov subspace solver is that one does not need to explicitly store the Jacobian matrix in each Gauss-Newton iteration, but only calculate the product of the Jacobian matrix or its transpose with the requested vector. This is done implicitly using a sequence of forward and pseudo forward modelling solutions with the same coefficient matrices in the left side, but distinct right-hand side vectors. These solutions are done for multiple frequencies using the parallelized version of the direct solver MUMPS (Amestoy et al., 2006). This makes our algorithm efficient, as only one factorization of the coefficient matrix (for each frequency) is required for all these forward and pseudo-forward solutions. The details of the inversion algorithm, including its forward modelling engine, is presented below. The performance and accuracy of the algorithm is also tested against a published synthetic model.

The minimum-structure inversion method aims at finding a plausible spatial variation of physical properties (i.e. conductivity) in a meshed model through an optimization routine that minimizes an objective function coupling data misfit and model structure measures. The general form for this objective function is:

$$\phi = \phi_d + \lambda \phi_m \quad (10)$$

Where ϕ_d and ϕ_m are data and model objective functions, respectively, and λ is a trade-off parameter. In particular, the term ϕ_d is the measure of data misfit defined using the conventional sum-of-squares misfit:

$$\phi_d = ||\mathbf{W}_d(\mathbf{d}^{obs} - \mathbf{d})||^2 \quad (11)$$

Here, $\mathbf{d}^{obs}$ is the observed field or synthetic data, $\mathbf{d}$ is the predicted data calculated for the model $\mathbf{m}$ and $\mathbf{W}_d$ is a diagonal weighting matrix with entries attributed to the reciprocals of the standard deviation of the noise for each data point. In equation (10) ϕ_m parametrizes a measure of the model structure, using 2-norm misfit terms:

$$\phi_m = \alpha_s||\mathbf{W}_s(\mathbf{m} - \mathbf{m}^{ref})||^2 + \alpha_m||\mathbf{W}_m\boldsymbol{m}||^2 \quad (12)$$

Here the first term on the right-hand side characterizes the closeness of the model ($\boldsymbol{m}$) to the reference model ($\mathbf{m}^{ref}$). Also, $\mathbf{W}_s$ is a diagonal weight matrix amounting for the degree of this closeness. The second term of the right-hand side controls the smoothness of the model through a choice of $\mathbf{W}_m$ matrix; for instance, an approximation of the conductivity gradient between neighbouring cells in the grid. Here also, α_s and α_m are scalar parameters. The coefficient λ in equation (10) is a trade-off parameter that is responsible for balancing the contributions from the data and model objective terms. The synthetic data for a particular model, $\mathbf{d}$ in equation (11), is calculated through a forward modelling procedure. This is implemented here using a finite-element solution to the conventional E-field equation (equation (3) above). The electric field computed after solving this equation is used to calculate the magnetic fields and subsequently the data vector $\mathbf{d}$ that contains both the diagonal and off-diagonal elements of the impedance tensor. Linearization of the non-linear equation forming the relationship between the data vector and the model parameter is done using the Taylor expansion series, for example, for the nth model:

$$\mathbf{d}^n = F(\mathbf{m}^{n-1}) + \mathbf{J}^{n-1}\delta\mathbf{m}^n \quad (13)$$

Where F is the forward functional (equation 3) and $\mathbf{J}$ is the Jacobian or sensitivity matrix, that is the derivate of the data vector with respect to the model parameter. The parameter $\delta\mathbf{m}^n$ is used to update the model using:

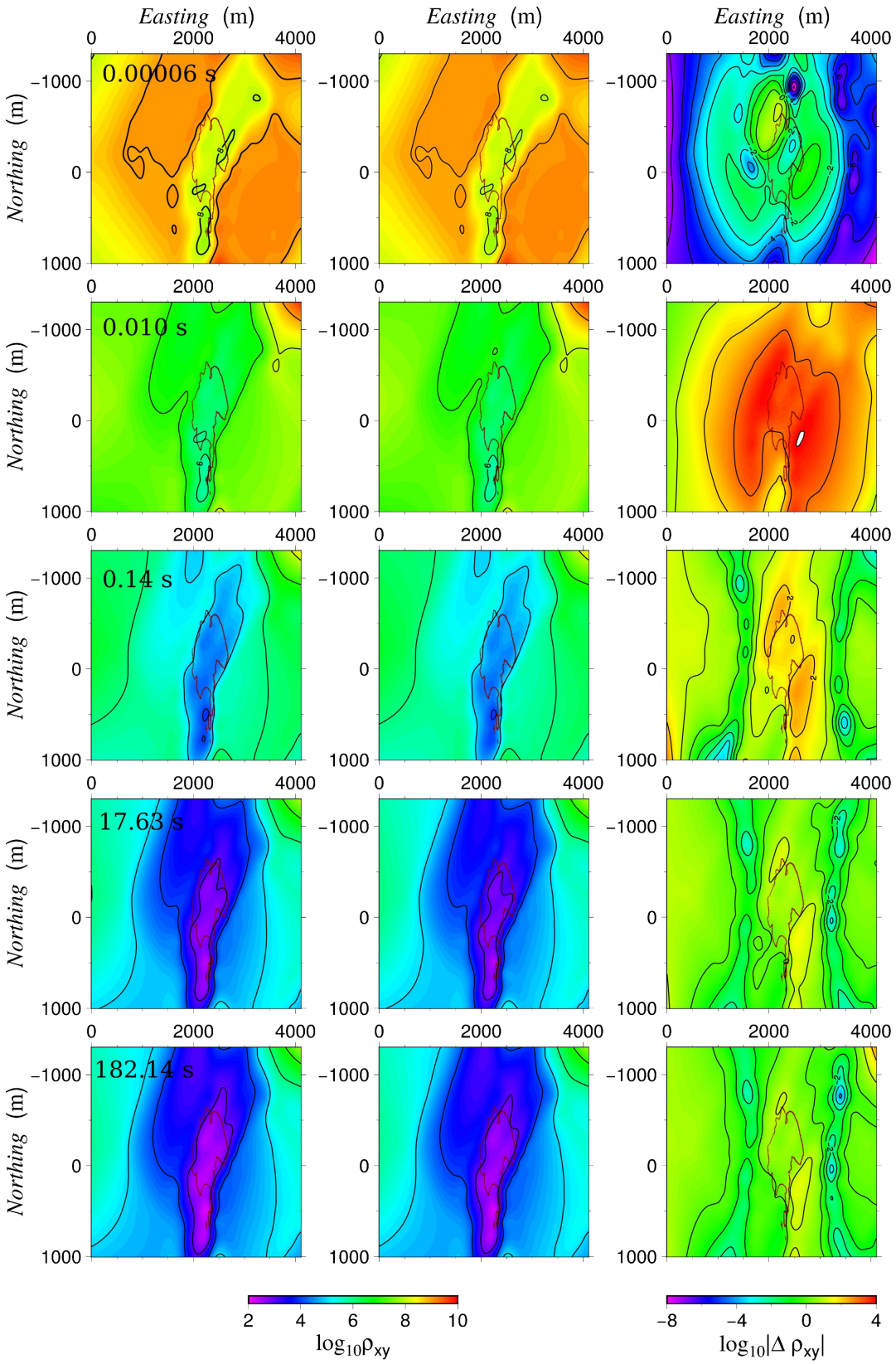

Figure 10. Contours of apparent resistivity for the xy polarization mode for 5 periods. The left panels show the responses of the original model with ore shells present. The middle panels show the corresponding responses without the ore shells. The right panels show the differences between the other two panels. Surface projections of the ore shell outlines, using the maximum and minimum lateral extents, are shown in dark red.

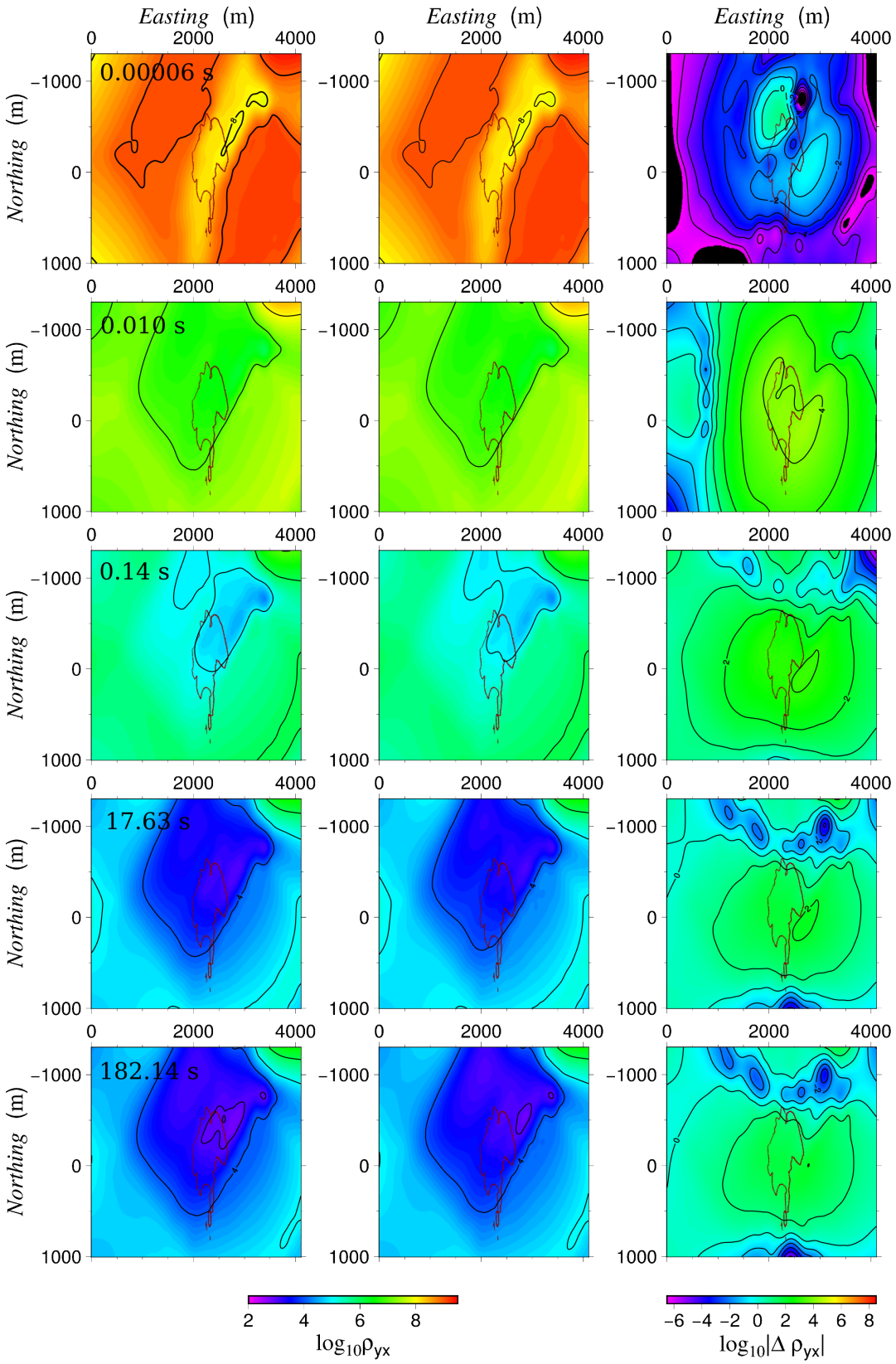

Figure 11. Contours of apparent resistivity for the yx polarization mode for 5 periods. The left panels show the responses of the original model with ore shells present. The middle panels show the corresponding responses without the ore shells. The right panels show the differences between the other two panels. Surface projections of the ore shell outlines, using the maximum and minimum lateral extents, are shown in dark red.

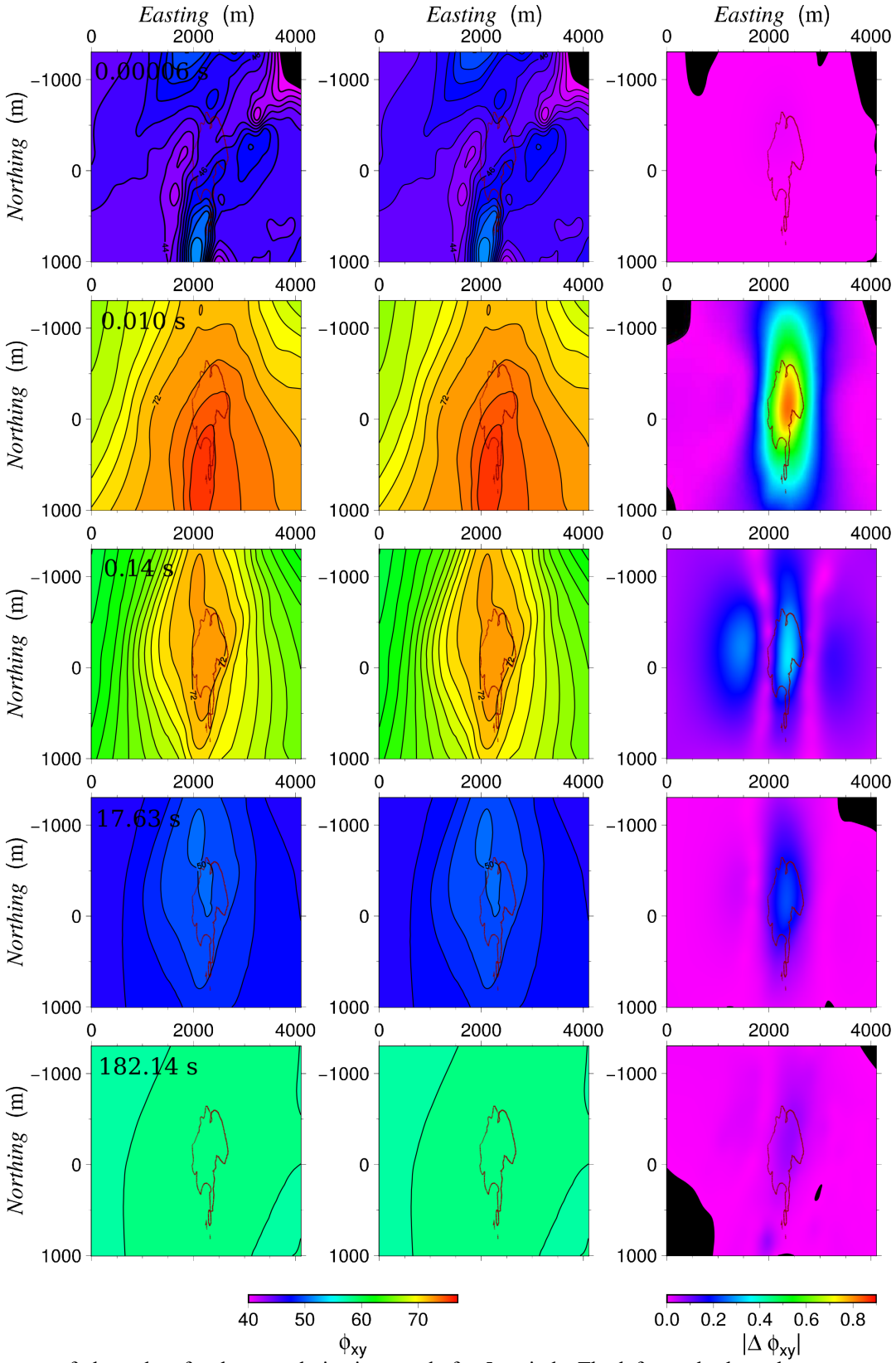

Figure 12. Contours of phase data for the xy polarization mode for 5 periods. The left panels show the responses of the original model with ore shells present. The middle panels show the corresponding responses without the ore shells. The right panels show the differences between the other two panels. Surface projections of the ore shell outlines, using the maximum and minimum lateral extents, are shown in dark red.

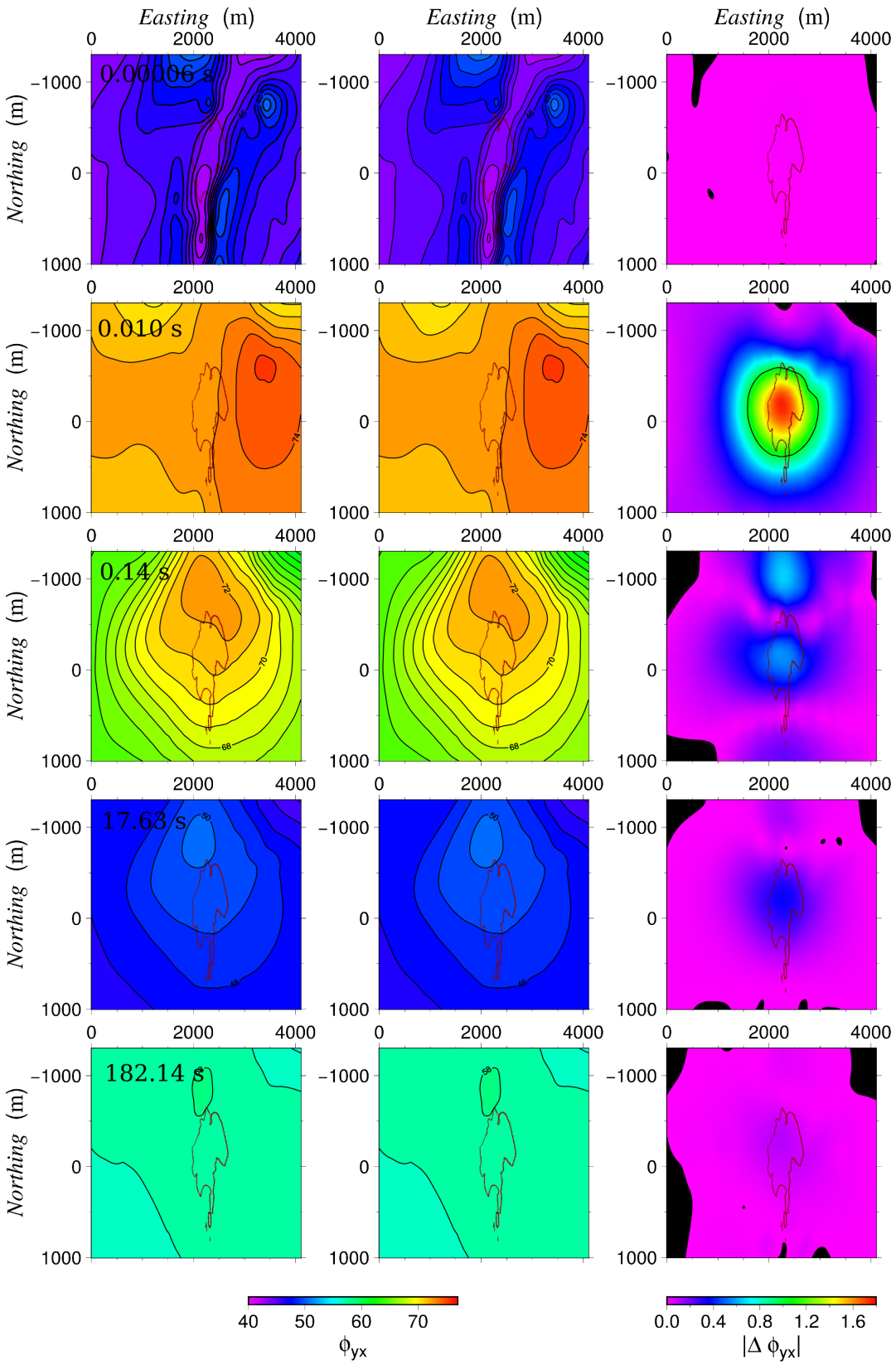

Figure 13. Contours of phase data for the yx polarization mode for 5 periods. The left panels show the responses of the original model with ore shells present. The middle panels show the corresponding responses without the ore shells. The right panels show the differences between the other two panels. Surface projections of the ore shell outlines, using the maximum and minimum lateral extents, are shown in dark red.

$$\mathbf{m}^n = \mathbf{m}^{n-1} + s\,\delta\mathbf{m}^n \quad (14)$$

Here the scalar parameter s is a step-length factor. By replacing equations (11) and (12) into equation (10), making use of equations (13) and (14), and then minimizing the modified objective function with respect to the model the following system is derived:

$$[\mathbf{J}^{n-1^T}\,\mathbf{W}_d^T\,\mathbf{W}_d\,\mathbf{J} + \lambda^n\alpha_m\mathbf{W}_m{}^T\mathbf{W}_m + \lambda^n\alpha_s\mathbf{W}_s^T\mathbf{W}_s]\delta\mathbf{m}^n = \mathbf{J}^{n-1^T}\,\mathbf{W}_d^T\,\mathbf{W}_d(\mathbf{d}^{obs} - \mathbf{d}^{n-1}) - \lambda^n\alpha_m\mathbf{W}_m{}^T\mathbf{W}_m\mathbf{m}^{n-1} - \lambda^n\alpha_s\mathbf{W}_s^T\mathbf{W}_s(\mathbf{m}^{n-1} - \mathbf{m}^{ref}) \quad (15)$$

For a given model, $\mathbf{m}^{n-1}$, the vector, $\mathbf{d}^{n-1}$, in the above equation is produced. The direct solver MUMPS is used for the forward problem. The solution to equation (15) is obtained in an iterative scheme using the Gauss-Newton method (Haber et al., 2000). For this, the product of the Jacobian matrix or its transpose with the relevant vectors are calculated in an implicit manner using multiple solutions of some pseudo-forward problems (e.g. see Mackie and Madden, 1993; Farquharson et al., 2002).

The equation of the pseudo-forward problem is, in principle, the derivative of the forward problem (discretized and linearized form of equation (4)) with respect to the model parameter (i.e. for cell k):

$$\mathbf{A}\frac{\partial\mathbf{E}_i}{\partial\mathbf{m}_k} = -\frac{\partial\mathbf{A}}{\partial\mathbf{m}_k}\,\mathbf{E}_i \quad (16)$$

Where $\mathbf{A}$ is the coefficient for the discretized form of equation (4) and $\mathbf{E}_i$ represents the electric field calculated along the edges of tetrahedral cells in the grid. The impedance data vector is a function of electric and magnetic fields at the observation locations. With its eventual form derived as a function of $\mathbf{E}$ combining x- and y-polarization modes, $\mathbf{d} = \mathrm{Q}(\mathbf{E}_{xpol}^{obs}, \mathbf{E}_{ypol}^{obs})$, the Jacobian matrix can be broken subject to the use of chain rule derivatives, and incorporating equation (16):

$$\mathbf{J} = \frac{\partial\mathbf{d}}{\partial\mathbf{m}} = \frac{\partial Q}{\partial\mathbf{E}_{xpol}^{obs}}\,\mathcal{N}\frac{\partial\mathbf{E}_{i\,xpol}}{\partial\mathbf{m}} + \frac{\partial Q}{\partial\mathbf{E}_{ypol}^{obs}}\,\mathcal{N}\frac{\partial\mathbf{E}_{i\,ypol}}{\partial\mathbf{m}} = \frac{\partial Q}{\partial\mathbf{E}_{xpol}^{obs}}\,\mathcal{N}\,\mathbf{A}^{-1}\,\mathbf{W}_{xpol} + \frac{\partial Q}{\partial\mathbf{E}_{xpol}^{obs}}\,\mathcal{N}\,\mathbf{A}^{-1}\,\mathbf{W}_{ypol}. \quad (17)$$

Considering the real and imaginary parts of the impedance, and real and imaginary parts of the $\mathbf{E}$ and $\mathbf{H}$ fields, $\frac{\partial Q}{\partial\mathbf{E}^{obs}}$ is an 8 x 8 block matrix for each observation location; the matrix N consists of basis function and its curl for x and y components of $\mathbf{E}$ and $\mathbf{H}$; the matrix $\mathbf{W}$ corresponds to the right hand side of equation (16) for the relevant polarizations. This modification of the Jacobian matrix gives the $\mathbf{J}.u$ and $\mathbf{J}^T.v$ products implicitly in our Gauss-Newton iterative solution of equation (15).

Test example

The above process is tested for the synthetic Commemi 3D - 2A model (Zhdanov et al., 1997; see Fig. 14). The model used for synthetic forward computations is a three-layered model with conductivities of 0.1, 0.01 and 10 S/m from top to basement respectively. A conductive 1 S/m block is also included in the top layer. The synthetic data are real and imaginary parts of the impedance tensor for five frequencies (0.001, 0.01, 0.1, 1, 10 Hz) for 40 observation locations on the surface. The actual data for the inversion is produced by adding random noise to synthetic data in the amount of 5% of the data itself or half of the magnitude of the average off-diagonal components of the impedance. The mesh used for the inversion consists of 355 739 cells, 57 221 nodes and 413 222 edges. As shown in Figure 14 the mesh is locally refined in the main area of investigation and also at the observation locations (the mesh used for calculating synthetic data was different). The inversion algorithm was started using a two-layered reference model, $\mathbf{m}^{ref}$ in equation (15), with background and basement conductivities of 0.02 and 10 S/m, respectively. In order to produce a smooth model for the first update the inversion is initiated with a large trade-off value of 108. Using a cooling strategy this parameter was halved at each Gauss-Newton iteration until the data misfit of the next produced model reached the predetermined target misfit. For each model update, equation (15) was solved using the iterative solver GMRES. Here the computation time for each model update was approximately 50 minutes considering a Krylov subspace of 500 and 250 iterations for GMRES. In terms of computer memory each MPI processor occupied 16 Gb of RAM to factorize the relevant coefficient matrix. The algorithms for the finite-element assembly associated with the forward and pseudo-forward problems are also coded in a multi-threaded OpenMP fashion on each MPI processor. The entire computation time for 20 model updates in our inversion was approximately 20 hours. Figure 15 shows the result of inversion including the behaviour of the data misfit, model roughness and smallness measures, and also the total objective function. A comparison of the observed and predicted data and also the produced model of the inversion for the 20th update is shown.

Summary

In this study, a workflow for constructing mesh-based models suitable for forward modelling and inversion of MT data is developed. Through the use of a combination of software packages and tools, the construction of a volumetric unstructured gird using meshed geological surfaces is demonstrated for a mineral sequence. We also combined lithofacies information and resistivity well log data through statistical methods to employ realistic resistivity to the geophysical modelling. A MT forward modelling algorithm was developed based on a finite-element discretization of the vector-scalar potential formulation on unstructured tetrahedral meshes. The code is successfully deployed for the Lalor VMS deposit, where the sensitivity of the MT signals to deep seated mineralization and host geometry is demonstrated for a range of frequencies typical of MT exploration. A slight sensitivity to the geometry of the Lalor ore zone is detected here. We are in the process of incorporating the full kernel density function petrophysical data into the

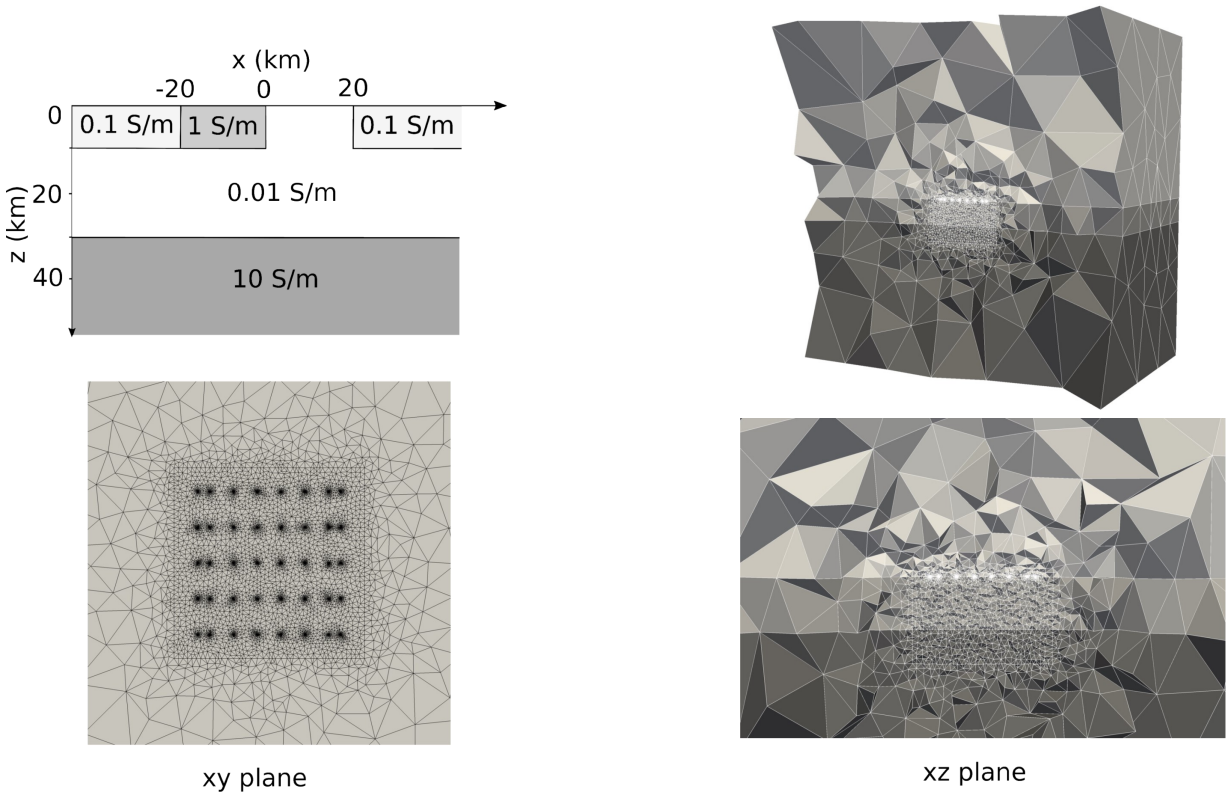

Figure 14. Commemi 3D-2A model and mesh used for inversion. Top right panel shows the entire view of the mesh. Figures at the bottom show central views of the mesh, including the refined regions.

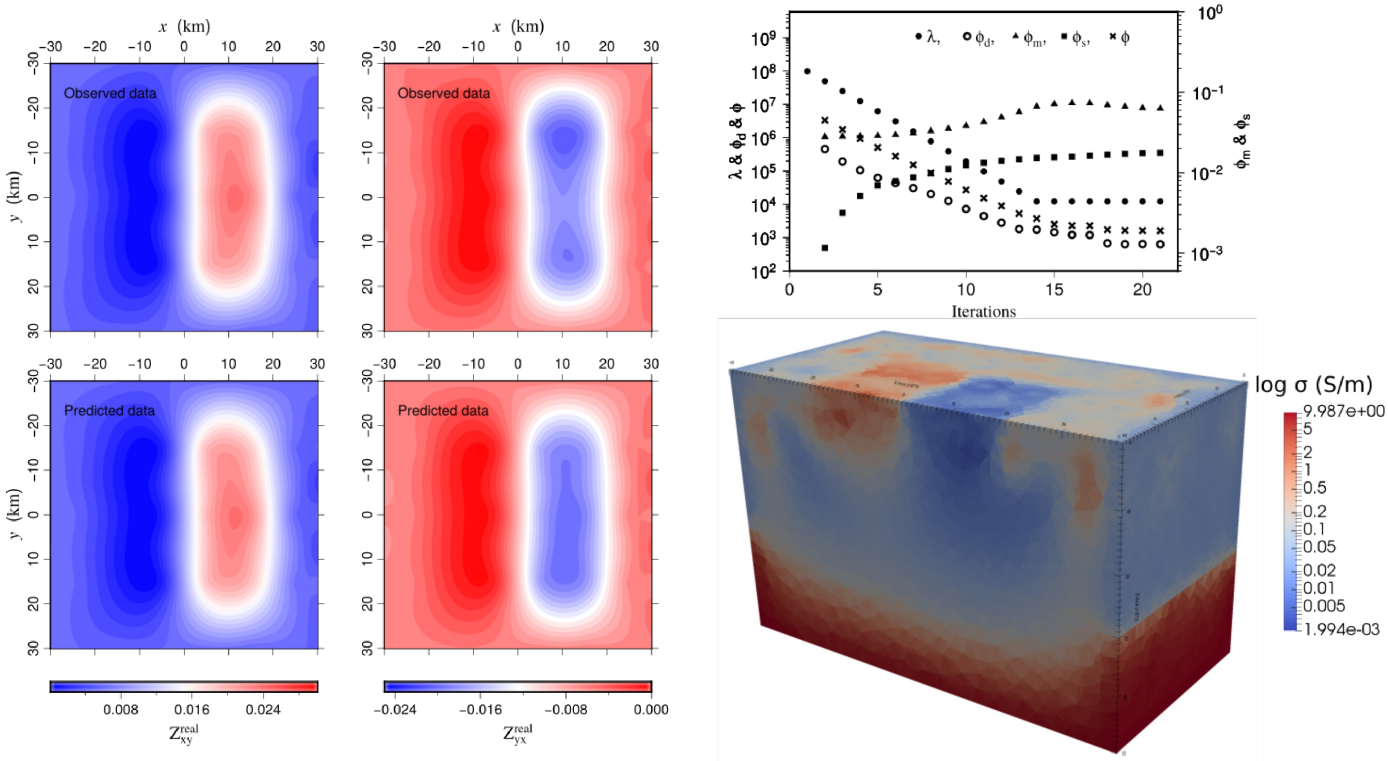

Figure 15. Inversion results: observed and calculated data for a frequency of 1 Hz on the Earth surface, behaviour of the trade-off parameter, data and model measures, and the 3D inversion model after 20 updates .

model, and developing efficient methodologies and algorithms for 3D inversion of MT data on unstructured meshes. Based on the primary results of the MT inversion presented here the electrical conductivity of the test model has been successfully recovered.

Acknowledgments

This report is a contribution to NRCan's Targeted Geoscience Initiative Program (TGI). Support for this study was provided through the Volcanic- and Sedimentary-Hosted Base Metal Mineralization Project's '*Activity VS-2.3: Elucidating VMS mineralizing fluid pathways from the geophysical responses to hydrothermal alteration*'.

Hudbay Minerals Inc. is gratefully acknowledged for providing access to data supporting this research. This report benefited from the review of Gilles Bellefleur, Vicki Tschirhart and Neil Rogers.

References

Amestoy, P.R., Duff, I.S., Koster, J., and L'Excellent, J.Y., 2001. A fully asynchronous multifrontal solver using distributed dynamic scheduling; SIAM Journal on Matrix Analysis and Applications, v. 23, p. 15–41.

Amestoy, P.R., Guermouche, A., L'Excellent, J.Y., and Pralet, S., 2006. Hybrid Scheduling for the parallel solution of linear systems; Parallel Computing, v. 32, p. 136–156.

Ansari, S.M., Farquharson, C.G., and MacLachlan, S.P., 2017. A gauged finite-element potential formulation for accurate inductive and galvanic modelling of 3-D electromagnetic problems; Geophysical Journal International, v. 210, p. 105–129.

Bailes, A.H. and Galley, A.G., 2007. Geology of the Chisel-Anderson lakes area, Snow Lake, Manitoba (NTS area 63K16SW and west half of 63J13SE); Manitoba Science, Technology, Energy and Mines, Manitoba Geological Survey, MAP Geoscientific Map 2007-1, scale 1:20 000.

Bailes, A., Rubingh, K., Gagne, S., Taylor, G., Galley, A., Bernauer, S., and Simms, D., 2013. Volcanological and structural setting of Paleoproterozoic VMS and gold deposit at Snow Lake, Manitoba; Geological Association of Canada – Mineralogical Association of Canada Joint Annual Meeting, Field Trip Guidebook FT-A2, Manitoba Innovation, Energy and Mines, Manitoba Geological Survey, Open File OF2013-3, 63 p.

Bailes, A. H., Galley, A. G., Paradis, S., and Taylor, B., 2016. Variations in large synvolcanic alteration zones at Snow Lake, Manitoba, Canada with proximity to associated volcanogenic massive sulphide deposits; Economic Geology, v. 111, p. 933–962.

Bournas, N., Türkoğlu, E., Clements, E., and Thomson, D., 2013. 3D MT inversion for the exploration of porphyry deposits; *in* Technical Program Expanded Abstract; Society of Economic Geologists, Annual meeting, Houston, p 1595–1600.

Caté, A., Mercier-Langevin, P., Ross, P.S., Duff, S., Hannington, M., Dubé, B., and Gangé, S., 2013. The Paleoproterozoic Lalor VMS deposit, Snow Lake, Manitoba: Observations on the nature and architecture of the gold and base metal-rich ore zones and associated alteration; Geological Survey of Canada, Open File Report 7483, p. 1–20.

Caumon, G., 2010. Towards stochastic time-varying geological modeling; Mathematical Geosciences, v. 42, p. 555–569

Dunham, M., Ansari, S.M., and Farquharson, C.G., 2018. Application of 3D marine CSEM finite element forward modeling to hydrocarbon exploration in the Flemish Pass Basin offshore Newfoundland, Canada; Geophysics, v. 83, p. WB33–WB49.

Farquharson, C.G., Oldenburg, D.W., Haber, E., and Shekhtman, R., 2002. An algorithm for the three-dimensional inversion of magnetotelluric data; SEG Technical Program Expanded Abstracts, p. 649–652.

Haber, E., Ascher, U.M., and Oldenburg, D.W., 2000. On optimization techniques for solving nonlinear inverse problems; Inverse Problems, v. 16, p. 1263–1280.

Jin, J.M., 2014.The finite element method in electromagnetics, 3rd Edition; John Wiley & Sons, New Jersey, 876 p.

Lelièvre, P.G., Carter-McAuslan, A.E., Dunham, W.M., Jones, D.J., Nalepa, M., Squires, C.L., Tycholiz, C.J., Vallée, M.A., and Farquharson, C.G., 2018. FacetModeller: Software for manual creation, manipulation and analysis of 3D surface-based models; Software X, v. 7, p. 41–46.

Mackie, R.L. and Madden, T.R., 1993. Three-dimensional magnetotelluric inversion using conjugate gradients; Geophysical Journal International, v. 115, p. 215–229.

Martinez, E. and Hearst, R., 2009. Geophysical survey interpretation report regarding the tensor MT, direct current resistivity and induced polarization surveys over Lalor Project, Northern Manitoba; report for Hudson Bay Mining & Smelting Co. Ltd. Flin Flon, Manitoba, Quantec Geosciences Ltd.

Miensopust, M.P, Queralt, P., Jones, A.G., and the 3D MT modellers, 2013. Magnetotelluric 3D inversion - a review of two successful workshops on forward and inversion code testing and comparison; Geophysical Journal International, v. 193, p. 1216–1238

Monk, P., 2003. Finite element methods for Maxwell's equations; Oxford University Press Inc., 472 p.

Newton and Vowles, 2017. Geophysical Overview of the Lalor VMS Deposit; *in P*roceedings of Exploration '17: 6th Decennial International Conference on Mineral Exploration, Toronto, Ontario, p. 619–635

Pellerin, J., Levy, B., Caumon, G., and Botella, A., 2014. Automatic surface remeshing of 3D structural models at specified resolution: A method based on Voronoi diagrams; Computer and Geosciences, v. 62, p. 103–116.

Pellerin J. Botella, A., Mazuyer A., Chauvin B., Bonneau, G., Caumon G., and Lévy, B., 2017. RINGMesh: A programming library for developing mesh-based geomodeling ap-

plications; Computers and Geosciences, v. 104, p. 93–100.

Puzyrev, V., Koldan, J., Puente, J. de la, Houzeaux, G., Vazquez, M., and Cela, J.M., 2013. A parallel finite element method for three-dimensional controlled-source electromagnetic forward modelling; Geophysical Journal International, v. 193, p. 678–693.

Schetselaar, E., 2013. Mapping the 3D lithofacies architecture of a VMS ore system on a curvilinear-faulted grid: a case study from the Flin Flon mining camp, Canada; Ore Geology Reviews, v. 53, p. 261–275.

Schetselaar, E., Bellefleur, G., Craven, J., Roots, E., Chraghi, S., Shamsipour, P., Caté, A., Mercier-Langevin, P., Goumi, N.E., Enkin, R., and Salisbury, M., 2017. Geologically driven 3D modelling of physical rock properties in support of interpreting the seismic response of the Lalor volcanogenic massive sulphide deposit, Snow Lake, Manitoba, Canada; Geological Society, London, Special Publication 453, p. 57–79

Si, H., 2007. TetGen, A quality tetrahedral mesh generator and three-dimensional Delaunay triangulator; Weierstrass Institute for Applied Analysis and Stochastics, Berlin, Germany. <http://wias-berlin.de/software/index.jsp?id=TetGen&lang=1> [accessed February 6, 2019]

Silvester, P.P. and Ferrari, R.L., 1983. Finite elements for electrical engineers; Cambridge University Press, 516 p.

Whitney, H., 1957. Geometric Integration Theory; Princeton University Press, 400 p.

Zehner et al., 2015. Workflows for generating tetrahedral meshes for finite element simulations of complex geological structures; Computers & Geosciences, v. 79, p. 105–117

Zhang, P. and Chouteau, M., 1991, The use of magnetotellurics for mineral exploration: an experiment in the Chibougamau region of Quebec; Canadian Journal of Earth Sciences, v. 29, p 621–635.

Zhdanov, M.S., Varentsov, I.M., Weaver, J.T., Golubev, N.G., and Krylov, V.A., 1997. Methods for modelling electromagnetic fields: results from COMMEMI — the international project on the comparison of modelling methods for electromagnetic induction; Journal of Applied Geophysics, v. 37, p. 133–271.

Analysis of wireline logs and vertical seismic profiling data acquired with fibre-optic cable at the copper-gold New Afton porphyry deposit, British Columbia

G. Bellefleur[1], E. Schetselaar[1], D. Wade[2], D. White[1], R. Enkin[3] and D.R. Schmitt[4]

[1]*Geological Survey of Canada, 601 Booth Street, Ottawa, Ontario K1A 0E8*

[2]*New Afton Mine, 4050 West Trans Canada Highway, Kamloops, British Columbia V1S 2A3*

[3]*Geological Survey of Canada, 9860 West Saanich Road, Sidney, British Columbia V8L 4B2*

[4]*Department of Earth, Atmospheric, and Planetary Sciences, Purdue University, 550 Stadium Mall Drive, West Lafayette, Indiana 47907*

Abstract

Wireline logs and vertical seismic profile (VSP) data were acquired in two boreholes intersecting the mineralized zone and alteration halo at the copper-gold New Afton porphyry deposit, Canada. Log data provide physical rock properties for the main lithologies and alteration zones. Calliper logs reveal many faults and caved-in zones indicating rocks with low integrity at the borehole wall. The preponderance of these zones as indicated by the logs suggests that their response may dominate the seismic reflection wavefield. Distributed acoustic sensing (DAS) was used to acquire VSP data in the boreholes surveyed with logs. Straight and helically wound fibre-optic cables used for the VSP survey housed standard fibres and a fibre engineered to increase the intensity of backscattering at the DAS interrogator. A new generation of DAS interrogator connected to the engineered fibres provided field data with lower noise level and higher signal-to-noise ratio. Data with higher signal-to-noise ratio from straight fibre-optic cable were processed and used for depth imaging. Depth images benefitted from new migration weights that account for the directional sensitivity of the straight fibre-optic cable and limit the extent of migration artefacts. Migration results show several reflectors with shallow dips to the northwest, some explained by faults intersecting the boreholes. The main sub-vertical lithological and alteration contacts at New Afton generated downgoing reflections that were not considered in the migration.

Introduction

Distributed acoustic sensing (DAS) is a distributed sensing technology that utilizes the optical scattering response to a laser pulse to measure changes of strain occurring along a fibre-optic cable (Hartog, 2018). DAS does not use point receivers but rather simultaneously senses the entire length of a fibre-optic cable for strain changes due to the passage of seismic waves. The ability to obtain measurements over the entire fibre -optic cable simultaneously is particularly advantageous and has led to the development of a variety of applications, primarily for the oil and gas industry (Hartog, 2018). Currently, there are a very limited number of publications of the application of DAS for mineral exploration and mining. DAS offers cost-effective solutions for mineral exploration, more particularly for vertical seismic profiling (VSP) surveys that are sometimes used for providing high-resolution images of the subsurface near known deposits or in prospective areas.

Here, we present results from one of the first applications of DAS-VSP for mineral exploration. DAS-VSP data were acquired as part of the Geological Survey of Canada's Targeted Geoscience Initiative for the development of an integrated geophysical imaging and 3-D geological modelling research study of the New Afton porphyry deposit located in the Canadian Cordillera of south-central British Columbia. This alkaline copper-gold porphyry deposit previously supported an open pit operation and is currently being mined at deeper levels through underground workings, providing geological constraints extending beyond 1.5 km in depth. This study intends to combine new VSP and 3-D magnetotelluric surveys, together with multi -parameter deep drillhole geophysical logs and 3-D modelling to elucidate the magmatic hydrothermal processes and structural controls responsible for concentrating metals in this porphyry deposit. Specifically, we present elastic rock properties from wireline logs and core samples, as well as results from a VSP survey acquired with DAS in two boreholes that intersect the main mineralized zone and alteration halo. At New Afton, the mineralization consists primarily of disseminated sulphides (≤4% in the economic ore zone) and will unlikely be detected directly on DAS-VSP data. Instead the focus is on fault zones, of which some may have acted as conduits that channelled hydrothermal fluid flow. In addition, lithologi-

Corresponding author: Gilles Bellefleur (gilles.bellefleur@canada.ca)

Bellefleur, G., Schetselaar, E.M., Wade, D., White, D., Enkin, E., and Schmitt, D.R., 2019. Analysis of wireline logs and vertical seismic profiling data acquired with fibre-optic cable at the copper-gold New Afton porphyry deposit, British Columbia; *in* Targeted Geoscience Initiative: 2018 report of activities, (ed.) N. Rogers; Geological Survey of Canada, Open File 8549, p. 235–241. https://doi.org/10.4095/313657

cal contacts and the potential signatures of hydrothermal alteration zones, which are key indicators for porphyry mineralization, were of interest. A 3-D geological model of the mine, wireline logging data and physical rock property measurements of core samples are used to support the interpretation of DAS-VSP data.

Geology

The copper-gold New Afton porphyry deposit is dominantly hosted by fragmental and crystalline volcanic rocks (hereafter referred to as BXF) of the Late Triassic Nicola Formation and to a lesser extent by the 204 Ma Cherry Creek monzonite of the Iron Mask batholith, the latter of which is interpreted as the heat source that caused alteration and mineralization in this alkalic porphyry (Lipske and Wade, 2014; Bergen et al., 2015). A subvertical southwest-plunging zone of primary hypogene mineralization, largely coincident with the potassic alteration zone, contains disseminated chalcopyrite and bornite (Fig. 1). This hypogene ore zone is structurally controlled by two subvertical northeast-striking fault zones, known as the footwall and hanging-wall faults. The hanging-wall fault juxtaposes BXF with a subvertical body of serpentinized picrite. This tectonic contact along the northern weakly serpentinized

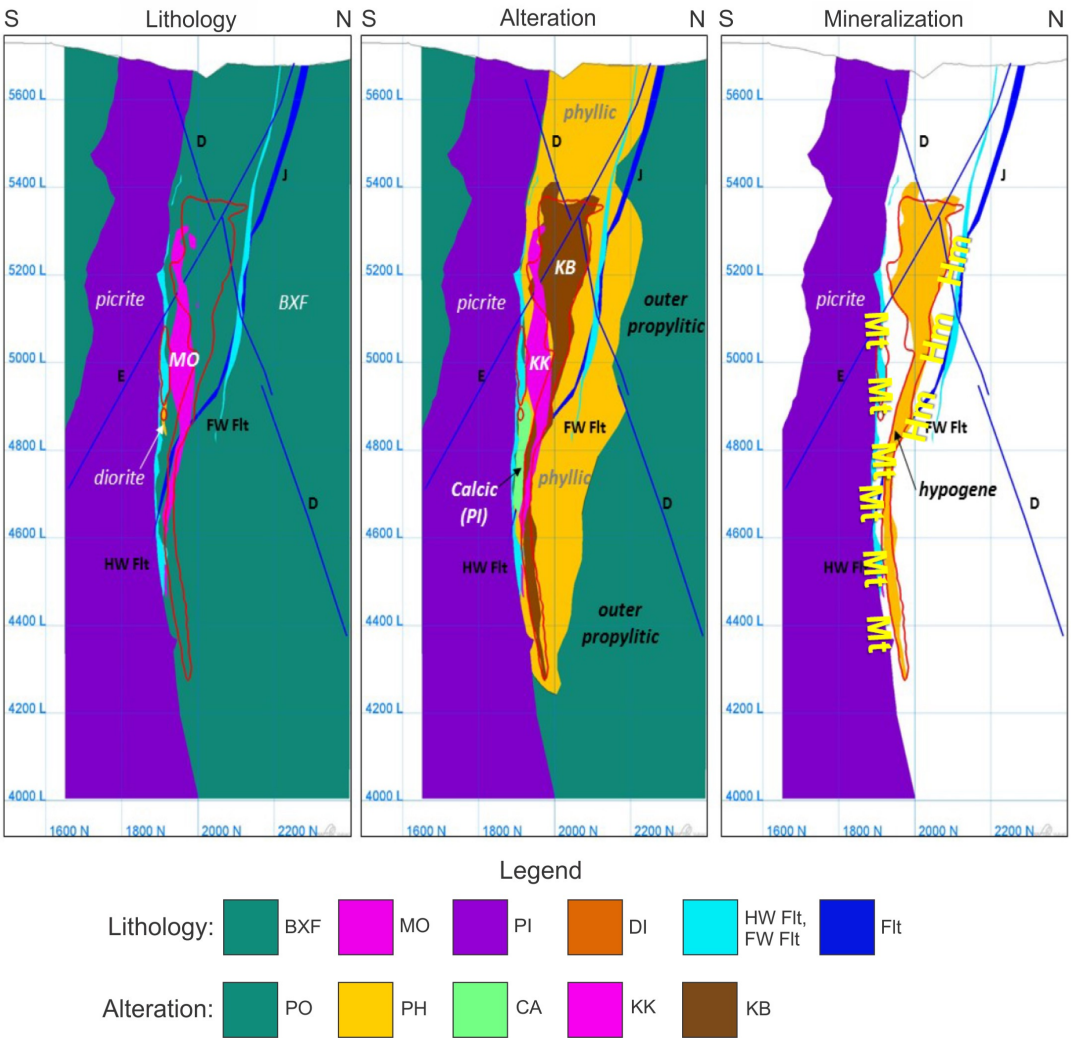

Figure 1. Section (looking west) of the main lithological units (left), alteration zones (middle) and mineralized zone (right) at the New Afton deposit. The main hypogene mineralized zone (0.4% Cu equivalent) is outlined in red and is primarily associated with the biotite-dominant potassic alteration zone. Propylitic alteration comprises chlorite, epidote, calcite and hematite. Phyllic alteration minerals consists of sericite, carbonate, pyrite, quartz and tourmaline. Calcic alteration minerals include magnetite, actinolite, apatite and epidote. The spatial coordinates shown are mine grid coordinates measured in metres (*modified from* Lipske and Wade, 2014). Abbreviations: BXF – volcanic fragmentals; CA – calcic; DI – diorite; D, E, J – faults; FW Flt – footwall fault; HW Flt – hanging wall fault; Hm – hematite; KB – biotite-dominant potassic alteration; KK – feldspar-dominant potassic alteration; MO – monzonite; Mt – magnetite; PH – phyllic; PI – picrite; PO – propylitic.

picrite margin is defined by a high-strain zone of brittle-ductile deformation and locally confines a zone of calcic alteration composed of magnetite, epidote, actinolite and apatite. The primary hypogene ore zone is cut by numerous moderately to steeply dipping fault zones that controlled secondary hypogene mineralization of tetrahedrite and tennanite. Supergene mineralization of native copper and chalcocite in hematite-rich oxidation zones is more abundant at higher structural levels near the open pit but native copper extends to 700 m below surface beneath the pit, along older long-lived structures (Lipske and Wade, 2014; Bergen et al., 2015).

Activity highlights

Wireline logging and physical rock properties

Wireline logs were acquired in two boreholes (EA16-171 and EA17-197) that emanate from the same underground drill bay located approximately 650 m below the surface (see Fig. 2 for location). The two boreholes have different lengths, dips and azimuths. Both boreholes intersect numerous faults that tend to collapse in open drill holes and that significantly complicated acquisition of the open-hole wireline logs. Open-hole logging measurements included 3-arm calliper, natural and spectral gamma-ray spectrometry, magnetic susceptibility, resistivity, induced polarization, induction conductivity and full-waveform sonic logs. Gamma-gamma density logging was conducted through drill rods and subsequently calibrated with values measured over a short section of stable open hole located near the surface. This approach minimized the risk of losing the radioactive source used for density measurements caused by obstructions in the borehole, an event that would have led to a temporary shutdown of mining operations.

Figure 3a presents selected logs for borehole EA16-171 plotted together with the main fault zones, alteration and lithological units from drill core geological logging conducted by the mine operator. The calliper track provides a good illustration of the difficult borehole conditions, with large values showing caved-in zones associated with brittle faults. Density

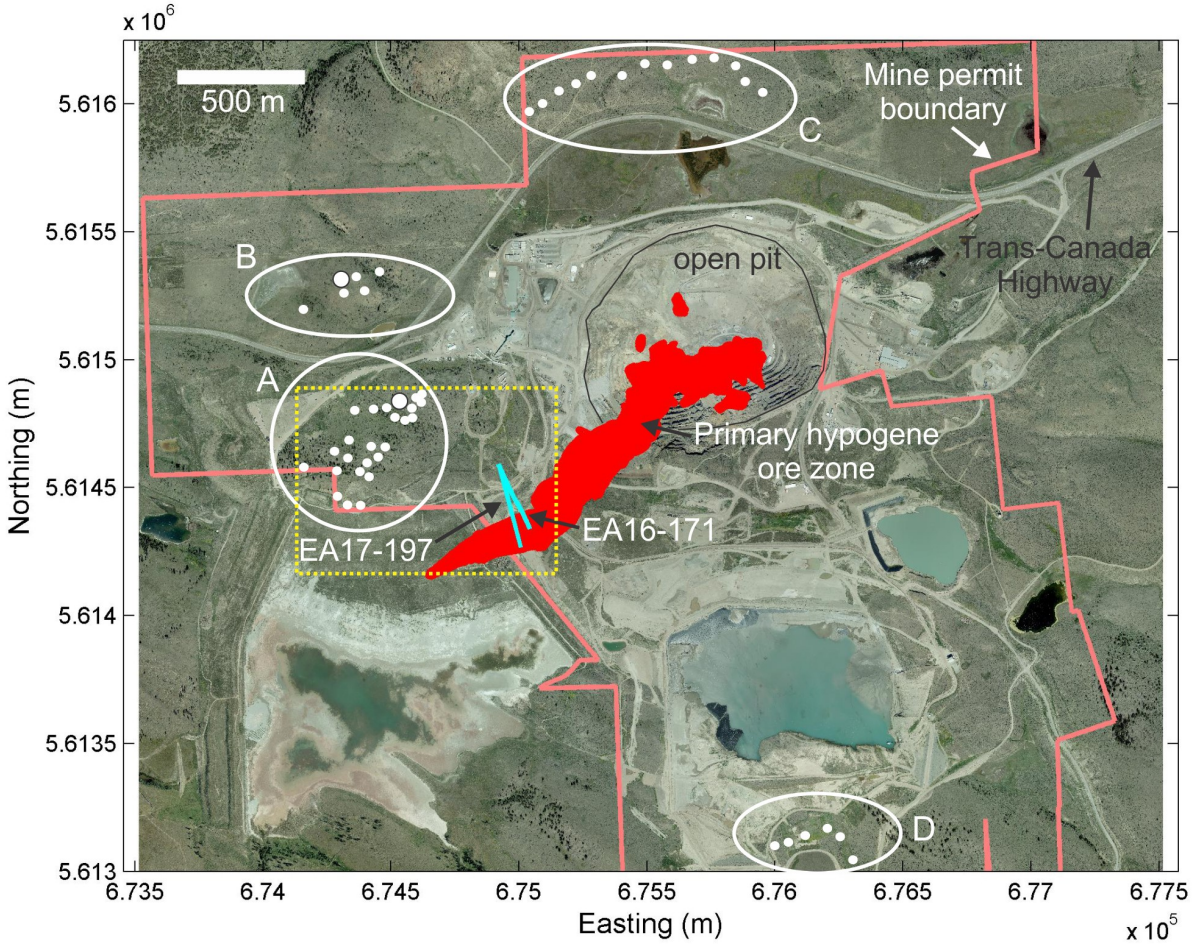

Figure 2. Map showing the surface location of seismic shot points (white dots), surface projection of the two surveyed boreholes (cyan) and surface projection of the hypogene mineralized zone (red). Seismic sources are located in four clusters labelled A, B, C and D. Boreholes EA17-197 and EA16-171 start from the same drill bay located approximately 650 m below the surface. Borehole EA16-171 dips at approximately 70° and is 870 m long. Borehole EA17-197 dips at approximately 60° and is 701 m long. The rectangle with yellow dashed line shows the lateral extent of velocity model and migrated volume in Figure 4.

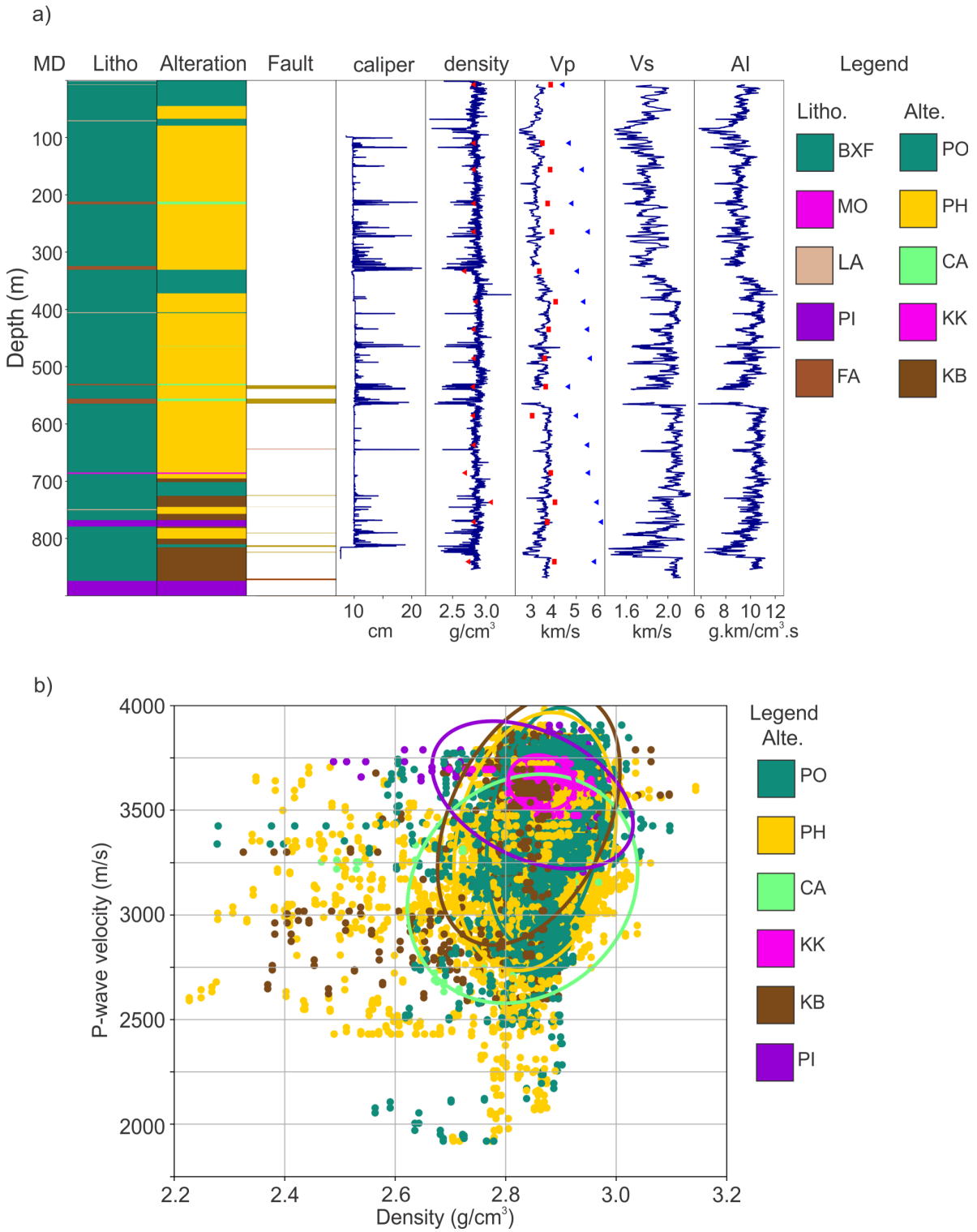

Figure 3. a) Logging data from borehole EA16-171. Tracks from left to right show, measured depth, lithology, alteration, faults, calliper, density, P-wave, S-wave velocity and acoustic impedance. Red squares and blue triangles are P-wave velocity measurements made on core samples at atmospheric pressure and 30 MPa, respectively. b) Plot of velocity versus density for different types of alteration. The main axis of each ellipse represents two standard deviations (from principal component analysis). Abbreviations: Alte. – alteration; BXF – volcanic fragmentals; CA – calcic; FA– faults (undifferentiated); KB – biotite-dominant potassic alteration; KK – feldspar-dominant potassic alteration; LA– latite; Litho. – lithology; MO – monzonite; PH – phyllic; PI – picrite; PO – propylitic.

and P- and S-wave velocity logs are of poor quality in areas with large calliper values due to the larger diameter of the borehole being filled with a mixture of rock and water. Outside the fault zones, the P- and S-wave velocity logs exhibit significant variability within the volcanic fragmental rocks of the Triassic Nicola Formation (BXF on Fig. 3a). This rock unit is heterogeneous and comprises clasts of varying size of porphyritic diorite, andesitic flow debris, mafic volcanic rocks, picrite and aphyric volcanic rocks within a fine- to coarse-grained matrix of intermediate to mafic composition. Hydrothermal alteration also changed the mineralogical composition of the volcanic fragmental rocks and other rock units near the deposit. In addition to the fault zones, the high variability of P- and S-wave velocities in Figure 3a is due to the heterogeneity of the volcanic fragmental rocks and alteration. An analysis of acoustic impedance of alteration at New Afton shows higher mean values and a narrow distribution of acoustic impedance for the potassic-dominant potassic alterations relative to the other altered rocks (Fig. 3b). In comparison, propylitic and phyllic alterations have a broader distribution of acoustic impedances and lower mean values. This suggests that reflections between potassic alteration (potassic-dominant) and other alteration zones are possible but will depend on local context. The contact between potassic alteration and picrite at the bottom of both boreholes may also generate a detectable reflection. No petrophysical measurements confirm this but core samples from the picrite are intensely serpentinized and are weaker than core samples from the potassic zone. No core samples from the picrite unit below the potassic zone remained sufficiently intact to allow for later pressurized velocity measurements. Geophysical logging tools did not reach the picrite located at the bottom of the two boreholes due to the presence of fallen rocks and debris that resulted from borehole reconditioning. Thus, our assessment of the reflectivity of the contact between potassic alteration and picrite is qualitative.

VSP with distributed acoustic sensing

The VSP survey at New Afton (Fig. 2) was conducted with an advanced DAS system (referred to as V3) achieving signal-to-noise ratio comparable to that generally obtained with geophones but offering simultaneous high-density spatial sensing over the entire length of the fibre-optic cable. Straight and helically wound fibre-optic cables specifically engineered for that system were installed in two boreholes and compared to standard telecommunication fibre-optic cables (referred to as V2) with similar configuration. The helically wound fibre-optic cables were deployed to assess the capability of omnidirectional sensing for various wave-modes and wave propagation directions. Such broadside sensing is desirable at New Afton due to its complex geological structure and the inclined and deviated geometry of the boreholes. Straight and helically wound fibre-optic cables were daisy-chained together to allow simultaneous recording along the length of the fibre-cable for each shot, thus minimizing the total number of shots required for the survey. A total of fifty shallow shot points consisting of 1 kg of explosives were distributed in four clusters around the boreholes (Fig. 2).

The VSP data recorded with straight fibre-optic cable and a V3 DAS interrogator for shot points located in cluster A (Fig. 2) were further processed and migrated to generate an image of the subsurface. Data from the helically wound cable or acquired with the V2 system were processed but not migrated due to the lack of reflections (helically wound cable) or lower signal-to-noise ratio (V2 data). Data processing focussed primarily on extracting the upgoing wavefield that was used for depth imaging. Processing included depth calibration of DAS channels, numerical integration of the measured signal with respect to time to convert strain rate to strain and align phases to geophone-like data (Daley et al., 2016), spectral balancing combined with band-pass filtering, fk-filtering to remove downgoing waves, median filtering to remove optical noise banding and muting of direct arrivals.

The processed DAS-VSP data were used to produce an image of the subsurface near the two boreholes of the VSP survey. Depth imaging was achieved using a 3-D Kirchhoff depth migration algorithm and a 3-D velocity model estimated from traveltime tomography of first arrivals. In applying depth migration to the data, we introduce novel migration weights that account for the directional sensitivity of straight fibre-optic cable. These weights act similar to parameters that control the aperture in standard depth migration and limit the extent of migration artefacts. In practice, weights defined from the angle of incidence of reflected waves on the fibre-optic cable enhance positions in the image space that are likely to exert longitudinal strain on the straight fibre-optic cable. An example of such weights for one receiver position near the collar of borehole EA17-197 is shown in Figure 4a. Figure 4 also compares vertical and horizontal sections obtained without and with the migration weights described above. Sections with weights still contain artefacts, but they are significantly reduced in comparison to migration results obtained using a full 3-D aperture. Artefacts are more prominent away from the two boreholes (i.e. areas east and above borehole EA17-197 and west and below borehole EA16-171 on Fig. 4). Results away from the boreholes are not reliable for geological interpretation.

The vertical section (Fig. 4c) shows many reflectors with a moderate dip to the north. In plan view (Figs. 4d and 4e), the reflectors are subparallel to the contact between the volcanic fragmental rocks with potassic alteration and the picrite unit intersected at the bottom of both boreholes, indicating that the true dip of the reflectors is approximately to the northwest. Such shallow dips are not characteristic of the main lithological contacts or contacts between different types of alteration observed on the 3-D geological model of the New Afton deposit. A possible explanation is that these reflectors are due to fault zones that were intersected in boreholes and that they have low acoustic impedances relative to the host rocks. The nearly vertical contact between volcanic fragmental rocks with potassic alteration and picrite, and other subvertical contacts between

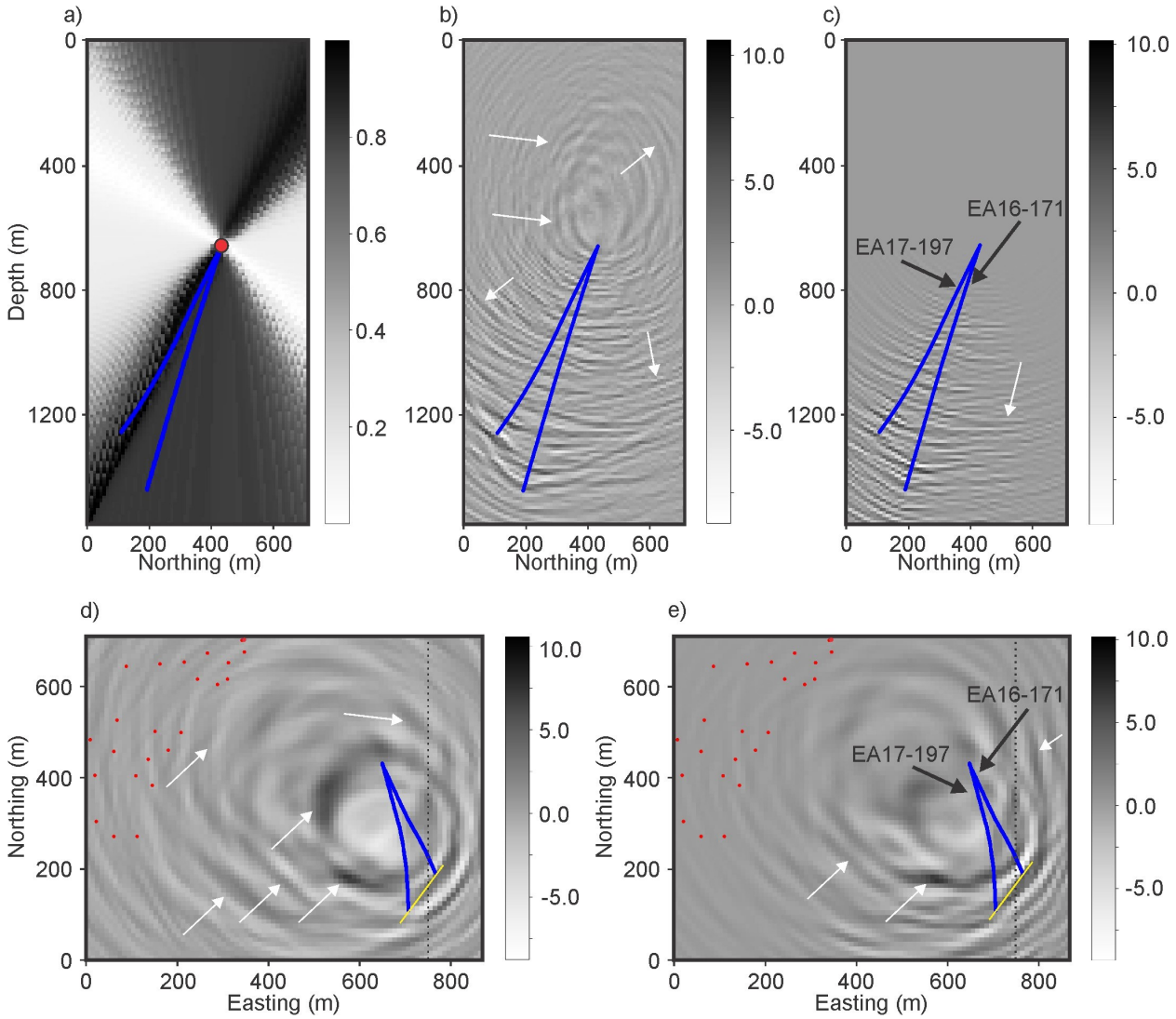

Figure 4. Results from the migration of V3 data recorded with straight fibre-optic cable. a) Vertical section showing the migration weights based on the angle of incidence of the reflected wave on the fibre-optic cable. The red dot shows the receiver position used to calculate the weights. b) Vertical section through the migrated results obtained with complete 3-D aperture. c) Vertical section showing the migration results obtained with the weights described in the text. d) and e) are slices at a depth of 1.35 km through the migrated results obtained without (d) and with (e) migration weights. Dashed lines in (d) and (e) show the location of the vertical sections in (a), (b) and (c). White arrows point to migration artefacts. Yellow lines are a projection at surface of the northern limit of the picrite body intersected near the bottom of the two boreholes. Red dots in (d) and (e) show location of shot points.

different alteration types are not imaged due to geometrical considerations. Contacts with steep dips most likely generated downgoing reflections that were not considered in the migration.

Next steps

Follow-up work will focus on the interpretation of the 3-D seismic volume and integration with other existing data sets from the New Afton deposit. More specifically, the cause of the moderately northwest-dipping reflectors observed on the DAS-VSP data will be further investigated using detailed geological information from the mine and physical rock properties (density and seismic velocity) from both logs and core samples. Currently, these moderately dipping seismic reflectors cannot be easily reconciled with any of the dominant geological structures of the deposit (e.g. lithological contacts, alteration zones). Although the geological significance of these seismic reflections is currently under investigation, this new information, will likely refine the 3-D geological model of the New Afton deposit, which may impact exploration. Integrated 3-D modelling of all existing data, including additional log properties and

results from geochemical analysis, will further help the understanding of the key ore system components near the New Afton deposit.

Conclusions

Wireline logs and for the first time DAS-VSP data were acquired in two boreholes intersecting the copper-gold New Afton porphyry deposit located in southeast British Columbia, Canada. Calliper logs reveal many faults and caved-in zones, indicating generally poor rock conditions in the immediate vicinity of borehole walls. Their significant number on logs suggests that their response may dominate the seismic wavefield. Outside fault zones, compressional and shear-wave velocities exhibit significant variability due to porosity, heterogeneity of volcanic fragmental rocks and alteration. Reflections between potassic alteration (potassic-dominant alteration) and other types of alteration may be possible but depend on local geological context. Contacts between potassic alteration and a picrite unit intersected at the bottom of the two boreholes may also generate detectable reflections.

The two boreholes surveyed with wireline logs were instrumented with straight and helically wound fibre-optic cables for the VSP survey. The fibre-optic cables included standard fibres and a fibre engineered to increase the intensity of backscattering at the DAS interrogator. Field data from the V3 DAS system have lower noise level and higher signal-to-noise ratio. Data from straight fibre-optic cable measured with the V3 DAS system were processed and used for depth imaging. Depth images benefitted from newly introduced migration weights that account for the directional sensitivity of straight fibre-optic cable and limit the extent of migration artefacts. Migration results show several reflectors with shallow dips to the northwest, some explained by faults intersected in the two boreholes used for the VSP survey. The nearly vertical contact between volcanic fragmental rocks with potassic alteration and picrite and other subvertical contacts between different alteration types most likely generated downgoing reflections that were not considered in the migration.

Acknowledgments

This report is a contribution to NRCan's Targeted Geoscience Initiative Program (TGI). Support for this study was provided through the Porphyry-style Mineral Systems Project's '*Activity P-1.3: 3D model of magmatic-hydrothermal conduits*'

We thank Atlas Drilling, Clean Harbors, DGI, Silixa and Western-Alliance for their diligent work and patience in the planning and execution of this project. DAS data were acquired by Silixa with the Carina® sensing system and iDAS™ interrogator. Processing of the DAS-VSP data (excluding traveltime tomography and depth imaging) was done with Globe Claritas™. This work would not have been possible without the outstanding support from New Gold. Sincere thanks to M. Della Libera, S. Davidson and all New Afton employees that provided support in one form or another and made this project possible. This report benefited from the review of Jim Craven, Vicki Tschirhart, SayadMasoud Anasri and Neil Rogers.

References

Bergen, D., Krutzlmann, H., and Rennie, D.W., 2015. New Gold Inc. – New Afton Project, Project #2400 Technical Report NI 43-101 – March 23, 2015; New Gold Inc., Toronto, Ontario, 256 p.

Daley, T.M., Miller, D.E., Dodds, K., Cook, P., and Freifeld, B.M., 2016. Field testing of modular borehole monitoring with simultaneous distributed acoustic sensing and geophone vertical seismic profiles at Citronelle, Alabama; Geophysical Prospecting, v. 64, p. 1318–1334.

Hartog, A.H., 2018. An Introduction to Distributed Optical Fibre Sensing; CRC Press, 442 p.

Lipske, J. and Wade, D., 2014. Geological Model of the New Afton Copper and Gold Deposit, British Columbia; internal report, New Gold Inc., Toronto, Ontario, 53 p.

.

Petrogenesis and associated mineralization of Acadian related granitoids in New Brunswick

Z. Azadbakht[1, 2], N. Rogers[2], D.R. Lentz[1] and C.R.M. McFarlane[1]

[1]*Department of Earth Sciences, University of New Brunswick, P.O. Box 4400, Fredericton, New Brunswick E3B 5A3*

[2]*Geological Survey of Canada, 601 Booth Street, Ottawa, Ontario K1A 0E8*

Abstract

The Acadian-related granitoids of New Brunswick are herein divided into geochemically defined groups to ascertain whether magmatic process related trends differentiate barren from mineralized granitoids. The Juniper Barren and Lost Lake granites have some similar characteristics (i.e. lowest SiO_2, highest transition element contents, high-K calc-alkaline, metaluminous), but do not constitute a defined geochemical group. They have the characteristics of unfractionated (oxidized) I-type granites, and neither are associated with significant mineralization.

Group NB-1 granites are metaluminous to peraluminous, high-K calc-alkaline, light rare-earth element (LREE) enriched with small negative Eu anomalies, and high Nb/Ta and Zr/Hf ratios. Group NB-1 intrusions are interpreted to be unfractionated reduced I-type granite formed via partial melting in an arc system and subsequently contaminated by reducing crustal rocks. The reduced component is critical for the formation of tungsten mineralization.

Group NB-2 granites are high-K calc-alkaline, metaluminous to peraluminous I-type granite characterized by K_2O contents greater than Na_2O, and are LREE enriched with pronounced negative Eu anomalies. Group NB-2 granites are unfractionated to weakly fractionated I-type granite generated from different degrees of partial melting of mixed mantle - older crustal protolith with an igneous quartzo-feldspathic composition.

Group NB-3 granites include the most evolved intrusions examined during this study. They are characterized by the highest SiO_2 content, Gottini index and K/Rb ratio, and have the lowest Zr/Hf, Nb/Ta, La/Sm and Eu/Eu* ratios. They are considered highly evolved I-type granite formed via crustal thinning related to crustal delamination following the juxtaposition of crustal terranes during the Acadian Orogeny.

Introduction

During the Palaeozoic, Atlantic Canada was involved in a series of accretionary orogenic events (Taconic, Salinic, Acadian and Neoacadian) that collectively constituted the Appalachian Orogen (van Staal et al., 2009). Voluminous syn-collisional felsic magmatism that occurred during the Taconic, Salinic, Acadian and Neoacadian orogenies has been linked to subduction and subsequent slab-breakoff (van Staal et al., 2009). In contrast, Early Devonian Acadian magmatism is associated with crustal shortening with magma characteristics previously associated with flat-slab subduction (van Staal et al., 2009).

Felsic intrusions emplaced during the later stages of the Appalachian orogenic cycle in New Brunswick have geochemical affinities ranging from primitive to highly evolved A-, S- and I-type granitoids (Whalen, 1993). However, only those associated with crustal thickening during the Acadian orogeny and post-Acadian uplift have associated granophile element mineralization (e.g. Burnthill, Mount Pleasant, Lake George and Sisson deposits: see Ruitenberg, 1967; Lentz, 1986; Taylor et al., 1987; Sinclair et al., 1988; MacLellan and Taylor, 1989; MacLellan, 1990; McLeod, 1990; Sinclair and Koomian, 1990; Whalen, 1993; Yang et al., 2002a, b, 2003, 2004; Inverno and Hutchinson, 2004; Leonard et al., 2006; Sinclair et al., 2006; Fyffe et al., 2008; Bustard et al., 2013; Zhang et al., 2016).

Twenty-five Late Silurian to Late Devonian intrusions (Fig. 1) were investigated in this study to ascertain whether there are whole-rock geochemical traits that reflect magmatic processes that differentiate barren from mineralized granitoids. When interpreting geochemical data it is crucial to appreciate granite petrogenesis and its association with mineralization. Previous studies on New Brunswick granitoids (e.g. Ruitenberg, 1967; Butt, 1976; Fyffe et al., 1981; Lentz et al., 1988; MacLellan, 1990; McLeod, 1990; Taylor, 1992; Whalen, 1993; Whalen et al., 1994a, b, 1996a, b, 1998; Thorn et al., 2002; Yang, 2005; Shinkle, 2011; Pilote et al., 2012; White, 2013; Zhang, 2015; Wilson and Kamo, 2016; Massawe, 2018) provide insight on the petrogenesis of these intrusions and relationships to mineralization. However, the studies are area specific and do not apply consistent geochemical approaches. The aim herein is to investigate what can be learnt in terms of source and petrogenetic controls of these granitoids by utilizing consistent treatment to petrochemistry.

Corresponding author: Zeinab Azadbakht (zeinab.azadbakht@canada.ca)

Azadbakht, Z., Rogers, N., Lentz, D.R. and McFarlane, C.R.M., 2019. Petrogenesis and associated mineralization of Acadian related granitoids in New Brunswick; *in* Targeted Geoscience Initiative: 2018 report of activities, (ed.) N. Rogers; Geological Survey of Canada, Open File 8549, p. 243–278. https://doi.org/10.4095/313658

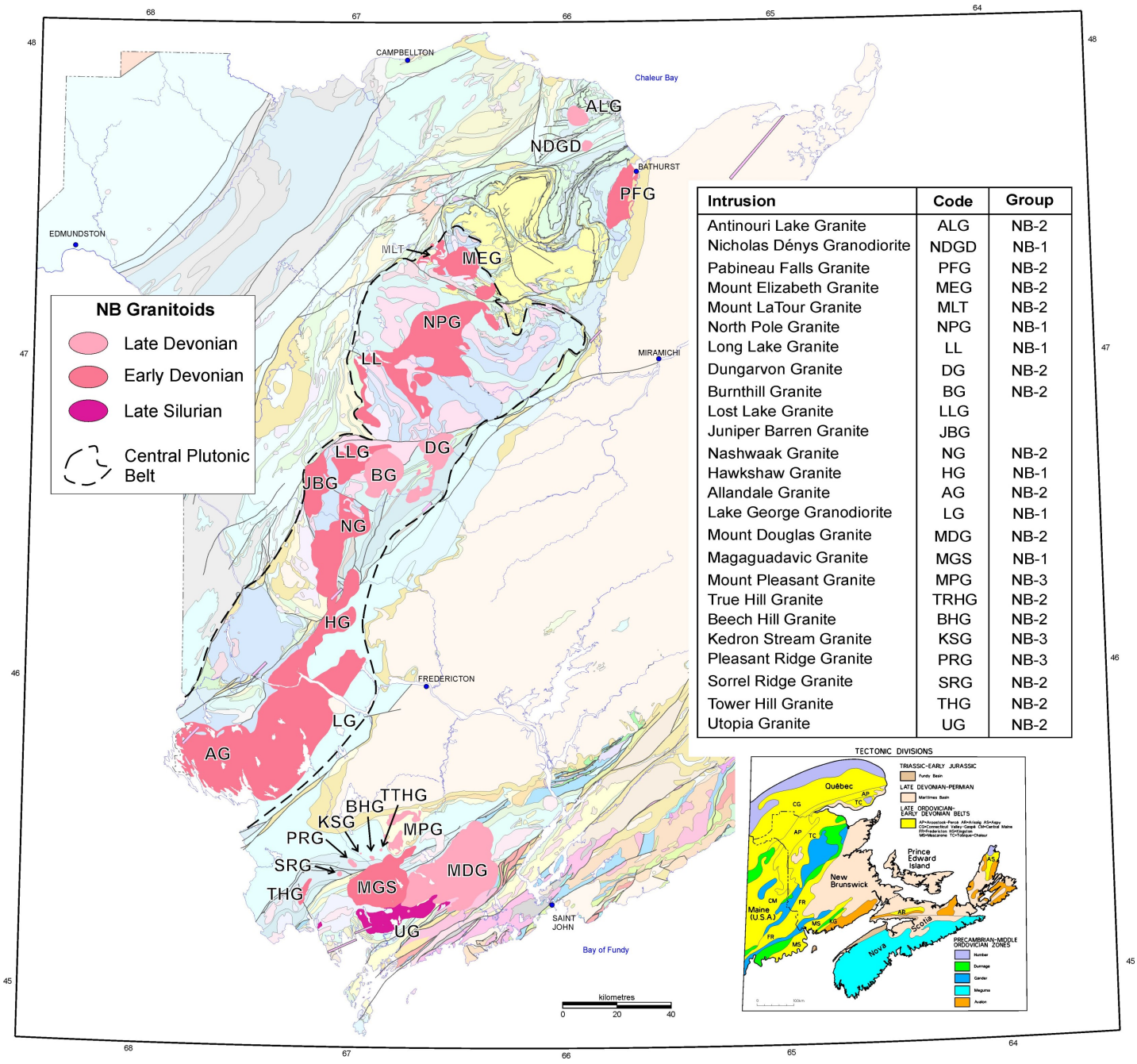

Intrusion	Code	Group
Antinouri Lake Granite	ALG	NB-2
Nicholas Dénys Granodiorite	NDGD	NB-1
Pabineau Falls Granite	PFG	NB-2
Mount Elizabeth Granite	MEG	NB-2
Mount LaTour Granite	MLT	NB-2
North Pole Granite	NPG	NB-1
Long Lake Granite	LL	NB-1
Dungarvon Granite	DG	NB-2
Burnthill Granite	BG	NB-2
Lost Lake Granite	LLG	
Juniper Barren Granite	JBG	
Nashwaak Granite	NG	NB-2
Hawkshaw Granite	HG	NB-1
Allandale Granite	AG	NB-2
Lake George Granodiorite	LG	NB-1
Mount Douglas Granite	MDG	NB-2
Magaguadavic Granite	MGS	NB-1
Mount Pleasant Granite	MPG	NB-3
True Hill Granite	TRHG	NB-2
Beech Hill Granite	BHG	NB-2
Kedron Stream Granite	KSG	NB-3
Pleasant Ridge Granite	PRG	NB-3
Sorrel Ridge Granite	SRG	NB-2
Tower Hill Granite	THG	NB-2
Utopia Granite	UG	NB-2

Figure 1. Lithological map of New Brunswick *modified after* Fyffe and Richard (2007) and New Brunswick Department of Natural Resources (2008) showing the location of the granitoids examined in this study. Inset map shows the general tectonic divisions of the Canadian Maritimes.

Geological setting

The Late Silurian to Late Devonian felsic intrusions in this study range in composition from granodiorite to alkali-granite (De La Roche et al., 1980). Most of the intrusions are located within the Central Plutonic Belt of New Brunswick (Fig. 1) that extends from Chaleur Bay, northeastern New Brunswick, to Maine in the southwest (Azadbakht et al., 2016). The belt includes many calc-alkaline, non-foliated to foliated Silurian-Devonian granitic intrusions. These granitoids intrude the Cambrian to Early Ordovician rocks of the Miramichi, Woodstock and Meductic groups, as well as the Bathurst Supergroup and the Trousers Lake Metamorphic Suite (Wilson and Kamo, 2016). The granitoid suites studied herein were produced primarily during the early to late Acadian (421–400 Ma) and Neo-

acadian (395–350 Ma) orogenies (Whalen 1993; van Staal et al., 2009).

To investigate potential petrogenetic trends whole rock geochemical data was compiled from previous studies (Table 1: McLeod, 1990; Whalen, 1993; Yang, 2005; Beal et al., 2010; Shinkle, 2011) and principal component analysis applied to define chemical variations (see Grunsky, 1997; Harris et al., 2000; Chandrjith et al., 2001; Garrett and Grunsky, 2001; Linhai Jing and Panahi, 2006; Cheng et al., 2011; Davis, 2011; Parsa et al., 2016). This approach treats data as a correlation matrix or eigenvector of a variance-covariance matrix and plots the result in terms of two components (e.g. component one and two). Component one (X-axis) represents the greatest possible variance among the data set, whereas component two (Y-axis) is calculated in the same way, but with the condition that is perpendicular (i.e. uncorrelated) with respect to the first component and it is considered the second highest variance in the data set (Davis, 2011).The results indicate Rb content as the most variable trace element followed by Mn, Zr and Ce (Fig. 2). These elements were plotted versus TiO_2, which behaves geochemically compatibly, to further granitoid classification. Several immobile major- and trace-element plots were useful in identifying three groups of intrusions (herein designated as NB -1, NB-2 and NB-3). Petrography, age data and mineralization are summarized for the studied granites in Appendix A.

Group NB-1 includes six granitoids that are further divided into three subgroups (NB-1-1 to NB-1-3), based on their litho-geochemical characteristics. Group NB-1-1 includes the multi-phase North Pole Stream Granite (NPG), Nicholas Dénys granodiorite (NDGD) and Magaguadavic Granite (MGS). Group NB-1-2 includes the Hawkshaw Granite (HG) and Long Lake Granite (LL), whereas NB-1-3 includes only the Lake George Granodiorite (LG). Group NB-2 incorporates fourteen intrusions: Allandale (AG), Antinouri Lake (ALG), Beech Hill (BHG), Burnthill (BG), Dungarvon (DG), Mount Douglas (MDG), Mount Elizabeth (MEG), Mount LaTour (MLT), Nashwaak (NG), Pabineau Falls (PFG), Sorrel Ridge (SRG), Tower Hill (THG), True Hill (TRHG) and Utopia (UG). The group is further divided into six subgroups (NB-2-1 to NB-2-6) based on minor geochemical variations. Group NB-3 intrusions include three Late Devonian granitoids, specifically Granite II of Mount Pleasant (MPG), the Pleasant Ridge Granite (PRG) and the Kedron Stream Granite (KSG).

The Juniper Barren (JBG) and Lost Lake (LLG) granites do not readily fit into any grouping, and thus are treated individu-

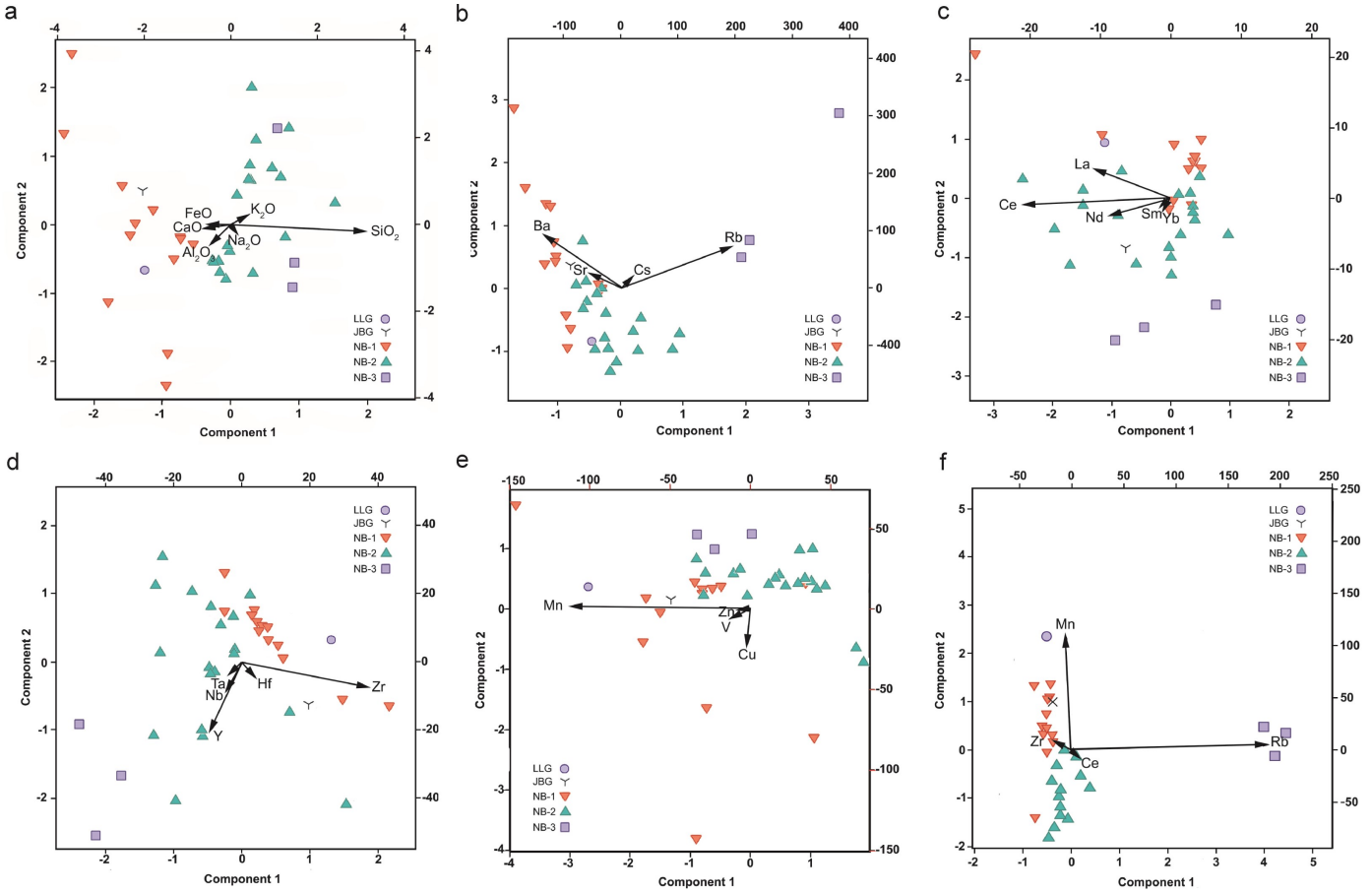

Figure 2. Principle component analysis (PCA) of the compiled whole rock data for the Acadian-related granitoids in New Brunswick: a) major elements; b) large ion lithophile elements; c) rare earth elements; d) high field strength elements; e) transition elements; and f) Zr-Mn-Rb-Ce.

Table 1. Representative geochemical analyses of Acadian-related granitoids in New Brunswick (*after* McLeod, 1990; Whalen, 1993; Yang, 2005; Beal et al., 2010; Shinkle, 2011).

Pluton	Code	Unit	Sample	SiO2	TiO2	Al2O3	FeOt	MnO	MgO	CaO	Na2O	K2O	P2O5	LOI	Total	As	Au	Ba
Magaguadaic Granite	MGS	NB-1-1	WX85NB-196	68.95	0.53	14.85	2.71	0.06	1.09	2.32	4.10	4.27	0.15	0.66	99.95	3.3	0.5	625
Nicholas Dénys Granodiorite	NDGD	NB-1-1	WX85NB-47	68.95	0.42	15.40	2.51	0.03	0.93	3.00	4.82	2.36	0.11	0.78	99.52	0.1	0.2	504
North Pole Stream Granite	NPG	NB-1-1	WX85NB-118	69.60	0.55	14.30	3.03	0.06	0.87	2.32	3.59	3.81	0.13	0.62	99.17	0.1	1.5	1000
Hawkshaw Granite	HG	NB-1-2	WX85NB-11	70.05	0.44	14.45	2.22	0.06	0.86	2.20	3.63	4.14	0.15	0.58	98.97	0.8	1.0	402
Long Lake Granite	LL	NB-1-2	DS06-077	68.81	0.51	16.17	3.69	0.10	1.85	0.68	3.43	3.40	0.19		101.11			691
Lake George Granodiorite	LG	NB-1-3	LG78-18-1190	65.71	0.60	14.83	3.78	0.07	1.53	3.35	3.90	1.57	0.14	4.40	101.00	31.9	2.0	260
Lake George Granodiorite	LG	NB-1-3	LG79-6-612	62.27	0.49	14.23	3.24	0.05	1.14	2.05	2.77	3.98	0.14	3.00	99.10	28.2	16.0	580
Lake George Granodiorite	LG	NB-1-3	LG80-36-1647	67.10	0.55	14.86	3.26	0.07	1.16	2.58	3.32	3.90	0.13	1.60	98.80	5.6	75.0	650
Lake George Granodiorite	LG	NB-1-3	LG81-12-1567	67.10	0.58	14.69	3.38	0.07	1.21	2.89	3.42	3.36	0.14	2.00	99.20	4.0	2.0	310
Lake George Granodiorite	LG	NB-1-3	LG81-14-1291	66.33	0.57	13.91	3.24	0.06	1.17	3.10	3.19	2.76	0.14	3.90	99.00	365.0	2.0	360
Lake George Granodiorite	LG	NB-1-3	LG81-14-1886	62.39	0.59	14.56	3.36	0.07	1.26	3.01	3.48	3.23	0.13	2.10	92.30	13.5	8.0	480
Lake George Granodiorite	LG	NB-1-3	LG81-19-1351	65.30	0.57	15.24	3.24	0.06	1.12	2.99	3.52	3.85	0.13	1.50	96.00	4.9	2.0	710
Lake George Granodiorite	LG	NB-1-3	LG81-2-1741	67.90	0.54	14.11	3.13	0.06	1.09	2.60	3.33	3.27	0.13	2.50	98.70	2.9	33.0	490
Allandale Granite	AG	NB-2-1	WX85NB-16	71.45	0.28	14.40	1.60	0.04	0.58	1.51	3.89	4.06	0.11	1.19	99.29	1.0	0.8	364
Allandale Granite	AG	NB-2-1	WX85NB-38	72.00	0.28	14.40	1.73	0.06	0.49	1.37	3.59	4.56	0.19	0.89	99.60	0.1	0.2	301
Tower Hill Granite	THG	NB-2-1	C80-5-254	71.40	0.22	14.32	2.24	0.05	1.33	0.36	4.45	3.63	0.15	0.42	98.30	1.7	2.0	403
Tower Hill Granite	THG	NB-2-1	WX85NB-214	73.40	0.15	14.60	3.03	0.03	0.19	0.87	3.91	4.95	0.09	0.74	99.99	0.1	1.0	423
Beech Hill Granite	BHG	NB-2-2	WX85NB-188	75.15	0.21	12.65	0.91	0.04	0.18	0.89	3.91	4.73	0.04	0.54	99.95	8.0	2.3	192
Mount Douglas Granite	MDG	NB-2-2	WX85NB-198	73.35	0.31	13.20	2.51	0.03	0.38	1.24	3.59	5.11	0.07	0.42	99.54	1.3	1.0	511
Mount Douglas Granite	MDG	NB-2-2	WX85NB-220	73.70	0.25	12.70	0.82	0.05	0.24	0.88	3.59	4.84	0.06	0.92	99.25	13.0	1.0	185
Mount Elizabeth Granite	MEG	NB-2-2	WX86NB-240	75.50	0.14	13.40	2.24	0.03	0.12	0.87	3.89	4.69	0.04	0.39	100.27	0.1	2.5	222
Antinouri Lake Granite	ALG	NB-2-3	WX85NB-52	74.45	0.21	12.70	0.41	0.04	0.24	0.87	3.97	4.74	0.05	0.47	99.47	1.0	1.5	182
Burnthill Granite	BG	NB-2-3	12-SHM-054	72.41	0.31	13.80	2.55	0.07	0.60	1.74	3.70	3.81	0.08	0.72	99.62	0.5	2.0	320
Dungarvon Granite	DG	NB-2-3	WX85NB-225	73.55	0.22	12.95	1.78	0.05	0.31	1.02	3.79	4.62	0.06	0.62	98.94	1.0	0.5	140
Dungarvon Granite	DG	NB-2-3	WX85NB-226	71.35	0.33	14.25	2.38	0.07	0.59	1.71	4.09	3.95	0.09	0.81	99.57	1.8	1.5	289
Mount LaTour Granite	MLT	NB-2-4	WX86NB-254	72.80	0.27	13.40	2.08	0.02	0.47	0.93	3.96	4.59	0.05	0.85	100.08	23.5	5.0	271
Mount LaTour Granite	MLT	NB-2-4	WX86NB-262	73.10	0.21	12.10	0.31	0.03	0.26	0.58	4.05	5.04	0.04	0.62	98.26	2.0	1.0	183
Utopia Granite	UT	NB-2-4	WX85NB-189	73.20	0.23	13.40	1.90	0.04	0.20	0.83	3.84	5.04	0.07	0.62	99.48	4.0	0.8	269
Sorrel Ridge Granite	SRG	NB-2-5	SR82-1-199	78.50	0.10	12.35	2.71	0.03	0.62	0.09	3.59	5.07	0.03	0.54	102.40	4.2	2.0	42
True Hill Granite	TRHG	NB-2-5	TH82-10-273	77.00	0.11	11.58	2.69	0.05	0.60	0.08	3.33	4.62	0.02	0.50	99.60	2.6	2.0	42
Nashwaak Granite	NG	NB-2-6	WX85NB-173	72.05	0.30	14.60	1.09	0.05	0.65	1.34	3.65	4.18	0.15	0.81	99.84	2.5	0.2	375
Pabineau Falls Granite	PFG	NB-2-6	WX85NB-46	71.10	0.31	14.50	2.13	0.06	0.62	1.63	3.98	4.20	0.12	0.85	99.33	0.5	0.2	432
Kedron Stream Granite	KSG	NB-3	BR84-4-129	75.90	0.02	13.20	1.23	0.10	0.51	0.02	4.06	3.74	0.03	0.82				18
Mount Pleasant Granite	MPG	NB-3	AM96-3-1223	74.90	0.02	12.15	1.31	0.08	0.04	0.36	3.76	4.60	0.02	0.58	97.80	8.7	2.0	22
Pleasant Ridge Granite	PRG	NB-3	WX85NB-187	75.75	0.04	13.70	0.82	0.06	0.01	0.21	4.63	4.19	0.02	0.66	101.19	2.0	0.5	12
Juniper Barren Granite	JBG		WX85NB-170	67.40	0.71	14.30	3.87	0.07	1.14	2.44	3.48	3.97	0.18	1.08	98.87	0.8	3.8	486
Lost Lake Granite	LLG		WX85NB-161	67.75	0.84	14.50	4.32	0.10	1.44	2.63	3.62	2.69	0.14	0.85	99.05	0.1	0.2	264

Major elements in weight %; minor and trace elements in ppm; Tzrn, Tmnt and Tap: estimates of liquidus temperatures from zircon, monazite and apatite saturation models after Watson and Harrison (1983), Montel (1993) and Harrison and Watson (1984) respectively, in °C.

Table 1. cont.

Sample	Be	Cd	Co	Cr	Cs	Cu	Ga	Hf	Mn	Mo	Nb	Ni	Pb	Rb	Sb	Sc	Se	Sn	Sr	Ta	Th	Tl	U
WX85NB-196	7	0.3	7.6	14	8.4	8.3	19	5.9	480	0.3	16.5	4.8	16	168	0.9	7.0	0.2	3.0	329	1.4	22.5	0.5	6.6
WX85NB-47	4	0.3	4.6	5	1.4	77.0	20	3.3	240	1.0	7.8	2.5	9	74	0.1	4.6	0.2	4.3	380	0.8	8.8	0.5	3.9
WX85NB-118	4	0.3	6.8	7	4.5	9.5	16	8.5	500	0.3	16.1	2.5	20	138	0.2	10.4	0.2	0.3	200	1.0	18.0	0.5	3.2
WX85NB-11	4	0.3	5.3	10	8.7	6.8	18	4.4	460	0.3	15.0	4.3	22	172	0.2	7.1	0.2	3.8	177	1.5	17.5	0.5	2.4
DS06-077	3	0.3		16		4.0	20	5.6			24.5	4.0	15	153		14.0			167	1.7	11.0		6.0
LG78-18-1190	3	0.3	10.0	30	6.0	14.0	16	5.0	623	2.0	12.5	17.0	27	68	4.6	9.2	0.6	1.0	317	0.5	12.2	0.3	6.4
LG79-6-612	5	0.3	8.0	10	6.0	56.0	16	6.0	430	1.0	15.5	5.0	25	139	27.9	7.9	0.6	1.0	177	5.0	14.9	1.0	9.2
LG80-36-1647	4	0.3	9.0	15	8.0	24.0	16	5.0	590	7.0	14.5	7.0	17	154	6.0	8.1	0.5	1.0	276	1.8	15.5	0.8	6.8
LG81-12-1567	4	0.3	8.0	10	8.0	72.0	16	4.0	482	4.0	14.5	6.0	18	119	2.6	7.4	0.7	1.0	232	1.8	14.4	0.5	8.4
LG81-14-1291	4	0.3	9.0	21	7.0	140.0	16	4.0	506	6.0	13.3	11.0	23	112	6.5	7.9	0.8	1.0	223	1.6	13.2	0.5	5.8
LG81-14-1886	4	0.3	7.0	12	9.0	41.0	15	4.0	628	2.0	12.6	6.0	18	159	5.6	8.2	0.4	1.0	300	0.5	14.1	0.9	6.6
LG81-19-1351	4	0.3	9.0	13	6.0	8.0	16	5.0	541	6.0	14.1	6.0	21	136	4.8	7.8	0.4	1.0	310	1.5	13.8	0.5	7.1
LG81-2-1741	4	0.3	8.0	16	6.0	9.0	16	5.0	584	3.0	14.3	7.0	15	142	4.3	8.8	0.3	1.0	288	2.5	12.8	0.6	6.3
WX85NB-16	5	0.3	3.3	5	7.6	5.3	18	4.6	345	2.5	13.4	2.5	21	166	0.2	5.1	1.7	4.8	114	1.4	16.5	0.5	13.9
WX85NB-38	6	0.3	3.4	6	10.4	3.3	17	3.1	435	3.0	16.5	2.5	28	235	0.2	5.3	0.2	13.5	102	2.4	13.3	0.5	2.9
C80-5-254		21.5	10.7	11	14.2	11.4	23	3.7		6.0	14.5	2.0	24	225	0.2	1.6	3.0	6.6	140	1.6	12.6		8.6
WX85NB-214	6	0.3	1.2	1	11.1	1.5	20	3.1	245	0.3	12.5	1.0	31	213	0.2	2.7	0.4	6.0	85	1.2	16.5	0.5	3.3
WX85NB-188	9	0.3	1.9	1	13.8	2.3	18	6.0	325	0.3	37.3	1.0	18	376	1.0	4.0	2.0	8.8	55	4.3	43.5	1.5	16.5
WX85NB-198	6	0.3	3.0	2	7.7	1.3	16	5.8	235	0.3	17.6	2.0	12	255	0.5	3.3	0.2	1.0	102	1.9	28.0	0.5	6.9
WX85NB-220	8	0.3	2.8	1	17.8	3.0	17	6.0	360	0.3	25.9	0.5	24	325	1.2	6.4	0.2	12.0	50	2.4	34.0	5.0	10.7
WX86NB-240	7	0.3	1.5	1	7.0	2.0	16	3.4	270	0.3	11.4	2.0	24	213	0.3	4.1	2.3	8.0	47	1.7	22.0	3.0	12.7
WX85NB-52	6	0.3	1.7	2	2.9	1.3	18	5.7	320	0.3	19.6	1.5	12	215	0.2	4.6	0.2	2.0	49	1.9	25.3	1.5	7.9
12-SHM-054	7	0.5	3.0	26	9.1	1.0	20	4.1		2.0	12.9	5.0	19	251	0.2	5.0		10.0	220	3.3	23.0	1.4	6.9
WX85NB-225	10	0.3	2.1	1	12.0	0.8	18	4.4	415	0.3	20.2	2.0	21	301	0.4	5.0	0.7	42.0	78	3.8	31.8	0.5	10.5
WX85NB-226	11	0.3	3.9	1	8.6	1.3	19	5.1	520	1.0	19.9	3.5	14	278	0.3	6.1	0.2	17.0	302	3.9	21.8	0.5	10.9
WX86NB-254	6	0.3	4.5	10	2.9	36.0	18	8.0	180	5.0	21.5	4.5	8	149	0.5	5.0	0.2	0.3	43	1.5	17.5	0.5	7.0
WX86NB-262	8	0.3	1.8	3	1.9	2.0	19	10.5	210	0.3	23.4	1.5	4	180	0.4	2.9	1.7	3.0	20	1.4	21.0	4.0	6.2
WX85NB-189	7	0.3	2.6	1	5.4	1.5	20	5.6	300	3.5	26.2	2.0	8	206	0.5	8.5	1.2	0.3	41	1.7	26.0	1.0	3.7
SR82-1-199		20.6	10.3	10	6.2	188.0	19	4.3		1.0	45.3	2.0	25	449	0.4	2.7	3.0	47.7	28	6.2	41.2		36.7
TH82-10-273		20.4	10.2	10	5.1	17.2	23	5.5		12.0	51.5	4.0	40	518	0.1	3.0	3.0	2.7	21	7.2	44.1		21.0
WX85NB-173	5	0.3	4.4	9	10.7	8.8	17	3.6	390	0.3	16.4	5.0	19	193	0.4	6.0	0.2	7.8	85	2.4	13.8	3.0	5.0
WX85NB-46	7	0.3	3.7	6	6.7	5.5	18	4.1	500	13.0	17.2	3.0	20	168	0.2	5.5	0.2	6.0	148	1.9	15.0	0.5	4.3
BR84-4-129					14.5		34	6.9			65.1			866				156.0	18	23.7	18.0		29.4
AM96-3-1223		22.3	11.2	11	20.5	5.6	33	6.1		1.0	64.5	16.0	24	933	0.8	2.0	3.0	43.1	8	15.3	32.7		20.3
WX85NB-187	11	0.3	0.8	1	54.8	2.3	29	5.0	485	0.3	43.6	0.5	19	1457	1.4	10.4	1.9	7.8	4	16.5	25.5	8.5	14.9
WX85NB-170	5	0.3	9.2	19	5.8	11.5	18	7.3	575	0.3	16.6	7.3	20	171	0.2	11.6	0.9	2.5	135	1.4	17.8	1.0	5.0
WX85NB-161	5	0.3	11.0	15	5.6	11.0	19	6.9	765	0.3	13.8	7.8	8	138	0.2	12.3	0.2	0.8	139	1.5	10.2	3.5	13.1

Major elements in weight %; minor and trace elements in ppm; Tzrn, Tmnt and Tap: estimates of liquidus temperatures from zircon, monazite and apatite saturation models after Watson and Harrison (1983), Montel (1993) and Harrison and Watson (1984) respectively, in °C.

Table 1. cont.

Sample	Bi	V	W	Y	Zn	Zr	La	Ce	Pr	Nd	Sm	Eu	Gd	Tb	Dy	Ho	Er	Tm	Yb	Lu	Tzrn	Tmnt	Tap
WX85NB-196		47	0.3	21.6	53.5	185.9	55.0	94.5		32.0	4.81	1.19		0.7					2.10	0.33	782	778	936
WX85NB-47	0.6	42	0.3	10.3	20.3	127.3	26.5	52.0	5.35	19.2	3.08	0.78	2.62	0.3	1.87	0.37	1.02	0.15	1.02	0.16	752	735	903
WX85NB-118	0.1	52	0.3	33.9	40.0	239.0	95.2	155.0		53.0	8.02	2.24		1.2					3.20	0.43	814	841	927
WX85NB-11	0.1	39	0.8	24.9	40.8	133.5	34.1	63.0		25.5	4.87	1.10		0.8					1.97	0.29	763	765	947
DS06-077		43		23.5	42.0	269.0	35.1	65.4	7.33	27.6	5.39	1.13	5.07	0.8	4.60	0.89	2.54	0.36	2.47	0.38	866	856	961
LG78-18-1190	1.7	60	1.0	20.0	59.0	174.0	29.5	50.0		12.0	3.90	1.00		0.5					1.90	0.30	785	721	881
LG79-6-612	3.8	49	4.0	22.0	38.0	179.0	30.1	51.0		8.0	4.10	1.10		0.5					2.30	0.30			
LG80-36-1647	11.9	52	6.0	23.0	48.0	166.0	37.0	62.0		16.0	4.90	1.20		0.5					2.60	0.30			
LG81-12-1567	0.4	51	31.0	16.0	42.0	173.0	29.4	49.0		15.0	4.00	1.10		0.5					2.20	0.30			
LG81-14-1291	0.8	59	1.0	13.0	39.0	167.0	31.4	52.0		15.0	4.10	1.00		0.5					1.90	0.30			
LG81-14-1886	0.2	59	5.0	19.0	51.0	160.0	30.4	51.0		13.0	3.90	1.10		0.5					1.90	0.30			
LG81-19-1351	0.2	59	1.0	28.0	47.0	194.0	32.5	52.0		19.0	4.40	1.20		0.5					2.10	0.30			
LG81-2-1741	10.5	55	8.0	19.0	50.0	168.0	31.5	50.0		14.0	4.20	1.00		0.5					2.20	0.30			
WX85NB-16	0.1	21	0.8	24.4	35.3	137.5	18.2	37.9	4.45	17.4	3.63	0.57	3.32	0.6	3.19	0.63	1.63	0.23	1.56	0.22	774	742	928
WX85NB-38	0.1	21	0.3	23.4	39.0	105.8	27.2	53.0		22.5	4.32	0.76		0.7					1.53	0.24	754	743	989
C80-5-254	0.4	16	1.0	10.0	95.7	145.6	27.1	57.1	5.90	20.6	3.85	0.66	2.90	0.4	2.10	0.30	0.80	0.10	0.60	0.10	790	792	959
WX85NB-214	0.7	4	0.8	14.2	39.5	79.4	29.7	49.5		18.5	3.41	0.59		0.4					0.74	0.10	733	770	927
WX85NB-188	0.3	12	3.5	69.6	21.0	147.0	56.6	103.0		39.0	6.99	0.58		1.6					8.49	1.35	773	802	868
WX85NB-198	0.5	19	3.3	35.9	18.0	154.6	48.2	86.5		30.5	5.09	0.85		0.9					4.26	0.67	776	783	902
WX85NB-220	0.1	15	3.5	72.9	31.0	145.8	59.2	117.0		48.0	8.43	0.56		1.5					7.57	1.19	776	821	891
WX86NB-240	0.5	7	1.0	29.2	16.0	79.4	30.3	53.0		21.0	3.75	0.52		0.6					3.07	0.50	729	764	872
WX85NB-52	0.1	11	1.0	52.1	22.0	137.3	36.3	81.6	9.41	34.6	7.57	0.34	7.16	1.3	7.93	1.73	4.85	0.73	5.01	0.72	767	779	882
12-SHM-054	0.4	29	1.0	36.2	75.0	157.0	29.5	59.7	7.08	25.5	5.50	0.62	4.83	0.9	5.21	1.03	3.30	0.57	3.90	0.54	783	771	906
WX85NB-225	0.3	18	0.3	49.6	27.3	106.6	32.1	65.0		30.0	6.28	0.32		1.2					5.09	0.83	749	772	890
WX85NB-226	0.9	25	4.8	49.2	31.8	145.0	29.8	64.0	7.64	29.0	6.38	0.64	5.69	1.1	6.83	1.52	4.35	0.70	4.95	0.74	772	771	907
WX86NB-254	0.1	19	2.5	50.0	18.0	202.1	55.1	102.0		43.0	8.25	0.88		1.4					4.94	0.73	804	813	866
WX86NB-262	0.2	6	0.5	78.6	30.0	254.1	74.9	126.0		58.0	11.70	0.69		1.9					6.77	1.00	815	810	849
WX85NB-189		12	3.3	45.9	24.3	142.2	45.1	86.0		35.5	6.81	0.59		1.5					4.80	0.71	773	797	901
SR82-1-199	1.7	10	4.0	75.2	52.1	112.0	27.5	64.6	7.40	26.6	6.30	0.15	6.80	1.2	9.70	2.10	7.20	1.20	8.30	1.30	763	787	863
TH82-10-273	3.0	10	4.0	99.6	43.1	138.6	49.7	112.7	12.10	40.1	8.80	0.15	8.50	1.6	12.50	2.70	9.20	1.60	10.60	1.60	784	838	828
WX85NB-173	1.0	29	0.5	25.7	37.3	120.6	29.5	54.5		22.5	3.95	0.85		0.8					2.23	0.33	768	783	967
WX85NB-46	0.2	26	0.5	28.8	31.0	134.6	34.1	59.0		25.0	4.28	1.03		0.7					2.77	0.43	768	770	934
BR84-4-129			8.0	97.6		95.4	26.0	75.5	9.10	31.3	9.30	0.03	8.50						21.50	3.20	761	807	839
AM96-3-1223	0.1	11	13.0	132.2	70.3	85.0	34.2	91.1	10.80	37.2	9.70	0.01	9.50	1.9	14.80	3.20	11.20	2.10	15.20	2.40	737	807	809
WX85NB-187	0.3	1	18.0	94.3	10.3	57.3	29.5	80.0		30.5	7.38	0.10		2.0					16.60	2.73	710	807	795
WX85NB-170	0.3	69	0.3	44.1	55.8	215.0	41.0	84.4	10.14	38.1	7.87	1.35	7.24	1.2	7.63	1.64	4.28	0.61	4.12	0.60	799	782	940
WX85NB-161	0.4	90	0.8	7.5	58.5	222.5	55.0	92.5		35.0	5.84	1.55		0.6					0.60	0.10	811	806	916

Major elements in weight %; minor and trace elements in ppm; Tzrn, Tmnt and Tap: estimates of liquidus temperatures from zircon, monazite and apatite saturation models after Watson and Harrison (1983), Montel (1993) and Harrison and Watson (1984) respectively, in °C.

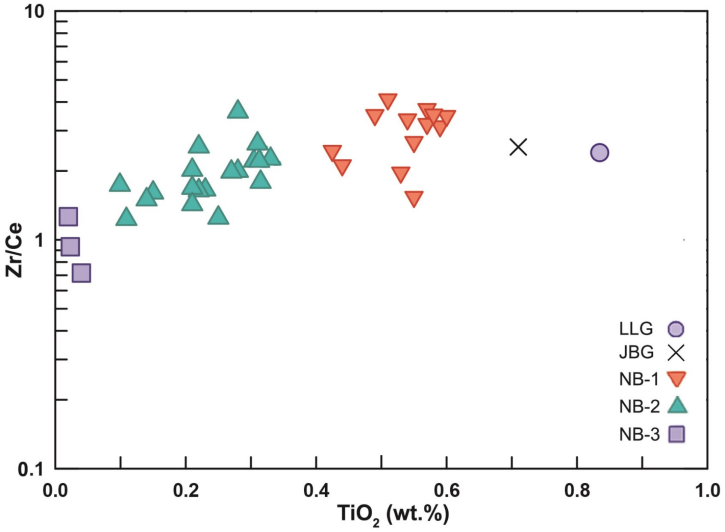

Figure 3. Discriminant plot of TiO_2 (weight %) vs. Zr/Ce discriminant plot for Acadian-related granitoids examined in this study. Abbreviations: JBG – Juniper Barren Granite; LLG – Lost Lake Granite.

ally herein. The TiO_2 versus Zr/Ce discrimination plot is very effective for distinguishing the four groups of granitoids (Fig. 3), but they are also evident by cluster analysis (Davis, 2011). It is notable that the chemically distinctive JBG and LLG are also the only granitoids in this study that intrude a high-grade metamorphic terrane (Cambrian to Ordovician Trouser Lake Metamorphic Suite consists primarily of gneissic rocks with local migmatite associated with the Ordovician McKiel Lake Granite (New Brunswick Department of Energy and Resource Development, 2018)). This distinctive setting would presumably make the source region for granite petrogenesis relatively 'dry', resulting in higher temperature partial melting. In turn, this could explain the atypical chemical characteristics, such as elevated TiO_2 due to involvement of titanite or related restite minerals.

Petrographic characteristics of granitoid intrusions

New Brunswick granitoids are typically characterized by a high abundance of quartz, K-feldspar and calcic plagioclase, with magnetite-ilmenite, apatite, zircon and monazite as common accessory phases. Granites from group NB-1, along with the JBG and LLG, are less evolved relative to the other two groups and plot in the granodiorite field using the IUGS classification scheme of Le Maitre et al. (2002). Conversely, plutons from groups NB-2 and NB-3 plot in the granite field of this classification. All of the granites examined contain both plagioclase and K-feldspar and display characteristics of haplogranite with plagioclase typically being more abundant than K-feldspar (sub-solvus). They display a variety of textures, including coarse- to fine-grained, equigranular, seriate and porphyritic, indicating a variety of crystallization environments, evolved characteristics and relatively high level of emplacement (Yang, 2005). Interestingly, the major rock-forming minerals show different physical characteristics among these groups. For example, quartz shows undulose extinction in the JBG, LLG and NB-1 group granites (Fig. 4a), whereas normal extinction is observed in groups NB-2 and NB-3. The presence of undulose extinction might indicate that these granites formed prior to the main phase of Acadian deformation/metamorphism.

Biotite is the most common ferromagnesian mineral within these granites; however, amphibole is present in some of the less-evolved intrusions, such as Lake George and Mount LaTour granites (Fig. 4b). Furthermore, the colour of biotite varies from reddish-brown to brown in NB-1 granites (Fig. 4c), indicating the relatively reduced nature of these intrusions, whereas it ranges from dark brown to greenish-brown in other granitoids (Fig. 4d) reflecting the more oxidized nature of these intrusions (cf. Lalonde and Bernard, 1993). Some of the most evolved intrusions examined in this study include Tower Hill, Burnthill, Beech Hill, Mount Douglas, Pleasant Ridge, Mount Pleasant and Kedron Stream granites all of which display granophyric to micrographic textures (Fig. 4e, f) indicating water saturation during their crystallization (Lentz and Fowler, 1992; Candela, 1997). Interestingly, NB-3 granites contain primary topaz, which might reflect a high halogen (specifically fluorine) content of these magmas (Yang et al., 2008). Additional information for the various intrusions is recorded in the New Brunswick bedrock lexicon (New Brunswick Department of Energy and Resource Development, 2018).

Economic geology

Tin, tungsten, molybdenum and antimony mineralization are commonly associated with highly fractionated intrusive phases that represent the late stage, incompatible element and fluid-enriched roof zones of large magma chambers (Wilson and Kamo, 2016). Highly evolved granites are characterized by elevated Rb/Ba and Rb/Sr ratios. Consequently, these ratios have been used as a proxy to target tin-bearing granitic rocks (Tauson and Kozlov, 1973; Neiva, 1984; Blevin and Chappell, 1992, 1995; Baker et al., 2005; Ng et al., 2015). Figure 5a shows that the MPG, PRG, KSG, TRHG, SRG, BHG, DG, MDG, MEG and UG are the most fractionated intrusions examined in this study. This suggests that these granites may be associated with tin mineralization; however, stanniferous granites typically contain more than 10 ppm Sn (Neiva, 1984; Lehmann et al., 1990). Bolded symbols on Figure 5a show the location of intrusions with known tin mineralization and dotted symbols show the distribution of the samples with more than 10 ppm Sn, which includes DG (17–42 ppm), BG (10 ppm), AG (14 ppm), MDG (12 ppm), SRG (48 ppm), MPG (43 ppm) and KSG (156 ppm). However, high Sn does not always correlate with high Rb/Ba and Rb/Sr ratios (Fig. 5a), thus this plot cannot be solely used to identify Acadian tin-bearing granites. On the other hand, most of the studied intrusions exhibit geochemical characteristics of highly evolved, tin-bearing granite

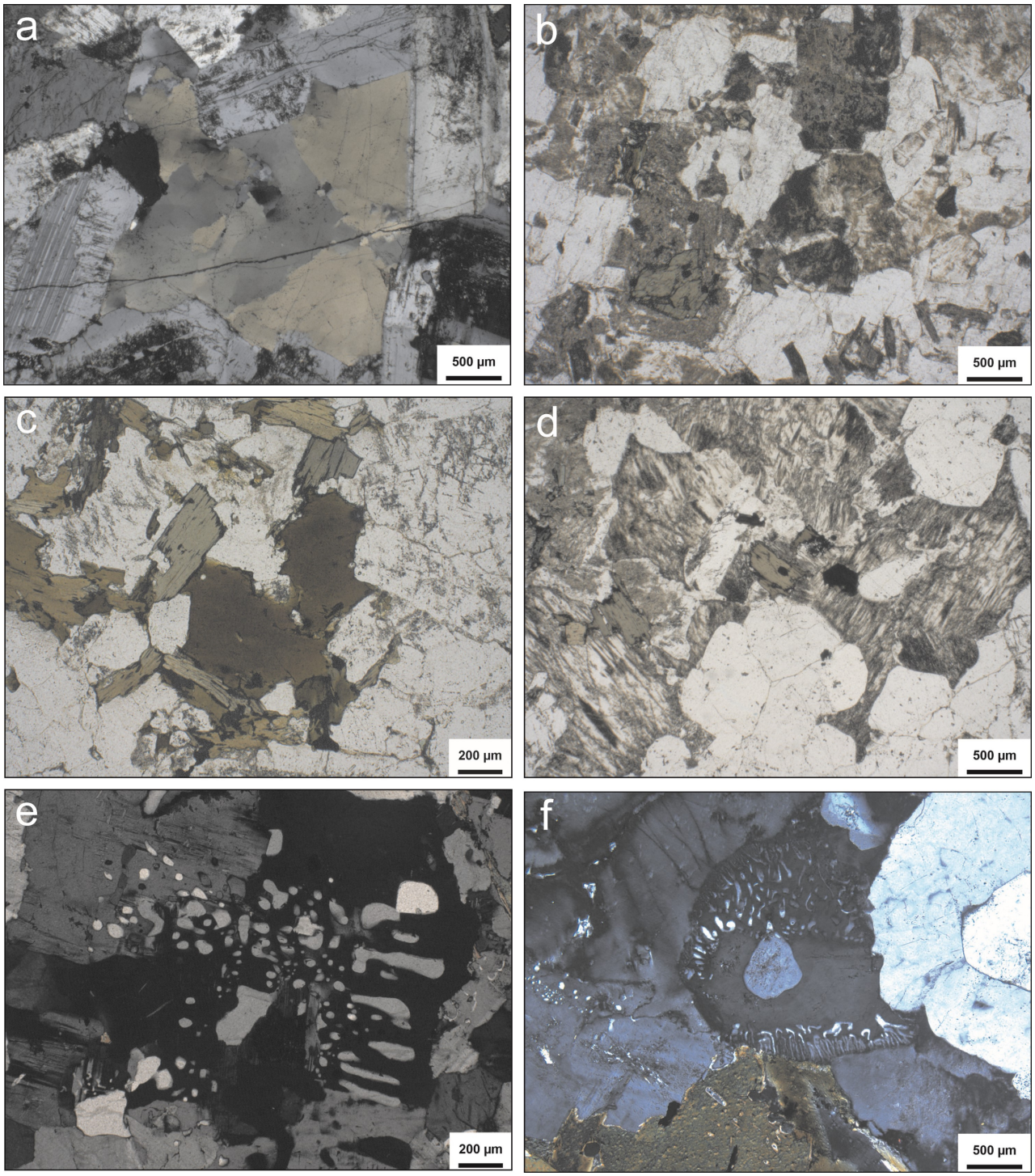

Figure 4. Photomicrographs showing variation in mineralogy and texture of some of the Siluro-Devonian granitoids examined in this study (PPL = plane polarized light and XPL = cross-polarized light). a) Partly resorbed euhedral quartz phenocryst displaying undulose extinction in the North Pole Granite (sample WX85NB-118: XPL). This texture may relate to a low degree of deformation and/or metamorphism in this rock. b) Xenocrystic amphibole is an accessory ferromagnesium mineral in the relatively lesser evolved Acadian-related granites (Mount LaTour Granite – sample WX86NB-262: XPL). c) Reddish-brown biotite phenocrysts in the Nicholas Dénys Granodiorite indicating the reduced environment of the formation (sample WX85NB-47: PPL). d) Light green biotite phenocrysts (Lost Lake Granite – sample WX86Nb-161: PPL). e) Micrographic texture in the Tower Hill Granite (sample WX85NB-214: XPL). f) Myrmekitic texture in the Mount Pleasant Granite (sample AM96-3-1223: XPL).

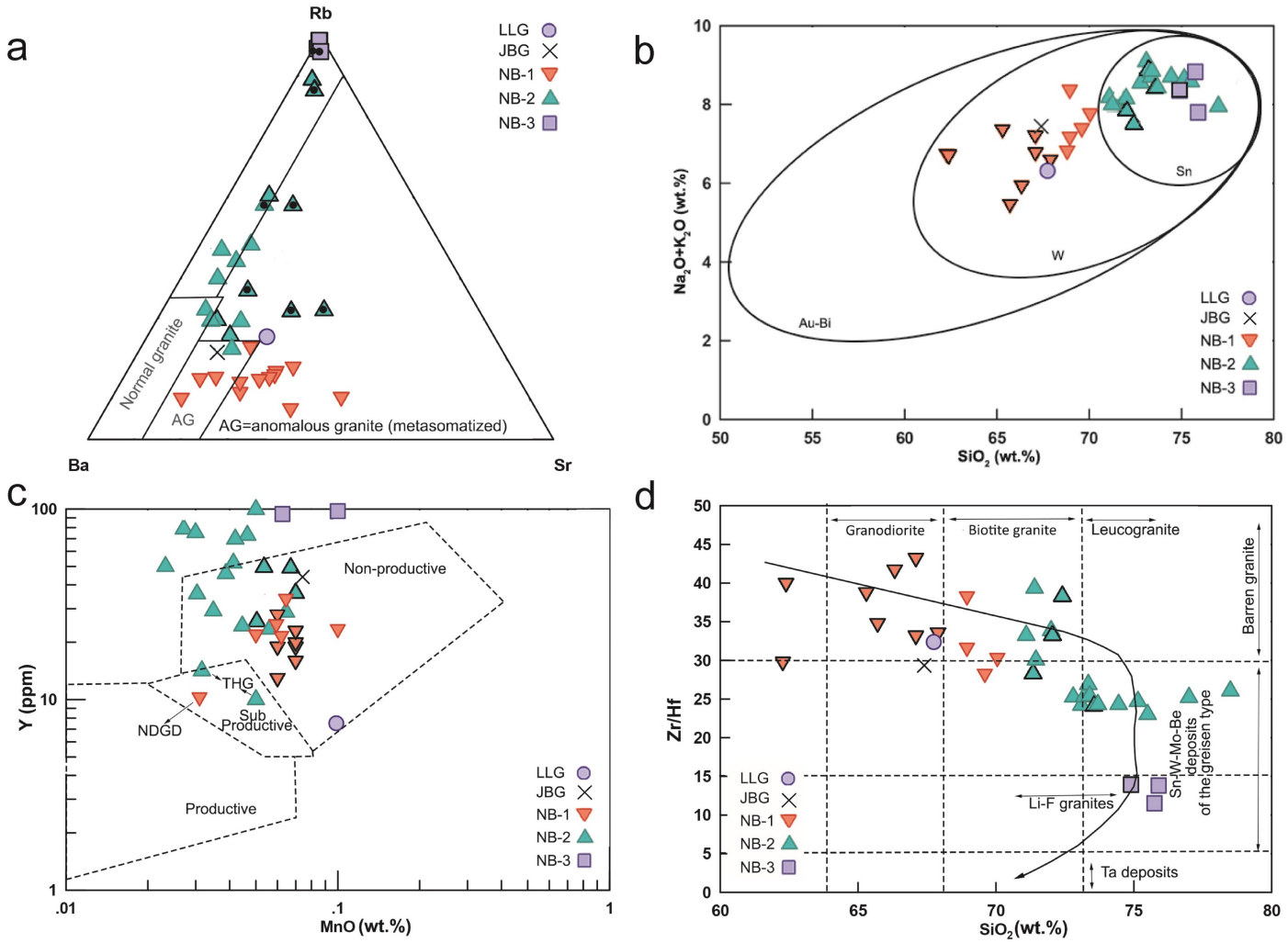

Figure 5. Trace- and/or major-element-based discrimination plots for Siluro-Devonian granites of New Brunswick. a) Ternary Ba-Rb-Sr plot with field boundaries *from* El Bouseily and El Sokkary (1975). Dotted symbols represent samples with more than 10 ppm Sn. Bolded symbols represent intrusions with known associated tin mineralization. b) Discrimination plot of Na_2O + K_2O vs. SiO_2 (field boundaries are *from* Le Maitre et al., 1989; Baker et al., 2005). Bolded symbols represent known mineralized samples. c) Discrimination plot of MnO vs. Y with field boundaries *from* Baldwin and Pearce (1982). Bolded symbols represent known mineralized samples. d) Discrimination plot of SiO_2 vs. Zr/Hf (Zaraisky et al., 2009). Bolded symbols represent known mineralized samples. Abbreviations: JBG – Juniper Barren Granite; LLG – Lost Lake Granite.

(Olade, 1980; Chatterjee and Muecke, 1982; Förster et al., 1999). Relative to the average upper continental crust values of Rudnick and Gao (2003) these intrusions are enriched in Ta, Sn, U, Rb, Li, Be, Th, W, Nb, Cs and F, and depleted in Zr, Ba, Sr, Sc and V (Table 1). The maximum Sn contents of SRG, MPG and DG are 48, 43 and 42 ppm, respectively (Table 1), which are comparable with stanniferous granites worldwide, especially to those of Nova Scotia (about 50 ppm; Chatterjee et al., 1983).

Le Maitre et al. (1989) and Baker et al. (2005) advocate the use of major element-based discrimination plots to estimate the type of associated mineralization. Figure 5b indicates that samples from the JBG, LLG and group NB-1 granites may potentially have tungsten mineralization, whereas NB-2 and NB-3 granites are more likely to have associated tin mineralization. Even though these granites have elevated Rb/Sr ratios of 0.1 to 10 (i.e. they are fractionated granites), most are not expected to have associated mineralization according to the classification schemes of Baker et al. (2005). Although tin, tungsten and molybdenum deposits are associated with fractionated granites (Rb/Sr = 0.1–10) they form from magmas of different oxidation states. Reduced magma is required for tin mineralization (Eugster, 1985), whereas intermediate oxidation state is needed for tungsten deposits. In contrast, molybdenum mineralization is associated with oxidized magmatic systems (Blevin and Chappell, 1992, 1995; Černý et al., 2005; Vigneresse, 2007). The JBG and LLG are not known to have associated tungsten mineralization, which is expected given their oxidized nature

(green biotite). Group NB-1 granites formed from reduced to intermediate oxidation state magmas (reddish-brown to greenish-brown biotite), although only the LG is known to be associated with tungsten mineralization. Granites from groups NB-2 and NB-3 are associated with many occurrences of tin mineralization, with the BG, MDG, SRG, BHG, TRHG and MPG hosting the best examples.

Baldwin and Pearce (1980) used whole rock MnO and Y content to differentiate productive and unproductive porphyritic intrusions. According to this classification, most of the Acadian-related granitoids in New Brunswick plot within the non-productive field due of their highly fractionated state. Two of the intrusions (THG and NDGD) plot within the sub-productive field (Fig. 5c). Although most of the intrusions are classified correctly, several that are known to be productive (e.g. ALG, PFG, UG and MGS) plot in the non-productive field. Therefore, this classification on its own cannot be relied upon to differentiate barren from mineralized Acadian-related granitoids in New Brunswick.

Zaraisky et al. (2009) used the Zr/Hf versus SiO_2 discrimination plot to differentiate between barren and mineralized granitic rare-earth element (REE)-bearing intrusions (Fig. 5d). They concluded that a Zr/Hf ratio below approximately 25 demarcates the boundary between tin, tungsten, molybdenum, beryllium and tantalum mineralized and barren granitoids (Zaraisky et al., 2009). Most of the intrusions examined during this study are correctly classified as barren or mineralized using these criteria (Fig. 5d). However, a few apparently barren intrusions (MLT and the Dmd1 phase of MDG) plot within the mineralized intrusion field. It is possible that this classification could be related to undiscovered mineralization or erosion of the mineralized portion.

The JBG, LLG and group NB-1 granites are typically barren in terms of granophile mineralization, however NB-1 granites may have been the source of the heat and water for circulating hydrothermal fluids, as suggested by their association with several large hydrothermal mineralizing systems. The LG is associated with antimony, gold, tungsten and molybdenum mineralization (Yang et al., 2002a, b). It is noteworthy that although the NG is spatially associated with exogranitic tungsten-molybdenum mineralization at Sisson Brook (McClenaghan et al., 2014), the mineralization significantly post-dates the NG and so they are not directly related (Zhang, 2015). Nevertheless, several greisen zones occur within the NG and this granite has one of the highest tin abundances (7.5 ppm) among the studied samples.

Conversely, granites of group NB-2 seem to be more strongly associated with granophile magmatic mineralization in the group NB-1 granites. These intrusions are associated with several tin-tungsten-molybdenum mineral occurrences associated with the BG and DG. The BG has mean contents of 10 ppm Sn, 1 ppm W, 2 ppm Mo and 7 ppm Be (Table 1) and is associated with both exo- and endogranitic tungsten, molybdenum, tin and beryllium mineralization.

Lastly, group NB-3 granites are the most shallowly emplaced and among the most highly mineralized intrusions investigated in this study. These intrusions have characteristics of topaz granite, which is rare in the geological record. Topaz granite is typically associated with economically important deposits of tin, tungsten uranium, lithium, tantalum and rubidium (Cuney et al., 1992). These granitic bodies could reveal critical information about the nature of magmatism, in particular the behaviour of various trace elements during late stages of the evolution of granitic magmas (Dostal and Chatterjee, 1995). The most significant mineralization associated with members of this group of intrusions are the Sn-W-Mo-Bi-In deposits associated with the MPG (Yang et al., 2003). The studied sample is from the youngest phase of this intrusion, and contains 43.1 ppm Sn, 13 ppm W, 1 ppm Mo, 0.8 ppm Sb, 20.3 ppm U and 32.7 ppm Th.

Petrochemistry

The representative geochemical data of the granitoid intrusions examined in this study are presented in Table 1. Most of the samples, with the exception of three from LG, have greater than 3.2 weight % Na_2O, have A/CNK ratio (molar ratio of $Al_2O_3/[CaO + K_2O + Na_2O]$) of less than 1.1 and have apatite as the dominant mineral inclusion in biotite. Therefore, they can be classified as I-type granite according to the classification of Chappell and White (1974, 1992, 2001). However, the muscovite bearing THG, LL and KSG display A/CNK ratios of greater than 1.1 and are more like S-type granite.

To help define the origin of these intrusions, P_2O_5 abundances and isotopic characteristics of these rocks were investigated. The abundance of P_2O_5 increases gradually with fractional crystallization in S-type granite, whereas the P_2O_5 rapidly drops to very low levels in strongly fractionated I-type (Chappell and White, 2001). In the granites examined in this study, P_2O_5 abundance decreases markedly from JBG and LLG to NB-3; this suggests that the granitoids are fractionated I-type granite rather than the S-type (Fig. 6).

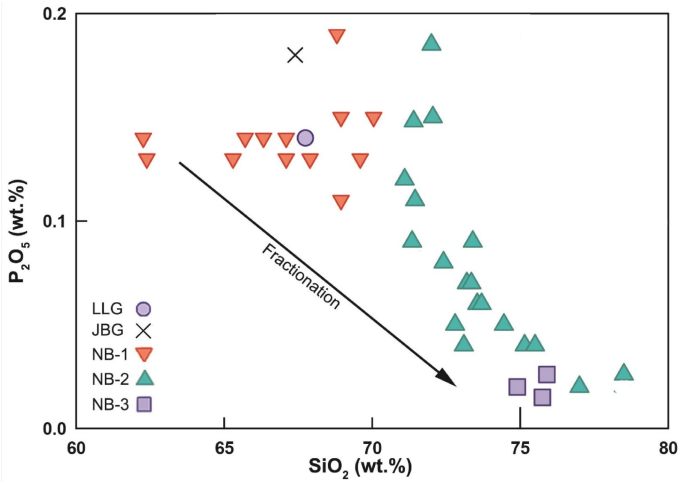

Figure 6. Discrimination plot of SiO_2 vs. P_2O_5, which shows a trend of increasing degree of fractionation.

Studied samples display a wide variation of alkali saturation index (A/CNK) values, which could be interpreted to reflect differences in the source material, degree of differentiation, crustal contamination and secondary hydrothermal activity (Clarke, 1992; Chappell, 1999; Yang et al., 2008). The general trend of increasing A/CNK from the JBG and LLG to group NB-3 granites suggests a higher degree of fractionation and supra-crustal contamination for the group NB-3 granites. This fractionation trend is identified using most geochemical indexes described above (Fig. 3, 5a–d, 6, 7) and reflects a general increase in the degree of fractionation from the JBG and LLG to NB-3 group granites.

Major elements

The JBG and LLG are the least fractionated granites examined in this study, as reflected by their high TiO_2 (0.77 and 0.89 weight %), FeO_T (2.65 and 3.15 weight %) and P_2O_5 (0.14 and 0.18 weight %). content. These intrusions have SiO_2 contents of less than 68 weight %, less K_2O than Na_2O and fall within the magnesian (calc-alkalic) granite field of Frost et al. (2001) (Fig. 8a, b). Furthermore, samples from both intrusions plot within the high-K calc-alkaline field of the Le Maitre et al. (2002) (Fig. 8c).

Group NB-1 granites have higher SiO_2 contents (65–70 weight %) and most plot within the high-K calc-alkaline series, the only exceptions being samples 47 and LG-1190 that plot in medium-K calc-alkaline field (Fig. 8c). However, both samples are highly altered (LG-1190 has a LOI of 4.40 weight %) suggesting the possibility of alkali (K) mobility. Furthermore, all granites in group NB-1 are magnesian (calc-alkalic) granites according to the classification scheme of Frost et al. (2001) (Fig. 8a, b). The granites in group NB-1 are peraluminous (A/CNK = 1.03–1.27) and have A/CNK and $FeO_{(total)}/(FeO_{(total)}$ + MgO) values that increase with increasing SiO_2 (Fig. 8d).

Group NB-2 granites have a higher SiO_2 content (71–78 weight %) and lower TiO_2 (mean 0.23 weight %), CaO (mean 1.01 weight %), P_2O_5 (mean 0.08 weight %), Al_2O_3 (mean 13.51 weight %) and MgO (mean 0.44 weight %) compared to group NB-1 granites. Most have more K_2O than Na_2O and almost the same A/CNK in comparison with the group NB-1 granites and all are high-K calc-alkaline (Fig. 8c). Most of the granitic bodies in this group can be classified as magnesian granites; however, some of the highly fractionated intrusions, (i.e. BH, MDG and MLT) are more precisely classified as ferroan granites (Fig. 8a, b). According to the modified alkali lime index (MALI: $Na_2O + K_2O$ - CaO; Frost et al., 2001) classification, group NB-2 granites are magnesian-ferroan and plot in an array from calc-alkaline to alkali-calcic fields (Fig. 8b). This indicates variation in composition and abundances of the feldspar in these rocks, which implies multiple sources for the parent magma (Frost et al., 2001).

Group NB-3 granites have the highest SiO_2 (>75 weight %) and Na_2O (mean 4.06 weight %) and the lowest Al_2O_3 (mean 13.02 weight %), FeO (mean 0.55 weight %), MgO (mean 0.19 weight %), CaO (mean 0.20 weight %) and P_2O_5 (>0.02 weight %) contents among the four groups of granites. Low TiO_2 (<0.04 weight %), MgO (<0.5 weight %), CaO (<0.3 weight %) and P_2O_5 (<0.02 weight %) are reflected by the Li-rich character of the mica (i.e. lithian siderophyllite) and the absence/low abundance of apatite as a common accessory mineral, which is not surprising given its high solubility in strongly peraluminous felsic melts (London, 1992; Chappell and White, 2001). The PRG and KSG have high Na_2O/K_2O, with the molar Na/K ranging from 1.30 to 1.63. In contrast, the MPG has K_2O contents in excess of Na_2O. Group NB-3 granites are considered high-K -calc-alkaline series (Fig. 8c). The PRG and

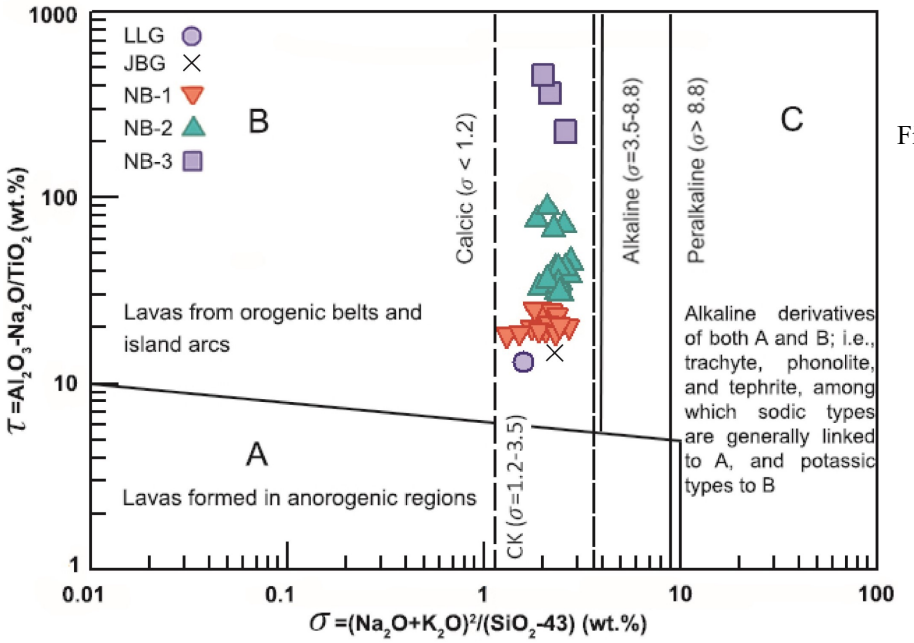

Figure 7. Discrimination plot of σ vs. τ for New Brunswick granitoids. Field boundaries from Yang (2007), modified after Rittmann (1973); values in weight %. $\tau = (Al_2O_3 - Na_2O)/TiO_2$ (Gottini, 1968) and $\sigma = (Na_2O + K_2O)^2/(SiO_2 - 43)$ (Rittmann, 1973). Fields of calcic series, calc-alkaline, alkaline and peralkaline igneous rocks are from Yang (2007). Abbreviations: JBG – Juniper Barren Granite; LLG – Lost Lake Granite.

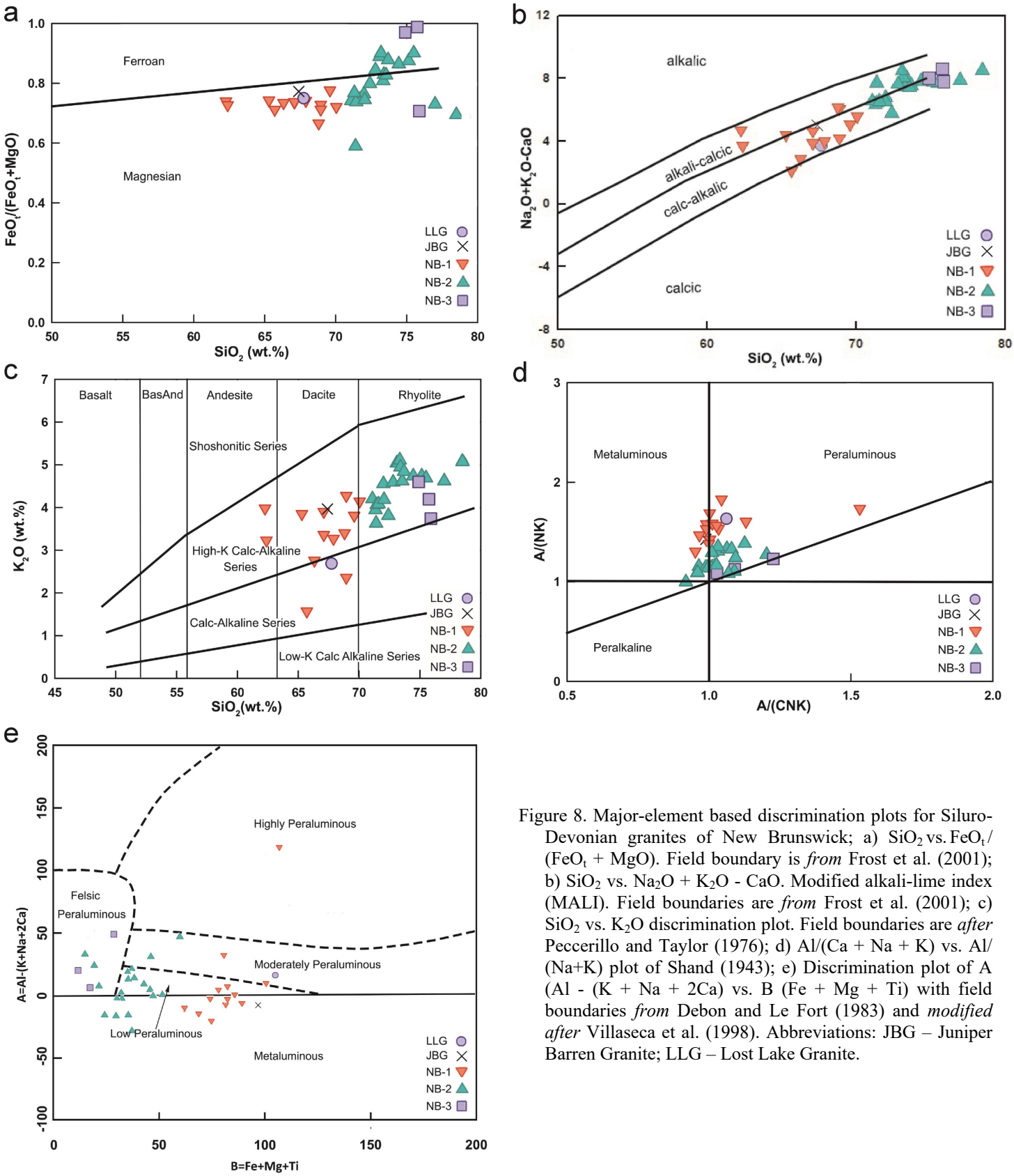

Figure 8. Major-element based discrimination plots for Siluro-Devonian granites of New Brunswick; a) SiO_2 vs. $FeO_t/(FeO_t + MgO)$. Field boundary is *from* Frost et al. (2001); b) SiO_2 vs. $Na_2O + K_2O$ - CaO. Modified alkali-lime index (MALI). Field boundaries are *from* Frost et al. (2001); c) SiO_2 vs. K_2O discrimination plot. Field boundaries are *after* Peccerillo and Taylor (1976); d) Al/(Ca + Na + K) vs. Al/(Na+K) plot of Shand (1943); e) Discrimination plot of A (Al - (K + Na + 2Ca) vs. B (Fe + Mg + Ti) with field boundaries *from* Debon and Le Fort (1983) and *modified after* Villaseca et al. (1998). Abbreviations: JBG – Juniper Barren Granite; LLG – Lost Lake Granite.

MPG are ferroan (alkali-calcic), whereas the KSG is a magnesian (alkali-calcic) granite (Fig. 8a, b). Also, according to the A versus B plot (A = Al - (K + Na + 2Ca vs. B = Fe + Mg + Ti), the LLG plots in the medium peraluminous field, whereas the JBG plots in metaluminous field (Fig. 8e). Granites from groups NB-1 and NB-2 plot in an array from metaluminous to weakly peraluminous (i.e. L-P – low peraluminous field in Fig. 8e). Lastly, two highly fractionated granites in group NB-2 (MDG and THG) plot within the felsic-peraluminous field on Figure 8e. The metaluminous nature of JBG and some less fractionated members of groups NB-1 and NB-2 can be attributed to the presence of Ca-bearing minerals such as apatite and titanite. Conversely, the peraluminous nature of other granites in groups NB-1, NB-2 and NB-3 may reflect either a higher degree of fractionation accompanied by hydrothermal alteration or extensive supra-crustal assimilation (Yang et al., 2008).

Large ion lithophile elements

The abundances of large ion lithophile elements (LILE: Rb, Cs, Sr and Ba) vary with the degree of differentiation (increasing SiO_2). In general, with increasing SiO_2 content both Rb and Cs increase, whereas Ba and Sr decrease. The Eu/Eu* values are negatively correlated with Rb content, whereas they positively correlate with Sr and Ba (Fig. 9a–c). These trends are consistent with the fractionation of plagioclase and K-feldspar (Clarke, 1992; Christiansen and Keith, 1996; Yang et al., 2003, 2008).

Using the Rb content (270 ppm) of the fractionated granites in the Lachlan Fold belt as a gauge (Chappell and White, 1992; Yang, 2005) many of the group NB-2 plutons (MDG, DG, BHG, BG, SRG, TRHG, DG and AG) and group NB-3 granites (MPG, PRG and KSG), are considered to be fractionated granites. In contrast, the other granites examined in this study are considered unfractionated, as their Rb contents are less than 270 ppm (Chappell and White, 2001). Some of the fractionated granites (SRG, TRHG, MPG, PRG and KSG) also have low Ba contents (<42 ppm); this combination of high Rb and low Ba are characteristics of highly evolved granites and is a function of Ba partitioning into K-feldspar and subsequent separation of K-feldspar from the melt (McLaughlin et al., 2003). The ternary Rb-Ba-Sr plot (Fig. 5a) is based on compatible Ba and Sr and incompatible Rb and is essentially a gauge of feldspar crystallization and fractionation. This plot identifies NB-3 group granites as the most evolved followed in order of decreasing degree of fractionation by group NB-2, NB-1 and JBG and LLG.

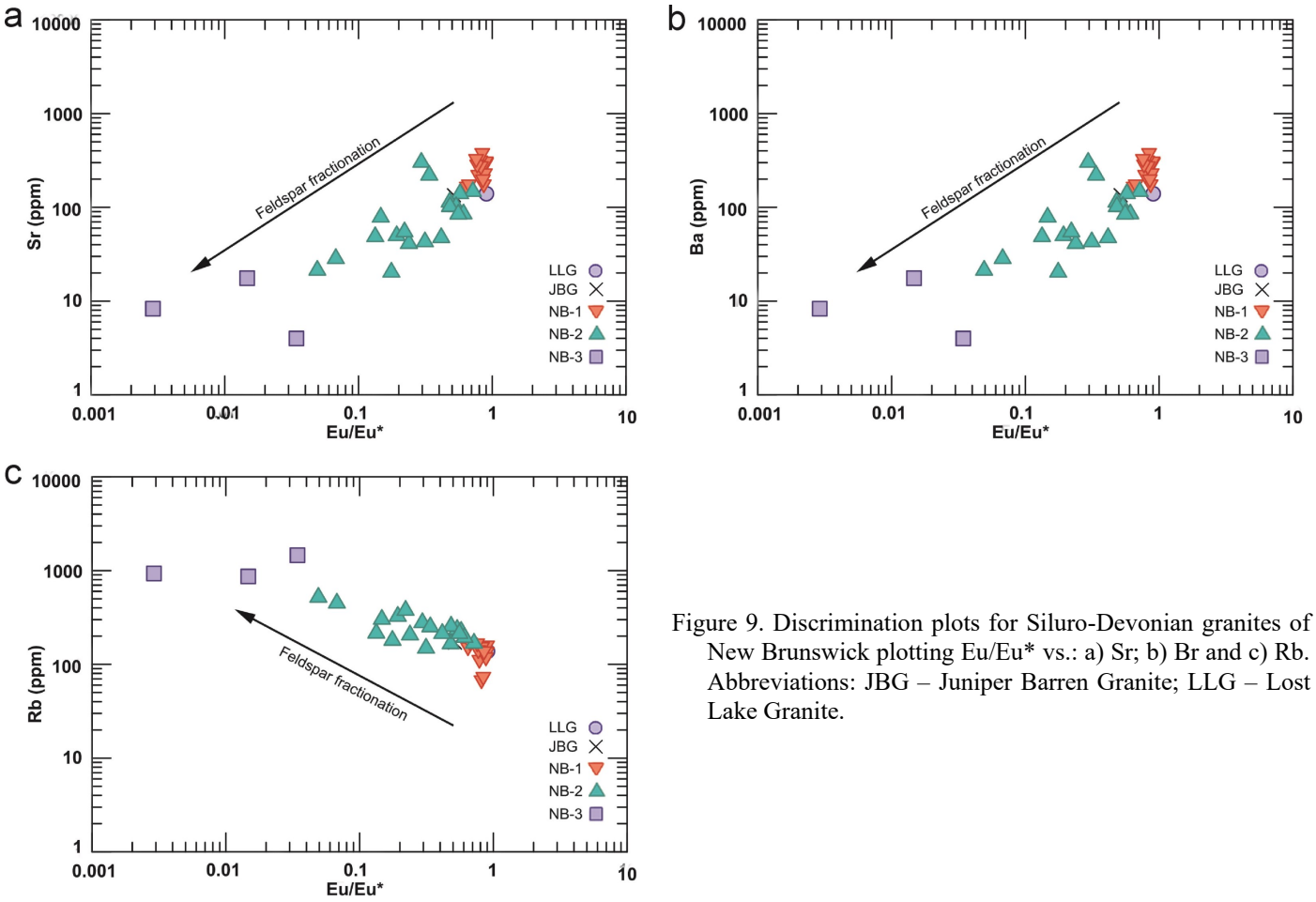

Figure 9. Discrimination plots for Siluro-Devonian granites of New Brunswick plotting Eu/Eu* vs.: a) Sr; b) Br and c) Rb. Abbreviations: JBG – Juniper Barren Granite; LLG – Lost Lake Granite.

Rare-earth elements

Each of the four groups of granites identified in this study have distinctive REE patterns (Fig. 10). Several common patterns are recognized among granites from groups NB-1 and NB -2, which suggests a similar petrogenesis in terms of source or melt evolution (Schofield and D'Lemos, 2000). These patterns were used to divide each group into several subunits. The JBG and LLG have different chondrite-normalized REE patterns; the LLG has a steep chondrite normalized REE pattern (mean $(La/Yb)_N = 66.30$) with no Eu anomaly (Fig.10a). The absence of a negative Eu anomaly suggests that little plagioclase was involved in the mineral-melt equilibria during melting or crystallization of this granitic body. In contrast, the JBG has a fairly steep REE pattern (mean $(La/Yb)_N = 7.14$) and a small negative Eu anomaly (Eu/Eu* = 0.51). This pattern is similar to those of groups in NB-1 and NB-2 (see below).

Granites in group NB-1 have LREE enriched chondrite-normalized REE patterns with no Ce anomaly. The mean $(La/Yb)_N$ ratios of the various subgroups range from 18.55 to 21.33 (group NB-1-1), 10.19 to 12.41 (group NB-1-2) and 9.38 to

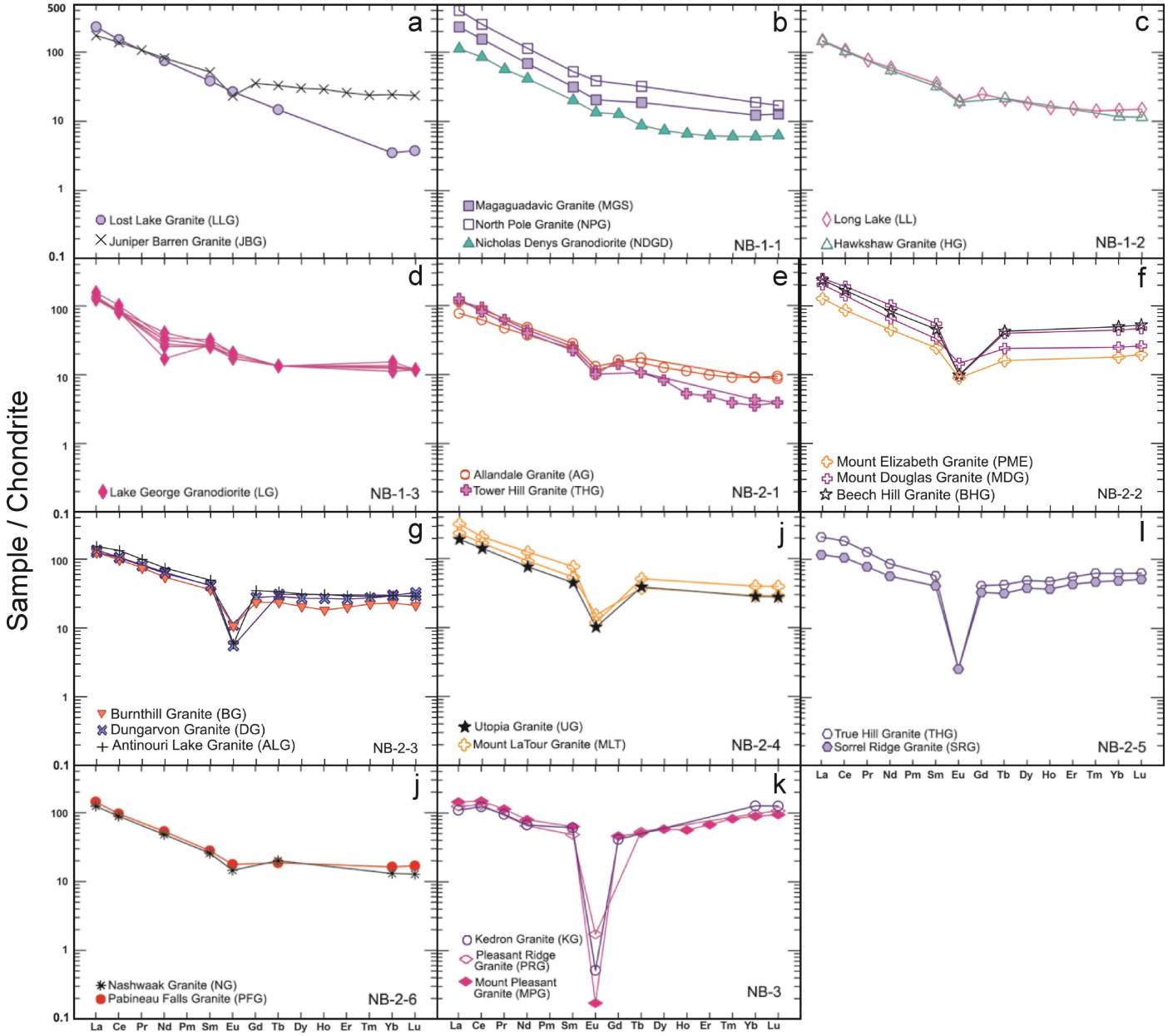

Figure 10. Chondrite-normalized rare earth element patterns for Acadian-related granitoids in New Brunswick: a) Juniper Barren Granite and Lost Lake Granite; b–d) group NB-1 granites; e–j) group NB-2 granites; and k) group NB-3 granites. Chondrite normalizing factors *from* Sun and McDonough (1989).

11.85 (group NB-1-3). The main difference among the subgroups NB-1-1 through NB-1-3 is the presence or absence of an Eu anomaly (Fig. 10b–d).

Group NB-2 granites also exhibit LREE enriched chondrite -normalized patterns, but have more pronounced negative Eu anomalies (Fig. 10e-l), which become more pronounced with higher SiO_2 content. NB-2 $(La/Yb)_N$ values that are lower than NB-1, varying mostly between 2.37 and 12.82. However, the THG shows a distinctly higher $(La/Yb)_N$ ratio of 30.28. All the members of this group have a few times greater heavy rare-earth element (HREE) and Y concentrations than average crust values of Wedepohl (1995), which suggests the absence of garnet in the source (Wilson, 2007). The group NB-2 is divided into six subgroups (NB-2-1 to NB-2-6) based on REE enrichment and the extent of negative Eu anomaly.

The highly fractionated granites of group NB-3 have flat, steer-horn-shaped chondrite-normalized REE patterns ($(La/Yb)_N$ = 0.86–1.61) with very pronounced negative Eu anomalies (Eu/Eu* = 0.002–0.03). The pronounced negative Eu anomalies reflects involvement of plagioclase feldspar fractionation in the mineral-melt equilibria during crustal melting and/or crystallization (Cullers and Graf, 1984; Taylor, 1992) (Fig. 10k). Furthermore, the low $(La/Yb)_N$ values of these rocks require that one or more LREE-enriched accessory minerals were involved during partial melting or subsequent crystallization of these magmas. Among these granites, monazite, primary topaz and Li-bearing mica are the most common accessory phase that could host the LREE (Charoy, 1986; Congdon and Nash, 1991; Taylor, 1992; Yang et al., 2003, 2008).

Several lines of evidence, including the positive correlation of Y and HREE with SiO_2 and negative correlation between $(La/Yb)_N$ and SiO_2, indicate an increasing degree of fractionation from the JBG and LLG to group NB-3 granites (cf. Chappell et al., 1998) (Fig. 11a). Furthermore, the negative correlation between $(La/Yb)_N$ and Yb_N suggests fractional crystallization as the primary evolutionary process among the plutons studied (Fig. 11b). The $(La/Yb)_N$ value decreases gradually from the JBG and LLG through groups NB-1, NB-2 and NB-3, suggesting a greater degree of feldspar fractionation in group NB-3 granites; this interpretation is supported by a decreasing Eu/Eu* ratio (cf. Li et al., 2015).

Acadian-related granitoids of New Brunswick have elevated $(La/Yb)_N$ values (Fig. 11b), which imply formation under deep, garnet stable, pressure-temperature conditions, such as those previously suggested for Archaean tonalite-trondhjemite-granodiorite (TTG) magmas (cf. Martin 1986; Martin et al., 2005; van Staal et al., 2009). High $(La/Yb)_N$ values in felsic rocks are recognized characteristics of granites formed during flat subduction in the central Chilean - -Argentinian subduction zone segment of the Andes (Kay et al., 2005). High-pressure metamorphism and partial melting of subducted fore-arc material as it entered the asthenospheric mantle wedge beneath the arc was introduced as the source for the elevated $(La/Yb)_N$ ratios (van Staal et al., 2009). However, the Acadian fore-arc was

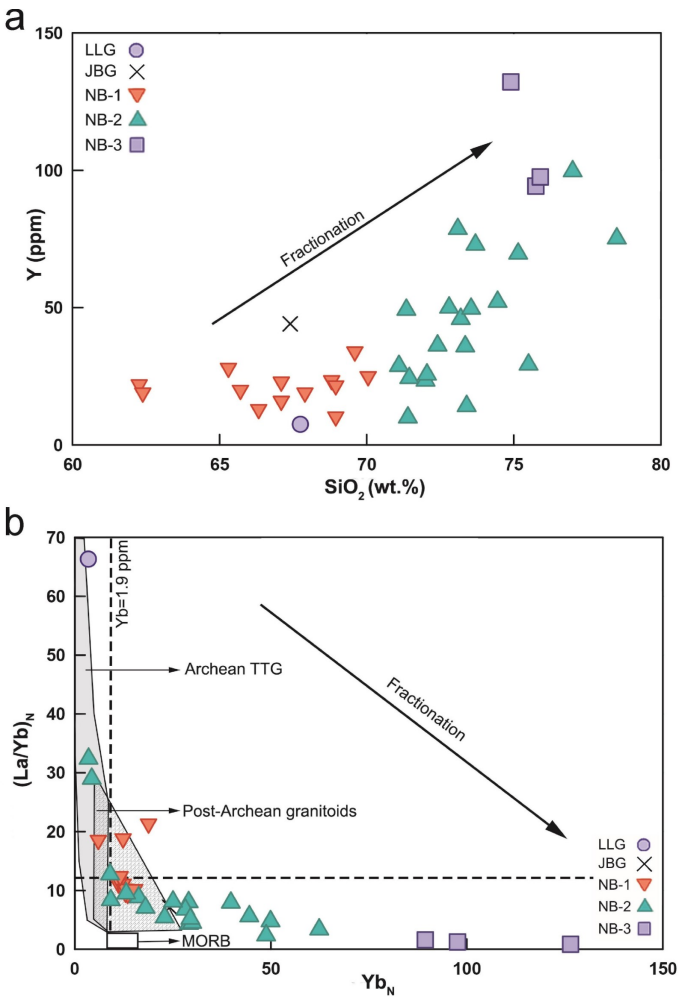

Figure 11. Discrimination plots for Siluro-Devonian granites from New Brunswick: a) SiO_2 vs. Y; and b) chondrite-normalized $(Yb)_N$ vs. $(La/Yb)_N$ discrimination plot. Field boundaries for Archean TTG (tonalite-trondhjemite-granodiorite), post-Archaean granitoids and Mid-Ocean ridge basalt (MORB) *from* van Staal et al. (2009). Chondrite normalizing factors *from* Sun and McDonough (1989).

tectonically removed and presumably subducted beneath the leading edge of Laurentia (van Staal et al., 2009). This feature together with the migration of the structural front towards the back-arc region, supports an Andean-type flat-slab subduction setting for the Early Devonian (416–400 Ma) Acadian felsic magmatism (van Staal et al., 2009). It is noteworthy to add that Acadian flat-slab magmatism likely involved progressive underthrusting of Avalonia beneath Laurentia (van Staal et al., 2009).

The JBG and LLG have Sr/Y values typical of crustally derived granite (S or I-type; Sr/Y = 2–20; Moyen, 2009); however, the LLG has a much higher Sr/Y (18.55) ratio relative to the JBG (Sr/Y = 3.06). The JBG has a very low $(La/Yb)_N$ value of 7.14, whereas the LLG has a $(La/Yb)_N$ of 66.30, which is

comparable to crustally derived granite ($(La/Yb)_N$ = 38–61; Taylor and McLennan, 1995; Wedepohl, 1995; Moyen, 2009). A number of process may account for enrichment of LREE and Sr over HREE, and yield high Sr/Y and $(La/Yb)_N$ ratios, namely: 1) fractionation of minerals with a high partition coefficient for HREE and Y (i.e. garnet and amphibole); 2) melting of a high Sr/Y (and La/Yb) source; 3) fractional crystallization or assimilation fractional crystallization (AFC); and 4) deep melting with abundant residual garnet or interactions of felsic melts with the mantle (Moyen, 2009).

Granites from groups NB-1 and NB-2 have Sr/Y and $(La/Yb)_N$ contents well within the range of typical crustally derived granite, whereas group NB-3 granites have significantly lower values (Sr/Y = 0.09 and $(La/Yb)_N$ = 1.25). No garnet or amphibole was observed in NB-3 group granites; however, xenotime, thorite, uraninite, rutile and columbite occur as accessory phases; all of which can partition HREE + Y, thereby accounting for the exceptionally low $(La/Yb)_N$ values in granite samples from this group.

High field strength elements

High field strength elements (HFSE: i.e. Ta, Nb, Zr, Hf, Th, U) are generally incompatible in granite melts; their concentration in the melt tends to increase with increasing fractionation. The HFSE abundances increase from the JBG and LLG to group NB-3 granites (Table 1), with the exception of Zr that, which decreases. Furthermore, both Nb/Ta and Zr/Hf values decrease markedly from group NB-1 to NB-2 to NB-3 (mean Nb/Ta of 11.91, 10.22 and 3.20, respectively; mean Zr/Hf of 36.29, 27.02 and 13.09, respectively). It is noteworthy that the Nb/Ta contents of all groups are higher than average continental crust (Wedepoh, 1995) and close to upper continental crust

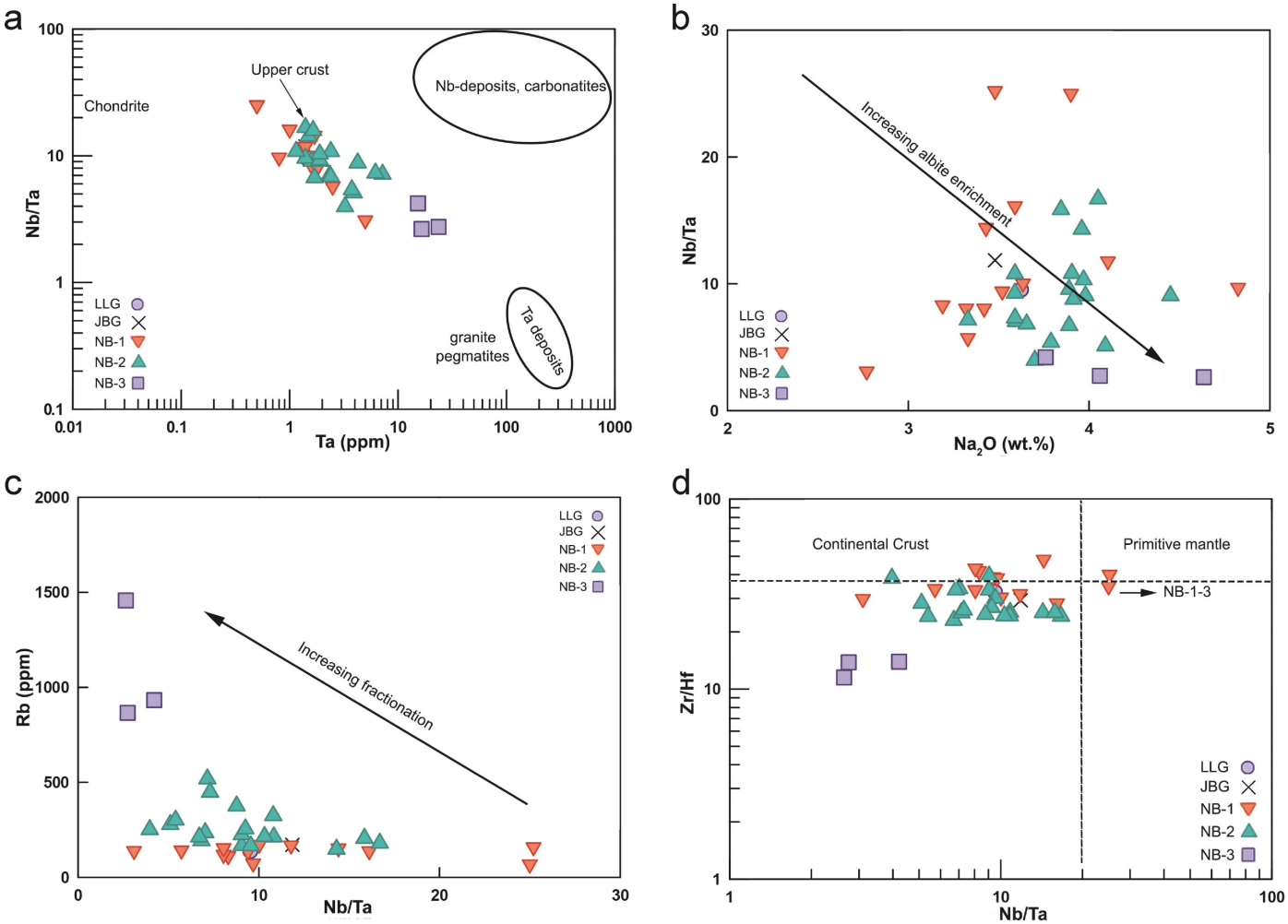

Figure 12. Discrimination plots for the determination of mineral potential of Siluro-Devonian granitoids in New Brunswick: a) Ta vs. Nb/Ta plot with field boundaries *from* Stepanov et al., (2014). Chondrite normalization factors are *from* Jochum et al. (2000) and the upper continental crust value (the source of granitic melts) is *from* Barth et al. (2000); b) Na_2O vs. Nb/Ta; c) Nb/Ta vs. Rb plot; and d) Nb/Ta vs. Zr/Hf discrimination plot of Acadian-related granitoids of New Brunswick. Continental crust data (CC) *from* Taylor and McLennan (1985). Primitive mantle data (PM) *from* McDonough and Sun (1995). Abbreviations: JBG – Juniper Barren Granite; LLG – Lost Lake Granite.

values (Barth et al., 2000; Fig. 12a). The negative correlation between Na_2O and Nb/Ta implies that tantalum evolution is related to albite enrichment (López Moro et al., 2017) (Fig. 12b). Furthermore, the negative correlation between Na/Ta and Li, F and Rb, and the positive correlation of Na/Ta with Rb/K suggests that fractional crystallization of albite was accompanied by fluid fractionation and the addition of mineralizing fluids in the more evolved group NB-3 granites (Fig. 12c: Dostal and Chatterjee, 1995, 2000; Halter et al., 1998).

The Zr/Hf ratios in the intrusions examined, with the exception of eight (LG, NDGD, PFG, AG, NG, THG, BG and LL), are lower than common igneous rocks, chondrite and bulk continental crust (Jochum et al., 1986; Taylor and McLennan, 1995; Wedepoh, 1995; Fig. 12d). The deviation from chondritic values could be explained by either metasomatism (Dupuy et al., 1992; Rudnick et al., 1993), internal fluid fractionation (Dostal and Chatterjee, 2000) or low temperature crystal fractionation involving accessory phases such as zircon (Linnen and Keppler, 2002; Yang et al., 2008). Moreover, the difference among the intrusions could be explained by the various degree of assimilation and fractional crystallization.

Decreasing Nb/Ta, Zr/Hf, $(La/Yb)_N$ and Eu/Eu^* (Fig. 10) suggests increasing degree of crystal fractionation from least evolved (JBG and LLG) to most evolved (group NB-3) granites (Linnen and Keppler, 1997; Stepanov et al., 2014). However, recent studies suggest that the decrease in Na/Ta in evolved peraluminous granites (i.e. NB-3 granites) could be caused by either interaction with late magmatic fluid (Dostal and Chatterjee, 2000; Tartèse and Boulvais, 2010; Ballouard et al., 2015, 2016; Dostal et al., 2015) or secondary hydrothermal alteration (Ballouard et al., 2016).

Transition elements

Transition elements behave compatibly in granitic systems and their abundances decrease with increasing silica within a magmatic suite, which is consistent with fractional crystallization. In general, the concentration of all of the elements, including Cr, Ni, Co, Sc, Zn and V, decreases from the JBG and LLG to NB-3 group granites, reflecting the more evolved nature of the latter group. However, the MPG and KSG have high Ni, Zn and Co concentrations despite their highly fractionated nature. This might be a function of the low abundance of ferromagnesian minerals in these intrusions. The low ferromagnesian mineral content may have caused the transition elements to behave incompatibly in these magmas, resulting in increasing concentrations with fractional crystallization in the parent magma. Yang et al. (2008) attributed the high Zn contents of these granites to fluid involvement, as Zn favours partitioning into a fluid phase (Yang et al., 2003).

Isotopic characteristics

Radiogenic and stable isotopes are useful for determining the source area of a granitoid magma. However, caution should be exercised when interpreting radiogenic isotopes as the effects of aging of the isotopic systems of the I-type source rocks cannot be readily quantified prior to the partial melting (Chappell and White, 2001).

Stable isotopes

Various geological reservoirs (i.e. mantle, crust and hydrosphere) commonly have distinctive isotopic compositions due to isotopic fractionation among mineral, melts and volatiles. The degree of isotopic fractionation depends on the mass differences between two nuclides of a particular element, temperature (inversely) and, in the case of sulphur, valences (Clark, 1992). Stable oxygen isotopes not only define source rock characteristics, but may also determine system equilibrium or disequilibrium, as well as examine the origin of fluids involved in granitic magmas (Rollinson, 1993; Whalen, 1993). The $\delta^{18}O$ values of the samples examined vary between 6 and10‰, which is within the range of most granitoids, including the I-type granites of Lachlan fold belt in Australia (Taylor, 1978; Chappell and White, 1992, 2001; Table 2).The values plot within the 'normal' granitoid field and includes rocks derived from mixed juvenile (mantle - lower crustal) and supracrustal sources (Taylor, 1978; Whalen et al., 1996a). High $\delta^{18}O$ values (>8‰) in most samples indicate a supracrustal component in their source areas, which is consistent with the peraluminous characteristics of these rocks.

Radiogenic Isotopes

Sr isotopes: Available initial $(^{87}Sr/^{86}Sr)_i$ data for the intrusions examined are consistent with published values for I-type granites ($(^{87}Sr/^{86}Sr)_i$ = 0.704–0.712; Table 2; Chappell and White, 2001). The LLG has one of the lowest $(^{87}Sr/^{86}Sr)_i$ values (0.703), which indicates a significant mantle contribution. Group NB-1 granites have initial $^{87}Sr/^{86}Sr$ values ranging from 0.703 to 0.707 suggesting a mantle or juvenile crustal source (I -type granite) along with a relatively minor older crustal component. Group NB-2 granites have a higher value (>0.705) compared to the group NB-1 intrusions and may reflect greater contribution of crustal material. The THG has the highest $^{87}Sr/^{86}Sr$ initial value (0.737) among group NB-2 granites. Yang et al. (2008) compared the isotopic characteristics of the THG to other intrusions and suggested contamination with supracrustal material, (i.e. Cookson Group slate and muscovite-garnet schist). Finally, group NB-3 granites have a constant value of 0.712, which implies derivation from a dominantly crustal source (i.e. the low-temperature I-type granite; Chappell and White, 2001). However, the low Sr content (<18 ppm) of these magmas suggest that the $^{87}Sr/^{86}Sr$ ratio might not accurately reflect a crustal source for the magmas (Eby, 1990).

Nd isotopes: Neodymium isotopic data is useful when studying mantle-crust differentiation and crustal recycling (DePaolo, 1981; Farmer and DePaolo, 1983). In general, ε_{Nd} values of all the granites examined are within the spectrum of I -type granites (Chappell and White, 2001). All group NB-1 granites, except for the MGS (ε_{Nd} = +1.5), have negative ε_{Nd} values, which may suggest an old continental crust or enriched

Table 2. Isotopic data for Acadian-related granitoids in New Brunswick (*after* Bevier, 1988; McLeod et al., 1988; Bevier and Whalen, 1990b; Whalen, 1993; Whalen et al., 1994b, 1996b, 1998; Yang, 2005; Beal et al., 2010; Shinkle, 2011; Azadbakht et al., 2016; Mohammadi et al., 2017).

Pluton	Sample	Group	δ18O‰	$(87Sr/86Sr)_i$	εNd
Hawkshaw Granite	WX85NB-11	NB-1-1	9.6	0.705	-2.5
Magaguadavic Granite	WX85NB-196	NB-1-1	8.2	0.707	1.5
Nicholas Dénys Granodiorite	WX85NB-47	NB-1-1	7.2	0.703	0.1
Long Lake Granite	DS06-077	NB-1-2	6.6–12.1		-0.5
North Pole Stream Granite	WX85NB-118	NB-1-2	8.2		-3.0
Lake George Granodiorite	LG78-18-1190	NB-1-3	9.4–10.7		-2.4
Allandale Granite	WX85NB-16	NB-2-1	9.5		-1.6
Allandale Granite	WX85NB-38	NB-2-1	9.5		
Tower Hill Granite	C80-5-254	NB-2-1	8.2	0.702	-0.4
Tower Hill Granite	WX85NB-214	NB-2-1	9.2	0.737	-0.4
Beech Hill Granite	WX-NB-188	NB-2-2	8.5	0.715	0.1
Mount Douglas Granite	WX85NB-198	NB-2-2	7.5	0.712	1.7
Mount Douglas Granite	WX85NB-220	NB-2-2	7.5	0.708	1.7
Mount Elizabeth Granite	WX-NB-240	NB-2-2	6.2–8.8		-6.1–2.2
Antinouri Lake Granite	WX85NB-52	NB-2-3	8.9		-1.6
Burnthill Granite	12-SHM-054	NB-2-3	9.2	0.705	-1.2
Mount LaTour Granite	WX86NB-254	NB-2-4	6.2–8.8		-6.1–2.2
Mount LaTour Granite	WX86NB-262	NB-2-4	6.2–8.8		-6.1–2.2
Utopia Granite	WX85NB-189	NB-2-4	9	0.705	2.0
Sorrel Ridge Granite	SR82-1-199	NB-2-5	8.0–9.4		0.6
True Hill Granite	TH82-10-273	NB-2-5	6.2–8.8		
Nashwaak Granite	WX-NB-173	NB-2-6	9.6		-3.4
Pabineau Falls Granite	WX85NB-46	NB-2-6	9.6		-2.5
Kedron Granite	BR84-4-129	NB-3	6.8–7.2		0.3
Mount Pleasant Granite	AM96-3-1223	NB-3	8.2–8.6	0.712	0.1
Pleasant Ridge Granite	WX85NB-187	NB-3	9.2	0.737	0.7
Juniper Barren Granite	WX85NB-170		8		-1.7
Lost Lake Granite	WX85NB-161		5.6	0.703	-1.1

mantle source. The ε_{Nd} values of group NB-2 have a wider range (-3.40 to + 2.20), which indicates various degrees of mantle-crust interactions. Some of the group NB-2 granites, (i.e. BHG (+0.1), THG (-0.4) and SRG (+0.6)), are located close to the Gander-Avalon boundary. Such a wide range in ε_{Nd} values is interpreted to reflect input from the various continental basement blocks underlying this major tectonic boundary (Whalen et al., 1996a).

Finally, group NB-3 granites have ε_{Nd} values ranging from 0.1 to 0.3, which indicates that melting of relatively young, juvenile material (i.e. depleted mantle) is the source for the granites in this group (Whalen, 1993).

Magma temperature

The temperature of granitic magmas can be independently estimated using zircon, monazite and apatite saturation temperatures (Table 1). These methods are briefly reviewed and applied to the Acadian-related granitoids of New Brunswick.

Zircon saturation temperatures

The mineral solubility experimental research of Watson and Harrison (1983) confirmed that zircon solubility is dependent on the temperature and felsic magma melt composition. This method applies to estimates of zircon saturation in metaluminous and peraluminous felsic melts (Yang et al., 2008), but not

peralkaline systems as the sum of Na and K exceeds Al. Zircon saturation temperature is calculated using the following equation:

$$\ln D_{Zr}^{zircon/melt} = \{-3.80-[0.85(M - 1]\} + 12900/T \quad (1)$$

Where $D_{Zr}^{zircon/melt}$ is the concentration ratio of Zr in the stoichiometric zircon to that in the melt, T is the absolute temperature in Kelvin and M is the cation ratio (Na + K + 2Ca)/(Al - Si) in the melt (Watson and Harrison, 1983). The result of this calculation should be used with caution as the effect of pressure and water content on zircon solubility in felsic magmas are not well constrained (Watson and Harrison, 1983). Furthermore, the calculation can yield a higher temperature than the real saturation temperature if Zr is hosted by any other Zr-bearing phases (e.g. zircophyllite or zirkelite; Yang, 2005). However, this is extremely rare in granite and these minerals were not observed in the examined samples. Most importantly, the calculation may result in the maximum zircon saturation temperature if the intrusion includes xenocrystic and/or residual zircon (Watson and Harrison, 1983; Yang, 2005).

Zircon saturation temperature (T_{Zircon}) was calculated using the bulk rock Zr and following equation (1) (Table 1). Figure 13a displays the relationship between the calculated zircon temperatures and the whole rock Zr content. In this plot, the solubility of zircon is a function of melt composition (M) ranging from 1.3 to 1.9 for tonalite to leucogranite (Miller et al., 2003). All of the Acadian-related granitoids plot in the 'leucogranite' field (Fig. 13a) and have melt compositions ranging from 1.6 to 1.9. Four of the intrusions with Zr greater than 200 ppm (i.e. Zr content greater than common crustal rocks that are typically 100–200 ppm; Taylor and McLennan, 1995), specifically MLT, NPG, LLG and JBG are considered to be hot granites as they have calculated temperatures higher than 800°C. Such high temperatures are expected in granite generated by dehydration melting in the crust or by fractionation of mantle melts (with or without crustal contamination) and transported in a crystal-poor state (Miller et al., 2003). An important influx of heat (i.e. presence of mafic magma), but not fluid, is believed to be required for the generation of hot granites (Miller et al., 2003). These hot granites are associated with large mafic bodies that may have acted as the heat source (Fig. 1). The rest of the intrusions examined are considered cold granites as their calculated zircon saturation temperatures are below 800°C. These granites are thought to be generated via fluid influx in tectonic settings (i.e. subduction, collision, post-orogenic) that do not reach high temperatures (Miller et al., 2003).

There is a similarity of temperature within each group and more precisely among the subgroups. As expected, the least fractionated granitoids (LLG and JBG) have the highest T_{Zircon} values of 811 and 799°C, respectively. Furthermore, the mean temperature decreases incrementally from 794°C to 770°C and 736°C for groups NB-1 through NB-3, supporting the more evolved (cooler) nature of group NB-3 granites. Inherited zircon is common among the Siluro-Devonian granitoids of New

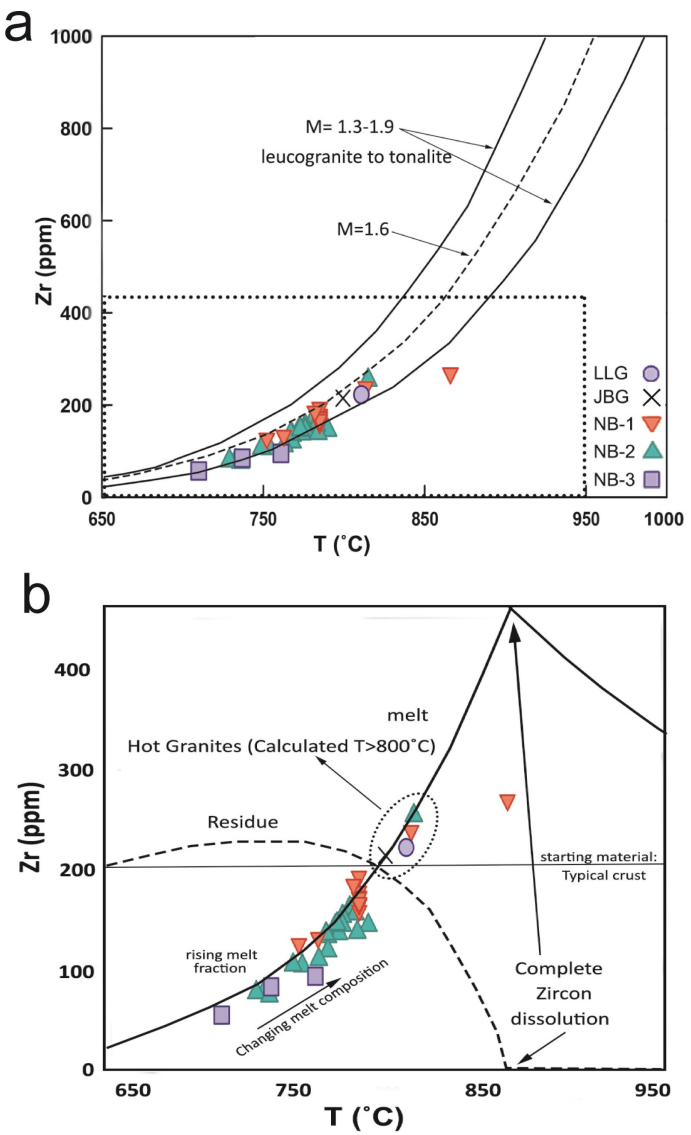

Figure 13. a) Solubility of zircon as a function of temperature (T in °C) and melt composition (M). Plot is *from* Miller et al. (2003), showing Zr solubility decreasing with decreasing temperature. Dotted area is enlarged in (b). b) Schematic plot for Zr budget during crustal melting. Abbreviations: JBG – Juniper Barren Granite; LLG – Lost Lake Granite.

Brunswick (Whalen, 1993; Roddick and Bevier, 1995; Azadbakht et al., 2016; Mohammadi et al., 2017), as a result the calculated temperatures are assumed to represent the maximum saturation temperatures or the initial magma temperature at the source (Miller et al., 2003; Yang et al., 2008).

The evolution of partial melts of common crustal rocks containing approximately 100 to 200 ppm Zr, was investigated using the schematic plot of Miller et al. (2003) (Fig. 13b). Inheritance-rich granite (i.e. cold granite) cannot be generated solely by dehydration of biotite or hornblende due to low tem-

peratures (<800°C) and is most likely to be generated when the residual melt is relatively zircon -rich and at the presence of fluid influx (Miller et al., 2003).

Monazite saturation temperatures

Montel (1993) proposed an empirical model using composition, temperature and water content of felsic melts, to calculate monazite saturation temperature in felsic magmas.

$$\ln(REE_t) = 9.50 + 2.34D + 0.3879\sqrt{H_2O} - 13318/T \quad (2)$$

Where $REE_t = \sum \frac{REE_i\ (ppm)}{at.weight\ (g\ mol^{-1})}$

And $D = \frac{(Na + K + Li + 2Ca)}{Al} \times \frac{1}{(Al + Si)}$

Na, K, Li, Ca, Al and Si are in atom %; H_2O is in weight % and T is in Kelvin. ∑REE is the sum of LREE from La to Gd (excluding Eu). Since natural monazite incorporates significant Th and U, which lower the activity of $REEPO_4$, it is highly recommended that the ratio REE_t/X_{REEPO_4} be used instead of REE_t in equation (2). Montel (1993) proposed the value of 0.83 for X_{REEPO_4}, based on 35 microprobe analyses of high-grade gneisses and peraluminous granites. This calculation can be applied to peraluminous, metaluminous and even peralkaline rocks, if Ca, Fe and Mg remain low.

Monazite saturation temperature ($T_{Monazite}$) was calculated using the whole rock REE composition as the melt composition and following equation (2) (Table 1). A water content of 5 weight % was assumed for calculation because of the subsolvus nature of the granites examined. In general, $T_{Monazite}$ values are lower than T_{Zircon} for most of the intrusions investigated. The LLG has one of the highest $T_{Monazite}$ temperatures (806°C). The mean monazite saturation temperature decreases to about 780°C for intrusions from group NB-1 and NB-2, whereas, the mean $T_{Monazite}$ temperature for group NB-3 intrusions unexpectedly increases to 814°C. The higher than expected calculated temperature in these more evolved and presumably lower temperature, intrusions suggests inaccurate assessment of REE content due the presence of other REE-bearing minerals in the system. The calculated saturation temperatures reflect either the equilibrium temperature of the grains and their parent melt in their source region or their liquidus temperature (Yang et al., 2008). Considering petrographic evidence (i.e. the presence of monazite as an early phase occurring primarily as inclusion in biotite) supports a liquidus temperature, thus it is better to consider the lowest temperature as the monazite saturation temperature.

Apatite saturation temperature

Harrison and Watson (1984) experimentally investigated apatite solubility in felsic magmas for a range of temperatures (850–1500°C), water contents (0–10 weight %) and pressures (1–8 kb). They concluded that apatite solubility is a function of temperature and melt composition (metaluminous to weakly peraluminous). Apatite saturation temperature is calculated following the equation below:

$$\ln D_P^{Apatite/melt} = \left[(8400 + ((SiO_2 - 0.5)2.64 \times 10^4)/T\right] - \left[3.1 + \left(12.4(SiO_2 - 0.5)\right)\right] \quad (3)$$

Where $D_P^{Apatite/melt}$ is the concentration ratio of P_2O_5 in stoichiometric apatite and that in apatite saturated melt, T is in Kelvin and SiO_2 is the weight fraction of silica in the melt. The relationship appears to be valid between 45% and 75% SiO2 (Harrison and Watson, 1984).

Using whole rock P_2O_5 and SiO_2 to represent the parent magma composition and the apatite solubility model of Harrison and Watson (1984), apatite saturation temperatures were calculated for the felsic intrusions examined in this study (Table 1). In general, Tapatite is higher than TZircon and TMonazite in all the samples examined and reflects the presence of another P-bearing mineral (monazite) in these systems; therefore, calculated Tapatite values likely reflect the maximum apatite-saturation temperatures (Yang et al., 2008). The JBG has one of the highest calculated Tapatite at 940°C, followed closely by LLG (Tapatite = 916°C). Furthermore, Tapatite also shows a systematic decrease from group NB-1 to NB-3 (935°C to 814°C, respectively) that is consistent with results from TZircon and, to some extent, TMonazite for these populations.

Tectonomagmatic characteristics

All the samples in this study plot in the calc-alkaline field of the AFM plot of Irvine and Baragar (1971) with a trend from the JBG and LLG to group NB-3 granites toward the alkali apex, which may indicate an increase in the degree of fractionation within these granites. They also plot in the B domain of the σ-τ plot of Gottini (1973) indicating an orogenic setting for these granites (Fig. 7).

The tectonic affinities of felsic rocks are commonly assessed using extended element spidergrams (Fig. 14), even though interpretation is complicated by fractionation of trace elements into mineral phases like monazite, zircon, Ti-bearing minerals and apatite. In the primitive mantle-normalized spidergrams for these intrusions, all the granites have apparent negative anomalies of Ba, Ce, Sr, P, Zr and Ti, which are indicative of differential partial melting and fractional crystallization of feldspars, Ti-rich phases, monazite, zircon and apatite in near equilibrium processes. In contrast, positive anomalies of Th, U, K, Pb and Nd suggest that assimilation fractional crystallization processes were involved in the evolution of these granites. The negative Nb anomalies present in all the granites are characteristic of igneous rocks formed in subduction settings, or inherited from crustal -source granites (Whalen et al., 1996a; Yang et al., 2002a).

On the Y + Nb versus Rb tectonomagmatic discrimination plots of Pearce et al. (1984) (see also Förster et al., 1997), the LLG plots within the volcanic-arc granite field (VAG; I-type),

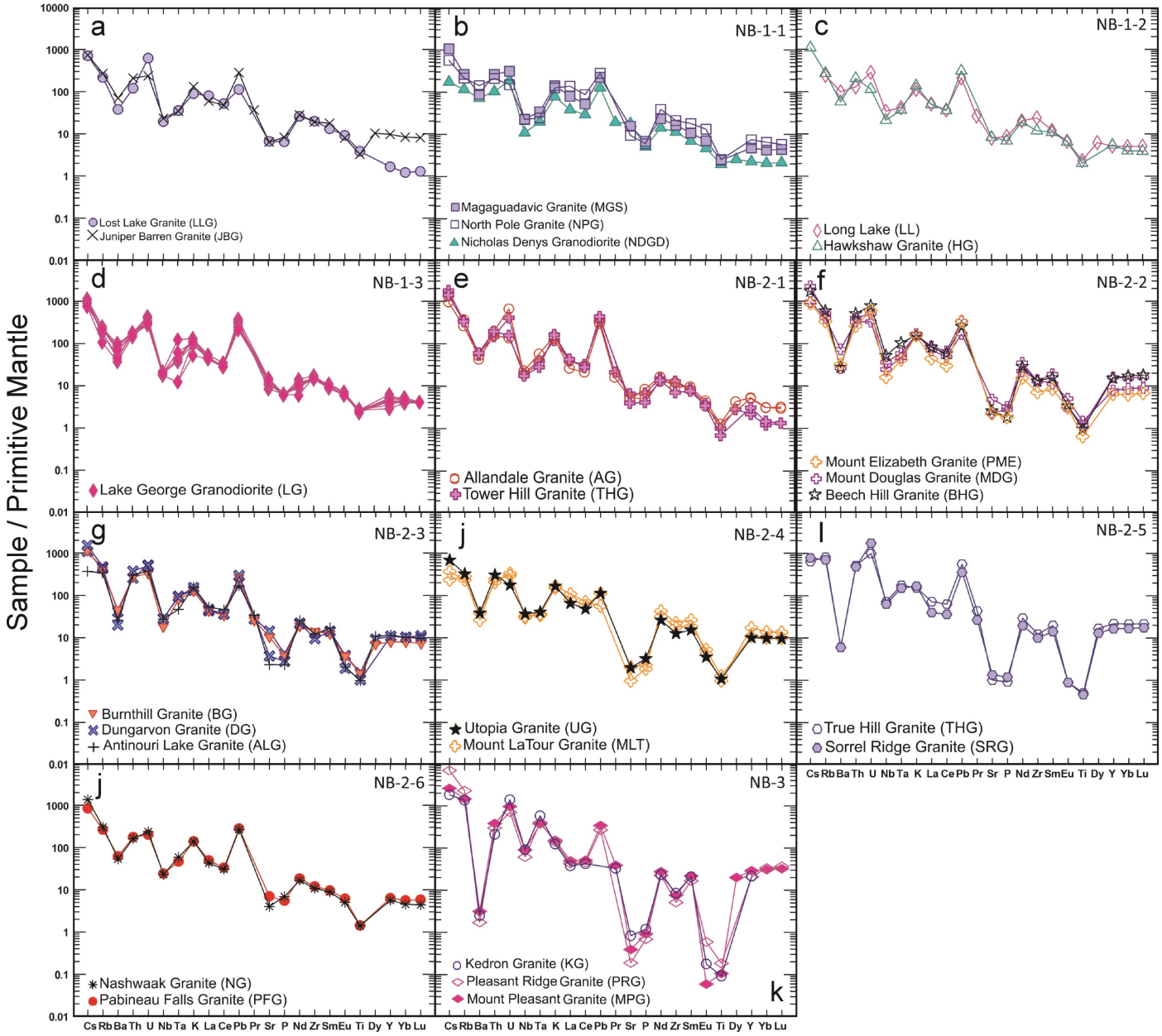

Figure 14. Primitive mantle-normalized spidergrams for Acadian-related granitoids in New Brunswick: a) Juniper Barren Granite and Lost Lake Granite; b–d) group NB-1 granites; e–j) group NB-2 granites; and k) group NB-3 granites. Primitive mantle normalizing factors *from* Sun and McDonough (1989).

whereas the JBG plots close to the boundary of VAG and within-plate granite fields (WPG; A-type) (Fig. 15a). Group NB-1 intrusions plot in the VAG field, whereas group NB-2 granites plot in an array from VAG toward the WPG field. This trend may reflect progressively increasing degree of fractional crystallization among the granites of this group, as extensive fractional crystallization can shift the data toward the WPG (crustal A-type) field (cf. Christiansen and Keith, 1996; Pearce, 1996; Förster et al., 1997). This agrees with previous studies in New Brunswick suggesting that the Acadian plutonic rocks are associated with continental collision events rather than subduction (Fyffe et al., 1981; McCutcheon and Robinson, 1987). All the granites in group NB-1 and most of the group NB-2 granites plot on the upper part of the VAG field, close to the boundary with the syn-collisional field (syn-COLG, S-type). This is consistent with a supracrustal contaminated mature arc setting (Pearce et al., 1984; Christianson and Keith, 1996; Bineli-Betsi and Lentz, 2011). Group NB-3 granites plot mainly in the WPG field close to the boundary with the syn-COLG field, due to their highly fractionated nature. However, the KSG plots within the syn-COLG field, reflecting a strong continental signature for this intrusion (Förster et al., 1997). The high incom-

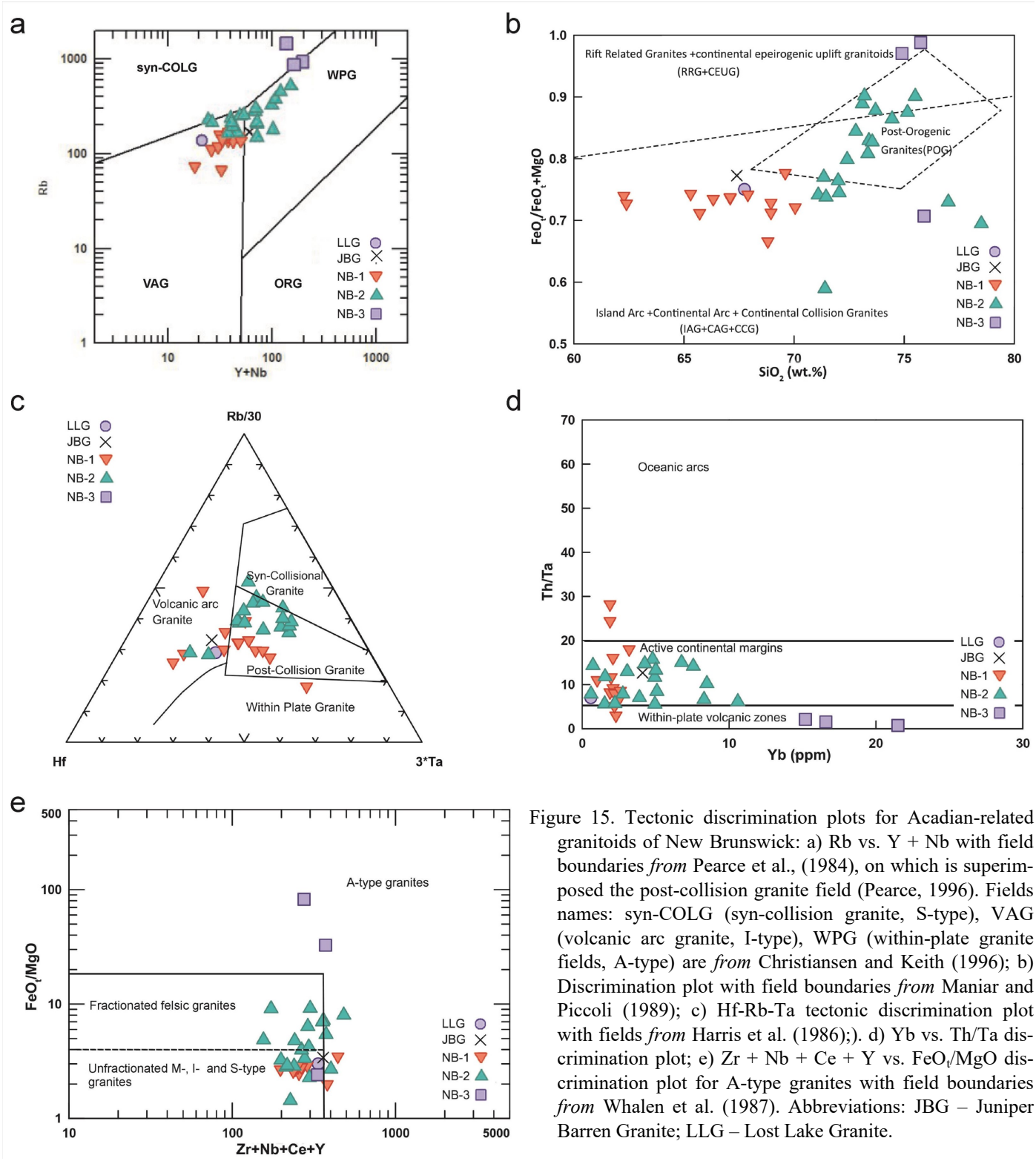

Figure 15. Tectonic discrimination plots for Acadian-related granitoids of New Brunswick: a) Rb vs. Y + Nb with field boundaries *from* Pearce et al., (1984), on which is superimposed the post-collision granite field (Pearce, 1996). Fields names: syn-COLG (syn-collision granite, S-type), VAG (volcanic arc granite, I-type), WPG (within-plate granite fields, A-type) are *from* Christiansen and Keith (1996); b) Discrimination plot with field boundaries *from* Maniar and Piccoli (1989); c) Hf-Rb-Ta tectonic discrimination plot with fields *from* Harris et al. (1986);). d) Yb vs. Th/Ta discrimination plot; e) Zr + Nb + Ce + Y vs. FeO_t/MgO discrimination plot for A-type granites with field boundaries *from* Whalen et al. (1987). Abbreviations: JBG – Juniper Barren Granite; LLG – Lost Lake Granite.

patible element content of the KSG may reflect a different source area, melting history and/or varying degree of assimilation fractional crystallization among these intrusions (i.e. the more fractionated members of group NB-2 intrusions and all the members of group NB-3; Förster et al., 1997). Moreover, with the exception of the MDG, DG, BG, MPG, PRG and KSG, all plot within the post-collision field of Pearce (1996).

According to the SiO_2 versus FeO_t/FeO_t + MgO discrimina-

tion plots of Maniar and Piccoli (1989) the JBG, LLG and NB-1 granites plot within the island arc – continental arc – continental collision granites (IAG-CAG-CCG) field, whereas the majority of group NB-2 intrusions fall within the post-orogenic granite field (POG, Fig. 15b). Lastly, the MPG and PRG plot within the rift related – continental epeirogenic uplift granitoids (RRG-CEUG) field, whereas the KSG plots within the IAG-CAG-CCG field, reflecting its different source materials (Fig. 15b).

The granite classification of Harris et al. (1986) was used to investigate the relationship among granites associated with various stages of the Acadian Orogeny (Fig. 15c). The JBG and LLG plot in the volcanic arc granite field, whereas group NB-1 granites plot in an array across the volcanic arc granite and post-collisional granite fields, which reflects the evolving nature of these I-type granites (Yang et al., 2002a). Group NB-2 intrusions mostly plot in the post-collisional granite field; the one exception being the MEG, which plots in the volcanic arc granite field. Furthermore, group NB-3 granites plot in an array across the syn-collisional granite and post-collisional granite fields. The PRG and MPG plot in the syn-collisional granite field, whereas the KSG plots in the post-collisional granite field. However, Yang et al. (2008) used petrographic and geochemical evidence to conclude that these post-collisional granites are associated with the terminal stage of the Acadian Orogeny, rather than the post-orogenic stage.

Gorton and Schandl (2000) classified felsic to intermediate plutonic rocks from oceanic arcs, active continental margins (ACM) and within-plate volcanic zones (WPVZ) using HFSE; such classification schemes should be equally applicable to plutonic rocks. On the Th/Ta versus Yb discrimination plot (Fig. 15d), most of the granitoids in this study plot within the active continental margin field. However, group NB-3 granites and one of the most evolved samples from LG plot in the within-plate volcanic zone field. Significant crustal contamination (addition of Ta and Yb) can cause granites that would otherwise plot in the active continental margin field to plot in the within-plate volcanic zone field (Gorton and Schandle, 2000; Fig. 15d). Furthermore, samples from the LG plot in the oceanic arc field due to their high Th content. This elevated Th may result from a higher degree of crustal assimilation or a higher contribution from the arc (Gorton and Schandle, 2000).

In the tectonic discrimination plots for anorogenic (A-type) granites (Whalen et al., 1987), group NB-1 granites plot entirely within the field of unfractionated I-type granites, whereas group NB-2 granites plot across the fractionated and unfractionated I-type fields (Fig. 15e). Moreover, BHG, MEG, UG, TRHG and SRG plot in the A-type field indicating the possibility of a mantle-related influence in the source area. Group NB-3 granites plot entirely in the A-type field (Fig. 15e). Fractionated I- and A-type granites are difficult to distinguish if the geochemical features of less-evolved phases in a particular igneous suite are not investigated (Whalen et al., 1987; Chappell, 1999). The data set used in this study (Table 1) suggests that the granitoids of New Brunswick are either normal I-type granite (i.e. NB-1 and most of the NB-2 granites) or fractionated I-types (more evolved phases of group NB-2, and all of group NB-3).

Petrogenesis of Acadian-related granitoid rocks in New Brunswick

Juniper Barren and Lost Lake granites

Several lines of geochemical evidence suggest that the JBG and LLG are unfractionated I-type granites (Fig. 6, 7, 9, 10, 11, 14). These granites have the lowest SiO_2 content (<68%) and Gottini index values of less than 15 and have the highest TiO_2, MnO, MgO, P_2O_5, Zr and V abundances. The $\delta^{18}O$ of these plutons (<10‰), is within the range of normal I-type granitoid rocks (Taylor, 1978; Chappell and White, 1992, 2001) for JBG. However, the LLG has a lower value ($\delta^{18}O$ = 5.6‰). These intrusions have the highest calculated $T_{Monazite}$, T_{Zircon} and $T_{Apatite}$ and the least evolved Nb/Ta and Zr/Hf values. They also have the lowest $(^{87}Sr/^{86}Sr)_i$ values (0.703) and slightly negative εNd value of -1.4 (mean). Their Sr/Y and $(La/Yb)_N$ values, along with the isotopic data, support the interpretation that their parent melt was formed from reworking an older crustal protolith through several different partial melting events (Whalen et al., 1996b). The LLG has the steepest chondrite-normalized REE pattern and no Eu anomaly. This unique pattern is due to minor HREE depletion accompanied by minimal feldspar fractionation. The strong LREE enrichment and very low HREE concentration of this sample suggests the presence of residual garnet in the source area (Wilson, 2007). In contrast, the JBG has an LREE-enriched pattern with a small negative Eu anomaly. These geochemical characteristics suggest that the JBG has an arc-related I-type affinity with a high amount of amphibole fractionation (Yang et al., 2002a).

The JBG and LLG are characterized as unfractionated (Whalen et al., 1987) and magnesian, calc-alkalic granites (Frost et al., 2001). The calc-alkalic characteristics of these granites may reflect partial melts of older (Avalonian?) calc-alkalic lower crustal protoliths, in response to Late Silurian to Early Devonian crustal thickening. These granites plot within the volcanic arc granite field (Pearce et al., 1984; Harris et al., 1986) and in the post-collisional granite field (Pearce, 1996). Negative Ba, Nb, Sr, P and Ti anomalies on the primitive mantle-normalized plot (Fig. 14) indicate that fractional crystallization of feldspar, apatite and Fe–Ti oxides played a role in the petrogenesis of these rocks, whereas positive U, K, Pb and Nd anomalies may indicate crustal contamination of these intrusions. All geochemical characteristics, including low silica, high P_2O_5, low incompatible elements, high Sr, Ba and Cs, and flat REE pattern with no significant negative Eu anomaly. Figures 10 and 14 suggest that reworking of an older crust (igneous source) in an arc environment was the source for the parent magmas of these intrusions; however, there is also evidence for a mantle contribution.

Group NB-1 granites

Group NB-1 granites have characteristics of unfractionated peraluminous I-type granites. These granites are amongst the least fractionated intrusions with the second highest MgO, TiO_2, CaO, FeO_t, P_2O_5, Ba, Sr, Zr and V, and the lowest SiO_2, K_2O, Rb, Nb, Ta and Gottini index (Table 1). These granitic intrusions are also characterized by low SiO_2 (<70 weight %), K_2O less than Na_2O and a relatively flat chondrite-normalized REE pattern with small negative Eu anomalies (Eu/Eu* = 0.66 –0.89), which are common characteristics of arc-related, I-type magmas that have undergone an appreciable amount of amphibole fractionation (Yang et al., 2003). The high CaO, P_2O_5 and LILE with low HFSE in these granites may indicate undifferentiated high-K calc-alkaline, I-type magmas in post-collisional settings (Landenberger and Collins, 1996; Barbarin, 1999). The small depletion of Ba, Sr and Ti on the mantle-normalized spidergram (Fig. 14), indicate that feldspar and iron -titanium oxide fractionation were involved in the petrogenesis of these rocks. NB-1 granites typically fall in the field of unfractionated granites of Whalen et al. (1987) and plot in an array across the calc-alkalic and alkali-calcic fields of magnesian granites on Frost et al. (2001). Such cross-field distribution trends are commonly observed in post-collisional magmatic suites, potentially reflecting magma mixing or partial melting of mixed protoliths for these granites (Clemens et al., 2009). Limited available initial $^{87}Sr/^{86}Sr$ (0.703–0.707) and $\delta^{18}O$ values are within the range of I-type granites (0.704–0.712 and less than 10‰, respectively; Chappell and White, 2001), the ε_{Nd} values are commonly higher and positive (+1.09 to -3.00) compared to I-type granites (ε_{Nd} = -3.5 to -8.9; Chappell and White, 2001). Furthermore, Sr/Y and $(La/Yb)_N$ ratios of these granites are within the range of normal crustally derived granite (S or I-type; Sr/Y = 2–20 and $(La/Yb)_N$ = 38–61; Wedpohl, 1995; Moyen, 2009), which suggests that supracrustal contamination played a role in their origin. To summarize, group NB-1 granites are unfractionated I-type granites generated from partial melting of the lower crust. These partial melts may have formed by advective heating by underplated mafic magmas. Varying degrees of fractional crystallization and crustal contamination could explain the geochemical variation between the subgroups.

Group NB-2 granites

Geochemical characteristics of group NB-2 granites suggest a fractionated metaluminous to peraluminous I-type affinity. These granites have geochemical values intermediate to those of two groups NB-1 and NB-3 and are characterized by SiO_2 contents of 71to 74 weight %, more K_2O than Na_2O and a LREE -enriched chondrite-normalized REE pattern. The REE patterns of group NB-2 granites have a more pronounced negative Eu anomaly (Eu/Eu* = 0.06–0.71) and display eight distinct shapes, reflecting a combination of various negative LREE and HREE slopes. NB-2 granites are also characterized by depletions of Ba, La, Ce, P, Sr and Ti on the primitive mantle-normalized plot, which indicate that feldspar, monazite, apatite and Fe-Ti oxide fractionation were involved in the petrogenesis of these rocks. Furthermore, enrichment in U, Th, Pb and K may reflect crustal contamination of the parent magmas. Group NB-2 granites plot within the unfractionated and fractionated granite field of Whalen et al. (1987) and in the magnesian granites of Frost et al. (2001). However, some of the more fractionated members of this group (i.e. MDG, DG, BHG, UG, MLT, MEG, ALG and THG) plot in the ferroan granite field (high $FeO_T/(MgO + FeO_T)$). Like the group NB-1 granites, the granites of NB-2 plot in an array across the calc-alkalic to alkali-calcic fields on the MALI plot of Frost et al. (2001: Fig. 8b), which is common for post-collisional magmatic suites and may indicate magma mixing or partial melting of mixed protoliths (i.e. tonalitic to granodioritic; Clemens et al., 2009). The combination of partial melting of tonalitic to granodioritic crust that produces alkali-calcic to calc-alkalic granitoids may play a key role in the formation of most ferroan granitoid rocks (Frost and Frost, 2011). In fact, the group NB-2 granites, with the exception of MDG, DG, BHG and BG, plot within the post-collisional field of Pearce (1996: Fig. 15a). Available $(^{87}Sr/^{86}Sr)_i$ is higher than 0.705 and $\delta^{18}O$ values (6–10‰) are within the published values of I-type granites (Chappell and White, 2001). Whalen (1993) concluded that the consistent negative ε_{Nd} value of both Ordovician and Siluro-Devonian granites of the Gander zone reflect reworking of the same (considerably older) crustal protolith through several different partial melting events. The positive ε_{Nd} of some of the members (i.e. MDG, BHG, UG, SRG, EGD and BGS) could also be explained by the melting of a young juvenile source. Furthermore, the $(La/Yb)_N$ and Sr/Y values of these granites are within the range of values typical of crustally derived granites (S or I-type; $(La/Yb)_N$ = 38–61) and Sr/Y (2–20); Wedepohl,1995; Moyen, 2009). However, the ε_{Nd} values of these samples are higher in comparison to the I-type granites of the Lachlan Fold Belt in Australia (ε_{Nd} = -3.5 to -8.9; Chappell and White, 2001). In summary, group NB-2 granites are unfractionated to fractionated I-type granites generated from varying degrees of partial melting of a mixed mantle - older crustal protolith. Different degrees of fractional crystallization, crustal contamination and secondary alteration could explain the geochemical differences between the subgroups.

Group NB-3 Granites

Several geochemical characteristics identify NB-3 granites as highly evolved peraluminous I-type granites. Granites of NB -3 are the most fractionated granites examined in this study and have the highest SiO_2 content (>74 weight %) and Gottini index (>350), and K/Rb ratios below 41. These granites are enriched in Rb, Li, Ta, Nb, Y, U and Sn, and depleted in Ba, Sr, Zr, Cr, Ni, Co, V, Cu and Mn. Group NB-3 granites are characterized by the lowest $(La/Yb)_N$ (< 2), highly fractionated HREE [$(Gd/Yb)_N$ < 1] and a strong negative Eu anomaly (Eu/Eu* = 0.002–0.03). Chondrite-normalized REE plots and primitive mantle-normalized spidergrams have several distinctive features: 1) flat REE patterns significant negative Eu anomalies

indicating that feldspar fractionation or restite feldspar in the source region played a major role in the petrogenesis of parent magmas (confirmed with the high negative Ba and Sr anomalies on the spidergrams); 2) Strong negative P, La, Ce and Ti anomalies indicating that monazite and Fe-Ti oxide fractionation, respectively; 3) LILE elements are significantly enriched according to the primitive mantle-normalized plot; 4) Group NB-3 granites have the lowest Zr/Hf and Nb/Ta values of all the intrusions investigated and negative correlation of Nb/Ta with Rb, Li and F indicates that extreme fractional crystallization of a quartzofeldspathic source was accompanied by fluid fractionation in the latest stages of fractionation for these granites (Creaser et al., 1991; Yang et al., 2003).

The similarities among granites of this group were previously documented by Taylor (1992), McLeod et al. (1994) and Yang (2005) who suggested that they were generated through extreme fractional crystallization from the MDG. Yang et al. (2003, 2008) suggested the involvement of fluid in their fractional crystallization. Several lines of evidences, including: 1) the existence of pod pegmatites; 2) the presence of micrographic and myrmekitic textures; 3) crystallization of primarily topaz and fluorite; 4) Zn enrichment; 5) low K/Rb and Nb/Ta ratios; 6) positive correlation of Rb, U, Ta and Sn with F; and 7) the high F content of the lithian siderophyllite (4.77–5.82 weight %) from these intrusions, indicate that fractional crystallization was accompanied by fluid fractionation, particularly in the later stages of crystallization. Fractional crystallization of the main phases, especially feldspars and lithium siderophyllite and accessory minerals (e.g. monazite, zircon, uraninite, fluorite and columbite), played important roles in the formation of these granites. The highly peraluminous nature of these granites (A/CNK = 1.02–1.20) indicates a significant supracrustal component in the source that is supported by high $\delta^{18}O$ (7.2–9.2‰) and $(^{87}Sr/^{86}Sr)_i$ (0.712) values. However, ε_{Nd} is close to zero and ranges from +0.1 to +0.3, which points to a slightly depleted mantle source or a mixture of depleted mantle and older crustal sources for these intrusions. Interestingly, NB-3 granites are located at the boundary between the Gander and Avalon zones and Whalen et al. (1996a) suggested that the differences in ε_{Nd} values reflects the presence of various continental basement blocks underlying the boundary area. These granites may classify as A-type granites based on the classification of Whalen et al. (1987), but they have much higher Rb/Sr and Rb/Ba ratios in comparison with typical A-type granites. Highly fractionated I- and S-type granites could display high Ga/Al ratios and other geochemical characteristics that overlap those of A-type granites (Whalen et al., 1987; Eby, 1992). Consequently, group NB-3 granites are interpreted to be highly fractionated I-type granites as all geochemical features support a crustal source for these highly evolved intrusions. Conversely, group NB-3 granites appear to be associated with the crustal thinning processes related to crustal delamination following the juxtaposition of various crustal blocks (i.e. Gander and Avalon zones) during the Acadian Orogeny (Whalen et al., 1996a; Sinclair et al., 2006).

Conclusions

The Late Silurian to Late Devonian granitoids of New Brunswick investigated for this study have been allocated to several geochemically defined groups. Chemical trends between the granitoid groupings indicate fractional crystallization has driven granitoid evolution. The degree of fractional crystallization reaches the maximum in the granites of group NB-3 and results in the formation of an exsolved fluid phase that is critical in ore-forming processes.

The barren JBG and LLG are characterized by the lowest SiO_2 contents and highest transition element contents. These metaluminous, magnesian granites have characteristics of unfractionated (oxidized) I-type granite, and would have formed from partial melting of an older crustal material (with some mantle input). Group NB-1 granites are peraluminous and characterized by SiO_2 ranging from 68 to 70 weight % and the highest Nb/Ta and Zr/Hf ratios. They have LREE-enriched chondrite-normalized REE patterns with small negative Eu anomalies and classify as unfractionated I-type granites and magnesian granites. The major difference between the granites of this group and the JBG and LLG is oxidation state (i.e. group NB-1 magmas were reduced as reflected by their reddish -brown biotite). The assimilation of reduced country rocks likely played an important role in generating the reduced state that is vital for the generation of the tungsten mineralization associated with some of these intrusions. In general, group NB-1 granites represent unfractionated reduced I-type granites that formed through partial melting in an arc system. Group NB-2 granites are metaluminous to peraluminous I-type granites, typified by SiO_2 contents of 71 to 75 weight % and more K_2O than Na_2O. Their chondrite-normalized REE pattern is LREE-enriched, with a more pronounced negative Eu anomaly than granites from the JBG, LLG and group NB-1 granites. Several geochemical characteristics, including negative Eu anomalies, high initial strontium and high oxygen isotopes, indicate a crustal source for these rocks. Specifically, the source magmas are unfractionated to fractionated I-type granites generated from various degrees of partial melting of an older crustal protolith with an igneous quartzofeldspathic composition. Finally, group NB-3 granites are the most fractionated intrusions in this study and are characterized by the highest SiO_2 content and Gottini index, and the lowest Zr/Hf and Nb/Ta ratios. Likewise, these granites have the lowest K/Rb, Nb/Ta, La/Sm and Eu/Eu* ratios, indicating that fluid fractionation played an important role in the genesis of these highly evolved intrusions. Group NB-3 intrusions have A-type affinities, but have much higher Rb/Sr and Rb/Ba values. Consequently, they are believed to be highly evolved I-type granites that formed in association with the crustal thinning related to crustal delamination following the juxtaposition of crustal terranes during the Acadian Orogeny.

Significantly the composition of granitoids that formed in different tectonic blocks, at different times, in response to different orogenic events are indistinguishable based on the available data (i.e. MEG and MDG; NG and PFG; DG and ALG:

see Fig. 1, 14). This data strongly suggests that the chemical traits exhibited by these granitoids are mostly related to process, rather than variations in source compositions (with the notable exception of JBG and LLG). Furthermore, within individual tectonic blocks, the granitoids display geochemical trends of progressive evolution over time that corresponds with increased prospectivity. For instance, in central New Brunswick the ca. 420 Ma NG hosts several minor occurrences of greisen-style mineralization, whereas the more evolved ca. 380 Ma BG and DG are associated with major deposits (i.e. Burnthill Mine, Tin Hill deposit). These relationships are consistent with the hypothesis that such granitoid prospectivity is enhanced through repeated orogenesis within a multiphase accretionary orogen, presumably through progressive seeding and batch processing concentrating ore minerals in source regions.

Acknowledgments

This report is a contribution to NRCan's Targeted Geoscience Initiative Program (TGI). Support for this study was provided through the Porphyry-style Mineral Systems Project's '*Activity P-1.4: Temporal and spatial controls on the nature and distribution of porphyry-style deposits*'.

This research forms part of Zeinab Azabackht's doctoral project at the University of New Brunswick. Support for this study has been provided by the Geological Survey of Canada as a part of the Targeted Geoscience Initiative and Natural Resources Canada and a Natural Sciences and Engineering Research Council Discovery grant. The authors would like to thank the staff of the New Brunswick Department of Energy and Mines for their ongoing support. We thank Malcom McLeod, Sean McClenaghan, Susan Johnson, Jim Walker and Joseph Whalen for their help with collecting samples and geochemical data. This report benefited from the review of Beth McClenaghan, Ian Honsberger (both GSC) and Jim Walker (E&RD). We also acknowledge Alex Zagorevski for providing editorial oversight.

References

Azadbakht, Z., McFarlane, C.R.M., and Lentz, D.R., 2016. Precise U-Pb ages for the cogenetic alkaline Mount LaTour and peraluminous Mount Elizabeth granites of the South Nepisiguit River Plutonic Suite, northeastern New Brunswick, Canada; Atlantic Geology, v. 52, p. 188–211.

Baker, T., Pollard, P., Mustard, R., Mark, G., and Graham, J., 2005. A comparison of granite-related tin, tungsten and gold-bismuth deposits: implications for exploration; Society of Economic Geologists Newsletter, v. 61, p. 5–17.

Baldwin, J.A. and Pearce, J.A., 1982. Discrimination of productive and non-productive porphyritic intrusions in the Chilean Andes; Economic Geology, v. 77, p. 664–674.

Ballouard, C., Boulvais, P., Poujol, M., Gapais, D., Yamato, P., Tartèse, R., and Cuney, M., 2015. Tectonic record, magmatic history and hydrothermal alteration in the Hercynian Guérande leucogranite, Armorican Massif, France; Lithos, v. 220, p. 1–22.

Ballouard, C., Poujol, M., Boulvais, P., Branquet, Y., Tartèse, R., and Vigneresse, J.L., 2016. Nb-Ta fractionation in peraluminous granites: A marker of the magmatic-hydrothermal transition; Geology, v. 44, p. 231–234.

Barth, M.G., McDonough, W.F., and Rudnick, R.L., 2000. Tracking the budget of Nb and Ta in the continental crust; Chemical Geology, v. 165, p. 197–213.

Barbarin, B., 1999. A review of the relationships between granitoid types, their origins and their geodynamic environments; Lithos, v. 46, p. 605–626.

Beal, K.L., Lentz, D.R., Hall, D.C., and Dunning, G., 2010. Mineralogical, geochronological and geochemical characterization of Early Devonian aquamarine-bearing dikes of the Zealand Station Beryl and molybdenite deposit, west-central New Brunswick; Canadian Journal of Earth Sciences, v. 47, p. 859–874.

Bevier, M.L., 1988. U-Pb geochronologic studies of igneous rocks in NB; *in* Thirteenth Annual Review of Activities, (ed.) S.A. Abbott; New Brunswick Department of Natural Resources and Energy, Minerals and Energy Division, Information Circular 88–2.

Bevier, M.L. and Barr, S.M., 1990. U-Pb age constraints on the stratigraphy and tectonic history of the Avalon Terrane, New Brunswick, Canada; The Journal of Geology, v. 98, p. 53–63.

Bevier, M.L. and Whalen, J.B., 1990a. Tectonic significance of Silurian magmatism in the Canadian Appalachians; Geology, v. 18, p. 411–414.

Bevier, M.L. and Whalen, J.B., 1990b. U-Pb geochronology of Silurian granites, Miramichi terrane, New Brunswick; *in* Radiogenic age and isotopic studies, Report 3; Geological Survey of Canada, Paper 89–2, p. 93–100.

Bineli-Betsi, T.B. and Lentz, D.R., 2011. Petrochemistry of subvolcanic dike swarms associated with the Golden Revenue Au-Cu and the Stoddart Mo-Cu±W mineralizations (Dawson Range, Yukon Territory, Canada) and implications for ore genesis; Ore Geology Reviews, v. 39, p. 134–163.

Blevin, P.L. and Chappell, B.W., 1992. The role of magma sources, oxidation states and fractionation in determining the granite metallogeny of eastern Australia; Earth Sciences, v. 83, p. 305–316.

Blevin, P.L. and Chappell, B.W., 1995. Chemistry, origin and evolution of mineralized granites in the Lachlan fold belt, Australia; the metallogeny of I-and S-type granites; Economic Geology, v. 90, p. 1604–1619.

Bustard, A., Zhang, W., McFarlane, C.R.M., and Lentz, D.R., 2013. Tungsten Mineralization Processes at the Sisson Brook W-Mo-Cu deposit, Central New Brunswick: the role of formation of titaniferous phases at reaction fronts; Acta Geologica Sinica, v. 87, p. 672–856.

Butt, K.A., 1976. Genesis of granitic stocks in southwestern

New Brunswick; Ph.D. thesis, University of New Brunswick, Fredericton, New Brunswick, 235 p.

Candela, P.A., 1997. A review of shallow, ore-related granites: textures, volatiles and ore metals; Journal of Petrology, v. 38, p. 1619–1633.

Černý, P., Blevin, P.L., Cuney, M., and London, D., 2005. Granite-related ore deposits; *in* Economic Geology 100th anniversary volume, (ed.) J.W. Hedenquist, J.F.H. Thompson, R.J. Goldfarb, J.P. Richards; Society of Economic Geologists, Colorado, p. 337–370.

Chappell, B.W., 1999. Aluminium saturation in I- and S-type granites and the characterization of fractionated haplogranites; Lithos, v. 46, p. 535–551.

Chappell, B.W. and White, A.J.R., 1974. Two contrasting granite types; Pacific Geology, v. 8, p. 173–174.

Chappell, B.W. and White, A.J.R., 1992. I-and S-type granites in the Lachlan Fold Belt; Geological Society of America, Special Papers 272, p. 1–26.

Chappell, B.W. and White, A.J.R., 2001. Two contrasting granite types: 25 years later; Australian Journal of Earth Sciences, v. 48, p. 489–499.

Chappell, B.W., Bryant, C.J., Wyborn, D., White, A.J.R., and Williams, I.S., 1998. High- and low-temperature I-type granites; Resource Geology, v. 48, p. 225–235.

Charoy, B., 1986. The genesis of the Cornubian batholith (South-West England): the example of the Carnmenellis pluton; Journal of Petrology, v. 27, p. 571–604.

Chandrajith, R., Dissanayake, C.B., and Tobschall, H.J., 2001. Application of multi-element relationships in stream sediments to mineral exploration: a case study of Walawe Ganga Basin, Sri Lanka; Applied Geochemistry, v. 16, p. 339–350.

Chatterjee, A.K. and Muecke, G.K., 1982. Geochemistry and the distribution of uranium and thorium in the granitoid rocks of the South Mountain Batholith, Nova Scotia; *in* Uranium in Granites (ed.) Y.T. Maurice; Geological Survey of Canada, Ottawa, Ontario, p. 2-17.

Chatterjee, A.K., Strong, D.F., and Muecke, G.K., 1983. A multivariate approach to geochemical distinction between tin-specialized and uranium-specialized granites of southern Nova Scotia; Canadian Journal of Earth Sciences, v. 20, p. 420–430.

Cheng, Q., Bonham-Carter, G., Wang, W., Zhang, S., Li, W., and Qinglin, X., 2011. A spatially weighted principal component analysis for multi-element geochemical data for mapping locations of felsic intrusions in the Gejiu mineral district of Yunnan, China; Computers and Geosciences, v. 37, p. 662–669.

Christiansen, E.H. and Keith, J.D., 1996. Trace element systematics in silicic magmas: a metallogenic perspective; *in* Trace element geochemistry of volcanic rocks: applications for massive sulphide exploration, (ed.) D.A. Wyman; Geological Association of Canada Short Course, v. 12, p. 115–151.

Clarke, D.B., 1992. Granitoid rocks; London, Springer Science and Business Media, 287p.

Clemens, J.D., Helps, P.A., and Stevens, G., 2009. Chemical structure in granitic magmas-a signal from the source?; Geological Society of America Special Papers 472, p. 159–172.

Congdon, R.D. and Nash, W.P., 1991. Eruptive pegmatite magma: rhyolite of the Honeycomb Hills, Utah; American Mineralogist, v. 76, p. 1261–1278.

Creaser, R.A., Price, R.C., and Wormald, R.J., 1991. A-type granites revisited: assessment of a residual-source model; Geology, v. 19, p. 163–166.

Cullers, R.L. and Graf, J.L., 1984. Rare earth elements in igneous rocks of the continental crust: intermediate and silicic rocks, ore petrogenesis; *in* Rare Earth Element Geochemistry, (ed.) P. Henderson; Amsterdam, Elsevier, p. 237–274.

Cuney, M., Marignac, C., and Weisbrod, A., 1992. The Beauvoir topaz-lepidolite albite granite (Massif Central, France); the disseminated magmatic Sn-Li-Ta-NB-Be mineralization; Economic Geology, v. 87, p. 1766–1794.

Davis, J.C., 2011. Statistics and data analysis in geology, India; Wiley, 638 p.

Davis, W.J., Chi, G., Castonguay, S., and McLeod, M., 2004. Temporal relationships between plutonism, metamorphism and gold mineralization in southwestern New Brunswick: U-Pb and $^{40}Ar/^{39}Ar$ geochronological constraints; Geological Survey of Canada, Current Research 2004–F2, 20 p.

Debon, F. and Le Fort, P., 1983. A chemical–mineralogical classification of common plutonic rocks and associations; Earth and Environmental Science, v. 73, p. 135–149.

De La Roche, H., Leterrier, J.T., Grandclaude, P., and Marchal, M., 1980. A classification of volcanic and plutonic rocks using R_1R_2-plot and major-element analyses—its relationships with current nomenclature; Chemical Geology, v. 29, p. 183–210.

DePaolo, D.J., 1981. Trace element and isotopic effects of combined wall rock assimilation and fractional crystallization; Earth and Planetary Science Letters, v. 53, p. 189–202.

Dostal, J. and Chatterjee, A.K., 1995. Origin of topaz-bearing and related peraluminous granites of the Late Devonian Davis Lake pluton, Nova Scotia, Canada: crystal versus fluid fractionation; Chemical Geology, v. 123, p. 67–88.

Dostal, J. and Chatterjee, A.K., 2000. Contrasting behaviour of Nb/Ta and Zr/Hf ratios in a peraluminous granitic pluton (Nova Scotia, Canada); Chemical Geology, v. 163, p. 207–218.

Dostal, J., Kontak, D.J., Gerel, O., Shellnutt, J.G., and Fayek, M., 2015. Cretaceous ongonites (topaz-bearing albite-rich microleucogranites) from Ongon Khairkhan, Central Mongolia: Products of extreme magmatic fractionation and pervasive metasomatic fluid: rock interaction; Lithos, v. 236, p. 173–189.

Dupuy, C., Liotard, J.M., and Dostal, J., 1992. Zr/Hf fractiona-

tion in intraplate basaltic rocks: carbonate metasomatism in the mantle source; Geochimica et Cosmochimica Acta, v. 56, p. 2417–2423.

Eby, G.N., 1990. The A-type granitoids: a review of their occurrence and chemical characteristics and speculations on their petrogenesis; Lithos, v. 26, p. 115–134.

Eby, G.N., 1992. Chemical subdivision of the A-type granitoids: petrogenetic and tectonic implications; Geology, v. 20, p. 641–644.

El Bouseily, A.M. and El Sokkary, A.A., 1975. The relation between Rb, Ba and Sr in granitic rocks; Chemical Geology, v. 16, p. 207–219.

Eugster, H.P., 1985. Granites and hydrothermal ore deposits: a geochemical framework; Mineralogical Magazine, v. 49, p. 7–23.

Farmer, G.L. and DePaolo, D.J., 1983. Origin of Mesozoic and Tertiary granite in the western United States and implications for Pre-Mesozoic crustal structure: 1. Nd and Sr isotopic studies in the geocline of the Northern Great Basin; Journal of Geophysical Research, v. 88, p. 3379–3401.

Förster, H.J., Tischendorf, G., and Trumbull, R.B., 1997. An evaluation of the Rb vs.(Y + Nb) discrimination plot to infer tectonic setting of silicic igneous rocks; Lithos, v. 40, p. 261–293.

Förster, H.J., Tischendorf, G., Trumbull, R.B., and Gottesmann, B., 1999. Late-collisional granites in the Variscan Erzgebirge, Germany; Journal of Petrology, v. 40, p. 1613–1645.

Frost, C.D. and Frost, B.R., 2011. On ferroan (A-type) granitoids: their compositional variability and modes of origin; Journal of Petrology, v. 52, p. 39–53.

Frost, B.R., Barnes, C.G., Collins, W.J., Arculus, R.J., Ellis, D.J., and Frost, C.D., 2001. A geochemical classification for granitic rocks; Journal of Petrology, v. 42, p. 2033–2048.

Fyffe, L.R., 1982. Geology in the vicinity of the 1982 Miramichi earthquake; *in* Preliminary Report of the Miramichi, New Brunswick, Canada Earthquake Sequence of 1982, Department of Natural Resources, Mineral Resources Division, p. 44–46.

Fyffe, L.R., 1992. Bedrock geology of the Beech Hill area (NTS 21G 7e), Charlotte County, New Brunswick; New Brunswick Department of Energy and Mines, Map Plate 1992-1, 1:50 000 scale.

Fyffe, L.R., 2001. Stratigraphy and geochemistry of the Ordovician volcanic rocks of the Eel River area, west-central New Brunswick; Atlantic Geology, v. 37, p. 81–101.

Fyffe, L.R. and Richard, D., 2007. Lithological map of New Brunswick; New Brunswick Department of Energy and Mines, Geological Surveys Branch. Map Plate 2007–18, 1:600 000 scale.

Fyffe, L.R., Pajari, G.E., and Cherry, M.E., 1981. The Acadian plutonic rocks of New Brunswick; Maritime Sediments and Atlantic Geology, v.17, p. 23–36.

Fyffe, L.R., Pickerill, R.K., and Stringer, P., 1999. Stratigraphy, sedimentology and structure of the Oak Bay and Waweig formations, Mascarene Basin: implications for the paleotectonic evolution of southwestern New Brunswick; Atlantic Geology, v. 35, p. 59–84.

Fyffe, L.R., Thorne, K., Dunning, G.R., and Martin, D.A., 2008, U-Pb geochronology of the Sisson Brook granite porphyry, York County, west-central New Brunswick; *in* Geological Investigations in New Brunswick for 2007, (ed.) G.L. Martin; New Brunswick Department of Natural Resources; Minerals, Policy and Planning Division, Mineral Resource Report 2008–1, p. 35–54.

Garrett, R.G. and Grunsky, E.C., 2001. Weighted sums–knowledge based empirical indices for use in exploration geochemistry; Geochemistry: Exploration, Environment, Analysis, v. 1, p. 135–141.

Gorton, M.P. and Schandl, E.S., 2000. From continents to island arcs: a geochemical index of tectonic setting for arc-related and within-plate felsic to intermediate volcanic rocks; The Canadian Mineralogist, v. 38, p. 1065–1073.

Gottini, V., 1968. The TiO_2 frequency in volcanic rocks; Geologische Rundschau, v. 57, p. 930–935.

Grunsky, E.C., 1997. Strategies and methods for the interpretation of geochemical data; *in* Current Topics in GIS and Integration of Exploration Datasets; Exploration ’97 Workshop, 145 p.

Halter, W.E., Williams-Jones, A.E., and Kontak, D.J., 1998. Modeling fluid–rock interaction during greisenization at the East Kemptville tin deposit: implications for mineralization; Chemical Geology, v. 150, p. 1–17.

Harris, N.B., Pearce, J.A., and Tindle, A.G., 1986. Geochemical characteristics of collision-zone magmatism; Geological Society of London, Special Publication No. 19, p. 67–81.

Harris, J.R., Wilkinson, L., and Grunsky, E.C., 2000. Effective use and interpretation of lithogeochemical data in regional mineral exploration programs: application of Geographic Information Systems (GIS) technology; Ore Geology Reviews, v. 16, p. 107–143.

Harrison, T.M. and Watson, E.B., 1984. The behaviour of apatite during crustal anatexis: equilibrium and kinetic considerations; Geochimica et Cosmochimica Acta, v. 48, p. 1467–1477.

Inverno, C.M. and Hutchinson, R.W., 2004. The endogranitic tin zone, Mount Pleasant, New Brunswick, Canada and its metallogenesis; Applied Earth Science, v. 113, p. 261–288.

Irvine, T.N.J. and Baragar, W., 1971. A guide to the chemical classification of the common volcanic rocks; Canadian Journal of Earth Sciences, v. 8, p. 523–548.

Jochum, K.P., Seufert, H.M., Spettel, B., and Palme, H., 1986. The solar-system abundances of Nb, Ta and Y and the relative abundances of refractory lithophile elements in differentiated planetary bodies; Geochimica et Cosmochimica

Acta, v. 50, p. 1173–1183.

Jochum, K. P., Stolz, A. J., and McOrist, G., 2000. Niobium and tantalum in carbonaceous chondrites: Constraints on the solar system and primitive mantle niobium/tantalum, zirconium/niobium, and niobium/uranium ratio; Meteoritics and Planetary Science, v. 35, p. 229-235.

Kay, S.M., Godoy, E., and Kurtz, A., 2005. Episodic arc migration, crustal thickening, subduction erosion and magmatism in the south-central Andes; Geological Society of America Bulletin, v. 117, p. 67–88.

Kooiman, G.J.A., McLeod, M.J., and Sinclair, W.D., 1986. Porphyry tungsten-molybdenum orebodies, polymetallic veins and replacement bodies and tin-bearing greisen zones in the Fire Tower Zone, Mount Pleasant, New Brunswick; Economic Geology, v. 81, p. 1356–1373.

Lalonde, A. and Bernard, P., 1993. Composition and color of biotite from granites: two useful properties in the characterization of plutonic suites from the Hefburn internal zone of Wopmay Orogen, Northwest Territories; The Canadian Mineralogist, v. 31, p. 203–217.

Landenberger, B. and Collins, W.J., 1996. Derivation of A-type granites from a dehydrated charnockitic lower crust: evidence from the Chaelundi Complex, Eastern Australia; Journal of Petrology, v. 37, p. 145–170.

Le Maitre, R.W.B., Dudek, P., Keller, A., Lameyre, J., Le Bas, J., Sabine, M.J., Schmid, P.A., Sorensen, R., Streckeisen, H., and Woolley, A., 1989. A classification of igneous rocks and glossary of terms; Recommendations of the International Union of Geological Sciences, Subcommission on the Systematics of Igneous Rocks, Oxford, Cambridge University Press, 300 p.

Le Maitre, R.W.B., Streckeisen, A., Zanettin, B., Le Bas, M.J., Bonin, B., Bateman, P., Bellieni, G., Dudek, A., Efremova, S., and Keller, J., 2002. Igneous rocks: a classification and glossary of terms; Recommendations of the International Union of Geological Sciences. London, Cambridge University Press, 235 p.

Lehmann, B., Ishihara, S., Michel, H., Miller, J., Rapela, C.W., Sanchez, A., Tistl, M., and Winkelmann, L., 1990. The Bolivian tin province and regional tin distribution in the Central Andes; a reassessment; Economic Geology, v. 85, p. 1044–1058.

Lentz, D.R., 1986. Geology and depositional conditions of tin lodes at True Hill, New Brunswick; M.Sc. thesis, University of New Brunswick, Fredericton, New Brunswick, 495 p.

Lentz, D.R., 1994. Multiple episodes of brecciation and mineralization associated with an epizonal granite porphyry, True Hill, southwestern New Brunswick; Exploration and Mining Geology, v. 3, p. 9–16.

Lentz, D.R. and McAllister, A.L., 1990. The petrogenesis of tin -and sulfide-lode mineralization at True Hill, southwestern New Brunswick; Atlantic Geology, v. 26. p. 139–155.

Lentz, D.R. and Fowler, A.D., 1992. A dynamic model for graphic quartz-feldspar intergrowths in granitic pegmatites in the southwestern Grenville Province; Canadian Mineralogist, v. 30, p. 571–585.

Lentz, D.R. and Gregoire, C., 1995. Petrology and mass-balance constraints on major-, trace- and rare-earth-element mobility in porphyry-greisen alteration associated with the epizonal True Hill granite, southwestern New Brunswick, Canada; Journal of Geochemical Exploration, v. 52, p. 303–331.

Lentz, D.R., Lutes, G., and Hartree, R., 1988. Bi-Sn-Mo-W greisen mineralization associated with the True Hill granite, southwestern New Brunswick; Maritime Sediment and Atlantic Geology, v. 24, p. 321–338.

Leonard, P.R.R., Lentz, D.R., and Poujol, M., 2006. Petrology, geochemistry and U-Pb (zircon) age of the quartz-feldspar porphyry dyke at the Lake George antimony mine, New Brunswick: implications for origin, emplacement process and mineralization; Atlantic Geology, v. 42, p. 13–29.

Li, J., Huang, X. L., He, P. L., Li, W. X., Yu, Y., and Chen, L. L., 2015. In situ analyses of micas in the Yashan granite, South China: Constraints on magmatic and hydrothermal evolutions of W and Ta–Nb bearing granites; Ore Geology Reviews, v. 65, p. 793–810.

Linhai Jing, Q.C. and Panahi, A., 2006. Principal component analysis with optimum order sample correlation coefficient for image enhancement; International Journal of Remote Sensing, v. 27, p. 3387–3401.

Linnen, R.L. and Keppler, H., 1997. Columbite solubility in granitic melts: consequences for the enrichment and fractionation of Nb and Ta in the Earth's crust; Contributions to Mineralogy and Petrology, v. 128, p. 213–227.

Linnen, R.L. and Keppler, H., 2002. Melt composition control of Zr/Hf fractionation in magmatic processes; Geochimica et Cosmochimica Acta, v. 66, p. 3293–3301.

London, D., 1992. Phosphorus in S-type magmas: the P_2O_5 content of feldspars from peraluminous granites, pegmatites and rhyolites; American Mineralogist, v. 77, p. 126–145.

López-Moro, F.J., Polonio, F.G., González, T.L., Contreras, J.L.S., Fernández, A.F., and Benito, M.C.M., 2017. Ta and Sn concentration by muscovite fractionation and degassing in a lens-like granite body: The case study of the Penouta rare-metal albite granite (NW Spain); Ore Geology Reviews, v. 82, p. 10–30.

MacLellan, H.E., 1990. Geology and geochemistry of middle Devonian Burnthill Brook granites and related tin-tungsten deposits, York and Northumberland Counties, New Brunswick; Minerals and Energy Division Department of Natural Resources and Energy, 104 p.

MacLellan, H.E. and Taylor, R.P., 1989. Geology and geochemistry of the Burnthill Granite and related W–Sn–Mo–F mineral deposits, central New Brunswick; Canadian Journal of Earth Sciences, v. 26, p. 499–514.

Maniar, P.D. and Piccoli, P.M., 1989, Tectonic discrimination

of granitoids: Geological Society of America, Bulletin, v. 101, p. 635–643.

Martin, H., 1986. Effect of steeper Archean geothermal gradient on geochemistry of subduction-zone magmas; Geology, v. 14, p. 753–756.

Martin, H., Smithies, R.H., Rapp, R., Moyen, J. F., and Champion, D., 2005. An overview of adakite, tonalite–trondhjemite–granodiorite (TTG) and sanukitoid: relationships and some implications for crustal evolution; Lithos, v. 79, p. 1–24.

Massawe, R.J.R., 2018. Petrogenesis of Cu–Ag skarn mineralization in the Mckenzie Gulch area, northern New Brunswick, Canada; Ph.D. thesis, University of New Brunswick, Fredericton, New Brunswick, 422 p.

McClenaghan, S.H., Thorne, K.G., and Rogers, N., 2014. Granite-related mineralization and alteration in the Acadian Plutonic Belt: Implications for Sn–W–Mo–Cu exploration in central New Brunswick; Geological Association of Canada/ Mineralogical Association of Canada Joint Annual Meeting, Field Trip Guidebook, 74 p.

McCutcheon, S.R., 1990. The Late Devonian Mount Pleasant Caldera Complex; Stratigraphy, Mineralogy, Geochemistry and Geologic Setting of Sn-W Deposit in Southwestern New Brunswick; Ph.D. thesis, Dalhousie University Halifax, Nova Scotia, 609 p.

McCutcheon, S.R. and Robinson, P.T., 1987. Geological constraints on the genesis of the Maritimes Basin, Atlantic Canada; *in* Sedimentary Basin and Basin-forming Mechanisms, (ed.) C. Beaumont and A.J. Tankard; Canadian Society of Petroleum Geology, Memoir 12, p. 287–297.

McCutcheon, S.R., Anderson, H.E., and Robinson, P.T., 1997. Stratigraphy and eruptive history of the Late Devonian Mount Pleasant Caldera complex, Canadian Appalachians; Geological Magazine, v. 134, p. 17–36.

McCutcheon, S.R., Sinclair, W.D., and Kooiman, G.J.A., 2001. The Late Devonian Mount Pleasant Caldera: Geological setting of a W-Mo-Sn-In deposit in southwestern New Brunswick; *in* Guidebook to Field Trips in New Brunswick and Western Maine, (ed.) R.K. Pickerill and D.R. Lentz; 93rd Annual Meeting New England Intercollegiate Geological Conference, University of New Brunswick, p. B5–B14.

McDonough, W.F. and Sun, S.S., 1995. The composition of the Earth; Chemical geology, v. 120, p. 223-–-253.

McLaughlin, K.J., Barr, S.M., Hill, M.D., Thompson, M.D., Ramezani, J., and Reynolds, P.H., 2003. The Moosehorn Plutonic Suite, southeastern Maine and southwestern New Brunswick: age, petrochemistry and tectonic setting; Atlantic Geology, v. 39, p. 123–146.

McLeod, M.J., 1990. Geology, geochemistry and related mineral deposits of the Saint George Batholith, Charlotte, Queens and Kings Counties, New Brunswick; New Brunswick. Minerals and Energy Division, Department of Natural Resources and Energy, 179 p.

McLeod, M.J. and Fyffe, L.R., 2002. Geology and gold occurrences, Clarence Stream area, southwestern New Brunswick; New Brunswick Department of Natural Resources and Energy, Minerals, Policy and Planning Division, Plate A 38.

McLeod, M.J., Taylor, R.P., and Lux, D.R., 1988. Geology, Ar/Ar geochronology and Sn-W-Mo-bearing sheeted veins of the Mount Douglas Granite, southwestern New Brunswick; Canadian Institute of Mining and Metallurgical Bulletin, v. 81, p. 70–77.

McLeod, M.J., Johnson, S.C., and Ruitenberg, A.A., 1994. Geological map of southwestern New Brunswick; New Brunswick Department of Natural Resources and Energy, Map NR-5.

Miller, C.F., McDowell, S.M., and Mapes, R.W., 2003. Hot and cold granites? Implications of zircon saturation temperatures and preservation of inheritance; Geology, v. 31, p. 529–532.

Montel, J.M., 1993. A model for monazite/melt equilibrium and application to the generation of granitic magmas; Chemical Geology, v. 110, p. 127–146.

Mohammadi, N., Fyffe, L.R., McFarlane, C.R.M., Thorne, K.G., Lentz, D.R., Charnley, B., and Butler, S., 2017. Geological relationships and laser ablation ICP-MS U-Pb geochronology of the Saint George Batholith, southwestern New Brunswick, Canada: implications for its tectonomagmatic evolution; Atlantic Geology, v. 53, p. 207–240.

Moyen, J.F., 2009. High Sr/Y and La/Yb ratios: the meaning of the "adakitic signature"; Lithos, v. 112, p. 556–574.

Neiva, A.M.R., 1984. Geochemistry of tin-bearing granitic rocks; Chemical Geology, v. 43, p. 241–256.

New Brunswick Department of Energy and Resource Development, 2018. New Brunswick Bedrock Lexicon; New Brunswick Department of Energy and Resource Development, <http://dnr-mrn.gnb.ca/Lexicon/Lexicon/Lexicon_Search.aspx?lang=e> [accessed November 11, 2018].

New Brunswick Department of Natural Resources, 2008. Bedrock geology of New Brunswick; Minerals, Policy and Planning Division, Map NR-1 (2008 Edition). Scale 1:500 000.

Ng, S.W.P., Chung, S.L., Robb, L.J., Searle, M.P., Ghani, A.A., Whitehouse, M.J., Oliver, G.J., Sone, M., Gardiner, N.J., and Roselee, M.H., 2015. Petrogenesis of Malaysian granitoids in the Southeast Asian tin belt: Part 1. Geochemical and Sr-Nd isotopic characteristics; Geological Society of America Bulletin, v. 127, p.1209–1237.

Olade, M.A., 1980. Geochemical characteristics of tin-bearing and tin-barren granites, northern Nigeria; Economic Geology, v. 75, p. 71–82.

Parsa, M., Maghsoudi, A., Yousefi, M., and Sadeghi, M., 2016. Recognition of significant multi-element geochemical signatures of porphyry Cu deposits in Noghdouz area, NW Iran; Journal of Geochemical Exploration, v. 165, p. 111–124.

Pearce, J., 1996. Sources and settings of granitic rocks; Episodes, v. 19, p. 120–125.

Pearce, J.A., Harris, N.B., and Tindle, A.G., 1984. Trace element discrimination diagrams for the tectonic interpretation of granitic rocks; Journal of Petrology, v. 25, p. 956–983.

Peccerillo, A. and Taylor, S.R., 1976. Geochemistry of Eocene calc-alkaline volcanic rocks from the Kastamonu area, northern Turkey; Contributions to mineralogy and petrology, v. 58, p. 63–81.

Pilote, J.L., Barr, S.M., Wilson, R.A., McClenaghan, S., Kamo, S., McNicoll, V.J., and Bevier, M.L., 2012. Precise age and petrology of Silurian-Devonian plutons in the Benjamin River-Charlo area, northern New Brunswick; Atlantic Geology, v. 48, p. 97–123.

Rittmann, A., 1973. Stable mineral assemblages of igneous rocks; Verlag Berlin, Springer, 262 p.

Roddick, J.C. and Bevier, M.L., 1995. U- Pb dating of granites with inherited zircon: Conventional and ion microprobe results from two Paleozoic plutons, Canadian Appalachians; Chemical Geology, v. 119, p. 307–329.

Rollinson, H., 1993. Using geochemical data; London, Longman, 352 p.

Rudnick, R.L. and Gao, S., 2003. Composition of the continental crust; Treatise on Geochemistry, v. 3, p. 1–64.

Rudnick, R.L., McDonough, W.F., and Chappell, B.W., 1993. Carbonatite metasomatism in the northern Tanzanian mantle: petrographic and geochemical characteristics; Earth and Planetary Science Letters, v. 114, p. 463–475.

Ruitenberg, A.A., 1967. Stratigraphy, structure and metallization Piskahegan-Rolling Dam area (northern Appalachians, New Brunswick, Canada); Ph.D. thesis, Leidse Geologische Mededelingen, v. 40, p. 79–120.

Schofield, D.I. and D'Lemos, R.S., 2000. Granite petrogenesis in the Gander Zone, NE Newfoundland: mixing of melts from multiple sources and the role of lithospheric delamination; Canadian Journal of Earth Sciences, v. 37, p. 535–547.

Shand, S. J., 1943, Eruptive rocks: their genesis, composition, classification, and their relation to ore deposits Wiley, New York, 444 p.

Shinkle, D.A., 2011. The Long Lake Uranium Prospect: Intragranitic Vein-type Uranium Mineralization in North-central New Brunswick, Canada; M.Sc. thesis, University of New Brunswick, Fredericton, New Brunswick, 297 p.

Sinclair, W.D. and Kooiman, G.J.A., 1990. The Mount Pleasant tungsten-molybdenum and tin deposits; *in* Mineral deposits of New Brunswick and Nova Scotia, (ed.) D.R. Boyle; Geological Survey of Canada, Open File 2157, p. 78–87.

Sinclair, W.D., Kooiman, G.J.A., and Martin, D.A., 1988. Geological setting of granites and related tin deposits in the North Zone, Mount Pleasant, New Brunswick (part B); Geological Survey of Canada, Current Research 88–1B, 7 p.

Sinclair, W.D., Kooiman, G.J.A., Martin, D.A., and Kjarsgaard, I.M., 2006. Geology, geochemistry and mineralogy of indium resources at Mount Pleasant, New Brunswick, Canada; Ore Geology Reviews, v. 28, p. 123–145.

Smith, E. and Fyffe, L.R., 2006. Bedrock Geology of the Hayesville area (NTS 21 J/10), Carleton, York and Northumberland Counties, New Brunswick; New Brunswick Department of Energy and Mines, Map Plate MP 2006–11. Scale 1:50 000.

Stepanov, A., Mavrogenes, J.A., Meffre, S., and Davidson, P., 2014. The key role of mica during igneous concentration of tantalum; Contributions to Mineralogy and Petrology, v. 167, p. 1–8.

Sun, S.S. and McDonough, W., 1989. Chemical and isotopic systematics of oceanic basalts: implications for mantle composition and processes; *in* Magmatism in the Ocean Basins, (ed.) A.D. Saunders and M.J. Norry; Geological Society of London, Special Publication No. 42, p. 313–345.

Tartèse, R. and Boulvais, P., 2010. Differentiation of peraluminous leucogranites "en route" to the surface; Lithos, v. 114, p. 353–368.

Tauson, L.V. and Kozlov, V.D., 1973. Distribution functions and ratios of trace-element concentrations as estimators of the ore-bearing potential of granites; *in* Geochemical Exploration 1972; London, Institute of Mining and Metallurgy, p. 37–44.

Taylor, H.P., 1978. Oxygen and hydrogen isotope studies of plutonic granitic rocks; Earth and Planetary Science Letters, v. 38, p. 177–210.

Taylor, R.P., 1992. Petrological and geochemical characteristics of the Pleasant Ridge zinnwaldite-topaz granite, southern New Brunswick and comparisons with other topaz-bearing felsic rocks; The Canadian Mineralogist, v. 30, p. 895–921.

Taylor, S.R. and McLennan, S.M., 1995. The geochemical evolution of the continental crust; Reviews of Geophysics, v. 33, p. 241–265.

Taylor, R.P., Sinclair, W.D., and Lutes, G., 1985. Geochemical and isotopic characterization of granites related to W-Sn-Mo mineralization in the Mount Pleasant area, New Brunswick. Granite-related mineral deposits; *in* Extended Abstracts; Canadian Institute of Mining and Metallurgy Conference, Halifax, Canada, p. 265–273.

Taylor, R.P., Lux, D.R., MacLellan, H.E., and Hubacher, F., 1987. Age and genesis of granite related W-Sn-Mo mineral deposits, Burnthill, New Brunswick, Canada; Economic Geology, v. 82, p. 2187–2198.

Thorne, K.G., Lentz, D.R., Hall, D.C., and Yang, X., 2002. Petrology, geochemistry and geochronology of the granitic pegmatite and aplite dikes associated with the Clarence Stream gold deposit, southwestern New Brunswick; Geological Survey of Canada, Current Research 2002-E12, 13 p.

Thorne, K.G., Fyffe, L.R., and Creaser, R.A., 2013. Re-Os geochronological constraints on the W-Mo mineralizing event in the Mount Pleasant Caldera Complex: implications for the timing of subvolcanic magmatism and caldera de-

velopment; Atlantic Geology, v. 49, p. 131–150.

van Staal, C.R., Whalen, J.B., Valverde-Vaquero, P., Zagorevski, A., and Rogers, N., 2009. Pre-Carboniferous, episodic accretion-related, orogenesis along the Laurentian margin of the northern Appalachians; *in* Ancient Orogens and Modern Analogues, (ed.) J.B. Murphy, J.D. Keppie and A.J. Hynes; Geological Society of London, Special Publication No. 327, p. 271–316.

Vigneresse, J.L., 2007. The role of discontinuous magma inputs in felsic magma and ore generation; Ore Geology Reviews, v. 30, p. 181–216.

Villaseca, C., Barbero, L., and Herreros, V., 1998. A re-examination of the typology of peraluminous granite types in intracontinental orogenic belts; Earth and Environmental Science, v. 89, p. 113–119.

Walker, J., Gower, S., and McCutcheon, S.R., 1991. Antinouri-Nicholas Project, Gloucester and Restigouche Counties, Northern New Brunswick; *in* Sixteenth Annual Review of Activities, (ed.) S.A. Abbon; New Brunswick, Mineral and Energy Division, Department of Natural Resources and Energy, p. 87–100.

Watson, E.B. and Harrison, T.M., 1983. Zircon saturation revisited: temperature and composition effects in a variety of crustal magma types; Earth and Planetary Science Letters, v. 64, p 295–304.

Wedepohl, K.H., 1995. The composition of the continental crust; Geochimica et Cosmochimica Acta, v. 59, p. 1217–1232.

Whalen, J.B., 1993. Geology, petrography and geochemistry of Appalachian granites in New Brunswick and Gaspésie, Quebec; Geological Survey of Canada Bulletin, v. 436, 124 p.

Whalen, J.B. and Theriault, R., 1990. K-Ar and Rb-Sr geochronology of granitoid rocks of Miramichi terrane, New Brunswick; *in* Radiogenic Age and Isotopic Studies: Report 3; Geological Survey of Canada, Paper 89–2, p. 100–107.

Whalen, J.B., Currie, K.L., and Chappell, B.W., 1987. A-type granites: geochemical characteristics, discrimination and petrogenesis; Contributions to Mineralogy and Petrology, v. 95, p. 407– 419.

Whalen, J.B., Jenner, G.A., Currie, K.L., Barr, S.M., Longstaffe, F.J., and Hegner, E., 1994a. Geochemical and isotopic characteristics of granitoids of the Avalon Zone, southern New Brunswick: possible evidence for repeated delamination events; The Journal of Geology, v. 102, p. 269–282.

Whalen, J.B., Jenner, G.A., Hegner, E., Gariépy, C., and Longstaffe, F.J., 1994b. Geochemical and isotopic (Nd, O and Pb) constraints on granite sources in the Humber and Dunnage zones, Gaspésie, Quebec and New Brunswick: implications for tectonics and crustal structure; Canadian Journal of Earth Sciences, v. 31, p. 323–340.

Whalen, J.B., Fyffe, L.R., Longstaffe, F.J., and Jenner, G.A., 1996a. The position and nature of the Gander-Avalon boundary, southern New Brunswick, based on geochemical and isotopic data from granitoid rocks; Canadian Journal of Earth Sciences, v. 33, p. 129–139.

Whalen, J.B., Jenner, G.A., Longstaffe, F.J., and Hegner, E., 1996b. Nature and evolution of the eastern margin of Iapetus: geochemical and isotopic constraints from Siluro-Devonian granitoid plutons in the New Brunswick Appalachians; Canadian Journal of Earth Sciences, v. 33, p. 140–155.

Whalen, J.B., Rogers, N., van Staal, C.R., Longstaffe, F.J., Jenner, G.A., and Winchester, J.A., 1998. Geochemical and isotopic (Nd, O) data from Ordovician felsic plutonic and volcanic rocks of the Miramichi Highlands: petrogenetic and metallogenic implications for the Bathurst Mining Camp; Canadian Journal of Earth Sciences, v. 35, p. 237–252.

White, T., 2013. The Early Devonian, Evandale Porphyry Cu-Mo-(Au) deposit, Southern New Brunswick: Petrologic, Geochemical, Geothermobarometric and Geochronologic Characterization of the Host Rocks and its Origin; B.Sc. thesis, University of New Brunswick Fredericton, New Brunswick, 72 p.

Wilson, B.M., 2007. Igneous petrogenesis a global tectonic approach; Netherland, Springer, 465 p.

Wilson, R.A., 2013a. Geology of the Bathurst area (NTS 21 P/12), Gloucester and Restigouche counties, New Brunswick; New Brunswick Department of Energy and Mines, Map Plate MP 2013–17. Scale 1:50 000.

Wilson, R.A., 2013b. Geology of the Point-Verte area (NTS 21 P/13), Gloucester and Restigouche counties, New Brunswick; New Brunswick Department of Energy and Mines, Map Plate MP 2013–18. Scale1:50 000.

Wilson, R. A. and Kamo, S. L., 2016. Geochronology and lithogeochemistry of granitoid rocks from the central part of the Central plutonic belt, New Brunswick: implications for Sn-W-Mo exploration; Atlantic Geology, v. 52, p. 125–167.

Yang, X.M., 2005. Petrogenesis of gold-related granitoid intrusions in southwestern New Brunswick, Canada; Ph.D. thesis, University of New Brunswick Fredericton, New Brunswick, 428 p.

Yang, X.M., 2007. Using the Rittmann Serial Index to define the alkalinity of igneous rocks; Neues Jahrbuch für Mineralogie-Abhandlungen, v. 184, p. 95–103.

Yang, X.M., and Lentz, D.R., 2005. Chemical composition of rock-forming minerals in gold-related granitoid intrusions, southwestern New Brunswick, Canada: implications for crystallization conditions, volatile exsolution and fluorine-chlorine activity; Contributions to Mineralogy and Petrology, v. 150, p. 287–305.

Yang, X.M., Lentz, D.R., and Chi, G., 2002a. Petrochemistry of Lake George granodiorite stock and related Au mineralization, York County, New Brunswick; Geological Survey of Canada, Current Research 2002-D7, 12 p.

Yang, X.M., Lentz, D.R., Hall, D.C., and Chi, G. 2002b. Petrology of the Lake George granodiorite stock, New Brunswick: implications for crystallization conditions, volatile exsolution and W-Mo-Au-Sb mineralization; Geological

Survey of Canada, Current Research 2002-E14, 12 p.

Yang, X.M., Lentz, D.R., and McCutcheon, S.R., 2003. Petrochemical evolution of subvolcanic granitoid intrusions within the Late Devonian Mount Pleasant Caldera, southwestern New Brunswick, Canada: comparison of Au versus Sn-W-Mo-polymetallic mineralization systems; Atlantic Geology, v. 39, p. 97–121.

Yang, X.M., Lentz, D.R., Chi, G., and Kyser, T.K., 2004. Fluid -mineral reaction in the Lake George Granodiorite, New Brunswick, Canada: implications for Au-W-Mo-Sb mineralization; The Canadian Mineralogist, v. 42, p. 1443–1464.

Yang, X.M., Lentz, D.R., Chi, G., and Thorne, K.G., 2008. Geochemical characteristics of gold-related granitoids in southwestern New Brunswick, Canada; Lithos, v. 104, p. 355–377.

Zaraisky, G.P., Aksyuk, A.M., Devyatova, V.N., Udoratina, O.V., and Chevychelov, V.Y., 2009. The Zr/Hf ratio as a fractionation indicator of rare-metal granites; Petrology, v. 17, p. 25.

Zhang, W., 2015. Petrological and Metallogenic Studies of the Nashwaak Granite and felsic dykes associated with the Sisson Book W-Mo-(Cu) deposit, west-central New Brunswick, Canada; Ph.D. thesis, University of New Brunswick, Fredericton, New Brunswick, 281 p.

Zhang, W., Lentz, D.R., Thorne, K.G., and McFarlane, C.R.M., 2016. Geochemical characteristics of biotite from felsic intrusive rocks around the Sisson Brook W–Mo–Cu deposit, west-central New Brunswick: An indicator of halogen and oxygen fugacity of magmatic systems; Ore Geology Reviews, v. 7, p. 82–96.

Appendix A: General descriptions of New Brunswick granitoids within this study

Group NB-1 granites

NB-1-1 North Pole Stream Granite (NPG): The Early Devonian NPG (U-Pb zircon age of 417 ± 1 Ma; Bevier and Whalen, 1990b) is a large multiphase intrusive body in northeastern New Brunswick. The main phase is a medium- to coarse-grained, equigranular to K-feldspar porphyritic biotite granite, which is cut by bodies of fine- to medium-grained white muscovite-biotite granite and quartz-feldspar porphyry (Whalen, 1993; Whalen et al., 1996a, b). The overlap between mineral ages, including a muscovite K-Ar age of 414 ± 5 Ma and a U-Pb monazite age of 417 ± 1 Ma, suggests a high-level of emplacement for this intrusive complex (Fyffe, 1982; Whalen and Theriault, 1990; Bevier and Whalen, 1990b; Whalen, 1993). A small area of alteration in the NPG contains minor disseminated to vein-type iron-lead-zinc sulphide mineralization.

NB-1-1 Nicholas Dénys Granodiorite (NDGD): The NDGD is a Late Devonian medium-grained, equigranular, biotite granodiorite (U-Pb zircon age of 381 ± 4 Ma; Walker et al., 1991; Whalen et al., 1994b) in northeastern New Brunswick immediately north of the Bathurst Mining Camp. The NDGD intrudes Silurian sedimentary rocks of the La Vieille and Petit Rocher groups (Wilson, 2013a). The NDGD has several associated exogranitic mineral occurrences: quartz veins, stockworks and disseminated and polymetallic base metal (mostly arsenic, zinc, lead, copper, iron, ±gold) and skarn copper-iron occurrences within its contact aureole with the highly fractured Silurian Chaleurs Group as well as several endogranitic molybdenum-copper occurrences.

NB-1-1 Magaguadavic Granite (MGS): This Early Devonian multiphase granite (U-Pb zircon age of 396 ± 1 Ma by Bevier and Barr, 1990; 403 ± 2 Ma by Davis et al., 2004; Mohammadi et al., 2017) is a large body that forms the western to central portion of the Saint George Batholith (SGB) in southwestern New Brunswick (McLeod, 1990). The MGS intrudes metasedimentary and metavolcanic rocks of the Silurian Mascarene Group and the Ordovician Cookson Group (Ruitenberg, 1967; Fyffe et al., 1999; Thorne et al., 2002). This intrusion varies from medium- to coarse-grained, porphyritic to megacrystic monzogranite to seriate, non-porphyritic monzogranite (McLeod, 1990). Pegmatitic to aplitic felsic dykes are associated with disseminated gold mineralization (Thorne et al., 2002). The MGS is also related to molybdenum-copper-bearing hornfels mineralization of Spring Brook and Clarence Brook.

NB-1-2 Hawkshaw Granite (HG): This Early Devonian granitic body (U-Pb titanite age of 411 ± 1 Ma; Bevier and Whalen, 1990a, b; Whalen et al., 1996b) in the eastern half of the Pokiok Batholith in southwestern New Brunswick. It consists of a mainly coarse-grained porphyritic biotite granite to granodiorite with minor equigranular biotite granite (Whalen, 1993). On its northwestern side, the HG intrudes Cambrian-Ordovician sedimentary rocks of the Woodstock Group (Fyffe, 2001). This intrusion is associated with minor greisen and stockwork vein Sn-Cu-Au-W-bearing quartz-carbonate veins and veins of purple fluorite.

NB-1-2 Long Lake Granite (LL): The LL is a high level, highly fractionated phase of the Devonian NPG. The LL is a uranium bearing, strongly peraluminous, slightly perphosphoric, muscovite leucogranite dyke, which crosscuts the NPG in the Long Lake area (Shinkle, 2011). An 11 Ma difference from the emplacement of the NPG ($^{40}Ar/^{39}Ar$ muscovite age of 406.1 ± 1.9 Ma; Shinkle, 2011) indicates that the LL formed during the later stages of the Acadian Orogeny. This dyke is associated with disseminated uranium-molybdenum mineralization and uranium-manganese mineralization.

NB-1-3 Lake George Granodiorite (LG): This small Devonian (U-Pb zircon age of 412 +5/-4 Ma; Yang et al., 2004) granodiorite stock is related to the HG through fractional crystallization (Yang et al., 2002a; b). It intrudes the Silurian metasedimentary rocks of the Kingsclear Group in which forms biotite- to cordierite porphyroblasts (Yang et al., 2002a, b). The LG is associated with early W-Mo-Au and later gold-antimony mineralization and at one time was the largest antimony producer in North America Yang et al., 2004).

Group NB-2 granites

NB-2-1 Tower Hill Granite (THG): The THG is an elliptical Early Devonian (Rb-Sr muscovite age of 401 ± 4 Ma; Whalen et al., 1996a) is a medium- to coarse-grained, fluorite- and topaz-bearing, equigranular, muscovite-biotite granite. The margin of the intrusion consists of a medium-grained, equigranular, muscovite granite. The THG intrudes the Foster Lake gabbro and Ordovician Kendall Mountain Formation of the Cookson Group in which is formed a contact metamorphic assemblage of biotite andalusite, staurolite, garnet, muscovite and quartz up to 500 m from the granite (Butt, 1976; Fyffe, 1992). The quartz veins related to this intrusion are associated with gold anomalies and base-metal mineralization, whereas pegmatitic dykes are associated with molybdenum mineralization.

NB-2-1 Allandale Granite (AG): This granite is the youngest (U–Pb monazite age of 402 ± 1 Ma; Bevier and Whalen, 1990b; Whalen et al., 1996b) and most evolved phase of the Pokiok Batholith. It intrudes the HG and dominantly consists of fine- to medium-grained equigranular muscovite-biotite granite. This intrusion has associated pegmatite-aplite dykes and vein-type Be-Mo-Nb-W mineralization at Zealand Station as well as gold mineralization (Beal et al., 2010).

NB-2-2 Mount Douglas Granite (MDG): This heterogeneous granitic body forms the eastern portion of the SGB in southwestern New Brunswick (Whalen et al., 1996b). McLeod (1990) divided this intrusion into three sequentially emplaced phases (Dmd_1 to Dmd_3), each of which was divided into several subunits based on texture and mineralogy. This intrusion contains mafic xenoliths similar of those in the UG (the oldest phase of the SGB; McLeod, 1990). An agreement between U-Pb zircon age (367 ± 1 Ma; Bevier, 1988) and ca. 367 Ma ^{40}Ar-^{39}Ar biotite ages reported by McLeod et al. (1988) identified this intrusion as the youngest phase of the SGB. The presence of aplite- pegmatitic dykes and pegmatite filled and miarolitic cavities in all the subunits (especially in $Dmd2_c$) indicates a shallow level of emplacement (Mohammadi et al., 2017). This leucogranite is related to significant endogranite Sn-W-Mo-As-Bi-Cu-Pb-Zn-bearing veins and related alteration in more than thirty localities.

NB-2-2 Mount Elizabeth Granite (MEG): The Early Devonian (U-Pb monazite age of 417.30 ± 0.96 Ma; Azadbakht et al., 2016) MEG in northeast New Brunswick, is a homogeneous equigranular, fine- to coarse-grained biotite granite. It intrudes sedimentary rocks of the Cambrian-Ordovician Miramichi Group as well as volcanic and sedimentary rocks of the Middle Ordovician California Lake Group and forms greisen alteration at the contact with the Ordovician - Meridian Brook Granite (Whalen et al., 1996b). The intrusion is associated with minor molybdenum mineralization at Mount Mitchell.

NB-2-2 Beech Hill Granite (BHG): BHG is a circular porphyritic biotite granite (Butt, 1976) that intrudes the contact between early Silurian siltstone and wacke of the Digdeguash Formation to the north and Late Ordovician sedimentary rocks of the Cookson Group (Kendall Mountain Formation) to the south (Fyffe, 1992). Quartz veins are common within the contact aureole of the intrusion but decrease rapidly with increasing distance from the intrusion (Yang et al., 2008). Mineralized fractures and veinlets in both the greisenized granite and the sedimentary rocks are associated with several tin, fluorine, zinc and molybdenum occurrences.

NB-2-3 Dungarvon Granite (DG): This composite Late Devonian (^{40}Ar-^{39}Ar muscovite age of 376 ± 4 Ma; MacLellan, 1990) pluton in central New Brunswick. It is composed mainly of medium- to coarse-grained equigranular to porphyritic biotite granite and an equigranular to porphyritic biotite microgranite with minor pegmatite, aplite and granophyric granite (MacLellan, 1990; Smith and Fyffe, 2006). The DG intrudes mafic volcanic and sedimentary rocks of the Miramichi and Tetagouche groups (MacLellan, 1990; Whalen et al., 1996b). This intrusion is related to several Sn-W-Mo-F vein occurrences. It is also associated with a vein uranium occurrence and disseminated copper mineralization.

NB-2-3 Burnthill Granite (BG): This Late Devonian (U-Pb zircon age of 380.6 ± 0.3 Ma; Wilson and Kamo, 2016) granite is the largest pluton of the Burnthill Brook area in central New Brunswick (MacLellan, 1990; Whalen et al., 1996b). It is a mineralogically heterogeneous biotite granite dominantly consisting of medium- to coarse-grained, equigranular to seriate and K-feldspar porphyritic biotite granite (MacLellan, 1990; Smith and Fyffe, 2006). This pluton intrudes Cambrian to Ordovician sedimentary rocks of the Miramichi Group and Trousers Lake Metamorphic Suite, Ordovician sedimentary and volcanic rocks of the Tetagouche Group, as well as the Early Ordovician McKiel Lake granite and the Early Devonian LLG (MacLellan, 1990). The BG is associated with several Mo-Sn-W-Be-F-bearing quartz veins and greisen occurrences, as well as Cu-Zn-F veins.

NB-2-3 Antinouri Lake Granite (ALG): This Late Devonian (U-Pb zircon age of 372 ± 4 Ma; Walker et al., 1991) circular stock is located in northeastern New Brunswick. It consists mainly of medium-grained, equigranular, biotite granite, which is cut by a quartz-feldspar porphyritic phase (Walker et al., 1991; Whalen et al., 1994b). The pluton intrudes Ordovician sedimentary rocks of the Elmtree Formation (Wilson, 2013b) and forms hornfels up to 2 km from the contact, except in the east where it extends to 4 km from the contact (Walker et al., 1991). The ALG is associated with several base metal skarn and quartz vein-type occurrences.

NB-2-4 Utopia Granite (UG): This Late Silurian (U-Pb monazite age of 425.5 ± 2.1 Ma; Mohammadi et al., 2017) medium- to coarse-grained, light to dark red syenogranite to monzogranite forms the southwestern part of the SGB (McLeod, 1990). The UG intrudes schistose bimodal volcanic and fossiliferous sedimentary rocks of the Eastport Formation with local development of biotite hornfels near the granite contact (McLeod, 1990). Mineralization associated with this intrusion includes disseminated molybdenum and copper, disseminated and vein

fluorine and silver, uranium and greisen molybdenum-tungsten.

NB-2-4 Mount LaTour Granite (MLT): The western portion of the South Nepisiguit River Plutonic Suite is composed of a number of phases. Whalen (1993) divided this portion into five phases: hybrid intrusive rocks, syenite, quartz monzonite, aplite and alkaline granite. The medium- to coarse-grained, equigranular alkaline granite contains only one feldspar (i.e. hypersolvus granite) is amphibole bearing and is the most abundant phase of the western suite. A sample of this granite gave a U-Pb monazite age of 417.7 ± 4.4 Ma (Azadbakht et al., 2016). The contact relationships among the various phases in the western part of the South Nepisiguit River Plutonic Suite are unknown, but they are presumed to be of similar age (Whalen, 1993). This intrusion is not known to have any associated mineralization.

NB-2-5 Sorrel Ridge Granite (SRG): This homogenous circular stock in southwestern New Brunswick is considered Late Devonian based on its association with the MDG (Sinclair et al., 1988; McLeod, 1990; Taylor, 1992). This fine-grained porphyritic granite intrudes the metasedimentary rocks of Ordovician Cookson Formation in which is developed a cordierite-biotite-quartz contact metamorphic assemblage up to 175 m from the intrusion (Whalen, 1993; Whalen et al., 1996a). The SRG is associated with disseminated and quartz vein copper, molybdenum, tin and tungsten mineralization in several localities.

NB-2-5 True Hill Granite (TRHG): This presumably Late Devonian (based on its genetic relationship to the MDG and its association with the Late Devonian rocks of the Mount Pleasant Caldera Complex (McLeod, 1990)) is a porphyritic to equigranular, fine-grained granite and subvolcanic that intrudes early Silurian sandstone and siltstone of the Sand Brook and Digdeguash formations (McLeod and Fyffe, 2002). Minimal hornfels is developed in the sedimentary country rocks, presumably due to the small size of the intrusions and its apparent shallow level of emplacement (Lentz et al., 1988). The porphyry-style greisen mineralization associated with this intrusion is similar to that at the Mount Pleasant W-Mo-Sn polymetallic deposit (Kooiman et al., 1986; Lentz, 1986, 1994; Lentz and McAllister, 1990; Lentz and Gregoire, 1995).

NB-2-6 Pabineau Falls Granite (PFG): This Early Devonian coarse-grained equigranular to sub-porphyritic biotite granite (U-Pb zircon age of 397.2 ± 1.9 Ma; Roddick and Bevier, 1995) is in the northeast part of the Bathurst mining camp (Whalen et al., 1996b). It intrudes sedimentary rocks of the Cambrian to Ordovician Miramichi Group in which cordierite andalusite and biotite porphyroblasts occur within 1 km of the pluton contact (Whalen, 1993). This intrusion hosts endogranitic disseminated and/or aplitic dykes associated molybdenum-beryllium mineralization and is associated with one gold-bearing quartz vein occurrence.

NB-2-6 Nashwaak Granite (NG): This large, Early Devonian pluton (U-Pb zircon age of 420.7 +1.8/-2.0 Ma; Wilson and Kamo, 2016) is dominantly medium-grained, equigranular to seriate, biotite granite but grades into muscovite-biotite granite in the north (Whalen, 1993). On its east side, the NG intrudes sedimentary rocks of the Cambro-Ordovician Woodstock Group, volcanic and sedimentary rocks of the Ordovician Meductic Group and the Howard Peak Granodiorite (Whalen, 1993; Whalen et al., 1996b). Andalusite and cordierite are developed in sedimentary rocks up to 2 km from the contact. To the north, the NG intrudes the Cambro-Ordovician Trousers Lake Metamorphic Suite, in which sillimanite is developed up to 1 km from the contact and the Ordovician McKiel Lake Granite.

Group NB-3 granites

Pleasant Ridge Granite (PRG): This Late Devonian low-P topaz granite ($^{40}Ar/^{39}Ar$ muscovite age of ca. 361 Ma; Taylor, 1992) that lies near the northwest margin of the SGB in southern New Brunswick, has yielded a broad range of δD (-66 to -106), has very low volatile contents and has pegmatitic pods that suggest magmatic degassing during emplacement (Yang et al., 2008). The PRG intrudes quartz arenite and shale of the Ordovician Kendall Mountain Formation (Fyffe, 1992) in which is developed a narrow contact aureole of biotite hornfels (Ruitenberg, 1967; Butt, 1976; Yang and Lentz, 2005). PRG is locally associated with disseminated ±Mo±Cu±Sn±Zn hydrothermal mineral occurrences.

Mount Pleasant Granite (MPG): The MPG consists of a highly altered and brecciated fine-grained equigranular granite (GR-I), aplitic to porphyritic granite (GR-II) and fine- to medium-grained equigranular granite (GR-III) (Kooiman et al., 1986; McCutcheon, 1990; McCutcheon et al., 1997, 2001; Yang et al., 2003; Sinclair et al., 2006). The MPG is comagmatic with the Late Devonian Mount Pleasant Caldera complex. Re-Os dating of molybdenite from the Fire Tower Zone yielded an age of 370 ± 2 Ma for the tungsten-molybdenum mineralizing event (GR-1): this age should also approximate the age of emplacement of the host to mineralization (Thorne et al., 2013). The breccia developed in the GR-I phase is associated with Sn-W-Mo-Zn mineralization, whereas the GR-II and GR-III phases host Sn-In-Zn deposits at the North Zone (Inverno and Hutchinson, 2004).

Kedron Stream Granite (KSG): This Late Devonian granite ($^{40}Ar/^{39}Ar$ muscovite age of 362 Ma; Taylor, 1992) is a cupola approximately 100 m in diameter (Taylor et al., 1985; Whalen et al., 1996a). The KSG, originally referred to as the Bonny River granite), is a lithian mica-topaz-bearing, fine- to medium-grained granite with an equigranular to seriate texture (Taylor, 1992) and similar to the PRG. This small cupola intrudes Early Silurian sandstone and siltstone of the Sand Brook Formation (Fyffe, 1992) along the northwestern margin of the SGB, to the west of the Mount Pleasant Caldera (Taylor, 1992; Whalen et al., 1996a). The KSG is associated with silica-rich, pegmatitic and greisen zones containing lead, copper, zinc, molybdenum, tin, tungsten and gold mineralization. These styles of alteration and metal assemblages of these occurrences are similar to those at the Mount Pleasant deposit.

Juniper Barren and Lost Lake granites

Lost Lake Granite (LLG): This Early Devonian heterogeneous granitic body (U-Pb zircon age of 409.7 ± 0.5 Ma; Wilson and Kamo, 2016) is in central New Brunswick. The southern part of the intrusion is composed primarily of medium-grained equigranular biotite-muscovite granite, with minor muscovite granite and pegmatite (Whalen, 1993; Whalen et al., 1996b). The northern part of the pluton is composed of a massive to weakly foliated, fine- to medium-grained equigranular biotite granite. The LLG intrudes the Middle Ordovician McKiel Lake Granite and Cambro-Ordovician metasedimentary rocks of the Trousers Lake Metamorphic Suite. The pegmatitic pods of LLG contain minor beryllium mineralization.

Juniper Barren Granite (JBG): This elongate Early Devonian (U-Pb zircon age of 415.8 ± 0.3 Ma, Wilson and Kamo, 2016) pluton is in central New Brunswick. It consists of medium- to coarse-grained, equigranular to sub-porphyritic biotite granite, with minor muscovite-bearing granite, aplite and pegmatite (Whalen, 1993; Whalen et al., 1996a, b). The JBG intrudes the Trousers Lake Metamorphic Suite to the east and the Ordovician Little Clearwater Brook Granite to the south. Quartz veins of JBG are associated with traces of molybdenite mineralization at Juniper Station.

The relationship between the Ganderian Aspy and Bras d'Or terranes explored using Devonian plutonic rocks, Cape Breton, Nova Scotia

C. Grant[1, 2], D.B. Archibald[1], D.A. Kellett[3] and J.M. Cottle[4]

[1]*Department of Earth Sciences, St. Francis Xavier University, 5009 Chapel Square, Antigonish, Nova Scotia B2G 2W5*

[2]*Department of Earth and Environmental Science, Acadia University, Wolfville, Nova Scotia B4P 2R6*

[3]*Geological Survey of Canada, 1 Challenger Drive, Dartmouth, Nova Scotia B2Y 4A2*

[4]*Department of Earth Science, University of California Santa Barbara, Santa Barbara, California 93106-9630*

Abstract

On Cape Breton Island, Nova Scotia, the Eastern Highlands Shear Zone bisects the Ganderia composite terrane, separating the Aspy and Bras D'Or terranes. The shear zone displays east-over-west, sinistral kinematics, and is intruded and stitched by plutonic rocks of the Devonian Black Brook Granite Suite. This study is utilizing whole rock geochemistry, U-Pb zircon geochronology and Hf isotopic analysis to constrain the petrogenesis of the Black Brook Granite Suite and other spatially associated granitoid plutons in northern Cape Breton. The granitoid-dominated plutonic suite is peraluminous, muscovite- and biotite-bearing, and interpreted to have formed from crustal anatexis. Published U-Pb monazite ages have constrained emplacement of the granite suite to ca. 375 Ma. Our new zircon geochronological data yielded weighted-mean U-Pb ages between ca. 396 and 399 Ma, but individual zircon grains recorded younger ages in all samples. Our interpretation is that many of the analyzed zircon grains are inherited from host rocks and/or protolith, or that the pressure-temperature conditions of the magma were only hot enough to grow long, slender zircon crystals not analyzed in this study. Thus, we interpret the timing of granitoid emplacement to be ca. 375 Ma. These results situate post-collisional plutonic rocks in northern Cape Breton Island in the temporal history of the Appalachian Orogen and can be used to constrain timing of deformation on the Eastern Highlands Shear Zone.

Introduction

Cape Breton Island, Nova Scotia, comprises four major Neoproterozoic to Devonian geological terranes (Hibbard et al., 2006) including, from west to east, the peri-Laurentian Blair River inlier, the Ganderian Aspy and Bras d'Or terranes, and the Avalonian Mira terrane (Fig. 1). These terranes represent distinctive tectonic components in the middle-Paleozoic accretionary orogen that comprises the northern Appalachian mountain belt (Hibbard et al., 2006). Appalachian orogenesis began in the Ordovician and concluded with the assembly of the supercontinent Pangea in the Carboniferous to Permian (e.g. Murphy et al., 2010; van Staal et al., 1998; van Staal et al., 2009; Williams, 1979). This project focuses on the internal relationship between the Aspy and Bras d'Or terranes of the Ganderia composite terrane (Fig. 1b). Ganderia accreted to the Laurentian margin in the late Silurian during the Salinic Orogeny (ca. 450–423 Ma; van Staal et al., 2009; Kellett et al., 2017). The Eastern Highlands Shear Zone (EHSZ) bisects the Ganderia composite terrane with the Bras d'Or and Aspy terranes on either side (Fig. 1b). The shear zone is characterized by an approximately 1 km wide mylonite zone (Barr and Raeside, 1989; Piette-Lauzière et al., 2018) that hosts ca. 375 Ma (Dunning et al., 1990) plutonic rocks that are interpreted as 'stitching granites' (Barr and Raeside, 1989).The EHSZ was interpreted to have east-over-west, reverse, and sinistral shear kinematics (Lin, 1995). Recent work (Piette-Lauzière et al., 2018; Piette-Lauzière et al., 2019) has distinguished two separate tectonic events affecting the EHSZ. D_1 had sinistral kinematics concurrent with the Acadian Orogeny (ca. 420-400 Ma; van Staal et al., 2009) and D_2 was a dextral transpression-dominated environment during the Neoacadian Orogeny (ca. 395–350 Ma; van Staal et al., 2009).

We studied the Black Brook Granite Suite (BBGS) because it is a Devonian granitoid that straddles the boundary between the Bras d'Or and Aspy terranes and was emplaced while the shear zone may have been active (Fig. 1b). Devonian granitoids in the Canadian Appalachians are regionally associated with intrusion-related mineralization, and crustal scale shear zones may provide the plumbing system for both the magmas and mineralizing fluids. We re-examined the petrogenesis and crystallization ages of the BBGS using in situ zircon U-Pb dating, new geochemical data, and zircon Hf isotopic data to es-

Corresponding author: Donnelly Archibald (darchiba@stfx.ca)

Grant, C., Archibald, D.B, J.M. Kellett, D.A., and Cottle, J.M., 2019. The relationship between the Ganderian Aspy and Bras d'Or terranes explored using Devonian plutonic rocks, Cape Breton, Nova Scotia; *in* Targeted Geoscience Initiative: 2018 report of activities, (ed.) N. Rogers; Geological Survey of Canada, Open File 8549, p. 279–286. https://doi.org/10.4095/313659

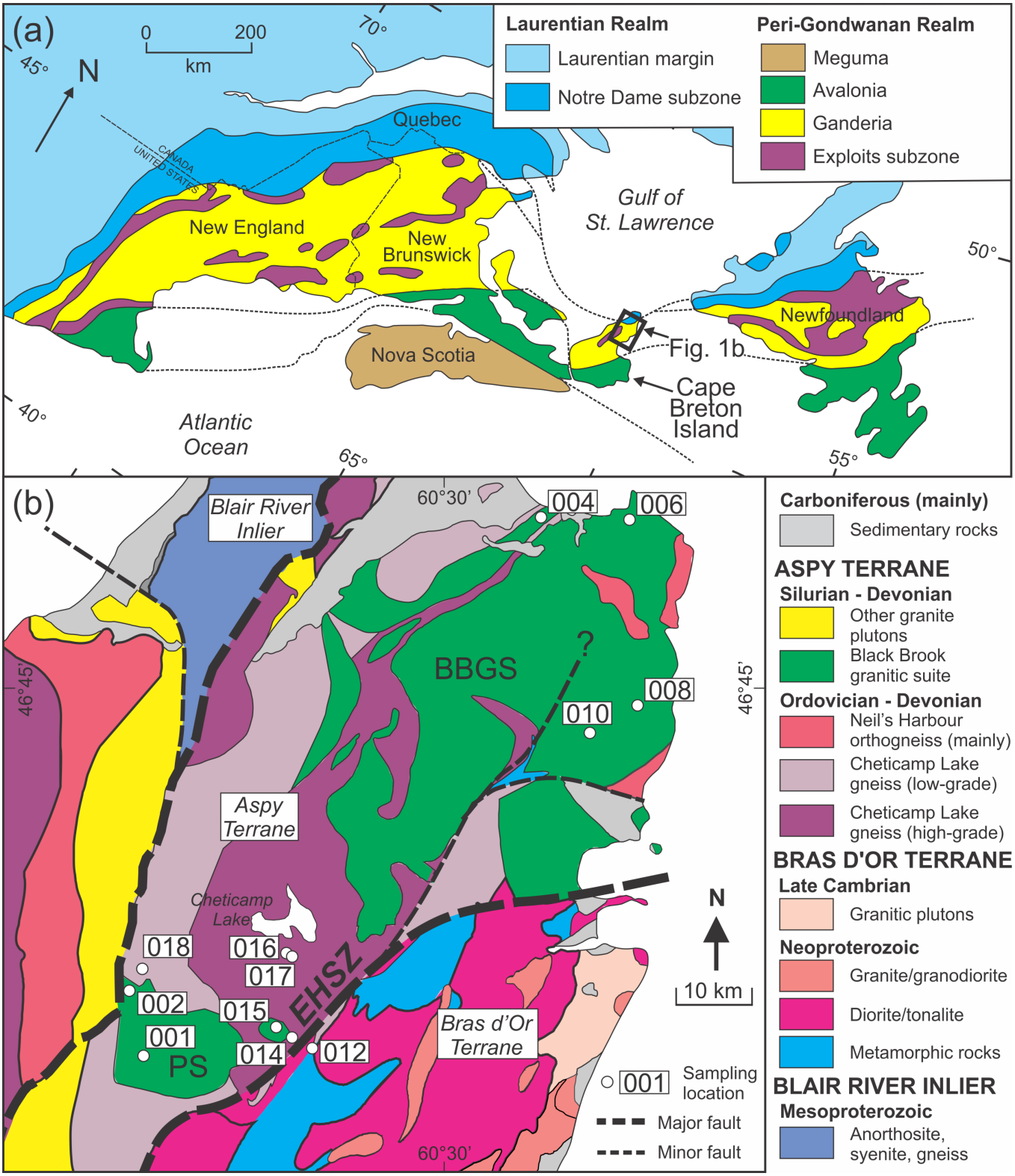

Figure 1. a) Regional terrane map of the late Neoproterozoic to mid-Palaeozoic northern Appalachian Orogen showing the study area on Cape Breton Island (Hibbard et al., 2006). b) Simplified geological map of northern Cape Breton Island showing the main geological units, the extent of the Black Brook Granitic Suite (BBGS) and Park Spur pluton (PS), sampling locations for this study, and the Eastern Highlands Shear Zone (EHSZ). 'CG17-' prefixes are omitted from sample labels for clarity. Map *modified from* Barr (2010), and Barr and White (2017).

tablish whether the BBGS formed as the result of a Devonian subduction event or due to late reactivation or emplacement during motion along the EHSZ (e.g. during or after the late Silurian to early Devonian accretion of Avalonia).

Geology of northern Cape Breton Island

Silurian-Devonian back-arc sedimentary and volcanic rocks and related plutonic rocks dominate the Aspy terrane (Dunning et al., 1990; Lin et al., 2007). These rocks experienced low-grade metamorphism during the late Silurian to early Devonian (ca. 420–400 Ma: Lin et al., 2007). The Cheticamp Lake Gneiss (Fig. 1b) is one of the largest metamorphic units in the Aspy terrane (Barr and White, 2017). Magmatic monazite crystals from the Cheticamp Lake Gneiss yielded a U-Pb age of 396 ± 2 Ma (Dunning et al., 1990). Neil's Harbour Gneiss (Fig. 1b) is a more restricted, metamorphic unit that crops out along the eastern coast (Barr and White, 2017) and is predominantly orthogneiss (Yaowanoiyothin and Barr, 1991). Metamorphic zircon from this unit yielded a U-Pb age of 403 ± 2 Ma (Dunning et al., 1990). The northeastern-most Aspy terrane is composed predominately of the Money Point Group, a metasedimentary-metavolcanic package (Barr and White, 2017). Keppie et al. (1991) dated rhyolite from the Money Point Group at 428 ± 2 Ma. Devonian plutonic rocks, which dominate the southeastern region of the terrane in the study area, are interpreted to have formed as a tectonic response to the accretion of outboard terranes (Mira and Bras d'Or) to the Aspy terrane (Lin, 1995).

The Bras d'Or terrane lies to the east of the Aspy terrane (Fig. 1b). It comprises mainly Neoproterozoic low-pressure gneissic units that are in faulted contact with metasedimentary and metavolcanic rocks (Raeside and Barr, 1990; Barr et al., 1998). Plutonic rocks are widespread in the Bras d'Or terrane, with zircon and monazite U-Pb crystallization ages ranging from late Ediacaran-early Cambrian (ca. 570–540 Ma) with younger plutonic activity in the Cambrian (ca. 520–490 Ma) and Silurian (ca. 440) (Barr et al., 2018; Barr et al., 1990; Dunning et al., 1990; Keppie et al., 1998). Amphibolite-facies metamorphism at ca. 564 Ma (Barr et al., 1990) differentiates Bras d'Or from the adjacent Mira terrane to the east (greenschist facies; Barr et al., 1998). The Bras d'Or terrane was juxtaposed against the Aspy terrane by ca. 450 to 423 Ma, during the Salinic Orogeny (Barr et al., 1998; van Staal et al., 2009).

Rocks of the BBGS are undeformed except near the EHSZ (Fig. 1b), where they exhibit a weak foliation (Piette-Lauzière et al., 2019). Previous work showed that the BBGS has the mineral assemblage plagioclase, quartz, perthitic microcline, biotite, and muscovite with accessory apatite, zircon, monazite, and ilmenite, while whole-rock geochemical data indicated that the plutonic rocks are S-type, biotite-muscovite granodiorite to alkali-feldspar granite (Yaowanoiyothin and Barr, 1991). Previous U-Pb dating of monazite from the BBGS yielded a date of 375 -4/+5 Ma (Dunning et al., 1990), interpreted to represent the age of emplacement of the BBGS.

Analytical methods

Sampling focused on collecting representative samples of the BBGS and the Park Spur pluton (Fig. 1b). Twelve samples were sent to Bureau Veritas Commodities Canada Ltd., Vancouver, for whole-rock geochemical data analyses. Major element data were collected by inductively coupled plasma optical emission spectrometry (ICP-OES) using a SPECTRO AS500 instrument and trace element data were collected by solution inductively coupled plasma mass spectrometry (ICP-MS) using a Perkin-Elmer ELAN 9000 system. Overburden Drilling Management (ODM) in Ottawa completed the mineral disaggregation and heavy mineral separation. Zircon grains were hand-picked from heavy mineral concentrates at St. Francis Xavier University, Nova Scotia, using a binocular microscope. Selected grains were mounted in epoxy resin and polished to expose the grain interiors.

Zircon U-Pb and trace element measurements were performed using a Nu Plasma high-resolution laser ablation multi-collector inductively coupled plasma mass spectrometer (LA-MC-ICP-MS) at the University of California, Santa Barbara. U-Pb data were collected during one analytical session. Data reduction, including corrections for baseline, instrumental drift, mass bias, down-hole fractionation, and primary-reference normalization, were carried out using Iolite v2.5 (Paton et al., 2011). Uncertainties for individual analyses are quoted at the 95% confidence or 2σ level and include contributions from the external reproducibility of the secondary reference material for the $^{207}Pb/^{206}Pb$ and $^{206}Pb/^{238}U$ ratios. Concordia diagrams and weighted-mean $^{206}Pb/^{238}U$ ages were calculated using IsoplotR (Vermeesch, 2018). The reader is referred to Grant (2018) for a complete description of the zircon U-Pb and trace element analytical procedures used in this study. Lu-Hf-Yb isotopes were measured in zircon following the methods outlined in Hagen-Peter et al. (2015) and Hagen-Peter and Cottle (2018) using the MC-ICP-MS at the University of California, Santa Barbara.

Results

Along the southern, western, and northern margins of the pluton, the BBGS intruded into the Ordovician-Silurian Cheticamp Lake Gneiss; on the eastern margin of the pluton, the BBGS intruded into the Neil's Harbour Gneiss (Fig. 1b, 2). The Park Spur pluton crosscuts the Cheticamp Lake Gneiss and Money Point Group (Yaowanoiyothin and Barr, 1991; Barr and White, 2017). Some samples collected proximal to the EHSZ demonstrate a weak foliation defined by the realignment of the mica minerals; however, most plutonic rocks show a hypidiomorphic granular texture.

Four samples, one sample from the Park Spur pluton and three samples from the BBGS, were selected for U-Pb zircon geochronology (Fig. 1). The Park Spur pluton sample (CG17-001) yielded a weighted mean $^{206}Pb/^{238}U$ date of 388 ± 5 Ma (n

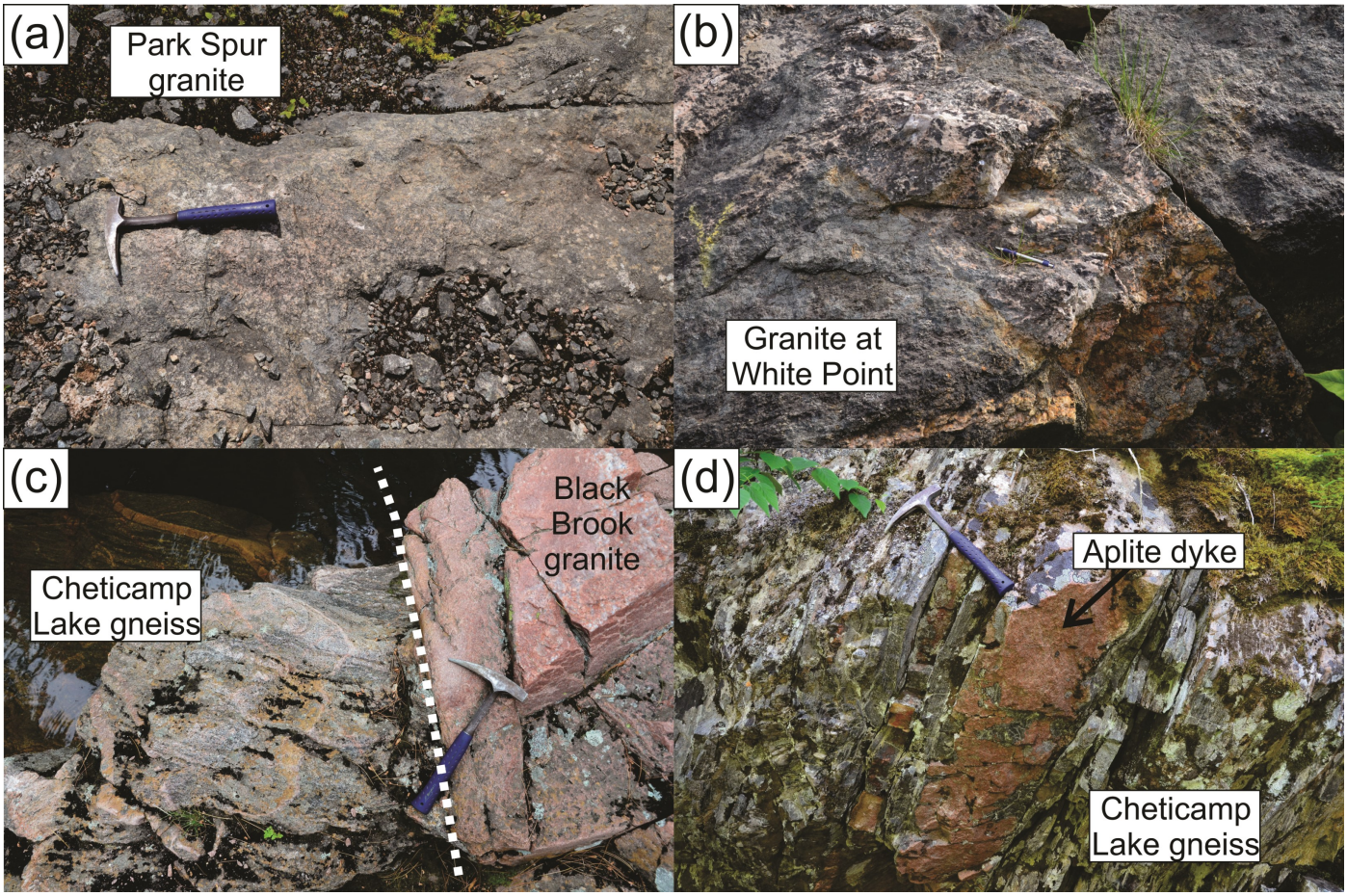

Figure 2. Representative field photographs of the Black Brook Granite Suite. a) Park Spur granite (sample CG17-001). b) White Point granite cropping out at White Point (sample CG17-006). c) Black Brook granite intruding the Cheticamp Lake Gneiss at Mary Anne Falls (sample CG17-010). d) Aplitic dyke crosscutting the Cheticamp Lake Gneiss in the Ingonish River near the Eastern Highlands Shear Zone (sample CG17-012). The hammer in (a), (c) and (d) is 33 cm in length and the pen in (b) is 15 cm in length.

= 9; MSWD = 2.7; Fig. 3a). A younger U-Pb zircon date of 379.1 ± 3.5 Ma (van Rooyen et al., 2018) was obtained from the same sampling location. Samples of the BBGS yielded weighted mean $^{206}Pb/^{238}U$ dates of 387 ± 5 Ma (sample CG17-010: n = 20; MSWD = 1.6; Fig. 3b), 398 ± 4 Ma (sample CG17 -017: n = 20; MSWD = 0.7; Fig. 3c), and 398 ± 6 Ma (sample CG17-019: n = 5; MSWD = 1.3; Fig. 3d), respectively. However, individual zircon U-Pb dates younger than the weighted-mean dates are common in all samples (Fig. 3). Previous geochronological data for the BBGS indicated that the pluton was emplaced ca. 20 to 25 Ma later (375 -4/+5 Ma) based on ID-TIMS U-Pb monazite dating (Dunning et al., 1990). A younger age (ca. 375 Ma) for the BBGS is also supported by unpublished ID-TIMS U-Pb zircon data from needle-shaped, acicular zircon crystals collected at the same sampling locality as sample CG17-010 (S.M. Barr and G.R. Dunning, pers. comm., February 2018). The age discrepancy could be explained by a metamorphic event related to movement along the EHSZ that resulted in the growth of new monazite crystals but the pressure-temperature (P-T) conditions were only hot enough to grow long, slender zircon crystals that were not selected in this study. An alternative explanation for the older U-Pb zircon dates is that the zircon analyzed here were inherited from the Cheticamp Lake Gneiss (U-Pb zircon age of 396 ± 2 Ma; Dunning et al., 1990). A third explanation is that the zircon could be partially metamict because of high U concentrations (range = 124–3530 ppm, mean = 1110 ppm). This can lead to increased elemental fractionation and a remobilization of lead from uranium in the zircon and in the plasma during laser ICP-MS analysis by a process of laser induced elemental fractionation (e.g. Kroslakova and Günther, 2007). Our interpretation is that the majority of the analyzed zircon grains were inherited from the host rocks or protolith and/or that the conditions allowed growth of monazite and only acicular zircon crystals. Thus, we interpret the timing of granitoid emplacement to be ca. 375 Ma. However, a more thorough analysis of zircon grain morphologies, internal zoning, and additional age and isotopic constraints on the host rocks are required to resolve the implications of the older zircon in the BBGS.

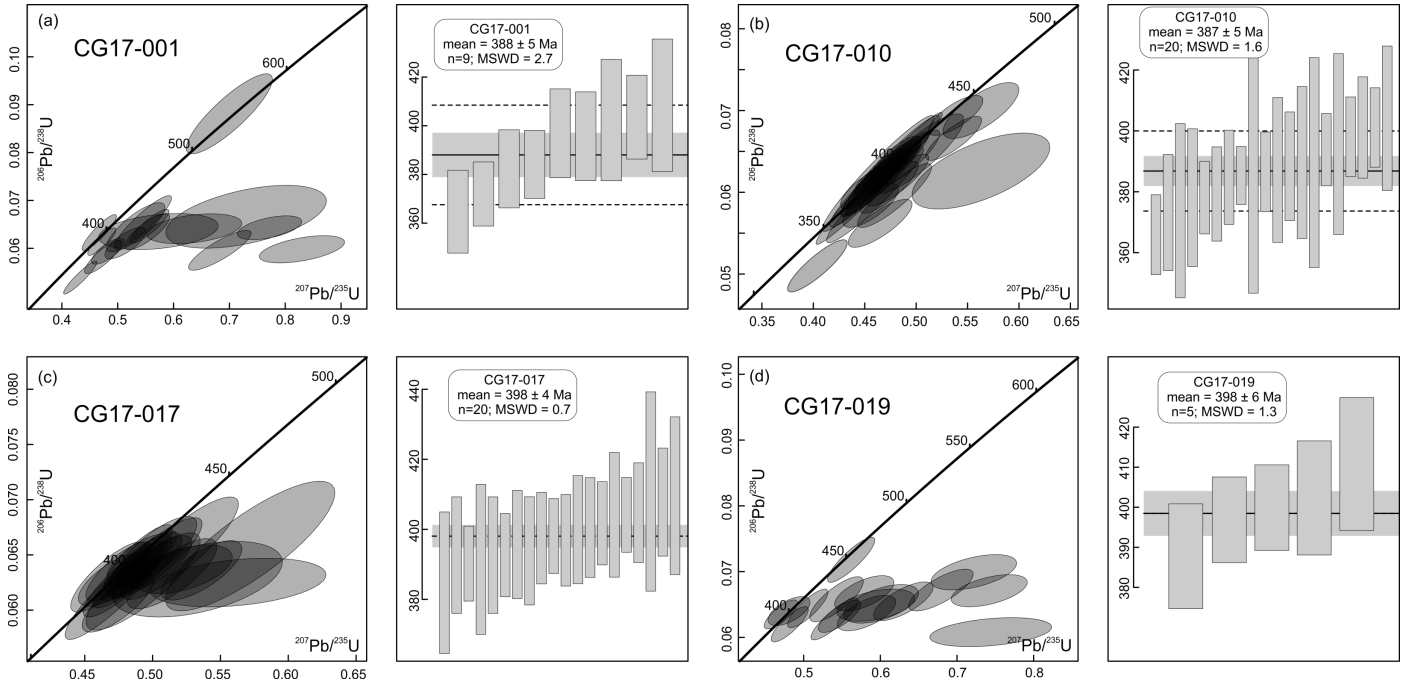

Figure 3. Concordia plots of zircon U-Pb analyses for (a) Park Spur sample CG17-001; and Black Brook Granitic Suite samples (b) CG17-010, (c) CG17-017, and (d) CG-17-019. Data point error ellipses are 2σ. The adjacent bar graphs show the number of concordant analyses used in the weighted-mean date calculations.

Rare earth element (REE) contents of zircon from the dated samples have common patterns that show depletion in LREEs (light REEs), enrichment in HREEs (high REEs), and positive Ce and negative Eu anomalies (Fig. 4a). Eu anomalies (Eu/Eu*) are between 0.15 and 0.89, values that indicate plagioclase fractionation and accumulation. The Park Spur sample shows a wider range in LREE to MREE (mid REE) concentrations compared to the BBGS samples (Fig. 4a). Zircon Th/U ratios are high, between 0.07 and 1.18, indicating an igneous origin (e.g. Rubatto, 2002). Hafnium isotopic data for zircon

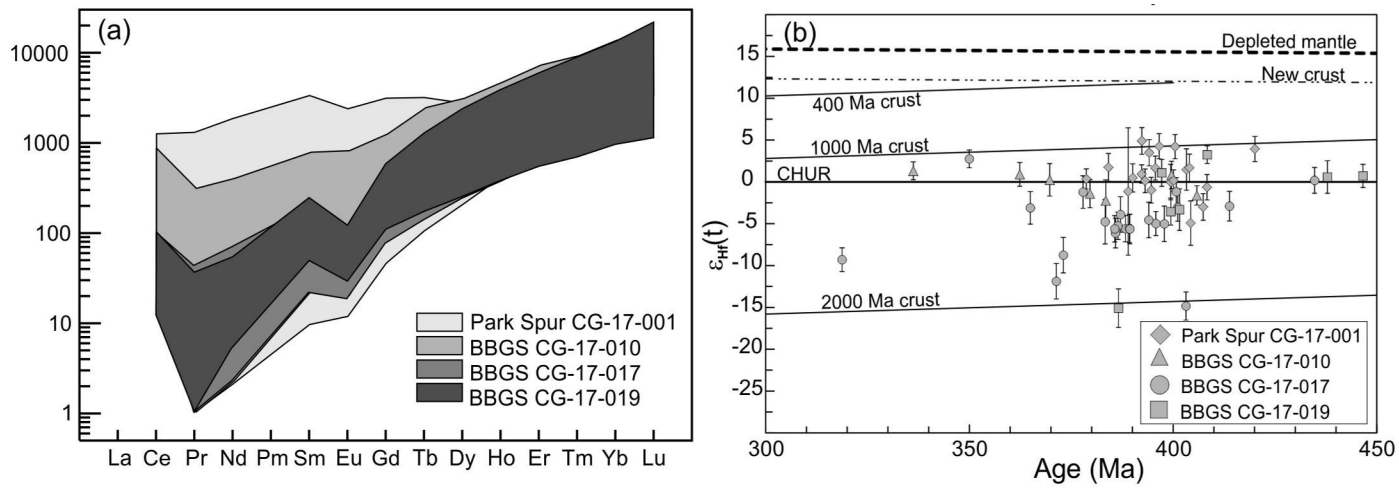

Figure 4. a) Rare earth element composition of zircon data. Lanthanum concentrations were below detection limit and are not plotted. Chondrite normalizing values *from* Sun and McDonough (1989). b) Values of $\varepsilon_{Hf}(t)$ plotted against the zircon crystallization age. Error bars on $\varepsilon_{Hf}(t)$ values are 2σ. In addition to CHUR, the evolution of depleted mantle (Griffin et al., 2002) and the evolution curve for new crust (Dhuime et al., 2011) are shown. The T_{DM} (crustal) Hf evolution lines at 1000 Ma and 2000 Ma are calculated using a $^{176}Lu/^{177}Hf$ ratio of 0.015 (Griffin et al., 2004). Abbreviations: BBGS – Black Brook Granitic Suite; CHUR – chondrite uniform reservoir.

from the Park Spur pluton have $\varepsilon_{Hf}(t)$ values between -2.2 and +3.6. In contrast, zircons from the BBGS have a wider range of $\varepsilon_{Hf}(t)$ values between -15.1 and +4.9. These isotopic data indicate mixing of mantle-derived melts with crustal melts or crustal melting of an unrecognized ca. 1200 to 1000 Ma crustal component. Additional dating and isotopic analyses of the host rocks are required to further resolve the significance of the Hf isotopic data.

Whole-rock geochemical data show a compositional overlap between the Park Spur and BBGS samples, which indicate the stitching granites in the Aspy terrane likely crystallized from a similar magma. Minor compositional variations probably reflect slight variations in magma sources or differentiation processes. Major element data show that the BBGS and Park Spur plutons are peraluminous and calc-alkaline (Fig. 5a, b). In addition, the mineralogy of these plutons indicates that they are S-type granitoids and are likely derived from a metasedimentary crustal material. Mineral compositional and whole-rock data indicate that the BBGS resulted from fractional crystallization of biotite, plagioclase, K-feldspar, zircon, and apatite from a parental peraluminous magma (Yaowanoiyothin and Barr, 1991). Based on similarities in trace element concentrations from the BBGS and one Cheticamp Lake Gneiss sample (Fig. 5c), we suggest that both rock suites were derived from a similar magma source at different times.

Future research directions

The fundamental contribution to knowledge of this work is the link between the so-called stitching granitoids in northern Cape Breton Island. Geochemical, geochronological, and isotopic data indicate that coeval emplacement of the Park Spur and BBGS occurred via lower crustal melting of the same source material. To test this and to better constrain the petrogenesis of granitoid rocks in northern Cape Breton Island, additional data are required. Further zircon geochronological, trace element, and isotopic data from the older host rocks may be used to characterize the geochemical and isotopic evolution of the Ganderian crust that the BBGS intruded. Similar data from other rock units in the region (e.g. rocks in the Bras d'Or terrane and Blair River Inlier) will better define the crustal components of Cape Breton. In addition, more detailed imaging and microbeam analysis of zircon grains, along with dating of other accessory minerals (e.g. apatite, titanite), could be applied to resolve the age discrepancies identified in this study. Improved resolution of the overall geology of Cape Breton Island will strengthen links with correlative terranes in Newfoundland and New Brunswick (Fig. 1a). This may lead to the discovery of economically viable mineral deposits in Cape Breton with genesis similar to deposits elsewhere in Atlantic Canada (e.g. van Staal, 2007).

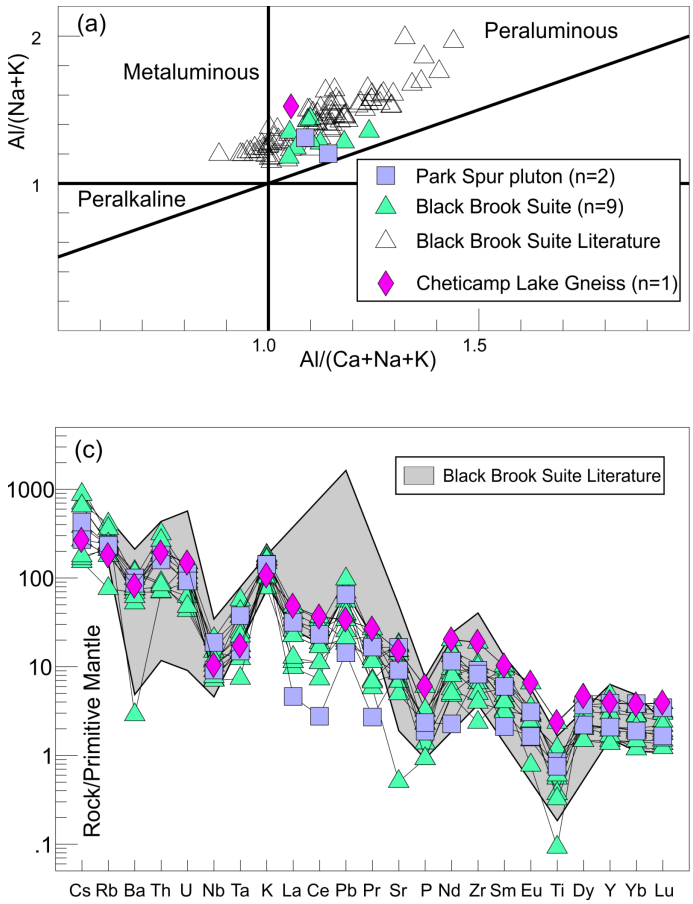

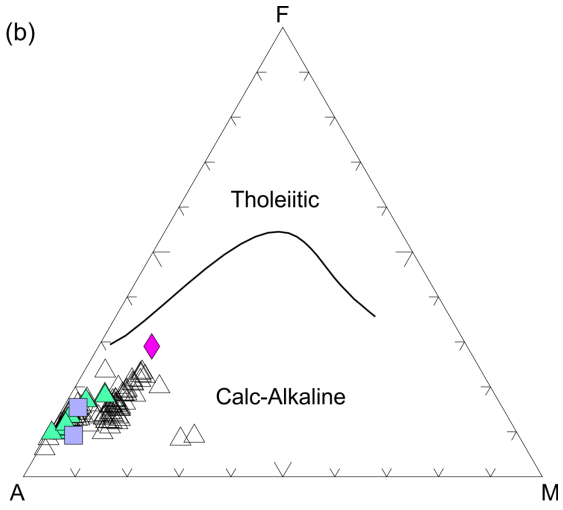

Figure 5. Whole-rock geochemical data. a) Binary plot of A/NK = molar $Al_2O_3/(Na_2O + K_2O)$ vs. A/CNK = molar $Al_2O_3/(CaO + Na_2O + K_2O)$. b) Ternary diagram of AFM (A = $Na_2O + K_2O$; F = $FeO + Fe_2O_3$; M = MgO) showing the boundary between calc-alkaline and tholeiitic trends (Irvine and Baragar, 1971). c) Primitive-mantle normalized trace-element spider plot. Normalization factors *from* Sun and McDonough (1989). Literature data for the Black Brook Granitic Suite *from* Yaowanoiyothin and Barr (1991).

Acknowledgments

This report is a contribution to NRCan's Targeted Geoscience Initiative Program (TGI). Support for this study was provided through the Porphyry-style Mineral Systems Project's '*Activity P-1.4: Temporal and spatial controls on the nature and distribution of porphyry-style deposits*'.

This report is based primarily on Caleb Grant's B.Sc. honours thesis. The authors are grateful to Sandra M. Barr and Chris E. White for in-depth discussions and sharing their knowledge about the geology of Cape Breton. Nicolas Piette-Lauzière (University of British Columbia, Okanagan) is acknowledged for his assistance in the field and for ongoing discussions. This report benefited from the review of Nicolas Pinet, Wouter Bleeker and Neil Rogers.

References

Barr, S.M., 2010. Granites and terranes in Cape Breton Island; *in* Eurogranites 2010 Field Excursion Guidebook, Nova Scotia, (ed.) D.B. Clarke; Atlantic Geoscience Society, Special Publication Number 37, p. 63–88.

Barr, S.M. and Raeside, R.P., 1989. Tectono-stratigraphic terranes in Cape Breton Island, Nova Scotia: Implications for the configuration of the northern Appalachian orogen; Geology, v. 17, p. 822–825.

Barr, S.M. and White, C.E., 2017. Overview map show locations of bedrock geology maps for Cape Breton Island, Nova Scotia; Department of Natural Resources, Geosciences and Mines Branch, Open File Map ME 2017-006, scale 1:220 000.

Barr, S.M., Dunning, G.R., Raeside, R.P., and Jamieson, R.A., 1990. Contrasting U–Pb ages from plutons in the Bras d'Or and Mira terranes of Cape Breton Island, Nova Scotia; Canadian Journal of Earth Sciences, v. 27, p. 1200–1208.

Barr, S.M., Raeside, R.P., and White, C.E., 1998. Geological correlations between Cape Breton Island and Newfoundland, northern Appalachian orogen; Canadian Journal of Earth Sciences, v. 35, p. 1252–1270.

Barr, S.M., van Rooyen, D., and White, C.E., 2018. Granitoid plutons in peri-Gondwanaan terranes of Cape Breton Island, Nova Scotia, Canada: new U-Pb (zircon) age constraints. Atlantic Geology, v. 54, p. 21–80.

Dhuime, B., Hawkesworth, C., and Cawood, P., 2011. When continents formed; Science, v. 331, p. 154–155.

Dunning, G.R., Barr, S.M., Raeside, R.P., and Jamieson, R.A., 1990. U-Pb zircon, titanite, and monazite ages in the Bras d'Or and Aspy terranes of Cape Breton Island, Nova Scotia: Implications for igneous and metamorphic history; Geological Society of America, Bulletin, v. 102, p. 322–330.

Grant, C., 2018. Investigating the relationship between the Bras d'Or and Aspy terranes in Cape Breton Island: Insights from Devonian plutonic rocks; BSc thesis, St. Francis Xavier University, Antigonish, Nova Scotia, 60 p.

Griffin, W.L., Wang, X., Jackson, S.E., Pearson, N.J., O'Reilly, S.Y., Xu, X., and Zhou, X., 2002. Zircon chemistry and magma mixing, SE China: In-situ analysis of Hf isotopes, Tonglu and Pingtan igneous complexes; Lithos, v. 61, p. 237–269.

Griffin, W.L., Belousova, E.A., Shee, S.R., Pearson, N.J., and O'Reilly, S.Y., 2004. Archean crustal evolution in the northern Yilgarn Craton: U-Pb and Hf-isotope evidence from detrital zircons; Precambrian Research, v. 131, p. 231–282.

Hagen-Peter, G. and Cottle, J., 2018. Evaluating the relative roles of crustal growth versus reworking through continental arc magmatism: A case study from the Ross orogen, Antarctica; Gondwana Research, v. 55, p. 153–166.

Hagen-Peter, G., Cottle, J.M., Tulloch, A.J., and Cox, S.C., 2015. Mixing between enriched lithospheric mantle and crustal components in a short-lived subduction-related magma system, Dry Valleys area, Antarctica: Insights from U-Pb geochronology, Hf isotopes, and whole-rock geochemistry; Lithosphere, v. 7, p. 174–188.

Hibbard, J.P., van Staal, C.R., Rankin, D.W., and Williams, H., 2006. Lithotectonic map of the Appalachian Orogen, Canada - United States of America; Geological Survey of Canada, "A" Series Map 02096A.

Irvine, T.N. and Baragar, W.R.A., 1971. A guide to the chemical classification of the common volcanic rocks; Canadian Journal of Earth Sciences, v. 8, p. 523–548.

Kellett, D.A., van Staal, C., Wilson, R.A., and Rogers, N., 2017. The age of Salinic deformation constrained by $^{40}Ar/^{39}Ar$ dating of multiple cleavage domains: Bathurst Supergroup, New Brunswick Appalachians; American Journal of Science, v. 317, p. 338–368.

Keppie, J.D., Nance, R., Murphy, J., and Dostal, J., 1991. Northern appalachians: Avalon and Meguma terranes; *in* The West African Orogens and Circum-Atlantic Correlatives, (ed.) R.D. Dallmeyer and J.P. Lécorché; Springer, p. 315–333.

Keppie, J., Dostal, J., Davis, D., and Horton, D., 1998. Earliest Silurian supra-subduction magmatism in central Cape Breton Island; Atlantic Geology, v. 34, p. 113–120.

Kroslakova, I. and Günther, D., 2007. Elemental fractionation in laser ablation-inductively coupled plasma-mass spectrometry: evidence for mass load induced matrix effects in the ICP during ablation of a silicate glass; Journal of Analytical Atomic Spectrometry, v. 22, p. 51–62.

Lin, S., 1995. Structural evolution and tectonic significance of the Eastern Highlands shear zone in Cape Breton Island, the Canadian Appalachians; Canadian Journal of Earth Sciences, v. 32, p. 545–554.

Lin, S., Davis, D.W., Barr, S.M., Van Staal, C.R., Chen, Y., and Constantin, M., 2007. U-Pb geochronological constraints on the evolution of the Aspy terrane, Cape Breton Island: implications for relationships between the Aspy and Bras d'Or terranes and Ganderia in the Canadian Appalachi-

ans; American Journal of Science, v. 307, p. 371–398.

Murphy, J.B., Keppie, J.D., Nance, R.D., and Dostal, J., 2010. Comparative evolution of the Iapetus and Rheic Oceans: A North America perspective. Gondwana Research; v. 17, p. 482-499.

Paton, C., Hellstrom, J., Paul, B., Woodhead, J., and Hergt, J., 2011. Iolite: Freeware for the visualisation and processing of mass spectrometric data; Journal of Analytical Atomic Spectrometry, v. 26, p. 2508–2518.

Piette-Lauzière, N., Larson, K.P., and Kellett, D.A., 2018. Field mapping of the Eastern Highlands shear zone, Cape Breton Island, Nova Scotia; *in* Targeted Geoscience Initiative: 2017 Report of Activities, volume 1, (ed.) N. Rogers; Geological Survey of Canada, Open File 8358, p. 23–29.

Piette-Lauzière, N., Graziani, R., Larson, K.P., and Kellett, D.A., 2019. Neoacadian reactivation of the Eastern Highlands shear zone, Appalachian Orogen; *in* Targeted Geoscience Initiative: 2018 report of activities, (ed.) N. Rogers; Geological Survey of Canada, Open File 8549, p. 295–305.

Raeside, R.P. and Barr, S.M., 1990. Geology and tectonic development of the Bras d'Or suspect terrane, Cape Breton Island, Nova Scotia; Canadian Journal of Earth Sciences, v. 27, p. 1371–1381.

Rubatto, D., 2002. Zircon trace element geochemistry: partitioning with garnet and the link between U-Pb ages and metamorphism; Chemical Geology, p. 184, p. 123–138.

Slaman, L.R., Barr, S.M., White, C.E., and van Rooyen, D., 2016. Age and tectonic setting of granitoid plutons in the Chéticamp belt, western Cape Breton Island, Nova Scotia, Canada; Canadian Journal of Earth Sciences, v. 54, p. 88–109.

Sun, S.-S. and McDonough, W.F., 1989. Chemical and isotopic systematics of oceanic basalts: implications for mantle composition and processes; *in* Magmatism in the Ocean Basins, (ed.) A.D. Saunders and M.J. Norry; Geological Society, London, Special Publications 42, p. 313–345.

van Rooyen, D., Barr, S.M., and White, C.E., 2018. New U-Pb (zircon and monazite) ages and Sm-Nd isotopic data from granitoid plutons in the Aspy and Bras d'Or terranes of Cape Breton Island, Nova Scotia: Implications for tectonic evolution and mineralization potential; *in* Targeted Geoscience Initiative: 2017 Report of Activities, volume 1, (ed.) N. Rogers; Geological Survey of Canada, Open File 8358, p. 37–45.

van Staal, C.R. 2007. Pre-Carboniferous tectonic evolution and metallogeny of the Canadian Appalachians; *in* Mineral Deposits of Canada: A Synthesis of Major Deposit-Types, District Metallogeny, the Evolution of Geological Provinces, and Exploration Methods, (ed.) W.D. Goodfellow; Geological Association of Canada, Mineral Deposits Division, Special Publication No. 5, p. 793–818.

van Staal, C.R., Dewey, J.F., Mac Niocall, C., and McKerrow, W.S., 1998. The Cambrian-Silurian tectonic evolution of the northern Appalachians and British Caledonides: history of a complex, west and southwest Pacific-type segment of Iapetus; *in* Lyell: the Past is the Key to the Present, (ed.) D.J. Bundell and A.C. Scott; Geological Society, London, Special Publication 143, p. 199–242.

van Staal, C.R., Whalen, J.B., Valverde-Vaquero, P., Zagorevski, A., and Rogers, N., 2009. Pre-Carboniferous, episodic accretion-related, orogenesis along the Laurentian margin of the northern Appalachians; *in* Ancient Orogens and Modern Analogues, (ed.) J.B. Murphy, J.D. Keppie and A.J. Hynes; Geological Society, London, Special Publications 327, p. 271–316.

Vermeesch, P., 2018. IsoplotR: A free and open toolbox for geochronology; Geoscience Frontiers, v. 9, p. 1479–1493.

Williams, H., 1979. The Appalachian Orogen in Canada; Canadian Journal of Earth Sciences, v. 16, p. 792–807.

Yaowanoiyothin, W. and Barr, S.M., 1991. Petrology of the Black Brook granitic suite, Cape Breton Island, Nova Scotia; The Canadian Mineralogist, v. 29, p. 499–515.

Contrasts in petrological features between Silurian-Devonian plutons in the Mira and Aspy terranes of Cape Breton Island, Nova Scotia: implications for porphyry-style mineralization

A. Moning[1], S.M. Barr[1], C.E. White[2] and D. van Rooyen[3]

[1]*Department of Earth and Environmental Science, Acadia University, Wolfville, Nova Scotia B4P 2R6*
[2]*Nova Scotia Department of Energy and Mines, Halifax, Nova Scotia B3J 2T9*
[3]*Department of Mathematics, Physics and Geology, Cape Breton University, Sydney, Nova Scotia B1P 6L2*

Abstract

The Devonian Gillis Mountain granitoid pluton in the Avalonian Mira terrane of southern Cape Breton Island hosts porphyry-style copper-molybdenum mineralization. In contrast, plutons of Silurian and Devonian age with similar rock types in the Leonard MacLeod Brook area of the Ganderian Aspy terrane of northern Cape Breton Island are not known to be mineralized. The Gillis Mountain pluton is calc-alkalic and likely formed as a result of slab failure in a subduction zone, whereas plutons in the Leonard MacLeod Brook area may have formed during within-arc extension followed by slab failure in the Devonian. Silurian plutons in the Leonard MacLeod Brook area are bimodal and intruded co-magmatic volcanic rocks, whereas the Devonian Gillis Mountain pluton intruded older shale and siltstone and is not associated with co-magmatic volcanic rocks.

Introduction

The Devonian Gillis Mountain pluton in the Avalonian Mira terrane of southern Cape Breton Island, Nova Scotia (Fig. 1), hosts porphyry-style copper-molybdenum mineralization (Kirkham and Soregaroli, 1975; O'Beirne, 1979; Barr and O'Beirne, 1981; Barr and Macdonald, 1992). In contrast, plutons of Silurian and Devonian age in the Leonard MacLeod Brook area of the Ganderian Aspy terrane in northern Cape Breton Island are not known to be mineralized (Barr et al., 1992; O'Neill, 1996). Hence this M.Sc. project was undertaken to compare the host rocks, depth of emplacement, mineralogy, and chemical composition the Gillis Mountain pluton with those of plutons in the Leonard MacLeod Brook area to provide insight about tectonic setting and factors controlling porphyry-style mineralization (Moning et al., 2018).

Plutons in the Leonard MacLeod Brook area were mapped and sampled in the summer of 2017 during regional mapping by the Nova Scotia Department of Natural Resources (Moning et al., 2018; White et al., 2018). Samples were also collected from drill core from the Gillis Mountain pluton (MacKinnon, 2008). In addition, archived sample powders from thesis work in the Leonard MacLeod Brook area by O'Neill (1996) and from thesis work in the Gillis Mountain pluton by O'Beirne (1979) were re-analyzed to obtain modern trace element data. This report summarizes some of the initial results from the field and petrological studies, and related U-Pb (zircon) dating.

Gillis Mountain pluton

The Gillis Mountain pluton is characterized by porphyry-style copper-molybdenum mineralization (Hawkes, 1967; Kirkham and Soregaroli, 1975; MacKinnon, 2008). Based on mapping and petrographic studies by O'Beirne (1979), Barr and O'Beirne (1981), and Barr et al. (1982), the Gillis Mountain pluton consists of three main units: quartz monzodiorite, porphyritic granite (grading to granodiorite), and fine-grained granite, intruded by aplitic, granitic, and mafic dykes. Chalcopyrite and pyrite occur in all units but molybdenite is mainly in the porphyritic granite. The pluton is characterized by typical porphyry-type hydrothermal alteration, including hematitization and sericitization of feldspar minerals and chloritization and possibly biotitization of mafic minerals (Barr and O'Beirne, 1981).

The Gillis Mountain pluton has sharp, discordant contacts with Middle Cambrian shale and siltstone. The contact metamorphic aureole is poorly exposed due to swampy terrain, but where observed the hornfels contains cordierite and andalusite, consistent with shallow emplacement (O'Beirne, 1979). Recent dating of the Gillis Mountain pluton yielded a crystallization age of 369.7 ± 2.3 Ma (U-Pb zircon: Barr et al., 2018), which confirms the Devonian age previously inferred from Rb-Sr dating by Cormier (1979).

No new mapping was done in the Gillis Mountain area for this study because access and outcrop are more limited now than they were during the work of O'Beirne (1979) when exploration trenches were well exposed. However, core from four holes drilled in the area by Globex Mining Enterprises Incorporated (MacKinnon, 2008) was sampled for petrographic study and whole-rock chemical analyses by XRF and ICP-MS at Bureau Veritas Ltd., Vancouver, BC. The same varieties of plutonic rocks were encountered in the drill core as were reported

Corresponding author: Alicia Moning (aliciamoning@acadiau.ca)

Moning, A., Barr, S.M., White, C.E., and van Rooyen, D., 2019. Contrasts in petrological features between Silurian-Devonian plutons in the Mira and Aspy terranes of Cape Breton Island, Nova Scotia: implications for porphyry-style mineralization; *in* Targeted Geoscience Initiative: 2018 report of activities, (ed.) N. Rogers; Geological Survey of Canada, Open File 8549, p. 287–294. https://doi.org/10.4095/313662

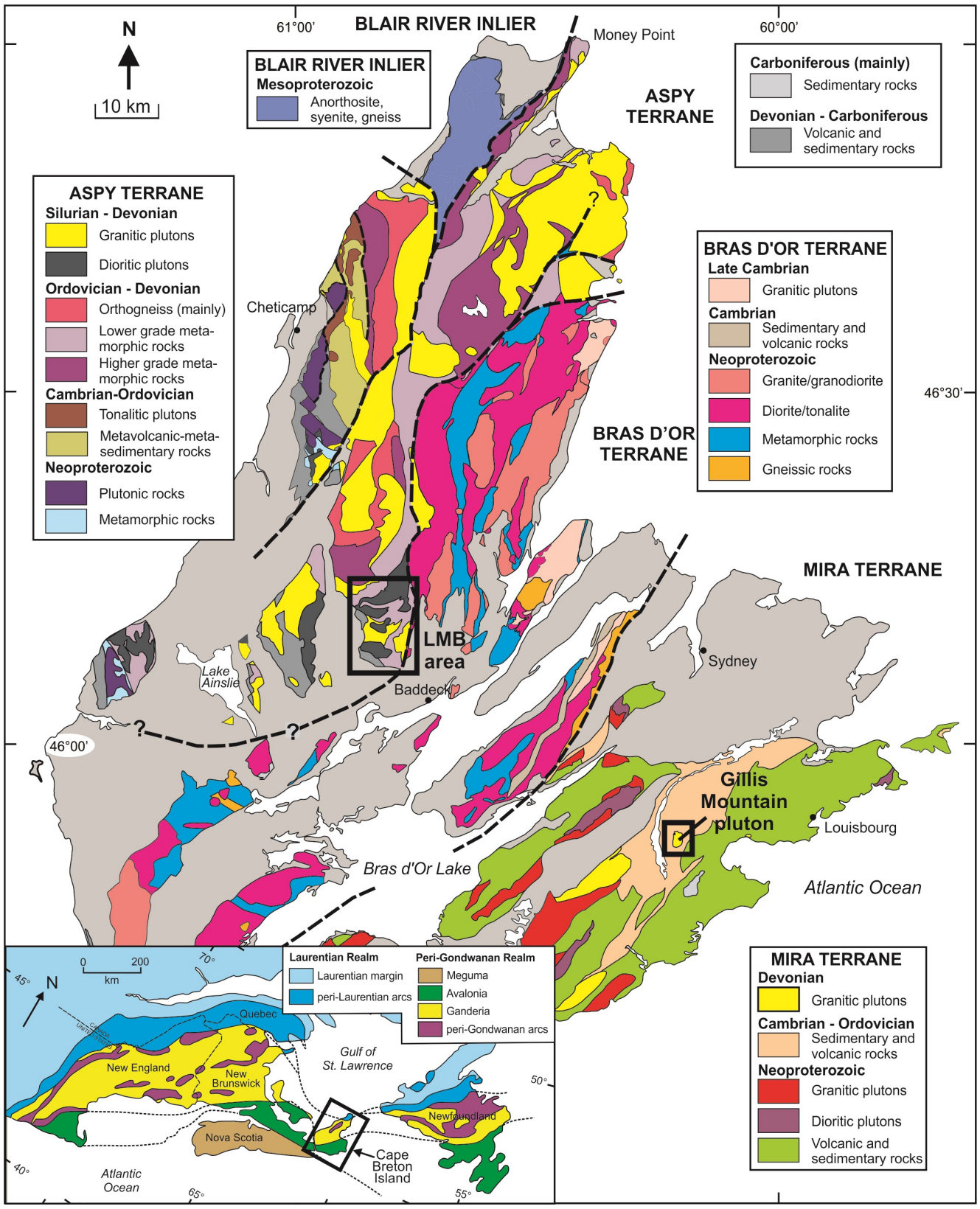

Figure 1. Simplified geological map of Cape Breton Island, *modified after* Barr et al. (2018), showing the locations of the Leonard MacLeod Brook (LMB) area and Gillis Mountain pluton in the Aspy and Mira terranes, respectively. Inset map shows the divisions of the northern Appalachian orogen *after* Hibbard et al. (2006).

at surface in previous studies (e.g., O'Beirne, 1979). Drillhole GM-11-08, in the western part of the pluton, intersected mainly quartz monzodiorite in the upper 280 m, with some sections of hornfels and minor zones of alteration and mineralization, mainly chalcopyrite and pyrite in veins. The quartz monzodiorite is intruded by dykes of porphyritic granite/granodiorite and aplite. The lower 80 m of the core consists of porphyritic granite/granodiorite and fine-grained granite. Drillhole GM12-08, in the east-central part of the pluton, is entirely in granitic rocks, varying from porphyritic (Fig. 2a) to medium-grained, also with zones of alteration and mineralization. The remaining two drillholes in the contact aureole east of the pluton are mainly in hornfels intruded by granitic dykes.

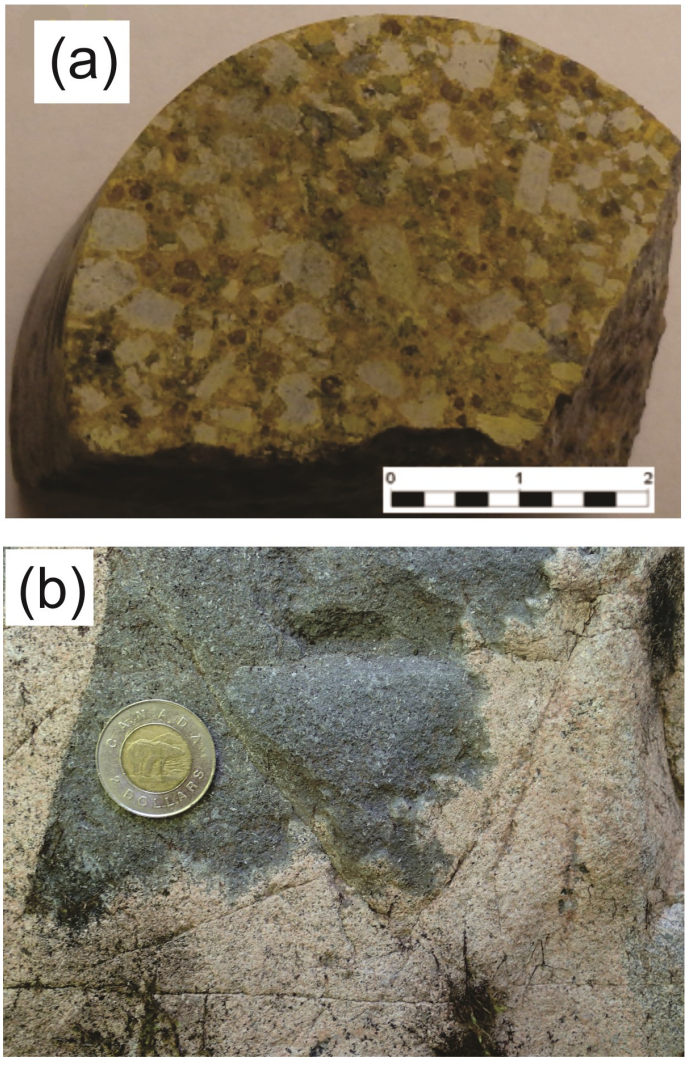

Figure 2. (a) Typical Gillis Mountain porphyritic granite from drillhole GM-12-08, depth 84.5 m. Slab has been etched and stained for potassium feldspar (yellow). Plagioclase is white, quartz is light grey, and biotite and amphibole are darker grey. (b) Outcrop photograph showing mingled diorite and syenogranite of the Easach Ban pluton (location UTM: 670215 E, 5120181 N; zone 20),

Leonard MacLeod Brook area

The Leonard MacLeod Brook area forms the southern tip of the central Cape Breton Highlands, adjacent to the shear zone between the Ganderian Aspy and Bras d'Or terranes and mostly surrounded by younger Carboniferous rocks (Fig. 1). Results of new mapping related to this project are consistent with the interpretations from previous work (Jamieson et al., 1987; Barr et al., 1992; O'Neill, 1996), which showed that the volcanic and sedimentary rocks that host the plutons belong to the Silurian Sarach Brook Formation (Fig. 3). A new U-Pb (zircon) date of 424.4 ± 5.7 Ma was obtained from a felsic tuff in the formation, not quite overlapping within error the previously reported age of date of 433 +7/-4 Ma from the Sarach Brook Formation farther north (Dunning et al., 1990). The names Leonard MacLeod Brook, Gillis Brook, and Easach Ban, assigned by O'Neill (1996) to the plutonic rocks in the area, are retained but their distribution is now better defined, and an additional pluton, Big Barren, has been recognized (Fig. 3). All four plutons vary in modal composition from gabbro and diorite to fine-grained alkali-feldspar granite and syenogranite. The mafic and felsic rocks typically display co-mingling and mixing textures (Fig. 2b), and locally intermediate hybrid rocks are present. Granitic components are fine-grained and consist of quartz, alkali feldspar, and plagioclase with minor amphibole and biotite (now chlorite) and opaque minerals. Syenogranitic samples have scattered phenocrysts of plagioclase in a groundmass of plagioclase, alkali feldspar and quartz with minor biotite. Some samples have interstitial granophyric texture consistent with high-level emplacement (e.g., Barker, 1970).

Although previously interpreted to be Devonian, three new U-Pb (zircon) ages (Barr et al., 2018; White et al., 2018) range from about 436 to 419 Ma, consistent with the ages obtained from the volcanic host rocks (Fig. 3). Although the ages are not precise enough to confirm the intrusive sequence, the dates are consistent with field relations, which suggest that Gillis Brook and Easach Ban are the oldest plutons and that undated Big Barren is the youngest (Fig. 3). The dates suggest that the magmas formed over a time span of as much as 15 m.y. The new dating also confirmed that tonalitic plutons along the eastern margin of the area are Ediacaran with ages of about 625 Ma (Fig. 3).

The Devonian Bothan Brook pluton, previously dated at 376 ± 3 Ma by Horne et al. (2003), consists of relatively homogeneous medium- to coarse-grained equigranular monzogranite with scattered mafic dykes but no co-magmatic gabbroic/dioritic components, in contrast to the Silurian plutons. Major minerals include plagioclase, quartz, alkali feldspar, and minor hornblende and biotite altered to chlorite. Accessory minerals include titanite, apatite, and zircon.

The geological relations in the Leonard MacLeod Brook area are complicated by widespread mylonitic shear zones that affect the Silurian plutons and their host rocks (Fig. 3). The Big Barren pluton is the least deformed by these shear zones, which may have been waning by the time of its emplacement in the

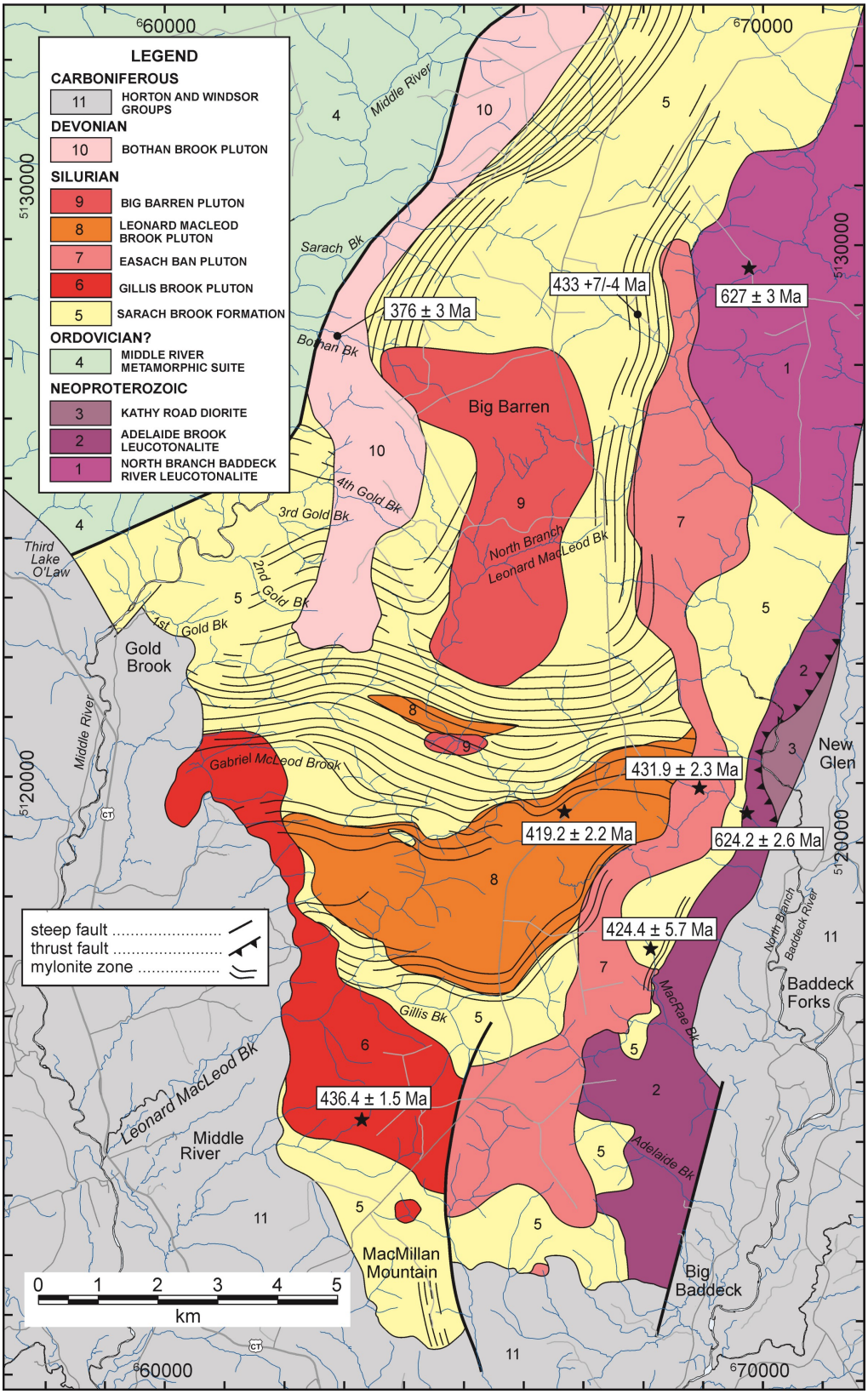

Figure 3. Geological map of the Leonard MacLeod Brook area *modified from* White et al. (2018) showing the Gillis Brook, Easach Ban, Leonard MacLeod Brook, Big Barren, and Bothan Brook plutons as described in the text. Mylonitic shear zones are shown schematically. Stars indicate locations of samples dated as part of or related to this project. Black dots indicate previously published U-Pb dates from Dunning et al. (1990) and Horne et al. (2003) as described in the text. Abbreviation: Bk – Brook.

late Silurian. The mylonitic fabrics trend northerly in the north and east, but turn to an easterly direction in the south and west. The Devonian Bothan Brook pluton cuts across the shear zones and is not deformed by them. Other than below 1 volume % pyrite in mylonitic rocks in shear zones, no sulphide mineralization was observed in any of these plutonic rocks.

Whole-rock chemistry

The porphyritic granite/granodiorite and fine-grained granite samples from the Gillis Mountain pluton have SiO_2 contents ranging from 65 to 70 weight %; because of their limited spread in composition, they are not distinguished from one another at the scales of the diagrams in Figures 4 and 5 but in general the porphyritic samples have lower SiO_2 than the fine-grained granite samples (O'Beirne, 1979). Aplitic dyke samples have higher SiO_2 content (about 76 weight %), and quartz monzodiorite samples have lower SiO_2 (58–62 weight %). Most of the analyzed samples plot in the high-K field on Figure 4a. They generally have Cu contents in the range 30-100 ppm but some samples of porphyritic granite have up to 4000 ppm Cu (Fig. 3b), although samples with visible sulphides were not generally selected for analysis. Both the granitic samples and quartz monzodiorite samples are calc-alkalic based on the modified alkali-lime index of Frost et al. (2001) (Fig. 4c) and are classified as magnesian based on FeOt/FeOt + MgO ratio (Fig. 4d). They trend along the calc-alkalic curve on the normative mineral classification diagram, and names based on normative minerals are consistent with those based on modal minerals (Fig. 4e). On tectonic setting discrimination diagrams, most samples cluster in the volcanic-arc field (Fig. 5a) but display the higher Nb values relative to Y indicative of plutons formed during slab failure (also known as slab breakoff) (Fig. 5b).

The whole-rock chemical data from the Silurian plutons in the Leonard MacLeod Brook area show the same bimodality that is apparent in their petrographic features. The gabbroic and dioritic components of the plutons have low SiO_2 content (47–54 weight %; samples <50 weight % are not shown on this diagram) whereas the granitic rocks have more than 70 weight % SiO_2 (Fig. 4a). Samples with intermediate compositions include hybrid rocks that have petrographic features indicative of mixing of the mafic and felsic end members, and altered rocks, in which K-feldspar has been replaced by albitic plagioclase, resulting in anomalously low K_2O content (Fig. 4a). None of the analyzed samples contained visible sulphide minerals, and none show elevated Cu, Pb, or Zn contents, as illustrated by the plot of Cu against SiO_2 (Fig. 4b). In comparison to the Gillis Mountain pluton, the values for Cu (as well as Pb and Zn, not shown) tend to be lower (Fig. 4b).

The analyzed samples from plutons in the Leonard MacLeod Brook area show wide variation in modified alkali-lime index and scatter through all of the fields defined by Frost et al. (2001), although the majority of samples are in the alkali-calcic field (Fig. 4c). On the plot of FeOt/FeOt + MgO versus SiO_2, the majority of felsic samples plot above the ferroan-magnesian dividing line and in the A-type granite field (Fig. 4d). The bimodality of the samples is apparent on the classification diagram based on CIPW normative mineralogy, on which the majority of samples plot in the diorite/monzodiorite or syenogranite/alkali-feldspar granite fields (Fig. 4e), consistent with their modal mineralogy. The intermediate samples are scattered, but both mafic and felsic samples follow the alkali-calcic trend in contrast to the calc-alkalic trend displayed by the Gillis Mountain pluton samples (Fig. 4e). On tectonic setting discrimination diagrams for granitoid rocks, the intermediate and felsic samples plot in the post-collisional and within-plate fields (Fig. 5a, b). The similarities in petrological features among the Silurian plutons in the Leonard MacLeod Brook area suggests that they are co-magmatic and related to the volcanic rocks of their host rocks of the Sarach Brook Formation, consistent with their age similarities. The larger chemical database enabled better definition of the chemical affinity and tectonic setting of these plutons than was apparent from the more limited database of O'Neill (1996).

In contrast to the bimodal Silurian plutons, the Bothan Brook pluton is entirely granitic, with more than 72% SiO_2 and high K_2O, and most samples plot in the shoshonitic field (Fig. 4a). All have low Cu content (Fig. 4b) and plot in the alkali-calcic to alkalic field in Figure 4c. They display wide range in FeOt/FeOt + MgO values and span the magnesian and ferroan fields in Figure 3d, although the majority are ferroan and appear to be A-type. However, they do not have other features of A-type granite such as high Zr, Y and Nb, and plot in the volcanic arc and slab-failure (slab breakoff) pluton fields on Figures 5a and b.

Preliminary conclusions

Significant results of this study so far include a new geological map of the Leonard MacLeod Brook area and the recognition based on U-Pb (zircon) dating that the majority of plutonic rocks in that area are Silurian rather than Devonian as was previously assumed. The chemical characteristics of the Gillis Mountain pluton contrast markedly with those of both the Silurian and Devonian plutons in the Leonard MacLeod Brook area. The Gillis Mountain pluton is calc-alkalic and likely formed as a result of slab breakoff in a subduction zone, whereas the tectonic setting for plutons in the Leonard MacLeod Brook area is more ambiguous, although within-arc extension is a possible model for the Silurian plutons and slab breakoff for the Devonian Bothan Brook pluton. Silurian plutons in the Leonard MacLeod Brook area intruded co-magmatic volcanic rocks, whereas the Devonian Gillis Mountain pluton intruded older shale and siltstone and is not associated with co-magmatic volcanic rocks. The Gillis Mountain pluton is characterized by higher Cu, Pb, and Zn values than the Silurian and Devonian plutons in the Leonard MacLeod Brook area. The differences in chemical affinity, tectonic setting, and host rocks all were likely factors in determining the presence or absence of porphyry-style mineralization in these plutons.

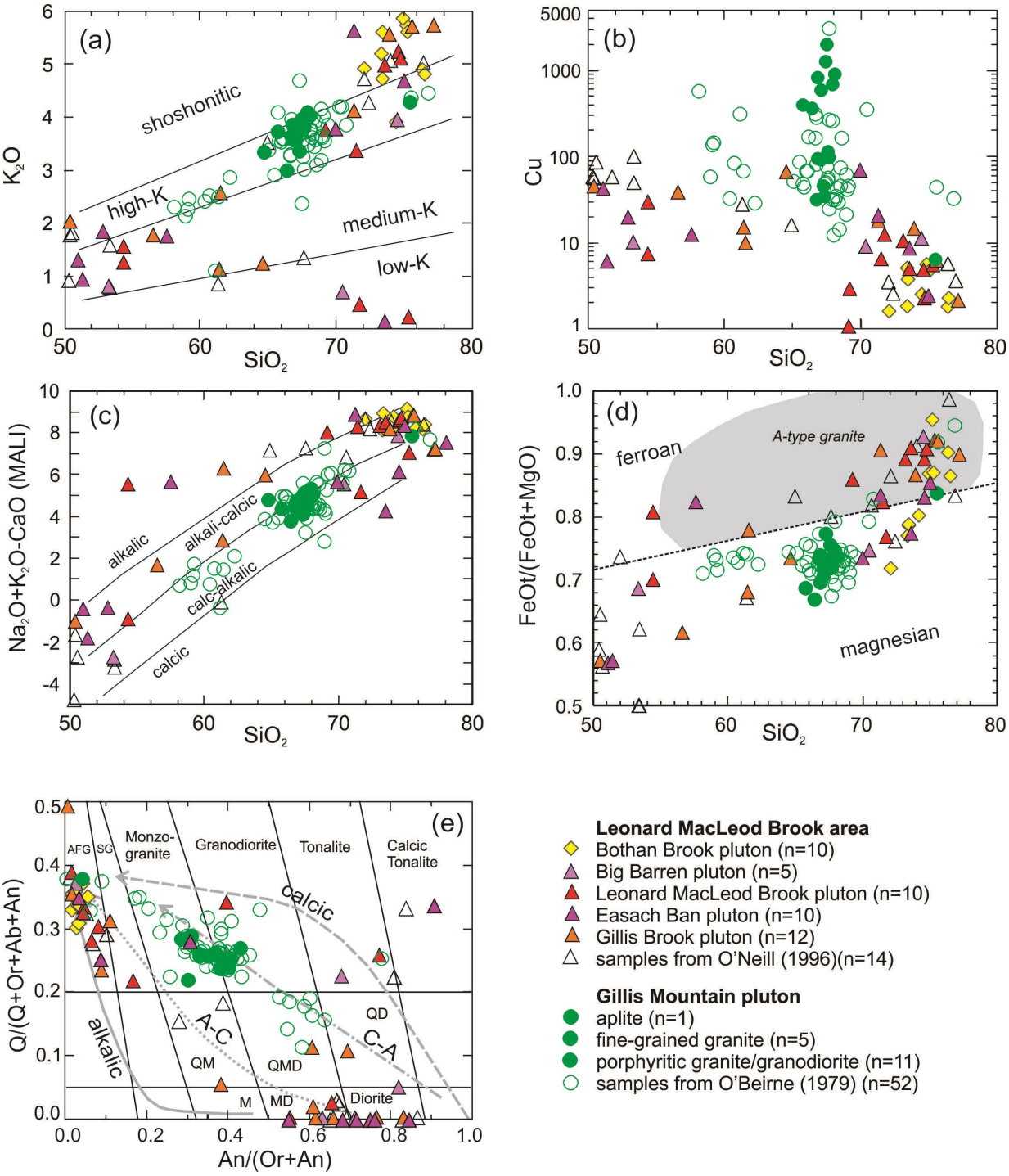

Figure 4. Chemical plots of the Gillis Mountain pluton and plutons in the Leonard MacLeod Brook area. a) K_2O vs. SiO_2 with low-, medium-, and high-K fields *after* LeMaitre (1989) and high-K and shoshonitic fields *after* Peccerillo and Taylor (1976). b) Cu (logarithmic scale) versus SiO_2. **c)** Modified alkali-lime index (MALI = Na_2O + K_2O - CaO) vs. SiO_2, fields *from* Frost et al. (2001). d) Fe-index (FeOt/FeOt + MgO) vs. SiO_2, fields *after* Frost et al. (2001). Ferroan-magnesian boundary *modified after* Frost and Frost (2008). e) CIPW normative Q/(Q+Or+Ab+An) vs. An/(Or+An) classification plot *after* Streckeisen and LeMaitre (1979). Also shown are compositional trends for types of plutonic suites *from* Whalen and Frost (2013). Abbreviations: A – alkalic; A-C – alkali-calcic; C-A – calc-alkalic; and C – calcic). CIPW normative mineralogy was calculated setting Fe_2O_3 at 0.15 of the total Fe.); 9 samples from the Gillis Brook, Easach Ban, Leonard MacLeod Brook, and Big Barren plutons have less than 50 weight % SiO_2 and are not shown on (a), (b), (c), or (d). Abbreviation "n" in the legend is the number of samples. Oxides are in weight %; Cu is in ppm.

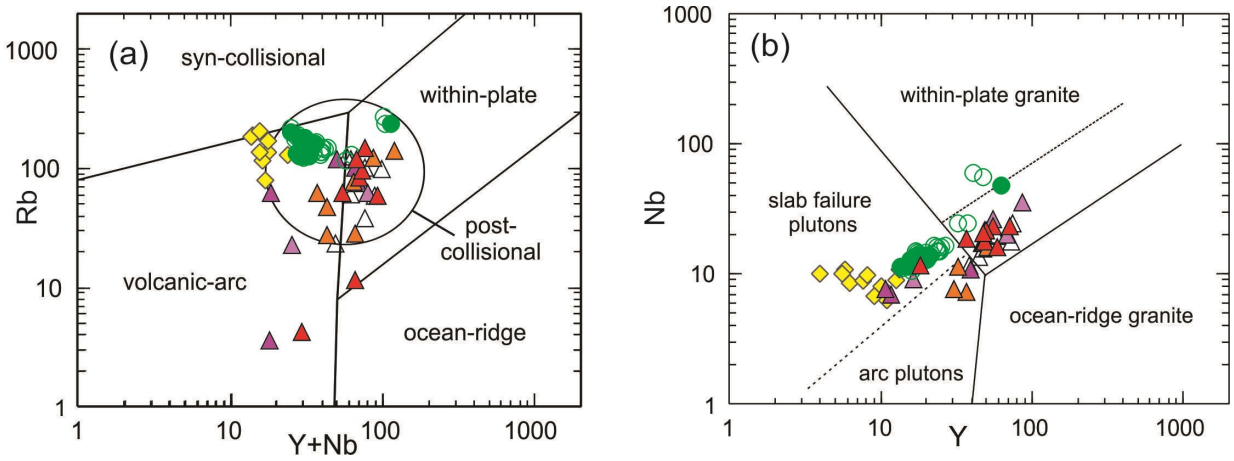

Figure 5. Tectonic setting discrimination diagrams for granitoid rocks with fields *from* Pearce et al. (1984) and Pearce (1996); fields in (b) have been *modified after* Hildebrand and Whalen (2015). Symbols are as in Figure 3, but only samples with greater than 60 weight % SiO_2 are included on these plots. Elements Rb, Y and Nb are in ppm.

Acknowledgments

This report is a contribution to NRCan's Targeted Geoscience Initiative Program (TGI). Support for this study was provided through the Porphyry-style Mineral Systems Project's '*Activity P-1.4: Temporal and spatial controls on the nature and distribution of porphyry-style deposits*'.

Alicia Moning is conducting a TGI-supported M.Sc. at Acadia University, Wolfville. Thanks to Perry MacKinnon for providing access to the Gillis Mountain drill core and Mick O'Neill for facilitating its transport to the core storage facility at Stellarton, Nova Scotia. This report benefited from the review of Benoit Dubé, Jean-Luc Pilote and Neil Rogers.

References

Barker, D. S., 1970. Compositions of granophyre, myrmekite, and graphic granite: Geological Society of America Bulletin, v. 81, p. 3339–3350.

Barr, S.M. and Macdonald, A.S., 1992. Devonian plutonism and related mineralization in southeastern Cape Breton Island; Atlantic Geology, v. 28, p. 101–113.

Barr, S.M. and O'Beirne, A.M., 1981. Petrology of the Gillis Mountain pluton, Cape Breton Island, Nova Scotia; Canadian Journal of Earth Sciences, v. 18, p. 394–404.

Barr, S.M., O'Reilly, G.A., and O'Beirne, A.M., 1982. Geology and geochemistry of selected granitoid plutons of Cape Breton Island; Nova Scotia Department of Mines and Energy Paper 82-1, 176 p.

Barr, S.M., Jamieson, R.A., and Raeside, R.P., 1992. Geology of northern Cape Breton Island, Nova Scotia; Geological Survey of Canada, Map 1752A, scale 1:100 000.

Barr, S.M., van Rooyen, D., and White, C.E., 2018. Granitoid plutons in peri-Gondwanan terranes of Cape Breton Island, Nova Scotia, Canada: new U-Pb (zircon) age constraints; Atlantic Geology, v. 54, p. 21–80.

Cormier, R.F., 1979. Rubidium/strontium isochron ages of Nova Scotian granitoid plutons; in Report of Activities 1978; Nova Scotia Department of Mines and Energy, Report 79-1, p. 143-147.

Dunning, G.R., Barr, S.M., Raeside, R.P., and Jamieson, R.A., 1990. U-Pb, zircon, titanite and monazite age in the Bras d'Or and Aspy Terranes of Cape Breton Island, Nova Scotia: Implications for igneous and metamorphic history; Geological Society of America Bulletin, v. 102, p. 322–330.

Frost, B.R. and Frost, C.D., 2008. A geochemical classification for feldspathic igneous rocks; Journal of Petrology, v. 49, p. 1955–1969.

Frost, B.R., Barnes, C.G., Collins, W.J., Arculus, R.J., Ellis, D.J., and Frost, C.D., 2001. A geochemical classification for granitic rocks; Journal of Petrology, v. 42, p. 2033–2048.

Hawkes, R.J., 1967. Exploration report on the McCormick Lake Granite, Noranda Exploration Company; Nova Scotia Department of Mines, Report 13-C-66, 10 p.

Hibbard, J.P., van Staal, C.R., Rankin, D.W., and Williams, H., 2006. Lithotectonic map of the Appalachian Orogen, Canada – United States of America; Geological Survey of Canada, "A" Series Map 2096A, 2 sheets, scale 1:1 500 000.

Hildebrand, R.S. and Whalen, J.B., 2015. Arc and slab-failure magmatism in Cordilleran batholiths II – The Cretaceous Peninsular Ranges Batholith of Southern and Baja California; in Stirring the Pot, A Celebration of the Career of Paul F. Hoffman, (ed.) J.B. Murphy, R.S. Hildebrand and G.P. Halverson; Geoscience Canada, Reprint Series v. 11, p. 239–267.

Horne, R.J., Dunning, G., and Jamieson, R., 2003. U-Pb age data for Belle Cote Road orthogneiss, Taylors Barren pluton, and Bothan Brook pluton, southern Cape Breton Highlands (NTS 11K/07, 11K/10, 11K/11): Igneous ages and

constraints on the age of host units and deformational history; in Mineral Resources Branch, Report of Activities 2002; Nova Scotia Department of Natural Resources Report 2003 -1, p 57–68.

Jamieson, R.A., Tallman, P., Marcotte, J.A., Plint, H.E., and Connors, K.A., 1987. Geology of the western-central Cape Breton Highlands, Nova Scotia; Geological Survey of Canada, Paper 87-13, 11 p.

Kirkham, R.V. and Soregaroli, A.E., 1975. Preliminary assessment of porphyry deposits in the Canadian Appalachians; in Report of Activities, Part A; Geological Survey of Canada, Paper 75-1A, p. 249–252.

LeMaitre, R.W., 1989. A Classification of Igneous Rocks and Glossary of Terms; Oxford: Blackwell, 193 p.

MacKinnon, P., 2008. Gillis Mountain Drill Program 2008; Assessment Report (Globex Mining Enterprises Inc.), Nova Scotia Department of Natural Resources, Report AR2008-234, 23 p plus appendices.

Moning, A., Barr, S.M., White, C.E., Sombini dos Santos, G., and van Rooyen, D., 2018. Factors controlling intrusion-related mineralization in Cape Breton Island, Nova Scotia: a comparison of Silurian-Devonian plutons in Avalonia and Ganderia; in Targeted Geoscience Initiative: 2017 Report of Activities, v. 1, (ed.) N. Rogers; Geological Survey of Canada, Open File 8358, p. 31–35.

O'Beirne, A.M., 1979. Geology of the Gillis Mountain Pluton, Cape Breton Island, Nova Scotia; M.Sc. thesis, Acadia University, Wolfville, Nova Scotia, 168 p.

O'Neill, M., 1996. Geology of the Leonard MacLeod Brook area, southern Cape Breton Highlands, Nova Scotia; M.Sc. thesis, Acadia University, Wolfville, Nova Scotia, 203 p.

Pearce, J.A., 1996. Sources and settings of granitic rocks; Episodes, v. 19, p. 120–125.

Pearce, J.A., Harris, N.W.B., and Tindle, A.G., 1984. Trace element discrimination diagrams for the tectonic interpretation of granitic rocks; Journal of Petrology, v. 25, p. 956–983.

Peccerillo, A. and Taylor, S.R., 1976. Geochemistry of the Eocene calc-alkaline volcanic rocks from Kastamonu area, northern Turkey; Contributions to Mineralogy and Petrology, v. 58, p. 63–81.

Streckeisen, A. and Le Maitre, R.W., 1979. A chemical approximation to the modal QAPF classification of the igneous rocks; Neues Jahrbuch für Mineralogie Abhandlungen, v. 136, p. 169–206.

Whalen, J.B. and Frost, C.D., 2013. The Q-ANOR diagram: A tool for the petrogenetic and tectonomagmatic characterization of granitic suites; in Abstracts, South-Central Section, Geological Society of America, Austin.

White, C.E., Sombini dos Santos, G., Moning, A.A., Barr, S.M., and van Rooyen, D., 2018. Geological and geochronological studies in the Middle River - Leonard MacLeod Brook area, central Cape Breton Island, Nova Scotia; in Geoscience and Mines Branch, Report of Activities 2016, (ed.) E.W. MacDonald and D.R. MacDonald; Nova Scotia Department of Natural Resources, Report ME 2018-001.

Reactivation of the Eastern Highlands Shear Zone, Cape Breton Island, Appalachian Orogen

N. Piette-Lauzière[1], R. Graziani[1], K.P. Larson[1] and D.A. Kellett[2]

[1]*Department of Earth and Environmental Science, University of British Columbia Okanagan, 3187 University Way, Kelowna, British Columbia V1V 1V7*

[2]*Geological Survey of Canada, 1 Challenger Drive, Dartmouth, Nova Scotia B2Y 4A2*

Abstract

The Eastern Highlands shear zone (EHSZ), in the Cape Breton Island portion of Appalachian Orogen, records two ductile deformation events (D_1 and D_2) from Early Silurian to Late Devonian. The Devonian is a key period for the economic endowment of the orogen during which intrusion-related mineralization may be associated with active and/or reactivated regional shear zones. The EHSZ is, therefore, a key structure to characterize shear zone reactivation and assess how this may have localized ore-bearing intrusive rocks. To accomplish this, we have first focused on linking local deformation events to the regional kinematic framework. New U-Pb geochronology of zircon from deformed specimens provide timing constraints on the two deformation events of the EHSZ. A rhyolite specimen with D_1 fabrics and a granite dyke specimen affected by D_2 deformation, both within the EHSZ, yielded weighted mean $^{206}Pb/^{238}U$ crystallization ages of 424 ± 4 Ma and 372 ± 4 Ma, respectively (2σ error). In addition, two foliated quartz-diorite specimens and a post-tectonic pegmatite specimen from the Chéticamp gneiss, west of the EHSZ, yielded weighted mean crystallization ages of 428 ± 9 Ma, 390 ± 8 Ma, and 391 ± 8 Ma, respectively. These new data constrain the EHSZ D_1 to between ca. 424 and 390 Ma, likely during the Acadian Orogeny. The EHSZ was then reactivated (D_2) after 372 Ma, which we attribute to the Neoacadian Orogeny. Considering the orientations and kinematics of the Neoacadian suture and the EHSZ, we interpret that the EHSZ was reactivated in a transpression-dominated environment.

Introduction

The Eastern Highlands shear zone (EHSZ) on Cape Breton Island (Fig. 1) is part of an orogen-wide shear system that is thought to have formed and variably reactivated during the multiple accretion events that formed the Appalachian Orogen (Lin, 1995). As a moderately well exposed shear zone with several described along-strike segments situated within a relatively well understood accretionary orogen, it is an ideal case study for understanding the role of crustal-scale shear zones as long-lived conduits for magmas and fluids in accretionary orogens. The EHSZ was examined extensively between 1990 and 2000, but little work has been completed since (Barr and Raeside, 1989; Dunning et al., 1990; Raeside and Barr, 1990; Lin, 1993, 1995, 2001; Chen et al., 1995). The paucity of available quantitative results to constrain the tectonic setting of the shear zone leaves three important questions unresolved: What was the tectonic setting, timing of deformation, and potential interactions with other contemporary shear zones? This report presents new zircon U-Pb geochronology results from pre- to post-kinematic lithologies that contribute to our understanding of the timing of deformation of the EHSZ.

Geological setting

Accretionary orogens develop along ocean-continent convergent margins. Their internal architecture results from multiple collisional events that incrementally add material to the continental margin, with some ancient examples terminating in a final continent-continent collision (Condie, 2007; Cawood et al., 2009). The Appalachian Orogen exemplifies this evolution, from the accretion of peripheral oceanic arcs and Ganderia, Avalonia, and Meguma terranes to the Laurentian margin during the Early to Middle Paleozoic, to a terminal collisional orogen between composite Laurentia and Gondwana (Hatcher, 2010; van Staal et al., 2015). The incremental accretion of crustal blocks to the Laurentian margin is associated with five distinct deformation and/or metamorphic episodes in Canada: the Taconic, Salinic, Acadian, Neoacadian, and Alleghanian orogenies (Fig. 1, 2; van Staal et al., 2009). Below we outline the events that, based on previous work, may have developed and (re)activated the EHSZ.

Salinic Orogeny

Gondwana-derived Ganderia forms a significant portion of Cape Breton Island. The accretion of Ganderia to the composite Laurentian margin resulted in the Salinic Orogeny, a complex sequence of collisional events that also involved the subduction and accretion of back-arc basins and associated volcanic arcs that separated Ganderia from Laurentia (Fig. 1, 2; van Staal et al., 2009). The suture is interpreted to correspond to the Bamford Brook-Liberty-Orrington fault system in northern New Brunswick, portions of the Wilkie Brook shear zone (WBSZ) in Cape Breton Island, and the Dog Bay Line in Newfoundland (van Staal et al., 2009). Recent in situ and step-heating $^{40}Ar/^{39}Ar$ muscovite geochronology has constrained the timing of the Salinic subduction and exhumation of the allochthonous volcanic units of the Bathurst Supergroup from ca. 452 to 437 Ma and the Ganderia collision at ca. 427 to 418 Ma in New Brunswick (Kellett et al., 2017).

Corresponding author: Nicolas Piette-Lauzière (nicolas.piette-lauzière @alumni.ubc.ca)

Piette-Lauzière, N., Graziani, R., Larson, K.P., and Kellett, D.A., 2019. Reactivation of the Eastern Highlands Shear Zone, Cape Breton Island, Appalachian Orogen; *in* Targeted Geoscience Initiative: 2018 report of activities, (ed.) N. Rogers; Geological Survey of Canada, Open File 8549, p. 295–305. https://doi.org/10.4095/313663

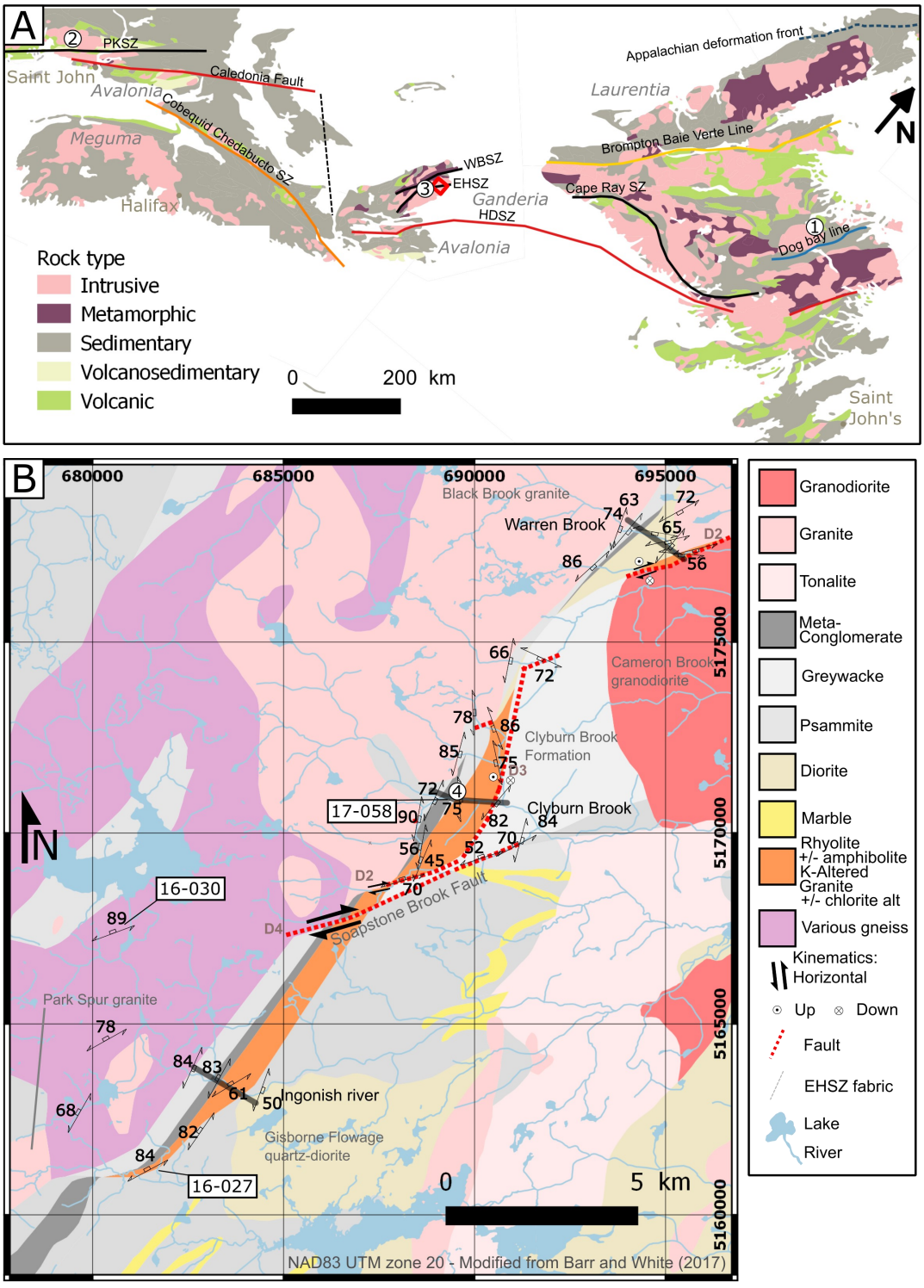

Figure 1. (a) Map of the Canadian Appalachian orogen excluding the Laurentian margin and some of its foreland with the principal Salinic (blue: Dog Bay line) Acadian (red: Hermitage Bay-Dover shear zone; HDSZ) and Neoacadian (orange: Cobequid Chedabucto shear zone) sutures, Caledonia fault, Cape-Ray shear zone, Eastern Highlands shear zone (EHSZ), Pocologan-Kennebecasis shear zone (PKSZ) Wilkie Brook shear zone (WBSZ), the location of the (1) Mount Peyton batholith, (2) Mount Pleasant deposit and (3) Inco showing. The red square indicates the position and orientation of map b. (b) Geological map of the EHSZ *modified from* Piette-Lauziere et al. (2017) with location of Figure 3 cross-sections, the Clyburn Brook gold veins (4) and outcrops 16-030, 16-027, 17-058. Maps *modified from* Wheeler et al. (1996), Barr and White (2017) and Hibbard et al. (2006).

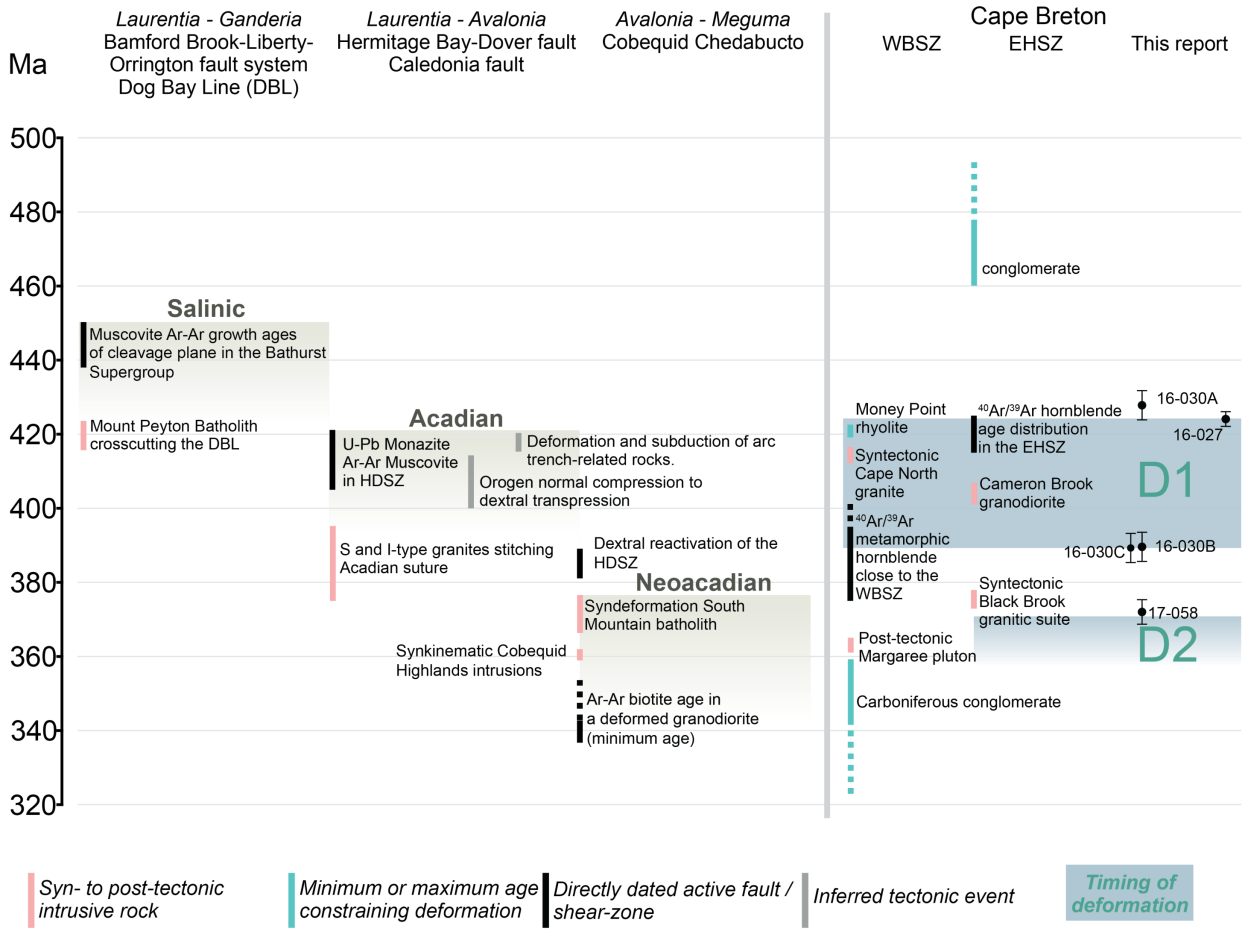

Figure 2. Published age constraints for Appalachian tectonic events compared to published and new age constraints from the Eastern Highlands shear zone (EHSZ) and Wilkie Brook shear zone (WBSZ) (Clarke and Halliday, 1980; Reynolds et al., 1989; Waldron et al., 1989; Keppie et al., 1992; Dallmeyer and Keppie, 1993; Chen et al., 1995; Benn et al., 1997; Lin, 2001; Pe-Piper et al., 2004; van Staal et al., 2009; Kellett et al., 2016, 2017). Abbreviations: CCSZ – Cobequid-Chedabucto shear zone; DBL – Dog Bay Line; HDSZ – Hermitage Bay Dover shear zone.

Acadian Orogeny

The collision of Gondwanan Avalonia with the amalgamated Laurentia-Ganderia margin resulted in the Acadian Orogeny (Fig. 1, 2). Contrasting isotopic signatures and tectonothermal histories mark the suture across the Caledonia fault in New Brunswick, the MacIntosh Brook fault in Cape Breton Island, and the Hermitage Bay-Dover shear zone (HDSZ) in Newfoundland (Fig. 1; van Staal et al., 2009). Dynamically recrystallized monazite and white mica in Dover fault sinistral mylonite indicate the bulk of Acadian deformation occurred between 422 and 405 Ma (Fig. 2; Kellett et al., 2016). Dextral transpression occurred along the eastern Ganderian margin during the Early Devonian (416–400 Ma) and perhaps as late as 385 Ma, resulting in west-verging folds and high-angle reverse faults (van Staal et al., 2009; Kellett et al., 2016).

Neoacadian Orogeny

The collision of Meguma, another Gondwana-derived microcontinent or promontory, with Avalonia, now part of the amalgamated Laurentian margin, initiated the Neoacadian Orogeny, which lasted from late Early Devonian to Early Carboniferous (van Staal et al., 2009). This event was accommodated along the dextral transpressive Coquebid-Chedabucto Fault (van Staal et al., 2009), the on-land expression of the Minas Fault zone that forms the suture between the two terranes (Murphy et al., 2011). An $^{40}Ar/^{39}Ar$ age of biotite in a deformed granodiorite is interpreted to constrain the last ductile movement of the shear zone at ca. 337 Ma (333 ± 4 Ma recalculated to 337 Ma; Pe-Piper et al., 2004, 2017).

Cape Breton Highlands

The Cape Breton Highlands form a plateau on Cape Breton Island that sits 300 to 500 m above sea level. The highlands comprise three distinct tectonic blocks: the Blair River Inlier to the northwest, which includes Precambrian rocks of Laurentian affinity, the Aspy terrane comprising Ordovician-Silurian volcano-sedimentary rocks and Devonian granitoids, and the Late Precambrian metasedimentary rocks and late Proterozoic dioritic to granitic plutons of the Bras d'Or terrane to the east (Barr and Raeside, 1989). The WBSZ and EHSZ are the main

structural breaks that separate the Blair River inlier from Aspy terrane and Aspy from Bras d'Or terrane, respectively.

The Wilkie Brook shear zone

The WBSZ is a sinistral strike-slip shear zone that juxtaposes the Precambrian Blair River inlier against Aspy terrane rocks in northwestern Cape Breton Highlands (Fig. 1; Dunning et al., 1990). Reusch and van Staal (2012) tentatively attributed the WBSZ to the main Salinic suture, the Dog Bay line (Fig. 1 of Reusch and van Staal, 2012), which has a minimum age constrained by the 420 ± 8 Ma Mount Peyton batholith (Williams et al., 1993). The WBSZ deformed the Money Point rhyolite (427 ± 4 Ma, U-Pb zircon) and is stitched by a syntectonic granitic pluton with a monazite $^{207}Pb/^{235}U$ crystallization age of 414 ± 3 Ma (Keppie et al., 1992). Therefore, at least some of the deformation of the WBSZ was nearly coeval with the 422 to 405 Ma Acadian deformation in the HDSZ, indicating it may have a complex reactivation history (Fig. 2; Kellett et al., 2016).

The Eastern Highlands shear zone

The EHSZ is a structural discontinuity in the central Cape Breton Highlands that has a complex displacement history (Fig. 1). Lin (1993) suggested that Aspy rocks sit unconformably on Bras d'Or lithologies: a conglomerate attributed to Aspy terrane includes clasts that yield crystallization ages consistent with a Bras d'Or terrane intrusive rock. From that interpretation, Lin (1993) suggested that Bras d'Or and Aspy have a basement-cover relationship and that they are both part of Ganderia (Fig. 1; Lin et al., 1994). Barr and Raeside (1989) and Reynolds et al. (1989) described the EHSZ as an east-over-west thrust whereas Lin (1993, 1995, 2001) described a multiphase structural history with two main deformation events, D_1 and D_2. Lin (1993, 1995, 2001) reported D_1 deformation characterized by steeply southeast-plunging mineral lineations and shear fabrics that indicate east-over-west thrusting with a minor sinistral transpressive component. According to Lin (1995), the minimum age of this event is constrained by the post-D_1 kinematic intrusion of the Black Brook granitic suite at ca. 375 Ma (Fig. 1, 2; Dunning et al., 1990; Yaowanoiyothin and Barr, 1991) and the maximum age by the deformation of conglomerate with a youngest zircon population of 462 ± 3 Ma (Chen et al., 1995). Hornblende $^{40}Ar/^{39}Ar$ ages range from ca. 561 Ma for a Bras d'Or terrane specimen geographically located ~16 km east of the EHSZ (Reynolds et al., 1989), to 415 ± 1 Ma within the EHSZ (Dallmeyer and Keppie, 1993). This difference in cooling age—young ages in the shear zone and progressively older cooling ages away from the shear zone into the interpreted hanging wall—has been interpreted to reflect east-over-west differential uplift across the EHSZ during D_1 deformation (Lin, 2001).

D_2 deformation occurred after intrusion of the Black Brook granitic suite and developed primarily along northeast-trending lithological contacts, in particular at the western edge of the metasedimentary Clyburn Brook formation (Fig.1; Lin, 1993, 1995). The associated mineral lineation (L2) plunges moderately to the southwest and locally northeast-striking zones of well-developed C-S-C' fabrics, mica fish, and drag folds indicate an oblique slip with west-side-up dextral kinematics. The maximum age of D_2 deformation is constrained by the Black Brook granitic suite at ca. 375 Ma (Fig. 2; Dunning et al., 1990; Yaowanoiyothin and Barr, 1991).

Mineralization

Numerous granite intrusions with related mineralization were emplaced during the Acadian and Neoacadian orogenies (van Staal, 2007; Bickerton et al., 2018). Notably, the Mount Peyton intrusive suite and the Mount Pleasant porphyry have well constrained tectonic settings (Fig.1). The Mount Peyton batholith is formed by co-magmatic granite and gabbro intrusive rocks (Strong, 1979) that crosscut the Dog Bay Line (Williams et al., 1993). The granite intrusion is interpreted to have formed through crustal melting during the gabbro emplacement (Strong and Dupuy, 1982) from 425 to 418 Ma (Sandeman et al., 2017). The intrusion-related mineralization includes gold, arsenic and antimony-bearing miarolitic cavities in monzogranite dykes intruding the Mount Peyton gabbro-diorite and associated gold, silver, arsenic and antimony-bearing veins (Sandeman et al., 2017). The timing of mineralization is interpreted to correspond to the crystallization age of the monzogranite dykes at 418 ± 2 Ma (U-Pb on zircon; Sandeman et al., 2017). The Mount Pleasant tungsten-molybdenum granite porphyry deposits were emplaced in an anorogenic or post-collisional, pre- to syn-extensional context following the Acadian Orogeny (Sinclair et al., 2006). The onset of mineralization has been constrained to ca. 370 ± 2 Ma by Re-Os dating of molybdenite (Thorne et al., 2013).

Locally, structurally-controlled gold veins have been reported in the EHSZ within the Kathy Road dioritic suite (Inco showing in Fig.1; Sangster et al., 1990; Mengel et al., 1991) and the MacMillan Flowage formation (Fig.1; Sangster et al., 1990). The Inco showing consists of a lens-shaped zone of sericitized felsic schists with 1-10 mm thick quartz veins. The quartz veins are interpreted to be late- to post-kinematic to the northwest-side-up mylonite fabric (Mengel et al., 1991). The gold veins in Clyburn Brook hosted by the the MacMillan Flowage formation appear to be east-west striking and highly deformed. They are interpreted by Sangster at al. (1990) to be older than the undeformed Cameron Brook granodiorite (U-Pb 402 ± 4 Ma; Dunning et al., 1990).

Observations

During the summers of 2016 and 2017, more than 200 outcrops were mapped on the EHSZ and WBSZ to characterize rock type, and the nature and extent of deformation. The work presented here builds upon observations summarized in Piette-Lauzière et al. (2018).

Lithologies

Ten rock types occur within the EHSZ (Fig. 3). The west side is bounded by quartz-diorite gneiss of the Chéticamp Lake gneiss, foliated granite of the Black Brook granitic suite and the massive Park Spur granite (379 ± 4 Ma, Dunning et al., 1990). Psammite, conglomerate, diorite, and rhyolite, with local tuff layers, form the core of the shear zone. The east side of the structure is bounded by an altered and brecciated granitoid, the 402 ± 4 Ma Cameron Brook granodiorite, metasedimentary rocks of the Clyburn Brook formation, and the 564 ± 5 Ma Gisborne Flowage quartz diorite (Dunning et al., 1990) (Fig. 1).

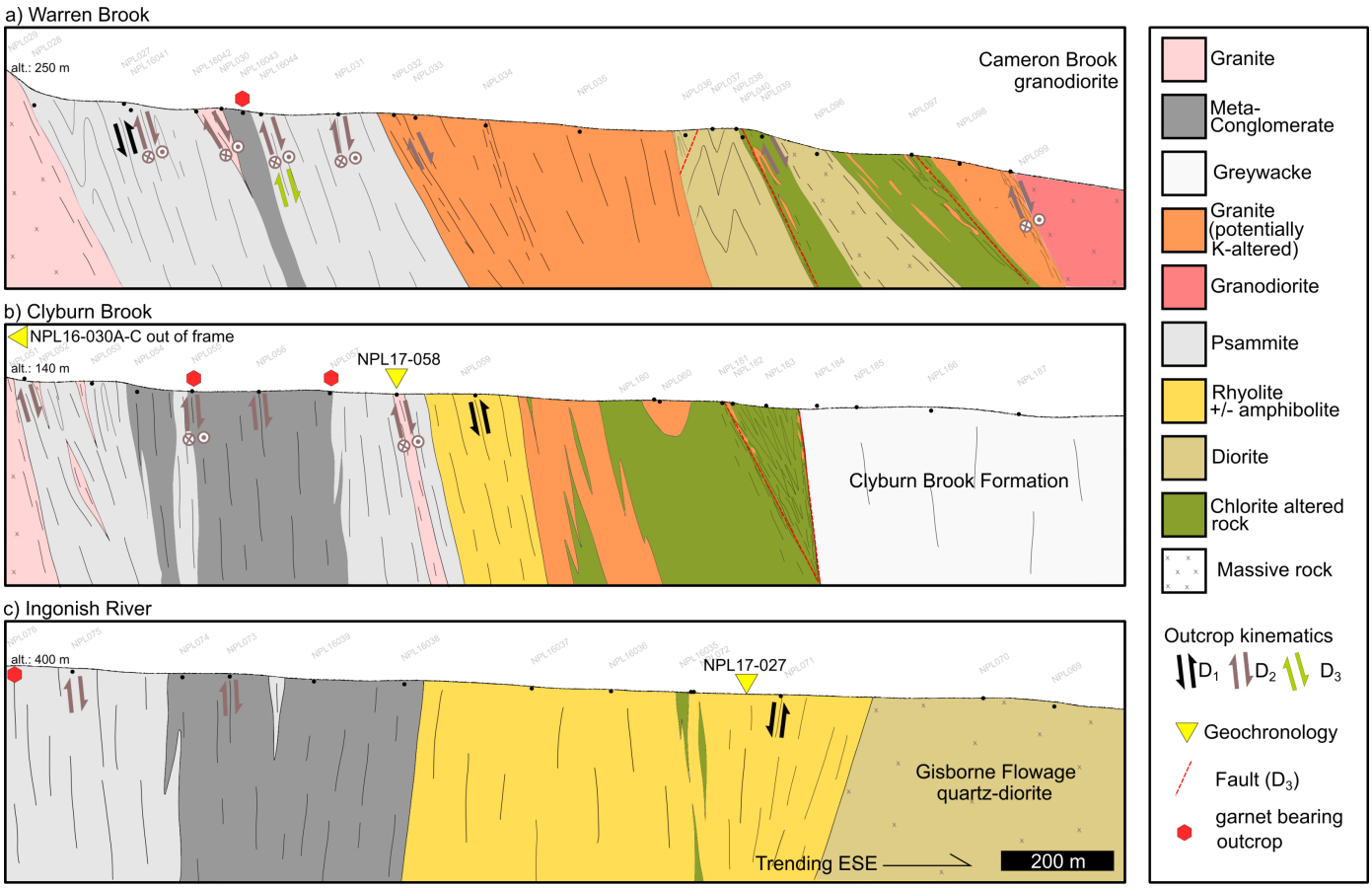

Figure 3. Cross-section of the Eastern Highlands shear zone (EHSZ) *modified from* Piette-Lauzière et al. (2018) with structural position of the specimens for geochronology along (a) Warren Brook, (b) Clyburn Brook, and (c) Ingonish River (c). *See* Figure 1b for cross-section locations.

Deformation

Three episodes of deformation have been identified within the EHSZ from field and thin section observations. The first episode, D_1, is associated with a subvertical fabric striking northeast-southwest, with a down-dip mineral lineation marked by oriented mica and amphibole, as well as by elongate conglomerate pebbles in the meta-conglomerate unit. C-S-C' fabrics and sigma-clasts indicate east-side-up kinematics as described by Lin (1995). The second deformational episode, D_2, is also associated with a northeast striking subvertical fabric, but its mineral lineation is marked by micas that plunge moderately to the southwest. East-northeast trending geological contacts along the Cameron Brook granodiorite are also dominated by D_2 fabrics oriented east-northeast and moderately dipping to the south-southeast with a mineral lineation plunging moderately to the south-southwest. C-S-C' fabrics indicate oblique, east-side-down dextral kinematics. A third deformational episode, D_3, is locally developed within chloritic-altered rock and brecciated potassic-altered granodiorite. This fabric forms northeast-oriented brittle-ductile faults within the main shear zone, with vertical slickenlines and elongation of K-altered granitic boudins. Sigma-shaped boudins indicate east-side-down kinematics. Locally, asymmetric crenulation of D_2 fabrics with sub-horizontal hinges indicate similar kinematics.

Methodology

Three variably deformed specimens from a single outcrop of the Chéticamp Lake gneiss were collected to assess the duration of D_1 deformation. The dominant lithology is a foliated quartz-diorite (Fig. 4: sample 16-030A) with quartz dynamic recrystallization microtextures that include subgrain rotation, bulging, and pinning (Fig. 5a). This unit is crosscut by a foliated quartz-diorite dyke (Fig. 3, 4: sample 16-030B) wherein quartz is characterized by chessboard-type extinction (Fig. 5b). Both lithologies are crosscut by a massive pegmatite dyke (Fig. 3, 4: sample 16-030C) in which quartz also displays chessboard -type extinction (Fig. 5c). The specimens were subjected to standard crushing and separation methods for zircon isolation at the University of California, Santa Barbara. Zircon grains were hand-picked, mounted in epoxy and polished to expose grain centres. The grains were then ablated with a 15 to 25 µm spot size using a Photon Machines 193 nm excimer laser and analyzed with a Nu Instrument Plasma HR-ES multi-collector inductively-coupled mass spectrometer (ICP-MS). Stern was used as the primary standard for U-Pb geochronology (Palin et al., 2013) and 44069 as the primary standard for trace elements measurements (Aleinikoff et al., 2006). Trebilcock (Tomascak et al., 1996) was treated as an unknown to assess the laboratory external error. Concordia plots and weighted means of results

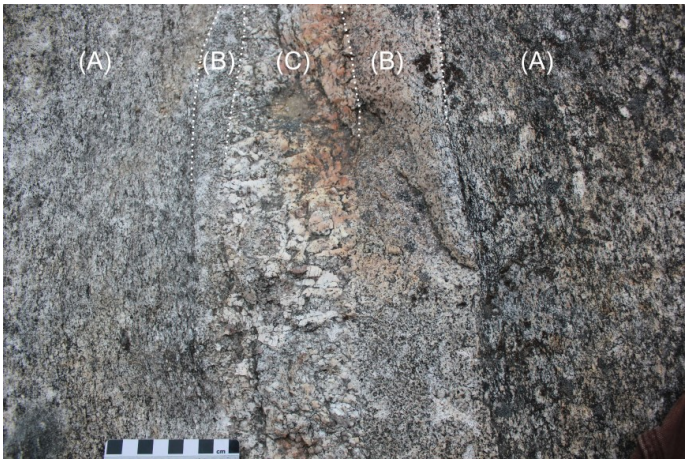

Figure 4. Field relationships between sampled rock units (A) 16-030A, (B) 030B, and (C) 030C (fully contained in A).

were plotted online using IsoplotR (Vermeesch, 2018) and calculated in Excel® using the Isoplot plugin (Ludwig, 1991).

Two additional specimens from the EHSZ were selected to constrain the maximum ages of D_1 and D_2 deformation. The first specimen is from a rhyolite within the shear zone (sample 16-027, Fig. 3), which is affected by D_1 deformation and the second is from a granite dyke that contains D_2 shear fabrics (sample 17-058, Fig. 3). Mineral separation was completed at Overburden Drilling Management Ltd. (Ottawa): disaggregation was performed using a Spark 2 Electric Pulse Disaggregator, heavy minerals were concentrated using a shaking table, and zircons concentrated with micro-panning. Zircon grains were then handpicked at the University of British Columbia and mounted in an epoxy puck, polished to expose grain mid-sections, and gold-coated at the Geological Survey of Canada geochronology laboratory (GSC) in Ottawa. Zircons were analyzed for U-Pb isotopes using the Sensitive High-Resolution Ion Microprobe (SHRIMP II) at the GSC. Temora (Black et al., 2003) was used as the primary standard for the U-Pb calibration, and 9910 Rambler secondary standard was used to assess the laboratory external error. An aperture of Kohler 50 was used and provided a 20 to 30 µm diameter analytical spot size at the sample surface.

Because ^{204}Pb measurements are possible on the SHRIMP, but not reliable on the ICP-MS, different common Pb corrections were used for each instrument. ^{204}Pb corrected $^{206}Pb/^{238}U$ ratios were used to calculate weighted mean ages for specimens 16-027 and 17-058 whilst ^{207}Pb corrected $^{206}Pb/^{238}U$ ratios were used to calculate weighted mean ages for specimens 16 -030A, B, and C.

Preliminary results

Tera-Wasserburg Concordia plots (Fig. 6-10; Tera and Wasserburg, 1972) show that most analyses of the youngest zircon plot in a concordant cluster in U-Pb space (Fig. 6–8). Zircon with dates plotting on Concordia, but off the main youngest cluster, are potentially inherited. Zircon analyses with

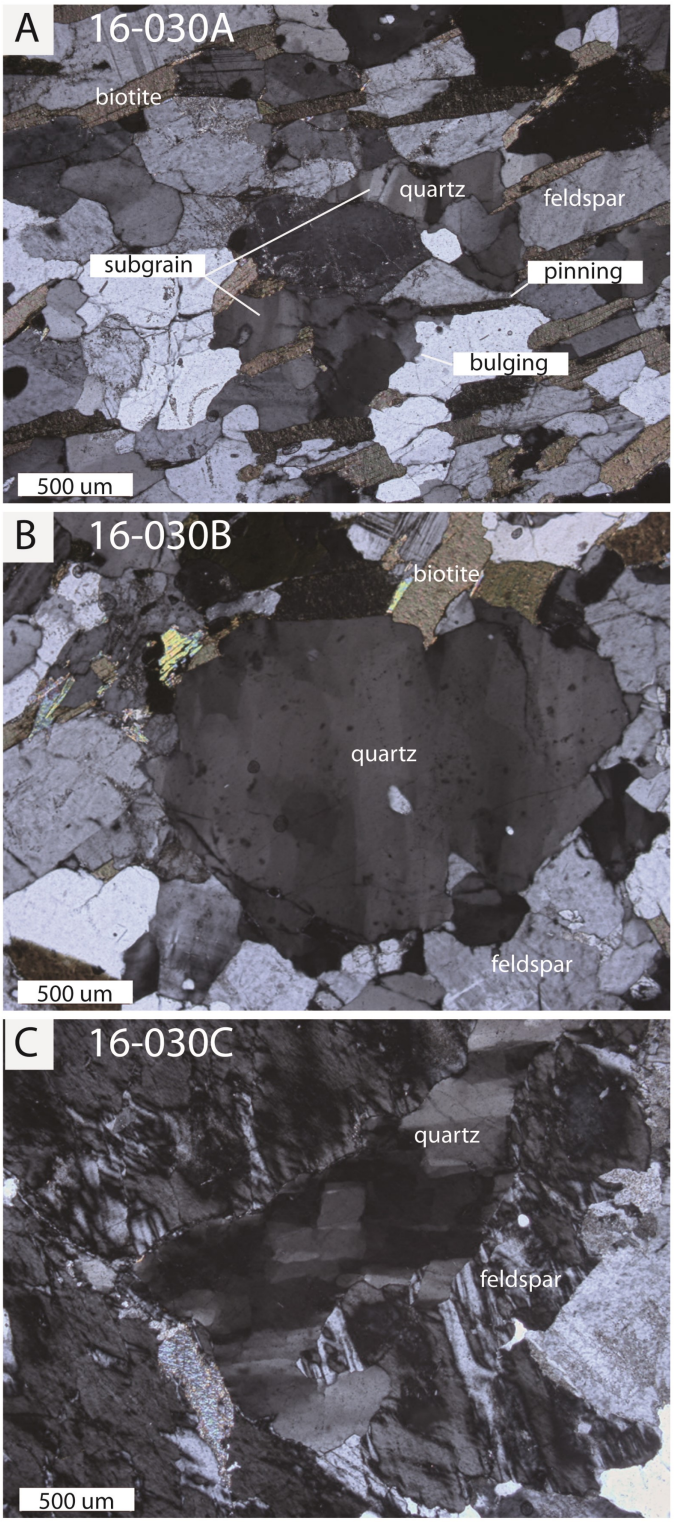

Figure 5. Quartz microfabrics in specimens 16-030A, B and C. a) Quartz subgrain rotation, bulging and pinned quartz grain against a biotite crystal. b and c) Chessboard-type quartz subgrain rotation.

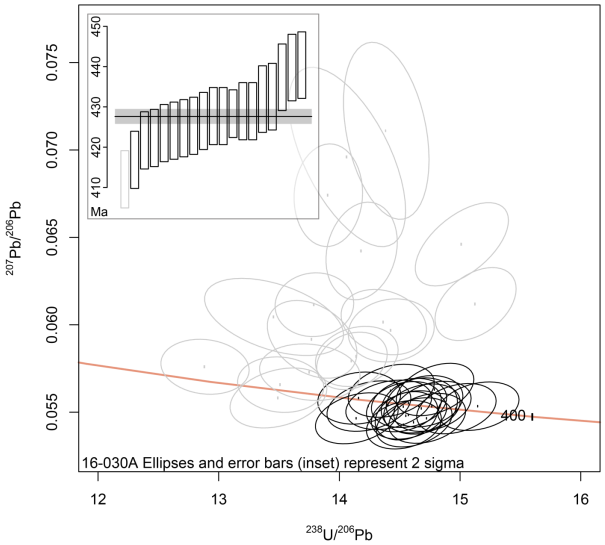

Figure 6. Tera-Wasserburg Concordia plot for specimen 16-030A Results for zircons that were discarded for excessive common lead or potential inheritance are shown in grey. Inset: ^{207}Pb-corrected $^{206}Pb/^{238}U$ zircon age distribution of remaining analyses with statistically rejected analyses in grey. Weighted mean age is 428 ± 9 Ma (n = 18, MSWD = 2.5).

excessive common lead were rejected for age determination. For specimen 16-030A, 17 core analyses yield a weighted mean age of 428 ± 9 Ma with a mean square weighted deviation (MSWD) of 2.5 (Fig. 6; note that all age results are reported with 2σ error). Similarly, 10 concordant core analyses of specimen 16-030B yield a weighted mean age of 390 ± 8 Ma with a MSWD of 10.4 (Fig. 7). Finally, 13 core analyses from

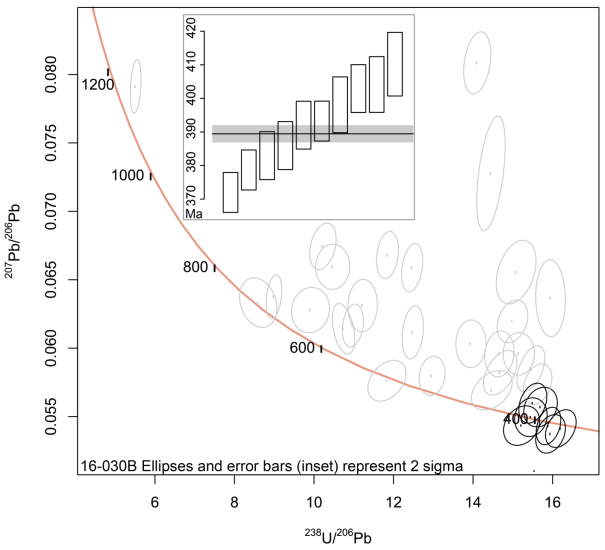

Figure 7. Tera-Wasserburg Concordia plot for specimen 16-030B. Results for zircons that were discarded as containing excessive common lead or potential inheritance are shown in grey. Inset: ^{207}Pb-corrected $^{206}Pb/^{238}U$ zircon age distribution. Weighted mean of 390 ± 8 Ma (n = 10, MSWD = 10.4).

16-030C yield a weighted mean age of 391 ± 8 Ma with a MSWD of 6.8 (Fig. 8). The weighted mean ages of specimens 16-030B and C have a high MSWD, which indicates that the weighted mean age has not been calculated on a single population and that these specimens might be younger. The U and REE composition of the zircon analyses from specimens 16-030A, B, and C plot along a trend that indicates progressive zircon enrichment in U, REE, and LREE with respect to the HREE (Fig. 11). This is consistent with the hypothesis that they may have crystallized from a common evolving source. For specimens 16-30A and B, we interpret the youngest significant population from each specimen to represent the timing of crystallization. Though the pegmatite dyke specimen (16-030C) yields an age indistinguishable from its host rock (16-030B), the analyses from this specimen have a distinct REE composition (Fig. 11) indicating that the zircons are likely not inherited and that the rock intruded nearly coeval with specimen 16-030B.

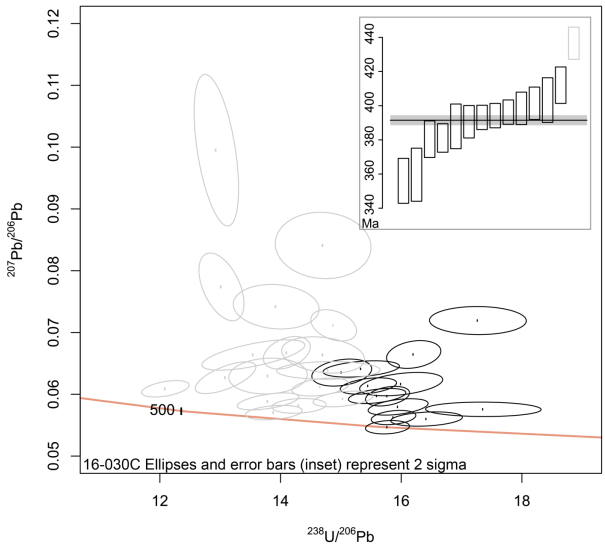

Figure 8. Tera-Wasserburg Concordia plot for specimen 16-030C. Results for zircons that were discarded for excessive common lead or potentially inherited are shown in grey. Inset: ^{207}Pb-corrected $^{206}Pb/^{238}U$ zircon age distribution with statistically rejected analyses in grey. Weighted mean age is 391 ± 8 Ma (n = 13, MSWD = 6.8).

For specimen 16-027, 53 grain cores were analyzed from which one discordant analysis and 4 inherited analyses (>550 Ma) were rejected before plotting (Fig. 8). The remaining 47 analyses yield a ^{204}Pb-corrected $^{206}Pb/^{238}U$ weighted mean age of 424 ± 4 Ma (external error of 0.85%) with a MSWD of 1.3 (Fig. 8). For specimen 17-058, 22 grain cores were analysed from which analyses for 8 highly radiogenic grains (U > 2000 ppm), one inherited analysis, and one discordant analysis were rejected. The remaining concordant analyses (Fig. 9) were used to calculate the ^{204}Pb-corrected $^{206}Pb/^{238}U$ weighted mean age of 372 ± 4 Ma with a MSWD of 1.7 (Fig. 9).

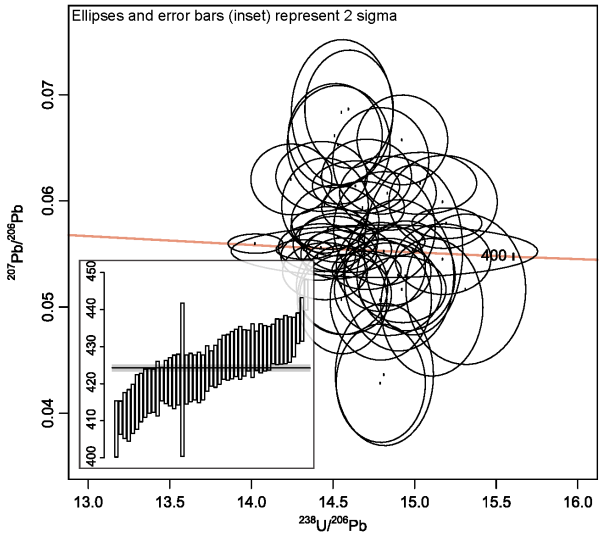

Figure 9. Tera-Wasserburg Concordia plot for specimen 16-027. Inset: ^{204}Pb-corrected $^{206}Pb/^{238}U$ zircon age distribution. Weighted mean age is 424 ± 4 Ma (n=46, MSWD = 1.3). Statistically rejected analyses are in grey.

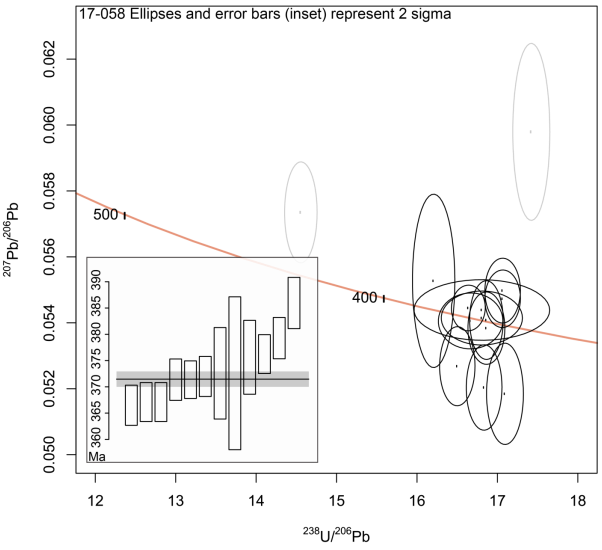

Figure 10. Tera-Wasserburg Concordia plot for specimen 17-058 with Results for zircons that were discarded for excessive discordance or potential inheritance are shown in grey. Inset: ^{204}Pb-corrected $^{206}Pb/^{238}U$ zircon age distribution. Weighted mean age is 372 ± 4 Ma (n=12, MSWD = 1.7).

Preliminary interpretations

Lin (1993) related the D_1 deformation, or formation of the EHSZ, to the Acadian Orogeny. With our new constraints on the timing of D_1 and D_2 deformation, we are now able to more conclusively relate the east-over-west kinematics in the EHSZ with sinistral strike-slip movement along the WBSZ (Keppie et al., 1992) and the HDSZ (Holdsworth, 1994) shown in Figure 1 (*see* also Fig. 2).

Preliminary U-Pb zircon geochronology results from pre- to post-kinematic (D_1 and D_2) samples presented in this report indicate that D_1 deformation in the EHSZ has a maximum age of 424 ± 4 Ma constrained by the rhyolite specimen with D_1 fabrics. The minimum age of D_1 deformation is constrained to ca. 390 Ma by the cogenetic quartz-diorite and pegmatite dyke crosscutting the Chéticamp gneiss (Fig. 4, lithologies B and C). These lithologies display chessboard-type quartz subgrains (Fig. 5b, c), which could represent near solidus strain (Lister and Dornsiepen, 1982; Mainprice et al., 1986). Due to the high MSWD of their calculated age, further work needs to be done to test if there is a younger zircon population for specimens 16-030B and C. The sinistral motion on the WBSZ has a maximum age of 427.5 ± 4.0 Ma constrained by the Money Point rhyolite (U-Pb on zircon, Keppie et al., 1992), is intruded by the 414 ± 3 Ma syntectonic Cape North granite (U-Pb on monazite, Keppie et al., 1992) and is crosscut by the 365.5 ± 3.3 Ma Margaree pluton (U-Pb on zircon, Sombini Dos Santos, 2018). Therefore, the D_1 movement along the EHSZ and the WBSZ were potentially coeval with east-side-up and sinistral kinematics, respectively. This deformation window coincides with the waning stages of the Salinic Orogeny, and the full duration of the Acadian Orogeny (Fig. 2 and references therein). The apparent sinistral reactivation of the Salinic WBSZ during D_1 deformation of the EHSZ is similar to the partitioning of the east-side-down and dextral kinematics observed along different strands of the Cape Ray shear zone by Dubé and Lauzière (1996).

The geochronology results also indicate that after 372 Ma the EHSZ alone reactivated with oblique east-side-down dextral kinematics (D_2) (Fig. 2, 10). This age likely corresponds to the Neoacadian Orogeny, which is broadly dated by 385 ± 4 Ma dextral reactivation of the Dover fault ($^{40}Ar/^{39}Ar$ muscovite: Kellett et al., 2016), the ca. 385 to 370 Ma syntectonic South Mountain Batholith that recorded regional stress during its cooling (Benn et al., 1997; Bickerton et al., 2018, 2019), and also by the syntectonic Hart Lake Byers Lake, Pleasant Hills, Cape Chignecto, and West Moose River plutons that crystallized in contact with the Cobequid-Chedabucto shear zone from 363 to 358 Ma (Doig et al., 1996). The minimum age for the Neoacadian ductile deformation is constrained by the minimum age of ductile deformation of the Cape Chignecto pluton at ca. 337 Ma ($^{40}Ar/^{39}Ar$ biotite age: Pe-Piper et al., 2004; 2017). Transpressional tectonics have been proposed, both at the local (Waldron et al., 1989) and regional scale (van Staal et al., 2009; Hatcher, 2010) for the Neoacadian Orogeny. Comparing the orientation and kinematics of the EHSZ to the CCSZ during this event, we suggest that reactivation of the EHSZ occurred in a transpression-dominated environment.

Future work

More zircon material will be processed to recalculate the ages of specimen 16-030B and C. In situ U-Pb monazite geochronology and $^{40}Ar/^{39}Ar$ geochronology of mica will provide further constraints on the timing of deformation and reactivation of the EHSZ and WBSZ. Additionally, the determination of vorticity axes information from quartz microfabrics of the EHSZ, WBSZ, and Pocologan-Kennebecasis shear zone (New Brunswick) will help to test if D_1 strain was partitioned between the EHSZ and WBSZ due to a promontory-promontory

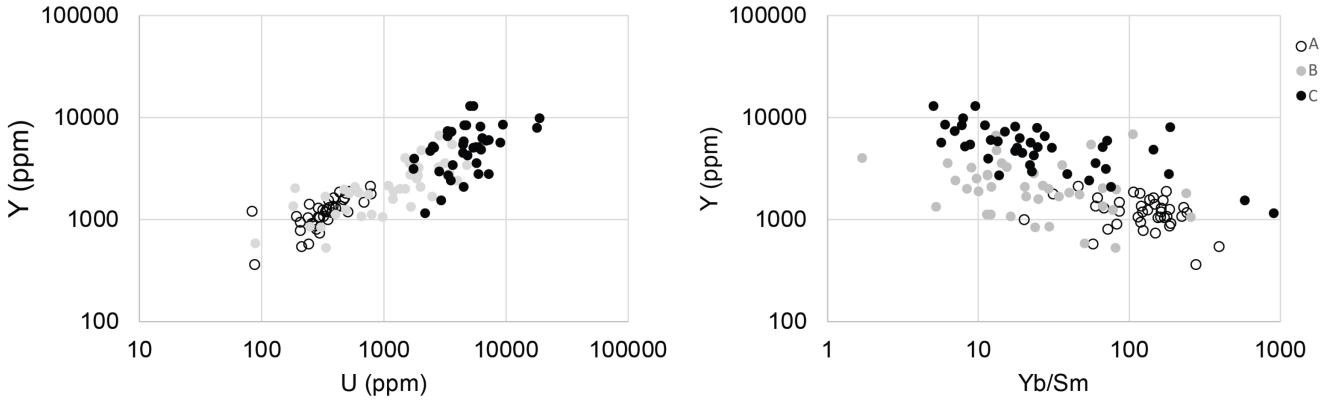

Figure 11. Y vs. U (left) and Y vs. Yb/Sm (right) plots of zircons grains from specimen 16-030 A, B and C.

collision during the Acadian Orogeny (Lin et al., 1994). Quartz crystallographic preferred orientation (CPO) plots and crystallographic orientations determined from Electron Backscatter Diffraction (EBSD) on specimens with D_2 fabrics will be used to determine the quartz vorticity axes, deformation temperatures for D_1 and D_2 deformation, and to test if D_2 EHSZ reactivation occurred in a transpression-dominated environment (Iacopini et al., 2008).

Conclusions

Our preliminary geochronology results indicate that D_1 deformation in the EHSZ occurred between ca. 424 and 390 Ma, based on a deformed rhyolite specimen that yielded a crystallization age of 424 ± 4 Ma and the crystallization ages of undeformed quartz-diorite and pegmatite dykes of 390 ± 8 Ma. The maximum age of D_2 is inferred to correspond to the crystallization age of a 372 ± 4 Ma granite dyke that displays D_2 fabrics. We interpret that D_1 deformation involved strain partitioning such that compression-dominated deformation of the EHSZ occurred concomitant with sinistral reactivation of the WBSZ during the Acadian Orogeny, and that the EHSZ was reactivated (D_2) during the Neoacadian Orogeny in a dextral, transpression-dominated environment. The results presented here confirm previous interpretations that the Black Brook granitic suite intruded the EHSZ between D_1 and D_2 deformation events. The transition from Acadian compression to extension appears to be a critical factor in the formation of the Mount Pleasant granite porphyry deposit at a similar time to the intrusion of the Black Brook granitic suite. Assuming that changes of tectonic environment from compression to extension contribute to form potentially ore-bearing magmas, we hypothesize that the change in shear zone kinematics contributes to form the space necessary to localize magmas in the upper crust. Therefore, this and further investigation into the precise timing and kinematics of reactivation of shear zones at the orogen scale may help determine the prospectivity of coeval intrusion-related mineralization.

Acknowledgments

This report is a contribution to NRCan's Targeted Geoscience Initiative Program (TGI-5). Support for this study was provided through the Porphyry-style Mineral Systems Project's '*Activity P-1.4: Temporal and spatial controls on the nature and distribution of porphyry-style deposits*'.

Nicolas Piette-Lauzière is conducting a TGI-supported doctoral study at University of British Columbia, Okanagan. The authors are indebted to John Cottle (UCSB) and Nicole Rayner (GSC) for assisting with U-Pb analyses and interpretation of results. Sandra Barr (Acadia), Chris White (NS-DNR), Deanne van Rooyen (CBU), Gabriel Sombini dos Santos (Acadia), and Rob Raeside (Acadia) are thanked for sharing their current research and helping our understanding of the Cape Breton Highlands geology; Donnelly Archibald and Caleb Grant (StFX) are thanked for bringing a different perspective to this project. Also, thanks go to James Bridgland and Gena Briand (CBH National Park) for facilitating our work in the Cape Breton Highlands National Park and field support, Zoïk Brault (UQAM) for his assistance in the field, and Jean-Philippe and Mary of the Maven Gypsy cottages in Wreck Cove for being great hosts. This report benefited from the review of Pedro Acosta-Góngora, Sébastien Castonguay and Neil Rogers.

References

Aleinikoff, J.N., Schenck, W.S., Plank, M.O., Srogi, L.A., Fanning, C.M., Kamo, S.L., and Bosbyshell, H., 2006. Deciphering igneous and metamorphic events in high-grade rocks of the Wilmington complex, Delaware: Morphology, cathodoluminescence and backscattered electron zoning, and SHRIMP U-Pb geochronology of zircon and monazite; Geological Society of America, Bulletin, v. 118, p. 39–64.

Barr, S.M. and Raeside, R.P., 1989. Tectono-stratigraphic terranes in Cape Breton Island, Nova Scotia: implications for the configuration of the northern Appalachian orogen; Geology, v. 17, p. 822–825.

Barr, S.M. and White, C.E., 2017. Bedrock Geology Map of the Cheticamp River Area, NTS Sheet 11/K/11, Inverness County, Nova Scotia; Nova Scotia Department of Natural Resources, Open File Map ME 2017-025, scale 1:50 000.

Benn, K., Horne, R.J., Kontak, D.J., Pignotta, G.S., Evans, N.G., 1997. Syn-Acadian emplacement model for the South Mountain Batholith, Meguma Terrane, Nova Scotia: magnetic fabric and structural analyses; Geological Society of America, Bulletin, v. 109, p. 1279–1293.

Black, L.P., Kamo, S.L., Allen, C.M., Aleinikoff, J.N., Davis,

D.W., Korsch, R.J., and Foudoulis, C., 2003. TEMORA 1: A new zircon standard for Phanerozoic U-Pb geochronology; Chemical Geology, v. 200, p. 155–170.

Bickerton, L., Kontak, D.J., Samson, I.M., Murphy, J.B., and Kellett, D.A., 2018. U-Pb geochronology of the South Mountain Batholith, Nova Scotia; *in* Targeted Geoscience Initiative: 2017 Report of Activities, (ed.) N. Rogers; Geological Survey of Canada, Open File 8358, p. 51–55.

Bickerton, L., Kontak, D.J., Samson, I.M., Murphy, J.B., and Kellett, D.A., 2019. SHRIMP U-Pb zircon dating of the South Mountain Batholith, Nova Scotia: Timing and duration of crystallization and evidence for inheritance; *in* Targeted Geoscience Initiative: 2018 report of activities, (ed.) N. Rogers; Geological Survey of Canada, Open File 8549, p. 307–320.

Cawood, P.A., Kröner, A., Collins, W.J., Kusky, T.M., Mooney, W.D., and Windley, B.F., 2009. Accretionary orogens through Earth history; Geological Society of London, Special Publication, v. 318, p. 1–36.

Condie, K.C., 2007. Accretionary orogens in space and time; Geological Society of America, Memoir 200, p. 145–158.

Chen, Y., Lin, S., and van Staal, C.R., 1995. Detrital zircon geochronology of a conglomerate in the northeastern Cape Breton Highlands: implications for the relationships between terranes in Cape Breton Island, the Canadian Appalachians, Canadian Journal of Earth Sciences, v. 32, p. 216–223.

Clarke, D.B. and Halliday, A.N., 1980. Strontium isotope geology of the South Mountain batholith, Nova Scotia; Geochimica et Cosmochimica Acta, v. 44, p. 1045–1058.

Dallmeyer, R.D. and Keppie, J.D., 1993. Ar-40/Ar-39 Mineral Ages from the Southern Cape-Breton Highlands and Creignish Hills, Cape-Breton Island, Canada - Evidence for a Polyphase Tectonothermal Evolution; Journal of Geology, v. 101, p. 467–482.

Doig, R., Murphy, J.B., Pe-Piper, G., and Piper, D.J.W., 1996. U-Pb geochronology of late palaeozoic plutons, Cobequid Highlands, Nova Scotia, Canada: Evidence for late Devonian emplacement adjacent to the Meguma-Avalon terrane boundary in the Canadian Appalachians; Geological Journal, v. 31, p. 179–188.

Dubé, B. and Lauzière, K., 1996. Structural evolution of a major fault zone: the Cape Ray Fault Zone, southwestern Newfoundland, Canada; Canadian Journal of Earth Sciences, v. 33, p. 199–215.

Dunning, G.R., Barr, S.M., Raeside, R.P., and Jamieson, R.A., 1990. U-Pb Zircon, Titanite, and Monazite Ages in the Bras-Dor and Aspy Terranes of Cape-Breton Island, Nova-Scotia - Implications for Igneous and Metamorphic History; Geological Society of America, Bulletin, v. 102, p. 322–330.

Hatcher, R.D., 2010. The Appalachian Orogen: A brief summary; *in* Rodinia to Pangea: The Lithotectonic Record of the Appalachian Region, (ed.) R.P Tollo, M.J. Bartholomew, J.P. Hibbard and P.M. Karabinos; Geological Society of America, Memoir 206, p. 1–19.

Hibbard, J.P., van Staal, C.R., Rankin, D.W., and Williams, H., 2006. Lithotectonic map of the Appalachian Orogen (North), Canada – United States of America; Geological Survey of Canada, Map 02042A, scale 1:1 500 000.

Holdsworth, R.E., 1994. Structural Evolution of the Gander Avalon Terrane Boundary - a Reactivated Transpression Zone in the NE Newfoundland Appalachians; Journal of the Geological Society of London, v. 151, p. 629–646.

Iacopini, D., Carosi, R., Montomoli, C., and Passchier, C.W., 2008. Strain analysis and vorticity of flow in the Northern Sardinian Variscan Belt: Recognition of a partitioned oblique deformation event; Tectonophysics, v. 446, p. 77–96.

Kellett, D.A., Warren, C., Larson, K.P., Zwingmann, H., van Staal, C.R., and Rogers, N., 2016. Influence of deformation and fluids on Ar retention in white mica: Dating the Dover Fault, Newfoundland Appalachians; Lithos, v. 254–255, p. 1–17.

Kellett, D.A., Van Staal, C., Wilson, R.A., and Rogers, N., 2017. The age of Salinic deformation constrained by $^{40}Ar/^{39}Ar$ dating of multiple cleavage domains: Bathurst supergroup, New Brunswick Appalachians; American Journal of Science, v. 317, p. 338–368.

Keppie, J.D., Dallmeyer, R.D., and Krogh, T.E., 1992. U-Pb and $^{40}Ar/^{39}Ar$ mineral ages from Cape North, northern Cape Breton Island: implications for accretion of the Avalon Composite Terrane; Canadian Journal of Earth Sciences, v. 29, p. 277–295.

Lin, S., 1993. Relationship between the Aspy and Bras d'Or "terranes" in the northeastern Cape Breton Highlands, Nova Scotia; Canadian Journal of Earth Sciences, v. 30, p. 1773–1781.

Lin, S., 1995. Structural evolution and tectonic significance of the Eastern Highlands shear zone in Cape Breton Island, the Canadian Appalachians; Canadian Journal of Earth Sciences, v. 32, p. 545–554.

Lin, S., 2001. $^{40}Ar/^{39}Ar$ age pattern associated with differential uplift along the Eastern Highlands shear zone, Cape Breton Island, Canadian Appalachians; Journal of Structural Geology, v. 23, p. 1031–1042.

Lin, S., Van Staal, C.R., and Dubé, B., 1994. Promontory-promontory collision in the Canadian Appalachians; Geology, v. 22, p. 897–900.

Lister, G.S. and Dornsiepen, U.F., 1982. Fabric transitions in the Saxony granulite terrain; Journal of Structure Geology, v, 4, p. 88–9.

Ludwig, K.R., 1991. ISOPLOT a plotting and regression program for radiogenic-isotope data, version 2.53; United States Geological Survey, Open file report 91-445.

Mainprice, D., Bouchez, J.L., Blumenfeld, P., and Tubià, J.M., 1986. Dominant c slip in naturally deformed quartz: Implications for dramatic plastic softening at high temperature; Geology, v. 14, p. 819–822.

Mengel, F., Godue, R., Sangster, A., Dubé, B., and Lynch, G., 1991. A progress report on the structural control of gold mineralizations in the Cape Breton Highlands; *in* Current Research, Part D; Geological Survey of Canada, Paper 91-1D, p. 117–127.

Mohammadi, N., Fyffe, L., McFarlane, C.R.M., Thorne, K.G., Lentz, D.R., Charnley, B., Branscombe, L., and Butler, S., 2017. Geological relationships and laser ablation ICP-MS U-

Pb geochronology of the Saint George batholith, southwestern New Brunswick, Canada: Implications for its tectonomagmatic evolution; Atlantic Geology, v. 53, p. 207–240.

Murphy, J.B., Waldron, J.W.F., Kontak, D.J., Pe-Piper, G., and Piper, D.J.W., 2011. Minas Fault Zone: Late Paleozoic history of an intra-continental orogenic transform fault in the Canadian Appalachians; Journal of Structural Geology, v. 33, p. 312–328.

Pe-Piper, G., Reynolds, P.H., Nearing, J., and Piper, D.J.W., 2004. Early Carboniferous deformation and mineralization in the Cobequid shear zone, Nova Scotia; an $^{40}Ar/^{39}Ar$ geochronology study; Canadian Journal of Earth Science, v. 41, p. 1425–1436.

Palin, R.M., Searle, M.P., Waters, D.J., Parrish, R.R., Roberts, N.M.W., Horstwood, M.S.A., Yeh, M.W., Chung, S.L., and Anh, T.T., 2013. A geochronological and petrological study of anatectic paragneiss and associated granite dykes from the Day Nui Con Voi metamorphic core complex, North Vietnam: Constraints on the timing of metamorphism within the Red River shear zone; Journal of Metamorphic Geology, v. 31, p. 359–387.

Pe-Piper, G., Piper, D.J.W., Papoutsa, A., Wisen, J., 2017. Fractured latest Devonian granites of the West Moose River pluton along the Cobequid Shear Zone, Nova Scotia: implications for regional mineralization; Canadian Journal of Earth Science, v. 54, p. 1119–1137.

Piette-Lauzière, N., Larson, K.P., and Kellett, D.A., 2018. Field mapping of the Eastern Highlands shear zone, Cape Breton Island, Nova Scotia; *in* Targeted Geoscience Initiative: 2017 Report of Activities, Volume 1, (ed.) N. Rogers; Geological Survey of Canada, Open File 8358, p. 23–29.

Raeside, R.P. and Barr, S.M., 1990. Geology and tectonic development of the Bras d'Or suspect terrane, Cape Breton Island, Nova Scotia; Canadian Journal of Earth Sciences, v. 27, p. 1371–1381.

Reusch, D.N. and van Staal, C.R., 2012. The Salinic Orogeny in northern New Brunswick: geochronological constraints and implications for Silurian stratigraphic nomenclature; Canadian Journal of Earth Science, v. 49, p. 222–238.

Reynolds, P.H., Jamieson, R.A., Barr, S.M., and Raeside, R.P., 1989. An $^{40}Ar/^{39}Ar$ study of the Cape Breton Highlands, Nova Scotia: thermal histories and tectonic implications; Canadian Journal of Earth Sciences, v. 26, p. 2081–2091.

Sandeman, H.A.I., Dunning, G.R., Mccullough, C.K., and Peddle, C., 2017. U-Pb Geochronology, petrologenetic relationships and intrusion-related precious-metal mineralization in the Northern Mount Peyton Intrusive suite: Implications for the origin of the Mount Peyton trend, Central Newfoundland (NTS 2D/04); *in* Current Research report 17-1, (ed.) C.P.G. Pereira, and D.G. Walsh; Newfoundland and Labrador Department of Natural Resources, p. 189–217.

Sangster, A.L., Thorpe, R.I., and Chatterjee, A.K., 1990. A reconnaissance lead isotopic study of mineral occurrences in pre-Carboniferous basement rocks of northern and central Cape Breton Island, Nova Scotia; *in* Mineral Deposit Studies in Nova Scotia, Volume I, (ed) A.L. Sangster; Geological Survey of Canada, Paper 90-8, p. 101–114.

Sinclair, W.D., Kooliman, G.J.A., Martin, D.A., and Kjarsgaard, I.M., 2006. Geology, geochemistry and mineralogy of indium resources at Mount Pleasant, New Brunswick, Canada; Ore Geology Reviews, v. 28, p. 123–145.

Strong, D., 1979. The Mount Peyton Batholith, central Newfoundland: a bimodal calc-alkaline suite; Journal of Petrology, v. 20, p. 119–138.

Strong, D. and Dupuy, C., 1982. Rare earth elements in the bimodal Mount Peyton batholith: evidence of crustal anatexis by mantle-derived magma; Canadian Journal of Earth Sciences, v. 19, p. 308–315.

Sombini Dos Santos, G., 2018. Petrology, geochemistry, age, and tectonic setting of the Margaree pluton, Aspy terrane, Cape Breton Island, Nova Scotia; M.Sc. thesis, Acadia University, Wolfville, Nova Scotia, 230 p.

Tera, F. and Wasserburg, G.J., 1972. U-Th-Pb systematics in three Apollo 14 basalts and the problem of initial Pb in lunar rock; Earth Planetary Science Letters, v. 14, p. 281–304.

Tomascak, P.B., Krogstad, E.J., and Walker, R.J., 1996. U-Pb monazite geochronology of granitic rocks from Maine: implications for Late Paleozoic tectonics in the Northern Appalachians; Journal of Geology, v. 104, p. 185–195.

van Staal, C.R., 2007. Pre-Carboniferous tectonic evolution and metallogeny of the Canadian Appalachian; *in* Mineral Deposits of Canada: A Synthesis of Major Deposit-Types, District Metallogeny, the Evolution of Geological Provinces, and Exploration Methods, (ed.) W.D. Goodfellow; Geological Association of Canada, Mineral Deposits Division, Special Publication No. 5, p. 793–818.

van Staal, C.R., Whalen, J.B., Valverde-Vaquero, P., Zagorevski, A., and Rogers, N., 2009. Pre-Carboniferous, episodic accretion-related, orogenesis along the Laurentian margin of the northern Appalachians; *in* Ancient Orogens and Modern Analogues, (ed.) J.B. Murphy, J.D. Keppie and A.J. Hynes; Geological Society of London, Special Publication 327, p. 271–316.

Vermeesch, P., 2018. IsoplotR: a free and open toolbox for geochronology; Geoscience Frontiers, v. 9, p. 1470–1493.

Waldron, J.W.F., Piper, D.J.W., and Pe-Piper, G., 1989. Deformation of the Cape Chignecto pluton, Cobequid Highlands, Nova Scotia: thrusting at the Meguma-Avalon boundary; Atlantic Geology, v. 25, p. 51–62.

Waldron, J.W.F., Barr, S.M., Park, A.F., White, C.E., and Hibbard, J., 2015. Late Paleozoic strike-slip faults in Maritime Canada and their role in the reconfiguration of the northern Appalachian orogen; Tectonics, v. 34, p. 1661–1684.

Wheeler, J.O., Hoffman, P.F., Card, K.D., Davidson, A., Sanford, B.V., Okulitch, A.V., and Roest, W.R., 1996. Geological Map of Canada; Geological Survey of Canada, Map 1860A, scale 1:5 000 000.

Williams, H., Currie, K.L., and Piasecki, M.A.J., 1993. The Dog Bay Line: a major Silurian tectonic boundary in northeast Newfoundland; Canadian Journal of Earth Sciences, v. 30, p. 2481–2494.

Yaowanoiyothin, W. and Barr, S.M., 1991. Petrology of the Black Brook granitic suite, Cape Breton island, Nova-Scotia; The Canadian Mineralogist, v. 29, p. 499–515.

SHRIMP U-Pb zircon dating of the South Mountain Batholith, Nova Scotia: Timing and duration of crystallization and evidence for inheritance

L. Bickerton[1], D.J. Kontak[1], I.M. Samson[2], J.B. Murphy[3] and D.A. Kellett[4]

[1]*Harquail School of Earth Sciences, Laurentian University, Sudbury, Ontario P3E 2C6*
[2]*Department of Earth and Environmental Sciences, University of Windsor, Windsor, Ontario N9B 3P4*
[3]*Department of Earth Sciences, St. Francis Xavier University, Antigonish, Nova Scotia B2G 2W5*
[4]*Geological Survey of Canada, 1 Challenger Drive, Dartmouth, Nova Scotia B2Y 4A2*

Abstract

The South Mountain Batholith (SMB) is the largest (7300 km^2) granitoid body in the Appalachian Orogen. It is a composite peraluminous intrusion with early stage biotite-granodiorite to biotite-monzogranite and later leucomonzogranite to leucogranite plutons. The latter are associated with subeconomic to economic polymetallic mineral deposits, including the past-producing (1985–1992) East Kemptville Sn-Cu-Zn-Ag(-In) deposit.

Sensitive High-Resolution Ion Microprobe (SHRIMP) analyses of zircon were used to constrain the timing of emplacement for phases across the SMB and to investigate potential sources of contamination to the magma. Zircon from four granodiorite to monzogranite samples and one from a more evolved leucogranite were analyzed to complement our previous SHRIMP U-Pb zircon dating of the more evolved phases (ca. 377–370 Ma). The granodiorite samples yielded ages between 384.9 ± 4.4 Ma and 375.9 ± 4.5 Ma whereas the leucogranite yielded an age of 377.7 ± 5.2 Ma (2σ errors). A late monzogranitic phase on the edge of the SMB also yielded an age of 367.7 ± 4.0 Ma. Collectively, the data sets indicate an apparent span of ca. 11 to 23 Ma for emplacement and assembly of the SMB, but with most ages between ca. 378 to 370 Ma.

The abundance of xenocrystic zircon cores varies throughout the complex; from common in less evolved granodiorite samples to rare in the more evolved leucogranite samples. The relative age population density pattern for the inherited cores is very similar to the detrital zircon signature for the upper stratigraphy of the Meguma Supergroup that hosts the SMB.

Introduction

The South Mountain Batholith (SMB) is a composite peraluminous intrusive complex of approximately 7300 km^2 located in southwest Nova Scotia. The batholith hosts numerous polymetallic (Sn, W, Mo, Cu, Ta, Nb, Zn) mineral occurrences, including the past-producing Sn-Zn-Cu-Ag(-In) East Kemptville deposit (MacDonald et al., 1992; MacDonald, 2001).

Tin-W with associated polymetallic base-metal (e.g. Cu, Zn, In) mineralization occurs as a range of deposit types (greisen-hosted, vein-hosted, skarn-hosted, porphyry-style, pegmatite) that are typically hosted in proximal evolved peraluminous granitic rocks (e.g. Taylor 1979). The nature and origin of enrichment for these metals in the granitic magmas remains contentious. Were Sn and W originally enriched in the crust that was subsequently assimilated/melted into the peraluminous magma (e.g. Lehmann, 1990; Romer and Kroner, 2016), or did mantle-derived melts contribute to and hybridize a magma that subsequently fractionated these elements into economic concentrations (e.g. Schuiling, 1967; Sillitoe, 1974)?

Studies on the setting and the petrology of the SMB and its proximal environment (e.g. Clarke et al., 2004, 2009; MacDonald and Clarke, 2017, and references therein) have shown 1) that the primary magma was significantly contaminated prior to undergoing extensive fractionation, and 2) magmatism was both mafic and felsic, with magma-mingling and hybridization having occurred along the perimeter of the SMB and in proximal satellite plutons (e.g. Tate and Clarke, 1997; Tate et al., 1997). The SMB represents, therefore, a hybrid product of contaminated, mantle-derived magmas. It remains to be determined whether or how the hybrid character of the magma relates to mineralization within the SMB. Another relevant issue is the duration of magmatism, recorded by the absolute age of the plutons that collectively make up the batholith. At present it is unclear whether the SMB represents episodic intrusive events or a single protracted magmatic event.

To address these issues, a detailed petrochronological study of the SMB using zircon (i.e. dating, in situ trace element chemistry, $\delta^{18}O$) was undertaken as part of the doctoral thesis of L. Bickerton. The initial results of SHRIMP U-Pb zircon dating revealed crystallization ages of an early granodiorite phase of the SMB to be 380.9 ± 3.0 Ma and later leucogranite phases to range between 376 ± 3 and 372.8 ± 3.0 Ma (Bickerton et al., 2018a). This indicated a significant span (ca.

Corresponding author: Luke Bickerton (lbickerton@laurentian.ca)

Bickerton, L., Kontak, D.J., Samson, I.M., Murphy, J.B., and Kellett, D.A., 2019. SHRIMP U-Pb zircon dating of the South Mountain Batholith, Nova Scotia: Timing and duration of crystallization and evidence for inheritance; *in* Targeted Geoscience Initiative: 2018 report of activities, (ed.) N. Rogers; Geological Survey of Canada, Open File 8549, p. 307–320. https://doi.org/10.4095/313664

5–15 Ma) between the crystallization of the oldest phase and the youngest phase in the SMB, representing a residence time that is problematic for a single intrusive event. In this contribution, new U-Pb SHRIMP zircon age data for samples from the earliest granodiorite phases of the SMB are reported, as well as age data for a single sample from a more evolved part of the batholith. We report the first ages for xenocrystic phases of the SMB, which permits, therefore, some insight into the nature of the contaminant and assessment of its relevance to the emplacement of the batholith and its metallogeny.

Regional geological setting

The geology of southern Nova Scotia is dominated by the metasedimentary rocks of the Meguma Supergroup and abundant peraluminous granitoid intrusive rocks comprising the SMB. The Meguma rocks, which include the Goldenville and Halifax groups, are an Ediacaran to Early Ordovician sequence of interbedded metasandstone, metasiltstone, and slate that, in this region, is unconformably overlain by a Silurian-Devonian sequence, which includes the volcanic rocks of the White Rock Formation (White, 2010). The Meguma Supergroup and overlying White Rock Formation make up the Meguma terrane, the most outboard of several Gondwana-derived terranes that accreted to the eastern Laurentian margin during the Paleozoic (i.e. Ganderia, Avalonia and Meguma; Fig. 1, inset; van Staal et al., 1998, 2009). Meguma terrane rocks were deformed during the ca. 400 Ma Neoacadian orogeny (van Staal, 2007) that recorded dextral oblique translation along the eastern composite Laurentian margin (e.g. Hicks et al., 1999). The Avalonia volcanic arc terrane, which had accreted to Laurentia during the Acadian orogeny (ca. 421–417 Ma), is thought to have underthrust the converging Meguma terrane at this time (e.g. van Staal et al., 2009). During the later accretionary stages of the

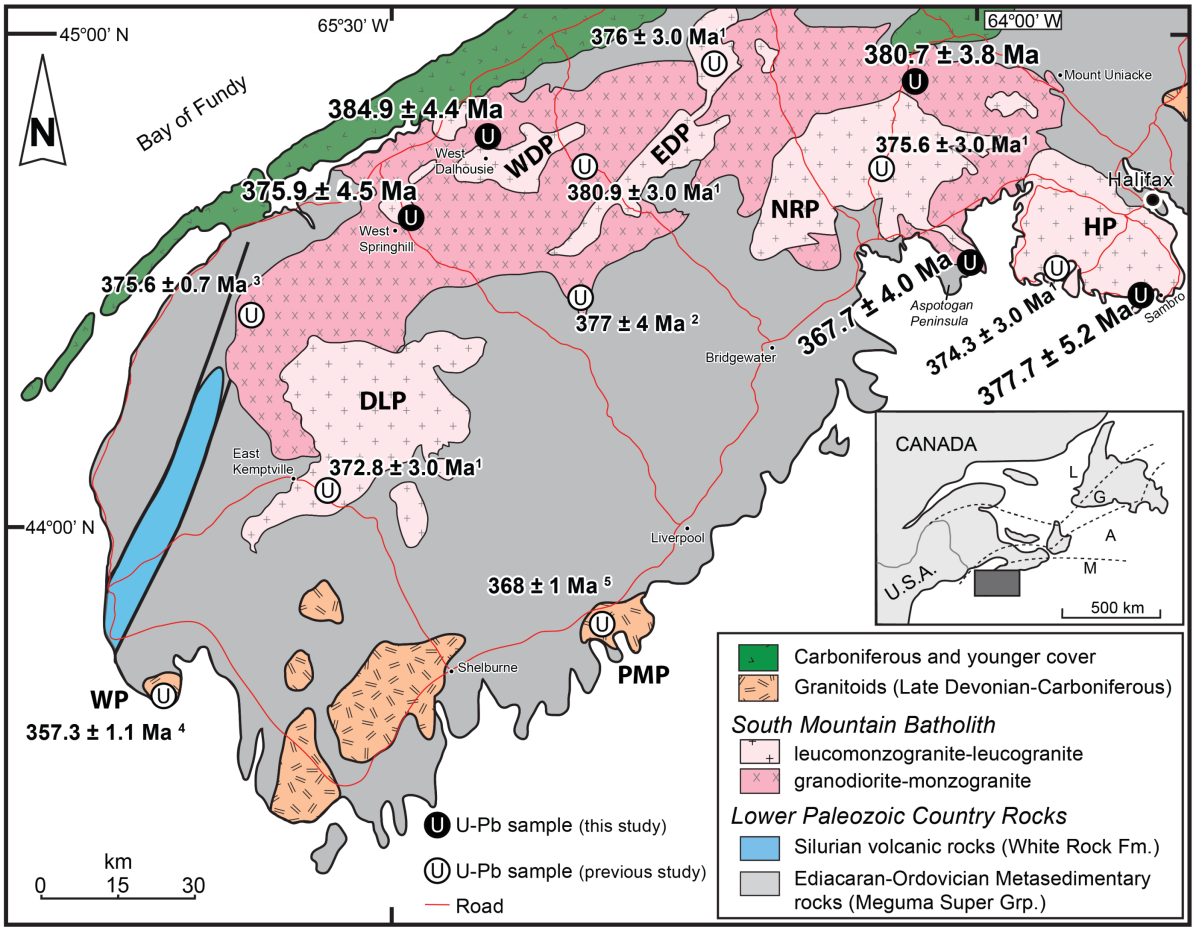

Figure 1. Regional bedrock geology of southwestern Nova Scotia (modified after Bickerton et al., 2018a, and references therein. Pink granitoids are the various phases of the South Mountain Batholith: the darker shade for the less evolved granodiorite and the lighter shade for more evolved plutons (abbreviations: DLP – Davis Lake Pluton; EDP – East Dalhousie Pluton; HP – Halifax Pluton; NRP – New Ross Pluton; and WDP – West Dalhousie Pluton). The inset shows the location of the study area in the northeastern Appalachians with regional tectonic boundaries: A – Avalonia; G – Ganderia; L – Laurentian margin; M – Meguma. Also shown are the locations of the U-Pb zircon geochronology samples from this study (black symbols) and previous studies (white symbols: 1 – Bickerton et al. 2018a; 2 – Keppie et al., 1993; 3 – unpub. U-Pb data, 2015; 4 – MacLean et al., 2004; 5 – Currie et al., 1998).

Neoacadian orogenic event, the Meguma terrane was intruded by voluminous metaluminous to peraluminous granitoids, the largest of which is the SMB. Field and geomagnetic studies indicate that basement faults controlled the emplacement of the SMB and were also important conduits for the later focusing of mineralizing fluids (e.g. Horne et al., 1992; Kontak, 1994; Benn et al., 1997; MacDonald, 2001).

Detailed mapping of the SMB (MacDonald, 2001) revealed that it is composite in nature, with an outer zone of granodiorite that was intruded by five more evolved leucogranitoid plutons (Fig. 1). From west to east, these evolved bodies are the Davis Lake Pluton (DLP), West Dalhousie Pluton (WDP), East Dalhousie Pluton (EDP), New Ross Pluton (NRP) and Halifax Pluton (HP). Prior to this study, four of five crystallization ages of these evolved plutons have been constrained based on U-Pb zircon dating (376.0 ± 3.0 to 372.8 ± 3.0 Ma: Bickerton et al., 2018a).

There are many centres of mineralization in the SMB that vary in both elemental association (i.e. Sn, W, U, Ta, Cu) and style of mineralization (e.g. pegmatites, veins, greisens). The most significant of these centres is the East Kemptville Sn-Zn-Cu-Ag(-In) deposit, which is hosted by the 800 km^2 zoned DLP. The nature and origin of this deposit, which has been the focus of many previous studies (e.g. Richardson, 1988; Kontak, 1990a, b, 1991, 1994; Halter et al., 1996, 1998; Kontak et al. 2001), is being re-evaluated as part of the current project (Bickerton et al., 2017a, b, 2018a, b). Lithophile-element-enriched deposits similar in age to the East Kemptville deposit are found elsewhere in the Appalachians and are hosted by late Devonian plutons that do not intrude the Meguma terrane; such as at Mount Pleasant, New Brunswick (hosted by Avalonia), and the Ackley granite, Newfoundland (hosted by Ganderia-Avalonia; van Staal, 2007; *see* Kontak et al., 2013, for a recent summary).

Analytical techniques

Zircon grains were separated from five approximately 10 kg rock samples using conventional methods of crushing followed by gravity and electromagnetic concentration. Zircon grains in the concentrates, which ranged from greater than 10 000 grains in the less evolved granodiorite samples to approximately 5000 grains in the more evolved leucocratic samples, were hand-picked and mounted in epoxy resin together with the zircon reference materials Temora-2 (primary), z9910, and z6266. The grain mount was subsequently polished to reveal approximate zircon midsections and imaged using back-scattered electron (BSE) and cathodoluminescence (CL) on a scanning electron microscope (SEM) at the Geological Survey of Canada, Ottawa. Abundances of U and Pb isotopes were measured in situ in individual zircon crystals by Sensitive High-Resolution Ion Microprobe (SHRIMP) using an approximately 20 µm diameter analytical volume. Sampling locations were selected by evaluating the internal structure of the grains as revealed in the BSE and CL images (Fig. 2). Standard operating techniques for the SHRIMP employed in this study have been described by Stern (1997). All reported errors are at 2 sigma and include the external long-term reproducibility of the 9910 reference zircon (constant external error of 0.59%, 95% conf.). The accuracy is measured against the reported TIMS age for z9910 of 441 Ma: the long-term average is 440.7 ± 7 Ma. In the 2018 analytical session, 9910 calibrated against 10493 Temora yielded 440.70 ± 0.70 Ma (n = 42, MSWD = 1.4).

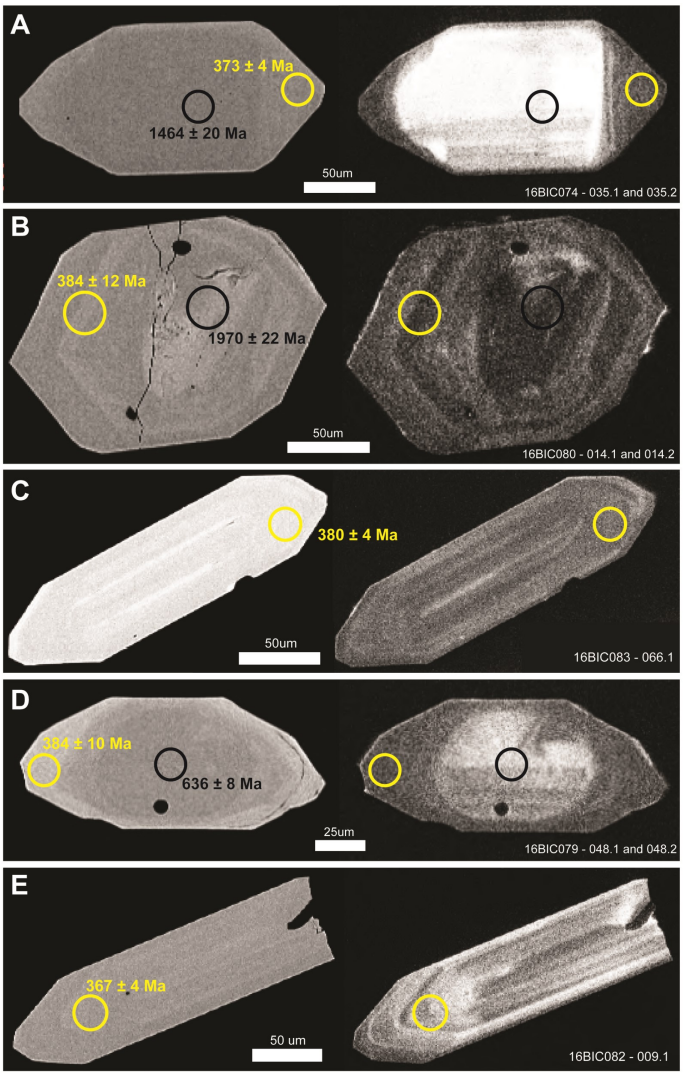

Figure 2. Representative zircon grains from the South Mountain Batholith. Backscatter electron (BSE) images (left) and cathodoluminescence (CL) images (right) of the same grains are juxtaposed and the SHRIMP analytical spot locations are indicated. Labels in the bottom right indicate U-Pb sample number and zircon grain-spot number. Labels beside the circles show the U-Pb age determinations (note $^{206}Pb/^{238}U$ ages are reported for ages younger than ca. 800 Ma and $^{207}Pb/^{206}Pb$ ages are reported for ages older than ca. 800 Ma). Yellow circles indicate crystallization ages and black circles indicated inherited xenocrystic core ages. The sample numbers are noted at the bottom right of each pair of images.

Results

The data reported below are from three samples collected along the periphery of the SMB, where the early, relatively less-evolved granodiorite phase of the SMB crops out, and from two samples of more evolved leucogranite units (i.e. West Dalhousie pluton and Halifax pluton) from the western and southeastern part of the batholith, respectively (Fig. 1). These samples complement the more-evolved leucogranitic samples previously collected and analyzed by Bickerton et al. (2018a). The locations of all samples from both studies are shown in Figure 1. Full results from the 2018 SHRIMP analyses are presented in Appendix 1, while full results for 2017 analyses previously reported in Bickerton et al. (2018a) are presented in Appendix 2.

Northwestern South Mountain Batholith (sample 16-BIC-074; 384.9 ± 4.4 Ma)

The perimeter of the SMB is dominated by a less evolved phase, a biotite-muscovite granodiorite that locally contains xenoliths of the adjacent metasedimentary wall rock. Sample 16-BIC-074 is a grey, medium-grained biotite-muscovite granodiorite from a roadside outcrop near the West Dalhousie area (Fig. 1). Zircon grains from this sample are relatively large (100–800 μm) compared to the other samples from the SMB and have a morphology that is dominantly equant to prismatic, with oscillatory to complex internal zoning. Many grains contain inherited xenocrystic cores, as revealed by BSE and CL imaging (e.g. Fig. 2a). Thirty-four spots across 24 grains were analyzed and yield a weighted mean ^{204}Pb-corrected ^{206}Pb/^{238}U age of 384.9 ± 3.8 Ma (4.4 Ma including external error; n = 16, MSWD = 1.7).

Eastern South Mountain Batholith (sample 16-BIC-080; 380.7 ± 3.8 Ma)

The granodiorite in the east-northeast part of the SMB is rich in metasedimentary xenoliths that show partial resorption textures. Sample 16-BIC-080 is a grey medium-grained biotite-muscovite(trace) granodiorite that is exposed along the highway in the Mount Uniacke area (Fig. 1). Zircon grains from this sample are highly variable in size (30–250 μm) with a relatively consistent stubby semi-prismatic morphology and thin oscillatory zones (Fig. 2b). Many of these zircon grains have inherited xenocrystic cores. Thirty-two spots across 27 grains were analyzed and the weighted mean ^{204}Pb-corrected ^{206}Pb/^{238}U date across the youngest concordant population yields 380.7 ± 3.1 Ma (3.8 Ma including external error; n = 22, MSWD = 1.3).

West Dalhousie Pluton (sample 16-BIC-083; 375.9 ± 4.5 Ma)

The west-southwestern part of the SMB is generally composed of less evolved biotite monzogranite to granodiorite and rare, more evolved muscovite-biotite(trace) leucogranitic phases (e.g. West Dalhousie Pluton). Sample 16-BIC-083 is one such leucocratic phase from this area and is a light-grey, medium- to coarse-grained leucomonzogranite from a roadside outcrop in West Springhill (Fig. 1). Zircon grains from this sample were relatively less abundant than the other SMB samples and are variable in both their size (50–250 μm) and morphology (from elongated to stubby prismatic grains). The grains typically showed thin oscillatory zones and, less commonly, complex internal zonation as seen in BSE and CL images (Fig. 2c). Inherited xenocrystic cores are notably rare in zircon from this sample, thus a population for the comparative xenocrystic core study was not obtained and this sample is not represented in Figure 3. Fourteen spots across 14 grains were analyzed and the weighted mean ^{204}Pb-corrected ^{206}Pb/^{238}U date across the youngest concordant population yields 375.9 ± 3.9 Ma (4.5 Ma including external error; n = 13, MSWD = 0.76).

Halifax Pluton (sample 16-BIC-079; 377.7 ± 5.2 Ma)

The zoned Halifax Pluton in the southeast SMB provides the best exposure in the batholith and is considered to be one of the more evolved phases of the complex. Sample 16-BIC-079 is a light-grey medium-grained biotite-muscovite granodiorite collected from a roadside outcrop near Sambro, near the southern margin of the pluton. This sample is more peripheral to the main mass of the pluton and is less leucocratic than a sample from the western part of the pluton previously dated at 374.3 ± 3 Ma (Fig. 1; Bickerton et al., 2018a). Zircon grains from this sample vary both in size (50–300 μm) and morphology (dominantly stubby equant with fewer prismatic and rare partially resorbed stubby prismatic crystals). Inherited xenocrystic cores are common in this sample (e.g. Fig. 2d). Twenty-six spots across 23 grains were analyzed and yield a weighted mean ^{204}Pb-corrected ^{206}Pb/^{238}U date across the youngest concordant population of 377.7 ± 4.7 Ma (5.2 Ma including external error; n = 12, MSWD = 2.0).

Southeastern South Mountain Batholith (sample 16-BIC-082; 367.7 ± 4.0 Ma)

The southern margin of the SMB contains sporadic leucocratic phases and less evolved, melanocratic and xenolith-bearing granodiorite phases. Sample 16-BIC-082 is a light-grey medium- to coarse-grained muscovite-biotite (accessory) monzogranite from a roadside outcrop on the Aspotogan Peninsula. Zircon grains from this sample are less abundant than other SMB samples from this study but are consistent both in size (100–250 μm) and morphology (dominantly equant prismatic with fewer stubby prismatic; Fig. 2e). Inherited xenocrystic cores are less common in this sample. Eighteen spots across 16 grains were analyzed and yield a weighted mean ^{204}Pb-corrected ^{206}Pb/^{238}U date across the youngest concordant population of 367.7 ± 3.4 Ma (4.0 Ma including external error; n = 15, MSWD = 1.5).

Inherited xenocrystic cores

Identification of inherited xenocrystic cores from zircon described both in Bickerton et al. (2018a) and in this study were recognized through a combination of BSE and CL imaging (e.g. Fig. 2a, b, d). Typically, the xenocrystic cores were manifested by an internal change of zonation (oscillatory zoning in zircon rims transitioning to complex zoning in zircon cores), and distinct CL and BSE responses compared to zircon

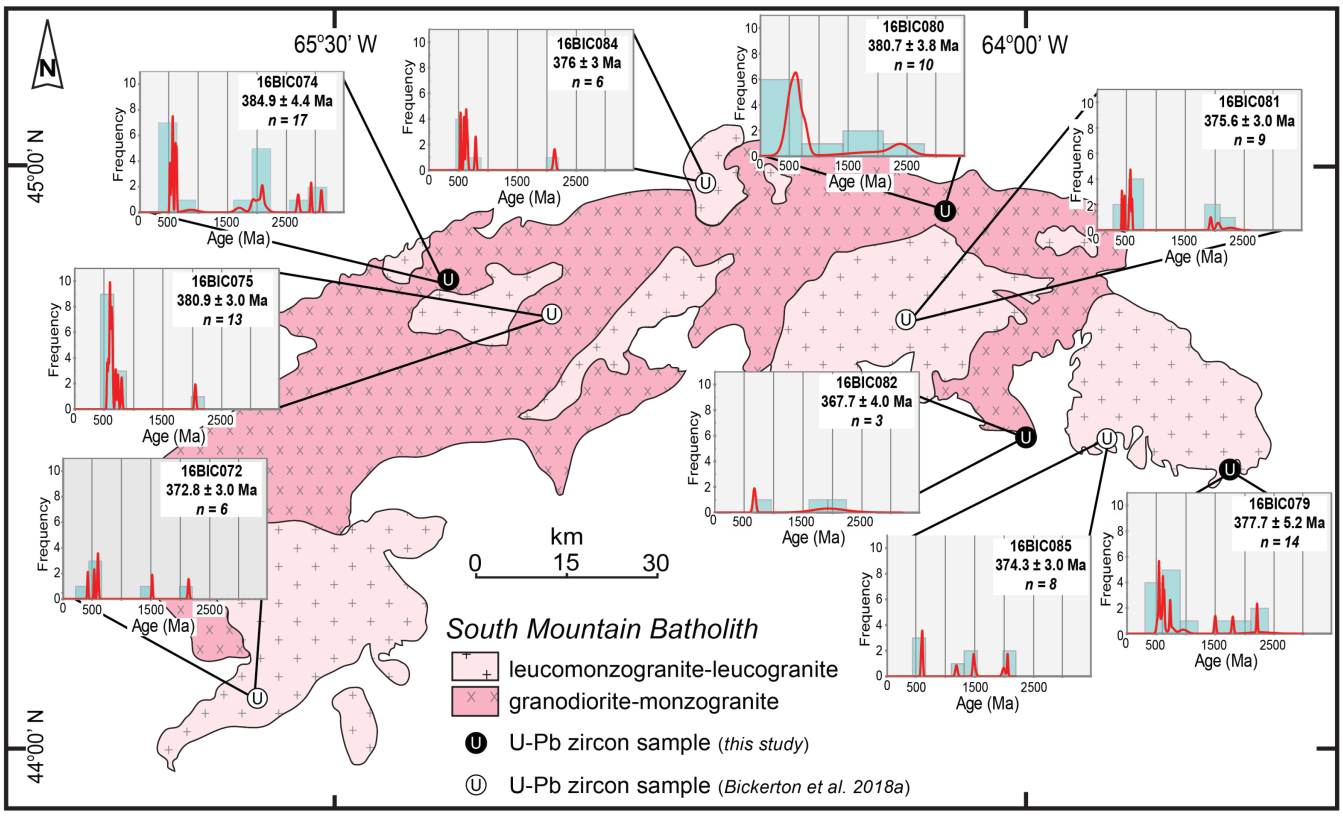

Figure 3. Overview of SMB phases with spatial distribution of age populations for the dated xenocrystic cores in each sample from this study and that of Bickerton et al. (2018a). Probability density distribution plots constructed using Isoplot 3 (Ludwig, 2003). Sample numbers and weighted average crystallization ages are indicated in the upper right corner for each plot. Plots show frequency of spots for a given age (histograms) and the relative probability density of ages for each inherited core population (lines).

rims, from relatively higher or lower HREE ± U, Th chemical signature (enrichment of these elements results in much brighter CL and darker BSE imagery). In total, 86 spots were analyzed on areas designated to represent inherited cores from nine different samples across the batholith. A summary of the spatial distribution of the nine samples from across the SMB and their age probability plots (i.e. age versus frequency) are shown in Figure 3. Typically, the more evolved leucocratic plutons contain fewer inherited cores relative to the more extensive granodiorite phases. In addition, the age results cluster around ca. 740 to 420 Ma and 2.22 to 1.91 Ga with less frequent but notable ages in both the Proterozoic and Archean (Fig. 4a).

Discussion

SHRIMP U-Pb dating of the spectrum of phases that represent the evolution of the SMB provides further constraints on both the timing of its emplacement and duration of its construction. Based on the new data presented here, the oldest age for the SMB is ca. 384 Ma, whereas the youngest is ca. 367 Ma, which provides an age span of ca. 17 ± 6 Ma for its emplacement. The latter clearly has ramifications regarding the processes required to generate magma for such a long duration and how these phases relate to each other. Future work will address these issues.

The above work is the most comprehensive dating study of the SMB to have been reported and these results will be integrated into research on the evolution of the SMB. The SMB has previously been dated using a variety of methods, including a single TIMS U-Pb zircon age of 375.6 ± 0.7 Ma (D.J. Kontak, work in progress, 2015) and a LA-ICP-MS U-Pb zircon age of 377 ± 4 Ma (Keppie et al., 1993). The zircon dates were an improvement on the Rb-Sr whole-rock ages of 374 ± 11, 371.8 ± 2.2 Ma (Clarke and Halliday, 1980) and ca. 374 Ma (Chatterjee and Cormier, 1991) as well as a Pb-Pb isochron age of ca. 366 Ma for granite and greisen at East Kemptville (Kontak and Chatterjee, 1992). The cooling K-Ar and $^{40}Ar/^{39}Ar$ ages for the batholith may approximate the time of crystallization, and vary from ca. 380 to 365 Ma (Reynolds et al., 2004, and references therein). The Re-Os molybdenite ages have been obtained from two localities: 371 ± 3 Ma for mineralized pegmatites in the New Ross area (Carruzzo et al., 2003; Selby and Creaser, 2004), and 376 ± 3 Ma for a pegmatite from East Kemptville (Kontak et al., 2003). We note that the historic U-Pb data are similar, within error, to the range of

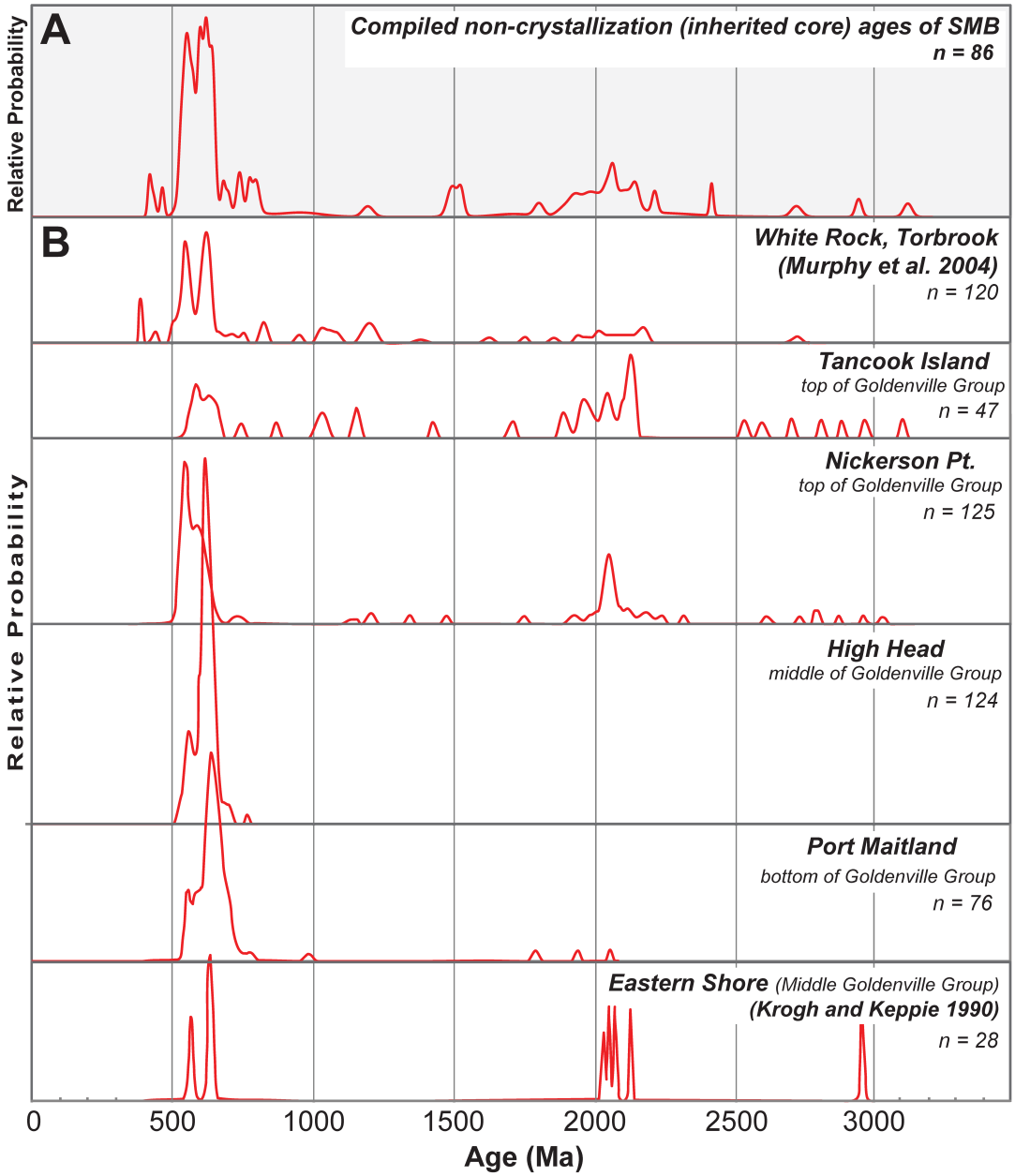

Figure 4. a) Compiled core ages (non-crystallization) from SHRIMP analysis of zircon across the SMB showing relative probability density for a spectrum of ages (note that $^{206}Pb/^{238}U$ ages were used for ages younger than ca. 800 Ma and $^{207}Pb/^{206}Pb$ ages were used for ages older than ca. 800 Ma). The plot constructed using Isoplot 3 (Ludwig, 2003). b) A series of relative probability density plots for detrital zircon age populations from Meguma Supergroup samples (*modified after* Waldron et al., 2009).

SHRIMP crystallization ages obtained in this study and that of Bickerton et al. (2018a; Appendix 2), whereas the less evolved phases are interpreted to have intruded at ca. 385 to 375 Ma and more evolved leucocratic phases at ca. 377 to 370 Ma (*see* Fig. 1).

The youngest SHRIMP age was obtained from a leucomonzogranite from the southeast SMB (sample 16-BIC-082) at 367.7 ± 4.0 Ma. Although the unit was mapped as Sandy Lake biotite monzogranite of the less evolved part of the SMB, the sample has characteristics that suggest the outcrop represents a more evolved phase of the batholith, perhaps the Panuke Lake leucomonzogranite that is exposed directly to the north (Fig. 1; MacDonald, 2001). Further work is required to address and resolve this apparent discrepancy of the anomalous young age for this part of the SMB.

The age populations obtained from the inherited cores from all samples dated by SHRIMP in this study and in Bickerton et al. (2018a) are displayed as probability density and frequency

plots in Figure 3. A comparison between the ages for the inherited zircon cores and detrital zircon hosted in metasedimentary rocks of the Meguma terrane (i.e. Meguma Supergroup, White Rock and Torbrook formations) is shown in Figure 4b. It is apparent from this plot that the age distribution for the SMB zircon grains is most similar in terms of proportion of age groups to samples from the upper part of the Meguma stratigraphy and overlying Silurian-Devonian rocks rather than the deeper exposed parts of the Meguma terrane. In addition, a small but anomalous population (6 analyses across 4 samples) at ca. 1500 Ma also occurs, which perhaps represents zircon cores that were brought from depth (basement to the Meguma terrane) by the SMB magmas. Based on the current data, the age profile of xenocrystic cores in the SMB suggest contamination of the magma from the upper strata of the Meguma Supergroup and overlying units.

Future work

The zircon grains selected for SHRIMP analysis in both this and our previous study (Bickerton et al., 2018a) will be analyzed for their geochemical and isotopic ($\delta^{18}O$, Lu-Hf) signatures, as part of a comprehensive study of zircon in the SMB (doctoral thesis of L. Bickerton) following an approach similar to that of Kemp et al. (2006, 2007). The zircon dated by SHRIMP will also be analyzed by laser-ablation inductively coupled plasma mass spectrometry (LA-ICP-MS) to quantify trace-element concentrations and determine the oxidation state and metallogenic affinity of the various SMB phases (cf. Gardiner et al., 2017). To resolve the overlap in age errors across all phases of the SMB (ca. 5 Ma), high-resolution thermal ionization mass spectrometry (TIMS) U-Pb dating of zircon is being conducted as part of the Doctoral study to determine whether there is a pause in igneous activity between the less evolved and more evolved phases of the SMB.

Conclusions

These new age data, in conjunction with previous work, generally characterize the chronologic evolution for the SMB as follows: 1) the least evolved component to the composite batholith was emplaced between 384.9 ± 4.4 Ma (U-Pb zircon, this study) and 375.6 ± 0.7 Ma (U-Pb zircon; unpub. U-Pb data, Kontak), 2) more evolved components in the SMB range in time emplacement between 377.7 ± 5.2 Ma and 367.7 ± 4.0 Ma (U-Pb zircon, this study), and 3) parts of the SMB cooled to below approximately 350°C (muscovite closure temperature) by ca. 380 Ma and either experienced prolonged cooling or underwent a reheating event at ca. 370 Ma (^{40}Ar-^{39}Ar, Reynolds et al., 2004). Dating the SMB by SHRIMP has also provided, for the first time, an opportunity to characterize inheritance by dating xenocrystic cores, which were common in zircon from less evolved samples but rare in more evolved samples. This has yielded an inherited age population with a signature similar to that of the upper parts of the Goldenville Group transition to Halifax Group metasedimentary rock (c.f. Waldron et al., 2009) as well as the volcanic sequences unconformably overlying the Meguma Supergroup (i.e., White Rock and Torbrook formations; Fig. 4).

Acknowledgments

This report is a contribution to NRCan's Targeted Geoscience Initiative Program (TGI). Support for this study was provided through the Porphyry-style Mineral Systems Project's '*Activity P-1.4: Temporal and spatial controls on the nature and distribution of porphyry-style deposits*'.

The authors thank Nicole Rayner and the personnel at the GSC SHRIMP laboratory for their analytical and technical expertise. This report benefited from the review of Alain Plouffe, Bill Davis and Neil Rogers.

References

Benn, K., Horne, R.J. Kontak, D.J., Pignotta, G.S., and Evans, N.G., 1997. Syn-Acadian emplacement model for the South Mountain Batholith, Meguma Terrane, Nova Scotia: Magnetic fabric and structural analyses; Geological Society of America Bulletin, v. 109, p. 1279–1293.

Bickerton, L., Kontak, D.J., and Samson, I.M., 2017a. A tale of two ore zones in the ca. 375 Ma East Kemptville granite-hosted Sn-Cu-Zn-Ag-In deposit, Nova Scotia, Canada; Atlantic Geoscience Society 43rd Colloquium & Annual General Meeting. Fredericton, New Brunswick, v. 53.

Bickerton, L., Kontak, D.J., Samson, I.M., and Murphy, J.B., 2017b. A mesothermal greisen-hosted Sn-Zn-Cu-Ag-In deposit at East Kemptville, Nova Scotia, Canada; *in* Proceedings of the Society of Geology Applied to Mineral Deposits (SGA) 14th Biennial Meeting, 20-23 August 2017, Québec, p. 1273.

Bickerton, L., Kontak, D.J., Samson, I.M., Murphy, J.B., and Kellett, D.A., 2018a. U-Pb geochronology of the South Mountain Batholith, Nova Scotia; *in* Targeted Geoscience Initiative: 2017 Report of Activities, volume 1, (ed.) N. Rogers; Geological Survey of Canada, Open File 8358, p. 51–55.

Bickerton, L., Kontak, D.J., Samson, I.M., Murphy, J.B., and Zajacz, Z., 2018b. Defining the fluid evolution of a mesothermal magmatic greisen-vein Sn-Cu-Zn-Ag-In deposit, East Kemptville, Nova Scotia, Canada; *in* Abstracts with Program; Society of Economic Geologists, Annual Meeting 2018, Keystone, Colorado.

Carruzzo, S., Kontak, D.J., Reynolds, P.H., Clarke, D.B., Dunning, G.R., and Selby, D., 2003. U/Pb, Re/Os, and Ar/Ar Dating of the South Mountain Batholith and its Mineral Deposits; Abstracts, Geochimica et Cosmochimica Acta, v. 67, Supplement 54.

Chatterjee, A.K. and Cormier, R.F., 1991. A Rb-Sr geochronological study of the Davis Lake pluton, South Mountain batholith, southern Nova Scotia: evidence for a 374 Ma

time of emplacement; Mines and Minerals Branch Report of activities, part A. Nova Scotia Department of Natural Resources Report 91-5.

Clarke, D.B. and Halliday, A.N., 1980. Strontium isotope geology of the South Mountain Batholith, Nova Scotia; Geochimica et Cosmochimica Acta, v. 44, p. 1045–1058.

Clarke, D.B., MacDonald, M.A., and Erdmann, S., 2004. Chemical variation in Al_2O_3-CaO-Na_2O-K_2O space: Controls on the peraluminosity of the South Mountain Batholith; Canadian Journal of Earth Sciences, v. 41, p. 785–798.

Clarke, D.B., Erdmann, S., Samson, H., and Jamieson, R.A., 2009. Contamination of the South Mountain Batholith by sulfides from country rocks; Canadian Mineralogist, v. 47, p. 1159–1176.

Currie, K.L., Whalen, J.B., Davis, W.J., Longstaffe, F.J., and Cousens, B.L., 1998. Geochemical evolution of peraluminous plutons in southern Nova Scotia, Canada — a pegmatite-poor suite; Lithos, v. 44, p. 117–140.

Gardiner, N.J., Hawkesworth, C.J., Robb, L.J., Whitehouse, M.J., Roberts, N.M., Kirkland, C.L., and Evans, N.J., 2017. Contrasting granite metallogeny through the zircon record: a case study from Myanmar; Scientific reports, v. 7, p. 748.

Halter, W.E., Williams-Jones, A.E., and Kontak, D.J., 1996. The role of greisenization in cassiterite precipitation at the East Kemptville tin deposit, Nova Scotia; Economic Geology, v. 91, p. 368–385.

Halter, W.E., Williams-Jones, A.E., and Kontak, D.J., 1998. Origin and evolution of the greisening fluid at the East Kemptville tin deposit, Nova Scotia, Canada; Economic Geology, v. 93, p. 1026–1051.

Hicks, R.J., Jamieson, R.A., and Reynolds, P.H., 1999. Detrital and metamorphic $^{40}Ar/^{39}Ar$ ages from muscovite and whole -rock samples, Meguma Supergroup, southern Nova Scotia. Canadian Journal of Earth Sciences, v. 36, p. 23–32.

Horne, R.J., MacDonald, M.A., Corey, M.C., and Ham, L.J., 1992. Structure and emplacement of the South Mountain Batholith, southwestern Nova Scotia; Atlantic Geology, v. 28, p. 29–50.

Kemp, A.I.S., Hawkesworth, C.J., Paterson, B.A., and Kinny, P.D., 2006. Episodic growth of the Gondwana supercontinent from hafnium and oxygen isotopes in zircon; Nature, v. 439, p. 580–583.

Kemp, A.I.S., Hawkesworth, C.J., Paterson, B.A., Woodhead, J.D., Hergt, J.M., Gray, C.M., and Whitehouse, M.J., 2007. Magmatic and crustal differentiation history of granitic rocks from Hf-O isotopes in zircon; Science, v. 315, p. 980–983.

Keppie, J.D., Dallmeyer, R.D., Krogh, T.E., and Aftalion, M., 1993. Dating mineralization using several isotopic methods: An example from the South Mountain Batholith, Nova Scotia, Canada; Chemical Geology, v. 103, p. 251–270.

Kontak, D.J., 1990a. The East Kemptville topaz-muscovite leucogranite, Nova Scotia. I. Geological setting and whole rock geochemistry; Canadian Mineral, v. 28, p. 787–825.

Kontak, D.J., 1990b. A sulfur isotopic study of main-stage tin and base metal mineralization at the East Kemptville tin deposit, Yarmouth County, Nova Scotia, Canada: evidence for magmatic origin of metals and sulfur; Economic Geology, v. 85, p. 399–407.

Kontak, D.J., 1991. The East Kemptville topaz-muscovite leucogranite, Nova Scotia: U. Mineral chemistry; Canadian Mineralogist, v. 29, p.37–60.

Kontak, D.J., 1994. Geological and geochemical studies of alteration processes in a fluorine-rich environment: the East Kemptville Sn-(Zn-Cu-Ag) deposit, Yarmouth County, Nova Scotia, Canada; *in* Alteration and Alteration Processes associated with Ore-forming Systems, (ed.) D.R. Lentz; Geological Association of Canada, Short Course Notes, v. 11, p. 261–314.

Kontak, D.J. and Chatterjee, A.K., 1992. The East Kemptville tin deposit, Yarmouth County, Nova Scotia. A Pb isotope study of the leucogranite and mineralized greisens: Evidence for a 366 Ma metallogenic event; Canadian Journal of Earth Sciences, v. 29, p. 1180–1196.

Kontak, D.J., Dostal, J., Ansdell, K., Halter, W., Martin, R.F, and Williams-Jones, A.E., 2001. The nature and origin of pegmatite in a fluorine-rich leucogranite, East Kemptville, Nova Scotia; Transactions of the Royal Society of Edinburgh: Earth Sciences, v. 92, p. 173–200.

Kontak, D.J., Dunning, G., and Creaser, R., 2003. U/Pb and Re/Os dating of the South Mountain and Musquodoboit batholiths, Nova Scotia: evidence for protracted magmatic-hydrothermal events; Joint Meeting Northeastern Section Geological Society of America-Atlantic Geoscience Society, Program with Abstracts.

Kontak, D.J., Horne, R.J., Creaser, R.A., Petrus, J., and Archibald, D., 2013. A petrological and geochronological study of a 360 Ma metallogenic event in Maritime Canada with implications for lithophile-metal mineralization in the Canadian Appalachians; Canadian Journal of Earth Sciences, v. 50, p. 1147–1163.

Krogh, T.E. and Keppie, J.D., 1990. Age of detrital zircon and titanite in the Meguma Group, southern Nova Scotia, Canada: Clues to the origin of the Meguma Terrane; Tectonophysics, v. 177, p. 307–323.

Lehmann, B., 1990. Metallogeny of Tin; Springer, Berlin. 177p.

Ludwig, K.R., 2003. User's Manual for Isoplot 3.00; Berkeley Geochronology Center, Special Publication 4.

MacDonald, M.A., 2001. Geology of the South Mountain Batholith, southwestern Nova Scotia; Nova Scotia Department of Natural Resources Open File Report ME2001-2, 280 p.

MacDonald, M.A. and Clarke, D.B., 2017. Occurrence, origin, and significance of melanogranites in the South Mountain Batholith, Nova Scotia; Canadian Journal of Earth Sciences, v. 54, p. 693–713.

MacDonald, M.A., Horne, R.J., Corey, M.C., and Ham, L.J., 1992. An overview of recent bedrock mapping and follow-

up petrological studies of the South Mountain batholith, southwestern Nova Scotia, Canada; Atlantic Geology, v. 28, p. 7–28.

MacLean, N.J., Barr, S.M., White, C.E., and Ketchum, J.W.F., 2004. New U-Pb (zircon) age and geochemistry of the Wedgeport pluton, Meguma terrane, Nova Scotia; Atlantic Geology, v. 39, p. 239–253.

Murphy, J.B., Fernández-Suárez, J., Keppie, J.D., and Jeffries, T.E., 2004. Contiguous rather than discrete Paleozoic histories for the Avalon and Meguma terranes based on detrital zircon data; Geology, v. 32, p. 585–588.

Reynolds, P.H., Clarke, D.B., and Bogutyn, P.A., 2004. $^{40}Ar/^{39}Ar$ Laser dating of zoned white micas from the Lake Lewis leucogranite, South Mountain Batholith, Nova Scotia, Canada; Canadian Mineralogist, v. 42, p. 1129–1137.

Richardson, J.M., 1988. Field and alteration relationships of alteration and greisen-hosted mineralization at the East Kemptville tin deposit, Davis Lake monzogranite, southwest Nova Scotia, Canada; *in* Granite-Related Mineral Deposits, (ed.) R.P. Taylor and D.F. Strong; Canadian Institute of Mining and Metallurgy, Special Volume 39, p. 265–279.

Romer, R.L. and Kroner, U., 2016. Phanerozoic tin and tungsten mineralization—Tectonic controls on the distribution of enriched protoliths and heat sources for crustal melting; Gondwana Research, v. 31, p. 60–95.

Schuiling, R.D., 1967. Tin belts on the continents around the Atlantic Ocean; Economic Geology, v. 62, p. 540–550.

Selby, D. and Creaser, R.A., 2004. Macroscale NTIMS and microscale LA-MC-ICP-MS Re-Os isotopic analysis of molybdenite: Testing spatial restrictions for reliable Re-Os age determinations, and implications for the decoupling of Re and Os within molybdenite; Geochimica et Cosmochimica Acta, v. 68, p. 3897–3908.

Sillitoe, R.H., 1974. Tin mineralisation above mantle hot spots; Nature, v. 248, p. 497.

Stern, R.A., 1997. A SHRIMP II Ion Microprobe at the Geological Survey of Canada; Geoscience Canada, v. 23, p. 73–76.

Tate, M.C. and Clarke, D.B., 1997. Compositional diversity among Late Devonian peraluminous granitoid intrusions in the Meguma Zone of Nova Scotia, Canada; Lithos, v. 39, p. 179–194.

Tate, M.C., Clarke, D.B., and Heaman, L.M., 1997. Progressive hybridisation between Late Devonian mafic-intermediate and felsic magmas in the Meguma Zone of Nova Scotia, Canada; Contributions to Mineralogy and Petrology, v. 126, p. 401–415.

Taylor, R.G., 1979. Geology of Tin Deposits; Elsevier, Amsterdam. 543p.

van Staal, C.R., 2007. Pre-Carboniferous tectonic evolution and metallogeny of the Canadian Appalachians; *in* Mineral Deposits of Canada: a synthesis of major deposit-types, district metallogeny, the evolution of geological provinces, and exploration methods (ed.) W.D. Goodfellow; Geological Association of Canada, Special Publication 5, p. 793–818.

van Staal, C.R., Dewey, J.F., Mac Niocaill, C., and McKerrow, W.S., 1998. The Cambrian-Silurian tectonic evolution of the northern Appalachians and British Caledonides: history of a complex, west and southwest Pacific-type segment of Iapetus; *in* Lyell: the Past is the Key to the Present, (ed.) D.J. Blundell and A.C. Scott; Geological Society, London, Special Publications, v. 143, p. 197–242.

van Staal, C.R., Whalen, J.B., Valverde-Vaquero, P., Zagorevski, A., and Rogers, N., 2009. Pre-Carboniferous, episodic accretion-related, orogenesis along the Laurentian margin of the northern Appalachians; *in* Ancient Orogens and Modern Analogues, (ed.) J.B. Murphy, J.D. Keppie, and A.J. Hynes; Geological Society, London, Special Publications, v. 327, p. 271–316.

Waldron, J.W., White, C.E., Barr, S.M., Simonetti, A. and Heaman, L.M., 2009. Provenance of the Meguma terrane, Nova Scotia: rifted margin of early Paleozoic Gondwana; Canadian Journal of Earth Sciences, v. 46, p. 1–8.

White, C.E., 2010. Stratigraphy of the Lower Paleozoic Goldenville and Halifax groups in southwestern Nova Scotia; Atlantic Geology, v. 46, p. 136–154.

Appendix 1: Table of SHRIMP analyzed U-Pb isotopes of zircon from the South Mountain Batholith (2018).

					Corrected isotope ratios										Apparent ages (Ma)				
Spot No.	U ppm	Th ppm	Th/U	^{206}Pb* ppm	^{204}Pb/^{206}Pb	±1s (%)	f(206)^{204} %	^{207}Pb*/^{206}Pb*	±1s (%)	^{207}Pb*/^{235}U*	±1s (%)	^{206}Pb*/^{238}U	±1s (%)	error coeff.	^{207}Pb*/^{206}Pb*	±1s (Ma)	^{206}Pb*/^{238}U*	±1s (Ma)	% disc.
16-BIC-074																			
12307-007.1	665	28	0.04	33.0	3.06E-04	19	0.53	0.0529	1.9	0.422	2.2	0.0578	1.1	0.494	326	43	**362**	**4**	-11
12307-045.2	660	32	0.05	33.5	1.43E-04	27	0.25	0.0541	1.7	0.441	3.8	0.0592	3.4	0.888	374	39	**371**	**12**	+1
12307-035.2	264	17	0.07	13.5	2.93E-04	29	0.51	0.0547	3.2	0.449	3.4	0.0596	1.1	0.329	401	72	**373**	**4**	+7
12307-032.2	264	12	0.05	13.6	1.72E-04	38	0.30	0.0521	2.3	0.430	3.3	0.0598	2.3	0.714	288	52	**375**	**8**	-31
12307-021.2	980	28	0.03	50.7	1.00E-04	26	0.17	0.0538	1.0	0.447	1.4	0.0603	1.1	0.730	361	22	**377**	**4**	-5
12307-056.1	244	39	0.17	12.7	2.97E-04	29	0.51	0.0551	2.7	0.460	7.0	0.0606	6.5	0.925	416	60	**379**	**24**	+9
12307-039.2	637	25	0.04	33.3	1.50E-04	26	0.26	0.0543	1.7	0.455	2.4	0.0608	1.7	0.697	382	39	**380**	**6**	+0
12307-026.2	1644	26	0.02	87.3	7.41E-06	71	0.01	0.0542	0.5	0.462	1.2	0.0618	1.0	0.895	380	12	**387**	**4**	-2
12307-024.1	271	78	0.30	14.4	5.01E-04	20	0.87	0.0513	3.2	0.438	3.4	0.0619	1.1	0.326	255	74	**387**	**4**	-53
12307-074.1	321	29	0.09	17.1	3.78E-04	23	0.66	0.0530	2.7	0.454	2.9	0.0622	1.1	0.377	327	62	**389**	**4**	-19
12307-093.1	111	23	0.21	5.9	2.20E-04	50	0.38	0.0649	3.1	0.557	8.6	0.0623	8.0	0.933	770	65	**389**	**30**	+51
12307-093.2	856	28	0.03	45.8	7.37E-05	30	0.13	0.0546	0.9	0.469	2.0	0.0623	1.7	0.888	397	20	**390**	**7**	+2
12307-024.2	634	20	0.03	34.0	2.35E-04	20	0.41	0.0530	1.5	0.456	1.9	0.0624	1.1	0.568	328	35	**390**	**4**	-20
12307-022.1	1055	41	0.04	56.8	1.24E-04	22	0.21	0.0539	1.3	0.466	1.7	0.0627	1.1	0.626	367	30	**392**	**4**	-7
12307-056.2	414	36	0.09	22.3	1.12E-04	38	0.19	0.0547	1.6	0.473	2.6	0.0628	2.1	0.802	400	35	**392**	**8**	+2
12307-043.1	306	17	0.06	16.5	3.07E-04	25	0.53	0.0558	2.3	0.484	3.4	0.0629	2.4	0.719	445	52	**393**	**9**	+12
12307-005.2	401	33	0.09	21.7	1.84E-04	29	0.32	0.0538	1.8	0.469	4.8	0.0631	4.4	0.927	364	40	**395**	**17**	-9
12307-061.1	51	26	0.53	3.7	1.09E-03	26	1.89	0.0607	8.0	0.709	8.1	0.0847	1.4	0.169	629	172	524	7	+17
12307-026.1	28	25	0.92	2.2	3.58E-03	20	6.20	0.0389	29.8	0.481	29.8	0.0896	2.0	0.067	-422	780	553	11	+241
12307-019.1	93	89	0.99	7.4	6.50E-04	26	1.13	0.0538	5.0	0.689	5.1	0.0928	1.2	0.239	363	112	572	7	-60
12307-045.1	38	35	0.95	3.0	1.65E-03	24	2.87	0.0562	12.0	0.722	12.1	0.0931	1.5	0.127	462	266	574	8	-25
12307-013.1	91	93	1.06	7.8	5.96E-04	27	1.03	0.0565	5.1	0.783	5.3	0.1006	1.2	0.232	471	113	618	7	-33
12307-038.1	23	7	0.32	2.0	3.18E-03	22	5.51	0.0453	25.9	0.639	25.9	0.1023	2.0	0.077	-38	628	628	12	+1860
12307-006.1	83	59	0.73	7.5	4.41E-04	30	0.77	0.0612	3.6	0.879	3.8	0.1043	1.2	0.319	645	77	640	7	+1
12307-032.1	48	145	3.10	7.0	8.39E-04	24	1.45	0.0685	5.9	1.604	6.1	0.1698	1.3	0.216	885	123	1011	12	-15
12307-035.1	23	34	1.55	5.0	1.06E-03	24	1.85	0.1048	3.8	3.742	4.1	0.2591	1.5	0.359	1710	71	1485	20	+15
12307-021.1	115	11	0.10	32.5	1.82E-04	24	0.32	0.1283	6.0	5.797	11.3	0.3276	9.6	0.848	2075	105	1827	152	+14
12307-064.1	199	110	0.57	59.2	8.70E-05	24	0.15	0.1314	3.5	6.269	6.5	0.3461	5.5	0.842	2116	62	1916	91	+11
12307-004.1	78	80	1.07	23.5	2.58E-04	24	0.45	0.1189	1.9	5.781	4.9	0.3527	4.5	0.921	1939	34	1948	75	-0
12307-075.1	1555	161	0.11	485.5	9.04E-06	26	0.02	0.1246	2.6	6.245	4.5	0.3634	3.7	0.822	2024	45	1998	64	+1
12307-017.1	52	28	0.54	17.7	3.10E-04	25	0.54	0.1305	1.1	7.047	1.6	0.3918	1.2	0.735	2104	20	2131	22	-2
12307-039.1	258	72	0.29	101.6	6.95E-05	21	0.12	0.1870	1.1	11.819	2.9	0.4584	2.6	0.917	2716	19	2433	53	+12
12307-005.1	2168	365	0.17	951.4	6.15E-06	22	0.01	0.2388	0.9	16.821	1.9	0.5109	1.6	0.860	3112	15	2660	35	+18
12307-063.1	217	132	0.63	101.0	7.24E-05	21	0.13	0.2142	0.7	16.019	2.2	0.5425	2.1	0.949	2937	11	2794	48	+6
16-BIC-080																			
12309-039.1	160	42	0.27	7.6	7.00E-04	24	1.21	0.0521	5.1	0.400	12.6	0.0557	11.5	0.914	288	117	**349**	**39**	-22
12309-101.1	192	50	0.27	9.6	5.74E-04	24	0.99	0.0543	5.6	0.438	6.1	0.0584	2.5	0.408	385	125	**366**	**9**	+5
12309-097.1	1816	124	0.07	91.9	1.24E-03	5	2.16	0.0544	2.8	0.443	3.4	0.0589	2.0	0.577	390	63	**369**	**7**	+5
12309-081.2	58	20	0.36	3.0	3.07E-03	22	5.33	0.0532	20.6	0.435	20.7	0.0592	1.8	0.088	339	466	**371**	**7**	-10
12309-041.1	123	48	0.40	6.3	1.33E-03	22	2.31	0.0576	9.9	0.471	10.7	0.0593	4.0	0.377	516	217	**372**	**15**	+29
12309-060.1	75	28	0.38	3.9	1.27E-03	25	2.20	0.0563	9.9	0.462	10.0	0.0595	1.4	0.139	466	219	**373**	**5**	+21
12309-078.2	69	37	0.56	3.5	3.38E-03	18	5.87	0.0408	29.4	0.335	29.4	0.0596	1.7	0.058	-300	750	**373**	**6**	+231
12309-078.1	322	69	0.22	16.6	7.30E-04	18	1.27	0.0507	4.0	0.420	4.9	0.0601	2.7	0.558	229	93	**376**	**10**	-66
12309-021.1	82	25	0.32	4.2	1.66E-03	21	2.87	0.0486	11.2	0.402	11.3	0.0601	1.4	0.124	127	263	**376**	**5**	-202
12309-097.2	53	29	0.56	2.7	3.73E-03	20	6.47	0.0376	41.2	0.312	41.6	0.0602	5.8	0.139	-515	1100	**377**	**21**	+178
12309-020.1	920	78	0.09	47.8	7.69E-05	30	0.13	0.0539	1.0	0.450	1.4	0.0605	1.1	0.743	368	21	**379**	**4**	-3
12309-063.1	910	72	0.08	47.3	1.31E-04	24	0.23	0.0539	1.4	0.450	2.2	0.0606	1.7	0.758	366	32	**379**	**6**	-4
12309-058.1	423	54	0.13	22.1	2.43E-04	24	0.42	0.0540	1.9	0.452	3.2	0.0608	2.6	0.801	369	43	**380**	**9**	-3
12309-009.1	963	70	0.07	50.3	8.69E-05	27	0.15	0.0543	0.9	0.455	2.0	0.0608	1.8	0.887	384	21	**380**	**6**	+1
12309-070.1	230	74	0.33	12.0	5.01E-04	23	0.87	0.0530	3.6	0.444	3.8	0.0608	1.1	0.305	328	81	**380**	**4**	-16
12309-081.1	287	72	0.26	15.1	5.76E-04	20	1.00	0.0529	3.9	0.446	4.6	0.0611	2.6	0.552	324	87	**383**	**9**	-19
12309-014.2	232	54	0.24	12.2	1.63E-03	15	2.82	0.0566	7.9	0.479	8.5	0.0614	3.1	0.371	476	174	**384**	**12**	+20
12309-005.1	102	27	0.27	5.4	7.69E-04	28	1.33	0.0533	8.1	0.452	8.2	0.0615	1.3	0.154	344	184	**385**	**5**	-12
12309-010.1	2041	125	0.06	107.9	7.64E-05	21	0.13	0.0542	0.6	0.460	2.0	0.0615	1.9	0.948	378	14	**385**	**7**	-2
12309-013.2	777	65	0.09	41.4	1.90E-04	21	0.33	0.0527	1.4	0.450	1.7	0.0619	1.1	0.618	316	31	**387**	**4**	-23
12309-059.1	399	47	0.12	21.4	2.24E-04	25	0.39	0.0550	1.8	0.474	2.6	0.0625	1.9	0.716	414	40	**391**	**7**	+6
12309-074.1	2195	118	0.06	118.3	1.28E-04	26	0.22	0.0549	1.0	0.475	1.4	0.0627	1.1	0.733	408	22	**392**	**4**	+4
12309-027.1	52	49	0.97	3.9	2.54E-03	18	4.40	0.0450	16.3	0.543	16.7	0.0876	3.8	0.229	-58	396	541	20	+1084
12309-053.1	172	67	0.40	13.0	1.49E-03	16	2.58	0.0567	6.6	0.689	7.1	0.0882	2.6	0.361	478	146	545	13	-15
12309-016.1	227	143	0.65	17.3	5.37E-04	18	0.93	0.0573	3.6	0.703	4.7	0.0889	3.1	0.654	504	79	549	16	-9
12309-011.1	38	30	0.82	2.9	1.77E-03	24	3.08	0.0592	14.0	0.731	14.6	0.0896	4.2	0.291	575	304	553	22	+4
12309-018.1	57	25	0.46	5.0	1.77E-03	19	3.07	0.0555	10.3	0.781	10.8	0.1022	3.3	0.304	432	229	627	20	-47
12309-103.1	136	123	0.94	12.3	1.19E-03	16	2.07	0.0630	5.5	0.914	5.6	0.1052	1.2	0.213	708	117	645	7	+9
12309-074.2	999	193	0.20	108.9	8.27E-05	19	0.14	0.0653	0.6	1.143	1.2	0.1269	1.1	0.881	784	12	770	8	+2
12309-014.1	687	602	0.91	146.9	2.30E-04	21	0.40	0.1210	1.2	4.153	6.0	0.2490	5.9	0.978	1970	22	1433	76	+30
12309-013.1	254	71	0.29	71.1	3.90E-05	33	0.07	0.1261	4.2	5.665	13.7	0.3258	13.0	0.952	2044	74	1818	206	+13
12309-037.1	222	250	1.16	82.1	1.07E-04	19	0.19	0.1561	0.4	9.256	1.2	0.4299	1.1	0.948	2414	6	2305	21	+5
16-BIC-082																			
12310-033.1	1221	137	0.12	59.4	6.54E-03	19	11.34	0.0489	59.0	0.382	59.1	0.0566	3.0	0.051	142	1384	**355**	**10**	-153
12310-034.1	160	75	0.48	7.8	1.27E-03	18	2.21	0.0500	7.1	0.390	7.2	0.0567	1.2	0.169	194	166	**355**	**4**	-86
12310-044.1	385	52	0.14	19.1	4.77E-04	19	0.83	0.0535	3.9	0.427	4.0	0.0579	1.1	0.274	351	87	**363**	**4**	-3
12310-009.1	192	61	0.33	9.6	5.06E-04	25	0.88	0.0558	4.2	0.450	4.3	0.0585	1.2	0.266	443	93	**367**	**4**	+18
12310-043.1	175	56	0.33	8.8	1.07E-03	18	1.86	0.0498	7.6	0.403	8.0	0.0587	2.4	0.305	186	177	**367**	**9**	-101
12310-026.1	889	35	0.04	44.8	1.57E-04	21	0.27	0.0530	1.1	0.429	1.6	0.0587	1.1	0.678	328	26	**368**	**4**	-13
12310-022.1	525	47	0.09	26.5	6.32E-04	17	1.10	0.0543	3.4	0.439	3.6	0.0587	1.1	0.311	382	77	**368**	**4**	+4
12310-010.1	999	86	0.09	50.5	3.21E-05	45	0.06	0.0536	0.8	0.435	1.3	0.0589	1.1	0.806	354	17	**369**	**4**	-4
12310-056.1	80	20	0.26	4.1	1.94E-03	20	3.37	0.0491	12.7	0.399	12.8	0.0590	1.5	0.114	153	297	**369**	**5**	-146
12310-037.1	1274	67	0.05	64.8	1.51E-04	18	0.26	0.0542	1.0	0.442	1.4	0.0592	1.1	0.738	379	22	**371**	**4**	+2
12310-055.1	1335	166	0.13	68.4	1.26E-03	10	2.19	0.0518	3.9	0.426	6.4	0.0597	5.0	0.792	277	89	**374**	**18**	-36
12310-021.1	1137	54	0.05	58.5	1.85E-04	18	0.32	0.0546	1.4	0.451	4.1	0.0599	3.9	0.941	395	31	**375**	**14**	+5
12310-057.1	1744	40	0.02	90.2	1.17E-04	18	0.20	0.0545	0.8	0.452	2.6	0.0602	2.5	0.955	391	17	**377**	**9**	+4
12310-012.1	370	31	0.09	19.2	3.30E-04	21	0.57	0.0550	2.7	0.457	2.9	0.0603	1.1	0.378	411	60	**378**	**4**	+8
12310-061.1	365	57	0.16	19.0	3.93E-04	21	0.68	0.0535	4.6	0.447	5.4	0.0606	2.8	0.515	350	104	**379**	**10**	-9
12310-060.1	422	502	1.23	40.2	2.15E-04	20	0.37	0.0634	1.7	0.969	2.0	0.1108	1.1	0.532	722	37	678	7	+7
12310-055.2	63	56	0.91	17.2	4.69E-04	20	0.81	0.1158	1.4	5.043	1.9	0.3159	1.3	0.673	1892	25	1770	20	+7
12310-057.2	106	75	0.73	32.4	2.09E-04	22	0.36	0.1271	1.8	6.222	2.1	0.3551	1.1	0.539	2058	31	1959	19	+6

Appendix 1: cont.

Spot No.	U ppm	Th ppm	Th/U	^{206}Pb* ppm	Corrected isotope ratios										Apparent ages (Ma)				
					^{204}Pb/^{206}Pb	±1s (%)	f(206)^{204} %	^{207}Pb*/^{206}Pb*	±1s (%)	^{207}Pb*/^{235}U*	±1s (%)	^{206}Pb*/^{238}U	±1s (%)	error coeff.	^{207}Pb*/^{206}Pb*	±1s (Ma)	^{206}Pb*/^{238}U*	±1s (Ma)	% disc.
16-BIC-079																			
12308-031.1	876	334	0.39	44.3	1.73E-04	21	0.30	0.0534	1.3	0.433	1.7	0.0589	1.1	0.646	345	29	**369**	**4**	-7
12308-018.1	305	184	0.62	15.5	2.10E-04	32	0.36	0.0573	2.1	0.468	2.4	0.0593	1.1	0.465	504	46	**371**	**4**	+27
12308-006.1	210	152	0.75	10.7	4.95E-04	24	0.86	0.0493	3.9	0.405	4.1	0.0596	1.1	0.279	162	92	**373**	**4**	-135
12308-002.1	110	65	0.61	5.6	1.45E-03	19	2.51	0.0499	10.4	0.412	11.0	0.0598	3.5	0.317	192	243	**374**	**13**	-98
12308-025.1	191	97	0.52	9.9	1.07E-03	22	1.85	0.0496	7.9	0.411	8.0	0.0601	1.2	0.152	177	184	**376**	**4**	-116
12308-017.1	711	68	0.10	36.9	1.71E-04	22	0.30	0.0530	1.3	0.442	2.3	0.0605	1.9	0.816	331	30	**378**	**7**	-15
12308-029.1	405	47	0.12	21.2	4.07E-04	20	0.70	0.0537	2.4	0.451	2.7	0.0609	1.1	0.409	360	55	**381**	**4**	-6
12308-050.1	213	74	0.36	11.2	6.04E-04	22	1.05	0.0555	5.3	0.467	6.1	0.0610	2.9	0.484	434	118	**382**	**11**	+12
12308-048.1	2381	44	0.02	125.6	9.30E-05	20	0.16	0.0537	0.7	0.455	2.8	0.0614	2.7	0.969	358	15	**384**	**10**	-7
12308-051.1	183	18	0.10	9.7	6.06E-04	23	1.05	0.0557	5.8	0.476	6.3	0.0620	2.6	0.416	440	128	**388**	**10**	+12
12308-033.2	1513	19	0.01	80.6	1.29E-04	19	0.22	0.0537	0.9	0.460	1.8	0.0620	1.5	0.870	360	20	**388**	**6**	-8
12308-057.2	428	82	0.20	22.9	1.84E-05	100	0.03	0.0552	2.1	0.474	2.3	0.0622	1.1	0.470	422	46	**389**	**4**	+8
12308-042.1	169	80	0.49	12.3	7.96E-04	21	1.38	0.0533	4.8	0.623	6.1	0.0848	3.7	0.608	341	109	525	19	-56
12308-020.1	69	51	0.77	5.2	1.19E-03	23	2.07	0.0626	6.9	0.764	7.0	0.0884	1.3	0.192	696	146	546	7	+22
12308-026.1	25	12	0.48	2.0	2.14E-03	26	3.72	0.0578	17.0	0.715	17.1	0.0897	1.8	0.104	523	374	554	9	-6
12308-010.1	224	84	0.39	18.3	3.26E-05	71	0.06	0.0616	2.2	0.808	5.1	0.0951	4.6	0.904	660	47	586	26	+12
12308-040.1	273	228	0.86	23.5	2.17E-04	24	0.38	0.0610	1.5	0.842	1.9	0.1000	1.1	0.580	641	33	615	6	+4
12308-014.1	357	546	1.58	31.0	2.43E-04	20	0.42	0.0596	1.4	0.831	5.4	0.1011	5.3	0.964	588	31	621	31	-6
12308-048.2	74	58	0.81	6.6	1.31E-03	19	2.26	0.0563	7.9	0.805	8.0	0.1037	1.3	0.164	465	175	636	8	-39
12308-038.1	61	32	0.54	6.4	1.51E-03	18	2.61	0.0613	7.3	1.024	7.4	0.1212	1.4	0.183	650	157	737	10	-14
12308-021.1	144	83	0.59	15.6	5.45E-04	20	0.94	0.0971	7.0	1.687	9.4	0.1260	6.2	0.662	1569	132	765	45	+54
12308-013.1	113	226	2.06	16.9	5.40E-04	19	0.94	0.0711	3.3	1.704	4.7	0.1739	3.4	0.712	960	68	1034	32	-8
12308-033.1	200	62	0.32	42.2	1.85E-04	21	0.32	0.0937	0.8	3.173	1.4	0.2456	1.1	0.804	1502	15	1416	14	+6
12308-039.1	308	154	0.52	76.9	7.75E-05	23	0.13	0.1101	0.9	4.412	1.4	0.2907	1.1	0.770	1801	16	1645	15	+10
12308-057.1	5	1	0.11	1.4	5.29E-03	20	9.16	0.1432	11.2	6.518	11.6	0.3301	3.0	0.260	2267	194	1839	48	+22
12308-060.1	146	68	0.48	49.1	1.21E-04	25	0.21	0.1388	0.5	7.477	2.1	0.3907	2.1	0.966	2212	10	2126	37	+5
16-BIC-083																			
12311-057.1	416	47	0.12	20.2	6.02E-04	20	1.04	0.0528	4.2	0.412	5.8	0.0567	4.0	0.683	319	96	**355**	**14**	-12
12311-058.1	654	32	0.05	32.1	1.02E-04	33	0.18	0.0537	1.3	0.423	4.2	0.0571	4.0	0.952	358	29	**358**	**14**	+0
12311-063.1	796	64	0.08	40.0	1.76E-04	24	0.31	0.0548	1.4	0.441	3.4	0.0584	3.1	0.912	402	31	**366**	**11**	+9
12311-038.1	443	38	0.09	22.6	4.43E-04	18	0.77	0.0557	2.8	0.457	3.0	0.0595	1.1	0.367	442	61	**372**	**4**	+16
12311-048.1	699	29	0.04	35.8	2.86E-04	22	0.50	0.0532	2.3	0.437	2.9	0.0596	1.9	0.633	337	51	**373**	**7**	-11
12311-068.1	349	136	0.40	17.9	5.04E-04	20	0.87	0.0538	4.9	0.444	5.6	0.0598	2.7	0.478	363	110	**375**	**10**	-3
12311-003.1	389	42	0.11	20.0	3.14E-04	23	0.54	0.0539	3.1	0.445	3.8	0.0600	2.1	0.559	365	71	**375**	**8**	-3
12311-045.1	1043	29	0.03	54.0	1.71E-04	19	0.30	0.0540	1.5	0.449	2.3	0.0603	1.7	0.756	373	34	**377**	**6**	-1
12311-046.1	394	31	0.08	20.5	3.35E-04	22	0.58	0.0552	3.0	0.461	5.1	0.0605	4.1	0.808	421	67	**379**	**15**	+10
12311-006.1	330	150	0.47	17.2	3.57E-04	23	0.62	0.0558	2.5	0.466	4.0	0.0606	3.2	0.789	446	55	**379**	**12**	+15
12311-066.1	276	30	0.11	14.4	5.03E-04	22	0.87	0.0547	3.3	0.458	3.5	0.0608	1.1	0.331	400	73	**380**	**4**	+5
12311-069.1	280	89	0.33	14.7	7.56E-04	21	1.31	0.0555	4.4	0.467	4.8	0.0610	2.0	0.411	433	98	**382**	**7**	+12
12311-001.1	719	38	0.06	38.1	2.76E-04	18	0.48	0.0540	2.6	0.459	3.4	0.0617	2.2	0.641	372	59	**386**	**8**	-4
12311-043.1	415	26	0.06	24.0	4.29E-04	18	0.74	0.0581	2.7	0.540	2.9	0.0674	1.1	0.374	533	59	**421**	**4**	+22

Note:

The probability density cores plot (Figs. 3 and 4) has ^{206}Pb/^{238}U to ^{207}Pb/^{206}Pb at 750 Ma, no filtering for discordance

Bolded apparent ages are included in weighted mean average crystallization age for sample

Spot name follows the convention x-y.z; where x = sample number, y = grain number and z = spot number. Multiple analyses in an individual spot are labelled as x-y.z.z

Uncertainties are reported at 1s and are calculated by using SQUID 2.23.08.10.21, rev. 21 Oct 2008

f(206)^{204} refers to mole percent of total ^{206}Pb that is due to common Pb, calculated using the^{204}Pb-method; common Pb composition used is the surface blank (4/6: 0.05770; 7/6: 0.89500; 8/6: 2.13840)

* refers to radiogenic Pb (corrected for common Pb using ^{204}Pb).

% disc: Discordance given as difference between measured ^{206}*Pb/^{238}U ratio and the expected ^{206}*Pb/^{238}U ratio at t=207*/206* age, in percent.

Calibration standard 10493; ^{207}Pb/^{206}Pb Age = 421 Ma

Error in ^{206}Pb/^{238}U calibration 1.5% (included)

Standard Error in Standard calibration was 0.34% (not included in above errors but required when comparing data from different mounts).

Appendix 2: Table of SHRIMP analyzed U-Pb isotopes of zircon from the South Mountain Batholith (2017), reported in Bickerton et al., 2018a

					Corrected isotope ratios										Apparent ages (Ma)				
Spot No.	U ppm	Th ppm	Th/U	^{206}Pb* ppm	^{204}Pb/^{206}Pb	±1s (%)	f(206)^{204} %	^{207}Pb*/^{206}Pb*	±1s (%)	^{207}Pb*/^{235}U*	±1s (%)	^{206}Pb*/^{238}U	±1s (%)	error coeff.	^{207}Pb*/^{206}Pb*	±1s (Ma)	^{206}Pb*/^{238}U*	±1s (Ma)	% disc.
16-BIC-072																			
12101-005.1	216	113	0.54	10.7	-1.7E-4	45	-0.29	0.0574	2.8	0.459	3.1	0.0580	1.5	0.466	506	61	**363**	**5**	29
12101-037.1	275	58	0.22	13.8	3.1E-13	--	0.00	0.0552	1.8	0.444	2.3	0.0583	1.4	0.609	421	41	**366**	**5**	+14
12101-100.1	190	71	0.39	9.6	4.4E-4	30	0.76	0.0508	4.6	0.411	4.8	0.0586	1.5	0.309	233	106	**367**	**5**	-59
12101-039.1	662	116	0.18	33.4	3.6E-4	23	0.63	0.0551	2.5	0.446	2.9	0.0587	1.4	0.474	417	56	**367**	**5**	+12
12101-065.1	334	121	0.38	16.8	-2.2E-5	100	-0.04	0.0542	1.8	0.438	2.3	0.0587	1.4	0.612	378	41	**368**	**5**	+3
12101-006.2	716	139	0.20	36.1	7.0E-5	38	0.12	0.0527	1.4	0.427	1.9	0.0587	1.3	0.696	317	31	**368**	**5**	-17
12101-002.1	374	88	0.24	18.9	1.5E-4	38	0.27	0.0521	2.4	0.423	2.8	0.0589	1.4	0.502	290	55	**369**	**5**	-28
12101-110.2	124	59	0.49	6.3	2.3E-4	50	0.41	0.0522	4.4	0.426	4.7	0.0592	1.6	0.333	293	101	**371**	**6**	-27
12101-028.1	268	71	0.27	13.7	1.4E-4	45	0.24	0.0541	2.6	0.442	3.0	0.0592	1.4	0.478	375	59	**371**	**5**	+1
12101-049.1	169	66	0.41	8.6	2.2E-4	45	0.38	0.0542	3.6	0.443	3.9	0.0593	1.5	0.381	379	82	**371**	**5**	+2
12101-110.1	858	42	0.05	43.8	-5.1E-5	41	-0.09	0.0541	1.2	0.443	1.8	0.0594	1.3	0.745	375	27	**372**	**5**	+1
12101-075.1	154	48	0.32	7.9	1.9E-4	50	0.33	0.0521	3.7	0.428	4.0	0.0595	1.5	0.376	289	86	**373**	**6**	-30
12101-124.2	1992	35	0.02	102.0	2.4E-5	38	0.04	0.0533	0.7	0.438	1.5	0.0596	1.3	0.877	343	16	**373**	**5**	-9
12101-029.1	708	47	0.07	36.2	8.3E-5	35	0.14	0.0538	1.4	0.442	2.0	0.0596	1.3	0.686	361	32	**373**	**5**	-3
12101-103.1	2095	77	0.04	107.4	1.5E-4	17	0.26	0.0538	1.0	0.442	1.6	0.0597	1.3	0.800	361	22	**374**	**5**	-4
12101-062.1	981	58	0.06	50.4	8.2E-5	30	0.14	0.0527	1.2	0.435	1.8	0.0598	1.3	0.737	316	28	**375**	**5**	-19
12101-019.2	992	62	0.06	51.0	2.4E-5	58	0.04	0.0529	1.1	0.437	1.7	0.0598	1.3	0.764	326	26	**375**	**5**	-16
12101-013.1	423	156	0.38	21.7	2.1E-4	30	0.36	0.0505	2.5	0.417	2.8	0.0599	1.4	0.490	218	57	**375**	**5**	-74
12101-073.1	1070	53	0.05	55.2	4.1E-5	41	0.07	0.0545	1.0	0.451	1.7	0.0600	1.3	0.785	391	23	**376**	**5**	+4
12101-036.1	285	66	0.24	14.7	-2.7E-5	100	-0.05	0.0568	2.0	0.471	2.4	0.0601	1.4	0.584	484	44	**376**	**5**	+23
12101-108.1	898	65	0.07	46.5	8.8E-4	20	1.52	0.0581	5.1	0.483	5.4	0.0602	1.5	0.280	535	113	**377**	**5**	+30
12101-019.1	290	86	0.31	15.0	1.6E-4	41	0.28	0.0491	2.9	0.408	3.2	0.0603	1.4	0.444	151	68	**378**	**5**	-154
12101-006.1	1241	71	0.06	64.4	6.8E-5	30	0.12	0.0542	1.1	0.452	1.7	0.0604	1.3	0.780	381	24	**378**	**5**	+1
12101-077.1	922	72	0.08	48.4	3.0E-5	50	0.05	0.0539	1.1	0.454	1.7	0.0611	1.3	0.777	368	24	**382**	**5**	-4
12101-121.1	498	55	0.11	26.2	1.3E-20	--	0.00	0.0542	1.4	0.458	2.0	0.0613	1.5	0.734	381	31	**383**	**5**	-1
12101-124.1	347	47	0.14	20.5	1.5E-4	35	0.27	0.0574	3.3	0.543	3.9	0.0686	2.2	0.552	508	72	428	9	+16
12101-062.2	258	93	0.37	19.3	7.2E-5	50	0.13	0.0600	1.7	0.720	2.3	0.0870	1.6	0.674	603	37	538	8	+11
12101-089.1	191	91	0.49	16.0	-2.4E-5	100	-0.04	0.0616	1.8	0.829	2.7	0.0976	2.0	0.752	660	38	600	12	+10
12101-072.1	1936	728	0.39	162.7	1.3E-5	41	0.02	0.0602	0.8	0.812	1.9	0.0978	1.7	0.900	610	18	602	10	+1
12101-124.3	495	162	0.34	104.6	2.3E-5	38	0.04	0.0948	0.5	3.216	1.6	0.2461	1.5	0.946	1524	10	1418	20	+8
12101-027.1	167	79	0.49	51.6	6.1E-5	35	0.11	0.1335	0.7	6.634	1.9	0.3605	1.8	0.931	2144	12	1985	30	+9
16-BIC-075																			
12102-085.2	315	215	0.71	16.0	1.8E-4	35	0.32	0.0530	2.5	0.432	2.9	0.0590	1.4	0.486	330	57	**370**	**5**	-12
12102-104.2	571	30	0.05	29.1	1.2E-4	32	0.20	0.0534	1.6	0.437	2.1	0.0594	1.4	0.638	345	37	**372**	**5**	-8
12102-043.1	165	35	0.22	8.5	2.2E-4	45	0.37	0.0520	5.1	0.429	5.4	0.0598	1.5	0.281	285	118	**374**	**5**	-32
12102-048.1	137	44	0.33	7.1	1.5E-4	58	0.26	0.0514	6.4	0.428	6.6	0.0605	1.5	0.232	259	148	**378**	**6**	-48
12102-087.1	507	22	0.04	26.4	9.7E-5	38	0.17	0.0528	1.7	0.442	2.2	0.0606	1.4	0.620	321	39	**379**	**5**	-19
12102-085.1	512	20	0.04	26.7	7.0E-5	45	0.12	0.0527	1.6	0.441	2.1	0.0607	1.4	0.638	315	37	**380**	**5**	-21
12102-036.1	196	48	0.25	10.2	1.8E-4	45	0.31	0.0518	3.3	0.434	3.6	0.0608	1.5	0.410	277	75	**381**	**5**	-38
12102-073.1	469	20	0.04	24.5	5.9E-5	50	0.10	0.0540	1.6	0.453	2.1	0.0609	1.4	0.645	370	37	**381**	**5**	-3
12102-042.1	316	46	0.15	16.5	1.5E-20	--	0.00	0.0553	1.7	0.465	2.2	0.0609	1.4	0.635	426	38	**381**	**5**	+11
12102-048.2	575	26	0.05	30.1	8.4E-5	38	0.15	0.0538	1.5	0.452	2.1	0.0609	1.5	0.687	363	35	**381**	**5**	-5
12102-009.1	217	42	0.20	11.4	3.6E-4	32	0.63	0.0503	4.1	0.423	4.4	0.0609	1.5	0.336	209	96	**381**	**5**	-85
12102-012.1	475	49	0.11	24.9	2.0E-4	28	0.34	0.0529	2.1	0.445	2.5	0.0610	1.4	0.544	323	48	**382**	**5**	-19
12102-066.1	294	27	0.09	15.4	1.2E-4	45	0.21	0.0533	2.3	0.449	2.7	0.0610	1.4	0.518	342	53	**382**	**5**	-12
12102-022.1	546	27	0.05	28.6	-6.6E-5	45	-0.11	0.0554	1.5	0.466	2.0	0.0611	1.4	0.672	427	33	**382**	**5**	+11
12102-106.1	695	25	0.04	36.7	2.1E-5	71	0.04	0.0538	1.3	0.455	1.8	0.0614	1.3	0.731	362	28	**384**	**5**	-6
12102-088.1	428	22	0.05	22.6	6.5E-5	50	0.11	0.0518	1.8	0.439	2.2	0.0614	1.4	0.614	278	40	**384**	**5**	-39
12102-096.2	640	35	0.06	33.9	2.2E-5	71	0.04	0.0541	1.3	0.459	1.9	0.0616	1.3	0.724	375	29	**385**	**5**	-3
12102-067.1	759	48	0.07	40.2	1.2E-4	28	0.20	0.0526	2.1	0.447	2.5	0.0616	1.3	0.537	312	48	**386**	**5**	-24
12102-020.1	271	26	0.10	14.4	1.0E-13	--	0.00	0.0555	1.8	0.472	2.3	0.0617	1.4	0.615	434	40	**386**	**5**	+11
12102-096.1	1178	60	0.05	62.7	2.4E-14	--	0.00	0.0546	0.9	0.467	1.6	0.0620	1.3	0.833	396	20	**388**	**5**	+2
12102-106.2	146	132	0.93	11.2	1.4E-4	50	0.24	0.0577	2.7	0.711	3.1	0.0893	1.5	0.482	519	60	552	8	-6
12102-074.1	278	146	0.54	22.2	-1.5E-5	100	-0.03	0.0604	2.7	0.774	3.0	0.0928	1.4	0.460	619	58	572	8	+8
12102-065.1	254	102	0.41	21.1	3.5E-5	71	0.06	0.0607	2.6	0.809	2.9	0.0968	1.4	0.479	627	55	595	8	+5
12102-090.1	105	37	0.37	8.8	3.8E-4	32	0.65	0.0558	3.9	0.746	4.2	0.0969	1.5	0.367	445	87	596	9	-35
12102-060.1	125	64	0.53	10.4	4.1E-4	28	0.72	0.0525	3.9	0.706	4.2	0.0976	1.5	0.360	306	89	600	9	-101
12102-080.1	80	31	0.40	6.9	1.4E-4	58	0.25	0.0551	3.4	0.767	3.8	0.1009	1.6	0.425	417	76	620	9	-51
12102-081.1	179	87	0.50	15.6	2.3E-4	32	0.41	0.0579	2.6	0.809	2.9	0.1013	1.5	0.494	527	56	622	9	-19
12102-015.1	81	68	0.86	7.2	-1.6E-4	58	-0.27	0.0625	3.2	0.893	3.6	0.1036	1.6	0.453	691	68	636	10	+8
12102-092.1	142	48	0.35	12.8	1.4E-4	45	0.25	0.0602	2.5	0.868	2.9	0.1045	1.5	0.518	611	53	641	9	-5
12102-059.1	389	224	0.60	38.0	6.5E-5	38	0.11	0.0650	4.0	1.020	4.2	0.1138	1.4	0.326	775	84	695	9	+11
12102-104.1	856	463	0.56	88.7	1.7E-4	17	0.29	0.0647	0.9	1.075	1.8	0.1206	1.5	0.848	764	20	734	10	+4
12102-043.2	573	217	0.39	64.7	1.7E-4	18	0.30	0.0675	4.0	1.224	4.3	0.1315	1.5	0.356	853	83	797	11	+7
12102-056.1	116	49	0.44	34.9	2.1E-5	71	0.04	0.1264	0.8	6.111	2.2	0.3506	2.0	0.926	2049	14	1938	34	+6

Appendix 2: cont.

Spot No.	U ppm	Th ppm	Th/U	$^{206}Pb^*$ ppm	Corrected isotope ratios										Apparent ages (Ma)				
					$^{204}Pb/^{206}Pb$	±1s (%)	$f(206)^{204}$ %	$^{207}Pb^*/^{206}Pb^*$	±1s (%)	$^{207}Pb^*/^{235}U^*$	±1s (%)	$^{206}Pb^*/^{238}U$	±1s (%)	error coeff.	$^{207}Pb^*/^{206}Pb^*$	±1s (Ma)	$^{206}Pb^*/^{238}U^*$	±1s (Ma)	% disc.
16-BIC-081																			
12103-047.1	170	280	1.70	7.7	-1.8E-13	--	0.00	0.0531	2.5	0.388	2.9	0.0530	1.5	0.512	332	57	~~**333**~~	~~**5**~~	0
12103-099.2	90	40	0.47	4.4	-3.5E-13	--	0.00	0.0527	3.5	0.410	3.9	0.0564	1.6	0.427	316	79	~~**354**~~	~~**6**~~	-12
12103-040.1	597	32	0.05	30.4	5.5E-5	45	0.09	0.0531	1.4	0.434	1.9	0.0592	1.3	0.695	334	32	**371**	**5**	-11
12103-047.2	310	320	1.07	15.8	1.8E-4	35	0.30	0.0538	2.4	0.440	2.8	0.0593	1.4	0.498	361	55	**371**	**5**	-3
12103-024.1	166	50	0.31	8.5	1.2E-4	58	0.21	0.0579	2.9	0.474	3.2	0.0594	1.5	0.457	527	63	**372**	**5**	+30
12103-055.1	313	334	1.10	16.0	2.0E-4	33	0.35	0.0544	2.5	0.446	2.9	0.0595	1.4	0.485	389	57	**372**	**5**	+4
12103-017.1	165	60	0.38	8.4	-7.9E-5	71	-0.14	0.0568	2.6	0.466	3.0	0.0595	1.5	0.491	485	58	**372**	**5**	+24
12103-002.1	338	109	0.33	17.3	3.9E-5	71	0.07	0.0553	1.8	0.454	2.2	0.0595	1.4	0.618	425	39	**373**	**5**	+13
12103-018.1	102	73	0.73	5.2	3.8E-4	41	0.67	0.0483	5.8	0.398	6.1	0.0598	1.6	0.264	114	138	**374**	**6**	-236
12103-112.1	787	52	0.07	40.5	1.5E-4	25	0.26	0.0531	1.5	0.439	2.0	0.0599	1.3	0.657	334	35	**375**	**5**	-13
12103-015.1	70	78	1.15	3.6	-3.9E-4	50	-0.68	0.0636	5.7	0.525	5.9	0.0599	1.7	0.295	730	120	**375**	**6**	+50
12103-020.1	776	63	0.08	39.9	9.4E-5	32	0.16	0.0529	1.4	0.437	2.0	0.0599	1.5	0.724	326	32	**375**	**5**	-16
12103-036.1	529	85	0.17	27.3	1.3E-5	100	0.02	0.0526	1.4	0.435	1.9	0.0601	1.4	0.698	310	32	**376**	**5**	-22
12103-066.1	453	278	0.63	23.4	2.0E-4	27	0.35	0.0528	2.1	0.437	2.5	0.0601	1.5	0.582	319	47	**376**	**5**	-19
12103-058.1	214	39	0.19	11.0	-1.7E-4	45	-0.29	0.0565	2.8	0.469	3.1	0.0601	1.5	0.463	473	62	**377**	**5**	+21
12103-076.1	715	57	0.08	37.0	4.5E-4	16	0.78	0.0560	2.2	0.465	2.6	0.0602	1.3	0.516	453	50	**377**	**5**	+17
12103-113.1	320	239	0.77	16.6	8.2E-5	50	0.14	0.0563	2.0	0.469	2.4	0.0604	1.4	0.581	463	43	**378**	**5**	+19
12103-060.1	372	54	0.15	19.3	7.8E-5	50	0.13	0.0520	2.0	0.433	2.4	0.0604	1.4	0.572	286	45	**378**	**5**	-33
12103-065.1	291	106	0.37	15.2	-2.4E-5	100	-0.04	0.0569	1.9	0.475	2.3	0.0606	1.4	0.605	486	41	**379**	**5**	+23
12103-103.1	398	54	0.14	20.7	1.1E-4	41	0.19	0.0540	2.0	0.452	2.4	0.0606	1.4	0.575	373	44	**379**	**5**	-2
12103-118.1	808	33	0.04	42.1	-3.9E-5	50	-0.07	0.0552	1.2	0.461	2.0	0.0606	1.6	0.787	419	28	**379**	**6**	+10
12103-089.1	294	39	0.14	15.4	-2.5E-5	100	-0.04	0.0548	2.0	0.460	2.4	0.0608	1.4	0.582	405	45	**381**	**5**	+6
12103-079.2	1082	56	0.05	56.6	9.6E-5	26	0.17	0.0533	1.2	0.447	1.8	0.0609	1.3	0.752	340	26	**381**	**5**	-12
12103-110.1	496	22	0.05	26.0	-2.9E-5	71	-0.05	0.0525	1.5	0.441	2.0	0.0609	1.4	0.671	306	34	**381**	**5**	-25
12103-044.1	560	37	0.07	29.4	2.5E-5	71	0.04	0.0523	1.4	0.440	2.0	0.0610	1.4	0.691	300	32	**382**	**5**	-28
12103-022.1	168	16	0.10	9.6	2.7E-4	38	0.47	0.0510	3.8	0.467	4.1	0.0665	1.5	0.363	240	88	415	6	-76
12103-013.1	115	53	0.47	7.4	2.3E-4	45	0.40	0.0551	3.8	0.564	4.1	0.0742	1.5	0.379	418	84	461	7	-11
12103-079.1	125	76	0.63	9.4	3.5E-4	35	0.60	0.0551	4.1	0.665	4.4	0.0875	1.6	0.354	417	92	541	8	-31
12103-104.1	537	391	0.75	41.8	7.6E-5	33	0.13	0.0577	1.2	0.720	1.9	0.0905	1.5	0.773	518	27	559	8	-8
12103-100.1	262	137	0.54	20.6	5.3E-5	58	0.09	0.0584	2.9	0.734	3.3	0.0912	1.4	0.430	544	64	563	8	-4
12103-105.1	538	170	0.33	44.1	6.9E-5	33	0.12	0.0595	1.1	0.783	1.8	0.0955	1.3	0.767	586	24	588	8	-0
12103-099.1	219	62	0.29	26.5	4.7E-13	--	0.00	0.1431	5.6	2.779	8.0	0.1408	5.8	0.718	2265	96	849	46	+67
12103-012.1	120	161	1.38	23.8	3.1E-5	71	0.05	0.1181	1.0	3.745	1.8	0.2299	1.5	0.823	1928	18	1334	18	+34
12103-012.2	123	170	1.43	31.2	-2.1E-5	71	-0.04	0.1267	1.8	5.160	2.4	0.2955	1.5	0.617	2052	33	1669	21	+21
16-BIC-084																			
12104-118.1	310	32	0.11	15.5	1.2E-4	45	0.20	0.0540	2.3	0.433	2.7	0.0582	1.4	0.529	370	52	**365**	**5**	2
12104-041.2	397	11	0.03	19.9	2.3E-4	28	0.40	0.0532	2.4	0.429	2.7	0.0585	1.4	0.504	339	54	**366**	**5**	-8
12104-090.1	173	26	0.16	8.7	1.4E-13	--	0.00	0.0566	2.2	0.457	2.6	0.0585	1.5	0.559	478	48	**366**	**5**	+24
12104-093.1	138	21	0.15	7.0	2.4E-4	45	0.41	0.0563	3.8	0.457	4.1	0.0589	1.5	0.374	463	84	**369**	**5**	+21
12104-032.1	273	27	0.10	14.0	3.9E-4	26	0.68	0.0496	3.7	0.408	3.9	0.0597	1.4	0.363	176	86	**374**	**5**	-116
12104-086.1	2001	32	0.02	102.8	3.5E-5	30	0.06	0.0540	0.7	0.445	1.5	0.0598	1.3	0.880	372	16	**374**	**5**	-1
12104-062.1	495	29	0.06	25.5	1.4E-4	32	0.25	0.0515	2.7	0.426	3.0	0.0599	1.4	0.450	265	62	**375**	**5**	-43
12104-096.1	413	27	0.07	21.3	1.9E-5	100	0.03	0.0530	1.7	0.438	2.2	0.0600	1.4	0.630	328	39	**375**	**5**	-15
12104-082.1	156	35	0.24	8.0	1.7E-4	50	0.29	0.0523	3.4	0.433	3.7	0.0600	1.5	0.403	299	77	**375**	**5**	-26
12104-040.1	474	30	0.07	24.5	9.1E-5	41	0.16	0.0551	1.9	0.457	2.3	0.0601	1.4	0.594	417	41	**376**	**5**	+10
12104-058.1	239	36	0.15	12.4	1.2E-4	50	0.22	0.0539	2.7	0.447	3.0	0.0602	1.4	0.474	367	60	**377**	**5**	-3
12104-037.1	367	24	0.07	19.0	2.3E-4	29	0.39	0.0525	2.5	0.435	2.8	0.0602	1.4	0.491	305	56	**377**	**5**	-24
12104-008.1	448	25	0.06	23.2	1.4E-4	33	0.25	0.0527	2.0	0.438	2.4	0.0602	1.4	0.566	315	46	**377**	**5**	-20
12104-044.1	392	25	0.07	20.3	-1.8E-5	100	-0.03	0.0555	1.6	0.461	2.1	0.0603	1.4	0.653	430	36	**377**	**5**	+13
12104-019.1	408	31	0.08	21.1	1.8E-4	32	0.30	0.0527	2.2	0.438	2.6	0.0603	1.4	0.527	315	51	**377**	**5**	-20
12104-009.1	582	35	0.06	30.1	2.4E-5	71	0.04	0.0553	1.3	0.460	1.9	0.0603	1.4	0.714	426	30	**377**	**5**	+12
12104-003.1	335	29	0.09	17.3	4.3E-5	71	0.07	0.0545	1.9	0.453	2.3	0.0604	1.4	0.595	391	42	**378**	**5**	+3
12104-039.1	473	19	0.04	24.5	2.6E-4	23	0.45	0.0538	2.8	0.448	3.2	0.0604	1.5	0.461	362	64	**378**	**5**	-5
12104-045.1	255	42	0.17	13.3	8.3E-5	58	0.14	0.0536	2.3	0.447	2.7	0.0605	1.4	0.520	353	53	**379**	**5**	-8
12104-066.1	596	30	0.05	31.0	2.4E-5	71	0.04	0.0542	1.3	0.453	1.9	0.0606	1.4	0.713	378	30	**379**	**5**	-0
12104-089.1	193	39	0.21	10.1	-7.9E-5	71	-0.14	0.0598	2.5	0.501	2.9	0.0607	1.5	0.503	598	55	**380**	**5**	+38
12104-052.1	437	19	0.05	22.8	9.7E-5	41	0.17	0.0544	1.8	0.456	2.3	0.0608	1.4	0.601	389	41	**380**	**5**	+2
12104-042.1	77	36	0.48	4.1	3.8E-4	50	0.67	0.0530	6.6	0.446	6.9	0.0610	1.7	0.254	331	151	**382**	**6**	-16
12104-024.1	702	37	0.05	36.8	1.1E-5	100	0.02	0.0539	1.2	0.454	1.8	0.0611	1.3	0.734	367	28	**382**	**5**	-4
12104-079.1	863	39	0.05	45.4	4.1E-5	45	0.07	0.0545	1.1	0.460	1.8	0.0612	1.3	0.759	392	26	**383**	**5**	+2
12104-113.1	337	44	0.14	18.4	1.9E-4	33	0.32	0.0534	2.4	0.468	2.8	0.0635	1.4	0.504	348	54	~~**397**~~	~~**5**~~	-15
12104-039.2	183	40	0.23	13.5	1.5E-4	41	0.26	0.0588	2.4	0.697	2.8	0.0860	1.4	0.524	560	51	532	7	+5
12104-026.1	217	120	0.57	17.9	1.1E-4	41	0.20	0.0614	1.9	0.812	2.3	0.0960	1.4	0.605	652	40	591	8	+10
12104-041.1	292	193	0.68	25.6	1.4E-4	32	0.25	0.0585	1.8	0.822	2.3	0.1019	1.4	0.617	548	39	626	8	-15
12104-114.1	86	79	0.95	7.8	5.8E-4	30	1.01	0.0635	5.9	0.923	6.2	0.1054	2.0	0.314	726	125	646	12	+12
12104-023.1	573	351	0.63	64.1	7.7E-5	28	0.13	0.0656	0.9	1.177	1.9	0.1302	1.7	0.876	793	20	789	13	+1
12104-042.2	175	39	0.23	58.0	-6.7E-6	100	-0.01	0.1327	1.2	7.061	2.0	0.3859	1.6	0.809	2134	20	2104	28	+2

Appendix 2: cont.

Spot No.	U ppm	Th ppm	Th/U	^{206}Pb* ppm	Corrected isotope ratios: ^{204}Pb/^{206}Pb	±1s (%)	f(206)^{204} %	^{207}Pb*/^{206}Pb*	±1s (%)	^{207}Pb*/^{235}U*	±1s (%)	^{206}Pb*/^{238}U	±1s (%)	error coeff.	Apparent ages (Ma): ^{207}Pb*/^{206}Pb*	±1s (Ma)	^{206}Pb*/^{238}U*	±1s (Ma)	% disc.
16-BIC-085																			
12105-032.1	169	61	0.37	7.4	3.6E-3	19	6.32	0.0561	####	0.396	19.7	0.0512	2.2	0.113	457	433	~~**322**~~	~~**7**~~	30
12105-082.2	433	28	0.07	21.1	4.2E-4	19	0.73	0.0569	2.5	0.445	2.9	0.0567	1.4	0.476	488	56	**356**	**5**	+28
12105-049.1	938	569	0.63	45.8	1.5E-3	16	8.92	0.0530	9.9	0.426	10.0	0.0583	1.4	0.141	327	224	**365**	**5**	-12
12105-033.1	89	25	0.29	46.9	-2.7E-13	--	2.59	0.0586	3.2	0.476	3.6	0.0588	1.6	0.457	554	70	**368**	**6**	+34
12105-105.1	236	73	0.32	4.5	2.3E-4	35	0.00	0.0525	3.0	0.427	3.3	0.0591	1.4	0.429	307	69	**370**	**5**	-21
12105-046.1	136	73	0.56	12.0	4.3E-4	35	0.39	0.0518	5.2	0.423	5.5	0.0592	1.6	0.286	276	120	**371**	**6**	-35
12105-009.2	567	51	0.09	6.9	3.3E-4	20	0.75	0.0535	2.2	0.437	2.6	0.0593	1.4	0.524	351	50	**371**	**5**	-6
12105-075.1	362	37	0.11	28.9	8.8E-21	--	0.56	0.0562	1.6	0.461	2.1	0.0595	1.4	0.658	459	35	**373**	**5**	+19
12105-035.1	243	23	0.10	18.5	8.9E-5	58	0.00	0.0528	2.5	0.433	2.9	0.0595	1.4	0.501	320	56	**373**	**5**	-17
12105-028.1	438	32	0.08	12.4	8.0E-5	45	0.15	0.0548	1.7	0.450	2.2	0.0595	1.4	0.619	404	39	**373**	**5**	+8
12105-018.1	152	56	0.38	22.4	2.1E-4	45	0.14	0.0534	4.7	0.439	5.0	0.0595	1.5	0.303	348	107	**373**	**5**	-7
12105-103.1	1252	49	0.04	7.8	6.3E-5	29	0.37	0.0534	1.0	0.441	1.6	0.0600	1.3	0.803	345	22	**375**	**5**	-9
12105-041.1	234	116	0.51	64.5	5.5E-5	71	0.11	0.0543	2.2	0.449	2.6	0.0600	1.4	0.544	382	49	**376**	**5**	+2
12105-019.1	441	61	0.14	12.1	6.3E-5	50	0.10	0.0535	1.7	0.443	2.2	0.0601	1.4	0.630	348	38	**376**	**5**	-8
12105-004.1	368	63	0.18	22.7	1.9E-5	100	0.11	0.0559	2.7	0.463	3.2	0.0601	1.7	0.524	449	60	**376**	**6**	+17
12105-023.1	581	66	0.12	19.0	1.1E-4	33	0.03	0.0533	1.7	0.442	2.2	0.0601	1.4	0.628	342	38	**376**	**5**	-10
12105-096.1	292	49	0.17	30.0	1.9E-4	35	0.20	0.0523	2.6	0.435	3.0	0.0603	1.4	0.472	299	60	**377**	**5**	-27
12105-029.1	505	342	0.70	15.1	7.8E-5	41	0.33	0.0534	1.6	0.444	2.1	0.0603	1.4	0.649	346	36	**377**	**5**	-9
12105-109.1	316	55	0.18	26.1	1.5E-4	38	0.14	0.0527	3.6	0.439	3.9	0.0604	1.4	0.362	318	82	**378**	**5**	-19
12105-110.1	1395	44	0.03	16.4	7.4E-5	26	0.26	0.0542	1.9	0.452	2.4	0.0604	1.4	0.573	381	44	**378**	**5**	+1
12105-071.1	666	97	0.15	72.4	-1.1E-5	100	0.13	0.0554	1.2	0.462	1.8	0.0604	1.3	0.743	430	27	**378**	**5**	+12
12105-031.1	1127	57	0.05	34.6	7.4E-5	29	-0.02	0.0535	1.1	0.446	1.7	0.0605	1.3	0.774	348	24	**379**	**5**	-9
12105-024.1	1064	72	0.07	58.6	3.2E-5	45	0.13	0.0539	1.0	0.450	1.7	0.0606	1.3	0.796	367	23	**379**	**5**	-3
12105-069.1	483	21	0.04	55.4	5.7E-5	50	0.06	0.0523	1.6	0.438	2.1	0.0607	1.4	0.641	300	37	**380**	**5**	-27
12105-085.1	969	57	0.06	25.2	1.9E-4	20	0.10	0.0534	1.5	0.447	2.0	0.0607	1.3	0.674	348	33	**380**	**5**	-10
12105-060.1	171	41	0.25	50.5	4.1E-5	100	0.33	0.0564	2.5	0.473	2.9	0.0608	1.5	0.504	468	56	**381**	**5**	+19
12105-008.1	99	80	0.83	8.9	3.7E-4	33	0.07	0.0586	3.9	0.777	4.2	0.0961	1.6	0.372	554	85	591	9	-7
12105-026.1	223	90	0.42	8.1	5.5E-4	21	0.64	0.0545	3.6	0.744	3.9	0.0990	1.5	0.371	393	82	608	8	-57
12105-026.2	157	96	0.63	19.0	1.6E-4	45	0.95	0.0588	2.7	0.811	3.2	0.1000	1.8	0.566	561	58	615	11	-10
12105-082.1	242	82	0.35	37.9	8.2E-14	--	0.00	0.0798	1.0	2.008	2.1	0.1825	1.9	0.889	1192	19	1081	19	+10
12105-028.2	294	95	0.34	58.5	5.2E-5	33	0.09	0.0928	0.7	2.970	1.6	0.2320	1.4	0.883	1485	14	1345	17	+10
12105-013.1	206	78	0.39	47.4	5.6E-5	38	0.10	0.0936	1.3	3.459	2.1	0.2680	1.6	0.760	1500	25	1531	21	-2
12105-016.1	262	41	0.16	80.8	2.9E-5	38	0.05	0.1275	0.5	6.304	2.0	0.3585	1.9	0.962	2064	10	1975	32	+5
12105-037.1	130	74	0.59	44.9	5.9E-5	35	0.10	0.1228	1.4	6.786	2.0	0.4008	1.5	0.720	1997	25	2173	27	-10

Note:

The probability density cores plots (Figs. 3 and 4) have ^{206}Pb/^{238}U to ^{207}Pb/^{206}Pb at 750 Ma, no filtering for discordance

Bolded apparent ages are included in weighted mean average crystallization age for sample

Ages with strikethrough indicate analysis was rejected; either due to inclusion, crack, high common Pb or a low U/altered zone

Spot name follows the convention x-y.z; where x = sample number, y = grain number and z = spot number. Multiple analyses in an individual spot are labelled as x-y.z.z

Uncertainties are reported at 1s and are calculated by using SQUID 2.23.08.10.21, rev. 21 Oct 2008

f(206)^{204} refers to mole percent of total ^{206}Pb that is due to common Pb, calculated using the^{204}Pb-method; common Pb composition used is the surface blank (4/6: 0.05770; 7/6: 0.89500; 8/6: 2.13840)

* refers to radiogenic Pb (corrected for common Pb using ^{204}Pb).

% disc: Discordance given as difference between measured ^{206}*Pb/^{238}U ratio and the expected ^{206}*Pb/^{238}U ratio at t=207*/206* age, in percent.

Calibration standard 10493; ^{207}Pb/^{206}Pb Age = 421 Ma

Error in ^{206}Pb/^{238}U calibration 1.5% (included)

Standard Error in Standard calibration was 0.34% (not included in above errors but required when comparing data from different mounts).

Discovering the next generation of copper porphyry deposits using mineral markers

A. Plouffe[1], I.M. Kjarsgaard[2], C.H. Kobylinski[3, 1], K. Hattori[3], D.C. Petts[1], K.E. Venance[1] and T. Ferbey[4]

[1]*Geological Survey of Canada, 601 Booth Street, Ottawa, Ontario K1A 0E8*
[2]*Mineralogical Consultant, 15 Scotia Place, Ottawa, Ontario K1S 0W2*
[3]*Department of Earth and Environmental Sciences, University of Ottawa, 25 Templeton Street, Ottawa, Ontario K1N 6N5*
[4]*British Columbia Geological Survey Branch, 1810 Blanshard Street, Victoria, British Columbia V8T 4J1*

Abstract

The composition of epidote and zircon in till and bedrock around copper porphyry mineralization in south-central British Columbia are investigated as an indicator towards deposits covered by glacial sediments. At the Gibraltar porphyry deposit, new dating reveals that the Mine phase of the Granite Mountain batholith was emplaced during three intrusive pulses at ca. 205, 213 and 219 Ma. Zircon Ce^{4+}/Ce^{3+} ratios, a potential fertility proxy, progressively decrease from an average of 681 in the earliest mineralized intrusive Mine phase (219 Ma) to 193 in the younger intrusive phase (202–207 Ma). Zircon with Ce^{4+}/Ce^{3+} values greater than 400, corresponding to a Ce/Nd ratio of 20, are most likely derived from the mineralized Mine phase. Two zircon grains with Ce/Nd ratios greater than 20 were identified in a till sample less than 1 km down-ice from mineralization. Epidote grains in till from three porphyry localities (Mount Polley, Woodjam, and Gibraltar) and bedrock from Woodjam were analyzed to test the hypothesis that a simple correlation plot of Sb versus As could be used to differentiate epidote that formed in metamorphic versus hydrothermal settings. Our preliminary results show a significant overlap between the As and Sb concentrations in epidote grains from till and epidote from the alteration zones at the Woodjam prospect. Future work will investigate whether epidote in till with low As (< 10 ppm) and Sb (<1 ppm) levels could be derived from regionally metamorphosed rocks of the Nicola Group.

Introduction

Plouffe et al. (2018) provided an overview on work in progress on the study of zircon, rutile and epidote grains from till and rock samples from the Gibraltar copper porphyry deposit of south-central British Columbia. The objective of this research is to study the geochemical composition of minerals from copper porphyry mineralization and associated alteration zones so that their composition can be linked to ore formation processes. These minerals could then be identified and traced in detrital sediments (e.g. till, stream sediments) to a mineralized source. Ultimately, a suite of porphyry copper indicator minerals (PCIM) identified in detrital sediments will serve to assess, at a regional scale, the fertility potential of a batholith and at a more detailed scale, detect the presence of buried copper porphyry mineralization. For PCIM to be effective in mineral exploration, their abundance or composition needs to be related to a porphyry source and they need to be resistant enough to survive glacial erosion, transport, and postglacial weathering.

We report on the work in progress on the study of zircon and epidote composition from rocks and till in the region of copper porphyry mineralization of south-central British Columbia including the Gibraltar copper-molybdenum deposit (active mine), the Mount Polley copper-gold deposit (active mine) and the Woodjam prospect. Zircon and epidote are selected for this study because they are known to be present in till and their composition has the potential to be indicative of a mineralized source.

Background

Hashmi et al. (2015), Ferbey et al. (2016), Plouffe and Ferbey (2016) and Plouffe et al. (2016) reported the abundance of PCIM in till in the region of the aforementioned porphyry copper study sites, Gibraltar, Woodjam and Mount Polley, plus the Highland Valley copper-molybdenum porphyry district which includes the Highland Valley Copper deposits (Fig. 1). Copper porphyry mineralization at these sites is hosted in Late Triassic to Early Jurassic felsic to intermediate intrusive rocks of the Quesnel volcanic arc terrane, composed predominantly of the sedimentary and volcanic rocks of the Nicola Group, which were accreted to North America during the mid-Jurassic (Byrne et al., 2013; Rees, 2013; Sherlock et al., 2013; van

Corresponding author: Alain Plouffe (alain.plouffe@canada.ca)

Plouffe, A., Kjarsgaard, I.M., Kobylinski, C.H., Hattori, K., Petts, D.C., Venance, K.E., and Ferbey, T., 2019. Discovering the next generation of copper porphyry deposits using mineral markers; *in* Targeted Geoscience Initiative: 2018 report of activities, (ed.) N. Rogers; Geological Survey of Canada, Open File 8549, p. 321–331. https://doi.org/10.4095/313666

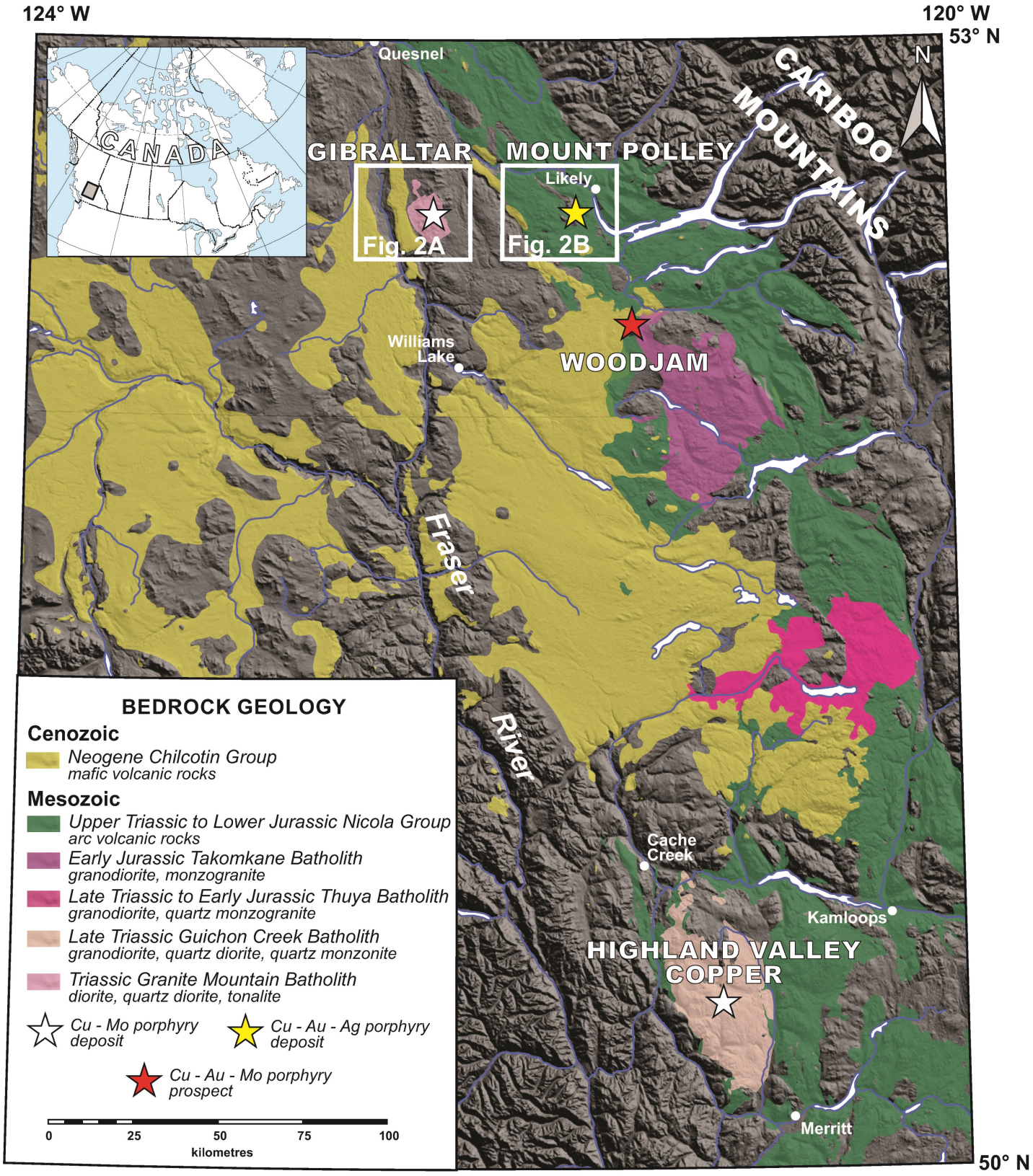

Figure 1. Location map with the four copper porphyry study sites mentioned in the text (*modified from* Ferbey et al., 2014).

Straaten et al., 2013). The investigation of till mineralogy showed the greater abundance of ore (e.g. chalcopyrite and gold) and alteration (e.g. epidote) minerals in till near porphyry mineralization compared to surrounding background regions, with distribution patterns influenced by ice-flow movements. These results complement, with some differences, the conclusions of Kelley et al. (2011) about the distribution of PCIM in till in the region of the Pebble Cu-Au-Mo porphyry deposit in Alaska. For instance, the presence of chalcopyrite in surface till samples is observed at the four sites in British Columbia but is absent at Pebble.

Using the till mineralogy results from British Columbia, Plouffe and Ferbey (2017) present a two-fold classification scheme for PCIM in till. Group 1 PCIM can be directly linked to copper porphyry mineralization because they are generally more abundant in till near mineralization and the associated alteration zones compared to surrounding regions with no mineralization. In addition, group 1 PCIM show distribution patterns in till influenced by ice-flow movements (Fig. 2a). Conversely, group 2 PCIM are not more abundant in till near copper porphyry centres and only their chemical or physical attributes can be linked to a porphyry source (Fig. 2b). Plouffe and Ferbey (2017) note that their classification scheme is site specific. We present the analytical results and preliminary interpretation for two minerals: zircon, which classifies as a potential group 2 PCIM, and epidote as a group 1 PCIM.

Methods

Zircon compositions at Gibraltar were determined by laser ablation inductively coupled plasma mass spectrometry (LA-ICP-MS) analyses conducted at the University of Ottawa. The analytical methodology is detailed in Kobylinski et al. (2018).

We also report on epidote trace element composition conducted on polished thin sections (thickness = 75 µm) of rock samples from the Woodjam prospect and grain mounts produced with epidote grains recovered from till at the three porphyry study sites. Epidote grains were recovered from till samples following heavy mineral separation procedures outlined in Plouffe and Ferbey (2016), and mounted in epoxy mounts. Epidote was analyzed by LA-ICP-MS at the Geological Survey of Canada (GSC) using a Photon Machines Analyte G2 (equipped with a dual-volume cell) connected to an Agilent 7700x ICP-MS. Laser conditions during this work included a laser fluence of 5 J/cm^2, a spot size of 50 to 65 µm, and a repetition rate of 10 Hz. Signals were acquired on the ICP-MS using time-resolved data acquisition mode, including a total mass cycle time of 456 ms (all 58 elements) and dwell times of 2 to 4 ms for major elements, 4 to 8 ms for most trace elements, and 12 to 16 ms for As, Ag, Pd, and Au. The total analytical time for each sample was 100 s, with 40 s of background measurement (laser-off) and 60 s of signal analysis (laser on). The United States Geological Survey glass standard GSE-1G was used as the primary calibration standard and was analyzed twice every hour to correct for instrument drift. Accuracy was assessed by analyses of secondary standards NIST-612, GSD-

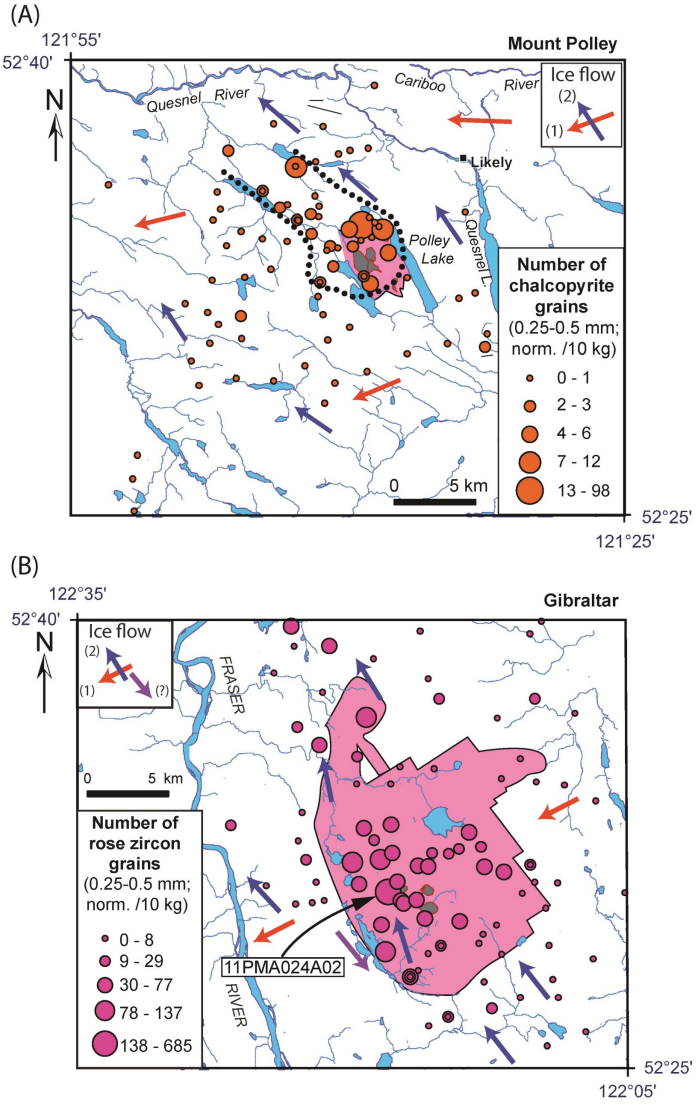

Figure 2. (A) Distribution of chalcopyrite grains in the 0.25 to 0.5 mm and greater than 3.2 SG fraction of till at the Mount Polley porphyry copper-gold deposit. The pink polygon represents the Mount Polley intrusive complex and the grey polygons the extent of the porphyry copper mineralization. (B) Distribution of zircon grains in the same size and density fraction of till at the Gibraltar porphyry copper-molybdenum deposit. The pink polygon represents the Granite Mountain batholith and the grey polygons the extent of porphyry copper mineralization. Grain counts normalized to 10 kg bulk material less than 2 mm. *Modified from* Hashmi et al. (2015), Plouffe et al. (2016) and Plouffe and Ferbey (2017).

1G, BCR-26, and Po689, with most elements falling between 5 and 10% of their accepted values. Secondary standards were analyzed once every hour. Analytical spectra were visualized and processed using Glitter software. Only a 'clean' portion of each spectrum with no evidence of contamination by inclusions (e.g. Ti or P spikes related to titanite and apatite inclusions,

respectively) was retained for data processing. Trace element concentrations of unknowns were calibrated using Ca as an internal standard, which was determined by electron microprobe analyses (EMPA) acquired on a JEOL8230 electron microprobe equipped with five wavelength spectrometers at the University of Ottawa, using Probe for EPMA software. The operating conditions were 20kV accelerating voltage, 20nA beam current and a spot size of 5 microns. Count times were 10 s on peak and 5 s on backgrounds either side of the peak. Calibration standards were a mix of natural and synthetic minerals. Raw data were processed with the CITZAF program of Armstrong (1988).

LA-ICP-MS analytical results were further filtered to remove mineral phases other than epidote using weight % oxides of major elements. Analyses with SiO_2 > 42 weight %, TiO_2 > 0.5 weight %, Al_2O_3 < 15 weight %, Fe_2O_3> 16 weight %, MgO > 0.5 weight %, CaO> 24 weight %, Na_2O>0.5 weight %, K_2O > 0.25 weight %, and P_2O_5> 0.5 weight % as well as those that had very high or low totals (<90 weight % and >105 weight %) were rejected from the interpreted data set. Europium anomaly (Eu/Eu*) corresponds to $Eu_N/(Sm_N \times Gd_N)^{0.5}$ where N denotes chondrites-normalised values using McDonough and Sun (1995).

Zircon

The composition of magmatic zircon in host rocks of porphyry deposits can be used to date the intrusive phases but can also provide an indication of the fertility potential of the intrusion. Porphyry copper deposits are typically associated with oxidized and hydrous magmas that facilitate the transport and concentration of chalcophile elements, such as copper, to the shallow crust (Sillitoe, 2010; Richards, 2011). Zircon in oxidized intrusions associated with copper porphyry mineralization typically shows higher Ce^{4+}/Ce^{3+} ratios compared to barren intrusions, and Eu anomalies greater than 0.4 (Ballard et al., 2002; Liang et al., 2006; Dilles et al., 2015; Shen et al., 2015; Hattori et al., 2016, 2017; Lee et al., 2017a, b). Consequently, identifying zircon from till or stream sediments with anomalous Ce^{4+}/Ce^{3+} or Eu/Eu* values could become an exploration tool for assessing the mineralization potential of large batholiths similar to the tracing of Cr-pyrope ('G10' garnets) in till or stream sediments to detect diamondiferous kimberlite (e.g. McClenaghan and Kjarsgaard, 2007).

To test the hypothesis of using zircon as a PCIM, Wolfe (2017) and Kobylinski et al. (2018) investigated the composition of zircon in till and bedrock at the Gibraltar copper-molybdenum porphyry deposit. As part of this investigation, U-Pb dating based on LA-ICP-MS analyses of zircon refines the emplacement history of the Granite Mountain batholith, which is host of the mineralization (Kobylinski et al., 2018). Not only was the batholith emplaced in compositionally different intrusive phases from ca. 222 to 202 Ma, but the Mine phase, which contains the bulk of the copper mineralization, is now recognized as three compositionally indistinguishable intrusive pulses at 202 to 207, 213 and 219 Ma (Kobylinski et al., 2018). Furthermore, the Ce^{4+}/Ce^{3+} values of zircon, calculated according to the method of Ballard et al. (2002), progressively decrease from an average of 681 in the earliest pulse of the mineralized Mine phase (219 Ma) to 193 in the youngest intrusive pulse (Fig. 3). Zircon Ce^{4+}/Ce^{3+} mean values in the unmineralized or sub-economically mineralized Mine, Border and Granite Mountain intrusive phases are all below 215 (Fig. 3).

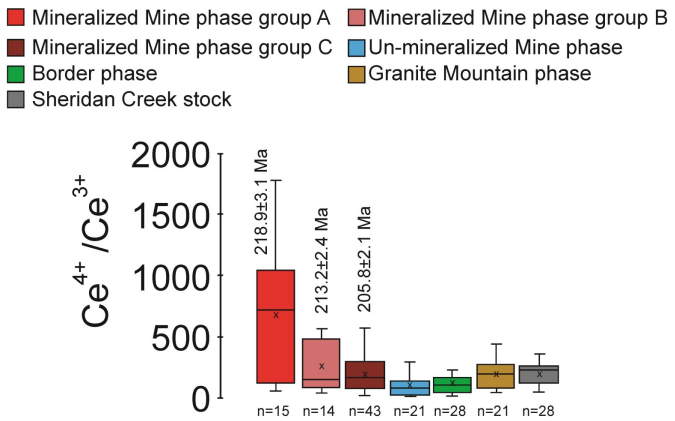

Figure 3. Box and whisker plots of Ce^{4+}/Ce^{3+} values in zircon calculated according to the method of Ballard et al. (2002). The "x" represents the mean value for each plot. U-Pb ages for the mineralized Mine phase are indicated. *Modified from* Kobylinski et al. (2018).

Although the highest Ce^{4+}/Ce^{3+} values are detected in the mineralized Mine phase at Gibraltar, not all zircon grains from this phase have high Ce^{4+}/Ce^{3+} values (Fig. 3). One of the challenges for mineral exploration is the ability to identify the presence of zircon in detrital sediments with anomalous Ce^{4+}/Ce^{3+} values. We address this challenge in two steps: 1) determine the anomalous fertility signal recorded in zircon in the intrusion; and 2) try to detect zircon grains in till with an anomalous signal. First, given that Ballard et al.'s (2002) method to calculate the Ce^{4+}/Ce^{3+} value requires bulk rock composition, it cannot be applied to detrital zircon grains detached from their source rock. However, recent work has shown that a strong correlation exists between Ce/Nd ratio and Ce^{4+}/Ce^{3+} in zircon (Fig. 4; Kobylinski et al. (2018) at Gibraltar and Chelle-Michou et al. (2014) at Coroccohuayco, in Peru). As such, the Ce/Nd ratio of detrital zircon could be used as a proxy for fertility similar to the Ce^{4+}/Ce^{3+} values. We conservatively estimate that zircon grains with Ce^{4+}/Ce^{3+} values greater than 400 (i.e. Ce/Nd ratio of 20; Fig. 4) are most likely derived from the mineralized Mine phase (Fig. 3). Our estimate of the threshold value for Ce^{4+}/Ce^{3+} at Gibraltar (400) is high in comparison to Ce^{4+}/Ce^{3+} ratios of 300 by Ballard et al. (2002) from the Chuquicamata-El Abra porphyry copper belt in Chile, 120 by Liang et al. (2006) at five ore-bearing porphyries and three barren ones in Tibet, and also 120 by Shen et al. (2015) at nine porphyry Cu deposits of the Central Asian Orogenic Belt. The

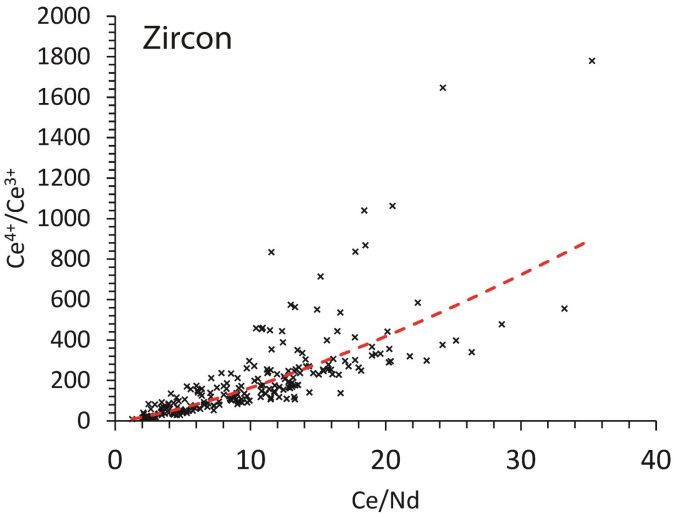

Figure 4. Correlation graph Ce^{4+}/Ce^{3+} vs. Ce/Nd in zircon from the Granite Mountain batholith at Gibraltar; the correlation coefficient is 0.90 following the equation: Ce/Nd = 7.28 $(Ce^{4+}/Ce^{3+})^{(1.35)}$ represented by the dash line. *Modified from* Kobylinski et al. (2018).

variability in the threshold value of Ce^{4+}/Ce^{3+} in zircon associated with a positive fertility signal amongst porphyry Cu deposits is likely related to the variability in the content of REE-bearing mineral phases in the intrusions at each site, which ultimately can influence the REE composition of zircon (c.f. Loader et al., 2017).

The second step is to test recoverability of zircon grains in detrital sediments that are associated with a positive fertility signal near a fertile intrusion. At Gibraltar, of the 45 zircon grains from the five till samples analyzed by Wolfe (2017), only one sample, collected less than 1 km from mineralization (sample 11PMA024A02; Fig. 2b), contained two grains with a Ce/Nd ratio of greater than 20, which is considered as a positive signal (Plouffe et al., 2018). Clearly, more zircon grains from more till samples need to be analyzed to verify the efficiency of this method at detecting a positive fertility signal. However, combining the presence of zircon grains with a Ce/Nd ratio greater than 20 with other alteration (e.g. epidote) and ore minerals (e.g. chalcopyrite) in detrital sediments would serve to define the mineralization potential of the Granite Mountain batholith (c.f. Plouffe et al., 2016; Plouffe and Ferbey, 2017). As such, zircon would classify as a group 2 PCIM as per Plouffe and Ferbey's (2017) classification scheme.

An analogue to the Ce anomaly, the Eu/Eu* in zircon is a proxy for the oxidation state of an intrusion and has been investigated at a number of porphyry deposits and barren intrusions as a potential fertility indicator (e.g. Ballard et al., 2002; Dilles et al., 2015; Lee et al., 2017a). In these studies, an Eu/Eu* value of 0.4 in zircon has been used as a threshold between mineralized and barren intrusions. At Gibraltar, Eu/Eu* in zircon is not an accurate indicator of fertility, given that zircon from the mineralized Mine phase have Eu/Eu* values of approximately 0.3 and are similar to or lower than the other unmineralized intrusive phases (Fig. 5). In contrast, in the Highland Valley porphyry district approximately 250 km to the south, zircon recovered from these rocks have Eu/Eu* values with large variance but display a trend of increasing values from 0.2 to 0.7, towards the mineralized phase (Lee et al., 2017b).

More studies that link REE distribution with the fertility signal in magmatic zircon, and its traceability in till, need to be pursued to better constrain the efficiency and limit of this method. For instance, the effect of titanite crystallization on zircon composition and the resulting potential overestimation of Ce^{+4}/Ce^{+3} and Eu/Eu* values in zircon (and hence a false-positive fertility signal) was pointed out by Loader et al. (2017). They suggest that low Ta and Nb content and high Yb/Gd ratios in zircon could be used to identify zircon crystals that were impacted by titanite crystallization.

In addition to our study of zircon at Gibraltar, the composition of zircon in bedrock and till is being investigated at the Highland Valley Copper deposit in collaboration with the Canada Mining Innovation Council research group.

Epidote

A number of studies have reported on the composition of epidote in the hydrothermal alteration zones of porphyry Cu deposits (Bowman et al., 1987; Norman et al., 1991; Cooke et al., 2014, 2015, 2017; Jago et al., 2014; Hart et al., 2017; Wilkinson et al., 2017a). Cooke et al. (2014) and Wilkinson et al. (2017a) surveyed the variability of epidote composition associated with copper porphyry mineralization by examining an extensive sample distribution that extends several kilometres from the core of mineralization. They show that the composition of epidote within the propylitic alteration halo around porphyry deposits varies with distance from mineralization. Higher concentrations of Cu, Mo, Au, Sn, Zn, La, Yb, Y and Zr were measured in epidote near or on a shoulder of copper mineralization, whereas As, Sb, Pb, Zn and Mn, are particularly low near mineralization.

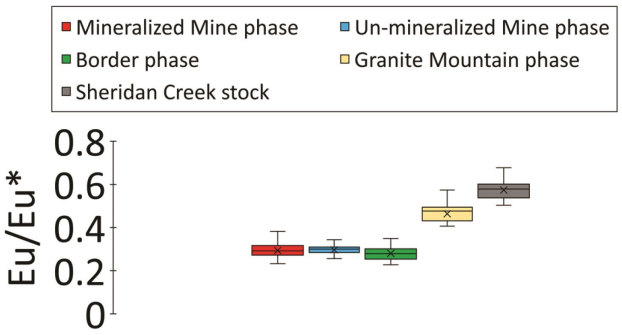

Figure 5. Box and whisker plots of the Eu/Eu* values in zircon from the Granite Mountain batholith at Gibraltar. The "x" represents the mean value. *Modified from* Kobylinski et al. (2018).

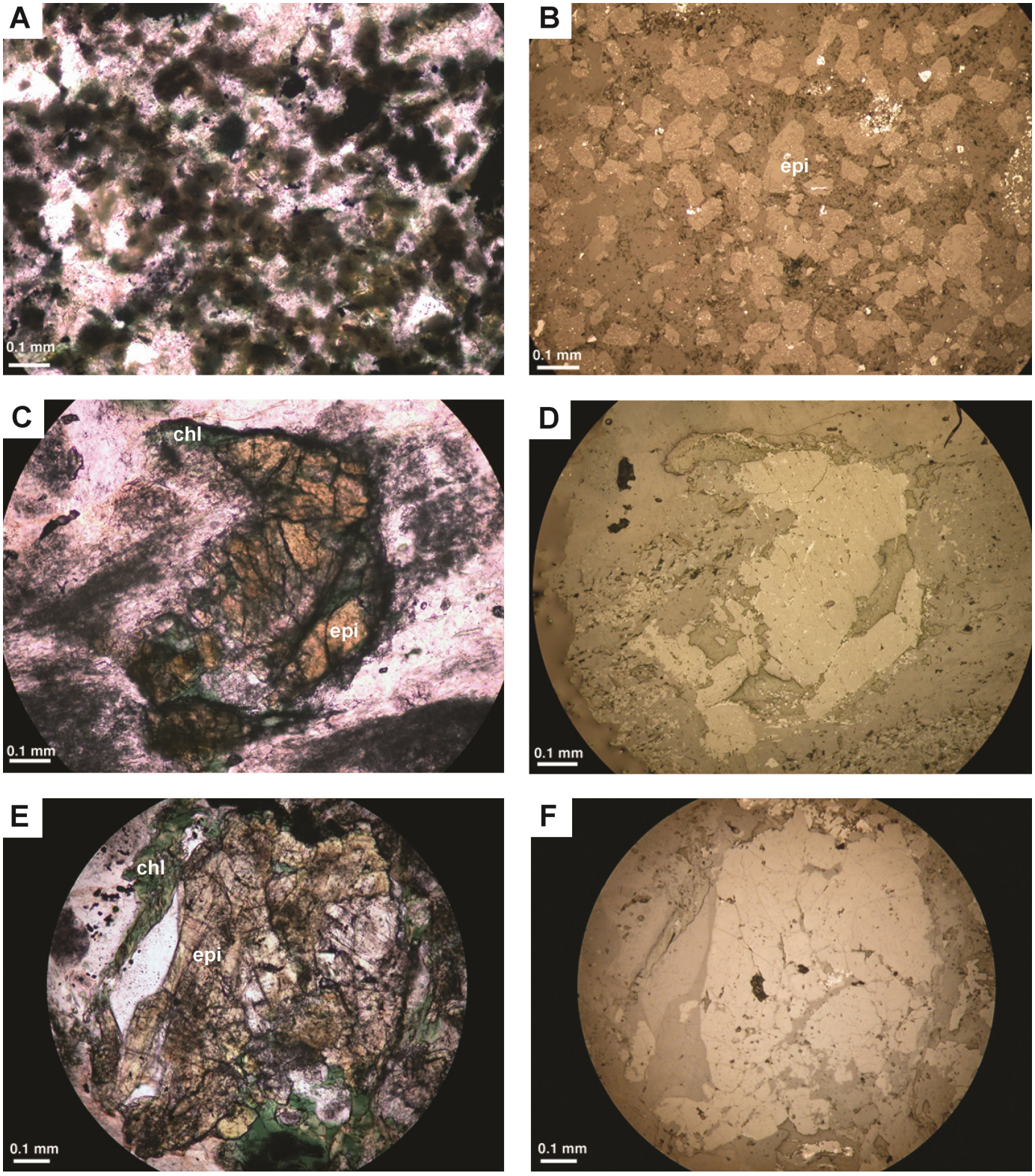

Figure 6. Photomicrographs in (a) plain polarized light (PPL) and (b) reflected light (RL) of poikilitic epidote (epi) overprinting chlorite and carbonate in volcaniclastic sandstones of the Nicola Group; field of view (fov): 1.02 x 1.36 mm. (c) PPL and (d) RL photomicrographs of anhedral epidote (epi) intergrowth with chlorite (chl) in the Sheridan Creek Stock south of the Granite Mountain batholith; fov: 1.05 x 1.40 mm. (e) PPL and (f) RL photomicrographs of anhedral epidote aggregate in green chlorite in the Granite Mountain batholith; fov: 1.13 x 1.50 mm.

Wilkinson et al. (2015, 2017b) and Baker et al. (2017) show that epidote in unmineralized metamorphic rocks and epidote from hydrothermal alteration zones of porphyry deposits could be differentiated with a simple correlation plot, such as As versus Sb. Such simple discrimination is possible because metamorphic epidote contains low levels of pathfinder elements, typically less than 10 ppm As and less than 3 ppm Sb. Although there is variability in the As and Sb content of epidote in porphyry alteration zones as indicated above, their concentrations are generally higher than in metamorphic epidote. However, the comparison presented by these authors is made between the composition of epidote from porphyry mineralization in Chile versus metamorphic rocks from Scotland and Australia. More areas need to be sampled to verify if the discrimination of epidote based on arsenic and antimony is universally applicable.

In addition to the detailed studies on epidote composition mentioned above, the greater abundance of epidote in till in the region of copper porphyry deposits were demonstrated by Hashmi et al. (2015), Plouffe et al. (2016), and Plouffe and Ferbey (2017) at four copper porphyry study sites in British Columbia (Fig. 1). At these sites, epidote in till is interpreted to be derived dominantly from alteration zones that extend outward from copper porphyry mineralization. However, some of the epidote in till may also be derived from the regional greenschist-facies metamorphosed rocks of the Nicola Group. Hence, it is critical to differentiate the provenance of epidote in till (alteration zones of porphyry mineralization versus metamorphic rocks) should its abundance be used to detect copper porphyry mineralization below the bedrock surface (i.e. with only the alteration zone exposed to glacial erosion; see Fig. 2 in Plouffe and Ferbey, 2017). In this scenario, ore minerals (e.g. chalcopyrite) would not be present in till but alteration minerals, such as epidote or tourmaline (Beckett-Brown, et al., 2019; McClenaghan et al., 2019) would be.

With the objective of differentiating metamorphic versus alteration epidote in detrital sediments, ongoing research includes petrographic, scanning electron microscopy (SEM), LA-ICP-MS, and EMPA analyses of 1) epidote grains recovered from till, 2) epidote from hydrothermally altered rocks associated with porphyry mineralization, and 3) epidote from unmineralized metamorphosed rocks of the Nicola Group. Preliminary petrographic results show three broad types of epidote in rocks:

1. Euhedral, and poikilitic epidote replacing feldspar or overprinting chlorite and carbonate is typical of the greenschist-facies regional metamorphism in Nicola volcanic and volcaniclastic rocks (Fig. 6a, b). Some of this epidote is very fine grained (<0.05 mm), which limits its presence in the 0.25 to 0.5 mm size fraction of till from which epidote abundance is determined.
2. Epidote replacing chlorite pseudomorphs after biotite is recognized by its layered, often deformed, wavy texture (inherited from the sheet silicates it replaces) and the presence of more or less fine-grained titanite inclusions. The presence of titanite likely reflects the titanium nature of the primary biotite. Because Ti is not incorporated in the chlorite lattice, it crystallizes separately as titanite. The origin of this epidote is uncertain but most likely hydrothermal (Fig. 6b).
3. More intensely coloured epidote (pistachio green), larger in grain size reaching greater than 0.25 mm, occurring in chlorite or together with quartz and/or sulphide in pockets and veins is interpreted to be hydrothermal in origin (Fig. 6c). Hydrothermal epidote may show blotchy colour distribution with some very intense yellow-green to olive areas. Hydrothermal epidote has a pitted texture due to abundant (fluid?) inclusions, which are common in hydrothermal minerals.

So far, two sets of LA-ICP-MS analytical results are availa-

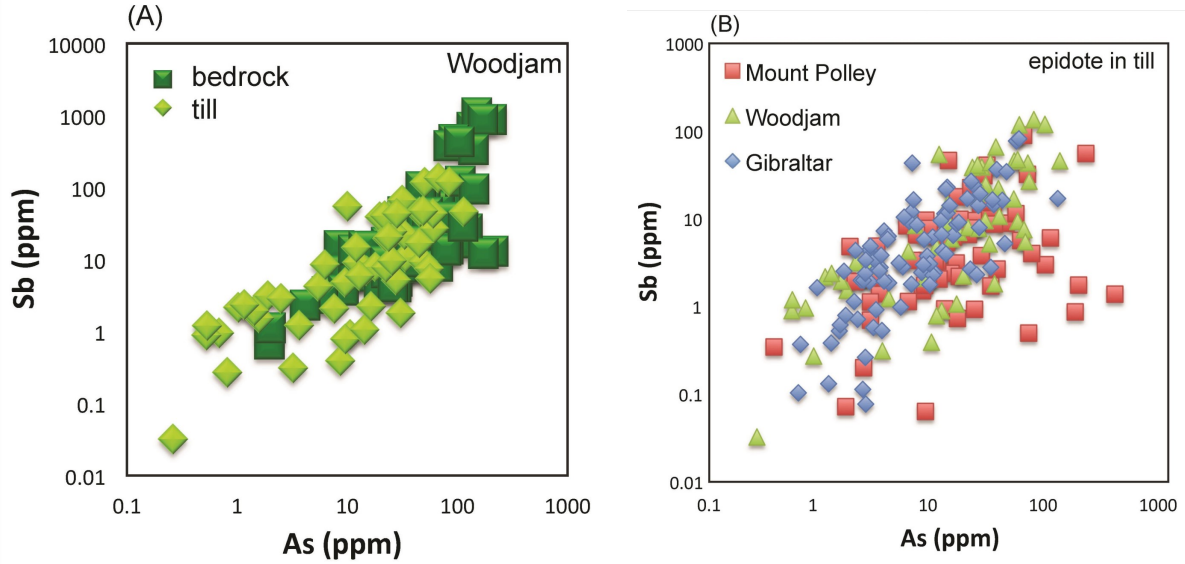

Figure 7. Sb vs. As plot for epidote grains in (a) till and bedrock from the Woojdam prospect, and (b) till in the region of the Gibraltar and Mt. Polley deposits, and the Woodjam prospect.

ble: 1) epidote associated with hydrothermal alteration zones of the Woodjam prospect; and 2) epidote grains from till in the region of the Gibraltar and Mount Polley mines, and the Woodjam prospect (Fig. 1). On a simple correlation diagram of As versus Sb (Wilkinson et al., 2017b; Baker et al., 2017), there is a wide overlap between the composition of epidote grains in till and alteration epidote from bedrock at Woodjam (Fig. 7a), suggesting that most of the epidote from till is derived from the alteration zones. The highest As (>120 ppm) and Sb (>100 ppm) values were found in bedrock epidote. Epidote grains with lower As (approximately <10 ppm) and Sb (approximately <1 ppm) are only found in till and could be derived from metamorphic rocks according to the composition of metamorphic epidote presented by Wilkinson et al. (2017b). Ongoing analyses of epidote from unmineralized regionally metamorphosed rocks of the Nicola Group is hoping to confirm this hypothesis. The till-derived epidote grains from the three study sites (Gibraltar, Mount Polley, Woodjam) show similar compositions (Fig. 7b).

Rare earth element patterns in bedrock epidote from Woodjam are variable, showing both light and heavy REE enrichment, resulting in La/Yb_N ratios from 0.07 to 83.28, with slightly negative to predominantly positive Eu anomalies (Eu/Eu*) smaller than 10 (Fig. 8a). Most of the epidote grains from till at Woodjam show similar REE ratios but a few grains have Eu/Eu* greater than 10. The ratios are similar in epidote grains from till at Gibraltar and Mount Polley (Fig. 8b), with Gibraltar showing the largest spread in both La/Yb_N and Eu/Eu* values and more negative Eu anomalies than observed at Woodjam and Mount Polley, which have generally positive Eu/Eu*. Wilkinson et al. (2015) noted Eu/Eu* values of greater than 1 in a limited number of epidote samples from porphyry mineralization. The variability in the REE content of the epidote is likely related to the inheritance from the precursor minerals (e.g. feldspar, chlorite), hydrothermal fluid and bulk rock compositions, pressure-temperature (P-T) conditions, and oxygen fugacity during epidote formation (Arnason et al., 1993). With these preliminary results, the distinction of metamorphic versus hydrothermal alteration epidote grains in detrital sediments based on their REE content is not straightforward. Analyses of epidote from rocks of the Nicola Group might elucidate the distinction based on REE content, if there is one.

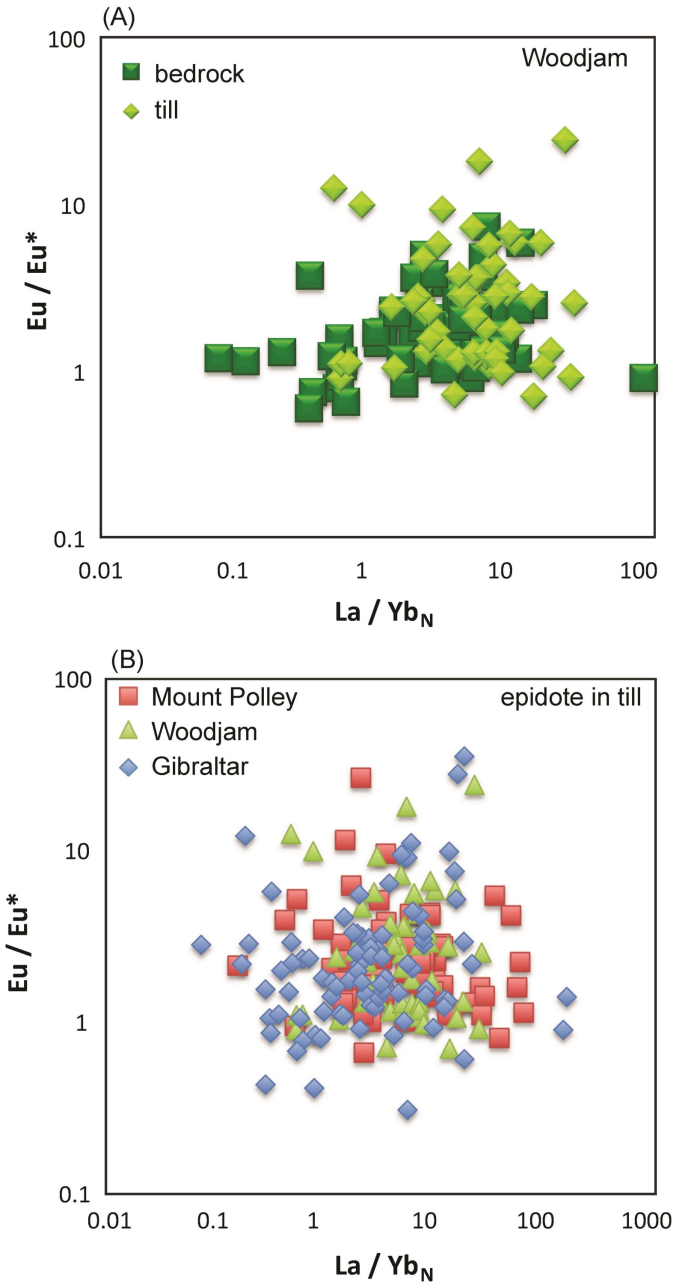

Figure 8. Eu/Eu* vs. La/Yb plot for epidote from (a) till and bedrock from the Woodjam prospect, and (b) epidote grains from till in the region of the Gibraltar and Mt. Polley deposits, and the Woodjam prospect.

Conclusions

Zircon and epidote are promising PCIM that could be used in mineral exploration, especially in glaciated landscapes such as the Canadian Cordillera, where prospective geology is covered by glacial sediments requiring innovative and effective mineral exploration methods to evaluate the mineral potential of vast underexplored areas. Combining the presence and composition of epidote and zircon grains in till with other PCIM could provide an indication of the mineralization potential of a batholith that is largely covered by sediments. Such innovative mineralogical exploration methods need to be developed to find the undiscovered mineral deposits for the needs of future generations.

Acknowledgments

This report is a contribution to NRCan's Targeted Geoscience Initiative Program (TGI). Support for this study was provided through the Porphyry-style Mineral Systems Project's '*Activity P-3.3: Mineralogical controls on the fertility of*

porphyry-style systems'.

Chris Kobylinski is a M.Sc. candidate at the University of Ottawa, under the supervision of Keiko Hattori, completing a thesis on the composition of zircon and epidote at the Gibraltar deposit. Cathryn Bjerkelund, Chris Hutton and Neil Rogers from the TGI management team provided the support to enable this project. John Chapman provided the rock samples from the Woodjam prospect. This report benefited from the review of Colter Kelly, Jean-Luc Pilote and Neil Rogers.

References

Armstrong, J.T., 1988. Quantitative analysis of silicates and oxide minerals: comparison of Monte-Carlo, ZAF and Phi-Rho-Z procedures; *in* Microbeam Analysis, (ed.) D.E. Newbury; San Francisco Press, San Francisco, p. 239–246.

Arnason, J.G., Bird, D.K., and Lion, J.G., 1993. Variables controlling epidote composition in hydrothermal and low-pressure regional metamorphic rocks; 125 years Knappenwand, Proceedings of a Symposium, Salzburg, Austria, p. 17–25.

Baker, M.J., Cooke, D.R., Hollings, P.N., and Piquer, J., 2017. Identification of hydrothermal alteration related to mineralisation using epidote mineral chemistry; 15th Biennial Society for Geology Applied to Mineral Deposits (SGA) Conference, Quebec City, August 20-23, 2017, p. 1069–1071.

Ballard, J.R., Palin, J.M., and Campbell, I.H., 2002. Relative oxidation states of magmas inferred from Ce(IV)/Ce(III) in zircon: application to porphyry copper deposits of northern Chile; Contributions to Mineralogy and Petrology, v. 144, p. 347–364.

Beckett-Brown, C.E., McDonald, A.M., and McClenaghan, M.B., 2019. Unravelling tourmaline in mineralized porphyry systems: assessment as a valid indicator mineral; *in* Targeted Geoscience Initiative: 2018 report of activities, (ed.) N. Rogers; Geological Survey of Canada, Open File 8549, p. 345–351.

Bowman, J.R., Parry, W.T., Kropp, W.P., and Kruer, S.A., 1987. Chemical and isotopic evolution of hydrothermal solutions at Bingham, Utah; Economic Geology, v. 82, p. 395–428.

Byrne, K., Stock, E., Ryan, J., Johnson, C., Nisenson, J., Alva Jimenez, T., Lapointe, M., Stewart, H., Grubisa, G., and Syroka, S., 2013. Porphyry Cu-(Mo) deposits in the Highland Valley district, south-central British Columbia; *in* Porphyry systems of central and southern British Columbia: Tour of central British Columbia porphyry deposits from Prince George to Princeton, (ed.) J.M. Logan and T.G. Schroeter; Society of Economic Geologists, Field Trip Guidebook, Series 43, p. 99–116.

Chelle-Michou, C., Chiaradia, M., Ovtcharova, M., Ulianov, A., and Wotzlaw, J.-F., 2014. Zircon petrochronology reveals the temporal link between porphyry systems and the magmatic evolution of their hidden plutonic roots (the Eocene Coroccohuayco deposit, Peru); Lithos, v. 198-199, p. 129–140.

Cooke, D.R., Baker, M., Hollings, P., Sweet, G., Zhaoshan, C., Danyushevsky, L., Gilbert, S., Zhou, T., White, N., Gemmell, J.B., and Inglis, S., 2014. New advances in detecting the distal geochemical footprints of porphyry systems - epidote mineral chemistry as a tool for vectoring and fertility assessments; *in* Building Exploration Capability for the 21st Century, (ed.) K.D. Kelley and H.C. Golden; Society of Economic Geologists, Special Publication No. 18, Littleton, Colorado, p. 127–152.

Cooke, D.R., Wilkinson, J.J., Baker, M., Agnew, P., Wilkinson, C.C., Martin, H., Chang, Z., Chen, H., Gemmell, J.B., Inglis, S., Danyushevsky, L., Gilbert, S., and Hollings, P., 2015. Using mineral chemistry to detect the location of concealed porphyry deposits - an example from Resolution, Arizona; *in* Abstracts; 27th International Applied Geochemistry Symposium, Tucson, Arizona, p. 1–6.

Cooke, D.R., Agnew, P., Hollings, P., Baker, M., Chang, Z., Wilkinson, J.J., White, N.C., Zhang, L., Thompson, J., Gemmell, J.B., Fox, N., Chen, H., and Wilkinson, C.C., 2017. Porphyry indicator minerals (PIMS) and porphyry vectoring and fertility tools (PVGTS) - Indicator of mineralization styles and recorders of hypogene geochemical dispersion halos; Proceedings of Exploration 17: Sixth Decennial International Conference on Mineral Exploration, p. 457–470.

Dilles, J.H., Kent, A.J.R., Wooden, J.L., Tosdal, R.M., Koleszar, A., Lee, R.G., and Farmer, L.P., 2015. Zircon compositional evidence for sulphur-degassing from ore-forming arc magmas; Economic Geology, v. 110, p. 241–251.

Ferbey, T., Plouffe, A., and Anderson, R.G., 2014. An integrated approach to search for buried porphyry-style mineralization in central British Columbia using geochemistry and mineralogy: a TGI-4 project; *in* Current Research 2014-2; Geological Survey of Canada, 15 p.

Ferbey, T., Plouffe, A., and Bustard, A.L., 2016. Geochemical, mineralogical, and textural data from tills in the Highland Valley Copper mine area, south-central British Columbia; British Columbia Geological Survey, GeoFile 2016-11 (also Geological Survey of Canada, Open File 8119).

Hart, L., Wilkinson, J.J., Armstrong, R., and Araujo, D., 2017. Classfifying propylitic alteration in complex porphyry systems; a case study of the Oyu Tolgoi Cu-Au porphyry deposits, southern Mongolia; Porceedings 14th Biennial Society of Geology Applied to Mineral Deposits (SGA) conference, Quebec City, August 20–23, p. 4 p.

Hashmi, S., Ward, B.C., Plouffe, A., Leybourne, M.I., and Ferbey, T., 2015. Geochemical and mineralogical dispersal in till from the Mount Polley Cu-Au porphyry deposit, central British Columbia, Canada; Geochemistry: Exploration, Environment, Analysis, v. 15, p. 234–249.

Hattori, K., Morfin, S., Baumgartner, R., Shen, P., and Petts,

D., 2016. Fertility of igneous rocks related to porphyry copper deposits: indications from zircon compositions; XVIII Peruvian Geological Congress, 3 p.

Hattori, K., Wang, J., Baumgartner, R., Kobylinski, C., Morfin, S., and Shen, P., 2017. Zircon composition: indicator of fertile igneous rocks related to porphyry copper deposits; 14th Society for Geology Applied to Mineral Deposits (SGA) Biennial meeting 2017, Québec City, Canada, Volume 1, p. 295–298.

Jago, C.P., Tosdal, R.M., Cooke, D.R., and Harris, A.C., 2014. Vertical and lateral variation of mineralogy and chemistry in the Early Jurassic Mt. Milligan alkalic porphyry Au-Cu deposit, British Columbia, Canada; Economic Geology, v. 109, p. 1005–1033.

Kelley, K.D., Eppinger, R.G., Lang, J., Smith, S.M., and Fey, D.L., 2011. Porphyry Cu indicator minerals in till as an exploration tool: example from the giant Pebble porphyry Cu-Au-Mo deposit, Alaska, USA; Geochemistry: Exploration, Environment, Analysis, v. 11, p. 321–334.

Kobylinski, C.H., Hattori, K., Smith, S.W., and Plouffe, A., 2018. High cerium anomalies in zircon from intrusions associated with porphyry copper mineralization in the Gibraltar deposit, south-central British Columbia; Geological Survey of Canada, Open File 8430, 19 p.

Lee, R.G., Dilles, J.H., Tosdal, R.M., Wooden, J.L., and Mazdab, F.K., 2017a. Magmatic evolution of granodiorite intrusions at the El Salvador porphyry copper deposit, Chile, based on trace element composition and U/Pb age of zircons; Economic Geology, v. 112, p. 245–273.

Lee, R.G., Byrne, K., Alfaro, M., D'Angelo, M., Hart, C.J.R., Hollings, P., and Gleezon, S.A., 2017b. Assessing the zircon compositional evolution from the Guichon Creek Batholith and Highland Valley Copper deposit, south-central B.C.; 14th Society for Geology Applied to Mineral Deposits (SGA) Biennial meeting 2017 Québec, Quebec, Volume 3, p. 1087–1090.

Liang, H.-Y., Campbell, I.H., Allen, C., Sun, W.-D., Liu, C.-Q., Yu, H.-X., Xie, Y.-W., and Zhang, Y.-Q., 2006. Zircon Ce^{4+}/Ce^{3+} ratios and ages for Yulong ore-bearing porphyries in eastern Tibet; Mineralium Deposita, v. 41, p. 152–159.

Loader, M.A., Wilkinson, J.J., and Armstrong, R.N., 2017. The effect of titanite crystallisation on Eu and Ce anomalies in zircon and its implications for the assessment of porphyry Cu deposit fertility; Earth and Planetary Science Letters, v. 472, p. 107–119.

McClenaghan, M.B. and Kjarsgaard, B.A., 2007. Indicator mineral and surficial geochemical exploration methods for kimberlite in glaciated terrain; examples from Canada; *in* Mineral Deposits of Canada: A Synthesis of Major Deposit-Types, District Metallogeny, the Evolution of Geological Provinces, and Exploration Methods, (ed.) W.D. Goodfellow; Geological Association of Canada, Special Publication No. 5, p. 983–1006.

McClenaghan, M.B., McCurdy, M.W., Garrett, R.G., Beckett-Brown, C.E., Leybourne, M.E., Casselman, S.G., and Pelchat, P., 2019. Mineral markers of porphyry copper mineralization: work in progress for the Casino Cu-Au-Mo-Ag porphyry deposit, Yukon; *in* Targeted Geoscience Initiative: 2018 report of activities, (ed.) N. Rogers; Geological Survey of Canada, Open File 8549, p. 333–344.

McDonough, W.F. and Sun, S.S., 1995. The composition of the Earth; Chemical Geology, v. 120, p. 223–253.

Norman, D.K., Parry, W.T., and Bowman, J.R., 1991. Petrology and geochemistry of propylitic alteration at southwest Tintic, Utah; Economic Geology, v. 86, p. 13–28.

Plouffe, A. and Ferbey, T., 2016. Till geochemistry, mineralogy and textural data near four Cu porphyry deposits in British Columbia; Geological Survey of Canada, Open File 8038 (and British Columbia Geological Survey Geofile 2016-10).

Plouffe, A. and Ferbey, T., 2017. Porphyry Cu indicator minerals in till: A method to discover buried mineralization; *in* Indicator Minerals in Till and Stream Sediments of the Canadian Cordillera, (ed.) T. Ferbey, A. Plouffe, and A. Hickin; Mineral Association of Canada, Topics in Mineral Sciences Volume 47, Geological Association of Canada, Special Paper 50, p. 129–159.

Plouffe, A., Ferbey, T., Hashmi, S., and Ward, B.C., 2016. Till geochemistry and mineralogy: vectoring towards Cu porphyry deposits in British Columbia, Canada; Geochemistry: Exploration, Environment, Analysis, v. 16, p. 213–232.

Plouffe, A., Kobylinski, C.H., Hattori, K., Wolfe, L., and Ferbey, T., 2018. Mineral markers of porphyry copper mineralization: Work in progress at the Gibraltar deposit, British Columbia; *in* Targeted Geoscience Initiative - 2017 Report of Activities: Volume 1, (ed.) N. Rogers; Geological Survey of Canada, Open File 8358, p. 59–69.

Rees, C., 2013. The Mount Polley Cu-Au deposit, south-central British Columbia, Canada; *in* Porphyry systems of central and southern British Columbia: Tour of central British Columbia porphyry deposits from Prince George to Princeton, (ed.) J.M. Logan and T.G. Schroeter; Society of Economic Geologists, Field Trip Guidebook, Series 43, p. 67–98.

Richards, J.P., 2011. Magmatic to hydrothermal metal fluxes in convergent and collided margins; Ore Geology Reviews, v. 40, p. 1–26.

Shen, P., Hattori, K., Pan, H., Jackson, S., and Seitmuratova, E., 2015. Oxidation condition and metal fertility of granitic magmas: zircon trace-element data from porphyry Cu deposits in the central Asian orogenic belt; Economic Geology, v. 110, p. 1861–1878.

Sherlock, R., Blackwell, J., and Skinner, T., 2013. NI 43-101 technical report for 2012 activities on the Woodjam North property; Gold Fields Horsefly Exploration Group, Consolidated Woodjam Copper Corporation, Cariboo Mining Divi-

sion, British Columbia, 275 p.

Sillitoe, R.H., 2010. Porphyry copper systems; Economic Geology, v. 105, p. 3–41.

van Straaten, B.I., Oliver, J., Crozier, J., and Goodhue, L., 2013. A summary of the Gibraltar porphyry copper-molybdenum deposit, south-central British Columbia, Canada; *in* Porphyry systems of central and southern British Columbia: Tour of central British Columbia porphyry deposits from Prince George to Princeton, (ed.) J.M. Logan and T.G. Schroeter; Society of Economic Geologists, Field Trip Guidebook, Series 43, p. 55–66.

Wilkinson, C.C., Harman, E.M., and Wilkinson, J.J., 2015. Epidote chemistry in contrasting hydrothermal and metamorphic environments; World- Class Ore Deposits: Discovery to Recovery, Society of Economic Geology 2015 Conference, September 27 ,2015 ,30–Hobart, Tasmania, poster.

Wilkinson, J.J., Baker, M.J., Cooke, D.R., Wilkinson, C.C., and Inglis, S., 2017a. Exploration targeting in porphyry Cu systems using propylitic mineral chemistry: a case study of the El Teniente deposit, Chile; Proceedings 14th Biennial Society of Geology Applied to Mineral Deposits (SGA) conference, Québec, Quebec, August 20–23, 4 p.

Wilkinson, J.J., Cooke, D.R., Baker, M.J., Chang, Z., Wilkinson, C.C., Chen, H., Fox, N., Hollings, P., White, N.C., Gemmell, J.B., Loader, M.A., Pacey, A., Sievwright, R.H., Hart, L.A., and Brugge, E.R., 2017b. Porphyry indicator minerals and their mineral chemistry as vectoring and fertility tools; *in* Application of indicator mineral methods to bedrock and sediments, (ed.) M.B. McClenaghan and D. Layton-Matthews; Geological Survey of Canada, Open File 8345, p. 67–77.

Wolfe, L., 2017. Chemistry of refractory indicator minerals in tills around the Gibraltar porphyry copper deposit, south-central British Columbia; B.Sc. thesis, University of Ottawa, Ottawa, Ontario, 56 p.

Mineral and geochemical signatures of porphyry copper mineralization: work in progress for the Casino Cu-Au-Mo-Ag porphyry deposit, Yukon

M.B. McClenaghan[1], M.W. McCurdy[1], R.G. Garrett[1], C.E. Beckett-Brown[2], M.I. Leybourne[3], S.G. Casselman[4] and P. Pelchat[1]

[1]*Geological Survey of Canada, 601 Booth Street, Ottawa, Ontario K1A 0E8*

[2]*Harquail School of Earth Sciences, Laurentian University, 935 Ramsey Lake Road, Sudbury, Ontario P3E 2C6*

[3]*Department of Geological Sciences and Engineering, Queen's University, 35 Union Street, Kingston, Ontario K7L 3N6*

[4]*Yukon Geological Survey, 300 Main Street, Whitehorse, Yukon Y1A 2B5*

Abstract

This paper reports preliminary results for a detailed indicator mineral and geochemical study of the Casino porphyry Cu-Au-Mo-Ag deposit, one of the largest and highest grade porphyry deposits in Canada. The calc-alkaline porphyry is hosted in a Late Cretaceous quartz monzonite and associated breccias in the west central Yukon. This deposit is an ideal study site because it has not yet been disturbed by mining, contains tourmaline, and metal-rich stream sediments were previously identified around the deposit. At 22 sites around the deposit, one bulk stream sediment sample for recovery of indicator minerals, two water samples and one stream silt sample for geochemical analysis, and one pebble sample were collected. Preliminary results indicate that chalcopyrite, pyrite, gold, molybdenite, sphalerite, scheelite and tourmaline in the heavy mineral fraction of stream sediments are indicators of the porphyry mineralization and demonstrate that indicator mineral methods are a viable exploration tool in this unglaciated terrain. The geochemical signature of the deposit is best defined by Ag, As, Au, Bi, Cd, Cu, Fe, Mn, Mo, Pb, U and Zn in stream silt (<0.177 mm), a well-established exploration method in the region, and by Cd, Co, Cu, Mo, Pb and Zn in stream water, a new tool for mineral exploration.

Introduction

Indicator minerals are an established exploration tool in glaciated terrain for gold (e.g. Averill and Zimmerman, 1986; Averill, 2001; McClenaghan and Cabri, 2011) and diamonds (e.g. McClenaghan and Kjarsgaard, 2007 and references therein), and more recently have been tested for porphyry copper deposits (e.g. Kelley et al., 2011; Chapman et al., 2015; Hashmi et al., 2015; Plouffe et al., 2016). The objective of the Geological Survey of Canada's (GSC) Targeted Geoscience Initiative (TGI) Porphyry Mineral Markers research activity is to further develop the porphyry copper indicator mineral suite that can be recovered from surficial sediments in both glaciated and unglaciated terrains. This new research includes the detailed examination and characterization of the chemistry of tourmaline (Beckett-Brown et al., 2019), as well as epidote, rutile and zircon (Kobylinksi et al., 2018; Plouffe et al., 2018, 2019).

This paper reports the preliminary results of a detailed indicator mineral and geochemical study of the Casino porphyry Cu-Au-Mo-Ag deposit, Yukon, one of Canada's largest and highest grade porphyry deposits. The deposit is located 300 km northwest of Whitehorse, Yukon (Fig. 1). The Casino deposit was chosen as a Geological Survey of Canada (GSC) test site for porphyry indicator mineral studies because it has not yet been disturbed by mining, is known to contain tourmaline, and metal-rich sediments are known to occur in local streams that drain the deposit (Archer and Main, 1971).

Bedrock geology

The bedrock geology of the deposit is briefly summarized below from detailed descriptions of its discovery history and geology reported by Archer and Main (1971), Godwin (1975, 1976), Bower et al. (1995), Casselman and Brown (2017) and Yukon Geological Survey (2018a). The deposit is a calc-alkaline porphyry intrusion that hosts Cu, Au and Mo mineralization in a Late Cretaceous quartz monzonite and associated breccias along the intrusion margins.

The earliest exploration in the deposit area was in the early 1900s for placer gold in Canadian Creek (Fig. 2), immediately north of the deposit. Over the years, placer gold mining has taken place in three locations proximal to the deposit (Fig. 2; Chapman et al., 2014). Early exploration of mineralized bedrock in the area focused on the silver-lead-zinc veins at the

Corresponding author: Beth McClenaghan (beth.mcclenaghan@canada.ca)

McClenaghan, M.B., McCurdy, M.W., Garrett, R.G., Beckett-Brown, C.E., Leybourne, M.I., Casselman, S.G., and Pelchat, P., 2019. Mineral and geochemical signatures of porphyry copper mineralization: work in progress for the Casino Cu-Au-Mo-Ag porphyry deposit, Yukon; *in* Targeted Geoscience Initiative: 2018 report of activities, (ed.) N. Rogers; Geological Survey of Canada, Open File 8549, p. 333–344. https://doi.org/10.4095/313667

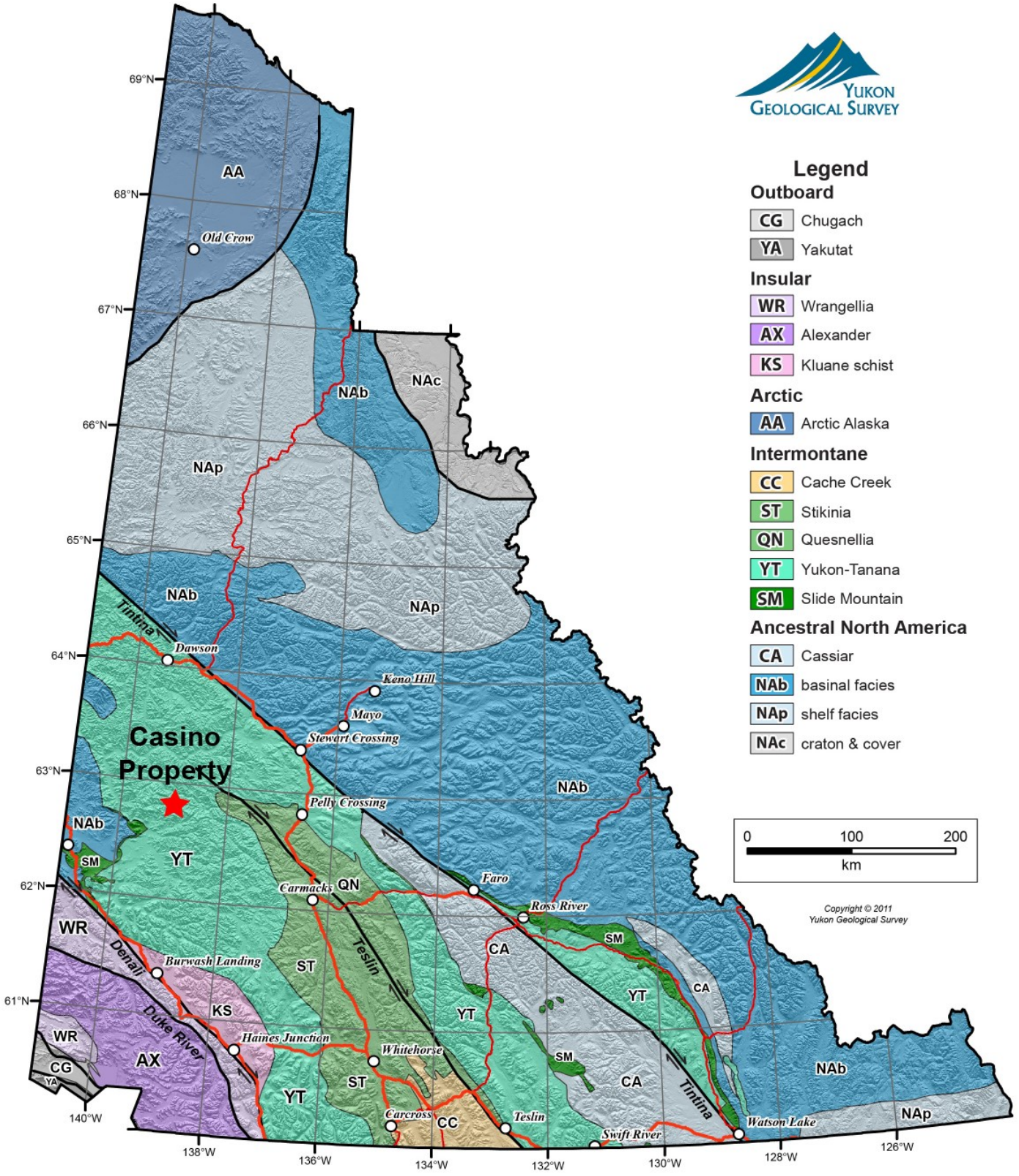

Figure 1. Location of the Casino porphyry copper deposit in west central Yukon (*modified from* Yukon Geological Survey, 2018b).

Bomber occurrence (Yukon Geological Survey, 2018d) on the south periphery of what is now known to be the Casino deposit (Fig. 2).

Porphyry-style mineralization on the Casino property was discovered in 1969. Current total measured, indicated, and inferred resources of the deposit are 101 million tonnes of 0.39 g/t Au in the oxide gold zone, 87 million tonnes grading 0.25 weight % Cu, 0.29 g/t Au, 0.02 weight % Mo, and 1.7 g/t Ag in the supergene oxide enriched zone, and 2.7 billion tonnes of sulphide ore grading 0.16 weight % Cu, 0.19 g/t Au, 0.02 weight % Mo and 1.5 g/t Ag in the supergene sulphide + hypogene zones (Casselman and Brown, 2017). The deposit displays primary alteration related to copper mineralization, consisting of a central potassic alteration zones that grades outwards to concentric phyllic and propylitic zones.

During the warm and wet climate of the Paleogene, the deposit was subjected to deep (up to 300 m) chemical weathering because of the porous nature of the breccias and strongly altered zones. The deep weathering profile is largely intact because of minimal to no glacial erosion of the region during the last 2 Ma (Bond and Lipovsky, 2011, 2012). Thus, the deposit has a well formed zonation consisting of a leached cap, supergene oxide mineralization, supergene sulphide mineralization, and hypogene (primary) mineralization. The leached cap is about 70 m thick and is enriched in gold, depleted in copper, and consists primarily of jarosite, limonite, goethite and hematite. The supergene oxide zone is copper-rich and contains chalcanthite, malachite and brocanthite along with minor cuprite, azurite, tenorite and neotocite, and trace molybdenite as coatings on fractures and in vugs. It is discontinuous to tens of metres thick. The supergene sulphide zone, on average 60 m thick, has Cu grades often almost double those in the hypogene zone. It consists of pyrite, chalcopyrite, bornite and tetrahedrite that may be altered along grain boundaries with chalcocite, digenite, or covellite, as well as molybdenite that may be altered to ferrimolybdite. Hypogene mineralization occurs in the potassic, phyllic, and propylitic alteration zones and includes pyrite, chalcopyrite, molybdenite, sphalerite, bornite and tetrahedrite. In the hypogene zone, gold occurs as discrete grains (50–70 µm) in quartz and as inclusions in pyrite and chalcopyrite (1–15 µm).

Methods

In 2017 and 2018, 37 bedrock samples were collected from drill core stored at the deposit (McClenaghan et al., 2018 – Appendix A) and 11 samples from core stored in the Yukon Geological Survey Core Library (McClenaghan et al., 2018). These samples, from all of the alteration and weathering zones, are being examined and analyzed as polished thin section and heavy mineral concentrates prepared at a commercial laboratory. Bedrock samples are being used to establish the indicator mineral suite and then will be compared to the stream sediment heavy mineral samples.

Stream sediment samples were collected at 22 sites around the Casino deposit in the fall of 2017 (Fig. 2). At each site, one bulk stream sediment sample for recovery of indicator minerals, two water samples and one stream silt sample for geochemical analysis, and one pebble sample were collected following GSC protocols described in Day et al. (2013). Bulk (10–15 kg) stream sediment samples were processed by a commercial laboratory to recover heavy (>3.2 specific gravity (SG)) and moderate-density (2.8–3.2 SG) fractions and examine them for key indicator minerals, including tourmaline (Beckett-Brown et al., 2019) and magnetite.

The <0.177 mm (-80 mesh) of stream silt/fine sand was analyzed using modified aqua regia digestion / inductively coupled plasma mass spectrometry (ICP-MS), instrumental neutron activation analysis, and fire assay/ ICP-MS procedures. A bulk dried, unsieved split of each sample was also analyzed at GSC-Ottawa using a portable X-ray fluorescence (pXRF) machine, with the mean value of two readings for each sample used for data interpretation.

Two stream water samples were collected: i) a filtered (0.45 µm), acidified sample for analysis of cations; and ii) a filtered, unacidified sample for analysis of anions. In addition to the GSC water samples, groundwater samples collected from drillholes in the fall of 2017 by Western Copper and Gold were also analyzed by the GSC. All water samples were analyzed for trace metal and major elements by ICP-ES and MS as well as conductivity, pH and alkalinity at GSC Laboratories in Ottawa. Selected water samples are also being analyzed for Cu isotopes at the Queen's Facility for Isotopic Research (QFIR). Surface water samples were also analyzed for $\delta^{18}O$, $\delta^{2}H$, and $\delta^{34}S$ (where sufficient SO_4) at QFIR.

Results

Indicator minerals

Indicator minerals recovered from bulk sediments immediately downstream of the Casino deposit (samples 115J17-007, -008, -010, -013, -014) include chalcopyrite (Fig. 3a), gold (Fig. 3b), molybdenite (Fig. 3c), tourmaline (Fig. 3d), sphalerite (Fig. 3e) and pyrite. Stream sediment sample 115J17-1003, collected downstream of the Cockfield porphyry Cu-Mo-Au occurrence (Yukon Geological Survey, 2018e), 18 km east of the Casino deposit, displays a similar indicator mineral signature that includes chalcopyrite, pyrite, molybdenite and tourmaline, as well as bismuthinite (Fig. 3f) and arsenopyrite. Green epidote, characteristic of the propylitic alteration at Casino (Godwin, 1975, 1976; Casselman and Brown, 2017), is abundant in most stream sediments sampled whether proximal or distal to the deposit and does not appear to have a distribution that is indicative of proximity to the Casino porphyry mineralization. Other potentially useful porphyry indicator minerals, apatite and andradite garnet, were not recovered from the stream sediments.

Gold grains from the Casino deposit and from known gold placers on Canadian Creek (Fig. 2), downstream of the Casino

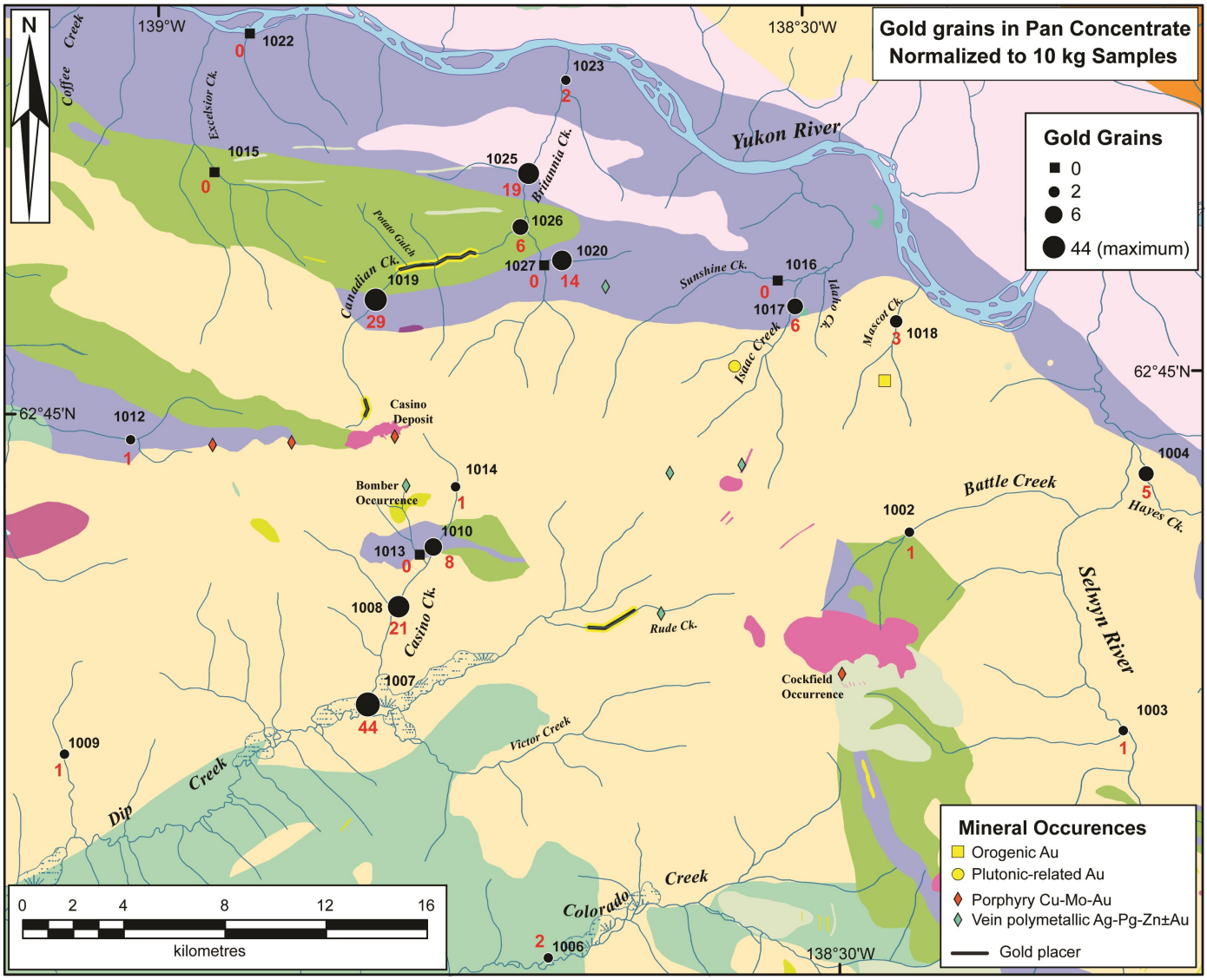

Figure 2. a) Local bedrock geology of the Casino deposit area and abundance of gold grains in the pan concentrate of bulk stream sediment samples. Data have been normalized to 10 kg mass of less than 2 mm material (table feed); b) Bedrock geology legend. Bedrock geology *from* Yukon Geological Survey (2018c). Sample numbers are shown in black beside each sample site. Abbreviations: Bt – biotite; Grt – garnet; Hbl – hornblende; Ms – muscovite; Qtz – quartz.

deposit, were previously examined in large heavy mineral samples prepared by a combination of sluicing and panning by Chapman et al. (2014, 2017). Based on gold alloy compositions and mineral inclusion assemblages, the authors concluded that gold in these placers was a mixture of grains derived from the Casino deposit and from shallow epithermal mineralization. To expand on this earlier research, our study recovered gold grains from bulk stream sediment samples collected proximal to, and distal from, the known placers on Canadian Creek as well as other streams across the Casino region (Fig. 2). Our results confirm that the Casino deposit is an important source of gold in local streams both on the north and south sides of the deposit, and that gold grains recovered from 10 to 14 kg stream sediment samples are a useful indicator mineral of the porphyry Cu mineralization. The largest dimension of the gold grains ranges from 50 to 1500 µm, with 60% of the grains between 50 and 150 µm. The chemistry and inclusion compositions of gold grains recovered from GSC samples are under investigation and will be compared to those reported by Chapman et al. (2014, 2017).

Pyrolusite (MnO_2) (Fig. 3g) and plumbojarosite ($PbFe_6(SO_4)_4(OH)_{12}$) (Fig. 3h) grains were recovered only from site 115J17-1013, close to the mouth of Meloy Creek where it joins Casino Creek (Fig. 2). This site is 3 km downstream from an



Figure 2. cont.

old adit excavated to access the original Pb-Ag-Zn veins. Some drill holes in this area are noted for containing high manganese values. Thus, the hard detrital pyrolusite grains in the sample were likely formed during Paleogene weathering of the deposit and eroded by stream sediments in modern time. Alternatively, a pipe draining the adit flows into the headwaters of Meloy Creek and may have contributed manganese to the stream and ultimately to the formation of pyrolusite.

As part of a Ph.D. thesis at Laurentian University, tourmaline zonation, chemistry and inclusion mineralogy within the Casino deposit are being characterized using EMP, LA-ICP-MS, and Raman spectroscopy and compared to other mineralized and unmineralized porphyries worldwide to better understand mineralizing processes and to develop chemical discrimination criteria that will assist in vectoring to porphyry mineralization (Beckett-Brown et al., 2019). The criteria will then be tested using the tourmaline grains recovered from stream sediments around the deposit and in background areas.

Recent studies of magnetite in copper porphyry deposits have indicated that trace element chemistry may be useful for



Figure 3. Colour photographs of indicator minerals recovered from the heavy mineral fraction of stream sediments collected around the Casino deposit: a) chalcopyrite; b) gold; c) molybdenite; d) tourmaline; e) sphalerite; f) pyrolousite; g) plumbojarosite; and h) bismuthinite.

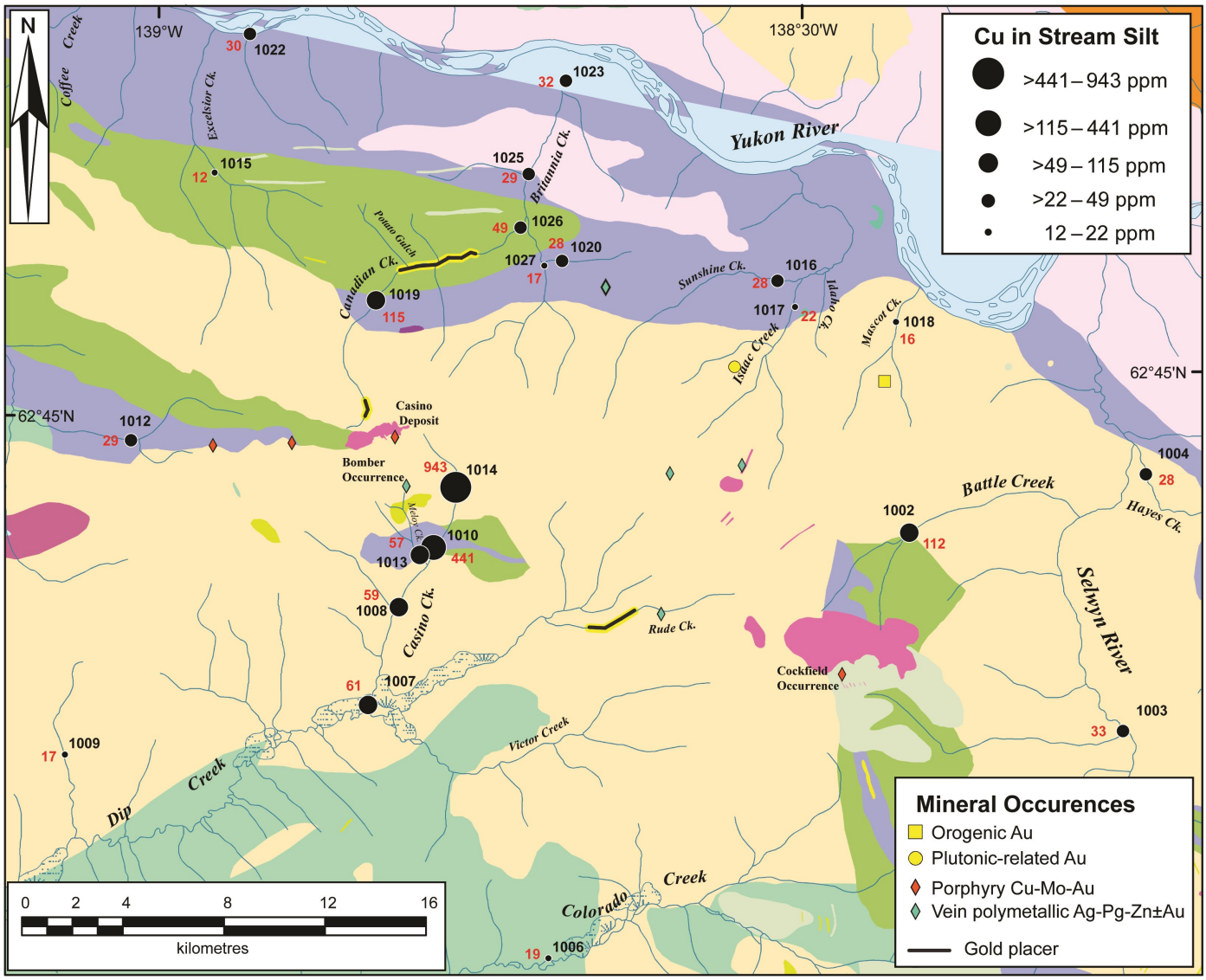

Figure 4. Distribution of Cu in the finer than 0.177 mm (-80 mesh) fraction of stream sediments collected around the Casino porphyry deposit, determined by aqua regia/ICP-MS. Bedrock geology from Yukon Geological Survey (2018c). *See* Figure 2b for bedrock legend. Sample numbers are shown in black beside each dot and have the prefix "115J17-".

identifying hydrothermal magnetite and vectoring to porphyry mineralization (Dupuis and Beadoin, 2011; Nadoll et al., 2014, 2015; Canil et al., 2016; Sievwright, 2017; Pisiak et al., 2017). Magnetite from the Casino deposit and GSC stream sediments will be used to test these published discrimination schemes as part of a M.Sc. thesis at Queen's University.

Stream sediment geochemistry

Archer and Main (1971) published the first stream sediment geochemical data for the Casino deposit. Subsequently, regional stream silt samples were collected across the Yukon by the GSC (Geological Survey of Canada, 1987). The GSC samples were re-analyzed and the data were published for the southern 2/3 of the Yukon, including the Casino deposit area (Jackaman, 2011; Mackie et al., 2017; Arne et al., 2018). The regional data indicate that there is a multi-element geochemical anomaly (Ag, Cu, Pb, Sb, W) in the streams draining the Casino deposit.

To further understand the stream sediment geochemical signature of the Casino deposit, stream silt samples were collected around the deposit as part of the GSC study. Using the published regional data to establish background concentrations, stream sediments in our study were found to contain elevated concentrations of elements in three key areas: 1) around the Casino deposit (Cu (Fig. 4), Ag, As, Au, Bi, Cd, Fe, Mn, Mo, Pb, U and Zn); 2) downstream of the Cockfield showing (As, Bi, Cu, Fe, Mo, Pb); and 3) in the mid to lower reaches of Ca-

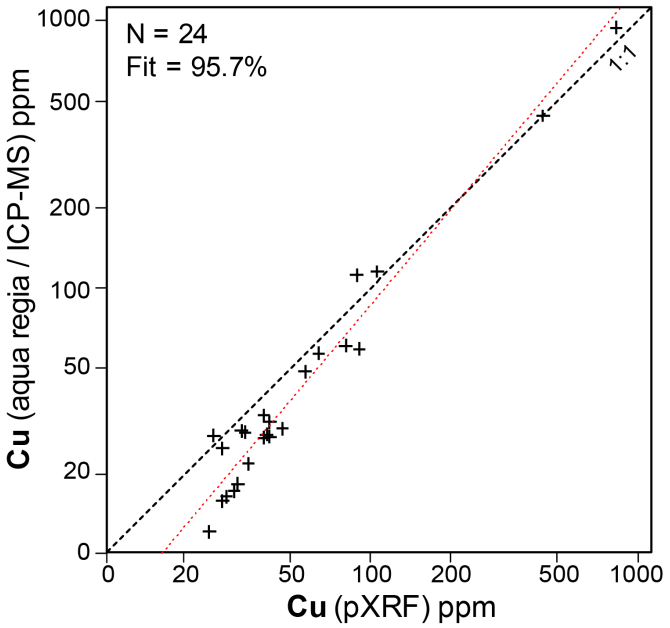

Figure 5. Comparison of Cu values for stream sediment samples determined by aqua regia ICP/MS on the finer than 0.177 mm fraction of stream sediment versus those determined by pXRF on dried unsieved stream sediment.

nadian Creek (As, Au, Bi, Mo, Sb) draining the Casino area northwards towards the Yukon River. Portable XRF (pXRF) data for dry unsieved splits of the stream sediments provide comparable data (Fig. 5) to commercial lab analysis by aqua regia/ICP-MS for As, Cu, Fe, Mn, Mo, S and Zn, and indicate that pXRF could be used in the field to follow up on anomalous values during the same field season. Further interpretation of the stream sediment data will include consideration of location of loess deposits, valley morphology, and stream order, as suggested by Bond and Lipovsky (2011).

Stream water geochemistry

Elevated Cu concentrations were detected in local stream water up to 3 km downstream of the south side of the Casino deposit by Archer and Main (1971). To investigate the applicability of water geochemistry to porphyry exploration, water samples were collected as part the GSC stream sediment survey. Stream waters from Casino Creek, draining the south side of the deposit, have elevated concentrations of Cu (Fig. 6), Mo, Zn, Pb, Cd and Co up to 14 km downstream. Ground and surface water pH values range from 6.7 to 8.3; values that are typical to slightly alkaline for ground and surface waters in crystalline rocks (Leybourne et al., 2006).

The Cu isotopic compositions of stream water (GSC samples) and groundwater collected from drillholes by Western Copper and Gold are being analyzed to investigate the fractionation of copper as a function of sulphide weathering and aqueous transport. Additionally, the isotopic signatures of water will be compared to that for oxidized and fresh mineralized bedrock, and stream sediments. These combined data will provide valuable information regarding the utility of Cu isotopes in aqueous samples as exploration vectors to sulphide mineralization. Further, the Cu isotopic composition of waters may be useful for indicating if isolated anomalies, such as in sample 115J17-1002, are related to mineralization.

The $\delta^{18}O$ and $\delta^{2}H$ of the surface water samples range from -23.0 to -21.8‰ and -172 to -160‰, respectively. The data are tightly clustered around the mean annual weighted average for precipitation in the Yukon, as recorded at stations in Mayo and Whitehorse (Fig. 7). This pattern indicates that the surface waters represent shallow groundwater discharge, with dampened seasonal fluctuations in the stable isotopic compositions. There was sufficient SO_4 to measure S isotopes in a small number of surface waters (N = 16), with resulting $\delta^{34}S$ values ranging from 3.9 to 14.1‰.

Discussion

Several studies of porphyry copper deposits in glaciated terrain have reported the presence of indicator minerals in the moderate density and heavy mineral fractions of till down ice of mineralization, including chalcopyrite, pyrite, gold, green epidote, apatite, andradite garnet and jarosite (Kelley et al., 2011; Hashmi et al., 2015; Plouffe and Ferbey, 2015; Plouffe et al., 2016). The Casino deposit area is largely an unglaciated terrain and sediments downstream of the deposit contain some of the same indicator minerals, including chalcopyrite, pyrite and gold. In this study, additional indicator minerals were identified in sediments downstream of the Casino deposit, including molybdenite, sphalerite, pyrolusite and plumbojarosite. The local distribution of scheelite and tourmaline in stream sediments may also reflect the Casino porphyry mineralization. Mineral chemistry studies underway will help refine our understanding of the signature for these two minerals. Unlike the porphyry indicator minerals studies in glaciated terrain, the distributions of green epidote, apatite, andradite garnet and jarosite in stream sediments in this study did not indicate the presence of the porphyry mineralization.

Conclusions and implications for exploration

This study is one of the first detailed indicator mineral studies around a major Canadian porphyry copper deposit in unglaciated terrain. Preliminary results indicate that the deposit has an obvious indicator mineral signature in stream sediments that includes chalcopyrite, pyrite, gold, molybdenite, sphalerite, scheelite and tourmaline. The signature is detectable at least 14 km downstream. Indicator mineral patterns also indicate the presence of the nearby porphyry mineralization at Mount Cockfield. The presence of fresh sulphide minerals in the stream sediments around Casino indicate that the streams are eroding, in places, less oxidized and more mineralized material than what is exposed in the leached cap. Detailed characteriza-

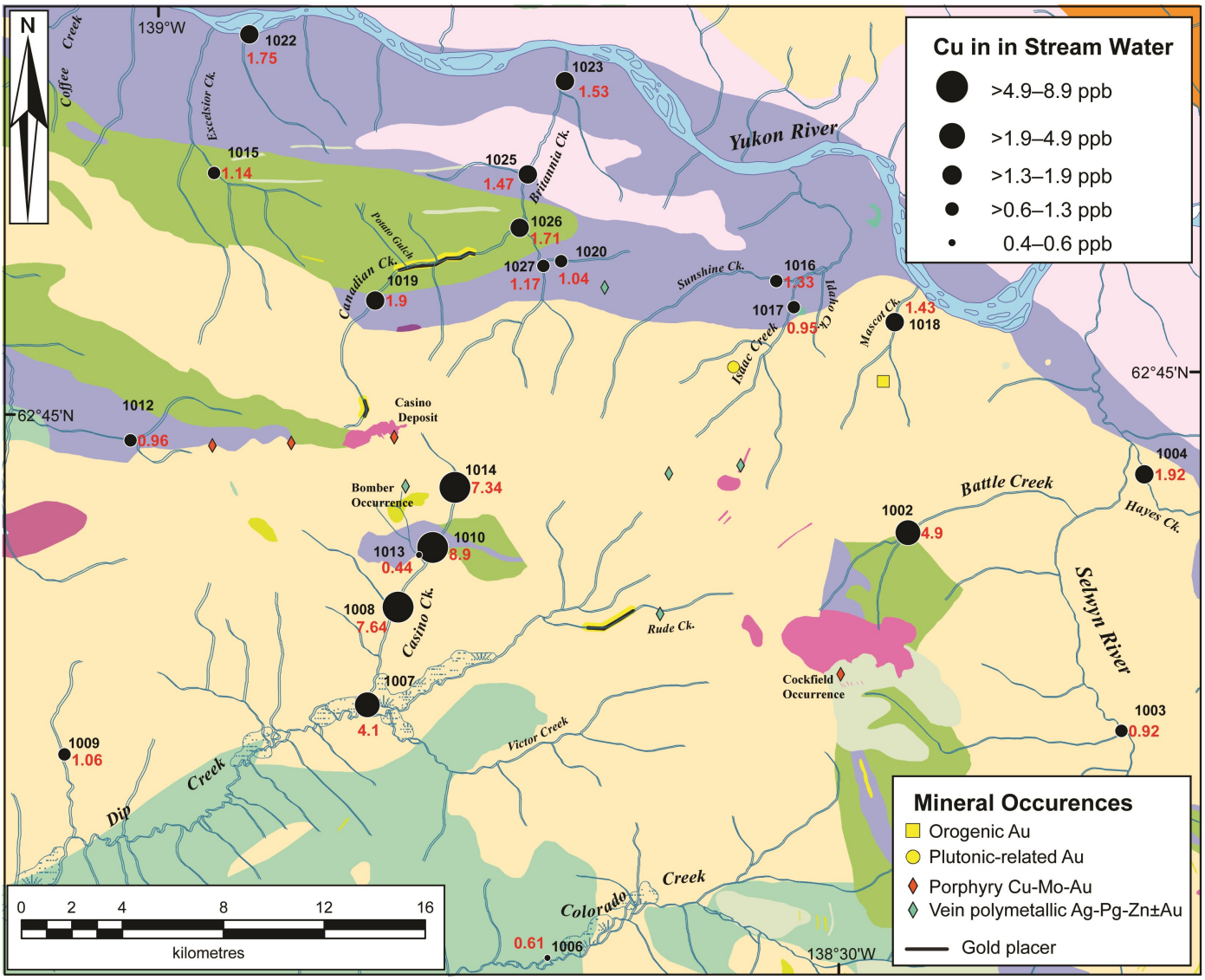

Figure 6. Distribution of Cu in stream waters around the Casino porphyry deposit, determined using ICP-ES and MS. Bedrock geology *from* Yukon Geological Survey (2018c). *See* Figure 2b for bedrock legend. Sample numbers are shown in black beside each dot and have the prefix "115J17-".

tion of the mineral chemistry of gold, tourmaline, scheelite and magnetite from samples in this study is underway to further enhance the applicability of indicator mineral methods for porphyry copper exploration.

Stream sediment geochemistry is an established exploration method in the region. In our study, the deposit has a geochemical signature in stream silts that is best defined by Ag, As, Au, Bi, Cd, Cu, Fe, Mn, Mo, Pb, U and Zn. Stream waters also define a geochemical anomaly around the deposit for Cd, Co, Cu, Mo, Pb and Zn. Elevated metal concentrations in both media are detectable up to 14 km downstream. Lab-based pXRF testing of stream sediments indicates that portable pXRF could be used to identify and investigate geochemical anomalies while still in the field.

The elemental abundances of porphyry copper associated metals in ground and surface waters are indicative of water-deposit interaction, suggesting that surface water chemistry is a viable tool for mineral exploration in this terrain. The $\delta^{18}O$ and $\delta^{2}H$ compositions of the surface waters are clustered around the mean annual value for precipitation at Mayo and Whitehorse. These values are expected as shallow groundwater typically represents the seasonal average of precipitation (Leybourne et al., 2006) The Casino surface waters represent base flow (shallow groundwater) and the data indicate that these surface waters were unaffected by recent precipitation, and therefore carry the elemental, and Cu isotopic composition, of shallow

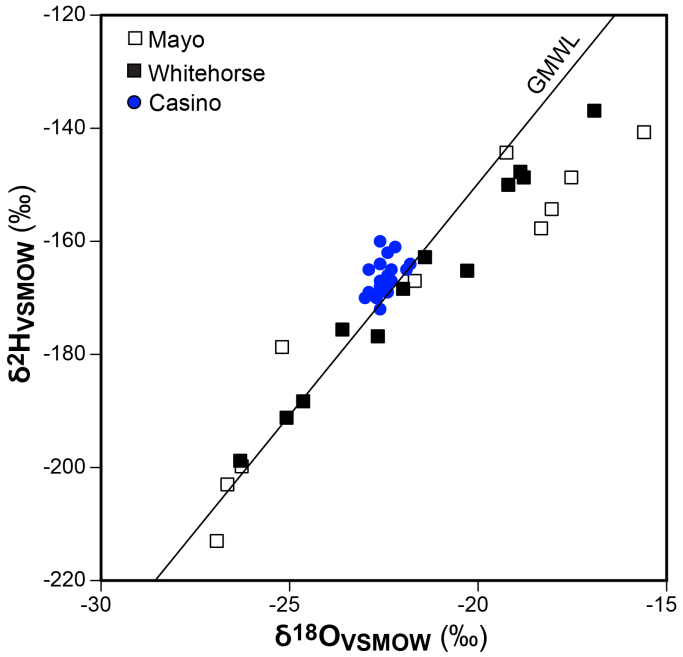

Figure 7. $\delta^{18}O$ and $\delta^{2}H$ for surface waters from Casino compared to weighted monthly averages for International Atomic Energy Agency stations at Mayo and Whitehorse. The Casino data fall near the annual weighted average value for precipitation. Abbreviations: GMWL – global meteoric water line.

groundwaters. Further work on the Cu isotopic composition of these waters will refine aqueous geochemistry as an exploration tool for porphyry-style mineralization.

Acknowledgments

This report is a contribution to NRCan's Targeted Geoscience Initiative Program (TGI). Support for this study was provided through the Porphyry-style Mineral Systems Project's '*Activity P-3.3: Mineralogical markers of fertility porphyry-style systems*'.

We gratefully acknowledge the support of Western Copper and Gold Corporation and the Casino Mining Corporation, and in particular Mary Mioska and Heather Brown. Jeff Bond, Yukon Geological Survey, is thanked for sharing geological information and advice for the Casino sampling program. This report benefited from the review of Eric Potter, Jeremy Powell and Neil Rogers .

References

Archer, A.R. and Main, C.A., 1971. Casino, Yukon- A geochemical discovery of an unglaciated Arizona-type porphyry; *in* Geochemical Exploration, Proceedings, 3rd International Geochemical Exploration Symposium, (ed.) R.W. Boyle; Canadian Institute of Mining and Metallurgy, Special Volume 11, p. 67–77.

Arne, D., Mackie, R., and Pennimpede, C., 2018. Catchment analysis of re-analyzed regional stream sediment geochemical data from the Yukon; EXPLORE, no. 179, p. 1–13.

Averill, S.A., 2001. The application of heavy indicator mineralogy in mineral exploration with emphasis on base metal indicators in glaciated metamorphic and plutonic terrains; *in* Drift Exploration in Glaciated Terrain, (ed.) M.B. McClenaghan, P.T., Bobrowsky, G.E.M. Hall, and S.J. Cook; Geological Society of London, Special Publication 185, p. 69–81.

Averill, S.A. and Zimmerman, J.R., 1986. The Riddle resolved: the discovery of the Partridge gold zone using sonic drilling in glacial overburden at Waddy Lake, Saskatchewan; Canadian Geology Journal of the Canadian Institute of Mining and Metallurgy, v. 1, p.14–20.

Beckett-Brown, C.E., McDonald, A.M., and McClenaghan, M.B., 2019 Unravelling tourmaline in mineralized porphyry systems: assessment as a valid indicator mineral; *in* Targeted Geoscience Initiative: 2018 report of activities, (ed.) N. Rogers; Geological Survey of Canada, Open File 8549, p. 345–351.

Bond, J.D. and Lipovsky, P.S., 2011. Surficial geology, soils and permafrost of the northern Dawson Range; *in* Yukon Exploration and Geology 2010, (ed.) K.E. MacFarlane, L.H. Weston and C. Relf; Yukon Geological Survey, p.19–32.

Bond, J.D. and Lipovsky, P.S., 2012. Surficial geology of Colorado Creek (NTS115J/10) Yukon; Yukon Geological Survey, Open File 2012-2.

Bower, B., Payne, J., DeLong, C., and Rebagliati, C.M., 1995. The oxide-gold, supergene and hypogene zones at the Casino gold-copper-molybdenum deposit, west central Yukon; *in* Porphyry Deposits of the Northwestern Cordillera of North America, (ed.) T.G. Schroeter; Canadian Institute of Mining, Metallurgy and Petroleum, Special Volume 46, p. 352–366.

Canil, D., Grondhal, C., Lacourse, T., and Pisiak, L.K., 2016. Trace elements in magnetite from porphyry Cu–Mo–Au deposits in British Columbia, Canada; Ore Geology Reviews, v. 72, p. 1116–1128.

Casselman, S.C. and Brown, H., 2017. Casino porphyry copper-gold-molybdenum deposit, central Yukon (Yukon MINFILE 115J 028); *in* Yukon Exploration and Geology Overview 2016, (ed.) K.E. MacFarlane; Yukon Geological Survey, p. 61–74.

Chapman, J.B., Plouffe, A., and Ferbey, T., 2015. Tourmaline: The universal indicator?; *in* Short Course 02 Application of Indicator Mineral Methods to Exploration, 27th International Applied Geochemistry Symposium, Tucson; Association of Applied Geochemists, p. 25–31.

Chapman, R.J., Grimshaw, M.R., Allan, M.M., Mortensen, J.K., Wrighton, T.M., and Casselman, S., 2014. Pathfinder signatures in placer gold derived from Au-bearing porphy-

ries; *in* Yukon Exploration and Geology 2014, (ed.) K.E. MacFarlane, M.G. Nordling, P.J. Sack; Yukon Geological Survey, p. 21–31.

Chapman, R.J., Allan, M.M., Mortensen, J.K., Wrighton, T.M., and Grimshaw, M.R., 2017. A new indicator mineral methodology based on generic Bi-Pb-Te-S mineral inclusion signature in detrital gold from porphyry and low/intermediate sulfidation epithermal environments in Yukon Territory, Canada; Mineralium Deposita, v. 58, p. 815–834.

Day, S.J.A., Wodicka, N., and McMartin, I., 2013. Preliminary geochemical, mineralogical and indicator mineral data for stream silts, heavy mineral concentrates and waters, Lorillard River area, Nunavut (parts of NTS 56 -A, -B, and -G); Geological Survey of Canada, Open File 7428.

Dupuis, C. and Beaudoin, G., 2011. Discriminant diagrams for iron oxide trace element fingerprinting of mineral deposit types. Mineralium Deposita, v. 46, p. 319-335.

Geological Survey of Canada, 1987. Regional stream sediment and water geochemical reconnaissance data, Snag area, Yukon; Geological Survey of Canada, Open File 1363.

Godwin, C.I., 1975. Geology of the Casino porphyry copper-molybdenum deposit, Dawson Range, Yukon Territory; Ph.D. thesis, University of British Columbia, Vancouver, British Columbia., 257 p.

Godwin, C.I., 1976. Casino; *in* Porphyry Deposits of the Canadian Cordillera, (ed.) A. Sutherland Brown; Canadian Institute of Mining and Metallurgy, Special Volume 15, p. 344–358.

Hashmi, S, Ward, B.C., Plouffe, A., Leybourne, M.I., and Ferbey, T., 2015. Geochemical and mineralogical dispersal in till form the Mount Polley Cu-Au porphyry deposit, central British Columbia; Canada; Geochemistry: Exploration, Environment, Analysis, v. 15, p. 234–249.

Jackaman, W., 2011. Regional stream sediment geochemical data Stevenson Ridge, Yukon (NTS 115J & K); Yukon Geological Survey, Open File 2011-28.

Kelley, K.D., Eppinger, R.G., Lang, J., Smith, S.M., and Fey, D.L., 2011. Porphyry copper indicator minerals (PCIMs) in glacial till samples as an exploration tool: example from the giant Pebble porphyry Cu-Au-Mo deposit; Geochemistry: Exploration, Environment, Analysis, v. 11, p. 321–334.

Kobylinksi, C.H., Hattori, K., Smith, S.W., and Plouffe, A., 2018. High cerium anomalies in zircon from intrusions associated with porphyry copper mineralization in the Gibraltar deposit, south-central British Columbia; Geological Survey of Canada, Open File 8430.

Leybourne, M.I., Clark, I.D., and Goodfellow, W.D., 2006. Stable isotope geochemistry of ground and surface waters associated with undisturbed massive sulfide deposits; constraints on origin and water-rock reactions; Chemical Geology, v. 231, p. 300–325.

Mackie, R.A., Arne, D.C., and Pennimpede, C., 2017. Assessment of Yukon regional stream sediment catchment basin and geochemical data quality; Yukon Geological Survey, Open File 2017-4.

McClenaghan, M.B. and Cabri, L.J., 2011. Gold and Platinum Group Element indicator minerals in surficial sediments; Geochemistry: Exploration, Environment, Analysis, v. 11, p. 251–263.

McClenaghan, M.B. and Kjarsgaard, B.A., 2007. Indicator mineral and surficial geochemical exploration methods for kimberlite in glaciated terrain: Examples from Canada; *in* Mineral Deposits of Canada: A Synthesis of Major Deposit-Types, District Metallogeny, the Evolution of Geological Provinces, and Exploration Methods, (ed.) W.D. Goodfellow; Geological Association of Canada, Mineral Deposits Division, Special Publication No. 5, p. 983–1006.

McClenaghan M.B., Beckett-Brown, C.E., McCurdy, M.W., McDonald, A.M., Leybourne, M.I., Chapman, J.B., Plouffe, A., and Ferbey, T., 2018. Mineral markers of porphyry Cu mineralization: Progress report on the evaluation of tourmaline as an indicator mineral; *in* Targeted Geoscience Initiative: 2017 Report of Activities, Volume 1, (ed.) N. Rogers; Geological Survey of Canada, Open File 8358, p. 69–77.

Nadoll, P., Angerer, T., Mauk, J.L., and Walshe, J., 2014. The chemistry of hydrothermal magnetite: A review; Ore Geology Reviews, v. 61, p. 1–32.

Nadoll, P., Mauk, J.L., Leveille, A., and Koening, A.E., 2015. Geochemistry of magnetite from porphyry Cu and skarn deposits in southwestern United States; Mineralium Deposita, v. 50, p. 493–515.

Pisiak, L.K., Canil, D., Lacourse, T., Plouffe, A., and Ferbey, T., 2017. Magnetite as an indicator mineral in the exploration of porphyry deposits: a case study in till near the Mount Polley Cu-Au deposit, British Columbia, Canada; Economic Geology, v. 112, p. 919–940.

Plouffe, A. and Ferbey, T., 2015. Till compositions near Cu-porphyry deposits in British Columbia: highlights for mineral exploration; *in* TGI 4 - Intrusion Related Mineralization Project: New Vectors to Buried Porphyry-style Mineralization, (ed.) N. Rogers; Geological Survey of Canada, Open File 7843, p. 15–37.

Plouffe, A., Ferbey, T., Hashmi, S., and Ward, B.C., 2016. Till geochemistry and mineralogy: vectoring towards Cu porphyry deposits in British Columbia, Canada; Geochemistry: Exploration, Environment, Analysis, v. 16, p. 212–232.

Plouffe, A., Kobylinksi, C.H., Hattori, K., Wolfe, L., and Ferbey, T., 2018. Mineral markers of porphyry copper mineralization: work in progress at the Gibraltar deposit, British Columbia; *in* Targeted Geoscience Initiative: 2017 Report of Activities, Volume 1, (ed.) N. Rogers; Geological Survey of Canada, Open File 8358, p. 57–67.

Plouffe, A., Kjarsgaard,I., Kobylinski, C.H., Hattori, K., Petts, D., Venance, K., and Ferbey, T., 2019. Discovering the next generation of Cu porphyry deposits using mineral markers**;** *in* Targeted Geoscience Initiative: 2018 report of

activities, (ed.) N. Rogers; Geological Survey of Canada, Open File 8549, p. 321–331.

Sievwright, R., 2017. Developing magnetite chemistry as an exploration tool for porphyry copper deposits. Ph.D. thesis, Imperial College, London, United Kingdom, 340 p.

Yukon Geological Survey, 2018a. Occurrence 115J 028; Yukon Geological Survey. <http://data.geology.gov.yk.ca/Occurrence/15019> [accessed: October 31, 2018]

Yukon Geological Survey, 2018b. Overview of Yukon geology; Yukon Geological Survey. <http://www.geology.gov.yk.ca/overview_bedrock_geology.html> [accessed: October 31, 2018]

Yukon Geological Survey, 2018c. Yukon digital bedrock geology; Yukon Geological Survey. <http://www.geology.gov.yk.ca/update_yukon_bedrock_geology_map.html> [accessed: October 31, 2018]

Yukon Geological Survey, 2018d. Occurrence 115J 027; Yukon Geological Survey. <http://data.geology.gov.yk.ca/Occurrence/14376> [accessed: October 31, 2018]

Yukon Geological Survey, 2018e. Occurrence 115J 017; Yukon Geological Survey. <http://data.geology.gov.yk.ca/Occurrence/14367> [accessed: October 31, 2018]

Unravelling tourmaline in mineralized porphyry systems: assessment as a valid indicator mineral

C.E. Beckett-Brown[1], A.M. McDonald[1] and M.B. McClenaghan[2]

[1]*Harquail School of Earth Sciences, Laurentian University, 935 Ramsey Lake Road, Sudbury, Ontario, P3E 2C6*

[2]*Geological Survey of Canada, 601 Booth Street, Ottawa, Ontario, K1A 0E8*

Abstract

Tourmaline has long been regarded as a petrogenetic indicator of its host environment, but its genesis in mineralized porphyry systems is poorly understood. Based on chemical and physical properties, tourmaline possesses essential features to be an effective indicator mineral. These properties, along with its abundant occurrence in mineralized copper-gold-molybdenum porphyry systems, make it potentially a key recorder of hydrothermal fluid composition, evolution and potential mineralization. A suite of tourmaline-bearing, barren and mineralized porphyry samples have been analysed as part of a broader study, including those from the Canadian Cordillera (Casino, Schaft Creek, Highland Valley and Woodjam) plus others, have been studied. Paragenetically, tourmaline is observed to be an early hydrothermal phase, predating both sulphide formation and any alteration. Tourmaline is observed to exhibit multiple growth zones, based on petrographic and electron microscope observations, which are also reflected in distinct trace-element variations. Three distinct textural types are recognized: breccia-style, vein-style and disseminated-style. Major element analyses based on SEM-EDS show a range between schorl (Na-Fe^{2+}-rich) to dravite (Na-Mg-rich) with some minor povondraite (Na-Fe^{3+}) component. Trace element analyses of porphyry related tourmaline *via* LAM-ICP-MS show distinct characteristics in comparison to that from non-porphyry settings, including redox sensitive elements (Mn, As and Sb) and large-ion lithophile elements (Sr, Ba). Elements not observed in significant concentrations include the light elements (Li, Be) and REEs, which commonly were below limit of detection. Current trace element analysis of tourmaline derived from surficial sediments points to tourmaline originating from the local porphyry system rather than an external source.

Introduction

Indicator minerals (including those belonging to specific groups such as garnet and apatite, and specific species such as rutile and zircon) are characterized by exhibiting both extensive chemical variation and combined resistance to both physical and chemical weathering in the surficial environment, have been effectively employed in the exploration for ore systems, including gold, diamonds and, more recently, porphyry copper (Averill and Zimmerman, 1986; Averill, 2001; McClenaghan and Kjarsgaard, 2007; Kelley et al., 2011; McClenaghan and Cabri, 2011; Hashmi et al., 2015; Plouffe et al., 2016). Tourmaline is a ubiquitous mineralogical component of many mineralized ore systems, including copper-gold-molybdenum porphyries, rare-earth pegmatites, orogenic-gold deposits and volcanogenic massive sulphide systems. Among these, its application to the exploration for mineralized porphyry systems has not been extensively employed, principally because there is a prevailing school of thought that mineralized systems need not be tourmaline-bearing. However, many prolific porphyry systems, such as the Los Bronces district are hosted in tourmaline breccias, making it paramount to understand the importance of this mineral (Warnaars et al., 1985). Tourmaline also possesses many key features that make it an effective indicator mineral including its resistivity to both chemical (stable across a wide-range of pH conditions) and physical (7 on Mohs' scale and poor cleavage) weathering as well as its ability to incorporate a wide range of major and trace elements. Tourmaline has been reported as a common accessory phase in some mineralized porphyry deposits (Sillitoe, 2010; Slack and Trumbull, 2011). Therefore, in order to create a baseline of knowledge of its occurrence, chemistry and textural variations, as well as to evaluate its application in exploration, a detailed study of tourmaline-bearing porphyry deposits has been undertaken. Furthermore, this study has sought to evaluate and test a broad selection of crystal chemical features of tourmaline that may serve as important discriminators in the differentiation between mineralized and barren porphyry systems and to apply these newly defined features to future mineral exploration programs.

Sample localities

The focus of this study is on porphyry deposits in the Canadian Cordillera (northern and southern British Columbia and the southern part of Yukon). These deposits include Casino, a calc-alkaline pre-accretion deposit (ca. 73 Ma); Schaft Creek, a deposit of calc-alkaline affinity situated within the post-accretion the Stikine terrain (ca. 220 Ma); and Woodjam copper, a deposit with an alkalic affinity positioned with in the

Corresponding author: Chris Beckett-Brown (ce_beckettbrown@laurentian.ca)

Beckett-Brown, C.E., McDonald, A.M., and McClenaghan, M.B., 2019. Unravelling tourmaline in mineralized porphyry systems: assessment as a valid indicator mineral; *in* Targeted Geoscience Initiative: 2018 report of activities, (ed.) N. Rogers; Geological Survey of Canada, Open File 8549, p. 345–351. https://doi.org/10.4095/313669

Quesnel terrain (ca. 200 Ma.) (Schroeter, 1995). It is important to note that both samples from the deposit (bedrock) and those from associated physically altered components (glacial till and stream sediments) have been included in this study to develop and define physical and/or chemical characteristics of grains in the surficial environment which reflect a potentially mineralized source. Tables 1, 2 and 3 list the bedrock, surficial and background sample data examined to date.

Table 1. Porphyry related tourmaline samples examined.

Deposit/ Property	Location	Metal Association	Notes	# of Samples
Casino	Yukon	Cu-Mo-Au	Large sample set collected from core samples throughout the deposit.	40
Mount Nansen	Yukon	Cu-Au	Core samples from the tourmaline breccia pipe.	5
Freegold Mountain Project	Yukon	Cu-Au	Bedrock samples of tourmaline.	3
Schaft Creek	British Columbia	Cu-Mo-Au	Large sample set collected from core.	35
Highland Valley Copper	British Columbia	Cu-Mo	Small sample set collected from GSC archives.	6
Woodjam Cu (Takom and Deerhorn)	British Columbia	Cu-Au	Large sample set collected from core and some grab samples around the deposit.	24
Red Spring Project	British Columbia	Au	Bedrock samples from exploration property.	6
New Afton	British Columbia	Cu-Au	Sample set of core from the phyllic zone.	10
Coxheath	Nova Scotia	Co-Mo-Au	Sample set from GSC archives.	7
Chibougamau	Quebec	Cu-Mo-Au	Sample set from GSC archives.	5
Soledad Project	Ancash, Peru	Cu-Au	Large sample set of tourmaline breccias from core.	13
El Correo	Sonora, Mexico	Cu-Mo-Sn	A transect of bedrock samples across deposit, from USGS archives	11
Los Bronces	Valparaiso Region, Chile	Cu-Mo	Bedrock sample.	1
El Teniente	Cachapoal Province, Chile	Cu	Sample set from GSC archives.	6

Table 2. Non-porphyry related tourmaline samples examined.

Deposit/ Property	Location	Rock Type/Metal Association	# of Samples
Seagull Batholith	Yukon	Granite	3
Seal Lake	Newfoundland and Labrador	Sediment hosted Cu	1
East Braintree	Manitoba	LCT Pegmatite	1
New Russels	Nova Scotia	Pegmatite	1
North Saddle	Northwest Territories	Pegmatite	1
Wakefield	Quebec	Pegmatite	1
Wolf Lake	Yukon	Granite	1
Canam Cu	British Columbia	Sediment Hosted Cu	1
Usakos Pegmatite	Namibia	NYF Pegmatite	1
Lost River	Alaska, USA	Skarn	1

Results

Tourmaline types – general observations

Three distinct genetic styles of tourmaline formation have been recognized in this study: 1) breccia; 2) vein; and 3) disseminated (Fig. 1). Tourmaline is generally found as acicular crystals that develop in radiating masses of black grains in hand sample. While many grains are observed to possess external, euhedral morphologies, back-scattered electron imaging shows internal textures that reveal evidence of complex chemical zonation, dissolution, overgrowths and various mineral inclusion types (quartz, iron-titanium oxides, zircon, apatite), all of which suggest multi-stage histories of crystallization. In general, breccia-type tourmaline is found within the core, with vein-style forming more proximal and disseminated forming more distal to the porphyry centres. Tourmaline is convention-

Table 3. Porphyry related surficial samples examined.

Deposit/ Property	Location	Type	# of Samples
Woodjam Cu	British Columbia	Glacial Till	16
Casino	Yukon	Stream Sediment, unglaciated	22
Soledad Project	Ancash, Peru	Stream Sediment, unglaciated	TBD

ally thought to form late in the paragenetic sequence of a porphyry, typically being classed as part of either periods of phyllic or propylitic alteration. However, detailed observations made as part of this study provide strong evidence that this is not the case: tourmaline is found to be one of the earliest forming hydrothermal phases and is almost always found predating the development of sulphide mineralization as well as alteration (Fig. 2), regardless of the tourmaline textural style and as such, tourmaline potentially records the earliest fluid composition.

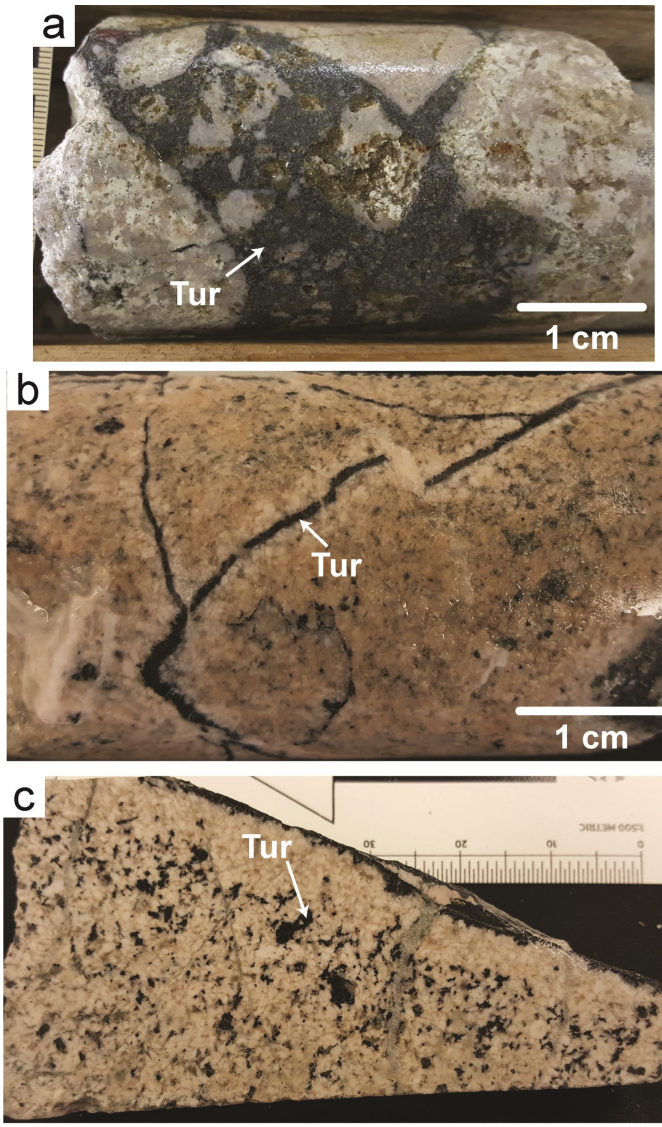

Figure 1. Photographs of hand samples showing the textural styles of tourmaline: a) breccia (black); b) vein (black); and c) disseminated (black).

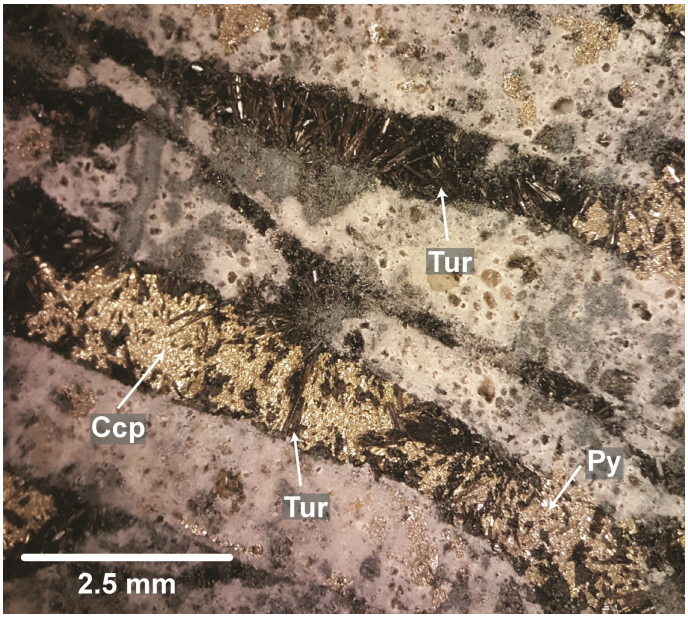

Figure 2. Microphotograph showing tourmaline (Tur) paragenesis. This is an example of a breccia cemented by tourmaline and sulphides (chalcopyrite and pyrite). Note the euhedral morphology of the tourmaline (black-brown).

Breccia-style tourmaline

Tourmaline-cemented breccias are relatively common in porphyry systems and contain tourmaline cementing or overgrowing the fragments (Fig. 1a). These cements also contain quartz and sulphide minerals (chalcopyrite, pyrite), all of which post-date the tourmaline. Polished thin section examinations show that the tourmaline gains are ubiquitously shattered, reflecting multiple periods of brecciation, with the fractures being infilled by secondary quartz, alkali-feldspar and sulphide minerals (pyrite, chalcopyrite). The tourmaline is generally jet black in colour, but under transmitted light it can appear pleochroic brown, pale green, or nearly colourless. Grains are typically prismatic to acicular and develop in radiating aggregates. Breccia-style tourmaline develops as grains that are 50 µm in diameter on average but are highly variable from submicrometre up to a millimetre in diameter. Grains are also observed to be colour zoned, both parallel and perpendicular to the elongation direction (Fig. 3).

Vein-style

Vein-style tourmaline (Fig. 1b) develops as the smallest grains of the three textural styles, these typically being approximately 20 µm in diameter and up to 100 µm in length. Such grains commonly develop in veins associated with paragenet-

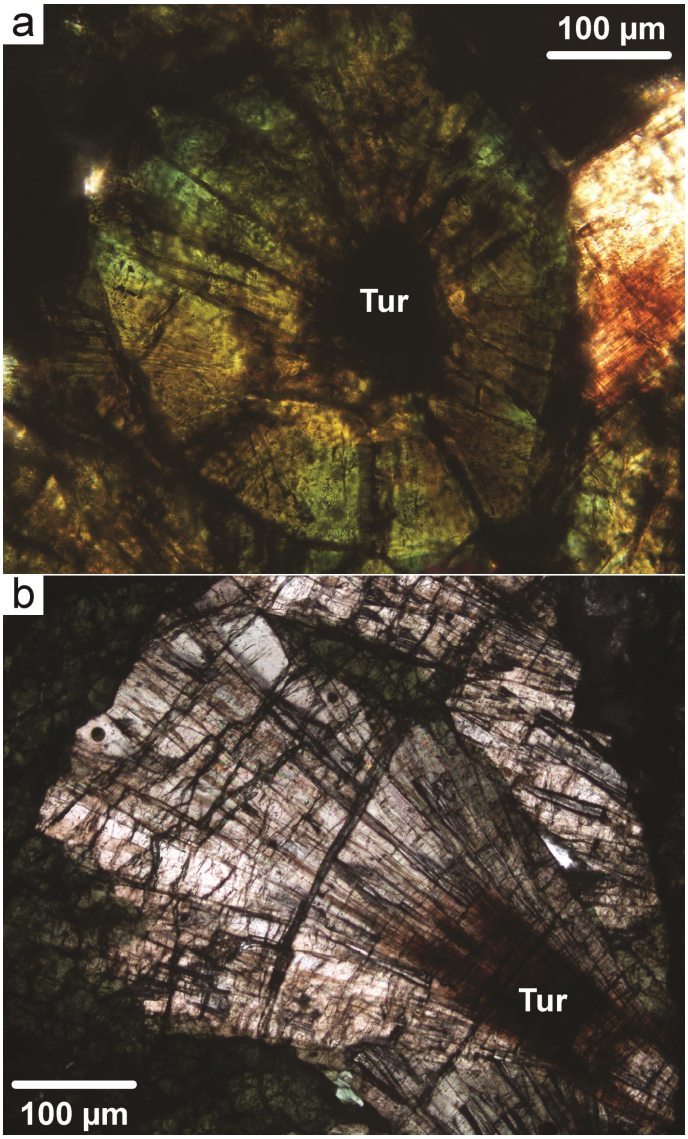

Figure 3. Transmitted light images showing the colour zonation of tourmaline: a) euhedral cross section of a grain showing the dark coloured core and green-yellow rim; b) euhedral long section of a grain showing the change in zonation from core to rim/nucleation to termination.

ically later quartz and sulphide minerals. In hand sample, the veins containing this textural type of tourmaline commonly have bleached white selvages that average 1 to 5 mm in width. The tourmaline colour in hand sample is generally dark brown to black. Tourmaline grains in the veins are randomly oriented (with respect to the other tourmaline grains) and tend to occur in densely packed aggregates, the interstices of which are predominantly occupied by quartz and, to a lesser extent, by sulphide minerals. Veins are commonly multigenerational denoted by multiple generations of quartz and the presence of broken tourmaline grains hosted in late quartz.

Disseminated-style

Disseminated-style tourmaline (Fig. 1c) forms the coarsest crystals observed in the porphyry system, with grains up to several millimetres in length. Texturally, such tourmaline closely resembles breccia-style tourmaline (i.e. acicular to prismatic radiating masses, commonly infilled by quartz) but can occur as individual clots, sometimes forming masses (Fig. 4). This tourmaline can also be observed forming in association with minor sulphide minerals (pyrite and chalcopyrite) (Fig. 2, 3). These grains are most commonly black to dark brown but more rarely can be observed as lighter colours.

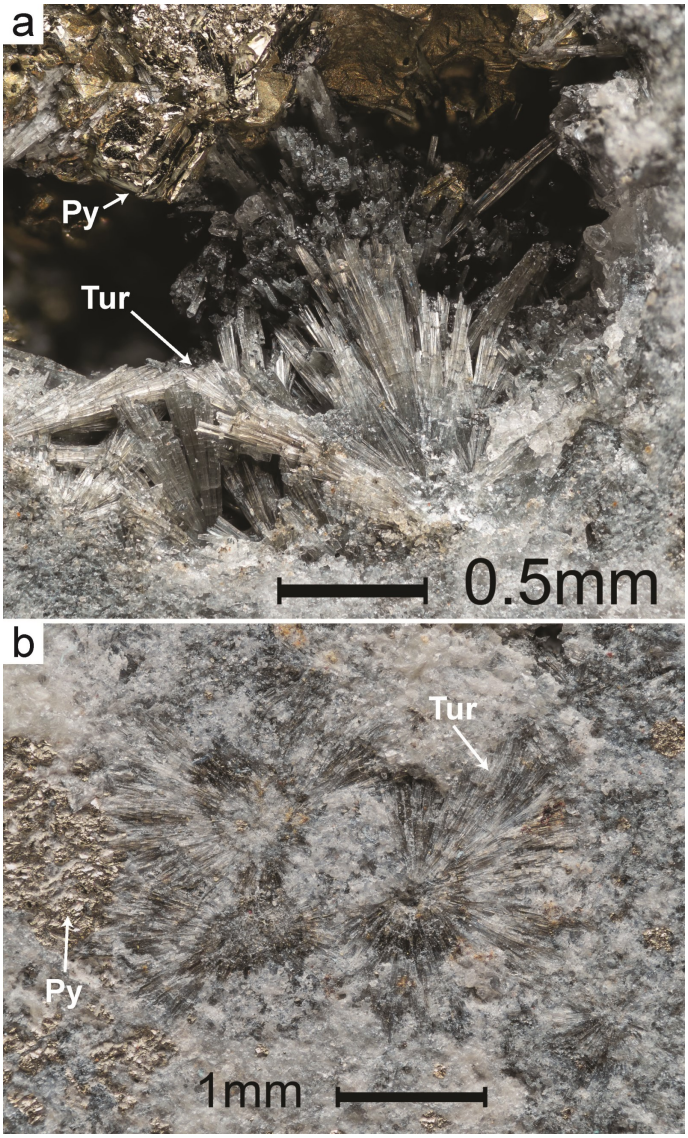

Figure 4. Microphotographs of radiating acicular tourmaline grains. Sulphides (pyrite, in this case) are intimately associated with tourmaline forming in the interstices between grains. The tourmaline grains also appear light in colour transitioning from a light green to nearly colourless at their termination: a) tourmaline forming in a vug; b) radiating tourmaline from a breccia sample. Photographs by Michael Bainbridge Photography.

Backscattered-electron imaging

The tourmaline mineral group can accommodate a wide range of elements, which reflects changes in the chemistry at the time of crystallization. It can also develop over multiple stages of growth as the fluid from which it crystallizes evolves. The combination of these features results in tourmaline exhibiting a high degree of chemical heterogeneity and zonation at the grain scale, these are observed through the use of backscatter electron (BSE) imaging (which reflects the contrast in average *Z*). Examination of the tourmaline grains with BSE imaging reveals numerous styles of chemical zonation within the tourmaline, including: oscillatory, patchy and diffuse (Fig. 5). These reflect the dynamic history of crystal growth of the tourmaline and can thus serve as graphical indicators of variations in pressure-temperature-fluid composition (*P-T-X*) conditions.

Major element chemistry (SEM-EDS)

Tourmaline from mineralized porphyry systems exhibits a wide range of major element chemistry. Tourmaline compositions primarily plot within the schorl, dravite, or povondraite compositional space, with minor additional components. The dominant substitution can be summarized by: $R^2 + Na^+ \leftrightarrow Al^{3+}$ + (vacancy) ($R^2 = 0.93$) and $Fe^{2+} + (OH)^- \leftrightarrow Al^{3+} + O^{2-}$ ($R^2 = 0.77$). The average (range) *apfu* (based on 15 cations) of the major elements are as follows; Na 0.71 (0.37–0.97), Ca 0.22 (<LOD to 0.70), Ti 0.06 (<LOD to 0.45), Mg 1.96 (0.69–2.89), Fe 1.38 (0.06–3.68), Al 5.64 (3.63–7.02) and Si 5.95 (5.32–6.42). In general, this variable chemistry corresponds to the species oxy-dravite – povondraite, the trend within this series reflecting an increase in Fe^{3+} (decrease in Al^{3+}) that may reflect the conditions of increasing oxidation (i.e. *f*O2) (Fig. 6). Such a trend has been previously documented in specific copper-gold-tin porphyry systems in Russia (Baksheev et al., 2012).

Trace element chemistry (LA-ICP-MS)

Tourmaline associated with mineralized porphyry systems (Cu, Cu-Au, Cu-Mo, Cu-Au-Mo) incorporates a wide range of trace elements due to the flexibility of its structure (van Hinsberg, 2011). A total of 51 elements have been sought and analyzed for *via* laser ablation-inductively coupled-mass spectrometry (LA-ICP-MS) most of which are considered trace in abundance. Table 4 highlights some tourmaline trace element generalizations. Specific to porphyry deposits, trace elements of interest include the redox sensitive elements (e.g. Mn, As, Sb), increased large-ion lithophile elements (e.g. Rb, Sr, Ba), and elevations of high field-strength elements (i.e. Ti, Zr, Th).

Ongoing/future tourmaline analysis

RAMAN spectroscopy: The determination of Fe^{2+}/Fe^{3+} in tourmaline is key to elucidating not only general trends in oxidation, but also in discriminating among processes (*e.g.* hydrothermal input, alteration, etc.). Typically, the Fe^{2+} and Fe^{3+} contents of tourmaline can be indirectly determined through mineral formula back calculations (based on mineral chemistry).

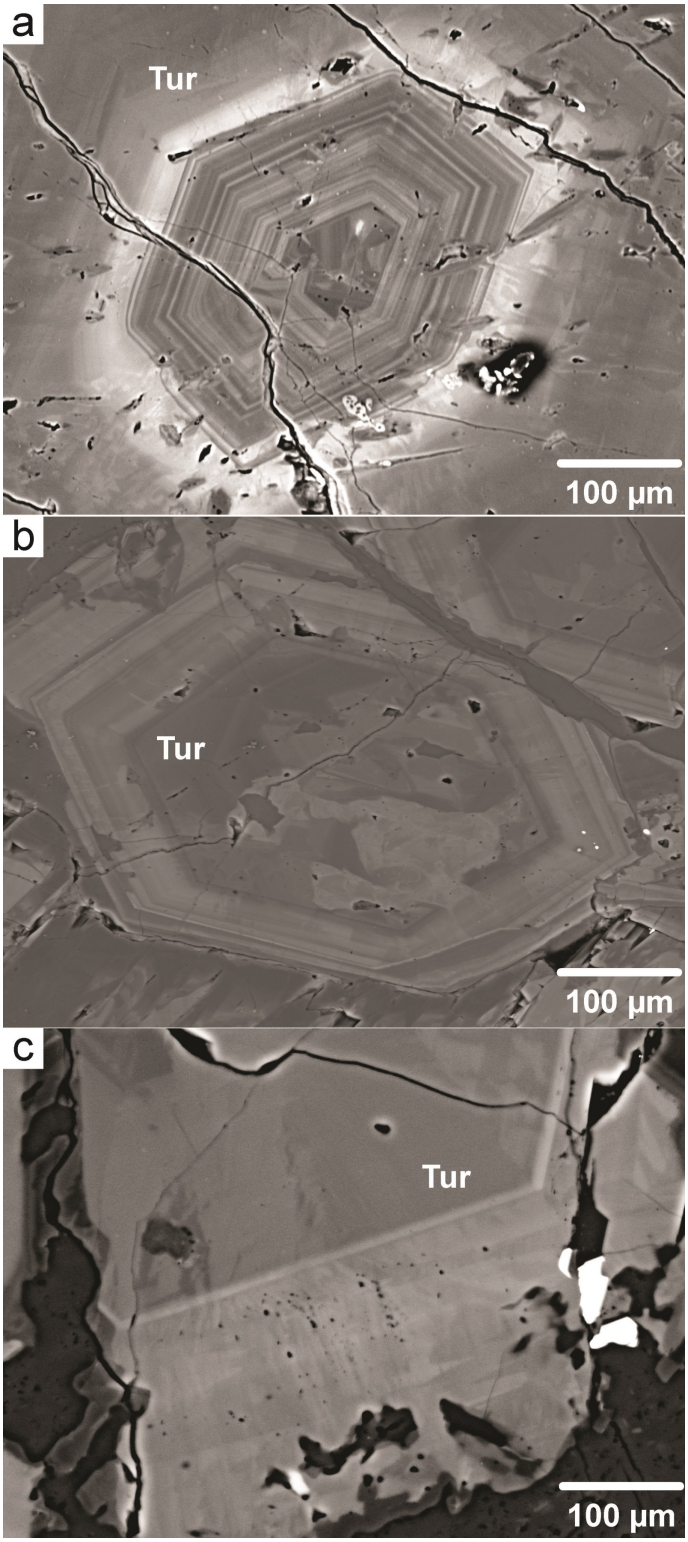

Figure 5. Backscattered electron images highlighting the varied nature of tourmaline zonation: a) chaotic zoned core followed by rhythmic oscillatory zonation; b) patchy zoned grain overgrown by oscillatory zonation; c) diffuse zonation appearing to overprint oscillatory zonation.

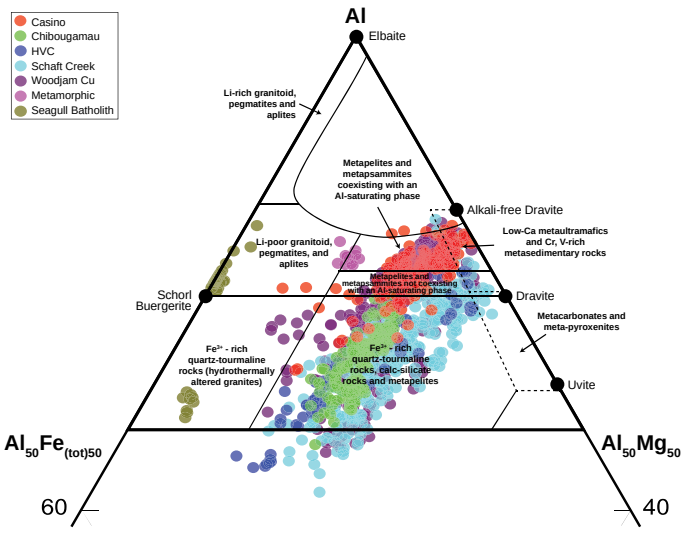

Figure 6. Ternary diagram of Al-Fe_{tot}-Mg (*after* Henry and Guidotti, 1985). Comparison of porphyry related and non-porphyry related tourmaline analyses. Porphyry tourmaline covers a large part of the plot, but all appear to follow an Al -Fe exchange along the oxy-dravite – povondraite trend.

Direct methodologies to obtain these data (Mossbauer and XANES) are not routine and generally difficult to both access and interpret. One powerful methodology that has shown promise is Raman spectroscopy (Watenphul et al., 2016). Following the methods of (Watenphul et al., 2016), the Fe valence will be assessed both on a grain-to-grain basis as well as between different growth zones within individual grains.

Table 4. Tourmaline trace element generalizations for different rock types or ore systems.

	Key trace-element signatures	References
Granitoids	Low Sr (<25 ppm) High Ga (100s of ppm) Sn (10s of ppm)	This study – Seagull batholith
Pegmatites	Enriched in REEs primarily LREEs High Sn (>50 ppm) Commonly contain Li and Be above LOD	1,2,3
Orogenic	Variable Li (tens to hundreds of ppm) Sr (1000s of ppm) Transition metals (100s to 1000s of Cr, Ni, Zn)	4
Volcanogenic Massive Sulfide	Low Ni (<5 ppm) Variable Zn (100s to 1000s of ppm) Enriched in Pb (>10 ppm)	5
Porphyries	<LOD light elements (Li and Be) Redox sensitive elements (>50 ppm Mn and As) Sr concentrations ~100s of ppm LREE enriched but low to <LOD concentrations	This study

[1]Novak et al. (2011), [2]Hazarika et al. (2017), [3]Marschall et al. (2013), [4]Kalliomäki et al. (2017), [5]Slack et al. (1999).

LA-ICP-MS: Full trace element results will be presented in an upcoming peer reviewed publication.

Isotope work: Isotopic analyses of boron will be conducted to assess the applicability of separating prospective tourmaline as well as determining the source of boron.

Surficial samples of tourmaline: Tourmaline recovered from surficial samples (till around the Woodjam deposit, stream sediments around the Casino deposit) will be analyzed and compared to that of the bedrock samples in terms of the criteria developed.

Acknowledgments

This report is a contribution to NRCan's Targeted Geoscience Initiative Program (TGI). Support for this study was provided through the Porphyry-style Mineral Systems Project's Activity 'P-3.3: Mineralogical controls on the fertility of porphyry-style systems'.

The authors acknowledge the support of Western Copper and Gold Corporation and the Casino Mining Corporation. The following companies have provided sample material to this study: Chakana Copper, New Gold, Jaxton Mining, Gold Fields Ltd. (now owned by Consolidated Woodjam Copper Corporation) and Triumph Gold. Scott Casselman, Yukon Geological Survey, is thanked for providing geological information, advice and access to samples from deposits in Yukon. John Chapman, Martin McCurdy and Dave Sinclair (GSC) are thanked for their contributions to this project. This report benefited from the review of Benoit Dubé, Chris Lawley and Neil Rogers.

References

Averill, S.A. and Zimmerman, J.R., 1986. The Riddle resolved: the discovery of the Partridge gold zone using sonic drilling in glacial overburden at Waddy Lake, Saskatchewan; Canadian Institute of Mining and Metallurgy, v. 1, p. 14–20.

Averill, S.A., 2001. The application of heavy indicator minerals in mineral exploration with emphasis on base metal indicators in glaciated metamorphic and plutonic terrain; *in* Drift Exploration in Glaciated Terrain, (ed.) M.B. McClenaghan, P.T. Bobrowsky, G.E.M. Hall and S. Cook; Geological Society of London, Special Volume 185, p. 69–82.

Baksheev, I.A., Prokof'ev, V.Y., Zaraisky, G.P., Chitalin, A.F., Yapaskurt, V.O., Nikolaev, Y.N., Tikhomirov, P.L., Nagornaya, E.V, Rogacheva, L.I., Gorelikova, N.V, and Kononov, O.V., 2012. Tourmaline as a prospecting guide for the porphyry-style deposits; European Journal of Mineralogy, v. 24, p. 957–979.

Hashmi, S, Ward, B.C., Plouffe, A., Leybourne, M.I., and Ferbey, T., 2015. Geochemical and mineralogical dispersal in till from the Mount Polley Cu-Au porphyry deposit, central British Columbia; Canada; Geochemistry: Exploration, Environment, Analysis, v. 15, p. 234–249.

Hazarika, P., Upadhyay, D., and Pruseth, K.L., 2017 Episodic tourmaline growth and re-equilibration in mica pegmatite from the Bihar Mica Belt, India: Major- and trace-element variations under pegmatitic and hydrothermal conditions; Geological Magazine, v. 154, p. 68–86.

Henry, D.J. and Guidotti, C.V., 1985. Tourmaline as a petrogenetic indicator mineral–An example from the staurolite-grade metapelites of NW Maine; American Mineralogist, v. 70, p. 1–15.

Kalliomäki, H., Wagner, T., Fusswinkel, T., and Sakellaris, G., 2017 Major and trace element geochemistry of tourmalines from Archean orogenic gold deposits: Proxies for the origin of gold mineralizing fluids? Ore Geology Reviews, v. 91, p. 906–927.

Kelley, K.D., Eppinger, R.G., Lang, J., Smith, S.M., and Fey, D.L., 2011. Porphyry Cu indicator minerals in till as an exploration tool: Example from the giant Pebble porphyry Cu-Au-Mo deposit Alaska, USA; Geochemistry: Exploration, Environment, Analysis, v. 11, p. 321–334.

Marschall, H., Wenzel, T., Jacob, D.E., Marks, M.A.W., Marschall, H.R., Schühle, P., Guth, A., and Wenzel, T., 2013. Trace element systematics of tourmaline in pegmatitic and hydrothermal systems from the Variscan Schwarzwald (Germany): The importance of major element composition, sector zoning, and fluid or melt composition Michael; Chemical Geology, v. 344, p. 73–90.

McClenaghan, M.B. and Cabri, L.J., 2011. Gold and Platinum Group Element indicator minerals in surficial sediments; Geochemistry: Exploration, Environment, Analysis, v. 11, p. 251–263.

McClenaghan, M.B. and Kjarsgaard, B.A., 2007. Indicator mineral and surficial geochemical exploration methods for kimberlite in glaciated terrain: Examples from Canada; *in* Mineral Deposits of Canada: A Synthesis of Major Deposit-Types, District Metallogeny, the Evolution of Geological Provinces, and Exploration Methods, (ed.) W.D. Goodfellow; Geological Association of Canada, Mineral Deposits Division, Special Publication No. 5, p. 983–1006.

Novák, M., Škoda, R., Filip, J., Macek, I., and Vaculovič, T., 2011. Compositional trends in tourmaline from intragranitic NYF pegmatites of the Třebíč pluton, Czech Republic: An electron microprobe, mössbauer and LA-ICP-MS study; The Canadian Mineralogist, v. 49, p. 359–380.

Plouffe, A., Ferbey, T., Hashmi, S., and Ward, B.C., 2016. Till geochemistry and mineralogy: Vectoring towards Cu porphyry deposits in British Columbia, Canada; Geochemistry: Exploration, Environment, Analysis, v. 16, p. 213–232.

Schroeter, T.G. (ed.), 1995. Porphyry deposits of the northwestern Cordillera of North America; Canadian Institute of Mining, Metallurgy and Petroleum, Special Volume 46, p. 888.

Sillitoe, R.H., 2010. Porphyry copper systems; Economic Geology, v. 105, p. 3–41.

Slack, J.F. and Trumbull, R.B., 2011 Tourmaline as a recorder of ore-forming processes; Elements, v. 7, p. 321–326.

Slack, J.F., Ramsden, A.R., Griffin, W.L., Win, T.T., French, D.H., and Ryan, C.G., 1999. Trace elements in tourmaline from the Kidd Creek massive sulfide deposit and vicinity, Timmins, Ontario: A proton microprobe study; *in* The Giant Kidd Creek Volcanogenic Massive Sulfide Deposit, Western Abitibi Subprovince, Canada, (eds.) M.D. Hannington and C.T. Barrie; Economic Geology, Monograph 10, p. 415–430.

van Hinsberg, V.J., 2011. Preliminary experimental data on trace-element partitioning between tourmaline and silicate melt; Canadian Mineralogist, v. 49, p. 153–163.

Watenphul, A., Burgdorf, M., Schluter, J., Horn, I., Malcherek, T., and Mihailova, B., 2016. Exploring the potential of Raman spectroscopy for crystallochemical analyses of complex hydrous silicates: II. Tourmalines; American Mineralogist, v. 101, p. 970–985.

Warnaars, F.W., Holmgren, C., and Barassi, S., 1985. Porphyry copper and tourmaline breccias at Los-Bronces-Rio-Blanco, Chile. Economic Geology, v. 80, p. 1544–1565.

Origin of boron-rich fluids in the formation of unconformity associated deposits of the Sibley Basin

C.J. Kelly[1], W.J. Davis[1], E.G. Potter[1], R. Metsaranta[2] and M. Puumala[3]

[1]*Geological Survey of Canada, 601 Booth Street, Ottawa, Ontario K1A 0E8*

[2]*Ontario Geological Survey, 933 Ramsey Lake Road, Sudbury, Ontario P3E 6B5*

[3]*Ontario Geological Survey, Suite B002, 435 James Street South, Thunder Bay, Ontario P7E 6S7*

Abstract

Hydrothermal magnesio-foitite or dravite (tourmaline) is common within the ore zones of unconformity associated uranium deposits globally. Magnesium-rich tourmaline ranging in composition from dravite to magnesio-foitite is identified in two uranium showings within the Sibley Basin. Hydrothermal dravite from the Malborne Lake showing ($\delta^{11}B$ = -22.5‰ to -20.2‰) is significantly isotopically lighter than dravite and magnesio-foitite analyzed from the Innis Lake showing ($\delta^{11}B$ = 16.5–20.0‰). The isotopically light $\delta^{11}B$ values of tourmaline from Malborne Lake is consistent with local metamorphic tourmaline, indicating that boron is primarily basement-derived. This contrasts with the isotopically heavy compositions of hydrothermal tourmaline from the Innis Lake showing that are comparable to values reported from the Athabasca Basin. A positive $\delta^{11}B$ value indicates that boron was sourced from, or potentially equilibrated with, the overlying marine evaporites, such as the chemical sediments of the Sibley Basin. The $\delta^{11}B$ values of hydrothermal tourmaline from the two occurrences are markedly different and suggest that vein-hosted mineralization in the basement rocks of the Sibley Basin did not form via a unique mechanism.

Introduction

Unconformity associated uranium deposits are pods, veins, and semi-massive replacements of uraninite that are the result of high-volume fluid flow at the interface between sedimentary basins, crystalline basement rocks, and fault systems (Jefferson et al. 2007). Economic deposits are best known from the Proterozoic Athabasca and Kombolgie basins in Canada and Australia. Unconformity associated uranium deposits represent more than 36% of the global uranium resources and are the sole producers of primary uranium in Canada (Organisation for Economic Co-Operation and Development, 2018). Figure 1a illustrates the distribution of Proterozoic basins within Canada that contain unconformity associated uranium (Jefferson et al., 2007). Alteration halos of illite, chlorite, and magnesium-rich tourmaline developed around uranium ore zones demonstrate the importance of magnesium and boron in the genesis of this deposit type. The origin and composition of the fluids responsible for the mobilization and mineralization of uranium, as well as the associated boron- and magnesium-rich alteration halos, is still contentious with some researchers suggesting that basinal marine brines were an important fluid source (Mercadier et al., 2012), while others suggest a basinal fluid that equilibrated with basinal sedimentary rocks (Adlakha et al., 2017).

Boron is a fluid-mobile, moderately volatile lithophile element with a low atomic mass. It has two stable isotopes ^{10}B and ^{11}B with isotopic abundances of 19.8 and 80.2%, respectively in nature. The boron isotopic composition is reported as a per mil (‰) deviation from the SRM 951 boric acid ($^{11}B/^{10}B$=4.04362) reference value as follows:

$$\delta\ ^{11}B = 1000 \times \left(\left[\frac{R_{Corr}}{R_{SRN951}}\right] - 1\right)$$

The large relative mass difference between the two isotopes (~10%) and the physiochemical properties of boron result in large isotopic fractionations between seawater (39.6‰) and average continental crust (-15–0‰; Bast et al., 2014). The global $^{11}B/^{10}B$ ratio varies by several tens of per mil in surficial environments (Palmer and Swihart, 1996; Marschall and Monteleone, 2014) with non-marine evaporites having $\delta^{11}B$ values as low as -27‰ (Palmer and Slack, 1989) whereas marine brines can be up to +55‰ (Vengosh et al., 1992). Continental rocks typically have negative $\delta^{11}B$ values, with positive $\delta^{11}B$ values indicating a marine contribution. The strong enrichment of B in the crust and its affinity for fluid phases coupled with the significant difference in the $\delta^{11}B$ of distinct geological reservoirs make boron a powerful tool for tracing hydrothermal fluids in metasomatic processes (Slack et al., 1993; Xavier et al., 2008; Marschall and Jiang, 2011; Slack and Trumbull, 2011; Tornos al et., 2012).

Tourmaline ($XY_3Z_6(T_6O_{18})(BO_3)_3V_3W$) is a chemically complex borosilicate with up to 3 weight % B (Henry and Dutrow, 2011). Tourmaline is resistant to chemical diffusion (van Hinsberg and Marschal, 2007) and isotope homogenization, even at high pressures and temperatures, meaning that primary chemical and isotopic signatures are often preserved up to upper amphibolite facies conditions (Henry and Dutrow, 1996; Dutrow et al., 1999; van Hinsberg et al., 2011). The ro-

Corresponding author: Colter Kelly (colter.kelly@canada.ca)

Kelly, C.J., Davis, W.J., Potter, E.G., Metsaranta, R. and Puumala, M., 2019. Origin of boron-rich fluids in the formation of unconformity associated deposits of the Sibley Basin; *in* Targeted Geoscience Initiative: 2018 report of activities, (ed.) N. Rogers; Geological Survey of Canada, Open File 8549, p. 353–363. https://doi.org/10.4095/313670

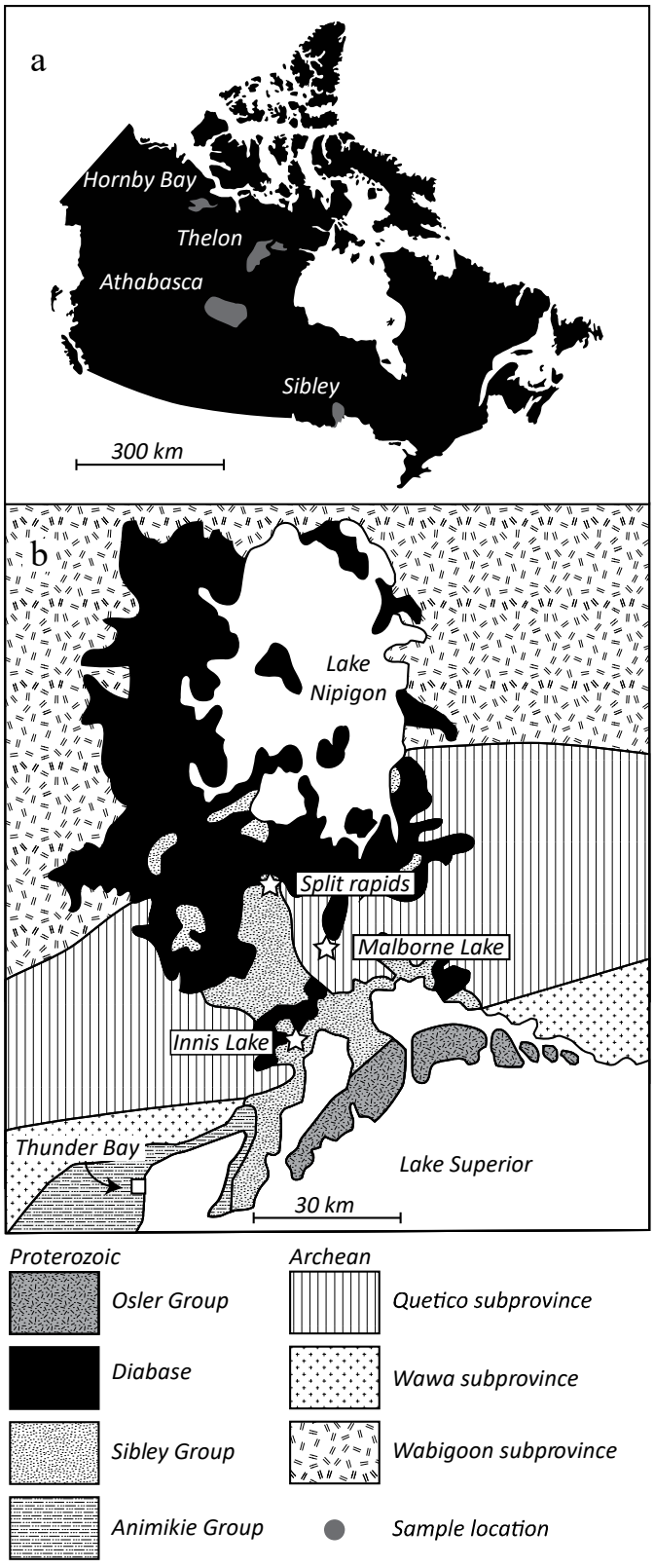

Figure 1. a) Simplified map of Canada illustrating the locations of the Proterozoic basins that contain unconformity-related uranium. b) Simplified geological map of the Thunder Bay – Nipigon Lake area (*modified after* Rogula et al., 2007).

bustness of tourmaline highlights its potential as a geochemical tracer of crustal evolution (van Hinsburg et al., 2017). As the fractionation factors between tourmaline and water have been calculated (Meyer et al., 2008; Marschall et al., 2009), it is possible to derive robust estimates of the fluid-boron composition from the isotopic composition of tourmaline. As such, the boron isotopic composition of hydrothermal tourmaline that formed synchronously with ore minerals has the potential to elucidate the origins of the ore-forming fluids as well as the source of coeval boron present within alteration haloes. This tool has been utilized for a plethora of ore deposit systems, including unconformity associated uranium (Mercadier et al., 2012; Adlakha et al., 2017).

The Sibley Basin is an intracontinental basin that shares a number of characteristics of the world-class Athabasca Basin, including depositional age, lithology, and mineral occurrences (Scott 1987). During uranium exploration of the 1970s and early 1980s, several unconformity associated uranium showings were discovered within the Sibley Basin, but significant uranium mineralization has not been documented (Smyk and Franklin, 2007). Two of the showings visited in this study contained vein-hosted tourmaline, a characteristic alteration mineral of Athabasca deposits. The major element and boron isotopic composition of the tourmaline is documented to allow comparisons with tourmaline occurrences of the Athabasca Basin. Specifically, the study tests if fluids related to alteration associated with uranium mineralization in the Sibley Basin have strongly positive boron isotopic values as in the Athabasca, which would suggest a similar source of boron and mineralization style.

Geologic setting

Hart et al. (2007) and Rogala et al. (2007) provide good reviews of the geology and stratigraphy of the Nipigon Embayment and the Sibley Basin and surrounding areas. Archean rocks of the Superior Province form the basement of the Sibley basin in the studied area (Fig. 1b), although the Sibley Group unconformably overlies weakly metamorphosed Paleoproterozoic rocks of the Animikie Group (Rove and Gunflint formations) farther to the south and is thought to overlie ca. 1.59 to 1.54 Ga anorogenic granite and volcanic rocks (English Bay Complex) and broadly contemporaneous gabbroic and syenitic plutons (Badwater intrusion) over portions of the northern part of the Sibley Basin (cf. Davis and Sutcliffe, 1985; Hollings et al., 2004; Heaman et al., 2007). Metavolcanic and associated metasedimentary rocks of the Wabigoon and Wawa subprovinces (ca. 3.0–2.68 Ga) underlie the northern and southern portions of the Sibley Basin, respectively, and metasedimentary rocks and a variety of felsic to intermediate intrusive rocks and local mafic-ultramafic intrusive rocks of the Quetico subprovince (less than ca. 2.7 Ga) underlie the central portion of the basin (Fig. 1b). Locally, uranium-bearing pegmatite dykes are associated with felsic plutonic rocks of the Quetico subprovince and were interpreted to represent the primary metal source

of mineralization for later uranium mineralization (Franklin, 1978).

Following deformation of the Archean basement rocks, a localized regolith developed prior to the deposition of the Animikie Group (Gunflint and Rove formations). The Gunflint Formation (ca. 1.88 Ga; Fralick et al., 2002) generally consists of local basal sandstone, chert, iron-rich carbonate rocks and argillite; greywacke and black shale dominate the Rove Formation (ca. 1.83 Ma; Addison et al., 2005). The two formations are interpreted to be separated by impact ejecta from the ca. 1.85 Ma Sudbury meteorite impact (Addison et al., 2005). Both these formations are relatively undeformed and unmetamorphosed (e.g. Franklin, 1970), although the Gunflint Formation is locally folded.

Essentially unmetamorphosed (except near intruding mafic sills and dykes) and undeformed, oxidized clastic, carbonate, and halite- and sulphate-bearing evaporate rocks of ca. 1.5 to 1.3 Ga (cf. Franklin et al., 1982; Heaman et al., 2007; Rogala et al., 2007) Sibley Group disconformably overlie the Animikie Group rocks. Evidence of halite (including bedded halite) and nodular gypsum in the Sibley Group is confirmation of deposition in a hot, semi-arid to arid climate (e.g. Cheadle, 1986; Metsaranta et al., 2007). The Sibley Group is intruded by numerous mid-continent rift-related mafic to ultramafic intrusive rocks of the Nipigon Embayment (e.g. Hart et al., 2007). Contact metamorphic aureoles of larger Nipigon diabase sills commonly effect Sibley Group rocks. The lithostratigraphy of the Sibley Group comprises five formations and it reaches a maximum thickness of approximately 950 m. The detailed lithostratigraphy of the Sibley Group is presented in Rogala et al. (2007). In general, it comprises a thin lower conglomerate and sandstone unit (braided fluvial, Pass Lake Formation) overlain by fine-grained mixed siliciclastic-carbonate-sulphate-halite rocks (Rossport Formation, saline lacustrine deposits), followed by a generally coarsening upwards mudstone-siltstone (Kama Hill Formation, deltaic) to sandstone (Outan Island Formation, deltaic to meandering fluvial) succession that is then overlain by a thick homogenous succession of sandstone (Nipigon Bay Formation, aeolian).

Generally, east- to northeast-striking structural fabrics and shear zones within Archean rocks underlying the Sibley Basin do not appear to have strongly influenced the geometry of the Sibley Basin, despite major regional-scale ductile shear zones, such as the Quetico and Gravel River faults underlying the basin (although this is not well established by existing mapping and drilling). The basin has a general half-graben morphology and units thicken towards the north-northwest-striking Black Sturgeon Fault and basin thickening to the east appears to have been accommodated by east-dipping, likely northwest-striking normal faults based on drill core and audiomagnetolelluric data (e.g. Craven et al., 2006; Rogala et al., 2007).

Scott (1987) described several different styles in which uranium is hosted in the Thunder Bay – Nipigon area:

1. Archean pegmatites in the Quetico Belt.

2. Fault-hosted veins at or near the unconformity between the Sibley Group and underlying Archean rocks. Regionally Archean host rocks include quartz monzonite (Greenwich Lake and Innes Lake occurrences), magnetite-chert iron formation (Black Sturgeon-Split Rapids occurrence), and Quetico metasedimentary rocks (Malbourne Lake occurrence).

3. Weakly radioactive Pb-Zn veins associated with Sibley Group/Archean unconformity.

4. Diatremes, alkalic intrusive rocks and carbonatite.

5. Mudball Tuff unit in the Gunflint Formation.

Occurrences examined during this study fall into the second class – fault-hosted veins near the Sibley-Archean unconformity. Note that no well substantiated occurrences of uranium mineralization are hosted in the Sibley Group rocks themselves. All are hosted in approximately north-striking oxidized vein systems in basement rocks and are interpreted to be the roots of a now eroded sandstone-hosted uranium occurrences.

Tourmaline was sampled from two uranium showings, Innis Lake and Malborne Lake. A third uranium occurrence (Black Sturgeon – Split Rapids Dam) was also investigated but tourmaline was not found in the alteration assemblage.

The uranium occurrence at Innis Lake is within a weakly foliated, but likely Archean, quartz monzonite intrusion. The relatively fresh, undeformed rock markedly contrasts with the enveloping metasedimentary rocks and migmatite of the Quetico gneiss belt. The uranium mineralization is associated with a hematitic quartz breccia, referred to as the Goodmorning Lakes fault (Yule, 1979). The Goodmorning Lakes fault contains fragments of the Sibley Group sedimentary rocks, illustrating the proximity to the unconformity with now eroded, overlying rocks of the Sibley Basin (Scott, 1987). Microscopic (>10 μm) and equant tourmaline is present at this showing as centimetre-wide, pale blue veins that formed early in the petrogenetic sequence relative to uranium (Yule, 1979). Tourmaline that is <5 μm long is intergrown with plagioclase, kaolinite, and contains millimetre-wide concordant seams of goethite. Petrographically, there are two generations of tourmaline evinced by a marked change in the abundance of coexisting phases, namely plagioclase, from the edge to the core of the vein, consistent with at least two episodes of crack and seal (Fig. 2a). Uranium mineralization at this location was interpreted to represent the roots of an unconformity associated deposit (Scott, 1987; Smyk and Franklin, 2007) wherein hydrothermal fluids were driven by mid-continental rift heating.

The Malborne Lake showing consists of a narrow high-grade fractured zone within Archean metasedimentary rocks. Hematitic quartz breccia is present, however proximity to the overlying unconformity is unknown (Scott, 1987). Centimetre-wide veins of illite/smectite, iron saponite crystallized with a blue-green tourmaline is present at this showing (Fig. 2b, c). At the outcrop, there is a dismembered pegmatite sill containing black tourmaline up to several centimetres in diameter. This tourmaline is inclusion-rich (quartz and plagioclase) and is

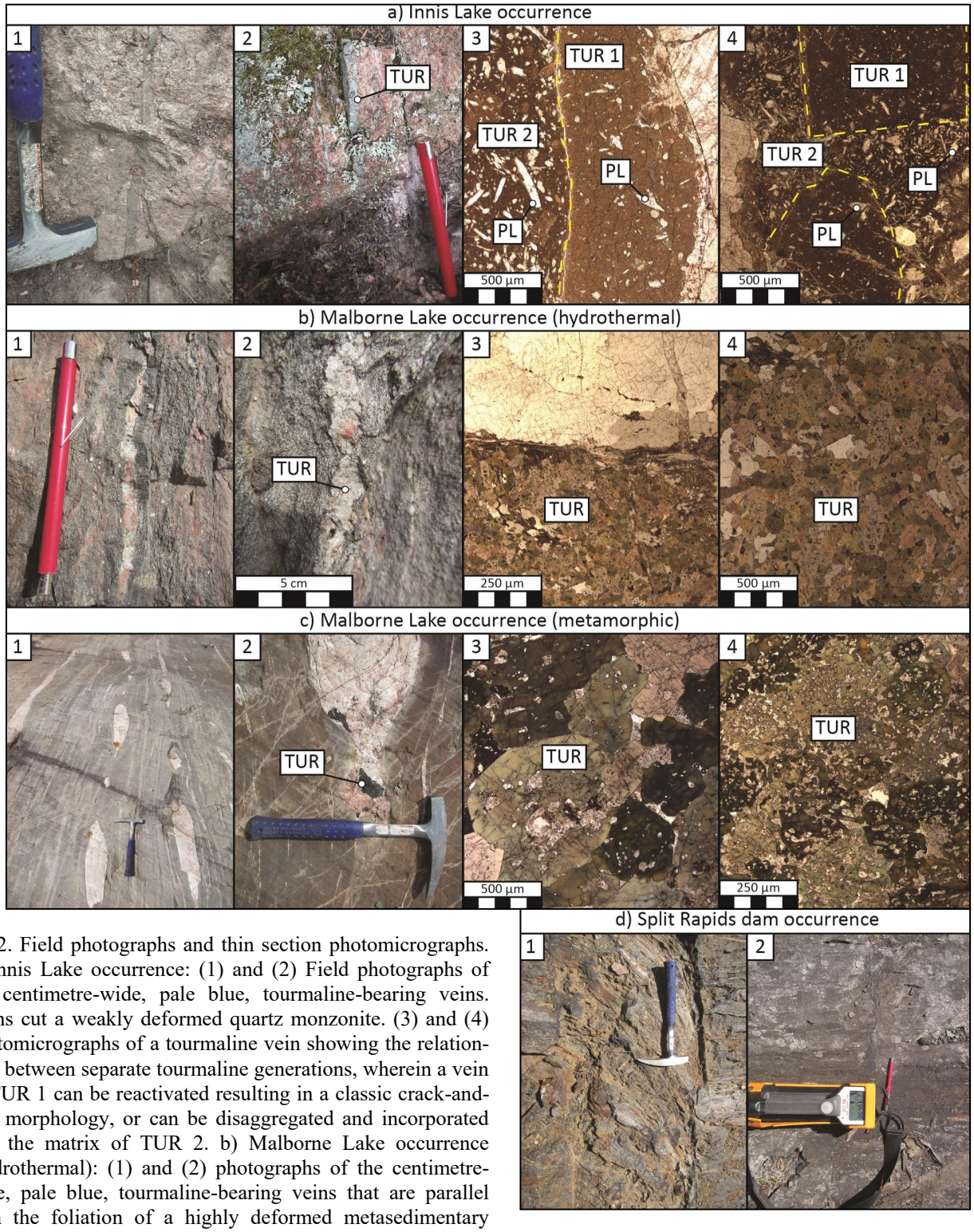

Figure 2. Field photographs and thin section photomicrographs. a) Innis Lake occurrence: (1) and (2) Field photographs of the centimetre-wide, pale blue, tourmaline-bearing veins. Veins cut a weakly deformed quartz monzonite. (3) and (4) Photomicrographs of a tourmaline vein showing the relationship between separate tourmaline generations, wherein a vein of TUR 1 can be reactivated resulting in a classic crack-and-seal morphology, or can be disaggregated and incorporated into the matrix of TUR 2. b) Malborne Lake occurrence (hydrothermal): (1) and (2) photographs of the centimetre-wide, pale blue, tourmaline-bearing veins that are parallel with the foliation of a highly deformed metasedimentary rock. (3) and (4) Photomicrographs illustrating the interlocking nature of the tourmaline crystals and the contact relationship with adjacent quartz flooding. c) Malborne Lake occurrence (metamorphic): (1) and (2) Field photographs illustrating the dismembered nature of the pegmatitic sill. Coarse-grained black tourmaline crystals observed at the margins of the 'pod' in (2). (3) and (4) Photomicrographs of a rich domain of pegmatite. Tourmaline is inclusion-rich and intergrown in appearance. d) Split Rapids Dam occurrence: (1) and (2) Field photographs of uranium bearing deformation zones and veins. Note hammer for scale is 26 cm long and red magnetic pen is 9.5 cm long. *TUR = tourmaline, PL = plagioclase.*

interpreted to be metamorphic—with boron associated with primary crystallization of the pegmatite.

The Black Sturgeon – Split Rapids Dam uranium occurrence is hosted in centimetre- to metre-scale deformation zones within Archean banded iron formation (Fig. 2d). Remobilized iron oxide is abundant within shear zones in addition to minor amounts of vermiculite, ferrihydrite, and clinopilillite. Despite the presence of tourmaline in drill core (Metsaranta and Metsaranta, 2008), it was not identified at the outcrop.

Analytical methods

Preliminary observation of alteration assemblages was completed on hand specimens using a TerraSpec Halo near-infrared spectrometer. Petrographic imaging at the Geological Survey of Canada, Ottawa using binocular microscope and back scattered electron (BSE) images using a Zeiss EVO 50 series scanning electron microscope (SEM) under high voltage set at 20 kV allowed for further evaluation of tourmaline crystals.

Electron probe micro-analyzer

Major element analyses using an electron probe micro-analyzer (EPMA) was completed using a JEOL JXA-8230 Superprobe at the University of Ottawa with an acceleration voltage of 20 kV, a beam current of 20 nA, and a beam diameter of 5 µm. Data collection times were 10 s for on peak and 5 s off peak. The calibration standards were as follows: sanidine (Si*K*α, Al*K*α, K*K*α), rutile (Ti*K*α), hematite (Fe*K*α), tephroite (Mn*K*α), sphalerite (Zn*L*α), diopside (Mg*K*α, Ca*K*α), albite (Na*K*α), tugtupite (Cl*K*α), sanbornite (Ba*L*α), fluorite (FKα), and celestine (Sr*L*α). Data reduction was carried out using a ZAF routine. Structural formulas were calculated for 31 anions where stoichiometric amounts of OH together with F correspond to four atoms/molecules per formula unit. The procedure assumes boron saturation of three atoms per formula unit and no boron on the tetrahedral position. Li was not analyzed but is assumed to fill up the Y site to a total of three cations. Charge balance calculations imply that Fe and Mn in the analyzed tourmalines are bivalent (Selway and Xiong, 2002; Tindle et al., 2002). Mean values of representative samples are presented in Table 1.

Secondary ion mass spectrometry

The boron isotope composition was measured using a sensitive high-resolution ion microprobe (SHRIMP II) at the Geological Survey of Canada, Ottawa, following methods described in Adlakha et al. (2017). Each analysis was composed of three sets of 10 scans measuring masses of ^{10}B, ^{11}B, and background in single Faraday collector peak jumping mode for a total analytical time of 20 minutes.

Two tourmaline reference materials (dravite H108796, and schorl 112566: Dyar et al., 2001, Leeman and Tonarini, 2001) were analyzed during each of the two analytical sessions (Table 2). The measured boron isotope compositions ($^{11}B/^{10}B$ = R) are consistently lower than the accepted values (cf. Leeman and Tonarini, 2001). An internal mass fractionation correction (IMF) factor was calculated as ($IMF = R_{cert} / R_{meas}$). Given that unknowns do not represent end-member compositions, an average value between those of dravite H108796 and schorl 112566 was utilized for the IMF corrections (1.0339 and 1.0314 for session one and two, respectively), this approach yields a repeatability of 1.1‰, which represents the predominant source of uncertainty in our analytical setup.

Tourmaline composition

Tourmaline from the Innes Lake occurrence ranges in composition from dravite $[NaMg_3Al_6(BO_3)_3Si_6O_{18}(OH)_4]$ to magnesio-foitite $[\square Mg_{1.5}Al_{7.4}Si_6O_{18}(BO_3)_3(OH)_4]$ (Fig. 3; Table 3). Variability in the X site magnesium#, X_{Mg} [Mg/(Mg+Fe)], is tightly constrained, with tourmaline from Innis Lake ranging between 0.88 and 0.91. The X site vacancy, $X_{\square}$ [$X_{\square}$/($X_{\square}$+Na)], is much less consistent, ranging from 0.24 to 0.55. The boron isotopic composition of tourmaline at Innis Lake range from $\delta^{11}B$ = 16.5 to 20.0‰. Variation within a single crystal is up to 1.8‰ with no systematic differences between rims and cores of individual crystals or from the edge of the veins to the centre, despite a notable shape in crystal habit.

Two generations of tourmaline are identified at Malborne Lake: metamorphic tourmaline with intermediate schorl $[NaFe^{2+}{}_3Al_6(BO_3)_3Si_6O_{18}(OH)_4]$–dravite $[NaMg_3Al_6(BO_3)_3Si_6O_{18}(OH)_4]$ compositions with limited alkali vacancies; and hydrothermal tourmaline dravitic in composition (Table 3). Variability in X_{Mg} is tightly constrained, with tourmaline from Malborne Lake ranging from 0.60 to 0.66 and $X_{\square}$ ranging from

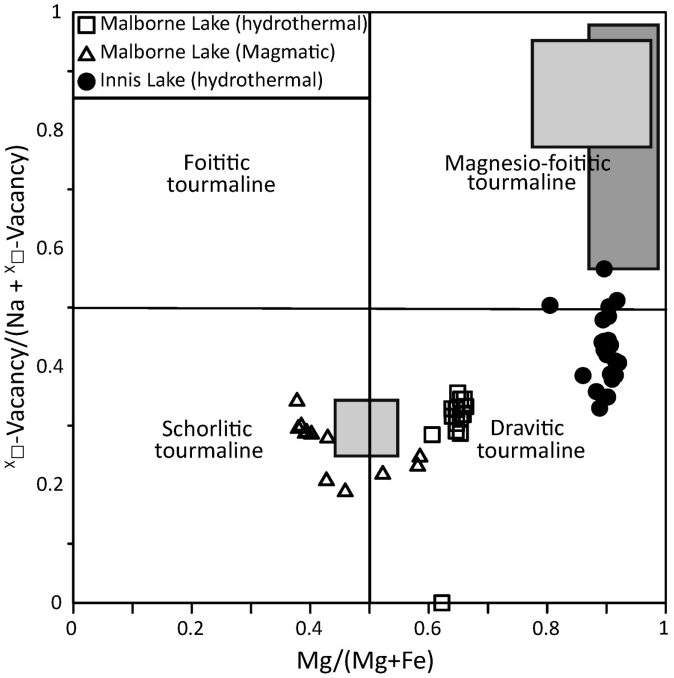

Figure 3. Tourmaline chemical classification diagram using the binary X_{mg} vs. $X_{\square}$ (Novák et al., 2009).

Table 1. Selected electron microprobe analyses of tourmaline from uranium showings of the Nipigon Basin.

	Innis Lake												Malborne lake								
	GML-17-01 (hydrothermal)			GML-17-02b (hydrothermal)			GML-17-02c (hydrothermal)			GML-17-03 (hydrothermal)			MBL-17-01a (hydrothermal)			MBL-17-01b (hydrothermal)			MBL-17-03b (Magmatic)		
SiO2	33.64	33.39	35.29	33.99	33.79	32.68	36.92	35.23	35.09	34.96	34.19	34.05	34.88	35.09	35.01	34.98	34.92	34.95	34.57	34.65	34.45
TiO2	0.03	0.05	0.04	0.03	0.02	0.01	0.05	0.06	0.05	0.06	0.63	0.33	0.99	0.72	0.82	0.52	0.42	0.64	0.59	0.58	0.46
Al2O3	30.01	29.41	30.54	30.50	31.21	31.72	30.97	30.78	31.47	32.16	30.83	31.36	30.36	31.78	31.83	31.27	31.01	32.34	31.90	31.76	31.31
V2O3	0.00	0.00	0.05	0.00	0.04	0.00	0.01	0.00	0.04	0.00	0.05	0.00	0.07	0.07	0.06	0.02	0.03	0.07	0.06	0.07	0.05
FeO	1.39	1.28	1.51	2.44	1.68	1.34	1.77	1.39	1.57	1.64	9.80	10.87	7.46	5.95	6.38	6.72	6.17	6.24	7.63	7.48	10.38
MgO	8.38	8.32	8.51	8.44	8.07	8.43	7.92	8.38	8.83	8.95	4.66	3.92	6.45	6.47	6.75	6.92	6.52	6.39	5.95	5.92	3.92
CaO	0.12	0.09	0.08	0.16	0.10	0.08	0.10	0.10	0.09	0.07	0.26	0.24	1.20	0.82	0.91	0.95	0.70	0.91	0.52	0.49	0.24
MnO	0.01	0.00	0.01	0.01	0.03	0.00	0.00	0.00	0.01	0.00	0.12	0.13	0.03	0.06	0.06	0.03	0.03	0.05	0.07	0.10	0.13
Na2O	1.65	1.57	1.61	1.72	1.42	1.38	1.53	1.58	1.78	1.67	2.30	2.02	1.70	1.70	1.84	1.70	1.80	1.73	2.10	2.08	2.02
K2O	0.19	0.21	0.53	0.05	0.46	0.01	1.12	0.39	0.08	0.04	0.00	0.00	0.00	0.01	0.00	0.00	0.01	0.00	0.03	0.00	0.02
F	0.08	0.34	0.24	0.16	0.21	0.30	0.31	0.42	0.00	0.05	0.27	0.37	0.14	0.17	0.00	0.21	0.08	0.32	0.50	0.00	0.00
H2O*	3.30	3.13	3.35	3.32	3.29	3.20	3.43	3.27	3.49	3.49	3.35	3.29	3.47	3.48	3.58	3.45	3.47	3.42	3.30	3.54	3.48
B2O3*	9.68	9.56	10.05	9.83	9.82	9.69	10.37	10.04	10.12	10.17	10.07	10.03	10.24	10.31	10.38	10.28	10.16	10.36	10.27	10.25	10.09
Li2O*	0.26	0.33	0.50	0.08	0.16	0.00	0.96	0.50	0.19	0.04	0.16	0.07	0.26	0.29	0.23	0.13	0.24	0.26	0.16	0.18	0.18
Total	88.74	87.69	92.30	90.75	90.31	88.84	95.47	92.12	92.82	93.29	96.67	96.68	97.24	96.93	97.84	97.18	95.56	97.69	97.65	97.08	96.72
O=F	0.03	0.14	0.10	0.07	0.09	0.13	0.13	0.17	0.00	0.02	0.11	0.16	0.06	0.07	0.00	0.09	0.04	0.13	0.21	0.00	0.00
Total*	88.70	87.55	92.20	90.68	90.22	88.72	95.34	91.94	92.82	93.27	96.56	96.52	97.18	96.85	97.84	97.09	95.52	97.56	97.44	97.08	96.72
Structural formula based on 31 anions (O, OH, F)																					
T: Si	6.042	6.071	6.105	6.007	5.982	5.863	6.187	6.100	6.026	5.975	5.901	5.898	5.921	5.916	5.865	5.912	5.973	5.862	5.851	5.877	5.935
Al	0.000	0.000	0.000	0.000	0.018	0.137	0.000	0.000	0.000	0.025	0.099	0.102	0.079	0.084	0.135	0.088	0.027	0.138	0.149	0.123	0.065
B	3.000	3.000	3.000	3.000	3.000	3.000	3.000	3.000	3.000	3.000	3.000	3.000	3.000	3.000	3.000	3.000	3.000	3.000	3.000	3.000	3.000
Z: Al	6.000	6.000	6.000	6.000	6.000	6.000	6.000	6.000	6.000	6.000	6.000	6.000	5.995	6.000	6.000	6.000	6.000	6.000	6.000	6.000	6.000
Mg	0.000	0.000	0.000	0.000	0.000	0.000	0.000	0.000	0.000	0.000	0.000	0.000	0.005	0.000	0.000	0.000	0.000	0.000	0.000	0.000	0.000
Y: Al	0.351	0.303	0.226	0.354	0.493	0.569	0.117	0.281	0.368	0.452	0.172	0.300	0.000	0.230	0.149	0.142	0.224	0.254	0.216	0.226	0.293
Ti	0.004	0.007	0.005	0.004	0.003	0.002	0.006	0.008	0.006	0.007	0.081	0.043	0.126	0.091	0.103	0.066	0.054	0.080	0.075	0.074	0.059
V	0.000	0.000	0.007	0.000	0.005	0.000	0.001	0.000	0.005	0.000	0.006	0.000	0.009	0.010	0.008	0.003	0.004	0.010	0.009	0.009	0.006
Mg	2.243	2.256	2.196	2.225	2.130	2.254	1.978	2.164	2.260	2.280	1.200	1.013	1.627	1.627	1.684	1.745	1.664	1.597	1.501	1.496	1.006
Mn	0.002	0.000	0.002	0.002	0.004	0.000	0.000	0.000	0.001	0.000	0.018	0.019	0.005	0.009	0.009	0.004	0.004	0.007	0.009	0.014	0.019
Fe2+	0.208	0.195	0.218	0.361	0.249	0.202	0.248	0.201	0.225	0.234	1.415	1.574	1.059	0.838	0.894	0.950	0.882	0.876	1.081	1.060	1.496
Li*	0.135	0.163	0.223	0.040	0.089	0.000	0.369	0.227	0.098	0.020	0.076	0.038	0.115	0.136	0.106	0.063	0.116	0.124	0.078	0.086	0.088
Mg	0.792	0.770	0.706	0.826	0.816	0.918	0.561	0.707	0.821	0.888	0.424	0.377	0.536	0.570	0.584	0.607	0.578	0.566	0.536	0.535	0.366
Fe2+	0.073	0.066	0.070	0.134	0.095	0.082	0.070	0.066	0.082	0.091	0.500	0.585	0.349	0.294	0.310	0.330	0.306	0.310	0.386	0.379	0.545
?Y	3.000	3.000	3.000	3.000	3.000	3.026	3.000	3.000	3.000	3.000	3.000	3.000	3.000	3.000	3.000	3.000	3.000	3.000	3.000	3.000	3.000
X: Ca	0.024	0.017	0.015	0.030	0.018	0.015	0.019	0.018	0.017	0.012	0.048	0.044	0.219	0.148	0.164	0.172	0.129	0.163	0.094	0.089	0.044
Na	0.574	0.554	0.539	0.590	0.489	0.479	0.498	0.529	0.594	0.552	0.769	0.677	0.559	0.556	0.596	0.557	0.597	0.562	0.688	0.683	0.676
K	0.043	0.050	0.116	0.012	0.105	0.003	0.239	0.086	0.018	0.008	0.000	0.001	0.000	0.003	0.000	0.000	0.002	0.000	0.007	0.000	0.005
Vacancy	0.359	0.380	0.329	0.369	0.388	0.503	0.245	0.367	0.372	0.427	0.182	0.277	0.222	0.293	0.240	0.271	0.272	0.275	0.211	0.228	0.275

*calculated stoichiometrically

Table 2. Summary of B isotope analyses by sensitive high-resolution ion microprobe (SHRIMP) on tourmaline reference materials.

Standard	Session	Accepted	Measured	SEM(%)	SD(%)	Constant external error applied	n	IMF	Accepted $\delta^{11}B$	Calculated $\delta^{11}B$
Dravite H108796	1	4.0169	3.8832	0.020	0.0259	0.025	5	1.0344	-6.6079	-6.5717
Schorl 112566		3.9931	3.8641	0.014	0.0365		10	1.0334	-12.4938	-11.4742
Dravite H108796	2	4.0169	3.8919	0.052	0.1318	0.1	7	1.0321	-6.6079	-6.8501
Schorl 112566		3.9931	3.8742	0.015	0.0479		6	1.0307	-12.4938	-11.3602

Table 3. Summary of B isotope analyses by sensitive high-resolution ion microprobe (SHRIMP) on tourmaline from uranium showings of the Nipigon basin.

		Title	Session	Measured $^{11}B/^{10}B$	1 S	corrected $^{11}B/^{10}B$ ††	total uncertainty†	correcte d $\delta^{11}B$	Error
Malborne lake	(hydrothermal)	MBL-17-01a.1c	1	3.8260	0.025	3.9574	0.0354	-21.3	0.3
		MBL-17-01a.2c	1	3.8238	0.023	3.9556	0.0340	-21.8	0.3
		MBL-17-01a.2r	1	3.8216	0.024	3.9527	0.0347	-22.5	0.3
		MBL-17-01a.3c	1	3.8256	0.023	3.9570	0.0340	-21.4	0.3
		MBL-17-01a.3r	1	3.8219	0.023	3.9535	0.0340	-22.3	0.3
		MBL-17-01a.4c	1	3.8264	0.021	3.9578	0.0326	-21.2	0.3
		MBL-17-01a.4r	1	3.8237	0.026	3.9548	0.0361	-22.0	0.4
		MBL-17-01a.5c	1	3.8237	0.024	3.9552	0.0347	-21.9	0.3
		MBL-17-01a.6c	1	3.8245	0.021	3.9561	0.0326	-21.6	0.3
		MBL-17-01a.7r	1	3.8248	0.023	3.9563	0.0340	-21.6	0.3
		MBL-17-01a.8c	1	3.8273	0.017	3.9589	0.0302	-20.9	0.3
		MBL-17-01a.9c	1	3.8230	0.024	3.9546	0.0347	-22.0	0.3
		MBL-17-01a.9r	1	3.8303	0.026	3.9621	0.0361	-20.2	0.4
		MBL-17-01a.10c	1	3.8225	0.019	3.9543	0.0314	-22.1	0.3
		MBL-17-01a.10r	1	3.8284	0.023	3.9599	0.0340	-20.7	0.3
	(magmatic)	MBL-17-03b.1c	1	3.8370	0.024	3.9690	0.0347	-18.5	0.3
		MBL-17-03b.1c	1	3.8327	0.022	3.9646	0.0333	-19.5	0.3
		MBL-17-03b.1c	1	3.8390	0.024	3.9707	0.0347	-18.0	0.3
		MBL-17-03b.2c	1	3.8356	0.022	3.9673	0.0333	-18.9	0.3
		MBL-17-03b.2r	1	3.8323	0.023	3.9642	0.0340	-19.6	0.3
		MBL-17-03b.3c	1	3.8345	0.019	3.9662	0.0314	-19.2	0.3
		MBL-17-03b.4r	1	3.8339	0.017	3.9661	0.0302	-19.2	0.3
		MBL-17-03b-2.1c	1	3.8326	0.018	3.9646	0.0308	-19.5	0.3
		MBL-17-03b-2.1c	1	3.8338	0.018	3.9653	0.0308	-19.4	0.3
		MBL-17-03b-2.1r	1	3.8291	0.019	3.9605	0.0314	-20.6	0.3
		MBL-17-03b-2.2c	1	3.8179	0.024	3.9490	0.0347	-23.4	0.3
		MBL-17-03b-2.2r	1	3.7882	0.028	3.9181	0.0375	-31.0	0.4
Innis Lake		GML-17-01.1	2	3.9929	0.042	4.1202	0.1085	18.9	1.1
		GML-17-01.2	2	3.9913	0.04	4.1185	0.1077	18.5	1.1
		GML-17-01.3	2	3.9925	0.04	4.1198	0.1077	18.8	1.1
		GML-17-01.5	2	3.9820	0.042	4.1089	0.1085	16.1	1.1
		GML-17-01.6	2	3.9970	0.04	4.1244	0.1077	20.0	1.1
		GML-17-01.7	2	3.9961	0.043	4.1235	0.1089	19.8	1.1
		GML-17-01.8	2	3.9834	0.043	4.1104	0.1089	16.5	1.1

† Indicates the 1σ observed uncertainty of the individual analysis based on the scatter of 40 isotope ratios recorded during the run as well as the calculated external error quadratically applied.

†† Corrected using insrumental mass fractionation formula

* Errors caluclated base off the method described in (†).The overall uncertainty for a given datum is estimated to be around ±1.2‰ (1 σ)

0.22 to 0.31 with a single analysis at 0.00. A generalized discriminatory diagram is presented in Figure 3. The $\delta^{11}B$ variation in of metamorphic tourmaline from Malborne Lake range from $\delta^{11}B$ = -18‰ to -31‰. The hydrothermal tourmaline crystals have similar compositions from -22.5‰ to -20.2‰.

Discussion

Magnesium-rich tourmaline compositions within the Sibley Basin are consistent with those documented within the Athabasca (Kotzer and Kyser, 1995; Mercadier et al., 2012; Adlakha and Hattori, 2016). The source Mg and B required to form the dravite, magnesio-foitite, and oxy-dravite of the Athabasca is debated. Kotzer and Kyser (1995) propose that Mg is derived from basement fluids and B is leached from clay and evaporite of the Athabasca Basin, whereas Mercadier et al. (2012) suggested that evaporated seawater supplied Mg and B for tourmaline based on high $\delta^{11}B$ values of magnesio-foitite.

The measured $\delta^{11}B$ for hydrothermal tourmaline crystals must be corrected for fractionation effects between the crystal and the fluid ($\Delta^{11}B_{tourmaline\text{-}fluid}$). There is no published isotopic fractionation factor at temperatures below 400°C, therefore the values determined by Meyer et al. (2008) for tourmaline and fluids between 750 and 400°C were extrapolated (cf. Mercadier et al., 2012; Adlakha et al., 2017) to the temperature of uranium mineralization (110°C; Scott, 1987, and references therein). A fractionation factor of -7.5‰ yields $\delta^{11}B$ values of the fluids ranging from -15 to -12.7‰ and 24 to 27.5‰ at Malborne Lake and Innis Lake, respectively.

The $\delta^{11}B$ of the fluids are very different between the two sampling sites (Fig. 4), suggesting that the tourmaline and uranium mineralizing at the two sites were formed from distinct and unrelated fluids. At the Malborne Lake showing, similarities between hydrothermal tourmaline and metamorphic tourmaline from the pegmatite suggest that the boron was sourced locally and subsequently remobilized to the nearby vein with little or no influence from an external fluid. The negative $\delta^{11}B$ values reported herein are consistent with global crustal reservoirs (Palmer and Swihart, 1996) and suggest minimal interaction with isotopically heavy reservoirs such as marine brines or marine carbonate or evaporite.

Conversely, the positive $\delta^{11}B$ values reported from the Innis Lake showing are consistent with carbonate rocks, marine salts, and non-marine brines. Evaporitic boron reservoirs within the Sibley Group are evinced by the presence of halite and gypsum casts as well as extensive carbonate sequences. The positive $\delta^{11}B$ values from the Innis Lake showing fall within the range of results of the two $\delta^{11}B$ studies conducted in the Athabasca Basin. Mercadier et al. (2012) emphasize the importance of basin-derived marine brines in the deposition of unconformity associated uranium deposits and Adlakha et al. (2017) suggest a basement-derived fluid that sources boron through the dissolution of carbonate or evaporitic rocks and later modified by the crystallization of minerals that preferentially incorporate ^{10}B (e.g. illite). Our data set cannot differentiate basement versus basinal brines, however it is clear that at the Innis Lake showing, the uranium-forming fluids were buffered by the basinal stratigraphy.

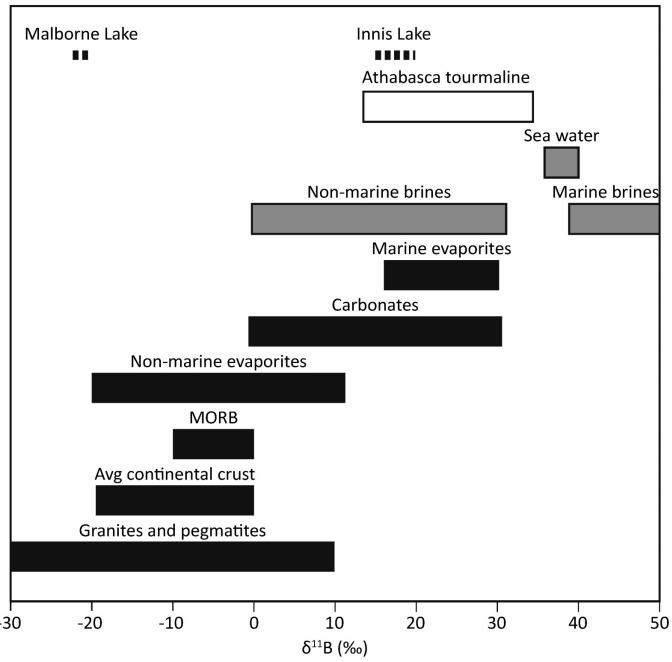

Figure 4. Range of B isotopic compositions from various geological/fluid reservoirs. Black dashed lines highlight analyzed tourmaline and vertical grey bars signify the composition of the fluids at equilibrium with the tourmaline (Marschall and Jiang, 2011; Mercadier et al., 2012; Tornos et al., 2012; Adlakha et al., 2017, and references therein).

The two generations of tourmaline within the vein at the Innis Lake showing are geochemically identical suggesting that the fluid from which they were crystallizing did not vary significantly over the lifetime of the vein. Boron isotopic variation between grains is limited and perhaps reflects fluctuations in crystallization temperature. Using the extrapolated data of Meyer et al. (2008), a 100°C change in temperature can result in a 2‰ change in the $\delta^{11}B$ of tourmaline. Or more likely, the boron isotopic composition of the fluid varied slightly over the lifespan of the vein.

Conclusions

The $\delta^{11}B$ values of magnesium-rich tourmaline from uranium occurrences in the Sibley Basin are distinctly different between the Innis Lake and Malborne Lake showings. The isotopically heavy tourmaline compositions from the Innis Lake showing are analogous with those of the Athabasca Basin. These results are consistent with the hypothesis of Franklin (1978) that the Innis Lake showing represents the roots of a now eroded, unconformity associated uranium deposit. Conversely, the Malborne Lake showing, which has isotopically light tourmaline, represents the remobilization of uranium and

boron from the nearby pegmatite.

Similarities between the Sibley and Athabasca basins have long been documented (*see* Scott, 1987), and this study illustrates that in addition to the timing and lithological similarities, the fluid responsible for transporting uranium in some instances is chemically similar. We provide evidence that there are at least two separate boron sources (magmatic versus basin-derived) within the Sibley Basin responsible for the development of uranium-bearing veins in the basement rocks. The Sibley Basin lacks the reactivated regional scale faulting present within the Athabasca basin, however; given the development and refinement of basement-hosted uranium deposits (e.g. Patterson Lake; Card and Noll, 2016) of the Athabasca Basin, there is sufficient evidence to re-evaluate uranium potential near the unconformity between the Sibley Group and underlying Archean rocks proximal to the north-trending deformation zones of the Archean basement.

Acknowledgments

This report is a contribution to NRCan's Targeted Geoscience Initiative Program (TGI). Support for this study was provided through the Uranium-rich Mineralization Project's '*Activity U-1.2: Role of marine brines in the formation of giant uranium deposits*'.

The authors would like to thank Brittany Ramsay, Jolee Stewart, and Matthew Greco for their insights into the regional geology and assisting in the collection of samples. Pat Hunt and Tom Pestaj are thanked for their assistance in sample preparation and imaging. This report benefited from the review of Ian Honsberger, Mike Gadd and Neil Rogers.

References

Addison, W.D., Brumpton, G.R., Vallini, D.A., McNaughton, N. J., Davis, D.W., Kissin, S.A., Fralick, P.W., and Hammond, A.L., 2005. Discovery of distal ejecta from the 1850 Ma Sudbury impact event; Geology, v. 33, p. 193–196.

Adlakha, E.E. and Hattori, K., 2016. Paragenesis and composition of tourmaline types along the P2 fault and McArthur River uranium deposit, Athabasca Basin, Canada; The Canadian Mineralogist, v. 54, p. 661–679.

Adlakha, E.E., Hattori, K., Davis, W.J., and Boucher, B., 2017. Characterizing fluids associated with the McArthur River U deposit, Canada, based on tourmaline trace element and stable (B, H) isotope compositions; Chemical Geology, v. 466, p. 417–435.

Bast, R., Scherer, E.E., Mezger, K., Austrheim, H., Ludwig, T., Marschall, H.R., Putnis, A., and Löwen, K., 2014. Boron isotopes in tourmaline as a tracer of metasomatic processes in the Bamble sector of Southern Norway; Contributions to Mineralogy and Petrology, v. 168, p. 1069.

Card, C.D. and Noll, J., 2016. Host-rock protoliths, pre-ore metasomatic mineral assemblages and textures, and exotic rocks in the western Athabasca Basin: ore-system controls and implications for the unconformity-related uranium model; Saskatchewan Ministry of the Economy, Miscellaneous Report, 4.

Cheadle B.A., 1986. Alluvial-playa sedimentation in the lower Keweenawan Sibley Group, Thunder Bay District, Ontario; Canadian Journal of Earth Sciences, v. 23, p. 527–541.

Craven, J.A., Shareef, S., Hart, T.R., Martí, A., and Farquharson, C., 2006. Preliminary results of the audiomagnetotelluric study of the Nipigon Embayment: Lake Nipigon Region Geoscience Initiative; Ontario Geological Survey, Miscellaneous Release Data 192.

Davis, D.W. and Sutcliffe, R.H., 1985. U-Pb ages from the Nipigon Plate and Northern Lake Superior; Geological Society of America Bulletin, v. 96, p. 1572–1579.

Dutrow, B.L., Foster, C.T., and Henry, D.J., 1999. Tourmaline-rich pseudomorphs in sillimanite zone metapelites: Demarcation of an infiltration front; American Mineralogist, v. 84, p. 794–805.

Dyar, M.D., Wiedenbeck, M., Robertson, D., Cross, L.R., Delaney, J.S., Ferguson, K., and Hughes, J.M., 2001. Reference minerals for the microanalysis of light elements; Geostandards and Geoanalytical Research, v. 25, p. 441–463.

Fralick, P.W., Davis, D.W., and Kissin, S.A., 2002. The age of the Gunflint Formation, Ontario, Canada: single zircon U-Pb age determinations from reworked volcanic ash; Canadian Journal of Earth Science, v. 39, p. 1085–1091.

Franklin, J.M., 1970. Metallogeny of the Proterozoic Rocks of Thunder Bay District, Ontario; Ph.D. thesis, University of Western Ontario, London, Ontario, 317 p.

Franklin, J.M., 1978. Uranium mineralization in the Nipigon Area, Thunder Bay District, Ontario; *in* Current Research Part A; Geological Survey of Canada, Paper 78-1A, p. 275–282.

Franklin, J.M., Mcllwaine, W.H., Shegelski, R.J., Mitchell, R.H., and Platt, R.G., 1982. Proterozoic Geology of the Northern Lake Superior Area; Geological Association of Canada - Mineralogical Association of Canada Joint Annual Meeting, Winnipeg, Field Trip Guidebook, Trip 4, 71 p.

Hart, T., Richardson, A., MacDonald, C.A., and Hollings, P., 2007. Geochemistry of the Mesoproterozoic intrusive rocks of the Nipigon Embayment, northwestern Ontario: evaluating the earliest phases of rift development; Canadian Journal of Earth Sciences, v. 44, p. 1087–1110.

Heaman, L.M., Easton, R.M., Hart, T.R., Hollings, P., MacDonald, C.A., and Smyk, M., 2007. Further refinement to the timing of Mesoproterozoic magmatism, Lake Nipigon region, Ontario; Canadian Journal of Earth Sciences, v. 44, p. 1055–1086.

Henry, D.J. and Dutrow, B.L., 1996. Metamorphic tourmaline and its petrologic applications; Reviews in Mineralogy and Geochemistry, v. 33, p. 503–557.

Henry, D.J. and Dutrow, B.L., 2011. The incorporation of fluorine in tourmaline: internal crystallographic controls or ex-

ternal environmental influences?; The Canadian Mineralogist, v. 49, p. 41–56.

Hollings, P., Fralick, P., and Kissin, S., 2004. Geochemistry and geodynamic implications of the Mesoproterozoic English Bay granite–rhyolite complex, northwestern Ontario; Canadian Journal of Earth Sciences, v. 41, p. 1329–1338.

Jefferson, C.W., Thomas, D.J., Gandhi,. S., Ramaekers, P., Delaney, G., Brisbin, D., Cutts, C., Portella, P., and Olson, R.A., 2007. Unconformity-associated uranium deposits of the Athabasca Basin, Saskatchewan and Alberta; *in* EXTECH IV: Geology and Uranium Exploration TECHnology of the Proterozoic Athabasca Basin, Saskatchewan and Alberta, (ed.) C.W. Jefferson and G. Delaney; Geological Survey of Canada, Bulletin 588, p. 23–67.

Kotzer, T.G. and Kyser, T.K., 1995. Petrogenesis of the Proterozoic Athabasca Basin, northern Saskatchewan, Canada, and its relation to diagenesis, hydrothermal uranium mineralization and paleohydrogeology; Chemical Geology, v. 120, p. 45–89.

Leeman, W.P. and Tonarini, S., 2001. Boron isotopic analysis of proposed borosilicate mineral reference samples; Geostandards and Geoanalytical Research, v. 25, p. 399–403

Marschall, H.R. and Jiang, S.Y., 2011. Tourmaline isotopes: no element left behind; Elements, v. 7, p. 313–319.

Marschall, H.R. and Monteleone, B.D., 2014. Boron isotope analysis of silicate glass with very low boron concentrations by secondary ion mass spectrometry; Geostandards and Geoanalytical Research, v. 39, p. 31–46.

Marschall, H.R., Meyer, C., Wunder, B., Ludwig, T., and Heinrich, W., 2009. Experimental boron isotope fractionation between tourmaline and fluid: confirmation from in situ analyses by secondary ion mass spectrometry and from Rayleigh fractionation modelling; Contributions to Mineralogy and Petrology, v. 158, p. 675–681.

Mercadier, J., Richard, A., and Cathelineau, M., 2012. Boron- and magnesium-rich marine brines at the origin of giant unconformity-related uranium deposits: $\delta^{11}B$ evidence from Mg-tourmalines; Geology, v. 40, p. 231–234.

Metsaranta, R.T. and Metsaranta, D.-A., 2008. Report on 2007 diamond drilling Black Sturgeon East Claim block, split rapids property; RPT Uranium Corp. (Rampart Ventures Ltd.), Black Sturgeon Uranium Project, Thunder Bay Mining Division, Northwest Ontario, 13 p.

Metsaranta, R.T., Fralick, P.W., and Bowdidge, C., 2007. Metamorphosed, halite-dominated evaporites of the Lower Sibley Group; *in* Proceedings and Abstracts; Institute on Lake Superior Geology, 53rd Annual Meeting, v. 53, p. 52–53.

Meyer, C., Wunder, B., Meixner, A., Romer, R.L., and Heinrich, W., 2008. Boron-isotope fractionation between tourmaline and fluid: an experimental re-investigation; Contributions to Mineralogy and Petrology, v. 156, p. 259–267.

Novák, M., Henry, D.J., Hawthorne, F.C., Ertl, A., Uher, P., Dutrow, B.L., and Pezzotta, F., 2009. Nomenclature of the tourmaline-group minerals; *in* Report of the Subcommittee on Tourmaline Nomenclature to the International Mineralogical Association's Commission on New Minerals, Nomenclature and Classification.

Organisation for Economic Co-Operation and Development, 2018. Uranium 2018: Resources, production and demand; Nuclear Energy Agency – International Atomic Energy Agency, NEA no. 7413, 462 p.

Palmer, M.R. and Slack, J.F., 1989. Boron isotopic composition of tourmaline from massive sulfide deposits and tourmalinites; Contributions to Mineralogy and Petrology, v. 103, p. 434–451.

Palmer, M.R. and Swihart, G.H., 1996. Boron isotope geochemistry; an overview; Reviews in Mineralogy and Geochemistry, v. 33, p. 709–744.

Rogala, B., Fralick, P.W., Heaman, L.M, and Metsaranta, R., 2007. Lithostratigraphy and chemostratigraphy of the Mesoproterozoic Sibley Group, northwestern Ontario, Canada; Canadian Journal of Earth Sciences, v. 44, p. 1131–1149.

Scott, J.F., 1987. Uranium occurrences of the Thunder Bay-Nipigon-Marathon area; Ontario Geological Survey, Open File Report 5634.

Selway, J.B. and Xiong, J., 2002. Tourmaline recalculation software; *in* Tourmaline in petalite-subtype granitic pegmatites: evidence of fractionation and contamination from the Pakeagama Lake and Separation Lake areas of northwestern Ontario, Canada, A.G. Tindle, F.W. Breaks and J.B. Selway; The Canadian Mineralogist, v. 40, p. 753–788.

Slack, J.F. and Trumbull, R.B., 2011. Tourmaline as a recorder of ore-forming processes; Elements, v. 7, p. 321–326.

Slack, J.F., Palmer, M.R., Stevens, B.P., and Barnes, R.G., 1993. Origin and significance of tourmaline-rich rocks in the Broken Hill district, Australia; Economic Geology, v. 88, p. 505–541.

Smyk, M.C. and Franklin, J.M., 2007. A synopsis of mineral deposits in the Archean and Proterozoic rocks of the Lake Nipigon Region, Thunder Bay District, Ontario; Canadian Journal of Earth Sciences, v. 44, p. 1041–1053.

Tindle, A.G., Breaks, F.W., and Selway, J.B., 2002. Tourmaline in petalite-subtype granitic pegmatites: evidence of fractionation and contamination from the Pakeagama Lake and Separation Lake areas of northwestern Ontario, Canada; The Canadian Mineralogist, v. 40, p. 753–788.

Tornos, F., Wiedenbeck, M., and Velasco, F., 2012. The boron isotope geochemistry of tourmaline-rich alteration in the IOCG systems of northern Chile: implications for a magmatic-hydrothermal origin; Mineralium Deposita, v. 47, p. 483–499.

van Hinsberg, V.J. and Marschall, H.R., 2007. Boron isotope and light element sector zoning in tourmaline: Implications for the formation of B-isotopic signatures; Chemical Geology, v. 238, p. 141–148.

van Hinsberg, V.J., Henry, D.J., and Marschall, H.R., 2011.

Tourmaline: an ideal indicator of its host environment; The Canadian Mineralogist, v. 49, p. 1–16.

van Hinsberg, V.J., Franz, G., and Wood, B.J., 2017. Determining subduction-zone fluid composition using a tourmaline mineral probe; Geochemical Perspectives Letters, v. 3, p. 160–168.

Vengosh, A., Starinsky, A., Kolodny, Y., Chivas, A.R., and Raab, M., 1992. Boron isotope variations during fractional evaporation of sea water: New constraints on the marine vs. nonmarine debate; Geology, v. 20, p. 799–802.

Xavier, R.P., Wiedenbeck, M., Trumbull, R.B., Dreher, A.M., Monteiro, L.V., Rhede, D., and Torresi, I., 2008. Tourmaline B-isotopes fingerprint marine evaporites as the source of high-salinity ore fluids in iron oxide copper-gold deposits, Carajas Mineral Province (Brazil); Geology, v. 36, p. 743–746.

Yule, G.R., 1979. Investigations of the Goodmorning Lake Radioactive Fault Breccia: Innes Lake Area, Dorion Township, Northwestern Ontario; B.Sc. thesis, Lakehead University, Thunder Bay, Ontario, 93 p.

Quantifying fertile alteration in the Patterson Lake corridor, Saskatchewan, through visible-near infrared-shortwave infrared spectroscopy

J.W. Powell[1], E.G. Potter[1], V. Tschirhart[1], J.B. Percival[1], S. Mount[2], B. McEwan[3], R. Ashley[4] and K. Wheatley[5]

[1]*Geological Survey of Canada, 601 Booth Street, Ottawa, Ontario K1A 0E8*
[2]*Department of Earth Sciences, Carleton University, 1125 Colonel By Drive, Ottawa, Ontario K1S 5B6*
[3]*NexGen Energy Ltd., 3150-1021 West Hastings Street, Vancouver, British Columbia V6E 0C3*
[4]*Fission Uranium Corp., 700-1620 Dickson Avenue, Kelowna, British Columbia V1Y 9Y2*
[5]*Forum Energy Metals Corp., 615-800 West Pender Street, Vancouver, British Columbia V6C 2V6*

Abstract

Visible-near infrared - shortwave infrared (VNIR-SWIR) spectroscopy, gamma-ray logs, and magnetic susceptibility measurements were taken on drill core samples that span the Patterson Lake exploration corridor (PLC) on the southwestern margin of the Athabasca Basin. Clay mineralogy and mineral properties (composition, crystallinity) derived from reflectance spectra were compared with gamma-ray and magnetic susceptibility profiles to assess relationships between uranium mineralization and alteration in the crystalline basement. In all drill core, the clay mineralogy is similar to the clay alteration in deposits of the eastern portion of basin, although in the PLC, dickite is uncommon and kaolinite horizons are associated with high-grade mineralization. Several drill core exhibit trends between spectral parameters related to the crystallinity and thermal maturity of clays (illite and kaolinite) and uranium mineralization. A non-mineralized drill core with moderate clay alteration was expectantly nonmagnetic. In comparison, the magnetic susceptibility within a mineralized hole that included multiple lithologies correlated with observed parameters computed from reflectance spectra. These results highlight the efficacy of VNIR-SWIR reflectance spectroscopy in characterizing clay alteration associated with uranium mineralization. As shown throughout the Athabasca Basin, mineralogy and spectral parameters may vector towards fertile fluid conduits when expanded to property- or corridor-scales.

Introduction

The Athabasca Basin remains the primary exploration target for uranium deposits in Canada. Within this Proterozoic basin and surrounding basement rocks, known uranium deposits are spatially associated with structural trends and/or intersections of crustal-scale faults that were likely the main fluid conduits during formation of unconformity-related uranium deposits (Jefferson et al., 2007, and references therein). Many of these structures show evidence of multiple deformation phases (e.g. brittle fabrics overprinting ductile fabrics) and alteration (new mineral growth: clay minerals, tourmaline, aluminium-phosphate-sulphate minerals, hematite, etc.), which is reflected in their petrophysical characteristics, and geophysical and isotopic signatures. This study investigates the role that reactivated faults played in the formation of unconformity-related uranium deposits and aims to quantify fertile alteration along such fluid pathways — specifically the Patterson Lake corridor (PLC) of northwestern Saskatchewan (Fig. 1). Whereas exploration has previously focused on relatively shallow targets near the unconformity in the eastern Athabasca Basin, recent discoveries of high-grade and large resources in the PLC on the southwest margin of the basin are challenging the existing exploration models. In the PLC, structurally controlled uranium deposits (e.g. Triple R and Arrow) and occurrences (e.g. Spitfire, Harpoon) are situated along a greater than 50 km long corridor, hosted in altered and metamorphosed mafic to ultramafic intrusive rocks and orthogneisses of the Taltson Domain, up to 900 m below the unconformity surface (Card and Noll, 2016; Card, 2017). In the summer of 2018, visible-near infrared-shortwave infrared (VNIR-SWIR) spectra were systematically collected on samples from ten drill core to determine mineralogy of alteration assemblages and track variations in reference spectra parameters (absorption features, clay crystallinity indices). Integration of these data with magnetic susceptibility measurements and gamma radiation profiles constrains expressions of fertile and barren alteration across the PLC to vector towards uranium mineralization.

Geology of the Patterson Lake corridor

The PLC basement comprises crystalline rocks of the southwest Rae Province of the Canadian Shield. The Athabasca Basin overlies this crystalline basement in the northeastern part of the PLC (Fig. 1). The basin consists of unmetamorphosed rocks of the Athabasca Supergroup (Bosman and Ramaekers,

Corresponding author: Jeremy Powell (jeremy.powell@canada.ca)

Powell, J.W., Potter, E.G., Tschirhart, V., Percival, J.B., Mount, S., McEwan, B., Ashley, R., and Wheatley, K., 2019. Quantifying fertile alteration in the Patterson Lake corridor, Saskatchewan, through visible-near infrared-shortwave infrared spectroscopy; *in* Targeted Geoscience Initiative: 2018 report of activities, (ed.) N. Rogers; Geological Survey of Canada, Open File 8549, p. 365–379. https://doi.org/10.4095/313671

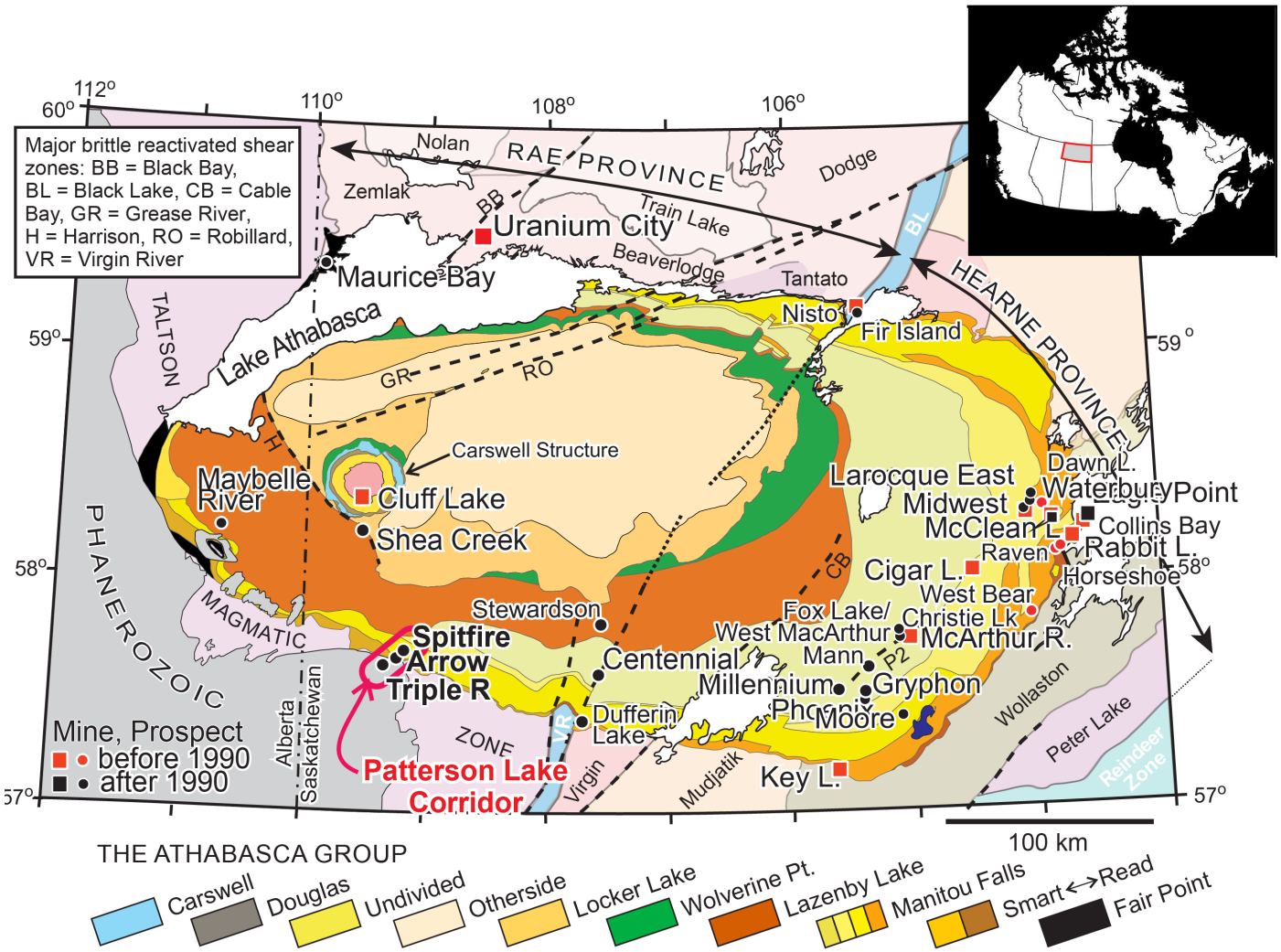

Figure 1. Location of the Patterson Lake corridor and associated uranium deposits and discoveries along the southwestern margin of the Proterozoic Athabasca Basin. *Modified from* Jefferson et al. (2007).

2015), and is primarily composed of continental clastic sequences that were deposited between 1.76 and 1.50 Ga (Ramaekers et al., 2007). Locally, mixed siliciclastic and carbonate strata of the Lower to Middle Devonian Elk Point Group and/or sandstone, mudstone, and coal of the Lower Cretaceous Manville overlie the Athabasca Supergroup. Additionally, a veneer of Quaternary sediments covers the entire study area. Although the high degree of hydrothermal-metasomatic alteration in the PLC is such that protoliths of the orthogneiss host rocks are difficult to determine, few fresh examples suggest a regionally extensive gneissic quartz diorite to diorite unit that is crosscut by a suite of metamorphosed mafic to ultramafic intrusive rocks (Card, 2017). These altered crystalline rocks are consistent in composition, and presumably age, with those known elsewhere in the southwestern Rae Province (e.g. ca. 2.53–1.97 Ga; Stern et al., 2003; Card et al., 2014; Powell et al., 2018).

Rocks of the southwest Rae Province have been strongly overprinted by kilometres-wide, steeply dipping corridors of heterogeneous ductile high-strain. Samples from uranium exploration drill core show that these high-strain corridors were flooded by blue quartz resulting in well-developed silicification fronts and strongly metasomatized rocks in which aluminium-bearing minerals were concentrated. These silicification textures were subsequently sheared suggesting that the quartz flooding occurred below the brittle – ductile transition (Card, 2017). The patches of chlorite- and white mica-altered, metamorphosed mafic to ultramafic rocks preserved within a matrix of blue quartz indicate that the crystalline basement was subjected to retrograde metamorphism prior to the flooding of blue quartz (Card and Noll, 2016). Graphite and sulphide minerals that postdate quartz flooding are common across the PLC and are structurally hosted in faults that formed above the brittle – ductile transition (Pană et al., 2007; Card, 2017). Both mineral species are of hydrothermal origin and predate uranium mineralization (Card, 2017). Hydrothermal-metasomatic mineral assemblages preserved in the high-strain corridors demonstrate long-term reuse of these major structural discontinuities and are speculated to have precipitated after regional metamorphic events ceased at ca. 1.90 Ga, but before uranium mineralization

began in the basin at ca. 1.6 Ga (Jefferson et al., 2007; Alexandre et al., 2009).

Although many studies detail the paragenesis of basement alteration in the eastern Athabasca Basin (e.g. Kotzer and Kyser, 1995; Kyser et al., 2000; Alexandre et al., 2005; Jefferson et al., 2007; Adlakha et al., 2013; Mathieu et al., 2017) very few studies have probed deposits in the PLC (Cerin et al., 2017). Observations from two field seasons suggest similarities between alteration PLC crystalline basement rocks with those in the eastern Athabasca Basin. For example, alteration of orthogneiss below the unconformity in the Arrow deposit (Fig. 2) exhibits similar patterns in zonation as paleoweathering-hydrothermal alteration in the eastern Athabasca Basin (e.g. Fraser et al., 1970; MacDonald, 1985). Specifically, the orthogneiss transitions from a clay-bleached zone directly below the unconformity between Athabasca Basin and basement rocks, through a hematitic zone (Fig. 2A) into a red-green zone in which the foliated orthogneiss is altered by chlorite, illite, and hematite (Fig. 2B). Within mineralized shear zones, high-grade uranium mineralization is often associated with reduction-oxidation (redox) fronts (Fig. 2C), intense clay alteration (Fig. 2D), and tourmaline breccias (Fig. 2E). Uranium mineralization at the Arrow deposit is structurally controlled and typified by uraninite with lesser coffinite and uranophane (Cerin et al., 2017). More research is required to understand the patterns in paragenesis and mineralization across the PLC, and their implications for regional ore-forming processes.

Methods

During the 2018 field season, spectral reflectance profiles were collected from ten drill core that intersect the two uranium deposits (Triple R, Arrow), the Harpoon discovery, and Forum Energy Metal Corp.'s Clearwater project. Reflectance spectroscopy is a useful, cost-effective tool in mineral exploration as measurements conducted on rock chips or core rapidly identify alteration mineralogy. Individual spectra were collected using the TerraSpec® Halo (Malvern Panalytical, Longmount Colorado, USA, formerly Analytical Spectral Device Inc., referred to here after as the Halo) portable mineral identifier, which is a handheld reflectance spectrometer that acquires reflectance spectra in the visible to near-infrared (VNIR: 350–1300 nm) and shortwave infrared (SWIR: 1300–2500) ranges (Percival et al., 2002; Mwenifumbo et al., 2007). Spectral absorption bands measure the radiation absorbed by vibrational processes between molecular bonds (Mathieu et al., 2017), and are diagnostic for many mineral groups, including clays, carbonates, sulphates, and ammonium-bearing minerals (Table 1). The Halo uses an internal wavelength reference to calibrate the positions of absorption features. Following acquisition, absorption features were accentuated relative to the background continuum via hull quotient normalization, which is computed via the ratio between the reflectance spectrum and a fitted convex hull (Clark and Roush, 1984). Since acquired spectra are generally a multi-mineral composite, the Halo identifies individual minerals through a pattern recognition process that compares

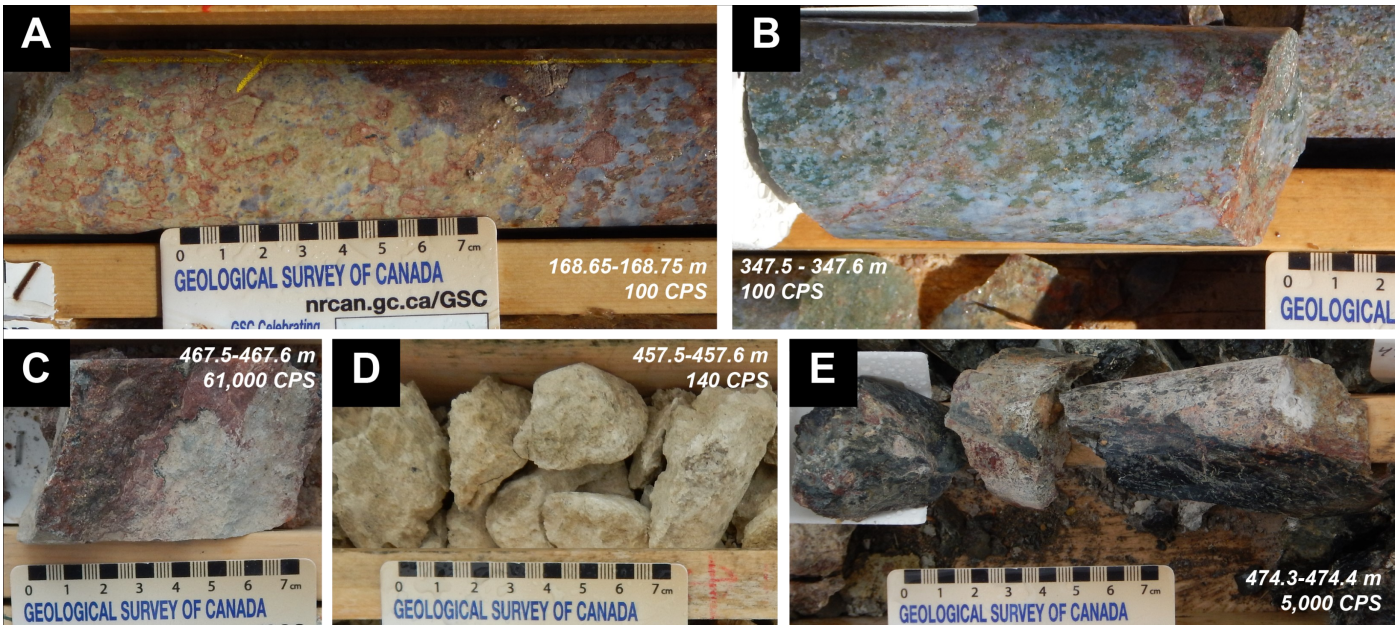

Figure 2. Examples of characteristic alteration assemblages from a drill core intersecting the Arrow deposit. a–b) Altered host rock outside of main shear zone: a) hematite and clay alteration in a silicified orthogneiss; b) chlorite, yellow-green clay and hematite alteration along foliation in the silicified orthogneiss. c–e) Alteration within the main shear zone: c) uranium redox front along sharp contact between hematite and clay in the vicinity of a horizon with massive uranium mineralization; d) non-mineralized clay alteration directly below and above two high-grade mineralized horizons; e) graphitic shear zone brecciated by chalky tourmaline.

Table 1. Wavelength bands of absorption features in the SWIR region and their correlative mineral groups (*after* Percival et al., 2018).

Position (nm)	Molecule	Mineral Group
1400 - 1500	OH and Water	Clays, sulfates, hydroxides, zeolites, prehnite
1560	NH_4	NH_4 species, epidote
1760 - 1800	OH	Sulphates
1900	Water	Clays, sulphates, hydroxides, zeolites, prehnite
2020, 2120	NH_4	NH_4 species
2160 - 2220	Al - OH	Minerals containing Al - OH bonds such as clays, sulphates, micas, etc
2230 - 2295	Fe - OH	Minerals containing Fe - OH bonds such as clays, amphiboles, sulphates, micas, etc
2300 - 2360	Mg - OH	Minerals containing Mg-OH bonds such as clays, amphiboles, chlorites, etc
2300 - 2350	CO_3^{2-}	Carbonates
2370 - 2400	Mg - OH	Amphiboles, talc, etc.

absorption features in the unknown spectra with an internal database of well characterized mineral samples. The Halo onboard library contains greater than 500 spectra of more than 150 reference minerals (Percival et al., 2018). Customized libraries are available through Malvern Panalytical. However, these can be supplemented by publically available spectral databases (U.S.G.S. Spectral Library: Kokaly et al., 2017; the NASA-Jet Propulsion Lab Spectral Library: Clark et al., 1990; the Kodama Clay Collection: Percival et al., 2016; and the GSC National Mineral Collection library; Percival et al., 2018).

In addition to mineral identification, the wavelength of specific absorption features (e.g. Al-OH, Mg-OH, Fe-OH) are indicative of the geochemical conditions of alteration. Specifically, the wavelength of the Al-OH feature provides insight into the geochemistry of phyllosilicate minerals. Chemical substitutions (Mg-Fe) in white micas result in a shift in the wavelength position of the Al-OH absorption feature, tracking the solid solution series between paragonite (Al-OH < 2195 nm), muscovite (2195 nm < Al-OH < 2216 nm) and phengite (2216 nm > Al-OH) (Herrmann et al., 2001). However, only Al-OH values from spectra containing white mica (±chlorite) can be related to phyllosilicate composition, as other minerals with prominent approximately 2200 nm absorption features (e.g. kaolinite, smectite) shift the wavelength of this scalar. Although clay crystallinity studies are generally conducted via X-ray diffraction (XRD; Wilson et al., 2009), semiquantitative scalar parameters correlating with kaolinite (Kx) and white mica (illite spectral maturity = ISM) crystallinity are computed from VNIR-SWIR data using ratios of reflectance values from hull quotient normalized spectra. The Kx scalar measures the ratio of the 2160 and 2177 nm absorption features, as increasing kaolinite crystallinity enhances the slope between the two wavelengths. Since kaolinite crystallinity is directly related to temperature of formation, Kx values greater than 1 tend to represent kaolinite that formed due to weathering, whereas Kx values less than 1 are indicative of highly crystalline kaolinite that formed under higher temperature conditions (Oluwadebi, 2015). Conversely, the ISM measures illite crystallinity by proxy of molecular H_2O in the crystal lattice, with crystallinity corresponding to a decrease in bound H_2O. The ISM values are calculated by dividing the relative depth of the Al-OH absorption feature (2200 nm) by the H_2O absorption feature (1900 nm) on a hull quotient-normalized spectra (Wilson et al., 2009). The ISM values are only calculated from spectra containing white mica + smectite, as other minerals with absorption features at approximately 1900 and 2200 nm (e.g. carbonate, gypsum, chlorite) will distort the scalar. Illite spectral maturity values greater than 1 indicate low-grade metamorphic illite whereas values less than 1 represent higher temperature alteration, with alteration temperatures increasing with decreasing ISM.

Our sampling strategy involved analyzing spectra at 2 to 5 m intervals throughout extensive sections of clay-altered orthogneiss, and in 0.5 to 1 m intervals within mineralized shear zones. To characterize the magnetic signature of the crystalline basement with regards to alteration assemblage, magnetic susceptibility was measured using a KT-10 susceptibility meter at 0.5 to 1 m increments on a mineralized drill core from the Arrow deposit and a non-mineralized drill core from the Clearwater project to the southwest. Drill core gamma-ray profiles were interpolated from company measurements.

In an effort to confirm the Halo results, the mineralogy of a sample from DDH-F (243.2–243.4 m) was determined using X-ray powder diffraction analysis (XRD). A less than 63 μm fraction was pulverized by hand in an agate mortar and pestle with distilled water. An aliquot was pipetted onto a zero-background slide and allowed to air-dry. X-ray patterns were recorded on a Bruker D8 Advance Powder Diffractometer equipped with a Lynx-Eye Detector, Co Kα radiation set at 35 kV and 35 mA. The smear mount was X-rayed, air-dried and then re-X-rayed following saturation with ethylene glycol.

Results

We collected 1565 spectra from samples from 10 drill core that span the PLC (Fig. 3). Mineralogy and spectra were exported using the program Halo Manager (Malvern Panalytical) and individual alteration minerals were sorted into 16 subgroups muscovite, biotite, other micas, illite, smectite, kaolinite, dickite, Mg-clays, chlorite, carbonate, tourmaline, epidote, amphibole, Fe-oxides, sulphate and others (Table 2). Mineralogy from spectra were binned at 10 m intervals for each drill core and are presented alongside their corresponding gamma-ray profiles (counts per second = CPS).

Note that the smectite-group minerals identified by the Halo (Table 2) are likely a mixed-layer (ML) clay mineral containing illite and chlorite (probably sudoite) based on preliminary X-ray diffraction analyses (Fig. 4). The 21.5 Å X-ray peak in the air-dried sample does not change with glycol saturation. If smectite was present, this X-ray peak would increase to greater than 24-25 Å. In addition, the mineral cookeite (Table 2) is the only di-trioctahedral chlorite in the onboard library. However, this is uncommon and has the same characteristics

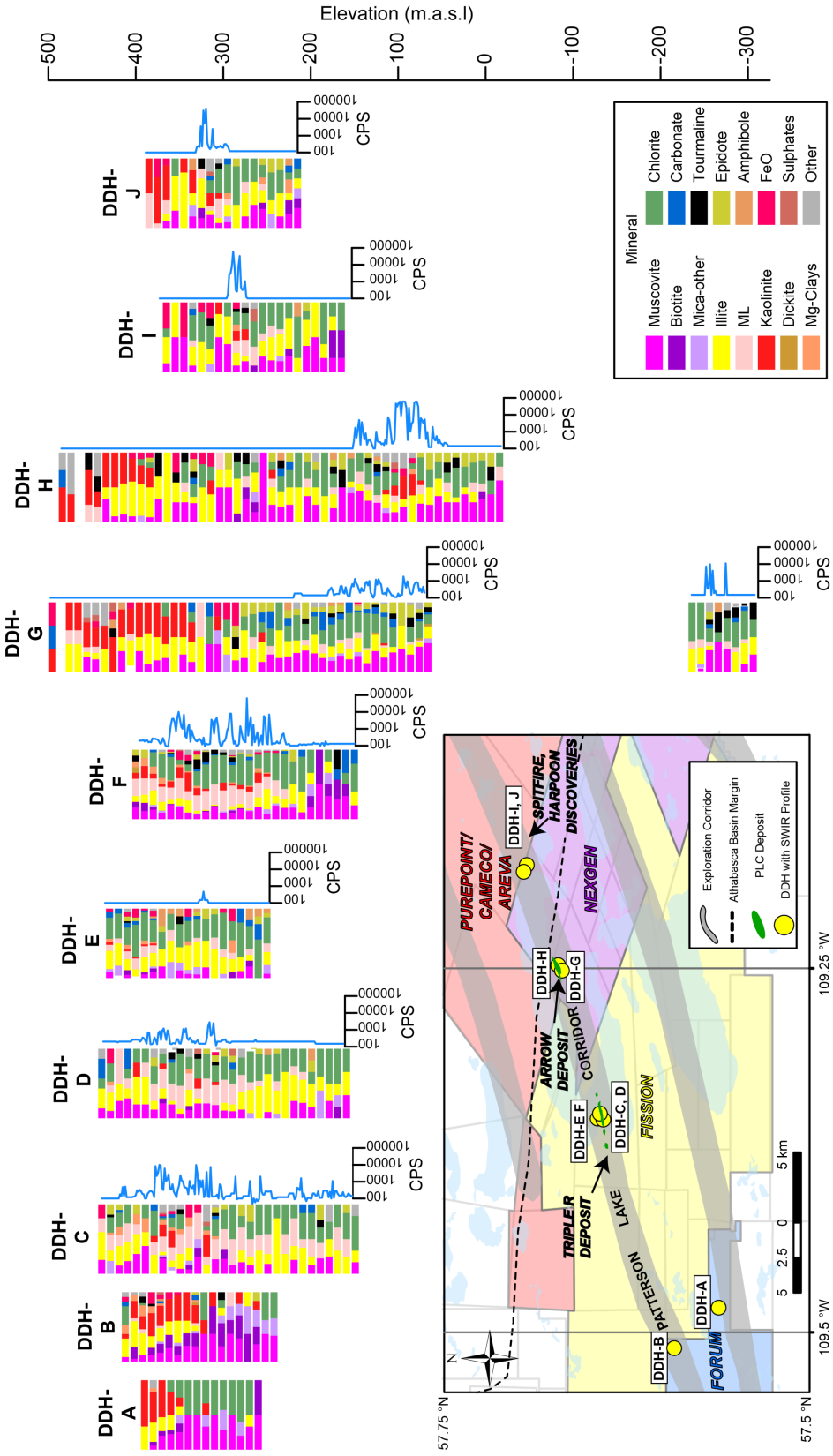

Figure 3. Comparison of clay distribution for ten diamond-drill holes (DDH) that span the Patterson Lake corridor. Modal mineralogy presented alongside profiles of gamma-ray emission (counts per second = CPS) and are plotted as a function of elevation. Mineralogy was identified by the Halo from individual VNIR-SWIR spectra and are binned for 10 m intervals. Gamma-ray profiles for DDH-A and DDH-B were less than 100 CPS. Dip and azimuth were not available for all drillholes, so plotted elevation is a function of total depth and surface elevation. Inset map shows drillhole locations, regional mineral disposition, exploration corridors and uranium deposits. Note: gap in the spectral log for DDH-G corresponds to a non-cored interval between upper and lower shear zone intersections. XRD studies to confirm VNIR-SWIR mineralogy are ongoing.

Table 2. Subgroup classification for mineral species identified by the Halo from VNIR-SWIR spectra.

Mineral Subgroups	Mineral species identified by the Halo
Muscovite	Muscovite, phengite
Biotite	Biotite, phlogopite
Other Micas	Lepidolite, margarite, paragonite
Illite	K-illite, Mg-illite, Na-illite
Smectite[1]	Allevardite, beidellite, montmorillonite, illite-smectite, rectorite, iron smectite
Kaolinite	Kaolinite, kaolinitePX, kaoliniteWX
Dickite	Dickite
Mg-Clays	Antigorite, palygorskite, sepiolite, stipnomelane, vermiculite
Chlorite	Cookeite[2], corrensite, Fe-chlorite, FeMg-chlorite, penninite, Mg-chlorite
Carbonate	Ankerite, calcite, dolomite, rhodochrosite, siderite, smithsonite, strontianite
Tourmaline	Tourmaline
Epidote	Epidote, clinozoisite
Amphibole	Cummingtonite, glaucophane, hornblende, kearstutite, nephrite, riebeckite, tremolite
FeO	Goethite, hematite
Sulphates	Alunite, brochantite, jarosite,
Other	Axinite, chabzite, chondrodite, dioptase, gmelinite-Na, montebrasite, natrolite

[1]XRD analyses indicate that smectite-group minerals identified by the Halo are likely a mixed-layer (ML) illite-chlorite clay mineral

[2]Cookeite is the only di-trioctahedral chlorite in the Halo reference library and is more likely sudoite

(in XRD) as sudoite, more commonly found in the Athabasca Basin (Percival and Kodama, 1989; Percival et al., 1993). More detailed XRD analyses are in progress.

Two drill core were logged from Forum Energy Metals Corp.'s Clearwater project to the southwest, including one drill core within the PLC (DDH-B) and another in a parallel exploration corridor to the south (DDH-A). Both of these holes are non-mineralized and have a prominent kaolinite-illite alteration assemblage that extends for tens of metres below the unconformity surface. In DDH-A, this upper zone becomes increasingly chloritic with depth, whereas DDH-B transitions into relatively unaltered, muscovite-biotite-rich host rock.

The four drill core from Fission Uranium Corp.'s Triple R deposit (DDH-C through H) are variably mineralized and have an upper bleached zone defined by low CPS and a higher proportion of white mica (muscovite+illite). In the three mineralized drill core from the Triple R deposit, the proportion of illite relative to ML decreases within the mineralized shear zones. Comparatively, the non-mineralized drill core (DDH-E) displays the opposite trend, with relatively little ML, and an increasing proportion of illite in proximity to a narrow horizon with higher CPS. Mineralization in NexGen Energy Ltd.'s Arrow deposit (DDH-G, -H) is substantially deeper than observed in the Triple R deposit. The upper, bleached, kaolinite+illite+muscovite horizon in these two holes extends for tens of metres below the unconformity with the Athabasca Group. Similar to the Triple R deposit, the highest grade mineralization in the two drill core that intersect the Arrow deposit correlate with a decrease in white mica content. However, no trends are overserved between the proportion of ML and degree of mineralization (CPS) in either of the Arrow drill core.

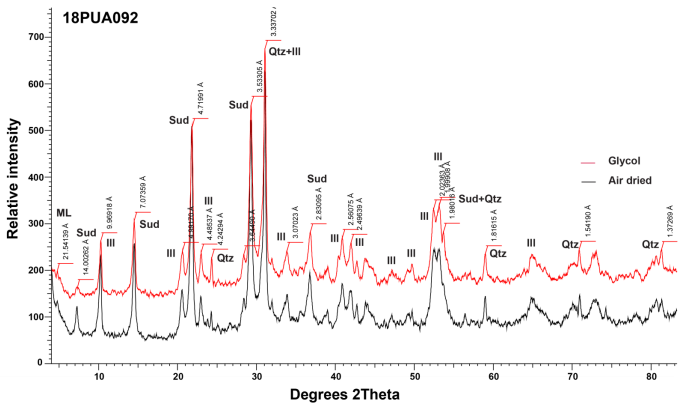

Figure 4. Stacked X-ray diffractograms of the air-dried and glycol saturated smear of sample 17PUA-092. Processing of diffractograms made using EVA (Bruker AXS, Inc.) software. Major X-ray peaks are identified (from left to right: ML: mixed-layer clay mineral; Sud: sudoite; Ill: illite; Qtz: quartz).

Two drill cores were logged from NexGen Energy Ltd.'s Harpoon discovery to the northeast (DDH-I, J). Mineralized shear zones in both drill core are narrow relative to those observed at the Triple R and Arrow deposits, and correspond with a decrease in white mica content and an increase in the proportion of ML relative to the surrounding basement. Kaolinite is closely associated with mineralization in all drill core investigated in this study. In the following section, we investigate spectral data from five of these drill core in detail to determine whether spectral parameters (Al-OH, Kx, ISM, Fe-OH, etc.) correlate with patterns in mineralization and rock properties (magnetic susceptibility).

DDH-A

Drill core from DDH-A (Fig. 5) transitions from a bleached and friable orthogneiss at the top of the drill core into a silicified orthogneiss with abundant hydrothermal graphite and sulphide minerals. Alteration in the bleached zone is characterized by kaolinite that decreases in crystallinity from the top of the horizon (Kx ≈ 0.98) to the bottom (Kx ≈ 1.05). The Al-OH values of white mica indicate that mica in the bleached zone is more phengitic in composition (Al-OH ≈ 2206 nm) relative to the paragonitic mica in the underlying orthogneiss (Al-OH ≈ 2196 nm). Illite spectral maturity values for all white mica spectra are greater than 1, which is indicative of low-grade, metamorphic micas. The magnetic susceptibility profile for DDH-A is subdued, with minimal variations over the length of the drill core.

DDH-C

DDH-C (Fig. 6) intersects the main Triple R shear zone between 120 and 340 m, with the highest grade mineralization between 120 and 185 m. Mineralization is associated with intense clay and hematite alteration, and is typified by bands of

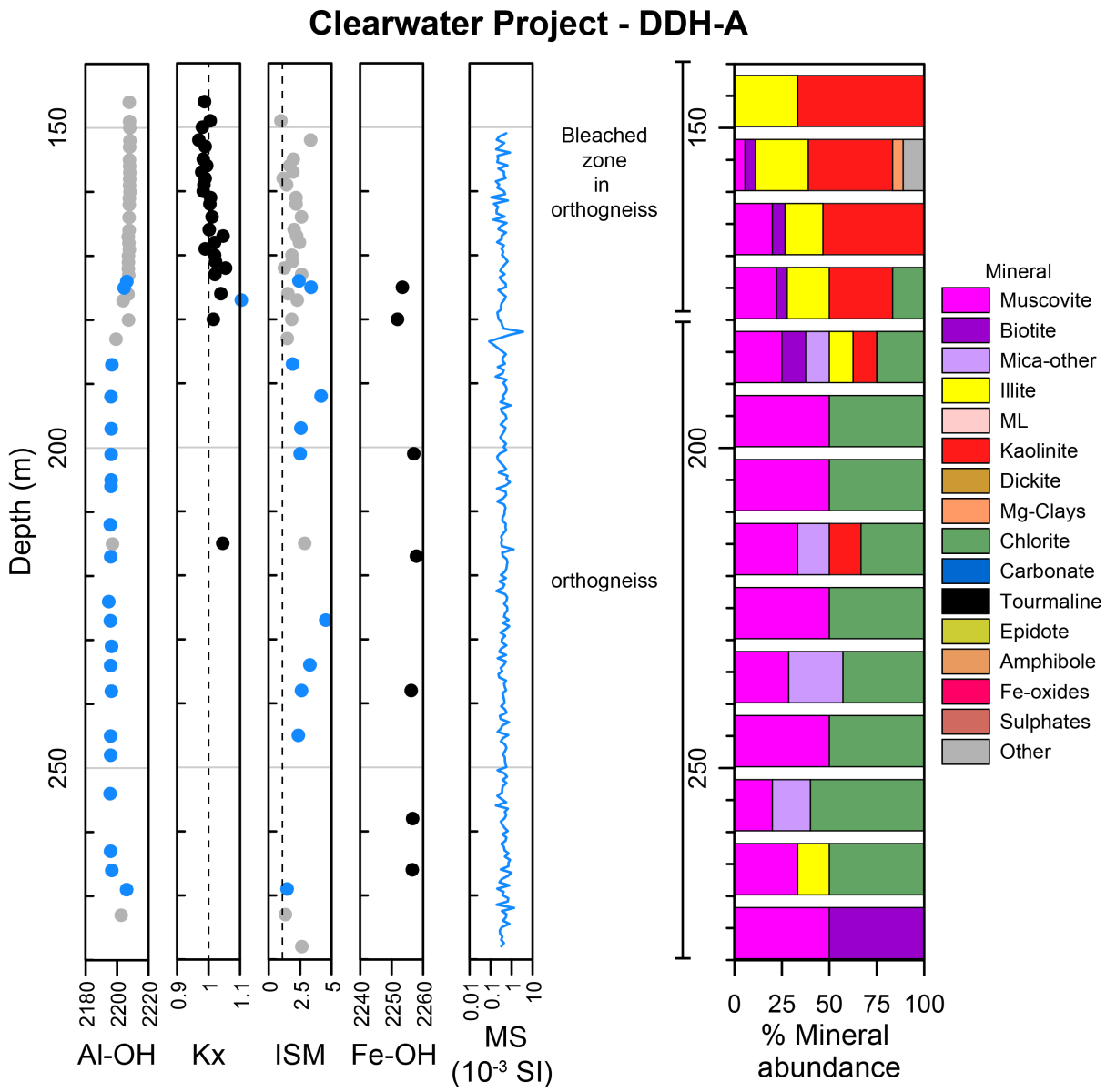

Figure 5. Multi-parameter logs for DDH-A from Forum Energy Metals Corp.'s Clearwater project. Spectral data are plotted along with important scalars (Al-OH = wavelength of AL-OH absorption feature; Kx = kaolinite crystallinity index; ISM = illite spectral maturity; Fe-OH = wavelength of Fe-OH absorption feature) and as strip log of % mineral abundance (binned over 10 m intervals). For AL-OH and ISM plots, grey data points represent scalars from mixed spectra, whereas blue data points indicate scalars representative of white mica (Al-OH) and white mica + ML (ISM). Abbreviation: MS = magnetic susceptibility. Gamma-ray profile not shown due to low CPS. Dashed line in Kx and ISM logs indicates a value of 1.

disseminated, nodular uraninite. The Al-OH scalar indicates that the white micas are muscovite in composition above the ore zone (Al-OH ≈ 2200 nm) but become increasingly phengitic (<2207 nm) with proximity to the highest grade interval (120–130 m; 10 000 CPS). Kaolinite is present as an alteration mineral associated with the highest grade mineralization. The Kx values in the 117 to 134 m interval indicate that kaolinite associated with high-grade mineralization has a lower crystallinity (larger Kx) than kaolinite from weakly mineralized horizons (Kx = 1.07 at 10 000 CPS; Kx = 1.00 at 270 CPS). The ISM values are negatively correlated with CPS throughout the ore zone, from a high of 1.32 (146 m, 120 CPS) to 0.5–0.8 (122–127 m; 2200–10 000 CPS), suggesting that the highest grade ore zones were also subject to the highest temperatures during clay alteration. The ISM scalars in the shallow, altered orthogneiss have a bimodal distribution, with lower values (0.4–0.9) signifying hydrothermal alteration of white mica, and larger values (1.3–4.8) indicating preservation of the original, low-grade metamorphic crystallinity. Unlike drill core from DDH-A, the magnetic susceptibility profile for DDH-C is highly var-

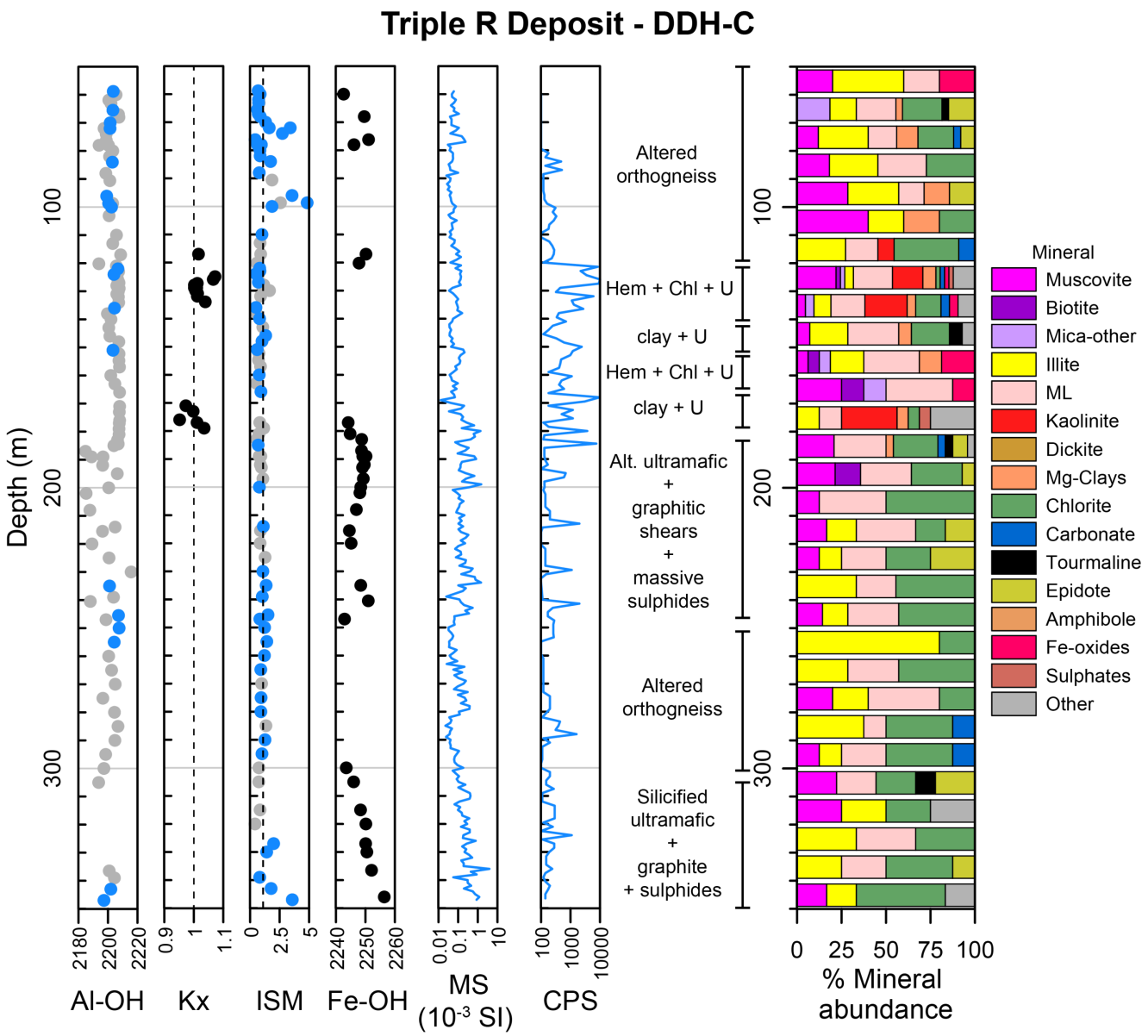

Figure 6. Multi-parameter logs for DDH-C from Fission Uranium Corp.'s Triple R deposit. Spectral data are plotted as important scalars (Al-OH = wavelength of AL-OH absorption feature; Kx = kaolinite crystallinity index; ISM = illite spectral maturity; Fe-OH = wavelength of Fe-OH absorption feature) and as strip log of % mineral abundance (binned over 10 m intervals). For AL-OH and ISM plots, grey data points represent scalars from mixed-spectra, whereas blue data points indicate scalars representative of white mica (Al-OH) and white mica + ML (ISM). MS = magnetic susceptibility. CPS = Gamma-ray counts per second. Dashed line in Kx and ISM logs indicates a value of 1.

iable and correlative to observed alteration. Magnetic susceptibility values throughout the main ore zone are generally low (<0.1 x 10^{-3} SI), but increase slightly in hematite-rich mineralized horizons relative to the interspersed, non- to weakly mineralized clays, as hematite is more magnetic than most clays. The largest values in the magnetic susceptibility profile are within chlorite-altered ultramafic intervals with abundant graphite and sulphide minerals. Whereas the magnetic signature is likely related to trace amounts of pyrrhotite and/or magnetite, these same intervals are delineated in the spectral data by an increase in the Fe-OH scalar that is representative of alteration assemblages increasingly dominated by Fe-and-Fe-Mg chlorite.

DDH-F

In DDH-F, the main Triple R shear zone begins directly below the glacial overburden (approximately 110 m) and extends to a depth of 250 m (Fig. 7). The style of mineralization changes from remobilized redox fronts at the top of the shear zone to fracture and fault related lower in the section, with a single interval of massive uraninite at approximately 227 m. Similar to DDH-C, kaolinite in DDH-F is associated with ore

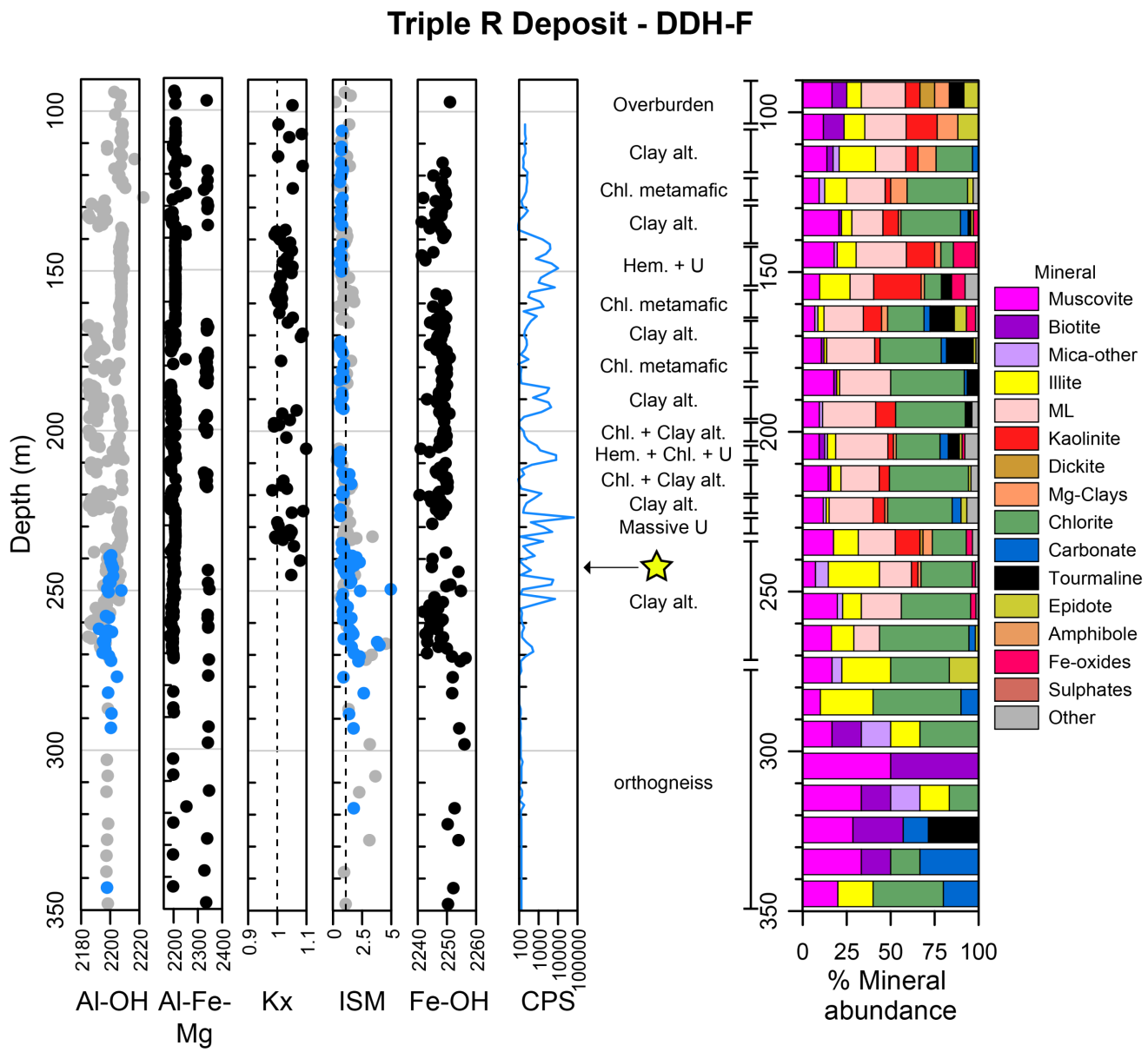

Figure 7. Multi-parameter logs for DDH-F from Fission Uranium Corp.'s Triple R deposit. Spectral data are plotted as important scalars (Al-OH = wavelength of AL-OH absorption feature; Al-Fe-Mg = deepest wavelength of the Al-OH, Fe-OH and MgOH absorption features; Kx = kaolinite crystallinity index; ISM = illite spectral maturity; Fe-OH = wavelength of Fe-OH absorption feature) and as strip log of % mineral abundance (binned over 10 m intervals). For AL-OH and ISM plots, grey data points represent scalars from mixed-spectra, whereas blue data points indicate scalars representative of white mica (Al-OH) and white mica + ML (ISM). CPS = Gamma-ray counts per second. Dashed line in Kx and ISM logs indicates a value of 1. Yellow star = location of XRD sample (Fig. 4).

zones and becomes increasingly crystalline (decrease in Kx) outwards from the highest grade horizons. The Al-Fe-Mg scalar indicates which of the Al-OH (2160–2200 nm), Fe-OH (2230–2295 nm), and Mg-OH (2300–2360 nm) absorption features corresponds with the deepest wavelength in the reflectance spectra. When plotted in profile, Al-Fe-Mg values are a useful visual tool to distinguish horizons in which chlorite is the dominant alteration mineral (Al-Fe-Mg ≈ 2340 nm) compared with background mixed-layer clay alteration assemblage (Al-Fe-Mg ≈ 2200 nm). In all cases, these narrow chloritic intervals correspond with non-mineralized horizons within the shear zone. Few of the mixed spectra from DDH-F contained only white mica and chlorite, and as a result, Al-OH scalars that correspond with white mica composition are only reported from spectra deeper than 240 m. These values suggest a standard muscovite composition with an interval of paragonitic mica between 260 and 270 m. The ISM values within the main shear zone decrease from greater than 1 to approximately 0.4 with increasing CPS, indicative of higher alteration temperatures in proximity to high-grade mineralization.

DDH-H

Over 35 m of Cretaceous Manville Group and approximately 10 m of the Proterozoic Athabasca Group sandstone overlie PLC basement in DDH-H (Fig. 8). The unconformity between PLC basement and the overlying sandstones is evident in the spectral data as a sharp increase in Kx values. The orthogneiss below the unconformity transitions from a kaolinite+illite bleached zone, through stacked hematite and chlorite-altered zones prior to intersecting the mineralized shear zone at 400 m. These alteration assemblages are evident in the spectral scalars, including the Kx (extent of kaolinite bleached zone), and Fe-OH (Fe-OH less than 2245 nm = hematite zone, Fe-OH greater than 2245 = chlorite zone) parameters. Similar to observations from the two drill core intersecting the Triple R deposit (Fig. 6, 7), the presence of kaolinite is associated with high-grade mineralization at the Arrow deposit. However, unlike clay alteration through the Triple R ore zone, ISM values for white micas associated with mineralization at the Arrow deposit are mostly greater than 1, with only a single ISM indicative of higher temperature alteration (0.6).

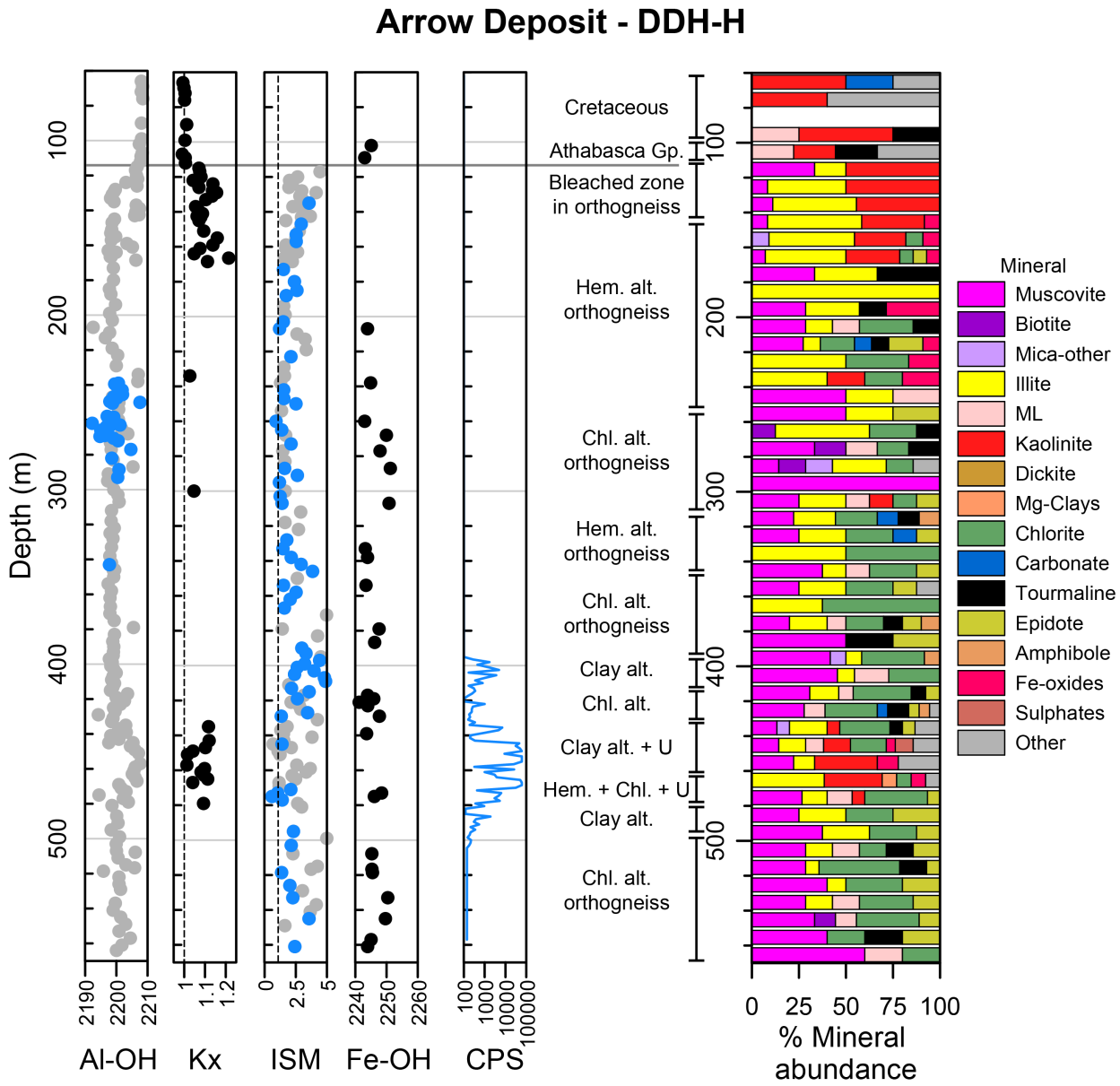

Figure 8. Multi-parameter logs for DDH-H from NexGen Energy Ltd.'s Arrow deposit. Grey horizontal line indicates the unconformity between Athabasca Group sandstones and underlying crystalline basement. Spectral data are plotted as important scalars (Al-OH = wavelength of AL-OH absorption feature; Kx = kaolinite crystallinity index; ISM = illite spectral maturity; Fe-OH = wavelength of Fe-OH absorption feature) and as strip log of % mineral abundance (binned over 10 m intervals). For AL-OH and ISM plots, grey data points represent scalars from mixed-spectra, whereas blue data points indicate scalars representative of white mica (Al-OH) and white mica + ML (ISM). CPS = Gamma-ray counts per second. Dashed line in Kx and ISM logs indicates a value of 1.

DDH-J

DDH-J intersects the unconformity between the Athabasca Supergroup and basement at 134.5 m, and the main Harpoon discovery shear zone at 175 to 212 m (Fig. 9). Similar to drill core DDH-H, the unconformity is apparent in the Kx profile, with consistent 0.98 values from the overlying Athabasca Supergroup that increase to greater than 1.0 below the unconformity. The Al-OH values indicate a range in white mica compositions from paragonitic to phengitic throughout the drillhole. However, no relationship is evident between composition and alteration related to uranium mineralization due to limited Al-OH values from mixed spectra in the primary ore zone. Similar to other drill core analyzed in this study, the presence of kaolinite below the upper weathering profile is coincident with high-grade uranium mineralization. The ISM values are indicative of low-grade metamorphic micas, with only a single value (0.8 at 297 m) indicative of increased crystallinity due to higher temperature alteration.

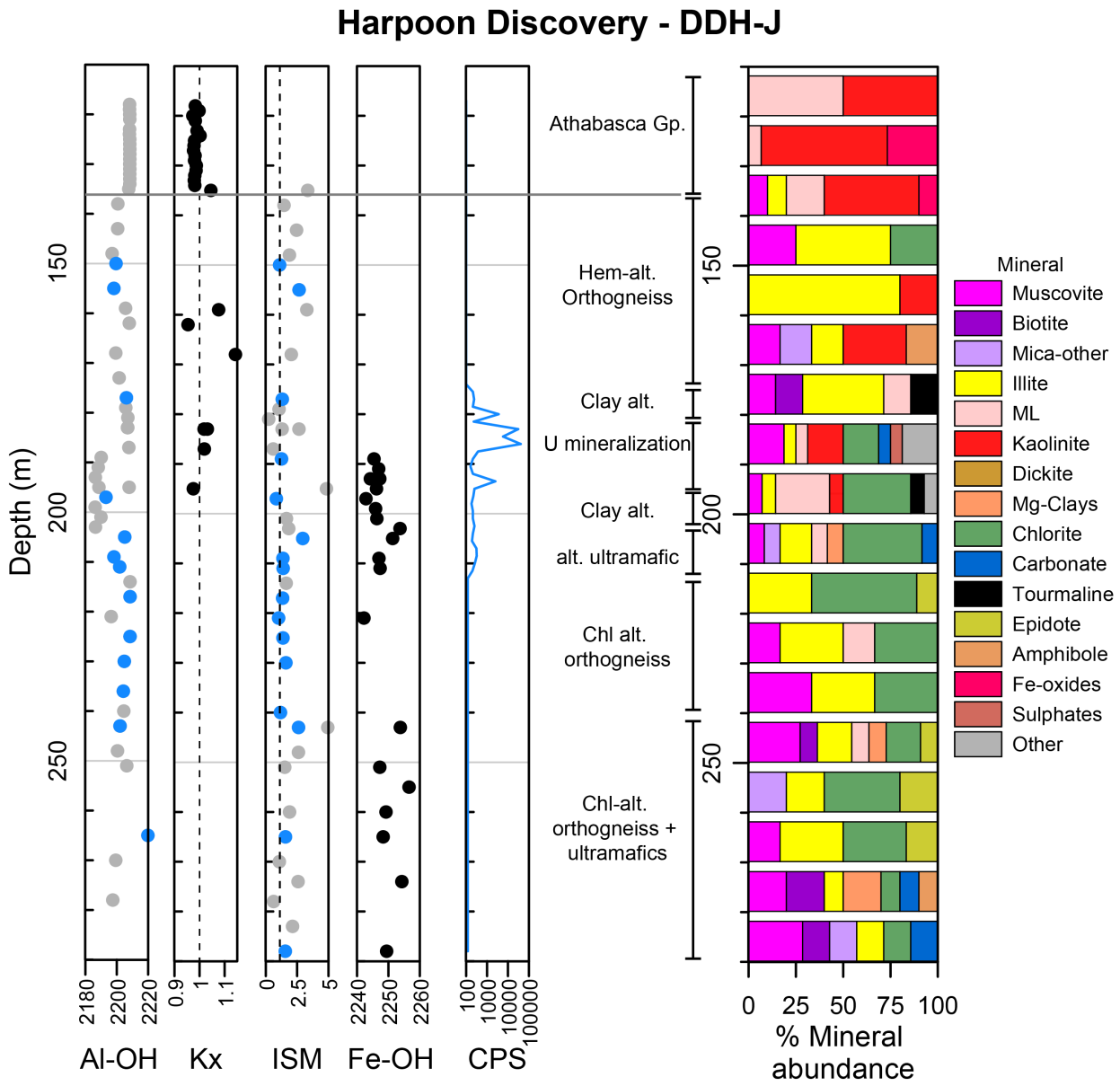

Figure 9. Multi-parameter logs for DDH-J from NexGen Energy Ltd.'s Harpoon discovery. Grey horizontal line indicates the unconformity between Athabasca Group sandstones and underlying crystalline basement. Spectral data are plotted as important scalars (Al-OH = wavelength of AL-OH absorption feature; Kx = kaolinite crystallinity index; ISM = illite spectral maturity; Fe-OH = wavelength of Fe-OH absorption feature) and as strip log of per cent mineral abundance (binned over 10 m intervals). For AL-OH and ISM plots, grey data points represent scalars from mixed-spectra, whereas blue data points indicate scalars representative of white mica (Al-OH) and white mica + ML (ISM). CPS = Gamma-ray counts per second. Dashed line in Kx and ISM logs indicates a value of 1.

Discussion and ongoing studies

Visible-near infrared - shortwave infrared reflectance spectroscopy is an efficient method to provide rapid and robust data of the chemical and physical properties of alteration assemblages. Results from this study highlight that detailed, metre-scale logs of mineral abundance are useful tools for evaluating the magnitude of fluid alteration in drill core. However, preliminary XRD analyses (Fig. 4) underscore the need to integrate quantitative mineral identification methods with spectral data. Research in progress incorporates XRD and SEM methods to confirm the VNIR-SWIR-derived clay mineralogy presented in this study. Our findings show that kaolinite is a useful mineral for distinguishing fluid pathways in the PLC, as it both denotes the depth that fluids circulated in the upper bleached zone (e.g. Fig. 5, 8), and is associated with highest grade mineralization in each drillhole (Fig. 10). Likewise, scalars derived from reflectance spectra provide information about the geochemical conditions at the time of alteration, and relative temperature of the circulating fluid. Many drill core investigated in this study exhibit correlations between clay crystallinity indices (Kx, ISM) and grade of uranium mineralization. Whereas these trends have limited interpretative ability in a single drillhole, they are likely vectors towards major fluid conduits when expanded to property- or corridor-scales.

Ongoing studies are incorporating geochronological, isotopic and geophysical methods to understand and track the temporal evolution of these fluid conduits, and determine the effect of fluid circulation and mineralization on the geochemical and physical properties of host rocks in the PLC. Current geochronology studies are integrating low-temperature thermochronometers ($^{40}Ar/^{39}Ar$ dating of micas, K-Ar dating of illite, (U-Th)/He dating of zircon) to constrain the hydrothermal-metasomatic history of the PLC through deep time.

Using mineralogical (primary minerals versus alteration assemblages) and isotopic data (Mg and Fe isotopes) in concert, there is also potential to define isotopic compositions that reflect redox reactions and changes in Fe and Mg bonding states characteristic of fertile hydrothermal uranium systems. Significant concentrations of hydrothermal Fe- and Mg-bearing minerals (e.g. Fe-oxides/hydroxides and chlorite) are often associated with Proterozoic unconformity-related uranium sys-

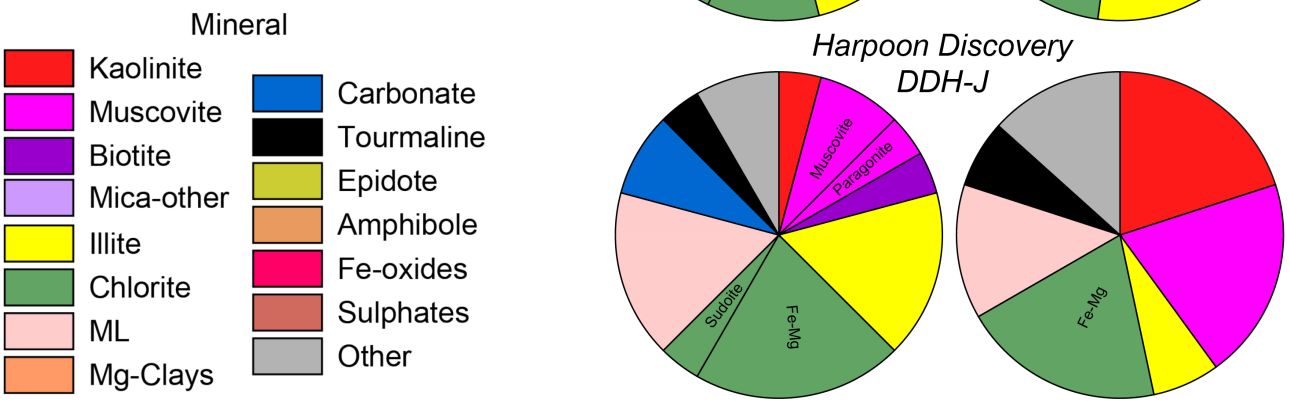

Figure 10. Comparison of the clay alteration associated with mineralization across the PLC (Fig. 6–9). Alteration within individual shear zones was classified as either a non- to weakly mineralized alteration halo (<1000 CPS) or high-grade mineralization.

tems, with their presence typically cited as a product of uranium precipitation mechanisms. The Fe^{2+} oxidized during the fluid-mineral reactions releases electrons that reduce U^{6+} in the oxidized fluids to immobile U^{4+} (uraninite), while the liberated Fe^{3+} and Mg^{2+} form Fe-oxide minerals and chlorite. As shown from the Bong uranium deposit in the Thelon Basin and the McArthur River deposit in the eastern Athabasca Basin, the alteration assemblages associated with uranium mineralization can record significant Fe and Mg isotopic fractionations (Acevedo and Kyser, 2015; Potter et al., 2015). These large Fe fractionations can occur during redox reactions, changes in bonding states, or leaching of Fe^{2+} species under acidic conditions (Johnson et al., 2008). Similar to Fe isotopes, there is a mineralogical control on the fractionation of Mg between carbonates, clay minerals, and waters during low-temperature processes such as weathering (Young and Galy, 2004; Pogge von Strandmann et al., 2008; Handler et al., 2009; Bourdon et al., 2010; Li et al., 2010; Wimpenny et al., 2014).

The heterogeneous lithology of many of the map units in the PLC, together with variable levels of alteration, result in a wide range of physical property values that might affect their overall geophysical signature depending on the depth of investigation and geophysical methodology used. Results from this study highlight the variable and complex alteration across the PLC and emphasize that in the absence of geological information, interpretation of geophysical data sets can be tenuous. For drill cores where magnetic susceptibility was measured, there is significant correlation between anomalous Fe-OH values and moderate to high magnetic susceptibilities, indicating the presence of hematite, pyrrhotite, and/or magnetite in the rocks. Geophysical studies are integrating magnetic susceptibility profiles and geological logs from 27 drill cores with airborne geophysical data to understand the relationships among magnetic-lithologic units, alteration, and geophysical signature. Additional samples collected from the PLC drill cores are undergoing measurements for density, electrical properties and remnant magnetization.

Acknowledgments

This report is a contribution to the Targeted Geoscience Initiative Program (TGI). Support for this study was provided through the Uranium Ore system '*Activity U-1.3: Fault reactivation, fluid flow and geophysical quantification of fertile alteration in unconformity-related uranium systems*'.

The authors would like to thank the collaboration of industry and the Alberta and Saskatchewan geological surveys in this study. Forum Energy Metals Corp., Fission Uranium Corp. and NexGen Energy Ltd. generously provided logistical support, and shared geological data and knowledge. Big Bear Contracting provided additional logistical support. We thank Igor Bilot for facilitating X-ray diffraction analyses, This report benefited from the review of Christopher Lawley, Jan Peter, SayadMasoud Anasri and Neil Rogers.

References

Acevedo, A. and Kyser, T.K., 2015. Fe isotopic composition of alteration minerals from McArthur River zone 4 deposit, Athabasca Basin, Saskatchewan; *in* Targeted Geoscience Initiative 4: Unconformity-Related Uranium Systems, (ed.) E.G. Potter and D.M. Wright; Geological Survey of Canada, Open File 7791, p. 61–73.

Adlakha, E.E., Hattori, K., Zaluksi, G., Kotzer, T., and Potter, E.G., 2013. Alteration within the basement rocks associated with the P2 fault and the McArthur River uranium deposit, Athabasca Basin; Geological Survey of Canada, Open File Report 7462, 35 p.

Alexandre, P., Kyser, K., and Polito, P., and Thomas, D., 2005. Alteration mineralogy and stable isotope geochemistry of Paleoproterozoic basement-hosted unconformity-type uranium deposits in the Athabasca Basin, Canada; Economic Geology, v. 100, p.1547–1563.

Alexandre, P., Kyser, K., Thomas, D., Polito, P., and Marlat, J., 2009. Geochronology of unconformity-related uranium deposits in the Athabasca Basin, Saskatchewan, Canada and their integration in the evolution of the basin; Mineralium Deposita, v. 44, p. 41–59.

Bosman, S.A. and Ramaekers, P., 2015. Athabasca Group + Martin Group = Athabasca Supergroup? Athabasca Basin multiparameter drill log compilation and interpretation, with updated geological map; *in* Summary of Investigations 2015, Volume 2; Saskatchewan Geological Survey, Saskatchewan Ministry of the Economy, Miscellaneous Report 2015-4.2, Paper A-5, 13 p.

Bourdon B., Tipper E. T., Fitoussi C., and Stracke A. 2010. Chondritic Mg isotope composition of the Earth; Geochimica et Cosmochimica Acta, v. 74, p. 5069–5083.

Card, C.D., 2017. Distribution and significance of crystalline rocks in the Patterson Lake uranium exploration corridor of northwest Saskatchewan; *in* Summary of Investigations 2017, Volume 2; Saskatchewan Geological Survey, Saskatchewan Ministry of the Economy, Miscellaneous Report 2017-4.2, Paper A-11, 19 p.

Card, C.D. and Noll, J., 2016. Host-rock protoliths, pre-ore metasomatic mineral assemblages and textures, and exotic rocks in the western Athabasca Basin: ore-system controls and implications for the unconformity-related uranium model; *in* Summary of Investigations 2016, Volume 2; Saskatchewan Geological Survey, Saskatchewan Ministry of the Economy, Miscellaneous Report 2016-4-2, Paper A-8, 19 p.

Card, C.D., Bethune, K.M., Davis, W.J., Rayner, N., and Ashton, K.E., 2014. The case for a distinct Taltson orogeny: Evidence from northwest Saskatchewan, Canada; Precambrian Research, v. 255, p. 245–265.

Cerin, D., Gotze, J., and Pan, Y., 2017. Radiation-induced damage in quartz at the Arrow uranium deposit, southwestern Athabasca Basin, Saskatchewan; The Canadian Mineralogist, v. 55, p. 457–472.

Clark, R. and Roush, T., 1984. Reflectance spectroscopy: quantitative analysis techniques for remote sensing applications; Journal of Geophysical Research, v. 89, p. 6329–6340.

Clark, R.N., King, T.V.V., Klejwa, M., and Swayze, G.A., 1990. High-spectral resolution reflectance spectroscopy of minerals; Journal of Geophysical Research, v. 95; p. 653–680.

Fraser, J.A., Donaldson, J.A., Fahrig, W.F., and Tremblay,

L.P., 1970. Helikian basins and geosynclines of the northwestern Canadian shield; *in* Symposium on basins and geosynclines of the Canadian Shield, (ed.) A.J. Baer; Geological Survey of Canada, Paper 70-40, p. 213–238.

Handler M., Baker J., Schiller M., Bennett V., and Yaxley G., 2009. Magnesium stable isotope composition of Earth's upper mantle; Earth and Planetary Science Letters, v. 282, p. 306–313.

Hermann, W., Blake, M., Doyle, M., Huston, D., Kamprad, J., Merry, N., and Pontual, S., 2001. Short wavelength infrared (SWIR) spectral analysis of hydrothermal alteration zones associated with base metal sulfide deposits at Rosebery and Western Tharis, Tasmania, and Highway-Reward, Queensland; Economic Geology, v. 96, p. 939–955.

Jefferson, C.W., Thomas, D.J., Gandhi, S.S., Ramaekers, P., Delaney, G., Brisbin, D., Cutts, C., Portella, P., and Olson, R.A., 2007. Unconformity-associated uranium deposits of the Athabasca basin, Saskatchewan and Alberta; *in* EXTECH IV: Geology and Uranium EXploration TECHnology of the Proterozoic Athabasca Basin, Saskatchewan and Alberta, (ed.) C.W. Jefferson and G. Delaney; Geological Survey of Canada, Bulletin 588, p. 23–67

Johnson, C.M., Beard, B L., and Roden, E.E., 2008. The iron isotope fingerprints of redox and biogeochemical cycling in modern and ancient Earth; Annual Review of Earth and Planetary Sciences, v. 36, p. 457–493.

Kokaly, R.F., Clark, R.N., Swayze, G.A., Livo, K.E., Hoefen, T.M., Pearson, N.C., Wise, R.A., Benzel, W.M., Lowers, H.A., Driscoll, R.L., and Klein, A.J., 2017. USGS Spectral Library Version 7: U.S. Geological Survey Data Series 1035, 61 p.

Kotzer, T.G. and Kyser, T.K., 1995. Petrogenesis of the Proterozoic Athabasca Basin, northern Saskatchewan, Canada, and its relation to diagenesis, hydrothermal uranium mineralization and paleohydrogeology; Chemical Geology, v. 120, p. 45–89.

Kyser, T.K., Hiatt, E., Renac, C., Durocher, K., Holk, G., and Deckart, K., 2000. Diagenetic fluids in paleo– and meso–Proterozoic sedimentary basins and their implications for long protracted fluid histories; *in* Fluid and Basin Evolution, (ed.) T.K. Kyser; Mineralogical Association of Canada, Short Course 28, p. 225–262.

Li, W.-Y., Teng F.-Z., Ke, S., Rudnick R.L., Gao, S., Wu, F.-Y., and Chappell B.W., 2010. Heterogeneous magnesium isotopic composition of the upper continental crust; Geochimica et Cosmochimica Acta, v. 74, p. 6867–6884.

MacDonald, C., 1985. Mineralogy and geochemistry of the sub -Athabasca regolith near Wollaston Lake; *in* Geology of Uranium deposits, (ed.) T.I.I. Sibbald and W. Petruk; Canadian Institute of Mining, Special Volume 32 p. 155–158.

Mathieu, M., Roy, R., Launeau, P., Cathelineau M., and Quirt, D., 2017. Alteration mapping in drill cores using a KySpex SWIR-320m hyperspectral camera: uranium deposit (Saskatchewan, Canada); Journal of Geochemical Exploration, v. 172, p. 71–88.

Mwenifumbo, J.C., Percival, J.B., Bernius, G., Elliott, B., Jefferson, C.W., Wasyliuk, K., and Drever, G., 2007. Comparison of geophysical, mineralogical, and stratigraphic attributes in drill holes MAC- 218 and RL-88, McArthur River uranium camp, Athabasca Basin, Saskatchewan; *in* EXTECH IV: Geology and Uranium Exploration TECHnology of the Proterozoic Athabasca Basin, Saskatchewan and Alberta, (ed,) C.W. Jefferson and G. Delaney; Geological Survey of Canada Bulletin 588, p. 507–520.

Oluwadebi, A.G., 2015. The significance of crystallinity in hydrothermal alteration mapping: a case study of Alem Tena area of Main Ethiopia Rift, Ethiopia; International Research Journal of Earth Sciences, v. 3, p. 12–17.

Pană, D., Creaser, R.A., Muehlenbachs, K., and Wheatley, K., 2007. Basement geology in the Alberta portion of the Athabasca Basin: context for the Maybelle River area; *in* EXTECH IV: Geology and Uranium EXploration TECHnology of the Proterozoic Athabasca Basin, Saskatchewan and Alberta, (ed.) C.W. Jefferson and G. Delaney; Geological Survey of Canada, Bulletin 588, p. 135–153.

Percival, J.B. and Kodama, H. 1989. Sudoite from Cigar Lake, Saskatchewan; The Canadian Mineralogist, v. 27, p. 633–641.

Percival, J.B., Bell, K., and Torrance, J.K., 1993. Clay mineralogy and isotope geochemistry of the alteration halo at the Cigar Lake uranium deposit; Canadian Journal of Earth Sciences, v. 30, p. 689–704.

Percival, J.B., Wasyliuk, K., Reif, T., Bernier, S., Drever, G., Perkins, T., and Jefferson, C.W., 2002. Mineralogical aspects of three drillholes along the McArthur River transect using a portable infrared spectrometer; *in* Summary of Investigations 2002, Volume 2; Saskatchewan Geological Survey, Saskatchewan Energy Mines, Miscellaneous Report 2002-4-2, Paper D-14, 15 p.

Percival, J.B., Olejarz, A.D., English, M.L.R., Belley, P.M., Flynn, T., Laudadio, A.B., and Stirling, J.A.R., 2016. Spectral Library: The Kodama Clay Collection; Geological Survey of Canada Open File 7923.

Percival, J.B., Bosman, S.A., Potter, E.G., Peter, J.M., Laudadio, A.B., Abraham, A.C., Shiley, D.A., and Sherry, C., 2018. Customized spectral libraries for effective mineral exploration: mining national mineral collections; Clay and Clay Minerals, v. 66, p. 209–226.

Pogge von Strandmann P.A.E., Burton K.W., James R.H., van Calsteren P., Gislason S.R., and Sigfússon B., 2008. The influence of weathering processes on riverine magnesium isotopes in a basaltic terrain; Earth and Planetary Science Letters, v. 276, p. 187–197.

Potter, E.G., Sharpe, R., Girard, I., Fayek, M., Gammon, P., Quirt, D., and Robbins, J., 2015. Fe and Mg signatures of the Bong uranium deposit, Thelon Basin, Nunavut; *in* Targeted Geoscience Initiative 4: Unconformity-Related Uranium Systems, (ed.) E.G. Potter and D.M. Wright; Geological Survey of Canada, Open File 7791, p. 52–60.

Powell, J.W., Pană, D.I., Card, C.D., Potter, E.G., Tschirhart, V., and Joyce, N., 2018. New geochronological insights into the Taltson Domain of northern Alberta and Saskatchewan; *in* Targeted Geoscience Initiative: 2017 Report of Activities, Volume 2, (ed.) N. Rogers; Geological Survey

of Canada, Open File 8373, p. 43–56.

Ramaekers, P., Jefferson, C.W., Yeo, G.M., Collier, B., Long, D.G.F., Drever, G., McHardy, S., Jiricka, D., Cutts, C., Wheatley, K., Catuneanu, O., Bernier, S., Kupsch, B., and Post, R.T., 2007. Revised geological map and stratigraphy of the Athabasca group, Saskatchewan and Alberta; *in* EXTECH IV: Geology and Uranium EXploration TECHnology of the Proterozoic Athabasca Basin, Saskatchewan and Alberta, (ed.) C.W. Jefferson and G. Delaney; Geological Survey of Canada, Bulletin 588, p. 155–191

Stern, R.A., Card C.D., Pană, D., and Rayner, N., 2003. SHRIMP U-Pb ages of granitoid basement rocks of the southwestern part of the Athabasca Basin, Saskatchewan and Alberta; *in* Radiogenic Age and Isotopic Studies, Report 16; Geological Survey of Canada, Current Research 2003-F, 20 p.

Wilson, C.J.L., McKnight. S.W., Dugdale, A.L., Rawling, T.J., Farrar, A.D., McKenzie, M.J., and Melling, W.D., 2009. Illite crystallinity and the b-spacing values of white micas and their implications for gold mineralisation in the Lachlan Orogen; Australian Journal of Earth Sciences, v. 56, p. 1143–1164.

Wimpenny, J., Colla, C.A., Yin, Q.Z., Rustad, J.R., and Casey, W.H., 2014. Investigating the behaviour of Mg isotopes during the formation of clay minerals; Geochimica et Cosmochimica Acta, v. 128, p. 178–194.

Young, E.D. and Galy, A., 2004. The isotope geochemistry and cosmochemistry of magnesium; Reviews in Mineralogy and Geochemistry, v. 55, p. 197–230.

Geochemistry of U±Cu±Mo±V mineralization, Central Mineral Belt, Labrador: differentiating between mineralization styles using a principal component analysis approach

P. Acosta-Góngora[1], E.G. Potter[1], L. Corriveau[2], C.J.M. Lawley[1] and G.W. Sparkes[3]

[1]*Geological Survey of Canada, 601 Booth Street, Ottawa, Ontario K1A0E8*

[2]Geological *Survey of Canada, 490 rue de la Couronne, Québec, Quebec G1K 9A9*

[3]*Geological Survey of Newfoundland and Labrador, 50 Elizabeth Avenue, P.O. Box 8700, St. John's, Newfoundland and Labrador A1B 4J6*

Abstract

The Central Mineral Belt, Labrador, has experienced intermittent uranium exploration since the late 1950s. It hosts multiple U±Cu±Mo±V showings, prospects and deposits in Neoarchean to Mesoproterozoic meta-igneous and -sedimentary rocks. Uranium mineralization occurs in metasomatic (albitite-hosted), magmatic- and magmatic hydrothermal-related (e.g. iron-oxide-carbonate-rich veins and breccias) and sedimentary-hosted (e.g. unconformity-related) systems.

In this contribution, we use the IOCG discrimination-alteration diagram and apply principal component analysis (PCA) to characterize hydrothermal alteration and ore element signatures at uranium occurrences included within the Central Mineral Belt Uranium Geochemistry database. Our results indicate that sodium and Na-Ca-Fe-(Mg) metasomatism is more pervasive and regionally widespread than previously reported, and commonly hosts uranium mineralization; albitization itself may not be directly associated with uranium mineralization. Other second-order factors (e.g. proximity to structures) are more likely to control uranium enrichment.

In the Jacques Lake and Michelin deposits and Two Time-Snegamook trend, uranium-mineralized samples yield positive PC2 scores and occur with Na- and Na-Ca-Fe-(Mg)-altered rocks. Our analysis also documents that PC3 represents a proxy for a second style of U-As-Mo mineralization that is better defined in basalt-argillite-hosted systems (e.g. Moran Lake Upper C zone and Anna Lake deposits). The unusual U-As-Mo hydrothermal fingerprint may indicate: i) a synsedimentary origin of uranium (i.e. U-rich black shales) that was remobilized to upper stratigraphic levels; and/or ii) argillitic and basaltic packages within the Moran Lake and Post Hill groups served as redox traps for oxidizing uranium-rich fluids that equilibrated with these rocks.

Introduction

The Central Mineral Belt (CMB; Fig. 1a) of Labrador hosts multiple U±Cu±Mo±V prospects and advanced exploration projects. The early exploration in the CMB was in the 1950s and up to the mid-1980s, prior to a significant uranium price drop in the world commodity markets. In the mid-2000s, the renewed commodity demand triggered extensive exploration resulting in large amounts of industry geophysical and geochemical data.

The recent work of Sparkes (2017) summarizes the geology and metallogeny of the CMB, and expanded the scope of previous studies carried out in this area (e.g. Gower et al., 1982; Ryan et al., 1983; Kerr, 1994; Wilton, 1996). The geological background provided by their work, coupled with the extensive geochemical and geophysical data generated during the latest exploration wave, provides an excellent framework to characterize the CMB uranium-rich systems within current ore deposit models.

The CMB U±Cu±Mo±V mineralization styles and associated alteration types are spatially linked to pervasive regional alkali-rich alteration followed by brecciation and iron oxide alteration. Such features resemble alteration typical of Iron-Oxide-Copper-Gold (IOCG; Williams et al. 2005) and albitite-hosted (also called sodium-metasomatic; Cuney 2009) uranium deposits. Thus, it is worthwhile to explore potential links among IOCG deposits, albitite-hosted deposits and the CMB uranium mineralization to advance exploration models and understanding of metal pathways and traps.

The CMB uranium geochemistry database (CMBUG; Acosta-Góngora et al., 2018) consists of over 40 000 samples compiled from the Geological Survey of Newfoundland and Labrador database and mineral assessment reports submitted between 2002 and 2011. In this report, we provide preliminary characterization of the CMB uranium systems and their associated hydrothermal alteration using the IOCG discriminant-alteration diagram of Montreuil et al (2013) and principal component analysis (PCA) with the samples taken/derived from the CMBUG database.

Corresponding author: Pedro Acosta-Góngora (pedro.acostagongora@canada.ca)

Acosta-Góngora, P., Potter, E.G., Corriveau, L., Lawley, C.J.M., and Sparkes, G.W., 2019. Geochemistry of U±Cu±Mo±V mineralization, Central Mineral Belt, Labrador: differentiating between mineralization styles using a principal component analysis approach; *in* Targeted Geoscience Initiative: 2018 report of activities, (ed.) N. Rogers; Geological Survey of Canada, Open File 8549, p. 381–391. https://doi.org/10.4095/313673

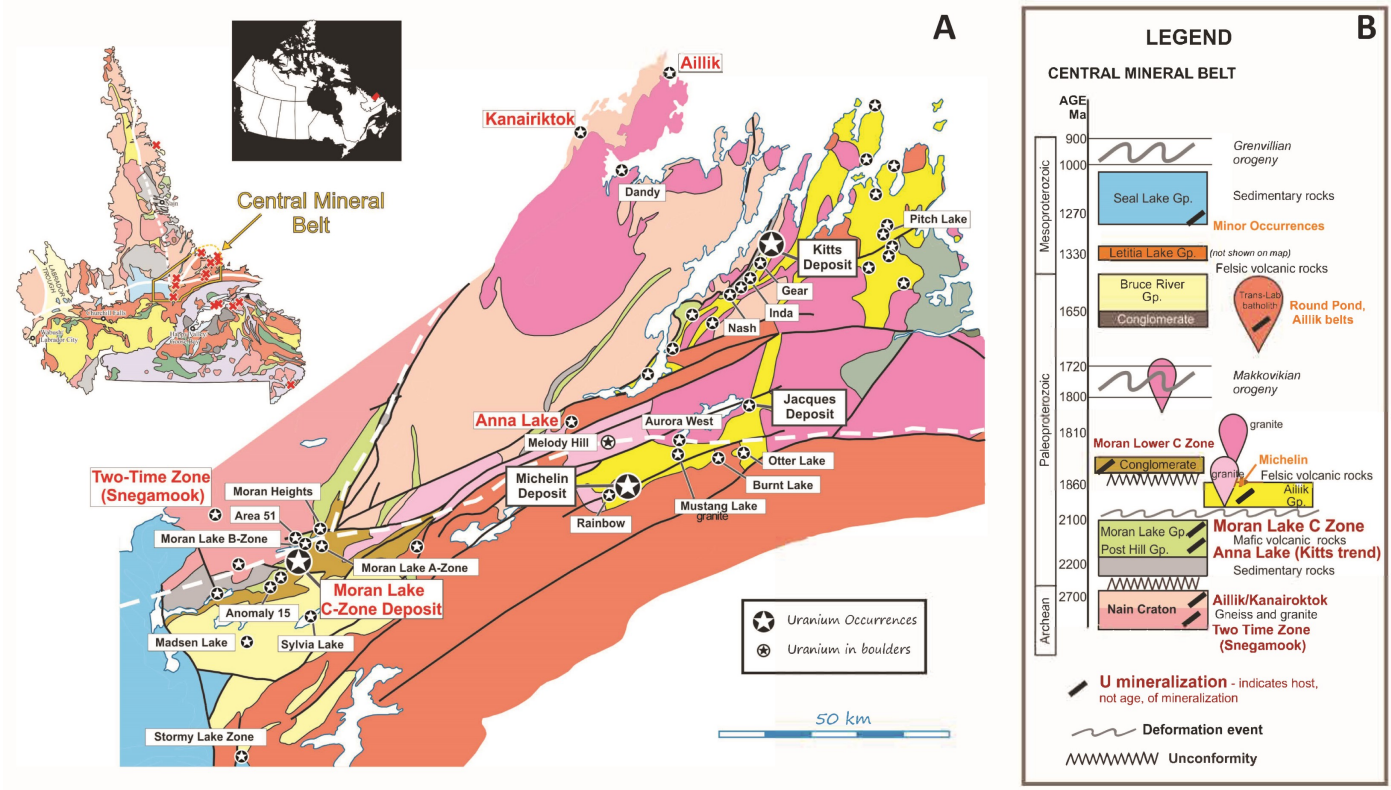

Figure 1. a) Simplified geological map of the Central Mineral Belt, Labrador, with locations of the principle uranium occurrences shown. b) Stratigraphy of the Central Mineral Belt, highlighting the host rocks of uranium mineralization. *Modified from* Sparkes (2017) and Kerr and Sparkes (2009).

Geology of the Central Mineral Belt

The regional geology of the CMB (Fig. 1) is described in detail by Gower et al. (1982), Ermanovics (1993), Wardle et al. (1997), Kerr (1994), Culshaw and Ketchum (1995), Kerr et al. (1996), Wilton (1996), Hinchey (2007), Hinchey and LaFlamme (2009), Sparkes et al. (2016) and Sparkes (2017). The oldest unit in the CMB is the Archean Nain Province gneiss, which is intruded by variably deformed tonalite, granodiorite and granite intrusions of the Kanairiktok Intrusive Suite (KIS) and overlain by Proterozoic meta-volcanic and -sedimentary packages (Ryan, 1984; Ermanovics, 1993; Kerr et al., 1996). The Archean gneiss and KIS intrusions are transected by the ca. 2.23 Ga Kikkertavak dykes (Cadman et al., 1993).

The Paleoproterozoic Moran Lake (southwest CMB) and Post Hill groups (northeast CMB) are considered stratigraphically equivalent (Fig. 1b) and are comprised of metamorphosed shale, sandstone and basalt, unconformably overlying the Archean gneiss and KIS intrusions (Fig. 1b). These rocks are not cut by the Kikkertavak dykes, giving a maximum depositional age of 2.2 Ga for the Moran and Post Hill groups (cf. Ermanovics, 1993; Wilton, 1996). In the Moran Lake area, shale of the Warren Creek Formation comprises the basement of the Moran Lake Group and is overlain by basaltic rocks of the Joe Pond Formation. In the Post Hill Group, the stratigraphy, in ascending order, comprises psammite, schistose mafic metavolcanic rocks and minor pelite (Culshaw and Ketchum, 1995).

The Post Hill Group is overlain by mixed metamorphosed sedimentary and bimodal volcanic rocks of the Aillik Group (Marten, 1977; Gower et al., 1982) (Fig. 1b). The Moran Lake Group is unconformably overlain by the Bruce River Group, which consists of conglomeratic arkose and sandstone overlain by a thick sequence of 1.7 Ga felsic volcanic rocks (e.g. Ryan, 1984; Schärer et al., 1998; Sparkes et al., 2017). However, tuff layers interbedded with basal sandstone units within the lower Bruce River Group yield a U-Pb age of ca. 1850 Ma (Sparkes et al., 2016, 2017), indicating the presence of unrecognized complexities within the stratigraphy of the Bruce River Group.

The youngest supracrustal sequences in the CMB are the Letitia and Seal Lake groups (Fig. 1b). The ca. 1.3 Ga Letitia Lake Group (Thomas, 1981; Gandhi et al., 1988) is dominated by alkaline volcanic rocks that underlie Seal Lake Group sedimentary and mafic volcanic rocks. The Archean intrusions and Paleoproterozoic sequences were metamorphosed (greenschist to amphibolite facies) and variably deformed by at least three orogenic episodes (Makkovikian: ca. 1.8–1.7 Ga; Labradorian: 1.7–1.6 Ga; Grenvillian: ca. 1.0 Ga; Sparkes, 2017).

Examples of CMB uranium mineralization occur, at least

locally, within the Archean to Paleo- to Mesoproterozoic intrusive (e.g. Two Time prospect), meta-volcanic (e.g. Moran Lake Upper C Zone and Michelin deposits) and -sedimentary (e.g. Moran Lake Lower C Zone) rock packages. Mineralization styles include breccia zones (e.g. Two Time and Moran lake Upper C zone), fracture-hosted (e.g. Anomaly No. 17 prospect and Two Time deposit) and disseminated (e.g. Anna Lake prospect). Commonly, ore-generating events are also preceded by moderate to pervasive alkali metasomatism (e.g. Michelin deposit) and iron oxide replacement or breccia infill (mainly hematite; Moran Lake Upper C Zone) (Sparkes and Kerr, 2008).

Uranium mineralization in the Central Mineral Belt

Uranium mineralization in the CMB occurs in magmatic, metamorphic, metasomatic and sedimentary formational environments (Sparkes, 2017). The magmatic systems can be roughly separated into magmatic and magmatic-hydrothermal. Examples of the former occurrences include the pegmatite-hosted Dandy and Kanairiktok prospects (Fig. 1a), whereas the latter include the Moran Lake Upper C Zone deposit (Fig. 2a, b), which exhibits IOCG-like features. This deposit is mainly contained in meta-basalt of the Joe Pond Formation (Moran Lake Group), where mineralization is hosted in iron oxide-carbonate breccias that post-date extensive alkali (Ca, Na) metasomatism in the area. The mineralized mafic volcanic rocks are thrusted to the northwest over younger, fluvial sedimentary rocks of the Heggart Lake Formation (Bruce River Group), which host the Moran Lake Lower C Zone deposit (Sparkes, 2017; Fig. 2a, b). Other less economically significant occurrences are hosted by felsic volcanic rocks of the Aillik Group (e.g. Harbinger , Benedict #1 and Benedict #2 prospects) in the Benedict Mountains and Bruce River Group (Madsen and Sylvia Lake prospects) in the Moran Lake area.

The metamorphic and metasomatic related uranium mineralization exhibits an overriding structural control and is hosted in cataclastic breccia zones (Sparkes, 2017). Examples of this mineralization type include the Two Time Trend, the Kitts deposit, and related occurrences along the Post Hill Trend (or Post Hill Belt), as well as the Michelin and Jacques Lake deposits (Sparkes, 2017; Fig. 1a). The Two Time Trend corresponds with a northwest-trending shear zone that connects the Two Time and Snegamook prospects, both hosted by Archean intrusions of the KIS with uranium mineralization occurring within iron-oxide breccia. According to Sparkes (2017), significant alkali metasomatism is not associated with the breccia or mineralization, suggesting an important structural control on fluid focusing and ore deposition. Uranium mineralization in the Kitts deposit and the Inda, Gear, Nash and Anna Lake prospects (Post Hill Trend) are hosted in mafic argillite and tuff of the Post Hill Group (e.g. Evans, 1980). These prospects locate within an inferred structural corridor, which at a regional scale defines the boundary between the Post Hill Group and the structurally overlying Aillik Group (Sparkes, 2017). Mineralization developed along the Post Hill Trend is not associated with a metasomatic footprint, and thus contrasts with the ore-style at deposits within the Moran Lake Upper C zone area

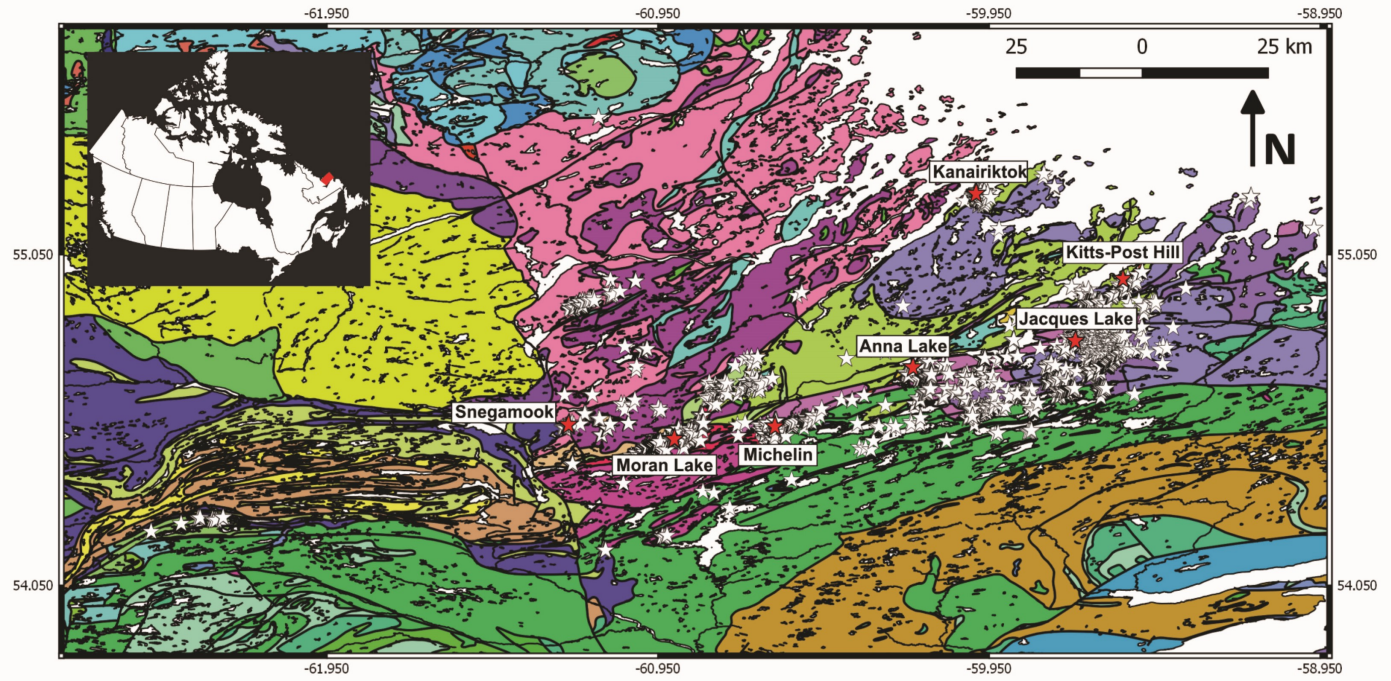

Figure 2. Map of the Central Mineral Belt geology (*after* Wardle et al., 1997) with the locations of the geochemistry samples and/or drillholes in the CMBUG database from which samples were obtained. The location of the main deposits/occurrences discussed in this study are highlighted.

(Sparkes, 2017). Within the Aillik Group, the Michelin and Jacques Lake deposits are the most important uranium occurrences, and are hosted in albitite corridors, similar to those reported in the Kirovograd district of Ukraine (Cuney et al., 2012), Valhalla deposit in Australia (Polito et al., 2009) and Southern Breccia Corridor in Canada (Montreuil et al. 2015; Potter et al., in press).

Sediment-hosted mineralization is mainly confined to the Bruce River Group, with minor occurrences also developed within sedimentary rocks of the Moran Lake Group (e.g. Area 51 prospect). The Moran Lake Lower C Zone deposit is the most important occurrence, and is primarily restricted to the ca. 1850 Ma Heggart Lake Formation (Sparkes et al., 2016). Mineralization occurs along and slightly above the unconformity between metabasalts the Joe Pond Formation (Moran Lake Group) and overlying metasandstone and -conglomerate packages of the Heggart Lake Formation (Bruce River Group; Fig. 2b). Uranium ore is associated with reduced zones in otherwise oxidized rocks, which resembles classic sandstone-hosted uranium mineralization. The sedimentary-hosted occurrences display a spatial association with regional fault structures.

The timing of CMB uranium mineralization is poorly constrained, principally defined by magmatic and detrital zircon dating from host meta-sedimentary and -volcanic packages, as well as crosscutting dykes. Overall, this mineralization is constrained to four main events (Sparkes 2017 and references therein). In the northeastern CMB, uranium mineralization was emplaced in two windows (2030-–1880 Ma (e.g. Kitts deposit), and 1860–1800 Ma (e.g. Michelin, Jacques Lake)), whereas in the southwest, uranium mineralization occurred between 1860 and 1660 Ma (e.g. Moran Lake Upper and Lower C Zone deposits), and after 1650 Ma (e.g. Madsen and Sylvia Lake prospects).

The Central Mineral Belt database

The CMB uranium geochemistry database (CMBUG; Acosta-Góngora et al., 2018) is a compilation of geochemical data from the Geological Survey of Newfoundland and Labrador (GSNL) and mineral assessment reports submitted to the Newfoundland and Labrador Mineral Assessment Database (NLAD) between 2002 and 2011 (Fig. 3). The majority of the data (82%) is derived from drill core assays, with the remainder from outcrop, channel, float, chip and boulders samples. The CMBUG is separated in two subsets, the NLAD and GSNL. Lithological descriptions, including rock type and alteration types, as well as analytical Si and loss-on-ignition (LOI) values are absent for the NLAD, but reported in the GSNL subset.

In this study, only data obtained via four acid digestion methods were used for statistical analysis. The ‘four acid’ or ‘near total’ digestion techniques use a combination of three or four different acids (hydrochloric, hydrofluoric, nitric and perchloric acids) to dissolve a sample that contains refractory minerals. However, some highly resistive minerals (e.g. zircon) may not be completely dissolved by this method and it is thus considered a ‘near total’ digestion. The near-total dissolution was analyzed using inductively coupled plasma mass spectrometry (ICP-MS) to provide results for a broad suite of major, minor, and trace elements. More details on the analytical techniques and laboratory protocols are outlined in Acosta-Góngora et al. (2018).

Data treatment

Prior to performing any statistical analysis, the data suite was inspected for negative values and duplicates, which were converted into “NA” expressions (not analyzed) and eliminat-

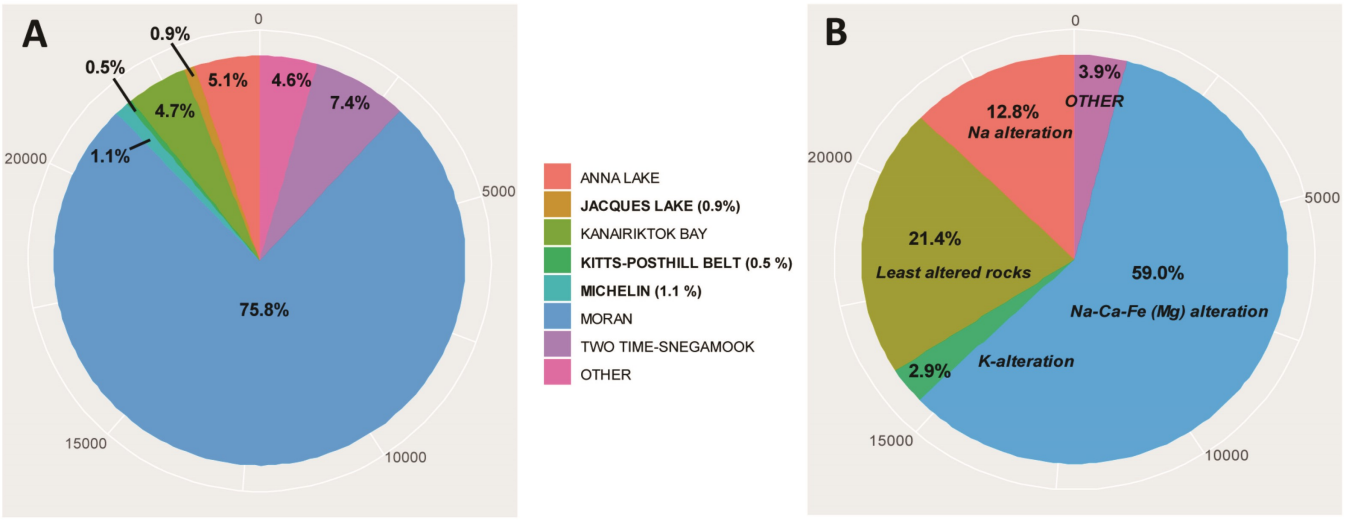

Figure 3. a) Geology of the Moran Lake C Zone area *modified from* Ryan (1984) and Gillies et al. (2009). b) Cross section along the A-B segment shown in a) and showing the mineralized Joe Pond Formation basalts (Moran Upper C Zone) thrusted over the sandstone-conglomerate of the Heggart Formation of the Bruce River Group, host to the Moran Lake Lower C Zone.

ed. It was found that approximately 40% of the data set contained analytical values only for U_3O_8 and selected base metals, and thus, these were removed from further statistical analysis. Given the variability of the element suites analyzed in each assessment report, we only selected elements with less than 30% of the data missing (e.g. not analyzed or below detection limits). Elements with a relatively large proportion of missing values impact log-ratio results based PCA and thus were removed for the purposes of this study. Censored compositional data were replaced using a method of k-nearest neighbours, which provides reliable estimates of replacement values (Hron et al., 2010). The robCompositions package in the R platform (R Core Team, 2018) was used for this calculation (impKNNa function). After data treatment, the resulting CMBUG database was reduced to 24 413 samples (GSNL: n = 653; NLAD: n = 23 760).

The Si values for the NLAD subset were approximated on an assumption that dissolution of the other major elements (as element oxides) and uranium (as U_3O_8) was nearly total. Therefore, the concentration of Si (as SiO_2 weight %) was estimated as Si* = 100 - (Na_2O + K_2O + CaO + MgO + Fe_2O_3 + Al_2O_3 + U_3O_8). However, for samples with relatively high LOI (>5 weight %) and/or U (>1 weight %) values, the Si* values are expected to be less accurate.

Compositional data are inherently closed because values sum to a constant (1 or 100%), resulting in forced inter-variable correlations if multivariate statistical analysis is directly applied to the raw data (Aitchison, 1986; Filzmoser et al., 2009). This is known as the 'closure problem' and is overcome by transforming the data using the centred-log ratio (clr) method (Thió-Henestrosa and Martín-Fernández, 2005). This transformation was applied to the CMBUG data set prior to performing PCA. PCA was done using the prcomp function of the stats package of the R platform. Concentrations in PCA biplots are log-ratio transformed.

Results

Geographical distribution and alteration classification

Figure 4a illustrates the CMB data distribution in terms of location. The Moran Lake area comprises 75.8% of the data, followed by the Snegamook (7.4%), Anna Lake (5.1%), and Kanairiktok Bay (4.7%) areas. Some of the most important deposits in the CMB such as Jacques Lake (0.9%), Michelin (1.1%), and the Kitts Post Hill Belt (0.5%) (host to the Kitts, Inda, Gear, and Nash systems) occur within underrepresented areas, and are shown for comparison. .

The Montreuil et al. (2013) IOCG discrimination-alteration diagram was used to classify the CMB data according to their alteration 'facies'. The 'facies' approach of metamorphic geology has been applied to IOCG and affiliated deposits (Corriveau, 2017; Corriveau et al., 2010, 2016, 2017, 2018; Montreuil et al., 2015, 2016a, b) as a means of grouping mineral assemblages that produce diagnostic whole-rock compositions (i.e. Na, Ca-Fe, K-Fe, K). This approach greatly simplifies descriptive nomenclature and alteration mapping protocols for the regional-scale iron oxide and alkali-calcic alteration systems that host iron oxide-apatite, IOCG and affiliated deposits.

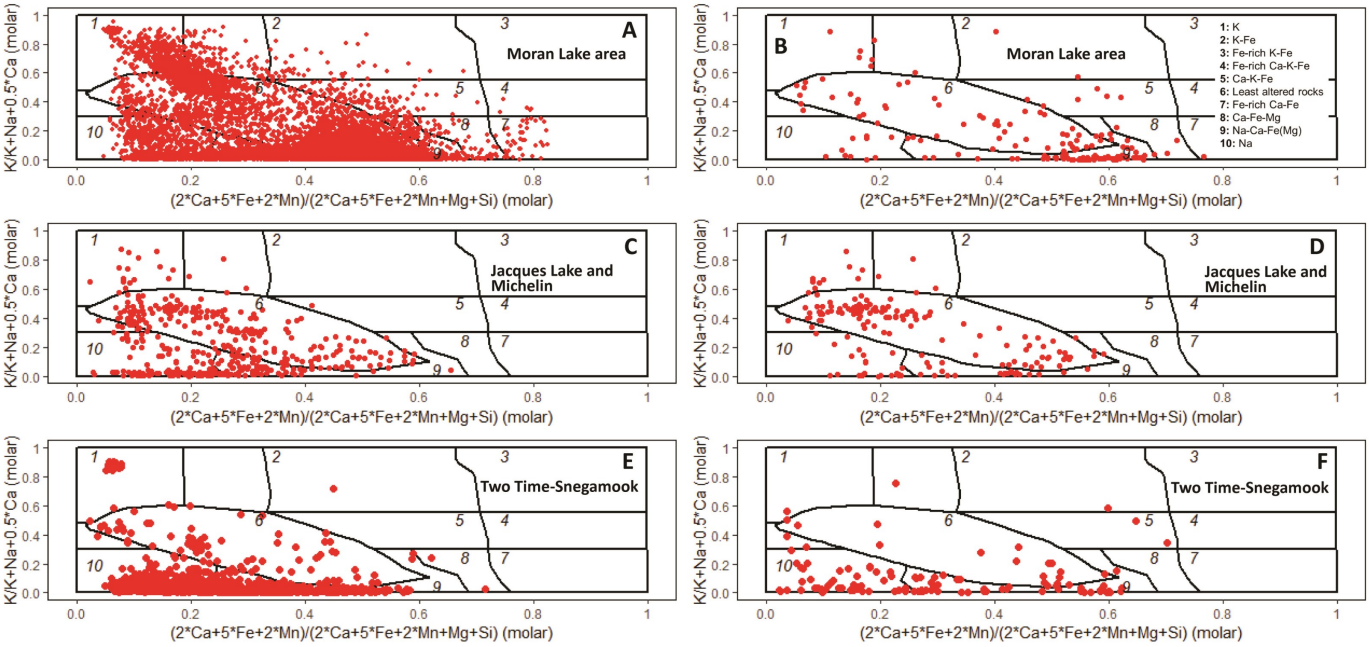

Figure 4. a) Proportions of samples in the CMBUG database by geographical area. b) Proportions of the iron oxide and alkali-calcic alteration facies present in the Central Mineral Belt after using the IOCG discrimination-alteration plot of Montreuil et al. (2013). The numbers displayed at the outermost circumference of the chart correspond to the number of samples.

Most of the data (96%) fall in only four fields of the plot, the Na-Ca-Fe-(Mg) (59.0%), Na (12.8%) and K (2.9%) alteration and least altered rock (21.4%) fields (Fig. 4b). This geochemical fingerprint is consistent across the CMB and is not an artefact of the dominant Moran Lake data population (Fig. 5). In Figure 5, the GSNL and NLAD subsets are plotted separately for distinct areas of the CMB to assess the validity of the Si* calculation. Both data sets (Si* versus Si) show very similar distributions, suggesting that Si* estimates are a good proxy for the true Si concentration for most samples.

Principal component analysis results

Three main principal components (PC) account for most of the data variability: PC1 (37.3%), PC2 (12.8%), and PC3 (11.2%). Along the PC1 axis, Fe, Ca, Mg, Mn and most base metals (V, Co, Ni, Cr) are tightly clustered and yield positive PC1 scores, whereas K, Rb, Th and Ba are associated with negative PC1 scores (Fig. 6a, b). These element associations suggest that lithology and/or alteration facies correspond to the largest source of data set variance (37.3%; Fig. 6a) and represent the dominant features of the CMBUG database. PC2 is the second largest source of variance (12.3%) and yields high component loadings for uranium (48% of U variability). The association between U, PC2, and PC3, suggests that these particular principal components represent an important proxy for uranium mineralization. The most uranium-rich samples are associated with Pb, which is likely radiogenic (Fig. 6c), and are antithetical to samples that yield a large ion lithophile element (LILE) signature (negative PC2 scores). PC3 represents the third largest source of data variance within the CMBUG database (Fig. 6d; 13% of U variability), and documents an association between As, U, Pb and Mo.

The U-Pb-As-Mo defined by PC3 is dominated by samples from the Moran Lake and Anna Lake areas (Fig. 6a–c). Felsic volcanic (Jacques Lake and Michelin) and intrusion-hosted (Snegamook and Kanairiktok Bay) occurrences are not associated with the U-Pb-As-Mo signature. The large data scatter observed for the Moran Lake area is due to most of the data coming from the Moran Lake C Zone deposit (Fig. 6c). Distinctions between the Upper (basalt-hosted) and Lower C zones (sandstone-hosted) were not provided with the data.

Discussion

This study further confirms that Na and Na-Ca-Fe(Mg) metasomatism is regionally widespread throughout the CMB (Fig. 4b; 5a–f), even in areas such as the Two Time Trend (Snegamook and Two Time prospects) and Kanairiktok Bay, where it has not been previously identified or considered as a relatively minor alteration feature. The scale and distribution of Na metasomatism within the CMB is similar to that observed in the Mount Isa and Cloncurry districts, which include IOCG (e.g. Cloncurry district: Ernest Henry) and albitite-hosted uranium (e.g. Mount Isa district: Valhalla) deposits (e.g. Oliver et al., 2004; Williams et al., 2005). At the deposit-scale, this Na metasomatism is also comparable with that of the Southern Breccia Corridor, in the southern Great Bear magmatic zone (GBMZ; Montreuil et al. 2015).

PC1 scores are an effective proxy for lithology and alteration due to component loadings that separate elements with felsic (K, Rb, Th, Ba, La) and mafic (Fe, Ca, Mg, V, Co, Ni, Cr) affinities. The GSNL subset shows that basaltic rocks hosting the Moran Lake Upper C Zone, and felsic volcanic and intrusions from the Michelin, Jacques Lake, Snegamook, and Kanairiktok Bay deposits/areas correspond to opposite ends of the PC1 versus PC2 biplot (Fig. 6e). In the following discussion, hydrothermal alteration and other processes that overprint the primary composition of the rocks are described along with the remaining PC scores.

The PC2 and PC3 relate to at least two distinct uranium mineralization styles. Mineralized samples from the first style yield variable PC1 and positive PC2 scores (Fig. 6c). In these samples uranium concentrations weakly correlate with lead, which is expected given the radiogenic decay of uranium to lead. Minor decoupling of uranium from lead may have occurred after the primary uranium mineralization as a result of later re-mobilization triggered by metasomatic fluids. The lack of association between uranium and other elements in the CMB suggests that sodium, potassium, calcium, and/or iron metasomatism reflects a broader hydrothermal alteration process that impacts uranium-rich and unmineralized rocks. Figure 6f shows how Na- and Na-Ca-Fe-(Mg)-altered rocks have the largest uranium contents, but that barren samples (PC2 < 0) are also overprinted by these alteration types.

Samples from the Jacques Lake and Michelin deposits yield negative PC1 and generally positive PC2 scores (Fig. 6d–f). At these deposits, uranium-rich rocks are typically associated with Na- and Na-Ca-Fe(Mg)-alteration facies, as suggested by the inverse correlation between U and K (Fig. 6d–f). This indicates that uranium enrichment likely overprints potassic alteration and/or that uranium precipitation favoured rocks with lower potassium contents. Porosity formation during albitization (cf. Putnis and Austrheim, 2010) can make the intensely sodic-altered rocks ideal fluid pathways, but also mechanically weaken the rocks. Considering that albitites commonly form along fault zones, the combination of syn-metasomatic active faulting and post-metasomatic system fault reactivation thereby preferentially partition brittle deformation and brecciation to form albitite-hosted uranium mineralization where albitization and uranium mineralization occurred as two separate events (e.g. Southern Breccia Corridor, GBMZ; Montreuil et al., 2015; Potter et al., in press).

PC3 represents a useful proxy for distinguishing the second uranium mineralization style within specific areas of the CMB. For example, uranium-rich rocks at the Anna Lake deposit (Fig. 6a) yield negative PC3 scores and a U-Mo-As-Pb signature that is distinct from the Jacques Lake and Michelin deposits. Host rock from the Anna Lake deposit also yield weakly negative PC1 scores, which is consistent with their mafic-intermediate compositions (Fig. 6a, b). In the Moran Lake area

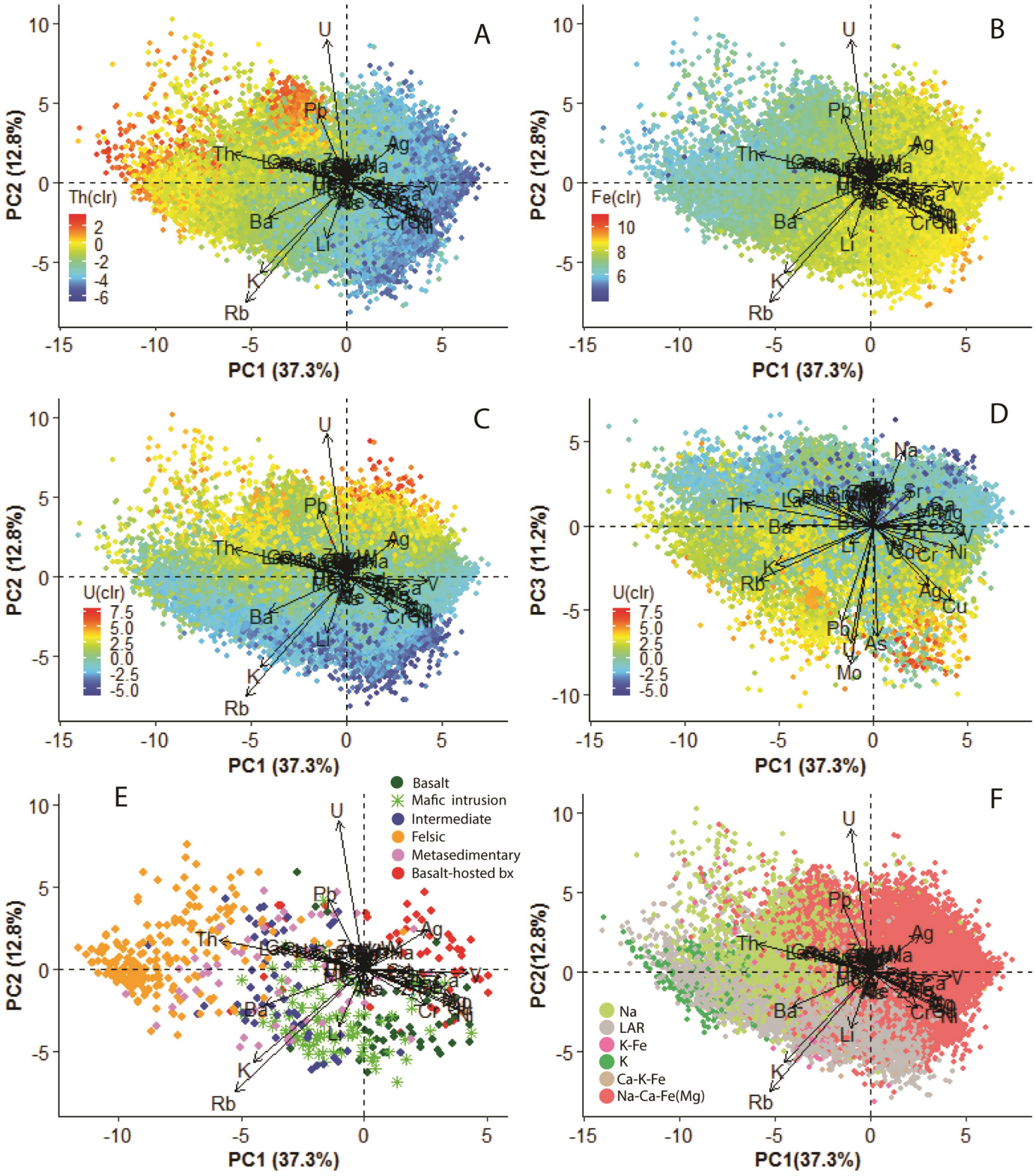

Figure 5.Classification of the CMBUG database on the Montreuil et al. (2013) iron oxide-copper-gold (IOCG) alteration discrimination plot for Moran Lake (a, b), Jacques Lake, Michelin (c, d) and Two Time-Snegamook (e, f). The left and right columns correspond with data from the NLAD (Si*) and GSNL (Si) subsets, respectively. Both subsets have similar distribution throughout the CMB.

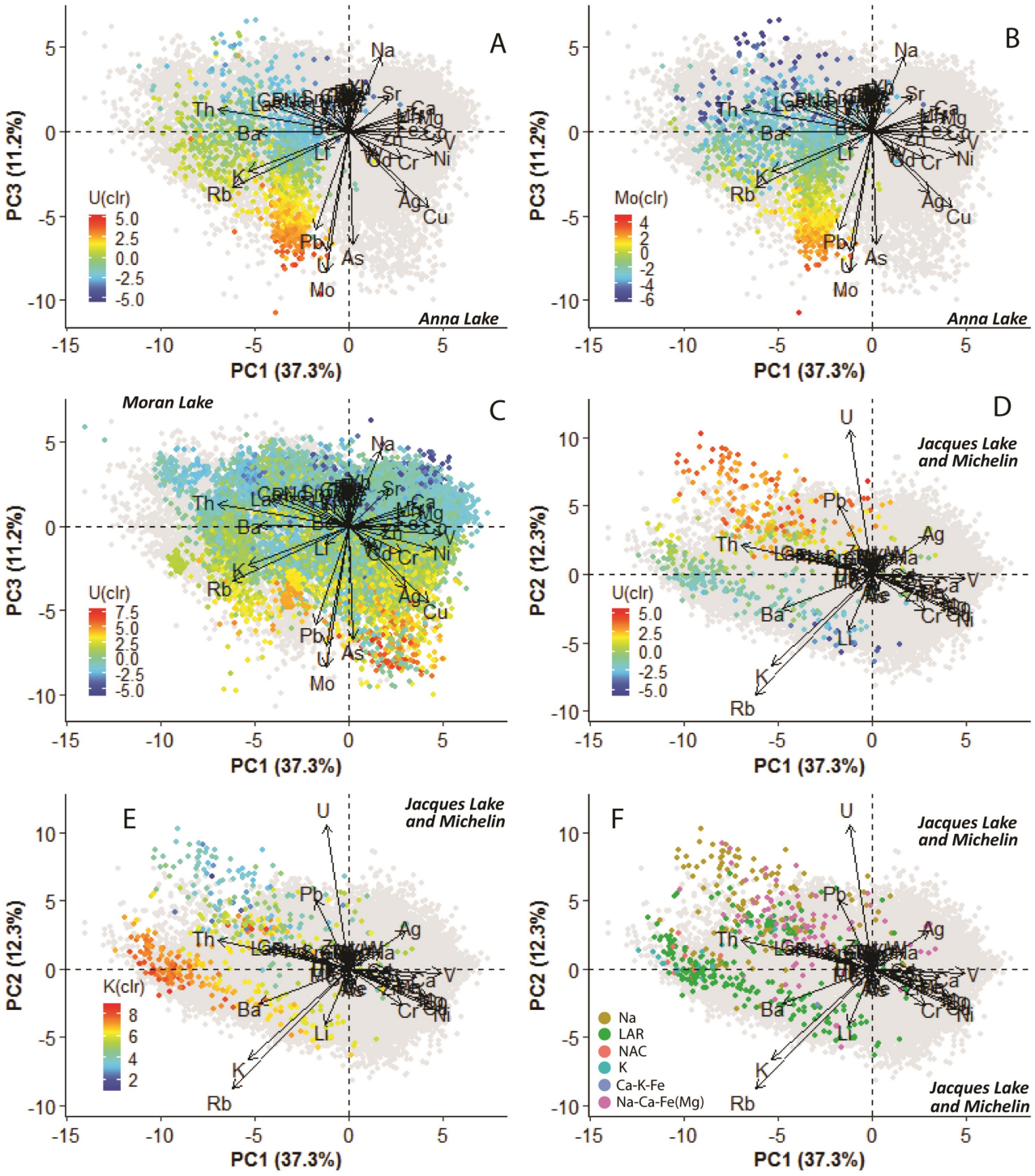

Figure 6. Principal component (PC) analysis on the Central Mineral Belt uranium geochemistry database (CMBUG). PC1 represents the largest source of variance and yields negative (K, Th, Ba) (a) and positive (Fe, V, Cr and Ni) (b) loadings that serve as a useful proxy for distinguishing rock types. PC2 (c) and PC3 (d) explain most of the uranium variability and point to at least two distinct styles of uranium mineralization. e) Data of the GSNL subset showing that primary lithology controls PC1 values. f) Classification of the CMBUG according to the Montreuil et al. (2013) alteration facies plot in PCA space. This plot shows that rocks with the highest uranium enrichments are sodic altered (Na or Na-Ca-Fe-(Mg)). However, this is not a systematic correlation as Na-Ca-Fe metasomatized rocks can also be barren. Abbreviations: bx = breccia; clr = center-log ratio transformed; LAR = least altered rocks.

(Fig. 6c), uranium-rich basaltic rocks of the Moran Lake Upper C Zone (PC1 approximately > 0) yield negative PC3 scores, suggesting a U-Mo-As association that is similar to the sedimentary-hosted and unconformity-related Moran Lake Lower C Zone deposit (PC1 approximately < 0) (Fig. 6c). These geochemical similarities may suggest that mineralization in the Moran Lake Group sediment-hosted occurrences resulted after remobilization of uranium from the underlying meta-basaltic and -pelitic packages of the Joe Pond Formation.

The Anna Lake argillite (Post Hill Group) and Moran Lake Upper C Zone basalt (Moran Lake Group) are roughly located at the same stratigraphic level. In fact, the Moran Lake Group basalt (Joe Pond Formation) overlies shale of the Warren Creek Formation, which is likely correlative with the Anna Lake argillite (Fig. 1b). The association between uranium, arsenic and molybdenum in these areas may either indicate (i) a synsedimentary origin of uranium (i.e. uranium-rich black shales) and local remobilization to upper stratigraphic levels (e.g. Joe Pond metabasalt) and/or (ii) the reducing argillitic and basaltic packages within the Moran Lake and Post Hill groups could have acted as redox traps for oxidizing uranium-rich fluids that equilibrated with these rocks.

Conclusions

The present study indicates that Na and Na-Ca-Fe-(Mg) metasomatism in the CMB is more pervasive and regionally widespread than previously thought. However, as noted elsewhere in other IOCG districts, alkali metasomatism is not directly associated with the uranium mineralization (e.g. Montreuil et al. 2015; Potter et al. in press). Thus, other second-order factors (e.g. structures, redox conditions, fluid-rock reactions) must control the precipitation of uranium ore.

Principal component analysis is a powerful approach for distinguishing primary host-rock compositions, even when such information was not available in the CMBUG, and provides evidence about the nature of uranium mineralization in the CMB. In the Jacques Lake and Michelin deposits, uranium mineralization occurs at the expense of potassium in Na- and Na-Ca-Fe-(Mg)-altered rocks. Conversely, in metamorphosed basalt-argillite-hosted systems (e.g. Moran Upper C zone and Anna Lake deposits), a correlation between uranium, arsenic and molybdenum may indicate: (i) a synsedimentary origin of uranium, which was followed by local remobilization to upper stratigraphic levels; and/or that (ii) argillitic and basaltic packages within the Moran Lake and Post Hill groups served as redox traps for oxidizing uranium-rich fluids that equilibrated with these rocks.

In summary, this work shows that, even in poorly characterized geochemical databases, the use of the IOCG discrimination-alteration diagram and multivariate statistical analysis enables: i) the identification of distinct lithologies; ii) the determination of alteration paths; and iii) speculatation about potential ore forming processes derived from specific element associations.

Acknowledgments

This report is a contribution to NRCan's Targeted Geoscience Initiative Program (TGI-5). Support for this study was provided through the Uranium-rich Mineralization Project's '*Activity U-2.1: Metal pathways and traps in polymetallic (U ± Fe, Cu, Au, REE) metasomatic ore systems project*'.

This report benefited from the review of Jennifer Smith, Mike Gadd and Neil Rogers.

References

Aitchison, J., 1986. The Statistical Analysis of Compositional Data; Chapman and Hall, London, United Kingdom, 302 p.

Acosta-Góngora, P., Duffett, C., Sparkes, G.W., and Potter, E.G., 2018. The Central Mineral Belt uranium geochemistry database; Geological Survey of Canada, Open File 8352.

Cadman, A.C., Heaman, L., Tarney, J., Wardle, R.J., and Krogh, T.E., 1993. U–Pb geochronology and geochemical variation within two Proterozoic mafic dyke swarms, Labrador; Canadian Journal of Earth Sciences, v. 30, p. 1490–1504.

Corriveau, L., 2017. Iron-oxide and alkali-calcic alteration ore systems and their polymetallic IOA, IOCG, skarn, albitite-hosted U±Au±Co, and affiliated deposits: A short course series. Part 1: Introduction; Geological Survey of Canada, Scientific Presentation 56, 80 p.

Corriveau, L., Williams, P., and Mumin, A.H., 2010. Alteration vectors to IOCG mineralization from unchartered terranes to deposits; *in* Exploring for Iron Oxide-Copper-Gold (Ag-Bi-Co-U) Deposits, Examples from Canada and Global Analogues, (ed.) L. Corriveau and A.H. Mumin; Geological Association of Canada, Short Course Notes 20, p. 89–110.

Corriveau, L., Montreuil, J.-F., and Potter, E.G., 2016. Alteration facies linkages among iron oxide-copper-gold, iron oxide-apatite, and affiliated deposits in the Great Bear magmatic zone, Northwest Territories, Canada; Economic Geology, v. 111, p. 2045–2072.

Corriveau, L., Potter, E.G., Acosta-Gongora, P., Blein, O., Montreuil, J.-F., De Toni, A.F., Day, W., Slack, J.F., Ayuso, R.A., and Hanes, R., 2017. Petrological mapping and chemical discrimination of alteration facies as vectors to IOA, IOCG, and affiliated deposits within Laurentia and beyond; *in* Proceedings of the 14th SGA Biennial Meeting, 20-23 August 2017, Québec, Quebec, p. 851–855.

Corriveau, L., Potter, E.G., Montreuil, J.-F., Blein, O., Ehrig, K., and De Toni, A., 2018. Iron-oxide and alkali-calcic alteration ore systems and their polymetallic IOA, IOCG, skarn, albitite-hosted U±Au±Co, and affiliated deposits: a short course series. Part 2: overview of deposit types, distribution, ages, settings, alteration facies, and ore deposit models; Geological Survey of Canada, Scientific Presentation 81.

Cuney, M., 2009. The extreme diversity of uranium deposits; Mineralium Deposita, v. 44, p. 3–9.

Cuney, M., Emetz, A., Mercadier, J., Mykchalov, V., Shunko,

V., and Yuslenko, A., 2012. Uranium deposits with Na-metasomatism from central Ukraine: A review of some of the major deposits and genetic constraints; Ore Geology Reviews, v. 44, p. 82–106.

Culshaw, N. and Ketchum, J., 1995. The Kaipokok zone of the Makkovik orogen – an early Proterozoic terrane boundary?; *in* Eastern Canada Shield Onshore-Offshore Transect (ECSOOT), Report of the 1994 Transect Meeting, (comp.) R.J. Wardle and J. Hall; University of British Columbia, Lithoprobe Secretariat, Lithoprobe Report 45, p. 7–21.

Ermanovics, I., 1993. Geology of Hopedale Block, southern Nain Province, and the adjacent Proterozoic terranes, Labrador, Newfoundland; Geological Survey of Canada, Memoir 431, 161 p.

Evans, D. 1980. Geology and petrochemistry of the Kitts and Michelin uranium deposits and related prospects, Central Mineral Belt, Labrador; Ph.D. thesis, Queen's University, Kingston, Ontario, 311 p.

Filzmoser, P., Hron, K., and Reimann, C., 2009. Univariate statistical analysis of environmental (compositional) data: Problems and possibilities; Science of the Total Environment, v. 407, p. 6100–6108.

Gandhi, S.S., Krogh, T.E., and Corfu, F., 1988. U–Pb zircon and titanite dates on two granitic intrusions of the Makkovik Orogen and a peralkaline granite of the Red Wine Intrusive Complex, central Labrador; Geological Association of Canada – Mineralogical Association of Canada – Canadian Society of Petroleum Geologists, Abstracts, v. 13, p. A42.

Gillies, S.L., Clarke, E.J., and Northcott, C., 2009. First, second, third, fourth, fifth and seventh year assessment report on geological, geochemical, geophysical, trenching and diamond drilling exploration for licences 9781M, 9783M, 10367M-10368M, 10715M-10720M, 10722M-10723M, 11395M, 11770M,11833M-11835M, 12616M-12618M, 13427M, 13634M-13635M and 14515M on claims in the Moran Lake-Otter Lake area, central Labrador, 2 reports; Newfoundland and Labrador Geological Survey, Assessment File13K/0313, 2723 p.

Gower, C.F., Flanagan, M.J., Kerr, A., and Bailey, D.G., 1982. Geology of the Kaipokok Bay–Big River area, Central Mineral Belt, Labrador; Government of Newfoundland and Labrador, Department of Mines and Energy, Mineral Development Division, Report 82-7, 77 p.

Hron, K., Templ, M., and Filzmoser, P., 2010. Imputation of missing values for compositional data using classical and robust methods; Computational Statistics & Data Analysis, v. 54, p. 3095–3107.

Hinchey, A.M., 2007. The Paleoproterozoic metavolcanic, metasedimentary and igneous rocks of the Aillik Domain, Makkovik Province, Labrador (NTS map area 13O/03); *in* Current Research; Newfoundland Department of Natural Resources, Geological Survey, Report 07-1, p. 25–44.

Hinchey, A.M. and LaFlamme, C., 2009. The Paleoproterozoic volcano-sedimentary rocks of the Aillik Group and associated plutonic suites of the Aillik domain, Makkovik Province, Labrador [NTS map area 13J/14]; *in* Current Research; Newfoundland Department of Natural Resources, Geological Survey, Report 09-1, p. 159–192.

Kerr, A., 1994. Early Proterozoic magmatic suites of the eastern Central Mineral Belt (Makkovik Province), Labrador: Geology, geochemistry and mineral potential; Government of Newfoundland and Labrador, Department of Mines and Energy, Geological Survey Branch, Report 94-03, 167 p.

Kerr, A. and Sparkes, G.W., 2009. Mineral commodities of Newfoundland and Labrador: Uranium; Geological Survey of Newfoundland and Labrador, Mineral Commodities Series, n. 5, 15 p.

Kerr, A., Ryan, B., Gower, C.F., and Wardle, R.J., 1996. The Makkovik Province: Extension of the Ketilidian Mobile Belt in mainland North America; *in* Precambrian Crustal Evolution in the North Atlantic Region, (ed.) T.S. Brewer; Geological Society of London, Special Publication 1112, p. 155–177.

Marten, B.E., 1977. The relationship between the Aillik Group and the Hopedale gneiss, Kaipokok Bay, Labrador; Ph.D. thesis, Memorial University of Newfoundland, St. John's, Newfoundland and Labrador, 389 p.

Montreuil, J.-F, Corriveau, L., and Grunsky, E.C., 2013. Compositional data analysis of hydrothermal alteration in IOCG systems, Great Bear magmatic zone, Canada: To each alteration type its own geochemical signature; Geochemistry: Exploration, Environment, Analysis, v. 13, p. 229–247.

Montreuil, J.-F., Corriveau, L., and Potter, E.G., 2015. Formation of albitite-hosted uranium within IOCG systems: the Southern Breccia, Great Bear magmatic zone, Northwest Territories, Canada; Mineralium Deposita, v. 50, p. 293–325.

Montreuil, J.-F., Potter, E.G., Corriveau, L., and Davis, W.J., 2016a. Element mobility patterns in magnetite-group IOCG systems, Northwest Territories, Canada; Ore Geology Reviews, v. 72, p. 562–584.

Montreuil, J.-F., Corriveau, L., Potter, E.G., and De Toni, A.F., 2016b. On the relation between alteration facies and metal endowment of iron oxide-alkali-altered systems, southern Great Bear magmatic zone (Canada); Economic Geology, v. 111, p. 2139–2168.

Oliver, N.H.S, Cleverley, J.S., Mark, G., Pollard, P.J., Fu, B., Marshall, L.J., Rubenach, M.J., Williams P.J., and Baker, T., 2004. The role of sodic alteration in the genesis of iron oxide-copper-gold deposits, eastern Mt Isa Block, Australia; Economic Geology, v. 99, p. 1145–1176.

Polito, P.A., Kyser, K.T., and Stanley, C., 2009. The Proterozoic, albitite-hosted, Valhalla uranium deposit, Queensland, Australia: a description of the alteration assemblage associated with uranium mineralisation in diamond drill hole V39; Mineralium Deposita, v. 44, p. 11–40.

Potter, E.G., Montreuil, J.-F., Corriveau, L., and Davis, W.J., in

press. The Southern Breccia metasomatic uranium system of the Great Bear magmatic zone, Canada: iron oxide-copper-gold (IOCG) and albitite-hosted uranium linkages; *in* Mineral Deposits: Origins and Exploration. (ed.) S. Decree; John Wiley and Sons Inc.

Putnis, A. and Austrheim, H., 2010. Fluid-induced processes: metasomatism and metamorphism; Geofluids, v. 10, p. 254–269.

R Core Team, 2018. R: A language and environment for statistical computer; R Foundation for Statistical Computer, Vienna, Austria. <https://www.r-project.org/> [accessed January 3, 2019]

Ryan, 1984. Regional geology of the central part of the Central Mineral Belt, Labrador; Government of Newfoundland and Labrador, Department of Mines and Energy, Mineral Development Division, Memoir 3, 185 p.

Ryan, A.B., Kay, A., and Ermanovics, I., 1983. The geology of the Makkovik Subprovince between Kaipokok Bay and Bay of Islands, Labrador; Government of Newfoundland and Labrador, Department of Mines and Energy, Mineral Development Division, Maps 83-38–83-41, scale 1:50 000.

Schärer, U., Krogh, T.E., Wardle, R.J., Ryan, B., and Gandhi, S.S., 1988. U-Pb ages of early to middle Proterozoic volcanism and metamorphism in the Makkovik Orogen, Labrador; Canadian Journal of Earth Sciences, v. 25, p. 1098–1107.

Sparkes, G.W., 2017. Uranium mineralization within the central mineral belt of Labrador: A summary of the diverse styles, settings and timing of mineralization; Government of Newfoundland and Labrador, Department of Natural Resources, Geological Survey, Open File LAB/1684, 198 p.

Sparkes, G.W., and Kerr, A., 2008. Diverse styles of uranium mineralization in the Central Mineral Belt of Labrador: an overview and preliminary discussion; *in* Current Research. Government of Newfoundland and Labrador Department of Natural Resources, Geological Survey, Report 08-1, p. 193–227.

Sparkes, G.W., Dunning, G.R., Fonkew, M., and Langille, A., 2016. Age constraints on the formation of iron oxide-rich hydrothermal breccias of the Moran Lake area: evidence for potential IOCG-style mineralization within the Central Mineral Belt of Labrador; *in* Current Research 2016; Newfoundland and Labrador Department of Natural Resources, Geological Survey Report 16-1, p. 71–90.

Thió-Henestrosa, S. and Martín-Fernández, J., 2005. Dealing with compositional data: the freeware CoDaPack; Mathematical Geosciences, v. 37, p.773–793

Thomas, A., 1981. Geology along the southwestern margin of the Central Mineral Belt, Labrador; Government of Newfoundland and Labrador, Department of Mines and Energy, Mineral Development Division, Report 81-4, 40 p.

Wardle, R.J, Gower, C.F., Ryan, B., Nunn, G.A.G., James, D.T., and Kerr, A., 1997. Geological map of Labrador; 1:1 million scale; Government of Newfoundland and Labrador, Department of Mines and Energy, Geological Survey, Map 97-07, scale 1:1 000 000.

Wilton, D.H.C., 1996. Metallogeny of the Central Mineral Belt and adjacent Archean basement, Labrador; Government of Newfoundland and Labrador, Department of Mines and Energy, Geological Survey, Mineral Resources Report 8, 178 p.

Williams, P.J., Barton, M.D., Johnson, D.A., Fontbote, L., De Haller, A., Mark, G., Oliver, N.H.S., and Marschik, R., 2005. Iron oxide-copper-gold deposits: geology, space-time distribution, and possible modes of origin; in 100th Anniversary Volume (1905-2005), (ed.) J.W. Hedenquist, J.F.H. Thompson, R.J. Goldfarb and J.P. Richards; Society of Economic Geologists, p. 371–405.

Volcanology, geochemistry and petrogenesis of the Expo-Raglan magmatic system in the eastern Cape Smith Belt, Nunavik, northern Quebec

D.J. McKevitt[1], C.M. Lesher[1] and M.G. Houlé[2, 1]

[1]*Mineral Exploration Research Centre, Harquail School of Earth Sciences, Laurentian University, 935 Ramsey Lake Road, Sudbury, Ontario P3E 2C6*

[2]*Geological Survey of Canada, 490 rue de la Couronne, Québec, Quebec G1K 9A9*

Abstract

The Paleoproterozoic volcano-sedimentary Cape Smith Belt in Nunavik (northern Quebec) contains a variety of mafic-ultramafic units classifiable by position in sequence, geometry, lithology, degree of differentiation and mineralization style. Non-differentiated to differentiated mafic flows/sills comprise the majority of the section as essentially non-mineralized massive-pillowed basalts, conformable gabbroic units and differentiated pyroxenite/gabbro/basalt flows. Differentiated mafic-ultramafic sills intrude sedimentary strata of the lower and upper Povungnituk Group and host reef-style PGE-(Cu)-(Ni) mineralization (e.g. Delta). Poorly differentiated ultramafic-mafic bladed dykes along the Expo Trend in the Povungnituk Group commonly host Cu-Ni-(PGE) sulphides along their margins (e.g. Expo-Ungava, Méquillon) and reach up to 35 weight % MgO in the most magnesian olivine pyroxenitic parts and up to 16 weight % MgO in their chilled melanogabbroic margins. Poorly differentiated ultramafic lava channels along the Raglan Trend at the base of the Chukotat Group host Ni-Cu-(PGE) mineralization at or near their lower contacts, and reach MgO contents of nearly 44 weight % in the most magnesian peridotitic parts and up to 20 weight % in their chilled pyroxenitic margins. Recent dating indicates a temporal overlap between the Expo and Raglan parts of the system; however, field and geochemical data suggest that the Expo dykes are derived from less magnesian magmas and formed mineralization with higher Cu/Ni ratios than the lava channels in in the Raglan Trend. The Expo dykes may have fed other parts of the system, but do not appear to represent direct feeders to the mineralized lava channels in the Raglan parts.

Introduction

The 1.8 to 1.9 Ga Cape Smith Belt in northern Quebec represents the northern segment of the approximately 2500 km-long Circum-Superior large igneous province that occurs along the margin of the Superior craton. The Southern Domain of the belt consists of a generally conformable sequence of volcanic and sedimentary strata that trend approximately east-west and dip and young northwards (Fig. 1; Lamothe, 2007). Previously, successive 'wedges' of sedimentary strata within the dominantly basaltic succession were all interpreted as thrust-faulted repetitions (e.g. St-Onge and Lucas, 1993); however, recent reassessment suggests there are fewer thrust-faulted contacts and more conformable/disconformable contacts (Lesher, 2007; Bleeker and Ames, 2017). A south-north section across the east-central Southern Domain includes siliciclastic rocks (siltstone to conglomerate) ± carbonate rocks and iron formation of the lowermost Povungnituk Group, tholeiitic basalt flows of the middle Povungnituk Group, locally sulphidic and graphitic siltstone/shale of the upper Povungnituk Group and olivine-phyric komatiitic, pyroxene-phyric komatiitic and plagioclase-phyric tholeiitic basalt of the Chukotat Group. Mafic to ultramafic sills, dykes, and flows occur throughout the Povungnituk-Chukotat stratigraphy and host several styles of magmatic sulphide mineralization.

Due to excellent exposure and low-grade metamorphism, the east-central region of the Cape Smith Belt is ideally suited to study the evolution of a mineralized Paleoproterozoic transcrustal magmatic system. The primary objective of this doctoral study, undertaken at Laurentian University, Sudbury, is to understand the temporal and petrogenetic relationships between various parts of this magmatic plumbing system by utilizing field mapping, geochronology and geochemistry. Poorly-understood or unstudied mafic-ultramafic units throughout the Southern Domain will be compared to previously studied units to determine key factors controlling mineralization and the prospectivity of different parts of the system (both laterally and stratigraphically).

This contribution focuses on the main characteristics of each type of mafic to ultramafic unit based on field investigations conducted in the summers of 2017 and 2018 in the east-central Cape Smith Belt. Previous regional-scale geological mapping has been checked and augmented by truck- and helicopter-supported visits to 537 localities spanning an approximately 60 x 35 km area, from which 348 rock samples have

Corresponding author: Dylan McKevitt (DMcKevitt@laurentian.ca)

McKevitt, D.J., Lesher, C.M. and Houlé, M.G., 2019. Volcanology, geochemistry and petrogenesis of the Expo-Raglan magmatic system in the eastern Cape Smith Belt, Nunavik, northern Quebec; *in* Targeted Geoscience Initiative: 2018 report of activities, (ed.) N. Rogers; Geological Survey of Canada, Open File 8549, p. 393–401. https://doi.org/10.4095/313674

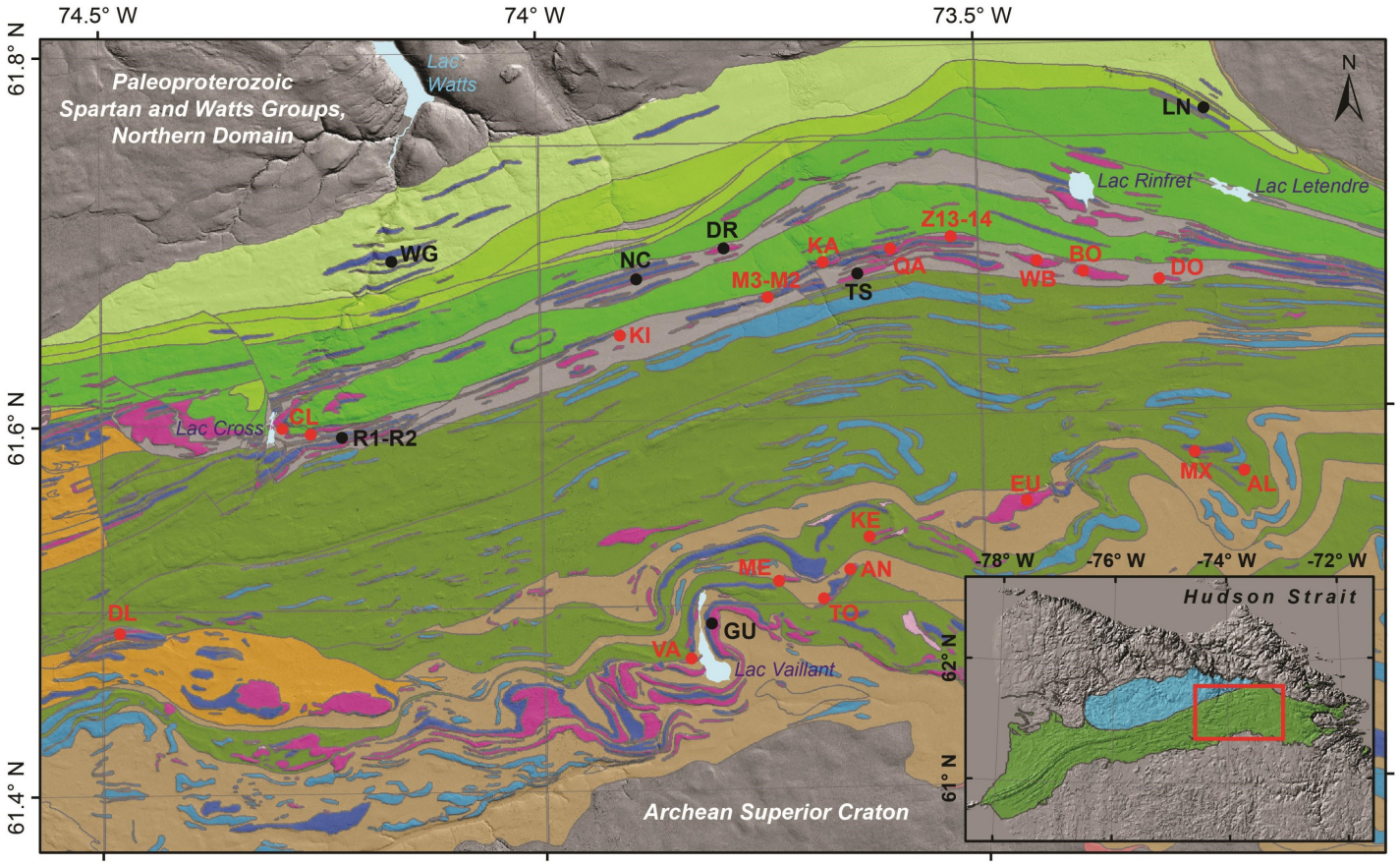

Paleoproterozoic Cape Smith Belt, Southern Domain

0 2.5 5 10 15 20 Kilometers

Chukotat Group
- dominantly plagioclase-phyric basalt
- dominantly pyroxene-phyric basalt
- dominantly olivine-phyric basalt

Esker Lake Suite
- gabbro
- pyroxenite
- peridotite
- dunite

Povungnituk Group
- Nuvilic Fm (sulfidic semipelite)
- Cécilia Fm (alkaline volcaniclastics)
- Beauparlant Fm (plagioclase-phyric basalt)
- Nituk Fm (siliciclastics, carbonates, iron fm)
- Kuuvvaluk Fm (quartzite, schist, iron fm)
- Bélanger Gabbroic Suite

Differentiated mafic-ultramafic sills
GU = Gulf sill
R1-R2 = Romeo 1&2 sills
NC = NC20C Gorge
DL = Delta sills

Poorly-differentiated ultramafic dikes
(Expo Trend)
VA = Vaillant
ME = Méquillon
AN = Annie
TO = Tootoo
KE = Kehoe
EU = Expo-Ungava
MX = Mesamax
AL = Allamaq

***RED** denotes mineralized units*

***BLACK** denotes essentially barren units*

Non-differentiated to differentiated mafic flows/sills
LN = Lac Letendre north
WG = Lac Watts gorge

Poorly-differentiated ultramafic flows/sills
DR = Deception Ridge
TS = T-Sill
(Raglan Trend)
CL = Cross Lake
KI = Kikialik
M3-M2 = Mine 3, Mine 2
KA = Katinniq
QA = Quakimajurq
Z13-14 = Zone 13-14
WB = West Boundary
BO = Boundary
DO = Donaldson

Figure 1. Regional geological map of the eastern Cape Smith Belt's Paleoproterozoic Southern Domain. Inset map shows Nunavik (northern Quebec), with the Cape Smith Belt coloured (Northern Domain = blue, Southern Domain = green) and the red rectangle outlining the geological map area. The four types of mafic-ultramafic units discussed in this report are shown; red symbols denote mineralized and black denotes essentially barren units. *See* Lamothe (2007) for descriptions of stratigraphic units. Geology *after* St-Onge et al. (2007). Underlying digital elevation model *from* Porter et al. (2018).

been collected for thin section and geochemical analysis. In particular, closely spaced samples were collected along transects across individual units in order to characterize them petrologically and geochemically. Additional data was compiled to provide coverage for the entire Cape Smith Belt, but with a primary focus on the east-central portion (Fig. 2).

Mafic to ultramafic units

The mafic-ultramafic units comprising most of the stratigraphy across the Povungnituk and Chukotat groups in the east-central Cape Smith Belt can be generally classified according to location in the sequence, geometry, lithology and degree of differentiation (including magnesian contents of cumulate parts and chilled margins), and style of magmatic sulphide mineralization. The intrusive versus extrusive nature of individual units is often difficult to determine in the absence of well exposed upper contacts (*see* Arndt et al., 2004), but can be inferred from cross-cutting relationships, inclusions of one unit in another, baked contacts or by comparing them with well exposed 'type units'. These representative type units include the Romeo 1 differentiated mafic-ultramafic sill near Cross Lake (Thibert, 1993; Picard et al., 1994), Expo-Méquillon poorly differentiated ultramafic bladed dykes (Mungall, 2007), the variably differentiated ultramafic channelized sheet flow at Cross Lake and the weakly differentiated lava channel at Katinniq (Lesher, 2007). Francis and Hynes (1979), Bédard et al. (1984) and Picard et al. (1990) provide a more comprehensive review of non-differentiated to differentiated mafic flows/sills in the Cape Smith Belt.

Non-differentiated to differentiated mafic flows/sills

Mafic volcanic flows occur throughout the Southern Domain of the Cape Smith Belt and comprise the majority of the stratigraphic sequence. The middle Povungnituk Group is dominated by 3 to 15 m thick massive-pillowed tholeiitic flows (typically plagioclase-phyric). Intimately associated, conformable, less than 50 m thick diabase/gabbroic horizons locally feature massive columnar jointing (Fig. 3) and have been interpreted as subvolcanic feeder sills to adjacent basalt flows (Beall, 1977; St-Onge and Lucas, 1993). Recent field observations show that some of these gabbroic units are thinner and less continuous than depicted on current regional geological maps, suggesting that, in some cases, they may actually be coarse-grained parts of thick lava flows (as also suggested by Mungall, 2007).

The Chukotat Group comprises pillowed, massive, and brecciated basalt flows ranging from komatiitic to tholeiitic upsection (Francis and Hynes, 1979; Bédard et al., 1984). The lower olivine-phyric and pyroxene-phyric members include massive, differentiated pyroxenite/gabbro/basalt flows/sills (Fig. 4) up to 80 m thick with columnar-jointed lower sections, exposed especially well along strike lengths of over 100 m along a gorge approximately 9 km south of Lac Watts and 4 km northwest of Lac Letendre (Fig. 1). Massive gabbroic units

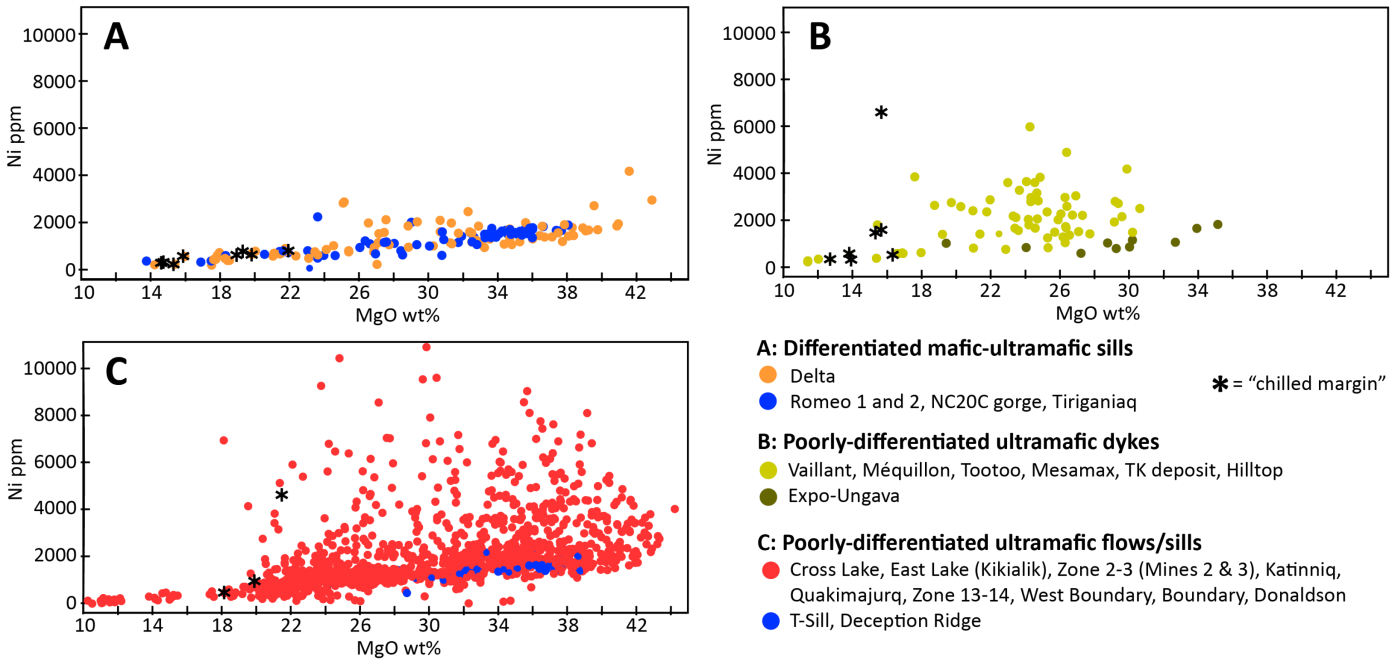

Figure 2. Binary plot of MgO vs. Ni of whole rock geochemical analyses of ultramafic rocks from three of the four types of mafic-ultramafic units discussed in this report. Data obtained from Ministère de l'Énergie et des Ressources naturelles du Québec (2018) and this study. Lithological classifications (including 'chilled margins') are as published. Only analyses containing less than or equal to 3 weight % S are shown.



Figure 3. Columnar-jointed, medium-grained microgabbro/diabase located conformably within middle Povungnituk Group basalts, about 8 km west of Donaldson. Columns are 2 to 3 m tall and approximately 0.5 m wide

occur in the upper, plagioclase-phyric member of the Chukotat Group, and are poorly and discontinuously exposed approximately 8 km south and 14 km east of Lac Watts.

Differentiated mafic-ultramafic sills

Well differentiated sills intrude the sedimentary sequences in the lowermost and uppermost Povungnituk Group (e.g. Gulf sill immediately east of Lac Vaillant; NC20C sill 3.5 km north of Kikialik; Romeo 1 and 2 sills 1–2 km southeast of Lac Cross; Fig.1). These units feature thin, basal pyroxenite margins, transitioning upwards into columnar-jointed olivine pyroxenite/peridotite that is sometimes in sharp, load-casted contact with overlying, layered mela- to leucogabbro (Fig. 5). Lithologies are consistently similar among these units, but the proportion of ultramafic to mafic zones is quite variable from one unit to the other. The ultramafic zone sometimes shows an upward progression of increasing size and decreasing abundance of clinopyroxene oikocrysts. Thin, pyroxenitic upper margins are normally sheared and only rarely exposed. Underlying and overlying sedimentary rocks, where exposed, are hornfelsed and may occur locally as rafted blocks within the uppermost gabbro. The most magnesian olivine pyroxenitic parts contain up to 38 weight% MgO and the chilled melagabbroic margins up to 19 weight % MgO (Fig. 2a).



Figure 4. A stratigraphically conformable 25 m thick differentiated ultramafic-mafic unit in the middle Chukotat Group, 9 km south of Lac Watts. Photograph was taken looking west. The lower fine-grained brownish coloured (olivine) pyroxenitic part (to left) narrows to the west and east. The overlying gabbroic part (to right) transitions upwards from medium-grained to fine-grained massive basalt. Green backpack (0.5 m tall) outlined at the centre for scale.

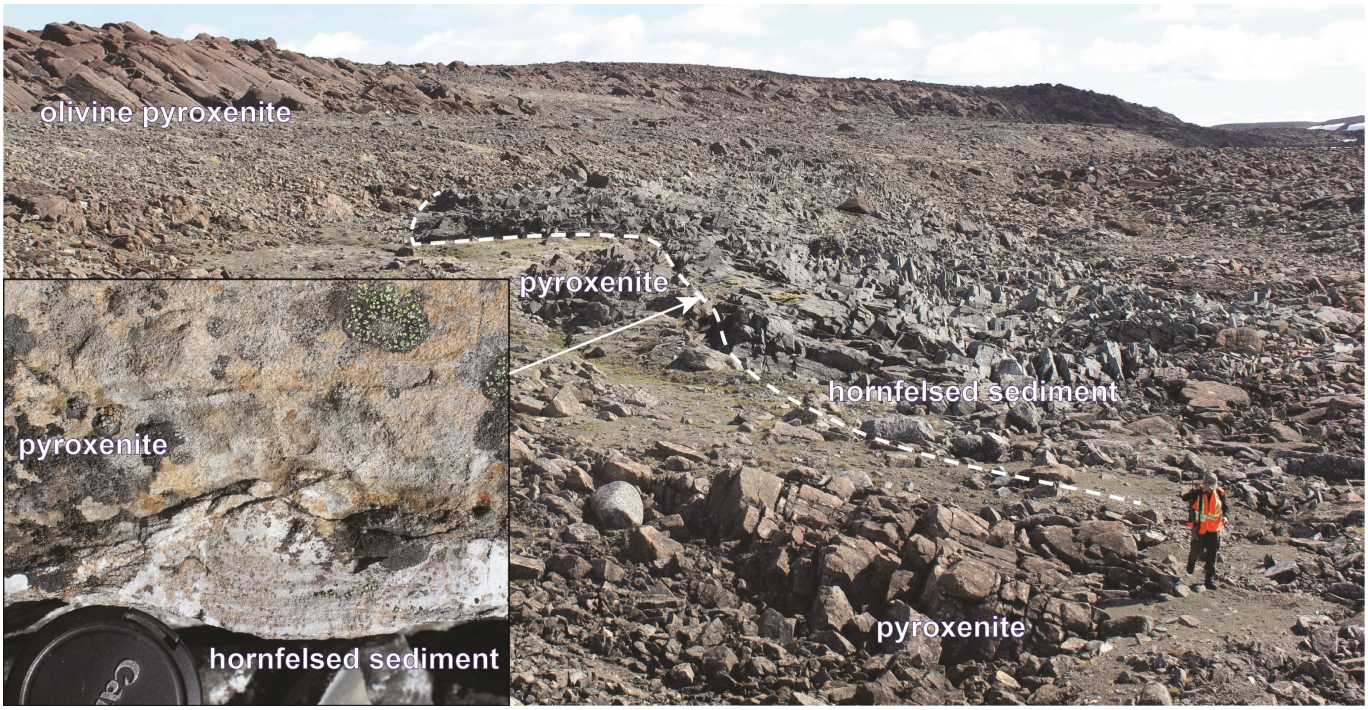

Figure 5. Base of the Romeo 1 sill, facing east. From right to left (upsection): light grey, hornfelsed semipelitic sedimentary rock; blocky, orange-weathering pyroxenitic chill margin; reddish brown, massive columnar-jointed olivine pyroxenite. White dashed line delineates lower sedimentary rock-pyroxenite contact (and approximates concealed contact). Inset shows a close-up of the chilled margin (lens cover is 6 cm in diameter).

Poorly differentiated ultramafic dykes

Ultramafic bladed dykes cross-cut stratigraphy along the southern 'Expo Trend' (e.g. Vaillant, Méquillon, Expo-Ungava, and Mesamax in Fig. 1: Mungall, 2007; Barnes and Mungall, 2018). They are typically 50 to 350 m thick (Expo-Ungava reaches 900 m wide) with 5 to 20 m thick melagabbroic margins and interiors of pyroxenite to olivine pyroxenite often in complex, uneven contact with each other and with localized magmatic layering (Fig. 6, 7). Where exposed, adjacent sedimentary rocks are hornfelsed. The most magnesian olivine pyroxenitic interiors are approximately 31 weight % MgO (with the exception of Expo-Ungava, which reaches up to 35 weight % MgO) and chilled melagabbroic margins are up to 16 weight % MgO (Fig. 2b).

Poorly differentiated ultramafic flows/sills

Ultramafic lava channels, invasive (downward burrowing) flows, and channelized sheet flows characterize the 'Raglan Trend' horizon at the Povungnituk Group – Chukotat Group transition (e.g. Cross Lake, Katinniq, Donaldson; Fig. 1, 8). They are composed predominantly of mesocumulate peridotite (often columnar jointed in the lower parts) with lesser olivine pyroxenite with 1 to 2 m thick lower pyroxenite margins and 2 to 5 m thick upper pyroxenite-basalt flow-top breccia. Channelized sheet flows may grade laterally into differentiated olivine pyroxenite and gabbro. Lower contacts with hornfelsed sedimentary rock are irregular due to thermomechanical erosion. Upper contacts with komatiitic basalt are conformable and lack evidence of contact metamorphism, although some of the overlying rocks are hydrothermally altered, consistent with the lava channels taking longer to cool. The most magnesian peridotitic parts are up to 44 weight % MgO, and chilled margins are up to 20 weight % MgO (Fig. 2c). The peridotitic parts are characterized by the presence of ubiquitous fine disseminated Fe-Ni-Cu sulphides.

Broadly similar units occur stratigraphically below the Povungnituk – Chukotat transition within upper Povungnituk sedimentary rocks, both along the Raglan Trend (e.g. T-Sill) and north of it in the Northern Permits (e.g. Deception Ridge and units south of Lac Rinfret; Fig. 1). They consist of olivine pyroxenite-peridotite and often exhibit columnar jointing. The most magnesian parts are up to 40 weight % MgO (Fig. 2c) and are distinguished from the mineralized units in the Raglan Trend by the absence of fine disseminated Fe-Ni-Cu sulphides. It is not yet clear whether they are sills or flows.

Mineralization

The middle and upper parts of the Povungnituk Group contain bladed olivine pyroxenite ± melagabbro dykes with Cu-Ni-(PGE) mineralization along their sides and keels (e.g. Expo-Méquillon: Mungall, 2007). Differentiated mafic-ultramafic



Figure 6. Looking south at the margin of the Annie-Tootoo dyke. Olivine pyroxenite (brownish coloured) transitions to melagabbroic margins (dark grey) downslope. The tundra (top of photo) covers middle Povungnituk Group pillowed basalt and sedimentary rock.

(gabbro-olivine pyroxenite) sills intrude all parts of the Povungnituk Group, some of which locally contain stratiform PGE-(Cu)-(Ni) mineralization (e.g. Delta: Giovenazzo, 1991). Weakly differentiated lava channels and the channelized parts of sheet flows at the base of the Chukotat Group contain Ni-Cu-(PGE) mineralization at or near their lower contacts (e.g. Raglan deposits: Lesher, 2007).



Figure 7. Complex magmatic layering in the internal olivine pyroxenite part of the Méquillon dyke. Note the pyroxene oikocrysts standing in relief. Lens cap is 6 cm in diameter.

Discussion

Early workers suggested that various components of the Expo-Raglan magmatic plumbing system were petrogenetically related (e.g. Francis and Hynes, 1979; Francis et al., 1981, 1983; Bédard et al., 1984; Giovenazzo et al., 1989). Based on a date from gabbroic units at Expo-Ungava (1882.7 ± 1.3 Ma: Randall, 2005), Mungall (2007) suggested that the units in the Raglan Trend, Chukotat Group, and Expo-Ungava Trend are part of the same magmatic system and should be considered as a single magmatic suite (model 1 in Fig. 9). New radiometric U-Pb dating has been conducted under the TGI program on several units along the Raglan Trend including a 'hanging-wall' gabbro (1883.0 ± 1.7 Ma) near Katinniq, a 'footwall' gabbro (1882.1 ± 2.0 Ma), and a differentiated gabbro sill at Cross Lake (1881.5 ± 0.9 Ma); ages that overlap with those for the Expo part of the system (Fig. 9; Bleeker and Ames, 2017; Bleeker and Kamo, 2018).

Some of the ultramafic sills below the Raglan Trend have weighted average MgO contents greater than their chilled margins (e.g. Bravo: Barnes and Giovennazo, 1990; Méquillon: Tremblay, 1990), indicating that they contain up to 40% excess olivine, which is consistent with them being dynamic feeder sills (Lesher, 2007). However, other sills have weighted average compositions similar to their chilled margins (e.g. Romeo 1: Thibert, 1993), suggesting that they did not accumulate significant amounts of olivine and that they represent simple (non-dynamic) sills rather than subvolcanic feeders (Lesher, 2007).

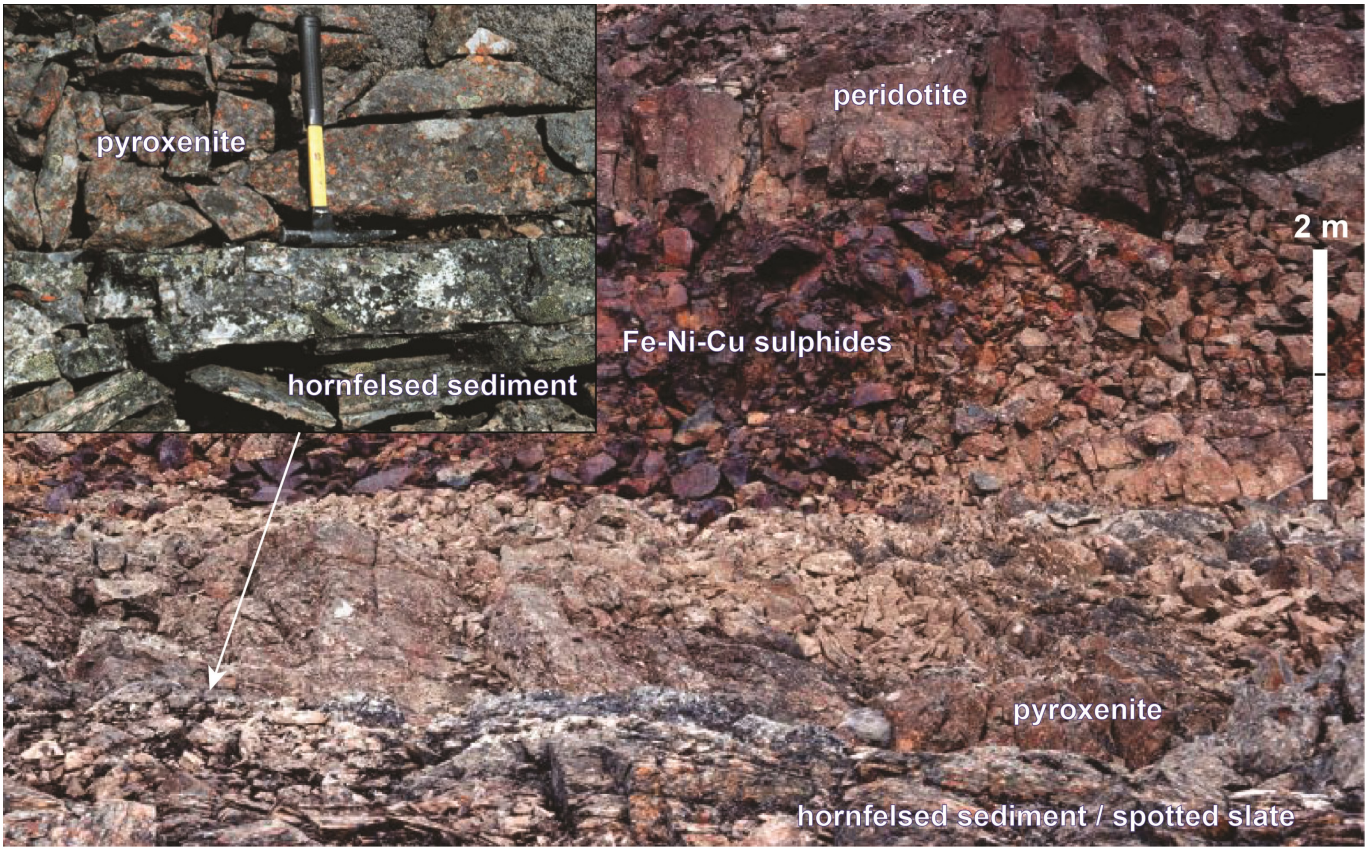

Figure 8. Lower contact of the Katinniq ultramafic complex with underlying hornfelsed sedimentary rock. Nickel-copper sulphide mineralization is localized in embayments where ultramafic lava flows have thermomechanically eroded down into uppermost Povungnituk Group sedimentary rock or gabbroic sills. Note columnar-jointed peridotite at the top of the photo. Inset is a close-up of the pyroxenitic chill margin (hammer for scale). Images *from* Lesher (2007) figures 14D and 19A.

Based upon available geochemical data (Fig. 2) and our recent field observations, the bladed dykes in the Expo-Ungava part of the system appear to be derived from less magnesian magmas (≤16 weight % based on the melagabbroic chilled margins) than the Raglan Trend units (≤20 weight % based on the pyroxenitic chilled margins) and may not represent direct feeders to lava channels and channelized sheet flows in the Raglan parts of the system (model 2 in Fig. 9). Ongoing geochemical, petrological, and geochronological analyses will test alternative relationships between bladed dykes, sills and lava flows to reveal the timing and distribution of this transcrustal magmatic plumbing system.

Acknowledgments

This report is a contribution to NRCan's Targeted Geoscience Initiative Program (TGI). Support for this study was provided through the Ni-Cr-PGE Systems Project's '*Activity NC-1.1: Extent, origin, and deposit-scale controls of the 1883 Ma Circum-Superior large igneous province, northern Manitoba, Ontario, Quebec, Nunavut, and Labrador'*.

We sincerely thank all who make this project possible, and who helped make this a safe, successful field season. Special thanks go to Glencore and the Raglan Mine exploration team (including Mathieu Landry, Adam White, François Baillargeon, François Gagnon, Jeremy Kilner, Benoit Soucy de Jocas, Neil Bradbury, Joe McLeod and Daryl Ball) for many years of consistent and friendly support through (in part) facilitating logistics, accommodation, training, and helpful discussions. Canadian Royalties Inc. (Denis Doucet and Michael Li) and the Nunavik Nickel Project security staff (Guy Chamard and Jean-Christophe Marceau) and geology exploration team (including Michel Cormier, Maxim Boisvert and Yueshi Lei) for continuing support in organizing training, logistics, access to data and property, and helpful discussions. The Geological Survey of Canada for financial and logistical support through TGI-5. Metal Earth (Laurentian University / Harquail School of Earth Sciences / Mineral Exploration Research Centre) for financial support. Wouter Bleeker (GSC) for joining us in the field and offering support and helpful geological and scientific insights. The helicopter pilot (Christophe Vani) and engineer of Nunavik Rotors, and Gardaworld guards (André Richer, Stéphane Ca-

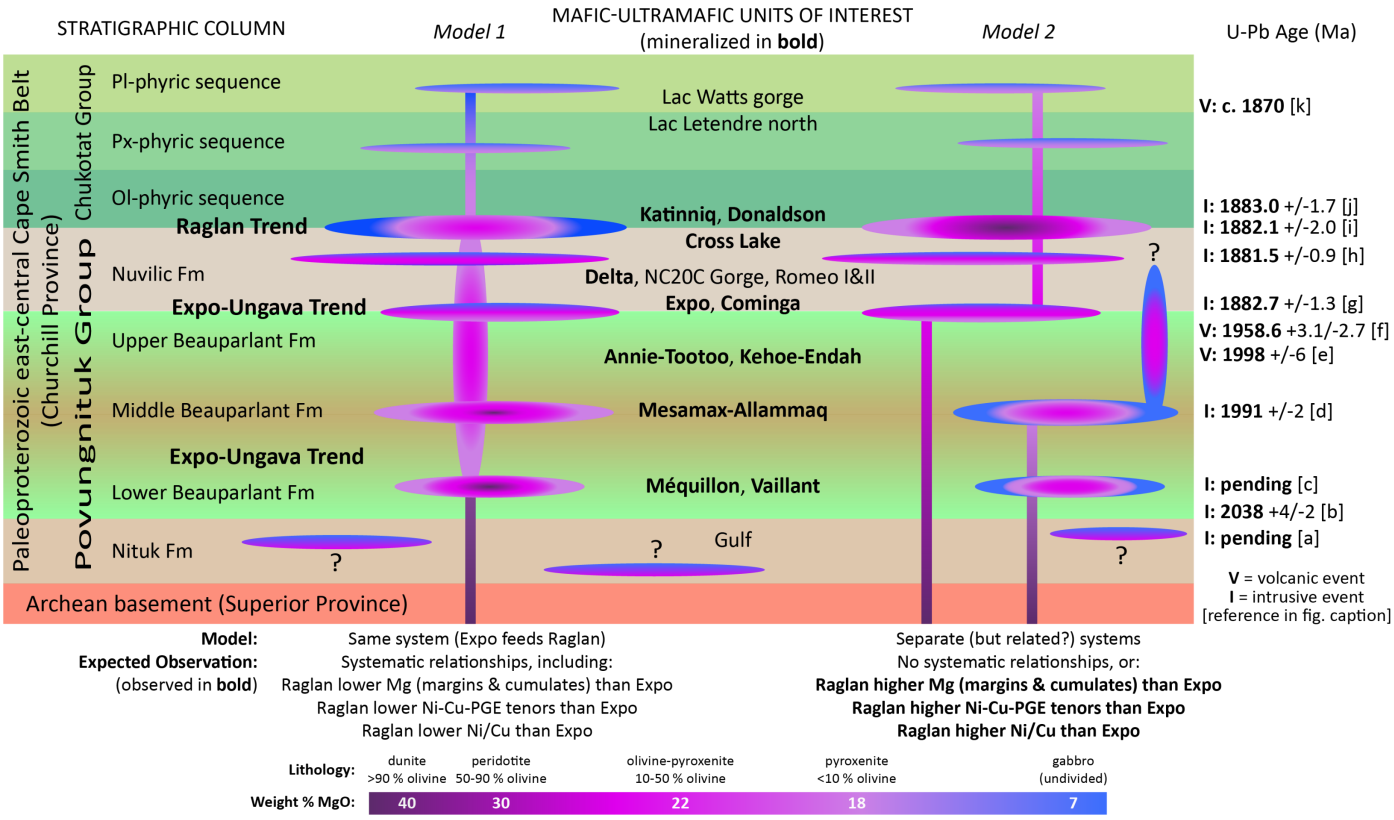

Figure 9. Schematic diagram showing two generalized models for the Expo-Raglan magmatic plumbing system. Select, representative units are placed in their approximate stratigraphic positions based upon field observations and current geological maps. Stratigraphic nomenclature is after Lamothe (2007). *See* Figure 1 for locations of units. U-Pb zircon/baddeleyite ages are shown in their approximate stratigraphic positions, and represent the most recent, lowest-error radiometric dates available for particular stratigraphic levels. Descriptions include [a] Gulf differentiated sill (this study, analysis pending); [b] Korak gabbro sill (Machado et al., 1993); [c] Méquillon dyke (this study, analysis pending); [d] granodiorite intrusion in pillowed basalts (Machado et al., 1993); [e] subvolcanic gabbroic unit (Kastek et al., 2018); [f] rhyolite near the top of the basalt sequence (Parrish, 1989); [g] vari-textured melagabbro from Expo-Ungava intrusion (Randall, 2005); [h] gabbro sill near Cross Lake, [i] Katinniq 'footwall' gabbro sill, [j] Katinniq 'hanging-wall' gabbro (Bleeker and Kamo, 2018); and [k] subvolcanic gabbroic unit (St-Onge et al., 1992).

drin, Eric Létourneau) who ensured our safe travel to and from field sites and security while in the field. S. Michel (M.Sc. candidate, Laurentian University) provided excellent field assistance. A. Morin, P. Brouillette, and F. Aucoin are gratefully acknowledged for thorough GIS support throughout the course of this research activity. This report benefited from the review of Ernst Schetselaar, Sébastien Castonguay and Neil Rogers. Metal Earth Contribution number MERC-ME-2018-101.

References

Arndt, N.T., Lesher, C.M., Houlé, M.G., Lewin, E., and Lacaze, Y., 2004. Intrusion and crystallization of a spinifex-textured komatiite sill in Dundonald Township, Ontario; Journal of Petrology, v. 45, p. 2555–2571.

Barnes, S.J. and Mungall, J.E., 2018. Blade-shaped dikes and nickel sulfide deposits: a model for the emplacement of ore-bearing small intrusions; Economic Geology, v. 113, p. 789–798.

Barnes, S.-J. and Giovenazzo, D., 1990. Platinum-group elements in the Bravo intrusion, Cape Smith Fold Belt, northern Québec; Economic Geology, v. 85, p. 1269–1272.

Beall, G.H., 1977. Final report on Cross Lake and Laflamme Lake areas; Ministère des Richesses naturelles du Québec; DP-460, 79 p.

Bédard, J.H., Francis, D.M., and Hynes, A.J., 1984. Fractionation in the feeder system at a Proterozoic rifted margin; Canadian Journal of Earth Sciences, v. 21, p. 489–499.

Bleeker, W. and Ames, D.E., 2017. System-scale and deposit-scale controls on Ni-Cu-PGE mineralization in cratonic areas and their margins; *in* Targeted Geoscience Initiative,

2016 Report of Activities, (ed.) N. Rogers; Geological Survey of Canada, Open File 8199, p. 47–53.

Bleeker, W. and Kamo, S.L., 2018. Extent, origin, and deposit-scale controls of the 1883 Ma Circum-Superior large igneous province, northern Manitoba, Ontario, Quebec, Nunavut and Labrador; *in* Targeted Geoscience Initiative: 2017 Report of Activities, Volume 2, (ed.) N. Rogers; Geological Survey of Canada, Open File 8373, p. 5–14.

Francis, D.M. and Hynes, A.J., 1979. Komatiite-derived tholeiites in the Proterozoic of New Québec; Earth and Planetary Science Letters, v. 44, p. 473–481.

Francis, D.M., Hynes, A.J., Ludden, J.N., and Bédard, J., 1981. Crystal fractionation and partial melting in the petrogenesis of a Proterozoic high-MgO volcanic suite, Ungava, Québec; Contributions to Mineralogy and Petrology, v. 78, p. 27–36.

Francis, D., Ludden, J. and Hynes, A., 1983. Magma evolution in a Proterozoic rifting environment; Journal of Petrology, v. 24, part 4, p. 556–582.

Giovenazzo, D., 1991. Géologie et caractéristiques géochimiques des minéralisations Ni-Cu-EGP de la région de Delta, Ceinture de Cape-Smith, Nouveau-Québec; PhD thesis, l'Université de Québec à Chicoutimi, Chicoutimi, Quebec, 238 p.

Giovenazzo D., Picard, C., and Guha, J., 1989. Tectonic setting of Ni-Cu-PGE deposits in the central part of the Cape Smith Belt; Geoscience Canada, v. 16, p. 134–136.

Kastek, N., Ernst, R.E., Cousens, B.L., Kamo, S.L., Bleeker, W., Söderlund, U. Baragar, W.R.A., , and Sylvester, P., 2018. U-Pb Geochronology and Geochemistry of the Povungnituk Group of the Cape Smith Belt: Part of a Craton-Scale Circa 2.0 Ga Minto-Povungnituk Large Igneous Province, Northern Superior Craton; Lithos, v. 320–321, p. 315–331.

Lamothe, D., 2007. Lexicon stratigraphique de l'Orogène de l'Ungava; Ressources naturelles et Faune Québec, DV 2007 -03, 63 p.

Lesher, C.M., 2007. Ni-Cu-(PGE) Deposits in the Raglan Area, Cape Smith Belt, New Québec; *in* Mineral Deposits of Canada: A Synthesis of Major Deposit-Types, District Metallogeny, the Evolution of Geological Provinces, and Exploration Methods, (ed.) W.D. Goodfellow; Geological Association of Canada, Mineral Deposits Division, Special Publication No. 5, p. 351–386.

Machado, N., David, J., Scott, D.J., Lamothe, D., Philippe, S., and Gariépy, C., 1993. U-Pb geochronology of the western Cape Smith Belt, Canada: new insights on the age of initial rifting and arc magmatism; Precambrian Research, v. 63, p. 211–223.

Ministère de l'Énergie et des Ressources naturelles du Québec (2018). SIGÉOM: Système d'information géominière of Québec; Ministère de l'Énergie et des Ressources naturelles du Québec. <http://sigeom.mines.gouv.qc.ca> [accessed December 28. 2018]

Mungall, J.E., 2007. Crustal contamination of picritic magmas during transport through dikes: the Expo Intrusive Suite, Cape Smith Fold Belt, New Québec; Journal of Petrology, v. 48, p. 1021–1039.

Parrish, R.R., 1989. U-Pb geochronology of the Cape Smith Belt and Sugluk block, northern Quebec; Geoscience Canada, v. 16, p. 126–130.

Picard, C., Lamothe, D., Piboule, M., and Oliver, R., 1990. Magmatic and geotectonic evolution of a Proterozoic oceanic basin system: the Cape Smith Thrust-Fold Belt (New-Quebec); Precambrian Research, v. 47, p. 223-249.

Picard, C., Giovenazzo, D., Thibert, F., and Tremblay, C., 1994. Petrographie, geochimie et gitologie des roches plutoniques ultramafiques et mafiques proterozoiques de la partie centrale de la Fosse de l'Ungava: implications sur la distribution des elements du groupe des platinoides; Ministère des Richesses naturelles du Quebec, MB 94-30, 402 p.

Porter, C., Morin, P., Howat, I., Noh, M.-J., Bates, B., Peterman, K., Keesey, S., Schlenk, M., Gardiner, J., Tomko, K., Willis, M., Kelleher, C., Cloutier, M., Husby, E., Foga, S., Nakamura, H., Platson, M., Wethington, M., Jr., Williamson, C., Bauer, Gregory, Enos, J., Arnold, G., Kramer, W., Becker, P., Doshi, A., D'Souza, C., Cummens, P., Laurier, F., Bojesen, M., 2018. ArcticDEM, Harvard Dataverse, V1; Polar Geospatial Center, University of Minnesota. <https://www.pgc.umn.edu/data/arcticdem/> [accessed January, 2018]

Randall, W., 2005. U-Pb geochronology of the Expo Igneous Suite, Cape Smith Belt, and the Kyak Bay intrusion, New Québec Orogen: implications for the tectonic evolution of the Trans-Hudson Orogen; M.Sc. thesis, University of Toronto, Toronto, Ontario, 51 p.

St-Onge, M.R. and Lucas, S.B., 1993. Geology of the eastern Cape Smith belt: parts of the Kangiqsujuaq, cratère du Nouveau-Québec, and lacs Nuvilik map areas, Quebec; Geological Survey of Canada, Memoir 438, 110 p.

St-Onge, M.R., Lamothe, D., Henderson, I., and Ford, A., 2007. Digital geoscience atlas of the Cape Smith Belt and adjacent domains, Ungava Peninsula, Quebec–Nunavut; Geological Survey of Canada, Open File 5117.

St-Onge, M.R., Lucas, S.B., and Parrish, R.R., 1992. Terrane accretion in the internal zone of the Ungava orogeny, northern Quebec. Part 1: Tectonostratigraphic assemblages and their tectonic implications; Canadian Journal of Earth Sciences, v. 29, p. 746–764.

Thibert, F., 1993. Petrogenese du filon-couche differencie Romeo I situe dans la cienture plissee-faillee du Cape Smith, Nouveau-Quebec; M.Sc. thesis, Univeriste de Montreal, Montreal, Quebec, 145 p.

Tremblay, C., 1990. Les éléments du groupe du platine dans le dyke de Mequillon, Ceinture de Cape Smith, Nouveau-Québec: M.Sc. thesis, Université du Québec à Chicoutimi, Chicoutimi, Quebec, 76 p.

Ni-Cu-PGE potential of the Nipissing sills as part of the ca. 2.2 Ga Ungava large igneous province

S. Davey[1, 2], W. Bleeker[2], S. Kamo[3], D. Davis[3], M. Easton[4] and R.H. Sutcliffe[5]

[1]*Department of Earth Science, Carleton University, Ottawa, Ontario K1N5B6*

[2]*Geological Survey of Canada, 601 Booth Street, Ottawa, Ontario K1A 0E8*

[3]*Jack Satterly Geochronology Lab, Department of Earth Sciences, University of Toronto, 22 Russell Street, Toronto, Ontario M5S 3B1*

[4]*Ontario Geological Survey, 933 Ramsey Lake Road, Sudbury, Ontario P3E 6B5*

[5]*Pavey Ark Minerals Inc., 100 Broad Leaf Crescent, Ancaster, Ontario L9G 3R8*

Abstract

This report summarizes mineralization associated with the Nipissing Diabase sills in the broader Sudbury area and evaluates the geochemical link between these sills and potential feeder dykes that are part of the broader ca. 2.2 Ga Ungava large igneous province. New whole-rock major and trace element data are presented for the Nipissing sills and these are combined with previously published data. Sm-Nd isotope data are presented for the Maguire, Senneterre and Klotz dykes, and the Triangle Mountain sill, providing key constraints on their magmatic sources and history of crustal assimilation. To help constrain the temporal evolution of the magmatic system, a new U-Pb baddeleyite age has been determined for the Triangle Mountain sill at 2216.5 ± 2.1 Ma. We also report a previously obtained, precise, U-Pb zircon age for the Ni-Cu-PGE mineralized Shakespeare intrusion at 2217.0 +1.7/-1.5 Ma. Together, whole-rock major and trace elements, Sm-Nd isotopes, and U-Pb geochronology are used to gain a more complete picture of how the mineralized components of the ca. 2.2 Ga Ungava large igneous province were generated.

Introduction

The ca. 2.2 Ga Ungava large igneous province (LIP) includes six discrete mafic dyke swarms and subswarms and one major sill province (Fig. 1; Ernst and Bleeker, 2010). Converging on the northeastern margin of the Superior craton, the Senneterre (2214 Ma), Maguire (2229 Ma), and Klotz (2209 Ma) dykes define a radiating dyke swarm pattern that can be followed laterally for over 1000 km (Buchan et al., 1998; Ernst and Bleeker, 2010). The Anuc (2220 Ma), Couture (2199 Ma), and Kogaluk Bay (2212 Ma) dykes are also recognized as part of the Ungava LIP but are volumetrically minor and localised within the Ungava Peninsula of northern Quebec (Table 1; Maurice et al., 2009; Ernst and Bleeker, 2010; Maurice and Francis, 2010). The Nipissing Diabase sills are the most distal component of the Ungava LIP, and are considered to have been fed by the Senneterre dykes because of their contemporaneity (Buchan et al., 1998). The Nipissing sills reach as far as 1500 km from the inferred magmatic centre. The sills are hosted within the Paleoproterozoic 2.5 to 2.3 Ga Huronian Supergroup (Bennett et al., 1991; Young et al., 2001) and are also found at or near the unconformity between the Huronian Supergroup and Archean basement rocks.

Long recognized as viable targets for magmatic Ni-Cu-PGE deposits, among other commodities such as hydrothermal Co-Ag-Au veins, the sills are also proposed to have contributed to the metal endowment of the Sudbury Igneous Complex (Fig. 2, Table 2; Card and Pattison, 1973; Lightfoot and Naldrett, 1996a; James et al., 2002; Sproule et al., 2007; Potter et al., 2010). Here we compile and summarize present knowledge on mineralization associated with the Nipissing sills, including a brief overview of the recently mined Shakespeare deposit (Sproule et al., 2007; Dasti, 2014). We include a refined U-Pb baddeleyite age of one Nipissing sill (Triangle Mountain), for which previously published results (Noble and Lightfoot, 1992) suggested a younger magmatic pulse. The new data for the Triangle Mountain sill suggests an age of ca. 2216 to 2217 Ma, in line with most other U-Pb ages of Nipissing sills and allowing for a single, short-lived, magmatic event. We also report a previously obtained but unpublished U-Pb zircon age for the mineralized Shakespeare intrusion at 2217.0 +1.7/-1.5 Ma, which supports the conclusion of a short-lived magmatic event at ca. 2217 Ma. This zircon-based age is arguably the most precise among a dozen or so ages for Nipissing sills and related units (most of which are relying on baddeleyite) and could be further refined using modern chemical abrasion methods. New geochemical data for the Nipissing sills (Easton and Hrominchuk, 2002; Easton, 2006, 2007; Easton and Sykora, 2007; Gordon, 2016; Jobin-Bevans, 2016) and bedrock mapping in the Sudbury area make it possible to refine decades-old genetic models (e.g. Lightfoot and Naldrett, 1996a; Jobin-Bevans, 2004) for this mineralized magmatic system. Although both the Nipissing sills and potential feeder dykes have been the subject of more recent local studies (e.g. Sproule et al., 2007; Maurice

Corresponding author: Sarah Davey (sarah.davey@carleton.ca)

Davey, S., Bleeker, W., Kamo, S., Davis, D., Easton, M., and Sutcliffe, R.H., 2019. Ni-Cu-PGE potential of the Nipissing sills as part of the ca. 2.2 Ga Ungava large igneous province; *in* Targeted Geoscience Initiative: 2018 report of activities, (ed.) N. Rogers; Geological Survey of Canada, Open File 8549, p. 403–419. https://doi.org/10.4095/313675

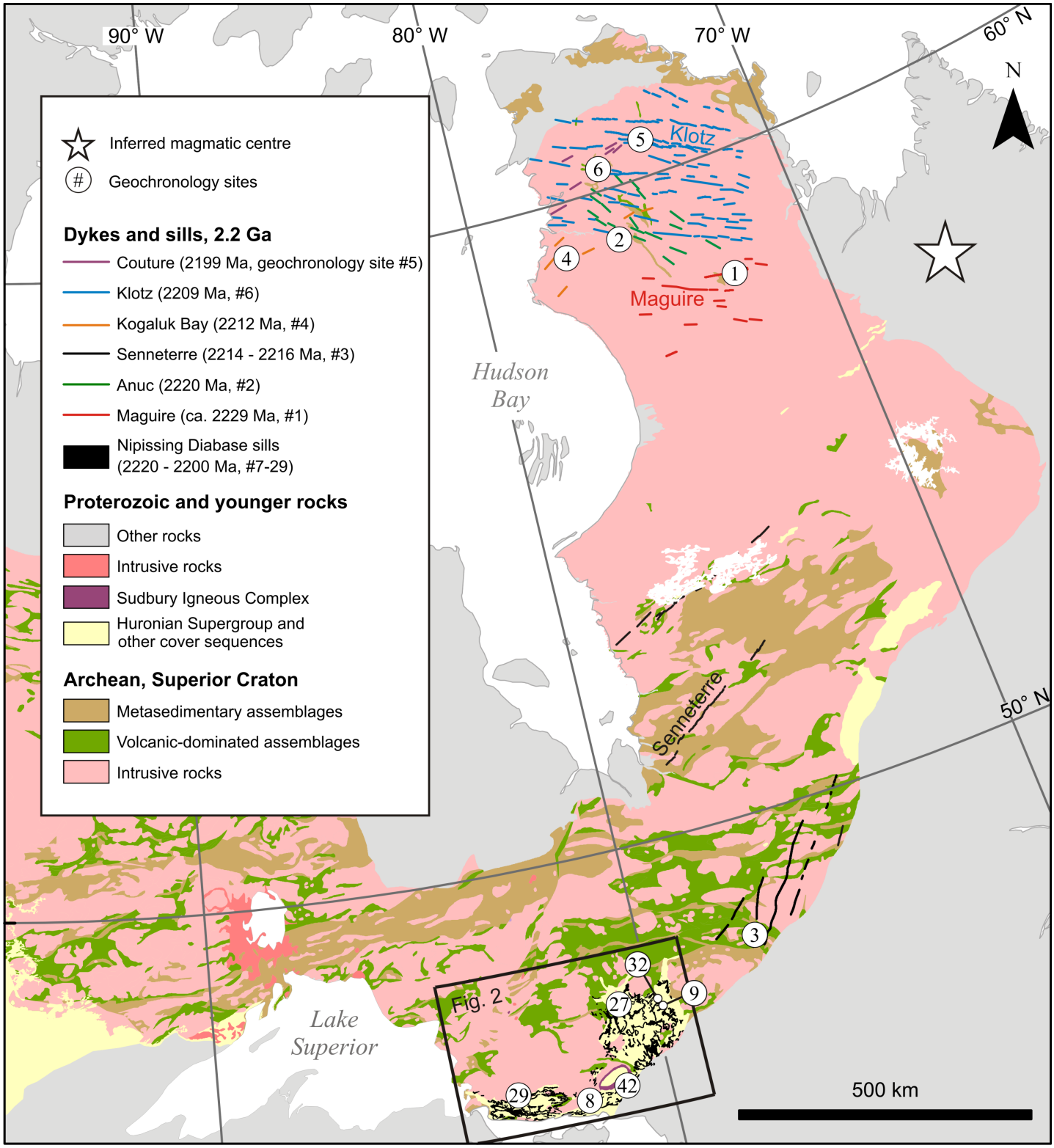

Figure 1. Map of the ca. 2.2 Ga Ungava large igneous province. Dykes and sills are *compiled from* Buchan and Ernst (2004), Maurice and Francis (2010) and the Ontario Geological Survey (2011). Geology of the Superior craton is *modified from* Goodfellow (2007). Locations of published ages relevant to this study are indicated by white circles with numbers that correspond to Table 1. Black box indicates the extent of Figure 2.

Table 1. Summary of U-Pb geochronology on mafic dykes and sills related to the Ungava large igneous province (LIP). Numbers correspond to Figure 1.

#	Locality	Longitude (W)	Latitude (N)	Method	Age (Ma)	References
	Dykes					
1	Maguire (site 71)	72.540	58.090	U-Pb, multigrain bd, ID-TIMS	2229 +35/-20	Buchan et al., 1998
2	Anuc	75.5151	59.1853	U-Pb, multigrain bd, ID-TIMS	2220 ± 1	Maurice et al., 2009
3	Senneterre (site 30)	77.36	48.19	U-Pb, single/multigrain bd, ID-TIMS	2214 ± 12.4; 2216 +8/-4	Buchan et al.,1993; 1996
4	Kogaluk Bay	77.2326	59.1407	U-Pb, multigrain bd, ID-TIMS	2212 ± 3.5	Maurice et al., 2009
5	Couture	75.4836	60.3462	U-Pb, multigrain bd, ID-TIMS	2199 ± 5	Maurice et al., 2009
6	Klotz (site 73)	73.89	60.58	U-Pb, multigrain bd and abraded zr, ID-TIMS	2209.7 ± 0.8	Buchan et al., 1998
	Nipissing Sills					
8	Shakespeare[1]	81.8327	46.3500	U-Pb abraded zr, TIMS	2217 ± 1.7	Davis, 2002a, b; this study
9	Triangle Mtn. (BNB-16-031)	79.8578	47.5365	U-Pb, multigrain bd, zr, TIMS	2209.6 ± 3.5; 2216 ± 2.1	Noble & Lightfoot, 1992; this study
27	Castle Mine	80.7412	47.6793	U-Pb, multigrain bd, ID-TIMS	2219.4 +3.6/-3.5	Corfu & Andrews, 1986
29	Morin-Otter (12CM228)	83.5200	46.5800	U-Pb, multigrain bd, TIMS	2214 ± 7.7	Gordon, 2016
32	Kerns	79.8418	47.5934	U-Pb, multigrain bd, ID-TIMS	2217.2 ± 4	Noble & Lightfoot, 1992
42	Clover leaf (BNB-13-048A)	80.9692	46.4373	U-Pb, zr and bd, CA-ID-TIMS	2215 ± 1 (minimum)	Bleeker et al., 2015

Notes:
Coordinates in WGS1984
CA-ID-TIMS – chemical abrasion isotope dilution thermal ionization mass spectrometry; ID-TIMS – isotope dilution thermal ionization mass spectrometry; TIMS – thermal ionization mass spectrometry; bd – baddeleyite; zr – zircon.
[1]Approximate location of the West Pit at the Shakespeare property (not an exact sample location).

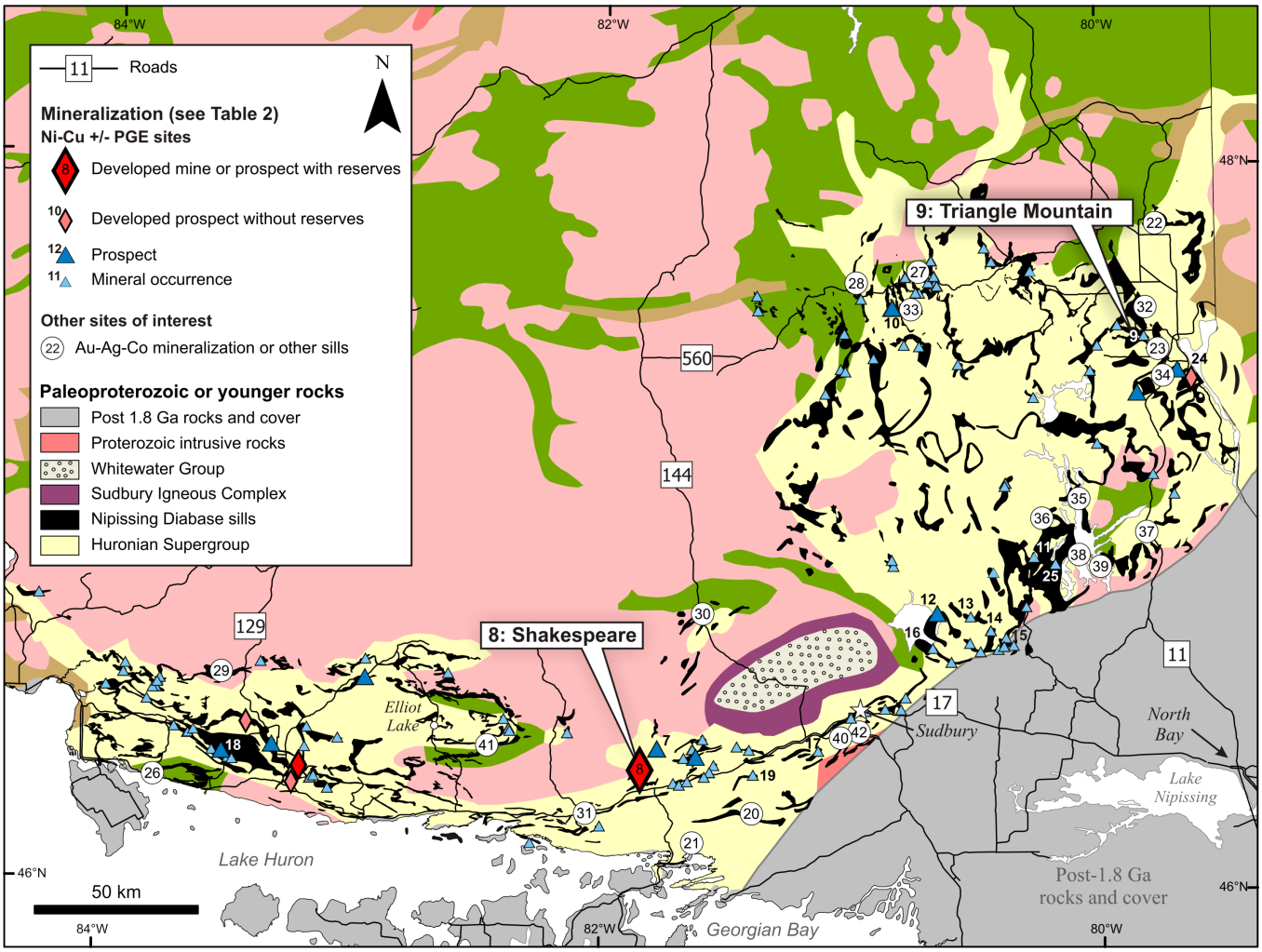

Figure 2. Distribution of the Nipissing Diabase sills highlighting the locations of the Shakespeare intrusion (#8) and Triangle Mountain (#9) sill (*modified from* Ontario Geological Survey, 2011). Numbered symbols correspond to Table 2. Locations of Ni-Cu±PGE developed mines, prospects, and mineral reserves from Ontario Geological Survey (2018). Geology of the Superior craton is *modified from* Goodfellow (2007).

Table 2. Summary of Nipissing sills discussed in literature with comments on Ni-Cu-PGE mineralization. Numbers correspond to Figure 2.

#	Locality	Longitude (W)	Latitude (N)	Mineralization comments[1]	References
	Mineralized Nipissing sills, Ni-Cu +/- PGE				
7	Big Swan	81.7667	46.4000	Ni-Cu-PGE occurrence/prospect	Turcott, 2002; Sproule et al., 2007
8	Shakespeare	81.8327	46.3500	Ni-Cu-PGE deposit	Sproule et al., 2007; Dasti, 2014
9	Triangle Mtn. (BNB-16-031)	79.8578	47.5365	Cu, Ni-Co, Ag occurrences	Lightfoot & Noble, 1992; this study
10	Milner Lake	80.8155	47.6243	Developed Ag prospect (no reserves); Ni-Cu-Co prospects/occurrences	Conrod, 1989; Lightfoot & Naldrett, 1996a, b
11	Emerald Lake	80.2263	46.9250	Cu occurrence	Lightfoot & Naldrett, 1996a, b
12	Wanapitei Lake	80.6762	46.7619	Ni-Cu-PGE prospect, Ag-Au and Au-Cu-Ni prospect	Rousell et al., 1988; Lightfoot & Naldrett, 1996a, b
13	Kukagami Lake/ Kelly	80.5035	46.7435	Ni-Cu-PGE and Au-Cu vein occurrence	Lightfoot et al., 1993; Lightfoot & Naldrett, 1996a, b; Sproule et al., 2007
14	Davis-Kelly	80.4556	46.7065	Ni-Cu-PGE and Au-Cu occurrence; Au prospect	Sproule et al., 2007
15	Janes	80.4063	46.6780	Occurrence Ni-Cu-PGE	Sproule et al., 2007
16	Bonanza Lake	80.7168	46.6740	Past producing Au mine (no reserves), occurrences Au, Ni-Cu	Conrod, 1989; Lightfoot & Naldrett, 1996a, b
17	Makada Lake	81.1475	46.3766	Occurrence Ni-Cu	Sproule et al., 2007
18	Basswood Lake	83.4403	46.3649	Occurrence/prospect Cu	Lightfoot et al., 1993; Lightfoot & Naldrett, 1996a, b
19	Louis Lake	81.3969	46.3156	Occurrence Ni-Cu	Sproule et al., 2007
20	Lac Panache	81.4105	46.2167	Occurrence Cu-Ni	Sproule et al., 2007
21	Casson Lake	81.5865	46.1504	Cu-Ni-Cr-(PGE) occurrence	Sproule et al., 2007
	Mineralized Nipissing sills, Ag-Co veins				
22	Englehart	79.7600	47.8343	Ag +/- Co-Cu-Au-Zn-Pb vein prospect/occurrence	Buchan et al., 1994; Lightfoot & Naldrett, 1996a, b
23	Portage Bay	79.7541	47.4887	Co-Ag vein occurrence	Conrod, 1989; Lightfoot & Naldrett, 1996a, b
24	Cross Lake	79.6418	47.4265	Past producing Cu (vein) mine (no reserves), Cu +/- Ni-Au vein	Conrod, 1989; Lightfoot & Naldrett, 1996a, b
25	Skunk Lake	80.1698	46.8990	Cu occurrence in quartz-carbonate veins	Simony, 1964; Lightfoot & Naldrett, 1996a, b
26	Bruce mines	83.7808	46.2926	Past producing mine Cu +/- Au-Ag vein (no reserves)	Lightfoot et al., 1993; Lightfoot & Naldrett, 1996a, b
27	Castle Mine/Miller lake	80.7412	47.6793	Past producing Ag +/- Ni-Co-Cu-Bi-Pb mine (no reserves)	Corfu & Andrews, 1986; Andrews et al., 1986; Lightfoot & Naldrett, 1996a, b
28	Duncan Lake	80.9810	47.6746	Ag-Au occurrence	Conrod, 1989; Lightfoot & Naldrett, 1996a, b
29	Morin-Otter (12CM228)	83.5217	46.5877	Ni-Co-Cu-Ag +/- Bi-Au vein prospect	Gordon, 2016
	Other sills				
30	HWY 144 (BNB-16-030)	81.5969	46.7621		Bleeker, work in progress, 2018
31	May Township (BNB-17-039)	82.0683	46.2170		Bleeker, work in progress, 2018
32	Kerns	79.8418	47.5934		Lightfoot & Noble, 1992; Lightfoot & Naldrett, 1996a, b
33	Beaton Bay	80.7909	47.6193		Conrod, 1989; Lightfoot & Naldrett, 1996a, b
34	Sharp Lake dyke (BNB-16-032)	79.7359	47.4149		This study
35	Slide Rock	80.0831	47.0775		Lightfoot & Naldrett, 1996a, b
36	Obabika Lake	80.2321	47.0248		Simony, 1964; Lightfoot & Naldrett, 1996a, b
37	Herridge Lake (BNB-16-033)	79.8099	46.9854		This study
38	Narrows Island	80.0884	46.9144		Simony, 1964; Lightfoot & Naldrett, 1996a, b
39	High Rock	80.0249	46.8990		Lightfoot & Naldrett, 1996a, b
40	Morin-Otter (BNB-16-029)	81.0440	46.4205		This study
41	Elliot Lake	82.4544	46.3934		Lightfoot et al., 1993
42	Clover leaf (BNB-16-028)	80.9700	46.4372		Bleeker et al., 2015

Notes:
Coordinates in WGS1984.
[1]Mineralization information from Ontario Geological Survey (2018).

and Francis, 2010), their genetic connection has not yet been tested through geochemistry nor has the overall magmatic system been considered in its entirety for the genesis and targeting of Ni-Cu-PGE mineralization.

Key scientific questions and progress

This study aims to conduct a survey of mineralization associated with the Nipissing sills, leading to a magmatic province-wide genetic model. In the process, we will address several questions about: a) the mineralization of the Nipissing sills in the Sudbury area; and b) genetic connections to the broader ca. 2.2 Ga Ungava LIP. Specific questions are:

i) Do detailed geochemical data allow the genetic link between the Senneterre and Maguire dykes and the Nipissing sills, as proposed by Buchan et al. (1998)?

ii) Relevant to the source of sulphur, is the negative εNd signature of the Nipissing sills reported by Lightfoot and Naldrett (1996a) exclusively a result of in situ crustal as-

similation, or was this signature acquired, at least partially, 'up stream' in the overall magmatic system, prior to final emplacement?

iii) Using geochemical approaches for evaluating metallogenic potential and generation of LIPs (e.g. Pearce, 2008, 2017; Jowitt and Ernst, 2013) combined with geochronology, can we identify new patterns in the geochemistry that may aid in the regional targeting of the Nipissing sills?

Characterization of the Nipissing Diabase sills

The Nipissing sills were emplaced between ca. 2220 Ma and ca. 2210 Ma and are exposed from across the Ontario-Quebec border in the east to Sault Ste-Marie in the west, over an extent of more than 400 km. Sills are generally (sub) concordant to bedding of the Huronian Supergroup or follow the unconformity between the Archean basement and overlying sediments (e.g. Fig. 3; Corfu and Andrews, 1986; Noble and Lightfoot, 1992; Buchan et al., 1993, 1996; Lightfoot et al., 1993; Bleeker et al., 2015). Less often, sills or sheets may be observed crosscutting Archean basement or stepping across Huronian stratigraphy (Lightfoot et al., 1993).

Geometric and petrological characteristics of the Nipissing sills vary between localities (Hriskevich, 1968; Conrod, 1989; Lightfoot et al., 1993). Intrusive bodies vary in thickness from tens to hundreds of metres and in strike length from one to ten kilometres or more. They vary in texture from homogeneous and undifferentiated lithologies to differentiated bodies with distinct lithological units (Lightfoot et al., 1993; Lightfoot and Naldrett, 1996a). Commonly, differentiated sills include bounding units with upper and lower chilled margins of diabase and quartz diabase (Conrod, 1989; Lightfoot et al., 1993; Lightfoot and Naldrett, 1996a). Overlying basal units, a typical differentiation series evolves from hypersthene gabbro to gabbronorite, all of which is capped by a pegmatoidal varitextured gabbro (Conrod, 1989; Lightfoot et al., 1993). In these upper units, angular to subangular rafts of host rock (e.g. Lorrain or Gowganda formations) and autoliths or xenoliths of diorite are common (Conrod, 1989; Lightfoot et al., 1993).

The differentiation series of the Nipissing sills and their geochemical evolution is attributed to coupled fractional crystallization and assimilation processes (Lightfoot and Naldrett, 1989, 1996a). The major element chemistry of the Nipissing sills varies with the degree of differentiation. Chilled margins and bounding quartz diabase units have major element chemistry typical of tholeiitic basalt (Lightfoot and Naldrett, 1989, 1996a, b; Lightfoot et al., 1993). In contrast, the upper differentiated units are characterized by more felsic and calc-alkaline signatures (Lightfoot et al., 1993). The sills are enriched in light rare earth elements (LREE) and large ion lithophile elements (LILE), and are depleted in Nb, TiO_2 and P_2O_5, with respect to primitive mantle (Lightfoot et al., 1993).

Lightfoot and Naldrett (1996a) conducted a Sm-Nd isotopic study across several differentiated sills (e.g. Kerns, Basswood Lake, Emerald Lake, Obabika, and Portage Bay) to better constrain the influence of assimilation of host rock on the overall composition of the Nipissing sills. Since the distinct lithological units within any given sill do not plot on a single isochron, and the most evolved lithologies trend towards host-rock signatures (Lorrain and Gowganda formations), it was concluded that the more evolved magmas were contaminated by in situ crustal assimilation (Lightfoot and Naldrett, 1989; Lightfoot and Naldrett, 1996a).

Geochemistry of the feeder systems

The geochemistry of Paleoproterozoic mafic dykes (2.5–2.0 Ga) of the Ungava Peninsula has been characterized using whole-rock major and trace element geochemistry by Maurice and Francis (2010). Their work included (but was not limited to) the Maguire, Anuc, Kogaluk Bay, Klotz, and Couture dyke swarms. Three distinct geochemical groups were recognized, including the (1) high iron-titanium, (2) low iron-titanium, and (3) low REE groups. These groups were identified based on abundances of Fe_2O_3 and TiO_2 weight % while tracking relationships with Fe, Ti and Al to Mg, and comparing relative enrichment of cations such as Na and trace element ratios, including Ti/V (Maurice and Francis, 2010). These three geochemical groups are not limited to particular dyke swarms or trends, and no secular evolution related to geochemistry has been recognized. Instead, the geochemical groups are found across various dyke swarms of different ages and trends (Maurice et al., 2009; Maurice and Francis, 2010).

The high iron-titanium group is defined by greater than 14 weight % Fe_2O_3, greater than 1.4 weight % TiO_2, and proportionally higher Na and Ti/V ratios (Maurice and Francis, 2010). There are two subgroups within the high iron-titanium group. These are distinguished by the relative proportion of Al cations; split below (low aluminium) and above (high aluminium) 12 weight % Al_2O_3. The low aluminium subgroup is further distinguished by higher CaO/Al_2O_3 ratios and steeper heavy rare earth element (HREE) slopes on a multi-element plot. The high iron-titanium (low aluminium) subgroup includes all samples belonging to the Kogaluk Bay and Anuc swarms as well as members of the Maguire swarm. The high iron-titanium (high aluminium) subgroup does not include any dykes dated at 2.2 Ga but includes numerous unclassified dykes. A peridotite and pyroxenite mantle that incorporated crustal and alkaline components is the proposed source for this geochemical group (Maurice and Francis, 2010).

Characteristics distinguishing the low iron-titanium group are greater than 11 weight % Fe_2O_3 and less than 0.8 weight % TiO_2, positive correlations between Fe, Ti and Al to Mg, low Ti/V values, and relatively high Mg with respect to SiO_2 (Maurice and Francis, 2010). Due to their characteristically low HREE and high field strength element (HFSE) abundances, a depleted refractory harzburgitic source is proposed for this geochemical signature (Maurice and Francis, 2010). This geochemical group includes members of the Maguire dykes.

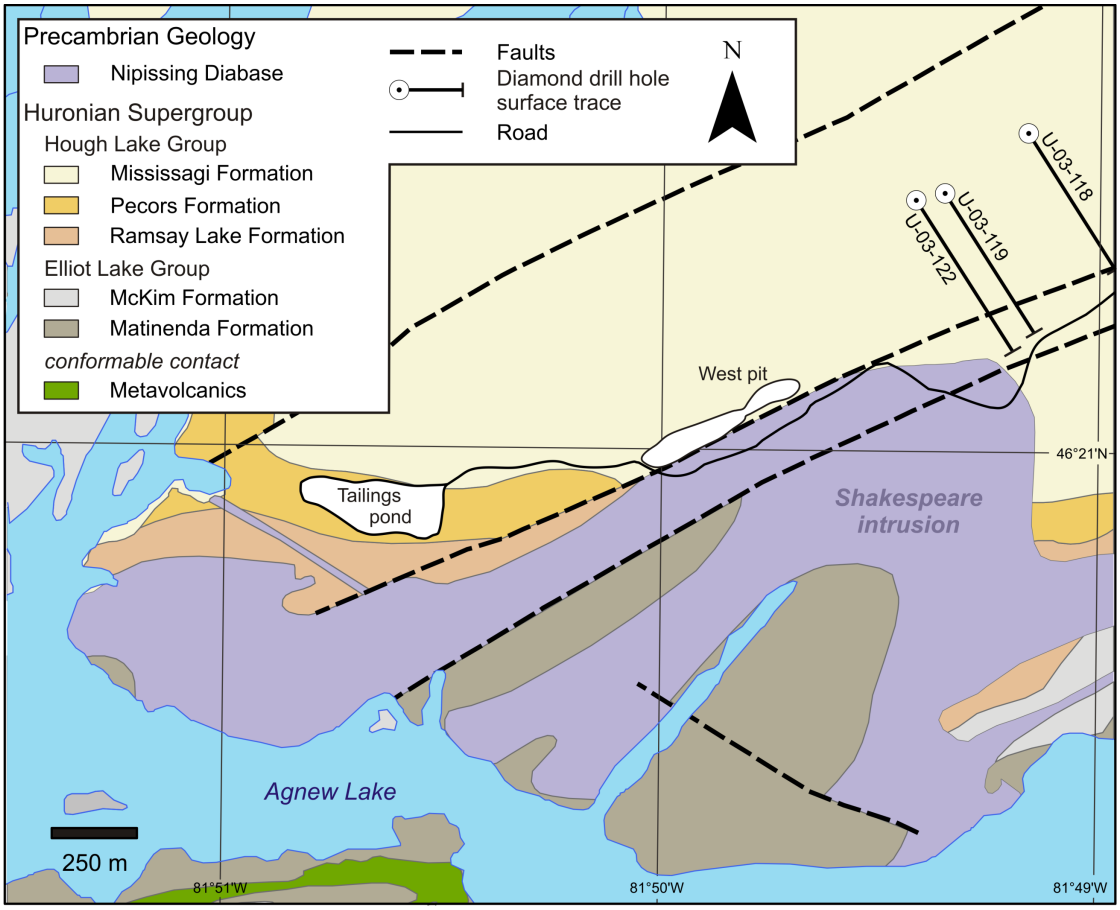

Shakespeare igneous stratigraphy from diamond drill holes (DDH), hung from upper contact

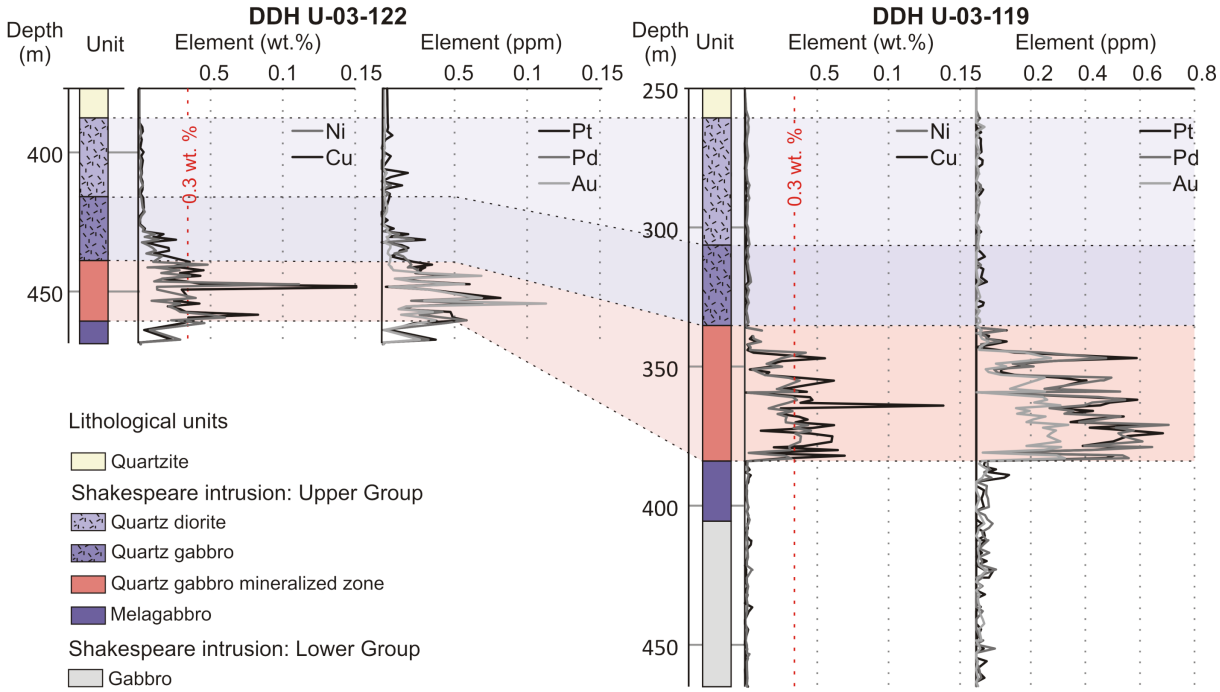

Figure 3. Geological map of the Shakespeare intrusion (*modified from* Card and Palonen, 1976). Diamond drillhole logs with Ni-Cu-PGE assays from Dasti (2014). All drillholes have an azimuth of 147°. Drillhole U-03-119 has an inclination of 65.9° and length of 531 m. Drillhole U-03-122 has an inclination of 75° and length of 624 m.

The low REE group includes dykes belonging to the Klotz and Couture swarms. With a broad range of Fe_2O_3 and TiO_2 concentrations overlapping with the high iron-titanium group, the low REE dykes are distinguished by lower Na_2O concentrations, Ti/V ratios of typical continental flood basalts and flat REE patterns. The quartz normative, low Mg characteristics of the low REE group are interpreted as resulting from fractionation and evolution of a melt extracted from a lherzolitic mantle source (Maurice and Francis, 2010).

Mineralization

General characteristics

Mineralization associated with the Nipissing sills occurs as magmatic Ni-Cu-PGE sulphides and secondary hydrothermal Co±Ag-Cu-Ni polymetallic veins (James et al., 2002; Vaillancourt, et al., 2003; Sproule et al., 2007; Potter et al., 2010). Historic operations include about a dozen past producing mines, which exploited the sills for their hydrothermal cobalt-silver vein deposits located within the Coleman, Gillies Limit, South Lorrain and Plummer Additional townships (Potter et al., 2010; Ontario Geological Survey, 2018). According to the Ontario Geological Survey *Mineral Deposit Inventory* (2018), the Nipissing sills include a number of developed prospects with (n = 1) and without (n = 3) reserves, prospects (n = 8), and occurrences (n = 98) reporting various combinations of Cu-Ni±PGE-Au-Ag (Fig. 2). Several styles of magmatic Ni-Cu-PGE mineralization are reported in the Nipissing sills. These include disseminated Cu-Ni-Cr-(PGE) pipes at Casson Lake, Ni-Cu-PGE sulphides disseminated internally at the Kelly and Davis-Kelly localities, massive to disseminated Ni-Cu-Co-PGE sulphides at the Louise and Waters localities, basal Ni-Cu-PGE sulphides with massive and disseminated textures at the Janes locality, and remobilized basal Ni-Cu-PGE at Rathburn Lake (Table 2; James, et al., 2002; Vaillancourt, et al., 2003; Sproule et al., 2007; Dasti, 2014).

The Shakespeare intrusion

The Shakespeare intrusion represents the largest documented occurrence of Ni-Cu-PGE mineralization and one of the most recent developments exploiting a Nipissing sill (Dasti, 2014). It is located 70 km west of Sudbury, near the northern shore of Agnew Lake. The sill-like intrusion has a thickness that varies from 300 to 430 m, and a strike length of 14 km, dipping north between 40 and 80° (Fig. 3; Sproule et al., 2007). The rusty detrital pyrite (and uraninite) bearing formations of the lower Huronian Supergroup (Young et al., 2001) which host the Shakespeare intrusion may have provided a local source of sulphur. The Shakespeare intrusion is identified as a Nipissing sill by its coeval U-Pb age at 2217 Ma and matching whole-rock major and trace element signatures (Sutcliffe et al., 2002). Although production is currently on hold, the mine was in operation from 2010 to 2012. The most recent resource estimates of the intrusion include 11.8 Mt of probable ore and 5.44 Mt of indicated and inferred resources with 0.33% Ni, 0.35% Cu, and 0.87 g/t PGM and Au (Dasti, 2014).

Consistent with many Nipissing sills, assimilation and fractional crystallization control the differentiation series within the Shakespeare sill. Sproule et al. (2007) explain that the lithologies of the sill can be divided into an uneconomic, sparsely mineralized Lower Group and an economic mineralized Upper Group. The Lower Group includes basal pyroxenite overlain by gabbro (Fig. 3; Sproule et al., 2007; Dasti, 2014). Chilled against the Lower Group, the Upper Group hosts mineralization starting from the lower contact melagabbro, which differentiates upwards to a quartz gabbro and biotite-quartz diorite (Sproule et al., 2007; Dasti, 2014). Also restricted to the Upper Group are lithic fragments of angular to subrounded quartzite, as well as autoliths and xenoliths of diorite (Sproule et al., 2007; Dasti, 2014). The lithological units of the Shakespeare intrusion exhibit pervasive alteration of pyroxene to chlorite, minor sericite alteration of plagioclase, and variable sulphide recrystallization observed in the pyroxenite, gabbro, and biotite-quartz diorite (Sproule et al., 2007; Dasti, 2014). Chlorite and sericite alteration intensity varies with metamorphic grade from greenschist to amphibolite facies and is related to the 1.9 Ga Penokean Orogeny (Sproule et al., 2007).

Mineralization styles observed in the Upper Group involve ore mineral assemblages of pyrrhotite, chalcopyrite, and lesser pyrite (Sproule et al., 2007; Dasti, 2014). Melagabbro belonging to the Upper Group is associated with sulphide abundances of 10 to 15% as disseminated, blebby (2–5 cm) to net-textured pyrrhotite, chalcopyrite, pentlandite, and gersdorffite (Sproule et al., 2007; Dasti 2014). Within the Lower Group, accessory (<1%) finely disseminated to blebby pyrrhotite and chalcopyrite are found at the contact between the basal pyroxenite and gabbro (Sproule et al., 2007; Dasti, 2014).

Methods

Geochronology

Geochronological analyses were completed at the Jack Satterly Geochronology Laboratory at the University of Toronto. Standard separation techniques were used to separate baddeleyite and zircon from approximately 10 kg samples of the Triangle Mountain sill and Shakespeare intrusion (Appendix 1: Methods).

Whole-rock major and trace element geochemistry

In addition to the 25 geochemical Nipissing sill samples analysed in this study, a further 765 whole-rock and/or trace element geochemical samples of Nipissing sills were compiled (Lightfoot and Naldrett, 1989, 1996b; Easton, 2006, 2007, 2013; Easton and Sykora, 2007; Ernst and Buchan, 2010; Gordon, 2016; Jobin-Bevans, 2016). A total of 59 whole-rock major and trace element geochemical analyses of dykes from the Kogaluk Bay (2), Couture (2), Anuc (4), Klotz (15), Maguire (10), and Senneterre (14) dyke swarms plus two analyses from unclassified dykes are also included in the database (Ernst and

Buchan, 2010; Maurice and Francis, 2010).

The compiled data set includes 843 analyses. Erroneous or incomplete analyses were removed based on the following criteria: 1) major element totals less than 97% (including loss on ignition); and 2) if any of the following trace elements were absent: Y, Zr, Nb, La, Sm, Tb, Yb or Th. To eliminate samples that may represent assimilation-fractional crystallization (AFC) processes, dyke and sill samples with greater than 54 weight % SiO_2 were also eliminated. These selection criteria resulted in a data set of 137 samples, comprising 48 dyke and 89 sill samples.

Sm-Nd isotope systematics

Sm-Nd isotope preparation and analyses were completed at the Isotope Geochemistry and Geochronology Research Centre (IGGRC) at Carleton University, Ottawa. For detailed protocols see Appendix 1: Methods.

Results

Triangle Mountain sill

Mineral separation of coarse-grained to pegmatoidal gabbro near the top of the Triangle Mountain sill yielded a reasonable amount of baddeleyite crystals and crystal fragments. One larger single grain and three multiple grain fractions (2–11 crystal fragments) were analyzed and resulted in weakly discordant data points that show minor scatter due to variable Pb-loss behaviour (Table 3; Fig. 4). In general, the data are similar to but extend the range of results reported earlier by Noble and Lightfoot (1992). In detail, our more precise data points better resolve the complex (early) Pb-loss behaviour often seen in baddeleyite (Bleeker, 2014; *see also* Davis and Sutcliffe, 1985), and the least discordant single-grain analysis indicates an older age than obtained by the earlier study. The $^{207}Pb/^{206}Pb$ age of this least-discordant single baddeleyite grain indicates a minimum crystallization age of 2214 ± 2.0 Ma. A regression through the three results that define the right edge of the combined population (i.e. analyses least affected by early Pb-loss behaviour) yields an upper intercept of 2216.5 ± 2.1 Ma, which we consider the best estimate for the crystallization age of the Triangle Mountain sill.

Shakespeare intrusion

A drill core sample from the upper portion of the Shakespeare intrusion, described by Davis (2002a, b) as quartz diorite, yielded a limited but distinct population of euhedral, pale brown, long-prismatic, and flat or platy zircon crystals devoid of cores. Apatite and rutile with a range of colours was also recovered but will not be discussed here (see report by Davis (2002a, b) for a detailed discussion).

Zircon crystals were air-abraded and five single grains were analyzed, resulting in variable discordance (0.6–4.6%). They proved to be relatively high in uranium, which is typical for late-stage platy zircons in mafic magmatic rocks, resulting in discordance but allowing for relatively precise analyses (Table 3; Fig. 4). All five analyses are collinear on a U-Pb concordia diagram, allowing for a precise upper intercept age of 2217.0 +1.7/-1.5 Ma, which is close to and within error of the $^{207}Pb/^{206}Pb$ age of the single least-discordant (0.6%) analysis at 2216.4 ± 1.9 Ma. Given this near-concordance, the lack of scatter, and the lack of inheritance, this upper intercept age of 2217.0 +1.7/-1.5 Ma dates the crystallization of the Shakespeare intrusion and represents one of the more precise age estimates for the Nipissing magmatic event.

Whole-rock major and trace element geochemistry

To demonstrate the variability of samples, especially those belonging to the Nipissing sill suite, all samples with major elements (n = 778) are plotted on a total alkali-silica (TAS) plot (Fig. 5; Le Bas et al., 1986). The Nipissing sills show a wide range of SiO_2 weight % content, from alkaline or subalka-

Table 3. U-Pb isotopic data of the Triangle Mountain sill and Shakespeare intrusion.

No.	Description	Wt. (mg)	U (ppm)	Th/U	PbCom (pg)	$^{207}Pb/^{204}Pb$	$^{206}Pb/^{238}U$	2 σ	$^{207}Pb/^{235}U$	2 σ	$^{207}Pb/^{206}Pb$	2 σ	$^{206}Pb/^{238}U$ Age	2 σ	$^{207}Pb/^{235}U$ Age	2 σ	$^{207}Pb/^{206}Pb$ Age	2 σ	Disc. %	Lab No.
Triangle Mountain sill - BNB-14-031D-E																				
1	1 bd	-	-	0.11	0.3	3550	0.40681	0.00078	7.792	0.018	0.13891	0.00012	2200.3	3.6	2207.2	2.1	2213.7	1.5	0.7	sk37p194
2	2 bd frgs	0.00034	701	0.13	0.5	1677	0.40599	0.00082	7.755	0.019	0.13853	0.00012	2196.6	3.8	2203	2.2	2208.9	1.6	0.7	sk37p195
3	3 bd	0.0011	682	0.08	1.7	1472	0.40297	0.0009	7.706	0.02	0.13869	0.00014	2182.7	4.1	2197.3	2.3	2210.9	1.8	1.5	sk37p196
4	11 bd	0.0025	495	0.48	2.7	1630	0.40114	0.0009	7.633	0.02	0.13801	0.00013	2174.3	4.1	2188.8	2.3	2202.4	1.6	1.5	sk37p197
Shakespeare sill - RHS02-1																				
1	1 Ab zr, eq pale brn	0.0007	697	0.4	0.18	9929	0.4077	0.0011	7.82	0.023	-	-	-	-	-	-	2216.4	1.9	0.6	dwd4207
2	1 Ab zr, flat, pale brn	0.0012	1741	0.43	1.78	4231	0.4031	0.0013	7.727	0.026	-	-	-	-	-	-	2215.2	1.6	1.7	dwd4163
3	1 Ab zr, eq, crk, pale brn	0.0019	1109	0.34	0.9	8373	0.4016	0.002	7.688	0.039	-	-	-	-	-	-	2212.9	1.6	1.9	dwd4162
4	1 Ab zr, eq pale brn	0.0002	679	0.36	0.39	1252	0.4002	0.001	7.665	0.021	-	-	-	-	-	-	2213.8	2	2.3	dwd4208
5	1 Ab zr, stubby, pale brn	0.0007	1348	0.46	1.2	2737	0.3902	0.001	7.46	0.021	-	-	-	-	-	-	2210.6	1.9	4.6	dwd4164

Notes:
Ab – abraded; bd – baddeleyite grain; brn – brownish; crk – cracked; eq – equant; frgs – fragment; zr – zircon grain
Th/U calculated from radiogenic $^{208}Pb/^{206}Pb$ ratio and $^{207}Pb/^{206}Pb$ age assuming concordance.
Pbtot is total amount of Pb in picograms excluding blank.
Pbcom is total amount of common Pb in picograms assuming the isotopic composition of laboratory blank:
Triangle Mountain sill (BNB-14-0.31D-E): $^{206}Pb/^{204}Pb = 18.49$; $^{207}Pb/^{204}Pb = 15.59$; $^{208}Pb/^{204}Pb = 39.36$ (errors of 0.4%)
Shakespeare sill (RHS02-1): $^{206}Pb/^{204}Pb = 18.221$; $^{207}Pb/^{204}Pb = 15.612$; $^{208}Pb/^{204}Pb = 39.360$ (errors of 2%).
Disc. - per cent discordance for the given $^{207}Pb/^{206}Pb$ age.
Uranium decay constants are from Jaffey et al. (1971). .

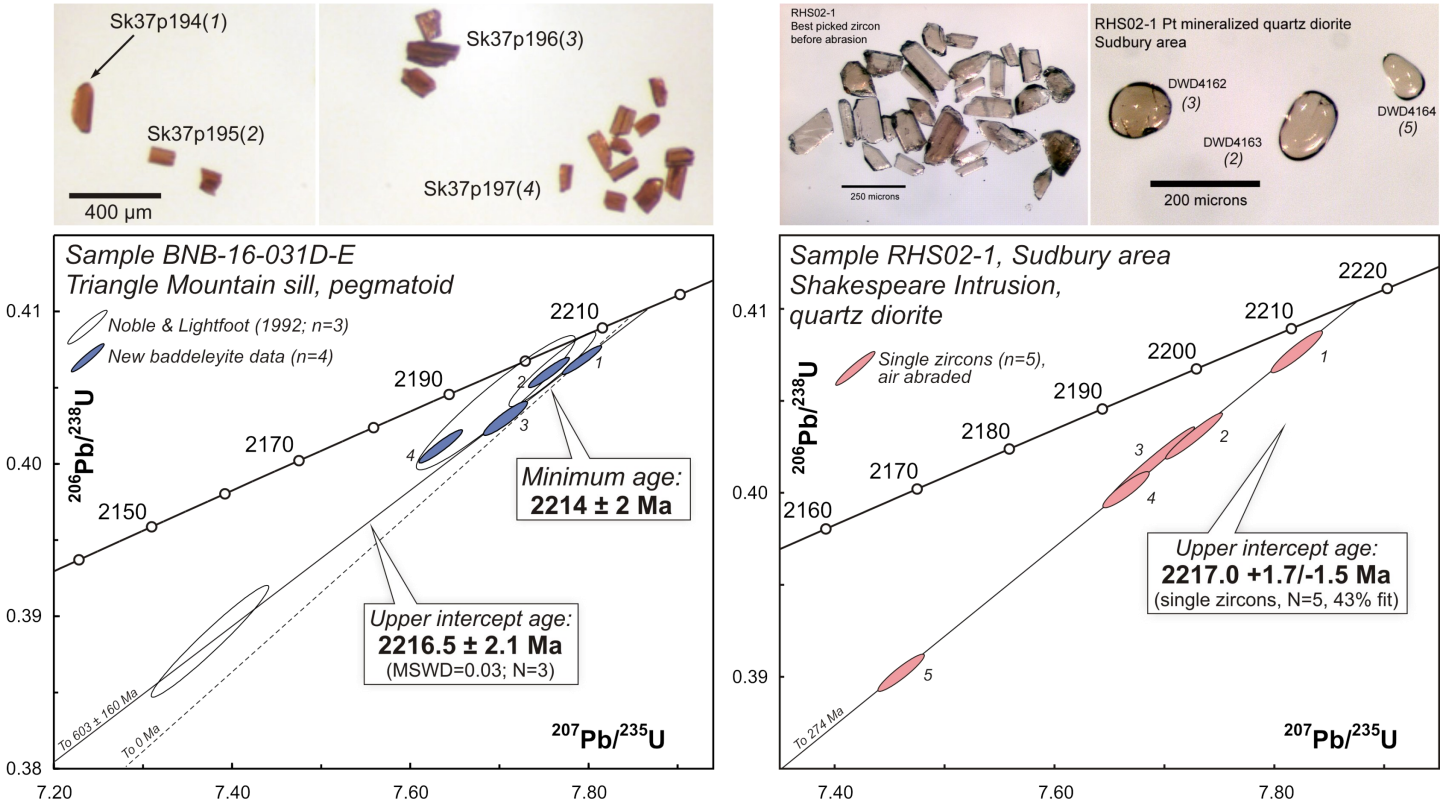

Figure 4. Geochronology of the Triangle Mountain sill (left; this study) and Shakespeare intrusion (right; *after* Davis, 2002a, b). Above each Concordia diagram are photos of baddeleyite and zircon grains analyzed. Analysis numbers and results correspond to Table 3. Previous data on the Triangle Mountain sill *from* Noble and Lightfoot (1992) are shown for comparison. *See* text for discussion.

line tholeiitic basalt to rhyolite compositions. The majority of dyke samples plot within the subalkaline basalt to basaltic andesite field. Results of the filtering procedure are shown on a second TAS plot (Fig. 6a). The Nipissing sills show a dramatic decrease in range and are confined to the subalkaline field from basalt to basaltic andesite. Two Nipissing sill samples plot as outliers from the general population including one melagabbro from the Shakespeare intrusion (no. 6 from Sproule et al., 2007) and a coarse-grained gabbro from Boon Township (sample 12RME-3404 from Easton, 2013). Results and discussion of data hereafter will pertain only to the filtered data set unless otherwise stated.

Nearly all dykes and sills classify as basalt on a Zr/Ti versus Nb/Y plot (Fig. 6b), with only a few exceptions plotting in the andesite/basaltic andesite field. Most samples have Ti/V ratios between 20 and 50, plotting within the continental basalt field of Shervais (1982), although three Nipissing sills, one Klotz dyke, and one Maguire dyke plot within the ocean island basalt (OIB) field, with Ti/V ratios over 50 (Fig. 6c). Conversely, there are other Nipissing sills and some Maguire and Senneterre dykes that have Ti/V ratios below 20.

Five distinct multi-element patterns are recognized within the ca. 2.2 Ga dykes and sills (Fig. 7). These patterns corre-

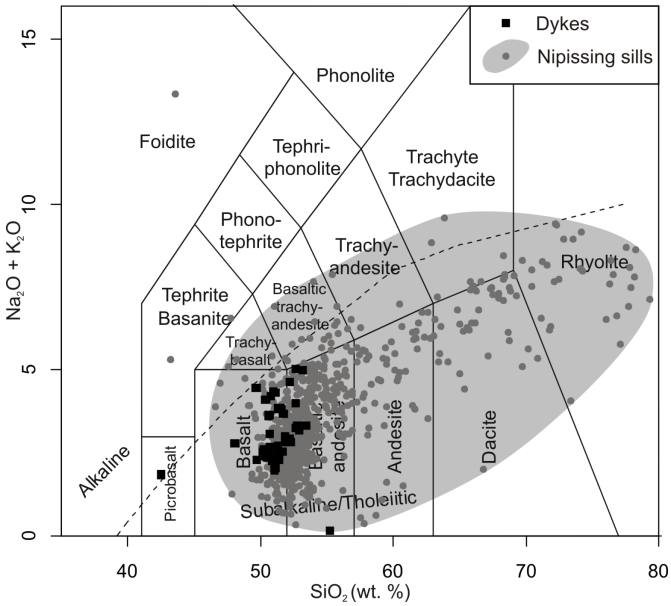

Figure 5. Total alkali versus silica plot (TAS; Le Bas, 1986), plotting all available data for sills and dykes. Data *from* Lightfoot and Naldrett, 1989, 1996b; Easton, 2006, 2007; Easton and Sykora, 2007; Maurice and Francis, 2010; Ernst and Buchan, 2010; Gordon, 2016; Jobin-Bevans, 2016; this study.

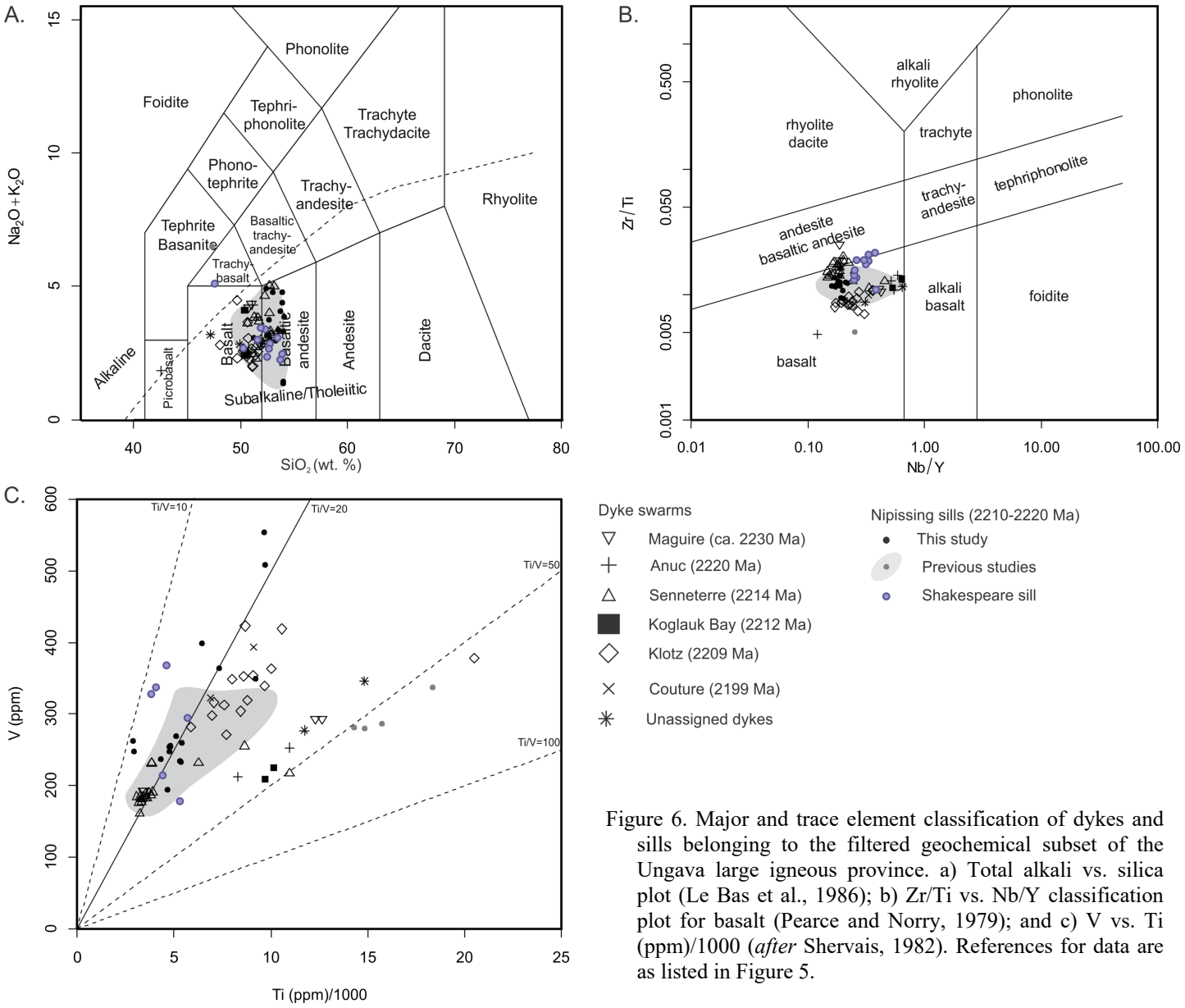

Figure 6. Major and trace element classification of dykes and sills belonging to the filtered geochemical subset of the Ungava large igneous province. a) Total alkali vs. silica plot (Le Bas et al., 1986); b) Zr/Ti vs. Nb/Y classification plot for basalt (Pearce and Norry, 1979); and c) V vs. Ti (ppm)/1000 (*after* Shervais, 1982). References for data are as listed in Figure 5.

spond to the geochemical groups defined by Maurice and Francis (2010), including the high iron-titanium (low and high aluminium subgroups), low iron-titanium and low REE groups.

The high iron-titanium group is characterized by Ti/V ratios greater than 15 and Nb/Yb ratios greater than 1.7, steep LREE slopes (La/Sm ratios between 1.5 and 3), a negative Nb anomaly, and Th enrichment (Fig. 6c, 7a, b). Two subgroups within the high iron-titanium group are distinguished by their HREE slopes (Tb/Yb ratios). These directly correspond to the low and high aluminium subgroups defined by Maurice and Francis (2010). With steep HREE slopes (Tb/Yb ratios >1.5), the low aluminium subgroup includes all dykes from the Anuc and Kogaluk Bay swarms as well as members of the Maguire and Senneterre swarms. The high aluminium subgroup, in contrast, has nearly flat HREE slopes (Tb/Yb ratios <1.5). These include two unclassified dykes from Maurice and Francis (2010) as well as members of the Nipissing sills from the Otter, Joubin and Boon townships near Elliot Lake.

The low iron-titanium group includes the majority of Nipissing sills, and Senneterre and Maguire dykes (70% of the filtered data set; Fig. 7c). Multi-element patterns of the low iron-titanium group include pronounced negative Nb anomalies, enrichment in Th with Nb/Yb ratios of approximately 1, steep LREE slopes (La/Sm 1.5–4), and flat HREE slopes. Sills belonging to this group tend to have more pronounced negative Nb anomalies, greater enrichment in Th, and slightly higher La/Sm ratios compared to dykes.

With nearly flat LREE and HREE slopes on a multi-

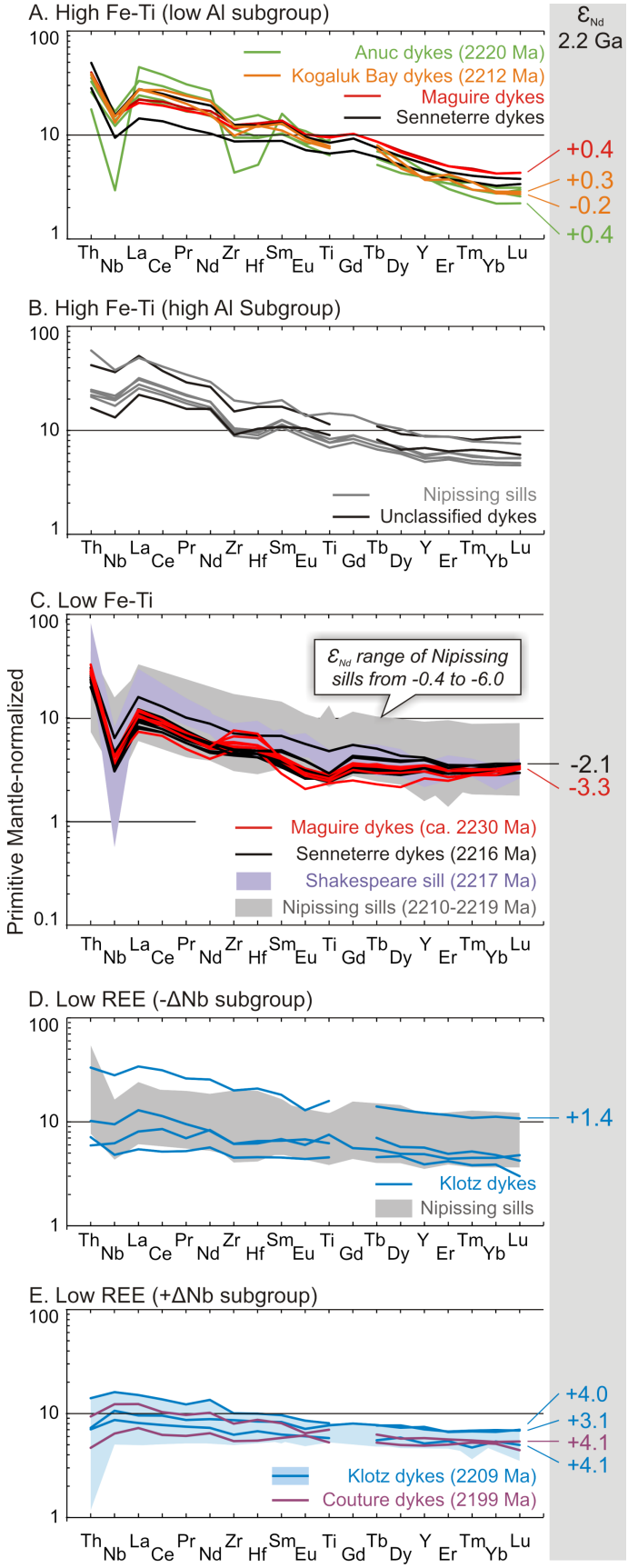

element plot, the low REE group has the most MORB-like pattern of all dykes and sills that are part of the Ungava LIP (Fig. 7d, c). Modified from Maurice and Francis (2010), the low REE group is divided into two subgroups by Th and Nb abundance. The low REE (-ΔNb) subgroup is slightly enriched in Th and has a negative Nb anomaly (Fig. 7d). This subgroup includes members of the Klotz dykes and Nipissing sills. The low REE (+ΔNb) subgroup is distinguished from all other groups as it lacks both a negative Nb anomaly and Th enrichment (ΔNb as calculated by Fitton et al., 1997; Fig. 7e). All of the Couture and some of the Klotz belong to this low REE (+ΔNb) subgroup.

Isotope geochemistry

Sm-Nd isotope analyses were completed for two Maguire dykes, one Senneterre and one Klotz dyke, as well as two samples from the Triangle Mountain sill (Table 4). The two Maguire dykes have distinct $\varepsilon Nd_{(t=2229\ Ma)}$ values at +0.4 and -3.3. The Senneterre dyke has an $\varepsilon Nd_{(t=2214\ Ma)}$ value at -2.1, matching one of the Maguire dykes. The Klotz dyke has an $\varepsilon Nd_{(t=2209\ Ma)}$ at +3.1 value, which is distinct from both Maguire and Senneterre dyke samples (Fig. 8).

The samples analyzed from the Triangle Mountain sill include a fine-grained gabbro (52.4 weight % SiO_2 and Mg# = 36.5) located near the basal contact of the sill, and a course-grained pegmatoidal varitextured gabbro located near the top of the sill (52.9 weight % SiO_2 and Mg# = 17.5). The samples produced $\varepsilon Nd_{(t=2214\ Ma)}$ values of -0.4 and -1.8, respectively, overlapping within analytical error (error margin of ±0.5 εNd units) with the Senneterre dyke and one of the Maguire dykes.

Discussion

Timing of Ungava magmatism

Magmatism of the Ungava LIP can be broadly categorized into three pulses: early (2229–2220 Ma), middle (2217–2214 Ma), and late (2209–2199 Ma) (Table 1). The early pulse is affiliated with swarms of limited areal extent (Anuc and possibly some members of the Maguire dykes) and represents volumetrically minor magmatism. The middle pulse includes most

Figure 7. Multi-element plots of the geochemical groups identified among the dykes and sills belonging to the Ungava LIP. Trace element concentrations are normalized to primitive mantle values of Sun and McDonough (1989). Where available, $\varepsilon Nd_{(t=2.2\ Ga)}$ are matched to corresponding samples. a) High iron-titanium (low aluminium subgroup); b) high iron-titanium (high aluminium subgroup); c) low iron-titanium group; d) low REE (-ΔNb subgroup); and e) low REE (+ΔNb subgroup). Trace element data sources as listed in Figure 5. Isotopic data are from this study, and compiled from Lightfoot and Naldrett (1996b) and Maurice and Francis (2010) .

Table 4: Sm-Nd isotope data for Triangle Mountain (Nipissing sill), Maguire, Senneterre and Klotz dykes.

Sample	Locality	Longitude (W)	Latitude (N)	Geochemical group	Nd (ppm)	Sm (ppm)	$^{143}Nd/^{144}Ndm$	$^{147}Sm/^{144}Nd$	$^{143}Nd/^{144}Ndi$	εNd_i
BNB-16-031B	Triangle Mtn.	79.7800	47.4946	Low Fe-Ti	9.74	2.72	0.512208	0.1687	0.509748	-0.4
BNB-16-031D	Triangle Mtn.	79.7942	47.4903	Low Fe-Ti	15.66	3.94	0.511895	0.1522	0.509675	-1.8
BXA91-7605	Maguire	75.044	57.212	High Fe-Ti, low Al	22.81	5.79	0.512024	0.1535	0.509770	+0.4
BXA91-7101	Maguire	72.540	58.090	Low Fe-Ti	8.23	1.87	0.511600	0.1377	0.509579	-3.3
TM34	Senneterre	81.794	47.665	Low Fe-Ti	8.91	2.35	0.511984	0.1593	0.509659	-2.1
BXA91-7302	Klotz	73.910	60.582	Low REE (+ΔNb)	11.99	3.6	0.512580	0.1817	0.509935	+3.1

Notes:
Coordinates in WGS1984
$^{143}Nd/^{144}Ndm$ is the measured present-day value, $^{143}Nd/^{144}Ndi$ is the initial ratio and $\varepsilon Nd_{(i)}$ based on crystallization ages of 2216 Ma for the Triangle Mountain sill, 2229 Ma for Maguire, 2214 Ma for Senneterre, and 2209 Ma for Klotz dykes.
Isotope ratios are normalised to $^{146}Nd/^{144}Nd = 0.72190$.
2σ uncertainties of $^{143}Nd/^{144}Ndm$ are 0.000011 based on reproducibility of the in-house Nd Standard.
2σ uncertainties of $^{147}Sm/^{144}Nd$ are 0.5% .

of the Maguire and Senneterre dykes, which define the radiating pattern of the Ungava LIP, as well as the local Kogaluk Bay dykes. Nipissing sills are also part of the middle pulse, which is confirmed by the new crystallization age of the Triangle Mountain sill at 2216.5 ± 2.1 Ma. Together, the Maguire, Senneterre, and Kogaluk Bay dykes and the Nipissing sills represent the most significant phase of the Ungava LIP volumetrically. The Klotz and Couture dykes belong to the late pulse. Though the Couture dykes are of limited area, the Klotz dykes are geographically more extensive and possibly expand the radiating pattern of the Ungava LIP to the north.

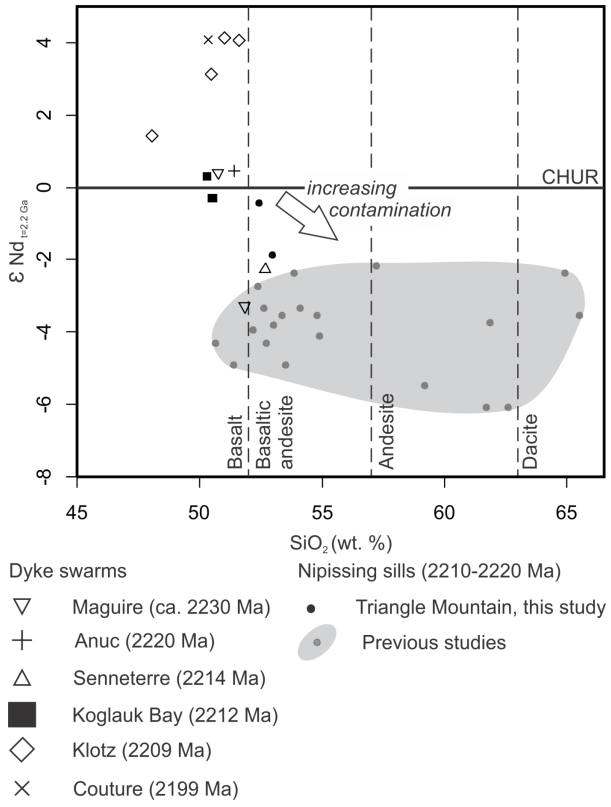

Figure 8. $\varepsilon Nd_{(t=2.2\ Ga)}$ versus SiO_2 weight % with chondrite uniform reservoir (CHUR) reference line. Sources as in Figure 7.

Feeders to the Nipissing sills

Three geochemical signatures are recognized within the Nipissing sills. These include the high iron-titanium (high aluminium), low iron-titanium and low REE (-ΔNb) groups (see Fig. 7b, c, d), each of which match different dyke swarms located within the Ungava Peninsula.

The Otter, Joubin, and Boon townships are host to the Nipissing sills with high iron-titanium (high aluminium subgroup) geochemistry (5 of 89 samples). Unlike the low iron-titanium and low REE (-ΔNb) groups, the high iron-titanium (high aluminium) subgroup does not have exact matches to dykes of the Ungava LIP. Instead, these sills match geochemistry of dykes not yet assigned to a particular swarm.

The majority of Nipissing sills (76 of 89 samples) belong to the low iron-titanium geochemical group, which also includes most of Maguire (7 of 9 samples) and Senneterre (12 of 14 samples) dykes. Matches in whole-rock major and trace element patterns (Fig. 7c), in addition to Nd isotopic ratios (Fig. 8), support their genetic relationship as proposed by Buchan et al. (1998).

Although less abundant, other geochemical signatures recognized within the Nipissing sills further support a link to the dykes of the Ungava LIP. Nipissing sills located within May, Baldwin, and Otter townships, for example, are less enriched in LREEs compared to those belonging to the low iron-titanium group. These sills (8 of 89 samples) are a closer match to the Klotz dykes of the low REE (-ΔNb) subgroup.

A preliminary tectono-magmatic interpretation

At least three distinct mantle end members are recognized as sources of Ungava LIP magmas feeding dykes and sills. These include the high iron-titanium (low and high aluminium) and low REE groups.

The high iron-titanium (low aluminium) group has $\varepsilon Nd_{(t=2.2\ Ga)}$ values of between -0.2 and +0.4 (Fig. 8; Maurice and Francis, 2010). Because these dykes are enriched in LREE, have high Tb/Yb_{PM} ratios, and have a negative Nb anomaly, deeper depths of melting can be inferred but their initial isotopic man-

tle-source signatures are obscured by the incorporation of a crustal component. Conversely, major and trace element patterns (e.g. flat HREEs, and negative correlation between Al_2O_3 and Mg#, as described by Maurice and Francis (2010)), indicate that magmas of the high iron-titanium (high aluminium) subgroup were generated at shallower depths and from a distinct mantle source compared to the high iron-titanium (low aluminium) subgroup.

The low REE (+ΔNb) subgroup has $\varepsilon Nd_{(t=2.2\ Ga)}$ values between +3.1 and +4.1 (Fig. 8; Maurice and Francis, 2010; this study). Paired with the nearly flat trace element patterns, their geochemical signature is characteristic of magmas generated by higher degrees of partial melting of upper mantle at shallow depths. The low REE (-ΔNb) subgroup is considered to have been derived from the low REE (+ΔNb) subgroup but was contaminated prior to final emplacement. Indicators of crustal contamination include a negative Nb anomaly, subtle Th and LREE enrichments, and a single $\varepsilon Nd_{(t=2.2\ Ga)}$ value of +1.4 (Maurice and Francis, 2010).

In similarity to the low REE group, flat HREE patterns of the low iron-titanium group are indicative of shallow melting. A crustal contamination signature suggested by enrichment in LREEs and Th, and prominent negative niobium anomalies are corroborated by $\varepsilon Nd_{(t=2.2\ Ga)}$ values at -2.1 and -3.3 in the Senneterre and Maguire dykes. Assimilation-fractional crystallization processes continued following emplacement of the Nipissing sills, indicated by progressively lower $\varepsilon Nd_{(t=2.2\ Ga)}$ with increasing SiO_2 weight % (Fig. 8). Whether the low iron-titanium group was generated from a distinct source or is a heavily contaminated phase derived from the low REE group requires further investigation.

Ni-Cu-PGE potential of the Nipissing sills

Jowitt and Ernst (2013) characterize LIPs with known Ni-Cu-PGE mineralization as having a basaltic composition with Ti/V ratios of less than 50, HREEs similar to primitive mantle, and enrichment in LREEs (monitored by La/Sm_{PM} and Th/Yb_{PM} ratios greater than 1). A magmatic system with these characteristics, however, does not explicitly indicate a fertile system. The magmatic system must also have been generated from a source undepleted in chalcophile elements and have undergone S-saturation (Jowitt and Ernst, 2013). The Ni versus MgO weight % plot can be used to evaluate S-saturation (Fig. 9a; Jowitt and Ernst, 2013). Samples with Ni concentrations less than the within-plate basalt array are inferred to have lost Ni to an immiscible sulphide melt; a deficit that occurs by early S-saturation (Jowitt and Ernst, 2013). With the exception of the samples from the mineralized Shakespeare deposit and two samples from the high iron-titanium (low aluminium) group, all samples plot either on or below the within-plate basalt array, suggestive of an early sulphur saturation event.

Ratios between chalcophile and lithophile elements of com-

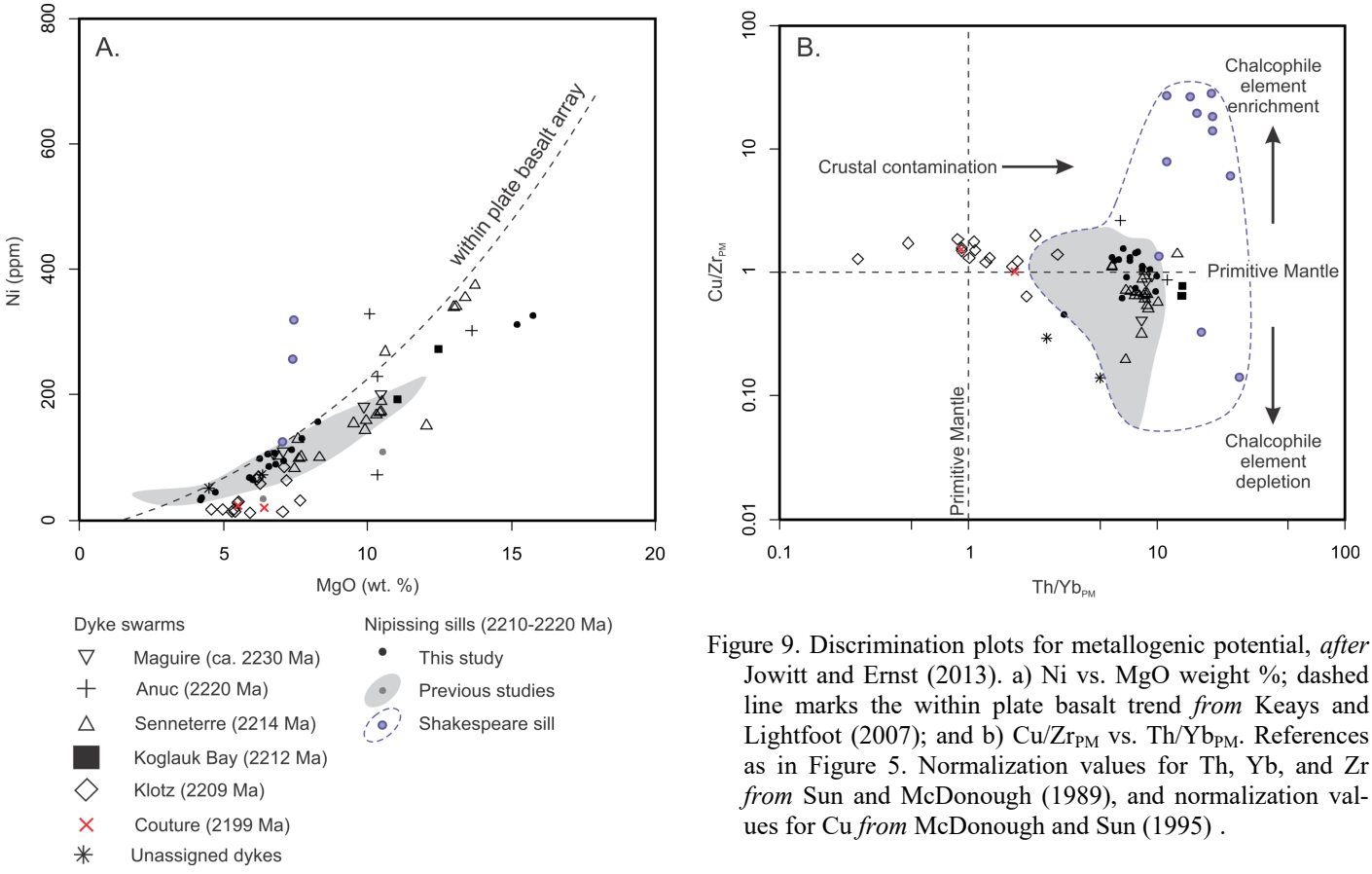

Figure 9. Discrimination plots for metallogenic potential, *after* Jowitt and Ernst (2013). a) Ni vs. MgO weight %; dashed line marks the within plate basalt trend *from* Keays and Lightfoot (2007); and b) Cu/Zr_{PM} vs. Th/Yb_{PM}. References as in Figure 5. Normalization values for Th, Yb, and Zr *from* Sun and McDonough (1989), and normalization values for Cu *from* McDonough and Sun (1995) .

parable incompatibilities offer a means of evaluating chalcophile element concentrations of a magma without influence from fractional crystallization processes (Jowitt and Ernst, 2013). Figure 9b compares ratios of Cu/Zr_{PM} against the crustal contamination proxy Th/Yb_{PM}. A magmatic group is considered prospective for Ni-Cu-PGEs when it includes signatures that are both undepleted (fertile) and depleted (loss of chalcophile elements to an immiscible sulphide magma; Jowitt and Ernst, 2013). Prospective geochemical groups include the low iron-titanium and low REE groups. The low iron-titanium group, which includes the Shakespeare deposit and most Nipissing sills, shows the widest variation in Cu/Zr_{PM} and high Th/Yb_{PM} values, consistent with high degrees of crustal assimilation (Fig. 9b) and local sulphur saturation. The low REE group with +ΔNb has Cu/Zr_{PM} values above primitive mantle, indicates that these are slightly enriched in chalcophile elements. Nipissing sills belonging to the low REE group consistently have -ΔNb signatures that follow a Cu/Zr_{PM}-depletion trend with Th/Yb_{PM} and for this reason, may be prospective.

Samples belonging to the high iron-titanium (low aluminium and high aluminium) group are considered less prospective. Although the high iron-titanium (low aluminium) group includes enriched and depleted chalcophile signatures, their steeper HREE slopes are uncharacteristic of mineralized intrusions. The high iron-titanium (high aluminium) subgroup is not considered prospective because all samples (sills and dykes) are depleted in chalcophile elements.

Summary

Geochemistry of dykes and sills belonging to the ca. 2.2 Ga Ungava LIP are compiled to gain a better understanding of the overall magmatic system and Ni-Cu-PGE prospectivity. Geochemical groups described by Maurice and Francis (2010), including the high iron-titanium (low and high aluminium), low iron-titanium and low REE groups, are recognized within the dykes and sills belonging to the Ungava LIP.

The high iron-titanium (low aluminium) group includes representatives of the Anuc, Kogaluk Bay, and some Maguire and Senneterre dykes. No Nipissing sill matches this geochemical signature. Trace element characteristics indicate that the group was generated from deeper depths (compared to the low REE and low iron-titanium groups) and incorporated a crustal component that may have influenced the +0.4 $\varepsilon Nd_{(t=2.2\ Ga)}$ signature.

The high iron-titanium (high aluminium) group has geochemical characteristics of melting at shallow depths but from a more enriched source compared to the low iron-titanium and low REE groups. Ubiquitous depletion of chalcophile elements indicates that the Nipissing sills belonging to this group are not prospective for Ni-Cu-PGE. No dykes with U-Pb ages dated at 2.2 Ga belong to this geochemical group.

Low iron-titanium chemistry is the most abundant geochemical group and includes the majority of samples belonging to the Senneterre and Maguire dykes and Nipissing sills. Heavy rare earth element patterns indicate that these magmas were generated at shallow mantle depths and LREE enrichment is ascribed to crustal contamination. Samarium-neodymium isotopes indicate that the Maguire and Senneterre dykes feeding the Nipissing sills incorporated a crustal component prior to emplacement as evidenced by low $\varepsilon Nd_{(t=2.2\ Ga)}$ values at -2.1 and -3.3. The mineralized Shakespeare deposit belongs to this geochemical group and the group as a whole is considered prospective.

A new crystallization age for the Triangle Mountain sill, part of the low iron-titanium group, is determined to be 2216.5 ± 2.1 Ma by U-Pb thermal ionization mass spectrometry (TIMS) of baddeleyite. Values of $\varepsilon Nd_{(t=2.2\ Ga)}$ of between -0.4 and -1.8 for the Triangle Mountain sill indicate that in situ crustal assimilation occurred but likely not to the same degree as other sills (e.g. Obabika and Kerns sills: Lightfoot and Naldrett, 1996a).

The low REE group is considered to have been generated by melting of the upper mantle at shallow depths. The group is divided into subgroups based on Th and Nb abundance. The +ΔNb subgroup lacks indicators of crustal contamination in terms of trace element patterns (absence of a negative Nb anomaly, and no Th enrichment). Samarium-neodymium isotopes with $\varepsilon Nd_{(t=2.2\ Ga)}$ values between +3.1 and +4.1 further support sourcing from uncontaminated upper mantle. This subgroup includes the Couture and Klotz dykes. The -ΔNb subgroup, on the other hand, is distinguished by subtle enrichment in Th and LREEs as well as a negative Nb anomaly. The single $\varepsilon Nd_{(t=2.2\ Ga)}$ value of +1.4 is indicative of input from a crustal component, especially when paired with its multi-element signature. The -ΔNb subgroup includes members of the Klotz dykes and some Nipissing sills, and is considered prospective for Ni-Cu-PGE.

Next steps

The analysis of a second batch of six samples for Sm-Nd isotopes is in progress, which will expand the isotope patterns identified in the Senneterre, Maguire, and Klotz dykes. These new data combined with the existing database will help determine a more detailed model of the evolution of the magmatic system to further constrain the crustal components recognized in the various geochemical groups, and whether the low REE and low iron-titanium groups are related within a single evolving magmatic system. Furthermore, the spatial distribution of the geochemical groups and their age relationships will also be evaluated.

Future geochronology is suggested for the Nipissing sills belonging to the high iron-titanium (high aluminium) and low REE geochemical groups. Precise ages for these specific geochemical groups can test their association with the Ungava event and help to constrain the overall secular evolution of the magmatic system (for example, do the low REE (-ΔNb) Nipissing sills match the age of the Klotz dykes?).

Acknowledgments

This report is a contribution to NRCan's Targeted Geoscience Initiative Program (TGI). Support for this study was provided through the Ni-Cu-PGE Systems Project's '*Activity NC-1.2: Localization of high-value footwall mineralization within the Sudbury Impact Structure*'.

The authors would like to acknowledge Ken Buchan and Henry Halls for providing some of the dyke samples. Shuangquan Zhang is thanked for his guidance in the isotope geochemistry laboratory at Carleton University. Brian Cousens and Richard Ernst are thanked for discussions and supervision of Ph.D. candidate Sarah Davey at Carleton University, Ottawa. This report benefited from the review of Dawn Kellett, Jeremy Powell and Neil Rogers.

References

Andrews, A.J., Owsiacki, L., Kerrich, R., and Strong, D.F., 1986. The silver deposits at Cobalt and Gowganda, Ontario. I: Geology, Petrography, and whole-rock geochemistry; Canadian Journal of Earth Science, v. 23, p. 1480–1506.

Bennett, G., Dressler, B.O., and Robertson, J.A., 1991. The Huronian Supergroup and associated intrusive rocks; *in* Geology of Ontario, (ed.) P.C. Thurston, H.R. Williams, R.H. Sutcliffe and G.M. Stott; Ontario Geological Survey, Special Publication 4, Part 1, p. 549–591.

Bleeker, W., 2014. The quest for better precision and more accuracy: Revisiting upper intercept ages; *in* Abstracts, Geological Association of Canada Annual Meeting, May 21 –23, Fredericton, v. 37, p. 31–32.

Bleeker, W., Kamo, S., Doreen, A.E., and Davis, D., 2015. New field observations and U-Pb ages in the Sudbury area: towards a detailed cross-section through the deformed Sudbury Structure; *in* Targeted Geoscience Initiative 4: Canadian Nickel-Copper-Platinum Group Elements-Chromium Ore Systems – Fertility, Pathfinders, New and Revised Methods, (ed.) D.E. Ames and M.G. Houlé; Geological Survey of Canada, Open File 7856, p. 151–166.

Buchan, K.L. and Ernst, R.E., 2004. Diabase dyke swarms and related units in Canada and adjacent regions; Geological Survey of Canada, Map 2022A, scale 1:5 000 000, 1 CD-ROM.

Buchan, K.L., Mortensen, J.K., and Card, K.D., 1993. Northeast-trending Early Proterozoic dykes of southern Superior Province: multiple episodes of emplacement recognized from integrated paleomagnetism and U-Pb geochronology; Canadian Journal of Earth Science, v. 30, no. 6, p. 1286–1296.

Buchan, K.L., Halls, H.C., and Mortensen, J.K., 1996. Paleomagnetism, U-Pb geochronology, and geochemistry of Marathon dykes, Superior Province and comparison with the Fort Frances swarm; Canadian Journal of Earth Science, v. 33, p. 1583–1595.

Buchan, K.L., Mortensen, J.K., Card, K.D., and Percival, J.A., 1998. Paleomagnetism and U-Pb geochronology of diabase dyke swarms of Minto block, Superior Province, Quebec, Canada; Canadian Journal of Earth Science, v. 35, p. 1054–1069.

Card, K.D. and Pattison, E.F., 1973. Nipissing diabase of the Southern Province, Ontario; *in* Huronian Stratigraphy and Sedimentation, (ed.) G.M. Young; Geological Association of Canada, Special Paper 12, p. 7–30.

Card, K.D. and Palonen, P.A., 1976. Geology of the Dunlop-Shakespeare area, District of Sudbury; Ontario Division of Mines, Geoscience Report 139, 52 p., Map 2313.

Corfu, F. and Andrews, A.J., 1986. A U-Pb age for mineralized Nipissing diabase, Gowganda, Ontario; Canadian Journal of Earth Science, v. 23, p. 107–109.

Conrod, D.M., 1989. The petrology and geochemistry of the Duncan Lake, Beaton Bay, Milner Lake, and Miller Lake Nipissing intrusions within the Gowganda area, District of Timiskaming; Ontario Geological Survey, Open File Report 5701, 210 p.

Dasti, I., 2014. The geochemistry and petrogenesis of the Ni-Cu-PGE Shakespeare deposit, Ontario, Canada; M.Sc. thesis, Lakehead University, Thunder Bay, Ontario, 233 p.

Davis, D.W., 2002a. U-Pb geochronology of a quartz diorite from the Sudbury area, September 23, 2002; *in* Report on Work 2002 Shakespeare Property, Volume 1 of 2, for Ursa Major Minerals Inc.; Ontario Assessment Record 4105SW2019, p. 498–504.

Davis, D.W., 2002b. U-Pb geochronology of a quartz diorite from the Sudbury area, October 11, 2002; *in* Shakespeare Project, Falconbridge Option Property, Report on Time Domain Electromagnetic Surveys, August 2002, Ursa Major Minerals Inc.; Ontario Assessment Record 4105SW2011, p. 52–62.

Davis, D.W. and Sutcliffe, R.H., 1985. U-Pb ages from the Nipigon plate and northern Lake Superior; Geological Society of America, Bulletin, v. 96, p. 1572–1579.

Easton, R.M., 2006. Geological, geochemical and geophysical data from the Porter and Vernon townships area, Southern Province, Ontario; Ontario Geological Survey, Miscellaneous Release-Data 197.

Easton, R.M., 2007. Geological, geochemical and geophysical data from the Baldwin Township mapping project, Southern Province, Ontario; Ontario Geological Survey, Miscellaneous Release – Data 212.

Easton, R.M., 2013. Geological, geochemical and geophysical data from the Elliot Lake area, Southern and Superior provinces, Ontario; Ontario Geological Survey, Miscellaneous Release – Data 305.

Easton, R.M. and Hrominchuk, J.L., 2002. Whole-rock and mineral chemistry, assay, and petrographic data for the River Valley intrusion, Crerar and Dana townships, Grenville Province, Ontario; Ontario Geological Survey, Miscellaneous Release – Data 95, 1 CD-ROM.

Easton, R.M. and Sykora, L.A. (comp.), 2007. Geochemical data from the East Bull Lake and Agnew intrusions, and the

Whiskey Lake and Ompa Lake greenstone belts, Districts of Algoma and Sudbury; Ontario Geological Survey, Miscellaneous Release – Data 223.

Ernst, R.E. and Bleeker, W., 2010. Large igneous provinces (LIPs), giant dyke swarms, and mantle plumes: significance for breakup events within Canada and adjacent regions from 2.5 Ga to the present; Canadian Journal of Earth Science, v. 47, p. 695–738.

Ernst, R.E. and Buchan, K.L., 2010. Geochemical database of Proterozoic intraplate mafic magmatism in Canada; Geological Survey of Canada, Open File 6016, 1 CD-ROM.

Fitton, J.G., Saunders, A.D., Norry, M.J., Hardarson, B.S., and Taylor, R., 1997. Thermal and chemical structure of the Iceland plume; Earth and Planetary Science Letters, v. 153, p 197–208.

Gerstenberger, H. and Haase, G., 1997. A highly effective emitter substance for mass spectrometric Pb isotope ratio determinations; Chemical Geology, v.136, p. 309–312.

Goodfellow, W.D. (ed.), 2007. Mineral Deposits of Canada: A Synthesis of Major Deposit-Types, District Metallogeny, the Evolution of Geological Provinces and Exploration methods; Geological Survey of Canada, Special Publication no. 5, 1068 p.

Gordon, C.A., 2016. Geological, geochemical, geophysical and geochronological data from the Morin and Otter townships bedrock geology mapping project, Southern and Superior provinces; Ontario Geological Survey, Miscellaneous Release – Data 332.

Hriskevich, M.E., 1968. Petrology of the Nipissing Diabase Sill of the Cobalt Area, Ontario, Canada; Geological Society of America, Bulletin, v. 79, p. 1387–1404.

Jaffey, A.H., Flynn, K.F., Glendenin, L.E., Bentley, W.C., and Essling, A.M., 1971. Precision measurements of half-lives and specific activities of ^{235}U and ^{238}U; Physical Review, v. 4, p. 1889–1906.

James, R.S., Jobin-Bevans, S., Easton, R.M., Wood, P., Hrominchuk, J.L., Keays, R.R., and Peck, D.C., 2002. Platinum group element mineralization in Paleoproterozoic basic intrusions in central and northeastern Ontario, Canada; in Geology, Geochemistry, Mineralogy and Mineral Beneficiation of Platinum Group Elements, (ed.) L.J. Cabri; Canadian Institute of Mining and Metallurgy, Special Publication 54, p. 339–365.

Jobin-Bevans, L.S., 2004. Platinum-group element mineralization in Nipissing gabbro intrusions and the River Valley intrusion, Sudbury region, Ontario; Ph.D. thesis, University of Western Ontario, London, Ontario, 572 p.

Jobin-Bevans, L.S., 2016. Geochemical data related to a study of platinum group element mineralization in Nipissing gabbro intrusions and the River Valley intrusion, Sudbury region, Southern Province; Ontario Geological Survey, Miscellaneous Release – Data 336.

Jowitt, S.M. and Ernst, R.E., 2013. Geochemical assessment of the metallogenic potential of Proterozoic LIPs of Canada; Lithos, v. 174, p. 291–307.

Keays, R.R. and Lightfoot, P.C., 2007. Siderophile and chalcophile metal variations in Tertiary picrites and basalts from West Greenland with implications for the sulphide saturation history of continental flood basalt magmas; Mineralium Deposita, v. 42, p. 319–336.

Krogh, T.E., 1973. A low contamination method for hydrothermal decomposition of zircon and extraction of U and Pb for isotopic age determinations; Geochimica et Cosmochimica Acta, v. 37, p. 485–494.

Le Bas, M.J., Le Maitre, R.W, Strekeisen, A., and Zanettin, B., 1986. A chemical classification of volcanic rocks based on the total alkali-silica diagram; Journal of Petrology, v 27, p. 745–750.

Lightfoot, P.C. and Naldrett, A.J., 1989. Assimilation and crystallization in basic magma chambers: trace-element and Nd-isotopic variations in the Kerns sill, Nipissing diabase province, Ontario; Canadian Journal of Earth Science, v. 26, p. 737–754.

Lightfoot, P.C. and Naldrett, A.J., 1996a. Petrology and geochemistry of the Nipissing Gabbro: Exploration strategies for nickel, copper, and platinum group elements in a large igneous province; Ontario Geological Survey, Study 58, 81 p.

Lightfoot, P.C. and Naldrett, A.J., 1996b. Analytical data for Nipissing Intrusions; Ontario Geological Survey, Miscellaneous Release – Data 19.

Lightfoot, P.C., De Souza, H., and Doherty, W., 1993. Differentiation and source of the Nipissing diabase intrusions, Ontario, Canada; Canadian Journal of Earth Science, v. 30, p. 1123–1140.

Maurice, C. and Francis, D., 2010. Enriched crustal and mantle components and the role of the lithosphere in generating Paleoproterozoic dyke swarms of the Ungava Peninsula, Canada; Lithos, v. 114, p. 95–108.

Maurice, C., David, J., O'Neil, J., and Francis, D., 2009. Age and tectonic implications of Paleoproterozoic mafic dyke swarms for the origin of 2.2 Ga enriched lithosphere beneath the Ungava Peninsula, Canada; Precambrian Research, v. 174, p. 163–180.

McDonough, W.F. and Sun, S.-S., 1995. The composition of the Earth; Chemical Geology, v. 120, p. 223–253.

Noble, S.R. and Lightfoot, P.C., 1992. U-Pb baddeleyite ages of the Kerns and Triangle Mountain intrusions, Nipissing diabase, Ontario; Canadian Journal of Earth Science, v. 29, p. 1424–429.

Ontario Geological Survey, 2011. 1:250 000 scale bedrock geology of Ontario; Ontario Geological Survey, Miscellaneous Release – Data 126 – Revision 1, scale 1:250 000.

Ontario Geological Survey, 2018. Mineral Deposit Inventory; Ontario Geological Survey. <www.ontario.ca/data/mineral-deposit-inventory-ontario> [accessed October 30, 2018]

Pearce, J.A. and Norry, M.J., 1979. Petrogenetic implications of Ti, Zr, Y and Nb variations in volcanic rocks; Contributions to Mineralogy and Petrology, v. 69, p. 33–47.

Pearce, J.A., 2008. Geochemical fingerprinting of oceanic basalts with applications to ophiolite classification and the search for Archean oceanic crust; Lithos, v. 100, p. 14–48.

Pearce, J.A., Ernst, R.E., Rogers, C., and Peate, D.W., 2017. LIP-Printing: A geochemical proxy approach to LIP Forensics; Geological Society of American Annual Meeting, Abstracts, v. 49, Paper 238-7.

Potter, E.G., Taylor, R.P., Jones, P.C., Rees, K., and Campbell, I., 2010. The geological setting, mineralogy, and paragenesis of gold-bearing polymetallic (Cu+Co+Ag+Au+Bi±Pb± Ni±U) veins of the Merico-Ethel property, Elk Lake, Northeastern Ontario, Canada; Exploration and Mining Geology, v. 19, p. 81–89.

Rousell, D.H. and Trevisiol, D.D., 1988 . Geology of the mineralized zone of the Wanapitei complex, Grenville Front, Ontario; Mineralium Deposita, v. 23, p. 138–149.

Simony, P.S., 1964. Geology of Northwestern Timagami Area District of Nipissing; Ontario Department of Mines, Geological Report No. 28, 46 p.

Shervais, J.W., 1982. Ti-V plots and the petrogenesis of modern and ophiolitic lavas; Earth and Planetary Science Letters, v. 59, p. 101–118.

Söderlund, U. and Johanssen, L., 2002. A simple way to extract baddeleyite (ZrO_2); Geochemistry, Geophysics, Geosystems, v. 3, p. 1–7.

Sproule, R.A., Sutcliffe, R. Tracanelli, H., and Lesher, C.M., 2007. Palaeoproterozoic Ni-Cu-PGE mineralisation in the Shakespeare intrusion, Ontario, Canada: a new style of Nipissing gabbro-hosted mineralisation; Applied Earth Science, v. 116, p. 188–200.

Sun, S.-S. and McDonough, W.F., 1989. Chemical and isotopic systematics of oceanic basalts: implications for mantle composition and processes; Geological Society, London, Special Publications 42, p. 313–345.

Sutcliffe, R., Tracanelli, H., and Davis, W., 2002. Shakespeare intrusion; *in* Abstracts; Ontario Prospectors and Developers Association Annual Meeting, Toronto, Ontario.

Turcott, M., 2002. Big Swan Property; Ursa Major Minerals Inc., Ontario Assessment Record 41I05NE2009, 130 p.

Vaillancourt, C., Sproule, R.A., MacDonald, C.A., and Lesher, C.M., 2003. Investigation of Mafic-ultramafic intrusions in Ontario and implications for platinum group element mineralization: Operation Treasure Hunt; Ontario Geological Survey, Open File Report 6102, 335 p.

Young, G.M., Long, D.G., Fedo, C.M., and Nesbitt, H.W., 2001. Paleoproterozoic Huronian basin: product of a Wilson cycle punctuated by glaciations and a meteorite impact; Sedimentary Geology, v. 141–142, p. 233–254.

Appendix 1: Methods

Geochronology

Sample preparation and analyses were completed at the Jack Satterly Geochronology Laboratory at the University of Toronto. Approximately 10 kg of coarse-grained, pegmatoidal varitextured gabbro of the Triangle Mountain sill and Shakespeare intrusion were crushed and pulverized in a jaw crusher and steel ring mill. Baddeleyite (Triangle Mountain sill) and zircon (Shakespeare intrusion) crystals were collected using a Wilfley table following the method of Söderlund and Johanssen (2002). Prior to dissolution, zircon grains from the Shakespeare intrusion were air abraded.

Isotope dilution thermal ionization mass spectrometry (ID-TIMS) was used to analyze U-Pb. Baddeleyite and zircon grains were rinsed with 8N HNO_3 before being loaded into a Teflon capsule spiked with a ^{205}Pb-^{235}U solution. The grains were dissolved in 0.10 ml of concentrated hydrofluoric acid and 0.02 ml of 7N HNO_3 for 3 to 5 days. Following dissolution, samples were dried down and dissolved in 0.15 ml of 3N HCl for 24 hours (Krogh, 1973). Anion exchange columns (50 µl) were used to extract U and Pb with HCl. Elutions were dried down with H_3PO_4 and loaded onto Re filaments with silica gel (Gerstenberger and Haase, 1997). U-Pb measurements were completed on a VG354 mass spectrometer using a Daly detector in pulse counting mode.

Geochemistry

Whole-rock major and trace element geochemical analyses were acquired for 25 samples from various Nipissing sill localities. Each sample was crushed with a steel jaw crusher and pulverized for 2.5 to 3 minutes using an agate mill at Carleton University, Ottawa. The pulverized samples were sent to ALS Laboratories for analysis of 13 major elements, and 42 minor and trace elements. A lithium borate fusion method was used to prepare the samples before being dissolved in acid and analyzed by inductively coupled plasma-atomic emission spectrometry (ICP-AES) and inductively coupled plasma-mass spectrometry (ICP-MS).

Isotope Geochemistry

Powdered samples weighing between 40 and 105 mg were spiked with a ^{148}Nd-^{149}Sm mixture and then dissolved in HNO_3 -HF on a hot plate for 5 days. Following complete dissolution, the solution was dried down and digested with HNO_3 and HCl. Rare earth elements (REE) were separated using cation chromatography (a Dowex 50-X8 column). The resulting REE solution was dried down and dissolved in 0.26 M HCl for extraction of Nd and Sm. Using an Eichrom chromatographic column, separate elutions of Nd and Sm were collected with 0.26 M HCl and 0.5 M HCl, respectively, and 5 µl of 0.3 M H_3PO_4 was added to each Teflon vial prior to being dried down. Samples were loaded onto Re filaments and ratios were measured between 1700 and 1800°C using a Thermo-Finnigan Triton TI thermal ionization mass spectrometer.

Characteristics of Ni-Cu-PGE sulphide mineralization within the 1.1 Ga Midcontinent Rift

J. Smith[1], W. Bleeker[1], D.A. Liikane[2], M. Hamilton[3], R. Cundari[4] and P. Hollings[5]

[1]*Geological Survey of Canada, 601 Booth Street, Ottawa, Ontario K1A 0E8*
[2]*Department of Earth Sciences, University of Toronto, Toronto, Ontario M5S 1A1*
[3]*Jack Satterly Geochronology Laboratory, University of Toronto, 22 Russell Street, Toronto, Ontario M5S 3B1*
[4]*Ontario Geological Survey, 435 James Street South, Thunder Bay, Ontario P7E 6S7*
[5]*Department of Geology, Lakehead University, 955 Oliver Road, Thunder Bay, Ontario P7B 5E1*

Abstract

Magmatic Ni-Cu-PGE deposits of the ca. 1.1 Ga Midcontinent Rift system occur in association with a diverse range of ultramafic-mafic intrusions, from small early rift conduits to large, layered, mafic intrusions such as the Duluth Complex. The nature and style of mineralization is variable throughout these intrusions, some conduit deposits such as Eagle and Tamarack host massive nickel-copper sulphides, whilst others are relatively sulphur-poor but show extreme PGE enrichment (e.g. Current Lake; Marathon Deposit of the Coldwell Complex). The addition of external sulphur (Proterozoic and/or Archean) is considered critical in the formation of many of the Ni-Cu-PGE deposits; however, the key factors controlling the style of mineralization and the base and/or precious metal content are yet to be determined. This research aims to address the processes that are fundamental for metal enrichment and how these may vary both temporally and spatially during the rift's development. Furthermore, the Midcontinent Rift provides an excellent base to study the critical differences between mineralized and unmineralized intrusions, therefore providing the opportunity to assess key controls on metal endowment.

Introduction

North America's Midcontinent Rift (MCR) represents one of the best preserved intra-continental rift systems of late Mesoproterozoic age (Wold and Hinze, 1982; Green, 1983; Van Schmus and Hinze, 1985; Hutchinson et al., 1990; Miller and Nicholson, 2013). The ca. 1.1 Ga failed rift system hosts a range of mafic-ultramafic, carbonatitic and alkaline intrusions (Fig. 1; Bleeker et al., 2018), many of which are actively being explored for a range of commodities (e.g. Ni, Cu, PGE, Co, Cr, V, Nb). The magmatic Ni-Cu-PGE sulphide deposits occur in association with a range of mafic and mafic-ultramafic intrusions. Like many other world class nickel-copper deposits (e.g. Norilsk, Voisey's Bay, Raglan), this mineralization shows a close spatial and temporal relationship with large volumes of magma erupted at or near the margins of Archean cratons (Begg et al., 2010; Barnes et al., 2016).

Within the MCR, the most prospective Ni-Cu-PGE targets (e.g. Eagle, Tamarack) are hosted by small, early rift (ca. 1117 –1106 Ma), mafic-ultramafic intrusions. These deposits are developed within the magmatic plumping system of the rift, within long-lived magma pathways, an environment known to be favourable for the development of high-grade massive sulphides (Song et al., 2011; Barnes et al., 2016). These conduit-type intrusions host a significant proportion of the world's mineable nickel-copper resources, and as a result remain the focus of much exploration. The ca. 1099 Ma Duluth Complex (Paces and Miller, 1993; Davis and Green, 1997; Hoaglund, 2010) and similar large, sill-like, mafic layered intrusions (e.g. Sonju Lake, Mellen Complex, Echo Lake, Crystal Lake, Coldwell Complex) are also known to host Ni-Cu-PGE sulphide mineralization (Bakheit, 1981; Good and Crocket, 1994; Joslin, 2004; Ripley, 2014). Although these intrusion types are characterized by disseminated sulphides and often lower grades than the conduit deposits, they remain prospective targets and are favourable settings for the development of stratiform reef-style PGE-Ni-Cu mineralization (e.g. Sonju Lake: Joslin, 2004; and Duluth Complex: Miller, 1998).

Although the MCR system has a rich legacy of past and ongoing research, the fundamental controls pertaining to the localization (e.g. mantle source characteristics, structural features and crustal contamination) and timing of mineralization remain poorly understood. Thus, the question remains: why is significant Ni-Cu-PGE mineralization not developed within all rift-related mafic-ultramafic intrusions? The answer will only become apparent once a more comprehensive understanding of the temporal relationship between the various mineralized and barren mafic and ultramafic intrusions is improved. Although a number of dating studies have been undertaken on the MCR (see Heaman et al., 2007, for a relatively recent compilation), many of the intrusions either lack the precision that is now possible with routine chemical abrasion U-Pb geochronology or are yet to be dated (e.g. Steepledge, Sunday Lake, Saturday Night, Eagle East, Bovine Igneous Complex, Roland Lake and

Corresponding author: Jennifer Smith (jennifer.smith6@canada.ca)

Smith, J., Bleeker, W., Liikane, D.A., Hamilton, M., Cundari, R., and Hollings, P., 2019. Characteristics of Ni-Cu-PGE sulphide mineralization within the 1.1 Ga Midcontinent Rift; *in* Targeted Geoscience Initiative: 2018 report of activities, (ed.) N. Rogers; Geological Survey of Canada, Open File 8549, p. 421–432. https://doi.org/10.4095/313676

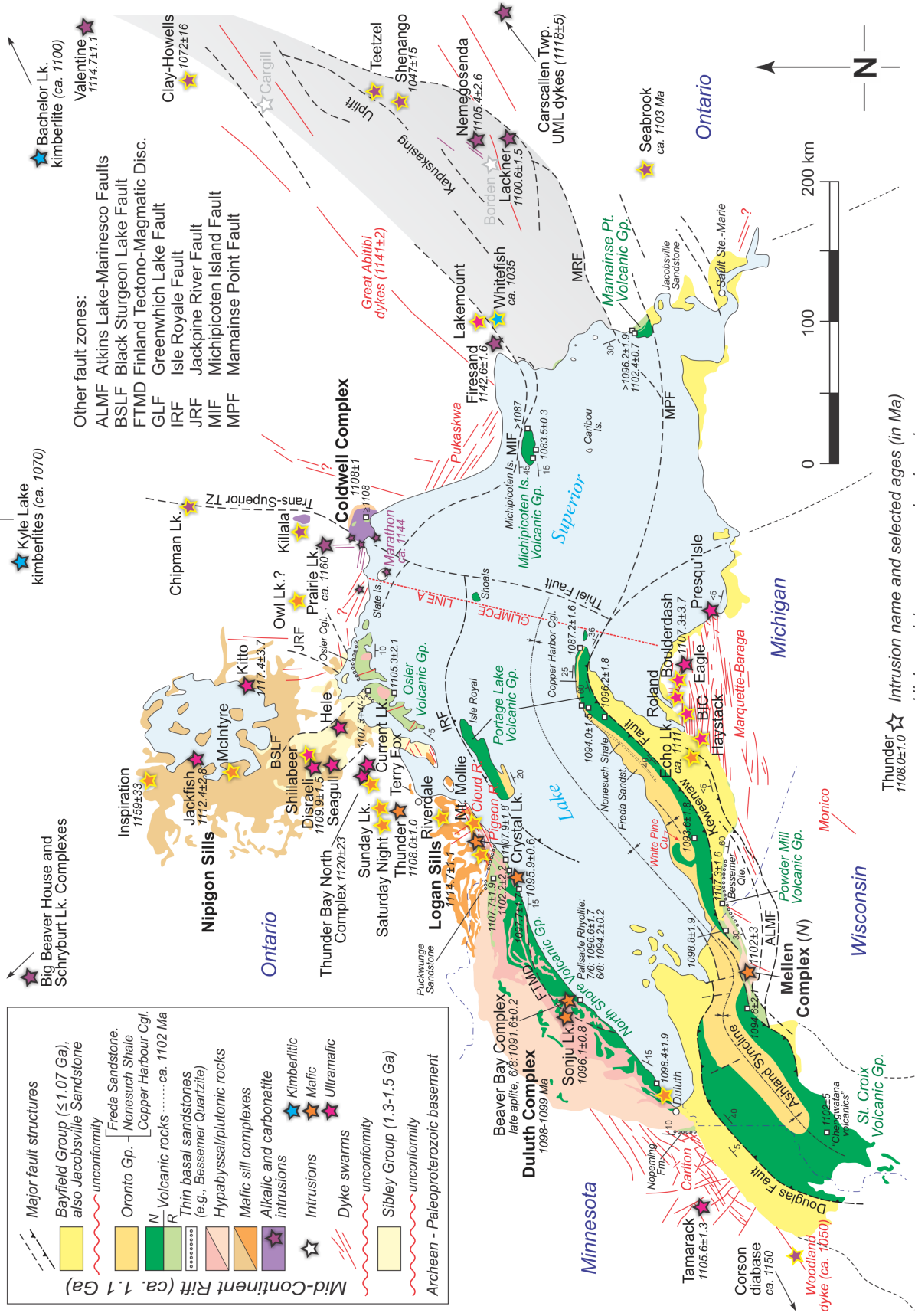

Figure 1. Summary map of the Midcontinent Rift from Bleeker et al. (2018), modified after Miller and Nicholson (2013) and references therein, highlighting the rift-related intrusions. Undated or poorly dated intrusions and/or ages that are otherwise problematic, are shown by stars with yellow outline. Only a selection of ages are shown, with the reader refereed to Bleeker et al. (2018) for additional age data and references. High-precision U-Pb ages on volcanic rocks are also shown for reference (Davis and Sutcliffe, 1987; Davis and Paces, 1990; Davis and Green, 1997; Zartman et al., 1997; Schoene et al., 2006; Swanson-Hysell et al., 2014; Fairchild et al., 2017).

Boulderdash). Through obtaining new and improved age constraints across the rift, we eventually aim to resolve the key processes relating to the rifts evolution. In addition, we aim to identify whether distinct mineralizing events can be directly related to discrete magmatic episodes, specific primitive melt compositions and/or mantle source regions or whether variations in local magma dynamics played the dominant role.

In this paper, we begin to document key characteristics of several of the mineralized mafic-ultramafic intrusions, highlighting the variability in the nature of magmatic Ni-Cu-PGE sulphide deposits within a single tectonic environment. A more detailed study is also underway on the Crystal Lake intrusion, west of Thunder Bay, Ontario, with the aim of (i) understanding the fundamental processes involved in ore genesis within the larger, main-rift-related intrusions; and (ii) constraining the relative timing of these mineralized intrusions with MCR related dykes that could represent potential feeders. This paper presents some preliminary observations from the 2018 field season.

Ni-Cu-PGE deposits of the Midcontinent Rift

The magmatic sulphide deposits developed within the MCR magmatic plumping system exhibit a variety of forms, occurring as tubular-shaped chonoliths, vertical/funnel dykes and lenticular/tabular bodies (Hart and Macdonald, 2007; Ding et al., 2010; Thomas et al., 2011; Taranovic et al., 2015; Barnes et al., 2016; Rose et al., 2018). Though many of these deposits are characterized by a circular magnetic anomaly (e.g. Eagle, Eagle East), several intrusions, including Tamarack, Steepledge and Current Lake, are characterized by a very distinctive magnetic anomaly that is 'tadpole-shaped' in appearance and extends in a NNW-SSE direction (Fig. 2). All of these intrusions contain a narrow, mineralized peridotite chonolith/dyke with an apparent deeper unmineralized lopolith-like intrusion to the southeast (Thomas et al., 2011; Taranovic et al., 2015). At present, the flow direction within these intrusion types is unconstrained. The 'bowl-like' intrusions are comparable, comprising a basal peridotite overlain by a thick differentiated oxide-rich gabbronorite

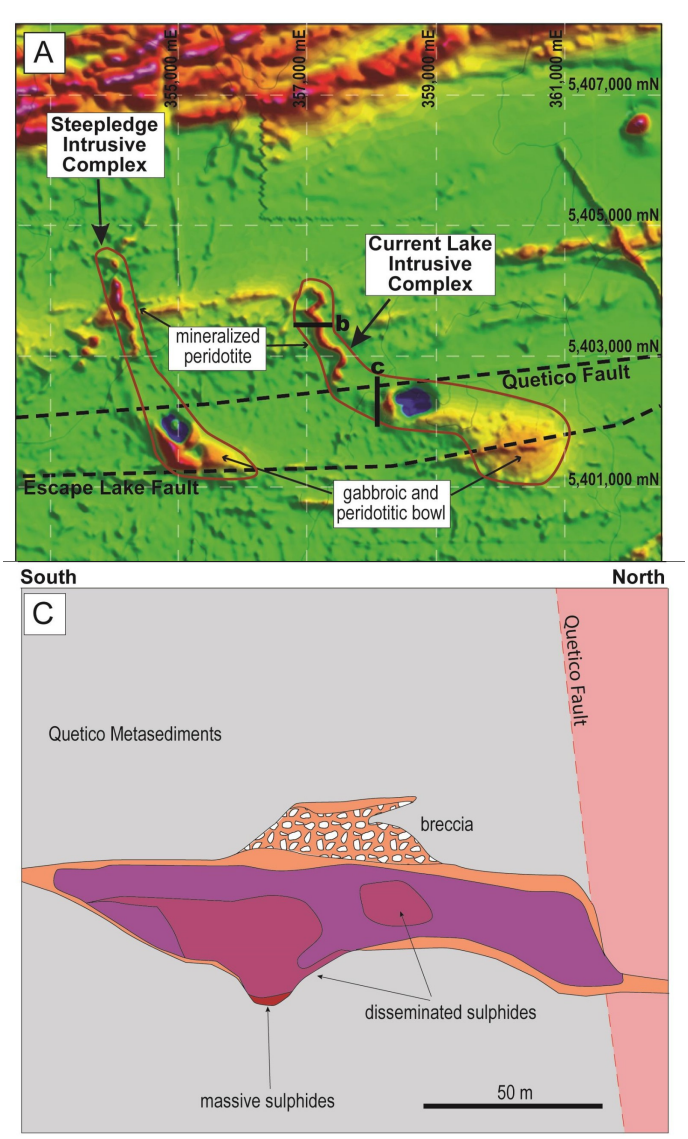

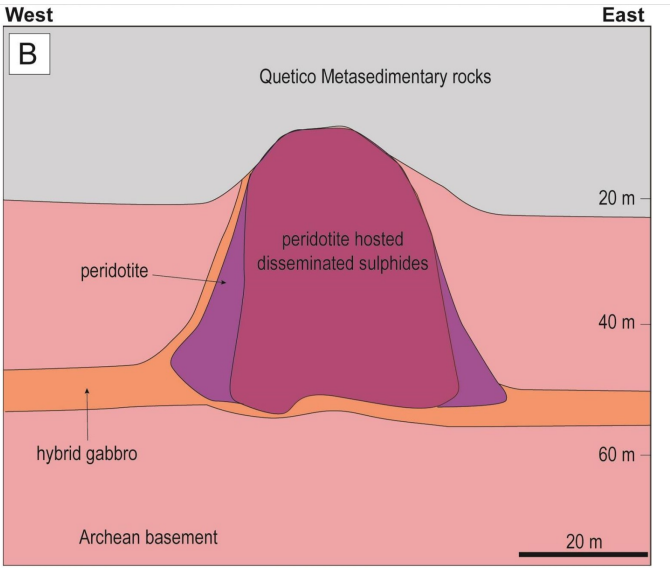

Figure 2. Geometry of the Current Lake Intrusive Complex. a) Total magnetic intensity map (image *from* A. Mactavish, Panoramic Resources, pers. comm., 2018) highlighting the NNW-SSE-trending 'tadpole' shape anomalies of the Current Lake and Steepledge Intrusive Complex. Intrusions comprise a narrow mineralized peridodite and a differentiated bowl. Location of cross-sections in (b) and (c) are also shown. b) Section through Current Lake (looking north), intrusion is tube-like in morphology with mineralization disseminated throughout the interior of the chonolith. c) Looking east through the Beaver Lake portion of the Current Lake Intrusive Complex. Note that the intrusion here is more tabular in geometry. Massive sulphides occur locally within footwall depressions. Cross-sections *from* Thomas et al. (2011) .

or monzogabbro. New, high-precision U-Pb age constraints will enable inferences on the spatio-temporal evolution of these intrusions to be made and placed in the context of the rifts development. Furthermore, an improved understanding of the dynamics of the MCR plumping system will also be gained. The geometry of conduit deposits is thought to result from the interplay of many factors, including pre-existing structures, thermal/mechanical erosion and stress fields (Barnes et al., 2016 and references therein). Within the MCR, Keays and Lightfoot (2015) suggested that the localization of the small, mineralized ultramafic intrusions is principally controlled by transpressional faults. The degree to which these faults control the geometry of the intrusions is yet to be constrained, however structural/lithological factors have been suggested to at least partially control the geometry of the Current Lake and Sunday Lake intrusions (Fig. 2c; Flank, 2017). Drilling indicates that the morphology of both intrusions, which are located within the Archean Quetico Subprovince, abruptly changes at the faulted contact between the Archean granodiorite and Quetico metasedimentary rocks (Fig. 2b, c; Thomas et al., 2011; Flank, 2017), from an irregular tube to a lopolith/tabular body, respectively.

The metal endowment and style of mineralization are also variable throughout the early rift mafic-ultramafic intrusions. Tamarack, Eagle and Eagle East are broadly similar, characterized by nickel-copper-enriched massive sulphide ores (Ni/Cu >1) developed within the keel or near the basal contact of the intrusion (Ding et al., 2010, 2012; Taranovic et al., 2016). In contrast, sulphide mineralization within other intrusions, particularly those hosted within the Quetico Subprovince (e.g. Current Lake, Sunday Lake), is PGE enriched and more disseminated in nature, with semi-massive sulphides only locally developed (Thomas et al., 2011; Flank, 2017). Subeconomic Ni-Cu-PGE occurrences have also been found within many of the small (<1 km thick) sheet/bowl-shaped mafic-ultramafic intrusions including Thunder, Bovine Igneous Complex and Seagull (Heggie, 2005; Laarman, 2007; Foley, 2011; Trevisan, 2014). Disseminated sulphide mineralization within many of these intrusions is developed within the basal ultramafic unit and as irregular horizons within the overlying differentiated gabbroic succession. At Seagull, Heggie (2005) also recognized stratiform PGE reef-style mineralization. The virtually barren early rift intrusions (e.g. Hele, Disraeli, Jackfish, Shillabeer and Boulderdash) are distributed throughout the rift, hosted by both Proterozoic sedimentary rocks and Archean basement. From the available literature there appears to be no clear spatial or temporal control on metal endowment throughout the rift. Consequently, the relationship of the unmineralized intrusions relative to those enriched remains poorly understood.

The addition of crustal sulphur is considered critical in the genesis of many of the MCR Ni-Cu sulphide deposits, which is supported by isotopic data (Ding et al., 2012; Ripley and Li, 2013; Ripley, 2014; Robertson et al., 2015). Externally derived sulphur is thought to be particularly important in the development of the high-grade massive sulphide conduit-type deposits (Ding et al., 2012; Hink, 2016; Taranovic et al., 2018), such as Eagle/Eagle East (4.8 Mt at 2.8 % Ni and 2.4 % Cu, Clow et al., 2017) and Tamarack (4.3 Mt at 1.58 % Ni, 0.92 % Cu, Fletcher et al., 2018). These three low tonnage, high-grade deposits are hosted within the correlative Animikie and Baraga basins, where they intrude sulphur-bearing Proterozoic sedimentary rocks of the Virginia, Thomson and Michigamme formations. These Proterozoic sedimentary rocks, which includes cherts, carbonates, greywackes and shales, appear to be favourable environments for the development of massive sulphides. Although $\delta^{34}S$ values are generally supportive of a local crustal sulphur source (Ding et al., 2012; Hink, 2016), Ding et al. (2012) highlight the potential contribution of multiple sources of sulphur, including a major contribution from a distal Archean source. The incorporation of significant Archean sulphur could explain the mantle-like $\delta^{34}S$ values recorded at Tamarack (Taranovic et al., 2018).

The addition of crustal sulphur (both Proterozoic and/or Archean) has also been shown to be critical in the genesis of sulphide mineralization within the large, sill-like mafic intrusions (e.g. Duluth Complex, Crystal Lake, Coldwell Complex; Ripley et al., 2007; Thomas, 2015; O'Brien, 2018; Shahabi Far et al., 2018). Basal- and stratiform-type deposits have been recognized within these intrusions, which host extensive disseminated, often low-grade Ni-Cu-PGE mineralization. The style and nature of this mineralization is variable amongst the intrusions, although it exhibits a close association with gabbroic rocks. Though many of the main-rift intrusions have been the subject of comprehensive studies, the relative timing of the various mineralizing events in the intrusions and MCR sills and dyke sets (e.g. Logan Sills, Pigeon River dykes, Cloud River dykes) remains unconstrained.

Crystal Lake intrusion

Geological Setting

A detailed geochemical and isotopic study is underway on the 1099.1 ± 1.2 Ma (Heaman et al., 2007) Crystal Lake intrusion, which has previously been compared to the proximal Duluth Complex (Thomas, 2015). The aim of this study is primarily to gain further insights into the controls on ore genesis within the main-rift intrusions.

The Crystal Lake intrusion, located 47 km southwest of Thunder Bay, outcrops as a prominent Y-shaped body (Fig. 3) within the Animikie basin, intruding sulphur-bearing shale, argillite and greywacke of the Paleoproterozoic Rove Formation (Geul, 1970, 1973). Although mineralization was first discovered in the 1950s and has been extensively explored since, the intrusion remains a prospective exploration target with Rio Tinto undertaking recent drill programs (2014–2018). Geochemically, the Crystal Lake intrusion can be distinguished from the more primitive conduit-type bodies by olivine composition (Fo_{51-79}), lower Ni/Cu and Pt/Pd ratios (<1), higher rare earth element (REE) abundances, light REE enrichment and minimal fractionation of heavy REEs (Gd/Yb <2).

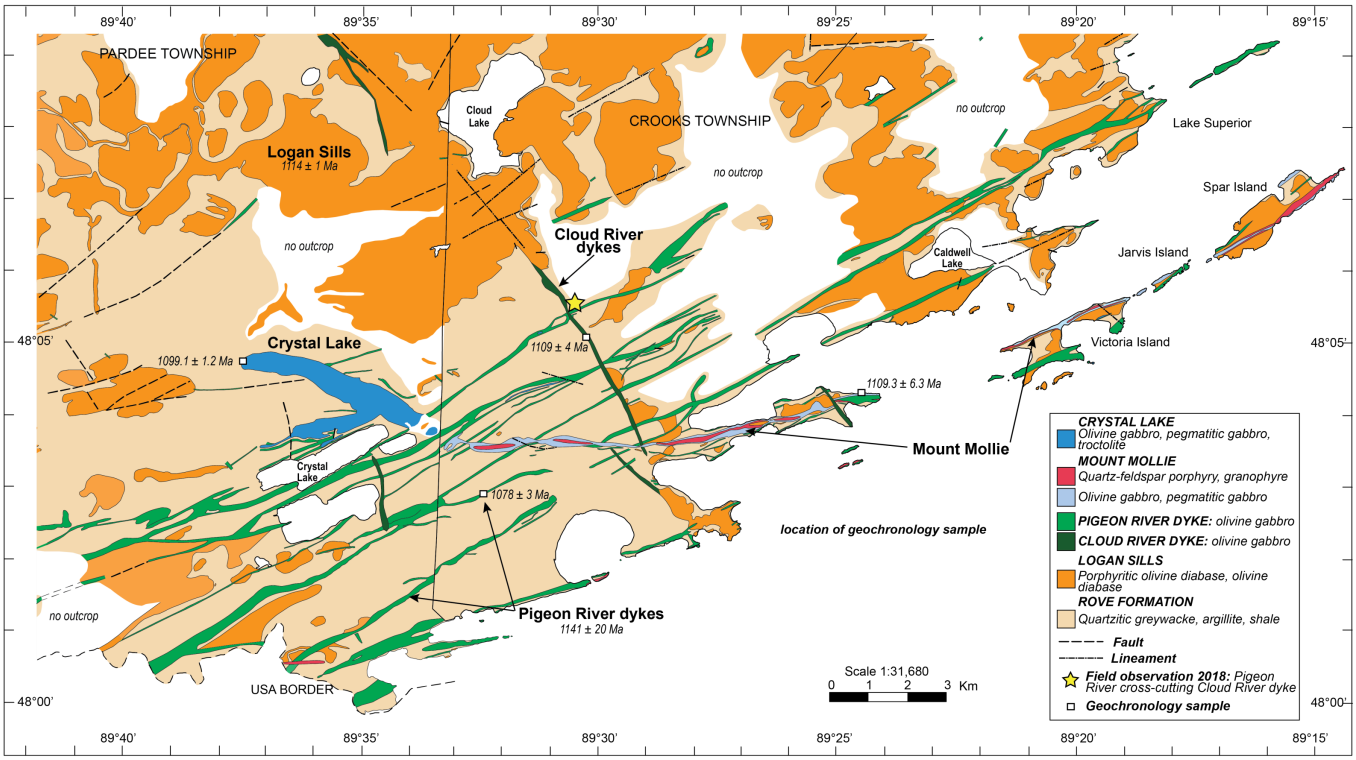

Figure 3. Geological map of the Pardee and Crook townships showing the location of Crystal Lake, Mount Mollie and the Pigeon River and Cloud River dyke sets.

Representative stratigraphic sections of the northern and southern limbs of the Crystal Lake intrusion are provided in Figure 4. There are notable differences between the limbs: (i) a magnetic anomaly is only identified along the southern limb, indicative of the thick unmineralized, magnetite-bearing olivine gabbro that has developed; (ii) an unmineralized, homogenous troctolite is present only within the northern limb; and (iii) to date, massive sulphides have only been intercepted within the northern limb. At present, there is uncertainty over the relationship between the two limbs, which we aim to resolve with high-precision U-Pb dating. Furthermore, we plan to untangle the timing of the Crystal Lake intrusion relative to the northeast-trending Pigeon River dykes and the sulphide-bearing Mount Mollie intrusion developed to the east. Crystal Lake has previously been suggested to be coeval with the Mount Mollie dyke (Smith and Sutcliffe, 1987; O'Brien, 2018). However, this is not supported by the current baddeleyite age date of 1109.3 ± 6.3 Ma (Hollings et al., 2010). Due to poor exposure, the timing relationships of the Crystal Lake intrusion with the Pigeon River, Mount Mollie and Cloud River dykes could not be successfully established from field observations. A cross-cutting relationship was however observed between the Cloud River and Pigeon River dykes within the Crooks Township (see Fig. 3 for location). At this location a Pigeon River dyke is seen to intrude the north-northwest-trending Cloud River dykes (Fig. 5), a cross-cutting relationship that disagrees with Geul's (1973) interpretation (Fig. 3).

Sulphide mineralization

Ni-Cu-PGE sulphide mineralization is developed within the northern and southern limbs of the Crystal Lake intrusion in association with vari-textured gabbro and irregular Cr-spinel-bearing horizons (Fig. 6). The association of sulphides and metal enrichment with pegmatitic/taxitic units is not unique to the Crystal Lake intrusion. It is also present within the ca. 1108 Ma (Heaman and Machado, 1992) Coldwell Complex and other major deposits (e.g. Merensky Reef, Norilsk, Voisey's Bay; Barnes and Campbell, 1988; Cawthorn, 2010; Good et al., 2015; Barnes et al., 2016). The upper troctolite and magnetite-bearing olivine gabbro of the northern and southern limbs, respectively, are completely barren of sulphides. With no apparent chill zone identified at the contact of these zones with the underlying mineralized vari-textured gabbros, the relative timing of these units is unclear.

Sulphide mineralization is largely disseminated, with massive sulphides developed only locally within the northern limb (Fig. 6c). The ores are dominated by the primary magmatic assemblage pyrrhotite, pentlandite and chalcopyrite, and are variable in texture with globule (capped and uncapped), blebby and interstitial sulphides identified (Fig. 7). The silicate-capped sulphide globules have been recognized in several other nickel-copper sulphide deposits (e.g. Norilsk, Insizwa Complex; Barnes et al., 2017; Le Vaillant et al., 2017) and are interpreted as being the remnants of a former magmatic vapour phase that

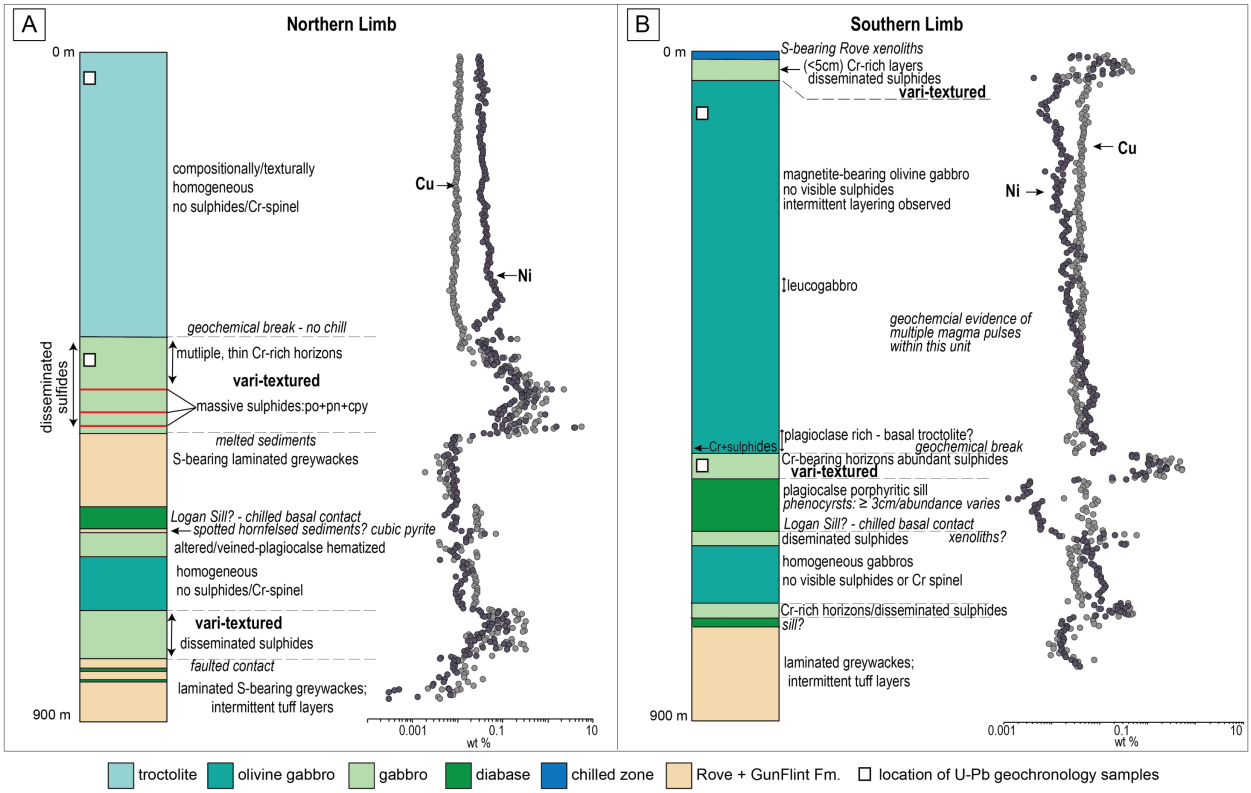

Figure 4. Representative stratigraphic columns of the (a) northern and (b) southern limbs of the Crystal Lake Intrusion. Metal concentrations *from* Goldner (2015, 2016).

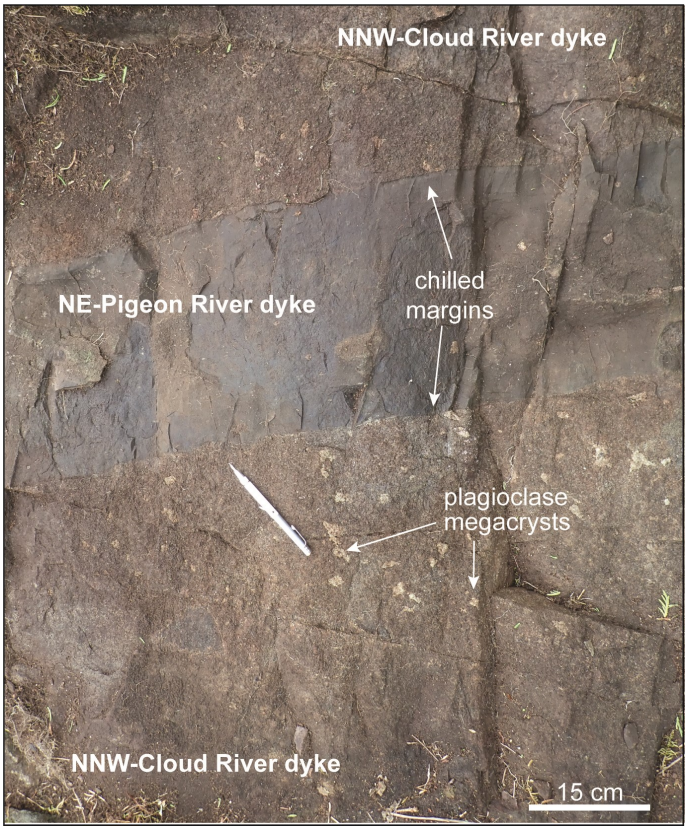

Figure 5. Observed cross-cutting relationship between the offshoot of the northeast-trending Pigeon River dyke and older north-northwest-trending Cloud River dyke where these two dyke trends intersect. Fine-grained, dark, Pigeon River dyke is cutting sharply across and chilled against the older coarse-grained Cloud River dyke. The central phase of the large Cloud River dyke carries 1 to 2 cm plagioclase megacrysts, visible as light coloured patches.

attached to an immiscible sulphide melt (Mungall et al., 2015). Within the Crystal Lake intrusion, the morphology of the vapour phase is variable. Convex silicate caps, identical to those modelled by Mungall et al. (2015), are present along with very irregular silicate attachments (Fig. 7e, f). Experimental studies have shown that these sulphide/vapour compounds are capable of floating under certain conditions, providing a mechanism for the upward movement of sulphides. Detailed work needs to be undertaken on the Crystal Lake intrusion to decipher the significance of these capped globules and their implications for sulphide transportation and deposition.

Partially assimilated, fine-grained greywacke xenoliths of the sulphur-bearing Rove Formation are present near the basal contacts of the gabbroic rocks (Fig. 8a; Smith and Sutcliffe, 1987; O'Brien, 2018). Based on isotopic data, the addition of crustal S from the Proterozoic country rocks is thought to have

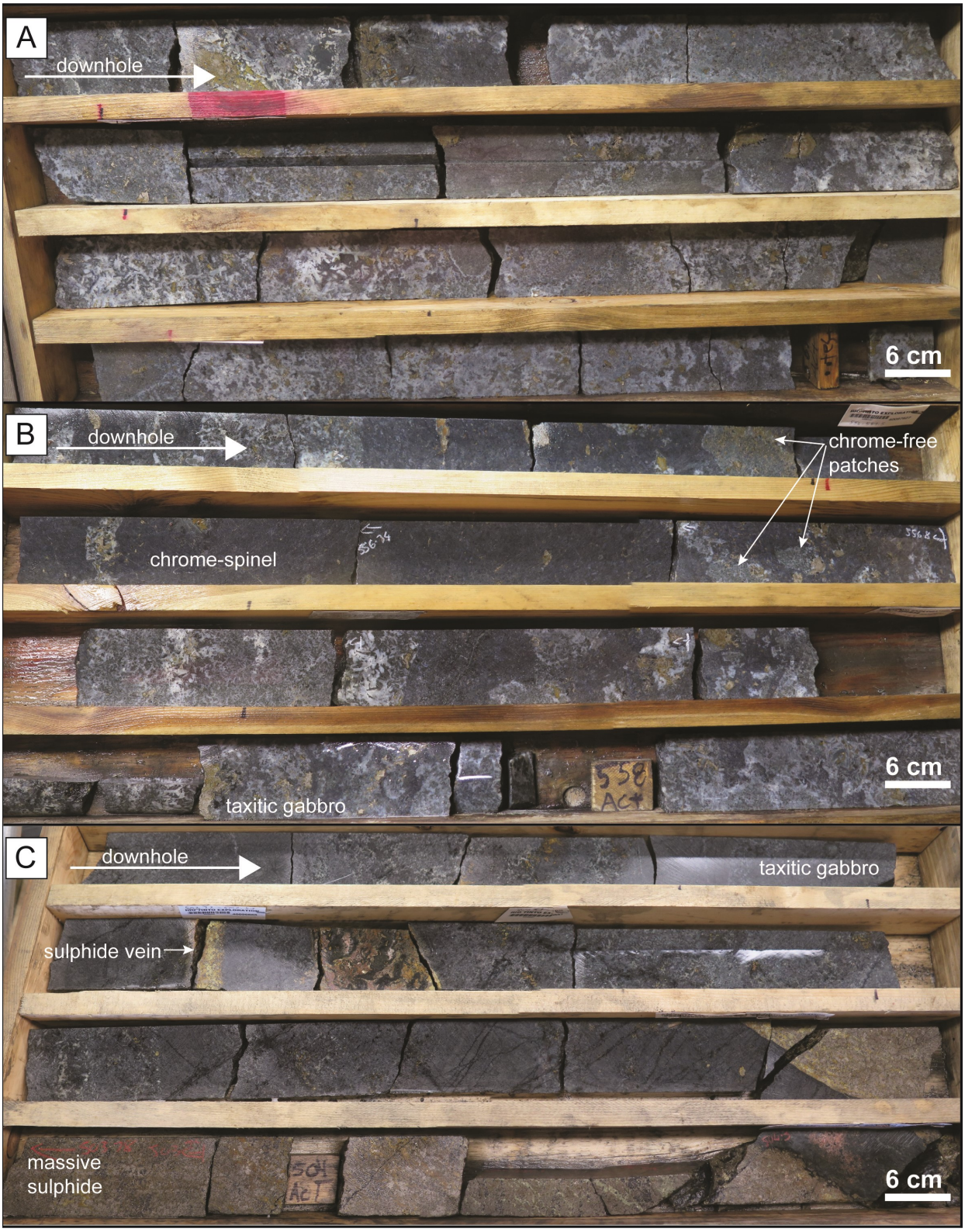

Figure 6. Representative photographs from the Crystal Lake intrusion. a) Vari-textured gabbro from the northern limb, with significant interstitial/blebby sulphide mineralization. b) Horizons rich in chrome-spinel intersected within the southern limb. Sulphide mineralization is disseminated and blebby in nature and is associated with the Cr-rich and Cr-free gabbro pockets. c) Massive sulphides developed within the northern limb. Note sharp upper contact with gabbro and the presence of sulphide veins.

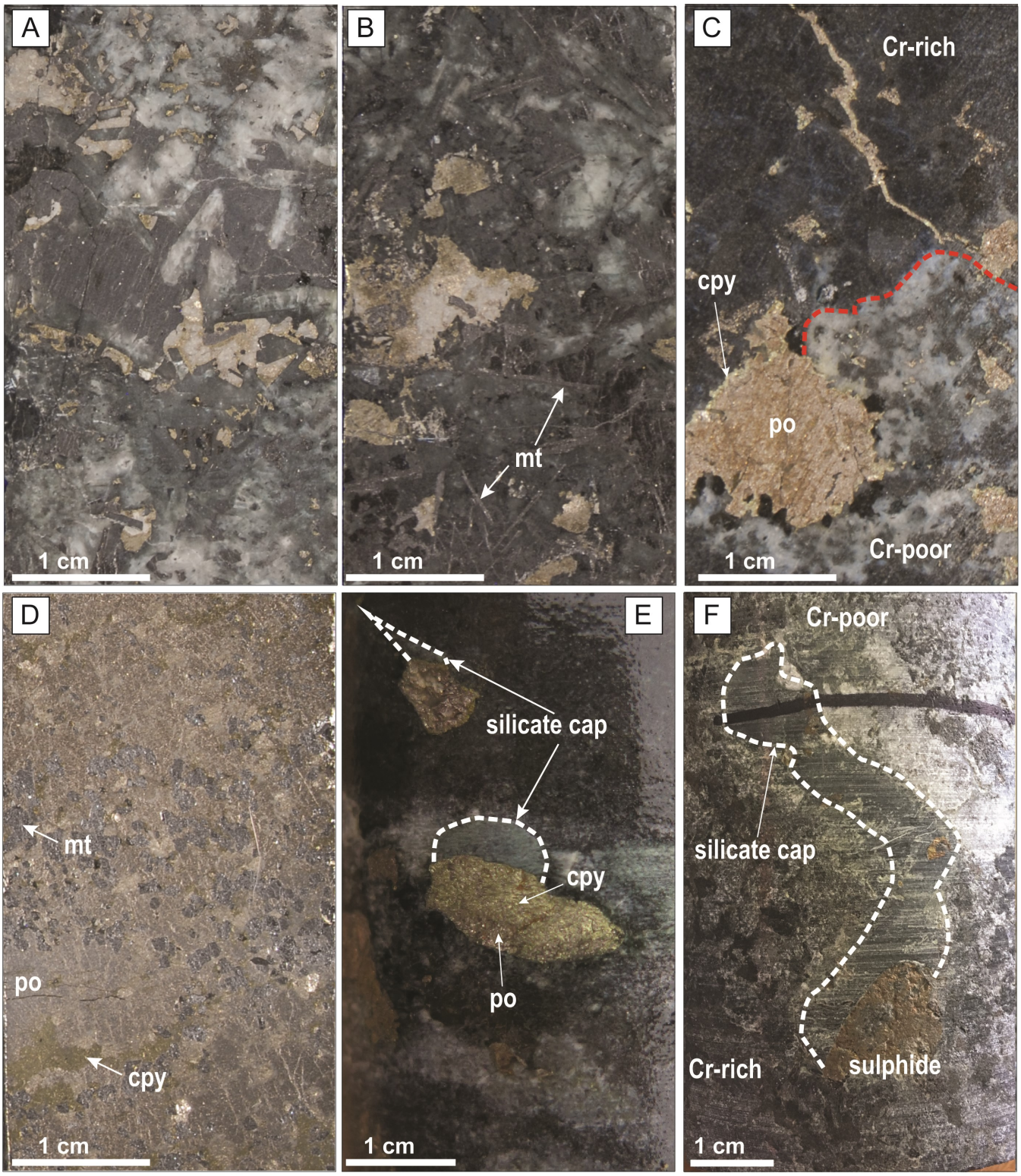

Figure 7. Sulphide textures observed within the Crystal Lake intrusion. a) and b) Interstitial, disseminated sulphides within variitextured gabbro. Note the abundance of magnetite needles within (b). c) Blebby and stringer sulphides observed within the Cr-rich horizons. Note sulphides occur within the Cr-rich and Cr-free areas. Sulphides comprise a pyrrhotite core, rimmed by chalcopyrite. d) Massive sulphides (pyrrhotite and chalcopyrite) from the northern limb, with magnetite. e) Globular sulphide consisting of chalcopyrite and pyrrhotite with silicate caps. f) Sulphide globule within Cr-horizon attached to an irregular silicate cap. Abbreviations: cpy – chalcopyrite; mt – magnetite; po – pyrrhotite.

occurred prior to emplacement. The *in situ* assimilation of the local footwall is not considered critical in inducing sulphur saturation (Thomas, 2011; O'Brien, 2018). Xenoliths of chrome-spinel and gabbro autoliths have been recognized within vari-textured gabbro (Fig. 8b–d), indicating some degree of reworking. Whether this reworking is localized or from a deeper source is yet to be determined.

Future work

High-precision age determinations are in progress or are planned for a selection of intrusions to resolve a number of the imprecise and/or problematic ages including Crystal Lake, Mount Mollie and the Pigeon River dykes. Zircon and baddeleyite mineral separates from dated intrusions are projected for further investigation by combined U-Pb, Lu-Hf and trace element studies to shed light on mantle sources of the mineralized intrusions.

A comprehensive suite of samples collected from the Crystal Lake intrusion during the 2018 field season will be used for detailed isotopic studies, including Sm-Nd, Rr-Sr and Lu-Hf. This data will provide an insight into the characteristics of the mantle source and the contamination history of the Crystal Lake intrusion. Multiple sulphur isotope studies have revealed that within the Eagle and Marathon deposits, sulphur is in part derived from Archean sources (Ding et al., 2012; Shahabi Far et al., 2018). Although intrusions such as Crystal Lake and the Duluth Complex are characterized by $\delta^{34}S$ values consistent with the incorporation of extensive crustal sulphur from the Paleoproterozoic rocks, determination of $\Delta^{33}S$ could provide evidence of a distal Archean source that has previously not been identified. Such a study could have implications for our understanding of ore genesis of Ni-Cu-PGE deposits within these large, mafic intrusions.

Acknowledgments

This report is a contribution to NRCan's Targeted Geoscience Initiative Program (TGI). Support for this study was provided through the Ni-Cu-PGE Systems Project's '*Activity NC-*

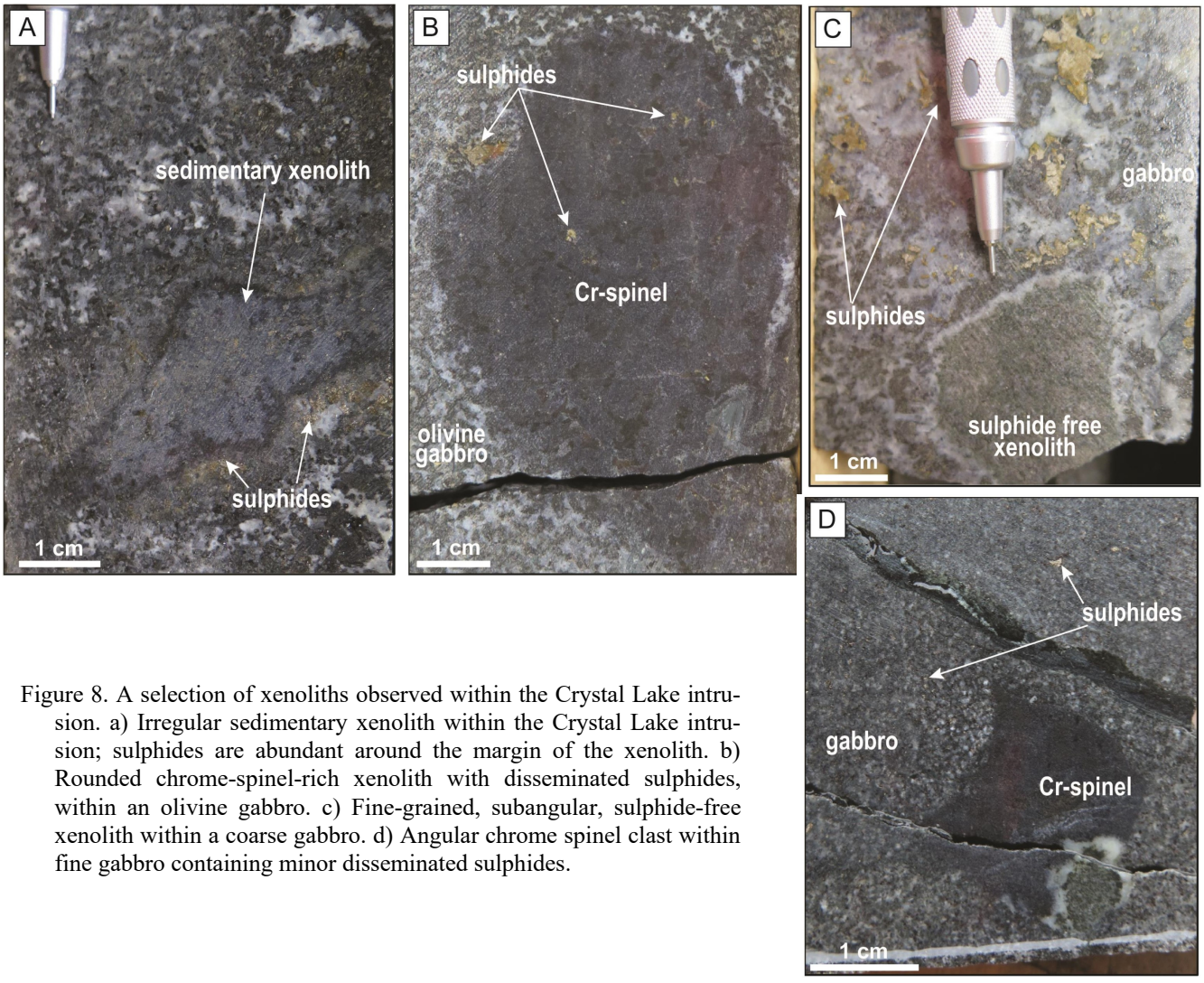

Figure 8. A selection of xenoliths observed within the Crystal Lake intrusion. a) Irregular sedimentary xenolith within the Crystal Lake intrusion; sulphides are abundant around the margin of the xenolith. b) Rounded chrome-spinel-rich xenolith with disseminated sulphides, within an olivine gabbro. c) Fine-grained, subangular, sulphide-free xenolith within a coarse gabbro. d) Angular chrome spinel clast within fine gabbro containing minor disseminated sulphides.

1.3: Controls on the localization and timing of mineralized intrusions in intra-continental rift systems, with a specific focus on the ca. 1.1 Ga Mid-continent Rift system'.

Dustin Liikane is conducting a TGI-supported Ph.D. at the University of Toronto, Toronto, Ontario. The authors thank our partners at Rio Tinto (Dean Rossell, Brian Goldner, Justin Laberge), North American Palladium (Dave Peck, Steve Flank), Transition Metals (Grant Moore, Scott McLean), Panoramic (Al MacTavish) and Stillwater Canada (Dave Good, John McBride) for their help and constructive discussions. The Ontario Geological Survey, particularly Mike Easton, Mark Puumala, Mark Smyk and Greg Paju, are also thanked for their logistical support throughout the 2018 field season and for sharing their knowledge of the geology of the Thunder Bay area. We also thank the Ministry of Natural Resources and Forestry for providing boat access and a crew (captained by Dave Montgomery), which enabled fieldwork to be carried out on various islands within Lake Superior. We also thank our field assistant Sarah Davey. Rhian Evans and other members of the TGI team are thanked for assistance in organizing the 2018 field season. This report benefited from the review of Benoît Dubé, Ernst Schetselaar and Neil Rogers.

References

Bakheit, A.K., 1981, Petrography of Cu-Ni mineralization in the Mineral Lake area, Ashland County, Wisconsin; M.Sc. thesis, University of Wisconsin, Madison, Wisconsin, 104 p.

Barnes, S.J. and Campbell, I.H., 1988. Role of late magmatic fluids in Merensky-type platinum deposits: A discussion; Geology, v. 6, p. 488–491.

Barnes, S.J., Cruden, A.R., Arndt, N., and Saumur, B.M., 2016. The mineral system approach applied to magmatic Ni–Cu–PGE sulphide deposits; Ore Geology Reviews, v.76, p. 296–316.

Barnes, S.J., Mungall, J., Le Vaillant, M., Godel, B., Lesher, M., Holwell, D., Lightfoot, P., Krivolutskaya, N., and Wei, B., 2017. Sulphide-silicate textures in magmatic Ni-Cu-PGE sulphide ore deposits: Disseminated and net-textured ores; American Mineralogist, v. 102, p. 473–506.

Begg, G.C., Hronsky, J.A., Arndt, N.T., Griffin, W.L., O'Reilly, S.Y. and Hayward, N., 2010. Lithospheric, cratonic, and geodynamic setting of Ni-Cu-PGE sulphide deposits; Economic Geology, v. 105, p. 1057–1070.

Bleeker, W., Liikane, D.A., Smith, J., Hamilton, M., Kamo, S.L., Cundari, R., Easton, M., and Hollings, P., 2018. Activity NC-1.3: Controls on the localisation and timing of mineralized intrusions in intra-continental rift systems, with a specific focus on the ca. 1.1 Ga Mid-continent Rift (MCR) system; *in* Targeted Geoscience Initiative: 2017 Report of Activities, Volume 2 (ed.) N. Rogers; Geological Survey of Canada, Open File 8373, p. 15–27.

Cawthorn, R.G., 2010. The platinum group element deposits of the Bushveld Complex in South Africa; Platinum Metals Review, v. 54, p. 205–215.

Clow, G.G., Normand L.L., Rennie, D.W., Scholey, B.J.Y., 2017. Lundin Mining Corporation Technical Report on the Eagle Mine, Michigan, U.S.A, NI 43-101 Report, 306 p.

Davis, D.W. and Green, J.C., 1997. Geochronology of the North American Midcontinent rift in western Lake Superior and implications for its geodynamic evolution; Canadian Journal of Earth Sciences, v. 34, p. 476–488.

Davis, D.W. and Paces, J.B., 1990. Time resolution of geologic events on the Keweenaw Peninsula and implications for development of the Midcontinent Rift system; Earth and Planetary Science Letters, v. 97, p. 54–64.

Davis, D.W. and Sutcliffe, R.H., 1985. U-Pb ages from the Nipigon plate and northern Lake Superior; Geological Society of America Bulletin, v. 96, p. 1572–1579.

Ding, X., Li, C., Ripley, E.M., Rossell, D., and Kamo, S., 2010. The Eagle and East Eagle sulphide ore-bearing mafic-ultramafic intrusions in the Midcontinent Rift System, Upper Michigan: Geochronology and petrologic evolution; Geochemistry, Geophysics, Geosystems, v. 11, 22 p.

Ding, X., Ripley, E.M., and Li, C., 2012. PGE geochemistry of the Eagle Ni–Cu–(PGE) deposit, Upper Michigan: Constraints on ore genesis in a dynamic magma conduit; Mineralium Deposita, v. 47, p. 89–104.

Fairchild, L.M., Swanson-Hysell, N.L., Ramezani, J., Sprain, C.J., and Bowring, S.A., 2017. The end of Midcontinent Rift magmatism and the paleogeography of Laurentia; Lithosphere, v. 9, p. 117–133.

Flank, S., 2017. The Petrography, Geochemistry and Stratigraphy of the Sunday Lake Intrusion, Jacques Township, Ontario; M.Sc. thesis, Laurentian University, Sudbury, Ontario, 71 p.

Fletcher, T., Peters, O., and Thomas B., 2018. Second Independent Technical Report on the Tamarack North Project – Tamarack, Minnesota, NI 43-101 Technical Report, 213 p.

Foley, D.J., 2011. Petrology and Cu-Ni-PGE mineralization of the Bovine Igneous Complex, Baraga County, Northern Michigan; M.Sc. thesis, University of Minnesota, Minneapolis, Minnesota, 109 p.

Geul, J.C., 1970. Geology of Devon and Pardee Townships and the Stuart Location; Ontario Department of Mines, Geological Report 87.

Geul, J.C., 1973. Geology of Crooks Township, Jarvis and Prince Locations, and Off-shore Islands, District of Thunder Bay; Ontario Department of Mines, Geological Report 102.

Goldner, B., 2015. Rio Tinto Exploration Canada Inc. Assessment Report on the Cu-Ni-PGE Crystal Lake Project. Pardee, Devon and Crooks Township, NTS 52A/04, Thunder Bay Mining Division, Ontario, 825 p.

Goldner, B., 2016. Rio Tinto Exploration Canada Inc. Assessment Report on the Cu-Ni-PGE Crystal Lake Project. Pardee, Devon and Crooks Township, NTS 52A/04, Thunder

Bay Mining Division, Ontario, 219 p.

Good, D.J. and Crocket, J.H., 1994. Genesis of the Marathon Cu-platinum group-element deposit, Port Coldwell Alkalic Complex, Ontario: A Midcontinent rift-related magmatic sulphide deposit; Economic Geology, v. 89, p. 131–149.

Good, D.J., Epstein, R., McLean, K., Linnen, R.L., and Samson, I.M., 2015. Evolution of the Main Zone at the Marathon Cu-PGE sulphide deposit, Midcontinent Rift, Canada: spatial relationships in a magma conduit setting; Economic Geology, v. 110, p. 983–1008.

Green, J.C., 1983. Geologic and geochemical evidence for the nature and development of the Middle Proterozoic (Keweenawan) Midcontinent Rift of North America; Tectonophysics, v. 94, p. 413–437.

Hart, T.R. and MacDonald, C.A., 2007. Geology and structure of the western margin of the Nipigon Embayment; Canadian Journal of Earth Sciences, v. 44, p. 1021–1040.

Heaman, L.M. and Machado, N., 1992. Timing and origin of midcontinent rift alkaline magmatism, North America: evidence from the Coldwell Complex; Contributions to Mineralogy and Petrology, v. 110, p. 289–303.

Heaman, L.M., Easton, R.M., Hart, T.R., Hollings, P., MacDonald, C.A., and Smyk, M., 2007. Further refinement to the timing of Mesoproterozoic magmatism, Lake Nipigon region, Ontario; Canadian Journal of Earth Sciences, v. 44, p. 1055–1086.

Heggie, G.J., 2005. Whole rock geochemistry, mineral chemistry, petrology and Pt, Pd mineralization of the Seagull intrusion, Northwestern Ontario; M.Sc. Thesis, Lakehead University, Thunder Bay, Ontario, 156 p.

Hink, B.D., 2016. Geochemical and Petrological Studies on the Origin of Nickel-Copper Sulphide Mineralization at the Eagle Intrusion in the Marquette County, Michigan; M.Sc. thesis, Western Michigan University, Kalamazoo, Michigan, 129 p.

Hoaglund, S.A., 2010. U-Pb geochronology of the Duluth Complex and related hypabyssal intrusions: investigating the emplacement history of a large multiphase intrusive complex related to the 1.1 Ga Midcontinent Rift; M.Sc. thesis, University of Minnesota Duluth, Duluth, Minnesota, 103 p.

Hollings, P., Smyk, M., Heaman, L.M., and Halls, H., 2010. The geochemistry, geochronology, and paleomagnetism of dikes and sills associated with the Mesoproterozoic Midcontinent Rift near Thunder Bay, Ontario, Canada; Precambrian Research, v. 183, p. 553–571.

Hutchinson, D., White, R., Cannon, W., and Schulz, K., 1990. Keweenawan hot spot: Geophysical evidence for a 1.1 Ga mantle plume beneath the Midcontinent Rift system; Journal of Geophysical Research, v. 95, p. 10 869–10884.

Joslin, G.D., 2004. Stratiform palladium-platinum-gold mineralization in the Sonju Lake intrusion, Lake County, Minnesota; M.Sc. thesis, University of Minnesota Duluth, Duluth, Minnesota,186 p.

Keays, R.R., and Lightfoot, P.C., 2015. Geochemical stratigraphy of the Keweenawan Midcontinent Rift volcanic rocks with regional implications for the genesis of associated Ni, Cu, Co, and platinum group element sulfide mineralization; Economic Geology, v. 110, p.1235–1267.

Laarman, J.E., 2007. Geochemistry and PGE mineralization of the Kitto intrusion: A product of Mesoproterozoic plume magmatism through fault bounded Archean crust, east Nipigon Embayment, northern Ontario; M.Sc. thesis, Lakehead University, Thunder Bay, Ontario, 276 p.

Le Vaillant, M., Barnes, S.J., Mungall, J.E., and Mungall, E.L., 2017. Role of degassing of the Noril'sk nickel deposits in the Permian–Triassic mass extinction event; Proceedings of the National Academy of Sciences, v. 114, p. 2485–2490.

Miller, J.D., 1998. Potential for reef-type PGE mineralization in the Duluth Complex: Evidence from the Layered Series at Duluth; The Minnesota Prospector, Special Issue, p. 8–12.

Miller, J.D. and Nicholson, S.W., 2013. Geology and mineral deposits of the 1.1 Ga Midcontinent Rift in the Lake Superior region – An overview; *in* Field Guide to the Cu-Ni-PGE Deposits of the Lake Superior Region, (ed.) J.D. Miller; Precambrian Research Center Guidebook 13-1, p. 1–50.

Mungall, J.E., Brenan, J.M., Godel, B., Barnes, S.J., and Gaillard, F., 2015. Transport of metals and sulphur in magmas by flotation of sulphide melt on vapour bubbles; Nature Geoscience, v. 8, p. 216–219.

O'Brien, S., 2018. Geology of the Crystal Lake Gabbro and the Mount Mollie Dyke, Midcontinent Rift, Northwest Ontario; M.Sc. thesis, Lakehead University, Thunder Bay, Ontario, 350 p.

Paces, J.B. and Miller, J.D., 1993. Precise U-Pb ages of Duluth complex and related mafic intrusions, northeastern Minnesota: Geochronological insights to physical, petrogenetic, paleomagnetic, and tectonomagmatic processes associated with the 1.1 Ga midcontinent rift system; Journal of Geophysical Research: Solid Earth, v. 98, p. 13 997–14 013.

Ripley, E.M., 2014. Ni-Cu-PGE mineralization in the Partridge River, South Kawishiwi, and Eagle intrusions: A review of contrasting styles of sulphide-rich occurrences in the Midcontinent rift system; Economic Geology, v. 109, p. 309–324.

Ripley, E.M. and Li, C., 2013. Sulphide saturation in mafic magmas: Is external sulphur required for magmatic Ni-Cu-(PGE) ore genesis?; Economic Geology, v. 108, p. 45–58.

Ripley, E.M., Taib, N.I., Li, C., and Moore, C.H., 2007. Chemical and mineralogical heterogeneity of the basal zone of the Partridge River intrusion, Duluth Complex: Evidence for Cu-Ni mineralization during early stages of rift development; Contributions to Mineralogy and Petrology, v. 154, p. 34–54.

Robertson, J., Ripley, E.M., Barnes, S.J. and Li, C., 2015. Sulfur liberation from country rocks and incorporation in mafic magmas; Economic Geology, v. 110 p. 1111–1123.

Rose, K., Essig, W., and Thakurta, J., 2018. Variation trends in sulphide isotope ratios at the Eagle and East Eagle intrusions and the surrounding country and basement rocks of the Baraga Basin, Upper Peninsula, Michigan; in Abstracts; Institute of Lake Superior Geology, 64th Annual Meeting, Iron Mountain, p. 87.

Schoene, B., Crowley, J.L., Condon, D.J., Schmitz, M.D., and Bowring, S.A., 2006. Reassessing the uranium decay constants for geochronology using ID-TIMS U-Pb data; Geochimica et Cosmochimica Acta, v. 70, p. 426–445.

Shahabi Far, M., Samson, I.M., Gagnon, J.E., Good, D.J., Linnen, R.L., Layne, G.D., and Wing, B.A., 2018. Identifying externally derived sulphur in conduit-type Cu–platinum-group element deposits: The importance of multiple sulphur isotope studies; Geology, v. 46, p. 235–238.

Smith, A.R. and Sutcliffe, R.H., 1987. Keweenawan intrusive rocks of the Thunder Bay area; Ontario Geological Survey, Miscellaneous Paper 137, p. 248–255.

Song, X., Wang, Y. and Chen, L., 2011. Magmatic Ni-Cu-(PGE) deposits in magma plumbing systems: Features, formation and exploration; Geoscience Frontiers, v. 2, p .375–384.

Swanson-Hysell, N.L., Burgess, S.D., Maloof, A.C., and Bowring, S.A., 2014. Magmatic activity and plate motion during the latent stage of Midcontinent Rift development; Geology, v. 42, p. 475–478.

Taranovic, V., Ripley, E.M., Li, C., and Rossell, D., 2015. Petrogenesis of the Ni–Cu–PGE sulphide-bearing Tamarack Intrusive Complex, Midcontinent Rift System, Minnesota; Lithos, v. 212, p. 16–31.

Taranovic, V., Ripley, E.M., Li, C., and Rossell, D., 2016. Chalcophile element (Ni, Cu, PGE, and Au) variations in the Tamarack magmatic sulphide deposit in the Midcontinent Rift System: implications for dynamic ore-forming processes; Mineralium Deposita, v. 51, p. 937–951.

Taranovic, V., Ripley, E.M., Li, C. and Shirey, S.B., 2018. S, O, and Re-Os isotope studies of the Tamarack Igneous Complex: melt-rock interaction during the early stage of Midcontinent Rift development; Economic Geology, v. 113, p. 1161–1179.

Thomas, B., 2015. Geochemistry, sulfur isotopes and petrography of the Cu-Ni-PGE mineralized Crystal Lake intrusion, Thunder Bay, Ontario; M.Sc. thesis, Indiana University, Bloomington, Indiana, 94 p.

Thomas, D.G., Melnyk, J., Gormely, L., Searston, S., and Kulla, G., 2011. Thunder Bay North polymetallic project, Ontario, Canada; Magma Metals Ltd., NI 43-101 Technical Report on Preliminary Assessment, p. 10-14–10-18.

Trevisan, B.E., 2014. The petrology, mineralization and regional context of the Thunder mafic to ultramafic intrusion, Midcontinent Rift, Thunder Bay, Ontario; M.Sc. thesis, Lakehead University, Thunder Bay, Ontario, 285 p.

Van Schmus, W.R. and Hinze, W.J., 1985. The midcontinent rift system; Annual Review of Earth and Planetary Sciences, v. 13, p. 345–383.

Wold, R.J. and Hinze, W.J., 1982. Geology and Tectonics of the Lake Superior Basin; Geological Society of America, Boulder, Colorado, Memoir 156, 280 p.

Zartman, R.E., Nicholson, S.W., Cannon, W.F., and Morey, G., 1997. U-Th-Pb zircon ages of some Keweenawan Supergroup rocks from the south shore of Lake Superior; Canadian Journal of Earth Science, v. 34, p. 549–561.

Overview of chromium, Fe-Ti-V and Ni-Cu-PGE metal endowment of the Superior Province

M.G. Houlé[1], C.M. Lesher[2] and A.-A. Sappin[1]

[1]*Geological Survey of Canada, 490 rue de la Couronne, Québec, Quebec G1K 9A9*

[2]*Mineral Exploration Research Centre, Harquail School of Earth Sciences, Goodman School of Mines, Laurentian University, 935 Ramsey Lake Road, Sudbury, Ontario P3E 2C6*

Abstract

This research activity investigates the metal endowments of magmatic ore deposits across the Superior Province in order to identify key metallogenic provinces and to develop an integrated genetic/exploration model. Almost all chromium deposits, including the world-class deposits in the McFaulds Lake greenstone belt (a.k.a. 'Ring of Fire'), are located in the northern part of the Superior Province, predominantly within the Meso- to Neoarchean supracrustal successions of the Bird River–Uchi–Oxford-Stull–La Grande Rivière–Eastmain domains, whereas the vast majority of the Ni-Cu-PGE deposits are located within the Wawa-Abitibi terrane. In this contribution, we present an initial compilation of chromium, Ni-Cu-PGE and Fe-Ti-V deposits hosted by ultramafic to mafic intrusions/flows in the Superior Province.

Introduction

The Archean Superior Province is well known for its endowment of numerous metals, including world-class lode gold and zinc-copper volcanogenic massive sulphides and to lesser extent for magmatic Ni-Cu-PGE, Fe-Ti-V and chromium deposits associated with mafic and ultramafic rocks. The Superior Province contains a significant proportion (approximately 12%) of the global nickel sulphide production and resources from sulphide deposits within Archean cratons worldwide (Fig. 1a; Mercier-Langevin et al., 2012), whereas no significant amounts of chromium or vanadium have been produced from the Superior craton or the rest of Canada. The bulk of chromium production in 2017 was from South Africa (primarily from the Bushveld Complex), Kazakhstan, India, Zimbabwe, Turkey, Finland and Brazil (Fig. 1b) and the bulk of vanadium production in 2016 was from China, Russia, South Africa and Brazil (Fig. 1c). Canada produces titanium, but most of the production comes from anorthositic complexes in the Grenville Province (e.g. Lac Tio and Lac Allard) and none is extracted from Archean deposits in the Superior Province as co-product (Fig. 1d).

The discovery of multi-commodity (chromium, Ni-Cu-PGE, Fe-Ti-V and zinc-copper) deposits in the Archean McFaulds Lake greenstone belt in northern Ontario (see Fig. 2), combined with the increased use of vanadium in a wider range of steel and its potential use in the energy storage market, have greatly renewed interest in orthomagmatic mineralization associated with mafic-ultramafic intrusions in the Superior Province. Importantly, potential future contribution from these magmatic ore deposits within the Superior Province could drastically change the global Canadian contribution to the overall production of many of these commodities. As an example, future chromium production from the 'Ring of Fire' (RoF) region, should position Canada as one of the five leading producers worldwide.

In this contribution, we present initial results from a compilation of chromium, Ni-Cu-PGE and Fe-Ti-V deposits in the Superior Province in order to develop an integrated model for key metallogenic provinces across the craton. This information contributes to a larger study, for which the main goals are establishing crucial parameters that control metal endowment in specific terranes, as well as resolving the potential ore environments that triggered the metal endowment.

Prospective units across the Superior Province

Spatial distribution of ultramafic to mafic intrusions

Ultramafic and mafic intrusions/flows are highly prospective units to host magmatic ore deposits and are ubiquitous throughout the Superior Province, although their abundance is extremely variable across the province. Several types of ultramafic to mafic magmatism have been identified across the craton, which can be grouped into four main types of ultramafic to mafic units: (1) ultramafic lavas and ultramafic intrusions of komatiitic affinity, (2) ultramafic-dominated intrusions, (3) mafic-dominated intrusions, and (4) differentiated ultramafic to mafic intrusions (Houlé et al., 2015).

Komatiitic ultramafic rocks are more spatially restricted across the craton than other types of ultramafic to mafic units. To date, komatiitic rocks have been recognized mainly in the Wawa-Abitibi terrane, largely in the central part, and in the Bird River, Uchi and Oxford-Stull domains of the North Caribou terrane and its eastern extensions, which include the La Grande and the Eastmain domains, collectively referred to

Corresponding author: Michel Houlé (michel.houle@canada.ca)

Houlé, M.G., Lesher, C.M., and Sappin, A.-A., 2019. Overview of chromium, Fe-Ti-V and Ni-Cu-PGE metal endowment of the Superior Province; *in* Targeted Geoscience Initiative: 2018 report of activities, (ed.) N. Rogers; Geological Survey of Canada, Open File 8549, p. 433–440. https://doi.org/10.4095/313677

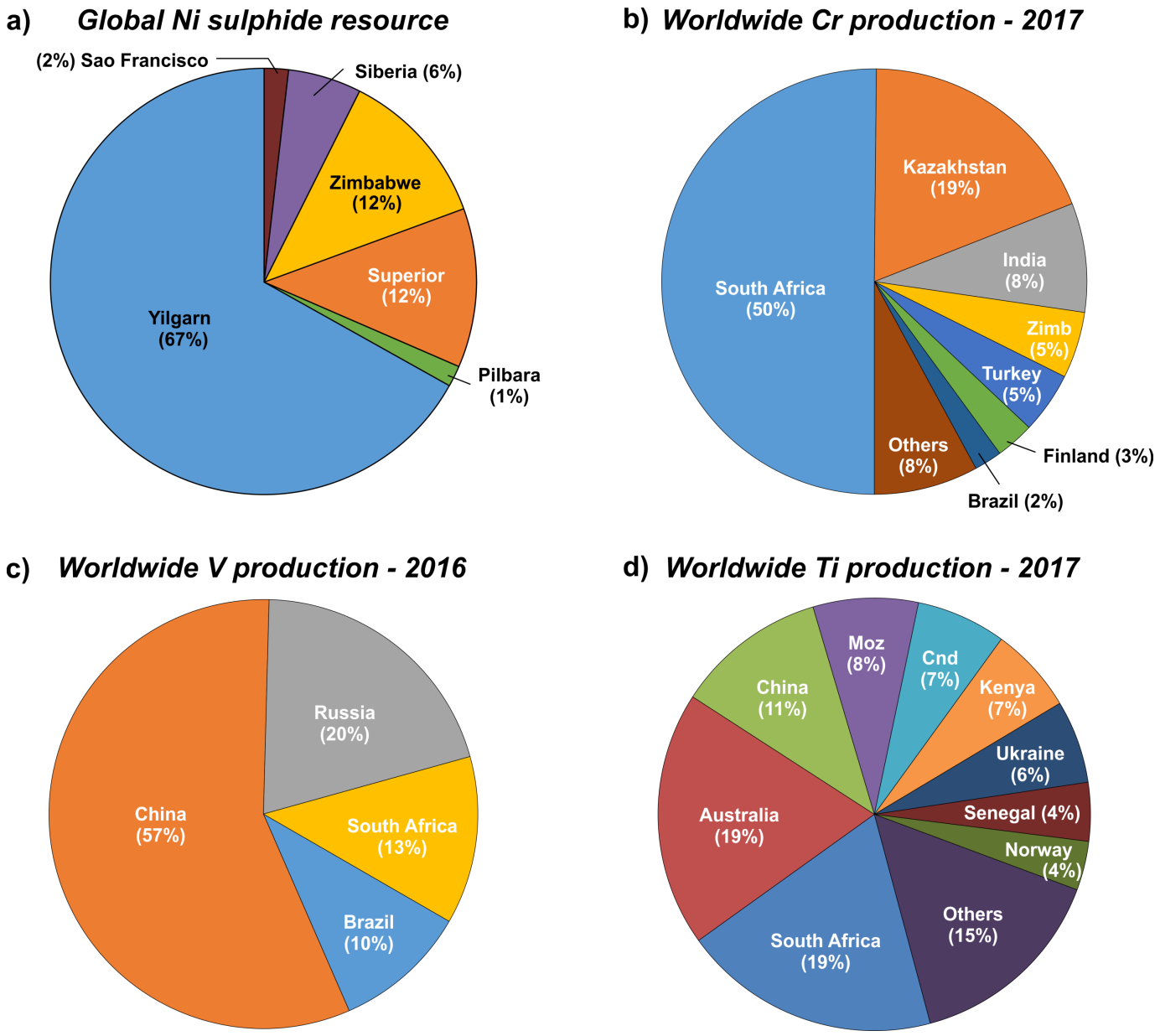

Figure 1. a) Global nickel resources in different Archean cratons, excluding lateritic deposits (Mercier-Langevin et al., 2012; *data from* Eckstrand and Hulbert, 2007). b) World chromite production in 2017. *Data from* S & P Global Inc. c) World vanadium production in 2016. *Data from* the USGS Mineral Resources Program. d) World titanium production in 2017. *Data from* the USGS Mineral Resources Program. Abbreviations: Zimb = Zimbabwe, Moz = Mozambique, Cnd = Canada.

herein as the BUOGE 'superdomain' (see Houlé et al., 2015, 2017). The highest volume of komatiitic rocks within the BUOGE superdomain occur within the western part of the Uchi domain (e.g. Wallace Lake, Garner Lake and Red Lake greenstone belts), the central part of the Oxford-Stull domain (e.g. Muskrat Dam, Caribou Lake and McFaulds Lake greenstone belts) and the central and northern part of the La Grande domain (e.g. Guyer and Venus greenstone belts). Outside these terranes, more sporadic but significant occurrence of komatiitic rocks also occur within the Western Wabigoon (e.g. Lake of the Woods greenstone belt and Grassy Portage area), within the central part of the North Caribou Core (e.g. North Spirit Lake, Favorable and Hornby greenstone belts) and also within the Goudalie domain (e.g. Duvert, Natuak and Morrice greenstone belts). The ultramafic-dominated, mafic-dominated and differentiated ultramafic to mafic intrusions are widespread across these terranes and domains and commonly coexist, but no obvious patterns have been determined.

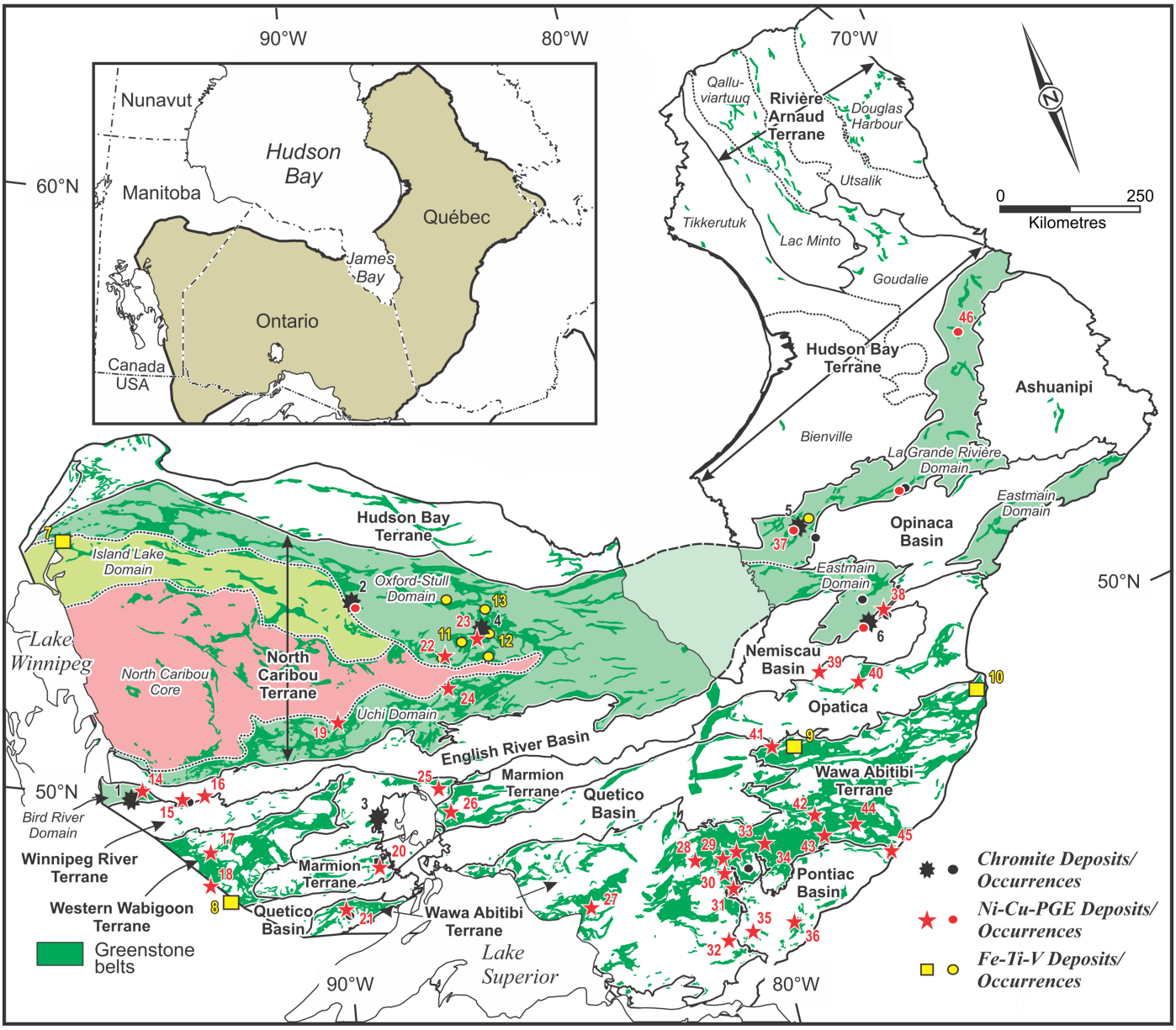

Figure 2. Schematic geological map showing the all chromium-(PGE), Ni-Cu-(PGE) and Fe-Ti-(V) deposits, main prospects and few occurrences of the Oxford–Stull, La Grande Rivière, Eastmain domains, the Bird River and Abitibi greenstone belts within the Superior Province. Terrane and domain boundaries are *modified from* Stott et al. (2010) and Percival et al. (2012).

Mineralization styles

Chromium-PGE mineralization

Fourteen chromite deposits and one prospect have been identified within the Superior Province (Fig. 2; Table 1). The vast majority of chromium deposits/prospect across the Superior Province occur within the Meso- to Neoarchean supracrustal successions of the BUOGE superdomain), which includes the deposits associated with the Bird River Sill in Manitoba (e.g. Chrome, Page, Bird Lake and Euclid) and also world-class chromite deposits of the RoF region (e.g. Blackbird 1, Blackbird 2, Black Horse, Big Daddy, Black Creek, Black Label and Black Thor). Outside this superdomain, only one other chromite deposit has been identified, occurring within the Winnipeg River terrane: the Chrome Lake deposit hosted within the Puddy-Chrome Lakes ultramafic intrusion. However, this chromite deposit is quite different from most other deposits in the Superior Province, exhibiting many similarities with podiform-type chromite deposits (e.g. Whitaker, 1986). A thick chromitite layer (up to 30 m thick) has also been observed at the

Table 1. Chromium-(PGE), Ni-Cu-(PGE) and Fe-Ti-(V) deposits and main mineral prospects in the Superior Province.

#	Deposits	Status	Intrusive Suite	Intrusive Unit		Deposit Type	Other mineral association	Terrane/domain
Chromium Mineralization								
1	**Bird River Area**							
	Chrome	Deposit	BR Suite	BR Sill	Chrome block	Stratiform Cr-PGE		WRT - BR domain
	Page	Deposit	BR Suite	BR Sill	Page block	Stratiform Cr-PGE		WRT - BR domain
	Bird Lake	Deposit	BR Suite	BR Sill	Bird Lake	Stratiform Cr-PGE		WRT - BR domain
	Euclid	Deposit	BR Suite	Euclid Lake		Stratiform Cr-PGE		WRT - BR domain
2	**Big Trout**	Deposit		Big Trout Lake		Stratiform Cr-PGE		NCT - Oxford-Stull
3	**Chrome Lake**	Deposit		Puddy-Chrome Lake		Stratiform Cr-PGE		WRT
4	**Ring of Fire' Region**							
	Blackbird 1	Deposit	RoF Suite	Double Eagle		Stratiform Cr-PGE		NCT - Oxford-Stull
	Blackbird 2	Deposit	RoF Suite	Double Eagle		Stratiform Cr-PGE		NCT - Oxford-Stull
	Black Horse	Deposit	RoF Suite	Double Eagle		Stratiform Cr-PGE		NCT - Oxford-Stull
	Big Daddy	Deposit	RoF Suite	Black Thor		Stratiform Cr-PGE		NCT - Oxford-Stull
	Black Creek	Deposit	RoF Suite	Black Thor		Stratiform Cr-PGE		NCT - Oxford-Stull
	Black Label	Deposit	RoF Suite	Black Thor		Stratiform Cr-PGE		NCT - Oxford-Stull
	Black Thor	Deposit	RoF Suite	Black Thor		Stratiform Cr-PGE		NCT - Oxford-Stull
5	**Menarik**	Deposit		Menarik		Stratiform Cr-PGE		La Grande domain
6	**Lac des Montagnes**	Prospect	Caumont	Lac des Montagnes		Stratiform Cr-PGE		Eastmain domain
	Total:	**15**						
Fe-Ti-V Mineralization								
7	**Pipestone**	Deposit		Pipestone		Fe-Ti-V		NCT - Island Lake/Oxford-Stull
8	**Seine Bay**	Deposit		Bad Vermillion		Fe-Ti-V		WWT
9	**Iron-T**	Deposit		Bell River Complex		Fe-Ti-V		WAT - Abitibi
10	**Chibougamau Area**							
	Lac Doré	Deposit		Lac Doré Complex - South		Fe-Ti-V		WAT - Abitibi
	Armitage	Deposit		Lac Doré Complex - South		Fe-Ti-V		WAT - Abitibi
	Southwest	Deposit		Lac Doré Complex - South		Fe-Ti-V		WAT - Abitibi
	Ile Portage	Deposit		Lac Doré Complex - North		Fe-Ti-V		WAT - Abitibi
	Mont Sorcier	Deposit		Lac Doré Complex - North		Fe-Ti-V		WAT - Abitibi
11	**Butler Area**							
	Butler West	Prospect	RoF Suite	Butler West		Fe-Ti-V		NCT - Oxford-Stull
	Butler East	Prospect	RoF Suite	Butler East		Fe-Ti-V		NCT - Oxford-Stull
12	**Thunderbird**	Prospect	RoF Suite	Thunderbird		Fe-Ti-V		NCT - Oxford-Stull
13	**Big Mac**	Prospect	RoF Suite	Big Mac		Fe-Ti-V		NCT - Oxford-Stull
	Total:	**12**						
Ni-Cu-PGE Mineralization								
14	**Bird River Area**							
	Ore Fault	Deposit	BR Suite	BR Sill	Page block	Ni-Cu-PGE		WRT - Bird River domain
	Maskwa	Past produce	BR Suite	BR Sill	Makwa block	Ni-Cu-PGE	Cr-PGE	WRT - Bird River domain
	Dunbarton	Past produce	BR Suite	BR Sill	Makwa block	Ni-Cu-PGE		WRT - Bird River domain
	New Manitoba	Deposit	BR Suite	Cat Lake		Ni-Cu-PGE		WRT - Bird River domain
	M2	Deposit	BR Suite	Mayville		Cu-Ni-PGE	Cr-PGE	WRT - Bird River domain
15	**Norpax**	Deposit				Ni-Cu-PGE		ERB
16	**Gordon**	Past producer				Ni-Cu-PGE		ERB
17	**Atikwa Lake Area**							
	Kenbridge	Deposit				Ni-Cu-PGE		WWT
	Apex	Deposit				Ni-Cu-PGE		WWT
18	**Nico 1**	Deposit		Dobie Intrusion		Ni-Cu-PGE		WWT
19	**Thierry**	Past producer				Ni-Cu-PGE		NCT - Uchi
20	**Lac des Iles**	Producer		Lac des Iles		Pd		Marion Terrane
21	**Shebandowan**	Past producer		Shebandowan		Ni-Cu-PGE	Cr-PGE	WAT - Shebandowan
22	**Lavoie Lake**	Deposit				Ni-Cu-PGE		NCT - Oxford-Stull
23	**Eagle's Nest**	Deposit	RoFS	Double Eagle		Ni-Cu-PGE		NCT - Oxford-Stull
24	**Norton**	Deposit				Ni-Cu-PGE		NCT - Uchi
25	**Juneau Lake Area**							
	B4-7 Deposit	Deposit				Ni-Cu-PGE		WRT
	VW Deposit	Deposit				Ni-Cu-PGE		WRT

Table 1. cont.

#	Deposits	Status	Intrusive Suite	Intrusive Unit	Deposit Type	Other mineral association	Terrane/domain
26	**Jacobus**	Deposit			Ni-Cu-PGE		Marmion Terrane
27	**Lakemount**	Deposit			Ni-Cu-PGE		WAT - Wawa
28	**Montcalm Area**						
	Montcalm	Past producer			Ni-Cu-PGE		WAT - Abitibi
	Loveland	Deposit			Ni-Cu-PGE		WAT - Abitibi
	Warran Claims	Prospect			Ni-Cu-PGE		WAT - Abitibi
29	**Shaw Dome Area**						
	Redstone	Past producer			Ni-Cu-PGE		WAT - Abitibi
	McWatters	Past producer			Ni-Cu-PGE		WAT - Abitibi
	Langmuir 1	Past producer			Ni-Cu-PGE		WAT - Abitibi
	Langmuir 2	Past producer			Ni-Cu-PGE		WAT - Abitibi
	Langmuir North	Deposit			Ni-Cu-PGE		WAT - Abitibi
	Langmuir South	Deposit			Ni-Cu-PGE		WAT - Abitibi
	Hart	Deposit			Ni-Cu-PGE		WAT - Abitibi
	W4	Deposit			Ni-Cu-PGE		WAT - Abitibi
30	**Bartlett-Halliday-Bannockburn Area**						
	Texmont	Past producer			Ni-Cu-PGE		WAT - Abitibi
	Sothman	Deposit			Ni-Cu-PGE		WAT - Abitibi
	Bannockburn	Prospect					
31	**Shining Tree**	Deposit			Ni-Cu-PGE		WAT - Abitibi
32	**Kanichee**	Past producer			Ni-Cu-PGE		WAT - Abitibi
	Temagami	Past producer			Ni-Cu-PGE		WAT - Abitibi
33	**Dundonald Area**						
	Alexo	Past producer			Ni-Cu-PGE		WAT - Abitibi
	Kelex	Past producer			Ni-Cu-PGE		WAT - Abitibi
	Dundeal	Deposit			Ni-Cu-PGE		WAT - Abitibi
	Dundonald South	Deposit			Ni-Cu-PGE		WAT - Abitibi
	Nickel Island	Deposit			Ni-Cu-PGE		WAT - Abitibi
34	**RM Nickel**	Deposit			Ni-Cu-PGE		WAT - Abitibi
35	**Lac Croche Area**						
	Alotta	Deposit			Ni-Cu-PGE		WAT - Abitibi
	Midrim	Deposit			Ni-Cu-PGE		WAT - Abitibi
36	**Lac Kelly Area**						
	Blondeau-Nickel	Deposit			Ni-Cu-PGE		WAT - Abitibi
	Lorraine	Deposit			Ni-Cu-PGE		WAT - Abitibi
	Lac Kelly	Deposit			Ni-Cu-PGE		WAT - Abitibi
	La Force	Deposit			Ni-Cu-PGE		WAT - Abitibi
37	**Menarik**	Deposit			Ni-Cu-PGE		La Grande - Yasinski
38	**Nisk**	Deposit			Ni-Cu-PGE		La Grande - Eastmain/Nemiscau
39	**Horden Lake**	Deposit			Ni-Cu-PGE		Opatica
40	**Lac Rocher**	Deposit			Ni-Cu-PGE		Opatica
41	**Grasset**	Deposit			Ni-Cu-PGE		WAT - Abitibi
42	**Dumont**	Deposit			Ni-Cu-PGE		WAT - Abitibi
43	**La Motte Area**						
	Marbridge 1	Past producer			Ni-Cu-PGE		WAT - Abitibi
	Marbridge 2	Past producer			Ni-Cu-PGE		WAT - Abitibi
	Marbridge 3	Past producer			Ni-Cu-PGE		WAT - Abitibi
	Marbridge 4	Past producer			Ni-Cu-PGE		WAT - Abitibi
	Québec Moly	Deposit			Ni-Cu-PGE		WAT - Abitibi
	Bilson-Cubric	Deposit			Ni-Cu-PGE		WAT - Abitibi
44	**Lac Tiblemont Area**						
	Vendôme	Deposit			Ni-Cu-PGE		WAT - Abitibi
	Commander-Zulapa	Deposit			Ni-Cu-PGE		WAT - Abitibi
45	**Villebon**	Deposit			Ni-Cu-PGE		WAT - Abitibi
46	**Gayot**	Prospect			Ni-Cu-PGE		La Grande - Gayot
	Total:	**46**					

Abbreviations: BR = Bird River, RoF = Ring of Fire, ERB = English River Basin, WRT = Winnipeg River Terrane, NCT = North Caribou Terrane, WWT = Western Wabigoon Terrane, WAT = Wawa-Abitibi Terrane

All deposits are mainly compiled and modified from Provincial mineral occurrences database (Mineral Inventory Card in Manitoba, Mineral Deposit Inventory in Ontario, SIGEOM in Quebec)

Shebandowan nickel-copper-PGE mine (Fig. 2; Table 1) during mining (M. Lavigne, A. Aubut and T. Hart, pers. comm., 2013 –2018), but has not been very well described. Interestingly, to the authors' knowledge, except for the RoF chromitite deposits, Shebandowan appears to be the only other location where a very thick chromitite layer has been found.

Iron-titanium-vanadium mineralization

Iron-titanium-vanadium mineralization associated with mafic and ultramafic intrusions is not uncommon across the Superior Province, but economic deposits are relatively rare. Eight Fe-Ti-V deposits and four prospects have been reported within the Superior Province (Fig. 2; Table 1). The only known examples occur at the margin of the Island Lake and the Oxford-Stull domains in Manitoba (Pipestone deposit), within the southern part of the Western Wabigoon terrane (Seine deposit within the Bad Vermillon intrusion) and in the northeastern part of the Wawa-Abitibi terrane in Québec (Iron-T deposit within the Bell River Complex near Matagami and numerous deposits within the Lac Doré Complex near Chibougamau). However, numerous prospects and occurrences of Fe-Ti-V mineralization occur across the Superior, the most important of which occur within the RoF region in northern Ontario (e.g. Butler East, Butler West, Thunderbird and Big Mac).

Ni-Cu-PGE mineralization

Magmatic Ni-Cu-PGE occurrences associated with mafic to ultramafic intrusions are ubiquitous across the entire Superior Province, but magmatic Ni-Cu-PGE deposits are not as widespread. Of the 65 Ni-Cu-PGE occurrences within the Superior Province, 20 are producers or past producers, 42 are unmined deposits and three are prospects (Fig. 2; Table 1). The Wawa-Abitibi terrane is by far the best endowed, where the vast majority of the deposits occur within the central portion of the terrane (Abitibi belt *sensu stricto*), grouped into numerous nickel districts characterized by clusters of deposits (e.g. Shaw Dome, Dundonald Township and La Motte Township). However, excluding the very large but low-grade nickel resources of the Dumont sill, the largest Ni-Cu-PGE deposit within this terrane is the past-producer Shebandowan Ni-Cu-PGE mine, which occurs as an isolated (so far) deposit in the Shebandowan greenstone belt. Another characteristic of this terrane is the presence of numerous Ni-Cu-PGE deposits around the periphery of Lake Superior that are related to the Mid-Continent Rift systems. In comparison, most of the other terranes within the Superior Province contain only sporadic and isolated Ni-Cu-PGE deposits.

Several Ni-Cu-PGE deposits also occur within sedimentary basin terrane, such as the Quetico basin (e.g. Current Lake), the English River basin (e.g. Norpax, Gordon Lake) and the Nemiscau basin (e.g. Nisk – at the margin between the Nemiscau basin and the Eastmain domain of the BUOGE superdomain). However, these are related or probably related to the Mid Continent Rift systems, to the eastern extension of the Bird River greenstone belt and to the Eastmain domain, respectively.

Discussion and next steps

The spatial distribution of magmatic chromium, Ni-Cu-PGE and Fe-Ti-V deposits throughout the Superior Province clearly shows that the Wawa-Abitibi and the BUOGE superdomain are certainly the most prospective to host these types of magmatic deposits. However, these terranes/superdomains also appear to be fundamentally different from each other in their metal endowment; the Wawa-Abitibi terrane is characterized by the presence of numerous, but small Ni-Cu-PGE deposits with a few large Fe-Ti-V deposits, whereas the BUOGE superdomain is characterized by numerous and very large chromite deposits with a few moderate to small Ni-Cu-PGE deposits and a few potentially large Fe-Ti-V deposits that are mainly prospects due to the lack of definition drilling. Many factors may be responsible for this distinctive metal endowment, but some critical features appear to be important and may represent efficient metallotects for Cr-(PGE) mineralization as proposed by Carson et al. (2015), Houlé et al. (2015) and Lesher et al. (2014) including the presence of: (1) a large magmatic event of primitive mantle-derived magmas emplaced over a short duration; (2) significant nearby crustal discontinuities that could have focused the passage of magma through the crust; and (3) favourable crustal architecture containing potential sulphur (e.g. sulphide-facies iron formation) and oxide reservoirs (e.g. oxide-facies iron formation) for generating the sulphide and chromitite within these ultramafic to mafic magmatic systems.

To advance our understanding of the metal endowment, a comprehensive, Superior craton-wide inventory of magmatic Cr-(PGE), Ni-Cu-(PGE) and Fe-Ti-V deposits associated with mafic and ultramafic intrusions (heat and metal sources), their main characteristics and country rocks (potential sulphur and oxide sources) is on-going. This database will constrain Ni-Cu-(PGE) and chromium metallotects at various scales and promote key criteria for improved exploration models. This comprehensive data set could also help provide better constraints on the genesis of these orthomagmatic deposits and indicate the likelihood of discovering additional mineral resources within the BUOGE metallogenic province and the Superior Province as a whole.

Furthermore, compiling existing and new mineral chemistry data (electron probe micro-analysis (EPMA) and laser ablation inductively coupled mass spectrometry (LA-ICP-MS)) of iron-titanium and chromium oxides for many intrusions are ongoing across the Superior Province to supplement the Superior magmatic ore deposits database. Oxide geochemistry may also be used as a petrogenetic indicator in mafic and ultramafic rocks (e.g. Irvine 1965), to discriminate between barren and mineralized komatiitic rocks (e.g. Lesher and Stone, 1996; Ames and Houlé, 2015 and references therein). Preliminary results have shown that oxide geochemistry (magnetite and chromite) could be used to define internal stratigraphy of mafic to ultramafic intrusions but also areas that could be more prospective to host orthomagmatic mineralization. For example, magnetite composition in compatible (e.g. Al, Mg, V, Ni, Cr) and incompatible

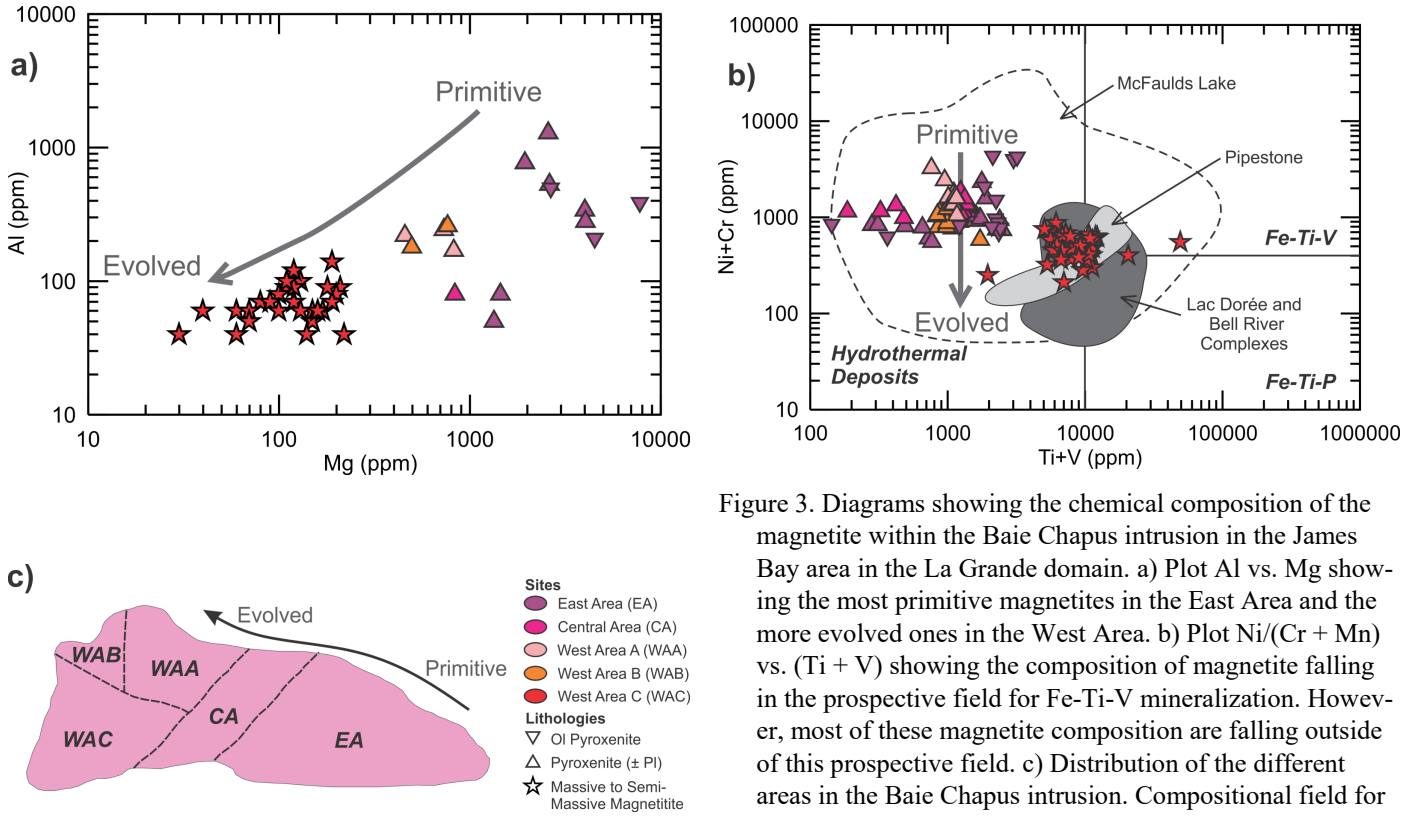

Figure 3. Diagrams showing the chemical composition of the magnetite within the Baie Chapus intrusion in the James Bay area in the La Grande domain. a) Plot Al vs. Mg showing the most primitive magnetites in the East Area and the more evolved ones in the West Area. b) Plot Ni/(Cr + Mn) vs. (Ti + V) showing the composition of magnetite falling in the prospective field for Fe-Ti-V mineralization. However, most of these magnetite composition are falling outside of this prospective field. c) Distribution of the different areas in the Baie Chapus intrusion. Compositional field for the Pipestone Deposit defined *from* Jobin-Bevans (1997); other fields defined in the course of this study.

elements (e.g. Ti, Mn, Zn) during fractionation in mafic magmas (Dare et al., 2014) shows a strong geographic-control, independently of the lithologies and the proportion of Fe-Ti oxides, that tracks efficiently the magmatic fractionation and indicates the way in several intrusions (Fig. 3), in which the geographic control and the most prospective areas are clearly shown for the Baie Chapus intrusion located in the James Bay area within the La Grande domain. In addition, high-precision age determination combined with Sm-Nd isotopic analyses of mafic to ultramafic intrusions are currently underway at the scale of the BUOGE superdomain as well as at a broader scale in order to establish their spatial and temporal distribution, magmatic affinities of the host units and to also assess the prospectivity of these intrusions. Targeted data collection (e.g. lithogeochemistry, geochronology and isotopic analyses) will continue to fill in knowledge gaps of key geological attributes of these mafic and ultramafic intrusions across the BUOGE superdomain, but also within the Superior Province.

Acknowledgments

This report is a contribution to NRCan's Targeted Geoscience Initiative Program (TGI). Support for this study was provided through the Ni-Cr-PGE Systems Project's '*Activity NC-2.2: Ni-Cr metallotect: Synthesis, updates and revised models for the Superior Province*'.

The authors are grateful to many mining exploration companies for their generous assistance, providing access to properties, permission to access diamond-drill cores and corporate geological databases over the years. Furthermore, we would like to express our appreciation to numerous federal and provincial colleagues, academic researchers and mining company geologists for discussions throughout project development and for their future involvement for the advancement of this cratonic-scale activity. Assistance of Marie-Pier Bédard was greatly appreciated for participating actively at the compilation of geological resources for these deposits/prospects. This report benefited from the review of Jean-Luc Pilote, Simon Jackson and Neil Rogers.

References

Ames, D.E. and Houlé, M.G., 2015. A synthesis of the TGI-4 Canadian nickel-copper-platinum group elements-chromium ore systems project – Revised and new genetic models and exploration tools for Ni-Cu-PGE, Cr-(PGE), Fe-Ti-V-(P), and PGE-Cu deposits; *in* Targeted Geoscience Initiative 4: Canadian Nickel-Copper-Platinum Group Elements-Chromium Ore Systems – Fertility, Pathfinders, New and Revised Models, (ed.) D.E. Ames and M.G. Houlé; Geological Survey of Canada, Open File 7856, p. 1–15.

Carson, H.J.E., Lesher, C.M., and Houlé, M.G., 2015. Geo-

chemistry and petrogenesis of the Black Thor intrusive complex and associated chromite mineralization, McFaulds Lake greenstone belt, Ontario; *in* Targeted Geoscience Initiative 4: Canadian Nickel-Copper-Platinum Group Elements-Chromium Ore Systems — Fertility, Pathfinders, New and Revised Models, (ed.) D.E. Ames and M.G. Houlé; Geological Survey of Canada, Open File 7856, p. 87–102.

Dare, S.A.S., Barnes, S.-J., Beaudoin, G., Méric, J., Emilie Boutroy, E., and Potvin-Doucet, C., 2014. Trace elements in magnetite as petrogenetic indicators; Mineralium Deposita, v. 49, p. 785–796.

Eckstrand, O.R., and Hulbert, L.J., 2007, Magmatic nickel-copper-platinum group element deposits; *in* Mineral Deposits of Canada: A Synthesis of Major Deposit Types, District Metallogeny, the Evolution of Geological Provinces, and Exploration Methods, (ed.) W.D. Goodfellow; Geological Association of Canada, Mineral Deposits Division, Special Publication No. 5, p. 205-222.

Houlé, M.G., Lesher, C.M., McNicoll, V.J., Metsaranta, R.T., Sappin, A.A., Goutier, J., Bécu, V., Gilbert, H.P., and Yang, X.M., 2015. Temporal and spatial distribution of magmatic Cr-(PGE), Ni-Cu-(PGE), and Fe-Ti-(V) deposits in the Bird River–Uchi–Oxford-Stull–La Grande Rivière–Eastmain domains: A new metallogenic province within the Superior Craton; *in* Targeted Geoscience Initiative 4: Canadian Nickel-Copper-Platinum Group Elements-Chromium Ore Systems – Fertility, Pathfinders, New and Revised Models, (ed.) D.E. Ames and M.G. Houlé; Geological Survey of Canada, Open File 7856, p. 37–48.

Houlé, M.G., Lesher, C.M., McNicoll, V.J., and Bécu, V., 2017. Ni-Cr Metallotect: Synthesis, updates, and revisted models for the Superior Province; *in* Targeted Geoscience Initiative – 2016 Report of Activities, (ed.) N. Rogers; Geological Survey of Canada, Open File 8199, p. 59–61.

Irvine, T.N., 1965. Chromian spinel as a petrogenetic indicator. Part I. Theory; Canadian Journal of Earth Sciences, v. 2, p. 648–672.

Jobin-Bevans, L.S., 1997. Geology, mineral chemistry and petrogenesis of the Pipestone Lake Anorthosite Complex; M.Sc. thesis, University of Manitoba, Winnipeg, Manitoba, 261 p.

Lesher, C.M. and Stone, W.E., 1996. Exploration geochemistry of komatiites; *in* Igneous Trace Element Geochemistry: Applications for Massive Sulphide Exploration, (ed.) D. Wyman; Geological Association of Canada, Short Course Notes 12, p. 153–204.

Lesher, C.M., Carson, H.J.E., Metsaranta, R.T., and Houlé, M.G., 2014. Genesis of chromite deposits by partial melting, physical transport, and dynamic upgrading of silicate-magnetite facies iron formation; 12th International Platinum Symposium, Yekaterinburg, Russia, Abstract Volume, p. 36–38.

Mercier-Langevin, P., Houlé, M.G., Dubé, B., Monecke, T., Hannington, M.D., Gibson, H.L., and Goutier, J., 2012. A Special Issue on Archean Magmatism, Volcanism, and Ore Deposits: Part 1. Komatiite-Associated Ni-Cu-(PGE) Sulfide and Greenstone-Hosted Au Deposits – Preface; Economic Geology, v. 107, p. 745–753.

Percival, J.A., Skulski, T., Sanborn-Barrie, M., Stott, G.M., Leclair, A.D., Corkery, M.T., and Boily, M., 2012. Geology and tectonic evolution of the Superior Province, Canada; *in* Tectonic Styles in Canada: The LITHOPROBE Perspective, (ed.) J.A. Percival, F.A. Cook and R.M. Clowes; Geological Association of Canada, Special Paper 49, p. 321–378.

Stott, G.M., Corkery, M.T., Percival, J.A., Simard, M., and Goutier, J., 2010. A revised terrane subdivision of the Superior Province; *in* Summary of Field Work and Other Activities 2010; Ontario Geological Survey, Open File Report 6260, p. 20-1–20-10.

Whittaker, P.J., 1986. Chromite deposits in Ontario; Ontario Geological Survey, Study 55, Toronto, 97 p.

Architecture of magmatic conduits in chromium-PGE and Ni-Cu-PGE ore systems in Superior Province: example from the 'Ring of Fire' region, Ontario

M.G. Houlé[1], C.M. Lesher[2], R.T. Metsaranta[3] and A.-A. Sappin[1]

[1]*Geological Survey of Canada, 490 rue de la Couronne, Québec, Quebec G1K 9A9*

[2]*Mineral Exploration Research Centre, Harquail School of Earth Sciences, Goodman School of Mines, Laurentian University, 935 Ramsey Lake Road, Sudbury, Ontario P3E 2C6*

[3]*Earth Resources and Geoscience Mapping Section, Ontario Geological Survey, 933 Ramsey Lake Road, Sudbury, Ontario P3E 6B5*

Abstract

One of the most prominent features of the McFaulds Lake greenstone belt (also known as the 'Ring of Fire'; RoF) in northern Ontario is an abundance of 2.7 to 2.8 Ga mafic to ultramafic intrusive rocks that host world-class magmatic chromium, significant magmatic Ni-Cu-PGE and potentially economically significant Fe-Ti-V mineralization. The Neoarchean intrusions in the RoF have been referred to as the Ring of Fire intrusive suite, which is here subdivided into two main magmatic subsuites: the spatially restricted ultramafic-dominated Koper Lake subsuite and the more widespread mafic-dominated Ekwan River subsuite. The Koper Lake subsuite includes the Esker intrusive complex, which comprises the Black Thor and Double Eagle intrusions that host the Black Thor, Black Label, Big Daddy, Black Creek, Black Horse and Blackbird chromite deposits and several Ni-Cu-PGE showings, the Blue Jay funnel, which hosts the Blue Jay Ni-Cu-PGE prospect, and the Eagle's Nest dyke, which hosts the Eagle's Nest Ni-Cu-PGE deposit. The Black Thor and Double Eagle intrusions are interpreted to have initially intruded separately, but to have coalesced over time with magma inflation within a dynamic komatiitic system to form the chromium and Ni-Cu-PGE -bearing Esker intrusive complex, one of the most important members of an increasingly important class of polymetallic magmatic ore systems.

Introduction

Mafic-ultramafic intrusions and ultramafic volcanic rocks are widespread throughout the Superior Province, but their association with subeconomic to economic chromium, Ni-Cu-PGE and Fe-Ti-V mineralization is not evenly distributed across the craton. Magmatic chromium and Ni-Cu-PGE deposits are both associated with ultramafic to mafic magmas, but a close association of these chromium and Ni-Cu-PGE mineralization within the same magmatic system is rare (e.g. Bird River Sill, Manitoba; Shebandowan, Ontario; and Uitkomst, South Africa) and few contain economic accumulation of both chromium and Ni-Cu-PGE. One of the most important examples of this association occurs within komatiitic ultramafic to mafic intrusions in the 'Ring of Fire' (RoF) region, which form part of the Meso- to Neoarchean McFaulds Lake greenstone belt (MLGB) in northern Ontario. The RoF region is even more unusual in that it also contains several Fe-Ti-V occurrences.

The primary goal of this research activity is to determine the architecture of known chromium and Ni-Cu-PGE mineralized komatiitic magmatic conduits in the MLGB. By resolving the geometries of the magma plumbing systems, the locations of mineralization within the systems and the dynamic conditions that led to the deposition and localization of magmatic sulphides and oxides within or proximal to the conduits, we will investigate the complete architecture (intrusive-subvolcanic-extrusive) of one mineralized mafic-ultramafic system from the magma conduits to the deposition sites (traps). Herein, we revise the lithodemic classification scheme for the best-constrained ultramafic to mafic intrusions in the RoF region and propose a preliminary emplacement model to explain the architecture of this subvolcanic magmatic plumbing system.

Ultramafic to mafic intrusions in the RoF

The abundance of mafic to ultramafic intrusive rocks is one of the most prominent features of the RoF region. The intrusions are part of the MLGB, an arcuate-shaped, Meso- to Neoarchean greenstone belt located in the central part of the Oxford-Stull domain of northern Ontario (Stott et al., 2010). The mafic-ultramafic intrusions range in age from ca. 2.81 Ga to ca. 2.73 Ga, but the metal endowments of chromium, Ni-Cu-PGE and Fe-Ti-V-(P) in the Neoarchean intrusions in the region greatly exceed those in the Mesoarchean intrusions (Fig. 1; Houlé et al., 2015).

The Neoarchean intrusions are known as the Ring of Fire intrusive suite (RoFIS) (Houlé et al., 2015; Metsaranta et al., 2015), which represents a dominantly mafic to ultramafic mag-

Corresponding author: Michel Houlé (michel.houle@canada.ca)

Houlé, M.G., Lesher, C.M., Metsaranta, R.T., and Sappin, A.-A., 2019. Architecture of magmatic conduits in chromium-PGE and Ni-Cu-PGE ore systems in Superior Province: example from the 'Ring of Fire' region, Ontario; *in* Targeted Geoscience Initiative: 2018 report of activities, (ed.) N. Rogers; Geological Survey of Canada, Open File 8549, p. 441–448. https://doi.org/10.4095/313678

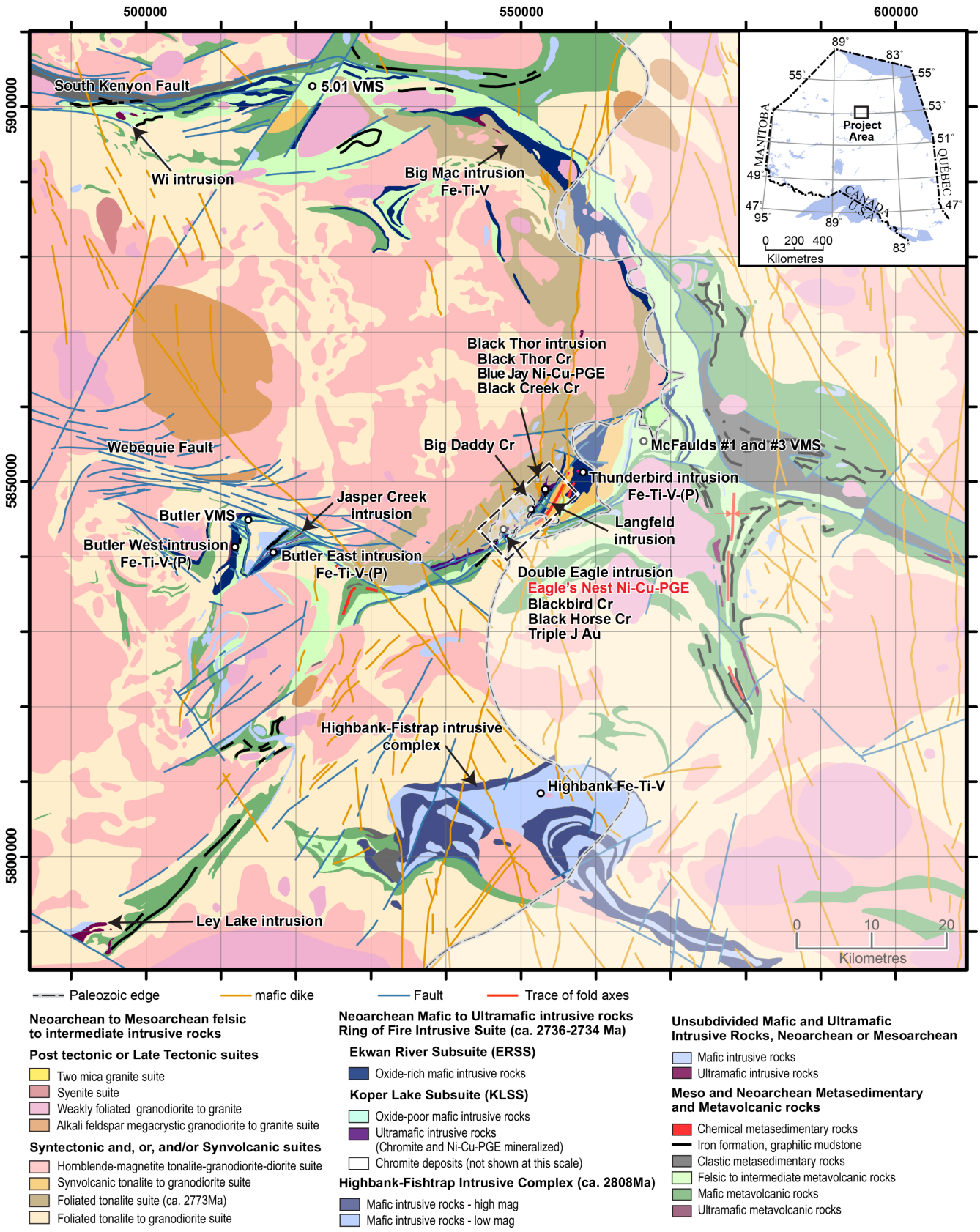

Figure 1. Simplified geological map of the McFaulds Lake greenstone belt showing the location of the main mineral deposits and occurrences in the 'Ring of Fire' region (*modified from* Metsaranta et al., 2015; Metsaranta and Houlé, 2017a–c). Paleozoic cover rocks occur to the east of the Paleozoic edge line. Dashed black box indicates the location of Figure 3.

matic event that was emplaced over the entire 175 km strike length of the MLGB in a relatively short time period of a few millions of years (ca. 2736–2732 Ma) (Fig. 1). The RoFIS is here subdivided, on the basis of their spatial distribution, lithological association, geochemical signature, and host mineralization, into the Koper Lake (KLSS) and the Ekwan River (ERSS) subsuites.

The KLSS is dominated by ultramafic rocks and is composed of variably serpentinized and/or talc carbonate-altered dunite, peridotite, chromitite, pyroxenite, and gabbro (Fig. 1). This subsuite is relatively restricted geographically, occurring predominantly in the central part of the MLGB, and it hosts most of the chromium and Ni-Cu-PGE mineralization. The best examples are the Black Thor (Carson et al., 2015, 2016) and the Double Eagle (Mungall et al., 2010; Azar, 2010) intrusions, referred to previously as the Black Thor and the Double Eagle intrusive complexes by Houlé et al. (2015, 2017).

The ERSS is dominated by mafic rocks and is composed of magnetite-bearing gabbro, layered gabbro, anorthosite, anorthositic gabbro and rare pyroxenite (Fig. 1). This subsuite occurs over the entire length of the MLGB and hosts most of the Fe-Ti-V-(P) mineralization. The best examples are the Thunderbird, Butler West and Butler East (Kuzmich, 2014; Kuzmich et al., 2015a), and Big Mac (Sappin et al., 2015) intrusions. All of these intrusions host significant accumulations of Fe-Ti-V (titanomagnetite, magnetite, ilmenite) mineralization.

Discussion

Stratigraphic and magmatic relationships

Mungall et al. (2010) suggested that the Black Thor and Double Eagle intrusions in the KLSS and the Thunderbird intrusion in the ERSS were once a single, large, layered ultramafic to mafic intrusion that was tectonically dismembered. Although these bodies have similar emplacement/crystallization ages (Houlé et al., 2015), they significantly differ in other respects: 1) the KLSS is spatially much more restricted than the ERSS (Fig. 1); 2) the ERSS does not contain any olivine-rich ultramafic rocks; 3) ERSS ferrogabbro locally crosscuts KLSS leucogabbro (Fig. 2), as well as other KLSS lithologies (evident in airborne magnetic maps); and 4) there are thin, highly deformed volcanic units between KLS/Black Thor Intrusion (BTI) leucogabbro and ERS/Langfeld ferrogabbro. Together, these observations indicate the presence of discrete ultramafic-dominated (KLSS) and mafic-dominated (ERSS) intrusions with complex contact relationships between each other, rather than a single, large, tectonically-dismembered layered ultramafic-mafic intrusion.

Other ultramafic-dominated intrusions (Wi, Ley Lake and Jasper Creek intrusions) occur in other parts the MLGB (Fig. 1). These are tentatively interpreted to be part of the KLSS, based on age (Wi intrusion) and/or lithological and geochemical similarities (Ley Lake intrusion) (Metsaranta and Houlé, work in progress, 2018). The Wi and Ley Lake intrusions are both composed predominantly of serpentinized dunite and peridotite with variable amounts of disseminated chromite with subordinate gabbroic units in their vicinity, supporting a magmatic connection with the KLSS. The Jasper Creek Ultramafic intrusion in the Butler east area is also olivine-rich and contains a significant amount of oxides, but the oxides component are predominantly magnetite and ilmenite rather than chromite and exhibit an iron-rich chemistry (Kuzmich, 2014; Kuzmich et al., 2015b), suggesting a link with ERSS rather than KLSS. However, several hypotheses could potentially explain the peculiar characteristic (iron-titanium oxides rather than chromium oxides) of the Jasper Creek intrusion: 1) it is an ultramafic component of the ERSS; 2) it belongs to a different subsuite than those already identified that exhibits an iron-rich and ultramafic chemical character; and 3) it belongs to the KLSS but

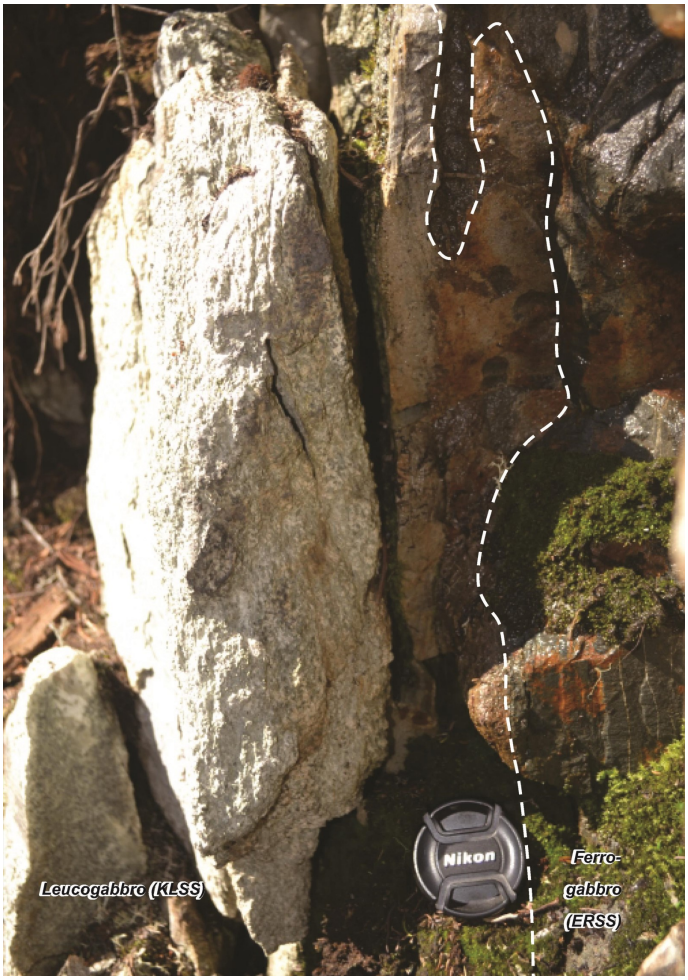

Figure 2. Field photograph showing iron- and titanium-enriched gabbroic dyke of the Ekwan River subsuite (ERSS) (on the right) cutting leucogabbro (on the left) of the upper part of the Black Thor intrusion that belongs to the Koper Lake subsuite (KLSS). The white dashed line highlights the sharp intrusive contact between the gabbroic rocks of the KLSS and the ERSS. Lens cap is 6 cm in diameter .

has assimilated magnetite-ilmenite rich layers from the Butler east intrusion (ERSS). More work is required to determine which of these hypotheses is correct. Currently, the third option appears to be most likely as ultramafic rocks in the Butler east area crosscut a magnetite-rich horizon of the Butler East intrusion (e.g. Kuzmich 2014) and Lesher et al. (2019) have shown that assimilation of ferrogabbro will produce a magnetite-ilmenite assemblage rather than chromite at the low magma/oxide ratios likely to have prevailed in this intrusion.

Classification scheme

The presence of numerous ultramafic to mafic intrusions in the RoF region leads us to propose a lithodemic classification scheme for the RoF region (Table 1) that combines aspects of the North American Stratigraphic Code (North American Commission on Stratigraphic Nomenclature, 2005; Easton et al., 2016) with the scheme developed by the British Geological Survey (Gillespie et al., 2008). This classification may still evolve based on the ongoing research conducted in the area, but it lays a foundation for grouping the various intrusions based on their field, petrographic and geochemical signatures, which will help determine the metallogenic prospectivity of these intrusions.

The scheme proposed here is similar to that proposed by Houlé et al. (2015), but names have been assigned to the ultramafic-dominated (KLSS) and mafic-dominated (ERSS) subsuites. Further, the name Esker intrusive complex (EIC) has been introduced, and the Black Thor and the Double Eagle complexes have been reclassified as intrusions that collectively comprise the EIC (Fig. 3). Because they appear to be cogenetic (but each with discrete feeders), we classify them here as being part of the EIC, along with the Eagle's Nest dyke (END) (Mungall et al., 2010; Zuccarrelli et al., 2018). The late websterite units described by Spath et al. (2015) in the BTI and by Zuccarelli et al. (2018) in the END, respectively, are assigned to the level of 'phase'. This will also permit subdivision of any additionally recognized intrusions within this system.

Magmatic Architecture of the EIC

Understanding the architecture of volcanic and intrusive plumbing systems is critically important in determining where chromite and Ni-Cu-PGE sulphides might be located within these mafic to ultramafic ore systems. However, establishing the architecture of the magmatic plumbing system is challenging, especially in a deformed and metamorphosed Archean greenstone belt like the MLGB.

Development of a 3D geological model has been undertaken in order to better understand the subsurface architecture and structural disposition of the DEI and the BTI (Laudadio et al., 2018a, b). Results from this 3D modelling study agree with the previous 2D geological interpretation of Metsaranta and Houlé (2017a) and support the linkage between the BTI and the DEI intrusions and their assignment to a single intrusive complex (A.B. Laudadio, pers. comm, 2018; Laudadio et al., 2018b), referred to here as the EIC (Table 1). The absolute timing and mode of emplacement of all phases of the EIC are not unequivocally determined, but based on geological relationships and age data at the BTI from Metsaranta and Houlé (2017b), we propose that the EIC resulted from the amalgamation of multiple ultramafic-(mafic) intrusions, and that the Thunderbird intrusion and other ERSS intrusions represent distinct, but broadly contemporaneous mafic intrusions emplaced into different locations and stratigraphic positions within the MLGB and tonalitic basement that existed at the time.

The EIC consists of semi-continuous, sill-like ultramafic-(mafic) complex that, after accounting for an apparent 90° south-southeast rotation, is underlain by several keel-like funnels and bladed dykes. This geometry has been interpreted to reflect a single, connected ultramafic complex (EIC), which was dissected and displaced with an apparent dextral sense of shear (A.B. Laudadio, pers. comm, 2018; Laudadio et al., 2018b).

The keels/dykes trend roughly northeast and southwest and include the END (host to the Eagle's Nest Ni-Cu-PGE deposit)

Table 1. Proposed lithodemic unit classification scheme for mafic-ultramafic intrusive rocks in the Ring of Fire intrusive suite.

Suite	Subsuite	Complex	Intrusion (Lithodeme)	Phase
Ring of Fire intrusive suite (RoFIS)	Koper Lake subsuite (KLSS)	Esker intrusive complex (EIC)	Black Thor intrusion (BTI)	Late websteritic phase
				Main phase
			Double Eagle intrusion (DEI)	Main phase
			Eagle's Nest dyke (END)	Late websteritic phase
				Main phase
			Wi intrusion (WII)	
			Ley Lake intrusion (LLI)	
			Jasper Creek intrusion (JCI)	
	Ekwan River subsuite (ERSS)		Butler West intrusion (BWI)	
			Butler East intrusion (BEI)	
			Thunderbird intrusion (TBI)	
			Big Mac intrusion (BMI)	
			Langfeld intrusion (LFI)	

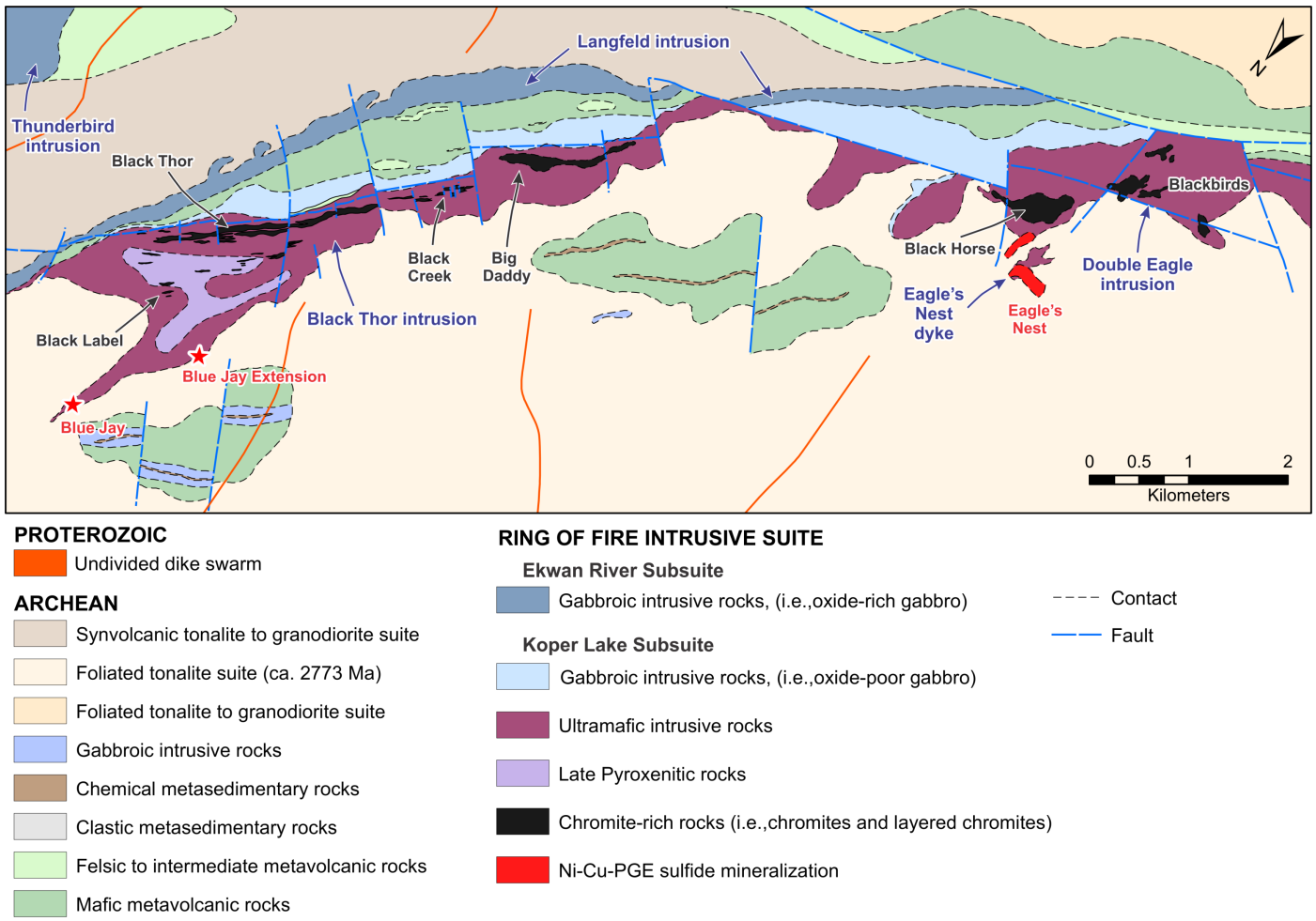

Figure 3. Geological map of the Esker intrusive complex, showing the location of the main mineral deposits in the 'Ring of Fire' region (*modified after* Houlé et al., 2017). The Eagle's Nest deposit occurs within the feeder system of the Double Eagle intrusive complex. Text in dark blue: intrusion names, in black: chromite deposits, and in red: Ni-Cu-PGE deposit/occurrences.

and the East dyke, AT-5, and Lobe 3 keels, which occur stratigraphically below the Double Eagle intrusion, and the AT-12 "keel" (host to the Blue Jay Ni-Cu-PGE prospect), which occurs stratigraphically below the Black Thor intrusion (Mungall et al., 2010, Metsaranta and Houlé, 2017a; Houlé et al., 2017). The area is transgressed by several strike-slip faults with offsets between 2.5km (Laudadio et al., 2018b); however, the irregular basal contacts of the EIC and clear interaction shown by on hornfelsed contact and sulphide veinlets within the granodioritic-tonalitic footwall rocks suggest that most or all of these keels are primary features.

The EIC comprises at least three distinct co-magmatic intrusions (BTI, DEI and END) (Fig. 4a). Long-term magma flux and crystallization/accumulation through these originally smaller, dynamic, komatiitic intrusions/conduits coalesced over time through magma inflation to form the EIC. The resulting composite architecture appears to preserve the elongate sill/chonolith geometry represented by the BTI and a funnel-tube-shaped intrusion geometry represented by the DEI, which are flanked by feeder funnels (Blue Jay funnel) and bladed dykes (Eagle's Nest), respectively (Fig. 4b). The exact mechanism of how the EIC formed remains unconstrained, but it may have started out as a bladed dyke that subsequently propagated laterally along a favourable horizon causing the dyke to transition into a funnel-tube intrusion and subsequently an elongate sill/chonolith similar to that proposed by Schofield et al. (2012), Magee et al. (2016) and Barnes and Mungall (2018).

Acknowledgments

This report is a contribution to NRCan's Targeted Geoscience Initiative Program (TGI). Support for this study was provided through the Ni-Cr-PGE Systems Project's '*Activity NC-2.1: Architecture of magmatic conduits in Cr-(PGE)/Ni-Cu-(PGE) ore systems*'.

We are grateful to Noront Resources Ltd., Cliffs Natural

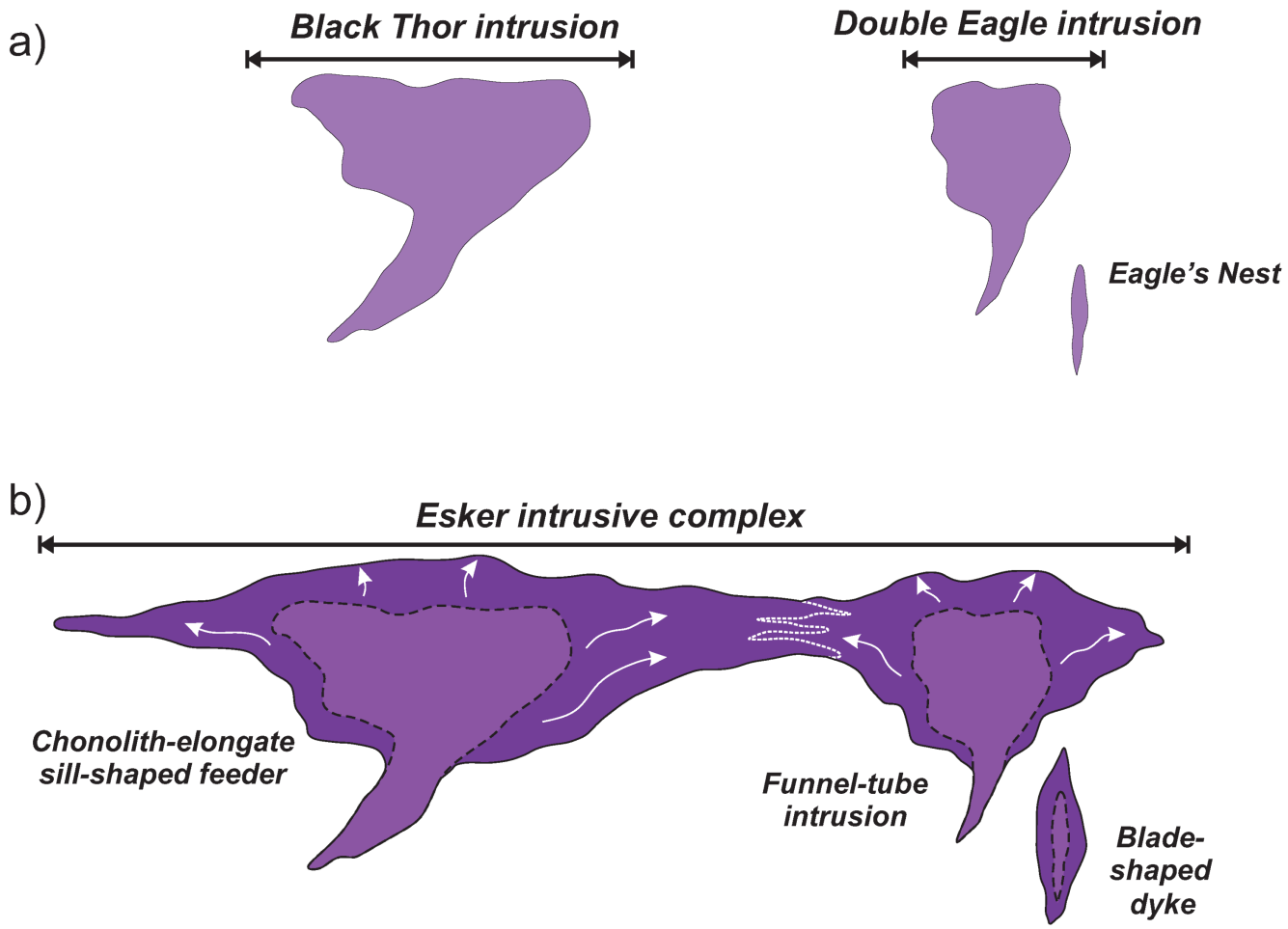

Figure 4. Schematic reconstruction (not to scale) of the evolution of the Esker intrusive complex (EIC). a) Initial emplacement of the Black Thor (BTI) and Double Eagle (DEI) intrusions. Light purple represents the initial komatiitic magmas emplaced respectively within the BTI and DEI. b) Continuation of magma flux through each system produced inflation of these intrusions and eventually they coalesced to form the EIC. Dark purple represents the full extent of the BTI and the DEI to form the EIC after lateral and vertical inflation from initial magma bodies. Medium purple represents the trace of the initial magma bodies emplaced in (a). White arrows indicate the displacement of magma throughout inflation processes that affected the EIC. White dashed line indicates the located of the coalescence of the BTI and the EIC. Not shown on the diagram but subsequently, the Frank Shear Zone faulted the EIC. Note the late websteritic phase has been left out from the schematic reconstruction for simplicity.

Resources/Freewest Resources, KWG Resources Inc., MacDonald Mines Ltd., Fancamp Exploration Ltd., Bold Ventures Inc., Probes Mines, UC Resources and Canterra Minerals for their generous assistance, providing access to properties, permission to access diamond-drill cores and corporate geological databases over the years. We also greatly appreciated the involvement and participation of numerous researchers and students (Heather Carson, Naghmeh Farhangi, Pete Hollings, Ben Kuzmich, Jordan Laarman, Alexandra Laudadio, Kaveh Merhmanesh, Jim Mungall, Claire Samson, Ernst Schetselaar, C.J. Spath and Natascia Zuccarelli) from the Ring of Fire Targeted Geoscience Initiative research group that have facilitated advances in our understanding of the RoF geology. Furthermore, we express our appreciation to numerous academic researchers and mining company geologists for geological discussions over the years, but especially geologists of Noront Resources (Ryan Weston, Matt Downey, Stephen Flewelling, Matt Deller, and Geoff Heggie) and KWG Resources (Moe Lavigne). This report benefited from the review of Jan Peter and Neil Rogers.

References

Azar, B., 2010. The Blackbird chromite deposit, James Bay Lowlands of Ontario, Canada: Implications for chromitite genesis in ultramafic conduits and open magmatic systems; M.Sc. thesis, University of Toronto, Toronto, Ontario, 154 p.

Barnes, S.J. and Mungall, J.E., 2018. Blade-shaped dikes and

nickel sulfide deposits: A model for the emplacement of ore -bearing small intrusions; Economic Geology, v. 113, p. 789–798.

Carson, H.J.E., Lesher, C.M., and Houlé, M.G., 2015. Geochemistry and petrogenesis of the Black Thor intrusive complex and associated chromite mineralization, McFaulds Lake greenstone belt, Ontario; *in* Targeted Geoscience Initiative 4: Canadian Nickel-Copper-Platinum Group Elements-Chromium Ore Systems — Fertility, Pathfinders, New and Revised Models, (ed.) D.E. Ames and M.G. Houlé; Geological Survey of Canada, Open File 7856, p. 87–102.

Carson, H.J.E., Lesher, C.M., and Houlé, M.G., 2016. Oxide chemostratigraphy of the Black Thor Chromitite Zone, Black Thor Intrusive Complex, McFaulds Lake, Canada; *in* Abstracts 13th International Ni-Cu-PGE Symposium, Fremantle, Australia, (ed.) B. Godel, S. Barnes, I. Gonzales–Alvarez, M. Fiorentini and M. Le Vaillant; Geological Survey of Western Australia, Record 2016/13, p. 19.

Easton, R.M., Edwards, L.E., Orndorff, R.C., Duguet, M., and Ferrusquía-Villafranca, I., 2016. North American Commission on Stratigraphic Nomenclature Report 12 – Revision of Article 37, Lithodemic units, of the North American Stratigraphic Code; Stratigraphy, v. 13, p. 220–222.

Gillespie, D., Stephenson, D., and Millward, D., 2008. BGS classification of lithodemic units: proposals for classifying units of intrusive rocks; British Geological Survey Research Report RR/08/05, 31 p.

Houlé, M.G., Lesher, C.M., McNicoll, V.J., Metsaranta, R.T., Sappin, A.A., Goutier, J., Bécu, V., Gilbert, H.P., and Yang, X.M., 2015. Temporal and spatial distribution of magmatic Cr-(PGE), Ni-Cu-(PGE), and Fe-Ti-(V) deposits in the Bird River–Uchi–Oxford-Stull–La Grande Rivière–Eastmain domains: A new metallogenic province within the Superior Craton; *in* Targeted Geoscience Initiative 4: Canadian Nickel-Copper-Platinum Group Elements-Chromium Ore Systems – Fertility, Pathfinders, New and Revised Models, (ed.) D.E. Ames and M.G. Houlé; Geological Survey of Canada, Open File 7856, p. 37–48.

Houlé, M.G., Lesher, C.M., McNicoll, V.J., and Bécu, V., 2017. Ni-Cr Metallotect: Synthesis, updates, and revisted models for the Superior Province; *in* Targeted Geoscience Initiative – 2016 Report of Activities, (ed.) N. Rogers; Geological Survey of Canada, Open File 8199, p. 59–61.

Kuzmich, B. 2014. Petrogenesis of the ferrogabbroic intrusions and associated Fe-Ti-V-P mineralization within the McFaulds Lake greenstone belt, Superior Province, northern Ontario, Canada; M.Sc. thesis, Lakehead University, Thunder Bay, Ontario, 486 p.

Kuzmich, B., Hollings, P., and Houlé, M.G., 2015a. Petrogenesis of the ferrogabbroic intrusions and associated Fe-Ti-V-(P) mineralization within the McFaulds greenstone belt, Superior Province, northern Ontario; *in* Targeted Geoscience Initiative 4: Canadian Nickel-Copper-Platinum Group Elements-Chromium Ore Systems — Fertility, Pathfinders, New and Revised Models, (ed.) D.E. Ames and M.G. Houlé; Geological Survey of Canada, Open File 7856, p. 115–123.

Kuzmich, B., Hollings, P. and Houlé, M.G. 2015b. Lithogeochemistry of iron-titanium-vanadium-phosphorus mineralized mafic intrusions in the McFaulds Lake area, northern Ontario; Ontario Geological Survey, Miscellaneous Release—Data 318.

Laudadio, A.B., Schetselaar, E., Houlé, M.G, and Samson, C., 2018a. 3D geological modelling of the Double Eagle – Black Thor intrusive complexes, McFaulds Lake greenstone belt, Ontario; *in* Targeted Geoscience Initiative: 2017 report of activities, volume 2, (ed.) N. Rogers; Geological Survey of Canada, Open File 8373, p. 35–41.

Laudadio, A.B., Schetselaar, E., and Houlé, M.G., 2018b. 3D Geological modelling of the Double Eagle - Black Thor Intrusive Complexes, McFaulds Lake greenstone belt, Ontario, Canada; Geological Survey of Canada, Scientific Presentation 82, 1 poster.

Lesher, C.M., Carson, H.J.E, and Houlé, M.G., 2019. Genesis of chromite deposits by dynamic upgrading of Fe±Ti oxide xenocrysts; Geology.

Magee, C., Muirhead, J.D., Karvelas, A., Holford, S.P., Jackson, C.A.L., Bastow, I.D., Schofield, N.J., Stevenson, C.T.E., McLean, C., McCarthy, W., and Shtukert, O., 2016. Lateral magma flow in mafic sill complexes; Geosphere, v. 12, p. 809–841.

Metsaranta, R.T. and Houlé, M.G., 2017a. Precambrian Geology Winiskisis Channel area, "Ring of Fire Region", north sheet; Ontario Geological Survey, Preliminary Map P.3804; Geological Survey of Canada, Open File 8200, scale 1:100 000.

Metsaranta, R.T. and Houlé, M.G., 2017b. Precambrian Geology of the McFaulds Lake area, "Ring of Fire Region" - Central Sheet; Ontario Geological Survey, Preliminary Map P.3805; Geological Survey of Canada, Open File 8201, scale 1:100 000.

Metsaranta, R.T. and Houlé, M.G., 2017c. Precambrian Geology of the Highbank Lake Area - "Ring of Fire Region", Southern sheet; Ontario Geological Survey, Preliminary Map P.3806; Geological Survey of Canada, Open File 8202, scale 1:100 000.

Metsaranta, R.T., Houlé, M.G., McNicoll, V.J., and Kamo, S.L., 2015. Revised geological framework for the McFaulds Lake greenstone belt, Ontario; *in* Targeted Geoscience Initiative 4: Canadian Nickel-Copper-Platinum Group Elements-Chromium Ore Systems — Fertility, Pathfinders, New and Revised Models, (ed.) D.E. Ames and M.G. Houlé; Geological Survey of Canada, Open File 7856, p. 61–73.

Mungall, J.E., Harvey, J.D., Balch, S.J., Azar, B., Atkinson, J., and Hamilton, M.A., 2010. Eagle's Nest: A magmatic Ni-sulfide deposit in the James Bay Lowlands, Ontario, Canada; *in* The Challenge of Finding New Mineral Resources: Global Metallogeny, Innovative Exploration, and New Dis-

coveries, Volume I: Gold, Silver, and Copper-Molybdenum, (ed.) R.J. Goldfarb, E.E. Marsh and T. Monecke; Society of Economic Geologists, Special Publication 15, p. 539–559.

North American Commission on Stratigraphic Nomenclature, 2005. North American Stratigraphic Code, 2005; American Association of Petroleum Geologists Bulletin, v.89, p. 1547–1591.

Sappin, A.-A., Houlé, M.G., Lesher, C.M., Metsaranta, R.T., and McNicoll, V.J., 2015. Regional characterization of mafic -ultramafic intrusions in the Oxford-Stull and Uchi domains, Superior Province, Ontario; *in* Targeted Geoscience Initiative 4: Canadian Nickel-Copper-Platinum Group Elements-Chromium Ore Systems — Fertility, Pathfinders, New and Revised Models, (ed.) D.E. Ames and M.G. Houlé; Geological Survey of Canada, Open File 7856, p. 75–85.

Schofield, N.J., Brown, D.J., Magee, C., and Stevenson, C.T.E., 2012. Sill morphology and comparison of brittle and non-brittle emplacement mechanisms; Journal of the Geological Society, London, v. 169, p. 127–141.

Spath, C.S., III, Lesher, C.M., and Houlé, M.G., 2015. Hybridized ultramafic rocks in the Black Label hybrid zone of the Black Thor intrusive complex, McFaulds Lake greenstone belt, Ontario; *in* Targeted Geoscience Initiative 4: Canadian Nickel-Copper-Platinum Group Elements-Chromium Ore Systems — Fertility, Pathfinders, New and Revised Models, (ed.) D.E. Ames and M.G. Houlé; Geological Survey of Canada, Open File 7856, p. 103–114.

Stott, G.M., Corkery, M.T., Percival, J.A., Simard, M., and Goutier, J., 2010. A revised terrane subdivision of the Superior Province; *in* Summary of Field Work and Other Activities 2010; Ontario Geological Survey, Open File Report 6260, p. 20-1–20-10.

Zuccarelli, N., Lesher, C.M., and Houlé, M.G., 2018. Sulphide textural variations and multiphase ore emplacement in the Eagle's Nest Ni-Cu-(PGE) deposit, McFaulds Lake greenstone belt, Ontario; *in* Targeted Geoscience Initiative: 2017 report of activities, volume 2, (ed.) N. Rogers; Geological Survey of Canada, Open File 8373, p. 29–34.